

NASA/CP-2014-217519



# 42<sup>nd</sup> Aerospace Mechanism Symposium

*Edward A. Boesiger and Claef Hakun, Editors*



Proceedings of a symposium held at  
Hyatt Regency, Baltimore, MD  
Hosted by NASA's Goddard Space Flight Center and  
Lockheed Martin Space Systems Company  
Organized by the Mechanisms Education Association

**May 14–16, 2014**

National Aeronautics and  
Space Administration

**Goddard Space Flight Center  
Greenbelt, Maryland 20771**

---

**MAY 2014**

## NASA STI Program ... in Profile

Since its founding, NASA has been dedicated to the advancement of aeronautics and space science. The NASA scientific and technical information (STI) program plays a key part in helping NASA maintain this important role.

The NASA STI program operates under the auspices of the Agency Chief Information Officer. It collects, organizes, provides for archiving, and disseminates NASA's STI. The NASA STI program provides access to the NASA Aeronautics and Space Database and its public interface, the NASA Technical Report Server, thus providing one of the largest collections of aeronautical and space science STI in the world. Results are published in both non-NASA channels and by NASA in the NASA STI Report Series, which includes the following report types:

- **TECHNICAL PUBLICATION.** Reports of completed research or a major significant phase of research that present the results of NASA Programs and include extensive data or theoretical analysis. Includes compilations of significant scientific and technical data and information deemed to be of continuing reference value. NASA counterpart of peer-reviewed formal professional papers but has less stringent limitations on manuscript length and extent of graphic presentations.
- **TECHNICAL MEMORANDUM.** Scientific and technical findings that are preliminary or of specialized interest, e.g., quick release reports, working papers, and bibliographies that contain minimal annotation. Does not contain extensive analysis.
- **CONTRACTOR REPORT.** Scientific and technical findings by NASA-sponsored contractors and grantees.

**CONFERENCE PUBLICATION.** Collected papers from scientific and technical conferences, symposia, seminars, or other meetings sponsored or co-sponsored by NASA.

- **SPECIAL PUBLICATION.** Scientific, technical, or historical information from NASA programs, projects, and missions, often concerned with subjects having substantial public interest.
- **TECHNICAL TRANSLATION.** English-language translations of foreign scientific and technical material pertinent to NASA's mission.

Specialized services also include organizing and publishing research results, distributing specialized research announcements and feeds, providing help desk and personal search support, and enabling data exchange services. For more information about the NASA STI program, see the following:

- Access the NASA STI program home page at <http://www.sti.nasa.gov>
- E-mail your question via the Internet to [help@sti.nasa.gov](mailto:help@sti.nasa.gov)
- Fax your question to the NASA STI Help Desk at 443-757-5803
- Phone the NASA STI Help Desk at 443-757-5802
- Write to:

NASA STI Help Desk  
NASA Center for AeroSpace Information  
7115 Standard Drive  
Hanover, MD 21076-1320

---



NASA/CP-2014-217519



# 42<sup>nd</sup> Aerospace Mechanism Symposium

*Edward A. Boesiger*  
*Mechanisms Education Association and*  
*Lockheed Martin Space Systems Company, Sunnyvale, CA*

*Clæf Hakun*  
*Goddard Space Flight Center, Greenbelt, MD*

Proceedings of a symposium held at  
Hyatt Regency, Baltimore, MD  
Hosted by NASA's Goddard Space Flight Center and  
Lockheed Martin Space Systems Company  
Organized by the Mechanisms Education Association

**May 14–16, 2014**

National Aeronautics and  
Space Administration

**Goddard Space Flight Center**  
**Greenbelt, Maryland 20771**

---

**May 2014**

This NASA conference publication contains both U.S. Government works and non-government works. NASA has been granted permission to publish and disseminate non-government works contained herein with all other rights presumably retained by the authors and/or copyright owners. For U.S. Government works, no copyright is claimed in the United States under Title 17, U.S. Code. All Other Rights Reserved.

Trade names and trademarks are used in this report for identification only. Their usage does not constitute an official endorsement, either expressed or implied, by the National Aeronautics and Space Administration.

*Level of Review: This material has been technically reviewed by technical management and professionally reviewed by NASA's Goddard Space Flight Center.*

---

Available from:  
NASA Center for AeroSpace Information  
7115 Standard Drive  
Hanover, MD 21076-1320

National Technical Information Service  
5285 Port Royal Road  
Springfield, VA 22161 Price Code: A17

---

## PREFACE

The Aerospace Mechanisms Symposium (AMS) provides a unique forum for those active in the design, production and use of aerospace mechanisms. A major focus is the reporting of problems and solutions associated with the development and flight certification of new mechanisms. Organized by the Mechanisms Education Association, responsibility for hosting the AMS is shared by the National Aeronautics and Space Administration and Lockheed Martin Space Systems Company (LMSSC). Now in its 42<sup>nd</sup> symposium, the AMS continues to be well attended, attracting participants from both the U.S. and abroad.

The 42<sup>nd</sup> AMS, hosted by the NASA Goddard Space Flight Center (GSFC) in Baltimore, Maryland, was held May 14, 15 and 16, 2014. During these three days, 43 papers were presented. Topics included payload and positioning mechanisms, components such as hinges and motors, CubeSats, tribology, and mechanism testing. Hardware displays during the supplier exhibit gave attendees an opportunity to meet with developers of current and future mechanism components.

The high quality of this symposium is a result of the work of many people, and their efforts are gratefully acknowledged. This extends to the voluntary members of the symposium organizing committee representing the eight NASA field centers, LMSSC, and the European Space Agency. Appreciation is also extended to the session chairs, the authors, and particularly the personnel at GSFC responsible for the symposium arrangements and the publication of these proceedings. A sincere thank you also goes to the symposium executive committee who is responsible for the year-to-year management of the AMS, including paper processing and preparation of the program.

The use of trade names of manufacturers in this publication does not constitute an official endorsement of such products or manufacturers, either expressed or implied, by the National Aeronautics and Space Administration.



## CONTENTS

Symposium Schedule .....	viii
Symposium Organizing and Advisory Committees.....	xii
An Innovative Aperture Cover Mechanism used on SDO/EVE and MMS/SDP.....1 Stephen Steg, William Vermeer, Scott Tucker & Heather Passe	
Metering Wheel-Wire Track Wire Boom Deployment Mechanism.....11 Mark Granoff	
Development of Cryogenic Filterwheels for the HERSCHEL Photodetector Array Camera & Spectrometer (PACS).....19 Christian Körner, Dirk Kampf, Albrecht Poglitsch, Josef Schubert, U. Ruppert & M. Schoele	
Development and Preliminary Testing of a High Precision Long Stroke Slit Change Mechanism for the SPICE Instrument .....	31
Gabriel Paciotti, Martin Humphries, Fabrice Rottmeier & Luc Blecha	
High Gain Antenna System Deployment Mechanism Integration, Characterization, and Lessons Learned .....	45
Fil Parlong, Blair Russell, Walter Garcen, Chris Rose, Chris Johnson & Craig Huber	
In-Orbit Performance of the MWRI Scanning Mechanisms .....	59
Manfred Schmid, Miao Jun & Yu Shuang	
Launch Load Resistant Spacecraft Mechanism Bearings Made From NiTi Superelastic Intermetallic Materials .....	73
Christopher DellaCorte & Lewis E. Moore III	
Reducing Wear of Steel Rolling Against Ti6Al4V Operating in Vacuum .....	87
Timothy Krantz	
Wear Potential due to Low EHD Films during elevated Temperatures .....	103
Alan Leveille & Peter Ward	
Observations of Spacecraft Bearing Lubricant Redistribution Based on Thermal Conductance Measurements .....	113
Yoshimi Takeuchi, Peter Frantz & Michael Hilton	
A Study on the Effects of Ball Defects on the Fatigue Life in Hybrid Bearings.....129 Ching-Yao Tang, Chad Foerster, Michael O'Brien, Brian Hardy, Vinay Goyal, Benjamin Nelson, Ernest Robinson, Peter Ward & Michael Hilton	
Design and Test of a Deployable Radiation Cover for the REolith X-ray Imaging Spectrometer .....	145
David Carte, Niraj Inamdar, Michael Jones & Rebecca Masterson	
The Development, Build and Environmental Testing of a Bi-Axis Solar Array Drive Mechanism.....	153
Noemy Scheidegger, Mark Ferris & Nigel Phillips	
Advances in Current Rating Techniques for Flexible Printed Circuits .....	161
Ron Hayes	

Design of 3D-Printed Titanium Compliant Mechanisms .....	169
Ezekial Merriam, Jonathan Jones & Larry Howell	
Magnetic Gearing versus Conventional Gearing in Actuators for Aerospace Applications .....	175
Gregor Puchhammer	
Flight Testing of a Low Cost De-orbiting Device for Small Satellites .....	183
Dana Turse, Phil Keller, Robert Taylor, Mark Reavis, Mike Tupper & Chris Koehler	
Deployment Methods for an Origami-Inspired Rigid-Foldable Array .....	189
Shannon Zirbel, Brian Trease, Spencer Magleby & Larry Howell	
ROPEC – ROTary PERcussive Coring Drill for Mars Sample Return.....	195
Philip Chu, Justin Spring & Kris Zacny	
Aperture Valve for the Mars Organic Molecule Analyzer (MOMA) .....	211
Charles Engler & John Canham	
Development of the RANCOR Rotary-Percussive Coring System for Mars Sample Return .....	217
Gabe Paulsen, Stephen Indyk & Kris Zacny	
Torque Tension Testing of Fasteners used for NASA Flight Hardware Applications. ....	231
Ed Hemminger, Alan Posey & Michael Dube	
Ultrasonic Method for Deployment Mechanism Bolt Element Preload Verification .....	245
Eric Johnson, Yong Kim, Fred Morris, Joel Mitchell & Robert Pan	
LARES Mission: Separation and Retention Subsystem .....	259
Alessandro Bursi, Pierluigi Camilli, Claudio Piredda, Gianni Babini & Elio Mangraviti	
Testing Orion's Fairing Separation System .....	273
Henry Martinez, Chris Cloutier, Heber Lemmon, Daniel Rakes, Joe Oldham & Keith Schlagel	
Design and Lessons Learned on the Development of a Pupil Select Mechanism to be used in the Testing and Calibration of the Integrated Science Instrument Module (ISIM) on the James Webb Space Telescope (JWST) .....	287
Alissa Mitchell, Thomas Capon, Jeffrey Guzek, Claef Hakun, Paul Haney & Corina Koca	
GMI Instrument Spin Balance Method, Optimization, Calibration and Test.....	303
Laoucet Ayari, Michael Kubitschek, Gunnar Ashton, Steve Johnston, Dave Debevec, David Newell & Joseph Pellicciotti	
The European Robotic Arm: A High-Performance Mechanism Finally on its Way to Space .....	319
Henk Cruijssen, Marcel Ellenbroek, M. Henderson, H. Petersen, P. Verzijden & M. Visser	
GPM Solar Array Gravity Negated Deployment Testing.....	335
Jonathan Penn, Chris Johnson, Jesse Lewis, Trevin Dear & Alphonso Stewart	
A Recommended New Approach on Motorization Ratio Calculations of Stepper Motors .....	349
Ruben Nalbandian, Thierry Blais & Richard Horth	

Magnetic Gearboxes for Aerospace Applications .....	365
Jose Luis Perez-Diaz, Efren Diez-Jimenez, Marco Antonio Alvarez-Valenzuela, Juan Sanchez-García-Casarrubios, Christian Cristache & Ignacio Valiente-Blanco	
Primer – Stepper Motor Nomenclature, Definition, Performance and Recommended Test Methods .....	375
Scott Starin & Cutter Shea	
Development Testing and Subsequent Failure Investigation of a Spring Strut Mechanism .....	391
Jared Dervan, Brandan Robertson, Lucas Staab, Michael Culberson & Joseph Pellicciotti	
Development of a Tendon-Actuated Lightweight In-Space MANipulator (TALISMAN) .....	405
William Doggett, John Dorsey, Thomas Jones & Bruce King	
The Use, Evolution and Lessons Learnt of Deployable Static Solar Array Mechanisms.....	421
Mark Ferris & Andrew Haslehurst	
Deployment Mechanism for Thermal Pointing System.....	435
Kraig Koski	
ISS Ammonia Pump Failure, Recovery, and Lesson Learned- A Hydrodynamic Bearing Perspective.....	451
Robert Bruckner & Richard Manco II	
Wide Range Vacuum Pumps for the SAM Instrument on the MSL Curiosity Rover.....	463
Paul Sorensen, Robert Kline-Schoder & Rodger Farley	
SLM Produced Hermetically Sealed Isolation Valve.....	463
James Richard	
DRAGON - 8U Nanosatellite Orbital Deployer .....	487
Marcin Dobrowolski, Jerzy Grygorczuk, Bartosz Kędziora, Marta Tokarz & Maciej Borys	
Mechanism Design and Testing of a Self-Deploying Structure Using Flexible Composite Tape Springs.....	497
Joseph Footdale & Thomas W. Murphey	
Innovative Escapement-Based Mechanism for Micro-Antenna Boom Deployment.....	511
Marta Tokarz, Jerzy Grygorczuk, Stanisław Jarzynka & Henryk Gut	
Design and Functional Validation of a Mechanism for Dual-Spinning CubeSats .....	523
Eric Peters, et al	

## SYMPOSIUM SCHEDULE

### WEDNESDAY, 14 MAY 2014

7:00 Wednesday Presenters' Breakfast - Pisces Room, 15th floor, Hyatt Regency

8:00 **CHECK-IN AND REFRESHMENTS** - Ballroom Foyer, Hyatt Regency

8:15 **INTRODUCTORY REMARKS** - Constellation Ballroom, Hyatt Regency

Joseph P. Schepis, Co-Host Chairman, NASA Goddard Space Flight Center, Greenbelt, MD  
Stuart Loewenthal, Deputy Chairman, Lockheed Martin Space Systems, Sunnyvale, CA  
Christopher Scolese, Director, NASA Goddard Space Flight Center, Greenbelt, MD

8:45 **SESSION I – PAYLOAD & DEPLOYMENT MECHANISMS**

James Wells, Session Chair  
NASA Langley Research Center, Langley, VA

- An Innovative Aperture Cover Mechanism used on SDO/EVE and MMS/SDP  
Stephen Steg, William Vermeer, Scott Tucker & Heather Passe, Laboratory for Atmospheric and Space Physics, University of Colorado, Boulder, CO
- Metering Wheel-Wire Track Wire Boom Deployment Mechanism  
Mark Granoff, University of New Hampshire, Durham, NH
- Development of Cryogenic Filterwheels for the HERSCHEL Photodetector Array Camera & Spectrometer (PACS)  
Christian Körner & Dirk Kampf, Kayser-Threde GmbH, Munich, Germany; Albrecht Poglitsch & Josef Schubert, Max Plank Institut für extraterrestrische Physik, Garching, Germany; U. Ruppert & M. Schoele, Freie Universität Berlin, Berlin, Germany
- Development and Preliminary Testing of a High Precision Long Stroke Slit Change Mechanism for the SPICE Instrument  
Gabriel Paciotti, Fabrice Rottmeier & Luc Blecha, Almatech, Lausanne, Switzerland; Martin Humphries, SpaceMech Ltd., Bristol, United Kingdom
- High Gain Antenna System Deployment Mechanism Integration, Characterization, and Lessons Learned  
Fil Parlong, Vantage Systems Inc., Lanham, MD; Blair Russell, Walter Garcen, Chris Johnson & Craig Huber, Stinger Ghaffarian Technologies Inc., Greenbelt, MD; Chris Rose, NASA Goddard Space Flight Center, Greenbelt, MD
- In-Orbit Performance of the MWRI Scanning Mechanisms  
Manfred Schmid, Airbus Defence & Space, Friedrichshafen, Germany; Miao Jun & Yu Shuang, Aerospace System Engineering, Shanghai, China

11:45 **LUNCH**

Lunch for AMS Attendees in the Atrium and Harborview, Hyatt Regency



12:30 **SESSION II – BEARINGS & TRIBOLOGY**

Michael Dube, Session Chair  
NASA Goddard Space Flight Center, Greenbelt, MD

- Launch Load Resistant Spacecraft Mechanism Bearings Made From NiTi Superelastic Intermetallic Materials  
Christopher DellaCorte, NASA Glenn Research Center, Cleveland, OH; Lewis E. Moore III, NASA Marshall Space Flight Center, Huntsville, AL
- Reducing Wear of Steel Rolling Against Ti6Al4V Operating in Vacuum  
Timothy Krantz, NASA Glenn Research Center, Cleveland, OH
- Wear Potential due to Low EHD Films during elevated Temperatures  
Alan Leveille, consultant, Las Vegas, NV; Peter Ward, The Aerospace Corporation, El Segundo, CA
- Observations of Spacecraft Bearing Lubricant Redistribution Based on Thermal Conductance Measurements  
Yoshimi Takeuchi, Peter Frantz & Michael Hilton, The Aerospace Corporation, El Segundo, CA
- A Study on the Effects of Ball Defects on the Fatigue Life in Hybrid Bearings  
Ching-Yao Tang, Chad Foerster, Michael O'Brien, Brian Hardy, Vinay Goyal, Benjamin Nelson, Ernest Robinson, Peter Ward & Michael Hilton, The Aerospace Corporation, El Segundo, CA

3:00 **BREAK**

3:15 **SESSION III – POTPOURRI OF POSTERS**

Don Sevilla, Session Chair  
Jet Propulsion Laboratory, Pasadena, CA

- Design and Test of a Deployable Radiation Cover for the REgolith X-ray Imaging Spectrometer  
David Carte, Niraj Inamdar, Michael Jones & Rebecca Masterson, Massachusetts Institute of Technology, Cambridge, MA
- The Development, Build and Environmental Testing of a Bi-Axis Solar Array Drive Mechanism  
Noemy Scheidegger, Mark Ferris & Nigel Phillips, Surrey Satellite Technology Ltd, Surrey, United Kingdom
- Advances in Current Rating Techniques for Flexible Printed Circuits  
Ron Hayes, Honeybee Robotics Spacecraft Mechanisms Corp., Longmont, CO
- Design of 3D-Printed Titanium Compliant Mechanisms  
Ezekial Merriam & Larry Howell, Brigham Young University, Provo, UT; Jonathan Jones, NASA Marshall Space Flight Center, Huntsville, AL
- Magnetic Gearing versus Conventional Gearing in Actuators for Aerospace Applications  
Gregor Puchhammer, Karl Rejlek GmbH, Vienna, Austria
- Flight Testing of a Low Cost De-orbiting Device for Small Satellites  
Dana Turse, Phil Keller, Robert Taylor, Mark Reavis & Mike Tupper, Composite Technology Development, Inc., Lafayette, CO; Chris Koehler, Colorado Space Grant Consortium, University of Colorado, Boulder, CO

- Deployment Methods for an Origami-Inspired Rigid-Foldable Array  
Shannon Zirbel, Spencer Magleby & Larry Howell, Brigham Young University, Provo, UT; Brian Trease, Jet Propulsion Laboratory, Pasadena, CA

4:30 **SESSION IV – MARS**

Louise Jandura, Session Chair  
Jet Propulsion Laboratory, Pasadena, CA

- ROPEC – ROtary PErcussive Coring Drill for Mars Sample Return  
Philip Chu, Justin Spring & Kris Zacny, Honeybee Robotics Spacecraft Mechanisms Corp., Pasadena, CA
- Aperture Valve for the Mars Organic Molecule Analyzer (MOMA)  
Charles Engler, NASA Goddard Space Flight Center, Greenbelt, MD; John Canham, ATK Space Systems, Beltsville, MD
- Development of the RANCOR Rotary-Percussive Coring System for Mars Sample Return  
Gabe Paulsen, Stephen Indyk & Kris Zacny, Honeybee Robotics Spacecraft Mechanisms Corp., Pasadena, CA

6:30 -10:00 **RECEPTION** - Ballroom Foyer, Hyatt Regency

Invited component suppliers display current products and provide tutorials. Local high school FIRST Robotics Team demonstrations, 4-H robotics and aerospace display and a light buffet meal.

**THURSDAY, 15 MAY 2014**

7:00 Thursday Presenters' Breakfast – Pisces Room, 15<sup>th</sup> floor, Hyatt Regency

8:00 **SESSION V – HOLD IT OR LET IT GO**

Wayne Jermstad, Session Chair  
NASA Johnson Space Center, Houston, TX

- Torque Tension Testing of Fasteners used for NASA Flight Hardware Applications  
Ed Hemminger, Alan Posey & Michael Dube, NASA Goddard Space Flight Center, Greenbelt, MD
- Ultrasonic Method for Deployment Mechanism Bolt Element Preload Verification  
Eric Johnson, Yong Kim & Robert Pan, The Aerospace Corporation, El Segundo, CA; Fred Morris & Joel Mitchell, Lockheed Martin Space Systems Co., Littleton, CO
- LARES Mission: Separation and Retention Subsystem  
Alessandro Bursi, Pierluigi Camilli, Gianni Babini & Elio Mangraviti, CGS S.p.A., Milan, Italy; Claudio Piredda, consultant
- Testing Orion's Fairing Separation System  
Henry Martinez, Chris Cloutier, Heber Lemmon, Daniel Rakes, Joe Oldham & Keith Schlagel, Lockheed Martin Space Systems Company, Littleton, CO

10:00 **BREAK**

10:15 **SESSION VI – TESTING**

Rob Mueller, Session Chair  
NASA Kennedy Space Center, FL

- Design and Lessons Learned on the Development of a Pupil Select Mechanism to be used in the Testing and Calibration of the Integrated Science Instrument Module (ISIM) on the James Webb Space Telescope (JWST)  
Alissa Mitchell, Thomas Capon, Claef Hakun, Paul Haney & Corina Koca, NASA Goddard Space Flight Center, Greenbelt, MD; Jeffrey Guzek, Stinger Ghaffarian Technologies, Greenbelt, MD
- GMI Instrument Spin Balance Method, Optimization, Calibration and Test  
Laoucet Ayari, Michael Kubitschek, Gunnar Ashton, Steve Johnston, Dave Debevec & David Newell, Ball Aerospace & Technologies Corp., Boulder, CO; Joseph Pellicciotti, NASA Goddard Space Flight Center, Greenbelt, MD
- The European Robotic Arm: A High-Performance Mechanism Finally on its Way to Space  
Henk Cruijssen, Marcel Ellenbroek, M. Henderson, H. Petersen, P. Verzijden & M. Visser, Dutch Space B. V., Leiden, The Netherlands
- GPM Solar Array Gravity Negated Deployment Testing  
Jonathan Penn & Chris Johnson, Stinger Ghaffarian Technologies, Greenbelt, MD; Jesse Lewis, Trevin Dear & Alphonso Stewart, NASA Goddard Space Flight Center, Greenbelt, MD

12:15 **LUNCH**

Lunch for AMS Attendees in the Atrium and Harborview, Hyatt Regency

1:00 **SESSION VII – MOTORS and GEARS**

Gérard Migliorero, Session Chair  
ESA/ESTeC, Noordwijk, The Netherlands

- A Recommended New Approach on Motorization Ratio Calculations of Stepper Motors  
Ruben Nalbandian, Moog, Chatsworth, CA; Thierry Blais, Astrium SAS, Toulouse, France; Richard Horth, MDA Corporation, Montreal, Canada
- Magnetic Gearboxes for Aerospace Applications  
Jose Luis Perez-Diaz, Efren Diez-Jimenez, Marco Antonio Alvarez-Valenzuela, Christian Cristache & Ignacio Valiente-Blanco, Universidad Carlos III de Madrid, Leganés, Spain; Juan Sanchez-García-Casarrubios, MAG SOAR S.L., Valdemoro, Spain
- Primer – Stepper Motor Nomenclature, Definition, Performance and Recommended Test Methods  
Scott Starin & Cutter Shea, Avior Control Technologies, Inc, Longmont, CO

2:30 **BREAK**

2:45 **SESSION VIII – DEPLOYMENTS**

Chris Lashley, Session Chair  
ATK Aerospace Systems, Beltsville, MD

- Development Testing and Subsequent Failure Investigation of a Spring Strut Mechanism  
Jared Dervan, NASA Marshall Space Flight Center, Huntsville, AL; Brandan Robertson, NASA Johnson Space Center, Houston, TX; Lucas Staab, NASA Glenn Research Center, Cleveland, OH; Michael Culberson, Lockheed Martin Space Systems Co., Littleton, CO; Joseph Pellicciotti, NASA Goddard Space Flight Center, Greenbelt, MD

- Development of a Tendon-Actuated Lightweight In-Space MANipulator (TALISMAN)  
William Doggett, John Dorsey & Thomas Jones, NASA Langley Research Center, Langley, VA;  
Bruce King, Northrop Grumman, Hampton, VA
- The Use, Evolution and Lessons Learnt of Deployable Static Solar Array Mechanisms  
Mark Ferris & Andrew Haslehurst, Surrey Satellite Technology Ltd, Surrey, United Kingdom
- Deployment Mechanism for Thermal Pointing System  
Kraig Koski, Laboratory for Atmospheric and Space Physics, University of Colorado, Boulder, CO

4:45 **INVITED PRESENTATION**

Mechanisms on the JWST mission

John Mather, Principal Investigator, Nobel Prize Awardee, NASA Goddard Space Flight Center,  
Greenbelt, MD

7:00-11:00 **BANQUET – National Aquarium**

Social Hour and Dinner, with 4-D movie presentations at 7:30 or 8:30 pm. Aquarium exhibits open  
from 7:00 to 11:00 pm.

**FRIDAY, 16 MAY 2014**

7:00 Friday Presenters' Breakfast – Pisces Room, 15<sup>th</sup> floor, Hyatt Regency

8:00 **SESSION IX – PUMPS & VALVES**

Steven Bauman, Session Chair

NASA Glenn Research Center, Cleveland, OH

- ISS Ammonia Pump Failure, Recovery, and Lesson Learned - A Hydrodynamic Bearing  
Perspective  
Robert Bruckner, NASA Glenn Research Center, Cleveland, OH; Richard Manco II, Sierra Lobo  
Inc., Cleveland, OH
- Wide Range Vacuum Pumps for the SAM Instrument on the MSL Curiosity Rover  
Paul Sorensen & Robert Kline-Schoder, Creare Incorporated, Hanover, NH; Rodger Farley,  
NASA Goddard Space Flight Center, Greenbelt, MD
- SLM Produced Hermetically Sealed Isolation Valve  
James Richard, NASA Marshall Space Flight Center, Huntsville, AL

9:30 BREAK

9:45 **SESSION X – SMALL SESSION ON SMALL SATELLITES**

William Niemeyer, Session Chair  
NASA Goddard Space Flight Center, Greenbelt, MD

- DRAGON - 8U Nanosatellite Orbital Deployer  
Marcin Dobrowolski, Jerzy Grygorczuk, Bartosz Kędziora, Marta Tokarz & Maciej Borys, Space Research Centre of the Polish Academy of Sciences, Warsaw, Poland
- Mechanism Design and Testing of a Self-Deploying Structure Using Flexible Composite Tape Springs  
Joseph Footdale, LoadPath, Albuquerque, NM; Thomas W. Murphey, High Strain Dynamics, Phoenix, NY
- Innovative Escapement-Based Mechanism for Micro-Antenna Boom Deployment  
Marta Tokarz, Jerzy Grygorczuk & Stanisław Jarzynka, The Space Research Center of the Polish Academy of Sciences, Warsaw, Poland; Henryk Gut, GUTRONIC Henryk Gut, Warsaw, Poland
- Design and Functional Validation of a Mechanism for Dual-Spinning CubeSats  
Eric Peters, et al, Space Systems Laboratory, Massachusetts Institute of Technology, Cambridge, MA; William Blackwell, et al, Lincoln Laboratory, Massachusetts Institute of Technology, Lexington, MA

11:45 **SPECIAL PRESENTATION**

The Challenge of Mechanism Development- Some Experiences and Guidelines to Avoid Trouble  
Manfred Schmid, Airbus Defence & Space, Friedrichshafen, Germany  
Manfred to provide insights into the mechanism development process and highlighting issues encountered and how to avoid or resolve them.

**TECHNICAL SESSIONS CONCLUSION**

Edward Boesiger, General Chairman, Lockheed Martin Space Systems, Sunnyvale, CA  
• Herzl Award Presentation

1:00 **LUNCH**

Lunch for AMS Attendees in the Atrium and Harborview, Hyatt Regency

1:45 – 4:30 **TOUR**

1:45 Buses depart hotel for NASA Goddard Space Flight Center  
2:15-4:30 Facility tour  
5:00 Buses return to hotel

## **SYMPOSIUM ORGANIZING COMMITTEE**

### **Host Chairs**

**Claf F. Hakun, NASA GSFC**

**Minh Phan, NASA GSFC**

**Joseph P. Schepis, NASA GSFC**

**General Chairman - Edward A. Boesiger, Lockheed Martin**

**Deputy Chairman - Stuart H. Loewenthal, Lockheed Martin**

**Steven W. Bauman, NASA GRC**

**William Caldwell, NASA ARC**

**Jared Dervan, NASA MSFC**

**Barry J. Dunn, NASA LaRC**

**Carlton L. Foster, NASA MSFC (retired)**

**Christopher P. Hansen, NASA JSC**

**Louise Jandura, JPL**

**Wayne Jermstad, NASA JSC**

**Alan C. Littlefield, NASA KSC**

**Ronald E. Mancini, NASA ARC (retired)**

**Fred G. Martwick, NASA ARC**

**Donald H. McQueen, Jr., NASA MSFC**

**Gérard Migliorero, ESA/ESTeC**

**Robert P. Mueller, NASA KSC**

**Donald R. Sevilla, JPL**

**Mark F. Turner, NASA ARC**

**Robin Tutterow, NASA LaRC**

**James E. Wells, NASA LaRC**

# An Innovative Aperture Cover Mechanism used on SDO/EVE and MMS/SDP

Stephen Steg<sup>\*</sup>, William Vermeer<sup>\*</sup>, Scott Tucker<sup>\*</sup> and Heather Passe<sup>\*</sup>

## Abstract

This paper describes an aperture cover mechanism that was successfully flown in four locations on SDO/EVE, and is awaiting launch in sixteen locations on MMS. This design uses a paraffin actuator and a latch that secures the cover closed and removes the actuator from the load path. This latch allows the assembly to operate both as a light weight contamination cover (SDO/EVE), and also as a high-strength sensor restraint mechanism (MMS/SDP). The paper provides design/analysis/test information about the mechanism.

## Introduction

The Solar Dynamics Observatory (SDO) EUV Variability Experiment (EVE) was launched in February 2010, and contains four optical channels, each protected with this cover mechanism. EVE has a cooled (-120°C) detector, grazing incidence optics, 35-micron entrance slits, and operates in the extreme ultraviolet. Together, these features make this instrument extremely sensitive to particulate and volatile contamination. The function of this mechanism is to keep the instrument free from contamination during ground assembly and test through launch and initial spacecraft outgassing.

The Magnetospheric Multiscale Mission (MMS) is a four spacecraft constellation. The Fields Investigation incorporates several instruments, including the Spin Plane Double Probe (SDP). The SDP instrument utilizes this same aperture cover mechanism; however, it is modified to restrain a preloaded sensor element. Both the SDO/EVE and MMS/SDP implementations of this mechanism are nearly identical. SDO/EVE was designed / fabricated / tested several years before MMS/SDP, but many of the design features are carried forward into the MMS/SDP implementation.

## Mechanism Requirements

- Dust / contamination seal (SDO/EVE)
- Sensor restraint (MMS/SDP)
- One time on-orbit release – open only
- Manual close
- <50 lifetime releases, pre-launch
- Design Life 500 cycles, limited by actuator
- Cover opens 120 degrees or more
- 1 G operation
- Force Margin 4x on passive deployment springs
- Redundant mechanical and electrical device
- No metal to metal contact
- A-thermalize design - Thermal gradient across hinge line
- Position sensors to power off actuator
- Window for instrument stimulus (SDO/EVE)
- >2 Hz deployed frequency
- Temp range -30 to +40°C, prior to actuation.
- Survive the radiation environment of geosynchronous orbit (SDO/EVE)

---

<sup>\*</sup> Laboratory for Atmospheric and Space Physics, University of Colorado, Boulder CO

### Mechanism Mechanical Design

A redundant torsion spring hinge line with redundant Vespel bushing surfaces is utilized. A unique latch restrains the mechanism for launch. A High Output Paraffin (HOP) actuator is configured in such a way that it expands, releases the latch, and provides a positive “kick-off” force on the cover to ensure that deployment motion is initiated. This kickoff force overcomes possible stiction at the cover interface. Ground testing is eased by removing the actuator and measuring the force required to release the latch. When the cover opens, the end of travel catch securely stops the motion.

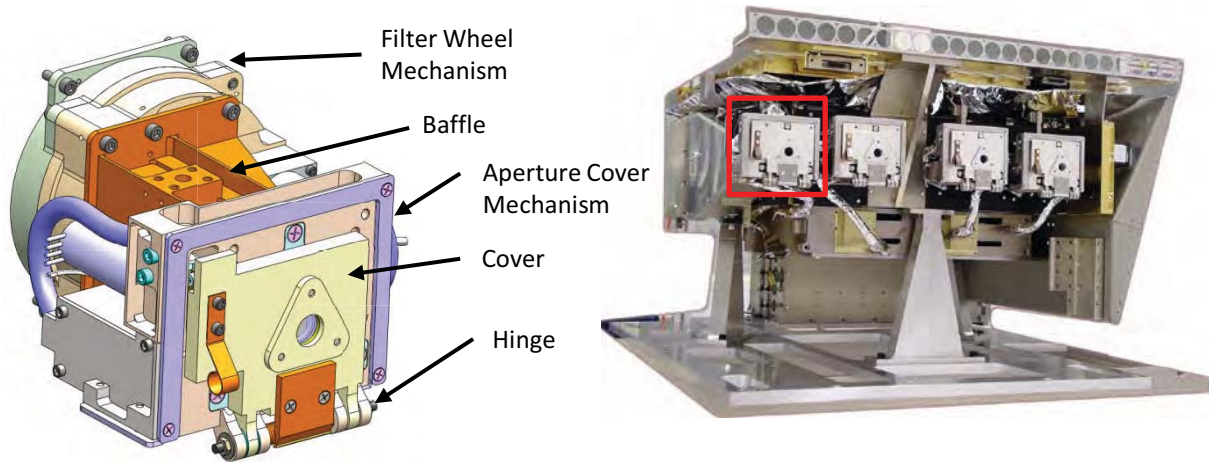


**Figure 1. SDO/EVE Aperture assembly with four aperture cover mechanisms**

Two limit switches sense cover motion and power off the HOP. The MMS/SDP implementation removed the limit switch from the redundant heater side, providing an innovative way to protect against the risk of limit switch failure, while still utilizing the limit switch to protect the integrity of the HOP before launch.

Figure 1 shows the location of the Aperture Cover Mechanism with respect to the EVE instrument. For this implementation, the primary function of the mechanism is to maintain cleanliness against particulate and volatile contamination.

Figure 2 shows the implementation for MMS/SDP. In addition to providing cleanliness, this mechanism functions to restrain the sensor element during launch. A large preload is applied to the sensor element, which is directly reacted by the cover and subsequently the catch. The over center latch is ideal because of its large load carrying capability as well as its low release force. Late in the MMS/SDP program, the sensor preload was significantly increased to mitigate an issue with vibration at the interface between the sensor-sphere and the restraint cover. This existing design handled the increased loading.



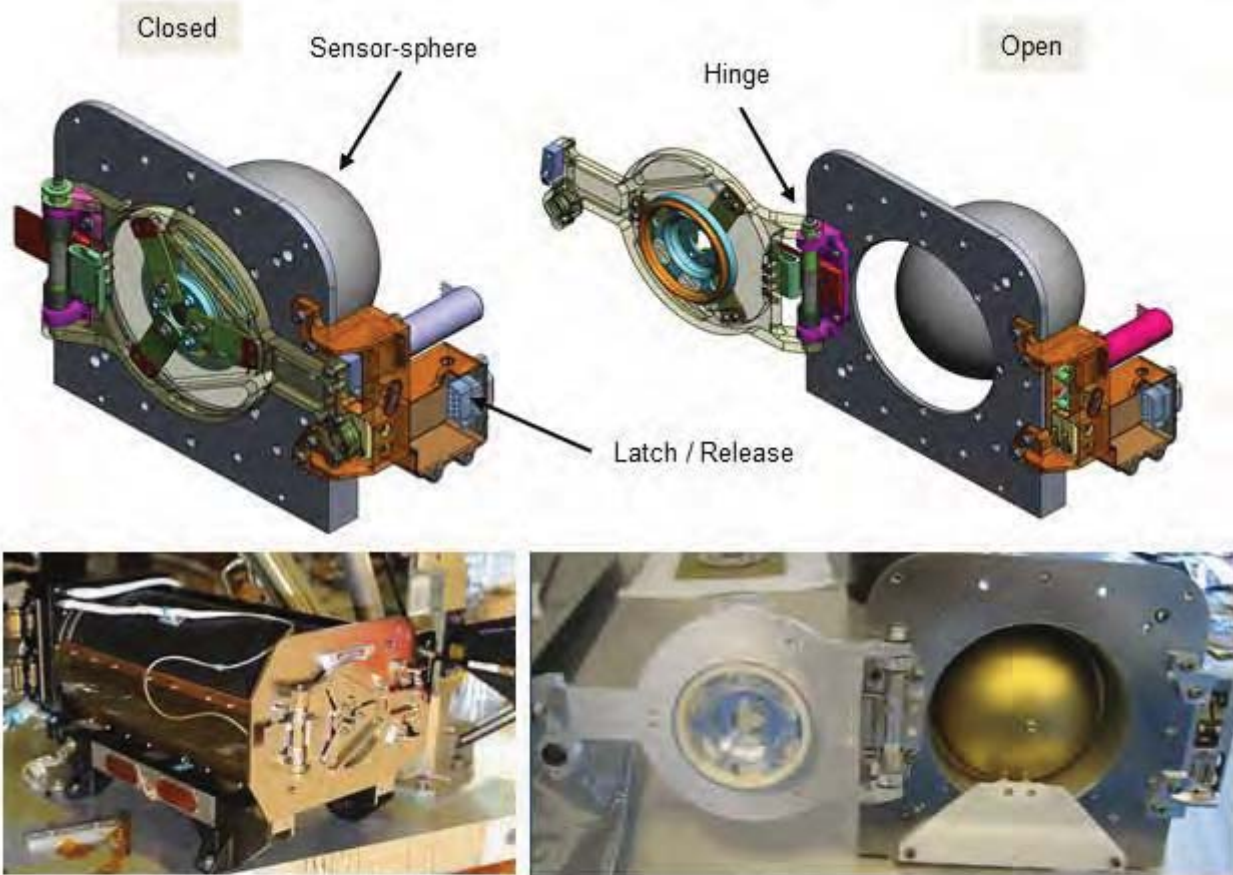


**Figure 2. MMS/SDP Sensor Restraint Mechanism**

Figure 3 shows the mechanism deployment sequence and details of the restraint latch. During launch, the latch hook secures the cover. This load is directly carried by the latch into the latch pivot. The loading from the cover (and the pre-loaded sensor element for MMS/SDP) is never applied to the actuator. This arrangement allows the actuator to be physically removed during ground testing to measure how much force is actually required to release the cover and establish a definitive actuator force margin. The latch rollers, latch pivot, and leaf spring bushings are all low friction Vespel SP3. The roller directly adjacent to the actuator is brass which dissipates any electrical charging due to the high radiation GEO environment. The latch hook is contoured which allows the kickoff roller to apply a direct force to the cover in the event that the cover is stuck. The over-center contour at the “latch roller / latch hook” interface prevents inadvertent release during launch. The latch hook has a ramp which allows the cover to be manually reset, simply by pushing the cover closed and visually observing the latch position.

When the cover is latched for launch, one of two limit switches is depressed. After launch, the cover is opened by powering the HOP. Initially it expands slightly as can be seen in Figure 3: “Released”. At this point, the redundant torsion springs are free to open the cover. However, the HOP is still powered, so its shaft will continue to axially deploy. In the event that the door is stuck, the HOP will expand until a roller is pushed firmly against the cover with 156 N (35 lb) of force. At the fully deployed position, the “cover closed switch” is released, and the “cover open” switch is engaged. Either of these events will nominally power off the HOP.

Table 1. Unique design features and benefits of this mechanism	
Feature	Benefit
Release latch, then "kick-off"	Ensures motion will start, particularly at the beginning of travel. 156N force available from HOP ensures large force margin of safety.
Actuator out of launch load path	No side load on pin puller. Design is insensitive to increased pre-load on cover
Manually open/close	Useful feature for ground testing
End of travel catch	Securely holds cover in open position
Redundant springs, bushing surfaces, HOP heaters	Higher reliability
Removable actuator	Allowed verification of force margin

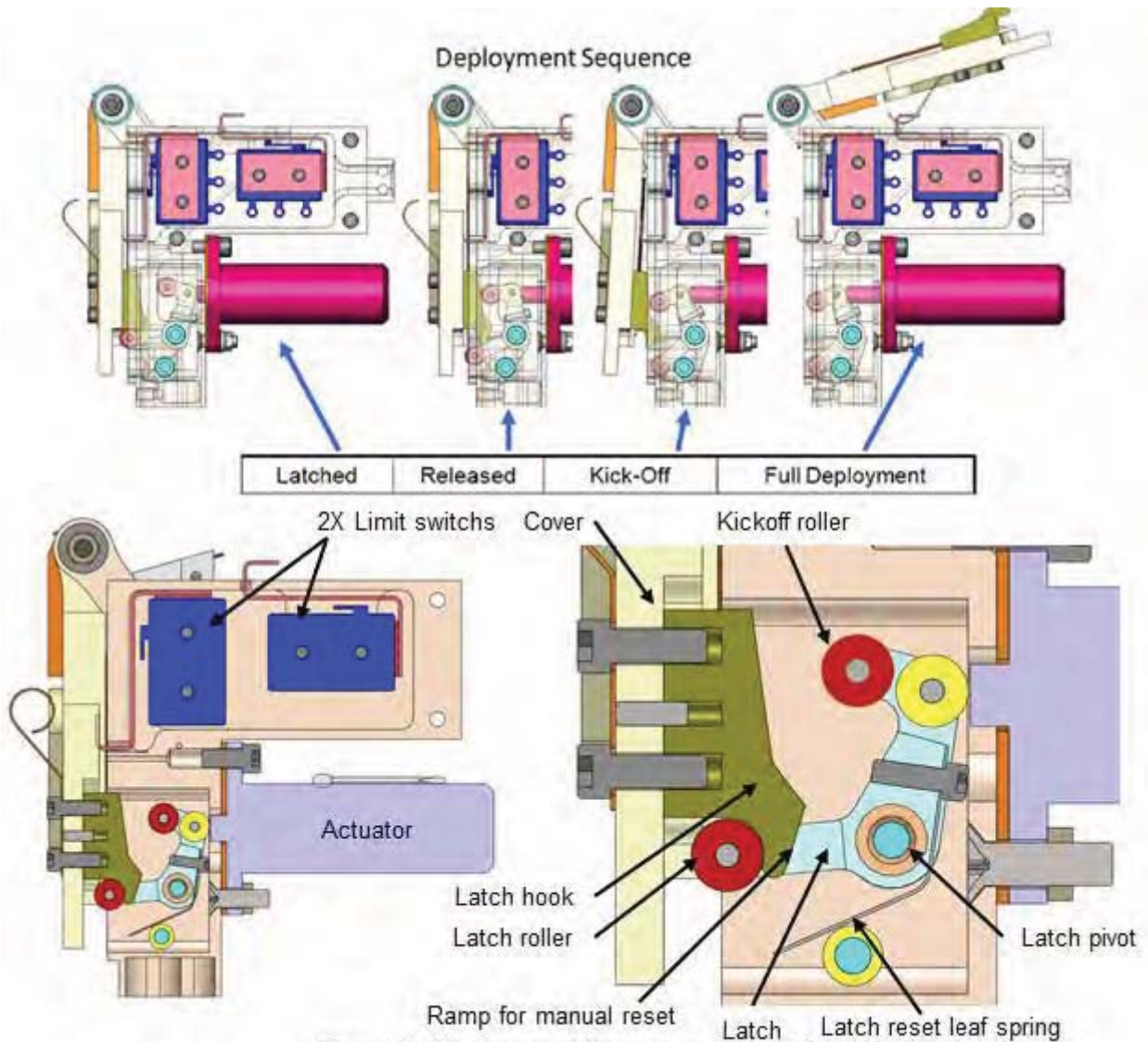


Figure 3. Deployment Sequence and Latch Details

In the event of a switch failure, the microprocessor can ignore the switches in the SDO/EVE implementation. The MMS/SDP implementation does not use switches on the redundant side, thus eliminating the risk of a limit switch anomaly preventing HOP actuation.

The MMS/SDP mechanism opens 180 degrees. The resultant spring torque at full open is sufficient to hold the cover against its open stop without an end-of-travel catch. For SDO/EVE, the cover opens 240 degrees and the spring torque at the fully opened position is small. Initial prototypes of the mechanism revealed 10-20 degrees of backlash of the cover when at its open position. To remedy this, stiffer torsion springs were used and a catch was added to hold the cover securely in the open position. Although this freedom of motion would not negatively affect the instrument, it would prevent the “cover open” switch from actuating reliably.

Initially, the catch was designed as a thin beryllium copper sheet metal component, as shown in Figure 4. After several actuations, it was discovered that the bounce-back of the door was loading the end of the sheet metal catch in compression, causing it to buckle and yield. The catch was redesigned out of a machined aluminum component, pivoting on a vespel bushing, and preloaded with a small torsion spring (Figure 4 and 5)

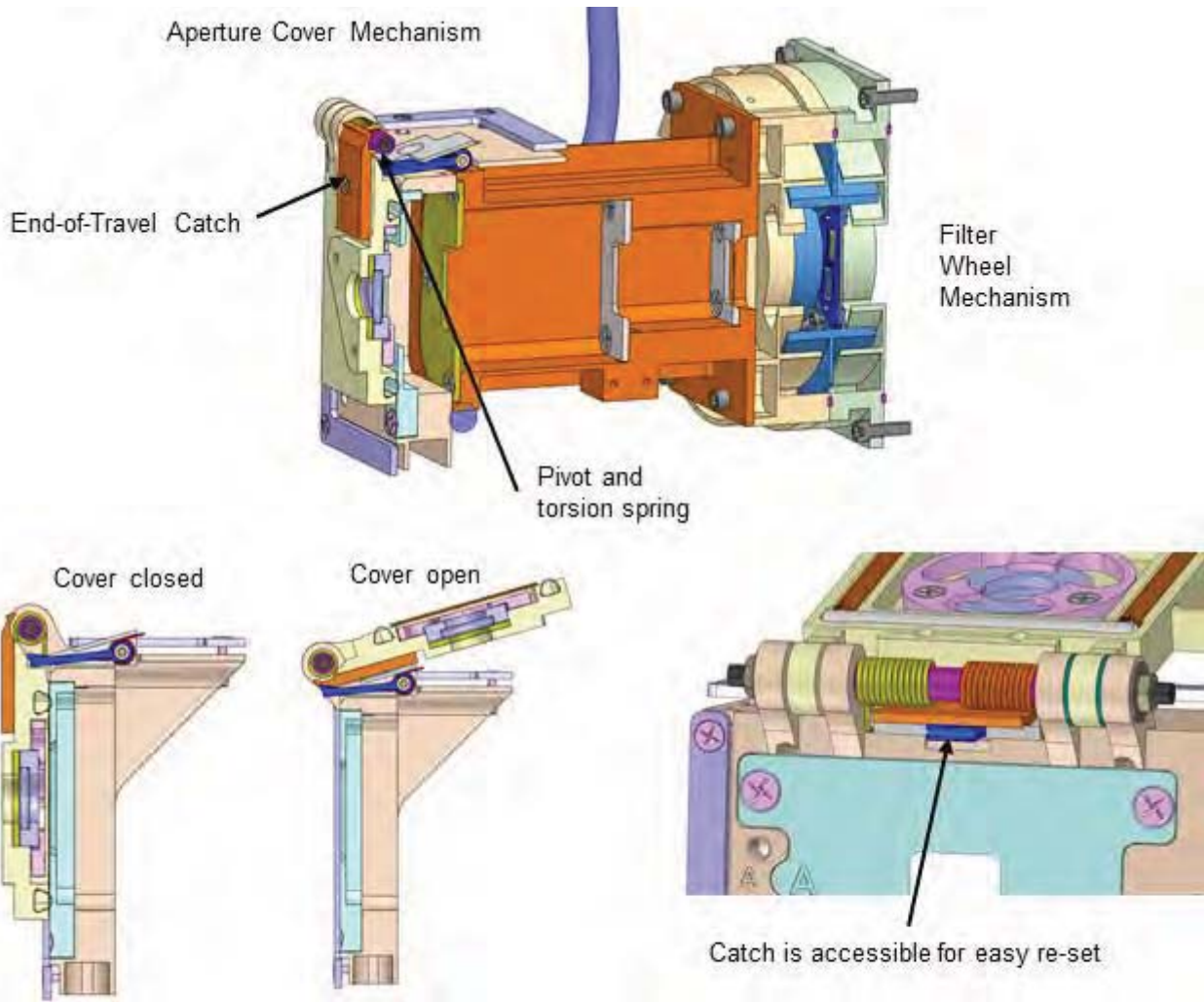


Figure 4. Initial and final catch designs

Details of the final end-of-travel catch are shown in Figure 5. Only after the cover has opened 180 degrees, and is completely outside the instrument’s glint free FOV, does the catch begin to engage with the cover. The location at the hinge line was selected to provide ready access to un-latch the catch, such that the cover could be manually closed without any disassembly or tools.

**Catch Anomaly:** During mechanism run-in testing, the catch always secured all four covers in the open position, reliably. However, upon close inspection it was found that two of the four mechanisms had catches that did not in fact capture the cover as it was initially deployed, but rather allowed these covers to bounce back about 45 degrees, then return to the catch, at which point they were securely captured. Many manual deployments were completed as this phenomenon was investigated. It appeared that slight variations in the end-of-travel springs and limit switch springs caused the catch to not engage on the first cover impact, but always engage on the second cover impact. This is considered acceptable because: 1) the catch always secures the cover in its open position, 2) the limit switches are redundant, and 3) a failure of the catch would not prevent the cover from properly opening.





**Figure 5. SDO/EVE final catch design**

Close attention was paid to the details of the hinge line, as shown in Figure 6. All moving surfaces were Vespel SP3, which contains  $\text{MoS}_2$  dry lubricant. The bushings were arranged such that redundant sliding surfaces exist at every interface. Axial bushings are used at one end of the hinge, but the other end is allowed to float axially. SDO/EVE faces the sun, so it was expected that the cover may get hot and that the hinge needs to allow for a large thermal gradient between the cover and the mechanism. Clearances are tightly controlled between bushings and mating surfaces to ensure that under the worst thermal conditions, a clearance would exist and prevent the hinge from binding. Hinge friction was measured for all flight units under the full survival temperature range (details to follow).

Thermal design features are shown in Figure 7. External metal surfaces are coated with silver composite coating CCaG, which prevent the cover from getting hot in direct solar illumination. This coating is sensitive to damage by handling, so great care was taken during mechanism assembly and test. The MLI attachment is considered a critical interface. Simple clamp plates are used (also CCaG coated) to compress the MLI securely around the apertures.

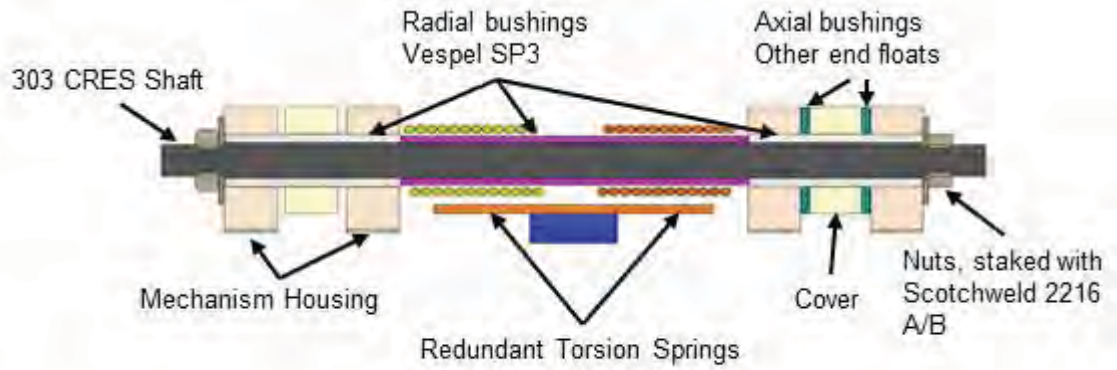


Figure 6. Hinge Line

MLI clamping was done to prevent any trapped particulate within the MLI from being vented at the aperture cover, and to prevent the MLI from obscuring the aperture. Thermally, the performance of the MLI is significantly reduced at this interface, but mechanically, this is very secure.

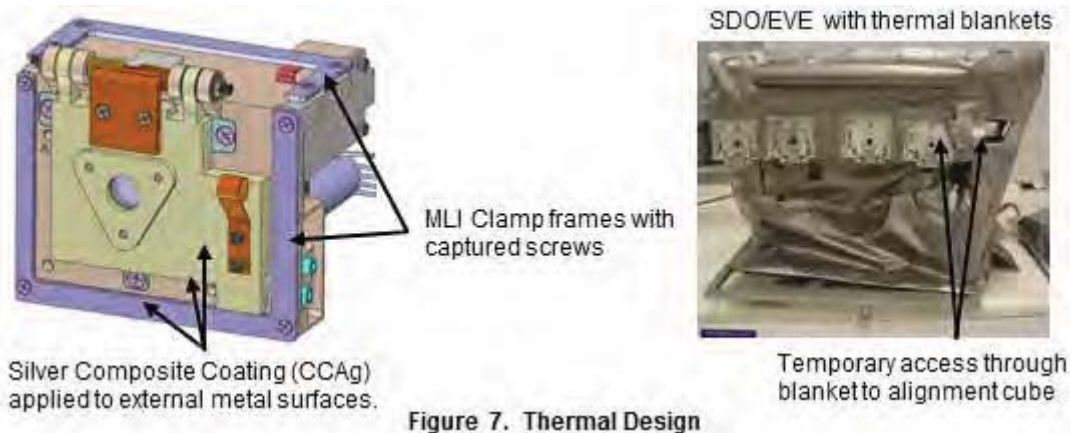


Figure 7. Thermal Design

The cover is machined Al6061T6, as shown in Figure 8. The actual seal was intended to be leaky and allow slow venting of the pre-launch purge N<sub>2</sub>. Additional larger vents are located on the instrument housing and they allow rapid instrument venting during launch. Viton O-rings are known to develop stiction, and would not allow the mechanism to slowly vent, so they are not used on this mechanism. The seal is fabricated from kapton tubes, fitted into dovetail O-ring grooves, and secured in place with an internal wire. Although this works fine, it turned out to be more complicated than necessary, and if done over again, they would be replaced with a simple machined Vespel seal. A window is included in the cover to allow for pre-launch instrument aliveness verification.

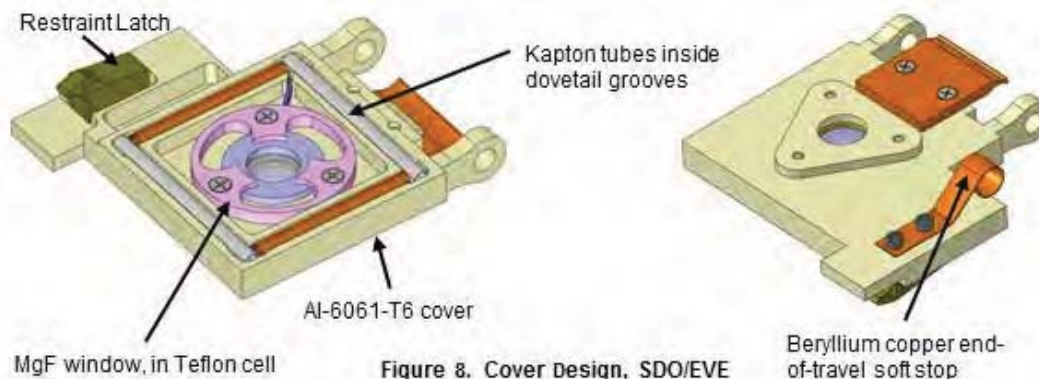
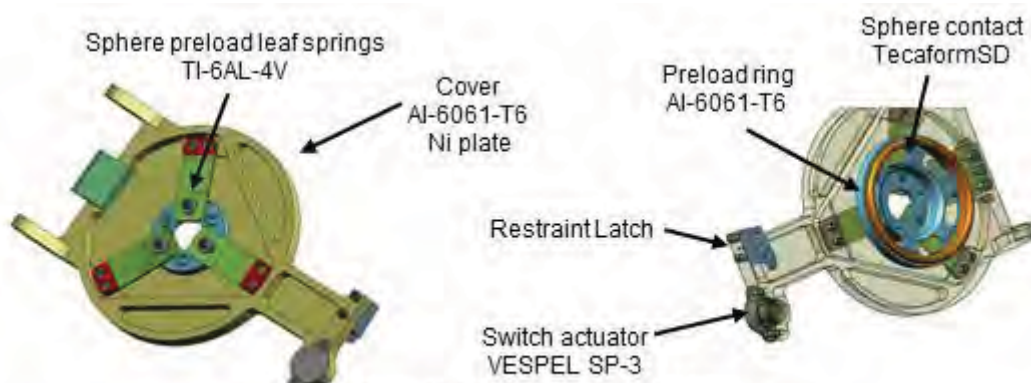


Figure 8. Cover Design, SDO/EVE

The MMS/SDP cover implementation is shown in Figure 9. The sensor sphere is titanium nitride, which has a known photo-emissive property. It is required that the door restrain the sphere carefully and firmly so that there will be no wear or transference of material that would damage the performance of the sensor-sphere surface and degrade the performance of the sensor. The sensor sphere was pre-loaded to 178 N with three Ti6Al4V leaf springs and contacted through a Tecaform SD ring.



### Testing SDO/EVE Mechanism

**Actuator Force Margin Test:** Early prototype testing (pre-PDR) was completed as a way to establish the force margin for the actuator and torque margin for the hinge springs. Figure 10 shows the setup and results of this early test. A prototype mechanism was placed in a thermal oven and purged with  $N_2$ . The actuator was removed for this test and substituted with a hand held force gage to measure the force required to unlatch and deploy the mechanism. This wasn't the perfect test – the oven door was opened repeatedly during the measurements which resulted in some frost build up. Dry ice was used to cool past the oven's cold temperature capability. Although this wasn't a perfect flight-like environment, it was considered very useful as a simple way to gain confidence, early in the mechanism development. The maximum force required to unlatch the mechanism was 6 N, which is very low considering the actuators 156-N capability.

**Hinge line friction test:** All mechanisms had hinge drag torque measurements performed during assembly, and had corresponding spring torque measurements completed after assembly. This verified a positive margin of safety for deployment torque.

**1G Orientation deployment:** One of the mechanisms was deployed in all six orientations, with respect to gravity, with no anomalies.



	Atm.	Temp C	Force to release N (lb)
10 cycles	Air	22	6 (1.3)
Hot	N2	50	6 (1.3)
Cold	N2	-39	6 (1.3)
Cold	N2	-33	5 (1.2)
Cold	N2	-49	5 (1.1)
Cold	N2	-62	6 (1.5)
Hot	N2	+50	3 (0.7)
Actuator Capability			156 (35.)



Aperture Cover Mechanism in thermal oven, with N2 purge

**Figure 10. Aperture Cover Force Margin**

**Final Run-In test:** All four flight mechanisms were deployed in a vacuum tank 45 times each in a matrix of 3 voltages and 3 temperatures for both primary and redundant windings. The deployment time was recorded for each actuator and typical values are noted in the table in Figure 11. The large variation in deployment times prevents a software time-out from being an effective method to power off the HOP. This result reaffirmed the necessity of end of travel switches.

Temp	Deployment time (s)		
	22V	28V	35V
-30 C	490	228	121
20 C	216	117	69
40 C	131	80	50

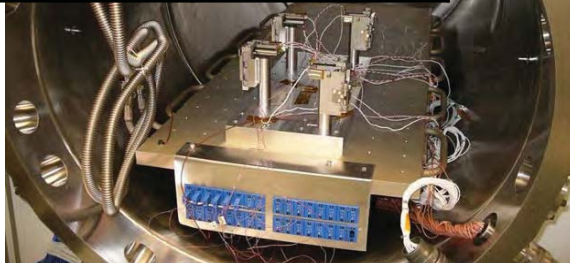


**Figure 11. Run-In Test**

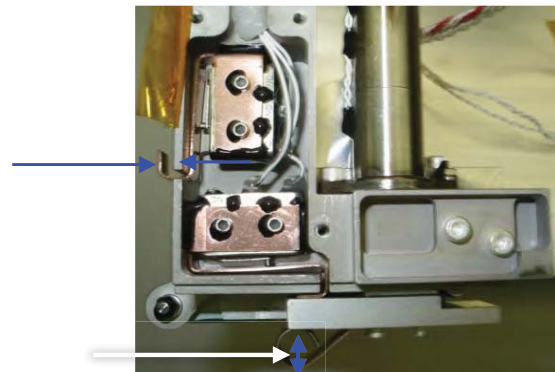


**Figure 12. Switch Spring Measurements**

**Switch Anomaly:** During the run-in test, one limit switch on one mechanism failed to properly indicate “door open” after 17 cycles. If this had happened in flight, it would neither have prevented the door from properly opening, nor prevented the actuator from being powered off. Nonetheless, the test was paused and the root cause was investigated.

Measurements of the height of the “end-of-travel” spring and the “switch spring” were made (Figure 12), and it was found that variations in the height of these 2 springs could prevent the switch from being fully depressed. The “end-of-travel” spring was shimmed to match the other mechanisms. The shimmed mechanism was then manually deployed 25 times in air at room temperature with zero anomalies. At this point, the final run-in test was resumed with no further issues.

**Vibration Testing:** An early prototype installed on a mass model was vibration tested to 10.0 grms and acoustic tested to 142 dB. The final flight mechanisms were vibration and acoustic tested after installation on the flight instrument.

### Testing MMS/SDP Mechanism

The engineering model was vibration tested with the integrated instrument. Following the test, the cover was deployed 14 total times, with 1 actuation at +50°C and 3 actuations at -30°C. These deployments were done in thermal convection chambers. The EQM was also vibration tested on the integrated instrument, followed by 23 total actuations. During TVAC, the unit was successfully deployed at both cold and hot survival limits. To date, a total of 16 flight units have undergone vibration and thermal vacuum testing. The only resulting anomaly was determined during a safe-to-mate check, and was related to a micro-switch. During the entire test campaign there has not been any premature deployments and all planned door actuations have been successful.



**Figure 13. MMS/SDP Latches**

### On-orbit experience

SDO/EVE covers were successfully deployed on orbit with no issues. The MMS/SDP covers are integrated onto the spacecraft, ready for launch.

### Conclusion

The SDO/EVE mechanism was a robust design that was easily scaled to a highly preloaded application for MMS/SDP. Building and testing the assembly early allowed for resolution of design issues associated with the original end-of-travel catch design. The capability of removing the actuator proved very helpful for testing the latch release force. Performing a run-in test over survival limits with many cycles was an effective way to uncover a limit switch adjustment issue, and provided a high degree of confidence in the design.



# Metering Wheel-Wire Track Wire Boom Deployment Mechanism

Mark S. Granoff\*

## Abstract

The NASA MMS Spin Plane Double Probe (SDP) Deployer utilizes a helical path, rotating Metering Wheel and a spring loaded Wire “Holding” Track to pay out a “fixed end” 57 meter x 1.5 mm diameter Wire Boom stored between concentric storage cylinders. Unlike rotating spool type storage devices, the storage cylinders remain stationary, and the boom wire is uncoiled along the length of the cylinder via the rotation of the Metering Wheel. This uncoiling action avoids the need for slip-ring contacts since the ends of the wire can remain stationary. Conventional fixed electrical connectors (Micro-D type) are used to terminate to operational electronics.

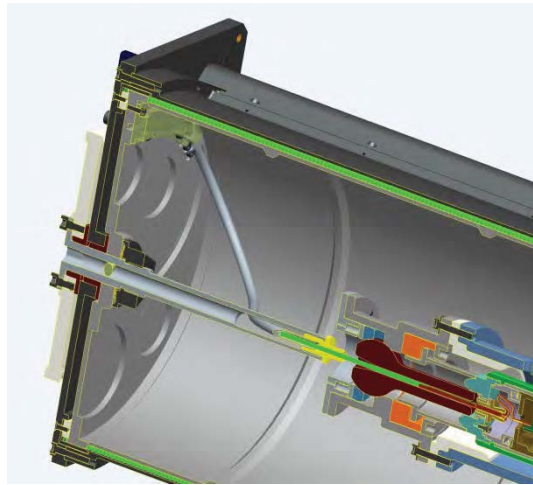


**Figure 1. SDP x-section, Wire Boom (green) between stationary cylinders & exiting on axis**

## Introduction

The original concept for this mechanism was first put forth by the Royal Institute of Technology (KTH) Stockholm, Sweden<sup>1</sup>. Engineering and manufacturing limitations at KTH necessitated the support of a strong design and flight fabrication capable institute to make SDP a reality. Collaboration with the University of New Hampshire Space Science Center was initiated and a competitive proposal was won, landing this challenging project and bringing this instrument from concept level to flight deliverable hardware in less than 36 months. A total of 16 flight-qualified SDP Deployers have been integrated, tested and delivered to NASA for the upcoming MMS mission. The unique approach toward wire coil storage and deployment provided by this instrument is the impetus for writing this paper.

## Metering Wheel & Wire Track Background

The Metering Wheel is keyed to the Metering Wheel Shaft which is supported in the instrument “Back Plate” via an integral Hub Bearing (journal type) made from SP-3 Vespel for low friction and good load carrying capacity. A Bellville washer and pre-load nut combine to provide a consistent pre-load of the

---

\* University of New Hampshire, Space Science Center, Durham, NH

Metering Wheel Shaft into the hub bearing. A polycarbonate cover, a polished stainless steel conduit tube and PEEK Exit Ferrule complete the subassembly.



**Figure 2. MMS SDP Metering Wheel Back Plate Sub-Assembly**

The Metering Wheel has opposing conduit ramps which simultaneously load the wire into the wire holding track, and uncoil the wire from the track. A hard-coat anodized “Outer Race” provides the reaction surface for the wire while under spring load in the track. As the wire moves relative to the metering wheel, the coils transition from the track and are linearly displaced within a helical tube conduit along the instrument principle axis. This mechanism operates clockwise and counterclockwise dependent upon commanded “deployment” or “stowage.”

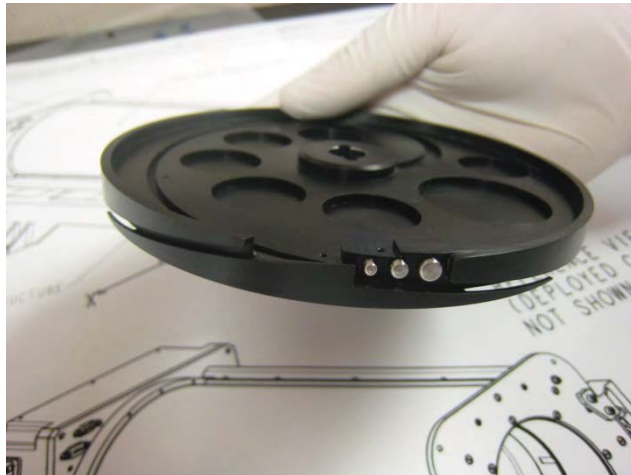


**Figure 3. SDP Metering Wheel, Conduit Ramps**

A key aspect of this instrument application is the ability of the Metering Wheel and Track to adequately hold the sphere and wire boom when exposed to the maximum centrifugal acceleration of the rotating MMS satellite. As calculated by the instrument P.I. P-A Lindquist<sup>2</sup>, KTH, this applied load is 5.22 N (1.17 lb) and occurs during spin up. Although a modest value, quantifying the load carrying capability of the SDP Metering Wheel & Track became paramount to design approval going forward. Early simplified models with high friction silicone races showed promise in generating holding power; however deflections of the non-linear elastomeric silicone, and unknown friction values were not quantifiable, leading to an ambiguous assessment of Metering Wheel & Wire Track load capability.

To quantify the load in the track, a series of simple, integral radial leaf springs, were machined into the PEEK Holding Track at an un-deflected radius. When the wire is loaded into the PEEK Track, the leaf springs deflect and a resultant spring load is generated for each spring, holding the wire in compression against the hard-coated Outer Race. The springs are implemented in opposing pairs so that the track will work equivalently for both deployment and stowage rotations. Shown in Figure 4 is a developmental one-piece track/race depicting the spring deflection and subsequent compression reaction against the outer race.

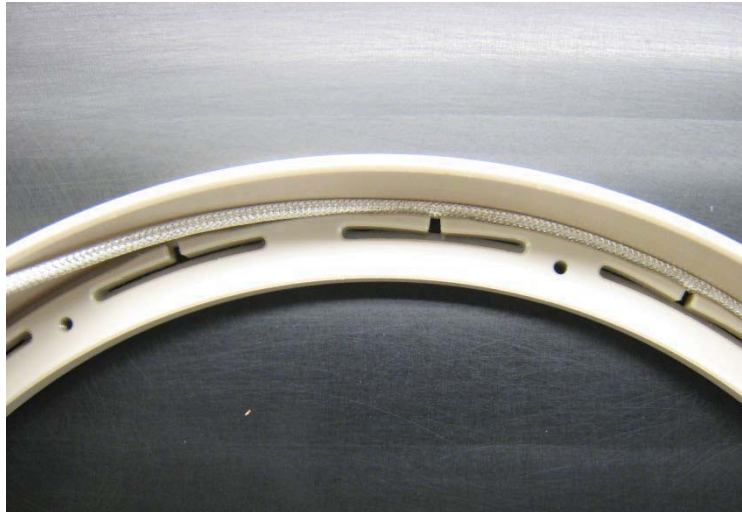


**Figure 4. PEEK Holding Track - spring deflection w/Wire (non-flight hardware)**

The following expression from Spott's<sup>3</sup> Fig. 1-13-5 is used to calculate the load generated by each spring deflection:

$$S_{\text{spring load}} = (Y_{\text{max}} \times 3 \times E \times I) / L^3 \text{ (multiply result by number of active springs)}$$

Where:

- $Y_{\text{max}}$  = deflection of spring 0.3 mm (0.012 in)
- $E$  = Young's Modulus for PEEK
- $I$  = MOI for Spring Section ( $bh^3/12$ )
- $L$  = length of spring arm

Due to the overlapping ramps of the Metering Wheel, about 259° (of 360°) of the of the Track, and hence springs, are active at any given moment. This results in 22 active springs for a total Normal load "N" of about 25 N (5.6 lb). Implementing the expression  $F=\mu \times N$  with  $\mu$  of PEEK<sup>4</sup> being about 0.3, the load in the track ( $F=T_T$ ) is calculated as about 7.5 N (1.7 lb). If the track was a linear or straight device, that would be your holding power. However, with the circular geometry of the Metering Wheel and Track, a "band brake" analogy is drawn and allows us to calculate the additional load holding capability of the Metering Wheel and Track via the following expression:

$$T_S = T_T \times e^{\mu\alpha} \text{ (Spott's Eqn. 18, 5}^{\text{th}} \text{ Edition, Chap. 6)}$$

Where:

- $T_S$  = load holding capacity at SDP Sphere end of wire boom, N (lb)
- $T_T$  = load in Track via spring normal force, friction coeff. & qty of active springs, N (lb)
- $\mu$  = Friction Coefficient of PEEK, 0.3
- $\alpha$  = 259° Boom wrap angle in track, =  $(259/360) \times 2\pi = 4.52$
- $\mu\alpha$  =  $0.3 \times 4.52 = 1.357$

Solving yields:  $T_s = 28.5 \text{ N}$  (6.4 lb)

This resultant load capacity of the SDP Metering Wheel and PEEK Wire Holding Track provides significant margin over the applied centrifugal load generated by the MMS spin rate. Load testing carried out with the SDP gear train engaged, i.e., with the Metering Wheel main gear locked through the engaged gear train all the way to the stepper motor pinion, yielded a pull test value of over 90 N (20 lb). This testing demonstrated analytical conservatism, and that there exists additional friction sources in our mechanism contributing to this robust margin for the flight assembly.

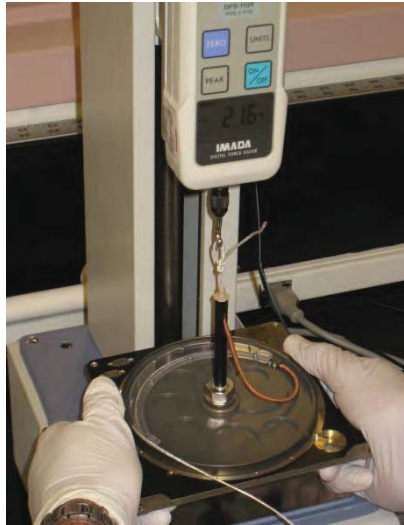


**Figure 5. MMS SDP Metering Wheel Pull Test slips at 21.6 lb (96 N)**

### **Stress**

The individual springs can be treated as classic cantilever beams with bending stress calculated via:

$$S_b = MC/I$$

Where:

M = bending moment of load P at deflection x moment arm length L

C = distance to neutral axis of spring

I = MOI for Spring Section ( $bh^3/12$ )

Solving yields 25.5 MPA (3700 psi) stress

With PEEK 450G having a tensile stress limit<sup>4</sup> of 97 MPA (14065 psi) and considering the NASA standard calculation for margin of safety,  $MSY > 0$ :

$$MSY = [\text{mat'l limit}/(1.6 \times \text{applied stress})] - 1 = [97/(1.6 \times 25.5)] - 1 = 1.37 > 0$$

With this resultant  $> 0$ , the stress margin is acceptable.

### **Fatigue**

Figure 6 depicts the Victrex PEEK 450G fatigue curve<sup>5</sup>. Extrapolating for 25.5 MPA, cycles to failure for the SDP Wire Track springs should exceed  $10e^7$  cycles. With each 57 meter SDP deployment, each spring sees approximately 170 actuations. With the Engineering Qualification Model demonstrating 14 complete deployments, along with 14 stowage cycles, the life test unit springs experienced more than 4700 actuations. With this significant margin of cycles to failure, and with the demonstrated life testing margin at 3.5 X flight model total actuations, fatigue of the PEEK Wire track springs is not considered significant.

Figure 14 Fatigue Stress Versus Cycles to Failure for Various High Performance Engineering Thermoplastic Matrices Containing the Same Reinforcement

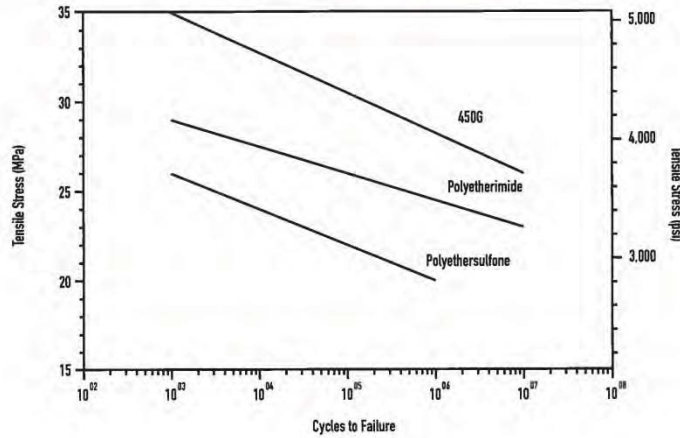


Figure 6. Victrex PEEK Fatigue Curve, 450G

**Thermal Considerations**

During developmental thermal testing at UNH<sup>6</sup> it was determined that there was too large a mismatch in Coefficient of Thermal Expansion (CTE) between the Habia Boom Wire ( $27.9e^{-6}/^{\circ}C$ ) and the original PEEK ( $42.4e^{-6}/^{\circ}C$ ) outer race feature leading to deployment of “small coils” during cold plateaus. The resultant was a binding of the coils along the inner storage cylinder. Subsequent testing determined that the CTE of the Habia wire was very close to that of Aluminum ( $23.4e^{-6}/^{\circ}C$ ) and the outer race feature was implemented into a separate part, a hard coat anodized Aluminum Outer Race. With CTE’s for the Habia wire, Outer Race and Inner Cylinder now all matched, successful thermal deployments were achieved.

Integration of the PEEK Track and Aluminum Outer Race into the SDP Back Plate is shown in Figure 7. The 16 pairs of opposing springs are relieved toward the Back Plate to allow unimpeded (non-rubbing) deflection. The track is held in place via 16 miniature M1.6 metric screws that thread directly into tapped holes in the track. Note the Vespel Hub Bearing shown installed at the Back Plate center.

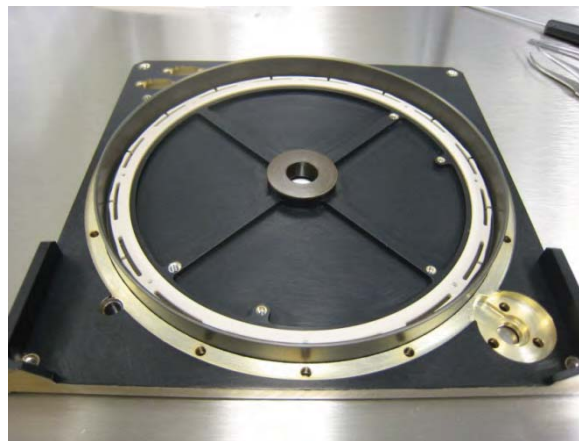
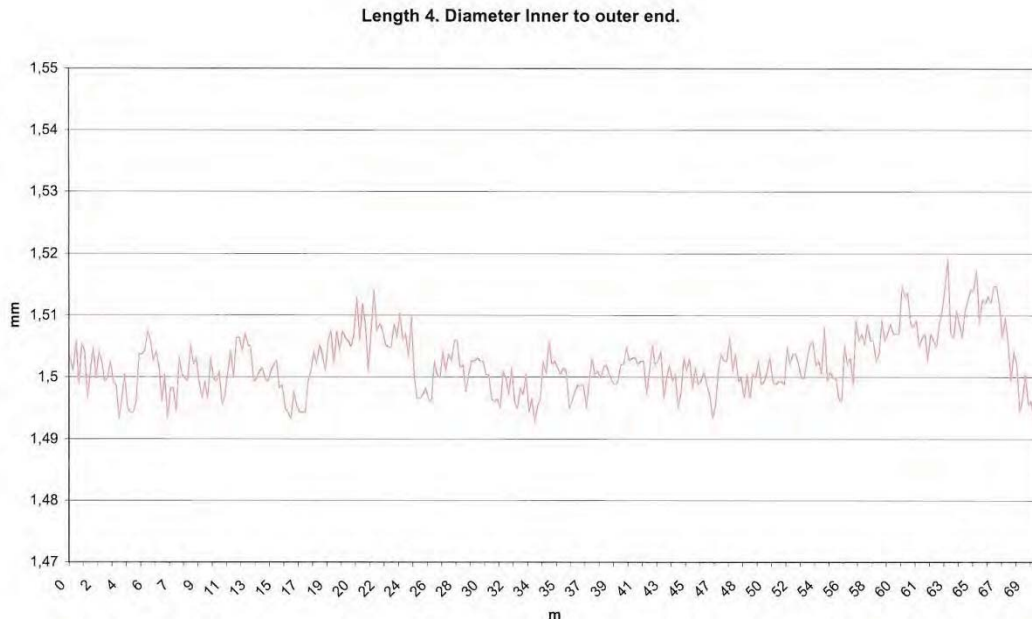


Figure 7. PEEK Wire Holding Track & Outer Race installed in SDP Back Plate (flight hardware)



### **Boom Wire**

The Wire used for the SDP Boom is manufactured by Habia Cable in Soderfors, Sweden<sup>7</sup>. Habia provided a custom 7 conductor, Kevlar/Kapton overwrap layup with a silver-plated copper GND shield. UNH worked closely with Habia to tailor the mechanical characteristics of the layup to ensure optimal consistency in cross sectional diameter as well as overwrap stiffness. The nominal diameter of the composite wire was specified to be held within  $1.50 \text{ mm} \pm 0.05 \text{ mm}$ , critical for consistent spring deflection in the PEEK Track/Outer Race geometry. Inspection data from Habia via laser measurement of each spool of wire for SDP demonstrated even tighter control of this important aspect of the wire. A sample plot of this diametral inspection is shown in Figure 8<sup>8</sup>. This modest actual variation in diameter,  $+0.02 \text{ mm} / -0.01 \text{ mm}$  was typical for SDP flight spools.



**Figure 8. Habia Boom Wire inspection data, diameter variation over 70 meter spool**

### **Material Specifications**

The materials used in manufacturing the SDP Metering Wheel and Wire Track sub-assembly were optimized during the comprehensive, and flight fidelity engineering model development at UNH. Surface treatments were optimized for friction and wear; all materials meet the stringent NASA Reference Publication 1124 for outgassing of materials intended for spacecraft use<sup>9</sup>. The materials list follows:

- Metering Wheel - 7075-T7351 Aluminum w/General Magnaplate Tuftram low friction plating
- Wire Track- PEEK Victrex 450G
- Hub & Thrust Bearings - Dupont Vespel SP-3
- Outer Race - 6061-T6 Aluminum w/clear hard-coat anodize
- Conduit Tube - 300 SS tube, custom formed and internally polished
- Belleville Spring - BeCu heat treated
- Cover - Lexan Polycarbonate
- Ferrule - PEEK Victrex 450G
- Nut & Key Pin - 6AL-4V Titanium
- Back Plate - 7075-T7351 Aluminum w/black hard-coat anodize
- Shaft - 7075-T7351 Aluminum w/black hard-coat anodize

### **Testing**

Comprehensive full deployment testing and powered stowage of each 57-meter SDP Boom is conducted at several junctures during flight integration and testing resulting in a minimum of 4 complete deployments and stowage operations. Developmental testing for life assessment was conducted on the flight-like Engineering Qualification Model which demonstrated 14 complete deployments and powered stowages, ensuring adequate margin over flight for the Metering Wheel-Wire Track deployment mechanism.

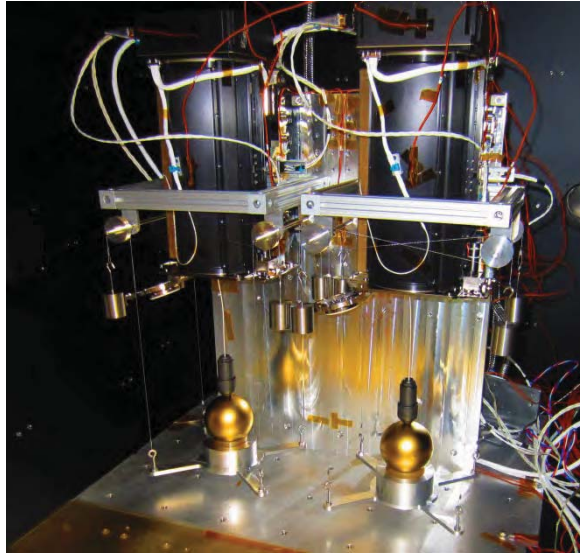


**Figure 9. MMS Flight Model SDP deployment testing, UNH vacuum chamber**

### **Conclusions**

The successful integration, test and delivery of the 16 MMS SDP instruments validated this unique approach to Wire Boom Deployer design. The integral Wire Track springs allowed quantification of the load in the track, and the Metering Wheel un-coiling rotation allowed the use of stationary storage cylinders and fixed electrical terminations.



**Figure 10. Flight Model MMS SDP instruments, fixed Wire Boom Termination at left**

## References

1. Göran Olsson, Royal Institute of Technology (KTH), "SCALE-UP Wire Boom Deployment Mechanism, Stockholm 2007"
2. Per-Arne Lindqvist, Royal Institute of Technology (KTH), "MMS SDP Wire Boom Deployment Plan" (15 February 2008)
3. M.F. Spotts, Design of Machine Elements, 5<sup>th</sup> Edition, Chapters 1 & 6 Section 9. Band Brake
4. Victrex PEEK Material Properties Guide, Table 2 & Figure 30 450G
5. Victrex PEEK Material Properties Guide, Figure 14, 450G plot
6. Ivan Dors, Garrett Roy, "EM SDP CTE Measurement Summary Revised," (28 September 2010)
7. H. Bertilsson, Habia Cable specification drawing 700016945 (2010-03-11)
8. B. King, UNH Project Manager, Habia Inspection Log, (26 October 2011)
9. NASA Reference Publication 1124, Outgassing Data for Selecting Spacecraft Materials



# Development of Cryogenic Filter Wheels for the HERSCHEL Photodetector Array Camera & Spectrometer (PACS)

Christian Körner\*, Dirk Kampf\*, Albrecht Poglitsch\*\*, Josef Schubert\*\*, U. Ruppert<sup>†</sup> and M. Schoele<sup>†</sup>

## Abstract

This paper describes the two PACS Filter Wheels that are direct-drive rotational mechanisms operated at a temperature below 5K inside the PACS focal plane unit of the Herschel Satellite. The purpose of the mechanisms is to switch between filters. The rotation axis is pivoted to the support structure via a slightly preloaded pair of ball bearings and driven by a Cryotorquer [1]. Position sensing is realized by a pair of Hall effect sensors. Powerless positioning at the filter positions is achieved by a magnetic ratchet system. The key technologies are the Cryotorquer design and the magnetic ratchet design in the low temperature range. Furthermore, we will report on lessons learned during the development and qualification of the mechanism and the paint.

## Introduction and Requirements

HERSCHEL is an ESA Cornerstone mission to study the origin and evolution of stars and galaxies. Three cryogenic instruments are accommodated in the focal plane of the Herschel telescope: HIFI, SPIRE and PACS. The giant infrared space observatory was launched on 14 May 2009 on an Ariane 5 and successfully operated in an orbit around L2 until end of April 2013, when the cryostat ran out of liquid helium coolant. The PACS instrument operates either as an imaging photometer or an integral field spectrometer over the spectral band from 57 to 210  $\mu\text{m}$ . Inside the PACS instrument, several mechanisms are accommodated: a Chopper to switch between the sky field of view and internal calibration sources, a Grating Drive to scan through the spectral band, and two Filter Wheels to select spectral bands for the observation which are subject of this paper. The main requirements for the Filter Wheels are listed in Table 1.

**Table 1: Filter Wheel Main Requirements**

	<b>Requirement</b>
Mass	Max. 1000 g
Quasi-static load	25g
No of revolutions incl. ground test and ECSS margins (qualification @ LHe)	40000
Operational temperature range	1K...350K
Amount of Filters	2 (initially 4)
Switching time (180°)	5 sec
Powerless position preservation	$\pm 30$ arcmin (0.5 Ncm @3°)
Stray light reduction (on instrument level)	$10^8$
Power dissipation 4K level:	50 mWs per switching

---

\* Kayser-Threde GmbH, Munich, Germany

\*\* Max Plank Institut für extraterrestrische Physik, Garching, Germany

<sup>†</sup> Freie Universität Berlin, Berlin, Germany

## Accommodation

In order to reduce the amount of sliding, rolling or flexing parts and due to mechanical and optical envelope reasons, a rotating system with a rotating cone supporting the filters was selected. The bearings are accommodated around the center of gravity of the rotating mass. The rotor of the Filter Wheel drive acts as a counterweight to the mass of the Filter Wheel and filters. To keep the wheel assembly compact, the position sensors and the magnetic ratchet system are accommodated in one plane with the lower bearing. The Filter Wheel drive, which was provided by FU Berlin, consists of a two-part rotor equipped with two sets of permanent magnets on both sides of the coils and a stator that is located between the magnets of the rotor and carries the windings (see Figure 6).

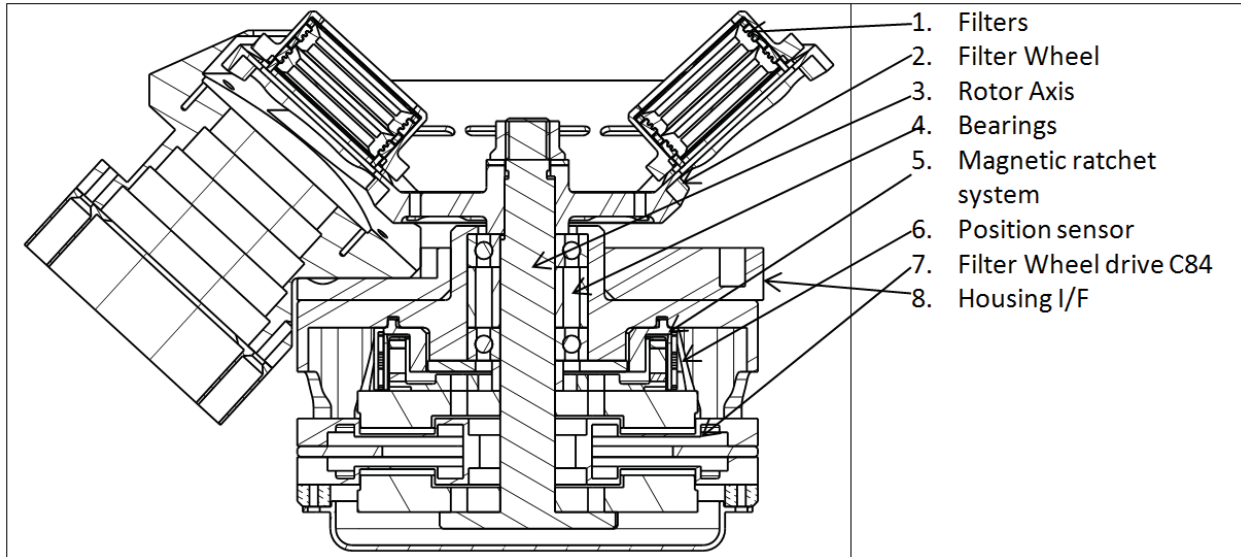


Figure 1. Filter wheel configuration

## Bearing system

The bearing is located in between the filters and the rotor of the motor. This allows a counterweighted configuration of the movable parts. The Filter Wheel with all the rotating parts (Cryotorquer Rotor, Wheel cone, Filters Axis...) has a mass of <600 g. The maximum quasi-static acceleration (derived from the Instrument FEM) is 26 g. To avoid gapping of the bearing, a preload of 126 N would have to be applied. But since the wheel shall be optimized to run with low power dissipation (50 mWs per switching), the preload is reduced to a minimum and the higher amplification and friction (during vibration) in the bearing is taken into account by a higher load capability. The selected bearing configuration is an O-configuration of two GRW SS6900 Z C10/15 GPR-1 J ball bearings.

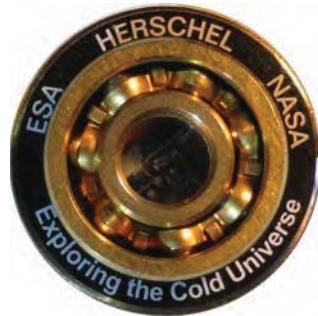


Figure 2. Gold-lubricated GRW SS6900 Z C10/15 GPR-1 J Ball bearing

Each of these bearings has 1130-N static load capability, which is assumed to be sufficient taking into account that the bearing adds damping due to friction (2% damping assumed). The low temperature forces the choice of a solid film lubrication. In order to avoid sensitivity to moisture, gold is selected. Gold lubrication shows a temperature and humidity independent behavior and is acceptable for this application due to the low number of revolutions.

Axial fit: To keep the preload constant over a temperature range of 300K, the bearings and the distance rings (which adjust the preload) have to be made out of the same material (or at least material with the same CTE). These distance rings are shimmed with precision shims to adjust a friction torque below 5 mN-m.

Radial fit: The housing material and all other parts of the PACS structure and mirrors are made of aluminum AA6061 in order to have an instrument that can be aligned at 293K and operated at 4K. The fitting of the bearing diameter therefore has to take into account the relative shrinkage between stainless steel and aluminum in the temperature range between 290K and 4K. The shrinkage can be approximated as a 5<sup>th</sup> order polynomial equation.

Polynomial equation for the temperature-dependent CTE (NIST) for Aluminium and Steel

$$a_{Al} := -4.1272 \cdot 10^{-2} \quad b_{Al} := -3.064 \cdot 10^{-1} \quad c_{Al} := 8.796 \cdot 10^{-3} \quad d_{Al} := -1.0055 \cdot 10^{-5} \quad T_{min} := 4$$

$$L_{293} := 22 \quad \text{Bearing outer Diameter @ 293K}$$

$$L_{AlT} := \left( a_{Al} + b_{Al} \cdot T_{min} + c_{Al} \cdot T_{min}^2 + d_{Al} \cdot T_{min}^3 \right) \cdot 10^{-5} \cdot L_{293} + L_{293}$$

$$L_{AlT} = 21.909 \quad \text{Housing Diameter @ 4K}$$

$$a_{SS} := -2.9546 \cdot 10^{-2} \quad b_{SS} := -4.0518 \cdot 10^{-1} \quad c_{SS} := 8.796 \cdot 10^{-3} \quad d_{SS} := -1.0055 \cdot 10^{-5}$$

$$e_{SS} := 1.8780 \cdot 10^{-8}$$

$$L_{SST} := \left( a_{SS} + b_{SS} \cdot T_{min} + c_{SS} \cdot T_{min}^2 + d_{SS} \cdot T_{min}^3 + e_{SS} \cdot T_{min}^4 \right) \cdot 10^{-5} \cdot L_{293} + L_{293}$$

$$L_{SST} = 21.935 \quad \text{Bearing Diameter @ 4K}$$

$$\Delta l := L_{SST} - L_{AlT} \quad \Delta l = 0.026 \quad \text{Differential shrinkage 293K...4K}$$

Therefore, the fitting diameter of the ball bearing housing is 26 μm larger in order to compensate for the shrinkage.

### Position Device

To ensure powerless positioning at the filter positions, the Filter Wheel is equipped with a magnetic position device. The setup of the magnetic position device (90°) is sketched in Figure 3.

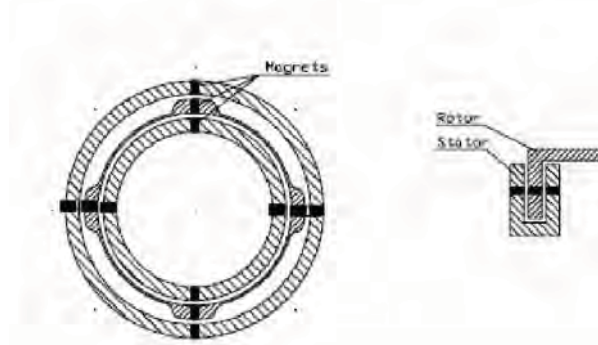


**Figure3. Locking system schematic**

By design, the Filter Wheel is balanced. Therefore, under gravity there are only extremely low torques (<1 mN-m) due to backdriving moments due to eccentricity or residual magnetic fields. In space, there will be almost no backdriving moment at all. The bearing friction cannot be assumed as a powerless positioning device. Therefore, a magnetic ratchet system was implemented. The torque of the actuator is linear to the current but the Ohmic power consumption goes with the second power of the current. Therefore, the ratchet torque is set to a low level (10 mN-m which is roughly twice the max friction). This value adds the functionality of automatic centering (without ECSS margins). The implemented solution is a set of 3 SmCo magnets in series where the middle one is mounted to the rotor. This configuration is repeated in a 90° pattern. To achieve the requested torque, SmCo magnets with a diameter of 1.5 mm and a length of 3 mm were selected.

### Position Sensor

In order to keep the dissipation in the system low and to increase reliability, the position sensor is implemented using contactless technology. The position sensing is performed by Hall effect sensors that detect the magnetic field of magnets mounted on the rotor.

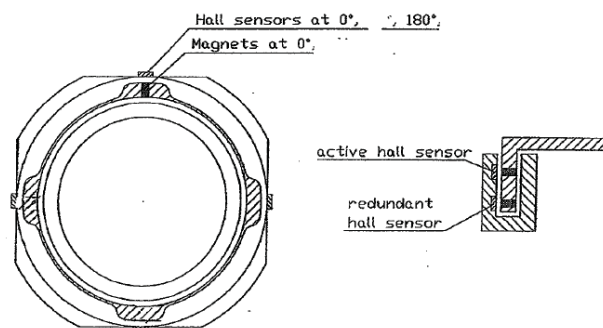


**Figure 4. Decoder system schematic**

The selection of the sensor is based on the following parameters: operating temperature range, low dissipation, and linearity. To work at the temperature range of 4.2K the Infineon ion-implanted GaAs hall generator KSY 10 was selected. The hall current was set from 7 mA to 0.75 mA, which reduces the hall voltage from 200 mV to ~20 mV. This is sufficient to detect the position with an accuracy better 10 arcmin

at the instrument level but at the same time reduces the power dissipation by a factor of 10. The dissipated power at 4.2K for a 180° switch is then:

$$0.85 \text{ mW} * 2 \text{ (positions nominal)} * 5 \text{ sec (switching time)} = 8.5 \text{ mWs.}$$

For this application, the SmCo magnets from the position device (dia.1.5 mm\*3 mm) are reused. Note: For the actual 90° ratchet system (double magnets) the torque has to be doubled.

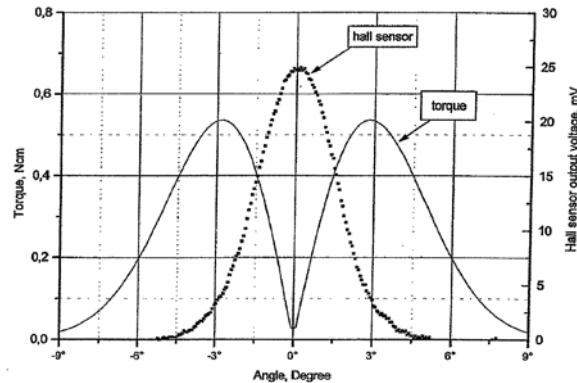


**Figure 5. Absolute value of the Hall sensor signal and the restoring torque for a 180° magnetic ratchet system**

### Actuator

In this application, the driving parameter for the sizing of the motor is not the motorization (as usual in space mechanisms), but power/heat dissipation since the lifetime of the mission is dependent on the dissipation inside the cryostat. In general, dissipation is minimized when the efficiency of the motor is high, friction is minimized, and the motor inertia and the actuated inertia are approximately equal. The Filter Wheel rotating parts have an inertia of ~0.1 g-m<sup>2</sup>; this fits into an already existing Cryotorquer developed by the FU Berlin (C 84) \*\* with an inertia of 0.12 g-m<sup>2</sup>. This Cryotorquer has also a high efficiency for slow rotating torque applications at low temperature. In addition, this Cryotorquer has heritage from several low temperature space projects. Therefore, this Cryotorquer was selected.

The pancake-shaped electronically commutated torque motor C84 developed by the FU Berlin is described in Figure 6.

The rotor consists of a package of alternating SmCo magnets on both sides of the coils (stator) that allows a comparable high air gap (0.5 mm) without decreasing performance. The magnetic loops are closed by means of the yoke rings made of good permeability material for low temperatures. The stator is composed of two redundant coil packages and each consists of one set of coils for phase 1 and a second set for phase 2. In normal operation, the two coil sets for each phase are interconnected. The current for each phase is supplied by the corresponding power source of the electronic control unit.

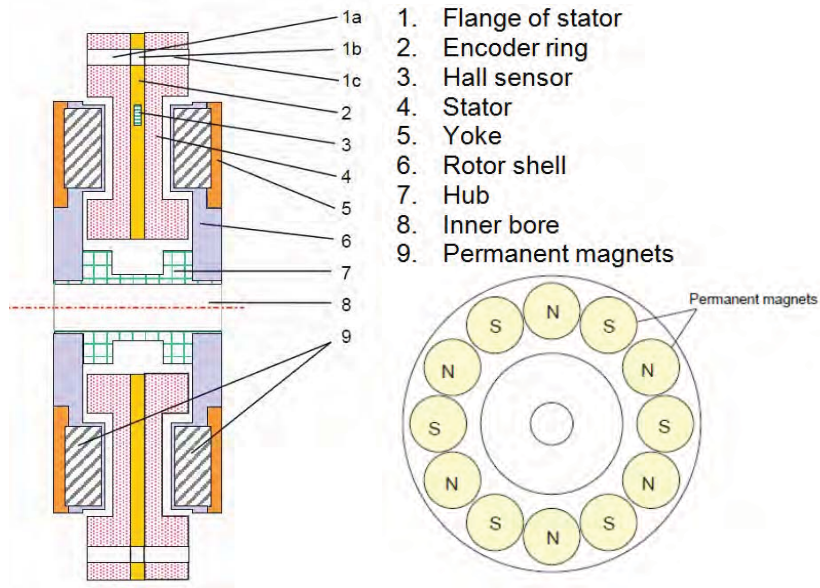


Figure 6. Schematic cross section of the Cryotorquer C 84 developed by FU Berlin

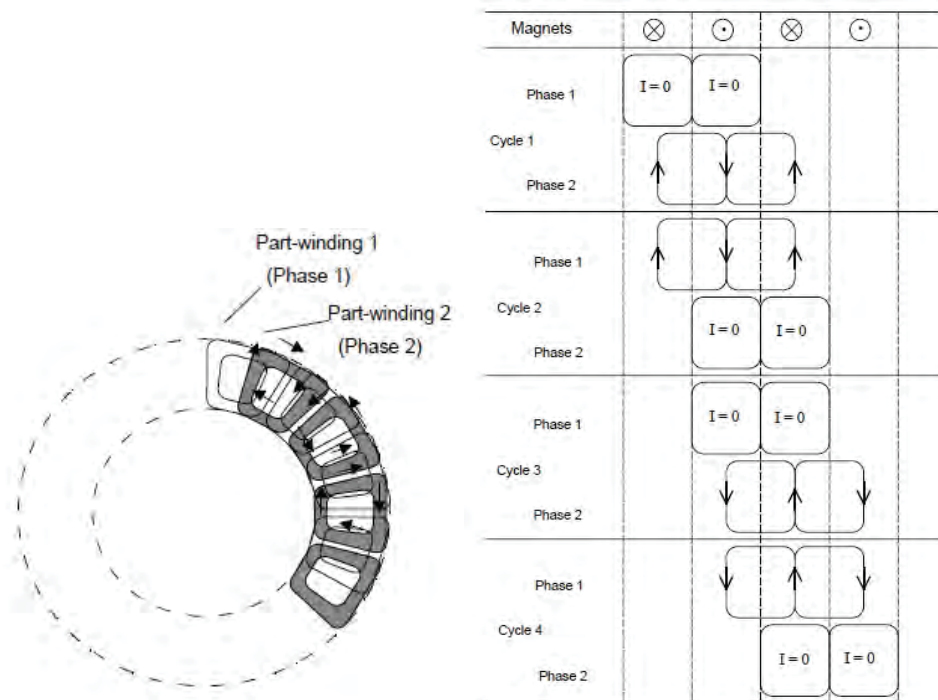


Figure 7. Position of the coil-sets of the two phase indicating the 15° angle shift of the two sets and an example for the current vectors of the two phases.

The torque capability of the motor at 250 mA is 142 N-mm. The maximum torque needed is 5 mN-m for the friction and 10 mN-m for the positioning device.



Worst case dissipation for 180° movement

$$\text{Current}_{\text{max}} := 27\text{mA}$$

$$T_{\text{switch}} := 5\text{s}$$

$$\text{Resistance}_{4k} := 3.6\Omega$$

$$P_{\text{max}} := (\text{Current}_{\text{max}})^2 \cdot \text{Resistance}_{4k}$$

$$P_{\text{max}} = 2.6 \times 10^{-3} \cdot \text{W}$$

$$k_m := 0.3 \frac{\text{N}\cdot\text{m}}{\sqrt{\text{W}}}$$

$$\text{Torque} := k_m \cdot \sqrt{P_{\text{max}}}$$

$$\text{Torque} = 0.015 \cdot \text{N}\cdot\text{m}$$

$$\text{Dis} := P_{\text{max}} \cdot T_{\text{switch}}$$

$$\text{Dis} = 13 \text{mW}\cdot\text{s}$$

### Development of the Coating

In order to achieve the demanding stray light reduction requirements, a new coating had to be developed since there is no coating commercially available that reduces the stray light at a wavelength of 57 to 200  $\mu\text{m}$  significantly. Therefore, KT has developed a coating (KT-72) which is indeed highly effective with respect to stray light reduction but at the same time bears some risks for the mechanisms.

In order to have reasonable stray light reduction, the effect of black paint in the optical path in the coating has to be of the order of magnitude of the wavelength or higher. The thickness of the paint inside the PACS instrument was therefore set in the range of 400 to 500  $\mu\text{m}$ , which is far away from the thickness of standard paints. In addition, the coating includes glass beads in order to change the direction of the light path into the plane of the coating.

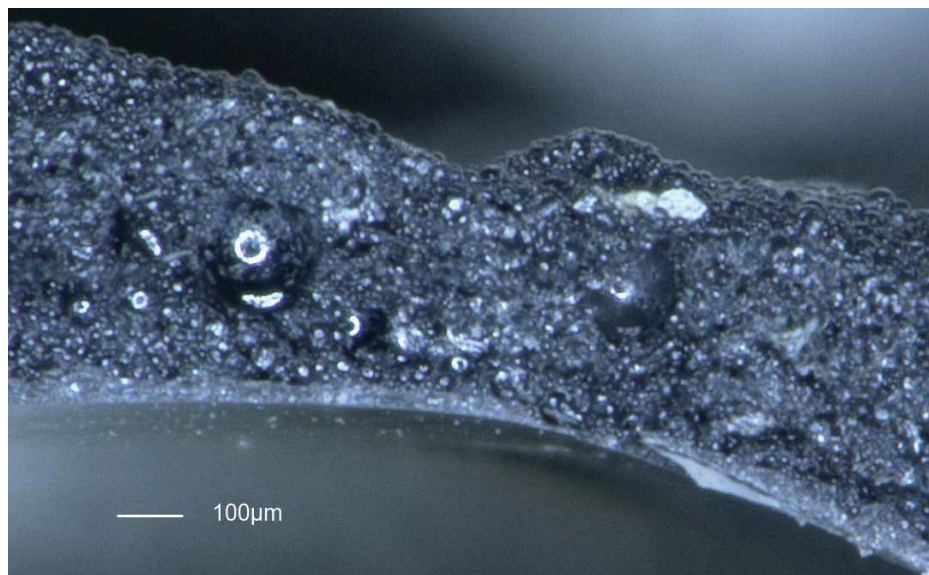


**Figure 8. Cut through a KT-72 sample.**

During the development of the coating, two effects drove the development, the delta CTE of the materials and the aerodynamic configuration.

The delta CTE of Paint ( $\sim 40\text{e-}6$ ) / Glass (6-) and Aluminum (14) (Housing) and a temperature gradient of 400K (bake out) to 4K leads to high stresses in the paint and between the coating and the base material,

which is at the limit of feasibility. Therefore, the connection between the different layers had to be optimized. One major parameter is time. The time-dependent oxidation and the contamination between the layers avoid a perfect adhesion. ALODINE is known as a very good surface to apply coatings. But for our coating, this turned out to be only sufficient when the coating was applied within 48 hours after ALODINE application. After this period, a reactivation of the surface became necessary.

First tests were made with flat samples. But this turned out to be not sufficient since the aerodynamic configuration of the parts have an influence to the distribution between large and heavy particles and paint  $\mu$ -particles. Therefore the result varies with the geometrical setup. The complex setup of the instrument did not allow a flat configuration of coating application. Therefore, KT did not change the source of the contamination but the effect.

The surfaces that had a “bad shape” and contained loose particles were “brushed” with a conventional electrical toothbrush. All parts were cleaned with a clean room vacuum cleaner.

### **Test Results**

The following development tests were performed by the FU Berlin:

- Vibration tests at 4.2K (sine search, sine, random)
- Functional and performance tests at 4.2K after vibration tests

For the tests at 4.2K, the Filter Wheel was placed in a sealed container.



**Figure 9. PACS FW in the sealed vibration adapter**

In Figure 10, the test results before and after the vibration tests are shown.

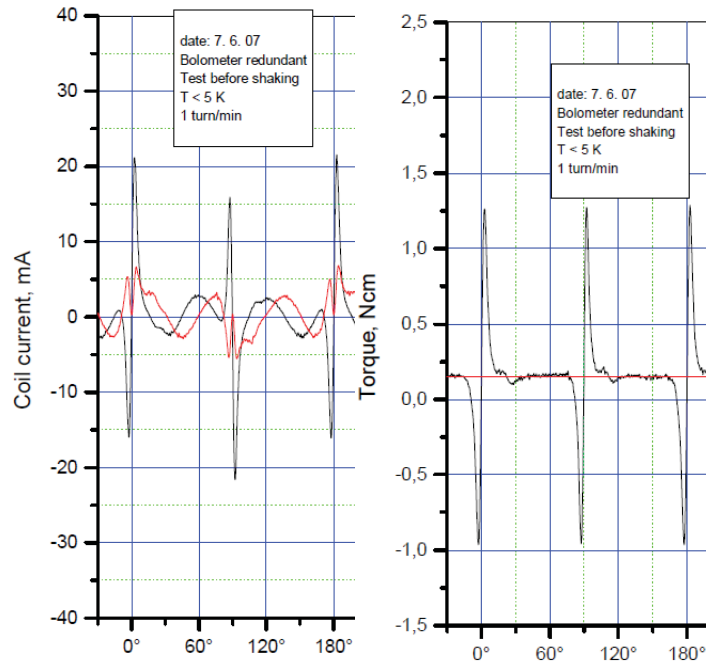


**Figure 10. Current (winding 1+2) and torque of the two redundant coils before vibration**

The functional test of the Filter Wheel shows very smooth rotation with 1.8 mN-m average torque. The high spikes ( $\pm 12$  mN-m) are due to the magnetic ratchet system

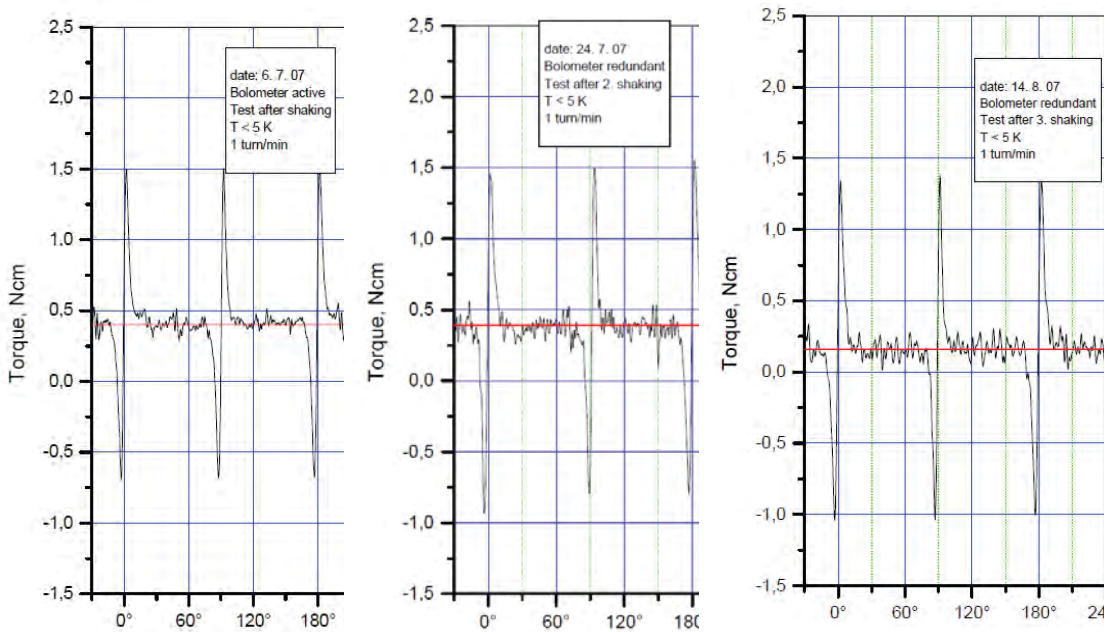


**Figure 11. Torque after vibration tests**

The first graph in Figure 11 shows the torque after the 0.5g sine search between 5 and 2000 Hz at 4.2K. The torque increased to 4 mN-m with a ripple of 1 mN-m. The second graph in Figure 11 shows the torque after the full sine vibration between 5 and 100 Hz with 19.8g max acceleration. The torque is

slightly decreased to 3.8 mN-m with a ripple of 1 mN-m. Torque after random vibration with 7.3g RMS → lower average torque but ~1.5 mN-m ripple.

The lifetime test at 4K (40000 start stop cycles) showed no increase in torque.

A failure of the Filter Wheel mechanism occurred during ground-testing of the flight spare instrument. While this failure (clamping) could be explained by exceeded manufacturing tolerances and recovered by shimming, it was nevertheless decided at instrument level to increase the motor current to gain a higher safety margin for the on-orbit operation.

### Flight Data

Over the whole mission (4 years in orbit and 2 years on ground) no failure occurred. The temperature over the whole in-orbit lifetime was stable at 2.92K. The wheel was driven with constant current sine of 70 mA which generates a torque of 56 mN-m for the nominal windings, a value which is considered as necessary and sufficient to overcome the bearing friction.

The photometer Filter Wheel performed ~6000 rotations the spectrometer Filter Wheel ~3000. The flight data we received for the evaluation are the Spectrometer Filter Wheel data from BOL (2009) and EOL (20013), which are shown hereafter.

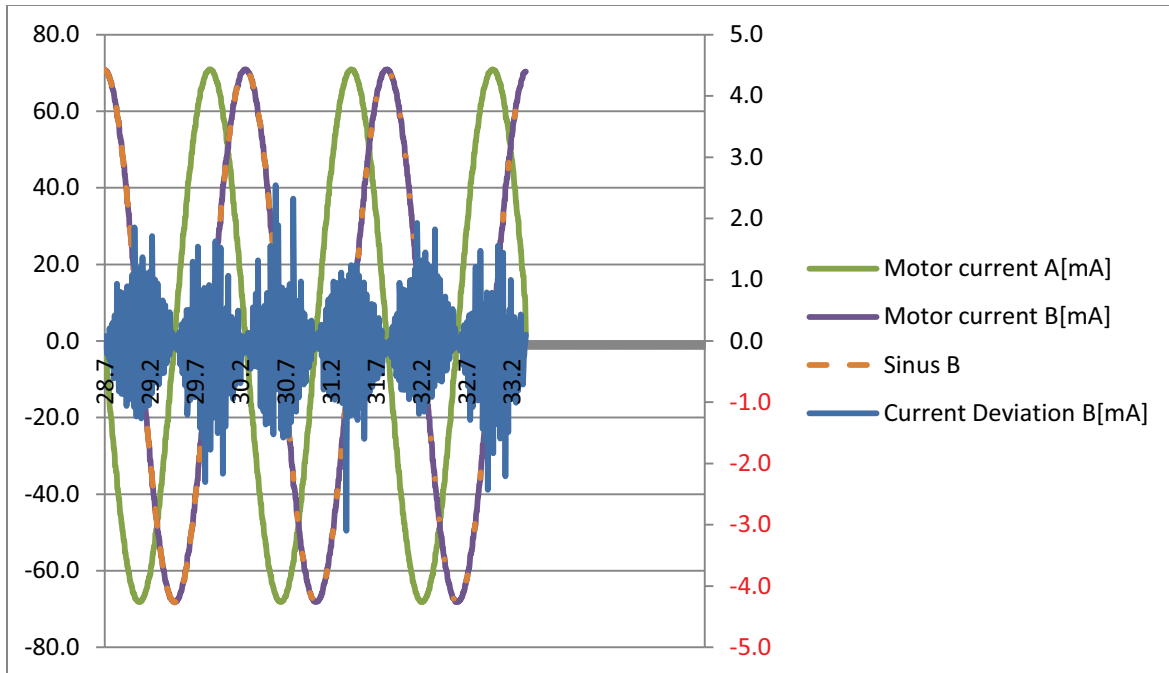


**Figure 12. Current and ripple of the nominal coils during flight**

The magnetic field readout of the motor hall sensors shows the smooth movement with no significant change between BOL and EOL. Since the Filter Wheels operated inconspicuously there are only very few high-speed data records from the operation of the wheels.

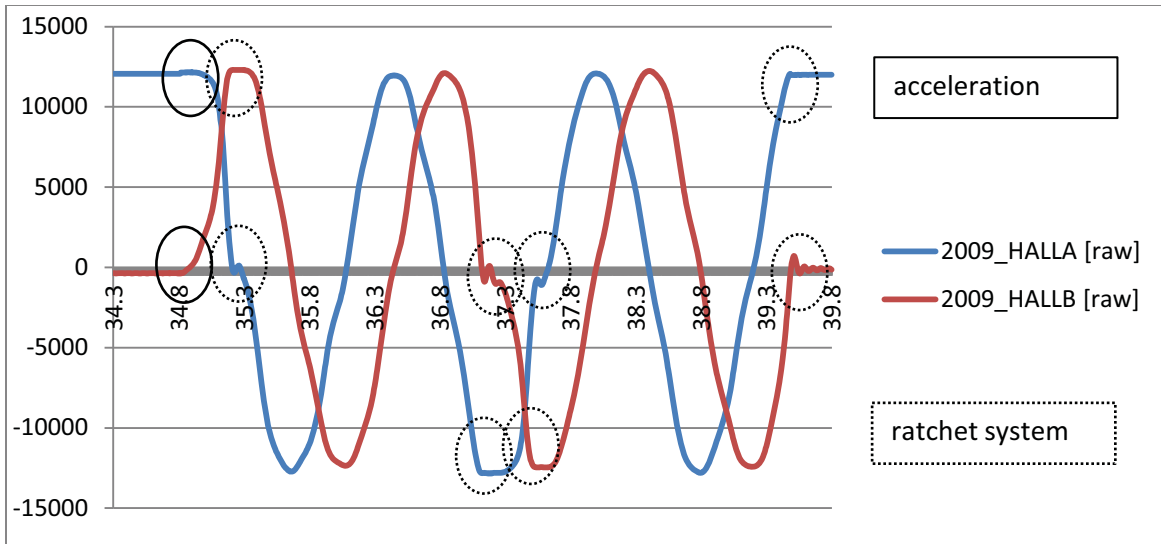


Figure 13. Signal of motor Hall sensors during commissioning

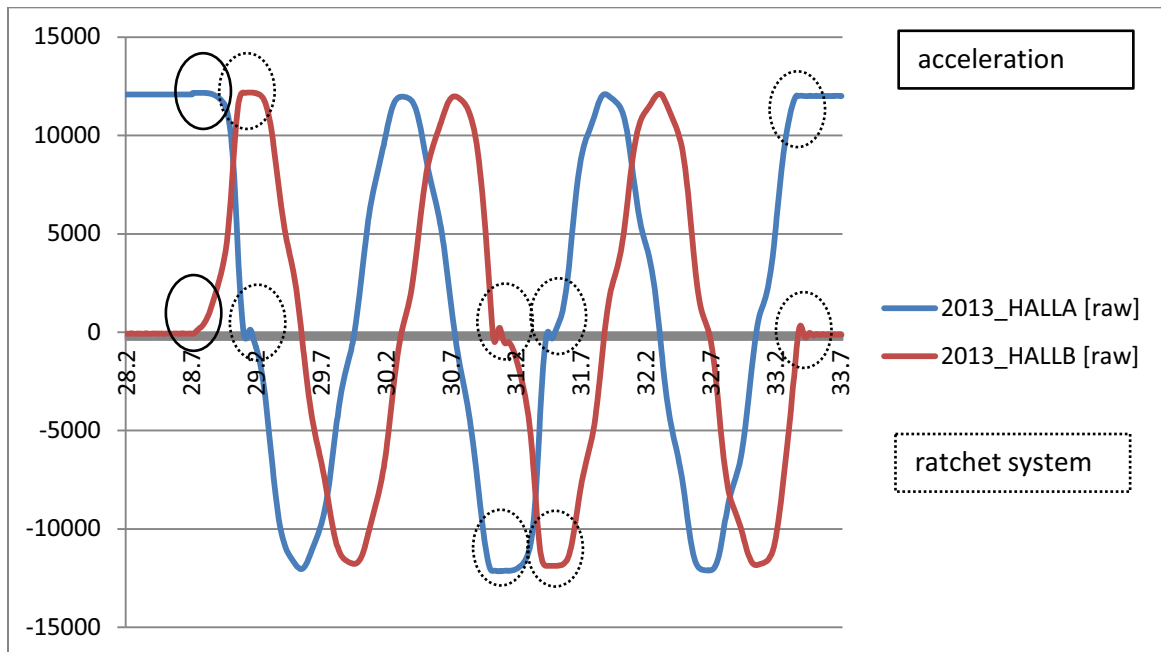


Figure 14. Signal of motor Hall sensors at end of life

### Conclusions and Lessons Learned

The development of the PACS Filter Wheels was successful and the two flight models performed well in the Herschel program. The usage of an already existing and proven cryotorquer eased the development. Also the contactless ratchet system and the contactless sensors were very predictable and reliable. Only the bearing showed some degradation during the vibration tests. The torque ripple increased to 1.5 mN-m and the overall torque showed some unpredictable variation after the vibration tests. In order to avoid such a variation, the complete bearing should be suspended in a setup where all CTE's are

matched to the bearing CTE. This homogeneous thermal shrinking setup was then isostatically mounted against the housing.

In addition, a deviation from the specified manufacturing tolerances in the flight spare model has led to a clamping in the flight spare mechanism that could be recovered by additional shimming.

The development of the paint was the highest risk for the function of the Filter Wheels since one of the 100- $\mu\text{m}$  glass beads could destroy a ball bearing and thus stop the Filter Wheel. The huge effort that was put into the development of the coating has paid off.

### **References**

1. M. Schoele, U. Ruppert,  
"CRYOGENIC MOTORS FOR HERSCHEL/PACS AND JAMES WEBB/MIRI AND NIRSPEC"  
FUB (Freie Universität Berlin), Department of Physics, Low Temperature Laboratory, Arnimallee  
14, 14195 Berlin, Germany



# Development and Preliminary Testing of a High Precision Long Stroke Slit Change Mechanism for the SPICE Instrument

Gabriel Paciotti\*, Martin Humphries\*\*, Fabrice Rottmeier\* and Luc Blecha\*

## Abstract

In the frame of ESA's Solar Orbiter scientific mission, Almatech has been selected to design, develop and test the Slit Change Mechanism of the SPICE (SPECTral Imaging of the Coronal Environment) instrument. In order to guaranty optical cleanliness level while fulfilling stringent positioning accuracies and repeatability requirements for slit positioning in the optical path of the instrument, a linear guiding system based on a double flexible blade arrangement has been selected. The four different slits to be used for the SPICE instrument resulted in a total stroke of 16.5 mm in this linear slit changer arrangement.

The combination of long stroke and high precision positioning requirements has been identified as the main design challenge to be validated through breadboard models testing. This paper presents the development of SPICE's Slit Change Mechanism (SCM) and the two-step validation tests successfully performed on breadboard models of its flexible blade support system.

## Introduction

While classical space mechanism design for significant displacements are generally based on linear or rotational sliding contact guiding systems, the optical cleanliness requirements of the SPICE instrument has channelled the selection of a flexible guiding system for supporting the slit changer inside the optical cavity, and the use of an actuation mechanism hermetically separated from it. Rotational slit changers concepts have been investigated and rejected due to the need of sliding contact feedthroughs, the presence of unwanted total optical obscuration of the instrument during slit changes, the elevated angular resolution to meet the position accuracy, and/or general geometrical constraints.

The selected linear Slit Change Mechanism design is presented in Figure 1. The slit carrier is supported by a pair of parallel metallic blades held by an external frame. The linear actuator design, separated by a hermetic metallic bellows assembly from the optical chamber, consists of the combination of a stepper motor and a satellite roller screw reduction drive. The mechanical link between the suspended slit assembly and the actuator is provided by a compliant rod connection.

The required total stroke of the linear actuator is 16.5 mm for the positioning of four different slits in the instrument's line of sight, requiring a highly flexible blade system for precise guiding over the full displacement range of the slit carrier. The requirement on the maximum induced translational and rotational inaccuracies, as well as their repeatability over life, are summarized in Table 2. The most demanding requirement is the positioning of the slit on the beam axis of the instrument (in X and Y) and the rotation around the Y-axis with the corresponding repeatability.

Considering these highly demanding performances to be demonstrated over 54000 cycles, a two-step breadboard model validation test program has been initiated before full SCM mechanism validation at qualification level.

---

\* Almatech, EPFL – Innovation Park, Lausanne, Switzerland

\*\* SpaceMech Ltd., Westbury-on-Trym, Bristol, U.K.

**Table 1. Contamination requirements for the SCM mechanism**

Contamination Type	Unit	Inside optical cavity	Outside optical cavity
Particulate (PAC)	ppm	30	100
Molecular (MOC)	ng/cm <sup>2</sup>	50	100

**Table 2. Positioning accuracy and repeatability requirements over 16.5-mm Z-displacement**

Direction	Positioning accuracy	Repeatability
X translation	±10 µm	±5 µm
Y translation	±50 µm	±3 µm
Z translation	±80 µm	±30 µm
Rotation around X	±5 arcmin	±30 arcsec
Rotation around Y	±50 arcsec	±25 arcsec
Rotation around Z	±10 arcmin	±5 arcmin

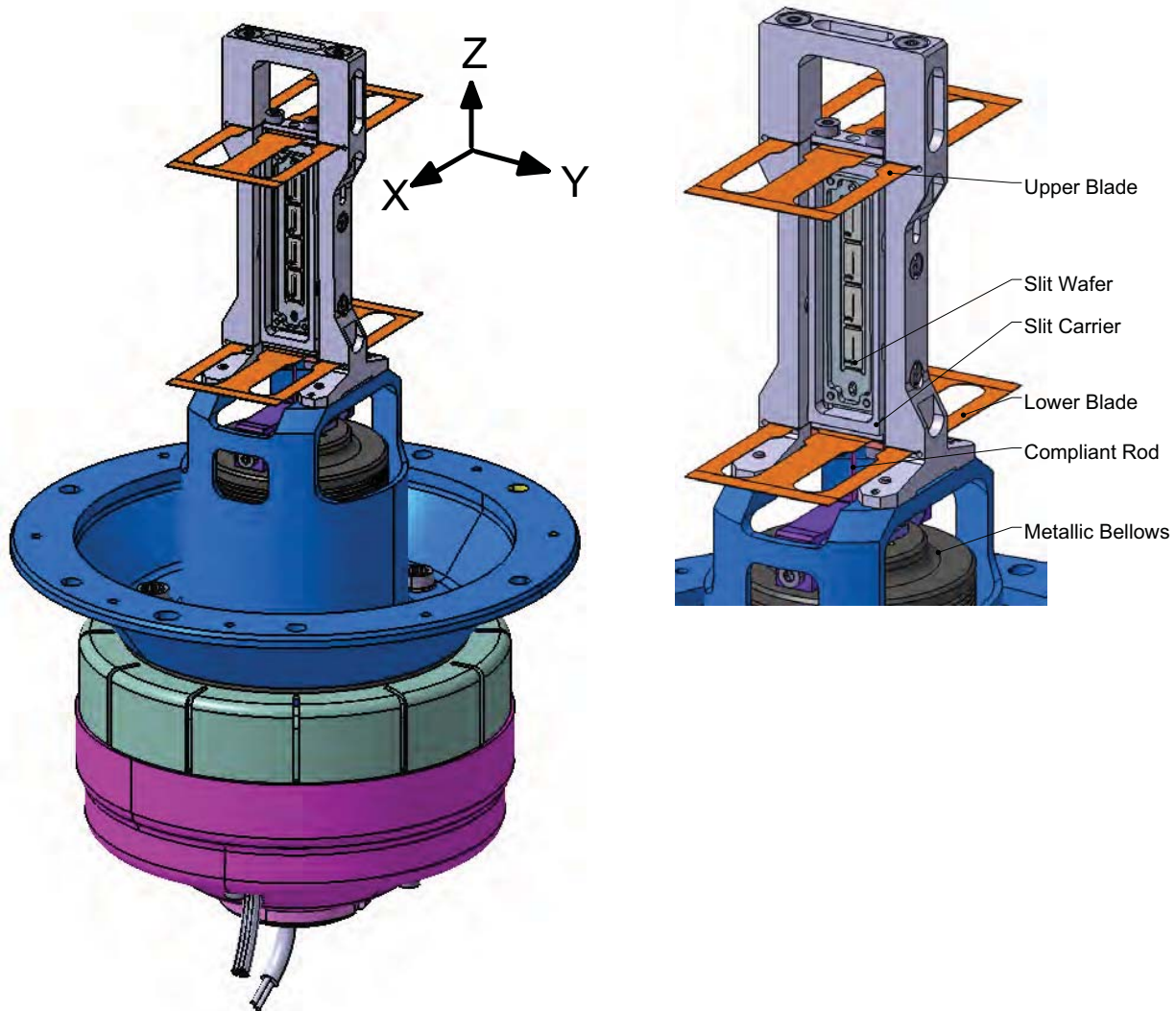


**Figure 1. Linear Slit Change Mechanism design**

## Flexible Guiding System Design

The flexible guiding system of the slit carrier is provided by a parallel blade arrangement illustrated in Figure 1. With no relative motion between contacting parts, the blade arrangement is free of any friction or wear as well as need for lubrication. Consequently, it inherently prevents the generation of particles or contaminants, one of the main design drivers with respect to the optical cavity cleanliness requirement defined in Table 1. The flexible blades are dimensioned such to limit the deformation stresses and subsequently the creep impact, ensuring the repeatability of the positioning over the full stroke of the slit carrier and operational lifetime.

In order to minimize thermo-elastic deformation-induced positioning inaccuracies over the wide operational thermal environment range of  $-30^{\circ}\text{C}$  to  $+60^{\circ}\text{C}$  of the SCM, all parts structurally supporting the slits from the instrument interface are designed in the same material, which is a titanium alloy.

Each blade is cut out of a thin titanium sheet using a photo-etching process to ensure high precision dimensions, manufacturing tolerances, and reproducibility. This is a key element in the precise guiding of this parallel flexure arrangement since it requires the assembly of several mechanical elements. The manufacturing tolerances of the blade support frame, slit carrier, and provided blade pin-alignment features are additional contributors to the precision guiding functionality of this system. Symmetry, parallelism and alignment of the flexible blades being a major driver in the positioning precision over the relatively long stroke, the characterization of the flex-blade guiding performances over the full stroke has been considered as the first step for the evaluation of the performance of the full mechanism. Initial characterization tests on a representative breadboard model have therefore been integrated in the validation test program of the SCM and are presented in this article.

Considering the importance of launch loads on space structural designs, the main drawback of such a thin blade parallel arrangement is the lateral load carrying capability (X-Y plane). While the presented design was compatible with the initial random specifications, their evolution have led to the integration of slit carrier displacement limiters (snubbers) between the slit carrier and blade support frame. This additional contact-free guiding feature is only provided in the launch configuration (slit 2 active) in order to limit the range of the provided tight clearance of 30 microns (in X & Y) over the axial direction Z. Their dimensioning is such to limit contact stresses and avoid generation of wear particles.

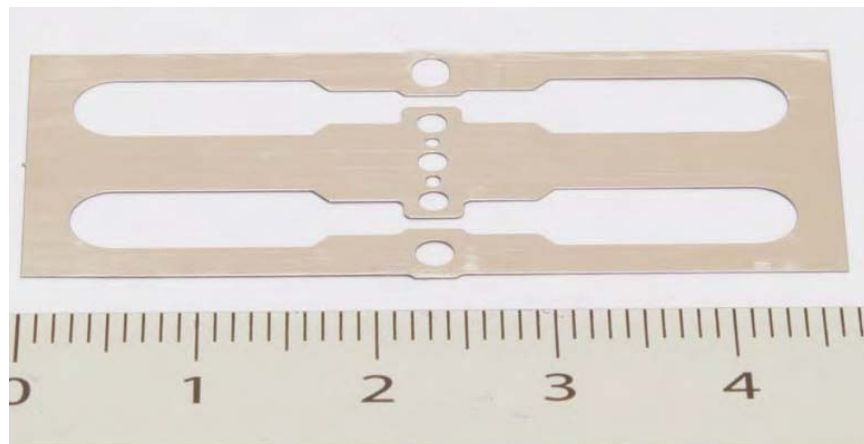


**Figure 2. Titanium alloy flexible blade - scale in cm**

## Compliant Rod Connection Design

In order to meet the slit positioning accuracies for the complete SCM mechanism, the centering and alignment of the linear actuator axis with respect to the flexible guiding system axis is essential over the full design stroke. With the aim of limiting the transfer of alignment perturbations between the linear actuator and the flexible guiding system, a compliant rod connection has been integrated between these mechanical systems. The optimization of the compliant rod design is essential for the minimization of the alignment and repeatability requirements to be imposed on the more complex design of the linear actuator mechanism. For this reason, a sensitivity analysis of the flexible guiding system (including connection rod) to actuator misalignment has been performed using FEM analyses during the initial design phase. These analyses included the consideration of thermal distortion effects, linear and rotational misalignments, as well as residual torque input from the linear actuator and for each of the four nominal slit positioning conditions. The studied misalignment inputs and the combined output inaccuracies are presented in Table 3 and Table 4, respectively. Table 5 presents the minimum reduction factors between the considered perturbations and its outputs on the slit positioning.

**Table 3. Linear actuator perturbation outputs**

Direction	Source	Perturbation
X translation	misalignment	10 $\mu\text{m}$
Y translation	misalignment	10 $\mu\text{m}$
Rotation around X	misalignment	1 arcmin
Rotation around Y	misalignment	1 arcmin
Rotation around Z	misalignment	30 arcmin

**Table 4. Total inaccuracies of slit positioning due to actuator input perturbations and thermal effects (absolute values)**

Direction	Unit	required	Slit 1	Slit 2 active	Slit 3	Slit 4
X translation	$\mu\text{m}$	$\pm 10$	2.04	2.77	3.5	4.22
Y translation	$\mu\text{m}$	$\pm 50$	1.19	1.6	2.01	2.42
Z translation	$\mu\text{m}$	$\pm 80$	30.2	27.9	25.5	23.1
Rotation around X	arcmin	$\pm 5$	0.26	0.26	0.26	0.26
Rotation around Y	arcsec	$\pm 50$	27	27	27	27
Rotation around Z	arcmin	$\pm 10$	0.05	0.06	0.07	0.08

**Table 5. Minimum reduction factor on slit positioning accuracy due to actuator perturbations**

Direction	Reduction factor
X translation	2.37
Y translation	4.13
Rotation around X	3.87
Rotation around Y	2.2
Rotation around Z	392

Note that the maximum displacement values presented in Table 4 are based on a single geometrical configuration consisting of the alignment of slit 2 on the optical axis (active slit), such that the results include the Z-offset of the other slits. Therefore, the lowest slit (slit 4) being the furthest away from the active slit, it presents the maximum absolute inaccuracies values in a worst case approach.

Based on the defined perturbation inputs from the linear actuator, the slit positioning combined responses are all compliant to the required values. More detailed analyses of the FEM model deformation results have shown that the major contribution to the X translation is a slight tilting of the whole blade support frame that has been stiffened in the QM/FM design. The transmission of X and Y misalignment are reduced by a minimum factor of 2.37 from the actuator to the slit positioning as shown in Table 5.

Z displacement inaccuracies are governed by the thermo-elastic behavior along this axis over the wide operational temperature range and the structural path from the SCM mechanical interface to the active slit position for this axis-symmetric mechanism design. All the parts involved in this structural chain are designed in the same material, titanium, such that the Z displacement inaccuracies are easily temperature compensated by the linear actuator control system. Mainly for this purpose, the resolution of the stepper motor driven linear actuator has been set to 5 microns; see the following paragraph for more detailed information on the linear actuator design. The design limitation for the compliant rod is its buckling stability during the dimensioning vibration loads, which provides the limit for the decoupling features of this compliant element.

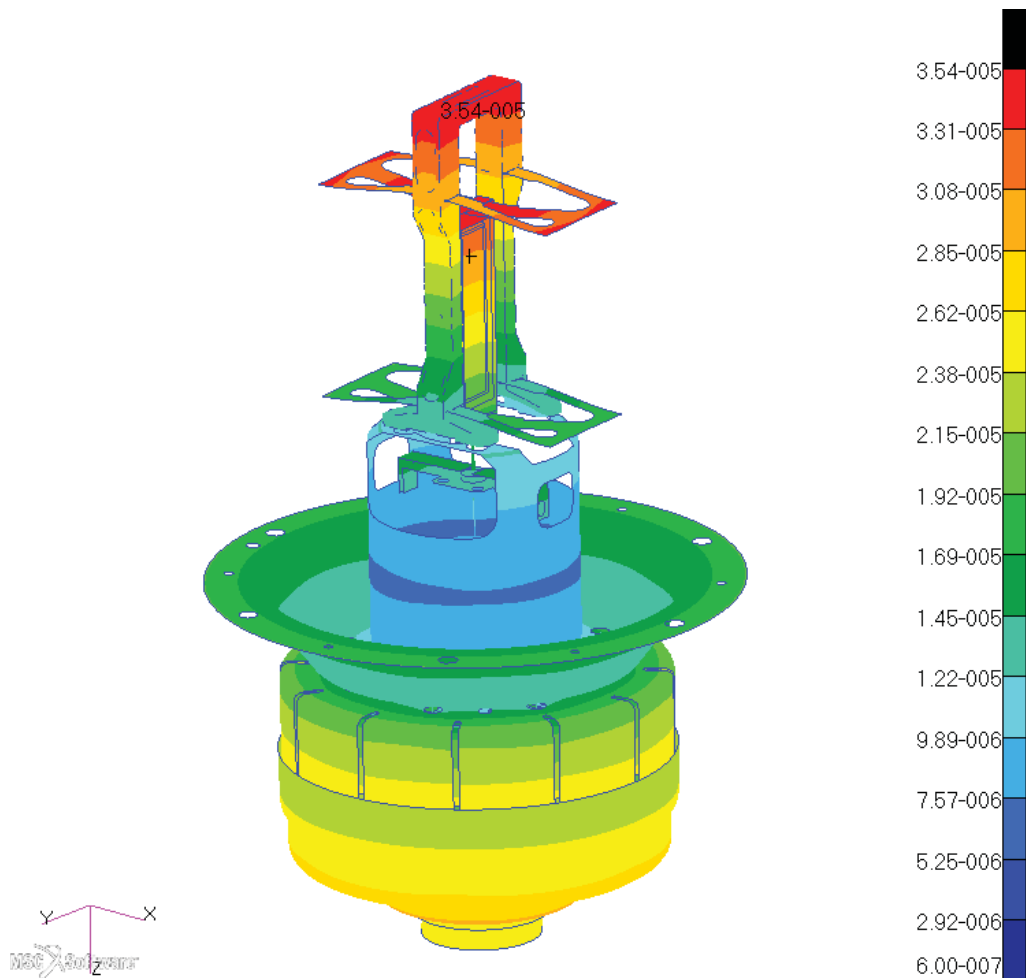


Figure 3. SCM temperature induced displacements from FEM sensitivity analyses over 50K – [m]

## Linear Actuator Design

In order to drive the linear positioning of the suspended slit carrier, a space-qualified low-power and reduced-thickness stepper motor has been selected and combined with a custom-designed satellite roller screw. The soft-preloaded satellite roller screw has been designed by Rollvis SA in close collaboration with Almatech to allow a direct and compact integration of the motor and bearings on the roller screw shaft, targeting the compliance to the required positioning accuracies and repeatability over the design life of the mechanism.

The advantages of a satellite roller screws over ball screw are mainly a higher number of points of contact that distributes the transmitted loads. This allows a higher static and dynamic load capacity, in particular during the launch environment. Moreover, it implies lower wear and longer lifespan which is one of the SCM's main design challenges and selection criteria. Another main advantage of satellite roller screw over ball screw linear drives are that they allow a more compact design. Furthermore, the ability to select at will the pitch of the planetary roller screw independently to available ball sizes has contributed to the advantages of such a solution. Based on the 200 steps per revolutions design of the selected motor, this feature allowed to set the resolution of the linear actuator to 5 microns per motor step, or 1 mm per rotor revolution. Finally, the design of the satellite roller screw dedicated to the SCM allowed the integration of custom mechanical end-stops directly on the non-rotating lead screw.



**Figure 4. Satellite screw design illustration (Courtesy of Rollvis SA)**

With the aim of assessing the guiding accuracy of the lead screw, measurements were performed on commercial off-the-shelf satellite roller screws directly by the manufacturer of this component. These tests have shown that the oscillation of the lead screw around the nut axis is better than  $\pm 5$  microns, confirming the selection of a satellite roller screw driving mechanism for a high precision positioning application such as the SCM. The off-axis error will be further reduced on custom-made systems especially designed for high-precision applications and by the matching of manufactured components resulting in the best final performances results.

The SCM's rotating assembly is supported by a pair of angular contact preloaded ball bearings in face-to-face configuration to lower the angular stiffness of the assembly and allow the integration of the bearing preloading systems on the outer rings.

In order to evaluate the guiding accuracy of the output lead screw of the fully assembled linear actuator and optimize the linear actuator design, a tolerance analysis has been performed. This study included the consideration of the all duplex bearing assembly parameters (type, size, tolerance class, arrangement, groove wobble, bearing seat coaxiality...) and all geometrical uncertainties due to the manufacturing of structural parts supporting the rotating equipment. Sensitivity analyses of these main parameters allowed



an optimization of the design and the definition of manufacturing tolerances for the most critical dimensions.

Figure 5 presents the tolerance analysis results for the baseline design configuration of the linear actuator and includes the roller screw’s radial run-out values based on the maximum measured values on commercial off-the-shelf roller screws. The prediction of the total run-out of the linear actuator lead at its maximum extension is 16.1 microns which can only comply with the X-axis positioning accuracy requirement by considering the lateral decoupling effect of the connection rod (i.e. minimum factor of 2.37 in Table 5). The predicted angular runout results of the lead screw is compliant with the requirements, in particular considering the reduction of the angular deflection due to the connection rod’s bending (minimum factor of 2.2).

In addition to the potential reduction of roller screw radial run-out on the custom SCM version, the static misalignment effect can be reduced by a precise alignment of the flexible guiding system’s axis to the linear actuator control axis. This alignment feature has been integrated in the SCM FM design and corresponding mounting procedures to further enhance the final positioning accuracies. It consists of the alignment, using an optical measuring technique, and high precision shimming of the blade support frame, followed by the clamping of the compliant rod connection. This later being specially designed to avoid the transmission of coupling stress during assembly.

Considering the criticality of the compliant rod connection design on the performances of the SCM’s positioning performances, it has been decided to assess its impact on the flexible guiding system using breadboard validation tests.

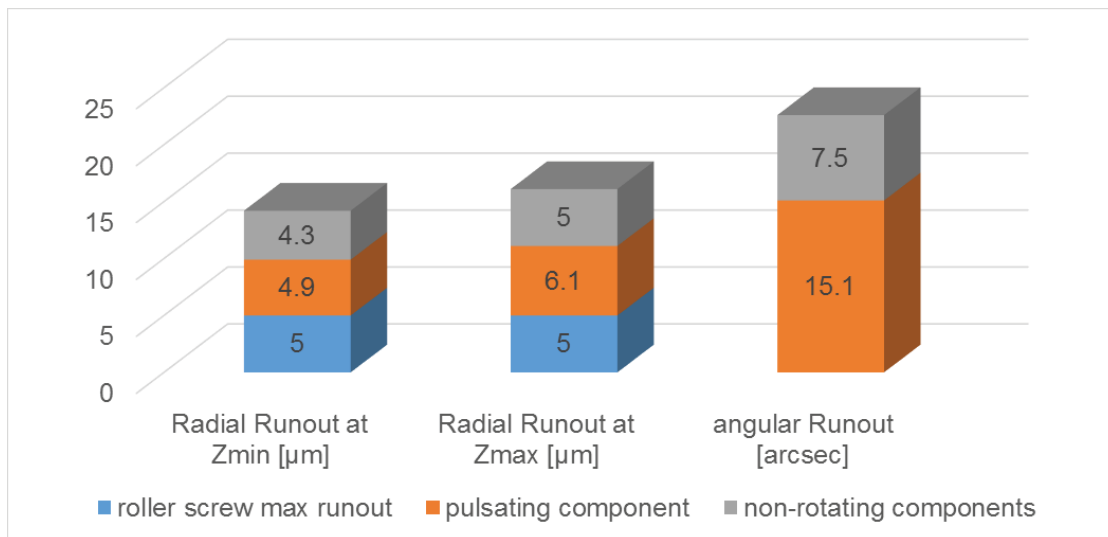


**Figure 5. Final configuration tolerance analysis results**

The positioning control of the SCM (along Z) is performed by step counts of the stepper motor. With the intention of allowing the initialization of the displacement control system, a high-precision switch ( $\pm 1 \mu\text{m}$ ) has been integrated in the SCM. It is triggered by the lower extremity of the lead screw as illustrated in Figure 6 and Figure 7.

Another key design challenge of the linear Slit Change Mechanism being its repeatability over the significant lifetime, careful attention has been given to the lubrication of the bearings and satellite roller screws. With the support of ESTL for the lubrication analyses (and for performing the lubrication of these components), lead lubricated bearings and hybrid lead/grease lubrication have been selected for the satellite roller screw.

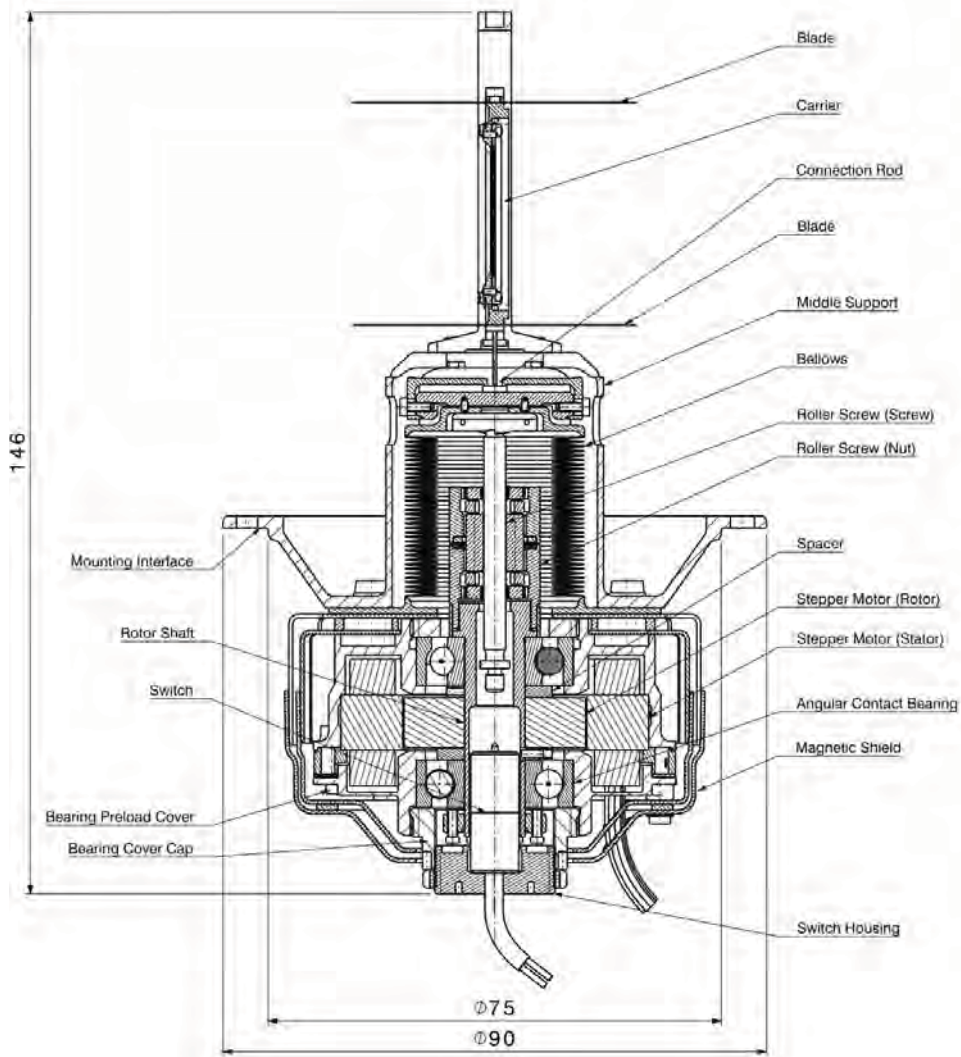


Figure 6. Cut view of the linear Slit Change Mechanism design – dimensions in mm

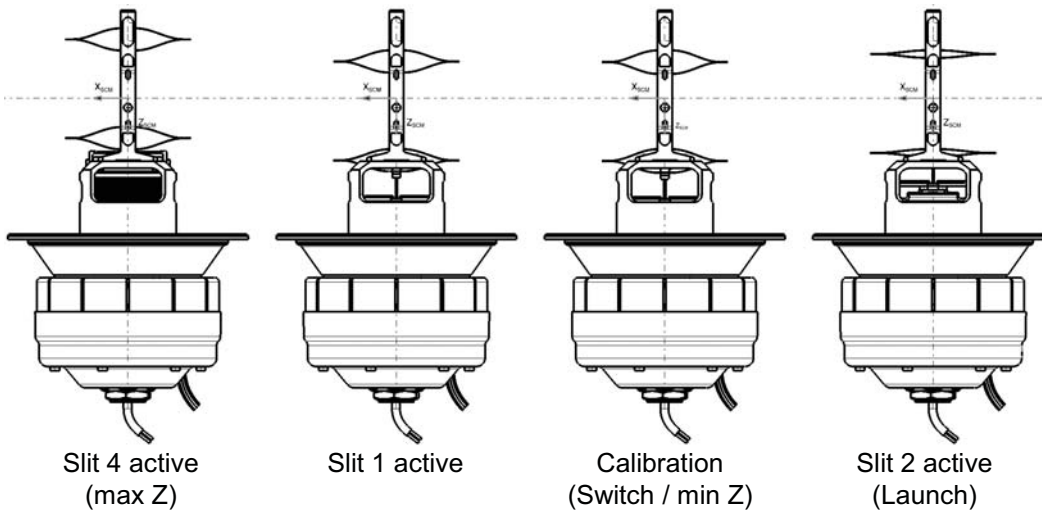


Figure 7. Linear Slit Change Mechanism design – configuration examples

## Validation Test Program

In order to assess the positioning performances of the Slit Change Mechanism in a step by step approach, it has been decided to proceed with the following validation test strategy:

1. Characterization of the flexible guiding system performances over the full stroke
2. Assessment of the influence of the compliant rod connection on flexible guiding performances
3. Performance measurements of the full mechanism on the SCM QM

In this article, the test apparatus and results for the two derisking steps are presented and discussed. The initial breadboard model test results performed on the flexible guiding system are presented hereafter. They are followed by the characterization test results of the influence of the compliance rod connection on the slit positioning accuracy. The performance measurements for the full SCM mechanism are not presented in this article.

### Flexible Guiding System Characterization Test Results

The initial breadboard tests were performed on a full-scale model of the flexible guiding mechanism, shown in Figure 8. These tests specifically aimed at measuring the geometrical positioning accuracy and repeatability over the full stroke for a limited number of cycles. The Z displacement was imposed using a steel wire tensioning system. Displacements were measured using two different high precision Laser Displacement Meters and rotations using a high-resolution Laser Diode Sensor Vector Autocollimator.

All X translation measurements were performed in a vertical configuration such to alienate gravity effects. The use of a traction system implied the need to perform +Z and -Z measurement tests separately and combine the test results.

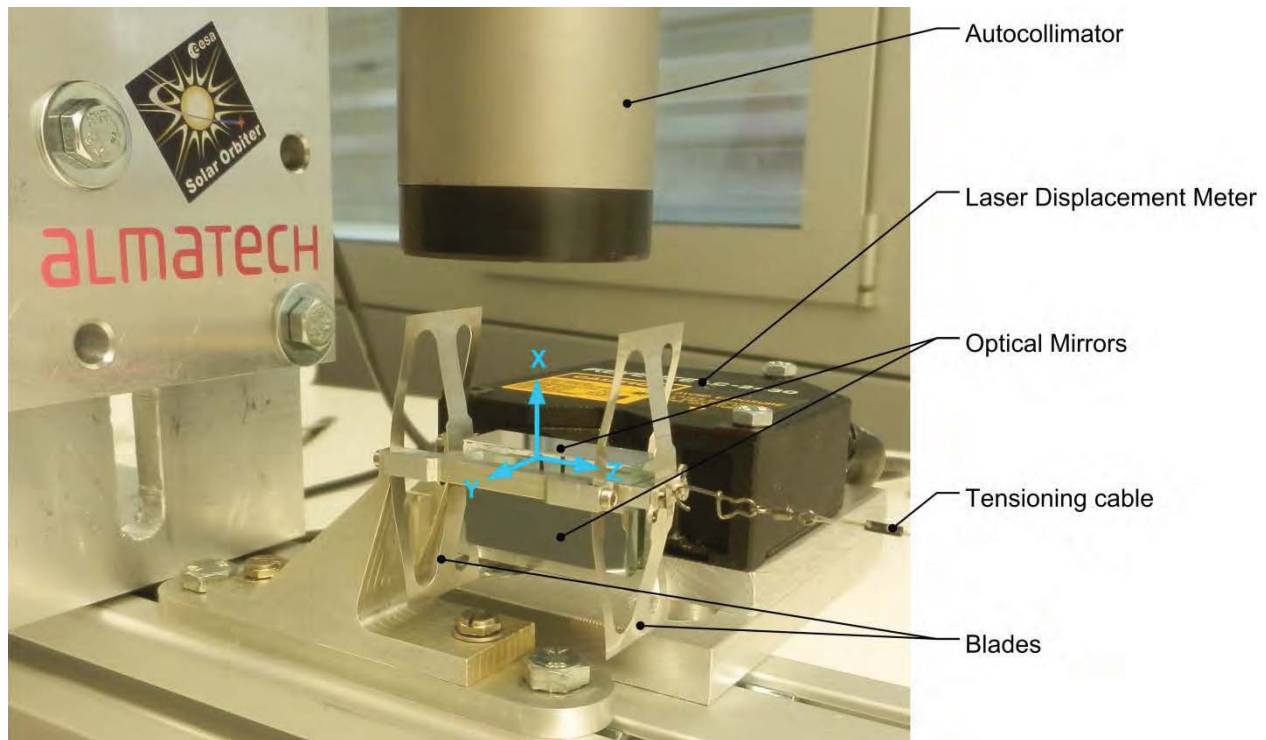
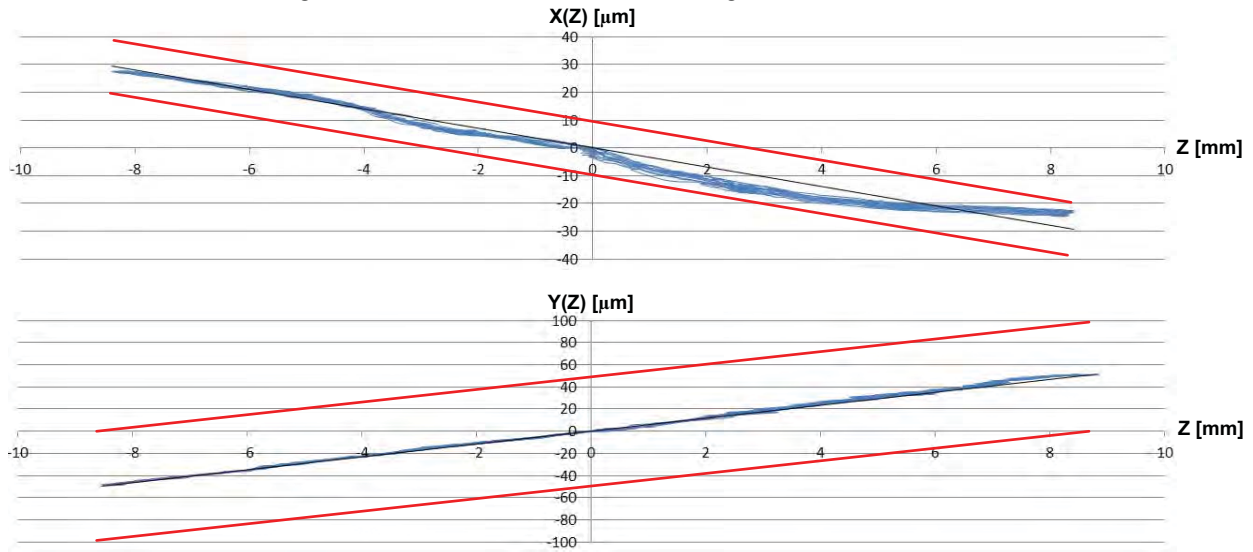
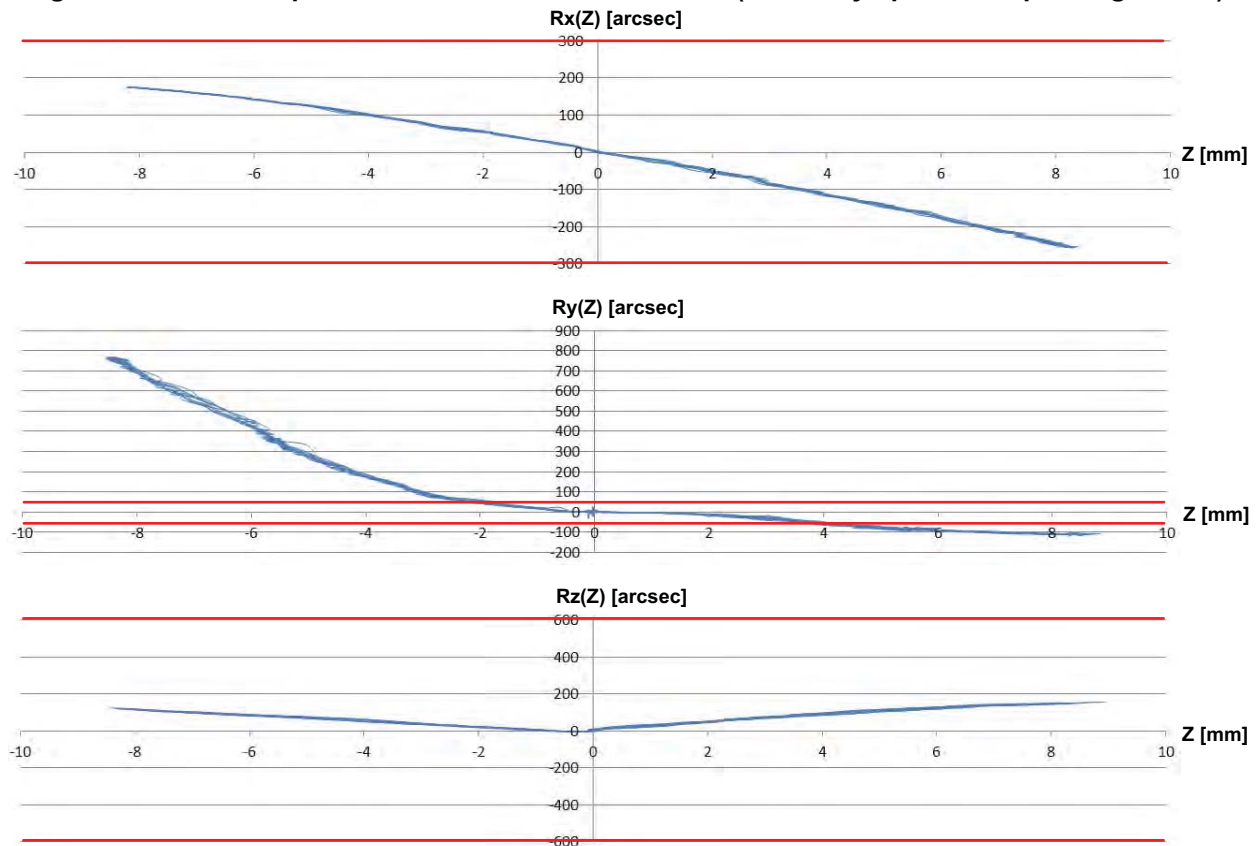


Figure 8. Breadboard model 1 test setup

Figures 9 and 10 present the slit carrier's displacement and rotational test results in function of the translation axis Z. High repeatability is observable between measured curves in each translation and rotation. All results are within the allowable limits with an exception for the  $R_y(Z)$  tests results. Following these tests, it has been observed that the tensioning cable fixation lug was slightly bent, introducing a perturbation moment around the Y axis for the  $-Z$  direction. For the  $+Z$  direction, the deviation from the requirement have been attributed to the breadboard's blade alignment system that has been further enhanced for the following breadboard tests and QM/FM design.



**Figure 9. Slit carrier position in function of the Z in mm (biased by optical setup configuration)**



**Figure 10. Slit carrier rotation in function of the Z-translation in mm**

Table 6 summarizes the initial breadboard model test results performed on the flexible guiding system presented above.

**Table 6. Max. positioning inaccuracy & worst case repeatability results from Z-displacement**

Direction	Position accuracy		Repeatability	
	Measured	Required	Measured	Required
X translation	$\pm 7.2 \mu\text{m}$	$\pm 10 \mu\text{m}$	$\pm 2.17 \mu\text{m}$	$\pm 5 \mu\text{m}$
Y translation	$\pm 5.1 \mu\text{m}$	$\pm 50 \mu\text{m}$	$\pm 0.71 \mu\text{m}$	$\pm 3 \mu\text{m}$
Rotation around X	$\pm 4.28 \text{ arcmin}$	$\pm 5 \text{ arcmin}$	$\pm 3.65 \text{ arcsec}$	$\pm 30 \text{ arcsec}$
Rotation around Y	$\pm 768 \text{ arcsec}$	$\pm 50 \text{ arcsec}$	$\pm 5.14 \text{ arcsec}$	$\pm 25 \text{ arcsec}$
Rotation around Z	$\pm 2.60 \text{ arcmin}$	$\pm 10 \text{ arcmin}$	$\pm 0.11 \text{ arcsec}$	$\pm 5 \text{ arcmin}$

**Flexible Guiding System Performance Test Results with Compliant Connection**

The second set of breadboard tests were performed on a full-scale model of the flexible guiding mechanism including the compliant connection rod and its clamping system. All design improvements identified during the initial flexible guiding system tests, presented above, have been implemented in the flexible guiding system design of the second Breadboard Model. This second set of tests specifically aimed at measuring the geometrical positioning accuracy and repeatability over the full stroke for a limited number of cycles (10). The Z-displacement was imposed using a micrometer in a vertical configuration. Displacements in X, Y and Z were measured using three high-precision Laser Displacement Meters. Rotations were measured using two high-resolution Laser Diode Sensor Vector Autocollimators. The test apparatus for these measurements, shown in Figure 11, included the use of an optical table with pneumatic vibration isolation system.

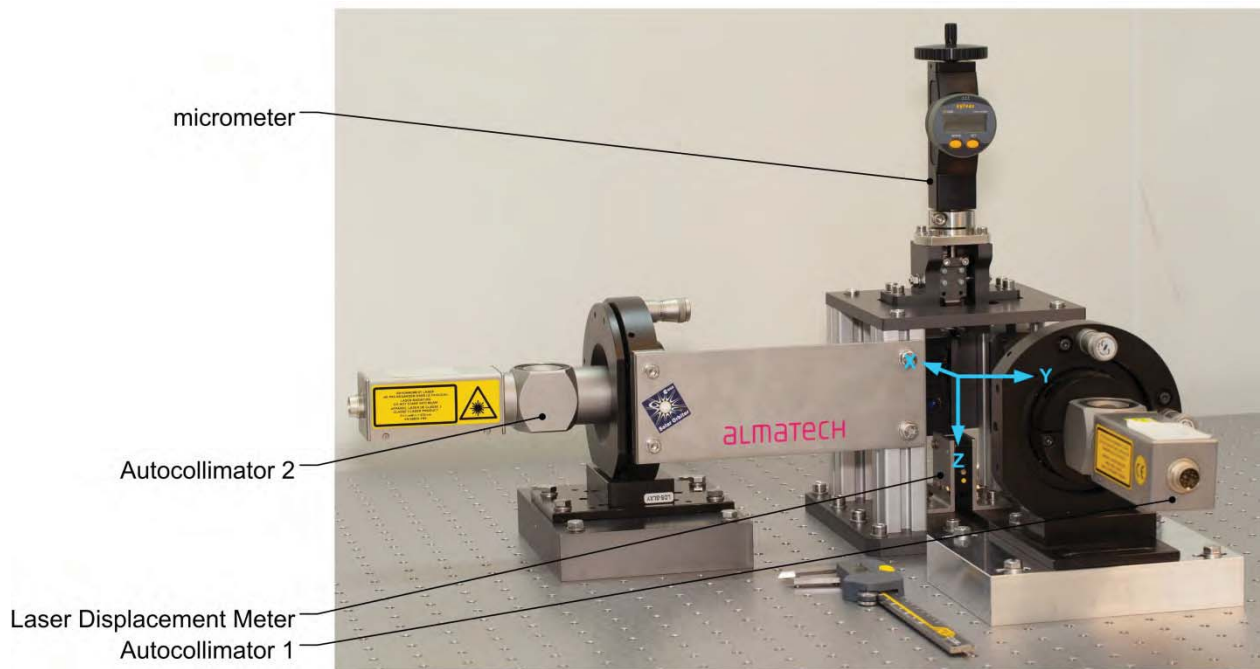


**Figure 11. Breadboard model 2 test setup**



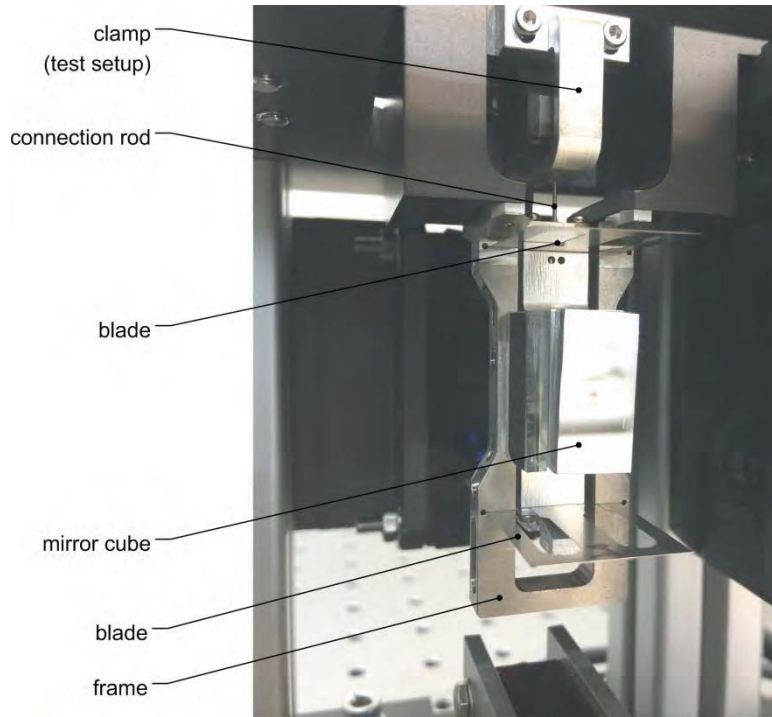


**Figure 12. Breadboard model 2 flexible guiding system**

Figures 13 and 14 present the slit carrier's displacement and rotational test results in function of the translation axis Z for the second test series (10 full strokes). Very high repeatability is observable between measured curves in each translation and rotation with a significant enhancement from the previous test result presented in Figures 9 and 10. The second set of results is well within the allowable limits with an exception for the  $R_y(Z)$  test results. In the corresponding figure, the four slit positioning locations are represented as circles. At these discrete locations where the positioning and repeatability requirements are applicable, they are just met. The origin of the behavior of the rotation around Y over the full stroke can be attributed to either a misalignment of the flexible blades in the X direction or some dissymmetrical behavior of the flexible blades.

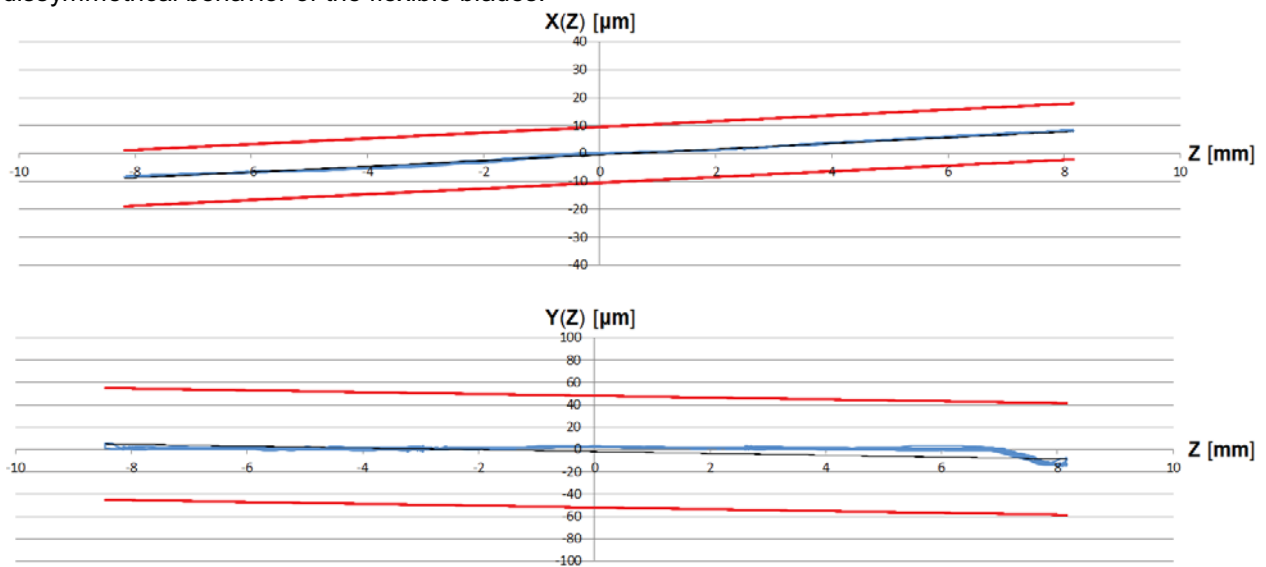


**Figure 13. Slit carrier position in function of the Z-translation in mm**



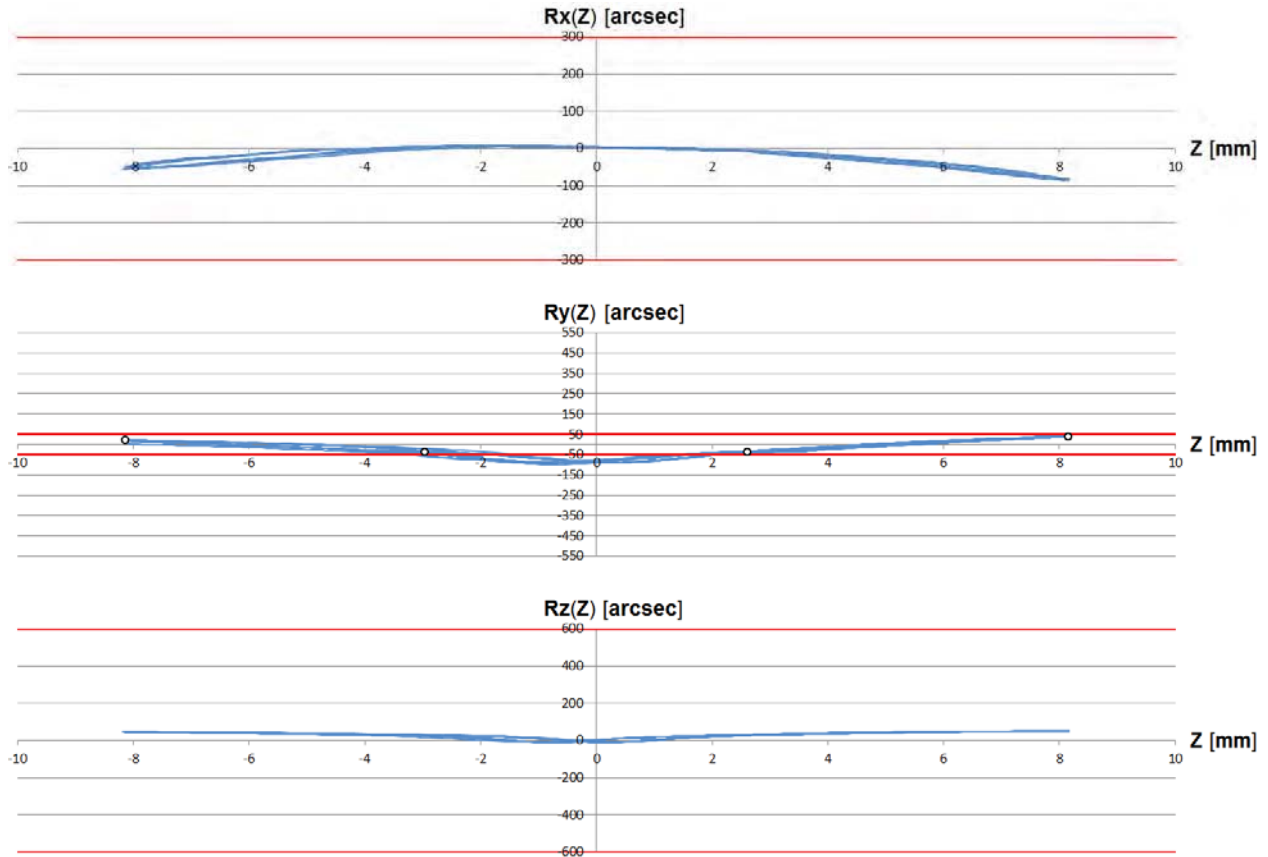


**Figure 14. Slit carrier rotation in function of the Z-translation in mm**

One potential enhancement of the flexible guiding system would be to connect both flexible blade ends together as they act as free pivot points (at +X and -X sides). However, this would make the design much more complex, in particular considering that these two additional mechanical structures would need to freely move along Z as well as to cope with the important launch environment and therefore be supported too. In any case, the requirements for the rotation around Y have been relaxed during the project. The design of the flexible guiding system with a connection rod is therefore considered fully suitable for the application and in compliance to the stringent positioning and repeatability requirements.

Table 7 summarizes the test results performed on flexible guiding system equipped with the compliant rod connection (breadboard model 2).

**Table 7: Max positioning inaccuracy & worst case repeatability test results from Z-displacement**

Direction	Position accuracy		Repeatability	
	Measured	Required	Measured	Required
X translation	$\pm 1.0 \mu\text{m}$	$\pm 10 \mu\text{m}$	$\pm 0.14 \mu\text{m}$	$\pm 5 \mu\text{m}$
Y translation	$\pm 8.5 \mu\text{m}$	$\pm 50 \mu\text{m}$	$\pm 2.36 \mu\text{m}$	$\pm 3 \mu\text{m}$
Rotation around X	$\pm 0.69 \text{ arcmin}$	$\pm 5 \text{ arcmin}$	$\pm 2.08 \text{ arcsec}$	$\pm 30 \text{ arcsec}$
Rotation around Y	$\pm 67 \text{ arcsec}$	$\pm 50 \text{ arcsec}$	$\pm 1.21 \text{ arcsec}$	$\pm 25 \text{ arcsec}$
Rotation around Z	$\pm 0.53 \text{ arcmin}$	$\pm 10 \text{ arcmin}$	$\pm 0.33 \text{ arcsec}$	$\pm 5 \text{ arcmin}$

## Conclusions

The validation test results have demonstrated the full adequacy of the flexible blade guiding system implemented in SPICE's Slit Change Mechanism in a stand-alone configuration. Further breadboard test results, studying the influence of the compliant connection to the SCM linear actuator on an enhanced flexible guiding system design have shown significant enhancements in the positioning accuracy and repeatability of the selected flexible guiding system. Preliminary evaluation of the linear actuator design, including a detailed tolerance analyses, has shown the suitability of this satellite roller screw based mechanism for the actuation of the tested flexible guiding system and compliant connection.

The presented development and preliminary testing of the high-precision long-stroke Slit Change Mechanism for the SPICE Instrument are considered fully successful such that future tests considering the full Slit Change Mechanism can be performed, with the gained confidence, directly on a Qualification Model.

The selected linear Slit Change Mechanism design concept, consisting of a flexible guiding system driven by a hermetically sealed linear drive mechanism, is considered validated for the specific application of the SPICE instrument, with great potential for other special applications where contamination and high precision positioning are dominant design drivers.

# High Gain Antenna System Deployment Mechanism Integration, Characterization, and Lessons Learned

Fil Parong<sup>\*</sup>, Blair Russell<sup>\*\*</sup>, Walter Garcen<sup>\*\*</sup>, Chris Rose<sup>+</sup>, Chris Johnson<sup>\*\*</sup> and Craig Huber<sup>\*\*</sup>

## Abstract

The integration and deployment testing of the High Gain Antenna System (HGAS) for the Global Precipitation Measurement mission is summarized. The HGAS deployment mechanism is described. The gravity negation system configuration and its influence on vertical, ground-based deployment tests are presented with test data and model predictions. A focus is made on the late discovery and resolution of a potentially mission-degrading deployment interference condition. The interaction of the flight deployment mechanism, gravity-negation mechanism, and use of dynamic modeling is described and lessons learned presented.

## Introduction

During testing and integration of the High Gain Antenna System to the core Global Precipitation Measurement (GPM) spacecraft, a potential deployment hardware interference issue was discovered. A release mechanism firing order change along with trimming a structurally critical bracket was chosen as a solution to increase clearance. A dynamic software model was built that predicted the worst-case, on-orbit deployment path of the HGAS. The model showed that the firing order change and the material removed from the HGAS hardware provided sufficient clearance margin for a successful deployment.

## GPM Mission Overview

The GPM core spacecraft will carry a high gain antenna system to provide command and control communications as well as a science data downlink through the Tracking and Data Relay Satellite System (TDRSS). The GPM mission is an international network of satellites that will provide the next-generation global observations of rain and snow. The GPM mission deploys a “core” satellite carrying an advanced radar/radiometer system to measure precipitation from space and serves as a reference standard to unify precipitation measurements from a constellation of research and operational satellites. The GPM team, initiated by National Aeronautic and Space Administration (NASA) and the Japan Aerospace Exploration Agency (JAXA), comprises a consortium of international space agencies. The GPM Core Spacecraft is qualified and scheduled to launch in late February 2014. [<http://pmm.nasa.gov/GPM>]

## HGAS Configuration and Design

The assembled HGAS system, shown in Figure 1, has a mass of 95 kg (210 lbm), including 24 kg (52 lbm) for the gimballed antenna assembly. When stowed, it occupies a roughly 2.8 m x 1.0 m x 0.9 m (110 in x 39 in x 35 in) volume, and deploys 3.6 m (140 in) from its base.

For antenna pointing, the GPM HGAS employs a two-axis gimbal configuration. Due to field-of-view requirements and packaging limitations, the HGAS boom assembly consists of two boom sections with shoulder and elbow hinges that contain coaxial deployment springs and dampers. A synchronization

---

<sup>\*</sup> NASA Goddard Space Flight Center, Greenbelt, MD

<sup>\*\*</sup> Stinger Ghaffarian Technologies Incorporated, Greenbelt, MD

<sup>+</sup> Vantage Systems Incorporated, Greenbelt, MD

(sync) cable provides redundancy for the dampers and deployment springs, allowing for system deployment in the event of a spring or damper failure. The sync cable also helps maintain the ratio of the two hinge angles to approximately 2:1, as the elbow and shoulder hinges open 180 and 90 degrees respectively during deployment.

HGAS contains five mechanisms: three Launch Restraint Mechanisms (LRM's), a Lower Boom Assembly (LBA), and the gimbal assembly. The upper boom connects the LBA to the gimbal assembly as shown in Figure 1. The entire HGAS assembly and associated mechanism are supported on an all-aluminum honeycomb plate. The LRMs and hinge line designs were developed from heritage Solar Dynamics Observatory hardware.

#### Launch Restraint Mechanism

The HGAS uses three LRMs (known as the A, B, and C devices) to restrain the upper boom and the gimbal assembly to the mounting plate prior to deployment. Each LRM is composed of a latch rod, securing the upper boom or gimbal assembly to two spring-loaded jaws. Each jaw is attached to a non-explosive actuator (NEA). After firing, the NEAs release the latch rods allowing the system to deploy. As designed, LRM C releases first, followed four seconds later by the LRMs A and B simultaneously. Deployment commences once all LRMs are released. Kick-off springs at LRM B and LRM C assist in separating the HGAS assembly from the LRMs.

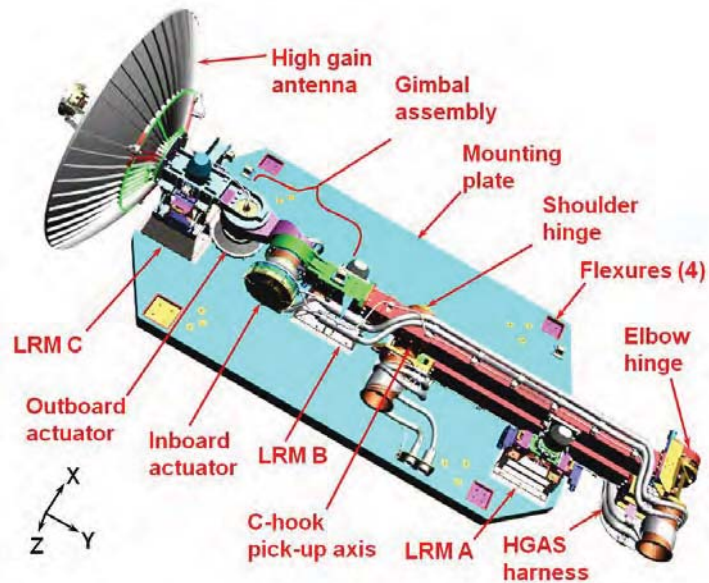


**Figure 1. HGAS Layout**

#### Lower Boom Assembly

The LBA, shown in Figure 2, is made up of the two deployment hinges; the elbow hinge and shoulder hinge, connected via a 0.77-m (30-in) long lower boom. Each hinge incorporates a constant torque deployment spring, a viscous fluid damper, and a potentiometer (for hinge angle telemetry).

#### Gimbal Assembly

The two-axis gimbal assembly consists of two actuators using a stepper motor and harmonic drive gear reduction in each axis. Both axes can rotate  $\pm 90^\circ$  in  $0.0075^\circ$  increments. The gimbal is commanded using pitch (local X) and yaw (local Y) axis design orientation made up of a lower actuator bracket that connects to the upper boom, a middle linkage bracket, and an antenna bracket mounted to the High Gain Antenna (HGA). The gimbal assembly provides the HGA with the capability to access multiple TDRSS satellite communication links continuously throughout the GPM mission.

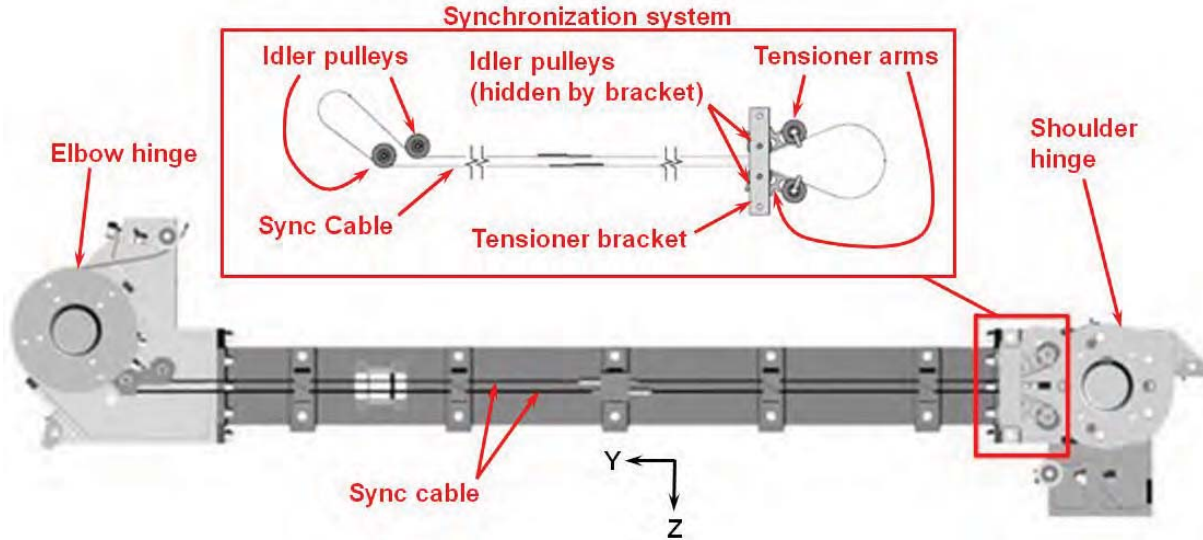


**Figure 2. Lower Boom Assembly, Key Components**

Hinge Spring and Damper Development and Sizing

Resistance torque testing of the hinge system was performed to determine the minimum torque required to deploy the system. A design deployment spring torque of 11.3 N-m (100 in-lbf) at both the elbow and shoulder hinges was selected, leaving adequate torque margin at each hinge.

The HGAS elbow hinge uses the same size and type viscous fluid damper as was already selected for GPM's solar array deployment system. Taking this known damping rate and design deployment spring torques as givens, along with the intent for the HGAS to deploy at a 2:1 ratio, the shoulder hinge's required damping rate was calculated. Since the damping varies strongly with temperature, both damper temperatures are actively controlled with external heaters to 30.0°C ± 2.0°C (86°F ± 3.6°F) for flight.

Synchronization System

A synchronization cable system was added to provide redundancy and control of the deployment path to the mechanism. The elbow and shoulder hinges are connected via a stainless steel sync cable, which helps to maintain the 2:1 intended hinge angle ratio. The pulleys connected to the hinges are sized for this 2:1 ratio. The sync cable's tension is maintained with a spring-loaded tensioning system that applies additional tension via two spring-loaded tensioner arms. This tensioning system was sized primarily for thermal gradient cases, as there can be a worst case 65°C (149°F) gradient along the lower boom. Since the ratio between elbow and shoulder hinges was designed as 2:1, a metric called the *elbow delta angle* ( $\Delta$ ) was defined as follows:

$$\Delta = \text{elbow angle} - 2x \text{ shoulder angle} \tag{1}$$

A positive  $\Delta$  indicates the elbow is leading the shoulder during deployment. A negative  $\Delta$  indicates the elbow is trailing the shoulder. *The design intent, and thus the expected value of  $\Delta$ , is zero or negligibly off zero throughout the deployment.*

**Gravity Negation System**

The gravity negation (g-negation) system enables a vertical deployment of the HGAS in a 1-g environment. Such deployments are required to characterize and qualify the HGAS system prior to flight. The HGAS deployment system qualification included three spacecraft integrated deployments; immediately after initial integration to spacecraft, after thermal vacuum testing (T-Vac), and after vibration testing. Due to packaging constraints, accommodations for other deployable systems, and configuration

requirements for operational tests on the ground, the HGAS g-negation system was required to enable vertical deployments. Other options such as deploying perpendicular to gravity (horizontally) on a low friction surface were not compatible with GPM program requirements.

The g-negation scheme utilizes three discreet counter mass elements sized to g-negate individual sections of the HGAS. The system is comprised of a four-bar mechanism, a concentrated mass/moment arm, and a counter mass connected by cables and pulleys through an overhead gantry. The g-negation system, attached to the HGAS, is sketched in Figure 3. Ground Support Equipment (GSE) is drawn in bold lines, while the HGAS flight hardware is drawn in thin lines. Shown partially deployed, heavy solid arrows indicate the direction of motion of the moving parts of the g-negation system.

### Counter Torque Assembly

The Counter Torque Assembly (CTA) imparts a torque to the HGAS shoulder hinge line. The intent of the CTA is to negate the effects of gravity on the lower boom of the HGAS assembly as it rotates through its 90 degree deployment. The torque is produced by an adjustable mass mounted to a moment arm. The torque is transmitted to the shoulder hinge line via a four-bar linkage. The magnitude of the torque decreases as the moment arm rotates through 90° from horizontal to vertical. In the absence of the deployable portion of HGAS above the elbow hinge, the CTA would negate the force of gravity on the lower boom throughout its rotation, assuming no applied torques from the harness or deployment springs.

### Elbow Counter Mass

The elbow counter mass balances the upper boom and gimbal assembly about the C-hook pickup axis. It consists of a mass block and a 'U'-shaped bracket; the mass of each may be adjusted. Were the lower boom absent, the upper boom and gimbal/HGA assembly would be torque balanced about the C-hook pickup axis, assuming no applied torques from the harness or deployment springs. The addition of the elbow counter mass to the upper boom requires that this mass is also negated by the C-hook counter mass.

### Gantry/C-Hook Counter Mass

The gantry/C-hook counter mass assembly is intended to negate the effects of gravity on the mass of the upper boom, gimbal assembly, and the elbow counter mass. The system consists of a modified commercial off-the-shelf gantry, a 'C'-shaped link (C-hook), a counter mass and a cable/pulley system. The gantry, in its configuration to support spacecraft integrated HGAS deployments, measured 7.6-m (25-ft) tall by 6.1-m (20-ft) wide and 3.6-m (12-ft) deep. It includes a substantial amount of ballast mass at its base to meet stability requirements. The total mass of the upper boom, gimbal/HGA assembly, and elbow counter mass is g-negated by the C-Hook counter mass.

Assuming a 2:1 ratio between the shoulder and elbow hinge angles is properly maintained and the HGAS mounting plate is parallel to the ground, the C-hook pick up axis on the upper boom should stay directly over the shoulder hinge axis. This allows a vertical cable to provide the g-negation for the upper boom/gimbal assembly through the C-hook pickup axis. The C-hook link allows the load path to go

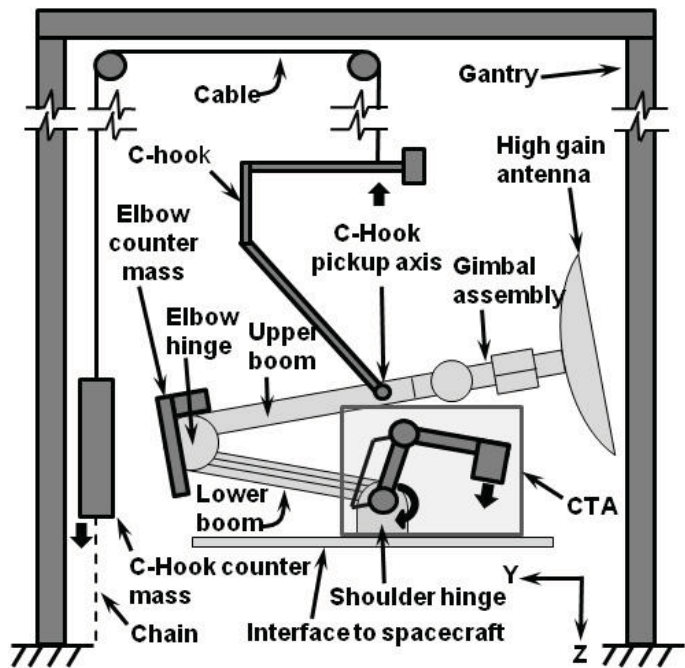


**Figure 3. HGAS G-Negation System**



around the antenna dish when the HGAS is deployed. The g-negation system, with HGAS integrated to the spacecraft, is shown in Figure 4.

### Stow/Deployment Bias

Ideally the system will exactly negate the effects of gravity on the HGAS for ground tests. As this is not feasible, the g-negation system will either hinder or aid in the deployment of the system. In order to confidently qualify the deployment system, it is important that the g-negation system does not assist deployment. To be conservative in ground testing, the system should be tuned to slightly hinder deployment or bias the system toward the stowed configuration. This is referred to as stow bias.

Stow bias is the load or torque applied by the g-negation system that retards system deployment compared to a “perfectly” gravity negated state. A deployment bias would be a load or torque that assists deployment.

The starting point for calculating the masses of the g-negation system’s three elements was the development of an accounting/moment balance spreadsheet. This spreadsheet tracked mass and moment arm for the lower and upper booms separately as well as the three g-negation elements. The mass and moment arm data was comprised of actual measured inertia, CAD-based inertial information, and engineering estimates. This data was used to sum the torques and masses and determine what counter mass was needed for each of the three g-negation elements. This g-negation configuration is specific to the flight hardware configuration for which it was determined.

During HGAS subsystem integration, the g-negation was verified by removing the deployment springs (harness was not present at this time) and observing system motion. Small changes to the mass configuration were made to fine tune the system.

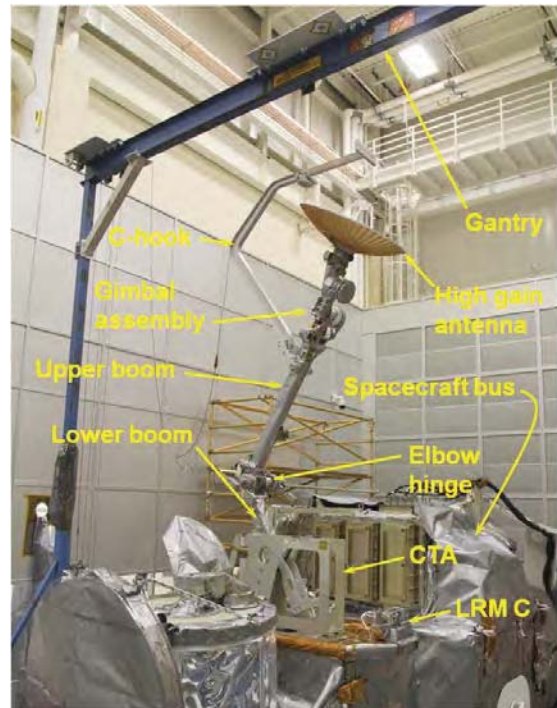


**Figure 4. HGAS during g-negated deployment testing, integrated to GPM spacecraft**

Any mass changes to the deployable section of the HGAS impacts the g-negation configuration. The addition of T-Vac test instrumentation, then vibration test instrumentation, and later removal of this hardware required changes to the g-negation mass configuration. These changes were determined analytically, with the balance spreadsheet, as it was no longer an option to remove the harness and deployment springs to verify the stow/deployment bias. This is a key limitation in ground testing.

### Deployment Instrumentation

As part of the ground support equipment, instrumentation was developed to document deployment tests. Inclinometers were added to the lower and upper booms to track their angles during deployment. Loads in the g-negation system were recorded via two load cells on either end of the C-hook cable assembly. The load cells were used primarily to ensure the stow/deployment bias did not change appreciably during deployment. Data from the inclinometers was more useful. From inclinometer data, the deployment rates for the shoulder and elbow hinge can be determined, as well as the elbow delta angle ( $\Delta$ ). This data is shown in Figure 5.

### Subtleties of G-negation System

There were several subtleties discovered during the early trials. While the gantry cable and pulley system is intended to only apply a vertical force to g-negate the upper boom/ gimbal assembly, any tendency of

the C-hook pickup axis to move laterally from a vertical path will be met with a centering reaction at the C-hook pickup axis (see Figure 9). This reaction is the horizontal component of the tension in the cable and increases as the cable angle deviates from vertical. This centering effect also increases as the HGAS deploys as cable length shortens and angle increases. For a deviation of 76 mm (3 in), the horizontal centering force would be on the order of 10 N (3 lb) for the fully deployed system. If HGAS deploys along its designed path this force is negligible.

Another subtlety discovered was the effect of cable length/mass switching sides of the g-negation cable/pulley system. As the system deployed, cable length on C-hook end of the cable/pulley system would shorten, while cable length on the C-hook counter mass end of the system would lengthen by an equal amount. The C-hook pickup axis moves vertically 1.9 m (75 in) during deployment. This effectively increased the counter mass on the C-hook counter mass side of the cable and thus decreased the amount of stow bias from the g-negation system by approximately 0.75 kg (1.65 lb) at the end of deployment. This feature was corrected by the addition of a length of chain (with the same linear density as the cable) to the C-hook counter mass. The chain was hung from the C-hook counter mass to a collection pan on the floor. As the length of cable shortened on the C-hook side of the cable/pulley system, the same length of chain piled up in the collection pan on the floor, balancing the effect.

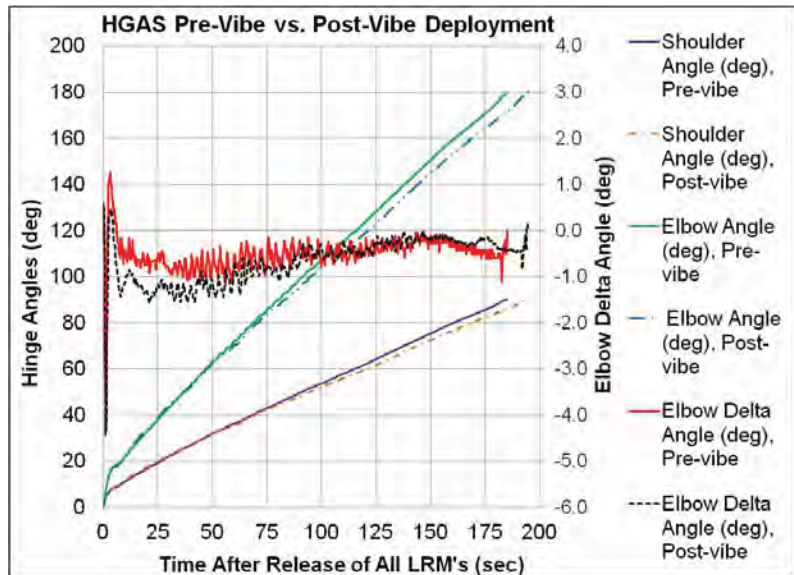


**Figure 5. Deployment Data for HGAS Qualification**

As the length of cable shortened on the C-hook side of the cable/pulley system, the same length of chain piled up in the collection pan on the floor, balancing the effect.

### Baseline (Flight-like) Dynamic Model

During the course of GPM HGAS manufacture and integration, a dynamic HGAS computer model was developed using MSC ADAMS to aid in predicting on-orbit deployment path and deployment time. Later, the model was enhanced by adding ground deployment GSE to simulate g-negated ground deployments.

The ADAMS model was very much a “living document”. It was first built with nominal values for spring torques, dampers, masses, etc. The model was continually updated as more accurate information of various flight components became available. Eventually, the model migrated towards representing the flight configuration in high fidelity with the exception of certain unknowns such as hinge friction coefficients and in-situ harness torques. Key features of the model are detailed below:

- *Hinge Deployment Spring Torque:* The deployment spring torque at both hinges used the torque vs. angle data gathered for the serialized flight springs during sub-component testing. While the springs were intended to be constant torque springs, the torque isn't truly constant and varies as a function of angle.
- *Variable Damping Coefficients:* The fluid hinge dampers have damping coefficients that are a function of angular velocity and temperature. In addition, the damping varies unit to unit. Damping performance at various temperatures and angular velocities was measured in the serialized flight units. Damping coefficient vs. angular velocity curves, at various temperatures, were generated based on that test data and incorporated into the ADAMS model.

- *Damper Deadband:* The dampers have a deadband, which is a span of a few degrees of rotation where there is no damping. Once the damper rotates past the deadband angle, damping suddenly comes into play. Some of the deadband is due to mechanical play in the damper attachment to the hinge while the rest is internal to the damper. Below the deadband angle, damping was simply switched off in the ADAMS model. Note that the deadband of the elbow damper and that of the shoulder damper were not the same.
- *Sync Cable Compliance:* Based on bench test data of a flight-like cable and tensioner, the compliance of the sync cable was incorporated into the ADAMS model. It was added as a non-linear spring function applied to the elbow hinge that was the  $\Delta$  function previously discussed. A positive  $\Delta$  indicates the elbow is leading the shoulder and an internal resistive torque would be applied to the elbow by the model. A negative  $\Delta$  indicates the elbow is trailing the shoulder and an internal assistive torque would be applied to the elbow. Larger magnitude  $\Delta$ 's would result in greater internal elbow torque magnitudes applied by the spring-like model. Whenever the  $\Delta$  was zero, the hinges are synchronized and no internal torque would be applied to the elbow by the model. An example of the  $\Delta$  is plotted as elbow angle delta in Figure 5. A mathematical construct known as a "coupler" in ADAMS was used to tie the elbow hinge to the shoulder hinge with a 2:1 ratio. The compliance torque function was serially applied at the elbow end of this coupler to simulate the compliance in the sync cable system.
- *Use of Measured Masses:* Actual measured masses were used for the booms, gimbal, and antenna. The mass used for HGAS harnesses were from the flight spares. Blanket and instrumentation masses are approximated. Center of gravity (CG) locations were not known for the flight subassemblies so the ADAMS model CG locations were matched to that of the CAD model.
- *Variable Harness Torque:* The HGAS harness torque as a function of angle imparted at each hinge was measured on the qualification unit at various temperatures. That data was incorporated into the ADAMS model.
- *Flexible Body Structures:* Both booms, the lower actuator bracket, middle linkage bracket, and the antenna bracket were modeled as flexible elements. ADAMS uses Timoshenko beam relations for such structures.
- *LRM Spring Energy:* The LRM retractor springs were assumed to be 90% efficient in terms of the energy they would deliver to the retractors when fired. The design value for the preload and stiffness was used for each retractor spring.
- *Friction:* Frictions in hinges, deployment springs, dampers, and cable pulleys were not load or rotation angle dependent. For these frictions, maximum expected vendor values were used.
- *Kick-off Springs at LRMs:* The kick-off springs at LRM B and LRM C are included in the model as preloaded linear springs.

The ADAMS model could be run either as an on-orbit model or as a ground test model ("g-negated"). Starting with the g-negated model, the ADAMS model could be easily converted to the on-orbit model by turning off gravity and disabling all the g-negating components of the model and vice-versa.

The model was calibrated using the results of g-negated ground tests. As the model evolved and more g-negated tests were performed, the model's calibration was iteratively tuned. The target for calibration was deployment time and damper deadband performance. The adjustments made to the model during calibration were to the hinge deadband angles and g-negation system stow bias.

On plots of hinge angles vs. time for ground tests, one can pick out the deadband angle of the particular dampers as there is an inflection point in the slope of the curve. The slope changes sign as the dampers activate outside their deadband angle. These characteristic inflection points are noted in Figure 6. Once the deadband angle was picked off the graph, that angle could be incorporated into the model. The model simulation would then be repeated to ensure that the inflection points occurred at approximately the same angle as seen in the test data.

As it could not be actually measured, the stow bias was the least certain value in the ADAMS model. To finalize calibration of the model, the stow bias was iterated until the latch time of both hinges closely matched the latching (i.e. fully deployed) times in the most current g-negated tests. The hinges would not latch at the exact same time due to compliance in the sync cable, allowing the small  $\Delta$  angle between the two hinges.

The final calibration to the ADAMS model was done using the post T-Vac, g-negated, deployment data. The hinge angles of the post T-vac test and the corresponding calibrated ADAMS model predictions are compared in Figure 6. The 3 N (0.7 lbf) of stow bias used to calibrate the model compares favorably to the 2 to 4.4 N (0.5 to 1.0 lbf) stow bias estimated by the test engineers prior to the test. This calibrated model became the baseline ADAMS model. This baseline model, run as a “on-orbit” (i.e. zero gravity and g-negation system model elements disabled) would be used to predict on-orbit performance of the flight configuration HGAS.

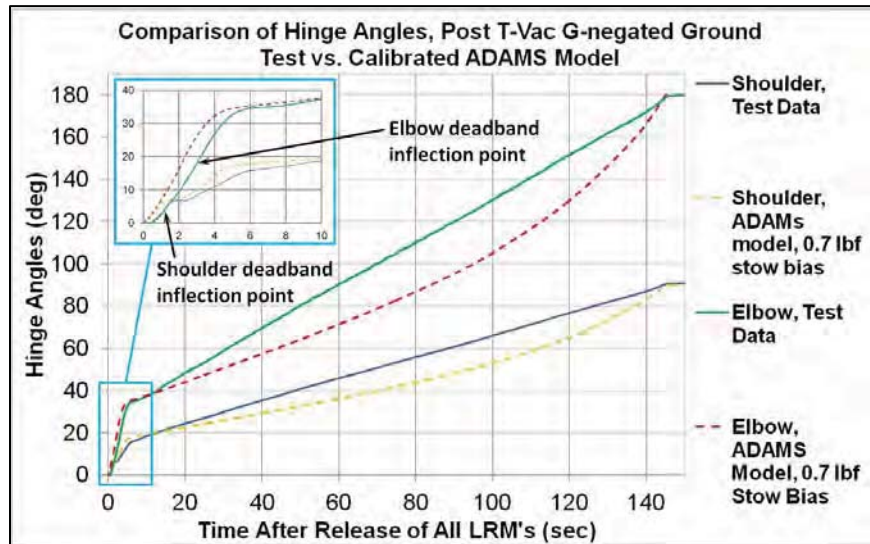


**Figure 6. Calibrated ADAMS Model Predicted Hinge Angles Compared to G-Negated Test Values**

### Potential Deployment Interference

After the HGAS subsystem was integrated to the spacecraft, a potential deployment interference issue between the outboard actuator of the gimbal assembly and LRM C was discovered (see Figure 7). The potential interference was discovered while doing an analysis run with the HGAS ADAMS model for another purpose (i.e. non-baseline), not to check for interferences between the gimbal assembly and LRM C.

The predicted interference was verified with a run of the baseline ADAMS model. It was noticed that the HGAS gimbal assembly penetrated into the rectangular solid representing LRM C (again, see Figure 7). While constraint (e.g. hinges) locations are based off the CAD model and thus accurately located in the HGAS ADAMS model, not all the geometry is accurately portrayed, so the ADAMS model, by itself, cannot be relied on to check for interferences.

The ADAMS model results for elbow and shoulder hinge angles were inserted into the CAD model to check for interferences. The CAD model also predicted an interference of the outboard actuator with LRM C (see Figure 8). In the event this interference led to a failed deployment by jamming the outboard actuator against LRM C, the core spacecraft would lose its high bandwidth communication ability and would have to rely on a much slower data rate. This would delay completing or possibly compromise the completion of mission objectives.



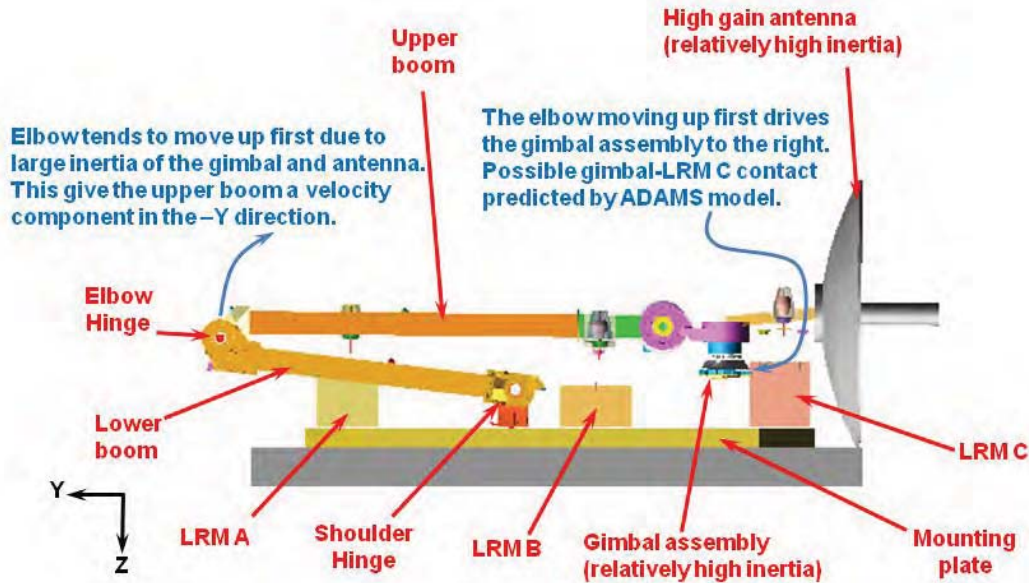


Figure 7. Potential Impact of Gimbal Section with LRM C (image from ADAMS model)

This discovery led to close examination of the HGAS deployable and the following revelation: The potential interference issue is rooted in a fundamental trait of the design. It is *kinematically indeterminate* with no set deployment path. The ramifications of this were not understood during the design phase or even early in the testing phase, as it was assumed that the sync cable would keep the elbow and shoulder hinges' rotation locked in a tight 2:1 ratio. In reality, compliance in the synchronization cable allows some independent rotation of the elbow hinge relative to the shoulder hinge. The ratio tends towards 2:1, but isn't necessarily 2:1. This kinematically indeterminate system resulting from the sync cable compliance allows the following to influence the HGAS deployment path:

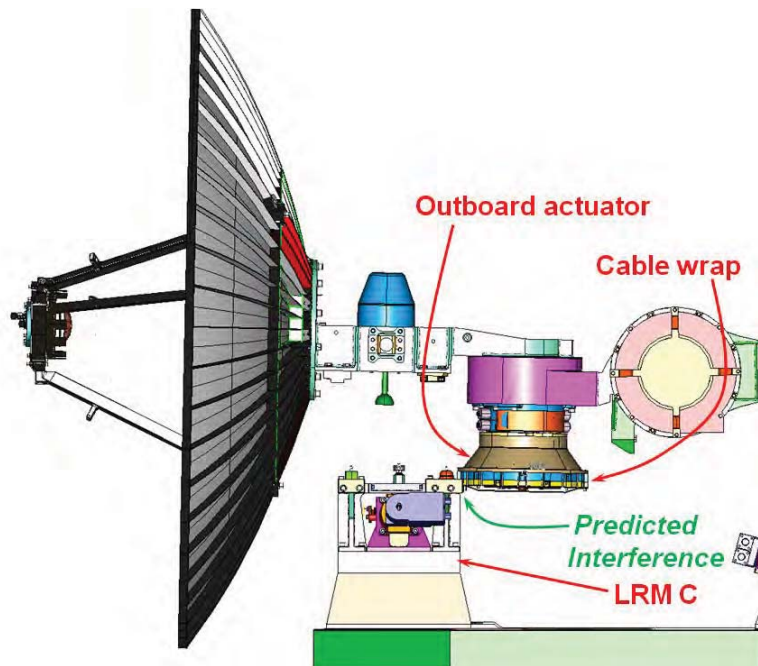
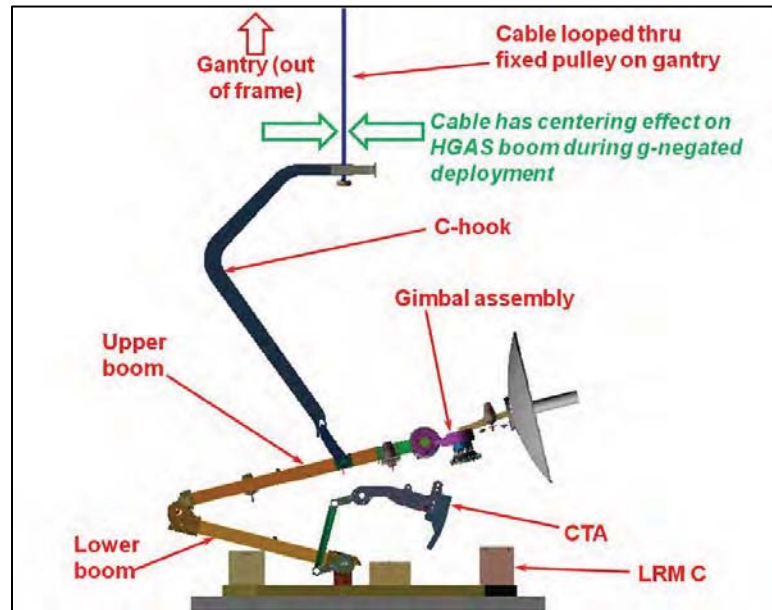


Figure 8. CAD Model Used to Verify Interference Predicted by Baseline Adams Model

- *Gimbal/Antenna Inertia*: The relatively large gimbal assembly and antenna inertia resists movement and thus the elbow end tends to lift off the deck first. Due to the geometry of the boom, this lifting of the elbow drives the gimbal assembly towards the non-deploying LRM C structure on the HGAS deck (see Figure 7).
- *Stored Energy in LRMS*: Impact energy from the firing of the launch restraint mechanisms and the force of the kick-off springs at each LRM can compound the issue. The LRM release order plays a significant role in the deployment path.

- *G-negation System Design:* G-negation system biases can influence the deployment path, masking the potential for on-orbit (i.e. zero-g) deployed interference (see Figure 9). During ground testing, contact was unlikely to be observed because the g-negation system biases the deployment path towards the intended design path (i.e. tends to center HGAS and assist the sync cable).

To check the validity of the baseline dynamics model and CAD predictions of the interference condition with LRM C, a hardware range of motion system check was performed. This check was done as early as the flight hardware was available. The HGAS was g-negated and all system preload was removed. Using careful hand manipulation, the system was moved through potential ranges of motion. From this study, it was verified that contact between deploying system members and non-deploying hardware could indeed occur. The principle point of contact was the outboard actuator with the +X, +Y corner at the top (-Z) edge of the spherical constraint tower assembly of the LRM C. The interference resolution was well under way at the time the issue was verified on the flight hardware.



**Figure 9. Gantry Cable tends to Center HGAS During G-negated Ground Deployment Tests (image from ADAMS model)**

### Interference-Biased ADAMS Model

Because the HGAS is kinematically indeterminate, whether there was sufficient clearance for the flight deployment path could not be determined without use of dynamic motion analysis. This analysis must include appropriate conservatism to ensure sufficient margin on clearance and a good design.

The calibrated baseline ADAMS model was key in developing a solution for the potential interference issue as the flight hardware was unavailable for detailed in situ subsystem study and testing. The HGAS was already integrated on the GPM spacecraft and the tight spacecraft integration and test schedule severely limited the team’s access to the hardware.

To use the dynamic HGAS ADAMS model to investigate potential solutions, appropriate conservatism was applied to the various parameters in the model. The type of conservatism applied to a dynamic model depends on the result one intends to study. For instance, with hinge deployment spring torque, if one wanted to be conservative with hinge “end of travel” impact velocity, you would use the high end of the deployment spring torque tolerance. If one wanted to be conservative on deployment time (i.e. the longest time) one would use the low end of deployment hinge spring torque tolerance, as lower torques translate to slower deployment speeds. When comparing and investigating the potential solutions of the interference issue, the metric used was the *minimum clearance between the gimbal assembly and LRM C* at any moment in time during the deployment.

Out of many dozens, the team identified 26 model parameters or factors that could have significant effect on this clearance. Using the baseline “on-orbit” model as the starting point, all these factors were biased



to reasonable extremes that *would minimize* clearance. For most of the 26 factors, those extremes were given by known tolerances. For the remaining factors, engineering judgment was used. This altered baseline model would become our *reasonable worst-case interference-biased model*, referred to hereafter as the “worst case” model. The team decided that a design solution was achieved if our ADAMS modeling efforts showed a minimum clearance of 6.4 mm (0.25 inch) between hard parts when running the on-orbit version of this worst case model.

This approach was considered robust because it was highly improbable that all 26 factors would be simultaneously biased towards minimum clearance in the actual flight hardware. Also, the HGAS ADAMS model had historically showed good correlation to the g-negated tests, especially in the first 15 degrees of shoulder hinge rotation.

As mentioned previously, the fidelity of the g-negation system to confidently test for interference of the gimbal with LRM C was insufficient due to the centering effect the gantry cable has on the HGAS during ground testing. Therefore, this worst case ADAMS model represented the best tool available to vet this issue.

There is insufficient space to describe the kinematic role of all 26 factors in this worst case model, but the three examples below demonstrate the typical methodologies used for biasing factors:

- *Shoulder Deployment Spring Torque*: A higher value of the shoulder spring torque would lift the elbow off the HGAS deck more quickly and thus further increase the interference of the gimbal assembly with LRM C (see Figure 7). Since the model was already using spring torques measured off the actual flight shoulder spring, variances in those torques would be driven by the error in the torque transducer used to measure the springs. The claimed accuracy of said transducer was  $\pm 4\%$ . Thus, it is possible for the measured torque to be up to 4% lower than the actual value. To be conservative on clearance in the worst case model, the torque vs. hinge angle curve for the shoulder deployment spring was multiplied by 1.04 (+4%)
- *Elbow Deployment Spring Torque*: Conversely, a lower value of elbow spring torque would result in a slower lifting of the gimbal assembly off LRM C and thus reduce clearance/increase interference. As with the shoulder, the model was already using spring torques measured off the actual flight elbow spring. The same transducer was used to measure the flight elbow spring torque. In this case, we wanted to minimize the spring torque in the worst case model to achieve the appropriate conservatism, so the elbow spring torque function was multiplied by 0.96 (-4%).
- *Elbow Damper Temperature*: Viscous dampers are used at each of the hinges. Thus the damping coefficients are functions of temperature. Decreasing temperature increases the damping. Heaters on the dampers control their temperatures to  $30^{\circ}\text{C} \pm 2^{\circ}\text{C}$  ( $86^{\circ}\text{F} \pm 3.6^{\circ}\text{F}$ ) As previously noted, hindering elbow rotation decreases clearance, thus the elbow damper temperature was set to  $28^{\circ}\text{C}$  ( $82.4^{\circ}\text{F}$ ) and the damping coefficient vs. hinge angular velocity curve in the model reflected the resulting increase in damping.

Both the baseline ADAMS model and the worst case model were used to determine the path forward. Due to time constraints, the early runs that illuminated the potential issue were used to guide potential hardware changes while the analysis team decided on the final conservative values for the aforementioned 26 critical factors of the worst case model. During this period, the baseline model was used to study the effect of proposed hardware and flight operation changes. Model hinge angle results were incorporated into the CAD model to check actual clearances.

### **Issue Resolution**

The solution to the interference issue was a combination of adjusting the firing/release order of the three launch restraint mechanisms (C then A/B became A/B then C) and trimming of non-deploying portions of the LRM C hardware to increase dynamic clearance.

Reversing the LRM release order improved the originally predicted 1.0-mm (0.04-inch) interference to 12 mm (0.46 inch) of clearance in the baseline model. With C firing first, followed by A/B four seconds later (i.e. the original firing order), the ADAMS model predicted that the retractor impact and kick-off spring energy at C was mostly absorbed by the x-axis gimbal actuator, contributing nothing to separating the HGAS from the surrounding structure. With the firing order reversed (A/B followed by C four seconds later), the model predicted that the firing of A and B does not change the hinge geometry significantly as the structure is still held down at C. But when LRM C is finally fired, the retractor and kick-off spring energy are efficiently used to rotate the HGAS away from the other structures about the elbow hinge axis. This operational change was implemented in the on-orbit deployment commands through the GPM engineering change request system. It was successfully utilized on all subsequent ground deployment tests.

Although the baseline model predicted 12 mm (0.46 inch) of clearance, the criterion for a successful design solution was 6.35 mm (0.25 inch) of predicted minimum clearance from the on-orbit version of the worst case model. A quick model run, assuming only one of the 26 factors biased towards interference (i.e. retractors transferring no impact energy to the booms), brought the predicted clearance back down to 4.8 mm (0.19 inch). A similar run with the worst case model was not done as the clearance was already below the target minimum. This necessitated trimming LRM C's tower assembly.

Figure 10 provides an overview of LRM C and the related constraint components. The spherical tower assembly of LRM C was nearest to the outboard actuator and was the location of predicted interference.

The most direct solution was to remove the corner material of each component in the tower assembly. At this stage of GPM testing and integration, HGAS had completed subsystem environmental test verification and had been delivered and integrated to the flight spacecraft. Thus modifying the test-verified hardware could create a programmatic risk by nullifying the test verification. However, spacecraft environmental testing had not yet begun and it was deemed that modification of constraint components would not violate previous verification so long as load path and contact stress were not compromised. Workmanship for reassembly would be verified through spacecraft-level environmental testing. Removal of tower component corner material up, to but shy of, the constraint contact region meant the removal of two tower assembly fasteners. Sub-assembly finite element analysis was performed with this change in place and yielded an acceptable margin.

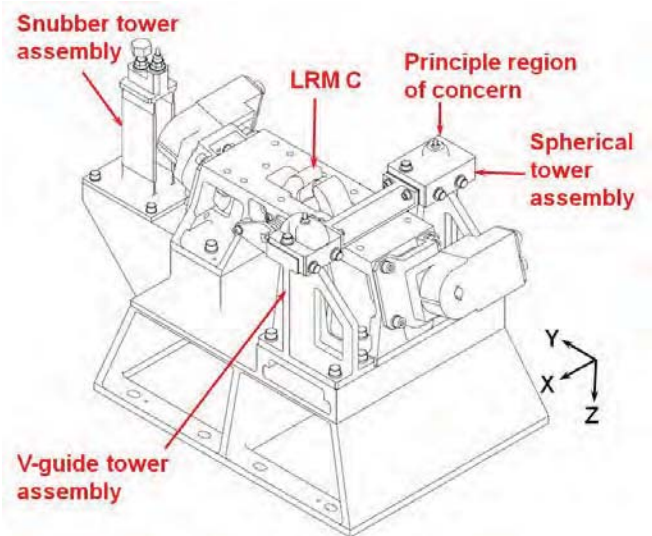


**Figure 10. LRM-C Constraint Component Assembly**

Modification of the constraint tower assembly components required tower assembly removal from HGAS. As the tower was pinned to the HGAS deck and already qualified, the decision was made to modify the installed components rather than flight spares. Positional relocation was not then a concern. Figure 11 illustrates the component modifications performed to ensure the desired deployment clearances.

Once removed from HGAS, the tower assembly was delivered to metrology for coordinate measuring machine documentation of tower assembly height and critical feature positions. In doing so, proper fitment of the modified and reassembled tower assembly could be verified.

The tower assembly was then disassembled and the individual components were modified via CNC machining. Piece part metrology verification was performed prior and after component modification.

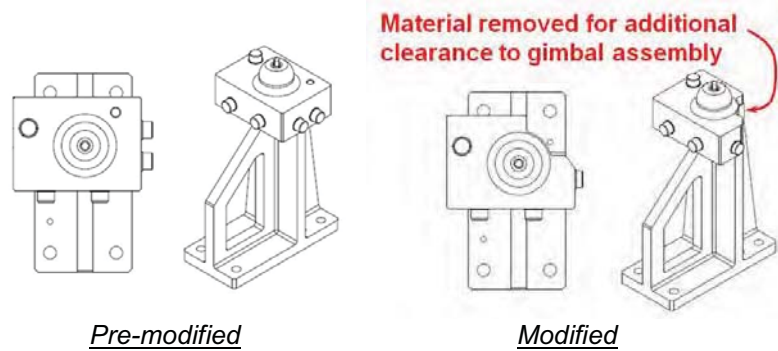


**Figure 11. LRM-C Spherical Tower Assembly**

Tower reassembly then occurred. The now modified spherical tower assembly itself received metrology verification. With spherical tower assembly modification complete, it was installed to its previously pinned HGAS location and its interface to the stowed HGAS constraints was verified by measurement.

The element of the gimbal assembly that could interfere with the constraint tower during deployment was the outboard gimbal cable wrap (see Figure 8). The cable wrap hardware was enveloped in a multi-layer thermal blanket. To maximize clearance at the potential location of contact, a section of blanket was removed from the gimbal harness wrap and replaced with a single layer of vapor deposited aluminum Kapton™ tape. Modification of the blanket was performed in situ.

With the trimmed hardware, the baseline simulations now indicated a 19-mm (0.76-in) clearance. Since the approval metric was based on using the worst case model, another simulation was run, which predicted a clearance of 12 mm (0.48 inch). This exceeds the minimum clearance of 6.35 mm (0.25 inch) by almost a factor of two. The design was acceptable.

The hand manipulation motion studies were repeated and clearance verified. Spacecraft level deployments and environmental testing followed. With respect to the component modifications performed, spacecraft environment testing was complete with the successful post-environmental test deployment. Functional and workmanship verification was achieved.

### **Lessons Learned**

The late discovery and resolution of a potentially mission degrading interference issue has yielded several pertinent lessons.

The compliance in cable synchronization systems in articulating multi-boom systems may allow significant non-kinematic behavior. A particular deployment travel path cannot be assumed. Designing to this assumption led to the development of a g-negation system that biases the deployment to the intended path. This can mask interference or other issues that ground testing is intended to uncover. In the present case, this was discovered during the integration and test phase of the spacecraft development, long after the design phase was complete.

Assuming the deployment path also led to giving up some clearance during the design phase in order to accommodate other packaging needs. If the kinematic indeterminate nature of this deployable was understood and appreciated at the time, clearance would not have been sacrificed. For such a system, more clearance should be kept in reserve. Although not always possible due to space constraints, a good “rule of thumb” is to avoid having deploying hardware below the break plane between the LRMs and the deploying hardware so that clearance increases monotonically during deployment.

The parallel development of a dynamic computer model of this complex deployable and its g-negation system proved indispensable. It allowed detection of the interference condition and informed the solution to the issue. It saved cost and schedule as much of the work was conducted offline while the spacecraft continued its integration and test program. As the HGAS subsystem hardware was integrated, the fidelity of the model was increased. As ground tests were performed, the model was calibrated. In the end, it was a very valuable tool that allowed the investigation and understanding of a complex deployable in a way that would have been difficult without it.

### **Acknowledgements**

The authors would like to acknowledge the all team members that were involved in the conception, development and delivery of HGAS to GPM as well as those that assisted in the issue resolution and editing of this paper. Specific acknowledgements to: Chris Strickland (Product Development Lead), Tim Pike (Designer/Engineer), Chris Mathews (Mechanical Technician), Danny Grove (Designer), Andrew Lea (Test Engineer), Bryon Stepp (Stress Analyst), John Tota (Quality Assurance), Wahid Zewari (Engineer), Minh Phan (Chief Engineer), Rodger Farley (Senior Staff Engineer), and Mark McGinnis (Reviewer).

# In-Orbit Performance of the MWRI Scanning Mechanisms

Manfred Schmid\*, Miao Jun\*\* and Yu Shuang\*\*

## Abstract

Scanning Equipment supporting the Millimeter Wave Radiometer Instrument (MWRI) are flying in a sun-synchronized orbit of 850-km altitude with an inclination of 98.8° on the FY-3 meteorological satellite (FY = Feng Yun, Wind and Cloud). MWRI is a linearly polarized, ten-channel passive Radiometer; it measures precipitation and water clouds, sea ice, snow/water equivalent, drought and flood index, land temperature and soil moisture.

Following the FY3-A, the FY3-B Satellite was launched in autumn 2010. Since that time, the Scanning Equipment was continuously operated. During the last three and a half years in orbit, the Scanning Mechanism has executed about 65 million revolutions, while the Scan Compensation Mechanism (SCM) - used for momentum compensation - has already successfully executed more than one billion revolutions.

During the commissioning phase of the instrument and during the first operation phase, random torque spikes, which manifested themselves as a motor current increase, were observed in the Scan Drive Mechanism, whereas the Scan Compensation drive operated nominally from the beginning.

The result of the root cause investigations performed in order to isolate the issue, and the consequences for the follow-on MWRI equipment which was successfully launched by end of September 2013 (now flying on the FY 3-C Spacecraft), are discussed.

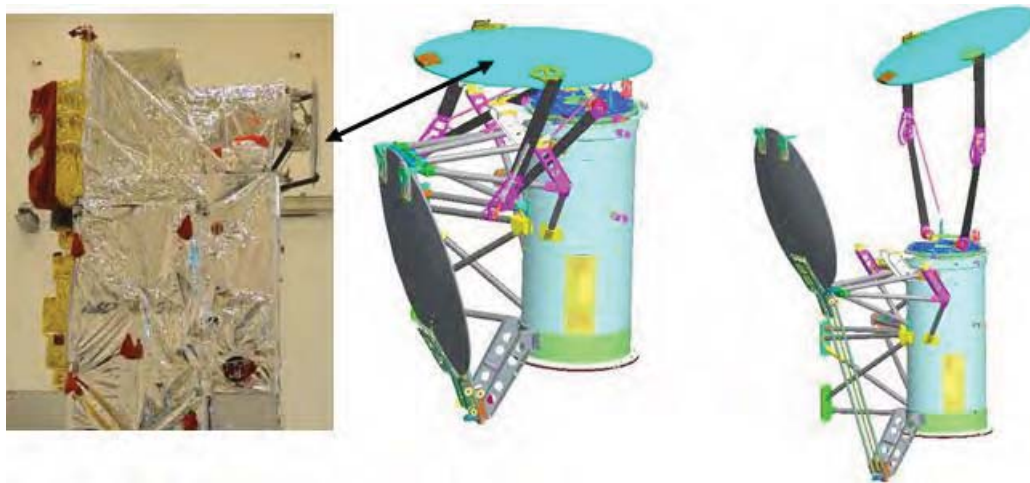


Figure 1. FY3 Spacecraft and Instrument Configuration

## Introduction

The scanning equipment consists of the Scan Drive Mechanism (SDM), a physically independent Scan Compensation Mechanism (SCM), and the Scan Drive Electronics (SDE). The conically scanning MWRI instrument with a mass of 60 kg is continuously operated by the Scan Drive Mechanism (SDM). The

---

\* Airbus Defence & Space (formerly Astrium GmbH Satellites), Friedrichshafen, Germany

\*\* ASES (Aerospace System Engineering), Shanghai, China

velocity of the Scan Compensation Mechanism (SCM) is electronically coupled by a fixed factor to the closed-loop-controlled Scan Drive Mechanism (SDM) in order to achieve momentum compensation during the instrument acceleration and deceleration and during normal operation phases.

The Scan Drive Electronics (SDE) controls and synchronizes the two mechanisms. The spin rate stability of the SDM is 0.3 ms. The spin stability is achieved by a closed-loop control scheme applied to the BDC motors and by a 16-bit encoder feedback device included in the SDM.

The nominal but adjustable spin rate of the SDM is 1.7 s/rev. The rotation speed of the counter-rotating Momentum Compensation Stage is coupled by a fixed factor to the SDM speed and is in the range of 560 revs/min.

During launch, the SDM mechanism bearings are off-loaded by a launch offload device attached to the SDM in the interface between mechanism and instrument. The instrument is supported during launch by instrument-provided holddown release mechanisms (HRMs) fixing the instrument to the S/C. By this design, parasitic loads introduced during launch by the heavy instrument into the SDM bearings are avoided.

After HRM release, the launch offload device - realized by a pre-loaded cup-cone element - provides a precise rotational axis for the Instrument and avoids potential run-out of the instrument CoG from the SDM rotation axis, what would lead to a cyclic excitation of the S/C.

The Flywheel of the Scan Compensation Mechanism with a mass of about 4 kg does not use a HRM. During launch, the flywheel is supported by the SCM bearings only.

### Instrument Description

Figure 2 shows the MWRI Instrument block diagram. After launch and HRM release, the antenna dish is deployed to its final configuration by means of a deployable support structure.

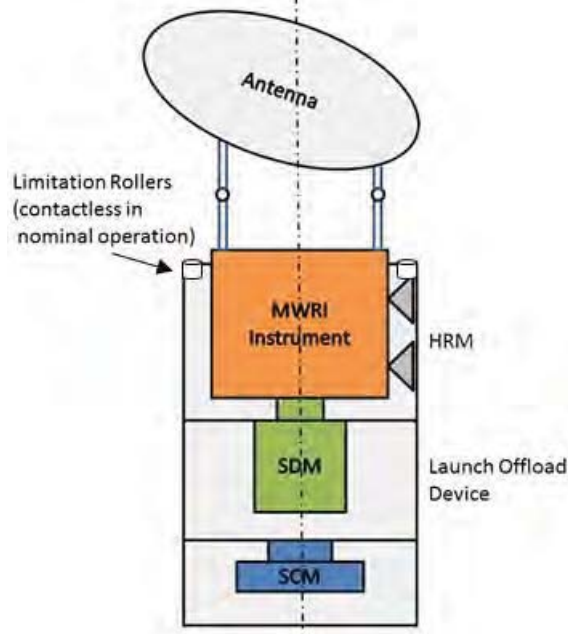
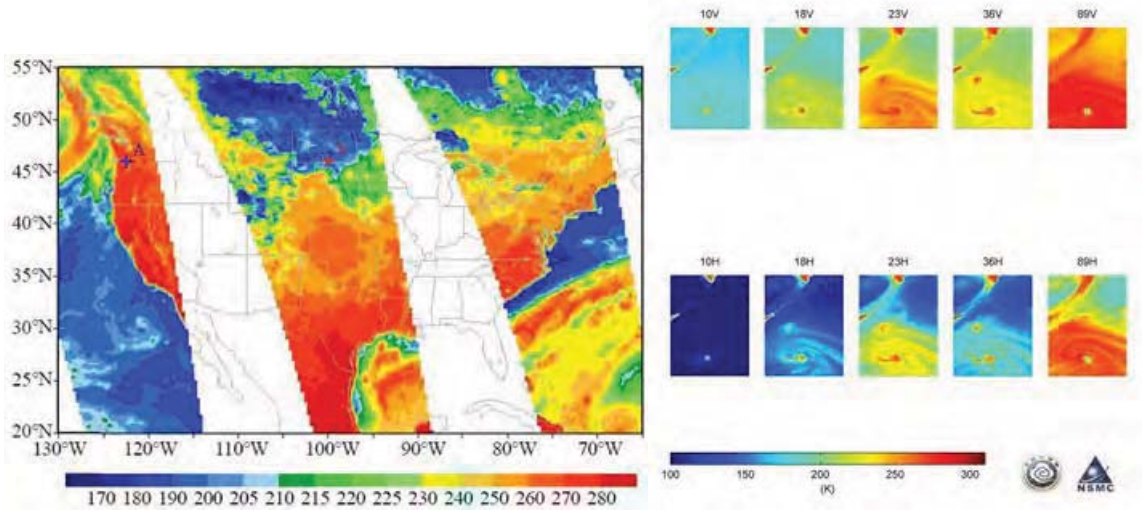


Figure 2. MWRI Instrument Block Diagram



The MWRI Instrument is rotated together with the antenna by means of the SDM in order to allow conical ground scanning. The SCM is used for momentum compensation during normal operation (scan rate changes) and during start-up and potential deceleration phases which take 180 s each, performed in a synchronized and controlled mode. MWRI receives data in 10 frequency channels from 10 GHz up to 89 GHz with a ground resolution of 0.25~1 km. A typical output is depicted in Figure 3.



**Figure 3. Spatial Distribution of Brightness Temperature and Tropical Storm over the Pacific**

### Scan Equipment Definition

The MWRI Scan Equipment consists of a Scan Drive Mechanism (SDM) including a Launch Offload Device, of a Scan Compensation Mechanism (SCM) and of a closed loop Scan Control Electronics (SCE).



**Figure 4. SDM (with Instrument Mol/Mass Simulator) and SCM**

## Scan Drive Mechanism Design (SDM)

The SDM consists of a drive module using two hard preloaded pairs of ball bearings, a redundant brushless DC motor and a redundant optical encoder for closed-loop velocity control. On the rear end of the drive module, a slip ring unit for power and signal transfer from / to the rotating Radiometer Instrument Package is attached. The Harness is guided through the hollow drive shaft to the slip ring rotor.

The I/F to the rotating instrument mounted on top of the SDM is formed by a launch off-load device. The launch off-load device consists of axially pre-loaded flexible metallic bellows and an accurately shaped conical Interface. The combination of both elements also provides high instrument alignment accuracy and torsional stiffness about the rotation axis during the mission. During launch, the conical I/F is lifted off from the mechanism I/F, so to de-couple the instrument load path from the mechanism. After release of the Instrument HRMs, the instrument is pulled back into its conical I/F and torque transfer from the SDM to the instrument is allowed.

The SDM rotor shaft is mounted via 2 pairs of hard preloaded angular contact ball bearings in face-to-face arrangement into the SDM housing (preload 400N). The bearings are manufactured from Stainless Steel 440C, the cages are manufactured from Phenolic Resin, vacuum impregnated and lubricated with Fomblin Z 25 (changed in the FY3C mission to Nye Oil/ Maplub for commonality reasons with the SCM).

The motor is a brushless DC type with completely cold redundant independent stators. The redundant optical Encoders provide position data with 16-bit resolution.

The slip ring for power and signal transfer to the instrument is composed of 19 solid gold tracks and redundant gold alloy brushes to achieve the expected orbit life of 3 years (3.5 years already achieved, corresponding to 60 million revs, 5 years goal).

The SDM mechanism design as used on the FY3-B Spacecraft is shown in Figure 5.

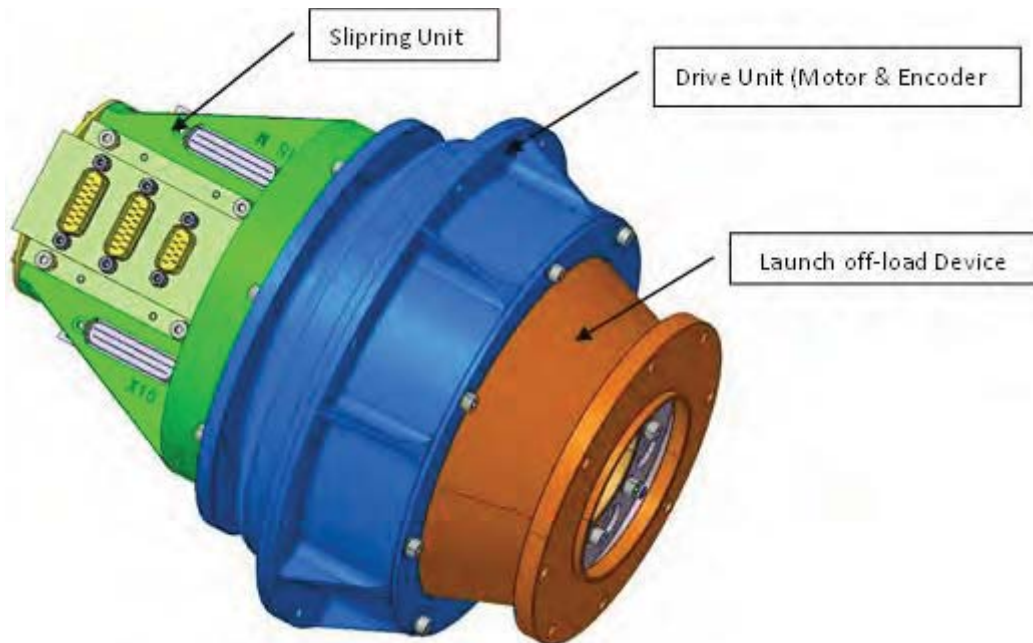


Figure 4. SDM Design as flown on FY3-B

## Scan Compensation Mechanism (SCM) Design

The SCM consists of a drive module using a brushless DC motor with redundant motor stators. The SCM motor is similar to the SDM motor, but optimized for the higher operation speed.

For rotation speed feedback, 3 Hall Sensors are included in each motor stator. A flywheel with trim masses is attached to the motor output shaft.

The SCM is lubricated with Nye Synthetic Oil 2001A and Maplub Grease SH051A. The bearings are identical to the SDM bearings. However, in the SCM only one pair of bearings is used in back-to-back arrangement. The bearing preload is set to 400 N.

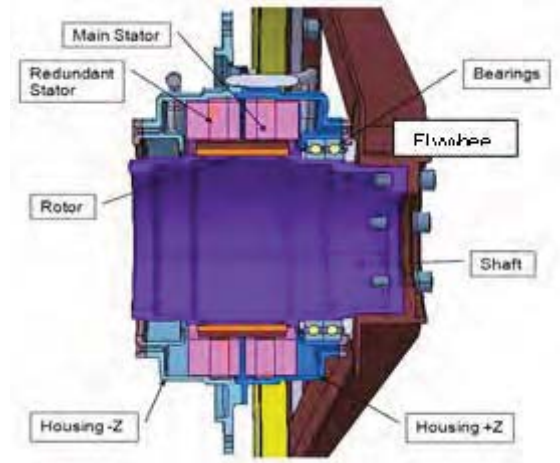


Figure 6. SCM Design

## Orbit Performance and Start-up Issue

During the instrument's in-orbit commissioning phase it was observed that the SDM current was not stable, but it was randomly varying over time. Nominally the current should have been in the range of slightly above 0.2 A, however, in reality current spikes up to the 1 A range were randomly observed along with long term current variations. From this behavior, the conclusion had to be drawn that the torque needed to operate the SDM together with its MWRI instrument module was varying over time.

It can be seen that after about 16 months of operation, the motor current stabilized back to the expected nominal current values of about 0.2 A and also the scan rate performance improved to nominal values.

In Figure 7, the SCM current is plotted for the observed mission time frame and we see that the motor current and consequently the mechanism friction looks very stable over all mission phases and it is well within the expected nominal range from the beginning.

From the telemetry data (current, temperature and scan rate stability), it was not clear which effect could have caused the friction variation in the SDM, leading to the controller current spikes and current variations as observed. In order to understand the issue better, an in-depth root cause investigation was performed.

In Figure 8, we see the typical current variation as received via Telemetry during the instrument start-up and first operation phase. A direct correlation between the motor current variation and the scan rate stability was observed, and the current variation leads also to a reduced controller performance.

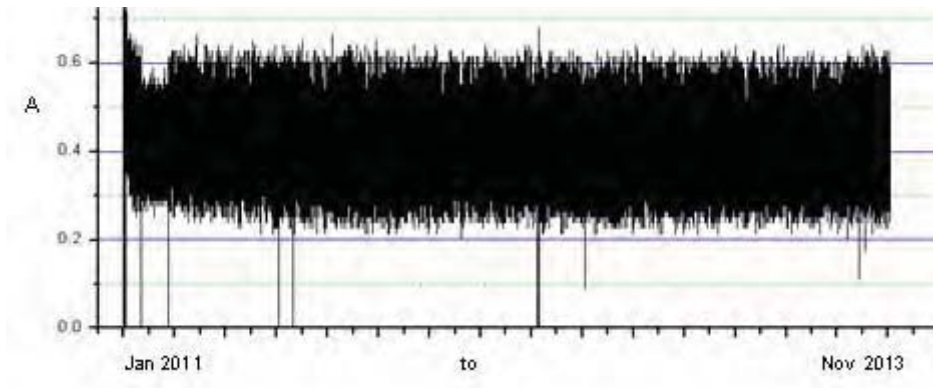


**Figure 7. Typical SCM Current over 34 Months**

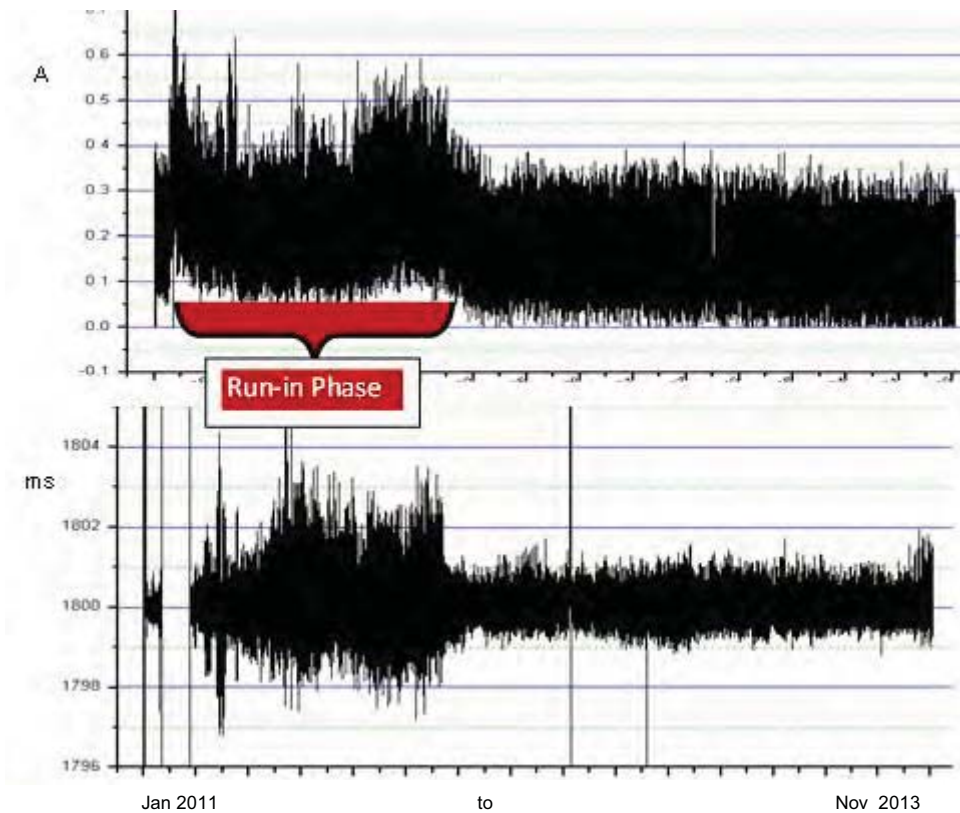


**Figure 8. SDM Motor Current Spikes and associated Scan Rate Stability over 34 Months**

### **Root Cause Investigation**

In order to identify the root cause for the current /friction anomaly observed, all potential disturbance sources were identified and investigated in detail. For initial identification of all potential root causes of the observed anomaly, a fish-bone diagram was used (Figure 9).

#### Identification of Potential Error Sources

Some of the potential root causes could be excluded very soon. These were:

- Transfer of wrong telemetry data --> eliminated due to the fact that all other data was transferred correctly; no anomalies
- Degraded slip rings --> slip rings are new in the first mission phase and no anomaly was observed during the limited number of ground test cycles.
- Bearing degradation --> bearings are new in the first mission phase and no anomaly was observed during any phase of ground testing or after environmental test.
- Bearing contamination by particles--> The probability of parasitic particles or contamination of the mechanism bearings could of course only be judged on the basis of the available documentation and photos and on the basis of discussions with the integration personnel. According to these investigations, and due to the fact that during all integration and test steps from equipment to system level a clean environment was provided, and due to the low probability that external particles could enter into the mechanism during any higher level integration stage, this option was also judged to be very unlikely.

Three different potential root causes could be isolated which might have caused the current issue.

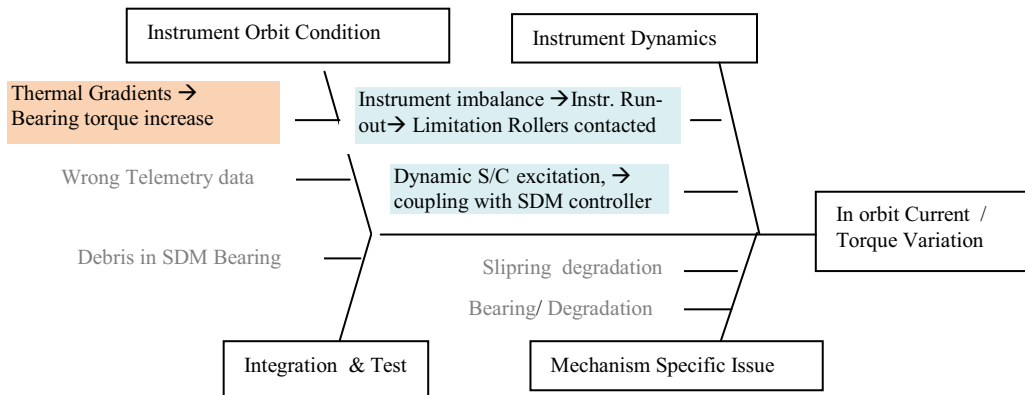


**Figure 9. Fishbone Diagram for Root Cause Investigation**

### Instrument Imbalance

A more likely scenario was seen in a potential misalignment of the rotating instrument axis with respect to the Scan Drive Mechanism, which could cause a lateral run-out and imbalance of the instrument compartment. Such a lateral run-out would lead to a contact of the (nominally contact-less) limitation rollers attached to the top of the instrument compartment with its rotating part. The friction of these rollers would influence the controller behavior and consequently also the current consumption of the mechanism. However, after checking all tolerances and after a proper check of the instrument center of gravity (CoG) and the subsequent calculation of the residual eccentric forces that would act on the off-load device of the mechanism, this possibility could also be excluded.

As a consequence, two remaining root causes were identified:

- Potential dynamic excitation of the quite large antenna on top of the instrument could have caused disturbances to the control loop due to the fact that the real orbit condition of the deployed antenna could not be simulated on ground (1 g condition).
- Thermal gradients in the mechanism that were not specified and not tested on ground.

### Dynamic Excitation of Deployable Antenna Appendage

Since quite a large appendage composed of the antenna dish and of a deployable antenna support structure is mounted on top of the instrument compartment, the possibility of a dynamic coupling between the appendage and the SDM controller was seen as a potential root cause for the observed current



increase. By nature, all on-ground tests on system level had been performed under 1 g conditions, so that influences on the dynamic behavior under 0 g condition could not be excluded.

Therefore the available engineering model (EM) Scan Mechanism was used to support a dynamic test with the goal to quantify potential influences of the antenna and its support structure on the mechanism performance. For this purpose, a test setup was built, simulating the instrument inertia and the mass and stiffness of the antenna deployment structure.

For this purpose the eigen-frequency results from the instrument analysis were used as reference and a spring blade test setup was designed and adjusted to the system reference eigen-frequency by means of a dedicated finite element model (Figure 10). The first rotational system frequency is at about 9 Hz, whereas the first lateral one is at about 5 Hz.

In this configuration, a dynamic test was carried out on the EM Scan Drive Mechanism, with the finding that the influence of the antenna and of its large deployable structure on the mechanism controller, and subsequently on the power consumption, was negligible.

In Figure 11, the H/W of the test setup as derived from the analytical model is depicted. The two masses on the both sides simulate the instrument inertia while the mass on top and the spring blades in between represent the antenna mass and the torsional stiffness of the antenna support structure.

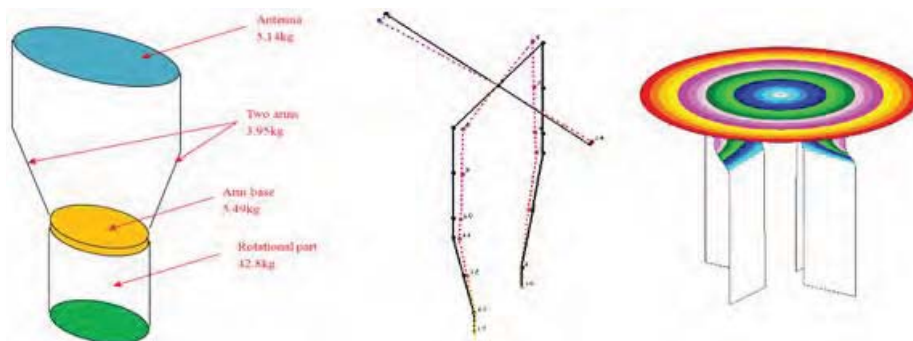


**Figure 10. FE Model of the Antenna Deployment Structure and Analogous Model for Test Setup**

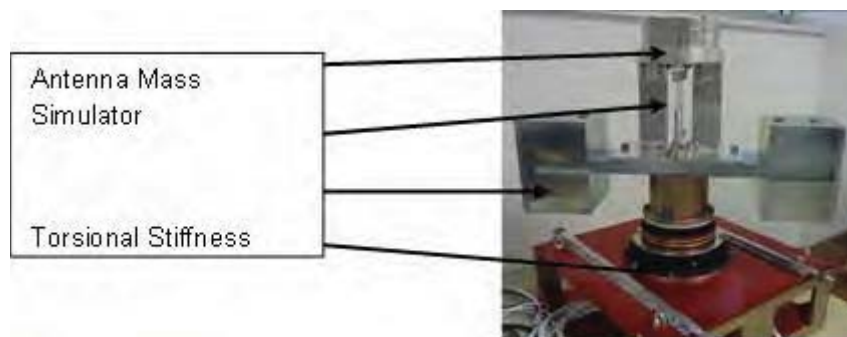


**Figure 11. Torsional Stiffness Test Setup**

Thermal Gradients as Root Cause

The MWRI Instrument is mounted on one side of the Spacecraft. This means that one side is exposed to space, while the other one is oriented towards the S/C structure. As a consequence, temperature gradients might act on the instrument structure, leading to a planarity change of the mechanism mounting I/F and of the mechanism housing itself.



The temperature range in the area of the Thermistors 149 and 150 is in the range of -6 to 0°C (Figure 12). The mechanism temperature (TMP 141/144) and SCM housing temperatures (TMP 132) are also at about 0 deg during operation, with only minor variation. However, the instrument I/F (attached to the mechanism rotor) has a temperature of about 23°C. Therefore, we see a lateral gradient acting through the mechanism mounting I/F to the structure, and also an axial gradient between the Instrument mounting I/F (rotor I/F) and the mechanism bearings.

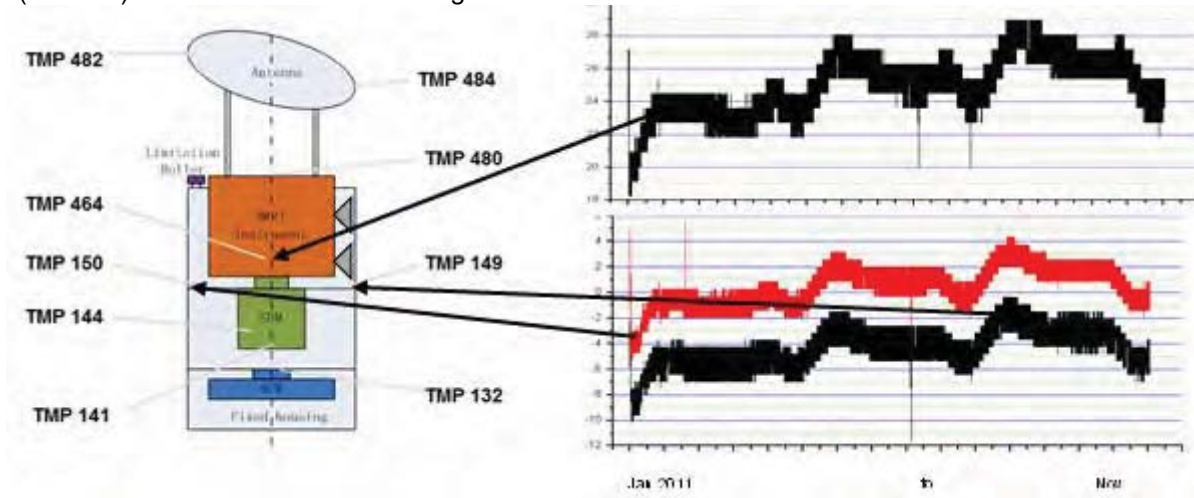


**Figure 52. Relevant Temperature Data (deg C°) of FY3-B over 34 months**

Based on the available orbit temperature data, a thermal deflection analysis was established in order to identify the maximum possible deviation of the mechanism I/F due to thermal gradients in its mounting structure (Figure 13). The analytical result was that the relative displacement of the mounting I/F flange along the mechanism rotation axis due to the gradient influence of the mounting flange is about 65  $\mu\text{m}$ .

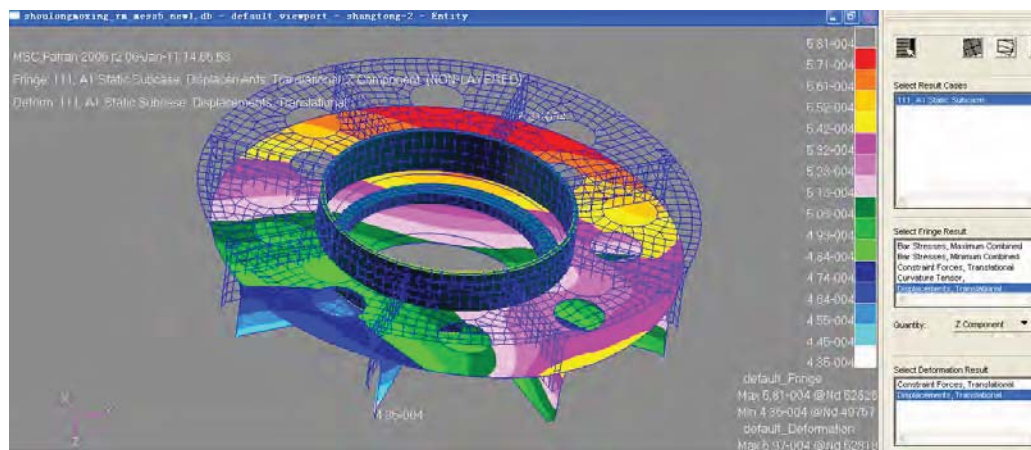


**Figure 13. Thermal Deflection Model Mechanism I/F to S/C**

Based on this result, and based on the fact that an additional axial temperature gradient from the warm instrument to the colder mechanism is observed, the assumption that the orbit current increase was resulting from such gradients which were not tested on equipment level during the qualification and acceptance test campaign, was valid.

In order to verify the findings, the available EM Scan Drive Equipment was submitted to a TV test campaign with the goal to apply realistic gradients as seen in orbit to the system and to prove the influence of such gradients to the motor current and control performance.

In this test, the baseplate (S/C I/F simulator) was cooled by means of cooling loops to the required low temperature, while the mechanism rotor was controlled to the Instrument I/F temperature (Figure 14). At the start of the test, the mechanism rotor I/F was heated to the orbit I/F temperature, while the S/C I/F temperature was at ambient. During continuous rotation of the mechanism, the S/C I/F temperature was decreased while maintaining the rotor I/F at the warm level. During the test, the rotation rate stability was also measured.

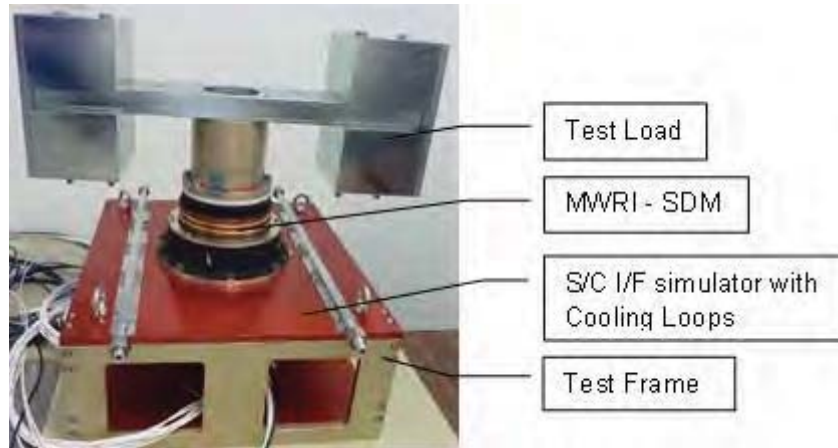


**Figure 14. TV Test Setup for Gradient Test**

A test result overview is depicted in Figure 15. One can clearly see the influence of the thermal gradients acting between the warm mechanism rotor and the cold S/C I/F flange on the motor current.

According to Figure 16, we can also confirm the influence of the thermal gradients to the scan rate stability. If the motor current rises due to thermal gradients in the system, the control performance of the scan rate decreases.

The effect can be explained by the fact that the SDM housing as flown on FY3B was manufactured from aluminium whereas the rotor shaft was manufactured from steel. Therefore the gradient between rotor and stator leads to a decrease in diameter of the outer rings of the thin ring bearings, while the inner ring stays stable. In addition, the deflection of the mechanism housing due to the lateral gradient over the SDM mounting I/F, as shown by the finite element model, will influence the bearing configuration.

The above findings explain well the mechanism behavior during the first mission phase and the associated current increase. The fact that the current and scan performance went back to nominal values after some months of operation can be explained by a run-in effect observed in the new (deflected) bearing configuration which established due to the thermal gradient effects. After a run-in phase of the bearings in the new slightly different configuration, the bearing friction adjusted back to nominal values.

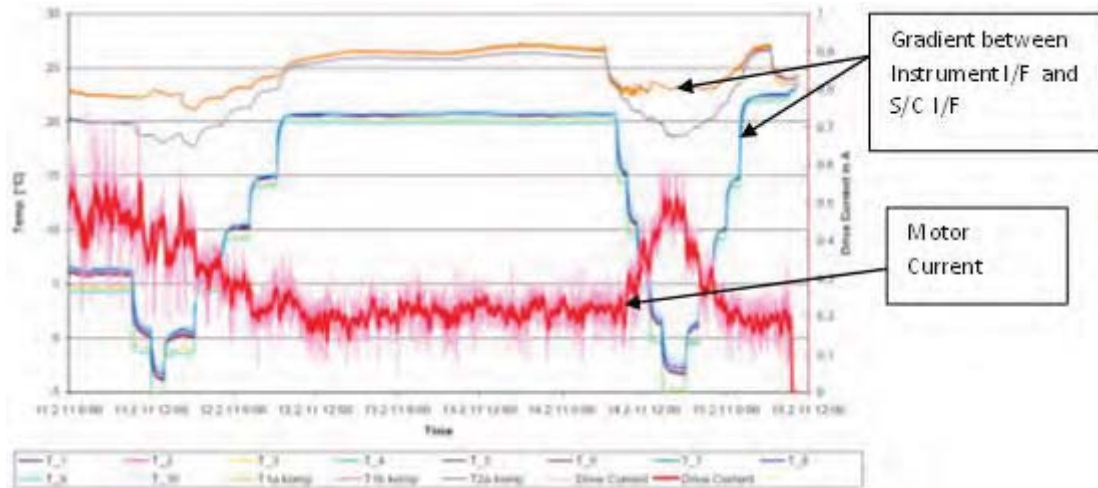


**Figure 15. Influence of the Thermal Gradient to the motor current**

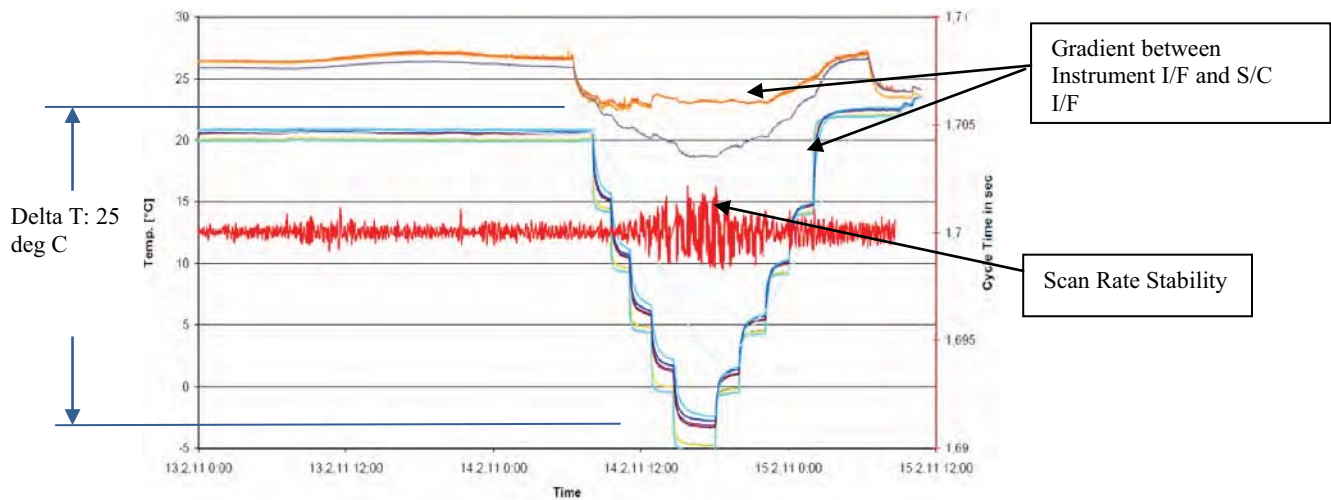


**Figure 16. Influence of the Thermal Gradient to the scan rate stability**

### Optimized Design of FY3-C Equipment

As a consequence of the root cause investigation that confirmed and correlated well with the observed orbit behavior, the relevant findings were transferred into a design modification on the FY3C flight equipment in order to avoid issues as observed on FY3B in the future (see also Figure 17).

- Change the SDM housing material from aluminium to titanium and add additional stiffening ribs:
  - improves insensitivity towards external stresses
  - reduces thermal mismatch due to gradients
- Modify conical I/F of the launch offload device (LOD) to steeper angle (general risk mitigation and improvement of design robustness):
  - improves capability to handle potential instrument CoG shift
  - improves mechanism rotation axis accuracy
- Set bearing preload to 400 N
- Add isolating Ti washer in the I/F to the instrument
  - reduction of thermal gradients in the mechanism

- Add mechanism cover (general risk mitigation and design robustness improvement):
  - dust /contamination protection cover

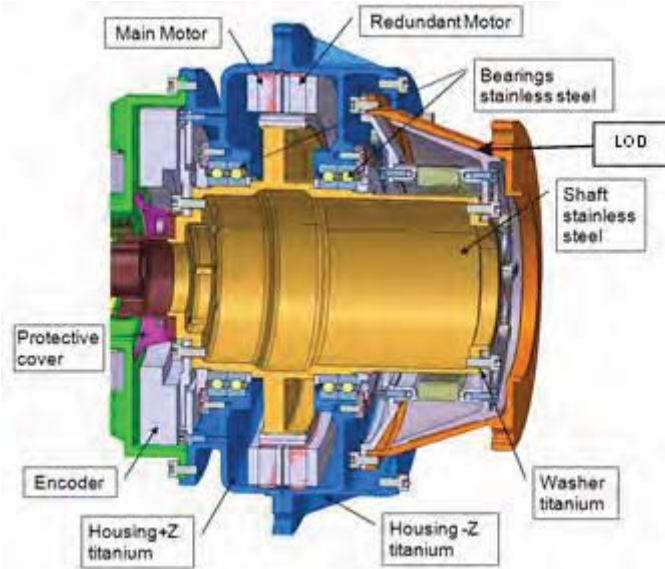


Figure 17. Optimized FY3-C Design

### Ground Test Results with Optimized Design

A summary of the TV ground test results after FY3C flight mechanism modification is depicted in Figure 18. It can be seen that the insensitivity of the Scan Drive Mechanism against thermal gradients has significantly improved and that the current only increases only marginally with the temperature gradient. Also the cycle time deviation stays well within the requirement. Due to the fact that the tested flight mechanism is new and un-used, we can expect an additional run-in effect which will decrease the motor current again over time and further improve the scan rate stability.

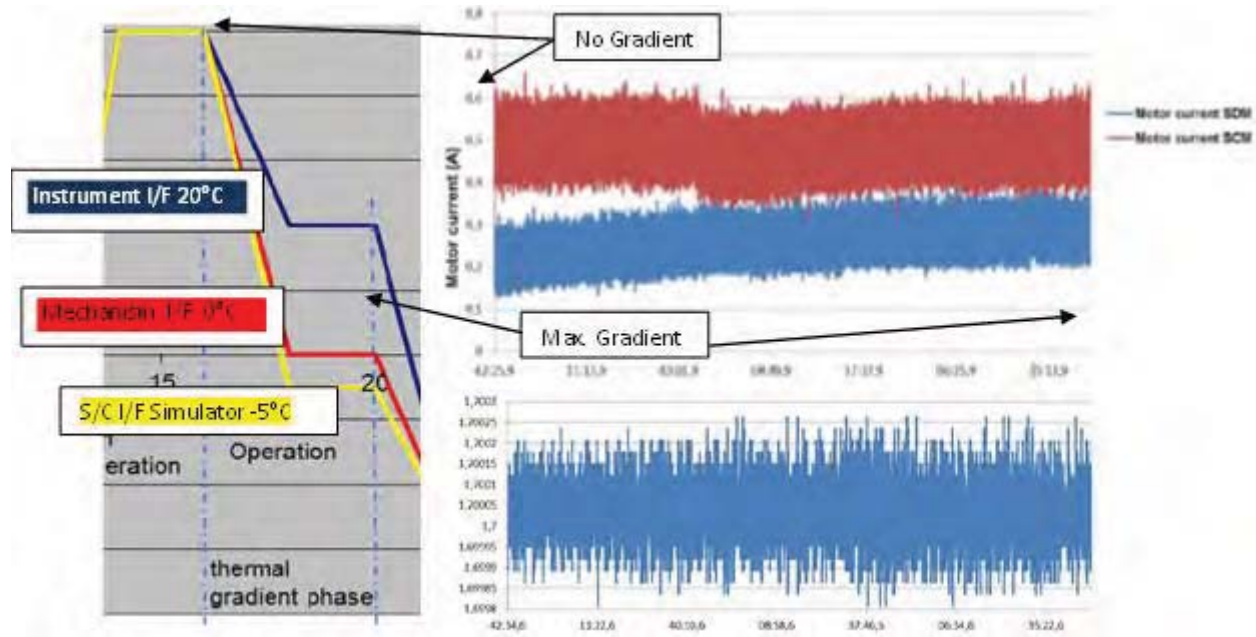


Figure 18. TV Gradient Test results



## SDM Orbit Performance with Optimized Design

The FY3C S/C was successfully launched at the end of September 1013 and the MWRI instrument went operational some days later. The first telemetry current and performance data achieved over a time frame of one week fully confirm the validity and efficiency of the chosen design modifications (Figure 19 and Figure 20).

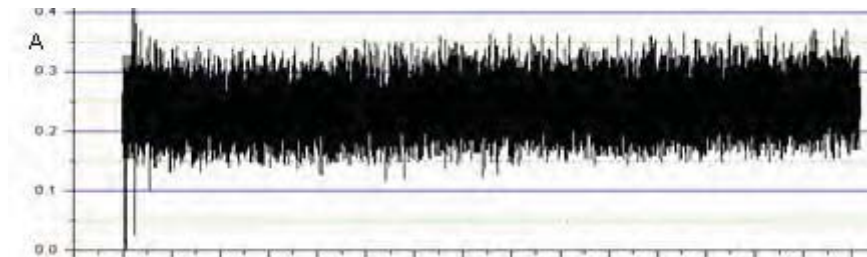


Figure 19. SDM current (A) of FY3-C over the first two Months of Mission Time

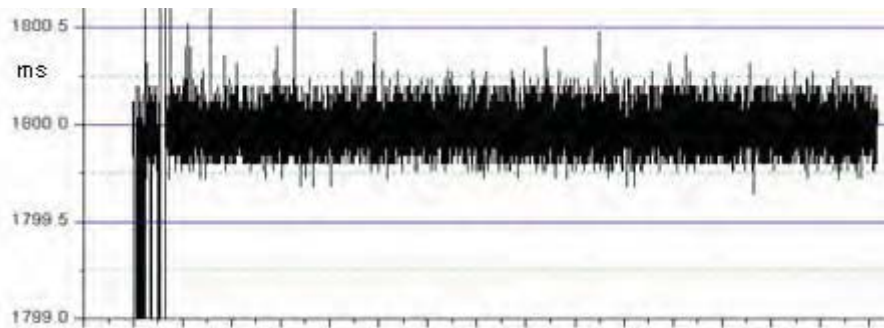


Figure 20. Scan Rate stability (s) of FY3-C over the first two Months of Mission Time

## Conclusions and Lessons Learned

- Check for sensitivity of mechanisms with respect to thermal gradients, even if gradients are not specified.
- In mechanisms with limited torque budgets or highly sensitive control loops such gradients might be critical.
- Limit by design the potential influence of thermal gradients
- Design the I/F to the S/C to be as stiff as possible in order to avoid planarity changes in the S/C I/F due to temperature changes and consequent setting effects influence the performance.
- If slight misalignment effects occur due to (more or less constant) gradients, a "healing effect" of the bearings over time may be observed due to run-in effects on a new ball track.





# Launch Load Resistant Spacecraft Mechanism Bearings Made From NiTi Superelastic Intermetallic Materials

Christopher DellaCorte\* and Lewis E. Moore III\*\*

## Abstract

Compared to conventional bearing materials (tool steel and ceramics), emerging Superelastic Intermetallic Materials (SIMs), such as 60NiTi, have significantly lower elastic modulus and enhanced strain capability. They are also immune to atmospheric corrosion (rusting). This offers the potential for increased resilience and superior ability to withstand static indentation load without damage. In this paper, the static load capacity of hardened 60NiTi 50-mm-bore ball bearing races are measured to correlate existing flat-plate indentation load capacity data to an actual bearing geometry through the Hertz stress relations. The results confirmed the validity of using the Hertz stress relations to model 60NiTi contacts; 60NiTi exhibits a static stress capability (~3.1 GPa) between that of 440C (2.4 GPa) and REX20 (3.8 GPa) tool steel. When the reduced modulus and extended strain capability are taken into account, 60NiTi is shown to withstand higher loads than other bearing materials. To quantify this effect, a notional space mechanism, a 5-kg mass reaction wheel, was modeled with respect to launch load capability when supported on standard (catalogue geometry) design 440C; 60NiTi and REX20 tool steel bearings. For this application, the use of REX20 bearings increased the static load capability of the mechanism by a factor of three while the use of 60NiTi bearings resulted in an order of magnitude improvement compared to the baseline 440C stainless steel bearings.

## Introduction

Spacecraft experience violent (shaking) and sustained (acceleration) inertial forces during launch because of the unsteady combustion provided by rocket propulsion systems (Ref. 1). Though each different launch vehicle presents a different vibration signature to its cargo, the launch load environments share certain characteristics. The launch loads are made up of a fairly steady average acceleration load of 3 to 6 g's plus a dynamic load that varies from 3 g's to over 9 g's depending upon whether the rocket utilizes solid propellants, liquid propellants, or a combination of the two. In addition, spacecraft mechanisms often must endure additional shock-type loads during deployment where the sudden release of spring energy and the use of pyrotechnic charges are encountered.

Such high environmental loads can lead to structural damage and payload damage, especially for delicate hardware. In response to these challenges, the space launch community has developed detailed design guidelines and testing protocols to mitigate negative outcomes (Ref. 1). One approach is to add design margin to flight hardware so that the damage load threshold is well above expected launch loads. This tends to add weight and expense. Another approach is to provide isolation of sensitive mechanisms to shield them from the launch environment. Such isolation systems can themselves be heavy and costly. In most instances, a combination of both approaches is used. Clearly, the development of more intrinsically robust mechanisms offers a path to ameliorate this issue.

Inside space mechanisms, the contacts between balls and races in ball bearings are a primary vulnerability for launch load damage. Spacecraft mechanisms rely on ball bearings for smooth and low friction operation of a wide array of systems such as deployment mechanisms, pointing gimbals and flywheels used in gyroscopes and reaction wheels. If a bearing raceway surface is dented by a static

---

\* NASA Glenn Research Center, Cleveland, OH

\*\* NASA Marshall Space Flight Center, Huntsville, AL

overload event, such as might occur during launch, the bearing may not run sufficiently smoothly and may fail prematurely (Ref. 2). Over the years, bearing and mechanism designers have developed at least four main strategies to overcome this problem.

One strategy is to devise mechanism locking features to divert loads around the bearings through other static structures thereby protecting precision bearing rolling surfaces. Another strategy is to carefully design and tailor internal bearing geometry to increase the load capacity of the ball-race contact. A third approach involves careful orientation of the mechanism with respect to the anticipated static load direction such that any damage that occurs is manifested outside the rolling contact zone. Finally, judicious material selection can be done leading to the use of race materials with heightened load capability. Unfortunately, each of these strategies carries inherent disadvantages.

Locking mechanisms can be complex to design, add weight and can fail to deploy correctly. This can lead to failure of the mechanism these devices are supposed to protect. Careful design of the bearing geometry, increasing conformity of the race-ball contact, can reduce stress levels but leads to increased operating friction. Further, such geometrical changes have only a marginal effect on load capability. The number and size of the bearing balls can be changed to maximize load capacity but this has the effect of increasing cage friction and reducing cage strength and lubricant reservoir capacity. Preferential orientation of a payload within the spacecraft can only alleviate predictable, directional launch loads such as vertical acceleration. Such an approach is ineffective for random vibrational loads. Finally, choosing higher strength materials such as substitution of high carbide tool steel for martensitic stainless steel has other tradeoffs like poor corrosion resistance (Ref. 3). Clearly there is a need for a fresh approach to enhance a bearing's ability to withstand static contact loads in spacecraft mechanisms. The use of superelastic intermetallic materials (SIMs) is such an approach.

Superelastic Intermetallic Materials like 60NiTi have been researched sporadically for over half a century but only recently have they been considered and matured for use in rolling element bearings (Refs. 4 and 5). Their use in highly loaded, high contact stress devices like bearings and gears initially appears counter intuitive. Traditional mechanical component materials like tool steel and silicon nitride have high hardness and elastic modulus and very limited elastic strain deformation range. These properties give components like bearings very high stiffness thus limiting deflection under load resulting in precise and predictable motion control, low friction, and long life. Superelastic materials, like 60NiTi, exhibit material properties that differ significantly from those for traditional bearing materials.

The NiTi alloys have an elastic modulus (stiffness) that is less than half that for steel and one third that of ceramics like silicon nitride. Despite developing high hardness comparable to tool steel through heat treatment, the superelastics can endure very large strains (5 percent or more) in a fully elastic manner. This elastic range is an order of magnitude or more higher than steel and ceramic. The unique combination of properties (high hardness, relatively low modulus, high elastic strain range) results in high resistance to concentrated contact damage such as Brinell indentation denting.

In a series of earlier studies, hardened 60NiTi flat plate surfaces were dented with silicon nitride balls to determine its resistance to damage and to establish stress limits for bearing design guidance (Ref. 6). It was shown that increases in contact stress led to an increase in permanent dent depth. Further it was found that, on a stress basis, 60NiTi's capability fell between that of 440C stainless steel and the high carbide content REX20 tool steel. Figure 1 depicts the stress-dent depth behavior.



**Figure 1. Dent Depth Versus Mean Contact Stress for 12.7-mm-Diameter  $\text{Si}_3\text{N}_4$  Ball Pressed Onto Flat Plate Specimens.**

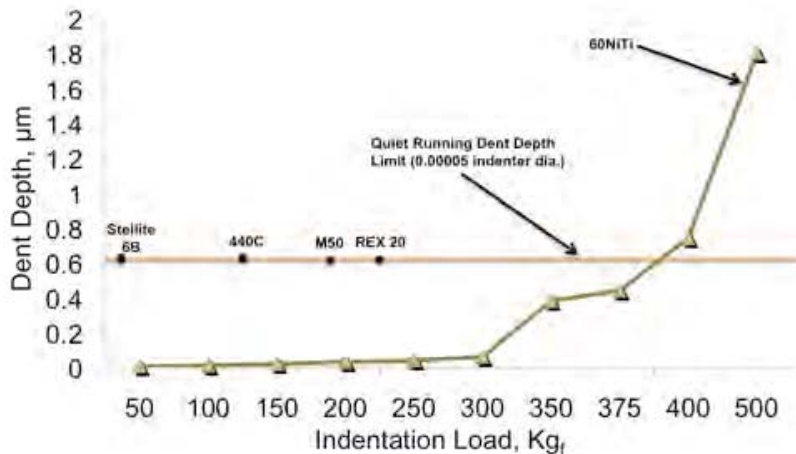


**Figure 2. Dent Depth Versus Indentation Load for 12.7-mm-Diameter  $\text{Si}_3\text{N}_4$  Ball Pressed Onto Flat Plate Specimens.**

When the same data is plotted on a load-dent depth basis, however, the rankings differ dramatically. The reduced modulus of elasticity for 60NiTi combined with its high elastic range enable very high loads prior to the formation of significant permanent dents. In fact, as shown in Figure 2, on the basis of applied load, 60NiTi can withstand 3 to 5 times higher loads than even the most advanced bearing steel.

The results shown in these two figures were then further extended to 60NiTi surfaces that were enhanced by pre-stressing. When pre-stressed by 2.70 GPa, the dent resistance increases by about 30 percent (Ref. 7). This stress capability increase translates into a 50 percent improvement in static load capacity. Figure 3 shows this data. Clearly, even at this nascent stage of technological development, the resilience of NiTi offers a potential path to very robust bearings and mechanisms.

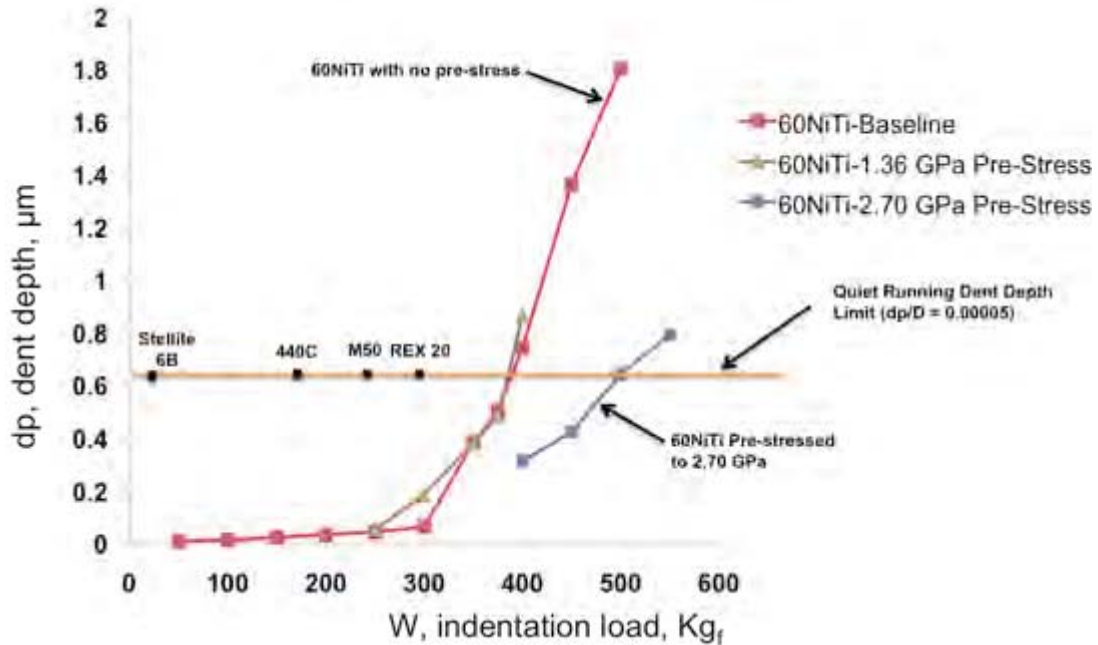


Figure 3. Dent Depth Versus Indentation Load for 12.7-mm-Diameter  $\text{Si}_3\text{N}_4$  Ball Pressed Onto Previously Stressed 60NiTi Flat Plate Specimens (Ref. 7).

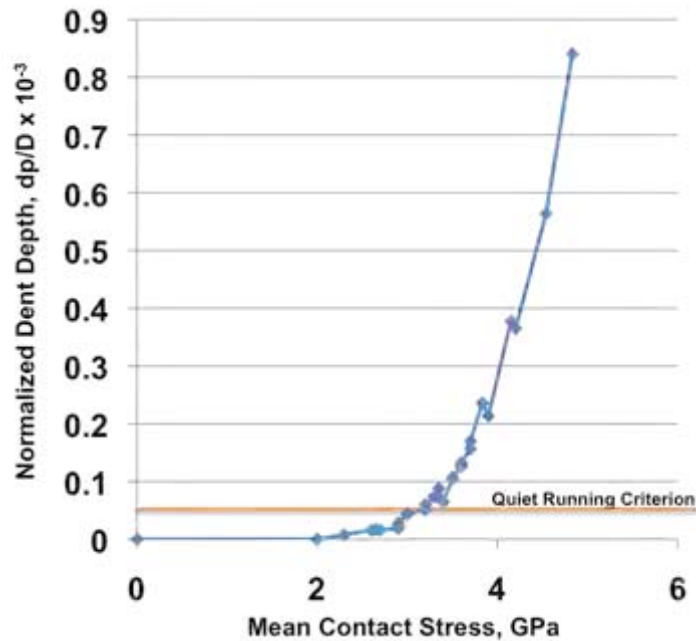


Figure 4. Normalized Dent Depth Versus Mean Hertz Contact Stress for  $\text{Si}_3\text{N}_4$  Balls From 6.4 to 12.7 mm Diameter Pressed Onto 60NiTi Flat Plate Specimens.

However, all of these early results were limited to indenters of the same size, 12.7-mm diameter. For design purposes, the stress and load capacity of NiTi must be evaluated for a wide range of indenter sizes. These experiments were recently reported for silicon nitride indenter balls from 6.35 to 12.7-mm diameter (Ref. 8, to be published). When the Hertz equations were used to collate the dent depth data as a function of stress, the data for all ball sizes fall onto the same curve as shown in Figure 4.

Based upon these flat plate results, one can conclude that the Hertz stress model is useful in predicting denting behavior of NiTi. Further, the behavior of NiTi to static loads is the same whether the indentation is from a small ball or a large ball. In order to complete the assessment and establish a stress capability limit that can be used with confidence for bearing design, however, the dent capability of a real bearing race, with dual curvature must be measured.

In the present study, a series of experiments are carried out in which the inner race of a 50-mm ball bearing is loaded by a single 8.74-mm (0.344-in) diameter silicon nitride ball under loads that range from 2200 to 11,000 N (1000 to 5000 lb). These loads correspond to mean Hertz contact stress from 2.1 to 3.5 GPa. The resulting dents are characterized for form, shape and depth. This data is then used to firmly establish load capability of 60NiTi bearing races. In addition, the newly established stress capability is then applied to the design of ball bearings that support a simple notional space mechanism, a reaction wheel. By analysis, the wheel assembly is then put through estimated space vehicle launch loads to determine its ability to survive without damage.

### Materials and Procedures

The test specimens consist of a ceramic indenter ball and a 60NiTi bearing race. The indenter is a standard grade 5 Si<sub>3</sub>N<sub>4</sub> bearing ball (8.74-mm dia.) and the inner race of a 50-mm bore ball bearing made from 60NiTi. The general material properties of these materials are shown alongside more conventional tool steel bearing materials in Table 1.

**Table 1. Nominal Properties for 60NiTi and Si<sub>3</sub>N<sub>4</sub> Test Specimens and Conventional Bearing Steels**

Property	60NiTi	440C	Si <sub>3</sub> N <sub>4</sub>	M-50
Density	6.7 g/cc	7.7 g/cc	3.2 g/cc	8.0 g/cc
Hardness	56 to 62 HRC	58 to 62 HRC	1300 to 1500 Hv	60 to 65 HRC
Thermal conductivity W/m-°K	~9 to 14	24	33	~36
Thermal expansion	~11.2×10 <sup>-6</sup> /°C	10×10 <sup>-6</sup> /°C	2.6×10 <sup>-6</sup> /°C	~11×10 <sup>-6</sup> /°C
Magnetic	Non	Magnetic	Non	Magnetic
Corrosion resistance	Excellent (Aqueous and acidic)	Marginal	Excellent	Poor
Tensile/(Flexural strength)	~1000(1500) MPa	1900 MPa	(600 to 1200) MPa	2500 MPa
Young's Modulus	~95 GPa	200 GPa	310 GPa	210 GPa
Poisson's ratio	~0.34	0.3	0.27	0.30
Fracture toughness	~20 MPa/√m	22 MPa/√m	5 to 7 MPa/√m	20 to 23 MPa/√m
Maximum use temp	~400 °C	~400 °C	~1100 °C	~400 °C
Electrical resistivity	~1.04×10 <sup>-6</sup> Ω-m	~0.60×10 <sup>-6</sup> Ω-m	Insulator	~0.18×10 <sup>-6</sup> Ω-m

Silicon Nitride is a hard ceramic material that is increasingly being used for balls in rolling element bearings because of its excellent corrosion resistance, low density, and fatigue life capability. Under the poorly lubricated conditions, ceramic-steel hybrid bearing configurations are typically more wear resistant than all-steel bearings.

The bearing race is made from powder metallurgy processed 60NiTi manufactured according to the steps detailed previously in the literature (Ref. 9). Briefly, pre-alloyed powder is made by atomization using 60 wt% nickel and 40 wt% titanium feedstock. The powder is placed inside an evacuated mild steel can that is then sealed by welding. The canned powders are consolidated under high pressure and temperature resulting in a fully dense 60NiTi ingot. The ingot is cut using a combination of electric discharge machining, turning and grinding operations to produce slightly oversized bearing races. The

aces are then heat treat hardened, finish ground and polished to produce bearing quality races as shown in Figure 5.



**Figure 5. 60NiTi Bearing Races.**

In order to estimate the static load capacity (permanent dent resistance) of a 60NiTi hybrid bearing one first needs to measure the load limit of a single ball-race contact. When one ball contacts a race, the load limit is reached when the Hertz contact stress exceeds that necessary to create a permanent dent whose depth is approximately 0.00005 times that of the ball diameter. This dent depth magnitude corresponds to a damage threshold which when exceeded leads to rough bearing operation and potentially reduced fatigue life (Ref. 2). The Hertz equations are used to calculate the contact stress. The stress is a function of the load, the geometries and material properties of the ball and race. The bearing geometry evaluated adheres to conventional design norms. The ball has a radius of 4.37 mm and the race curvatures are nominally 4.55 and 27.4 mm in the cross race and ball path (circumferential) directions, respectively. This gives the bearing ball-race conformity a value of 52 percent, a value very typical for ball bearings (Ref. 10). Since the inner race-ball contact represents the most severe stress location in a ball bearing, it is selected in the present study as the location of interest.

A special fixture was designed and fabricated to firmly hold the inner race and present it to a single ceramic ball for loading experiments. Figure 6 shows the fixture that is made up of two V-blocks that cradle a solid steel shaft onto which the bearing race is mounted. The steel shaft is marked to aid in placing the indents and is easily rotated while the fixture is mounted in a standard materials test load frame.

To conduct a test, the race fixture is placed on the lower platen of the load frame and held in place with two C-clamps. The ball pushrod is placed in the hydraulically actuated grip of the upper platen. A small amount of silicone vacuum grease is placed into the hemispherical cavity machined into the lower end of the ball pushrod. The ceramic indenter ball is placed into the cavity and the grease prevents the ball from falling out during unloaded periods of testing. The load frame is computer controlled using the desired test load as the control parameter.

To run a test, the ball pushrod is lowered at low speed by the computer until contact with the race is detected. The test load is then gently applied over approximately a five second ramp-up period and then held for 60 seconds. The load is then removed and the race shaft is rotated to the next desired test location. Dent locations are spaced equally  $12^\circ$  apart around the circumference of the race. After the dent experiments are complete, the fixture is removed and placed into an optical surface profilometer for dent depth characterization.



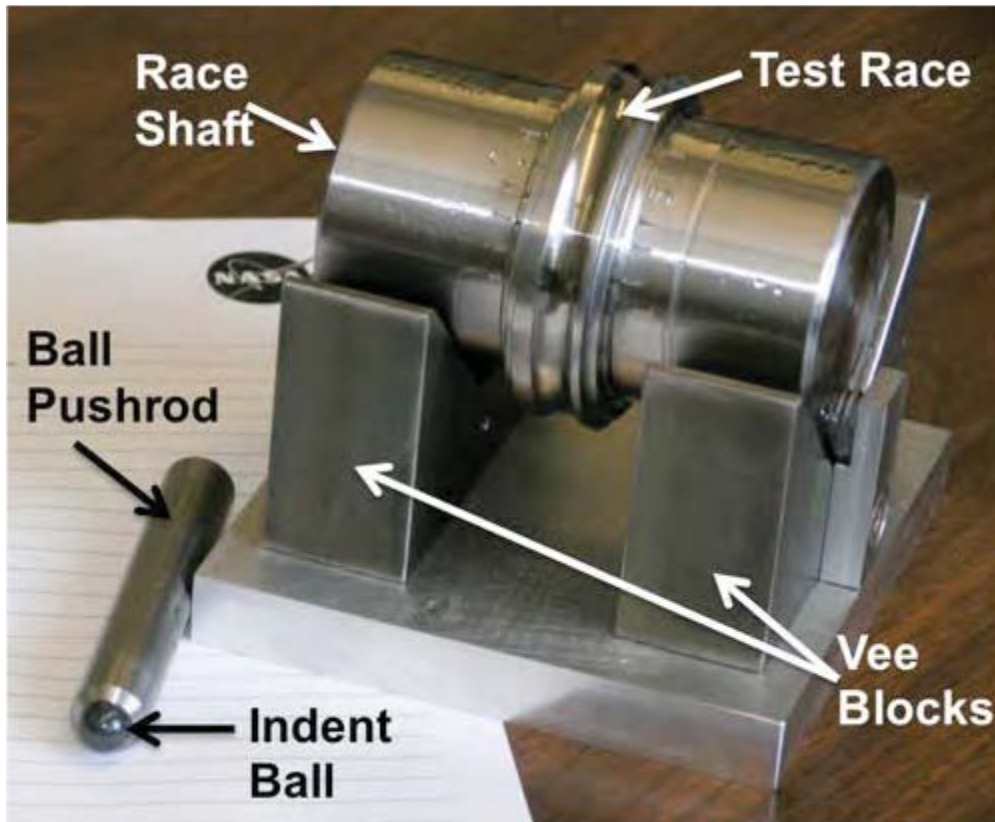


Figure 6. Bearing Race-Ball Dent Fixture.

### Results and Discussions

The single ball versus race static load capacity of a hybrid  $\text{Si}_3\text{N}_4$ -60NiTi bearing was evaluated and the results are shown in Table 2. In the table, the dent depth, dent depth normalized by the ball diameter, the peak stress, and the mean stress are listed. The normalized dent depth as a function of mean stress is plotted in Figure 7.

The dent depth data for the ball-race contact agrees reasonably well with the more generalized ball-flat plate dent depth data collected previously (Ref. 8). This agreement, despite differences in contact geometry, further support the argument that the Hertz stress relations for contacting bodies can be confidently applied to bearing design. Using the generally accepted dent depth criteria ( $d_p/D \sim 0.00003$  to  $0.00010$ ), the data indicate that the damage threshold for 60NiTi is around 2.8 to 3.3 GPa. This is slightly lower than the value estimated from flat plate dent studies but within data scatter and is to be considered in good agreement. Further experiments with additional race sizes are warranted to narrow the stress limit more precisely. For the present, a reasonable stress limit, when designing bearings to withstand high static load, is 3.1 GPa.

In the section that follows, a notional spacecraft mechanism, a small reaction wheel assembly (RWA), will be assessed to determine how the substitution of 60NiTi for steel in the bearings can affect the ability to withstand the rigorous launch vibration load environment. Through such an assessment it is hoped that pathways to performance improvement, weight reduction or enhanced robustness will be revealed.

**Table 2. Indentation Depth Data Summary**

[{Si<sub>3</sub>N<sub>4</sub> Ball (8.74-mm dia.) loaded against hardened (HRC 60.5) polished 60NiTi inner race}  
 Inner Race Curvature Radii: ball-path, 4.25 mm; cross-race, 1.27 mm.]

Indent load, kg <sub>f</sub> (lb)	Mean stress, GPa (ksi)	Peak stress, GPa (ksi)	Dent depth, <sup>a</sup> μm (μin.)	Dent depth/Ball dia., × 10 <sup>-4</sup>
493 (1000)	2.05 (298)	3.07 (446)	None detected	-----
741 (1500)	2.40 (348)	3.52 (511)	None detected	-----
988 (2000)	2.59 (375)	3.88 (562)	0.19 (7.5)	0.22
1111 (2250)	2.69 (390)	4.03 (585)	0.12 (4.8)	0.14
1235 (2500)	2.79 (404)	4.18 (606)	0.59 (23.3)	0.68
1358 (2750)	2.88 (417)	4.32 (626)	0.55 (21.8)	0.63
1482 (3000)	2.96 (429)	4.44 (644)	0.80 (31.4)	0.92
1605 (3250)	3.04 (441)	4.53 (661)	1.20 (47.4)	1.37
1729 (3500)	3.12 (452)	4.68 (678)	1.84 (72.6)	2.11
1852 (3750)	3.19 (463)	4.79 (694)	1.76 (69.3)	2.01
1976 (4000)	3.26 (473)	4.89 (709)	2.53 (99.8)	2.89
2100 (4250)	3.32 (482)	4.99 (723)	3.68 (145)	4.21
2223 (4500)	3.39 (492)	5.08 (737)	4.01 (158)	4.59
2346 (4750)	3.45 (500)	5.18 (751)	5.53 (218)	6.33
2470 (5000)	3.51 (509)	5.27 (764)	4.62 (182)	5.29

<sup>a</sup>Typical data scatter range ±5 percent.

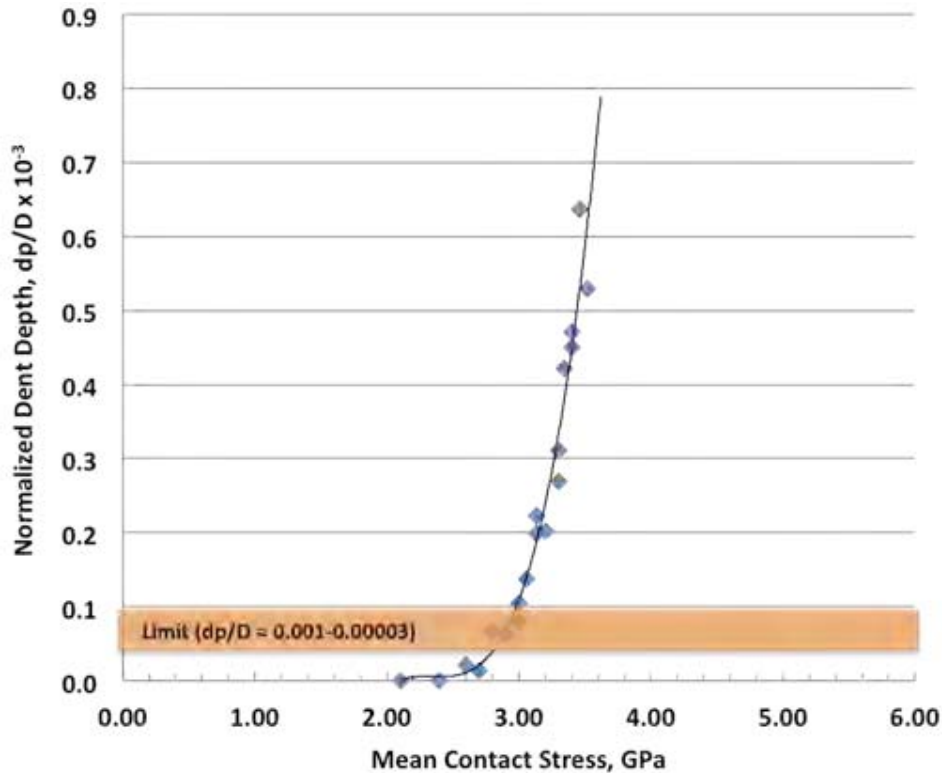


**Figure 7. Normalized Dent Depth Versus Mean Hertz Contact Stress for Inner Race of a 50-mm 60NiTi Bearing Loaded by a Si<sub>3</sub>N<sub>4</sub> Indenter Ball (8.74-mm dia.).**

## Notional Design Test Case

Spacecraft often use reaction wheel assemblies (RWA) for motion control functions. These assemblies consist of an electric-motor-driven heavy wheel supported on ball bearings. RWA's are typically hard mounted to a spacecraft structure in order to impart stabilizing forces and moments through inertial phenomena. A more complex device, the control moment gyroscope (CMG), employs multiple spinning wheels housed in one degree of freedom swivel mounts (gimbals) and can provide stabilization as well as pointing forces to the spacecraft. Both of these devices work in conjunction to traditional thrusters (chemical propulsion devices) to accurately position a spacecraft. To function properly, the bearings must provide low and stable running torque for the entire mission life that can span a decade or more. Despite modest operation loads and speeds, long life is assured only if the bearings are lubricated properly and survive the rigors of launch without damage.

While spinning in orbit, bearing loads are low but during launch while the wheels are stationary the vibration and acceleration load environment can be severe. It is during this period of high load that bearing balls can dent bearing races affecting the long-term life and smooth operation of the device. The contact between the balls and inner race surface are particularly vulnerable due to geometrical effects. The ball-inner race contact areas are very small because of the race curvature and this leads to high stresses even at modest bearing load.

Estimating launch loads and designing robust yet lightweight mechanical systems capable of withstanding these loads can be as much an art as a science. Each rocket launch vehicle has its own unique vibration signature and, depending upon the payload configuration and isolation techniques used, random and steady acceleration loads transmitted to a particular payload can vary widely. These uncertainties often lead to the requirement that both analytical and experimental methods be used to verify that a device, such as a reaction wheel, can withstand anticipated load levels before being approved for flight.

The use of superelastic 60NiTi in reaction wheel bearing applications offers the potential for increased static load margins. To determine the potential magnitude of these improvements, a small rotor (5 kg) supported by two duplex pairs of small (R4 size) deep groove bore ball bearings is considered. Maximum contact stress limits for 60NiTi, 440C and the high carbide content REX20 tool steel are applied to the ball-inner race contact to estimate the maximum allowable g-forces the assembly can withstand. By comparing these resulting maximum load values, the benefits of using superelastic materials for races, and balls in wheel bearings can be determined.

A commercially available reaction wheel assembly shown in Figure 8 is the basis for the load modeling (Ref. 11). R4 ball bearing design and internal geometry is based upon catalogue values and are typical for such bearings (Ref. 12).

For simplicity, the rotor is modeled as being axially and radially symmetric. Bearing preload is neglected and the load case considered is a radial load passing through the center of mass equally counteracted by all four bearings. This calculation does not require a priori knowledge of the wheel geometry or inertia properties and thus can be undertaken without revealing any manufacturer's proprietary information. Radial bearing load capacity is lower than thrust load capacity because less than half the rolling elements support the load whereas for thrust load support all the ball-race contacts share the load equally. Examination of the radial load capability of bearings made with varying materials helps to clearly reveal the potential of using superelastic bearing materials.

Determining a specific launch load value is difficult. Developing a more generalized range of expected maximum loads is fairly straightforward. NASA provides a standard (GSFC-STD-7000) in which the maximum expected random vibration levels for payload components of various sizes (mass) are given (Ref. 1). By adding the random level to the steady acceleration g-forces one can establish a reasonable load level to impose when making the bearing load calculation. For payload components with masses less than 22.7 kg, the random load levels are 14.1  $G_{rms}$  for qualification and 10.0  $G_{rms}$  for acceptance.

Typical steady acceleration forces for rocket launch are 1 to 3 g's. Thus for the RWA example being considered, a 5-kg wheel, the maximum applied rotor load is 17.1 g's (14.1 + 3).

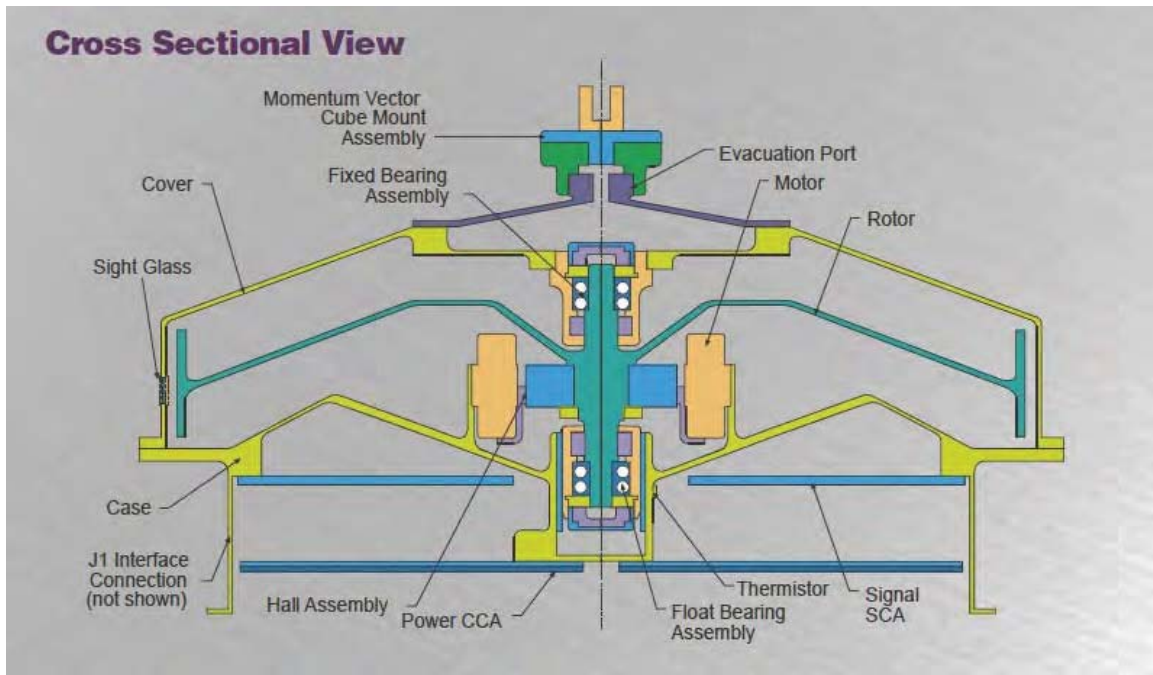


**Figure 8. Typical Reaction Wheel Assembly. Figure Based Upon Honeywell Corporation Model HR 0610 Design (Ref. 11). 5-kg Wheel Supported on Four R4 Ball Bearings With Standard (Catalogue Values) Design (Ref. 12).**

**Table 3. Reaction Wheel Assembly Bearing Configurations Assessed**

[Ball: 8.74-mm dia., Inner Race Curvature Radii: ball-path, 4.25 mm; cross-race, 1.27 mm.]

Configuration no.	Ball material	Race material	Limiting contact Stress, <sup>a</sup> GPa (ksi)	Single ball-race load limit, N (lb)
I	440C	440C	2.5 (350)	196 (44)
II	Si <sub>3</sub> N <sub>4</sub>	440C	2.5 (350)	138 (31)
III	60NiTi	440C	2.5 (350)	463 (104)
IV	60NiTi	60NiTi	2.5 (350)	846 (190)
V	Si <sub>3</sub> N <sub>4</sub>	60NiTi	2.5 (350)	374 (84)
VI	60NiTi	60NiTi	3.1 (450)	1780 (400) <sup>c</sup>
VII	Si <sub>3</sub> N <sub>4</sub>	60NiTi	3.1 (450)	801 (180)
VIII	<sup>b</sup> REX20	REX20	3.8 (550)	587 (132)
IX	Si <sub>3</sub> N <sub>4</sub>	REX20	3.8 (550)	467 (105)

<sup>a</sup>Mean Hertz contact stress.

<sup>b</sup>REX20 properties: Young's Modulus (E): 234 GPa; Poisson's Ratio (ν): 0.30.

<sup>c</sup>Hertz calculations may be invalid due to excessively deformed geometry.

Table 3 shows the bearing material configurations considered along with the bearing geometry assumptions and other pertinent details needed for the calculations.

The load capacity of the RWA bearing utilizing one of the configurations shown in Table 3 is determined by combining Hertz stress calculations with generally accepted bearing design relations that correlate ball-race contact stress to radial load capacity. For the Hertz calculations, an automated spreadsheet is used in which the contact material properties, geometry and single ball-race load is input. The

spreadsheet provides the mean and peak stress along with the contact area using the stress approximation equations developed by Antoine et al. (Ref. 13). The last column in Table 3 gives the single ball-race static load capacity for the nine materials and stress limit configurations considered.

To relate the single ball-race load capacity to radial load capacity of the R4 bearing, the relationships presented by Derner and Pfaffenberger and shown below are employed (Ref. 14):

$$F_R = 9Q_{\max}/5 \quad (1)$$

In Equation (1),  $F_R$  is the bearing load capacity and  $Q_{\max}$  is the single ball load capacity. The R4 bearing radial load capacity is then multiplied by four to account for the use of two duplex pairs of bearings in the RWA to get the overall wheel load capacity. This value is compared to the launch forces on the wheel to determine launch design margins for the various configurations. The calculation results are shown in Table 4.

**Table 4. Reaction Wheel Launch Load Capacity**  
[5-kg wheel mass supported on two duplex pairs of R4 bearings.]

Configuration no.	Ball material	Race material	Shaft load capacity, kN (lb)	RWA load capacity, g
I	440C	440C	1.4 (316)	28.6
II	Si <sub>3</sub> N <sub>4</sub>	440C	1.0 (223)	20.2
III	60NiTi	440C	3.3 (748)	67.9
IV	60NiTi	60NiTi	6.1 (1368)	124.4
V	Si <sub>3</sub> N <sub>4</sub>	60NiTi	2.7 (604)	54.8
VI	60NiTi	60NiTi	<sup>a</sup> 12.8 (2880)	<sup>a</sup> 261.2
VII	Si <sub>3</sub> N <sub>4</sub>	60NiTi	5.8 (1296)	118
VIII	REX20	REX20	4.2 (950)	86.2
IX	Si <sub>3</sub> N <sub>4</sub>	REX20	3.4 (756)	68.5

<sup>a</sup>Load beyond yield strength of RWA shaft.

The load capacity results reveal some interesting insights. The two conventional bearing configurations (I-440C/440C and II-Si<sub>3</sub>N<sub>4</sub>/440C) have load capacity values near the g force requirements for rocket launch with additional margin to accommodate bearing preload and other forces neglected in the present simplified analyses. Another insight is that the use of a high performance material like REX20 offers a significant improvement in the load capacity, about 3-fold over the 440C bearing. It is this very improvement that drove the development of such high-carbide tool steels for heavy reaction wheels despite the poor corrosion resistance and higher production costs of REX20 (Ref. 15).

Finally, the estimated shaft load capacity for the all superelastic bearing configuration (VI) shows a value well beyond the bending load capability of an RWA wheel shaft sized for the bore of R4 bearings. This revelation suggests that in such an application, a superelastic bearing is essentially shockproof in that the bearing capability is beyond any load the rest of the instrument could withstand. Of course, designing a space mechanism with load capacity far in excess of requirements is unrealistic. Excess launch load capacity margins do not enhance system performance. However, the availability of more robust bearing materials, like 60NiTi may enable the use of fewer and smaller bearings thus reducing weight, power consumption, and potentially cost. In addition, the enhanced corrosion resistance and non-magnetic properties of the NiTi alloys could enable mechanism designs with new capabilities.



## Summary Remarks

This investigation confirms that bearings made with low modulus, hard and superelastic 60NiTi material exhibits extraordinarily high static load capacity. Indentation experiments using the inner race of a 50-mm-bore ball bearing contacting a ceramic ball can withstand about 3 GPa mean stress before dents deeper than accepted limits are reached. This limiting stress value is consistent with the results obtained previously using flat plate 60NiTi specimens with indentation balls of varying diameters. The good agreement of the load capacity data collected under differing contact geometry configurations indicate that the Hertz stress relations can be used with confidence when designing bearings with respect to static load capacity.

Using a conservative stress limit of 3.1 GPa, the launch load tolerance of a small notional Reaction Wheel Assembly (RWA) supported on R4 sized bearings utilizing different materials was evaluated. The results show that the baseline RWA supported by 440C steel bearings can withstand launch vibration levels of about 25 g's. The use of the super-hard tool steel REX20 increases the launch load tolerance by a factor of three or more albeit while introducing bearing corrosion concerns. The use of 60NiTi provides an order of magnitude more load tolerance than the baseline 440C steel bearing case while imparting improved corrosion protection.

The enhanced load capacity enabled by the use of superelastic bearing materials like 60NiTi offer the opportunity to utilize smaller and fewer support bearings with commensurately lower operating friction. In future systems that may require larger wheels, the ability to withstand higher static loads may be an even stronger design driver for the continued development of superelastic bearings.

## Acknowledgements

The authors wish to acknowledge NASA's ISS Project Office and the NASA Engineering and Safety Center for their support of this work. The authors also acknowledge the technical contributions made to this work by NASA Glenn Research Center's Nathan Wilmoth, Walter Wozniak, and Fransua Thomas and also the valuable race dent measurements made by Justin Rowe of the Oregon State University during his internship at NASA Marshall Space Flight Center (MSFC). Without their assistance in specimen preparation and testing have enabled this work.

## References

1. General Environmental Verification Standard-Goddard Space Flight Center Standard-STD-7000, NASA GSFC, Greenbelt, MD, April 2005.
2. A.R. Leveille and J.J. Murphy, "Determination of the Influence of Static Loads on the Output Torque of Instrument Ball Bearings," in Proceedings of the Charles Stark Draper Lab. International Ball Bearings Symposium, (1973).
3. D.W. Smith, A.R. Leveille, M.R. Hilton, and P.C. Ward: "REX 20/Si<sub>3</sub>N<sub>4</sub> Control Moment Gyroscope Bearing Development," Proceedings of the 32<sup>nd</sup> Aerospace Mechanisms Symposium, May 13-15, 1998, Cocoa Beach, FL, NASA CP-1998-207191, pp. 223-235, 1998.
4. C. DellaCorte, S.V. Pepper, R. Noebe, D.R. Hull, and G. Glennon, 2009, "Intermetallic Nickel-Titanium Alloys for Oil-Lubricated Bearing Applications," NASA/TM—2009-215646.
5. C. DellaCorte, R. Noebe, M.K. Stanford, and S.A. Padula, "Resilient and Corrosion-Proof Rolling Element Bearings Made From Superelastic Ni-Ti Alloys for Aerospace Mechanism Applications," Proceedings of the 2011 ASTM Rolling Element Bearings Conference, Anaheim, California, April 13-15th, 2011 and NASA/TM—2011-217105.
6. C. DellaCorte, L.E. Moore, III, and J.C. Clifton: "Static Indentation Load Capacity of the Superelastic NiTi for Rolling Element Bearings," NASA/TM—2012-216016, May 2012.
7. C. DellaCorte, L.E. Moore, III, and J.C. Clifton: "The Effects of Pre-Stress on the Static Indentation Load Capacity of the Superelastic NiTi," NASA/TM—2012-216479, January 2013.



8. C. DellaCorte, L.E. Moore, III, and J.C. Clifton: "The Effects of Indenter Ball Radius on the Static Load Capacity of the Superelastic 60NiTi for Rolling Element Bearings," NASA/TM—2014-216627, 2014. To be published.
9. C. DellaCorte and W.A. Wozniak: "Design and Manufacturing Considerations for Shockproof and Corrosion-Immune Superelastic Nickel-Titanium Bearings for a Space Station Application," NASA/TM—2012-216015 and Presented at the 41<sup>st</sup> Aerospace Mechanisms Symposium, Pasadena, CA, May 2012.
10. B.J. Hamrock, S.R. Schmid and B.O. Jacobson: Fundamentals of Fluid Film Lubrication, 2<sup>nd</sup> Edition, Chapter 21, Marcel-Dekker, 2004, NY.
11. Data Sheet: Honeywell Model HR 0610 Reaction Wheel, Document #DFOISR:03-S-1924, December 2003, Honeywell Corporation, Phoenix, AZ.
12. Barden Super Precision Ball Bearings Catalogue, D/SPC/1/USA/113/T, Danbury, CT, 2013.
13. J.F. Antoine, G. Abba, C. Visa, and C. Sauvey: "Approximate Analytical Model for Hertzian Elliptical Contact Problems," ASME Journal of Tribology, volume 128, issue 3, pp. 660-664, March 2006.
14. W.J. Derner, and E.E. Pfaffenberger: "Rolling Element Bearings," in CRC Handbook of Lubrication: Theory and Practice of Tribology-volume II-Theory & Design, edited by E.R. Booser, pp. 495-537, 1983.
15. W. Park, M.R. Hilton, P.C. Ward, G.W. Henderson, A. R. Leveille, D.E. McClintock, and D.W. Smith, "Microstructure, Fatigue Life and Load Capacity of PM Tool Steel REX20 for bearing Applications," Lubrication Engineering, volume 55, number 6, pp. 20-30, 1999.



# Reducing Wear of Steel Rolling Against Ti6Al4V Operating in Vacuum

Timothy L. Krantz\*

## Abstract

This work was motivated by a qualification test of a mechanism for a space telescope. During the test undesired wear debris was formed. In this project alternative materials and coatings were tested with intent to reduce wear and debris when steel has a misaligned rolling contact against Ti6Al4V. Testing was done using a vacuum roller rig mimicking the mechanism's contact conditions. Ten configurations were tested. Most configurations resulted in significant debris. A sputtered 1-micrometer-thick nanocomposite molybdenum disulfide (MoS<sub>2</sub>) film provided the best wear protection. The best configuration made use of the MoS<sub>2</sub> coating on both materials, and in preparing for sputtering the anodized Ti6Al4V working surface was smoothed using an ultrasonic process.

## Introduction

This work was motivated by results of a qualification test of a mechanism to be used for the James Webb Space Telescope. The mechanism is used to move a magnet for certain operations of the telescope's near infrared spectrograph (NIRSpec) instrument. The motion of the magnet is guided by a set of preloaded steel rollers in contact with anodized Ti6Al4V flat surfaces. The qualification testing was accomplished in a cold vacuum chamber to match as closely as possible the extreme deep space environment. Post-test inspections of the qualification test article revealed some wear of the steel rollers and mating Ti6Al4V surfaces, and some loose debris was found. The NASA Engineering Safety Center (NESC) investigated the potential risk of the wear and resulting debris to hinder the full capability of the NIRSpec instrument. This article describes results of roller tests of ten material configurations with the project intent to minimize wear debris.

## Background – Qualification Test Article and Test Results

Following is a description of the qualification test article, test conditions, and results that motivated this research [1]. The mechanism of interest is a translator assembly that features a set of 11 rollers to guide the motion of a magnet (Figure 1). The translation of the magnet is used to control the positions of micro-shutters. The in-plane position is established by a set of four rollers contacting both sides of a guide rail defining the direction of motion. The out-of-plane position and motion is guided by a set of seven rollers. Three rollers are in contact with a base plate defining one plane and four rollers are in contact with a cover defining a second parallel plane. A motor and linkages provide the motive force. The translator assembly moves in a straight line for approximately 200 mm on each stroke. The translation time in one direction during testing was 10.5 seconds. The test duration was 96,000 forward and return motions.

Roller preload was established by a shimming procedure to provide a nominal normal load of 38 N. The roller profile was a circular crown with a flat feature superimposed on the center of the crown. Assuming line contact across the flat, the Hertz contact maximum pressure was 240 MPa. The rollers were machined from free machining 440F steel, annealed and passivated. Each roller was supported by a pair of deep groove ball bearings. The fastener securing the roller bearings to the axle was a locking style bolt assembled with a small amount of axial play. The rollers were in contact with Ti6Al4V that had been stress relieved and anodized.

---

\* NASA Glenn Research Center, Cleveland, OH

After completion of the qualification test, wear was visible on the rollers of the translator assembly and on the mating surfaces. Figure 2 shows the condition of one qualification test roller. Some loose particulate debris was also found, which was collected and analyzed [1-2]. The worn surfaces and wear debris provide evidence that the wear process was primarily adhesive wear. In the net it appears that the steel has transferred to the mating Ti6Al4V surfaces. The loose wear debris included both the steel and titanium alloy materials. The severity of wear was not the same on all rollers.

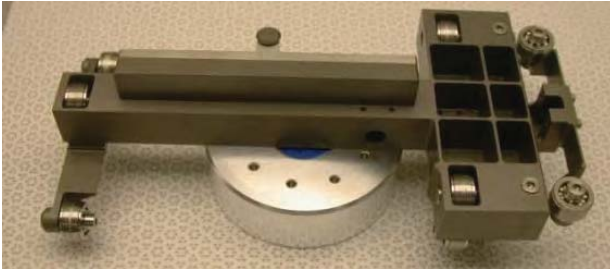


**Figure 1. Translator Assembly [Ref. 1]**

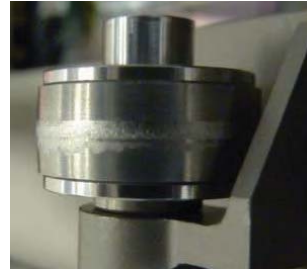


**Figure 2. Condition of Roller After Completion of Qualification Test [Ref. 2]**

The NASA Engineering and Safety Center (NESC) conducted an assessment to better understand the wear and provide recommendations that could reduce mission risk [3-4]. Experiments conducted by the NESC demonstrated that misalignment of a roller axis relative to the direction of travel is a key parameter influencing the propensity for wear. The NESC recommended two design changes for the rollers as follows. It was recommended that the roller material be changed from annealed 440F steel to 440C steel hardened to 58-60 Rockwell C. It was also recommended to change the roller profile geometry to eliminate the flat section superimposed in the center of the crown and to increase the crown radius. The NESC also recommended optimizing the assembly procedure to minimize roller misalignment.

The NESC has now completed additional work, reported herein, with goal to reduce mission risk from wear debris. There is little guidance in the open literature concerning detailed characterization of wear particles and transport of such particles. This is perhaps because for most applications small amounts of wear debris are of no consequence. The manufacture of semiconductors in a vacuum environment is one situation with similarity to the NIRSpec device in that high cleanliness is desired and wear particles can be of concern. For the manufacturing of semiconductors, proper bearing seals in combination with solid film lubrication has been proposed and studied to minimize adverse effects of wear debris [5]. The scope of the effort reported herein is evaluation of “alternative materials” for this mechanism. The words “alternative materials” includes coatings and solid lubrication films even if applied to the baseline substrate materials. For purposes on this study, it was assumed that the flight unit configuration would use a cover and baseplate made from anodized Ti6Al4V.

### **Laboratory Test Apparatus**

Testing was done using the NASA Glenn Research Center Vacuum Roller Rig (VRR). Previous work has shown that the VRR can effectively simulate the mechanism contact conditions and wear phenomena [3,4]. The VRR data are also useful to supplement results of qualification tests. The rig allows for application and measurement of a load pressing the rollers together while having a purposely misaligned and adjustable shaft angle. The rig is depicted in schematic form in Figure 3. A drive motor provides motion to the driving roller. A second drive motor provides some motive power to the output roller to overcome bearing and seal friction. The output shaft roller is driven through a torque-limiting permanent magnet clutch. The clutch torque and the output shaft motor speed settings resulted in a net torque of 1 Nm through the output shaft and rolling slip of less than 2 percent. This closely approximates the mechanism rollers that are essentially free-rolling but with some support bearing and seal drag torque. The normal load pressing the rollers together is provided by an air cylinder. The cylinder acts through a pivot point to rotate the plate that mounts the driving shaft and drive motor in an arc motion. The pressure

to the cylinder, and thereby the load between the contacting rollers, is adjusted by a hand-operated valve (open-loop control). A turbomolecular pump assisted by a scroll pump provides vacuum in the test chamber. The typical condition in the test chamber is a pressure of about  $4 \times 10^{-5}$  Pa ( $3 \times 10^{-7}$  torr). The most prevalent remaining constituent in the chamber during testing is water vapor as determined by residual gas analyzer [6]. The residual gas analyzer was used regularly to monitor the test chamber environment with no irregular results.

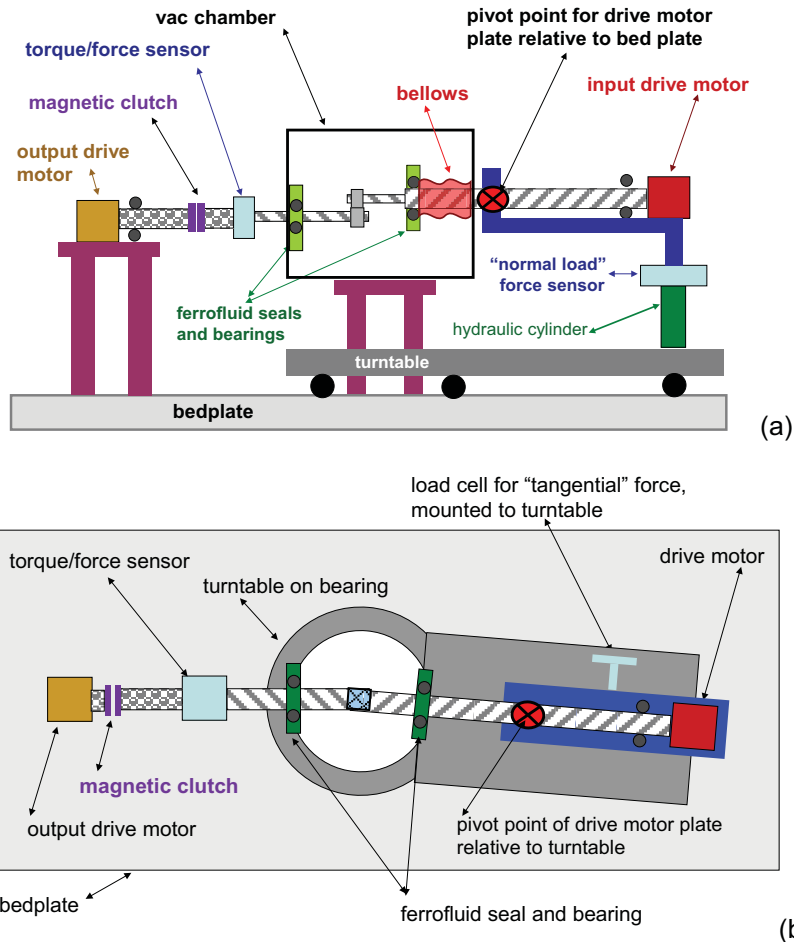


**Figure 3. Schematic views of the vacuum roller rig. (a) Schematic, side view. (b) Schematic, overhead view with shaft misalignment depicted and exaggerated.**

A set of sensors on the test apparatus monitors the test conditions. The outputs of the analog sensors were digitized at a rate of up to 0.66 Hertz. The misalignment of the driving roller shaft and driven roller shaft is depicted in an exaggerated manner in Figure 3. The misalignment is measured via a linear variable differential transformer (LVDT) attached to the bedplate. The LVDT tip moves against a stop on the turntable. To establish the aligned condition, special tooling blocks were machined to position the roller mounting surfaces as parallel to each other. The precision of this method for aligning is within 0.08 degree. The angular displacement from the aligned condition was calibrated by mounting a laser light source on the moving shaft at the roller mounting location and directing the light onto a paper placed at a known radial distance from the center of the turntable. The movement of the laser light was marked on the paper, and the distance between the points used to calculate the angular movement of the turntable and thereby relate this motion to the LVDT sensor output (voltage). The torque on the output shaft is monitored by a strain-gage torquemeter of 22 N-m (200 in lb) torque capacity. Calibration was done in place using deadweights on a torque arm. Figure 4 provides a schematic of the test roller setup labeled with some of the nomenclature used herein. The load pressing the rollers together is termed the "normal

load”. The normal load is applied via an air piston that acts through a load cell to move the drive motor plate that is pivot-mounted relative to the test chamber. Pressurizing the piston moves the input shaft in an arc motion toward the test roller. The arc motion is measured by an LVDT. Once the rollers are in contact, additional pressure to the air piston increases the normal load between the test rollers. Careful calibration processes allow calculating the test roller load using the sensor outputs from the load cell and the LVDT that measures the input shaft angular orientation [4]. Shaft speeds and total number of shaft revolutions were measured using encoders on each shaft. The encoder pulses were counted and recorded via a digital pulse counter. The encoders provide 6,000 pulses for each shaft revolution.

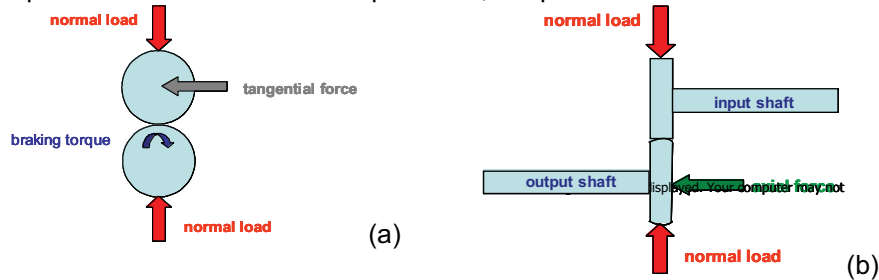


**Figure 4. Simplified schematic view including some of the important sensed data.(a) Schematic, front view. (b) Schematic, side view.**

When rollers operate in a misaligned condition, a force will develop in the direction of the shaft axis [7-10]. In such a condition points on the two rollers in intimate contact and within a “stick” zone of the contact patch are constrained to move in unison. If the points were not in contact the kinematic constraints would provide a slightly different path of motion. The difference in the actual path of motion and the motion that would occur if the points were not in contact gives rise to surface strains and a resultant axial force. A sensor to measure this force is labeled as the “axial force” sensor in Figure 4. The axial force sensor is co-located on the output shaft with the torquemeter.

The visual appearance of the test rollers were documented by digital photographs obtained through a viewport using a single-lens reflex camera with a 150-mm lens and a 12-million pixel image sensor. Wear debris was captured onto a flat rectangular pan located below the rollers. The analysis of such captured debris is beyond the scope of this article.

### Contact Analyses and Test Conditions

Hertz contact analyses were completed to guide use of the VRR to best mimic the contact conditions of the NIRSspec mechanism. Results of the analyses were also used to guide selections of materials for evaluation. Although the actual contact conditions of rough surfaces differ from Hertz models that assume perfectly-smooth surfaces, the Hertz model solutions provide useful design indices. The Hertz contact solutions herein were produced using the approximate solution technique of Antoine, et al [11]. The mechanism makes use of steel rollers contacting a Ti6Al4V plane surface while the VRR tests a pair of rollers. The contact solutions for the mechanism are for roller geometry having a circular crown with 510-millimeter radius and with a 38-N (8.5-lbf) normal load pressing the steel roller to the Ti6Al4V plane. Contact solutions for VRR are for a normal load of 130 N (30 lbf) pressing the two rollers together. The VRR rollers are 35.6-mm outer diameter, the upper roller has a circular crown of 400 mm, and the lower roller has a flat profile. The Hertz contact condition solutions are summarized in Table 1. The contact ellipses are short in the rolling direction (labeled “b” in the diagram contained in the table) and have similar aspect ratios, 14.3 for the mechanism and 11.3 for the VRR. The contact ellipse is somewhat larger for the VRR because of the larger diameters of the VRR rollers. The contact pressure magnitudes are somewhat larger in the VRR, approximately 40% larger comparing the maximum contact pressures. Use of a lower normal load in the VRR would have provided a closer match of the contact conditions, but because of VRR constraints the 130-N load was used for the experiments.



The misalignment of the roller rotation axis relative to the actual direction of rolling motion is an important parameter influencing the wear rates. In this work the VRR was operated with misalignment angle of 0.9 degree as such misalignment had produced relevant wear phenomena in previous work [3,4]. The sliding distance that promotes wear of slightly misaligned rollers may be approximated as proportional to the product of misalignment angle and the width of the contact region. This approximate sliding distance concept is depicted in Figure 5. The approximate sliding distance per contact pass was 3.1 micrometer for the VRR. If operating at the same misalignment angle of 0.9 degree the approximate sliding distance per contact pass for the mechanism would be 1.9 micrometer. The speed of the test rig was 20 revolutions per minute. The speed was selected to provide a contact passing time of same order as the mechanism but the test was operated with a slightly faster rate to obtain the desired number of contact passes in practical calendar time. The contact passing times were 0.009 second for the mechanism and 0.005 second for the VRR tests.

There was no single VRR test duration that could mimic the duration needed for the mechanism. The VRR makes use of equally sized rollers and so VRR roller surfaces experience equal number of contact pass cycles per unit of time. For the mechanism, the steel rollers and titanium-alloy planes have differing numbers of contact cycles. Using 48,000 actuations of the mechanism as the needed life, with each actuation requiring a forward and reverse traverse, the duration for some points on the mechanism's titanium-alloy plate is 96,000 contact cycles. Other points of the mechanism's plate are passed over by two rollers for each traverse, requiring 192,000 contact cycles. The mechanism steel roller surfaces experience up to three contact cycles per traverse, requiring 288,000 contact cycles. Further complicating selection of the VRR test duration, the lifetime of a solid lubricating film is not reliably calculated for all situations by simple proportionality to contact cycles. For mild wear, the wear rate is often modeled, to a first approximation, using the Archard wear model [12] as proportional to the product of contact pressure and sliding distance. The VRR test duration was selected as 90,000 contact cycles. This selection enabled a desired testing pace of two tests per week and was considered to provide a reasonable match of both total contact cycles and a simple wear index (product of sliding distance and contact pressure) in comparing the VRR to the mechanism. Table 2 summarizes some of the key engineering parameters one might use to compare VRR to the mechanism in terms of contact conditions and durability concepts. The VRR can be considered as an accelerated wear test in terms of higher contact pressures and faster speeds. In this way the alternative materials were evaluated on a relative basis with good relevance to the application. The VRR tests were intended to complement but not substitute for qualification testing.

**Table 1. Hertz Contact Conditions**

	mechanism	test rig
pressure, max. (MPa)	330	460
pressure, mean (MPa)	220	310
a (mm)	1.77	2.30
b (mm)	0.124	0.200
aspect ratio, a/b	14.3	11.3

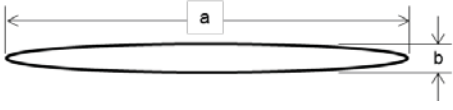



**Figure 5. Approximate model of sliding distance of a misaligned roller contact. (a) Elliptical contact ellipse of width R, misalignment angle  $t$ , and actual rolling path  $R'$ . (b) Approximate sliding distance  $S \approx R \cdot \tan(\tau) \approx R \cdot \tau$ .**

**Table 2 – Comparison of the Test Rig and Mechanism Contact and Durability Metrics**

	VRR	mechanism		
		steel roller	Ti6Al4V, two rollers, same track	Ti6Al4V, one roller only in track
duration, contact passes	90,000	288,000	192,000	96,000
wear index (Pa·m/10E6) <sup>a</sup>	86	120	80	40
pressure, max (MPa)	460	330		
rolling speed (mm/sec)	37.2	13.3		
contact passing time (sec)	0.005	0.009		

<sup>a</sup> wear index defined as product of mean of Hertz pressure-sliding distance-number of contact passes for 0.9-degree misalignment angle for both system per the approximate sliding distance concept of Figure 5.

### Selections of Alternative Materials and Configurations

A set of potential alternative materials were selected based on study of the literature, discussions with experts in the field, and implementation constraints. Liquid lubrication was not considered because of the extreme cold temperature of this application. Two review papers provide direct guidance and a substantial listing of relevant solid lubrication information [13,14]. Five different fundamental alternative material candidate solutions were selected for evaluation, as follows:

1. Use of polyimide rollers rather than steel rollers. Such material has been used for space applications and has been proposed for use as traction rollers. The experiment made use of a readily available VRR roller made from an unfilled base polyimide resin [15].
2. Use of a bonded, PTFE-type solid lubricant coating on the steel roller. The binder was an inorganic type with highest available strength.
3. Use of an alternative surface treatment to the currently employed anodizing treatment of the Ti6Al4V material, with intent to provide an adherent, hard, wear resistant layer of oxides. The selected treatment of the Ti6Al4V was a plasma electrolytic oxidation process [16].
4. Use of metal-doped diamond-like carbon coatings applied one or both surfaces to provide an adherent layer of high hardness and toughness. Some success has been reported for this approach for prevention of cold welding of Ti6Al4V in vacuum [17]. Such an approach has also been reported to improve durability of oil-lubricated bearings under certain operating conditions [18]. Two such coatings were selected, one a (TiC)<sub>a</sub>C:H type and one a (WC)<sub>a</sub>C:H type. The coatings were applied by physical vapor deposition.
5. Use of a molybdenum-disulfide (MoS<sub>2</sub>) type sputtered solid lubricant film applied to one or both contacting surfaces. The selected film is a nanocomposite coating with composition including antimony oxide and gold. Such compositions have been studied by others for use in vacuum conditions [19]. MoS<sub>2</sub> has an extensive heritage as an effective solid lubricant for cold vacuum conditions. The coating thickness was intended to be 1 micrometer.

The material configurations selected for testing evolved as test results were obtained. Ten configurations were tested as listed in Table 3.

**Table 3 – Tested VRR roller-pair configurations.**

Configuration	Upper roller	Lower roller
1	440F ; annealed ; passivated	Ti6Al4V ; anodized
2	440C ; hardened ; passivated	Ti6Al4V ; anodized
3	polyimide	Ti6Al4V ; anodized
4	440C ; hardened ; passivated; bonded PTFE solid lube	Ti6Al4V ; anodized
5	440C ; hardened ; passivated	Ti6Al4V ; PEO; bonded solid lube
6	440C ; hardened ; passivated	Ti6Al4V ; (WC)aC:H DLC
7	440C ; hardened ; (TiC)aC:H DLC	Ti6Al4V; (TiC)aC:H DLC
8	440C ; hardened ; passivated ; nanocomposite MoS <sub>2</sub>	Ti6Al4V ; anodized
9	440C ; hardened ; passivated ; nanocomposite MoS <sub>2</sub>	Ti6Al4V ; anodized; nanocomposite MoS <sub>2</sub>
10	440C ; hardened ; passivated ; nanocomposite MoS <sub>2</sub>	Ti6Al4V ; anodized;ultrasonic smoothing nanocomposite MoS <sub>2</sub>

### Experiment Procedures and Results

#### Experiment Procedures

The upper roller material for one test was made was polyimide material, otherwise the upper roller was 440 steel. The upper roller in all cases had a 400-mm crown radius and had a width of 13 mm. The lower roller for all testing was made from Ti6Al4V, had a flat profile, and had a width of 16.5 mm. Rollers were tested in a “tribologically clean” condition. For cases of rollers that had a coating by sputtering or physical vapor deposition, the rollers were stored in vacuum-sealed bags immediately following deposition and then were opened just prior to installation, and so special cleaning was not required. For cases of rollers with hard surfaces, rollers were scrubbed using 0.05-micron alumina powder suspended in deionized water. After appropriate scrubbing the roller was rinsed in deionized and filtered water. The cleaning procedure was different for the cases of the polyimide roller and the roller with the bonded type lubricant film. Alumina powder was not used to avoid possibility to imbed the powder into the relatively soft materials. In these cases, the rollers were cleaned using isopropanol rinse followed by ultrasonic cleaning in deionized water. It was confirmed that surfaces were clean of all oils by checking for uniform and full wetting of the surfaces. Water was then removed using dry, pressurized nitrogen. Once cleaned, the rollers were handled only with gloved hands and were transported to the rig using closed glass jars.

Just prior to installation, the surface textures of rollers were documented by tracing with a stylus profilometer using a 2-micrometer-radius conisphere-tipped stylus. Traces were recorded in the both circumferential (rolling) direction and in the profile (axial) direction. The final step prior to installing rollers into the test chamber was to measure the mass using a scale with 0.0001 gram resolution. After installing the rollers onto the test shafts, the hinged chamber door was immediately closed and the vacuum system operated to bring the chamber to a partial pressure of 6.7 Pa ( $50 \times 10^{-3}$  torr) within one minute. The test chamber was then brought to a pressure of  $1 \times 10^{-3}$  Pa ( $7.5 \times 10^{-6}$  torr) or less before beginning testing of the rollers. Roller mass and stylus profilometer data were obtained after testing.

#### Experiment Results

Following is a discussion of the roller wear test results. The information is organized to aid the discussion. The order of the discussion does not match chronological order of testing. The experimental data to be discussed herein includes the visual appearance of the roller surfaces as testing progressed, amounts of visible wear debris, the change of mass of rollers both individually and as a pair, and roller surfaces conditions at start and end of test as revealed by stylus profilometer measurements.

*Configuration 1 – Results:* The first configuration for discussion is the upper roller 440 F steel, annealed and passivated and the lower roller material Ti6Al4V, anodized. This configuration matches that of a tested qualification unit [1,2]. A motivation for this test was to demonstrate that the test conditions selected for this work (i.e. the speed, load, misalignment angle, and duration) would produce the relevant wear phenomena. One test was completed using this configuration. Significant adhesive wear and plastic flow of material occurred throughout the test. After 78,000 cycles high vibrations were occurring, and the test was stopped early of the targeted 90,000 cycles to avoid damage to the apparatus. The final roller conditions for this test are provided in Figure 6(a). The upper steel roller lost 0.0710 g mass while the lower Ti6Al4V roller gained 0.059 g mass. As a pair the rollers lost 0.011 g mass. Stylus profile inspections of the tested upper roller revealed a material peak along one edge of the contact, likely from plastic flow, reaching over 100 micrometer heights. Similar inspection of the tested lower roller revealed added material in the contact region reached 60 micrometer of height. This test confirmed that the operating conditions selected for this study reproduced the relevant wear phenomena of the qualification test unit.

*Configuration 2 – Results:* The second configuration for discussion is the upper roller 440 C steel hardened to HRC 58-60 and passivated and the lower roller anodized Ti6Al4V. The three tests completed using this configuration all had similar wear behavior. Significant adhesive wear had occurred after 25 percent of the test duration. The final conditions of the rollers featured distinctive worn surface topographies and significant adhesive wear had occurred; see Figure 6(b). From profilometer inspections the steel roller wear valleys had typical depths of 15 micrometers. The Ti6Al4V roller had a region with material removed and just adjacent another region with material added. Mass measurements confirmed that in the net the steel rollers lost mass and Ti6Al4V rollers gained mass. The sizes of the valley features of the steel roller and the peak features of the Ti6Al4V roller for this configuration were of smaller magnitudes by a factor of two to three as compared to Configuration 1. This result is consistent with the general trends observed in the earlier NESC study [3-4] that had quantified wear rates being less by order of two to three for hardened 440C rollers compared to annealed 440 F rollers.

*Configuration 3 – Results:* The third configuration for discussion comprises one test with the upper roller material polyimide and the lower roller anodized Ti6Al4V. The lower anodized roller abraded the upper polyimide roller like a machining process. The test created a great amount of polyimide debris [Figure 6(c)], and the test was stopped after 38,000 cycles far short of the intended 90,000 cycle duration. After cleaning with a soft-bristle brush, rollers look almost like the new condition. This material configuration might be suitable for situations where the polyimide wear debris could be tolerated, but it is not suited for the present application.

*Configuration 4 – Results:* The fourth configuration for discussion is the upper roller material of hardened and passivated 440C steel with a solid lubricant bonded film. The bonded film was a commercially available PTFE type with an inorganic binder. The product vendor considered the mean test pressure as “uncomfortably close to” the binder strength limit. The lower roller material was anodized Ti6Al4V. One test comprising 83,000 cycles of this configuration was completed. The bonded film was abraded and worn away by the anodized surface of the lower roller. A great volume of powdery debris was formed and transported toward one edge of the roller contact by the sweeping action of the misaligned rollers [Figure 6(d)]. Once the bonded film was compromised, adhesive wear occurred with similar wear rate of uncoated rollers. It appears that the binder strength was indeed insufficient, per the concerns expressed by the product provider. This configuration is obviously not suited for the present application.



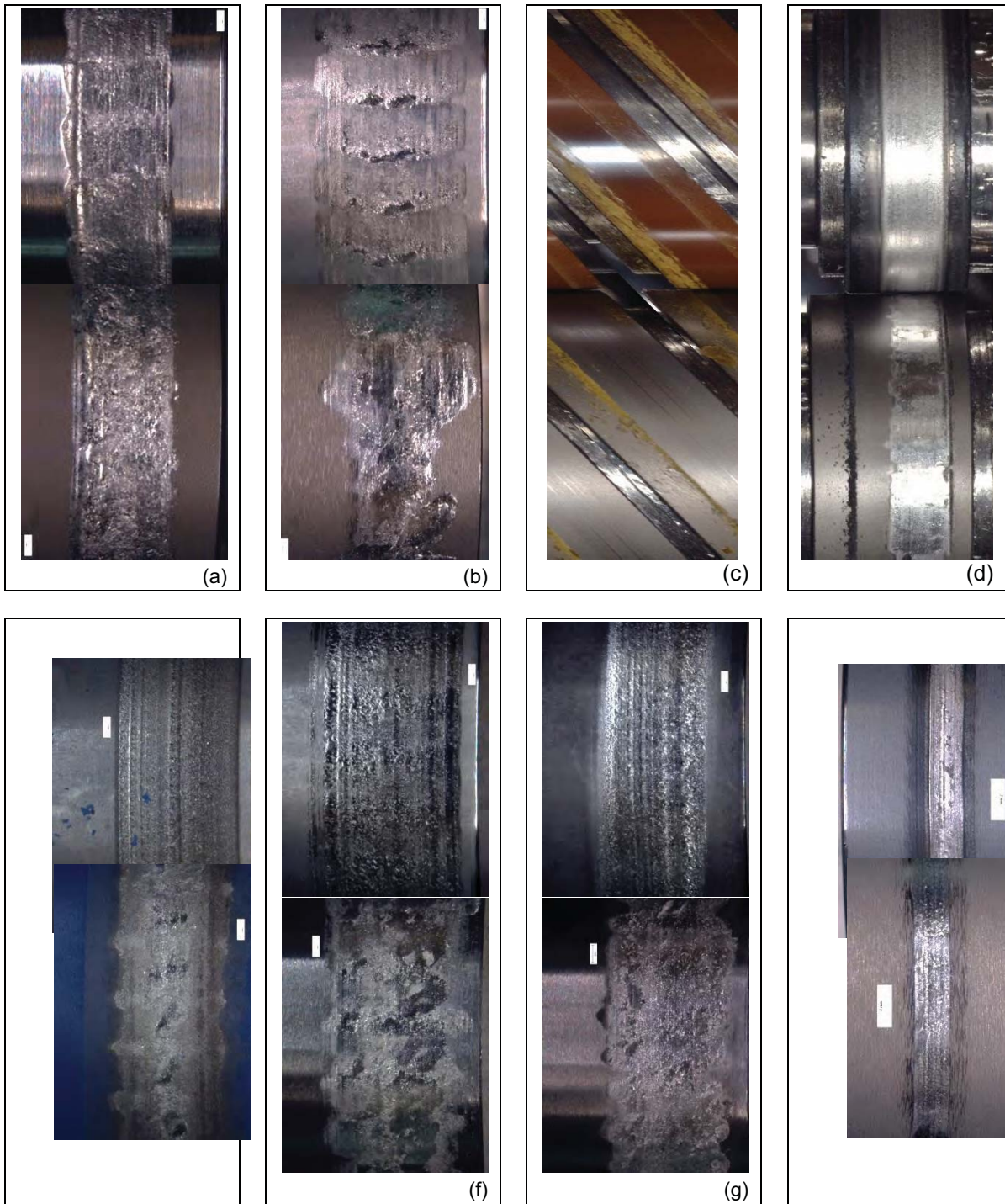


**Figure 6. Conditions of rollers at end of test.**  
**(a) Config. 1, annealed 440F steel. (b) Config. 2, hardened 440C steel.**  
**(c) Config. 3, polyimide upper roller.**  
**(d) Config. 4, bonded film.**  
**(e) Config. 5, PEO of Ti6AL4V.**  
**(f) Config. 6, lower roller coated with (WC)aC:H**  
**(g) Config. 7, both rollers coated with (TiC)aC:H.**  
**(h) Config. 8, upper roller coated with nanocomposite MoS<sub>2</sub>**

*Configuration 5 – Results:* The fifth configuration for discussion is the upper roller material hardened and passivated 440C steel. The lower roller was Ti6Al4V material treated by plasma electrolytic oxidation (PEO). The vendor of the PEO process also chose to apply on top of the PEO treated surface a bonded solid lubricant film, a combination that in their experience performed well. The configuration was put to test with the philosophy that failure of the bonded film need not define the capability of the PEO surface itself. One 93,000 cycle test was completed. The blue-colored solid lubricant film wore away and created a mixture of powder and large flakes of debris. The blue-colored bonded film transferred onto the upper steel roller during the early part of the testing, but later this transferred film was almost completely removed from the upper roller [Figure 6(e)]. There was significant adhesive wear. The final condition of the rollers for this configuration appeared visually similar to that of Configuration 2. The net mass lost from the upper 440C roller was 0.002 gram, also similar to the result of Configuration 2. Given the result of this test and given the lack of experience using the PEO process for space mechanisms, it was decided not to further pursue evaluations of PEO-treated Ti6Al4V for this application.

*Configuration 6 – Results:* The sixth configuration for discussion is the upper roller material hardened and passivated 440C steel and the lower roller material Ti6Al4V with a PVD-applied coating of a (Wc)aC:H diamond-like-carbon (DLC) composition. One test was completed to 91,000 cycles. In this test configuration the problematic Ti6Al4V alloy was coated with a galling-resistant composition hoping to defeat the adhesive wear mechanism. However, for these particular contact conditions wear occurred to both rollers throughout the course of the test. As the wear occurred a significant amount of debris was noted on the debris tray. During the first 25 percent of the test duration, the rollers surfaces appeared to have relatively low surface roughness suggestive of abrasive wear. By the end of the test the rollers surfaces conditions suggested the process had become primarily adhesive wear [Figure 6(f)]. Profilometer inspections of the rollers confirmed that the wear behavior of this configuration was different from the other configurations. The lower Ti6Al4V roller had a prominent wear valley with roughness features within the wear region, and by mass measurements the lower roller net mass lost was 0.007 gram. This was the only configuration where the majority of mass loss was only from the lower Ti6Al4V roller. This configuration is not suited for the present application.

*Configuration 7 – Results:* The seventh configuration for discussion is the upper roller material of hardened 440C steel and the lower roller Ti6Al4V. The surfaces of both rollers were coated with a (TiC)aC:H DLC composition applied by PVD. One test was completed to 96,000 cycles. The wear progression had some similarities to the test of configuration 6. Wear occurred to both rollers throughout the course of the test. As the wear occurred, a significant amount of debris was noted on the debris tray. Early in the test the wear may have been abrasive wear, but as the test progressed the surface roughness features became more apparent and end of test conditions suggested adhesive wear [Figure 6(g)]. Profilometer inspections of the rollers at the end of test show differing behaviors for Configuration 6 (lower roller only coated) compared to Configuration 7 (both rollers coated). The (Wc)aC:H coated lower roller of configuration 6 that was mated to an uncoated upper roller had no peak features and one prominent wear valley. On the other hand, for configuration 7 with (TiC)aC:H coating on both rollers, the lower roller had both peak and valley features. The upper rollers for Configurations 6 and 7 have similar surface profiles at the end of the test having a combination of peak and valley features of about 5 micrometer size. The use of the DLC coatings changed the wear behavior compared to tests without any coatings or solid-film lubrication. While DLC coatings may have a place for space mechanisms with more optimization and research, further consideration and testing of DLC coatings was not pursued for this application.

*Configuration 8 – Results:* The eighth configuration for discussion is the upper roller material hardened 440C steel and the lower roller anodized Ti6Al4V. The upper roller only was provided a MoS<sub>2</sub> nanocomposite coating by PVD sputtering. Four tests were completed using this configuration. The steel upper rollers with the sputtered coatings were passivated prior to coating except for one test the roller was not passivated because of testing schedule. The lack of passivation for one test probably did not have a big influence on performance, as the rollers are processed by a high-energy ion beam just prior to sputtering. The ion beam likely removes most or all of the oxides created during passivation. The test



durations ranged from 90,000 to 97,000 cycles. The wear behavior was not fully consistent for this set of four tests. In two cases there was moderate wear by the end of test. For these two tests the steel rollers lost mass and the Ti6Al4V rollers gained nearly equal mass. The mass change was of the order 0.020 gram for each roller of the two tests having moderate wear. For the other two tests with minor wear, the roller mass changes were nearly an order of magnitude less compared to the two tests with moderate wear. The photograph of Figure 6(h) shows a representative end-of-test condition for this configuration. Considering the four tests of this configuration as one grouping, the adhesive wear phenomenon was delayed and the overall wear rate was reduced as compared to tests without a solid lubricant film.

The reasons for the differing behaviors of the four tests of this configuration have not been determined conclusively. For one of the two tests with moderate wear, the coating thickness was about one-half of the intended thickness because of a temporary problem with the coating process. The thinner film was likely at least partially responsible for the less effective wear protection. From scanning-electron microscope inspections, for the other test with moderate wear, little transfer of sputtered film to the mating roller was observed. However, significant transfer did occur for a test that resulted in better wear protection. The reason for the lack of film transfer has not been determined. The scanning-electron microscope inspections revealed trace organics on some rollers from this configuration, and the likely source was a temporary coating-equipment problem. It is possible that the trace organics could have interfered with the solid lubricant film-transfer process, but this speculation is uncertain as trace organics and film transfer was found together for one of the low-wear cases from this configuration.

During a fifth test of this configuration, a mechanical failure of a rig part prevented rotation of the lower roller. The rollers operated in rolling condition for approximately 7,000 cycles, then ran unattended for an additional 47,000 revolutions of the upper roller with the lower roller stalled, not rotating. Although the full sliding does not represent the relevant contact conditions, the result is included herein as one that was quite striking. The final conditions of the test rollers showed some minor wear and perhaps some compromise of the MoS<sub>2</sub> coating, but large-scale adhesive wear was prevented (Figure 7). This test demonstrated effective wear protection. One can consider that once the lower roller stalled, a very small distance on the uncoated lower roller was in contact with a long distance of coated surface on the upper roller, the ratio being about 140:1. This experience illustrates the difficulty of extrapolating tribology test results from pin-on-disk or block-on-ring configurations of pure sliding to a different type of rolling-sliding contact condition. Still, this test produced evidence that the selected coating system is one that can provide effective wear protection in vacuum. The words “coating system” here indicates both the coating elemental composition and the process for coating application.

*Configuration 9 – Results:* The ninth configuration for discussion used the same nanocomposite MoS<sub>2</sub> coating as was used for Configuration 8, but in this configuration both rollers were coated. The upper roller substrate was passivated, hardened 440C steel. The lower roller substrate was anodized Ti6Al4V. Two tests of this configuration were completed, for 93,000 and 90,000 cycles, respectively. The test results for these two tests were consistent with good wear protection demonstrated. After some running-in of the surfaces, the underlying surface texture of the upper roller became visible. The lower roller surfaces developed a reflective sheen texture [Figure 8(a)]. All rollers lost some mass; none gained net mass by adhesive wear of the mate as occurred for uncoated roller pairs. The masses lost were small, less than 0.0003 gram mass lost per roller. From these visual assessments the wear protection was judged as excellent. However, the debris pans of these tests had a significant number of bright particles that were reflecting light and easy to see without aid of magnification. Profilometer inspections showed essentially no wear on the upper roller. Inspection also revealed a wear valley of about 2 to 3 micrometer depth on the lower roller [(Figures 8(b-c)]. Although this configuration prevented large-scale adhesive wear, the debris released from the lower roller was still significant, and such debris could pose some mission risk.

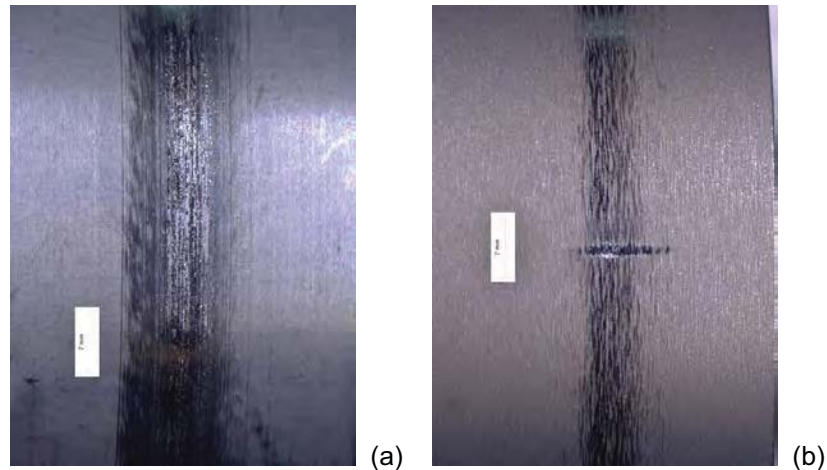


**Figure 7 – Conditions of rollers at end of test from an unintended but interesting full sliding test. (a) Upper MoS<sub>2</sub> nanocomposite coated roller. (b) Uncoated lower roller, stalled member.**

*Configuration 10 – Results:* The tenth and final configuration for discussion was almost identical to Configuration 9, except there was one additional processing step by the vendor in preparing Ti6Al4V rollers for sputtering. The nanocomposite MoS<sub>2</sub> coating was present on both upper and lower rollers for this configuration. It was noticed that the anodized surface of the titanium alloy rollers were quite rough, and roughness of such magnitude was judged as not favorable for minimizing wear. The lower titanium-alloy roller surfaces were smoothed by directing ultrasonic energy to the surfaces using a hand held probe. Aside from this added “smoothing” step for the anodized Ti6Al4V rollers that was done just prior to application of the coating, Configurations 9 and 10 were otherwise identical. Six tests were conducted for this configuration to more than 87,800 cycles for each test. Four of the tests provided excellent wear protection. Two of the tests, while slightly lesser performing, still provided very good wear protection. For one of the two lesser performing tests, the coating thickness was about one-half of the intended thickness because of a temporary problem with the coating process. The thinner film was likely at least partially responsible for the less effective wear protection. For the other lesser-performing test, a narrow wear track developed after about 60,000 cycles covering about one-third of the contact width. The photograph of Figure 9 shows typical end-of-test conditions of the rollers for the four tests that provided excellent wear protection.

Profilometer inspections showed essentially no wear, to the precision that could be measured by the stylus inspection technique, for both rollers. Typical lower roller inspections at start and end of test are provided in Figure 9(b-c). The undetectable wear on the lower roller is in quite contrast to the behavior of Configuration 9, per Figure 8(c) whereby a distinct wear valley was produced. It is interesting that the asperity features within the wear track of Figure 8(c) are very similar in shape and magnitude to the asperity features of the ultrasonically-smoothed and coated, but untested, roller of Figure 9(b). The many bright particles of debris easily seen without magnification on the debris pan during tests of Configuration 9 were absent during all tests of Configuration 10. Comparing the profilometer inspections of the lower rollers before test shows the effect of the ultrasonic smoothing process. Without the ultrasonic smoothing, the surface has asperities with high slopes as had resulted from the anodizing process. The asperity peaks are removed and/or deformed by the ultrasonic smoothing process [compare Figure 8(b) to Figure 9(b)] providing a more favorable surface for avoiding wear.

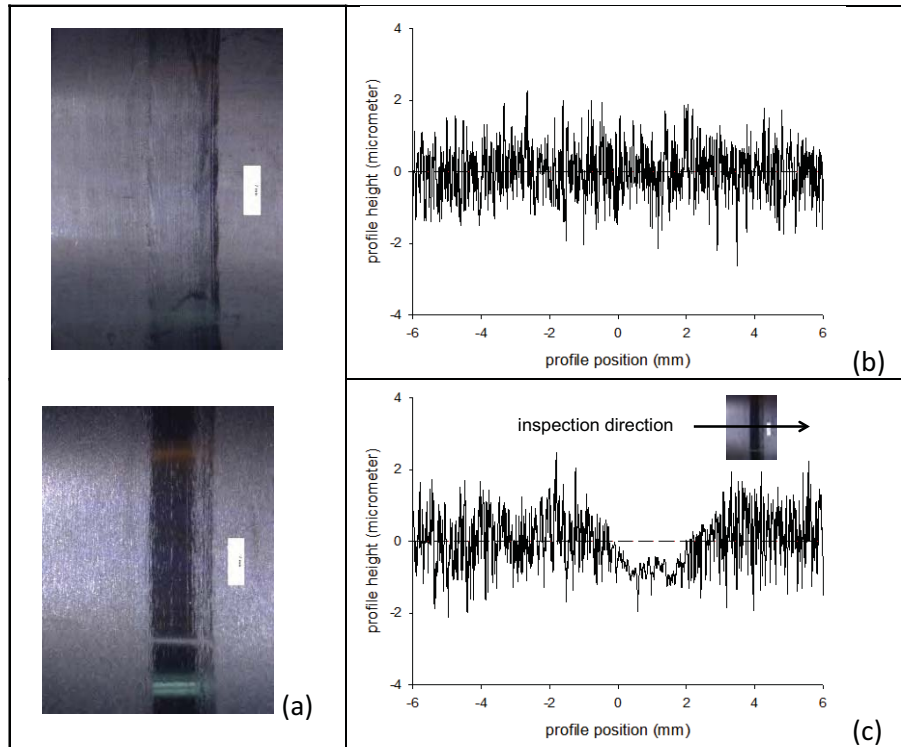


**Figure 8 – Data from Configuration 9. (a) Conditions of rollers, end of test. (b) Profilometer inspection, lower roller, start of test. (c) Profilometer inspection, lower roller, end of test.**

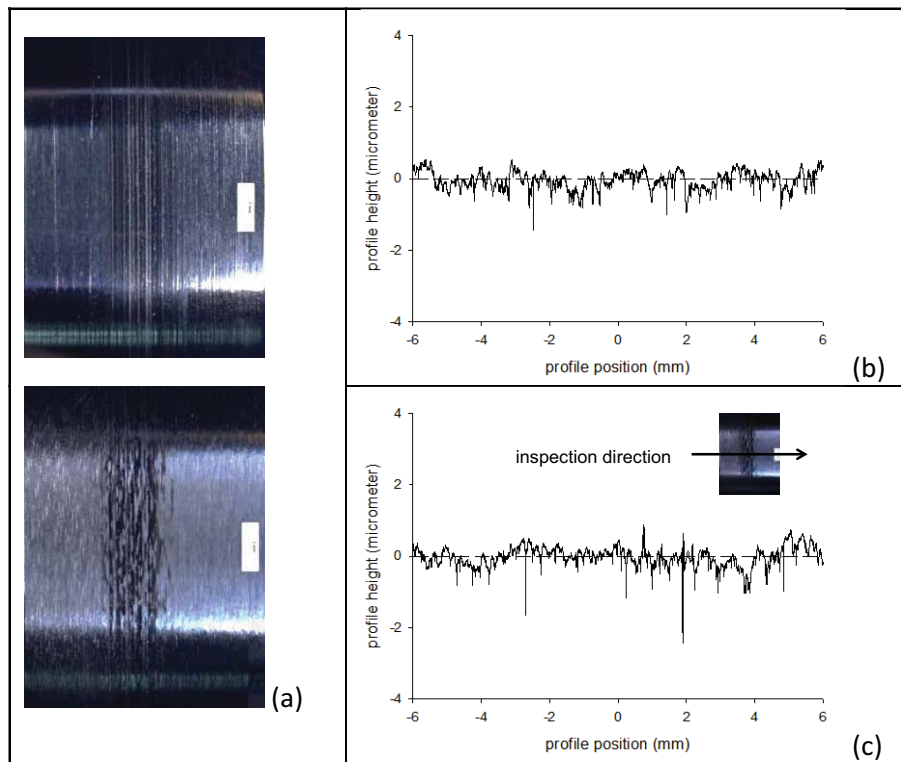


**Figure 9 – Data from Configuration 10. (a) Conditions of rollers, end of test. (b) Profilometer inspection, lower roller, start of test. (c) Profilometer inspection, lower roller, end of test.**

Configuration 10 provided the best wear protection and least amount of visible wear debris of all configurations tested. This conclusion is supported each and every aspect of the experimental data, that is: (1) excellent wear protection per qualitative assessment of the roller surface conditions; (2) low mass loss for both rollers, (3) wear depths were too small to be detected by profilometer inspection. It is recommended that this configuration should be carefully considered for implementation including durability and performance evaluations of the mechanism subsystem in appropriate cold-vacuum conditions.

### Summary

After a qualification test of a mechanism for a space telescope, roller wear and particulate debris from adhesive wear was noted. With intent to minimize wear and resulting debris, sets of experiments were completed using a vacuum roller rig to mimic the mechanism contact conditions. Ten configurations were tested. The roller-pair material configurations were evaluated on basis of qualitative assessment of roller surface conditions, mass lost or gained by each roller, and wear phenomena as could be assessed by stylus profilometer and scanning-electron-microscope inspections. Specific findings were:

1. Changing the roller material from annealed 440F steel to 440C steel hardened to HRC 58-60 resulted in a reduction of overall wear by a factor of two to three.
2. Use of a polyimide roller instead of a steel roller is not suited for this application as the anodized Ti6Al4V surface created polyimide debris in a manner like a machining process.
3. The bonded solid lubricant film that was applied to the steel roller was abraded and/or broke down from the contact pressure. Large amounts of debris were created.
4. While diamond-like-carbon coatings altered the wear behavior, large amounts of debris were created. The investigated diamond-like-carbon coatings are not suited for this application.
5. Application of a nanocomposite MoS<sub>2</sub> film significantly reduced the wear and production of wear debris.
6. Application of the nanocomposite MoS<sub>2</sub> film to both rollers provided better wear protection than providing the coating to the upper hardened 440C steel roller only.
7. Smoothing of the anodized Ti6Al4V prior to coating with the nanocomposite MoS<sub>2</sub> film resulted in better wear protection and the least amount of visible debris.
8. It is recommended that Configuration 10 should be carefully considered for implementation. Configuration 10 is use of a nanocomposite MoS<sub>2</sub> film sputtered on passivated 440C steel hardened to HRC 58-60 and also sputtered on anodized Ti6Al4V that has been ultrasonically smoothed after anodizing and prior to sputtering.

### Acknowledgements

This research was initiated and supported by the NASA Engineering Safety Center. The author thanks the following for extended technical discussions, providing data and technical papers, and/or timely response in the processing of test rollers:

J. Zabinski	Army Research Laboratory
C. Beal	Everlube Products Company
M. Dugger	Sandia National Laboratories
S. Prasad	Sandia National Laboratories
G. Doll	The University of Akron
A. Korenyi-Both	Tribologix Inc.

Trade names and trademarks are used in this report for identification only. Their usage does not constitute an official endorsement, either expressed or implied, by the National Aeronautics and Space Administration

## References

1. McClendon, M., "NIRSpec MSS Magnet Actuator Life Test Unit Wear Particle Evaluation", no report number, document obtained by Krantz, T., May 16, 2011
2. Authors unstated, "Micro Shutter Subsystem (MSS) Qualification Unit Test Report", JWST-RPT-013819, Rev. A, June 2010.
3. Krantz, T., Shareef, I, "Wear of Steel and Ti6Al4V Rollers in Vacuum", proceedings of the 41<sup>st</sup> Aerospace Mechanisms Symposium, also NASA TM-2012-217610, 2012.
4. Pellicciotti, J. (*submitted by*), "JWST NIRSpec Micro Shutter Subsystem", NESC-RP-11-00701, 2012.
5. Nishimura, Makoto, and Mineo Suzuki. "Solid-lubricated ball bearings for use in a vacuum—state-of-the-art." *Tribology International* 32, no. 11, 1999.
6. Pepper, S., "Research Note-Characterization of the Test Environment of JWST Roller Wear Evaluation at NASA-GRC", Aug. 1, 2011.
7. Johnson, K.L., **Contact Mechanics**, Cambridge University Press, 1985.
8. Kalker, J.J., "Rolling contact phenomena: linear elasticity", *Rolling Contact Phenomena CISM Courses and Lectures*, Issue 411, Springer-Verlag, 2000.
9. McGinness, H., "Lateral forces induced by a misaligned roller", DSN Progress Report 42-45, March and April 1978, Jet Propulsion Laboratory, Pasadena, Calif., 1978.
10. Krantz, T., DellaCorte, C., Dube, M., "Experimental Investigation of Forces Produced by Misaligned Steel Rollers", proceedings of the 40<sup>th</sup> Aerospace Mechanisms Symposium, NASA/CP-2010-216272, also NASA/TM-2010-216741, 2010.
11. Antoine, J. F., et al. "Approximate Analytical Model for Hertzian Elliptical Contact Problems." *Journal of Tribology* Vol. 128, 2006.
12. Archard, J. F., &Hirst, W. "The wear of metals under unlubricated conditions.", *Proceedings of the Royal Society of London. Series A. Mathematical and Physical Sciences*, Vol. 236, 1956
13. Roberts, E. W. "Space tribology: its role in spacecraft mechanisms." *Journal of Physics D: Applied Physics* 45, no. 50 , 2012.
14. Scharf, T. W., and S. V. Prasad. "Solid lubricants: a review." *Journal of Materials Science* 48, no. 2, 2013.
15. Authors not stated, "Properties of Du Pont VESPEL® Parts", Brochure Number H-15724-1, Du Pont Corporation, 1993.
16. Wheeler, J. M., C. A. Collier, J. M. Paillard, and J. A. Curran. "Evaluation of micromechanical behaviour of plasma electrolytic oxidation (PEO) coatings on Ti-6Al-4V." *Surface and Coatings Technology* 204, no. 21, 2010..
17. Santos, Lucia V., Vladimir J. Trava-Airoldi, Evaldo J. Corat, JadirNogueira, and Nélia F. Leite. "DLC cold welding prevention films on a Ti6Al4V alloy for space applications." *Surface and Coatings Technology* 200, no. 8, 2006.
18. Eckels, M., M. N. Kotzalas, and G. L. Doll. "Attaining High Levels of Bearing Performance with a Nanocomposite Diamond-Like Carbon Coating." *Tribology Transactions* 56, no. 3, 2013.
19. Scharf, T. W., P. G. Kotula, and S. V. Prasad. "Friction and wear mechanisms in MoS2/Sb2O3/Au nanocomposite coatings." *Acta Materialia* 58, no. 12, 2010.





# Wear Potential due to Low EHD Films during Elevated Temperatures

Alan Leveille\* and Peter Ward\*\*

## Abstract

An earlier study showed that EHD films could be accurately measured in a running bearing and that the EHD film eventually runs-in to a steady state value [1]. In the present paper, we report on additional tests conducted on bearings with more lubricants, wider speeds, and higher temperatures. The new results consistently show that all lubricants tested, including MAC-based lubricants have EHD film levels that are lower than model predictions in some situations. In addition, the MAC lubricants studied have lower film thickness than traditional hydrocarbons. Figure 1 is taken from [1] and shows room temperature data of MAC oil and Corey 100 oil, illustrating the smaller EHD film results when using this MAC oil.

Since higher temperatures produce lower films by changing the viscosity, the concern we have is that the EHD films may be too small to prevent ball/race metal contact and resulting wear at lower speeds. Best bearing practices would have the EHD film thickness be at least three (3) times the composite surface roughness. In this paper, we will present measured EHD thicknesses of lubricant films at speeds up to several thousand RPM for bearing bore sizes from as low as 6 mm (0.2 in) to as large as 35 mm (1.4 in) using MAC, Corey and KG-80. Ambient temperatures from room temperature to 52°C (125°F) are used. Testing was done with the base oils as well as formulated greases. Greases eventually ran in to the same EHD values as the base oil but took longer times to get there.

The results clearly indicate that wear is very possible in all steel bearings when using MAC lubricants and that this condition worsens with higher temperatures and smaller bearing size.

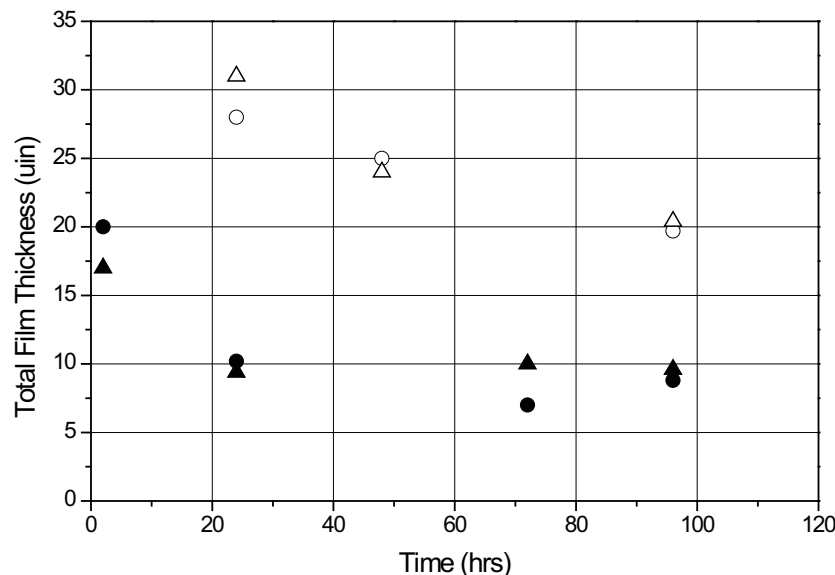


**Figure 1. Total Film thickness (in microinches) as a function of cumulative time operating at 6000 rpm with neat base oils formulated with TCP. Open symbols represent Corey and filled symbols represent MAC. Triangles and circles are the results from two independent measurement techniques**

\* Independent Consultant, Las Vegas, NV

\*\* The Aerospace Corporation, El Segundo, CA

## Introduction

Coincident with the use of MAC-based lubricants in the 90's was the observation of wear magnitudes in all-steel components that struck most bearing engineers as larger than previously seen and had expected. In 2008, Ward, Frantz, and Leveille presented the first publication [1] of a new instrument that could measure EHD films in real bearings over hundreds of hours. These initial but limited tests showed that MAC-based lubricants produced EHD films about 50% smaller than previous hydrocarbon-based lubricants such as KG-80 and Corey 100. Additional testing done over the past few years has confirmed that initial observation. We also observed that all of the EHD film thicknesses were thinner than predicted by calculations using the method developed by Hamrock-Dawson [2] with the Coy-Zaretsky [3] starvation factors that we have been using in our bearing modeling tools.

The smaller EHD films raised the concern of how thin do the lubricant films become at elevated temperatures? Will the EHD films be too thin to prevent wear due to ball/race metal contact? We will present measured EHD films at speeds up to several thousand RPM for bearing bore sizes from as low as 6 mm (0.2 in) to as large as 35 mm (1.4 in) using MAC, Corey and KG-80. All the test data was at ambient of 24°C (75°F) except for the 6-mm (0.2-in) bearing size for which data was obtained up to 52°C (125°F). We picked the 6-mm (0.2-in) size for the higher temperature testing because a smaller bearing would inherently have a smaller film at any given speed. The results are that we see the potential for EHD films that may be bordering on marginal or a Lambda of 1 and therefore, may be a cause of wear that could affect longevity in the presence of wear acceleration factors.

### Results from Earlier Testing at Room Temperature

A review of data from our EHD test apparatus for actual bearings over the years of use for various problems was done. It showed a general trend that MAC lubricants were about 50% or lower in EHD film thickness than the old hydrocarbon lubricants such as KG80 and Corey 100. Table 1 summarizes some of this data over the years. Table 1 is a summary at 3000 or 6000 RPM at room temperature.

**Table 1. Summary of Results at Room Temperature**

LUBRICANT	BEARING SIZE (mm) [in]	RPM	TOTAL MEASURED FILM THICKNESS (μm) [μin]	MULTIPLIER TO MATCH H-D + C-Z
Corey 100	12 [0.47]	3,000	0.66 [26]	0.46
Corey 100	20 [0.79]	6,000	0.51 [20]	0.13
Corey 100	25 [0.98]	6,000	0.71 [28]	0.25
KG80	35 [1.4]	6,600	0.46 [18]	0.43
MAC oil	6 [0.24]	3,000	0.2 [7]	0.375
MAC oil	12 [0.47]	3,000	0.38 [15]	0.52
MAC oil	20 [0.79]	6,000	0.2 [9]	0.11
MAC oil	25 [0.98]	6,000	0.38 [15]	0.23
MAC grease	25 [0.98]	6,000	0.25 [10]	0.14
MAC grease	25 [0.98]	6,000	0.30 [12]	0.2

NOTE: The EHD values listed in Table 1 is the sum of the EHD film at the inner race plus the EHD film at the outer race. H-D+C-Z is the DYBA model calculation of film thickness using Hamrock-Dowson with Coy-Zaretsky reduction factors.

The data in Table 1 seem to illustrate around 50% less EHD measured values than modeling predictions for the older oils. Additionally, the EHD film thicknesses for MAC oil are lower than the older oils.

### Testing up to 52°C (125°F)

Further work was executed recently on a 6-mm (0.2-in) bore size bearing while using increased capability of the EHD test apparatus. Specifically, the test ambient temperature was varied using a heat lamp. The bearings and the entire test housing are allowed to reach a steady state ambient before starting the EHD test. Thermocouples measure the test bearing outer ring temperature rise above ambient to obtain accurate “actual average lubricant temperature” for modeling purposes.

EHD data was taken for various speeds from 3000 rpm to less than 1000 rpm to show the speed effect on EHD thickness. The actual EHD data was gathered, first on a bearing pair using just a small amount of MAC oil, which is Case 1. Each bearing had just a small meniscus of oil at the ball/race interface when viewed at rest (see Figure 2). Weight checks showed 30 mg of lubricant. The phenolic cage was properly impregnated with the oil prior to test. The intent was to mimic adequate but minimal amount of lubricant oil. The EHD measurement is taken within a few seconds of a spin-motor stop, allowing the endplay changes associated with EHD film collapse at 0 rpm to be captured isothermally.



**Figure 2. An impregnated phenolic cage with just an adequate amount of oil to show a small meniscus at start.**

Next, another bearing pair was assembled with the same impregnated phenolic cage. Then typical cleaning sloshes with an oil/heptane mixture were done to assure bearing cleanliness followed by the addition of 25 milligrams of MAC grease. This Case 2 test shows a different lubricant procedure that represents methods known to be commonly used in industry, i.e., the use of grease lubricants.

The two lubricant cases were then subjected to a moderate amount of time at 52°C (125°F) running temperature while at 1000 rpm, approximating a beginning “run-in” process.

EHD data was then taken at various speeds from 3000 to less than 1000 rpm. Two running temperatures are shown in Figures 3 and 4, room temperature and 52°C (125°F). The EHD data is shown as a function of temperature and speed for the two lubricant cases. The overall intent is to show general operating lubricant amounts, coupled with running effects theoretically known to thin an operating lubricant film. We then correlate actual changes in EHD film thickness due to running conditions, with the modeling of EHD film thickness using the 50% reduction factor, over and above the standard Coy/Zaretsky reduction factor.

## Results and Discussion

The data presented in Figure 3 is on the 6-mm (0.2-in), all-steel bearing pair. It is the first lubricant case with a barely adequate amount of oil. As noted before, this data is collected after a brief “run-in” to distribute the lubricant and establish a steady-state condition. Then, the hot ambient tests are executed at different speeds followed by room temperature ambient tests after achieving the new steady state. This approach is used in an attempt to keep the lubricant condition in the bearing as identical as possible.

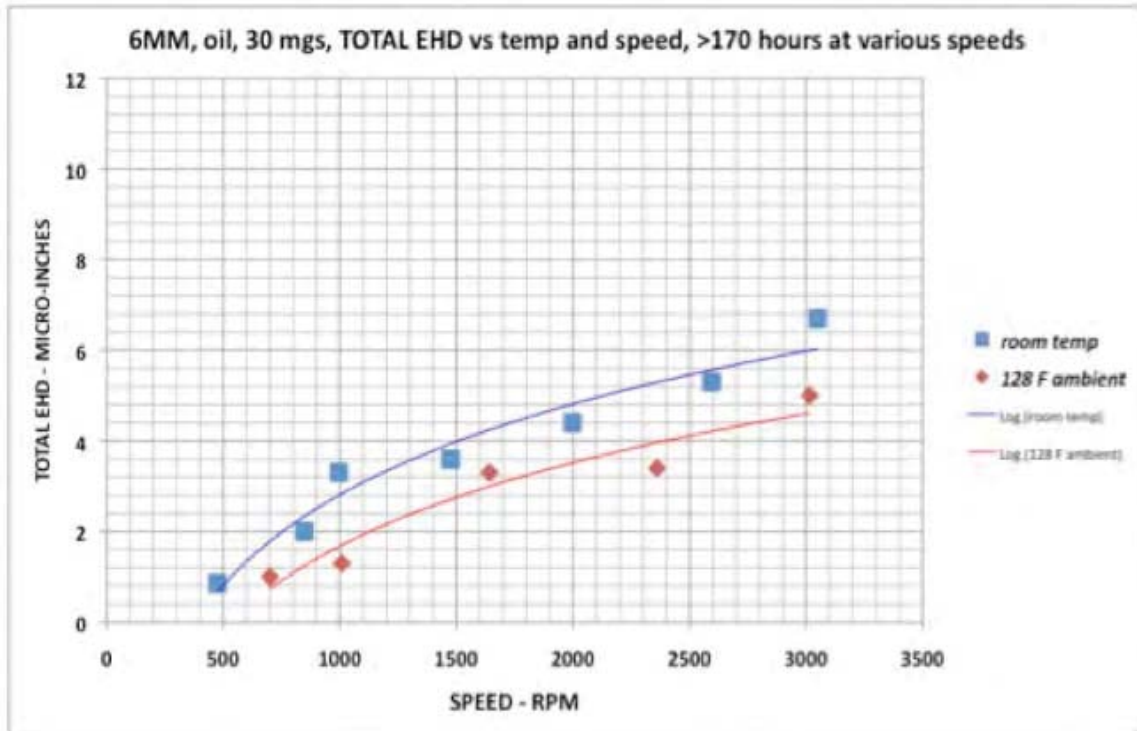


**Figure 3. Room Temperature and 52°C (125°F) EHD total values for the 6-mm (0.2-in) bore bearing lubricated with oil (Case 1).**

The data clearly shows the reduction of EHD film thickness due to the actual bearing running temperature and the accompanying viscosity change.

Next, Figure 4 shows data from the second lubricant case of tests with oil and grease. Again, the bearing is “Run-In” first at 1000 rpm in an elevated temperature condition, then data is taken.

As before, the chamber temperature was elevated to 52°C (125°F) steady state before starting bearing rotation. The bearing temperature during rotation was approximately 54°C (130°F). Note at the high temperature and 1000 RPM, the total EHD film thickness has decreased to less than 1 micro-inch (0.03 micro-meters). This bearing is definitely starved.

The difference between this lubricant condition with oil and grease versus the previous test with only oil is rather minimal and close to the EHD measurement error. The results indicate that the extra grease did not provide better protection in the first few hundred hours of operation. However, the grease/oil mixture may act differently from pure oil as operational time continues.

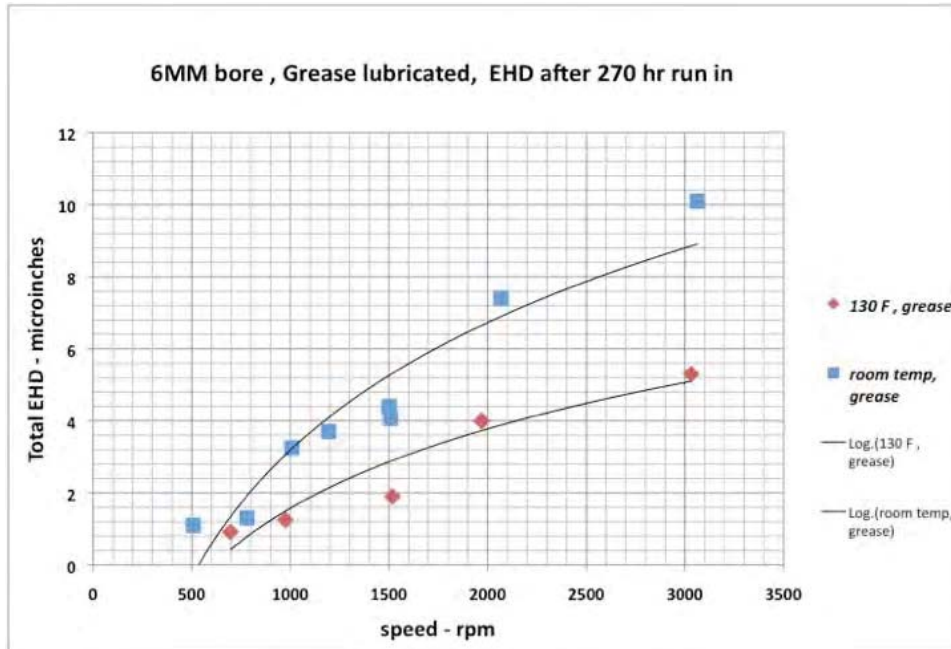


**Figure 4. The “oil plus grease” bearing (Case 2) pair at room temperature and 52°C (125°F).**

In the next few figures, the bearing race surfaces from these tests are depicted. It is evident some non-EHD conditions were established as there is evidence of beginning wear present.



**Figure 5. 6-mm (0.2-in) inner ring race of an original test with a hybrid bearing of silicon nitride ceramic balls and steel rings after the “Run-In”.**

**Note there is no evidence of race wear with this dissimilar ball material on the steel ring.**



Figure 6. 6-mm (0.2-in) race that generated the data shown in Figure 3, oil - only test. Note the worn ball path where hone lines have been eliminated when all-steel balls and rings/races are used.



Figure 7. Inner ring that generated the data in “Oil and Grease Test” shown in Figure 4. Again, there is wear in the ball path of the raceways that were tested against steel balls.





**Figure 8. A higher magnification view of the race in Figure 7, clearly showing the worn off hone lines and darkened grease in upper portion of the photomicrograph.**

#### **Modelling Estimates of Inner Race (IR) EHD Values over a Range of Speed and Temperatures**

The measured EHD data was the total EHD at the inner ring plus at the outer ring.

That is: 
$$EHD_{Dir} + EHD_{Dor} = EHD_{total} \quad (\text{Eq. 1})$$

The Hamrock-Dowson equations estimate that the inner ring lubricant film thickness is about 40% of the total. While not exact, assuming that the inner ring EHD is 40% of the total EHD measured should be sufficient for illustrating the inner ring behavior over a range of speed and temperature versus bearing size.

All the modeling estimates of EHD films shown in this paper were based on the software “DYBA” [4]. The MAC lubricants “multiplier” factors needed to match the Hamrock-Dowson + Coy-Zaretsky starvation factors are plotted in Figure 9. Applying a linear fit, we see the reasonably expected reduction as bore size increases, i.e., the larger bearing would have higher starvation at a given speed. We candidly admit that the correlation coefficient is not good but we would need significantly more testing to assure that we have really good control on the test variables. Nevertheless, we will use the multipliers as deduced by Table 1 to make comparative estimates of  $EHD_{Dir}$  vs. speed at 24°C (75°F) and 52°C (125°F) from 200 to 6000 RPM.

Conservative practice to prevent ball to race contact and wear is to have a value of  $\lambda \geq 3$  where:

$$\lambda = (\text{EHD film thickness}) / (\text{Composite ball and raceway surface roughness}) \quad [\text{Eq. 2}]$$

Using a composite bearing race/ball roughness of 2.0, a condition of  $3\lambda$  would require an EHD film of 6 micro-inches (0.2 micro-meters). The test bearings are at least this good.

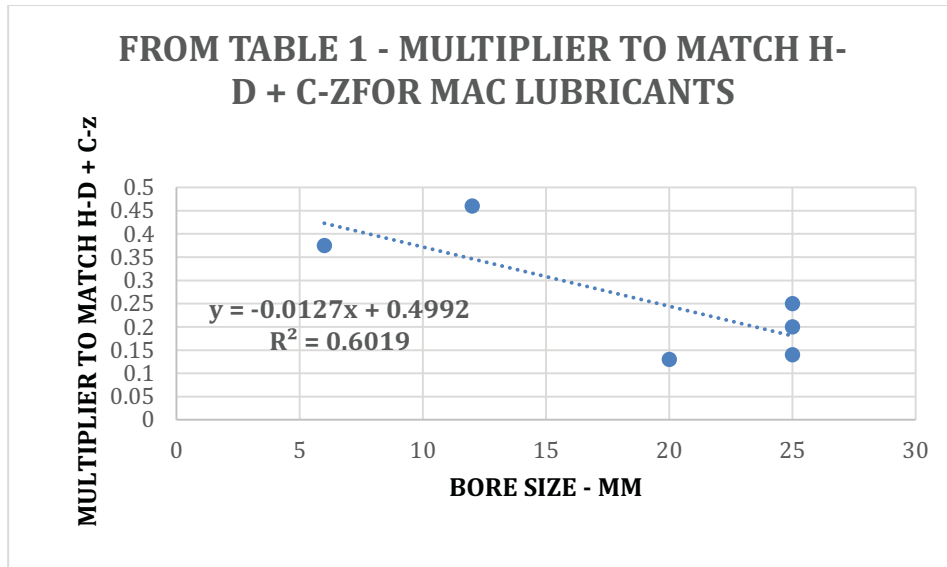


**Figure 9. Multiplier Factors from Table 1, to Match Hamrock-Dawson + Coy-Zaretsky EHD Predictions**

From Figure 9, the multiplier factors used in the analysis were: 6 mm (0.2 in) = 0.42, 12 mm (0.47 in) = 0.35, 20 mm (0.8 in) = 0.25 and 25 mm (0.98 in) = 0.18.

Figure 10 shows plots of the analytical estimates for the EHD film thickness at the inner race for the 6-mm (0.2-in) and 12-mm (0.47-in) bore bearings. Figure 11 shows similar plots for the 20-mm (0.8-in) and 25-mm (0.98-in) bore bearing estimates. To illustrate what might be an adequate lambda, we have placed an arbitrary line at 4 micro-inches (0.1 micro-meters) in Figures 10 & 11.

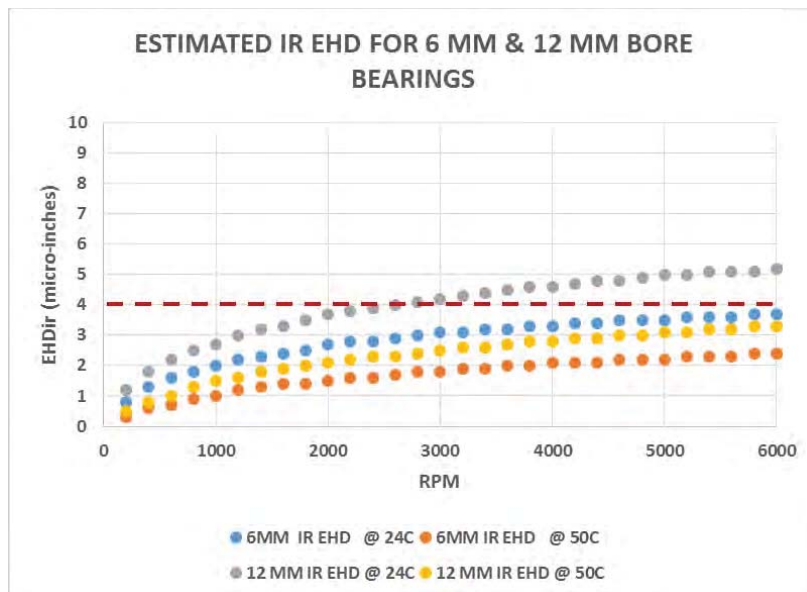


**Figure 10. Estimated IR EHD for 6-mm (0.2-in) and 12-mm (0.47-in) bore bearings at 24°C and 50°C**

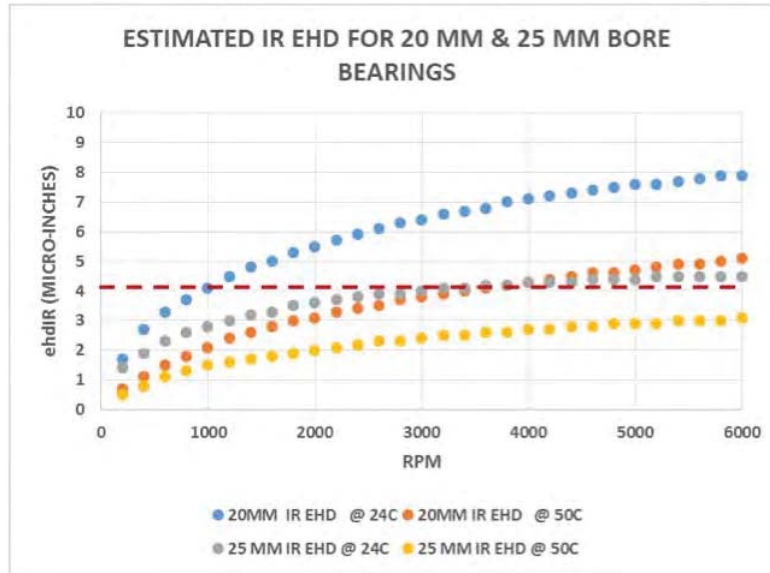


**Figure 11. Estimated IR EHD for 20-mm (0.8-in) and 25-mm (0.98-in) bore bearings at 24°C and 50°C**

The results shown in Figures 10 and 11 illustrate that MAC-based lubricants do not have large margins to separate the balls and raceways and that elevated temperatures and/or smaller bearing sizes increase that danger.

### Conclusions and Observations for Future Work

MAC lubricants have thinner EHD films at comparable bearing running conditions than older natural hydrocarbon lubricants.

Both lubricant types, using EHD predictions with approximately 25% to 50% reduction, seem to agree with actual data on films present.

The thinner films react predictably to raising bearing operating temperatures and speeds, and the resulting film thicknesses at high temperatures and at low speeds in actual applications need to be approached with caution in terms of resulting ball to race contact and possible wear. The low film thicknesses do seem to allow ball metal to race metal wear to start. Both tests presented showed polished wear bands in the race and darkening lubricant with metallic fines in the lubricant. When silicon nitride balls are substituted, the wear is totally mitigated.

Varying the lubricant quantity and examining long term run-in effects on EHD films are obvious next directions for future experiments. In this preliminary study of two lubrication cases, oil and oil with grease added, the EHD thickness values appear to be equivalent. However, long term effects have not been studied.

## References

1. Ward, P. C., Leveille, A. R., "Measuring the EHD Film Thickness in a Rotating Ball Bearing" , *Proceedings of the 39<sup>th</sup> Aerospace Mechanisms Symposium, NASA Marshall Space Flight Center, May 7-9, 2008*
2. Hamrock, B.J. and Dowson, D. "Isothermal Elastohydrodynamic Lubrication of point contacts, Part IV, Starvation Results" *ASME J. Lubr. Technol.* 99 (1977), 15-23
3. Coy, J.J., and Zaretsky "Some Limitations in Applying Classical EHD Film Thickness Formulas to a High-Speed Bearing" *ASME J. Lubr. Technol.* 103 (1981), 295-301
4. Leveille, A. R> "DYBA – A New Dynamic Bearing Analysis Software Tool" International Symposium on Rolling Element Bearings, Baja Hotel, San Diego, CA May 8, 2007

# Observations of Spacecraft Bearing Lubricant Redistribution Based on Thermal Conductance Measurements

Yoshimi R. Takeuchi<sup>\*</sup>, Peter P. Frantz<sup>\*\*</sup> and Michael R. Hilton<sup>\*</sup>

## Abstract

The performance and life of precision ball bearings are critically dependent on maintaining a quantity of oil at the ball/race interface that is sufficient to support a robust protective film. In space applications, where parched conditions are intentionally the norm, harsh operating conditions can displace the small reserves of oil, resulting in reduced film thickness and premature wear. In the past, these effects have proven difficult to model or to measure experimentally. This paper describes a study addressing this challenge, where bearing thermal conductance measurements are employed to infer changes in lubricant quantity at the critical rolling interfaces.

In the first part of the paper, we explain how the lubricant's presence and its quantity impacts bearing thermal conductance measurements. For a stationary bearing, we show that conductance is directly related to the lubricant quantity in the ball/race contacts. Hence, aspects of bearing performance related to oil quantity can be understood and insights improved with thermal conductance data. For a moving bearing, a different mechanism of heat transfer dominates and is dependent on lubricant film thickness on the ball.

In the second part of the report, we discuss lubricant quantity observations based on bearing thermal conductance measurements. Lubricant quantity, and thus bearing thermal conductance, depends on various initial and operating conditions and is impacted further by the run-in process. A significant effect of maximum run-in speed was also observed, with less oil remaining after obtaining higher speeds. Finally, we show that some of the lubricant that is displaced between the ball and race during run-in operation can be recovered during rest, and we measure the rate of recovery for one example.

## 1.0 Introduction

Bearing life and performance is critically dependent on lubricant. Heat transfer is also dependent on lubricant in space, therefore the two are linked. This paper will show bearing thermal properties depend on lubricant and its quantity, then, show how the conductance measurements can be used to infer lubricant behavior.

The requirements for operation of space mechanisms present bearings a very different thermal environment than mechanisms used in a terrestrial environment. In terrestrial applications, convection dominates the cooling mechanism. If air is not enough to cool it, the bearing is typically flooded with lubricant for additional cooling. Thus, bearing thermal conductance tends to be a second or third order effect in most terrestrial applications.

However, in the vacuum of space, essentially no air is present and flooding with lubricant is not feasible. Furthermore, in most cases, the bearing must operate with parched lubricant quantities and perform for years under these conditions. In the absence of convection, bearing raceway temperatures are a product of bearing thermal conductance, heat generation, and the operational environmental temperature. In most

---

<sup>\*</sup> The Aerospace Corporation, El Segundo, CA

<sup>\*\*</sup> The Aerospace Corporation, Colorado Springs, CO

vacuum situations, thermal conductance through the bearing and housing becomes a primary driver in maintaining stable temperatures.

Bearing thermal conductance and heat generation are dependent on a complex interaction of secondary factors, including the bearing geometry, internal loads, materials properties, operating and environmental conditions, and lubricant distribution. Heat generation within the bearing is the thermal energy gained and is equal to the mechanical energy lost based on the energy conservation concept. Thus, heat generation is the product of torque and rotational bearing speed. Since torque and speed are commonly measured values, bearing heat generation tends to be a commonly known quantity. Thermal conductance represents the bulk effective heat transfer between inner and outer race; the inverse of thermal resistance. The value of this parameter tends to be poorly known. Bearing thermal conductance and heat generation are dissimilar and respond to thermal and mechanical environments in very different ways. By measuring the lesser known parameter, thermal conductance, a different set of observations on bearing lubricant behavior can be made.

This paper will show that for static bearings, thermal conductance depends on lubricant distribution in the ball to race contacts. For example, a meniscus of oil collected at the interface between a ball and race provides for a larger effective area of contact and heat transfer between the two stationary bodies. This paper will also show that for a bearing in motion, the mechanism of heat transfer differs. The lubricant distribution on the ball dominates the thermal conductance measurement.

In the first part of the paper, we describe the use of thermal conductance measurements to establish the mechanisms of heat transfer, which are sensitive to lubricant distribution. Once the relation between bearing thermal conductance and the lubricant is demonstrated, we show that thermal conductance measurements can be used as a qualitative indicator of lubricant quantity, to monitor behavior during the run-in process, and to deduce the impact of lubricant recovery during bearing rest times.

### 1.1 Nomenclature

$G$  – ( $W/^\circ C$ ) bulk effective conductance across the bearing

$A_i$  – ( $m^2$ ) ball to inner race Hertzian contact area

$A_o$  – ( $m^2$ ) ball to outer race Hertzian contact area

$A$  – ( $m^2$ ) average inner and outer ball to race Hertzian contact area

$A_{oi}$  – ( $m^2$ ) area due to lubricant in ball to inner race contact area meniscus

$A_{oo}$  – ( $m^2$ ) area due to lubricant in ball to outer race contact area

$A_0$  – ( $m^2$ ) average inner and outer lubricant areas

$P$  – (N) axial load

$R_i$  – ( $^\circ C/W$ ) thermal resistance from the inner race to the ball in a bearing

$R_o$  – ( $^\circ C/W$ ) thermal resistance from the outer race through the ball of a bearing

$R_b$  – ( $^\circ C/W$ ) total thermal resistance across a single bearing ball

$a_i$  – (m) major axis of the Hertzian contact ellipse between the ball to inner race

$b_i$  – (m) minor axis of the Hertzian contact ellipse between the ball to inner race

$a_o$  – (m) major axis of the Hertzian contact ellipse between the ball to outer race

$b_o$  – (m) minor axis of the Hertzian contact ellipse between the ball to outer race

$a$  – (m) average of the inner and outer race major axis of the Hertzian contact ellipse

$b$  – (m) average of the inner and outer race minor axis of the Hertzian contact ellipse

$k_1$  – ( $W/m-^\circ C$ ) thermal conductivity of the race materials

$k_2$  – ( $W/m-^\circ C$ ) thermal conductivity of the ball material



## 2.0 Test Set Up

A test facility at The Aerospace Corporation was used to measure thermal conductance under controlled thermal and mechanical conditions [1]. The test rig allows the measurement of thermal conductance across a single bearing under controlled axial loads and speeds, and provides the ability to vary and monitor the thermal boundaries, all under a vacuum environment. The speed refers to the angular velocity of the inner race, where the shaft is driven by a motor. The other race is held stationary. A single test bearing is held under a constant load applied by the axial load device. Photos of the test facility used to measure the larger bearing's thermal conductance and its fixture are shown in Figures 2.0.1 and 2.0.2 respectively. A similar test set up was created to measure small and medium size bearing thermal conductance.

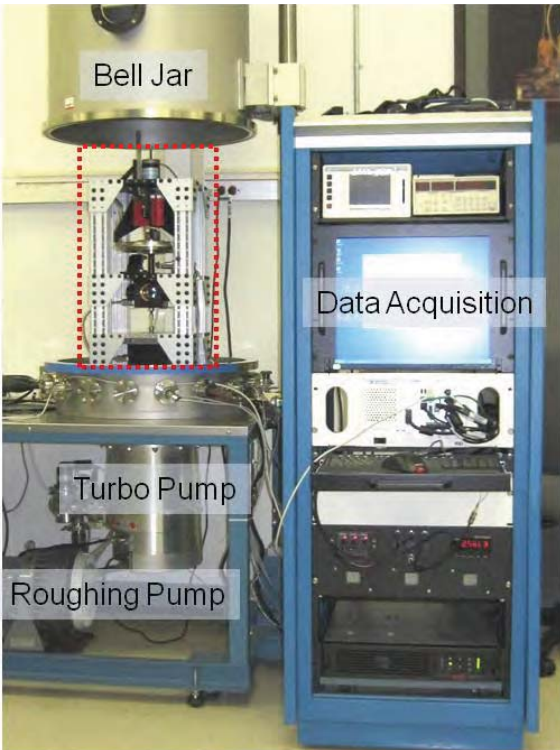


**Figure 2.0.1 Test Facility, Including the Electronics, and Part of the Open Vacuum Chamber**



**Figure 2.0.2 Bearing Test Fixture**

The sizes, geometry, and material information for the bearings that were tested are listed in Table 2.0.1. They are all conventional angular contact bearings with inner ring piloted phenolic retainers. Bearing sizes range from 28 mm to 62 mm outer diameter (OD). None of the test bearings are sealed or shielded.

**Table 2.0.1 Bearing sizes, materials, and lubricant quantities**

Sample Description	OD (mm)	Race material	Ball material	Dry Bearing weight (g)	Initial lubricant weight (mg)
Large bearing, steel	62	52100 steel	52100 steel	228.54	130
Large bearing, hybrid	62	52100 steel	Silicon Nitride	188.05	130
Medium bearing, steel	47	52100 steel	52100 steel	63.4076	96.9
Small bearing, steel	28	52100 steel	52100 steel	19.8058	49.9

The lubricant used for the bearings was NYE 2001 Penzance synthetic oil, Nye Lubricants, Fairhaven, MA. The bearings were cleaned and the retainers impregnated with the test oil [2]. A thin film of oil was cast on all surfaces from immersion in dilute solution, and excess oil was removed by centrifugation at 3000 rpm. The dry bearing weight is measured and compared with the weight after lubrication. The difference represents the lubricant weight. Table 2.0.1 documents the initial lubricant weight in each test bearing.

### 3.0 Test Results: PART 1 – Effect Of Lubricant On Bearing Thermal Conductance

The presence and location of lubricant affects bearing thermal properties. This relationship was explored here by first studying a base case of a dry (no oil), static (non-moving) bearing in vacuum. We then introduced oil into a static bearing to draw a comparison. Data was collected and an example compared the analytical predictions with that of experimental thermal conductance measurements for a small bearing size.

#### 3.1 Test Method

All tests were conducted under steady state thermal environmental conditions, where the thermal and mechanical boundary conditions were fixed and temperatures were allowed to equilibrate. Bearing thermal conductance measurements in section 3.2 through 3.4 were made under static conditions, 0 rpm, and dynamic measurements in section 3.5 were made at 6000 rpm. One of the challenges of the dynamic tests is that the variables, temperature and speed, are not designed to operate independently. To resolve this issue, a matrix of tests was used to perform a parametric study, where both parameters were varied. This enabled the sequential isolation of single independent variables. In this section, the test data set presented is for the average bearing temperature of 20 °C, determined by interpolation over a range of test data.

#### 3.2 Dry Static Bearing

Bearings are generally thermally insulative. The reason for the high thermal resistance is the bearing geometry. Two small contact areas are present, per ball, at the ball-to-inner race and ball-to-outer race interfaces generating a thermal constriction region, through which the heat must pass. A closed form analytical model to calculate the effect of the thermal constriction was developed by Yovanovich [3]. Yovanovich calculated the thermal resistance across a dry, static bearing by modeling the ball and races as semi-infinite half-planes with the elliptical Hertzian contact area serving as the thermal contact region. The basic equations to calculate thermal resistance across each of the ball-to-race contacts are:

$$R_i = \Psi_i/4k_1a_i + \Psi_i/4k_2a_i \quad \text{inner race to ball thermal resistance} \quad (3.1)$$

$$R_o = \Psi_o/4k_2a_o + \Psi_o/4k_1a_o \quad \text{ball to outer race thermal resistance} \quad (3.2)$$

$$R_b = (R_o + R_i) \quad \text{total thermal resistance across the bearing} \quad (3.3)$$

where  $\Psi$  is a non-dimensional geometric factor accounting for the ball contact areas and defined as:

$$\Psi_n = \frac{2}{\pi} \int_0^{\pi/2} \frac{d\theta}{\left(1 - \frac{a_n^2 - b_n^2}{a_n^2} \sin^2 \theta\right)^{1/2}} \quad (3.4)$$

Where the subscript  $n$  is designated either  $i$  or  $o$  for the inner or outer race. The Hertzian contact area is elliptical in shape and the geometry is represented by:

$a_n$  – major Hertzian contact axis

$b_n$  – minor Hertzian contact axis

The relationship between the major and minor axis dimensional geometries and load, P, is documented in the reference by Yovanovich [3]. A simplified summary:

$$a_n \propto P^{1/3} \quad (3.5)$$

$$b_n \propto P^{1/3} \quad (3.6)$$

Conductance is the inverse of the resulting calculated Yovanovich bearing thermal resistance equations.

$$G = \frac{1}{R_b} \quad (3.7)$$

Simplification is required to gain a basic understanding of the relationship between conductance and axial load and area. Substituting and simplifying with the following assumptions:

$$a_i \approx a_o \quad (3.8)$$

$$b_i \approx b_o \quad (3.9)$$

We obtain a relationship between bearing thermal conductance and load.

$$G \propto P^{1/3} \quad (3.10)$$

The Hertzian contact area is also defined as:

$$A_n = \frac{\pi}{4} \cdot a_n \cdot b_n \propto P^{2/3} \quad (3.11)$$

Thus,

$$A \approx A_n \propto P^{2/3} \quad (3.12)$$

and

$$G \propto \sqrt{A} \quad (3.13)$$

Equation 3.13 also means that the dependence of conductance on contact area weakens as the contact area increases. As the contact area grows, conductance becomes less sensitive to further increases. Equation 3.10 shows a similar, but stronger attenuation for the effect of increasing preload on conductance.

The relationship between a bearing's thermal conductance and axial load is demonstrated in Figure 3.2.1. This figure compares measured and calculated conductance values for the small (Table 2.0.1), dry (non-lubricated), static (non-moving) 52100 steel bearing. The conductance analysis utilized the Yovanovich method. Note the conductance vs. axial loads relationship demonstrates the  $P^{1/3}$  curve, where low values of axial loads result in high conductance sensitivity, but with higher loads the sensitivity gradually diminishes, evidenced by a decreased slope. A comparison between the calculated and measured values of thermal conductance indicates that the trends correlate well.

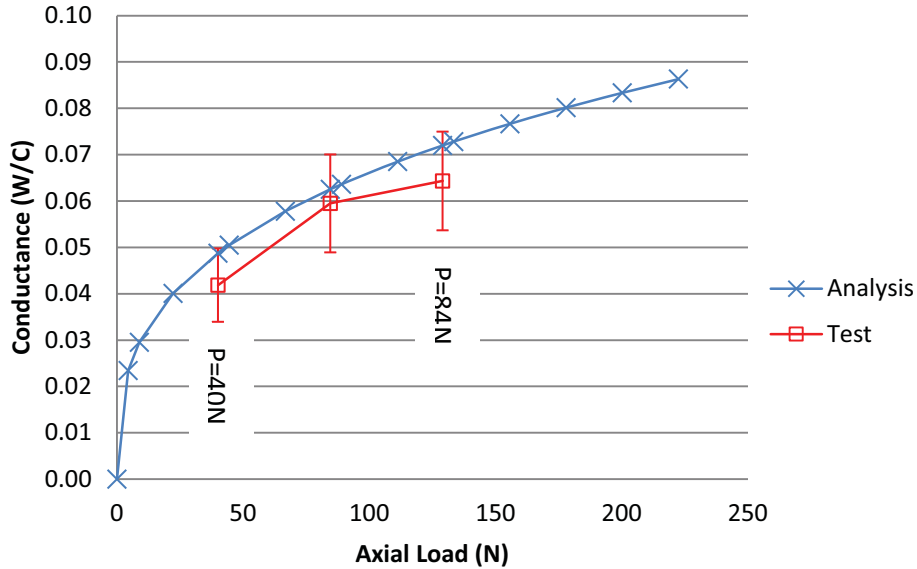


**Figure 3.2.1 Theoretical and Experimental Conductance vs. Axial Load for a 28-mm OD Dry Static Steel Bearing**

### 3.3 Oil Lubricated Static Non-Run-In Bearing

Once oil was introduced into the bearing, thermal conductance increased significantly and became relatively insensitive to axial loads. Figure 3.3.1 compares the conductance of a dry static bearing with the same bearing after the addition of oil. The small bearing was used for this experiment, after oil was added according to the method described above. The bearing was not operated to run-in the lubricant.

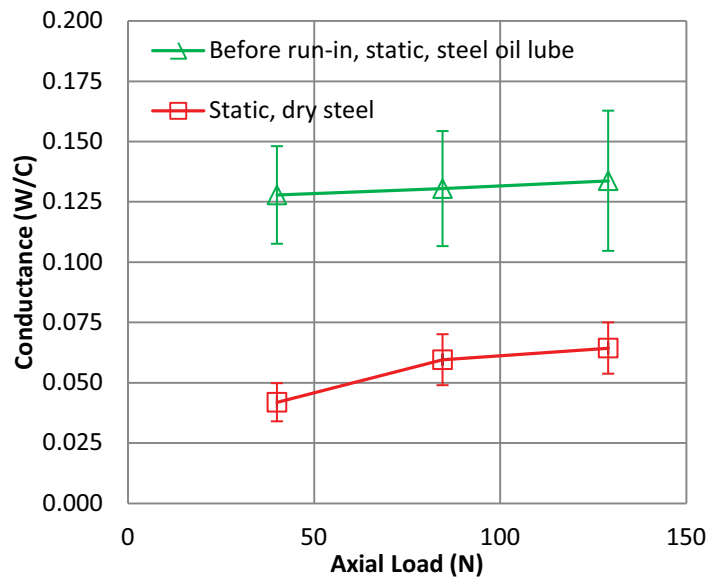


**Figure 3.3.1 Experimental Thermal Conductance vs. Axial Load for a Static 28-mm OD Oil Lubricated Non-Run-In and Dry Steel Bearing**

The green triangles in Figure 3.3.1 (oiled bearing) show a significant increase in conductance over the red squares (dry bearing); this is attributed to the increase in ball-to-race contact area due to the presence of the oil between the contacts. We surmise that increased conductance is due primarily to the

oil meniscus surrounding the contact and secondarily due to the liquid mediated Hertzian contact (filling the microscopic pores between the rough contacting surfaces). In essence, the oil increases the thermal pathway, decreasing resistance and increasing conductance.

The decreased sensitivity to axial loading can also be attributed to the increased initial area due to the presence of the oil lubricant. With a much larger initial area, a subsequently greater increased area change is needed to affect bearing thermal conductance. Figure 3.3.2 shows the relation between total ball-to-race contact area and conductance. The red dots indicate the increased contact area in a dry bearing showing the change in conductance as a function of load. The yellow dots show the increased contact area in an oil-lubricated bearing due to the same increase in load, and its influence on conductance. The change in an oil-lubricated bearing is dramatically less pronounced because the relevant contact area is already an order of magnitude larger due to the oil.

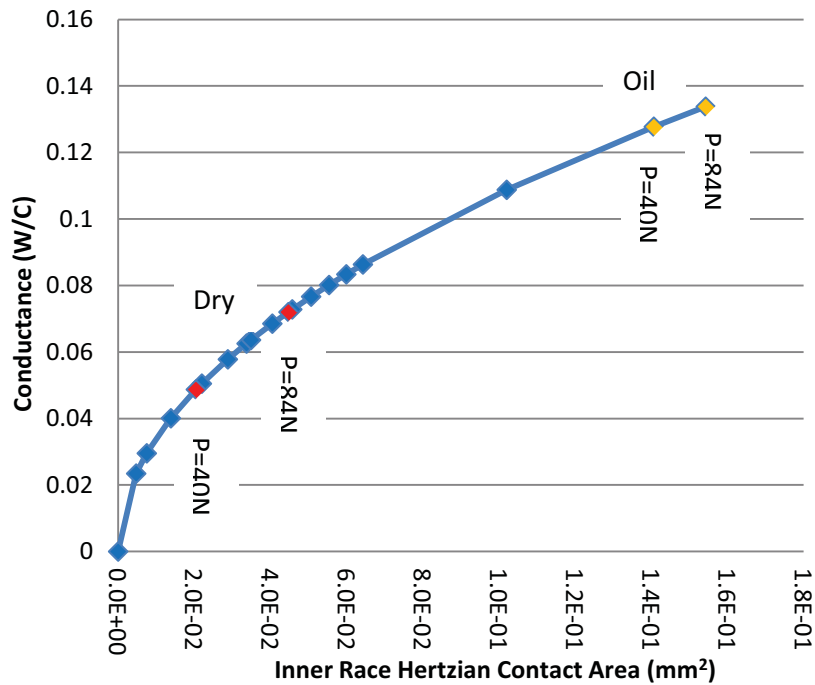


**Figure 3.3.2 Theoretical Conductance vs. Total Inner Race Contact Area for a 28-mm OD Steel Bearing: Change in Area for a Dry and Oil Lubricated Case**

The exact thermal conductance magnitude depends on the initial quantity and distribution of the lubricant. If we assume that the contact area of the lubricant,  $A_0$ , is constant, then, bearing thermal conductance is proportional to the square root of the total area of the lubricant and the ball to race contact:

$$G \propto \sqrt{A + A_0} \quad (3.14)$$

The ball to race contact area,  $A$ , is still proportional to the axial load to the 2/3 power:

$$A \propto P^{2/3} \quad (3.15)$$

Measuring conductance,  $G$ , the Yovanovich model can be used to estimate the total area  $A+A_0$  [3], then, the ball to race contact area can be calculated based on knowledge of the load,  $P$  [3]. The assumption is that the thermal resistance due to the lubricant is negligible, despite the thermal conductivity of oil being only 0.3% of the 52100 steel. The thermal resistance is still insignificant because the thickness of the lubricant in the meniscus at rest is, on average, approximately 0.3 microns. This assumption introduces

about a 3.5% error into the analysis, where the resulting contact area is under-estimated by that amount. Assuming that the thermal resistance across the metal and lubricant contact is small compared to the resistance generated due to the thermal constriction of ball to race geometry, the Yovanovich model can be used to estimate the lubricant area once the thermal conductance is measured across the bearing.

Thus, the total lubricant area,  $A_0$ , can be determined. Based on the analysis method, the contact areas due to the lubricant and the metal-to-metal Hertzian contact are shown in Table 3.3.1. The values depicted represent the lubricant and metal contact area between the inner race and one ball. Note that the initial lubricant area is dependent on the amount applied to the bearing system before testing began. In this case, the 62-mm OD bearing had a larger relative lubricant amount in the ball-to-race pathway than the smaller 28-mm OD bearing. In the next section, we'll explore how the run-in process impacts lubricant quantity in the ball-to-race contact.

**Table 3.3.1 Static Bearing Ball-to-Race Hertzian and Lubricant Area Before Run-In**

Bearing Details			Area – (Inner Race)			
Bearing Size	OD (mm)	Load, P (N)	Hertzian Contact Area (mm <sup>2</sup> )	Lubricant Area (mm <sup>2</sup> )	Total Area (mm <sup>2</sup> )	Lubricant/Hertzian Area (%)
Large bearing, steel	62	133	8.2E-02	45.E-02	53.E-02	550
Small bearing, steel	28	129	4.5E-02	11.E-02	15.E-02	245

### 3.4 Oil Lubricated Static Run-In Bearing

Oiled bearings (small and large, steel) were then run-in in the following manner: As the bearings turned continuously at 6000 rpm, the conductance, temperatures, and heat generation were observed to gradually decrease. Changes were most pronounced early in the test and gradually decreased in intensity over time. Each bearing was considered to be completely run-in when no additional changes in these variables could be detected with additional operational time. Measurements of thermal conductance resumed after bringing the bearing to rest (static conditions) and compared with the results before run-in conditions were established.

Observations on the run-in process indicated that the larger bearing runs-in significantly faster. While the small bearing took 5 days to run-in, the large bearing took significantly less time (less than 3 hours). It was not known exactly how long run-in conditions were reached for the largest 62-mm OD bearing tested because the thermal equilibrium in the test set up itself took 3 hours to occur and by then the bearing was run-in. A possible explanation for the much shorter run-in times for the larger bearing was that a much larger centrifugal force on the larger 62-mm OD bearing caused more lubricant to be thrown out initially.

Table 3.4.1 shows the impact of a 6000-rpm run-in on lubricant in the ball-to-race pathway. The data presented in the table represents the lubricant and metal contact area between the inner race and one ball, and provides a relative feel for the amount of lubricant present in the raceway.

Before run-in, the lubricant area in the race for the large bearing was significantly larger than the small bearing, but *after* run-in, the reverse occurred. While the lubricant contact area size was initially larger in the 62mm OD bearing, relatively, the lubricant was only 138% larger than its Herzian contact area compared with 183% for the smaller 28mm OD bearing.

This large decrease in lubricant was reflected in a large drop in thermal conductance measurements described next. Figure 3.4.1 shows the bearing thermal conductance as a function of axial loads for a 28-mm OD bearing, both before and after run-in and Figure 3.4.2 depicts the results for the large 62-mm OD bearing.



**Table 3.4.1 Static Bearing Ball-to-Race Hertzian and Lubricant Area After 6 krpm Run-In**

Bearing Details			Area – (Inner Race)			
Bearing Size	OD (mm)	Load, P (N)	Hertzian Contact Area (mm <sup>2</sup> )	Lubricant Area (mm <sup>2</sup> )	Total Area (mm <sup>2</sup> )	Lubricant/Hertzian Area (%)
Large bearing, steel	62	133	8.2E-02	11.4E-02	19.6E-02	138
Small bearing, steel	28	129	4.5E-02	8.2E-02	12.7E-02	183

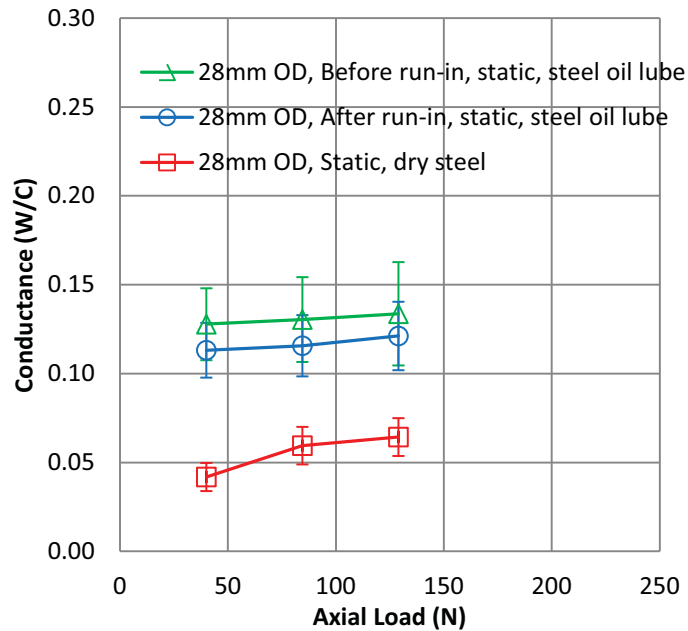


**Figure 3.4.1 Comparison of Thermal Conductance vs. Axial Load for an Oil Lubricated Static Before Run-In, After Run-In, and Dry Conditions for a 28-mm OD Steel Bearing**

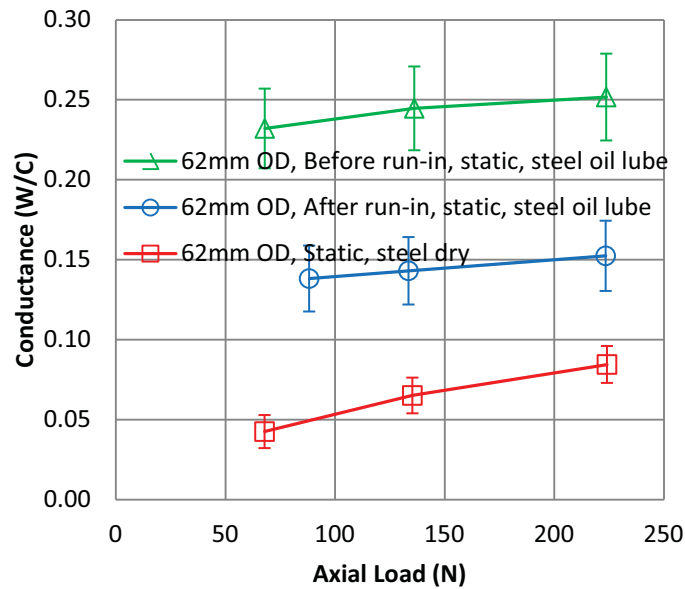


**Figure 3.4.2 Comparison of Thermal Conductance vs. Axial Load for an Oil Lubricated Static Before Run-In, After Run-In, and Dry Conditions for a 62-mm OD Steel Bearing**

We find changes in conductance that are caused by this run-in process. Bearing thermal conductance decreases in magnitude after run-in in both cases, as expected due to the smaller lubricant area. However, the thermal conductance in the larger bearing decreases significantly more than the smaller bearing, possibly due to a combined initial larger amount of lubricant and higher centrifugal force acting on the bearing during run-in, throwing out more lubricant. The final lubricant contact area is slightly greater in the larger bearing and likewise, the thermal conductance is slightly higher for the larger bearing.

In both cases, the final thermal conductance is still higher than the dry condition as would be expected. The dry case represents the lowest possible bearing thermal conductance value for a given bearing, geometry, materials, and load condition.

The total amount of lubricant in the bearing was measured before and after run-in for three different bearing sizes. The results are shown in Table 3.4.2, with additional initial weight data from a fourth bearing.

**Table 3.4.2 Lubricant Loss as a Function of Run-In Speed**

Bearing Details			Lubricant Weight		
Bearing Size	OD (mm)	Dry Bearing Weight (g)	Initial Lubricant Weight (mg)	After 6krpm Run-in (mg)	After 10 krpm Run-in (mg)
Large bearing, steel	62	228.54	130	100	not weighed
Large bearing, hybrid	62	188.05	130	90	70
Medium bearing, steel	42	63.4076	96.9	not operated	not weighed
Small bearing, steel	28	19.8058	49.9	39.2	not operated

In each case, we find that the conductance reached a steady state after prolonged operation at its run-in speed. The measured amount of lubricant loss can be attributed to the initial quantity and maximum run-in speed. In the case of the large hybrid bearing the weight fell further after additional testing at 10 krpm, showing that as run-in speeds increase, the amount of lubricant left in the bearing decrease. In section 4.4 below, we will show how this decrease affects conductance. Even though most of this lubricant weight is not distributed in the ball to race pathway, there is a corresponding drop in lubricant in the critical areas, resulting in lower bearing thermal conductance with increase run-in speeds.

### 3.5 Oil Lubricated Dynamic Run-In Bearing

Next, dynamic (constant speed motion at 6000 rpm) thermal conductance measurements were taken at various thrust loads for the small and large sized bearings. While the bearing is in motion at high speed, the heat transfer mechanism changes. For a static bearing, the mechanism of heat transfer was conduction through the contact pathway, through the ball, and finally through the outer contact pathway. However, once the bearing rotates at a significant speed (such as 6000 rpm), our data suggests that the mechanism of heat transfer changes to mass transport, as warm lubricant picks up heat at the hotter raceway and gets transported with the ball. It then deposits heat at the cooler raceway. Thus, the lubricant film thickness on the ball becomes important, and the Yovanovich analysis no longer holds. Comparisons of the conductance during both dynamic and static states as well as oiled and dry conditions were made for both bearing sizes in Figures 3.5.1 and 3.5.2.

For all of the dynamic test cases, bearing thermal conductance was stable for a given set of conditions once the bearing had fully run-in. To produce the test data shown below, the test fixture thermal conditions were adjusted and the data set was interpolated for a constant average bearing temperature of 20°C throughout. Despite the differences in bearing sizes, the behavioral *trends* were similar between the 28mm OD and 62mm OD bearing sizes. Conductance *magnitudes*, however, were very different, with the

larger bearing having much higher conductance than the smaller bearing and rising more steeply with axial load.

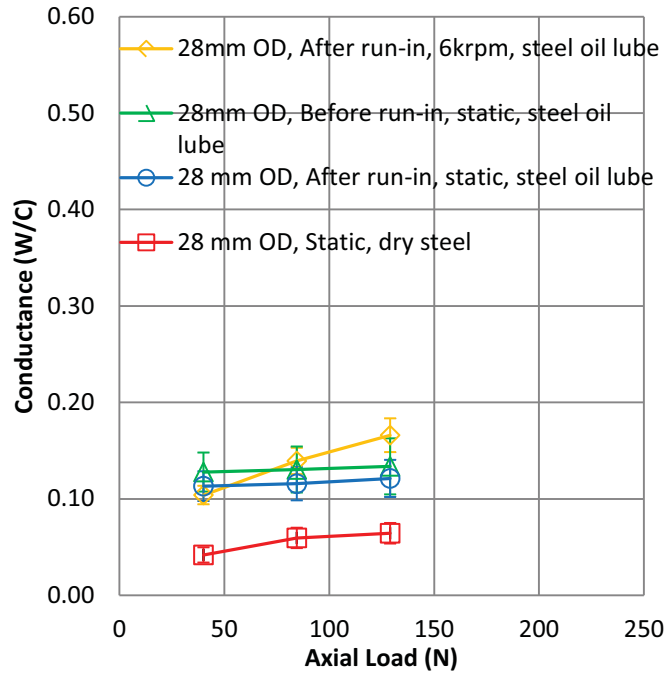


**Figure 3.5.1 Comparison of Thermal Conductance vs. Axial Load for an Oil Lubricated Static And Dynamic States of Motion for a 28-mm OD Steel Bearing**

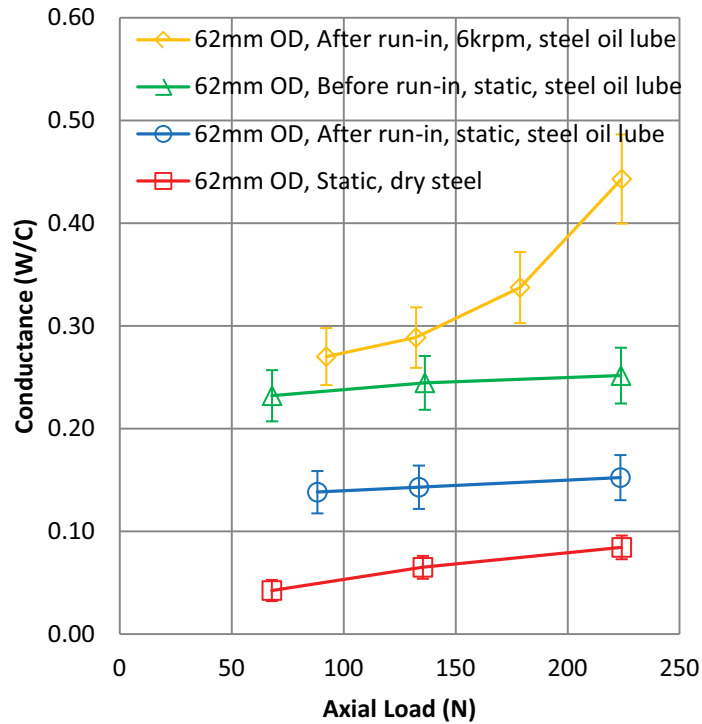


**Figure 3.5.2 Comparison of Thermal Conductance vs. Axial Load for an Oil Lubricated Static And Dynamic States of Motion for a 62mm OD Steel Bearing**

The reason for sensitivity to load is not yet fully understood, and is the subject of ongoing investigation. One possible explanation being explored is based on the mechanism of heat transfer. Once the bearing moves at a significant speed, the heat transfer process is very different than a static bearing. Significant motion would prevent conduction process through the contact points and ball. Instead, we believe that mass transport takes place, where the lubricant picks up heat at the hotter race, gets carried by the ball as it rotates, then deposit heat at the cooler race. As the axial load increases, this band of lubricant exposed to the mass transport process increases, resulting in greater heat transfer rates, thus higher bearing conductance.

#### **4.0 Test Results: PART 2 –Bearing Lubricant Behavior Observations Based on Thermal Conductance Measurements**

This section explores lubricant behavior observed through conductance changes during the run-in process. The impact of changing the maximum run-in speed was studied. The impact of bearing rest was also described below. From these measurements, we infer changes in lubricant quantity.

##### 4.1 Test Method

The bearing inner ring raceway was rotated in vacuum at constant speed and environmental temperature. After thermal equilibrium was established, the conductance was measured while operating at the indicated speed. The speed was then changed, and the system was allowed to establish a new equilibrium before the next data point was measured. The resulting thermal conductance was collected for speeds ranging from a minimum of 0 rpm to a maximum of 10,000 rpm.

Because we were establishing the influence of run-in, a test matrix was *not* performed on each data point, making it impossible to separate out the influence of temperature and speed. Hence the temperature was allowed to vary with speed in the data set shown below.

##### 4.2 Influence of Run-In on Bearing Lubricant Distribution

Two medium-sized bearings were tested as described above. The first bearing, labeled medium A in Figure 4.2.1, was freshly lubricated and had not been previously run-in. The second bearing, labeled medium B in Figure 4.2.2, had been run-in and tested previously but rested for months before the tests shown here. The curves on each of the plots show a set of runs that has the bearing tested at successively increasing or decreasing speeds.

The initial running cycles of the virgin bearing (blue diamonds, Figure 4.2.1) show erratic behavior caused by rapid changes in lubricant distribution. The high initial conductance at rest indicates a significant amount of oil in the menisci. As the first speed cycle returned to rest from 10,000 rpm, the conductance was less than initial, but still above the fully run-in value. With additional speed cycles, the conductance settled down to a continuous decrease with speed, showing the hypothetical effects of heat transport described above. After the multiple speed cycles, the static conductance leveled off at approximately 0.10 W/°C. At this point, we believe the bearing was fully run-in, as excess oil between the ball and race interfaces were displaced.

The used bearing, Figure 4.2.2, had been through a similar suite of testing, and then rested for months. We found that although the high-speed conductance changed little with additional run-in cycles, the conductance at rest (and, by inference, the quantity of oil in the static menisci) fell slowly with progressively greater accumulated operating time and as the bearing became run-in. The static conductance began at 0.13 W/°C, and fell with additional speed cycles to a stable value nearly equal to the static conductance of the virgin bearing after several speed cycles.

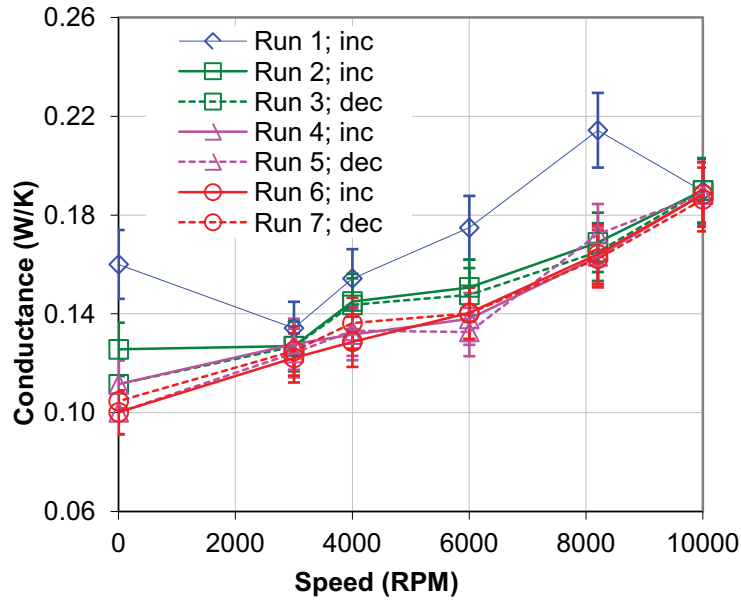


**Figure 4.2.1 Run-In Effects on Thermal Conductance of a Virgin Bearing; Medium Bearing A**

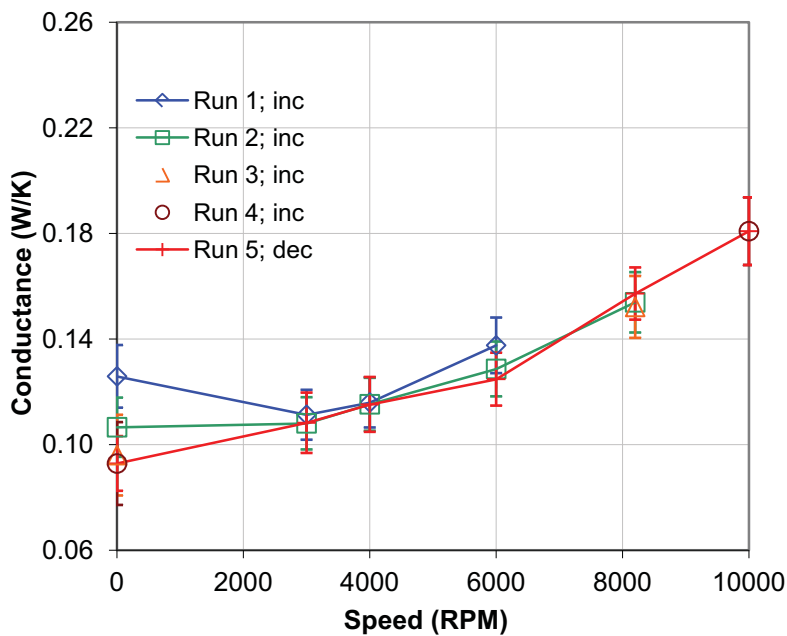


**Figure 4.2.2 Run-In Effects on Thermal Conductance of a Previously Used Bearing; Medium Bearing B**

We conclude from this that a bearing of this size, lubricated as these were, will have enough excess oil to enable a static conductance of  $0.16 \text{ W/}^\circ\text{C}$ . After run-in, a portion of this oil is displaced from the rolling path, but remains close, while another portion is displaced to a location where it is far from the rolling path. This loss results in a smaller oil meniscus and conductance of  $0.10 \text{ W/}^\circ\text{C}$ . With prolonged rest, the oil that remained close by is able to creep back to the ball-to-race interface, causing a recovery of the conductance to about  $0.13 \text{ W/}^\circ\text{C}$ .

In both cases, additional run-in resulted in a decrease in static thermal conductance. However, the dynamic bearing thermal conductance behavior began quite differently between A and B. For the virgin bearing A, the thermal conductance began high, but with additional run-in the value decreased. We suggested earlier that the mechanism of heat transfer in a dynamic bearing was mass transport. The test data indicates that the lubricant film thickness decreases with time then stabilizes after the bearing is completely run-in. That film thickness is established by the centrifugal forces generated by the maximum run-in speed. The film thickness on the ball should *not* be confused with the Elastohydrodynamic (EHD) film as the EHD film is the minimum oil thickness separating the ball and race during operation. Instead, the film thickness that we are referring to is the lubricant riding on the outer diameter of the ball.

The second bearing, B, had previously been run-in and clearly shows that the dynamic conductance values are repeatable. This suggests that the lubricant film on the ball does not recover after run-in.

The testing of both medium bearings varied in the number of start/stop cycles and the operational time, but both had seen maximum run-in speeds of 10,000 rpm and were operated at the same temperature. The conductance values after multiple speed cycles, shown in Figures 4.2.1 and 4.2.2, are very similar. Both the static and dynamic bearing thermal conductance values ended up comparable, suggesting final run-in lubricant quantity and distribution in the bearing is similar and is governed primarily by maximum run-in speeds.

#### 4.3 Influence of Maximum Run-In Speed on Lubricant Loss

The bearing thermal conductance profile changes, as the bearing is run-in at even higher speeds (20,000 rpm). This effect is shown in Figure 4.3.1.

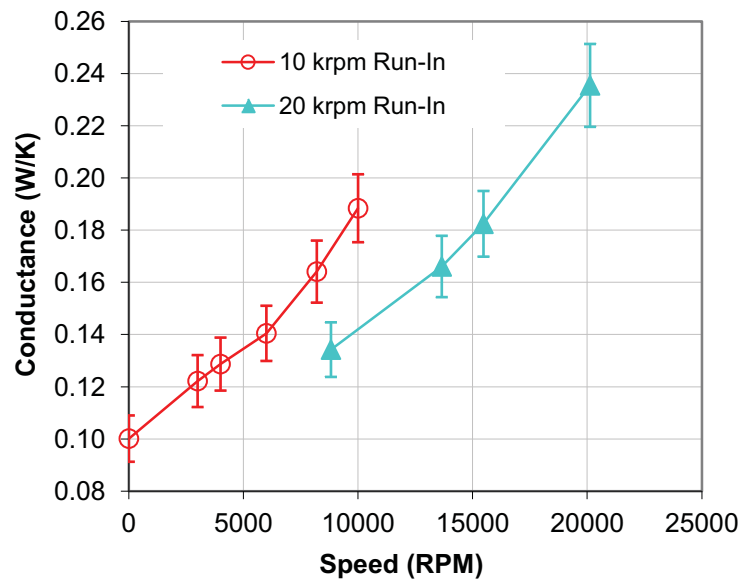


**Figure 4.3.1 Effect of Preconditioning Bearing at 10 krpm and 20 krpm Run-in on Final Bearing Thermal Conductance for Medium Sized Steel Bearings**

After operating at higher speeds, the thermal conductance decreases indicating that more oil has been displaced. We surmise that this oil has been driven away predominantly by higher centrifugal forces and possibly to a lesser extent by higher thermal gradients.

#### 4.4 Influence of Rest Time on Lubricant Redistribution

For the final series of tests, one medium bearing (Medium Bearing B) was allowed to rest to observe the recovery of oil that had been displaced in earlier tests. After the suite of testing shown above, the test fixture remained dormant for three months at room temperature. During this time, the bearings did not



spin. However, at three points in time during this interval, the static conductance was measured. Figure 4.4.1 indicates a slow growth in the static conductance. This growth is consistent with the recovery of oil at the ball/race menisci.

We find a slow equilibration process, resulting in a thermal conductance increase of about 45% after resting for four months. This corresponds to a lubricant area increase of over 160% in the ball-to-race pathway for a bearing at static rest. This suggests a possible strategy for remediation of mechanisms that are suffering from lubricant depletion.

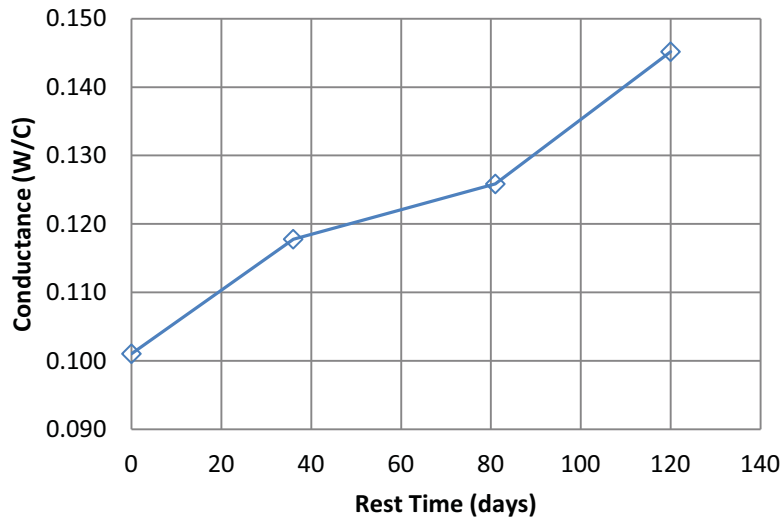


**Figure 4.4.1 Static Bearing Thermal Conductance vs. Rest Time For Steel Medium Bearing A**

## 5.0 Summary and Conclusions

The lifetime of precision bearings in space applications, where typically only a single charge of lubricant is expected to provide for the entire mission life, is closely tied to the lifetime of that lubricant. Mechanisms often function well until the lubricant is depleted, and then rapidly deteriorate. Some lubricant may be lost to thermo-chemical degradation during normal operation. However, in many situations much of it is simply displaced from the critical interfaces. Among this displaced lubricant some may be recovered by surface creep when the force balance is changed, while some is unrecoverable due to its having been thrown from the bearing or located with other impediments to migration. It would be helpful to understand the mechanisms of lubricant loss and recovery.

These experiments have shown that thermal conductance measurements are sensitive to lubricant quantity. For this reason, thermal conductance measurements can be used as a tool to make observations on lubricant behavior, such as run-in effects, and impact of rest times on lubricant redistribution. We show that conductance after run-in can be sensitively dependent on bearing geometry and operating speed, and less dependent on initial lubricant state, in the conditions studied here. These results imply that lubricant distribution is impacted by operational conditions, changing thermal conductance in logical ways. Some of the oil that is displaced by run-in can be recovered during rest, presumably by surface migration back to the contact, increasing conductance, but this process required months of time in the case studied here.

## References

1. Y. R. Takeuchi, S. E. Davis, M. A. Eby, J. K. Fuller, D. L. Taylor, M. J. Rosado, "Bearing Thermal Conductance Measurement Test Method and Experimental Design," Rolling Element Bearings: 9th Volume, ASTM STP 1542, Y. R. Takeuchi and W. F. Mandler, Eds., West Conshohocken, PA, 2012.
2. P. A. Bertrand, D. J. Carré, Reinhold Bauer, "Oil Exchange Between Ball Bearings and Cotton-Phenolic Bail-Bearing Retainers", Tribology Transactions, 1995; 38:342-352.  
DOI:10.1080/10402009508983414
3. Yovanovich, M. M., Analytical and Experimental Investigation on the Thermal Resistance of Angular Contact Instrument Bearings, Instrumentation Laboratory, E-2215, Massachusetts Institute of Technology, Cambridge, Massachusetts, Dec. 1967.

# **A Study on the Effects of Ball Defects on the Fatigue Life in Hybrid Bearings**

Ching-Yao (Tony) Tang\*, Chad E. Foerster\*, Michael J. O'Brien\*, Brian S. Hardy\*, Vinay K. Goyal\*, Benjamin A. Nelson\*, Ernest Y. Robinson\*\*, Peter C. Ward\* and Michael R. Hilton\*

## **Abstract**

Hybrid ball bearings using silicon nitride ceramic balls with steel rings are increasingly being used in space mechanism applications due to their high wear resistance and long rolling contact fatigue life. However, qualitative and quantitative reports of the effects of ball defects that cause early fatigue failure are rare. We report on our approach to study these effects. Our strategy includes characterization of defects encountered in use, generation of similar defects in a laboratory setting, execution of full-scale bearing tests to obtain lifetimes, post-test characterization, and related finite-element modeling to understand the stress concentration of these defects. We have confirmed that at least one type of defect of appropriate size can significantly reduce fatigue life. Our method can be used to evaluate other defects as they occur or are encountered.

## **Introduction**

Recently, silicon nitride ( $\text{Si}_3\text{N}_4$ ) ceramic balls have become an important component of advanced bearings used in a wide range of applications. The greatest commercial success for  $\text{Si}_3\text{N}_4$  balls have been in hybrid bearings, which combine the ceramic balls with steel races. Compared to the steel balls that they replace, the ceramic balls are harder and less dense and offer many other advantages, such as higher compressive strength, better corrosion resistance, and reduced susceptibility to lack of lubricant or lubricant breakdown. These benefits make the hybrid bearings ideal for severe high-speed applications.

However, during the development of hybrid bearings for space mechanism applications, we became aware of ball flaws, particularly scars, scratches, C-cracks, and traction cracks that could induce early fatigue failure [1]. Implementation of visual screening methods subsequently eliminated the most severe of these incidents. However, we realized that available data on flaw definition, size, stress concentrations, and life-limiting effects of ball defects in general were limited or included specific varieties of hybrid materials used under specific conditions [2-6].

In response, The Aerospace Corporation embarked on a long-term Independent Research and Development program to develop appropriate laboratory and analytical tools to improve the understanding and criteria for screening defects that induce infant mortality fatigue failure. To that end, full-scale bearing rolling contact fatigue testers (Figure 1) have been used to study the fatigue life of newer classes of properly-inspected, defect-free hybrid bearings.

In this paper, we present our approach to study the effects of ball defects on fatigue life. Our strategy included characterization of defects encountered in use, generation of similar defects in a laboratory setting, execution of full-scale bearing tests to obtain lifetimes, post-test characterization, and related finite-element modeling to understand the stress concentration of these defects. The rolling contact fatigue life was measured for as-manufactured bearings and for bearings with artificially-induced defects on the  $\text{Si}_3\text{N}_4$  balls.

---

\* Engineering and Technology Group, The Aerospace Corporation, El Segundo, CA

\*\* Civil and Commercial Operations, The Aerospace Corporation, El Segundo, CA



**Figure 1. Rolling contact fatigue testers at The Aerospace Corporation.**

### **Experimental Procedure**

#### Full-Scale Rolling Contact Fatigue (RCF) Testing

A test series was undertaken to demonstrate the rolling-element fatigue life of advanced material bearings consisting of  $\text{Si}_3\text{N}_4$  and CRU20 inner and outer races. These advanced material bearings are called “hybrid” bearings because they combine both steel (raceways) and ceramic (balls) components. The  $\text{Si}_3\text{N}_4$  balls were MgO doped, hot isostatically pressed, and lapped to AFBMA (Anti-Friction Bearing Manufacturers Association) Grade 3 surface finish and dimensional control. The balls have also undergone a thorough visual inspection with fluorescent penetrant dye under 40x magnification. CRU20 is the vacuum induction-melted version of REX20, which is an air-melted powder metallurgy version of M62 tool steel. The CRU20 steel was quenched and triple tempered to achieve a hardness of HRC 66-67 with a retained austenite of less than 5% by volume.

The bearings tested were of the 101H size and the 304H size, which are standard catalog bearings. The type 101H bearing has an outer diameter of 28.0 mm, an inner bore diameter of 12.0 mm, an external width of 8 mm, and a ball diameter of 4.763 mm (3/16 in). The type 304H bearing has an outer diameter of 52.0 mm, an inner bore diameter of 20.0 mm, an external width of 15.0 mm, and a ball diameter of 11.113 mm (7/16 in).

Fatigue testing was performed on full-scale bearings using a standard bearing tester (Figure 1). The bearings were thrust loaded to either 330 ksi (2.3 GPa) or 400 ksi (2.8 GPa) mean contact stress between the  $\text{Si}_3\text{N}_4$  balls and the inner race, rotated at 5000 rpm (524 rad/s), and lubricated with a continuous flow of MIL-L-7808 oil at 0.95 l/min/bearing. The oil was maintained at 60 °C (140 °F) and filtered to the 3- $\mu\text{m}$  level. These conditions resulted in  $\lambda = 1$ , where  $\lambda$  is the ratio of the calculated lubricant film thickness to the mean surface roughness of the races.

Test protocol was sudden-death statistics with four bearings using the least-of-four technique to obtain a Weibull distribution. The RCF testers use accelerometers to shut down the testers when a bearing failure raises the vibration level above a pre-determined limit. For tests involving the fatigue life of as-manufactured bearings, the first failure in each group of four bearings suspended the test of the other three bearings, resulting in an estimate of the life. For tests involving the fatigue life of bearings with artificially-induced scars (method of scar creation is explained in the next section), the first failed bearing of each group of four bearings was then replaced by a new bearing to obtain the second failure for the group. All  $\text{Si}_3\text{N}_4$  balls with scars were inspected before being re-used after the first bearing failure. This practice was employed mainly to conserve the number of bearings expended and to minimize the arduous process of preparing scars and documenting their progression in a new group of four bearings with scarred balls.

After each test, a scanning electron microscope (SEM) was used to conduct a fractographic examination of the failed bearing component (inner race, outer race, or ball) to identify the micro-structural feature

responsible for its failure. The SEM used a cold-field emission electron source with tungsten single-crystal tip. The sample chamber operated at a vacuum of  $4 \times 10^{-7}$  Torr. To prevent charging, if necessary, a low accelerating voltage of 1kV was used to image the bearing component, particularly the  $\text{Si}_3\text{N}_4$  ball. At such a low accelerating voltage, it was not necessary to coat the ball being examined with a conducting layer, such as pyrolytic carbon or gold.

#### Inducing Artificial Scars on $\text{Si}_3\text{N}_4$ Balls

A technique was created to generate scars with dimensions and morphology that are comparable to the distinctive features observed from contractors and in as-manufactured  $\text{Si}_3\text{N}_4$  balls (Figure 2). The technique involves controlled back-and-forth sliding contact of two  $\text{Si}_3\text{N}_4$  balls. This ball-on-ball apparatus is shown in Figure 3. The apparatus consists of a linear stage to enable precise relative translational motion between the balls, and two ball holders with conforming hemispherical sockets. The balls rest inside the sockets and their rotational movement is constrained by rubber-tip set screws.

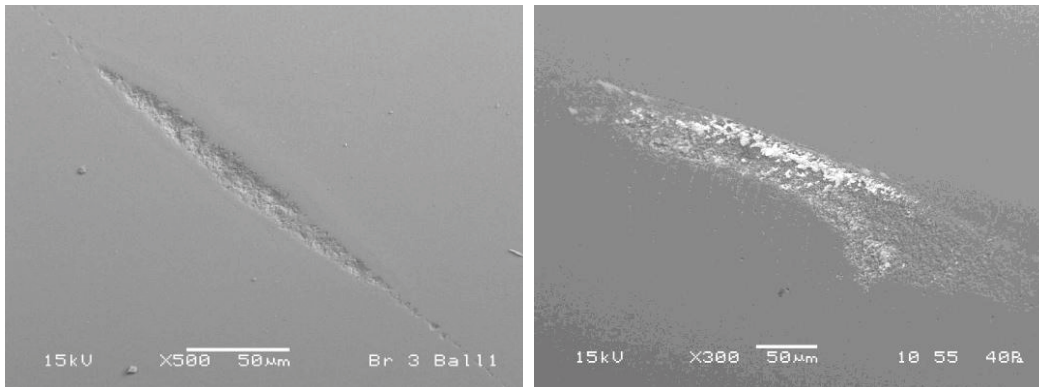


**Figure 2. A typical scratch found on  $\text{Si}_3\text{N}_4$  ball (left), and a distinctive feature observed by contractors (right).**

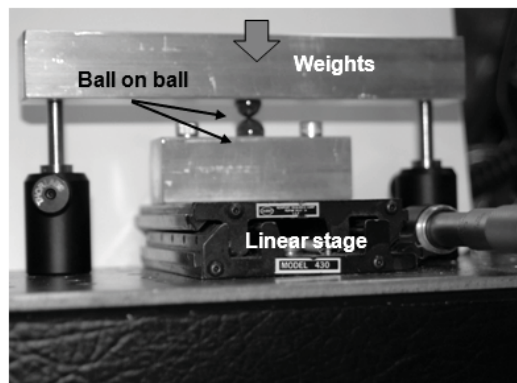


**Figure 3. Ball-on-ball test fixture used in generating artificial scars on  $\text{Si}_3\text{N}_4$  balls.**

Because it was necessary to generate scars of the same size and morphology on the  $\text{Si}_3\text{N}_4$  balls for each RCF test campaign, a technique was developed to improve the consistency and reproducibility of the scars. The  $\text{Si}_3\text{N}_4$  balls had to be cleaned by soaking in a warm bath of isopropyl alcohol for a few minutes and drying completely with lint-free cloth. Two balls were then placed in the ball-on-ball apparatus and locked in place. As a check for cleanliness, a clean swab with a spongy tip was moved across the surface of the ball. The surface of the ball was deemed clean when it felt like the ball was “grabbing” onto the moving swab. A final quick cleaning with a cotton/sponge swab removed any dust/lint that might have deposited in the contact zone. An aluminum block of a known mass was placed on top of the fixture to supply a load, which set the amount of material removed from the ball per pass and, ultimately, the final depth of the scar. Several back-and-forth passes were induced. The total travel per pass was 1.27 mm (0.050 in) for the “large” scars with a width of approximately 100  $\mu\text{m}$ , and 0.64 mm (0.025 in) for the

“small” scars with a width of approximately 40  $\mu\text{m}$ . The mean depth of the scars, for all scar sizes, was kept constant at approximately 2  $\mu\text{m}$ . Representative images of the “large” scar and the “small” scar are shown in Figure 4.

Two defects were induced on each  $\text{Si}_3\text{N}_4$  ball in a set of bearings. The scars on each ball were placed approximately 45 degrees apart and oriented roughly 45 degrees relative to each other. The number of balls in each bearing with scars varied depending on the purpose of the test. If the test was conducted to study the influence of scar size on bearing fatigue life, then all the balls in the bearings contained scars for a total of 64 scars (4 bearings per test, 8 balls per bearing, and 2 scars per ball). Statistical analysis showed that 2 scars on each 7/16-inch-diameter ball ensured (with 99.9% probability) that at least one of the 64 scars would be run over during the test, assuming that the balls maintained orientation through the entire duration of the test. On the other hand, if a test was conducted to study the influence of scar frequency on bearing fatigue life, then only two balls (ball 1 and ball 5) in each bearing contained scars for a total of 16 scars.

It was also necessary to track the balls inside each bearing in order to properly document the progression of the scars after testing. A small slit was gently scribed onto the phenolic cage (ball retainer) using a razor blade prior to inserting the balls. The slit provides a reference to identify the location of the first ball, e.g., ball 1 is the first ball to the right of the slit.

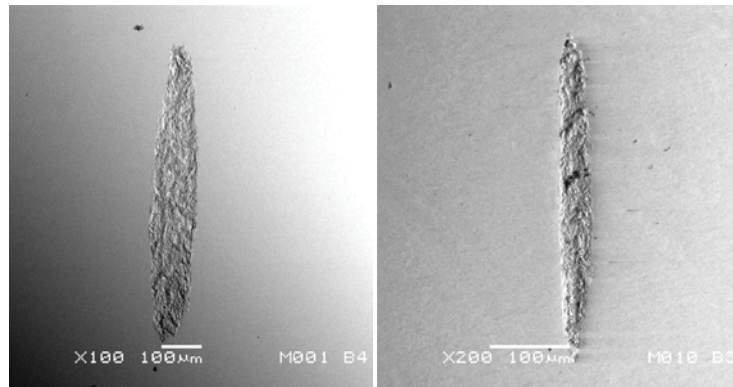


**Figure 4. Examples of artificially-generated scars: “large” scar (left) and “small” scar (right).**

### **Finite-Element Modeling**

#### Development of Finite-Element Models for Parametric Studies

Three-dimensional finite-element models (FEMs) of  $\text{Si}_3\text{N}_4$  balls contacting steel raceways were developed and compared against the analytical Hertzian contact stress solution. The FEM results for the elliptical contact patch size and parabolic contact stress distribution on the surface of the ball within the contact zone matched the Hertzian solution. Similar partial validations were completed for ball bearings contacting a flat surface. In addition, a subroutine was written to simulate the normal and traction loads generated from a ball bearing contacting either a curved or flat surface. This subroutine allowed the non-linear contact conditions present in the original FEMs to be replaced, significantly reducing the solve time for the models. These prior FEMs were leveraged and improved upon in preparation for the numerical FEM validation (Figure 5).

The high fidelity models included elements in the grain-size level (microns). These models were enhanced to provide more flexibility for future parametric studies. The FEMs were split into regions of varying mesh density based on the required stress resolution. Therefore, a large portion of the quarter symmetry model was changed to quadratic tetrahedral elements that could rapidly reduce in size in the contact region. Constraint equations were developed using the “tie” command in ABAQUS to enforce surface to surface continuity and facilitate coarse-to-fine mesh transitions. This strategy allowed for multiple model variations with different element sizes in the contact region, as shown in Figure 6.



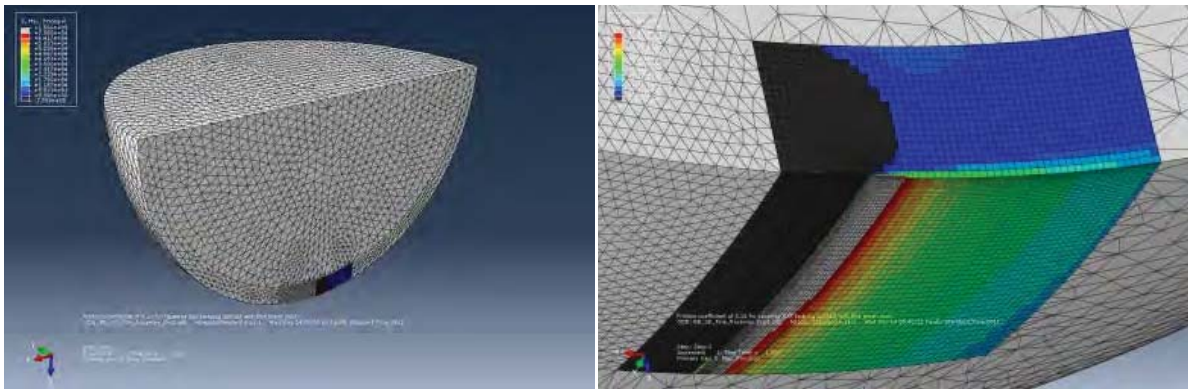


**Figure 5. Micron element size FEM (left) and whole model (right) region of interest showing the high tensile stresses created by the traction load.**

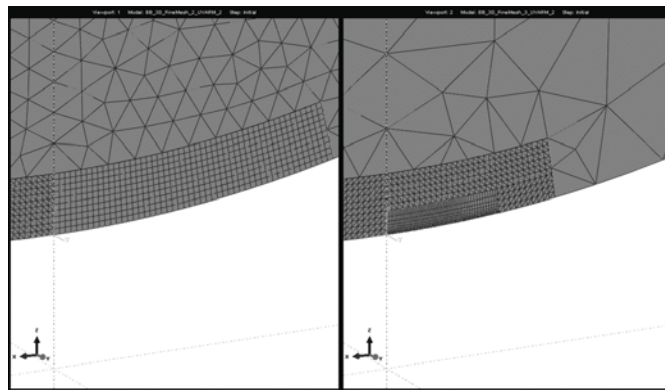


**Figure 6. Close up views of two parametric models showing the tie command regions with one significant mesh size transition (left) and two significant mesh size transitions (right).**

Validating Finite-Element Models with Three-Dimensional Explicit Equations for Sliding Spherical Contact

Additional confidence in the three dimensional stress results from the FEMs was required to predict the stress distribution and propensity for crack propagation due to scars and cracks on a  $\text{Si}_3\text{N}_4$  ball. There are numerous variables that can influence the validity of a FEM solution. Therefore, the three-dimensional stress field of the finite-element analysis was compared to an explicit closed-form analytical solution. After conducting a literature search, an appropriate set of equations was identified for sliding spherical contact [7]. This analytical solution could determine the interior stresses as well as the surface stresses of the ball due to sliding contact, differentiating it from the Hertzian solution used in previous FEM validation efforts. Validating the FEM stress results from the ball's interior was integral to establishing realistic stress fields for common ball defects. For visualization purposes, the analytical solutions were programmed into a subroutine that was executed by the finite-element analysis program. Stress results from the analytical solution were calculated at each integration point in the FEMs and saved to the output database. This procedure enabled side-by-side comparisons between the analytical and the numerical results.

Normal and shear stress results from both the explicit solutions and FEMs showed good agreement. The overall character of each stress measure from both the analytical and numerical results matched, while the absolute maximum and minimum stresses differed. The FEM results consistently presented higher maximum stresses and lower minimum stresses for each stress measure. Stress results in compressive regions were within five percent of each other, while differences in the tensile regions varied more.

Effect of Scars on the Life of a  $\text{Si}_3\text{N}_4$  Ball

Modeling efforts supported rolling contact fatigue testing to determine the effect of scars on hybrid ball bearing life. Scars were modeled in the FEMs by deleting elements in a manner to mimic the geometry of

a typical lab generated scar. The scar was placed in the high tensile region of the FEM caused by the traction load because that was the most probable failure initiation region. A raceway contact simulation was run and the FEM results demonstrated little change in the  $\text{Si}_3\text{N}_4$  ball's stress field around the contact region due to the presence of the scar (Figure 7). Therefore, a scar was deemed benign in terms of the effect on the life of the  $\text{Si}_3\text{N}_4$  ball.

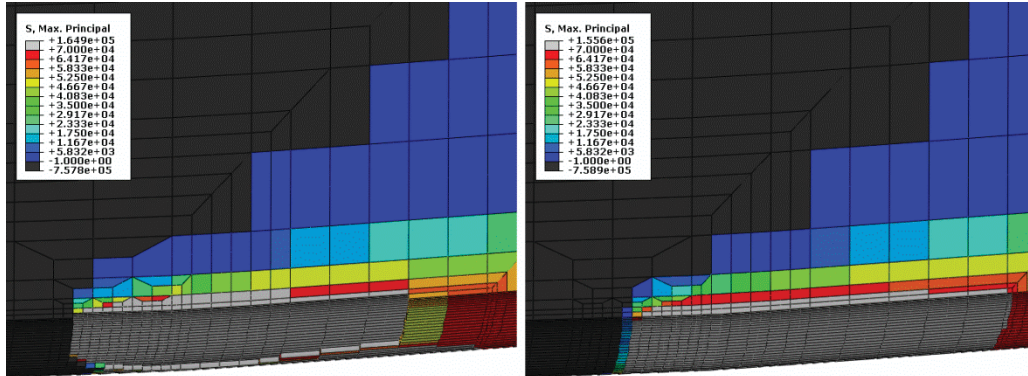


Figure 7. Maximum principal stress of contact with a scar (left) and without a scar (right).

However, during experimental testing, early failures in the hybrid ball bearings with scars indicated the bearing was affected by the presence of scars. Spalls prematurely developed in the steel raceways. When the hybrid bearings were disassembled, the scars on the  $\text{Si}_3\text{N}_4$  balls showed signs of wear but did not demonstrate any catastrophic growth.

#### Effect of $\text{Si}_3\text{N}_4$ Ball Scars on the Steel Raceway

A pristine contact condition produced high von Mises stresses in the steel raceway directly under the contact patch (Figure 8). This high stress region did not extend to the surface of the raceway. The ball scars changed the shape of the stress field, shifting the high von Mises stress region closer to the surface while creating a low stress region directly under the scar. In addition, at the scar edge a local stress concentration appeared in the steel raceway and connected with the high stress region.

As future work, elastic-plastic analysis will be used to determine the fatigue life of the raceway based on the abnormal cyclic loading due to the ball scars. An explicit integration two-dimensional FEM is being developed to resolve the stress field in the  $\text{Si}_3\text{N}_4$  ball and raceway when a ball scar is located within the contact patch.

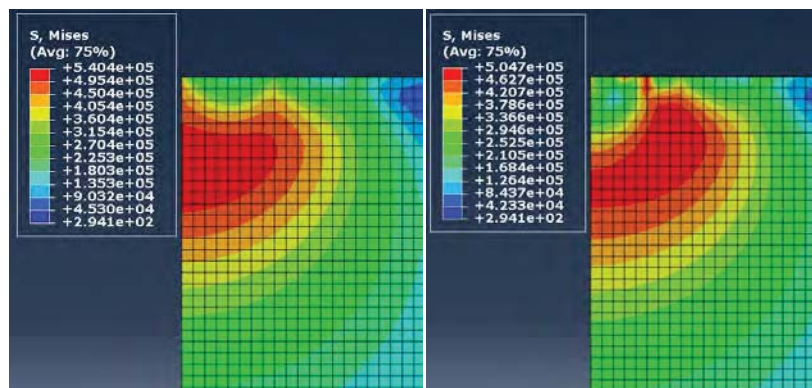


Figure 8. Stress contours in the steel from pristine ball contact (left) and contact with a 100- $\mu\text{m}$  wide ball scar (right).

## Database of Full-Scale RCF Tests

### Baseline (As-Manufactured) Hybrid Bearings

#### *101H Bearings*

A summary of the test results for the 101H bearings is presented in Table 1. All six tests have been completed. All tests were conducted at 400 ksi (2.8 GPa) mean contact stress. Out of the six tests, four tests ended due to fatigue failures and two tests reached 3000 hours without failing. For the four tests that resulted in failures, the spall(s) responsible for the failure occurred either in the ball, the inner (IR), or the outer (OR) race. One of the tests that reached 3000 hours was allowed to run until an outer race spall formed, which gave a total of five fatigue failures from the original six tests. The bearing that had OR dents for Test #4 was replaced with a new bearing, and the test (Test #7) was restarted and run until a ball spall eventually suspended the test.

**Table 1. Test results of 101H bearings at 400 ksi (2.8 GPa) mean stress**

Test #	Test Time (hours)	Failure Type
1	383	IR spall
2	3054	dents (run-on)
3	38	ball spall & IR spall
4	359	OR dents, replaced (restarted as Test 7)
5	1728	ball spall
6	3353	OR spall
7	1121	ball spall

#### *304H Bearings*

A summary of the test results for the 304H bearings is presented in Table 2. These tests were conducted at 400 ksi (2.8 GPa) mean contact stress. Out of the seven tests, six tests have been completed. The six completed tests all developed fatigue failures, but two of the tests surpassed 4000 hours. The failures were a combination of ball and raceway spalls. One test is still in progress during the preparation of this manuscript with a total run-time surpassing 8000 hours.

**Table 2. Test results of 304H bearings at 400 ksi (2.8 GPa) mean stress**

Test #	Test Time (hours)	Failure Type
1	2373	ball spall
2	1876	IR spall
3	4821	IR spall & OR spall
4	515	IR spall
5	4384	ball spall & IR spall
6	64	OR spall
7	8000+	still in progress

### Hybrid Bearings with Artificially-Scarred Si<sub>3</sub>N<sub>4</sub> Balls

A summary of the test results for the 304H bearings with scarred Si<sub>3</sub>N<sub>4</sub> balls is presented in Table 3. All tests were conducted at 330 ksi (2.3 GPa) mean contact stress. Fractographic images of failure features are presented in the next section.

**Table 3. Tests results of 304H bearings with scarred Si<sub>3</sub>N<sub>4</sub> balls at 330 ksi (2.3 GPa) mean stress**

Test #	Scar Size (μm)	Scar Frequency	Test Time (hours)	Failure Type
1	100	2 per ball	81	IR spall
2	100	2 per ball	87	IR spall
3	100	2 per ball	27	IR spall
4	100	2 per ball	42	IR spall
<b>5</b>	<b>40</b>	<b>2 per ball</b>	<b>4500+</b>	<b>still in progress</b>
6	100	2 per ball on balls 1 & 5	120	IR spall
7	100	2 per ball on balls 1 & 5	668	IR spall

*Influence of Scar Size on Fatigue Life*

Four tests have been completed where all the balls in each bearing contained two “large”, 100-μm wide scars. All four tests resulted in infant mortality of the bearings, with lives of less than 100 hours, due to the formation of an inner race spall. One test (Test #5) is still in progress at time of manuscript preparation, which involves bearings with balls that contain two “small”, 40-μm wide scars. The influence of the scar size on fatigue life is evident, as demonstrated by the drastic improvement in fatigue life (of a couple orders of magnitude) for bearings with “small” scars compared to bearings with “large” scars.

*Influence of Scar Frequency on Fatigue Life*

The influence of scar frequency on bearing fatigue life was also investigated. Two tests were completed where only two of the balls (ball 1 and ball 5) in each bearing contained two “large”, 100-μm wide scars. Preliminary results show that the fatigue life improved marginally with a reduction in the total number of scars in each bearing, but the life was lower than scar-free bearings. Based on the limited data available, the size of the scars seems to be driving force that dictates fatigue life.

**Post-Test Characterization of Bearings with Scarred Si<sub>3</sub>N<sub>4</sub> Balls**

The recent focus of our research has been on investigating the influence of surface defects, specifically scars, in Si<sub>3</sub>N<sub>4</sub> balls on fatigue life. Scars are shallow (0.5-5 microns in depth), elliptical surface defects that can be induced during the manufacturing process or from user mishandling and unintentional scratching. The scars were artificially duplicated, and bearings with these ball scars have undergone a series of fatigue testing to evaluate their effect on fatigue life. The fatigue testing showed that the bearings with ball scars actually failed by developing raceway spalls, which are presented and discussed for the tests listed in Table 3, as are representative images showing the progression of the scars on the Si<sub>3</sub>N<sub>4</sub> balls.

Raceway Fatigue Spalls

A set of four bearings were used in the first-ever RCF test with scarred balls. The total test time before failure was 81 hours. The first failure was an inner race spall of one bearing. This rather early failure was followed up by more testing to increase understanding. The same set of hybrid bearings that produced the failure was restarted. The Si<sub>3</sub>N<sub>4</sub> balls were reused and a new set of inner and outer races were replaced in the failed bearing. The goal was to observe further progression of the ball scars. The restarted test was continued under the same contact stress. The additional test time before failure the next failure was 6 hours. Combined with the first test, the total run time was 87 hours for all the Si<sub>3</sub>N<sub>4</sub> balls and the three original bearings. Failure for the restarted test occurred because of an inner race spall of one of the original bearings, which was similar to the spall that was responsible for the first failure.

To augment the RCF tests of the bearings with scars, a new set of bearings from a different manufacturer, but with the same type and source of Si<sub>3</sub>N<sub>4</sub> balls, was tested with identical ball defects. The goal was to determine whether the failures were caused by the race manufacturing processes of a particular manufacturer.



The first failure for the bearings from the second manufacturer was also an inner race spall of one bearing. The total test time before failure was 27 hours. Again, the root cause is uncertain, but due to the short fatigue life of the bearings and the similarity in spall characteristics, the failure most likely initiated in the same fashion for the two manufacturers' bearings.

The test that produced the failure was restarted. The  $\text{Si}_3\text{N}_4$  balls were reused and a new pair of inner and outer races was replaced in the failed bearing. The goal again was to observe further progression of the ball scars. The additional test time before the next failure was 15 hours. Combined with the first test, the total test time was 42 hours for all the  $\text{Si}_3\text{N}_4$  balls and the original bearings. Failure for the restarted test was an inner race spall of one of the original bearings. The root cause of the failure of the restarted and initial tests is likely the same because both inner race spalls looked very similar.

All RCF tests resulted in inner race spalls with a similar characteristic "surface initiation site" pattern (Figure 9). The spalls were most likely caused by the stress riser from rolling over the scar features on the  $\text{Si}_3\text{N}_4$  balls.

The reduction in the number of scars by 75% (64 scars to 16 scars) delayed, but did not eliminate, the onset of damage leading to inner race spall. Figure 10 shows the SEM images of the resulting damage that occurred after 120 hours and 668 hours of operation. The failure after 120 hours is perhaps the earliest initiation of a spall that has ever been captured before any significant material had been expelled. Our experience in setting the vibration limit of the RCF testers enabled us to capture the initiation stage. The feature that caused the second failure after 668 hours resembles the spalls previously discussed. Scanning electron microscopy coupled with our experience in setting the vibration limit of the RCF testers enabled us to capture the progression of damage leading to inner race spalls in a RCF test.

The root cause of the main spall is still unclear, but a few possibilities based on post-mortem characterization are: 1) debris shedding from  $\text{Si}_3\text{N}_4$  ball, 2) subsurface void in inner race steel because the spall is uncharacteristically deep for typical debris-induced damage, and 3) scar-induced localized stress riser on surface of steel races. The first scenario is unlikely because the RCF testing of "small" scars (Test #5 in Table 3), which is still in progress with over 4500 hours, would also have shed debris. Furthermore, the lubricant oil in the testers is constantly filtered. The latter scenario is the most likely explanation because of the observation of scar witness marks in the raceway and insights from finite-element modeling showing high subsurface stress of the raceway near the edge of the scars.

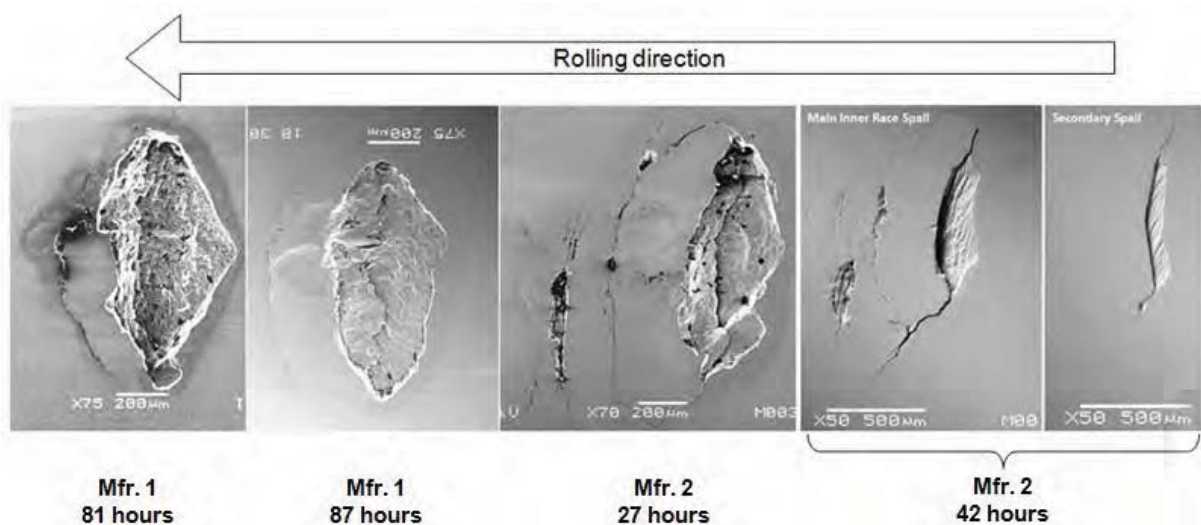
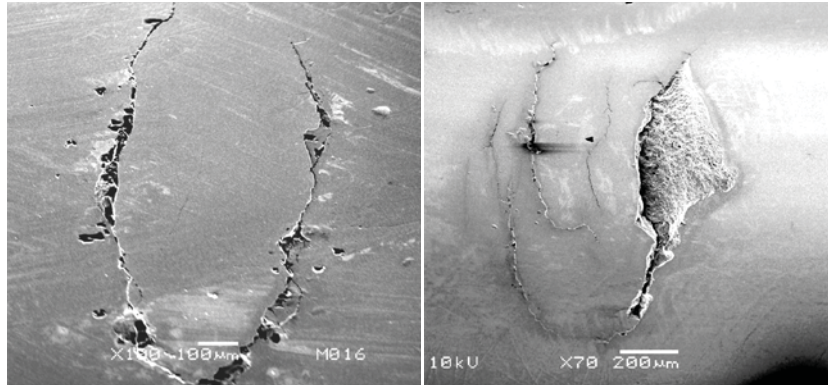


Figure 9. Inner race spalls of hybrid bearings with "large" scars on every ball.



**Figure 10. Inner race spalls of hybrid bearings with “large” scars on only 2 balls in each bearing. First failure occurred after 120 hours (left), and second failure occurred after 668 hours (right).**

Progression of Scars on Si<sub>3</sub>N<sub>4</sub> Balls

At the conclusion of each test, SEM was used to document the progression of the scars on the Si<sub>3</sub>N<sub>4</sub> balls, and to assess the resulting damage to the bearings and identify the potential cause of the failure.

Figure 11 shows the typical progression of a scar after testing, which provides two significant findings. First, all the scars on the Si<sub>3</sub>N<sub>4</sub> balls (64 scars in 4 bearings) had been run over, as evidenced by the apparent halo around and widening of each scar. This key finding suggests that, contrary to initial assumption, balls with scars do not track or maintain their orientation inside a bearing. This finding is further supported by the lack of a wear band on each ball, regardless of the number of hours in operation, which is typically observed in unscarred balls after RCF testing. The reason for the lack of ball tracking could be due to the ball being pivoted each time the scar enters the contact patch. Another reason could simply be because at such a high rate of rotation, any minute change in an otherwise pristine surface of the ball creates a misalignment between the ball’s center of mass and its axis of rotation, leading to rotational imbalance.

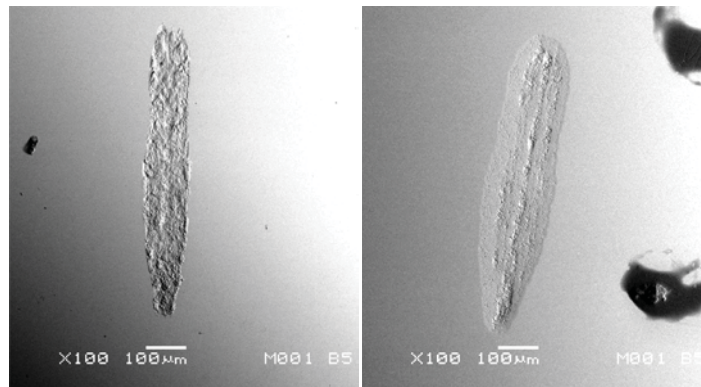


**Figure 11. Representative artificially-generated scar: before (left) and after (right) RCF testing. This particular test lasted 28 hours at 5000 rpm with a mean contact stress of 330 ksi (2.3 GPa).**

The second finding is the burnishing of the scars during testing. From Figure 11, it is apparent that the peaks within the scars have either been flattened or completely removed, leaving behind only the valleys and remnants after material removal.



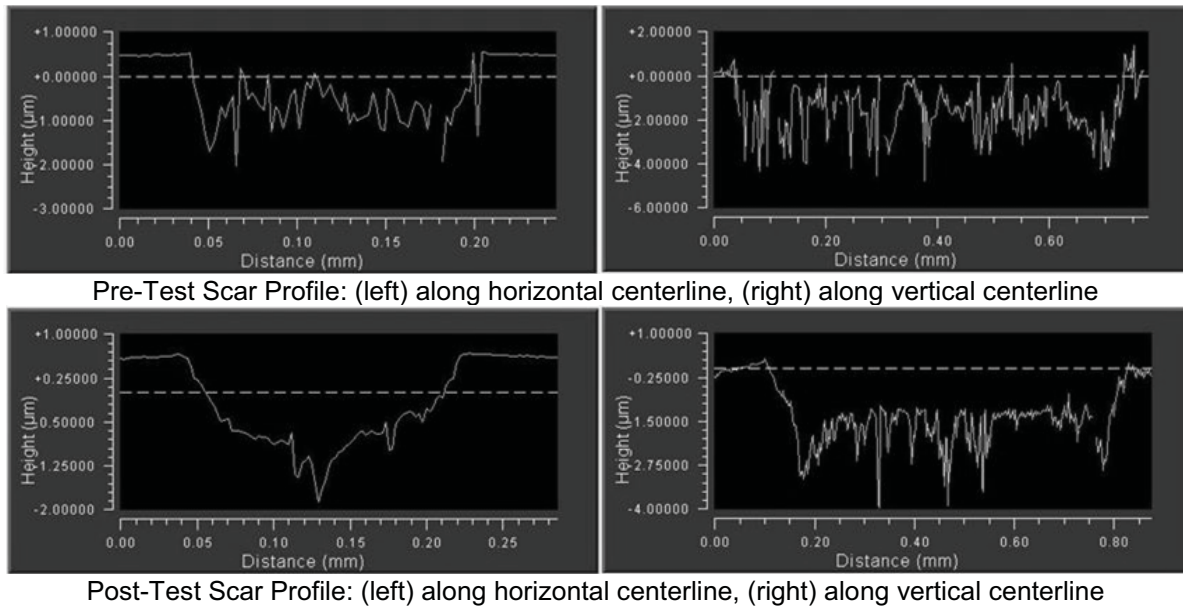


**Figure 12. Optical surface profilometry trace of a scar before (top) and after (bottom) RCF testing**

Further investigation of the apparent burnishing of the scars was conducted using optical (white-light) surface profilometry before and after testing (Figure 12), which provides a quantitative comparison of the roughness and morphology. Traces were taken near the major and minor axes of the scar ellipse, and the corresponding profiles are shown in the plots in the left column and right column, respectively. As the roughness decreased, the scar effectively became more benign, which could suggest that most of the raceway damage occurred very early in testing.

### Data Analyses and Statistical Methods

#### Data Processing and Distribution Models

The purpose of data analysis is to estimate the distribution of strength, the distribution of fatigue life, and to, if possible, combine the two distributions to create a reliability forecast chart that accounts for the effects of load and service life. The cumulative plotting position used here is the median rank estimate [8] given by:

$$F = (j - 0.3)/(N + 0.4) = 1 - S, \quad (1)$$

where  $F$  is the cumulative failure probability and is the complement of  $S = 1 - F$ ,  $j$  is the rank number, and  $N$  is the sample size.

The model for rolling contact fatigue life that accounts for both load level and fatigue life is the bivariate model [9] given by:

$$S = (S_r)^{**}(R/R_r)^m (t/t_r)^b, \quad (2)$$

where  $S$  is, again, the cumulative survival probability,  $R$  is the applied ball contact stress scaled by  $R_r$ , the reference strength,  $t$  is the observed fatigue life scaled by  $t_r$ , the reference life (such as the median life), and  $m$  and  $b$  are the Weibull modulus for strength and life distributions, respectively. Subscript  $r$  denotes reference scaling values for cumulative survival, strength and fatigue life, typically taken from the observed data and representing median reference values wherever possible. Solving for  $R$  gives:

$$\text{Log}(R) = \text{Log}(R_r) - b/m \text{Log}(t/t_r) + (1/m)[\text{Log}([1/S]/(1/S_r))]. \quad (3)$$

Equation (3) produces a family of straight lines as shown in Figure 15A, constant reliability contours, of slope  $-b/m$  on  $\text{Log}(R)$  versus  $\text{Log}(t)$  coordinates, provided that the distributions of strength and fatigue life are each consistent with Weibull distributions having time-invariant shape factor. However, this is not the case for the RCF data examined here, and some modification of the model is explored.

Following the line in [9], this equation is modified to account for augmented degradation to the bearings:

$$R = 1 - f[1 - \exp(-t/t_c)] \cdot R_r(t_r/t)^{b/m} [\text{Ln}(1/S/\text{Ln}(2))]^{(1/m)}, \quad (4)$$

where the reference survival probability  $S_r = 0.5$  and parameters  $f$  and  $t_c$  represent the fraction of strength being reduced by a first order corrosion or degradation process with time constant  $t_c$ . This equation underlies the probability contours of Figure 15B, with parameters shown in the text box. This graph suggests that, within perhaps the decade of time beyond the observed data for the parameters chosen, that the life is predicted to drop.. Substantial amount of data, at low load levels and relatively long lives, are required to get an approximate value for the turn-down model parameters. We would also caution that though such degradation has been observed in glass composite materials [9], we are not aware of any reports of similar degradation in silicon nitride bearings in ambient or vacuum environments. That is, it is not clear if the turn-down is real or of practical significance.

#### Ball Strength Distribution

The strength distribution shape factor estimate,  $m$ , was obtained from experimental data using Aerospace-developed strength tester [10] of  $\text{Si}_3\text{N}_4$  balls. Although based on a partial sample of the first 17 out of 131 specimens, this  $m = 8$  is a very good data fit, especially since it conforms to the weakest data (Figure 13). The estimated median strength is 725 ksi (5.0 GPa).

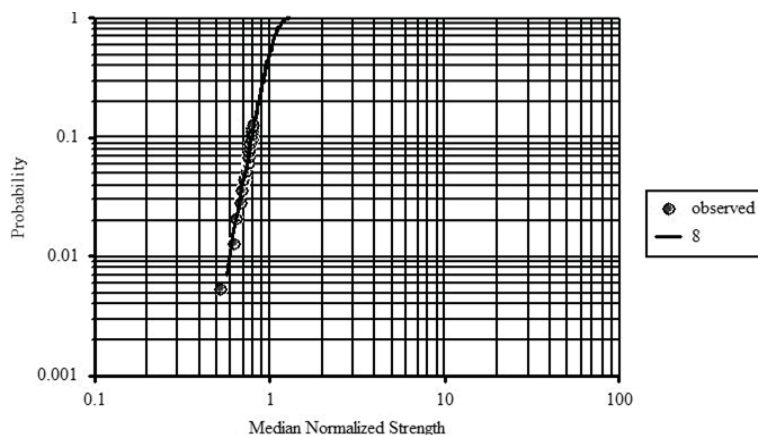


**Figure 13. Strength distribution of  $\text{Si}_3\text{N}_4$  balls**

#### Rolling Contact Fatigue Tests of As-Manufactured Hybrid Bearings

The individual data (first of four) for sizes 101 and 304 are collected and shown in Figure 14. The similarity of the distribution shapes allows these data to be pooled, forming a mixed population distribution. Unlike the expected inflection near the central values of life, these data show a monotonic increase in failure probability to the longest observed life. Fortunately the service life design is defined by the short observed lives, and, while the distribution at long life is of academic interest, it has little impact on the practical design operating life. The strength shape factor,  $m = 8$ , and life shape factor  $b = 0.55$  were combined to create a Reliability Forecast Chart shown in Figure 15, that gives a projected view for the combination of load, life, and reliability at very long service lives.

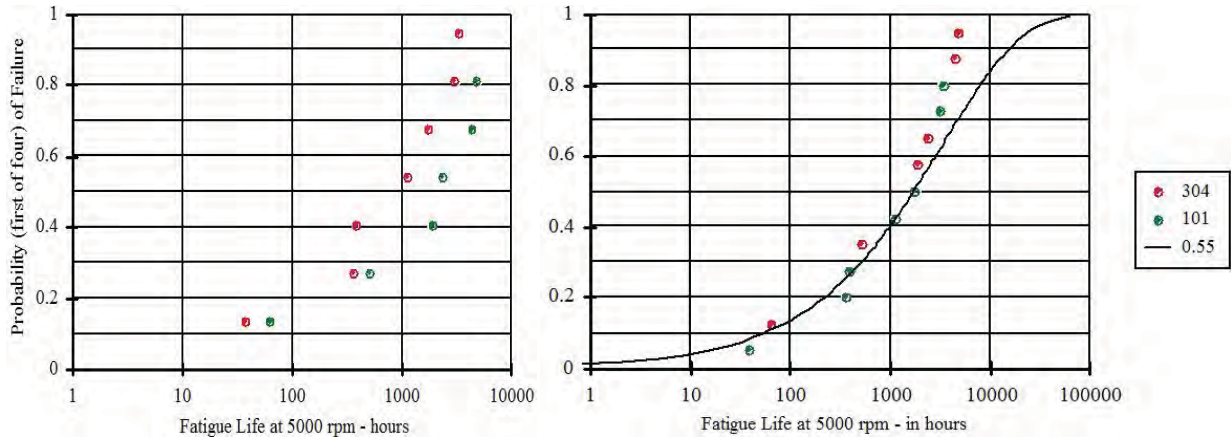


**Figure 14. Individual probability distributions (left) and combined RCF lifetime distribution (right) of as-manufactured hybrid bearings for 101H and 304H sizes**

Rolling Contact Fatigue Tests of Hybrid Bearings with Scarred  $\text{Si}_3\text{N}_4$  Balls

Figure 16 shows the pronounced reduction of fatigue life and lowered life scatter. However, the monotonic increase of failure probability seen with the pristine bearings is not present with the damaged bearings. The median life of the scarred bearings was about 5% of the pristine bearing life, and there was no similarity observed in the distribution plots

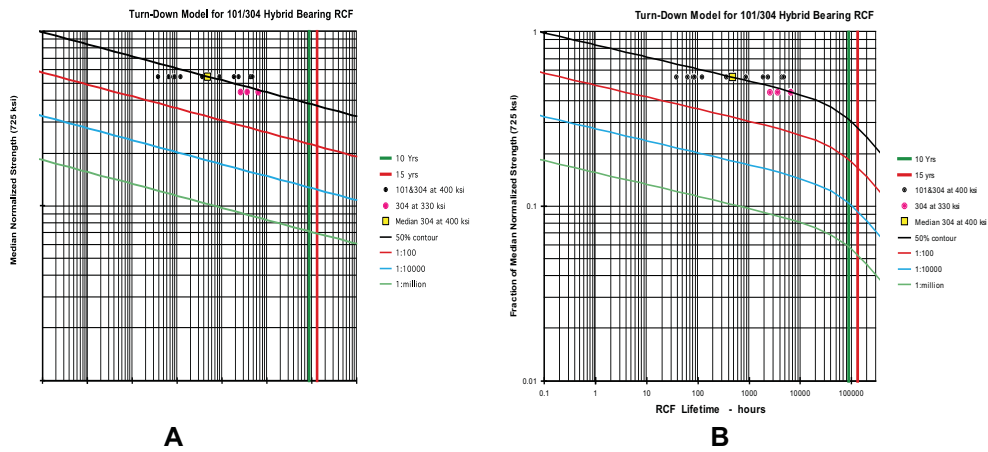


**Figure 15. Turn-down model for as-manufactured 101H and 304H bearings. A) No turn down, B) Notional turndown for one particular set of parameters shown here. More data would be needed to confirm or refute if a turn down effect is present in these materials.**

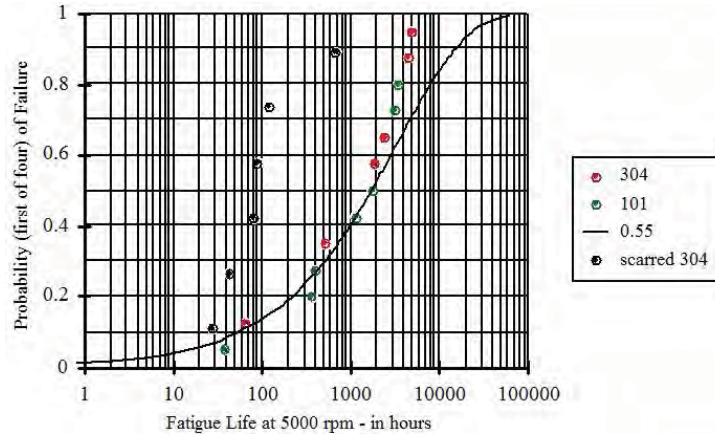


**Figure 16. Combined lifetime distribution of mixed as-manufactured 101H and 304H bearings and 304H bearings with scarred  $\text{Si}_3\text{N}_4$  balls.**

### Conclusions

Hybrid ball bearings using  $\text{Si}_3\text{N}_4$  balls with steel rings are increasingly being used in space mechanism applications due to their high wear resistance and long rolling contact fatigue life. However, qualitative and quantitative reports of the effects of ball defects that cause early fatigue failure are rare. We reported on our approach to study these effects. Our strategy included characterization of defects encountered in use, generation of similar defects in a laboratory setting, execution of full-scale bearing tests to obtain lifetimes, post-test characterization, and related finite-element modeling to understand the stress aspects of these defects. We have confirmed that at least one type of defect of appropriate size can significantly reduce fatigue life. Our method can be used to evaluate other defects as they occur or are encountered.

Based on recent RCF testing of hybrid bearings with scarred  $\text{Si}_3\text{N}_4$  balls, the size (width) of the scars dictates bearing fatigue life, whereas the frequency of scars has a much lesser influence on life. Scanning electron microscopy images from two tests captured the progression of damage leading to inner race spalls. Infant mortality was observed in all hybrid bearings with “large” (100- $\mu\text{m}$  wide) scars on the balls. Every one of those early failures was a result of inner race spall, and no damage growth was observed in the vicinity of the artificial defects on the  $\text{Si}_3\text{N}_4$  ball. Post-test microscopy of the scars revealed that the initially sharply-defined edges appear to be smoothed and burnished.

Finite-element modeling work focused on understanding the effects of  $\text{Si}_3\text{N}_4$  ball scars on the stress field in the steel raceway during rolling contact. The ball scars change the shape of the stress field, shifting the high von Mises stress region closer to the surface while creating a low stress region directly under the scar. This is a mechanism to create the observed raceway spalls. The modeling supports that the cause of the inner race spalls is the stress riser from rolling over the scar features on the  $\text{Si}_3\text{N}_4$  balls.

According to statistical data analysis, the RCF data of as-manufactured bearings for the 101H and 304H bearings exhibited similar lifetime distributions, which allowed pooling the data in a mixed population. The observed fatigue lifetime distributions of the as-manufactured hybrid bearings are highly scattered with a Weibull modulus fit (to the lower portion of the distribution) of  $b = 0.55$ , so the spread of life is over two orders of magnitude. Both data sets exhibited a progressive increase of failure probability with increasing life. This implies a turn-down of probability contours at long life, though experimental data is needed for validation, and the parameters chosen are speculative as shown here. A mathematical model that can forecast such turn-down was described.

The life degradation associated with the artificially damaged bearings amounted to a 95% reduction of the median life compared with the baseline (as-manufactured) counterparts. Further testing to assess

damage effects in hybrid bearings is planned. To date, no infant mortality of the hybrid bearings has been observed in tests with “short” (40- $\mu\text{m}$  wide) scars on the  $\text{Si}_3\text{N}_4$  balls.

Some test time savings may result from testing only slightly more than half the test specimens, thus avoiding the longest lived members of the populations. The Reliability Forecast Chart presented in this paper could be a useful tool in estimating load conditions of high projected reliability at long lives.

### Acknowledgements

This work was funded by the Independent Research and Development program of The Aerospace Corporation supported by USAF Space and Missile Systems Center (contract no. FA8802-09-C-0001).

### References

- [1] Park, W., et al., “Rolling Contact Fatigue and Load Capacity Tests of M62 Bearing Steel”, 32<sup>nd</sup> Aerospace Mechanisms Conference, NASA/CP-1998-207191, pp. 237-251, NASA Kennedy Space Center, FL, 13-15 May 1998.
- [2] Popp, M. and Sternagel, R., “Hybrid Ceramic and All Ceramic Anti-Friction Bearings”, Proceedings of the 8<sup>th</sup> European Space Mechanisms and Tribology Symposium, ESA SP-438, Sept., 1999.
- [3] Hutchings, I. M., Tribology: Friction and Wear of Engineering Materials, Arnold, London, 1992.
- [4] Gibson, H., Moore, C., and Thom, R., “Marshall Space Flight Center High Speed Turbopump Bearing Test Rig”, Proceedings from the 34<sup>th</sup> Aerospace Mechanisms Symposium, 10 May, 2000.
- [5] Kang, J. and Hadfield, M., “Comparison of 4-ball and 5-ball Rolling Contact Fatigue Tests on Lubricated  $\text{Si}_3\text{N}_4$ /Steel Contacts”, *Materials and Design*, Vol. 24, No. 8, pp. 595-604, 2003.
- [6] Warrior, S. Jarmon, D.C., and Chin, H.A., “Finite Element Analysis of the Critical Flaw Size in Hybrid Silicon Nitride Ball Bearing”, and references therein, Proc. ASME Turboexpo 2000, Paper 2000-GT-65, Munich Germany, 8-11 May 2000.
- [7] Hamilton, G. M., “Explicit equations for the stresses beneath sliding spherical contact”, Proc. Instn. Mech. Engrs, 197C, 53-59, 1983.
- [8] Johnson, L. G., *The Median Ranks of Sample Values in Engineering Experiments*, McGraw-Hill, New York, 1973.
- [9] Robinson, E. Y., “A Universal Bivariate Weibull Model for Static and Dynamic Fatigue Reliability Forecasting,” 2011 ASTM International Symposium on Rolling Element Bearings, STP 1542, pp. 26-46, Anaheim, CA, April 13–15, 2011.
- [10] O’Brien, M. J., de la Cruz, A. R., and Nguyen, E. A., “A Novel Proof Test for Silicon Nitride Balls”, *Journal of the American Ceramic Society*, Vol. 94, Issue 2, pp. 597-604, February 2011.





# Design and Test of a Deployable Radiation Cover for the REgolith X-ray Imaging Spectrometer

David B. Carte<sup>\*</sup>, Niraj K. Inamdar<sup>\*\*</sup>, Michael P. Jones<sup>\*</sup> and Rebecca A. Masterson<sup>\*</sup>

## Abstract

The REgolith X-ray Imaging Spectrometer (REXIS) instrument contains a one-time deployable radiation cover that is opened using a shape memory alloy actuator (a “Frangibolt”) from TiNi Aerospace and two torsion springs. The door will be held closed by the bolt for several years in cold storage during travel to the target asteroid, Bennu, and it is imperative to gain confidence that the door will open at predicted operational temperatures. This paper briefly covers the main design features of the radiation cover and measures taken to mitigate risks to cover deployment. As the chosen FD04 model Frangibolt actuator has minimal flight heritage, the main focus of this paper is the testing, results and conclusions with the FD04 while discussing key lessons learned with respect to the use of the FD04 actuator in this application.

## Introduction

REXIS is a student collaboration experiment aboard the Origins, Spectral Interpretation, Resource Identification, and Security Regolith Explorer (OSIRIS-REx) spacecraft. OSIRIS-REx is a NASA New Frontiers mission planned for launch in 2016 that will travel to near-Earth asteroid 101955 Bennu and return at least 60 g (0.013 lbm) of asteroid regolith to Earth in 2023. REXIS uses coded-aperture imaging X-ray spectroscopy to image Bennu in the soft X-ray range of 0.5-7.5 keV and develop an elemental abundance map of the asteroid [1]. REXIS is engineered primarily by students, with supervision and support from professional scientists and engineers at the MIT Space Systems Laboratory; MIT Department of Earth, Atmospheric, and Planetary Sciences; Harvard-Smithsonian Center for Astrophysics; the MIT Kavli Institute; MIT Lincoln Laboratories; and Aurora Flight Sciences.

REXIS requires a one-time deployable cover door to protect its charge-coupled device (CCD) imagers from radiation damage during the three-year cruise to Bennu. The door is positioned on top of the instrument and is closed from launch in 2016 until asteroid observation in 2019, at which point the door will be opened, providing the CCDs a view of the asteroid. Without this cover, space radiation will cause displacement damage in the detectors and degrade spectral resolution [2]. Use of a radiation cover will limit damage so that the REXIS detectors can meet measurement objectives in its primary mission phase.

In this paper, we focus on the mechanical design of the radiation cover and the opening mechanism. The 4-mm (0.2-in) thick aluminum (Al) cover rotates about a custom spring hinge and is opened upon arrival at Bennu through the use of an FD04 Frangibolt from TiNi Aerospace, which is part of a newly- introduced Mini Frangibolt family. This family of Frangibolts incorporates cylinders made from Single Crystal Shape Memory Alloy that offer 3 times the stroke performance of equivalent products from the Standard Frangibolt family (FCx). Other advantages of this product are its low power requirement, small form factor, and low cost. However, the Mini Frangibolt product family has minimal flight heritage. Successful actuation of the FD04 Frangibolt is highly sensitive to the thermal and structural design of the bolted joint. Given the minimal flight heritage for FD04, prototype testing of the REXIS radiation cover has focused on establishing confidence in the FD04 Frangibolt mechanism as a reliable actuator for this application and creating a robust design for the radiation cover. This paper presents the overall radiation cover design, provides an overview of the testing performed, and discusses the lessons learned.

---

<sup>\*</sup> Space Systems Laboratory, Massachusetts Institute of Technology, Cambridge, MA

<sup>\*\*</sup> Department of Mechanical Engineering, Massachusetts Institute of Technology, Cambridge, MA

## Design Overview

Requirements on the REXIS radiation cover flow from instrument measurement objectives as well as interface and environmental requirements. In order to meet REXIS science goals, the cover must provide a sufficient level of radiation protection for the CCDs. However, as a student instrument, the mass and power available to the REXIS instrument is limited. The “not to exceed” values for REXIS are 6.5 kg (14 lbm) mass and 15 W average power. Therefore a low mass and low power actuation device is desired. During the cruise to the asteroid, REXIS will experience very cold temperatures. All components of the mechanism must be kept warm enough to ensure successful cover opening. Lastly, as an asteroid-sample return mission, OSIRIS-Rex has strict contamination requirements. These constraints flow to REXIS, and it is imperative that the opening of the door does not release particulates or molecular contaminants that could endanger the integrity of the asteroid sample.

The REXIS radiation cover is located on top of the instrument and covers the coded-aperture mask so there is no direct line of sight for radiation to impinge on the CCDs. The cover design is shown in Figure 1a in the closed configuration. The 4-mm-thick (0.2-in) aluminum radiation cover rotates about a custom spring hinge with a 3/16-in (4.76-mm) diameter stainless steel shaft. The mechanism rotates about Vespel SP-3 bushings. Additional bushings made of Rulon J are also placed in between the torsion springs and the shaft to reduce friction and prevent cold welding of the springs to the shaft. The door is held in the stowed position by an FD04 Frangibolt actuator and custom notched titanium (Ti) bolt. The FD04 was largely chosen due to its large stroke performance over equivalent products in the Standard Frangibolt family (FCx), along with its low power requirements, low mass, and low cost.

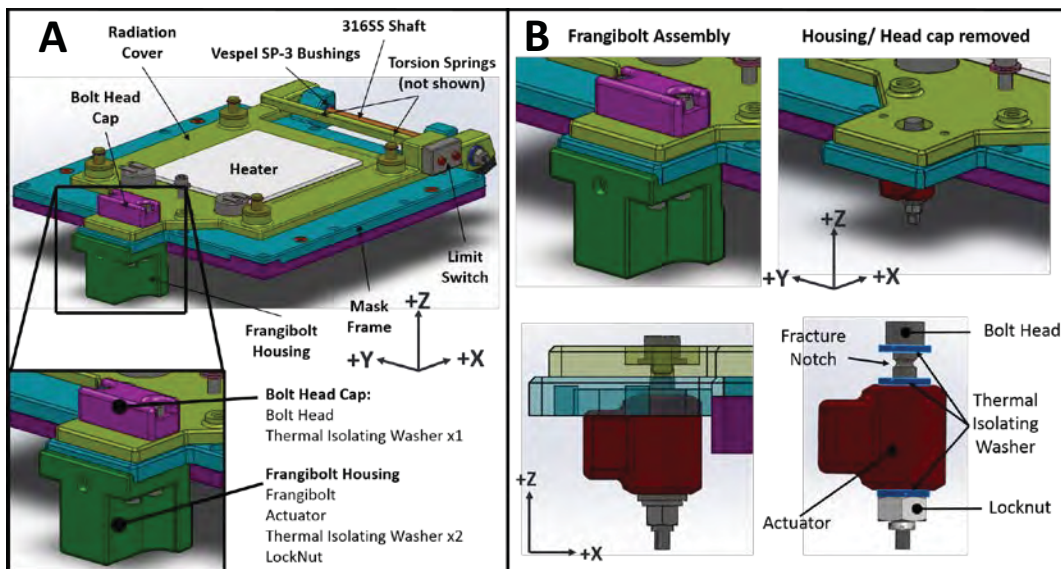


**Figure 1. (a) The REXIS radiation cover in closed configuration (b) detail of the Frangibolt assembly**

The FD04 is part of the recently introduced Mini Frangibolt product family and has flight heritage on the DICE CubeSat [4]. It consists of a Copper-Aluminum-Nickel shape memory alloy cylinder and provides ~550 lb (2450 N) of force to fracture the fastener in tension during actuation. This model is the smallest in size and requires the least power of the TiNi Frangibolts. It has a compressed length of 0.500 in (12.7 mm), and a stroke of 0.040 in (1.0 mm). Although shorter in length than a typical Nitinol alloy actuator (such as the FC2, which at a length of 1.000 in (25.40 mm) is the next size up), the FD04 has a larger stroke and is therefore less sensitive to preload [3]. The Frangibolt fastens two tabs together, one on the cover and one on the mask frame to hold the door closed. When power is applied to the Frangibolt, an internal heater (with redundant capacity) heats up the memory shape alloy, placing the bolt under tension and causing it to fracture. Once the Ti bolt is fractured, the door is released and opened by stainless steel

torsion springs that are wrapped around the hinge. To ensure the door will open, the springs are sized to provide sufficient torque margin to overcome expected resistive torques such as friction in the hinge and the resistance from the flight harness. Throughout cruise, a heater on the radiation cover will keep the Frangibolt assembly and hinge components well above their survival cold temperatures.

The implementation of the FD04 Frangibolt actuator on REXIS includes a custom housing, stiff joint design, and appropriate thermal path. In Figure 1b, the housing is hidden from view to show the Frangibolt stack-up including the bolt, thermal isolation washers, actuator, and locknut. It is important to thermally isolate the FD04 Frangibolt actuator from the surrounding structure in order for the cylinder to reach actuation temperature upon application of power. Custom low-conductivity washers are placed between the FD04 Frangibolt and its surroundings to achieve the required thermal isolation. For the FD04 Mini Frangibolt actuator to operate properly, careful attention must be paid to the fastener and the joint design. A stiff joint design is necessary to ensure that there are no gaps, the joint fits inside the grip length of the fastener, and the fastener is properly torque loaded in order to achieve the required preload. The housing, shown in Figure 1a, is necessary to capture the parts that become free after the bolt fractures. The main Frangibolt housing mounts to the lower tab and contains the Frangibolt actuator, two thermal isolation washers, the lower portion of the bolt, and a locknut that holds everything in place. The top portion, the bolt head cap, fastens to the top tab and retains the head of the fractured bolt as well as one thermal isolation washer.

### Test Effort

Prototypes of the REXIS radiation cover were developed, designed, and tested as part of the REXIS instrument engineering test unit (ETU) effort during the summer and fall of 2013. The main objectives of the REXIS prototype radiation cover testing were to validate the design of the REXIS bolted joint, establish confidence in the reliability of the Frangibolt actuator to operate successfully at predicted temperatures, determine an expected range for actuation times at a given temperature, and gain experience with installation and use of the FD04 actuator. Two prototypes were tested: a smaller ETU-1 model, and a larger ETU-2 model (Figure 2). The ETU-1 design represents an earlier concept that was later updated to a larger design (ETU-2) to accommodate moving the cover from the CCD assembly to the coded-aperture mask.

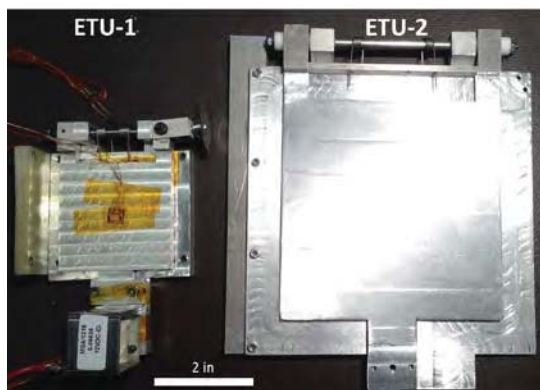
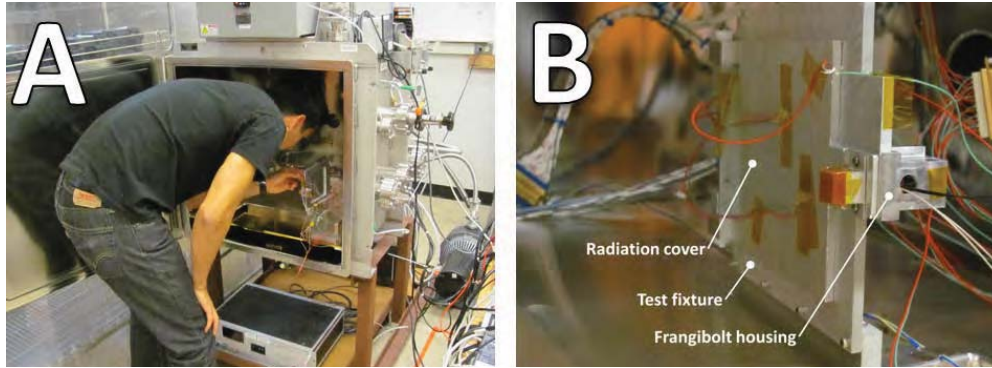


Figure 2. ETU-1 and ETU-2 prototypes

Actuation and deployment of the cover was tested in thermal vacuum (T-Vac) chambers at temperatures as low as  $-48^{\circ}\text{C}$  (shown in Figure 3). Each test specimen was mounted to an interface that was conductively cooled with liquid nitrogen. The mechanism was instrumented with resistance temperature detectors (RTDs) to track the temperature history of critical features on the mechanism during testing. Tests were performed with both Ti and G10 fiberglass washers to determine the impact of the washers on the thermal path. Electrical lines were fed through the chamber outside to a workstation, power supply, and multimeter as required. Tests were also performed at both 9 and 10 VDC to assess the impact of input power on actuation time. Power was applied and manually controlled from an external source during testing. In each test, power was applied to the Frangibolt and the actuation times and temperature histories were recorded.



**Figure 3. (a) Large T-Vac chamber used for ETU-2 (b) ETU-2 mounted to cold baseplate**

### Results

The FD04 successfully fractured the fastener and opened the radiation cover in 19 of 22 tests attempted. The tests in which actuation did not occur were all early  $-20^{\circ}\text{C}$  attempts before the thermal isolation issues were completely understood. In order not to risk damaging the FD04 Frangibolt, the power to the Frangibolt was shut off at 70 seconds. Once the thermal isolation issues were understood and power was applied for greater duration, the same FD04 Frangibolts actuated successfully. The actuation times for the successful tests can be seen in Figure 4. This figure shows the test temperature and the time required to achieve actuation. In general, we see a trend of longer actuation times with colder temperatures. However, the results also show that at a given temperature, actuation time decreases as the power applied to the FD04 increases. Actuation at  $-40^{\circ}\text{C}$  took more than 120 seconds with Ti washers and 9 V. The same test configuration at a similar temperature actuated in only 80 seconds when 10 V was applied. During the testing period, TiNi Aerospace provided the REXIS team with an alternate washer design made from G10 in order to reduce the actuation time at low temperatures. The results show that the use of G10 washers consistently reduces the Frangibolt actuation time when compared to the use of Ti washers at similar temperatures and the same input voltage. Near  $-40^{\circ}\text{C}$  and with an input power of 10 V the actuation time was reduced from 80 seconds to 40 seconds by changing from Ti to G10 washers. These results verify expectations based on the thermal conductivities between G10 and Ti and correlate with similar tests performed by TiNi. Finally, one test was performed at a very low preload (torqued to  $\sim 0.5$  in-lb (0.06 N-m)) as opposed to the specified 2.7 in-lb (0.3 N-m)) to confirm that the stroke of the FD04 could fracture the fastener under these conditions. This test was performed with G10 washers at room temperature and with 9 V applied. The fastener broke in less than 20 seconds. As shown in Figure 4, this actuation time is in family with all other room temperature tests conducted with both G10 and Ti washers at the specified installation preload.



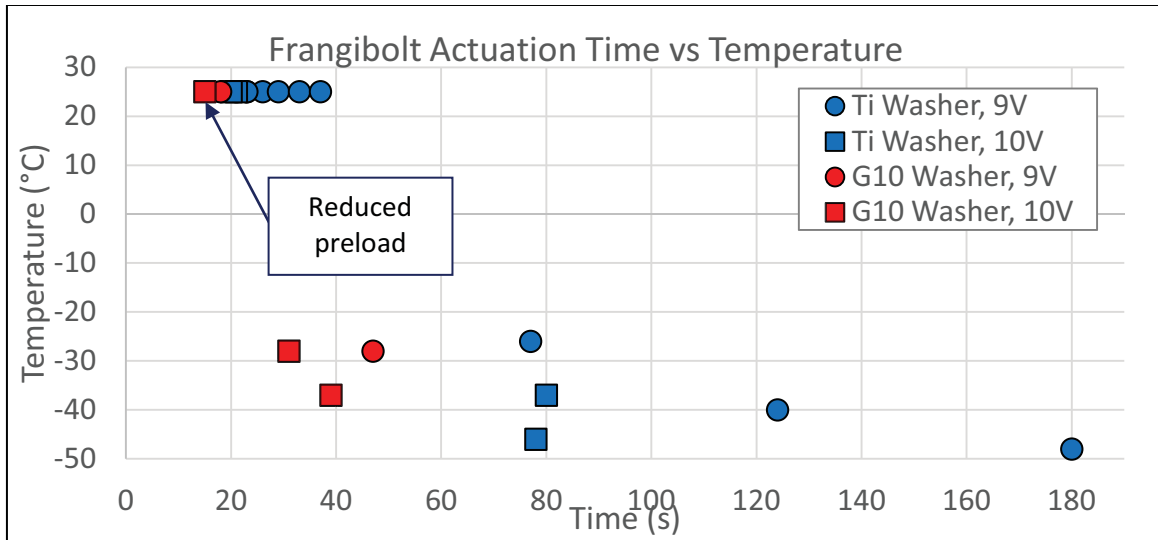


Figure 4. Actuation times for ETU-1 and ETU-2 as a function of temperature

Despite successful bolt fracture upon Frangibolt actuation, there were a few post-actuation observations worth noting. During the test protocol, four distinct FD04 actuators were used. In the course of testing, the first two actuators developed a tear along the seam of the insulation as shown in Figure 5. In addition, after the change from ETU-1 to ETU-2 a chip was observed in the actuator jacket (also shown in Figure 5). Upon actuation, the FD04 does move significantly, and it is believed that this damage to the Frangibolt jacket was due to impact with the aluminum housing around the Frangibolt. The tearing and damage to the jacket is cosmetic in nature and does not affect the performance of the FD04. Further tests with both actuators resulted in successful cover openings. However, given the strict contamination requirements on OSIRIS-REx it is important to avoid this type of damage to the actuator on REXIS. To mitigate the issue, the AI housing was modified to remove sharp edges, allow more movement clearance for the actuator, and include cushioning. Once these changes were made, no further damage to the jacket occurred.

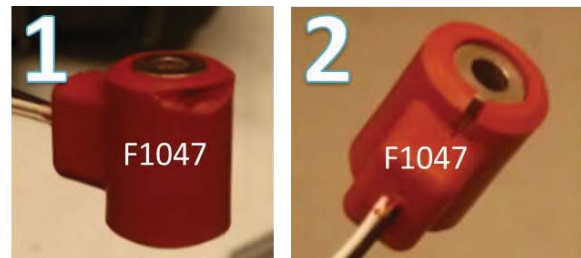


Figure 5. Cosmetic damage to the FD04 jacket post-actuation. The numbers are the actuator serial number.

After two particular tests, the power to the Frangibolt actuator was not cut immediately after actuation and white smoke was observed emitting from the actuator in one of the tests. In these cases the actuators were irreparably damaged. Once the fastener has broken, the FD04 is essentially floating free in the housing and the thermal path to the rest of the structure is broken. In this state, the actuator heats up very quickly and can easily exceed its high temperature limit. The FD04 as designed does not include a temperature sensor. Therefore, a limit switch of some type must be used to confirm actuation and ensure that power is cut.

### Discussion and Lessons Learned

The testing of the REXIS radiation cover prototypes validated the functionality of the deployment mechanism. The cover actuated successfully in 19 tests at a range of temperatures from -48°C to 25°C and both in air and in vacuum. It was shown that the springs open the cover once the fastener has fractured and that the cover remains open. It was noted that a large kick-off force is provided by the FD04 actuation, and systems that are sensitive to shock or jitter may require damping. The REXIS radiation cover design was modified to include bumper tabs with Poron 4701-40 to reduce the impact of the door

opening. It is important to note that a flight harness will need to pass over the hinge of the door in order to power the radiation cover heater. Testing with an appropriate mockup of this harness in place is planned. The testing also revealed a few lessons learned about working with the FD04 Frangibolt. These lessons include the importance of the thermal isolation of the FD04, the need for additional telemetry to signal actuation and cut power to the FD04, and the need for careful housing design to avoid cosmetic damage to the actuator jacket.

#### Actuation Time and Thermal Path

As expected, actuation time increases at lower test temperatures. This trend is likely a combination of two phenomena. First, it naturally takes the actuator heater longer to heat the shape-memory alloy to the necessary temperature when starting at colder temperatures. Secondly, at colder temperatures and once the Frangibolt starts heating, there is a greater temperature difference between the Frangibolt and its surroundings. As the heat transfer rate due to conductance is based on the temperature gradient between two surfaces, heat is lost from the Frangibolt to its surroundings at a higher rate when at colder temperatures. This increased heat transfer rate and demand for heat directly correlates to an extended amount of time power must be applied to achieve the necessary stroke on the actuator to fracture the bolt. Therefore, the specific structural/thermal path within the Frangibolt mechanism directly impacts this temperature vs. actuation time relationship. Testing has shown that the use of G10 washers and the application of 10V both significantly reduce the actuation time at low temperature. The G10 washers better thermally isolate the actuator, allowing for quicker actuation when compared to the Ti washers and the increase in input power allows the heater to come to temperature more quickly.

The use of G10 washers raises several questions and potential issues, however. The heater installed on the radiation cover is meant to ensure the Frangibolt mechanism stays above survival temperatures during its cruise to Bennu. A trade exists between power allocation and actuation time. On the one hand, good thermally isolating washers such as G10 will enable a quick and efficient actuation. On the other, they make it more difficult for the heater to keep the Frangibolt warm during cruise and therefore demand a larger power allocation from the spacecraft. There was an additional concern that G10 washers may reduce the preload of the Frangibolt at actuation. As G10 is a much softer material than Ti, it is unknown whether compression under long periods of time will cause the washer material to creep and cause the bolt to lose its desired installation preload. However, due to the large stroke on FD04, there is a significant margin of safety against bolt preload, such that the Frangibolt should be able to actuate even with zero installation preload. A test was performed successfully with G10 washers and significantly reduced preload (test annotated in Figure 4) to verify the insensitivity of the FD04 to preload.

#### Application of Power Post-Actuation

Once the bolt breaks, there is no longer a thermal path or heat sink to absorb heat from the actuator. Therefore, if power is applied to the FD04 actuator post actuation, the shape-memory alloy can overheat and outgas. With strict outgassing and contamination control requirements in place, REXIS must ensure that its operations do not contaminate the regolith sample collected by OSIRIS-REx. Unlike other Frangibolt models, the FD04 does not have an internal temperature sensor. For this reason, it is not possible for REXIS to prevent overheating by monitoring the Frangibolt temperature and control power based on this temperature. REXIS must incorporate additional hardware and software modifications as a means to determine successful actuation. One solution is to incorporate a limit switch that is compressed when the door is closed and released when the cover opens. This switch is constantly monitored by the instrument's main electronics board and allows for immediate power cutoff upon Frangibolt actuation.

There is some coupling between the actuation time and the concern of power post-actuation. While it is not necessary for REXIS to experience short actuation times, it has been found that longer actuation times result in a greater uncertainty of actuation time. There is more spread in the data at colder temperatures because small differences between tests amplify over time. The faster the Frangibolt can be actuated, the greater certainty there is that it will do so closer to an expected time. Since failure to cut power to the actuator within several seconds after actuation can potentially cause outgassing issues, it is crucial that the actuation time for the Frangibolt be characterized and fully understood.



Through the performed tests, we have seen significant differences in actuation times between tests with 9 and 10 VDC applied to the Frangibolt actuator. This result can be attributed to two factors. By observing the electrical power equation ( $P = \frac{V^2}{R}$ ), one can see that an increase in voltage has a squared effect on the power applied. Therefore, a change from 9 to 10 VDC has a large impact on how quickly the Frangibolt heats. Secondly, the faster the Frangibolt can be heated to its actuation temperature, the less time there is available for heat to be lost to the environment.

### Housing Design

Testing showed that there is a significant kickoff force caused from bolt fracture. This force can cause damage to the actuator insulation if allowed to impact edges of the housing, as was observed. Care must be taken to ensure any Frangibolt housing design will provide clearance to the actuator and not cause damage from the reaction of the actuation. Figure 6 shows some of the features made in the housing to provide freedom of movement for the actuator. It was noticed that during actuation the heater wires that exit the housing were

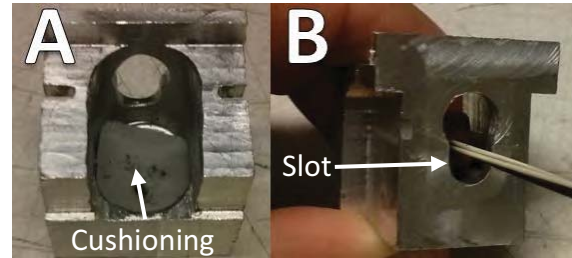


**Figure 6. Frangibolt housing shown with features used to avoid actuator damage**

impacting the edge of the existing cut, causing the actuator to twist and inadvertently impact other edges. The slot shown in Figure 6b was extended so that the wires did not catch upon actuation and cause damage. Additionally, all sharp edges were filed as to avoiding cutting of the actuator jacket. The addition of cushioning to the inside of the actuator housing is another way to mitigate this issue. Although the tearing of the jacket does not impact the performance of the FD04, it was found that resetting the FD04 and subsequent actuations do cause tearing to propagate. Therefore, the actuator should be carefully inspected before and after each test.

### **Conclusion**

Overall, testing of the radiation cover prototypes and Frangibolt implementation provided valuable insight, considerable knowledge, and a number of lessons learned regarding the thermal and mechanical sensitivity of the FD04 Frangibolt actuator. The prototype cover successfully opened 19 times at a range of temperatures. It was confirmed that a clear relationship between actuation time and testing temperature exists and is closely related to the established thermal path. Lessons were learned about implementing the FD04 on an instrument like REXIS. The power applied has a strong impact on actuation time. Likewise, if power is applied to the Frangibolt post-actuation the heater can burn and smoke, causing outgassing and contamination issues. The insulating jacket on the space-rated FD04 actuators is sensitive to impact so any housing around the actuator must be designed with that point in mind. The REXIS ETU radiation cover design and test enabled characterization of this mechanism within the relevant environments, and the lessons learned from these efforts will form the basis for a robust flight model radiation cover design.

### **Acknowledgements**

This work was conducted under the support of the OSIRIS-REx program through research funds from Goddard Space Flight Center. TiNi Aerospace provided valuable technical support during the testing of the FD04 actuators. The test effort was also made possible thanks to the help of the REXIS student team, especially Mr. Harrison Bralower, Mr. Nhat Cao, Ms. Sara Falcone and Mr. Derek Barnes.

## References

1. Allen, B. et al. "The REolith X-Ray Imaging Spectrometer (REXIS) for OSIRIS-REx: identifying regional elemental enrichment on asteroids." *SPIE Conference Series 2013*, 8840.
2. Strüder, L., et al. "The European photon imaging camera on XMM-Newton: the pn-CCD camera." *Astronomy and Astrophysics* 365 (2001): L18-L26.
3. Martynov, V., TiNi Aerospace, Inc. "Cu-Al-Ni Single Crystalline Shape Memory Alloy (SCSMA), Properties and Prospective for Application" *24<sup>th</sup> Annual AeroMat Conference and Exposition*.
4. Fish, et al. "DICE Mission Design, Development, and Implementation: Success and Challenges". *26<sup>th</sup> Annual AIAA/USU Conference on Small Satellites*, SSC-12-XI-1.

# Bi-Axial Solar Array Drive Mechanism: Design, Build and Environmental Testing

Noémy Scheidegger\*, Mark Ferris\* and Nigel Phillips\*

## Abstract

The development of the Bi-Axial Solar Array Drive Mechanism (BSADM) presented in this paper is a demonstration of SSTL's unique space manufacturing approach that enables performing rapid development cycles for cost-effective products that meet ever-challenging mission requirements: The BSADM is designed to orient a solar array wing towards the sun, using its first rotation axis to track the sun, and its second rotation axis to compensate for the satellite orbit and attitude changes needed for a successful payload operation. The tight development schedule, with manufacture of 7 Flight Models within 1.5 year after kick-off, is offset by the risk-reduction of using qualified key component-families from other proven SSTL mechanisms. This allowed focusing the BSADM design activities on the mechanism features that are unique to the BSADM, and having an Engineering Qualification Model (EQM) built 8 months after kick-off. The EQM is currently undergoing a full environmental qualification test campaign. This paper presents the BSADM design approach that enabled meeting such a challenging schedule, its design particularities, and the ongoing verification activities.



**Figure 1. BSADM Track Axis Assembly**

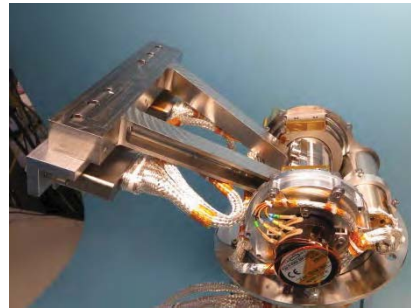


**Figure 2. BSADM Trim Axis Assembly**

## Introduction

Surrey Satellite Technology Ltd (SSTL) is a key supplier of small satellites based near London (United Kingdom) providing complete in-house design, manufacture, launch and operation of small satellites. SSTL also has an office and Assembly Integration and Test facilities based in Colorado in the U.S., SSTL-US. Heritage designs, commercial off-the-shelf technology, combined with a common sense and pragmatic approach to manufacture and low-cost operations enable SSTL to ensure that program economics are kept as low as realistically possible. The SSTL development approach focuses on the experience gained from previous missions. Extensive portions of new projects are evolved from flight-proven design, enabling SSTL to provide custom-designed solutions with high confidence founded on in-orbit performance. Satellite capabilities improve in line with technology developments, allowing the SSTL satellites to fulfill ever-challenging mission objectives. SSTL has an experienced mechanisms skillset; proven by the mechanisms successfully operating in orbit including reaction wheels (with both dry and wet lubrication), Antenna Pointing Mechanisms (APM), imager focusing mechanisms, solar array hold down and release systems (including hinges), and a variety of optical scanning mechanisms. SSTL has

---

\* Surrey Satellite Technology Ltd, Surrey, United Kingdom

now extended its mechanism's product range and developed a Bi-Axial Solar Array Drive Mechanism (BSADM) for advanced Low Earth Orbit missions.

### Heritage

The first solar array drive mechanism engineering model developed by SSTL - the SADM-Twist - is based on the APM's azimuth axis (illustrated in Figure 3), and mainly consists of a stepper motor with an integrated planetary gear box driving a spur gear transmission assembly to rotate the central shaft, which is supported by a duplex bearing. Magnetic encoders are used for position feedback. Like the APM, the SADM-Twist has a flexible printed circuit board (flexi-PCB), which is coiled up inside the large-diameter bearings and allows transmitting power and telemetry across the rotation axis. The APM's baseline flexi-PCB was scaled up for the SADM-Twist, to include 20 power lines (rated at 1.5 A), 6 signal lines (rated at 0.5 A) and 5 sections. This allowed the SADM-Twist to transfer 300 W from its rotating part to its stationary part. While the flexi-PCB provides a cost-effective solution, it does have limited rotation range and power handling capabilities – the latter influenced by track sizing and associated stiffness/bending effects over life. SSTL qualified the low-power SADM-Twist over a 350° movement range to 88000 cycles, at which point the flexi-PCB tracks started to degrade. While this proven life was far superior to the requirement of 36000 orbit cycles, it did highlight a limitation to the power-transfer capability of the flexi-PCB technology.



**Figure 3. Left: APM, Right: SADM-Twist**

The higher power requirement for the new SADM development and the need for continual rotation forced the replacement of the flexi-PCB with a more conventional slip ring. In addition to that, the SADM had to be equipped with a second rotation axis to cope with regular satellite orbit and attitude changes. These considerations were the main drivers for the enhancement of the SADM-Twist design leading to the Bi-Axial Solar Array Drive Mechanism (BSADM) development presented in this paper. The modular nature of SSTL's mechanisms allowed using qualified components for most of the BSADM design to retain heritage and reduce risk:

- The track / trim axis bearings are from the same family as the APMs bearings
- The track / trim axis stepper motor and gearbox are from the same family as used within the APMs and the Imager Focus Mechanisms
- The spur gear transmission is based on the design used within the APMs and the Imager Focus Mechanisms
- The BSADM is commanded by a Bi-Axial Solar Array Drive Electronics, which is based on the APM drive electronics.

### Requirements

The BSADM key requirements are detailed in Table 1. The BSADM has furthermore to provide full internal electrical redundancy, position feedback, and the capability to sustain a solar array deployment moment of 50 N-m. In addition, the BSADM had to be modular in design such that the tracking axis can exist as an entity in its own right (without trim axis) for use as a conventional tracking SADM.

**Table 1. BSADA Requirements Specification**

<b>Operation Characteristics</b>	<b>Track Axis</b>	<b>Trim Axis</b>
Motion Range	Unlimited continuous rotation	±60°
Rotation Speed	< 2°/s	< 2°/s
Position Accuracy	Absolute: ±3° Relative: < 0.01°	Absolute: ±3° Relative: < 0.01°
In-Orbit Duty	30800 rotations of 360°	675 sweeps of ±60°
Qualification Cycles	64000 rotations of 360°	3160 sweeps of ±60°
<b>Physical Properties</b>	<b>BSADM</b>	
BSADM Mass	< 6 kg	
Volume	Diameter 150 x 150 mm	
<b>Power/Signal Transfer</b>		
Number of Circuits	60 @ 1.6 A max	
Voltage	Nom. 32 V	
<b>Operation Characteristics</b>		
Mission Life	5.5 years	
Temperature Range	Operational: -30 to +60°C	Non-Operational: -40 to +80°C
Motor Power Consumption	1.6 W (Nominal Operation)	

### **Design**

The Bi-Axial Solar Array Drive Mechanism includes two rotation axis assemblies as illustrated in Figure 4: The lower axis assembly consists of a traditional SADM and is responsible for continual tracking of the sun. The upper axis (hinge) is responsible for the array trimming to compensate the satellite orbit and attitude changes needed for a correct payload operation. Both rotation axis assemblies are characterized by

- A stepper motor generating the torque needed for the axis rotation
- A planetary gear box and a spur gear that transmit and amplify the motor torque
- Angular contact bearings to support the rotation axis, lubricated with Maplub pf101A
- A redundant potentiometer that generates an analog signal between 0 to 5 V, proportional to the absolute angular position of the rotation axis.

The drive electronics shown in Figure 4 are from the APM housed in a standard module tray preventing the need for any non-recurring engineering. In addition to these ‘standard’ mechanism features, there are some particularities in the BSADM design as presented hereafter.

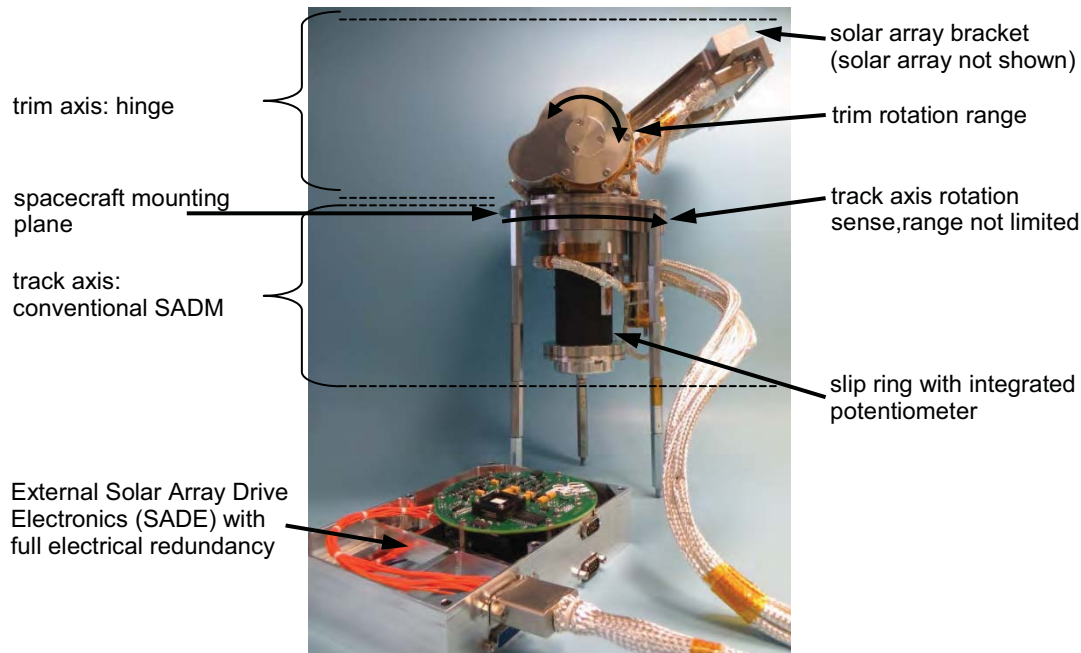


**Figure 4. BSADM Design Overview**

#### Angular Range Lock

During launch, the solar array will be folded and the BSADM hinge oriented perpendicular to the satellite surface panel as shown in Figure 5.a. Once the solar array has been deployed, the hinge will be rotated towards its nominal operation range which is between  $+60^{\circ}$ / $-70^{\circ}$ . An angular range lock has been implemented on the hinge rotation axis to prevent the hinge (and the solar array) to exceed this operation range. This is particularly important as the solar array might collide with other satellite instruments if the track axis was rotated while the hinge is positioned outside this range.

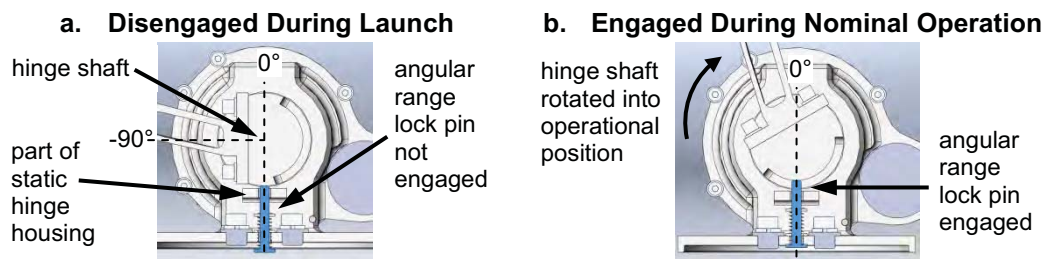


**Figure 5. Angular Range Lock**

#### Deployment Lock

Under conventional circumstances, without damping, the solar array wing used for the SSTL satellite would bounce back after deployment and come to a rest at an unknown position. A back-driving torque of 50 N-m is needed during the deployment to reasonably limit this solar array wing back-bouncing. In order to accommodate this requirement within a compact and lightweight product, an additional locking mechanism has been incorporated into the hinge assembly. The solar array deployment lock operation method is illustrated in Figure 6 and includes the following operation steps:

- a. During the solar array deployment, the hinge rotation is blocked through a pin which is in contact with an end stop on the hinge static housing. The translational displacement of this pin is prevented through an add-on feature of the gear, which forces the pin to remain in its position. The pin-carrier is mounted to the hinge shaft, onto which the solar array bracket is also attached.

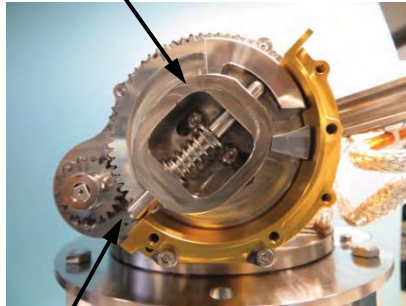


The rotation of the solar array is thus prohibited, and the required high back-driving torque resistance is provided through this locked pin.

- b. Once the solar array has been deployed and settled, the hinge motor is actuated and the gear begins to rotate. Since at this point the hinge shaft and the gear are still disengaged, the gear rotates, while the pin's position remains static until it reaches the gear opening allowing the pin to push through.
- c. The pin pushes through into a cavity in the gear add-on feature, forming thus a rigid connection between the gear and the hinge shaft (on which the solar array is attached). The hinge drive is now engaged; the rotation of the gear is transmitted through the pin to the shaft and the solar array. Nominal operation can be started.

**a. Hinge Locked**

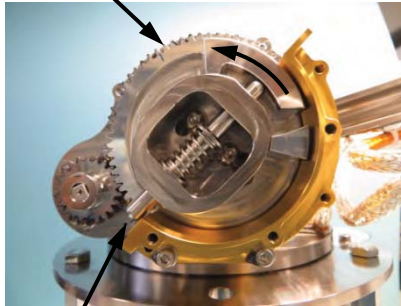
pin-carrier mounted on hinge shaft



pin against stop on static housing

**b. Un-Locking Operation**

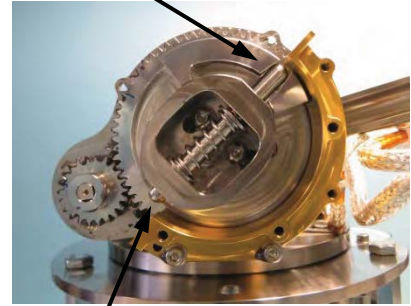
gear rotates



pin constrained against housing

**c. Drive Engaged**

pin engages into the gear, locking shaft and gear together



pin is no longer constrained by housing, hinge shaft is free to rotate

**Figure 6. Solar Array Deployment Lock Operation Method**

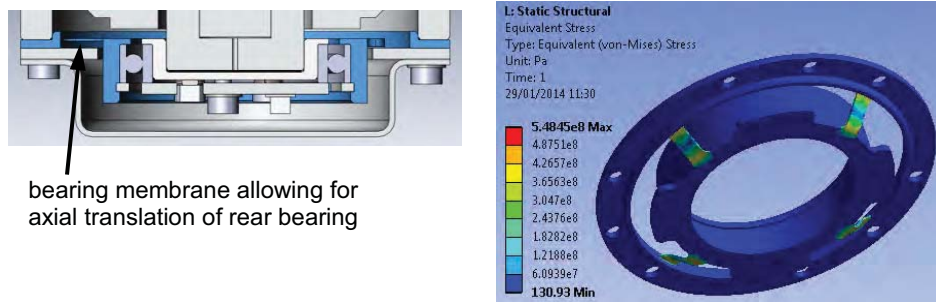
Track Axis Rear Bearing and Membrane

The track axis shaft is mainly supported by its front duplex bearing. These bearings will take most of the axial and radial loads during launch. An additional single-row bearing has been implemented at the rear end to further restrict radial displacements and guarantee that the shaft (especially the slip ring shaft) remains properly aligned with respect to its stationary counterpart.

The rear bearing is supported by a flexible membrane which allows translation along the rotation axis. This membrane compensates thus for shaft elongation/retractions due to temperature gradients between the shaft and the housing, and hence prevents significant variations of the bearing load.

Slip Ring

The slip ring allows the transmission of power and electrical signals from the stationary to rotating structure of the track axis. Its core consists of 60 current transfer rings made from gold plated brass, each of them having the capability to transfer 1.6 A. The molding of the rings within a space-qualified epoxy provides a very high electrical insulation between the tracks. The counter parts for these rings are gold brushes, wiping over the gold rings and thus providing electrical connection between the rotating and the stationary part of the track axis. Due to the criticality of the gold-on-gold contact between the brushes and the gold rings, the slip ring was purchased in order to benefit from existing heritage of such a sophisticated element. The slip ring will none the less be completely re-qualified within the BSADM as its performance significantly depend on the method how it's supported.



a. Rear Bearing Support Arrangement    b. Max. Flexible Membrane Deformation

**Figure 7. Trim Axis Rear Bearing Membrane**

### Verification

The BSADM qualification test campaign allows proving the mechanism's performance during the ground testing, the launch and its whole orbital lifetime. It includes

- A bench test to calibrate both rotation axis and to verify the mechanism's functional performances prior to its submission to thermal and mechanical loading
- Vibration tests to demonstrate that the mechanism is able to sustain launch loads
- A deployment test to show that the deployment torque generated by the solar array wring will not damage the mechanism (and in particular the deployment lock pin)
- A thermal test to verify the mechanism's robustness to temperature changes and its capability to provide the required performance over the whole operational temperature range
- A life test performed with temperature changes in vacuum, to prove that the targeted mechanism performances are provided during the whole orbital lifetime

Functional tests are performed regularly throughout the entire qualification test campaign to closely analyze and monitor the evolution of the mechanism's performance under the various circumstances/operation scenarios.

#### Bench Test

The bench test focuses on the verification of the BSADM key functions, consisting of the measurement of the operation accuracy (relative & absolute angular position accuracy), the torque margin and the deployment lock release capability.

#### Vibration Test

The vibration tests are started with a resonance search (low-level sine sweep) followed by a high-level sine vibration conducted to confirm the structural integrity of the BSADM. An intermediate-level random vibration test is then performed at -6 dB to assess the mechanism's responses before it is finally submitted to the full-level random vibrations that simulate flight-launch representative loading. The random vibration spectrum is unique for each test axis. Figure 9 shows the z-axis test level and the mechanism's response as example. The resonance searches done before and after the high-level sine and the full-level random vibration did not show significant Eigenfrequency changes, especially for the critical mechanism elements. The visual inspection and the performance tests done after the vibration tests did not reveal any damage and reinforce the confidence that the mechanism is able to sustain the predicted launch loads.

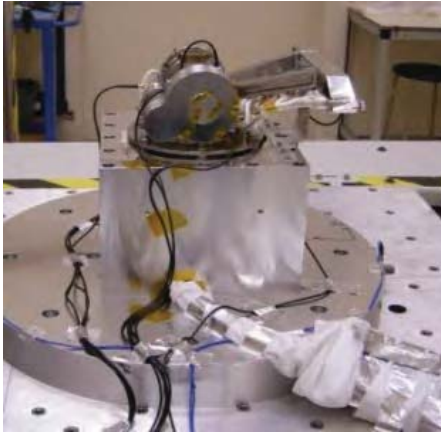


**Figure 8. BSADM Vibration Test Set-Up**

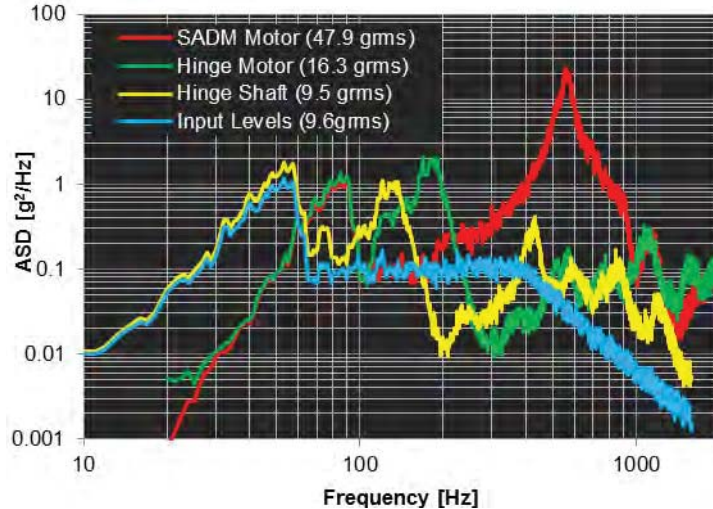


**Figure 9. BSADM Z-Random Vibration Response**

#### Deployment Test

A static torque of 60 N-m is applied on the solar array bracket to demonstrate that the deployment lock pin will not be damaged through the loads generated by the solar array deployment. A smooth and controlled release of the deployment lock after this test confirms that the deployment lock pin is robust enough to sustain the solar array deployment torque.

#### Thermal & Thermal Vacuum Life Test

The BSADM is submitted to 4 cycles between +50°C and -20°C during the thermal tests, and to 12 additional cycles in vacuum between +80°C and -30°C during the thermal-vacuum life test. The first cycle of each test sequence is used to verify the structural integrity of the mechanism under thermal loading. Mechanism start-up and functional tests are then done at hot and cold temperature during the second cycle. During the remaining thermal cycles, the mechanism track axis is continuously rotated, while the trim axis performs sweeps of ±60°. The BSADM performs 64000 continuous rotations of 360° with its track axis and 3160 sweeps of ±60° with its trim axis in overall, and will therefore be qualified as per ECSS for the targeted in-orbit life.

### **Conclusion**

The BSADM design approach – based on heritage, focused on the analysis of critical elements and the performance enhancement through particular features – lead to a rapid manufacturing of an EQM that allowed facing the environmental qualification testing with high confidence. The success of the EQM observed throughout the qualification tests done so far reinforce the expectation that the BSADM will pass the whole qualification campaign without major issue, and that 7 Flight Model mechanisms will be delivered ready to fit to the spacecraft by August 2014. This is a 17-month program from kick-off to completion – a good example of the successful, unique and highly efficient SSTL approach to design and development.



# Advances in Current Rating Techniques for Flexible Printed Circuits

Ron Hayes\*

## Abstract

Twist Capsule Assemblies are power transfer devices commonly used in spacecraft mechanisms that require electrical signals to be passed across a rotating interface. Flexible printed circuits (flex tapes, see Figure 2) are used to carry the electrical signals in these devices. Determining the current rating for a given trace (conductor) size can be challenging. Because of the thermal conditions present in this environment the most appropriate approach is to assume that the only means by which heat is removed from the trace is thru the conductor itself, so that when the flex tape is long the temperature rise in the trace can be extreme. While this technique represents a worst-case thermal situation that yields conservative current ratings, this conservatism may lead to overly cautious designs when not all traces are used at their full rated capacity. A better understanding of how individual traces behave when they are not all in use is the goal of this research.

In the testing done in support of this paper, a representative flex tape used for a flight Solar Array Drive Assembly (SADA) application was tested by energizing individual traces (conductors in the tape) in a vacuum chamber and the temperatures of the tape measured using both fine-gauge thermocouples and infrared thermographic imaging. We find that traditional derating schemes used for bundles of wires do not apply for the configuration tested. We also determine that single active traces located in the center of a flex tape operate at lower temperatures than those on the outside edges.

## Introduction

Electrical power transmission across rotating interfaces (such as in SADAs) is typically accomplished using slip rings, twist capsules, or wire wraps depending on the degree of rotational freedom required by the application. Slip rings permit continuous rotation in either direction but can be expensive and complex, which can be considered a liability in terms of reliability in some cases. Some applications do not require continuous rotation and therefore can forgo slip rings in favor of the other, more cost-effective options listed above. While wire wraps can be very simple, they are also difficult to adequately characterize in terms of parasitic torque and life, with these parameters varying widely depending on many factors in the design. A much more common, more predictable, and higher reliability option is the twist capsule. This device makes use of flexible printed circuit tapes to carry the electrical signals between a rotor and stator. These tapes are typically constructed of a single-layer copper conductor layer sandwiched between layers of Kapton film using acrylic adhesive to bond the whole thing together.

A critical aspect to the design of any conductor in a space environment is the temperature rise in that conductor due to Joule ( $I^2R$ ) heating; this is especially true for flex tapes used in twist capsules. The standard means for rating conductors in flex tapes has been to use nomographs derived from the electronics industry such as in MIL-P-50884. These techniques leave much to be desired, as experience has shown that in a vacuum the temperature rise in the conductors is highly dependent on the unsupported length of the flex tape. The heritage rating technique does not take this into account. A more physically representative technique was developed in the 1990's that took this length into account, and was based on a temperature-dependent finite-difference model (Hayes and Allen). This model has been used successfully for two decades, and has been tested and confirmed to be conservative in most cases. Results from a modified version of this model (modified to approximate radiative losses) are shown in

---

\* Honeybee Robotics Spacecraft Mechanisms Corporation, Longmont, CO

Figure 1. What this model does not do is account for a duty factor in the flex tape itself, meaning that if only a portion of the traces in a tape are in use at full capacity the model must be factored without much engineering basis. This approach yields a robust design but not fully understanding some of these intra-tape thermal effects limit how far we can push the envelope in terms of current carrying capacity and unit density. We are currently involved in a program that is focused on a better understanding of these duty factor effects as well as a more complete model verification. For this paper, tapes were tested in a vacuum chamber using thermal imaging instruments and specialized view ports and chamber configurations.

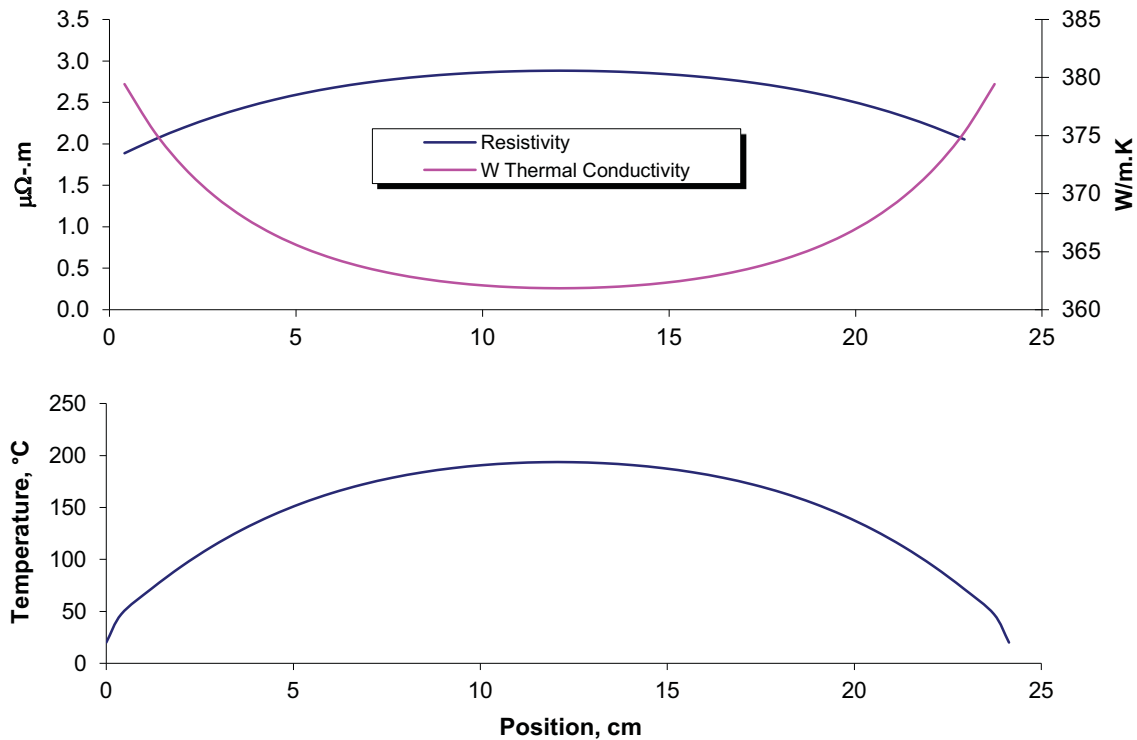


**Figure 1. Example predicted temperature profile (bottom) and material properties (top) along the length of a flex tape in vacuum at 10A. In the case presented here the radiation has been added in order to approximate the test conditions in the experiments conducted. For a flight application, the radiative effect would be removed yielding a much higher temperature and therefore a lower suitable maximum current.**

### Experimental

A flex tape from a recent solar array drive flight application was used for testing (shown in Figure 2). Jumpers were soldered between the exposed solder pads at the ends of the tape in a “daisy chain” configuration so that a single power source could be used to energize all of the traces in series, but also allow for connection to individual traces using alligator clips.

The flex tape (construction details in Table 1) was mounted to an aluminum alloy support structure using low outgassing double-sided tape. Type K thermocouples (TCs) were attached using aluminum tape to each end of the flex tape where it contacted the aluminum supports, additional TCs were attached using aluminum tape to the aluminum supports themselves and to the chamber platen. Additionally a single fine-gauge type K thermocouple was attached using Kapton tape to the flex tape under test, near the center of the length and width of the tape; this was done to calibrate the thermographic camera. The chamber was pumped down and current applied to all traces of the tape, once stabilization had occurred



a thermographic image was recorded of the region in which the TC had been attached. The emissivity setting in the camera was adjusted so that it indicated the temperature measured with the TC. Once this baseline was established, the mid-tape TC was removed.

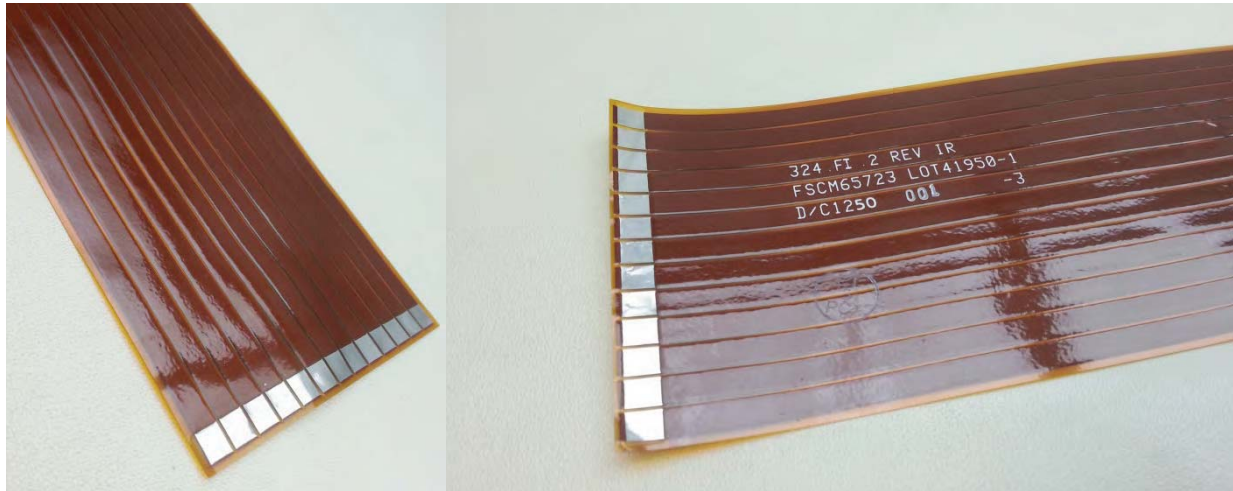


**Figure 2. Flex tape used in tests.**

A 40-mm-diameter CaF<sub>2</sub> window was used to view the tapes in far IR (where the FLIR operates). This material is transparent over most of the spectrum in that range. Calcium fluoride does not transmit all wavelengths in the far IR range with complete transparency, but since the previously described calibration procedure was performed thru the window we expect reasonable results.

**Table 1. Construction details of the flex tape used in the testing performed here.**

<i>Parameter</i>	<i>Value</i>
Overall Length	0.61 m (24 in)
Active Tape Length	0.24 m (9.5 in)
Overall Tape Width	0.061 m (2.4 in)
Number of Traces	13
Trace Width/Spacing	4.2x10 <sup>-3</sup> m / 8.9x10 <sup>-4</sup> m (0.16 5in / 0.035 in)
Trace Thickness Material	7.1x10 <sup>-5</sup> m (2 oz = 0.0028 in) Rolled Annealed Copper (IPC W7)
Tape Construction	Kapton/Acrylic Adhesive/Cu Single Layer

Power was supplied to the flex tape via a bench power supply. Current was monitored using a handheld DMM. Temperatures were monitored using handheld thermocouple readers. The thermographic instrument used was a FLIR i3. This FLIR unit was positioned above the IR window in the top of the chamber (Figure 4) using a ball vise.

For each test, the chamber was evacuated using a mechanical roughing pump to a pressure of approximately 0.13 Pa (1 torr) and power was applied. Tests were done with current levels ranging from 1 A to 11 A. The current used for the tests reported on here was 10 A in every case; this value was chosen because it gave good signal to noise ratio on the FLIR and allowed us to see more subtle variations in unpowered trace temperatures. The temperature of the tape was allowed to stabilize in order

to approximate the steady-state condition and a thermographic image recorded, as well as the temperature of all thermocouples, chamber pressure, current and the thermal image data file were logged. The chamber was brought back to atmospheric pressure trace connections modified and the process started again.

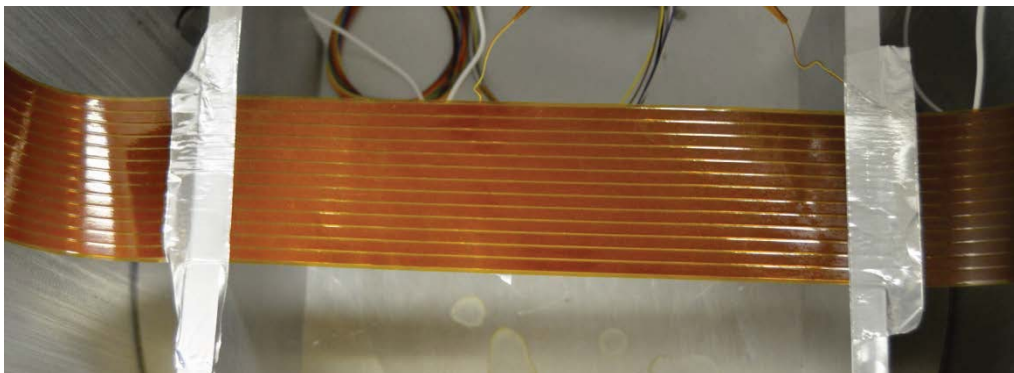


**Figure 3. General tape configuration in chamber. The boundary temperature thermocouple can be seen on the right side of this photo.**



**Figure 4. Thermographic (FLIR) instrument positioned above CaF<sub>2</sub> port in top of chamber.**

## Results

FLIR images were translated to .csv files and then imported into Microsoft Excel for analysis. The output from the FLIR takes the form of a 60x60 matrix of temperatures. For the data presented here in Figure 6, a column of data near the center of the image was taken. The column number and method of extraction are consistent for all the results here. During periods of testing, a K-type thermocouple was attached to the exposed surface of the flex tape using acrylic adhesive Kapton tape, the temperature read was used to calibrate the FLIR by adjusting the emissivity input. The emissivity of the flex tape Kapton surface was found to be 0.37. No uncertainty was calculated for this result as the absolute value of the emissivity is not critical for this work. In all cases reported here, “temperature rise” indicates raw temperatures that have been modified by subtracting the aluminum support fixture temperature thereby negating any heating of the fixture and chamber.

A sample of image files from the FLIR are shown in Figure 5 where a photo of the flex tape is shown for reference and images from the cases where only trace #1 is powered, traces 1-7 are powered, and all traces are powered. In each case, 10 A is applied to every trace. Data like these were taken for 10 A applied to traces in the series 1, 1-2, 1-3 and so on until all traces were powered. Similar data were gathered for the cases where only trace 1 is powered, then only trace 2 and so on thru trace 6. These results are given in Figure 7.

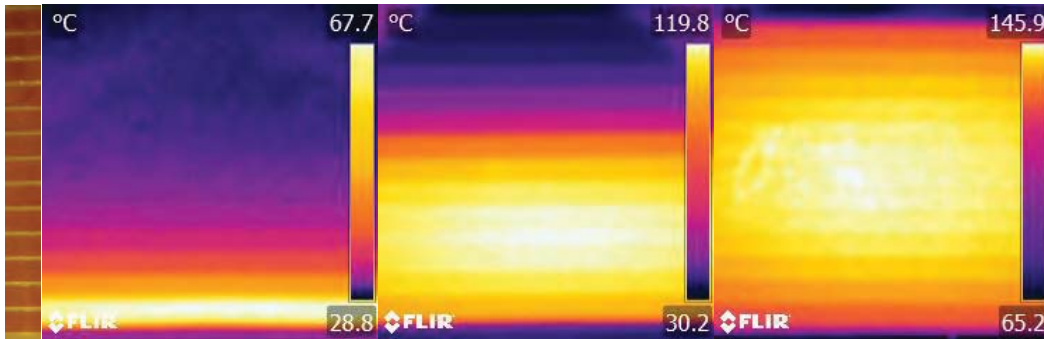


**Figure 5. FLIR images of flex tape tests. Leftmost image is a photograph of a segment of the flex tape tested shown for context. The other images, left to right, are of trace#1 (bottommost trace) active, traces 1-7 active, and all thirteen traces active.**

The numerical results from the series of images in Figure 5 are given in Figure 6. This graph shows the progression of the maximum temperature rise in the flex tape as more and more traces are energized. Here we can see that when three or fewer traces are energized near the edge of the tape the maximum temperature is less than the other cases. In every other case shown, the maximum temperature is relatively unchanged. This result is expressed in Figure 8 as a derating factor similar to those defined in MIL-STD-975.

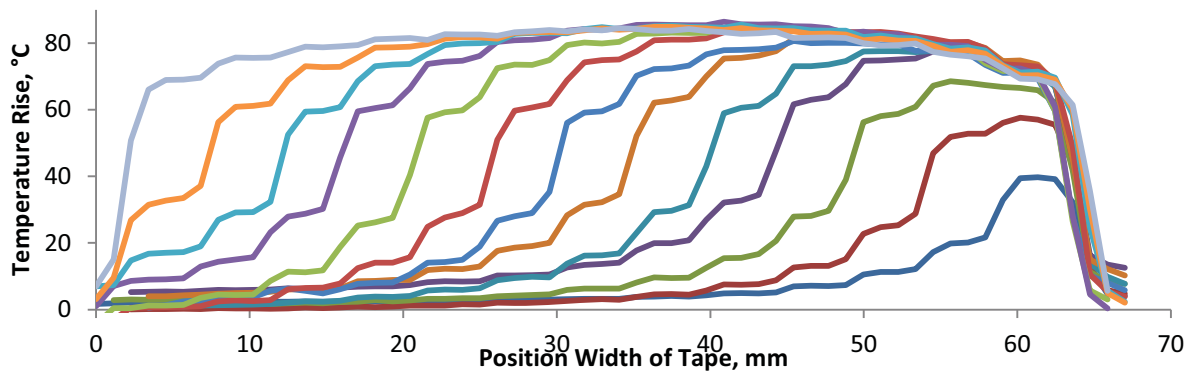




**Figure 6. Temperature profiles across the width of the flex tape. Starting at the right side of the graph trace number one has 10A applied, the next data set is with two traces activated, and so on until all thirteen are active with 10A (corresponding to right-most image in Figure 5)**

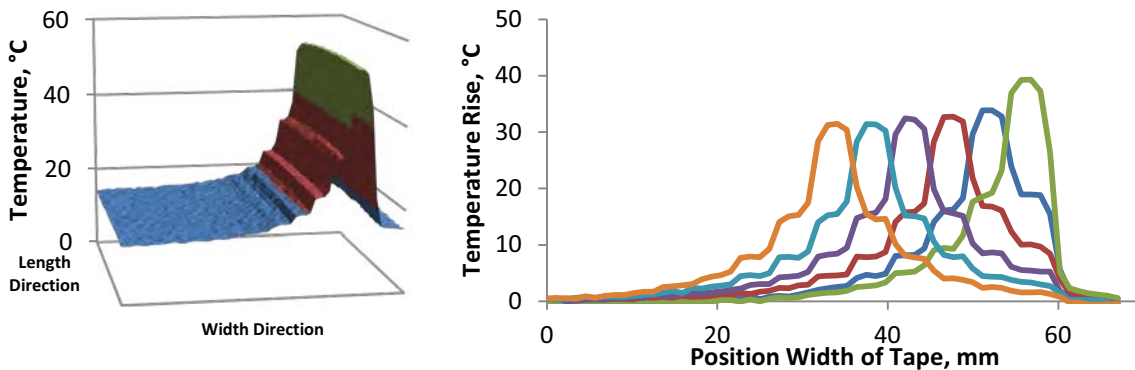


**Figure 7. 3D plot of temperature output file from FLIR converted in Excel and corresponding to the single trace image in Figure 5. The graph to the right shows the results from individual, discrete loading of tapes 1-6 showing the more benign maximum temperatures associated with moving the active trace toward the center of the flex tape.**

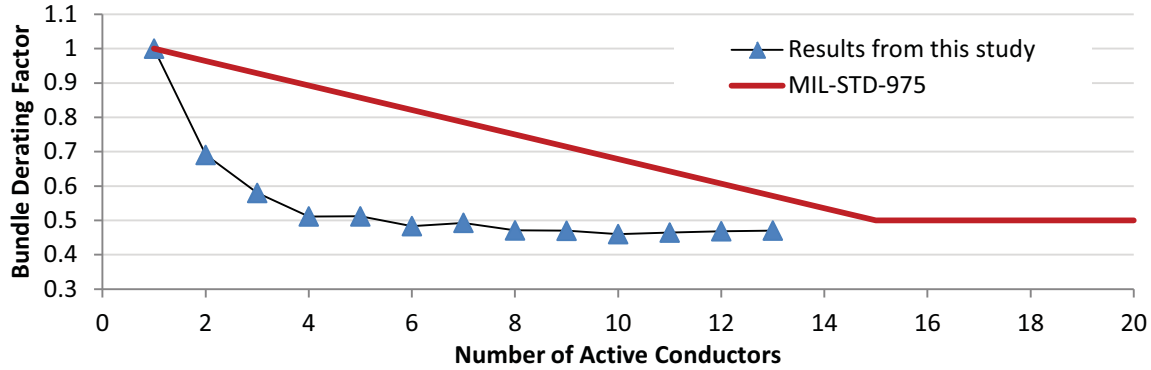


**Figure 8. Results of trace loading tests (from Figure 6) represented as a derating factor and compared to MIL-STD-975.**

### Remarks and Conclusions

More work will need to be done in order to fully characterize and draw definitive conclusions about the thermal relationship between individual traces and their adjacent traces with flex tapes in other common configurations (trace widths, thicknesses and spacing) but for this particular tape we have found the following:

1. Radiative cooling of exposed (not wound into a twist capsule) flex tape can be substantial and the results of these tests, or any not done in a flight-like configuration, should be taken in context. Traces of the dimensions used in these tests should not be used at 10 A in a flight twist capsule configuration. In fact, for the application for which these particular tapes were designed and used the maximum current is 2.5 A per trace.
2. Interior traces run cooler than exterior traces. Those traces in the middle of the tape spread heat across several adjacent neighbor traces; those on the edges of a tape can only dissipate heat in one direction and can be several degrees hotter than equivalently loaded interior ones.
3. Traces on a single tape do not follow the rules for leadwire bundle derating per MIL-STD-975. Once more than three adjacent traces are fully loaded, the maximum temperature rise in the tape has reached its maximum, though placing active traces on either side of a tape, keeping the middle for low power traces, should result in lower overall temperatures.

A practical application of conclusion 3 above is that the conservative current rating approach outlined at the beginning of this article can be modified for cases where the power traces can be allocated in groups of three or less. More work needs to be done with other flex tapes and rating models updated in order to determine how this relief should be applied.

### References

1. Military Standard. "NASA Standard Electrical, Electronic, and Electromechanical (EEE) Parts List", MIL-STD-975L, 31 January 1994.
2. Military Standard. "Printed Wiring Board, Flexible or Rigid-Flex, General Specification For", MIL-P-50884E, 1 September 2010.
3. Hayes, Ron L and Blair R Allen. "Temperature-Based Current Derating of Monofilament Slip Ring Brush Wire for Space Applications." *43<sup>rd</sup> International SAMPE Symposium and Exhibition*, Volume 43, May 31-June 4, 1998, pp. 1883-1893.





# Design of 3D-Printed Titanium Compliant Mechanisms

Ezekiel G. Merriam<sup>\*</sup>, Jonathan E. Jones<sup>\*\*</sup>, and Larry L. Howell<sup>\*</sup>

## Abstract

This paper describes 3D-printed titanium compliant mechanisms for aerospace applications. It is meant as a primer to help engineers design compliant, multi-axis, printed parts that exhibit high performance. Topics covered include brief introductions to both compliant mechanism design and 3D printing in titanium, material and geometry considerations for 3D printing, modeling techniques, and case studies of both successful and unsuccessful part geometries. Key findings include recommended flexure geometries, minimum thicknesses, and general design guidelines for compliant printed parts that may not be obvious to the first time designer.

## Introduction

A compliant mechanism derives its motion from the deflection of its constituent members. Compliant mechanisms offer decreased part count, decreased complexity, lower weight, longer life, and lower cost. Since compliant mechanisms can be designed with no surface contact, wear and all its associated issues are eliminated. In many cases, bearings may be eliminated, along with their weight, complexity, and failure modes [1]. Preliminary work has shown the applicability of compliant mechanism technology to space applications [2]. Additionally, compliant mechanisms lend themselves to monolithic construction through additive manufacturing processes.

Advances in Electron Beam Melting (EBM) enable additive manufacturing (also referred to as rapid manufacturing) in a variety of metals, including alloys of Titanium. The EBM process is well documented [3] [4]. Case studies have shown that rapid manufacturing offers reduced costs when production volumes are low, many design iterations are to be explored, high geometric complexity is needed, or when new materials are to be explored [5] [6]. Additionally, material scrap rate can be significantly reduced by printing a near-net-shape part rather than machining it from solid billet [7]. Combining compliant mechanisms with rapid manufacturing techniques opens up interesting possibilities for creating compliant space mechanisms that have unprecedented performance.

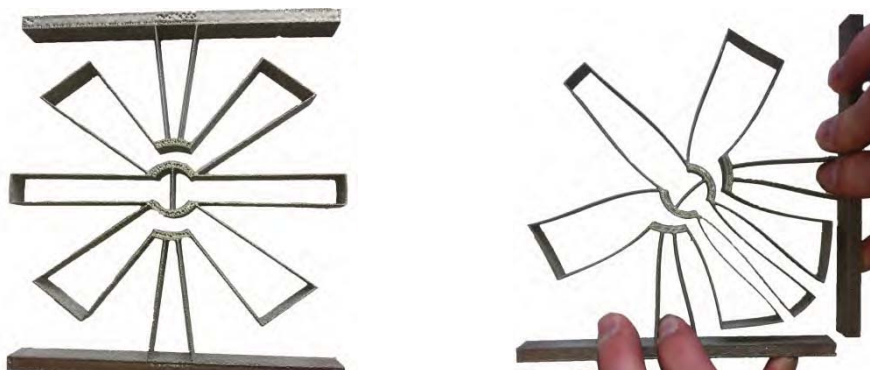


**Figure 1. A compliant titanium hinge produced with EBM. This hinge is capable of  $\pm 90^\circ$  of motion. Images provided courtesy of Robert Fowler. [8]**

<sup>\*</sup> Brigham Young University, Provo, UT

<sup>\*\*</sup> NASA Marshall Space Flight Center, Huntsville, AL

Rapid manufacturing processes have been used in multiple aerospace applications, including ductwork [5] [6] and a capacitor housing on the International Space Station [9]. These applications used selective laser sintered nylon parts, which established a basis for rapid manufacturing as a viable method for producing parts. Structural brackets [3], a shrouded cryogenic impeller [3] [10], and brackets for the Juno spacecraft [7] have also been manufactured in titanium using rapid manufacturing processes. While most parts built thus far have been structural members (brackets, etc.) or non-structural assemblies (ductwork and housings), in our work we use additive manufacturing to create monolithic mechanisms for aerospace applications. As part of that effort, it is desirable to know what to expect when printing slender geometries, and maximum allowable stresses in EBM-produced titanium parts.

### **Material Considerations**

#### Porosity of EBM produced parts

EBM produced parts can achieve full density [11]. Wooten and Dennies claim that the fully dense region occurs in bulk parts about 1.25 mm (0.05 in) below the surface [3], but give no explanation of how this figure was arrived at. This depth is more than the thickness of many printed flexures. While the region near the surface may not be fully dense, Murr et al, mention that such micropores have no effect on short-term tensile properties [12]. However, surface roughness and micro-cracks contribute to reduced fatigue life. Because of the slender geometry, machining of flexures is often impractical, so surface porosity is difficult to eliminate and must be accounted for in the design. This surface porosity constitutes a major obstacle to high cycle fatigue life. Hot isostatic pressing (HIP) improves the fatigue life of EBM produced parts [13]. If HIP treatment is impractical, property data obtained from raw (not treated with HIP or finish machined) tensile samples are available [14].

#### Thickness Correction Factor

Early design work for a two-degree-of-freedom (2 DOF) pointing mechanism [15] required testing the fabrication and performance of cross-axis flexural pivots. These flexures have a number of good characteristics, including good stability and load carrying capacity [16]. The flexure was modeled in ANSYS to predict its torsional stiffness, which was compared to analytical solutions. Finally, the flexures were produced using EBM, and an example is shown in Figure 2, along with the pointing mechanism.

The torque and deflection characteristics of three printed flexures were found. The FE model significantly over-predicted (~30%) the stiffness of the printed. Because of high surface roughness, it was thought that perhaps not all of the thickness of the flexure contributes to its bending stiffness. Applying a correction factor of 0.83 to the thickness resulted in good agreement between the FEA and measured stiffness of the flexures. Later this correction factor was used to predict the overall stiffness of the pointing mechanism, again resulting in good agreement. Therefore, when using thin flexures, a thickness correction factor of 0.83 is recommended to accurately predict the torsional stiffness of printed flexures.

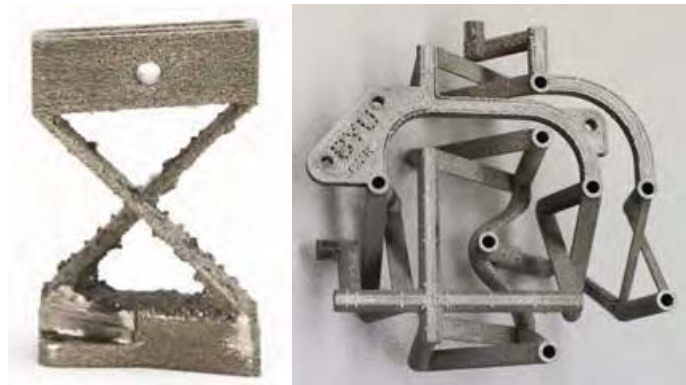


**Figure 2. Cross-axis flexural pivot and 2 DOF pointing mechanism used to compare FEA and analytical models to measured stiffness.**

### Allowable Stress

Two grades of titanium powder are currently produced for use in EBM machines: Ti6Al4V and Ti6Al4V ELI (ELI is “extra low interstitials,” which improves ductility and fracture toughness of the alloy). These two alloys have slightly different strength characteristics, but Ti6Al4V has slightly higher strength [13]. Table 1 presents strength data from several sources. These data were gathered from samples prepared in different ways; some used highly polished samples while other samples are tested in the as-built condition, with no post-processing or heat treatment. Rafi et al, found a strong correlation between build orientation and strength [14], while the manufacturer data make no distinction between build orientations [13].

**Table 1. Summary of strength data gathered from other sources.  
(\* ) indicates that sample underwent HIP process.**

Material	$S_y$	$S_{ut}$	$S_e$	Notes
Ti6Al4V	950	1020	600*	Manufacturer data [13]
Ti6Al4V ELI	930	970	600*	Manufacturer data [13]
Ti6Al4V ELI	782	842	120	As-built vertical [14]
Ti6Al4V ELI	844	917	225	As-built horizontal [14]
Ti6Al4V ELI	869	928	325	Machined vertical [14]
Ti6Al4V ELI	899	978	300	Machined horizontal [14]

### **Geometry Constraints**

#### Feature Geometry

Minimum wall or flexure thickness depends on feature orientation. A minimum thickness of 0.75 mm is recommended for flexures that have the thickness orthogonal or parallel to the build direction. If the flexure is built at other angles, 1.00 mm is recommended as the minimum thickness. If the flexure is built at some angle from the vertical, the larger dimension is recommended. Figure 3a illustrates this orientation dependence. The authors have had good success building flexures that rise at 45° from the horizontal when the flexures are 1.00-mm thick.



**Figure 2. (a) - Flexures built at angles not orthogonal or parallel to build plate should be slightly thicker. (b) - Horizontal flexures build more successfully when supported by build plate as shown on the right.**

#### Thermal Stresses and Part Warping

Because the build chamber is maintained at between 500°C and 700°C, most stresses are relieved during the part’s build cycle [11, 3], but some warping due to thermal stresses has been observed. Figure 4 shows a part where enough warping occurred that the part failed to build correctly. Although not fully understood, it is thought that this warping is due to stresses that occur when the molten metal solidifies but are subsequently relieved as the part is held at high temperature. Usually the part is bulky enough

that these low stresses do not cause warping. For the geometry shown in Figure 4, the part was redesigned to have the flexures rest on the build plate (illustrated in Figure 3b). Supporting the flexures in this way eliminated the warping and allowed a successful build. It is postulated that other ways to avoid warping include better support of the cantilevered flexure from underneath (by having it connect to another portion of the part) or making it wider. In general, narrow, unsupported flexures are to be avoided.



**Figure 3. Build failure due to warping of slender flexures.**

#### Manufacturing Clearances

Clearances are important to ensure that the completed mechanism can move freely, without fusing sections that should move relative to one another. On a number of mechanisms with small (<2 mm) gaps, the final gap dimension was significantly less than was specified in the part file. Additionally, gaps must be wide enough that un-melted powder can be easily removed to allow motion in the mechanism. Experience with successful mechanisms suggests a minimum gap of 1.0 mm. The final gaps are less than the specified gap. In one instance, a gap as small as 0.66 mm was specified and the part successfully printed without fusing the two sections together; the measured clearance was 0.23 mm. These clearances were measured in the horizontal direction (parallel to the build plate). Vertical clearances should be specified larger, especially in areas where powder removal is difficult.

#### Powder and Support Removal

Another design consideration is that the geometry must allow for removal of un-melted powder and any support structure. Closed geometries should be avoided, or openings should be provided to allow access to loosen packed powder with hand tools or media blasting. In some cases this may not be possible, and post machining using special fixtures or tooling must be used. Figure 5 shows the tooling required to allow machining the inside of a particular feature. In another case example, a linear spring was printed that consisted of Belleville washers stacked end-to-end. The internal areas of the spring were inaccessible, but by using a press to compress the spring, enough powder was removed from between each washer segment to allow the spring to function as intended.



**Figure 4. The 2 DOF pointer mechanism in fixture for removal of powder and supports from inside a split-tube flexure.**

### **Summary**

The following checklist can be used for designing compliant mechanisms for EBM manufacturing:

- Select minimum thickness for desired flexure orientation (0.75 mm for horizontal or vertical flexures and 1.0 mm for other angles)
- Find flexure length sufficient to bring stress into allowable range, subject to deflection and thickness
- Select flexure width to support applied loads without requiring excessive actuation torque
- Ensure minimum gap width is observed (1.0 mm)
- Ensure horizontal flexures are supported at both ends
- Ensure that geometry allows powder removal
- If post-machining is necessary, provide geometry for fixturing
- Orient part so that every feature is built up from build plate or supported in some way

### **Acknowledgements**

This work was supported by a NASA Office of the Chief Technologist's Space Technology Research Fellowship. The support of NASA Marshall Space Flight Center in the fabrication of titanium parts is gratefully acknowledged.

## References

- [1] L. Howell, *Compliant Mechanisms*, John Wiley Sons, Inc, 2001.
- [2] R. M. Fowler, L. L. Howell and S. P. Magleby, "Compliant space mechanisms: a new frontier for compliant mechanisms," *Mechanical Sciences*, vol. 2, pp. 205-215, 2011.
- [3] J. Wooten and D. P. Dennies, *Electron Beam Melting Manufacturing for Production Hardware*, Paper number 08AMT-0061, SAE International, 2008.
- [4] L. E. Murr, S. M. Gaytan, D. A. Ramirez, E. Martinez, J. Hernandez, K. N. Amato, P. W. Shindo, F. R. Medina and R. B. Wicker, "Metal Fabrication by Additive Manufacturing Using Laser and Electron Beam Melting Technologies," *Journal of Materials Science & Technology*, vol. 28, pp. 1-14, 2012.
- [5] B. Fox, "Rapid Manufacture in the Aeronautical Industry," in *Rapid Manufacturing: An Industrial Revolution for the Digital Age*, N. Hopkinson, R. Hague and P. Dickens, Eds., Chichester, West Sussex: John Wiley & Sons, Ltd, 2006, pp. 221-231.
- [6] J. Wooten, "Aeronautical Case Studies Using Rapid Manufacturing," in *Rapid Manufacturing: An Industrial Revolution for the Digital Age*, Chichester, John Wiley & Sons, Ltd, 2006, pp. 233-239.
- [7] S. Rawal, J. Brantley and N. Karabudak, "Additive manufacturing of Ti-6Al-4V alloy components for spacecraft applications," in *Recent Advances in Space Technologies (RAST), 2013 6th International Conference on*, 2013.
- [8] R. M. Fowler, "Investigation of Compliant Space Mechanisms with Application to the Design of a Large-Displacement Monolithic Compliant Rotational Hinge," Harold B Lee Library, Provo, 2012.
- [9] R. Spielman, "Space Applications," in *Rapid Manufacturing: An Industrial Revolution for the Digital Age*, Chichester, John Wiley & Sons, Ltd, 2006, pp. 241-248.
- [10] J. Halchak, J. Wooten and B. McEnerney, "Layer Build of Titanium Alloy Components for Complex-Geometry Rocket Engine," 2005. [Online]. Available: [http://www.calraminc.com/newsletters/Impeller\\_Paper.pdf](http://www.calraminc.com/newsletters/Impeller_Paper.pdf). [Accessed 10 October 2013].
- [11] Arcam, AB, "EBM® Electron Beam Melting - in the forefront of Additive Manufacturing," [Online]. Available: <http://www.arcam.com/technology/electron-beam-melting/>. [Accessed 17 October 2013].
- [12] L. E. Murr, S. M. Gaytan, A. Ceylan, E. Martinez, J. L. Martinez, D. H. Hernandez, B. I. Machado, D. A. Ramirez, F. Medina, S. Collins and R. B. Wicker, "Characterization of titanium aluminide alloy components fabricated by additive manufacturing using electron beam melting," *Acta Materiala*, vol. 28, no. 5, pp. 1887-1894, 2010.
- [13] Arcam AB, "EBM-Built Materials - way beyond average," Arcam AB, [Online]. Available: <http://www.arcam.com/technology/electron-beam-melting/materials/>. [Accessed 20 September 2013].
- [14] K. H. Rafi, N. V. Karthik, T. L. Starr and B. E. Stucker, "Mechanical property evaluation of Ti-6Al-4V parts made using Electron Beam Melting".
- [15] E. G. Merriam, J. E. Jones, S. P. Magleby and L. L. Howell, "Monolithic 2 DOF Fully Compliant Space Pointing Mechanism," *Mechanical Sciences*, vol. 4, pp. 381-390, 2013.
- [16] B. D. Jensen and L. L. Howell, "The modeling of cross-axis flexural pivots," *Mechanism and machine theory*, vol. 37, no. 5, pp. 461-476, 2002.



# Magnetic Gearing versus Conventional Gearing in Actuators for Aerospace Applications

Gregor Puchhammer\*

## Abstract

Magnetic geared actuators (MGA) are designed to perform highly reliable, robust and precise motion on satellite platforms or aerospace vehicles. The design allows MGA to be used for various tasks in space applications. In contrast to conventional geared drives, the contact and lubrication free force transmitting elements lead to a considerable lifetime and range extension of drive systems. This paper describes the fundamentals of magnetic wobbling gears (MWG) and the deduced inherent characteristics, and compares conventional and magnetic gearing.

## Introduction

Actuators are widely used on satellite platforms and will be a necessity for future space missions. There are numerous potential applications of actuators, such as antenna and solar arrays steering, robotic arms, rovers, and optical instrumentation. Gearboxes with conventional toothed gear wheels are the state-of-the-art solution for such actuator gears. Mechanical gear performance is highly affected by the vacuum conditions and wide temperature range of the space environment [1]. During launch, high vibrational loads and fretting leads to contact adhesion due to wearing-out of solid lubricants. In vacuum, evaporation leads to loss of oil and a subsequent contamination of satellite surfaces or optical components. Additionally, radiation can degrade some polymers or oxidize solid lubricants. Extended temperatures can cause an ineffective lubrication at temperature extremes. However, these gears require some sort of lubrication to maintain functionality throughout their entire lifetime.



**Figure 1. MWG with Hollow Input and Output Shaft**

The problem of compromised lifetime and degradation in gears can be identified as a problem of contacting surfaces and their proper lubrication [1]. In different kinds of gears, sliding contact is a critical issue. Friction losses and wear often limits the efficiency and lifetime. As it is commonly known, lubrication and space tribology are still areas of intense research aimed at reducing the effects of wear and tear. Until now, these harsh environmental conditions and the availability of appropriate lubricants often make it difficult to fulfill these needs in a satisfying manner.

---

\* Karl Rejlek GmbH, Vienna, Austria

## Magnetic Wobbling Gears

No contact, no sliding, no need of lubrication!

This is the simple answer to overcome lubrication problems in general, and particularly in space-related issues. Triggered by an idea for powerful and quiet actuation drives, the MWG emerged several years ago with astonishing properties. Beside quietness, which is not a main focus for space-related applications, the non-contact power transmission particularly seems to match most of the needs in space. Once the problem of lubrication has been overcome due to the lack of lubrication needs, the usual boundaries of conventional gearing no longer exist. Temperature ranges, lifetime cycles, and wear and tear problems are transferred to the question of proper dimensioning of bearings, where well-established solutions exist, starting from few Kelvins in cryogenic temperatures up to a few hundred degrees Centigrade for extended temperature ranges.

### MWG Background

For a short time, conventional gears can be replaced by powerful magnetic gearing systems. In magnetic gears, the traditional load- and friction-bearing elements are replaced by preferably strong permanent magnets to transmit energy. There is absolutely no contact between the acting magnetic surfaces. The gearing parts are friction free and perform consistently without lubrication.

Regarding magnetic gearing in general, there are many different functional principles comparable to those in conventional gears. Besides the proposed MWG system, possible candidates for magnetic gears include magnetic worm gears, magnetic spur gears, magnetic bevel gears, magnetic planetary gears, magnetic cycloid gears and even magnetic superconducting harmonic gears. Table 1 shows a comparison of the performances of torque conversion devices with respect to different criteria.

**Table 1. Comparison of Magnetic Gears**

Torque Conversion Device / Year From: [5]	Torque Density [Nm/l]	Magnetic Syst TD [Nm/l]	Magnetic Syst TD [Nm/kg]	Maximum Torque [Nm]	Torque Stiffness [Nm/rad]	Gear Ratio
Magnetic worm gear / 1993 <sup>[5]</sup>	2	2				
Magnetic spur gear / 1974 <sup>[5]</sup>	20	20				10
Liquid cooled PM BL machine <sup>[5]</sup>	30	30				1
Magnetic planetary gear / 1991 <sup>[5]</sup>	90	90				8
2-stage high ratio magnetic cycloid gear / 2006 <sup>[4]</sup>	75	120				360
1-stage low ratio magnetic cycloid gear / 2006 <sup>[4]</sup>	183	295				20
Harmonic magnetic gear / 2007 <sup>[5]</sup>	110	-				210–860
Magnetic superconducting harmonic drive / 2013 <sup>[3]</sup>	50 – 100	50 – 100				
MWG, Type B (fully magnetic) / 2009 <sup>[2]</sup>	135	350	58	11	250	45
MWG, Type C (fully magnetic) / 2009 <sup>[2]</sup>				11	250	2025
MWG, Type B (fully magnetic) / 2012 <sup>[2]</sup>	170	500	82	50	1250	49
MWG, Type A / 2013 <sup>[2]</sup>		605	110	55	2500	51
MWG, Type A / 2014 (targeted data)			(>110)	(35)	(5000)	120

Selection criteria for the 'best suited in space' magnetic gear are shown in Table 1. As the required amount of space on a satellite platform seems to be of importance, weight is of much higher priority. To get an idea of the magnetic performance, the magnetic system torque density rated in [Nm/kg] describes the amount of material of the magnetic system itself, which is necessary to produce the maximal torque. It consists of magnets and back iron, and defines the weight. This seems to be an effective way to compare the power of different torque conversion devices, including conventional gearing systems as well as magnetic systems in general and magnetic gearing systems alone. This is also a better method than regarding only the magnetic system, rated in [Nm/l], without bearings but including the amount of internal magnetic working range.

### Different Types of MWG

There are several possibilities for setting up a magnetic gear based on wobbling kinematics (Fig. 2). As basic kinematics, a wobbling motion must be generated by a rotating input shaft, which has a cranked region (dash-dotted line) onto which the wobbling bearing (not shown in Fig. 2) is fixed. The outer race of the bearing is coupled with the magnetic wobbling wheel (Wh2, Wh2-3). The input shaft is rotating with the input speed. The wobbling wheel performs the wobbling motion with the same frequency as the input shaft, and has a superimposed rotation with the reduced speed of the output shaft. Both magnetic wheels (Wh1, Wh2) are magnetically coupled over an air-gap and perform the magnetic gearing due to a difference in 'magnetic pole pairs on wheel' numbers between them. The gear ratio in MWG can be computed in the same simple manner as for conventional wobbling gears by substituting the number of teeth with the number of 'pole pairs on wheel'. Whereas the basic kinematics of wobbling gears is the same for all three MWG types, there are some possibilities for generating the actual output shaft rotation. As the wobbling wheel's useful output rotation is superimposed by the wobbling motion, a functional element for 'dewobbling' action is needed for all three MWG types.

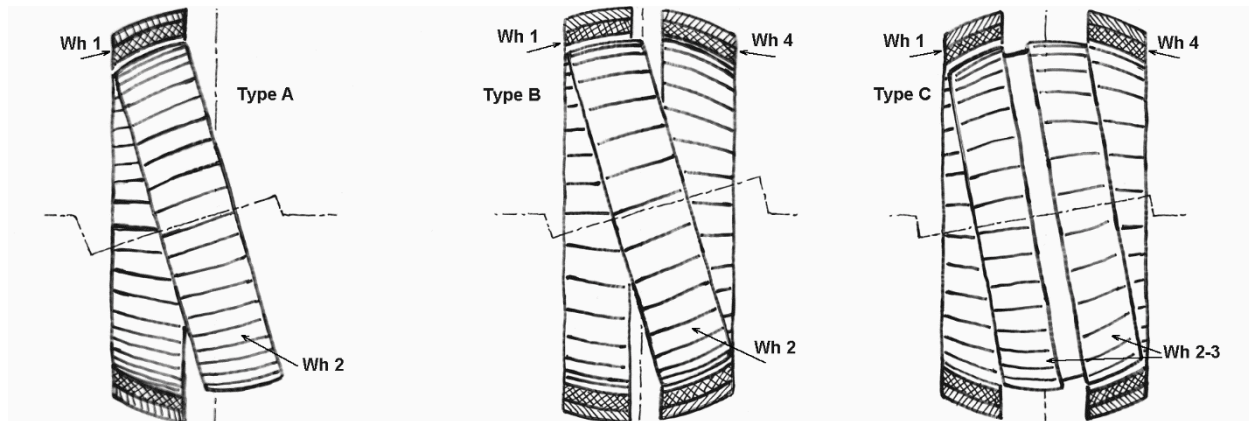


**Figure 2. Working Principle of Three Different Types of MWG**

- Type A consists of two single magnetic wheels. Wheel1 (Wh1) is fixed within the gear housing. Wheel2 (Wh2) generates the output motion by magnetic gearing. The 'dewobbling' motion is done by a universal joint, such as a cardan or a homokinetic joint, coupled between Wheel2 and the output shaft.
- Type B shows a MWG with three different types of magnetic wheels. Whereas Wheel1 and Wheel2 are acting in the same manner as in Type A, Wheel4 (Wh4) is part of the output shaft. The 'dewobbling' motion is performed by the magnetic clutch setup of the wheel-pair Wh2 and Wh4.

- Type C shows an arrangement with four different magnetic wheels, in which Wheel2 and Wheel3 are mechanically fixed and mounted on a common, single wobbling wheel Wh2-3. In contrast to the clutch setup of Type B, the magnetic wheel pair Wh3-Wh4 acts also as a magnetic gearing stage. The whole magnetic setup of Type C provides the possibility of generating extremely high reduction ratios with a squared ratio at the most, if compared to Type A and Type B.

All three types of MWG benefit from a ripple-free smooth output rotation. For space applications, Type A and Type C are the candidates of interest:

- Type A is characterized by one single magnetic coupling between Wheel1 and Wheel2, resulting in maximized torque stiffness, as well as torque density. As MWG can be easily scaled, it is a good choice for gear stages providing strong and powerful output shaft motion.
- Type C benefits from the potential of extremely high reduction ratios in only one single gear stage, and is useful as a small and compact first gear stage for high speed reduction.

### **General Characteristics of MWG**

New properties must be considered when using magnetic gears. Most of these properties are highly favorable and are described in brief below. Some of these are related only to MWG.

- High precision: Magnetic systems in general are known for their extremely precise operation. Because of the absence of mechanical interaction, MWG deliver constant precision in both low and high load cycles. Mechanical backlash is approximately an order of magnitude less than in conventional precision gears.
- Abrasion free: As it is friction free, MWG perform consistently without lubrication.
- Overload friendly: At overload, the magnetic transmission acts naturally as a clutch, but remains fully functional. The elasticity avoids unnecessary stress to related components. The safety clutch is an extremely reliable component and also works without electronics. Hitting an emergency hard end stop after the failure of some control or due to excessive vibrational loads may not result in the degradation of the performance of a mechanism.
- Highly efficient: Magnetic gearboxes offer highly economical energy transfer. Energy conversion is practically seamless: losses via rolling friction and low magnetic hysteresis phenomena are minimal in operation.
- High transmission ratio: Because of the unique concept of MWG, only one gear stage is necessary to achieve high transmission ratios (Type A) or even extremely high ratios (Type C).
- Lifetime: All characteristics are quite constant all over the estimated life cycle and ageing effects are predictable. This is a new feature for gears. Lifetime is only dependent on the lifetime of bearings and not on wear and tear.
- Temperature operating conditions: One temperature limit for magnetic systems is the Curie temperature ( $T_c$ ), in which a material's permanent magnetism changes to induced magnetism. Motors, steppers and also magnetic gears with permanent magnets are affected by this temperature and will lose their permanent magnetism at temperatures exceeding the  $T_c$  limit. The  $T_c$  depends mainly on the composition of materials with different properties and is a material property.
- High-torque capability: The MWG mechanism takes advantage of a constant air gap over the entire active area, which makes it superior to other magnetic concepts (Table 1). The result is a compact design with maximized torque, a crucial precondition for lightweight design.
- Elasticity: The inherent elasticity caused by the magnetic transmission in a powertrain can be very desirable, for example for compliant robotic applications. For other applications such as rigid structures, elasticity may be unacceptable. However, elasticity is a design target and can be influenced within certain limits. Recently, tremendous progress has been achieved (Table 1) by enhancing the torsional stiffness of the output shaft.

### MWG Compared to State-of-the-art Mechanical Gears

Due to different available data of gears it is difficult to compare gears one with another. All data were taken from actual catalogues, and all gears were compared with the same reduction ratios, the same nominal torques and the same operating conditions, if possible.

As seen in [6] and [7], there are many different definitions of torsional loads: 'Limit for momentary peak torque', 'Limit for repeated peak torque', 'Limit for average torque', 'Rated torque at rated speed', or 'Limit for maximum overload torque'. In MWG, there is only one limiting torque, the so-called 'Maximum Torque'. Therefore, the definition of different rated torques is no longer necessary in MWG.

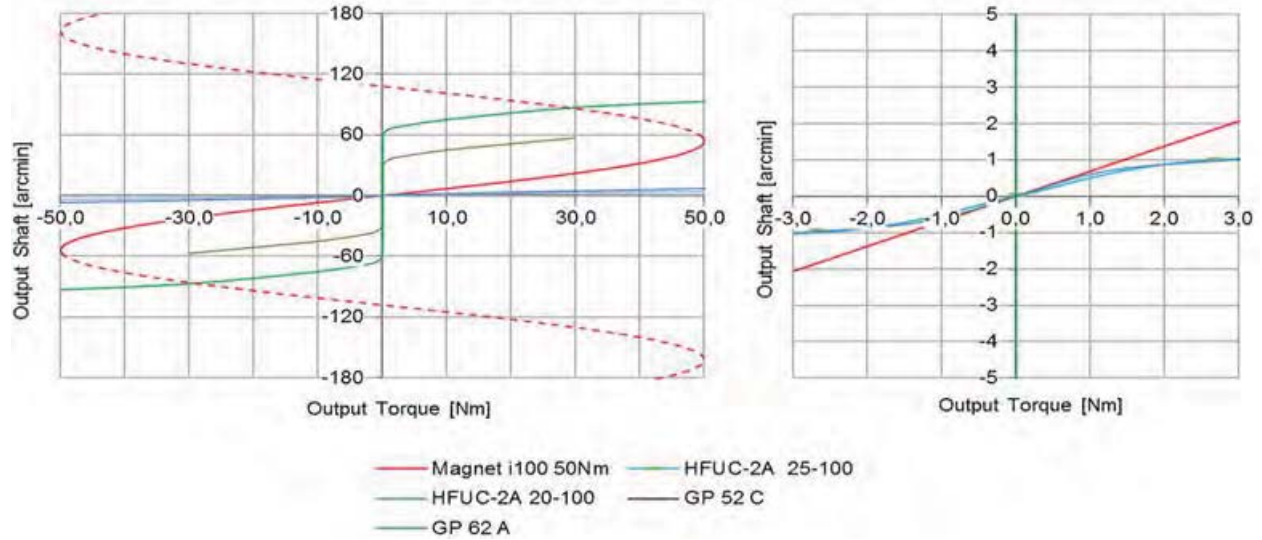


Figure 3. Torsional Stiffness with Blocked Input Shaft at Gear Ratio=100 and Nominal Torque=50 Nm: MWG, HFUC and Planetary Gear

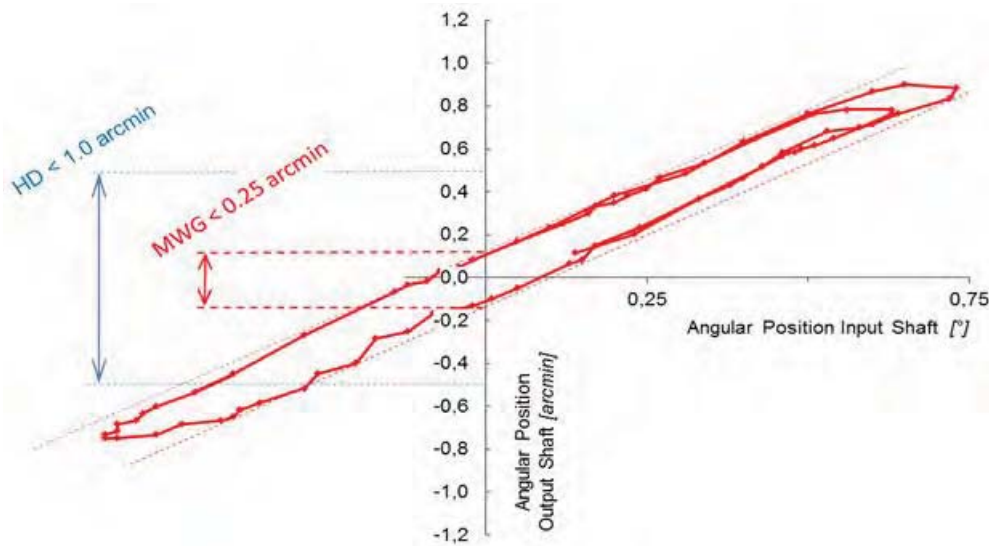
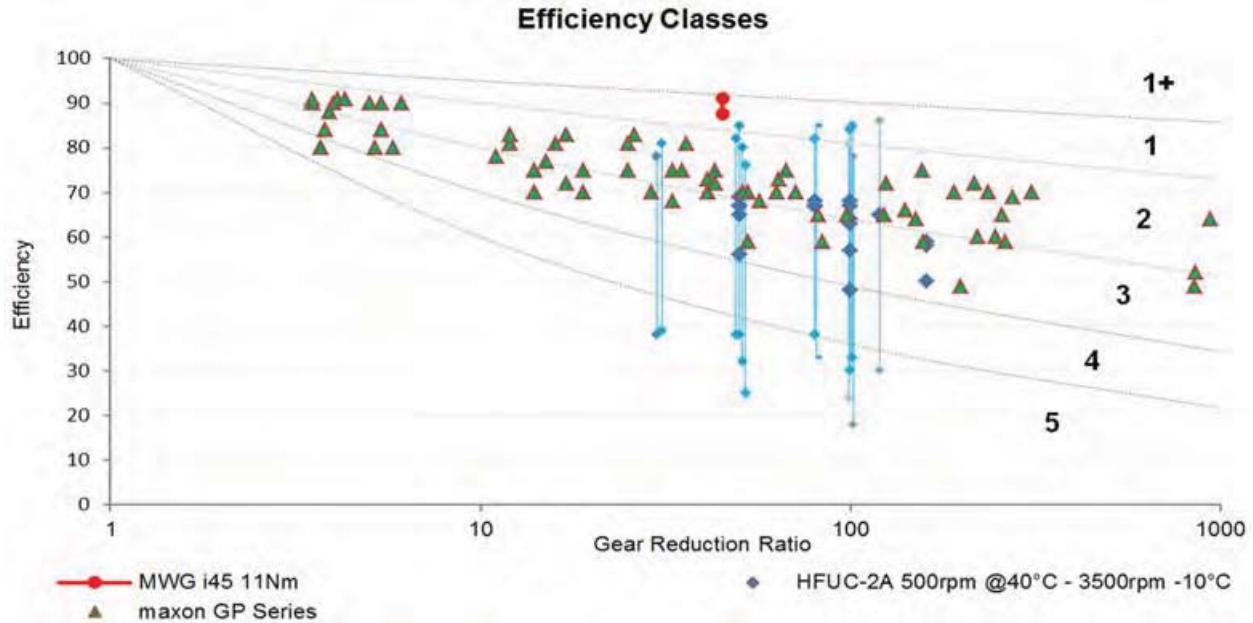


Figure 4. Hysteresis Loss of MWG ( $i=45$ , 11Nm)





**Figure 5. Efficiencies of MWG, HDG and Maxon GP's Series**

The gear can be operated up to that torque at full input speed. If that torque is exceeded (Fig. 3, red dotted line), the output shaft will lose its torsional coupling and the gear will act as a safety clutch, unless the torque has decreased. No harm will result after a one-shot or repeated transgression of the maximal torque.

Torsional operation is the most important task of gears. As seen in Fig. 3, the torsional stiffness is also strongly related to mechanical backlash. Whereas most planetary gears (GP52C, GP62A) have nearly no stiffness in the region of zero torque transition, MWG and HD are nearly free of backlash and therefore can provide a significant amount of torsional stiffness. Although harmonic drive gears (HDG) are overall much stiffer than MWG, one interesting phenomenon around the region of zero torque transition (Fig. 3, right side) can be observed. The 'Lost Motion' in HDG leads to degradation of the torsional stiffness of these gears. In this region, the stiffness of HDG and MWG is approximately the same size. This can be important with respect to resonant frequencies of coupled mechanisms or space applications.

The mechanical backlash or hysteresis loss of planetary gears is considerably bigger than in HDG or MWG. HDG shows a hysteresis loss less than 1 [arcmin], whereas MWG shows even less hysteresis due to its friction-free force transmission (Fig. 4).

After introducing efficiency classes [11], it is easy to compare the efficiencies of various gears with respect to their reduction ratio and operating conditions. MWG shows an energy conversion rate in efficiency class 1 (Fig. 5) within different operating speeds. The planetary gear stages of Maxon GP-series define industrial standard quality (class 2 and 3). HDG can hit the efficiency class 1 but is restricted to optimized operating conditions such as 40°C and low input speed. Lowering the operational temperatures to -10°C, the efficiencies of HDG can reach class 5. This results from the HDG lubrication needs.



## Conclusion

MWG is a gear designed to operate without contact between the force transmitting elements. It therefore overcomes the problem of lubrication and related problems in a new manner. Temperature-dependent lubrication effects, problematic contact stresses on the meshing gearing parts, hardening procedures of teeth and all related problems are no longer existent. The question of lifetime is transferred to the much simpler question of proper dimensioning of bearings. MWG benefits from extended lifetime and from extended operational temperature ranges with fairly constant mechanical properties.

Magnetic gears have less torsional stiffness than conventional, mechanically geared systems. Despite this fact, the torsional stiffness of MWG is partly equal (HDG) or even higher (planetary gears) than in conventional gearing systems. The torque density of MWG is steadily increasing, also lightweight design applications benefit from that new technology. MWG offers a simple internal structure with only a few components, and has the potential as high reduction, high precision gearing system.

MWG and its unique combination of features give way to new prospects in future space applications.

## References

1. Space Tribology Handbook, 5th edition (v2), pp.41 ff. and pp.132 ff., ESR Technology Ltd., 2013
2. Puchhammer, G. (2013). Magnetic Gears – New Approaches in Aerospace Applications, 'Workshop - Electromagnetic Devices in Aerospace Applications', ESA-W13, ESA, Noordwijk, The Netherlands
3. Perez-Diaz, J-L, Diez-Jimenez, E.; MAGDRIVE: 'A Non-Contact Magnetic Superconducting Harmonic Drive', ESMATS 2013, ESA, Noordwijk, The Netherlands
4. Jørgensen, F. T., Andersen, T. O. and Rasmussen, P. O. (2008) The Cycloid Permanent Magnetic Gear, IEEE Transactions on Industry Applications, Vol. 44, No. 6, November/December 2008, pp. 1659 - 1665
5. Hatch, G. P. (2010). Recent Developments In Permanent Magnet Gear Systems & Machines, 'Magnetics 2010 Conference', Lake Buena Vista, Florida, USA
6. General Catalogue, [www.harmonicdrive.de](http://www.harmonicdrive.de)
7. Maxonmotor Catalog, Program 2013/2014



# Flight Testing of a Low Cost De-Orbiting Device for Small Satellites

Dana Turse<sup>\*</sup>, Phil Keller<sup>\*</sup>, Robert Taylor<sup>\*</sup>, Mark Reavis<sup>\*</sup>, Mike Tupper<sup>\*</sup>, Chris Koehler<sup>†</sup>

## Abstract

Use of small and very small spacecraft is rapidly becoming more common. Methods to intentionally de-orbit these spacecraft at the end of useful satellite life are required. A family of mass efficient Roll-Out De-Orbiting devices (RODEO™) was developed by Composite Technology Development, Inc. (CTD). RODEO™ consists of lightweight film attached to a simple, ultra-lightweight, roll-out composite boom structure. This system is rolled to stow within a lightweight launch canister, allowing easy integration to the small satellite bus. The device is released at the end of useful lifetime and the RODEO™ composite boom unrolls the drag sail in a matter of seconds. This dramatically increases the deployed surface area, resulting in the higher aerodynamic drag that significantly reduces the time until reentry. A RODEO™ flight demonstration was recently conducted as part of the Colorado Space Grant Consortium's (COSGC) RocketSat-8 program, a program to provide students hands-on experience in developing experiments for space flight. The experiment was ultimately a success and RODEO™ is now ready for future CubeSat missions.

## Introduction

Operational satellites are at risk from a growing threat of orbital debris generated by satellite explosions and collisions. There are currently 19,000 objects larger than 10 cm being tracked by the U.S. Space Surveillance Network and an estimated 500,000 particles between 1 and 10 cm in diameter that are hazardous to satellites but are too small to be tracked.<sup>1</sup> The risk of orbital debris is also self-propagating, as the recent collision of the Iridium 33 communications satellite and the derelict Russian Cosmos 2251 satellite demonstrated by generating more than 500 pieces of debris large enough to be tracked.<sup>2</sup>

Addressing this concern, NASA has created a specification that requires all new satellites to launch with a known reentry plan. According to NASA technical standard NASA-STD-8719.14, "Process for Limiting Orbital Debris", one of the three options for disposal includes atmospheric reentry where 1) the space structure is left in an orbit in which natural forces will lead to atmospheric reentry within 25 years after completion of the mission; or 2) the space structure is maneuvered into a controlled de-orbit trajectory as soon as practical after completion of mission.<sup>3</sup>

However, the challenge faced by many small satellite mission teams is that small satellites are often designed for rideshare opportunities without full knowledge of the final orbit where they will be placed. In this case, the mission team must assume the highest possible orbit for calculation of the de-orbit time. Also, many small satellites have high mass-to-area ratios because they are designed with body-mounted solar arrays and minimal other deployable structures, such as a whip antenna. This lack of deployed area combined with a high possible orbit can lead to de-orbit times in excess of the NASA standard.

To enable small satellites to meet the 25-year requirement, CTD has developed a family of highly mass efficient Roll-Out De-Orbiting devices (RODEO™). Depicted in Figure 1 is a 3U CubeSat version of the RODEO™ de-orbit system. RODEO™ consists of lightweight film deployed and supported by a simple roll-out composite boom. RODEO's dramatic increase in the deployed surface area significantly reduces the time until reentry for satellites within low earth and elliptical orbits.

---

<sup>\*</sup> Composite Technology Development, Inc., Lafayette, CO

<sup>†</sup> Colorado Space Grant Consortium, University of Colorado, Boulder, CO

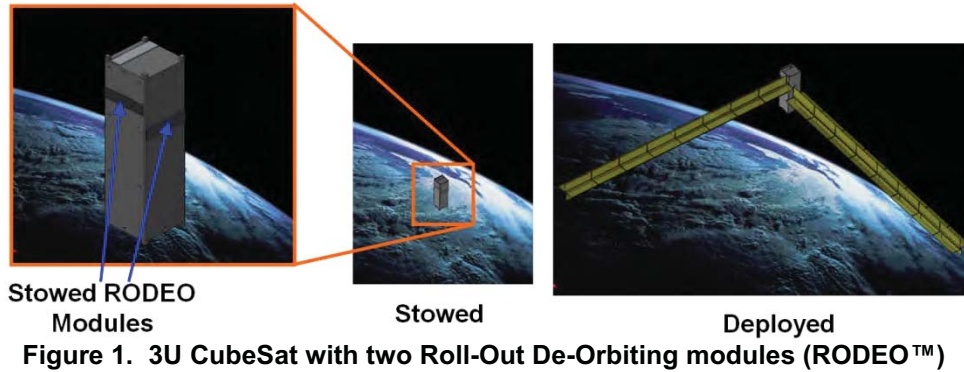


**Figure 1. 3U CubeSat with two Roll-Out De-Orbiting modules (RODEO™)**

### RODEO™ Overview

RODEO™ is a “turn-key” self contained de-orbiting system with everything required to operate the system included within each RODEO™ canister. This includes the composite roll-out boom fitted with robust thin film drag sail material, and the operational electronics with a built-in timing system and batteries. The mechanical system is extremely simple with a very low mechanical part count and complexity. The use of a high specific stiffness carbon fiber reinforced composite boom minimizes system mass yet provides a very robust deployed structure. The electronic system is also simple, providing an intentional release circuit and a timed release circuit. The timed release will execute if end-of-life is detected by a lack of power to the charging circuit for a preset amount of time.

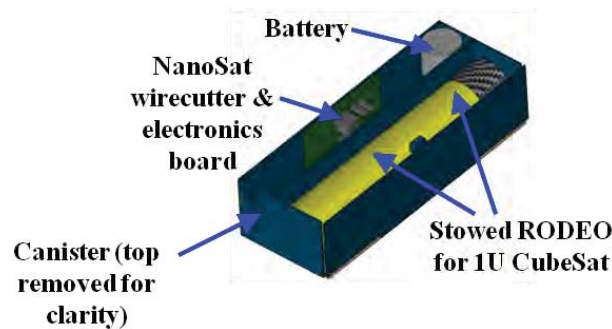


**Figure 2. Stowed CubeSat RODEO™**

Fundamentally the RODEO™ structure is easily scaled in length and width and has an extremely high packaging efficiency (greater than 100:1) allowing for integration upon “under-utilized” portions of the spacecraft, such as behind deployable solar panels.

#### Multifunctional Composite Slit-Tube Boom

The key technology for RODEO™ is the rolled composite boom. CTD has developed a wide variety of deployable composite slit-tube booms that range from 12.7 mm (0.5 in) to 127 mm (5.0 in) diameter (see Figure 3) and up to 23 meters (75 ft) in length. Common to all of these structures (including the RODEO boom) are robust composite slit-tube booms that can be flattened and rolled for storage (see Figure 4). This method of stowage and deployment is highly efficient, allowing large structures, in comparison to the spacecraft, to be stored within very small volumes. The material and composite laminate properties of rollable composite booms are highly tailorable and can be optimized to meet the specific requirements for a given application. Additionally, because the boom and drag sail are rolled together in one piece, the mechanical system has a very low part count with minimal complexity.

The RODEO™ boom is self deploying, meaning the stored strain energy of the packaged boom provides the necessary deployment force. The design of such a boom is challenging since the composite must survive the mechanical strain of being stowed within a very small volume, while also having adequate

deployment torque and significant axial stiffness upon deployment. The multi-functionality of the boom results in minimal parasitic mass, stowed footprint, and cost, making these booms attractive for a variety of applications, including within roll-out de-orbit devices.

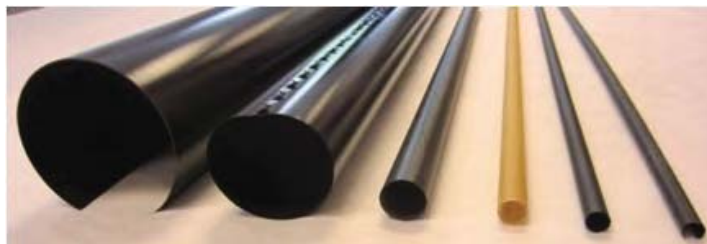


**Figure 3. Wide range of deployable slit-tube booms developed by CTD**



**Figure 4. Deployable composite slit-tube boom used for RODEO™**

#### Concept of Operations

Inside the RODEO™ housing, CTD has included a very simple electronic circuit board and battery. The board only has two inputs and a ground wire. The first input is to initiate a commanded release by supplying spacecraft voltage. The second input supplies a very small trickle charge to the battery and resets a timer circuit so that RODEO™ will remain stowed. However, if the spacecraft loses functionality and stops supplying the trickle charge, the timer circuit initiates and begins counting. After a pre-determined period of time with no trickle charge supplied, the timer circuit executes an automatic command to deploy the RODEO™ drag sail. Once the command to deploy is sent (either manually or via the timer circuit) an internal hot wire will release the spring-loaded hinged door, and the RODEO™ de-orbit wing will deploy. Deployment occurs via the single-degree of freedom composite roll-out boom that is restrained by the hinged door of the RODEO™ canister.



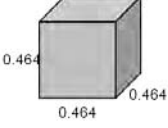
#### RODEO Sizing

To demonstrate the benefits of RODEO™, CTD ran an orbital decay analysis using NASA's DAS 2.0 software in order to identify the minimum surface area required to de-orbit each size of satellite. This RODEO™ sizing analysis has been summarized in Table 1 for a 25-year reentry timeframe, and is based on a 700-km circular orbit. Table 2 provides estimates for volume and mass for the three RODEO™ systems assessed.

### **RocketSat-8 X Flight Experiment**

RocketSat-8 was the eighth RocketSat student project at the Colorado Space Grant Consortium (COSGC) since the program began in 2006. RocketSat-8 flew as part of the national program called RockSat-X. This program allows university-level students to fly experiments on board a sub-orbital rocket launched out Wallops Flight Facility each August. The flight reaches an altitude of approximately 160 km and provides experiments with full access to the space environment including 30 to 180 seconds of stable microgravity. Experiments also have access to power and telemetry. There is a fee to fly on the flight, which helps foster partnerships with industry, universities, and students. CTD partnered with COSGC to develop the RODEO™ experiment, enabling the students to cover their required fee to fly. Students worked side by side with engineers from CTD in the development of RODEO™. The experience in developing RODEO™ with CTD enriched the experience for each of the students involved.

**Table 1. Required RODEO sizes for 25-year reentry**

System	Satellite Mass (kg)	RODEO Area
3U CubeSat 	6.00	0.150 m <sup>2</sup>
Nanosatellite 	15.0	0.526 m <sup>2</sup>
ESPA-Class Small Satellite 	100	3.74 m <sup>2</sup>

**Table 2. Estimated volume and mass for three RODEO™ configurations**

Satellite	RODEO Performance Metrics	
	Stowed Volume	System Mass
3U CubeSat (6kg)	140 cm <sup>3</sup>	96 g
Nanosatellite (15kg)	175 cm <sup>3</sup>	131 g
Small Satellite (100kg)	270 cm <sup>3</sup>	472 g

Flight Configuration

For the flight design, CTD selected a RODEO™ that would provide approximately 0.15 m<sup>2</sup> deployed surface area, enough area to de-orbit a 3U CubeSat in a period of 25 years (see Table 1). This area is achieved using three pop-out “wings” from a central 127-cm diameter boom as pictured in Figure 5. The wings are formed 120° apart to provide area in multiple planes. Structural “battens” bonded to the backbone of the boom and extending out to the edge of the Mylar are used to support the wings and enforce the deployed position. These battens are flexible and allow the three wings to be wrapped around to one side of the boom and stacked for stowage, as can be seen in Figure 6.

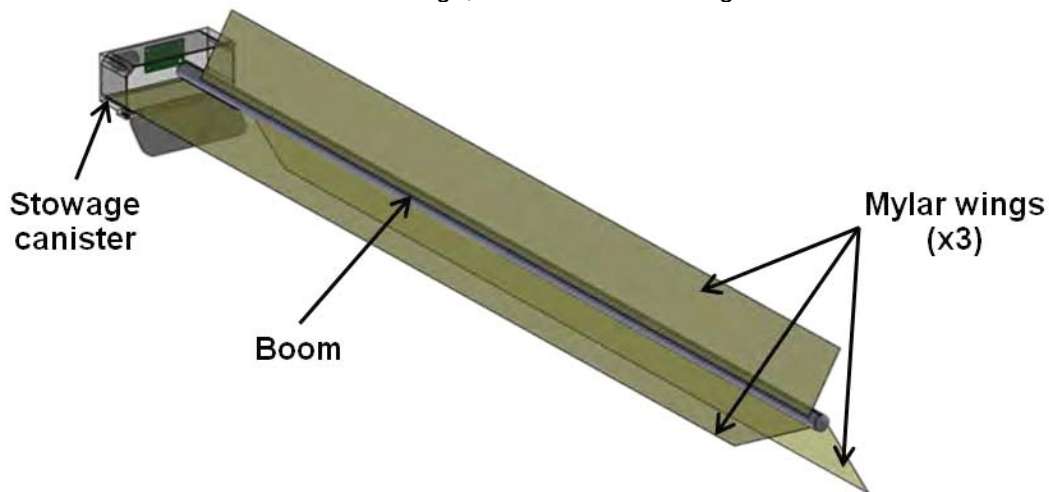


**Figure 5. 3U CubeSat RODEO™ configuration**





**Figure 6. Stowage of 3U CubeSat RODEO™ model**



**Figure 7. Deployment progression for 3U CubeSat RODEO™**

The stowed RODEO™ is held constrained within an aluminum box with a hinged door (see Figure 6). When the door is released, RODEO™ deploys in less than 1 second (see Figure 7). The flight hardware was fabricated using space-qualified materials. Multiple stowage/deployment cycles were completed in CTD's laboratory. The RODEO™ was found to deploy reliably without any deployment snags, or stalls.

#### Flight Testing

On August 13, 2012 RockSat-8 was lofted to an altitude of approximately 160 km above the Atlantic Ocean before landing via parachute about 145 km from the Wallops Flight Facility. The payload was recovered and high definition video of the RODEO™ experiment was retrieved from the payload. The video showed a complete, but off-nominal deployment. The deployment was slower than expected but continued in short bursts until reaching full deployment. Images from the RODEO™ flight experiment are pictured in Figure 8.



**Figure 8. Images from RODEO™ flight experiment**

This anomalous deployment was shown to be caused by moisture saturation in the composite boom. In the dry environment of Colorado, the boom always deployed nominally. When the students from the COSGC took their 2012 RockSat-8 payload, including RODEO™, to Wallops, located on the very humid coastal region of Virginia, they found that the RODEO™ boom did not deploy properly in final system tests and checks prior to integrating the payload into the rocket. CTD determined that the high humidity caused the composite to absorb moisture, plasticizing the resin and significantly reducing the stiffness and stored strain energy of the boom. The effect was duplicated in laboratory conditions and is completely reversible. The boom would deploy as expected after drying out.

The moisture issue was discovered two weeks before payload integration. To mitigate the issue, desiccant was packed within the RODEO™ canister to keep it dry for several days during launch preparation. Unfortunately, the launch was delayed by several weeks and the desiccant became saturated, allowing RODEO™ to also become saturated with moisture. As a result, the boom did not immediately deploy. However, the multiple starts and stops observed indicated that as the outer layers of the boom dried out, the boom was gradually able to reach full deployment.

Moisture would not be an issue for a CubeSat or small satellite mission since the boom would have ample time (months to years) to completely dry out in the hard vacuum of space prior to deployment. In addition, CTD has since incorporated a different moisture-resistant polymer matrix into the boom and has shown that deployment is no longer affected by moisture.

### **Conclusions**

The most responsible and proactive method of mitigating orbital debris caused by small and very small spacecraft is to incorporate an effective de-orbit device. To this end, CTD has developed RODEO™; a family of ultra-lightweight de-orbiting devices. All RODEO™ devices are capable of de-orbiting both functional and non-responsive satellites within NASA's required timeframe. RODEO™ modules utilize extremely lightweight, mass efficient composite slit-tube boom elements to deploy the drag film in a controlled, reliable fashion.

CTD recently worked with the Colorado Space Grant Consortium to demonstrate a RODEO™ deployment on a suborbital platform as part of the RocketSat-8 experiment. While high-definition video taken during the experiment showed that RODEO™ did eventually deploy, the deployment was off nominal. Moisture contamination was found to be the cause, which was only an issue for the sub-orbital demonstration due to the very short duration of the flight. At this point, RODEO™ is ready for future CubeSat missions.

### **References**

1. NASA Orbital Debris Program Office, <http://orbitaldebris.jsc.nasa.gov>
2. Iannotta, Becky and Makil, Tariq, "U.S. Satellite Destroyed in Space Collision," [space.com](http://space.com), February 11, 2009
3. NASA technical standard NASA-STD-8719.14, obtained from <http://www.hq.nasa.gov/office/codeq/doctree/871914.pdf>

# Deployment Methods for an Origami-Inspired Rigid-Foldable Array

Shannon A. Zirbel<sup>\*</sup>, Brian P. Trease<sup>\*\*</sup>, Spencer P. Magleby<sup>\*</sup> and Larry L. Howell<sup>\*</sup>

## Introduction

The purpose of this work is to evaluate several deployment methods for an origami-inspired solar array at two size scales: 25-meter array and CubeSat array. The array enables rigid panel deployment and introduces new concepts for actuating CubeSat deployables.

The design for the array was inspired by the origami flasher model (Lang, 1997; Shafer, 2001). Figure 1 shows the array prototyped from Garolite and Kapton film at the CubeSat scale. Prior work demonstrated that rigid panels like solar cells could successfully be folded into the final stowed configuration without requiring the panels to flex (Zirbel, Lang, Thomson, & al., 2013). The design of the array is novel and enables efficient use of space. The array can be wrapped around the central bus of the spacecraft in the case of the large array, or can accommodate storage of a small instrument payload in the case of the CubeSat array. The radial symmetry of this array around the spacecraft is ideally suited for spacecraft that need to spin.

This work focuses on several actuation methods for a one-time deployment of the array. The array is launched in its stowed configuration and it will be deployed when it is in space. Concepts for both passive and active actuation were considered.

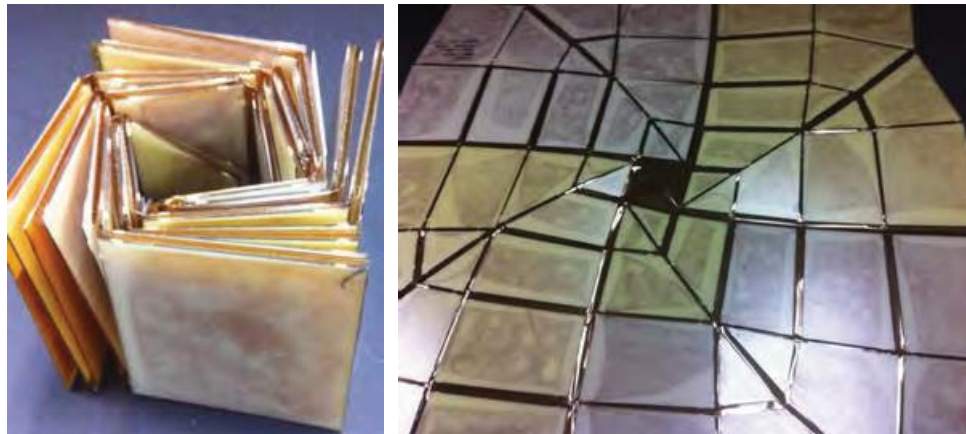


Figure 1. (left) Folded form of the four-sided CubeSat array. (right) Deployed configuration

## Actuation Concepts

Several methods of actuation have been explored, including a motor-driven perimeter truss, pneumatic actuation, centripetal acceleration, stored strain energy, and thermal activation (with a shape memory plastic). Because of the size of the panels in the 25-meter array, the perimeter truss is desirable to support the deployment motion. For the CubeSat array, a less bulky actuation method is preferable. Pneumatic actuation, centripetal acceleration, stored strain energy, and thermal activation of a shape memory plastic were demonstrated at that scale.

---

<sup>\*</sup> Department of Mechanical Engineering, Brigham Young University, Provo, UT

<sup>\*\*</sup> Jet Propulsion Laboratory, Pasadena, CA

### Motor-driven perimeter truss

A scale model of an array and truss, shown in Figure 1, were prototyped to demonstrate the functionality and interaction of the two. The truss was SLA-printed, the connecting flexures were 3D-printed in Nylon, and the array was prototyped from Garolite and Kapton. Astromesh, which has a motor-driven actuation, is flight-proven and would likely be used in the final design, should the array be selected for a flight project. Since our objective is primarily to show the interface between the array and the truss, we have sought to imitate the deployment of the AstroMesh without motorizing the model.



**Figure 2. Partially opened model of the array and truss**

Torsion springs, shown in Figure 3, were attached to the truss to bias the truss open; i.e., the springs are deflected when the array and truss are stowed. This method of stored strain energy makes the array self-deploy; however, we've guided the deployment to mimic motorization. The goal was to demonstrate a fixed rate of extension for each of the six sectors of the array. There is some clearance in the joints that prevent the truss from being a single-degree-of-freedom system, and therefore must be actuated at several points to deploy synchronously. When the center of the array is fixed, the truss rotates around the fixed point about 1.5 times to deploy the array.



**Figure 3. Torsion springs were affixed to the truss to bias the truss open**

We considered two different attachment points on the array: directly on the panels or at the membrane between panels. To avoid ripping the Kapton film, we opted to attach directly to the panels. The challenge with attaching to the panels is that they undergo a complex rotation from the deployed to stowed position.



The joint needs to undergo a 90° torsion as well as bend 90° to one side. We chose a serpentine flexure, shown in Figure 4, to accomplish this rotation.

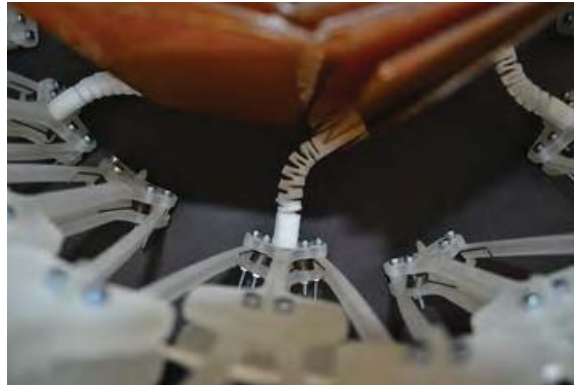


**Figure 2. Serpentine flexures enabled the complex motion needed to connect between the truss and the array**

The primary drawback of this joint is that it doesn't constrain any degrees of freedom. However, it does allow the complex rotation and allows for some extension of the joint as the distance between the array and the truss isn't necessarily constant, especially considering the rotation of the panels. Having a compliant joint that can accommodate that change in distance as well as complete the two-axis rotations is beneficial. In fact, it enables the two to interface.

The flexures are secured to the truss with screws. We opted to glue the flexures to the panels, although they could also be pinned or bolted to the panels. There is some slight interference with the ends of the flexures and the final folded form of the array (i.e., the outermost panels cannot sandwich perfectly flat against each other).

We tested a cable-driven actuation method on a portion of the bays from the perimeter truss, shown in Figure 5. The cable-driven prototype has a good mechanical advantage when the input cable is perpendicular to the truss members, but the low transmission angle that occurs when the bays are fully stowed results in binding if the actuation cable is pulled straight down.

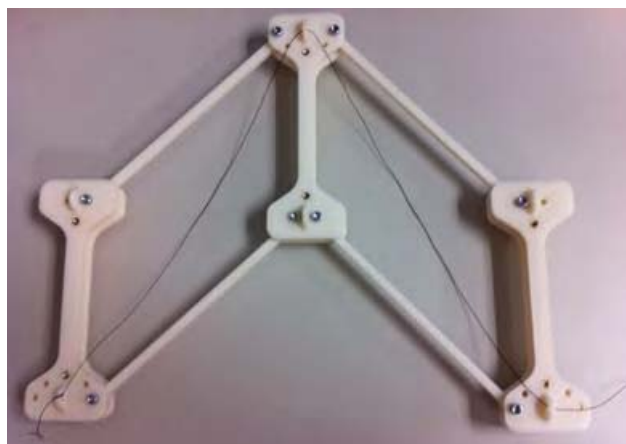


**Figure 3. Cable-driven actuation on a few bays from the square truss**

### Pneumatic actuation

For pneumatic actuation, a plastic bladder was adhered to the back of the array and inflated with compressed air. If the bladder were designed to be air tight, it would remain inflated after the array opened and provide a semi-stiff support for the array.

### Centripetal acceleration

Centripetal acceleration is the easiest to implement, as it can be accomplished by spinning the satellite. We demonstrated a concept for centripetal acceleration using a central torsion spring.

A torsion-spring deployer, shown in Figure 6, was prototyped to actuate the array. The array fits snugly over the small hexagon to hold it in place as the spring is displaced. We have demonstrated a rapid deployment of the small arrays with the centripetal acceleration from the torsion spring, as it is released.

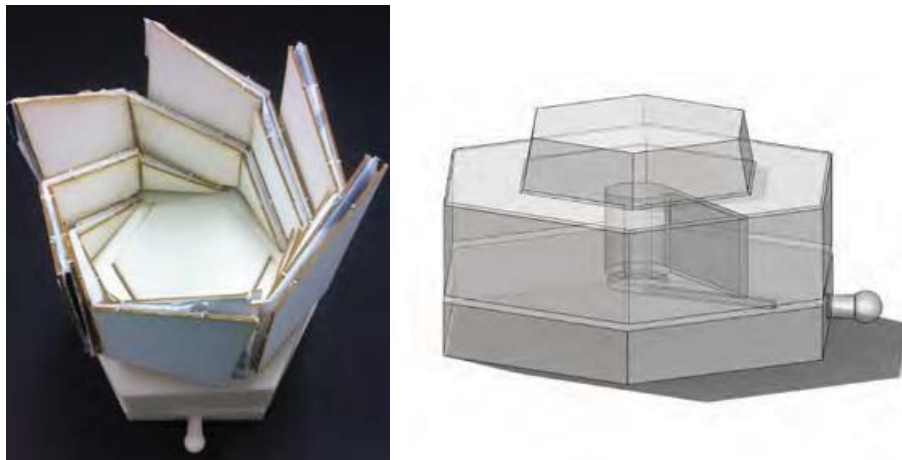


**Figure 4. (left) Prototype of the torsion spring test base with array. (right) Translucent rendering of CAD model, showing the cavity for the torsion spring**

### Stored strain energy

Strain energy can be stored in the array in a variety of ways. One approach evaluated at the CubeSat scale is to affix tape springs radially along each sector. The prototype array opened quickly, but did not lay perfectly flat; therefore, a mechanism to lock the panels in their deployed configuration may be desirable.

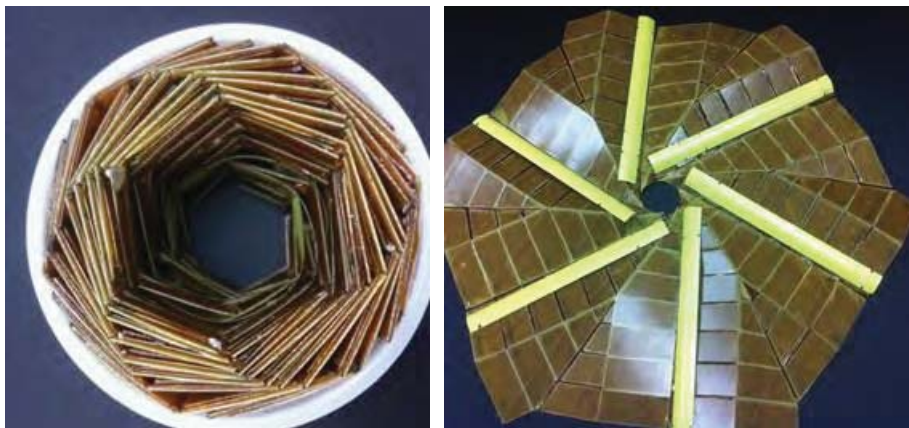


**Figure 5. (left) Stowed configuration of the array with radial tape springs. (right) Deployed configuration**



### Thermal activation

Shape memory polymers (SMPs) are specialized plastics with a low transition temperature (relative to its melting temperature), at which the plastic becomes malleable and can be molded into a new shape. When cooled, the plastic retains that new shape until heated again past its transition temperature. We experimented with 0.79-mm (1/32-in) thick sheets of shape memory plastic as a means of actuating a deployable solar array, as can be seen in Figure 8.

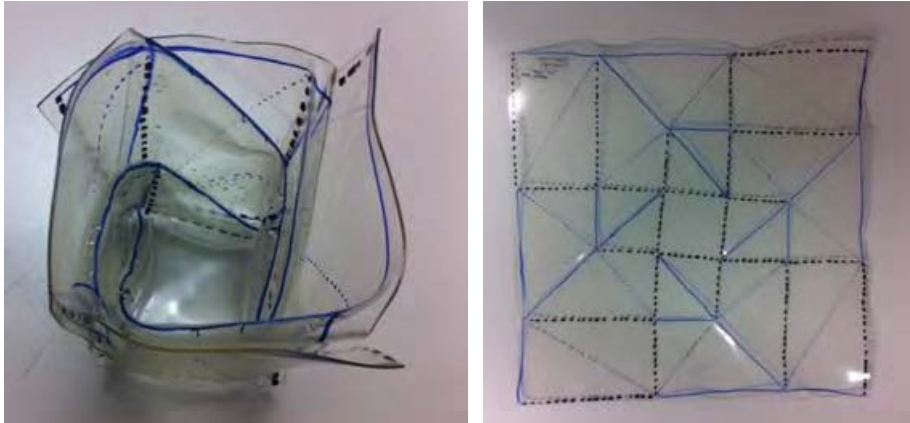


**Figure 6. (left) The shape memory plastic folded into a quad-flasher. (right) Deployed configuration**

The shape memory plastic can be folded into the pattern for the array and then thermally activated to return to the flat (or deployed) configuration. Alternatively, strips of the plastic can be affixed to the rows of panels that wrap around the central bus, rather than having the shape memory plastic cover the entire back surface of the solar array. This reduces the material thickness that must be added to the array, but may complicate the thermal activation if the strips are fully isolated from one another. As the added volume of the SMP to the array is very slight, this method of actuation has potential application to deployable arrays on CubeSats or other small satellites, where volume is especially critical.

### **Lessons Learned**

Once deployed, certain methods of passive actuation (such as centripetal acceleration and stored strain energy) may require an additional mechanism to lock the panels into their deployed state to keep the array flat. As uncontrolled methods of deployment are undesirable, such a latching mechanism is necessary to reduce the chance for failure with these methods of actuation.

For communications applications, the requirements for the final shape are more stringent than for some other applications. At this stage, the flatness of the final deployed configuration has not been evaluated, but the latching mechanism described above could provide a solution to keep the panels at a consistent flatness.

During testing, we observed that some of the actuation methods caused strong vibration loads on the panels. This was especially the case for the centripetal acceleration method and stored strain energy method, but was also observed to a lesser degree in the pneumatically actuated model. Further analysis and selection of final materials are needed to determine how detrimental these vibration loads will be to the structure and wiring.

If thermal activation of a shape memory polymer can be achieved for in-space deployment, this method will be most promising for the CubeSat array. The actuation is slow enough to not induce vibration loads in the panels, and the material has a thin profile which takes up little of the constrained volume.

## References

Lang, R. (1997). *Origami in Action*. St. Martin's Griffin.

Shafer, J. (2001). *Origami to Astonish and Amuse*. St. Martin's Griffin.

Zirbel, S., Lang, R., Thomson, M., & al., e. (2013). Accommodating Thickness in Origami-Based Deployable Arrays. *Journal of Mechanical Design*, Vol. 135, paper no. 111005, DOI: 10.1115/1.4025372.

# ROPEC – ROTary PERcussive Coring Drill for Mars Sample Return

Philip Chu\*, Justin Spring\* and Kris Zacny\*

## Abstract

The ROTary Percussive Coring Drill is a light weight, flight-like, five-actuator drilling system prototype designed to acquire core material from rock targets for the purposes of Mars Sample Return. In addition to producing rock cores for sample caching, the ROPEC drill can be integrated with a number of end effectors to perform functions such as rock surface abrasion, dust and debris removal, powder and regolith acquisition, and viewing of potential cores prior to caching. The ROPEC drill and its suite of end effectors have been demonstrated with a five degree of freedom Robotic Arm mounted to a mobility system with a prototype sample cache and bit storage station.

## Introduction

The mobility platform for the recently announced surface mission to Mars launching in the year 2020 is based on the Mars Science Laboratory rover [1]. This rover will conduct rigorous in-situ science assessments of the Martian surface with the goals of characterizing the local geology, looking for signs of an ancient habitable environment, and searching for signs of ancient life on the red planet. In addition to these science goals, the Mars 2020 mission will also acquire a number of physical samples, storing them within a sample cache for potential return to Earth at a later stage. These samples will likely include rock cores, regolith samples, and atmospheric gas. The ROTary PERcussive Coring (ROPEC) Drill has been designed to meet the needs of a Mars Sample Return mission by providing a platform that can produce rock cores, powder and regolith samples, and can abrade the surface of rocks. This last function serves to remove the weathered layer and expose a fresh rock face similar to the Rock Abrasion Tool on the Mars Exploration Rovers [2]. These functions are accomplished using a variety of bits, most of which can then be inserted into a Sample Cache within the rover body for storage.

The ROPEC Drill is the latest in a series of rock coring mechanisms aimed at planetary exploration developed by Honeybee Robotics over the past two decades [3]. The ROPEC Drill design builds on previous drilling systems such as the Mini Corer, Corer Abrader Tool, and SASSI Drill; improving upon them to achieve a light weight, compact, and highly capable mechanism. This drill can be mounted to a multi-degree of freedom robotic arm similar to the Instrument Deployment Device on the Mars Exploration Rovers or the Robotic Arm on the Mars Science Laboratory. A robotic arm is used to place the ROPEC drill on the desired rock target, holding the drill in position using a pair of preload tines. The ROPEC Drill then utilizes a rotary percussive action which can penetrate a wide range of rock targets ranging from high strength basalts to highly porous low strength sedimentary rocks. Once the drill has reached its target depth, an internal mechanism shears the rock core at the base of the drill bit. This shearing action simultaneously separates the core from the base rock and captures the core within the bit; preventing it from falling out while the bit is retracted from the rock. The entire drill bit, with rock core inside, can then be delivered to the Sample Cache.

This paper focuses on lessons learned throughout the design and development of the ROPEC Drill, as well as distinctive design features and the decisions and testing that contributed to their final implementation. There are a number of unique design features on the ROPEC Drill which should be brought to the attention of the spacecraft mechanisms community. These features could be used on future space flight mechanisms and prototypes. An overview of the ROPEC Drill and its operational usage

---

\* Honeybee Robotics Spacecraft Mechanisms Corporation, Pasadena, CA

is discussed below, followed by details of the design which are critical for understanding the lessons learned and any unique mechanism features. The objective of this publication is to provide detailed information on the design of the ROPEC Drill, focusing on educating future mechanism designers of similar devices. This work was funded by the National Aeronautics and Space Administration (NASA) Planetary Instrument Definition and Development Program.

### Driving Requirements

The ROPEC drill is designed to support a “One Bit-One Core” approach to delivering rock samples to a sample return canister [4]. This method dedicates a single drill bit to the acquisition of each returned rock core, as shown in Figure 1. After the core has been separated from the base rock and captured within the drill bit, the entire bit is delivered to and stored within the sample cache in an enclosed casing, to ultimately be returned to Earth. This method simplifies the process of caching rock cores by eliminating additional mechanisms required to extract rock cores from drill bits and place them within sealed canisters. The “One Bit-One Core” technique lead to one of the driving requirements on the ROPEC drill which was the ability to autonomously change end effectors. Since each core would have a dedicated drill bit for sample caching, the ROPEC drill and its bits have been designed with dedicated tool change features. This also allows for alternate end effectors, such as the Rock Abrasion Brushing Bit (RABBit), Powder and Regolith Acquisition Bit (PRABit), and Core PreView Bit. The ability to change bits drives many aspects of the ROPEC design.

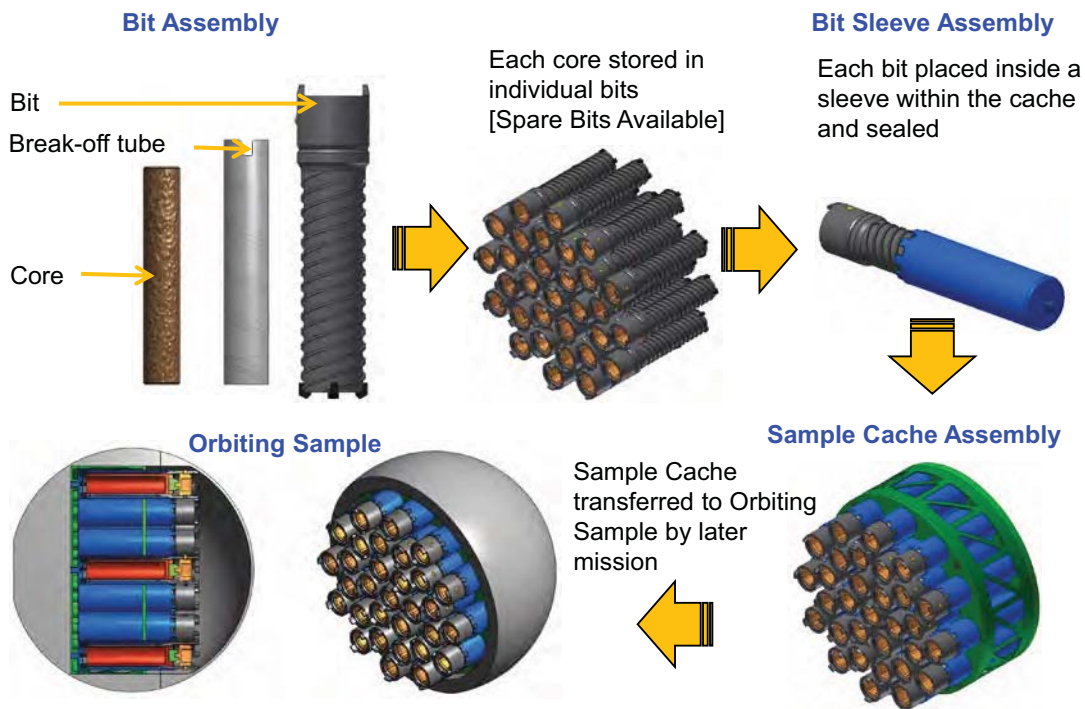


**Figure 1. “One Bit One Core” Mars Sample Return Architecture**

The “One Bit-One Core” architecture also requires that each drill bit be as light weight and volume efficient as possible to ensure that they could be returned to Earth at a later stage. At present, the return of the cached samples has not been explicitly defined as a mission by NASA. However, if approval for the mission is obtained, it will likely consist of two separate missions [5]. The first mission will consist of a Lander, Fetch Rover and a Mars Ascent Vehicle. Landing close to the sample cache, the small Fetch Rover would drive to the cache, retrieve it, and return it to the Lander, where it would be placed inside the Orbiting Sample (OS) within the Mars Ascent Vehicle (MAV). The MAV would then launch from the

surface, escape Martian gravity, and jettison the OS into Mars orbit. The second mission would retrieve the OS some time later and return it to Earth onboard an Earth Entry Vehicle. While the design of the MAV has not been finalized, Volume and Mass dedicated to the Sample Cache and OS is likely to be highly constrained. This drives the Bit Assembly to be as small in diameter and length and as low mass as possible. The small form factor of the bit is a significant driver on the allowable size of internal components within the ROPEC drill.

An animation showing this Mars Sample Return architecture is available at the following URL:  
<http://www.youtube.com/watch?v=NphWPvi9cy4>

Another driving requirement on the ROPEC design was the ability to lock the Auger stage rotation position during the Core Breakoff routine. Previous coring drill designs have had difficulty shearing rock cores, particularly in high strength igneous rocks. It was found that rotation of the bit inner shearing tube within the main drill bit would sometimes cause the latter to rotate with the shearing tube due to friction between the tubes overcoming the Auger actuator holding torque. This would negate the breakoff effect, and simply cause the entire bit to spin around the rock core, which was still attached to the base rock. For this reason, the SASSI drill was the first coring drill to implement an Auger Locking Mechanism to lock the position of the Auger during the breakoff sequence. This requirement has since been implemented on the ROPEC drill and all other Honeybee Robotics coring drills that use the eccentric tubes method of breaking off rock cores. This requirement is a significant design driver for the ROPEC drill.

Lessons learned from previous Honeybee Robotics developed coring drills suggested that the core breakoff mechanism worked well in shearing the rock core from the base rock, but that core quality needed to be improved in order to maximize science return. Figure 2 illustrates a number of different rock cores collected using Honeybee Robotics' SASSI Drill, showing the range of core quality obtained. While core quality depends on a number of different factors including rock type, internal bit clearance and cutter design, one of the ways to minimize the chance of low grade cores is to couple the Bit Breakoff Tube rotation with respect to the Bit Auger Tube during drilling. These two are then decoupled during the core breakoff routine so that the Bit Breakoff Tube can be rotated with respect to the Bit Auger Tube. The SASSI drill did not initially have this capability and thus was more likely to produce lower quality cores. The prerequisite to couple and decouple these tubes within the drill bit is one of the driving requirements in the ROPEC design. This eccentric tube core breakoff mechanism is explained in further detail in the following sections.

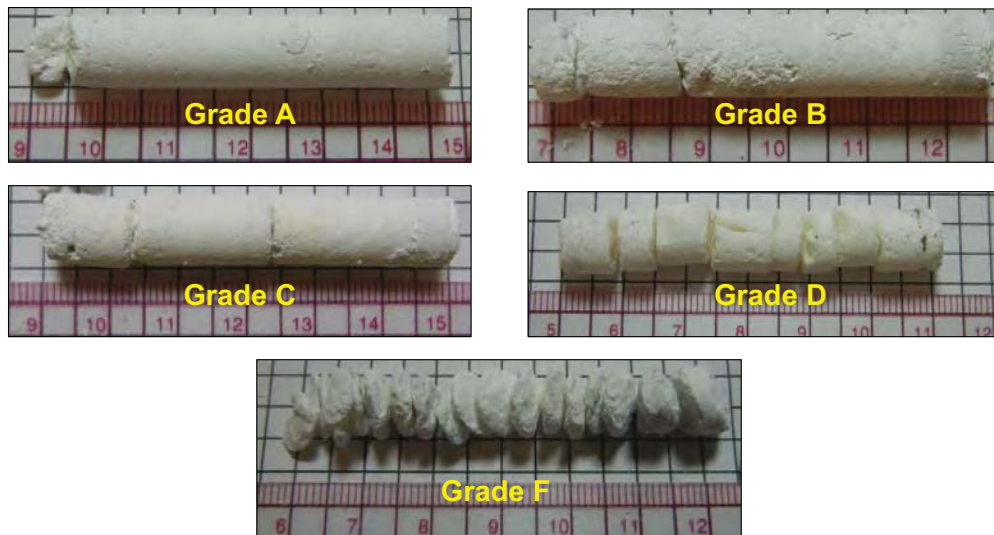


**Figure 2. Core Quality Grading Scheme**

Another significant design driver is the ability to separate the Auger rotary drivetrain from the Percussive hammer system. Rotary only drilling is ideal for weak rocks or while performing a hole-starting routine, while rotary-percussive drilling is best suited for penetrating harder rocks but may ruin a softer rock sample. Hammering action alone can be used for hole starting routines in rocks with steeply sloped or very rough surfaces. Hammering alone can also be used to dispense regolith, powder, and cores, if desirable. These operational modes were successfully demonstrated on previous drilling systems, leading to the requirement to separate Auger rotation from Percussive hammering.

In addition to various performance requirements (Auger speed greater than 350 RPM, percussion frequency of 1500 BPM, percussive energy greater than 0.5 Joules, breakoff torque greater than 10 Newton-meters, weight on bit greater than 40 Newtons) dictated by previous successful rotary percussive drilling systems, the mass of the ROPEC drill was desired to be less than 4 kg. During the requirements derivation phase, the Mars Sample Return architecture at the time assumed that the drilling and caching rover would be slightly larger than the Mars Exploration Rovers. This rover would use a Robotic Arm similar in design but larger than the Instrument Deployment Device (IDD) on the Mars Exploration Rovers (MER). The IDD has an approximately 2-kg end of arm payload capacity, and it was estimated that a drill weighing less than 4 kg could be deployed using a robotic arm suitable for the larger, MER Plus rover. After completing design and assembly of the ROPEC drill in December of 2012, it was announced that the initial drilling and caching rover would utilize a Mars Science Laboratory rover, which enables a significantly larger Robotic Arm and end of arm payload. While mass is no longer a significant design driver, during the development phase, it was critical that the ROPEC drill be as light weight as possible. As a result, the ROPEC drill mass is less than 4 kg.

## **Design Discussion**

### Mechanism Overview

The ROPEC Drill is a flight-like prototype, five actuator system. Four of these actuators are mounted to a linear translation stage driven by a ball screw. These actuators are used to drive the Auger axis, Breakoff mechanism, Percussive system, and Pushrod mechanism. The linear translation stage is driven by the Z-Axis actuator. The ROPEC Drill uses these actuators, as well as a number of electronic sensors to perform various tasks, described as follows. Figure 3 illustrates the ROPEC drill and its corresponding actuators with the latest flex cable design and Figure 4 shows the fully assembled drill with standard cable harnesses and a cable guide.



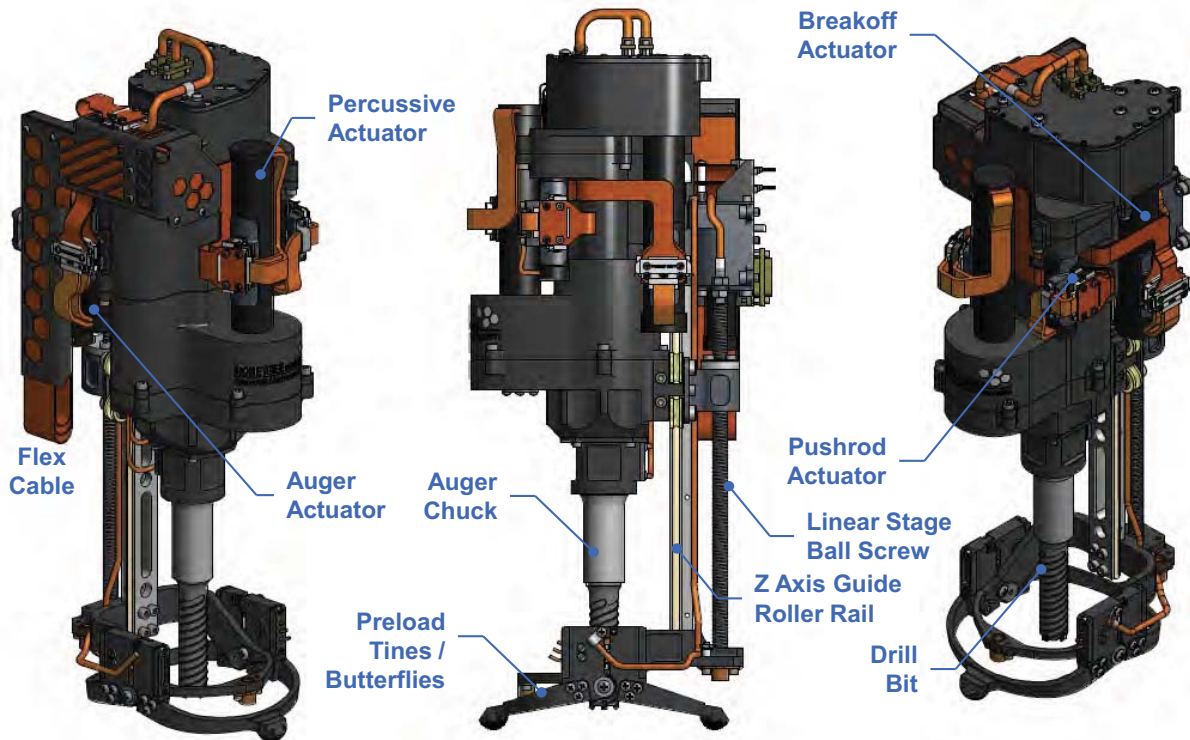


**Figure 3. ROPEC Drill Design with Revised Flex Cable**

- **Auger Actuator** – The Auger actuator is the primary driving force behind the drilling action. The drill bit is connected to the auger and needs to rotate continuously during drilling. The auger axis can be locked in position during the core breakoff routine where the rock core is sheared from the base material. The absolute position of the auger’s output can be determined using a reed switch and a magnet located on the auger output shaft.
- **Breakoff Actuator** – The Breakoff actuator is not used during the drilling process. During the core breakoff routine, the Breakoff actuator uses a high gear reduction to shear the core. Due to the high gear reduction, this actuator is normally not engaged with the drill output drivetrain during drilling; however an automated gear meshing routine is used to couple the Breakoff actuator to the drill output drivetrain during the core breakoff routine. This eliminates excessive drag torque associated with back-driving the high-reduction Breakoff Actuator while drilling.
- **Percussive Actuator** – The Percussive actuator drives a cam, spring, and follower mechanism that produces high-frequency, high-impact loads on the auger output shaft. The percussive wave from these impacts is then transferred through the drill bit down to the cutting elements and into the rock. The percussive mechanism uses a helical rotating cam to drive a rotating follower that is spring preloaded against the internal drill housing. As the helical cam rotates, it contacts the follower, which rolls along the surface of the cam until it reaches a drop off point. At the drop off point, the follower is released, and the potential energy stored in the spring is used to create the percussive impact by way of a hammer and anvil arrangement.
- **Pushrod Actuator** – The Pushrod actuator is used to control a long pushrod within the center of the ROPEC Drill. In a previous Mars Sample Return architecture developed by Honeybee Robotics, it was determined that a pushrod could be useful for inserting the drill bit and rock core into the Sample Cache. In the current “One Bit-One Core” architecture, it is no longer required. While the pushrod has the capability to extend far outside the drill, it is also used in a number of internal routines, such as

locking the auger axis during core breakoff, and coupling the breakoff actuator to the output drivetrain while shearing the core.

- Z Axis Actuator – The Z-Axis actuator drives a precision ball screw which controls the depth of penetration of the drill bit during drilling operations. Motor current feedback from the actuator can be used to estimate weight on bit. A non-contact inductive proximity sensor is used to home the linear extension stage.
- Preload Tines – The Preload Tines, or “Butterflies” are used to stabilize the ROPEC drill during drilling. These tines are placed on a rock surface, and a pair of limit switches within the Butterflies provides feedback as to whether the tines have made contact. Once contact is confirmed, the Robotic Arm continues to preload the tines against the rock, stabilizing ROPEC for drilling operations.

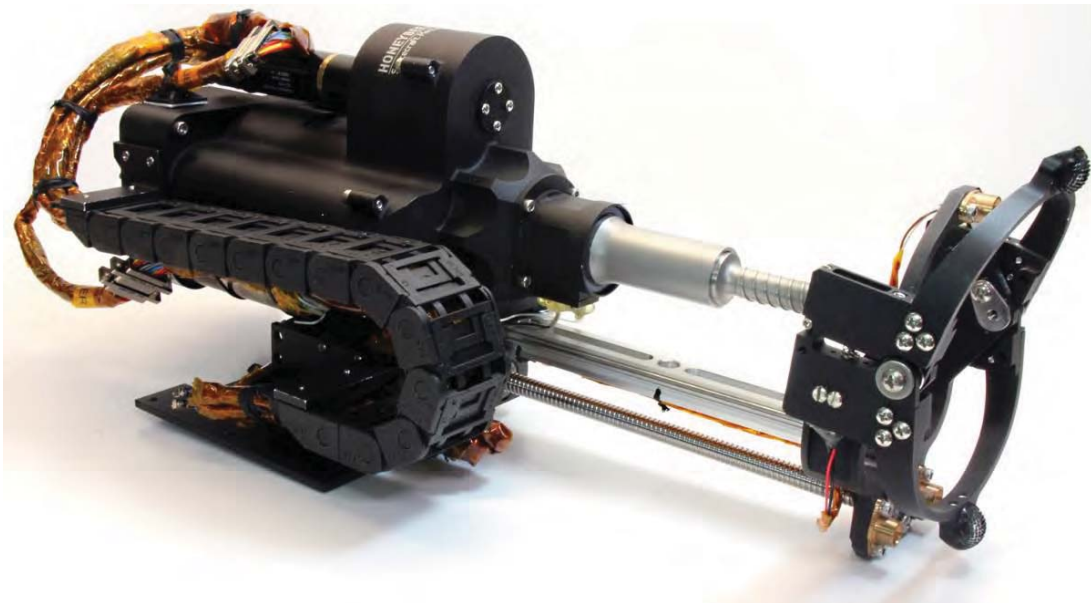


**Figure 4. Assembled ROPEC Drill without Flex Cable**

#### Auger Subsystem Design

The ROPEC Auger sub-system is shown in Figure 5. The maximum auger output speed is 375 RPM. The 90 Watt Auger Actuator (1) transmits power to the Auger Gear (4) through a system of Idler and Transfer gears. The Transfer Gear (3) also has a tab feature which allows it to lock, preventing the auger drive train from moving in one direction. Locking the Auger drivetrain is accomplished by allowing the torsion spring-loaded Auger Lock (6) to pivot into position, where it eventually contacts a tab on the Transfer Gear; temporarily acting as a hard stop. During drilling, the Auger Lock is pivoted out of the way of the Transfer Gears locking tab. This allows the Auger drivetrain to spin continuously. Pivoting of the Auger Lock is performed by raising and lowering the position of the Auger Locking Cam (7), which is controlled by the position of the Pushrod, as discussed in follow on sections.

Calculations were performed to size the actuator and drivetrain based on previous drilling data obtained using a similar drilling system. As shown in Figure 5, the Auger Transfer Gear transmits power from the Auger actuator to the Auger Gear (4). A spline in the Auger Gear (not shown) transmits torque to the Auger Chuck, while allowing the Chuck to slide axially over a short distance. With the Auger Chuck connected to the Drill Bit, this axial motion is necessary in order to allow impact energy from the percussive system to be transmitted to the Drill Bit without significant losses. A spring energized seal (5) around the Auger Chuck prevents debris from migrating into the mechanism.

The Auger Gear is constrained with a duplex pair of angular contact bearings which support Weight on Bit loads. While the Auger Chuck (12) is free to slide within the Auger Gear along the spline connection, it is constrained on one end by a flange on the chuck itself, and by a thrust needle bearing below (11).

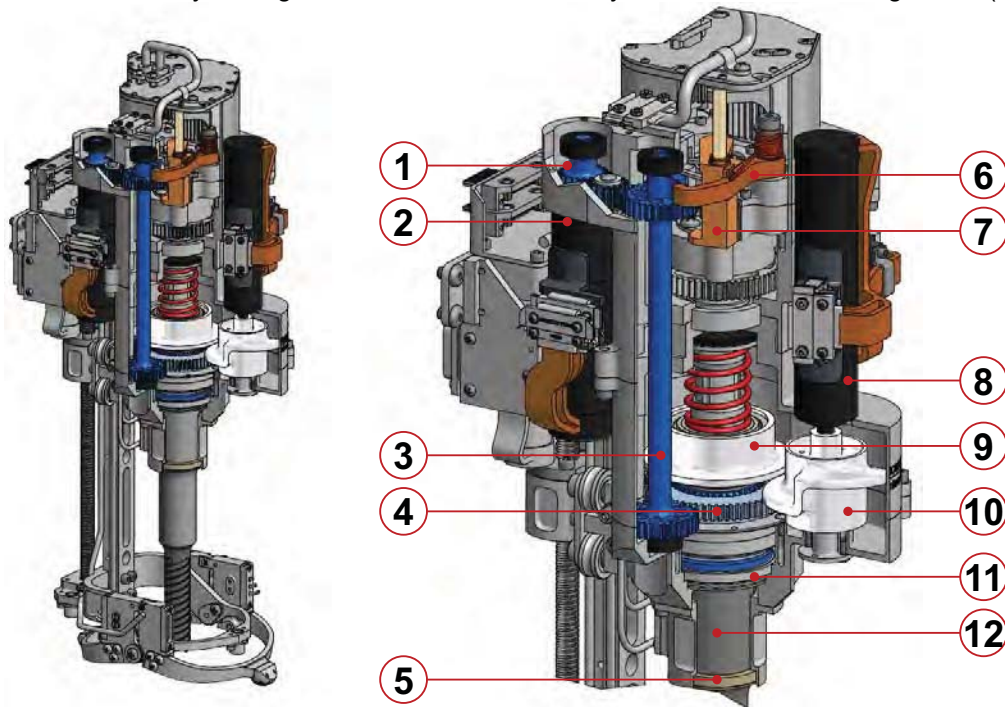


**Figure 5. ROPEC Drill Auger Subsystem (1) Auger Pinion Gear (2) Auger Actuator (3) Auger Transfer Gear (4) Auger Output Gear and Spline (5) Auger Dust Seal (6) Auger Lock (7) Auger Locking Cam (8) Percussive Actuator (9) Percussive Follower and Hammer (10) Percussive Cam (11) Thrust Needle Bearing (12) Auger Chuck**

#### Percussive Subsystem Design

The 100-Watt Percussive Sub-System delivers 0.56 Joule per blow at up to 1500 blows per minute and is also shown in Figure 5. The percussive system uses a helical Percussive Cam (10) which is driven by the Percussive Actuator (8). As the helical cam rotates, it raises a Percussive Follower and impact Hammer (9), preloading a spring. The helical cam raises the follower for approximately 3/4 of its revolution, and then releases it. Once released, the follower and impact hammer contact the top surface of the Auger Chuck, sending a percussive wave through the chuck and drill bit, ultimately impacting the rock surface. The Percussive Follower is mounted on preloaded angular bearings which allow the follower to rotate relative to the hammer. This rotation is critical in order to reduce friction and wear between the cam and follower. The hammer utilizes a custom ball spline, allowing it to move axially with minimal frictional losses.

The cam and follower percussive system has been employed in all of Honeybee Robotics' rotary-percussive drills. The percussive system in the SASSI drill has been successfully operated for 2 million cycles in a vacuum chamber at Mars pressure, which is equivalent to approximately 19 hours of operation.

#### ROPEC Breakoff Subsystem Design

The ROPEC Breakoff subsystem uses two nested tubes to shear the rock core at the bottom, and capture it for extraction from the base material [7]. The outer tube forms the main drill bit consisting of the bit shank, which connects to the ROPEC Auger Chuck, the helical fluting for cuttings removal and the tungsten carbide cutters at the base. The center bore of this outer tube is offset from the central axis of the exterior of the bit. The bore of the inner tube has the same offset. When the tubes are nested

together, they can be aligned such that the bore of the inner tube is coaxial with the outer surface of the outer tube. During the drilling process, these tubes are in this orientation, and need to spin simultaneously to avoid prematurely shearing the core.

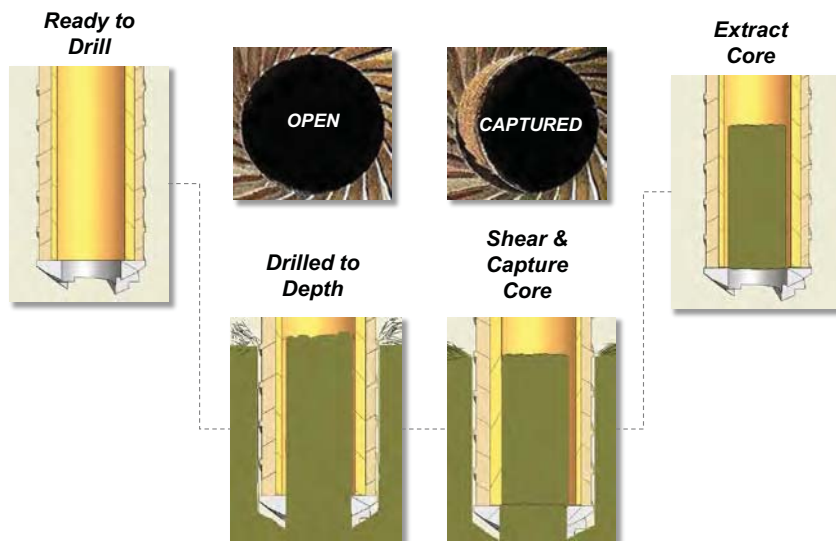


**Figure 6. Core Breakoff Method**

When core breakoff is desired, the outer tube is held stationary, while the inner tube is rotated using the Breakoff Shaft. This rotation shifts the bore of the inner tube relative to the central axis of the outer tube. This small shift is enough to shear the rock core at the base, and also capture it inside the bit, preventing it from falling out during extraction from the base material. This process is illustrated in Figure 6. This method is patented by Honeybee Robotics and has been used on a number of successful coring drill designs.

A recently concluded study with the SASSI drill and 140 coring tests in several rock types has shown that the inner breakoff tube successfully sheared and captured cores in 94% of cases, while partial core loss was observed in 6% of tests [8]. No full length core loss was observed. Some of the cores successfully captured included the “F” grade cores shown in Figure 2.

The Breakoff subsystem is shown in Figure 7. This drivetrain has the ability to selectively mesh and de-mesh the main Breakoff Output Gear (3). This subsystem is designed to produce enough torque to shear a rock core. This high torque is based on data from similar mechanisms, including a comfortable amount of torque margin. Due to this high torque requirement, the planetary gearhead on the breakoff motor has a multiple stage reduction, making the back-drive torque very high. Since the breakoff shaft needs to be coupled to the auger shaft during drilling, if the breakoff drivetrain were permanently coupled to the motor, the auger actuator would need to back-drive the breakoff motor. This back-driving rotation would require a prohibitively large amount of torque, which would result in a significantly larger auger actuator. The solution to this problem is to selectively decouple the breakoff drivetrain from the main breakoff shaft. This is accomplished by moving the Breakoff Cluster Gear (2) axially to de-mesh the drivetrain during drilling, and mesh the drivetrain during core breakoff. A magnetic Absolute Position Sensor (6) is used to provide position feedback to the control system, telling it exactly what position the breakoff drivetrain is in so that gear meshing is performed smoothly. The Breakoff Cluster Gear is translated using the Pushrod sub-system.



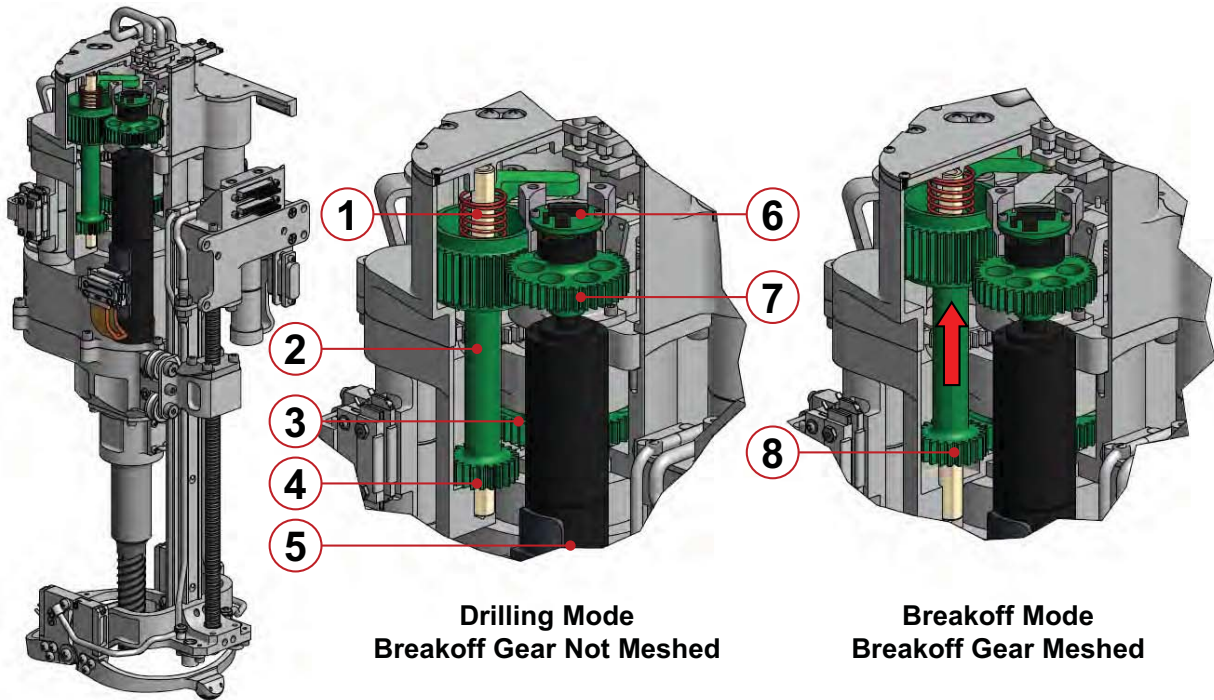


**Figure 7. ROPEC Drill Breakoff Subsystem (1) Return Spring (2) Breakoff Cluster Gear (3) Breakoff Output Gear (4) Non-Meshed Gears (5) Breakoff Actuator (6) Absolute Position Sensor (7) Breakoff Pinion Gear (8) Meshed Gears**

#### ROPEC Pushrod Subsystem Design

The Pushrod subsystem is shown Figure 9. In a previous iteration of the “One Bit-One Core” architecture, a pushrod was necessary in order to load a drill bit containing a rock core into the sample cache for sample return. The current “One Bit-One Core architecture does not require a Pushrod any longer, however due to the original requirement, a Pushrod with a long stroke has been included in the ROPEC design. The pushrod system uses a 1/4-28 threaded leadscrew and nut arrangement. The Pushrod Actuator drives a series of gears, which ultimately rotates the Pushrod Nut (5). As the Pushrod Nut rotates, the threads cause the Pushrod (1) to move axially. The Pushrod Ground Tube (3) is connected to the surrounding housing structure. The Pushrod is keyed rotationally with respect to the Ground Tube but is able to slide axially relative to it.

In addition to the option of pushing a drill bit into a sample cache, the Pushrod also helps actuate a number of different mechanisms within the ROPEC drill itself. The Pushrod is shown in both the drilling position and in its fully extended position in Figure 9. Once drilling is complete, the Pushrod is retracted further into the drill. This motion raises the Auger Locking Cam (Component 7 as shown in Figure 5), which actuates the Auger Lock (Component 6 as shown in Figure 5) near the top of the drill, which locks the Auger Transfer Gear in place, preventing the Auger drivetrain from rotating during the core breakoff routine, as described previously.

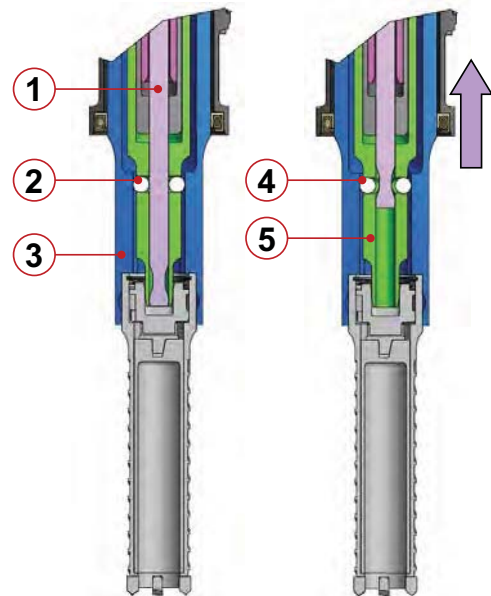


**Figure 8. ROPEC Drill Pushrod Subsystem (1) Pushrod (2) Locked Balls (3) Auger Chuck (4) Unlocked Balls (5) Breakoff Shaft**

As the Pushrod is retracted still further into the drill, it de-couples the Auger Chuck from the Breakoff Shaft as shown in Figure 8. During the drilling routine, the Auger Chuck (3) and Breakoff Shaft (5) are coupled together by way of a pair of locking balls held in place by the Pushrod (1). After drilling is complete, the Pushrod is retracted upwards until the balls are unlocked by “falling into” a groove in the Pushrod (4). This decouples the Auger Chuck from the Breakoff Shaft, allowing the latter to rotate relative to the chuck so that the rock core can be sheared.

Finally, as the Auger Chuck and Breakoff Shaft are decoupled, this movement raises the Breakoff Cluster Gear (Component 2 as shown in Figure 7), engaging the teeth with the main Breakoff Gear (Component 3 as shown in Figure 7) as previously described. The drill is now ready to break off a core.

While the Pushrod is no longer necessary in the “One Bit-One Core” architecture, it serves an important role in the ROPEC Drill by actuating a number of critical mechanisms.

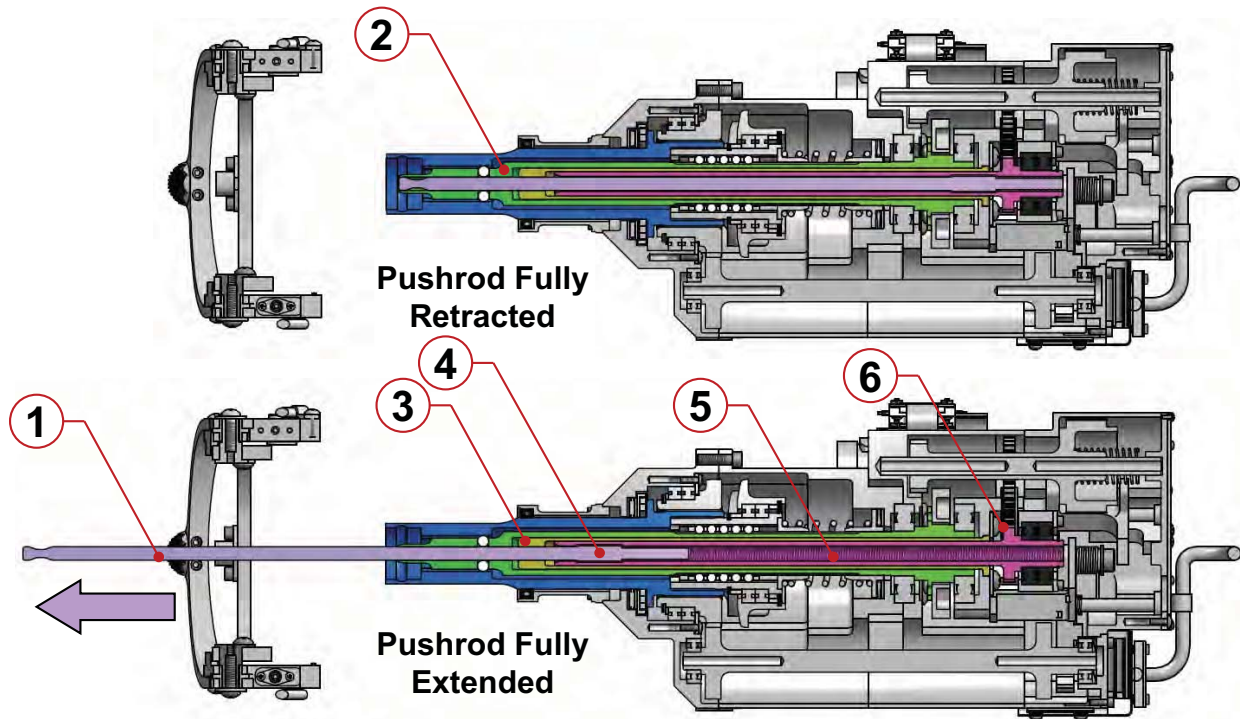


**Figure 9. ROPEC Drill Pushrod Subsystem (1) Pushrod (2) Breakoff Shaft (3) Ground Tube (4) Pushrod Threaded Section (5) Pushrod Deep Threaded Nut (6) Pushrod Output Gear**

#### ROPEC Butterfly Subassembly Design

The Butterfly sub-assembly design is based on a similar mechanism on the MER Rock Abrasion Tool, and is shown in Figure 10. This sub-assembly is connected to the base of the Z-Axis Guide Roller Rail. The Butterfly sub-assembly allows the ROPEC drill to be placed on the surface of a rock at an angle of up to 15 degrees from the local surface normal of the target. This angle is limited by mechanical Angular Hard Stops (3). Once placed on the target, the Butterfly sub-assembly is preloaded against the rock to help stabilize the drilling process. Contact Tines (2) have a raised diamond pattern knurl feature on them to help grip uneven rock surfaces.

The Butterfly sub-assembly utilizes two micro Contact Switches (1) for redundancy. These switches can be used by the control system as a safeguard in case the drill loses preload during an operation. A



change in state of the contact switch might indicate that preload was lost, or the drill slipped off the rock surface.

A compression spring keeps the switches normally open. As the Butterfly is preloaded against a surface, the spring is compressed, and the switches are closed. The Butterfly sub-assembly also includes a set of three Alignment Cup (5) features. Currently these features are designed as simple tapered bushings. These bushings can be used to mate with a Bit Storage Station or Sample Cache, providing a more accurate interface.

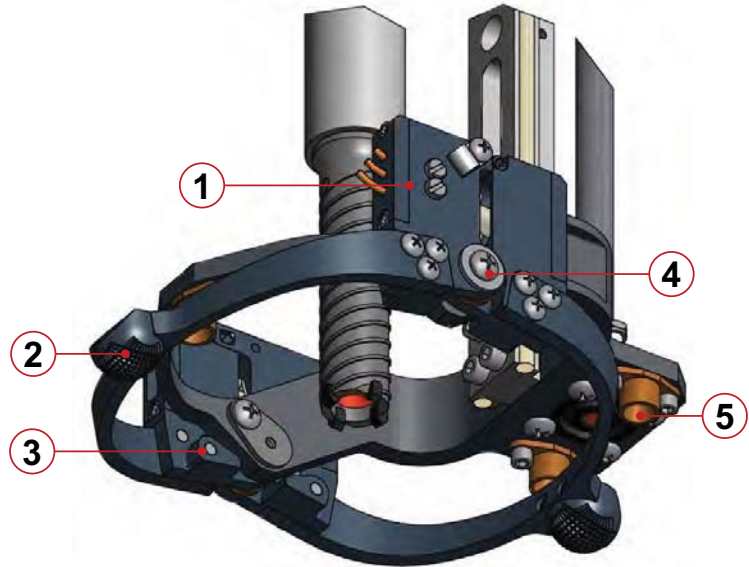


**Figure 10. ROPEC Drill Butterfly Subsystem (1) Contact Switch Housing (2) Contact Tine (3) Angular Hardstop (4) Pivot Shaft / Bushings (5) Alignment Cups**

#### ROPEC Z Axis Subassembly Design

The Z-Axis sub-assembly utilizes an off the shelf ballscrew and nut, as well as an off the shelf linear rail and rollers. The ballscrew is driven by a set of spur gears, and a felt seal prevents debris from migrating into the drivetrain housing. The ballscrew itself has a set of seals which seal the nut, preventing debris from jamming the reciprocating balls. An inductive proximity sensor is used as a limit switch to home the Z-Axis mechanism, providing a consistent starting position. A thin strip of sheet metal is cantilevered off of the moving carriage. This strip of sheet metal triggers the Proximity Sensor.

#### ROPEC Flex Cable Design

In order to consolidate cabling on the ROPEC drill, a custom flex cable was designed. A set of two almost identically shaped flex cables are laid on top of one another with a third cable in between to act as shielding. One flex cable has traces for motor power, and the other for encoder and hall sensor signals.

A detailed investigation was performed early in the design process to determine the amount of layers required on each flex cable. More layers typically results in a higher cost of the flex cable, as well as a stiffer cable with a larger bend radius. It was important that the flex cable have a low stiffness in this design because the flex cable needs to bend as the drill head is moved along the length of the Z-Axis Guide Rail. To keep the overall volume of the drill low, it was desirable to have as small a bend radius as possible. To perform this analysis, the number of wires for each motor, limit switch and other sensors was tabulated, along with the peak electrical current which that wire was expected to experience. Using the peak expected current, a maximum copper trace width was determined, based on standard industry practice for flex cables and printed circuit boards. Adding all of these widths together and accounting for gap space between each trace, the required width of the flex cable was determined.

#### ROPEC End Effectors

The ROPEC Auger Chuck is able to autonomously lock and unlock a drill bit. With this ability, and the degrees of freedom available, a number of end effectors have been designed to increase the versatility of the ROPEC Drill to different mission architectures. These end effectors are shown in Figure 11 and discussed as follows. These end effectors are demonstrated in the video at the URL below.

<http://www.youtube.com/watch?v=VhfL3htrtZ8>



**Figure 11. ROPEC Drill End Effectors (1) Standard Coring Bit (2) Rock Abrasion Brushing Bit (3) Powder and Regolith Acquisition Bit (4) Core PreView Bit (5) Slot Bit**

1. Standard Coring Bit – The current ROPEC Coring Bit is designed to obtain a 1-cm diameter by 5-cm rock core. This size was based on Mars Sample Return requirements at the time of requirements definition. Honeybee Robotics has also developed a BigTooth cutter arrangement [3] where a single larger tooth cuts the outer diameter of the core. This allows the rock core to be ejected using a combination of gravity and drill percussion.
2. Rock Abrasion Brushing Bit (RABBit) – The RABBit adds rock abrasion and brushing capability to the ROPEC similar to the Rock Abrasion Tool on the MER rovers. The RABBit allows the ROPEC Drill to penetrate through the weathered surface rind of Martian rocks, allowing science instruments to view the actual rock composition. The RABBit can also be integrated with a small scoop for capture and delivery of abraded rock cuttings, rock cuttings remaining from a drilling operation, or surface regolith.
3. Powder and Regolith Acquisition Bit (PRABit) – The PRABit is a full-faced drill bit attachment that can be used to collect drill cuttings or regolith samples. Cuttings from the drilling process are transported up the drill flutes and into a collection chamber. The internal sleeve collection chamber can be fully open, fully closed, or rotated to expose up to two different sized sieve screens, such as a 1-mm or 150-micron screen. Using the sieve screens, powder can be delivered to science instruments at a desired size fraction. A prototype bit has been successfully tested in five different rock powders [9].
4. Core PreView Bit – This bit enables science instruments and imaging systems to view a small core from a rock target before the decision is made to cache a full length core. Once a core is acquired, the PreView Bit “window” can be exposed through rotation of the inner sleeve to view the core. Figure 11 shows the PreView window partially open with a core inside.
5. Slot Bit – This bit allows science instruments and imaging systems to view a small width of the core along its entire length prior to caching the Slot Bit in the Sample Cache. This allows mission planners to have a better understanding of the quality of core that they will ultimately return to Earth. Figure 11 shows the Slot Bit fully open with a partially fractured core inside.

### **Mechanism Design and Test Lessons Learned**

#### Flex Cable Design

As shown in Figure 3, the ROPEC Flex Cable makes a number of complex bends in order to reach four actuators. In the first iteration of the design, not all of the connectors were on one side of the flex cable. This was not communicated appropriately to the team responsible for fabricating the flex cable, and it was assumed that all connectors were on the same side. Prior to integrating the flex cable with the control system, a pin-to-pin continuity test was performed, and the results showed that the main input connector

pins were “mirrored” from what they needed to be. Fortunately, this was caught prior to attempting to run the actuators, and a new cable was made between the controller and the mirrored connector.

*Lesson Learned: Be very careful when designing flex cables with multiple bends and changes in direction. Make sure that the engineers designing the cable routing properly communicates what side of the flex cable the connector is mounted on to the team responsible for mounting the connectors. During assembly, always perform a full continuity test on the flex cable, just like any other cable, even if the manufacturer guarantees that it was made according to specifications. It is always possible that the specifications inadequately described the connector locations.*

On the first iteration of the Flex Cable, the two 51 pin connectors were not properly strain relieved to the flex cable. The connectors were soldered directly to the flex cables, but no other strain relief was provided. The connectors were then screwed into a base structure, which offered the strain relief. Any time the connector was removed from the base structure during the assembly and debugging process, there was no longer anything providing strain relief between the connector and flex cable. This ultimately resulted in debonding of the connector from a number of the solder pads.

*Lesson Learned: Always provide a permanent mechanical strain relief method between connectors and a flex cable, even if the cable will later be integrated into a structure that provides strain relief. The second iteration of the flex cable is shown in Figure 12. This was designed to have permanent metallic backing plates (2) attach the flex cable (3) to the 51 pin connector (5) using fasteners (1). This backing plate would be fabricated, and then sent to the vendor integrating the connector to the flex cable. The vendor would then mount the backing plate and verify continuity before delivery. After receiving the flex cable, this backing plate never has to separate from the flex cable again. The backing plate itself is then fastened to the drill structure (4) using fasteners (6). This results in a permanent strain relief between the connector and the flex cable. The 51 pin connector is then mated with the controller cable (7). Currently, the design of the second flex cable iteration has not been integrated into the ROPEC Drill.*

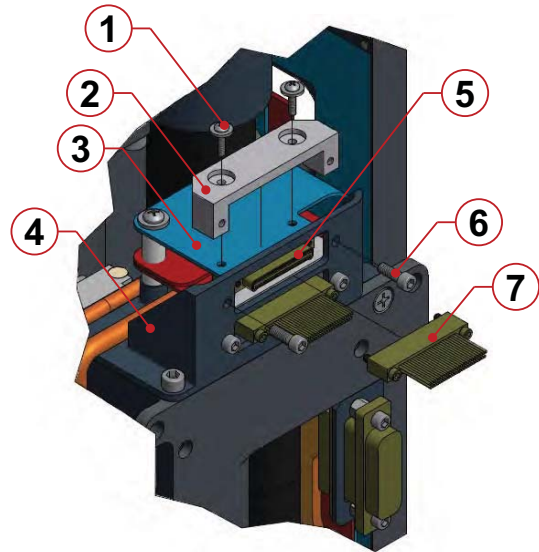


**Figure 12. Revised ROPEC Flex Cable Connector Strain Relief**

### Coatings under High Contact Stress

The ROPEC percussive axis uses a hardened helical cam and rotating follower arrangement to preload and release a spring loaded impact device. This mechanism experiences over 10,000 cycles during one drilling operation alone. The majority of contact between the cam and follower is rolling contact, with a small amount of sliding contact as the follower climbs the “ramp” of the cam, and a moment of impact when the follower first contacts the cam. In an attempt to reduce friction and increase efficiency, a high contact strength, low friction coating was applied to the cam and follower surfaces (Magnaplate Nedox FM-5 and Magnaplate Nedox SF-2 respectively) as recommended by the plating manufacturer. These coatings were applied on top of the Vascomax C300 base material. After only a few short operations, an anomaly within the drill auger mechanism was detected. Upon disassembly, it was found that the coatings were in the process of flaking off of the cam as shown in Figure 13. These flakes had become lodged in an open bearing, creating a torque anomaly. As seen in the figure, flaking of the coatings was so bad that it was decided to simply remove the coatings from the area and allow the base material to act as the contact surface. The drill housings were then cleaned and reassembled. This issue has not appeared again, however, it is expected that a small amount of base material is gradually wearing away as the drill

is used. The open bearing has since been replaced with a shielded bearing to further minimize the chances of debris migrating into the bearing.

*Lesson Learned: Honeybee Robotics has attempted to use a number of different coatings for percussive cam and follower mechanisms in the past. Due to the high number of cycles and the high contact stress on the cam and follower surfaces, none of these coatings seem to last more than a dozen drilling operations, where each operation requires at least 10,000 cycles. It is advised that future mechanisms with similar requirements consider not applying any coatings to the surface. It is highly recommended to build a breadboard to test material wear rates if particulate accumulation will cause problems with other mechanisms. In addition, be sure to shield any bearings in the vicinity of such mechanisms. It is likely that the percussive vibration helped migrate particles into the unshielded bearings.*

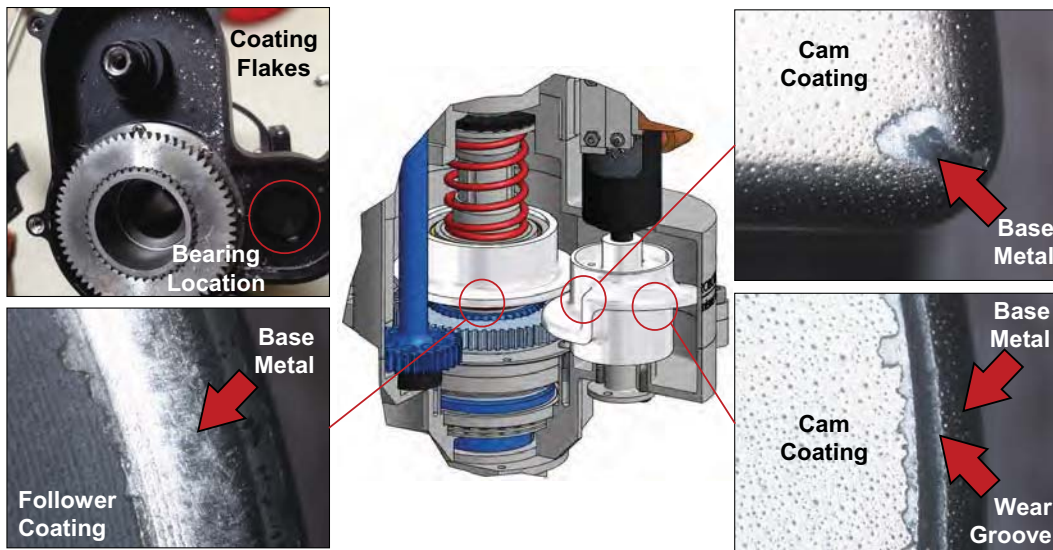


**Figure 13. ROPEC Cam and Follower Coating Issues**

#### Autonomous Gear Meshing

The ROPEC Drill requires that the Breakoff Cluster Gear be de-meshed from the Breakoff Output Gear during the drilling process, and meshed during the core breakoff routine. This mechanism is shown in Figure 7 and discussed in previous sections. In theory, if the absolute position is known for each of the gears, they can be meshed together after a short calibration. In practice, this method of gear meshing required a significant amount of software development and trial and error during the assembly and integration phase. Ultimately, the software routine is able to position the gears close to where they need to be, then a stepping routine is implemented which incrementally moves the Breakoff Pinion Gear, then raises the Breakoff Cluster Gear using the Pushrod. If Pushrod stall is detected prematurely, the routine repeats, stepping the Pinion Gear a small amount. This routine typically works, but sometimes fails to mesh the gears within the set number of incremental steps. The routine then needs to be run again. This trial-and-error method is not ideal for a flight system.

*Lesson Learned: Meshing and de-meshing gears is not an ideal choice when designing a high reliability mechanism. If it is a requirement on the mechanism, which is the case for ROPEC, it is recommended that axial meshing / demeshing not be used unless there is very high precision control over the absolute position of each gear. One of the two gears had this amount of control on ROPEC, and meshing is not 100% reliable. If meshing / demeshing is required, a "Missing Tooth" method can be used instead. This method was successfully implemented on a previous coring drill (SASSI Drill), and is shown in detail in Figure 14. Using this method, the absolute position of the Breakoff Cluster Gear and Breakoff Output Gear is known using a set of magnetic absolute position*



encoders. Both the Breakoff Output Gear and the Breakoff Cluster Gear have one or more missing teeth. As shown in the figure, the Breakoff Output Gear is first oriented in position as shown in (1). At this point, the Auger drivetrain is able to control the position of the Breakoff Output Gear. Both gears are then rotated simultaneously as shown in (2) until they are meshed. As shown in (3), the Breakoff drivetrain can now control the position of the Breakoff Output Gear, allowing the higher torque produced by the Breakoff Actuator to help shear the core.

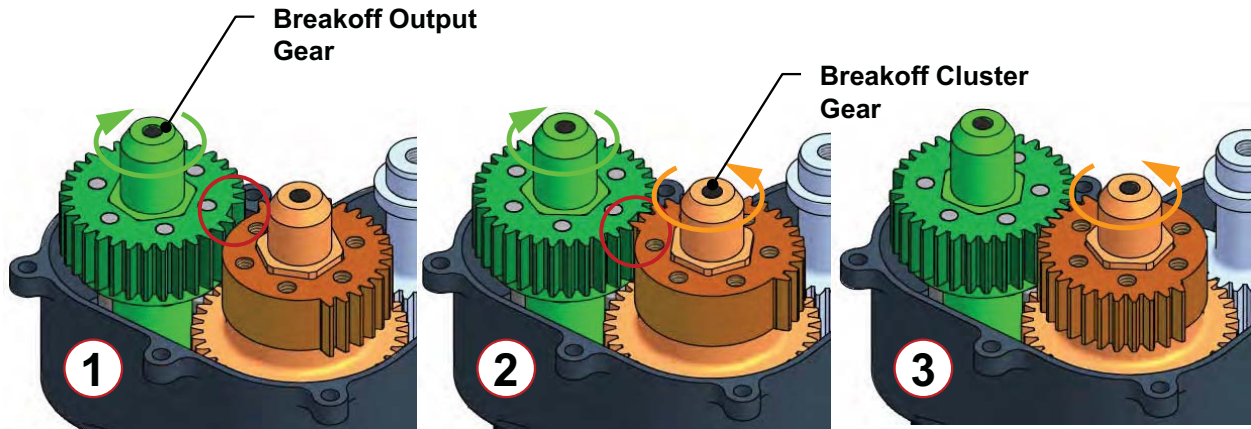


**Figure 14. SASSI Drill Missing Tooth Gear Coupling Method**

### Conclusion

The ROTary Percussive Coring Drill is a light weight, flight-like, five actuator drilling system prototype designed to acquire core material from rock targets for the purposes of Mars Sample Return. The ROPEC Drill is designed to integrate with a “One Bit-One Core” approach to returning samples from the Martian surface. The ROPEC Drill has a number of different attachments which expand its capability to include rock abrasion, brushing, powder and regolith acquisition, and viewing of rock cores for sample triage purposes.

A number of issues have been encountered with the ROPEC drill including flex cable development, coatings under high stress and cyclic loading, and meshing / demeshing of spur gears, resulting in a number of lessons learned which can be applied to similar prototype or flight mechanisms.

The ROPEC Drill has recently been integrated with a five degree of freedom Robotic Arm and mobility system, and has demonstrated docking with a prototype Bit Station, obtaining a Coring Bit, drilling and acquiring a rock core sample, and delivering the bit to a prototype Sample Cache. All drill attachments have similarly been demonstrated from the same platform.

## References

1. Mustard, et al, (2013). Report of the Mars 2020 Science Definition Team. Online at [http://mepag.jpl.nasa.gov/reports/MEP/Mars\\_2020\\_SDT\\_Report\\_Final.pdf](http://mepag.jpl.nasa.gov/reports/MEP/Mars_2020_SDT_Report_Final.pdf) (as of July, 2013).
2. Gorevan, S., et al. (2003). Rock Abrasion Tool: Mars Exploration Rover Mission. *Journal of Geophysical Research*, 108(E12), 8068
3. Zacny K., Chu, P., Davis K., Paulsen, G., Craft, J. (2014). Mars 2020 Sample Acquisition and Caching Technologies and Architectures. In *IEEE Aerospace Conference*, Big Sky, Montana.
4. Zacny K., Chu, P. et al. (2013). Sample Acquisition and Caching Architecture for the Mars Sample Return Mission. In *IEEE Aerospace Conference*, Big Sky, Montana.
5. Mattingly, R. (2005). The many faces of the Mars Sample Return Mission Architecture. In *Guidance and Control Conference*, Breckenridge, CO
6. Zacny, K., Wilson, J., Chu, P., Craft, J. (2011). Prototype Rotary Percussive Drill for the Mars Sample Return Mission. In *IEEE Aerospace Conference*, Big Sky, Montana.
7. Myrick, T., Core Break-off Mechanism. US Patent No. 6,550,549, April 22, 2003.
8. Zacny K., et al. (2013). Sample Acquisition and Caching Architectures for the Mars 2020 Rover Mission. In *AIAA Space 2013*, San Diego, CA.
9. Zacny K., et al. (2011) Development of the Brushing, Abrading, Regolith, Core PreView and the Coring Bits for the Mars Sample Return Mission. In *AIAA SPACE 2011 Conference & Exposition*, Long Beach, CA



# Aperture Valve for the Mars Organic Molecule Analyzer (MOMA)

Charles Engler\* and John Canham\*\*

## Abstract

NASA's participation in the multi-nation ExoMars 2018 Rover mission includes a critical astrobiology Mass Spectrometer Instrument on the Rover called the Mars Organic Molecule Analyzer (MOMA). The Aperture Valve is a critical electromechanical valve used by the Mass Spectrometer to facilitate the transfer of ions from Martian soil to the Mass Spectrometer for analysis. The MOMA Aperture Valve development program will be discussed in terms of the initial valve design and subsequent improvements that resulted from prototype testing. The initial Aperture Valve concept seemed promising, based on calculations and perceived merits. However, performance results of this design were disappointing, due to delamination of TiN and DLC coatings applied to the titanium base metals, causing debris from the coatings to seize the valve. While peer reviews and design trade studies are important forums to vet a concept design, results from testing should not be underestimated.

Despite the lack of development progress to meet requirements, valuable information from weakness discovered in the initial Valve design was used to develop a second, more robust Aperture Valve. Based on a check-ball design, the ETU / flight valve design resulted in significantly less surface area to create the seal. Moreover, PVD coatings were eliminated in favor of hardened, non-magnetic corrosion resistant alloys. Test results were impressive, with the valve achieving five orders of magnitude better sealing leak rate over end of life requirements. Cycle life was equally impressive, achieving 280,000 cycles without failure.

## Introduction

By studying organic molecules (the chemical building blocks of life as we know it), MOMA is designed to help answer questions about whether life existed on Mars, as well as its potential origin, evolution, and distribution on the Red Planet. The MOMA Instrument is principally a mass spectrometer used to detect the masses and relative concentrations of atoms and molecules in a substance. MOMA is designed to analyze the types and amounts of chemicals that make up organic and inorganic compounds found in rock and soil samples on Mars. The instrument will address a top science goal seeking the signs of past or present life on Mars. Since the surface of Mars is bathed in ultraviolet and cosmic radiation, complex organics in the uppermost surface layers could be degraded. The 2018 Rover will be equipped with a drill to obtain samples from as deep as 2 meters in the hope that organics at that depth would still be viable. Core samples of Martian soil will be ablated by a UV laser, producing ions which pass thru the Aperture Valve and are subsequently trapped and analyzed by the Mass Spectrometer to determine the molecular composition of the ion, which then determines the molecular composition of the sample.

The MOMA Mass Spectrometer illustrated in Figure 1. Principle components are the Mass Spectrometer Housing, 266-nm UV Laser Head, and Aperture Valve. The Martian sample is moved to the ultra-clean zone directly below the Aperture Valve. A laser mounted onto the Mass Spectrometer Housing creates a focused beam of energy which oblates the soil and ionizes soil particles. The valve opens, allowing ions to flow into the Mass Spectrometer, then quickly closes. Ions are trapped by a Linear Ion Trap, scanned for molecular composition, then ejected.

---

\* NASA Goddard Space Flight Center, Greenbelt, MD

\*\* ATK Space Systems, Beltsville, MD

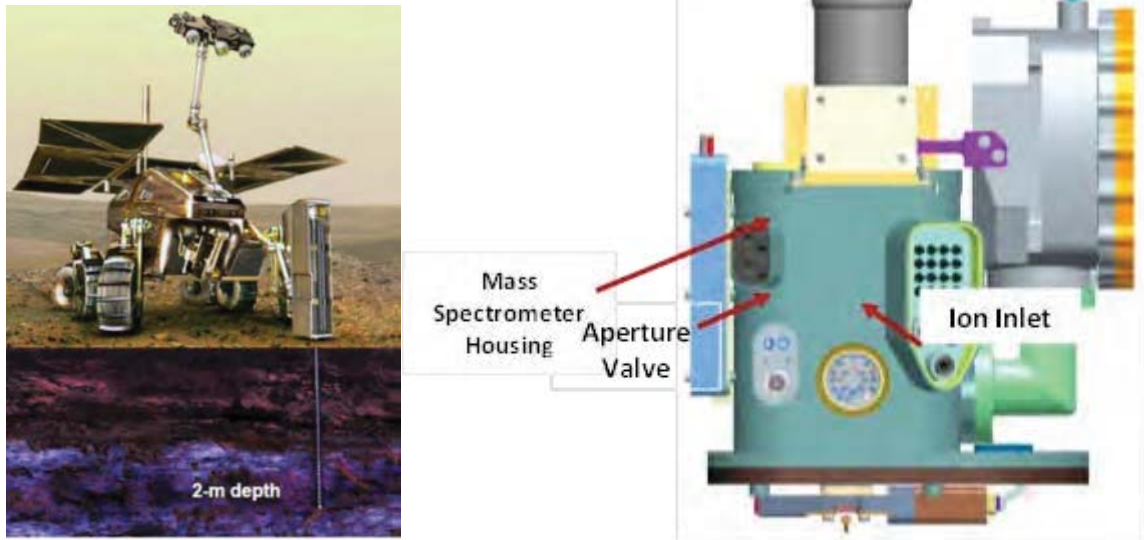


**Figure 1. MOMA Mass Spectrometer with Aperture Valve**

**Initial Aperture Valve Design**

Over 125 requirements for the valve were levied, which were then ranked according to importance and distilled down to the 25 top “driving” requirements. The initial Aperture Valve design is illustrated in Figure 2. Sealing the inlet was accomplished by means of a Sliding Pin, which operated to open and close off the Ion Tube. A solenoid was connected to the sliding pin connected to a pull-type solenoid, which when energized, pulled the Pin to the open position, allowing ions to travel from a Martian sample below the valve, up the inlet cone and thru the hole at the base of the cone. After power to the solenoid was removed, the solenoid rapidly closed from stored energy in a recoil spring. Close tolerance between the sliding Pin and Valve Body produced a pressure leak rate consistent with the requirement of 10E-3 cc/sec He for beginning of life and 10E-2 cc/sec He, end of life, which was defined as 125,000 actuation cycles.

**Table 1. Requirements**

Pressure leak rate	10E-3 cc/sec He
Operational cycle life	125,000 cycles
Operational temperature	-20°C to 50°C
Valve open/close time	<50 ms
Mass	90 grams
Failure Mode	Fail closed
Power	5 watts
Material limitations	Non-magnetic

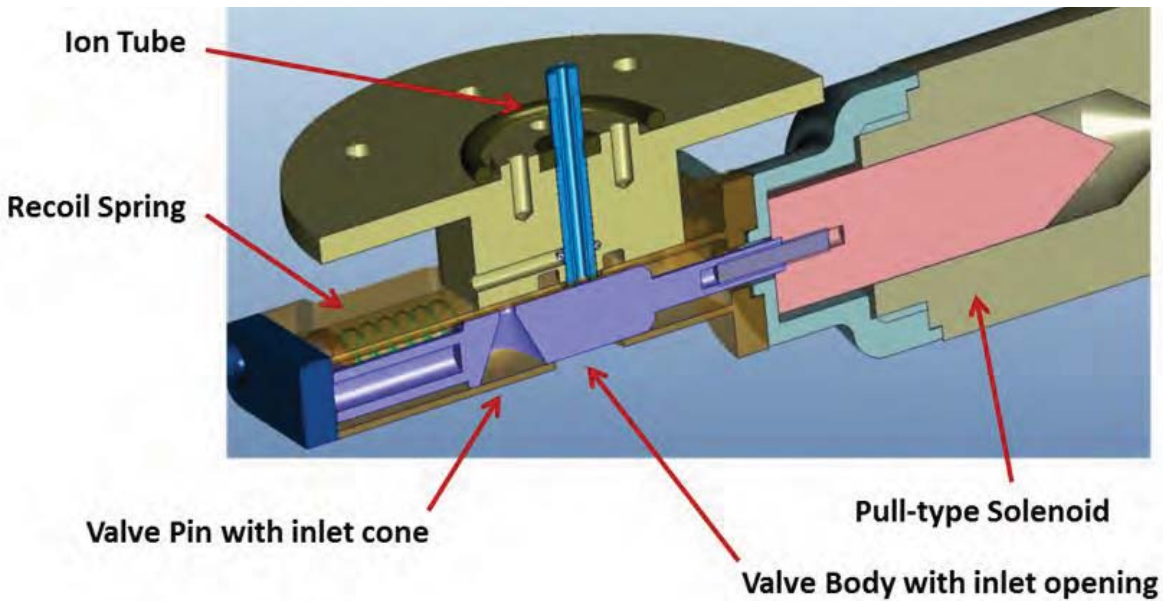


**Figure 2- Aperture Valve early design**

To meet operational and performance requirements, materials for Aperture Valve components were comprised of Titanium 6AL-4V. Titanium is well known material of choice for aerospace design with benefits including: high strength-to-weight ratio, corrosion resistance and non-magnetic. Coatings applied to the Titanium were added for surface hardness, lower coefficient of friction, and prevented galling between the Sliding Pin and Valve body. The choice of coatings on these parts and application of the coatings to the Titanium base metal would prove problematic. Figure 3 illustrates two versions of the initial Valve design. Both feature the same mechanical sliding pin type concept. Clearance between the outside diameter of the Sliding Pin and bore hole within the Valve body were tightly controlled to 5 micron (.0002 in) clearance. The valve body was coated with Titanium Nitride (TiN) by means of physical vapor deposition or PVD, a process of sublimating pure titanium with nitrogen in a high energy, vacuum oven. The result is an extremely hard, thin, gold-colored film, commonly found on tool bits. The sliding pin was coated with Diamond-Like Carbon (DLC), another PVD coating having a desirable combination of a low coefficient of friction and high micro hardness. In general, PVD coatings have a micro-hardness greater than 80Rc, well above the hardness of tool steel. Both coatings were applied at 2.5 micron (.0001 in) thickness.

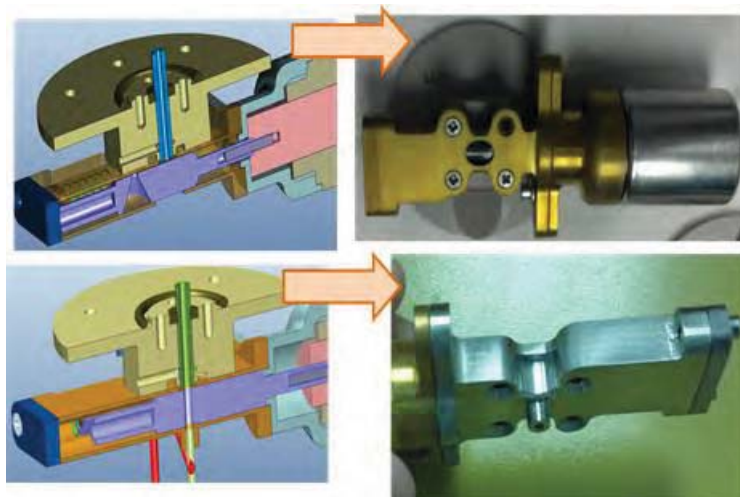


**Figure 3. variations of coated valves**

## Problems with TiN and DLC Coatings

Traditionally, the largest inherent problem with ceramic based coatings such as TiN and DLC has been the issue of adhesion; typically the higher the diamond percentage in a DLC film, the harder the DLC film but the higher the compressive stress within that film. In extreme cases, such stresses can create unstable interfaces (i.e., adhesion and/or cohesion issues) and the film may become prone to delamination.

Figure 4 illustrates the results of Aperture Valve testing after less than 100 actuations. Figure 4 (left) illustrates the bore of the valve body coated with TiN. Flaking of gold colored material inside the bore and complete film separation from the base substrate is evident. From our experience, the PVD process used to apply TiN onto internal cavities and bore holes does not produce acceptable adhesion of the TiN film. It is not clear whether additional factors associated with substrate preparation within the bore were contributing factors. Figure 4 (right) illustrates excessive wear of DLC coating on the Sliding Pin. This was probably the result of delaminated TiN flakes abrading the DLC surface. TiN on the cone and smaller shaft feature on the Sliding Pin were requested by the science team. While monolithic coatings are most common, multi-layer PVD coatings are applied with acceptable results, depending on number of layers, layer thickness, hardness of the coatings, etc. In this case, TiN was applied over the DLC coating with poor results, as flaking was evidenced here as well.

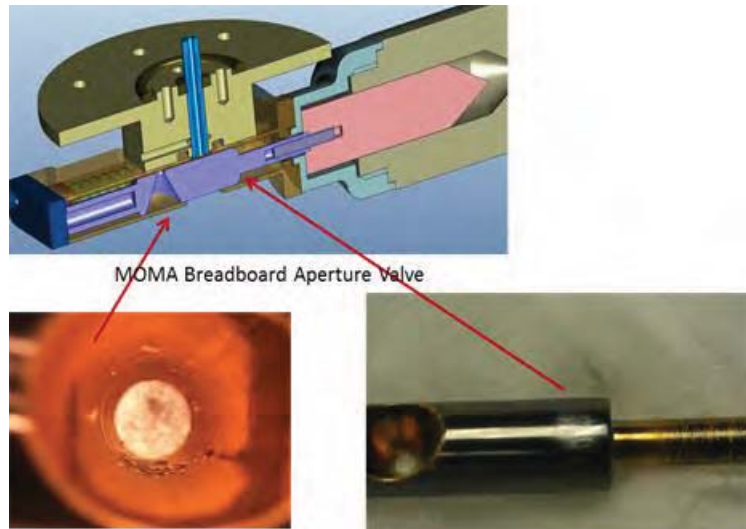


**Figure 4. Coating delamination on valve parts**

In the laboratory, the assembled valve initially operated well, meeting open and close times of <math><50\text{ ms}</math> per the requirement. Leak rate on the valve was also initially within requirement of  $1\text{E-}3\text{ cc/sec He}$ . After less than 100 open-close cycles however, there was a notable sticking of the sliding pin; the solenoid could quickly open the valve, however the recoil spring could not return the pin quickly due to particulates generated from TiN fragments. Finally, the valve pin ceased to open or close, overwhelmed by friction between sliding surfaces. Moreover, scratches on the sliding surfaces prevented the valve from being refurbished resulting in a failure. The valve test chamber is illustrated in Figure 5. The Valve operates at 5-7 torr (Mars ambient pressure) in a  $\text{CO}_2$  environment. Upper Chamber (not shown) operates at  $1\text{E-}6$  torr. Physical dimensions of the initial Valve are 98 mm x 20 mm x 20 mm (LxWxH).





**Figure 5. Aperture Valve test chamber**

### **ETU / Flight Aperture Valve design**

The second generation Aperture Valve for ETU and Flight was designed to specifically avoid the issues associated with PVD coatings and the Sliding Pin sealing concept requiring 5 micron (.0002 in) clearance to the Valve body bore to create the seal. While the previous design was based on creating hard, durable sliding surfaces between the Sliding Pin and Valve Body to minimize friction and particulate wear, the initial Aperture Valve never achieved more than 1200 cycles before failing due to particulates. Obviously, the initial Valve design could not meet the open-close requirement of 125,000 cycles. Therefore, another valve design was developed which specifically avoided the design weaknesses described. Figure 6 illustrates the improved valve design. Common features to the initial Valve include a pull-type solenoid, sliding carrier (not pin), valve body and recoil spring. Figure 6a illustrates the principle components of the new valve design. The innovation in the design may be found in the method of sealing the valve open and closed, similar to a check-ball design, whereby a ball fits into a spherical seat to create the seal. In this design, the ball is placed into a socket forcing the ball onto the seat by a small spring. A sliding Carrier containing the ball assembly translates to the right when pulled by the solenoid. Translation of the Carrier forces the ball out of the valve seat and into the Carrier. A hard stop prevents further motion of the Carrier, allowing a hole in the carrier to provide an open path for ions to travel thru the valve and up the inlet tube. When power to the solenoid is removed, the recoil spring sends the Carrier back, returning the ball to the valve seat to complete the seal.

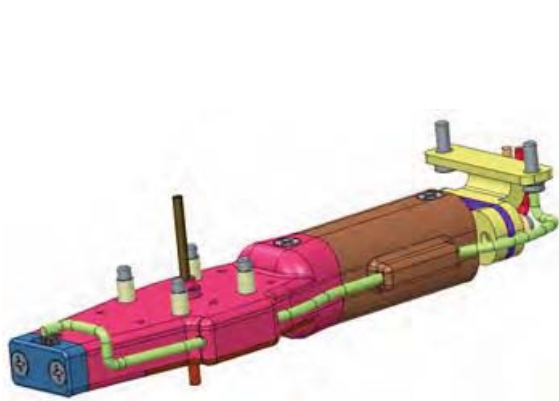


**Figure 6. ETU /Flight Aperture Valve**

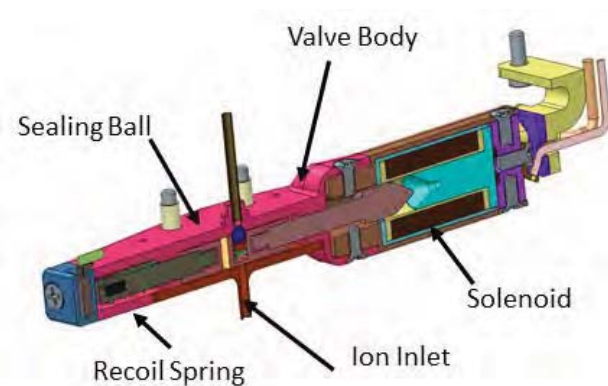


**Figure 6a. ETU /Flight Valve Section**

## **Results of ETU / Flight Aperture Valve Testing**

The ETU / Flight Aperture Valve design exceeded expectations for sealing and performance. The valve seat design was unique for this application and routinely achieved sealing leak rates as high as  $<E-9$  cc/sec He. In fact,  $5E-9$  cc/sec in Helium was measured even after 125,000 cycles. Closure times also exceeded requirements; open and closure times of  $<50$  ms (each way) were observed with a typical time of 26 ms. The ETU / Flight Aperture Valve design proved superior to the original valve in meeting or exceeding design requirements. Tests were conducted on valve endurance beyond requirements, finding a small reduction in sealing leak rate after 250,000 cycles. Additional testing was subsequently performed on the same valve to assess endurance when contaminants were introduced into the test chamber environment. Mars regolith, an Earth-based concoction of materials to simulate a typical Martian bedrock soil was used for the test. The test valve was run again for an additional 30,000 cycles in the contamination environment without failure. Leak rate was measured at  $2E-8$  cc/sec He, approximately 5 orders of magnitude higher than the end of life requirement ( $1E-3$  cc/sec He EOL spec vs.  $2E-8$  cc/sec He on test valve).

### **Conclusion**

The MOMA Aperture Valve development program was briefly discussed in terms of design improvements resulting from prototype test results. The initial Valve design was based on over 125 requirements which were distilled down to the top 25 “driving” design requirements. The initial Aperture Valve concept seemed promising, based on calculations and perceived merits. However, performance results of this design were disappointing, due to delamination of TiN and DLC coatings applied to the titanium base metals, causing debris from the coatings to seize the valve.

Despite the loss, valuable information from weakness discovered in the initial Valve design was used to develop a second, more robust Aperture Valve. Based on a check-ball design, the ETU / flight valve design resulted in significantly less surface area to create the seal. Moreover, PVD coatings were eliminated in favor of hardened, non-magnetic corrosion resistant alloys. Test results were impressive, with the valve achieving five orders of magnitude better sealing leak rate over end of life requirements. Cycle life was equally impressive, achieving 280,000 cycles without failure. Due to schedule constraints, the ETU / flight valve was never tested to actual end of life, however, it is estimated that the valve could achieve 500,000 cycles, due to the relatively few particulates discovered during post-test inspection of valve components.

### **Acknowledgements**

The authors would like to thank Ken Blumenstock for engineering the solenoid design and Willie Barber for his manufacturing expertise and support on this project.



# Development of the RANCOR Rotary-Percussive Coring System for Mars Sample Return

Gale Paulsen<sup>\*</sup>, Stephen Indyk<sup>\*</sup> and Kris Zacny<sup>\*</sup>

## Abstract

A RANCOR drill was designed to fit a Mars Exploration Rover (MER) class vehicle. The low mass of 3 kg was achieved by using the same actuator for three functions: rotation, percussions, and core break-off. Initial testing of the drill exposed an unexpected behavior of an off-the-shelf sprag clutch used to couple and decouple rotary-percussive function from the core break off function. Failure of the sprag was due to the vibration induced during percussive drilling. The sprag clutch would back drive in conditions where it was expected to hold position. Although this did not affect the performance of the drill, it nevertheless reduced the quality of the cores produced. Ultimately, the sprag clutch was replaced with a custom ratchet system that allowed for some angular displacement without advancing in either direction. Replacing the sprag with the ratchet improved the collected core quality. Also, premature failure of a 300-series stainless steel percussive spring was observed. The 300-series percussive spring was ultimately replaced with a music wire spring based on performances of previously designed rotary-percussive drill systems.

## Introduction

In 2010, NASA considered three mobility architectures for the next Mars mission. These included the MER-size rover, MER+ rover which was approximately 30% heavier than MER, and the MSL-size rover [1]. Since the goal of the future mission was to capture rock cores and cache them for potential sample return, Honeybee Robotics was tasked with a development of a core drilling system. The drill had to be mass optimized to fit either the MER or the MER+ platforms. It should be noted that the MER robotic arm, called the Instrument Deployment Device or IDD, was designed to carry approximately 2 kg of payload at its end. It was assumed that a slightly larger arm on MER or MER+ could potentially carry 3 or even 4 kg of payload. With that in mind, the driving goal of the project was to design a drill that would weigh approximately 3 kg or less. It should be noted that at the same time parallel drill development efforts focused on other aspects of the rotary-percussive coring systems such as reducing the sampling complexity [2].

To help reduce the mass of the RANCOR drill, a number of mechanisms were designed to be driven by a single actuator. The result was a two actuator drill that drives 4 degrees of freedom.

One of these actuators drives three degrees of freedom. These are the auger and bit rotation, percussive mechanism, and the mechanism used to break off the core. The second actuator is used to lock and unlock the drill bit from the chuck so that bits can be removed and inserted into the drill head and also to enable bits to be removed from the drill head at any time (i.e. if the bit is stuck in a rock). When complete,



**Figure 1. Weigh-in picture of the final mechanical assembly of the RANCOR drill**

<sup>\*</sup> Honeybee Robotics Spacecraft Mechanisms Corporation, Pasadena, CA

these design choices helped in reaching a final drill mass of 2.9 kg, including cable harnessing (2.8 kg without the cable harness as shown in Figure 1).

Another major requirement was for the drill to interface with an existing Integrated Mars Sample Acquisition and Handling (IMSAH) architecture developed by the Jet Propulsion Laboratory (JPL) [3, 4]. This architecture relies on an embedded sample tube that collects the core during drilling. Once a core is drilled and captured, the bit must be docked to IMSAH and subsequently detached from the drill head. At this stage, a mechanism within IMSAH is inserted into the back end of the drill bit to remove the sample tube with the core. This full sample tube is then cached into a separate caching mechanism and a new clean sample tube is collected and reinserted into the back end of the drill bit. At this point the drill head can mate with the drill bit again to drill and capture a new core.

### RANCOR Drill Overview

The core mechanical components of the RANCOR drill are shown in Figure 2. This includes everything except for the drive motor, spring Z stage, and proximity sensor for homing the auger axis. In this cross section it is evident how the auger and breakoff shaft are driven together with the cam/follower percussive mechanism while rotating the Cam Shaft Upper in one direction. When rotating this shaft in the opposite direction, the overrunning clutch (eventually replaced with a ratchet) decouples rotation of the cam and auger, thus rotating only the breakoff shaft. This is the mechanism that enables relative rotation between the breakoff shaft and auger to shear and capture cores.

#### RANCOR Drill Bit

At the working end of any drill is the drill bit. The RANCOR coring drill bit is comprised of 3 main components: the auger, breakoff tube, and JPL sample tube (Figure 3 and Figure 4). The auger was designed around the JPL Sampling tube and requirements for collecting a core sample of 6-cm length and 1-cm diameter. To break and capture the core, the Honeybee Robotics patented eccentric tube technology was used [5]. The auger shank was designed to fit with the three sets of guide wheel rollers found on the chuck. To make the chuck as compact as possible, the shank of the drill bit became an almost equilateral hexagon. Weight reduction features were created in the auger since this component alone comprised about 8% of the overall drill mass. Hence, there are three pockets on the alternate hexagon surfaces. It should be noted that the bit was designed to survive the load from the theoretical rover slip condition under Mars gravity. A 180-kg rover on a 20-degree slope would apply approximately 173-N side force to the bit.

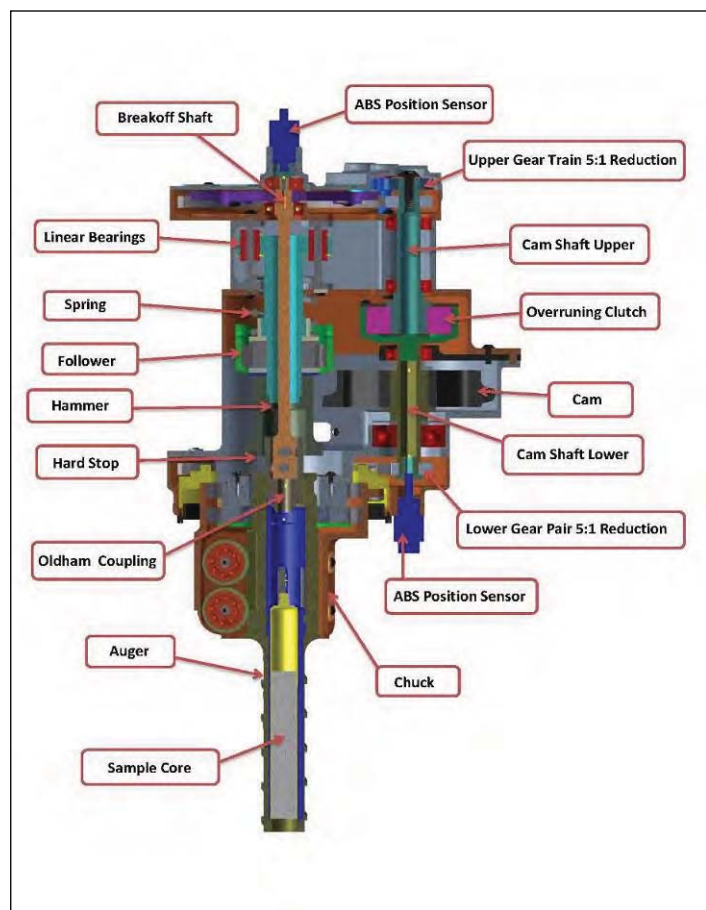
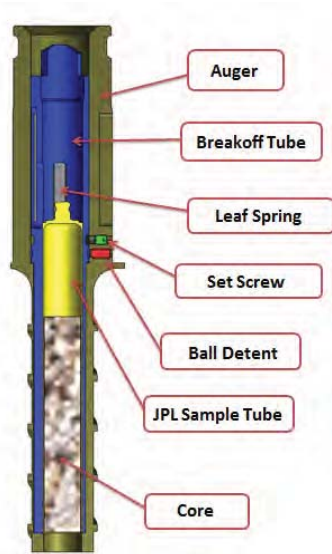
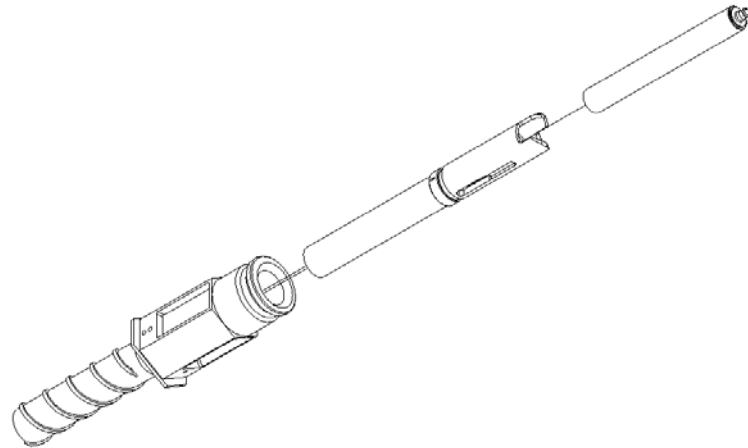


Figure 2. Details of the RANCOR drill components



**Figure 3. CAD image of the drill bit with its components labeled**



**Figure 4. Picture of the drill bit in an exploded drawing view, Auger, Breakoff Tube and JPL Sample Tube Visible**

Constraining the auger vertically in the drill are the small flanges that protrude from the hexagonal surface. The side of this feature fits in flats in the front end of the chuck. The groove in the shank is for mating with a cam in the bit lock mechanism to constrain the drill bit from falling out. Additionally, the rounded surface at the shank end mates with a seal to prevent dust or cuttings from entering the drill when the auger is in place. Caution should be taken in regards to cuttings and other debris since the complete drill bit assembly (complete with the JPL sample tube) should be in place to form a dust protective seal. However it is important to note that this assembly is not a perfect seal.

Material selection for the auger was decided based primarily on previously designed and tested Honeybee bit designs. The RANCOR bit uses a 455 stainless steel that has been heat treated to condition H900. This specialty steel was selected for its high performance characteristics of strength, toughness, and hardness. After manufacturing and heat treatment of the auger was complete, four rotary grade carbide inserts were brazed into place at the nose of the auger to serve as the cutting surfaces. Harder grade carbide was selected because this grade of carbide has been shown to survive percussion well when operating at relatively low percussive energy levels. At approximately 0.6 J/blow, the RANCOR drill falls into the category of low percussive energy. The advantage to using harder grade carbide is increased bit life, so long as the carbide doesn't fracture.

The breakoff tube (Figure 5) was also designed around the existing JPL Sampling tube. This mechanism interfaces with an Oldham coupling which is part of the core breakoff system. Design challenges for the breakoff tube included manufacturing for tight tolerances and clearances between the auger and the Oldham coupling interfaces. Different JPL sample tubes were expected to be inserted into the breakoff tube. Interfacing with multiple JPL sample tubes was expected to be difficult from a tolerance standpoint as they are thin walled structures and are vulnerable to deformation. To finalize the ID of the breakoff tube, multiple JPL sample tubes were measured and the statistical deviation of the maximum sample tube diameter was determined. Then the breakoff tubes were appropriately reamed to 0.4440 inch (11.28 mm) to accommodate all of the existing JPL sample tubes. The material used for the breakoff tube was 416 Stainless Steel which allowed for design flexibility in that a harder metal could be obtained through heat treatment if it was deemed necessary.



**Figure 5. RANCOR breakoff tube**

It is expected that the life of the breakoff tube will be able to outlive the life of the auger. In future designs, the following items should be considered to improve the design of the mechanism:

- Minimize the sliding friction between the inside surface of the auger and the outside surface of the breakoff tube. This could be done by using bronze bushings or even a concentric turning of the middle section of the breakoff tube.
- A better system of constraining the breakoff tube should be considered. Primarily, this concerns the replacement of the set screws. From test results, it is evident that the set screws have the potential of backing out if not installed correctly. Because of this, gouging can occur between the auger and breakoff tube, potentially causing them both to become jammed. The primary reason for using set screws here was to enable frequent disassembly of the drill bit assembly to monitor component wear and dust migration.

The final component that comprises the RANCOR coring drill bit is the JPL sample tube (Figure 6). This component is manufactured by JPL and is made of stainless steel. From an operational perspective, once the drill bit is docked with the JPL IMSAH system, the drill head separates from the drill bit and the JPL sample tube is extracted through the back end of the bit using an internal IMSAH mechanism. It is then cached within IMSAH for sample collection and analysis.



**Figure 6. JPL Sample tube**

#### RANCOR Chuck

Bridging the coring drill bit to the rest of the drill body is the chuck (Figure 7). Studied extensively during the concept and breadboarding phase of the project, the architecture of the chuck did not change dramatically from its initial concept. One of the driving requirements on the RANCOR drill was the ability to sustain the loads induced on the drill body and bit should the rover be drilling on a sloped surface and lose traction, or slip. The chuck serves as the primary interface for surviving and handling the load from the theoretical rover slip condition under Mars gravity. Slip conditions of a 180-kg rover on a 20-degree slope were needed to be survivable with the final chuck design. Under this loading condition the RANCOR chuck and drill bit would be expected to survive side loads as high as 173 N, as well as be able to safely eject the bit. Both conditions were met.





**Figure 7. RANCOR drill chuck and drill bit**



**Figure 8. Side view of the guide wheel roller, clearly showing the Nedox coating, and the two curved contact surfaces for maintaining near line contact with the bit shank**

RANCOR's final chuck design is comprised of six guide wheel rollers arranged in 3 pairs, 120 degrees apart from each other to constrain the drill bit. This configuration was chosen as a superior weight reduction design as opposed to a more conventional eight roller set in a 90-degree separated orientation. Utilizing guide wheels in this chuck is a key feature for enabling successful ejection of the drill bit under high loading conditions. The design also helps guide the drill bit insertion and minimizes percussive energy loss by allowing a small amount of axial motion during drilling. As shown in Figure 8, the surface of the guide wheel rollers is curved in two positions to help maintain line contact with the bit shank and still provide a means for transmitting torque to the bit. Maintaining the four surface contacts on each wheel set ensures that the auger is constrained in that plane and only allows axial motion from the drill bit. The drawback from this design is the relative size of the chuck required to house the rollers. However, this design still enables a maximum drill angle relative to the normal vector to the rock to be as large as 26 degrees and still allow for a 6-cm-long core to be captured before the chuck touches the rock. This allows for significant margin in the angular positioning accuracy of a robotic arm relative to the local surface normal of the rock.

The geometry of the chuck housing was optimized to minimize weight. CNC milling was required to fabricate the chuck housing out of a single piece of 6061 aluminum. Material for the guide wheels were selected as 455 stainless steel heat treated to condition H900 and plated with a Nedox SF-2 coating to reduce the rolling friction and increase the surface hardness. Steel pins were pressed through the bearings in the guide wheel rollers. Post-assembly, dimension checks were performed by inserting the drill bit augers into the chuck. Any tolerance corrections were then made by removing small amounts of material from the hexagonal faces of the bit shank. Interfacing the auger with the rest of the drill housing required a durable bearing interface. Sealed Silverthin JSA020 four point contact bearings were chosen for this purpose. Matched in pairs, these bearings are capable of sustaining thrust loads up to 3527 N under dynamic conditions and 7615 N under static conditions. Life expectancy of these bearings under expected loads show that these bearings should out last other bearings and components of the drill system. Overall, the functionality of the chuck and its minimal weight were favorable over other design alternatives designed to the same requirements. This chuck design has proven to be a reliable and robust component of the drill. Mass of the chuck was calculated to be 0.444 kg, approximately 15% of the overall drill weight.

Driving the chuck is the main drive motor for the drill, a Maxon 22-mm size brushless motor. In an effort to minimize weight and simplify operation, coupling the percussion mechanism with the auger rotation

allows for utilizing one actuator instead of two. Three Maxon motor combinations were tested for the drill unit. This was done to allow a high RPM as well as a high torque option to be evaluated during testing. Outputs from these various combinations were 272 RPM at 3.1 N-m continuous, 188 RPM at 4.3 N-m continuous, and 103 RPM at 6.7 N-m continuous. The high speed option worked well at speeds above 20 RPM. However, lower speeds were required for initializing and aligning the auger and breakoff tube when the system starts. The easiest solution to this was to simply exchange the planetary gearhead on the motor. The next size that fit the existing pinion gear on the motor produced the 103-RPM drill rate. This solution was not ideal from a drilling perspective, but met the system requirements and functioned well. Later the 188-RPM solution was implemented (this required a longer lead time) and also fit the requirements, but improved the performance of the drill. Ultimately, this option was selected as the final version.

#### RANCOR Overrunning Clutch (Sprag)

As previously mentioned, the rotation, percussion, and breakoff axes are driven by a single actuator. During a drilling operation, the actuator drives the auger and breakoff shaft simultaneously while the percussion axis rotates at 5 times the rate of the auger / breakoff axes. After drilling, the rock core is sheared at the base to capture it within the bit. To accomplish this, a clutch was implemented to separate the percussion cam and auger from the breakoff axis while driven in the opposite drilling direction. This allows the breakoff axis to rotate while the percussion and auger remain stationary. The drive train path is highlighted in Figure 9 with the blue path representing the breakoff axis and the red path representing the percussion and auger axes.

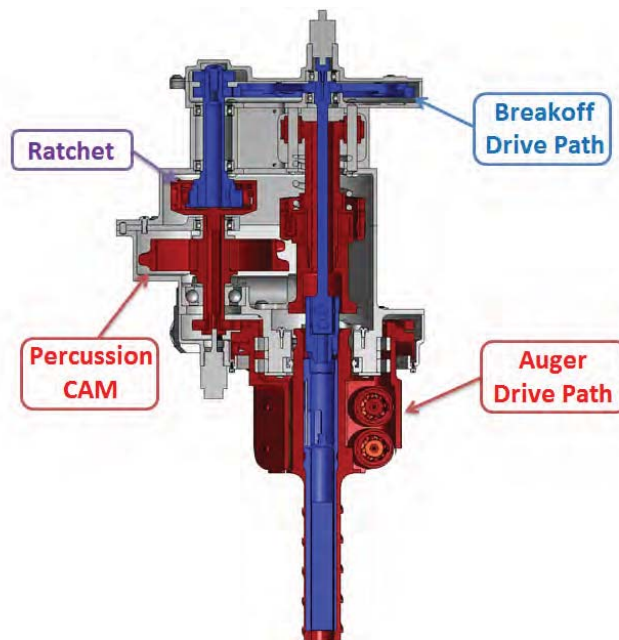


**Figure 9. Ratchet used to couple / decouple the percussion & auger rotation from the breakoff axis**

Initially an over running clutch, which utilizes sprags, was implemented. Though this mechanism performed as it should have, there was an operational behavior that was overlooked. Since the CAM must compress a spring and release the load over a short duration, there is a highly cyclical load on the CAM shaft. When the load is released there seems to be a combination of inertial effects and physical effects with the interface between the follower and the CAM that causes the CAM, and therefore the Auger axis to advance ahead of the breakoff axis. This effect caused poor quality cores to be produced, as shown in the bottom left image of Figure 10. Given the fine resolution of the sprag, these small advancements are captured, which causes relative motion between the auger and breakoff axes during a



drilling operation. At 100-RPM auger rotation, it takes about 500 percussion impacts to create a full 360° relative displacement between the auger and breakoff axes. Tests have shown that lower velocities generate higher displacements per blow and that when drilling into harder materials, this relative motion can be contained. However, this motion is unacceptable from a performance perspective. To solve this problem, a custom ratchet mechanism was designed to replace the sprag clutch.

The ratchet design shown in Figure 10 required more components and was significantly more expensive than the off the shelf sprag clutch. However, it offers two key features that make it an ideal solution to the problem of the auger advancing ahead of the breakoff axis. The first feature is the more coarse resolution. In this case, the cam would have to advance 18° ahead of the input shaft upon release to cause a shift in one tooth of the ratchet. This is far more than the average 4° shift that was observed with the sprag. The second key feature offered by the ratchet is that a more controllable force is required to cause the ratchet to advance. In the ratchet designed for this application, it takes approximately 0.5 N-m to advance the outer housing for the ratchet (well within the capabilities of the drive motor). This excludes frictional forces which are difficult to characterize and vary with temperature, pressure, vibration, and a number of other factors. In the case of the sprag, there were only rolling contact frictional forces to overcome to advance the outer race of the sprag. After implementing the ratchet mechanism into the final RANCOR drill assembly, the auger no longer advanced ahead of the breakoff shaft during drilling, resulting in a significant improvement in core quality, as shown in the bottom right image of Figure 10.

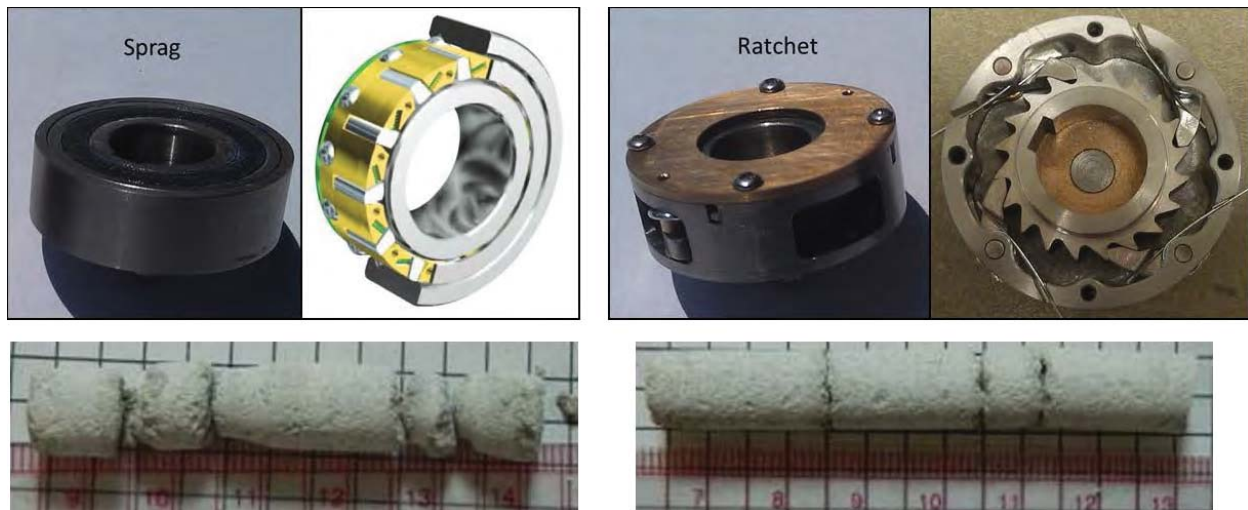


**Figure 10. Sprag (left) [7] and Ratchet (right) mechanisms and corresponding core qualities**

#### RANCOR Percussive Mechanism

Following the heritage of previous Honeybee drills, the RANCOR percussive mechanism was built upon existing successful designs. Mechanically, the percussion depends on employing a rotating cam to lift the follower fixed on the hammer, which then compresses a spring. Once the follower reaches the end of the cam, the spring potential energy is released and the hammer is free to impact the rear end of the drill bit, delivering the 0.6 joules per blow of energy.

A unique feature of the Honeybee CAM follower mechanism is the canted follower concept (Figure 11). This concept utilizes a follower mounted on bearings and tilted to match the slope of the CAM. By using this approach, the interaction between the CAM and follower is primarily rolling contact. However, there is sliding contact at the point where the CAM releases the follower. This approach also increases the operating efficiency of the mechanism. In the IceBreaker drill for instance, the CAM / follower mechanism operated at about 70% efficient [9, 10]. In alternative approaches where the follower is perpendicular to the vertical axis, efficiencies were typically in the 30% to 40% range.

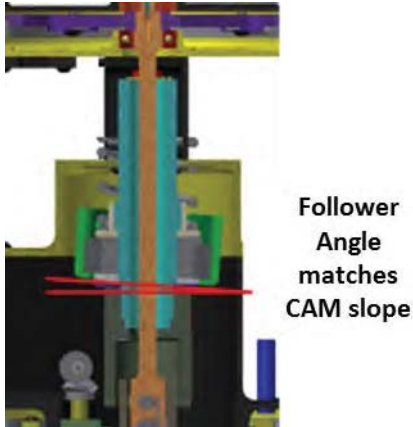


**Figure 11. Canted Follower matches slope of CAM**



**Figure 12. Wear on SASSI CAM**

Another advantage to the canted follower design is an increased life of the CAM / follower mechanism. Two RANCOR units were assembled and tested; a Honeybee and a JPL unit. After over 50,000 percussive cycles with the Honeybee RANCOR unit and over 30,000 percussive cycles with the JPL RANCOR unit, there is little wear on the mechanism (Figure 13). The only obvious wear location is the end of the ramp on the CAM where the follower is released. The follower also had a lubricious coating (Magnaplate Nedox FM-5) that has been worn off on the contact area which was anticipated. At the end of the CAM ramp the Magnaplate Nedox SF-2 plating has been worn off entirely. In designs where the follower is not canted (Figure 12) this plating is removed over essentially the entire contact area of the CAM after only a few thousand cycles.



**Figure 13. Images of wear in CAM and Follower for Honeybee unit after 50,000+ cycles (top 3 images) and the JPL unit after 30,000+ cycles (bottom 3 images)**

The method for constraining the percussive hammer had a large impact on the overall mass of the drill. Originally a ball spline was considered to constrain the motion of the hammer mechanism (left of Figure 14). However, this required a large amount of volume and added a large amount of mass. For the percussive cam system to work, a fixed amount of vertical travel of the hammer is required. The volume

due to this travel is fixed; however, the height of the linear slide mechanism can be reduced to only accommodate the required stroke plus some margin.

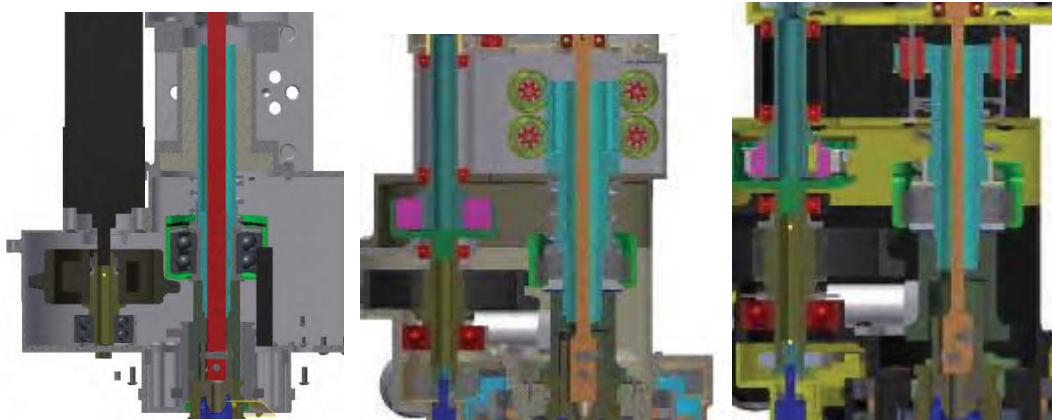


**Figure 14. Image of evolution of the hammer assembly. Initial concept on the left and final design on the right**

To reduce the mass of the hammer assembly, an alternative for the ball spline was sought. The first alternative approach considered, took inspiration from the chuck roller mechanism. This concept utilized 4 rollers to constrain a custom shaft to axial motion only (center of Figure 14). Due to the complexity of the mechanism and concerns over holding tolerances another alternative mechanism was designed. The final iteration of the design involved two linear bearings (right of Figure 14), which were later replaced by SAE 841 Bronze journal bearings. This is because the linear bearings did not prove durable enough to handle the shock loads of the percussing hammer. This design ended up being the most compact and had the greatest impact in mass reduction of all the designs considered for constraining the hammer motion.



**Figure 15. Hammer Sub Assembly**

Another unexpected failure was the spring responsible for generating percussive energy (Figure 15). The original spring selected for the mechanism was a 303 Stainless Steel compression spring. Failure of the spring occurred towards the end of an extended test of 2 hours (typical tests would run for 10 min to 15 min). Testing conditions were earth ambient temperature and pressure. The spring selected had a free length of 2.54 cm, 2.78-cm outside diameter, a wire diameter of 0.285 cm and 4.1 coils and the designated part number LC112M00S. In the RANCOR application, the spring was constrained by its inside diameter against the fixed, steel backed aluminum housing and the reciprocating follower on top of the drill's hammer. The spring carried an initial preload of 13.9 N due to its compression of 0.081 cm. At maximum compression, caused by the cam lifting the follower, the spring exerted 147.5 N of force under

0.864 cm of compression. At its release, this spring was calculated to provide 0.63 J of energy. The cam operated at 1400 RPM; lifting the follower and subsequently the spring once per revolution, the operation frequency of the spring was 23.33 Hz. Critical frequency of the spring was calculated to be 517 Hz [6]. This is more than 15 to 20 times the operating efficiency which is typically recommended for compressive springs. The Gerber method was used for calculating spring fatigue life [6]. Fatigue analyses concluded the spring should last above  $10^7$  cycles. However, after about 250,000 cycles, less than  $1/40^{\text{th}}$  the calculated design life of the spring, failure occurred.

Since no material certification was requested at the time of purchase of the springs, it is difficult to trace the pedigree of the failed spring. Contacting the manufacturer, Lee Spring, post failure investigation revealed the springs were manufactured in either China or Mexico from a 300-series stainless steel, out of cold drawn stock as according to ASTM A313. The spring also underwent stress relief between 315 - 371 °C after forming and had not been shot peened.

Potential reasons for failure were classified into operation or manufacture. Initial reasons investigated for the spring failure were thought to relate to low cycle failure since initial calculations indicated the spring should have a much longer cycle life than what was measured in testing. High cycle failure is typically caused by subsurface failure from inclusions and low cycle failure, such as perceived in this case, is a symptom of surface imperfections, or surface scratches [8]. Since the operational environment conditions did not exceed the spring's specifications, handling and assembly of the spring were looked at. The possibility of additional surface scratches during assembly was not ruled out. Magnified inspection of the spring under stereo microscope did not indicate any noticeable surface scratches, though a defect as small as 40  $\mu\text{m}$  in length (and hence difficult to see without the use of a Scanning Electron Microscope) could cause fracture initiation. A close up of the fractured surfaces is shown in Figure 16. The granular area in the image indicates brittle fracture. The fracture was at 45 degree (Figure 17) and hence followed the maximum principal stress plane. It should be noted that the gold material shown in Figure 16 is contamination from a bronze sleeve that had started to wear during this 2 hour test.

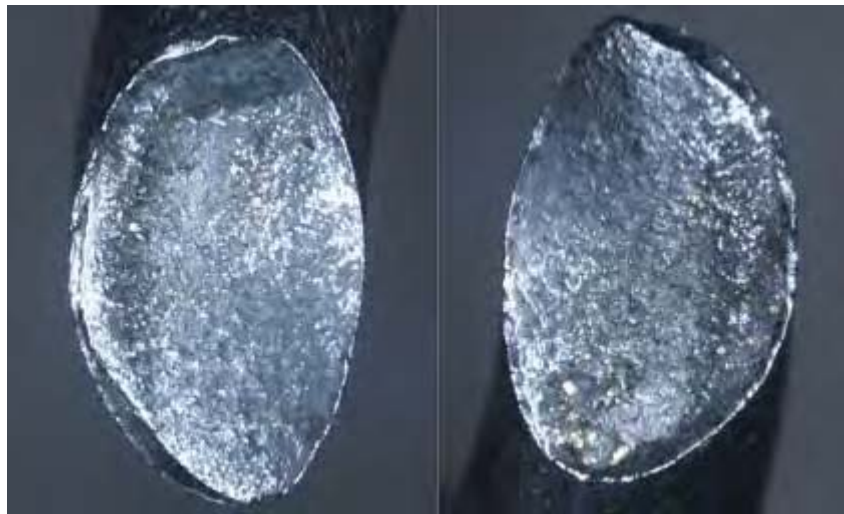


**Figure 16. Enlarged imaging of the fracture. Actual wire diameter is 0.285 cm. Side one of the fracture (left). Side two of the fracture (right).**



## Testing

Two RANCOR drills were built to support this effort. These units are referred to as the Honeybee Support unit and the JPL unit (Figure 18). During the testing phase, two distinct changes to the system were made that impacted the performance of the drill. The first was changing the motor planetary gearhead assembly to provide an increased auger velocity. This change more than doubled the rate of penetration (ROP) in most cases which helped to reduce the overall cycles on the actuator. Interestingly, the number of percussion and auger cycles remained relatively constant. The second change was switching from the sprag overrunning clutch to a ratchet design. This change improved the core grade from primarily D and F grades (generally meaning several fragments and reassembly of core stratigraphy is not obvious as shown in the left of Figure 10) to mostly A, B, and C grades (generally cores that are in-tact or in only a few fragments with a stratigraphy that can be reconstructed as shown in the right of Figure 10). In general, the JPL drill had lower quality cores. This is likely because this system was not positioned well with respect to the linear stage. That is, the drill bit axis and linear deployment stage axis had some noticeable angular misalignment in the mounts to the deployment stage. Therefore the drill bit was penetrating at an angle. Selected telemetry from these lab tests are shown in Table 1.



**Figure 17. Post failure spring, side 1 on the left, side 2 on the right. An approximate 45 degree failure to the surface of the spring corresponds with the maximum principal stress plane.**

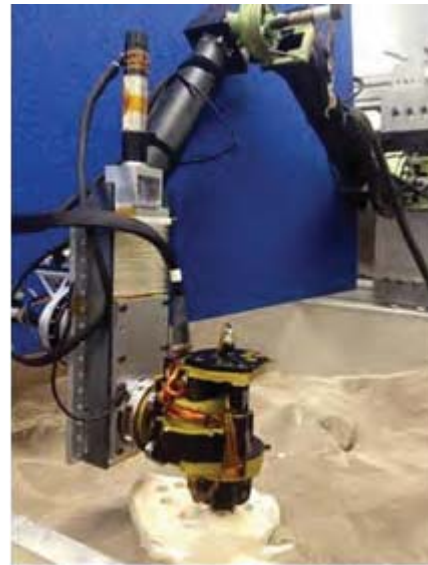


**Figure 18. Lab Testing at Honeybee with the Honeybee Support unit (left) and the JPL delivered unit (right).**

**Table 1. Selected Drill Telemetry from Controlled Laboratory Tests. (Tests marked with an \* were tests in a brown Gypsum. All other tests were in Indiana Limestone. Test 015 is marked with a \*\* because the core breakoff was in the wrong position which resulted in a very poor core grade.)**

Test	Drill	RPM	Sprag / Ratchet	ROP (mm/s)	WOB (N)	Energy/core (Whr)	Motor Cycles	Percuss Cycles	Core Grade
001	HBR	99	Sprag	0.94	39	2.07	168662	3182	D
002	HBR	100	Sprag	0.64	26	2.78	253687	4787	F
003	HBR	100	Sprag	0.56	27	3.19	293248	5533	F
004	HBR	100	Sprag	0.51	27	3.52	331758	6260	C
005	HBR	100	Sprag	0.41	25	4.21	411291	7760	F
006	HBR	100	Sprag	0.49	28	3.91	360050	6793	D
007	HBR	179	Sprag	1.20	37	3.46	146721	5059	F
008	HBR	179	Sprag	1.26	38	3.35	142357	4909	F
009*	HBR	179	Sprag	1.38	36	2.82	116164	4006	D
010*	HBR	179	Sprag	1.39	36	2.82	124202	4283	D
011*	HBR	178	Ratchet	1.24	36	2.37	109073	3761	A
012*	HBR	179	Ratchet	1.26	40	3.13	141429	4877	B
013	HBR	179	Ratchet	1.12	40	3.46	155186	5351	C
014	HBR	179	Ratchet	0.89	40	4.02	189509	6535	C
015**	HBR	179	Ratchet	0.78	40	4.56	222700	7679	F
016	HBR	179	Ratchet	0.81	41	4.42	208367	7185	A
017	HBR	179	Ratchet	0.90	39	3.85	188187	6489	C
018	JPL	179	Ratchet	1.15	37	3.26	149220	5146	A
019	JPL	179	Ratchet	1.01	39	3.44	167460	5774	D
020	JPL	179	Ratchet	0.88	39	3.78	198538	6846	D
021	JPL	179	Ratchet	1.04	37	3.48	173618	5987	A

### Lessons Learned

A number of useful lessons were learned from the design and testing of the RANCOR drill. As with any design, there is still room for improvement, but in the end the drill was more than capable of performing coring tasks in medium to low strength rock targets. Also as requirements for Mars Sample Return (MSR) mature, there may be more mass and volume available to the drill design that can be utilized to increase the reliability and robustness. Lessons learned from the RANCOR drill include the following:

1. In this case, the cost and simplicity of an off-the-shelf sprag clutch versus the design and build of a custom ratchet and pawl system led to the decision to use the sprag clutch. Although there was nothing functionally wrong with the sprag in this design, it enabled a degree of freedom that should have been locked out during the release of the hammer on the RANCOR. Therefore, the sprag mechanism was replaced with a ratchet and pawl system. The result was a large improvement in core quality (from D through F grades to A and B grades).
2. If a single drill bit is to be used for multiple holes (i.e. 10, 20, 30), care must be taken to design a proper kinematic constraint for rotation of the inner breakoff tube with the outer auger tube. Also seals should be used to prevent rock cuttings from migrating between the breakoff and auger tubes. In the region near the cutting edge of the bit, there should be sufficient clearance between the breakoff tube and auger tube to allow rock cuttings to flow in and out more freely. If there is not sufficient clearance, the cuttings will pack up and seize rotation between the breakoff and auger axes. This can happen after drilling only a few cores if spacing is not sufficient and seals are not in place.



3. Using rollers in the drill chuck to constrain the drill bit offers many benefits over traditional spline joints. These benefits are as follows:
  - a. Rotating joints are much easier to protect from dust than linear spline type joints.
  - b. When docking with a bit, the relatively large rollers on the RANCOR chuck helped account for some misalignment between the drill chuck axis and the axis of the docked drill bit.
  - c. The rolling interface between the chuck and the bit is a highly efficient joint that enables an efficient transfer of the percussive energy to the bit. Also, this interface greatly reduces the force required to remove the drill head from the drill bit if there is a large side load present on the system.
  
4. As with all drill bit designs, the grade of carbide makes a big difference in the life of the bit. In general, at low percussive energies, harder, more brittle carbide can be used to extend the life of the drill bit by reducing wear. In the case of the RANCOR drill bit design, the harder carbide performed well in relatively soft rocks (~40-MPa UCS). However, when drilling the ~120-MPa Saddleback Basalt, these cutters fractured and became less effective. Therefore, for the RANCOR drill, softer grade carbide is preferred. It is recommended that a number of carbide grades should be tested to determine the optimum combination of hardness and toughness for 0.6 J/blow hammer system in hard rocks. It should be noted that for alternative sample caching architectures, where the bit is used only once and cached together with a core sample, the bit life is less of a concern and hence softer carbide could be selected [11].

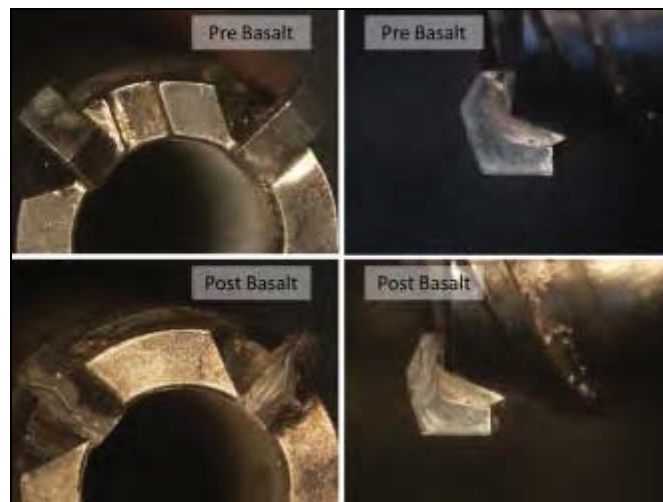


**Figure 19. RANCOR drill bit with a harder, more brittle, rotary grade carbide before and after drilling into Saddleback Basalt.**

5. For all spring loaded percussive designs, it's important to life test the percussive mechanism using components from a batch process with certification. Spring analyses for the RANCOR concluded that the original stainless steel spring selected for the RANCOR drill should have survived more than  $10^7$  cycles. However, this spring failed on the support unit after only 250,000 cycles. Currently the music wire spring that replaced the stainless steel spring is at greater than 375,000 cycles.
  
6. Using a canted or sloped follower for the hammer mechanism (i.e. follower is tilted to match the slope of the cam) is an ideal solution for the percussive mechanism. This type of solution has now been implemented on its third Honeybee drilling system and has performed efficiently on all systems. When compared to a more traditional follower design where the follower is perpendicular to its axis of travel, the canted follower is about twice as efficient and the wear in the mechanism is significantly reduced.

## Conclusions

A 3-kg rotary percussive core acquisition drill was developed under this effort. The system consists of two actuators and was able to drill cores, break and capture cores, and actively mate and de-mate with drill bits. This design fits within the JPL-derived IMSAH architecture and has mass, volume, power, and energy specifications that would enable deployment and operation from an MER or MER+ class rover or larger. Results from tests performed with this RANCOR drill proved that this design is fully capable of meeting the goals of a MSR mission. However, there were lessons learned here that would help to improve future designs of this type of drill and future drill systems. Also, much more testing is necessary to help ensure the life of the components within the drill will be sufficient for providing up to 30 cores plus margin for a MSR mission. Tests also should be performed at Mars atmospheric pressure.

## Acknowledgements

This work was funded by the NASA Small Business Innovative Research (SBIR) Program. We owe our sincere thanks and appreciation to the NASA SBIR program and the COTRs: Paul Backes, Kristo Kriechbaum, Kerry Klein, and Lori Shiraishi.

## References

1. S. Hayati, Technology Planning for Future Mars Missions, MEPAG, 29-30 July 2009
2. Chu P., J. Spring, K. Zacny, ROPEC – ROTary PERcussive Coring Drill for Mars Sample Return, 42nd Aerospace Mechanisms Symposium will be May 14-16, 2014 in Baltimore, Maryland.
3. K. Klein, et al. "Rotary Percussive Sample Acquisition Tool (SAT): Hardware Development and Testing." Proceeding of the 41<sup>st</sup> Aerospace Mechanism Symposium, Jet Propulsion Laboratory, May 16-18, 2012.
4. Backes, P.; Lindemann, R.; Collins, C.; Younse, P.; An integrated coring and caching concept, Aerospace Conference, 2010 IEEE, 10.1109/AERO.2010.5446985
5. Myrick., T., US Patent No. 6,550,549, "Core Break-off Mechanism"
6. Joseph E. Shigley and Charles R. Mischke. *Mechanical Engineering Design Sixth Ed.* McGraw-Hill, 2001.
7. GotTransmissions.com. (2014, January 3). *Automatic Transmission Sprag Clutches Defined.* <http://www.gottransmissions.com/blog/transmission-components-technology-defined-explained/automatic-transmission-sprag-clutches-defined>.
8. Pytel et al. "Fatigue behavior of helical compression springs at a very high number of cycles – Investigation of various influences." *International Journal of Fatigue* (2013).
9. Paulsen, G., K. Zacny, M. Szczesiak, C. Santoro, B. Mellerowicz, J. Craft, C. McKay, B. Glass, A. Davila, M. Marinova. *Testing of a 1 meter Mars IceBreaker Drill in a 3.5 meter Vacuum Chamber and in an Antarctic Mars Analog Site.* AIAA SPACE 2011 Conference & Exposition, Long Beach, September 26-29, 2011
10. Zacny K., Paulsen G., McKay C. P., Glass B., Davé A., Davila A.F., Marinova M., Mellerowicz B., Heldmann J., Stoker C., Cabrol N., Hedlund M., and Craft J. *Reaching 1 m Deep on Mars: The Icebreaker Drill.* *Astrobiology.* December 2013, 13(12): 1166-1198. doi:10.1089/ast.2013.1038.
11. Zacny, K., J. Wilson, P. Chu, and J. Craft, Prototype Rotary Percussive Drill for the Mars Sample Return Mission, Paper #1125, IEEE Aerospace conference, 5-12 March 2011, Big Sky, Montana.

# Torque Tension Testing of Fasteners used for NASA Flight Hardware Applications

Ed Hemminger\*, Alan Posey\* and Michael Dube\*

## Abstract

The effect of various lubricants and other compounds on fastener torque-tension relationships is evaluated. Testing was performed using a unique test apparatus developed by Posey at the NASA Goddard Space Flight Center. A description of the test methodology, including associated data collection and analysis will be presented. Test results for 300 series CRES and A286 heat resistant fasteners, torqued into various types of inserts will be presented. The primary objective of this testing was to obtain torque-tension data for use on NASA flight projects.

## Introduction

Threaded fasteners are used extensively in flight hardware assembly at the Goddard Space Flight Center. The reliability and safety of the assembly is dependent primarily on the preload which is applied by trained and certified technicians using a calibrated torque wrench of the proper size. It has been shown that most of the applied torque is used in overcoming the head bearing and thread friction leaving only a small fraction for fastener elongation or tension resulting in joint pre-load application. The torque tension relationship is therefore highly dependent on the friction coefficients and lubrication applied to the threads and washer-to-bolt head bearing surfaces. Even the most reliable torque application methods have been shown to result in wide scatter and do not accurately predict the joint preload. This can result in premature joint or fastener failure due to over or under estimation of the applied preload. Typical failure mechanisms are vibration loosening, fastener fatigue due to insufficient preload, or joint failure due to excessive preload.

Alan Posey has developed a new bolt preload measurement system which incorporates three miniature load cells and an instrumented torque wrench for measurement of applied torque and joint preload (see Figures 1 and 2).



Figure 1. Bolt Preload Test Fixture & Test Plate

---

\* NASA Goddard Space Flight Center, Greenbelt, MD



**Figure 2. Bolt Preload Measurement System**

In the past, one load washer was typically used for torque tension testing but this was not practical for the smaller #0 (1.5-mm) to #6 (3.5-mm) size fasteners as load washers this size were not available. The system consists of three load cells mounted in a high-strength steel fixture plate in an equilateral triangle configuration. A counter-bored bushing, sized for the fastener being tested, is centered in this triangular pattern. The system is connected to a laptop computer with LabVIEW and MATLAB software for data collection and analysis (Figure 3). Fasteners from size #0 (1.5-mm) to ¼-in (6.3-mm) diameter have been tested using this system.

**Governing Equation:**

- $T=KDP$
- 
- $T=Torque,$
- 
- $K=Torque$   
 $Coefficient,$
- 
- $D=Bolt Dia,$
- 
- $P=Preload$

**Testing to Determine “K”**

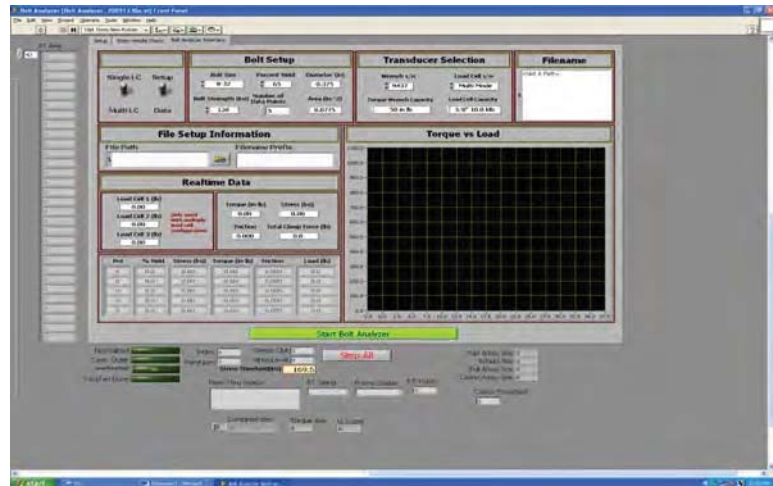


**Figure 3. Bolt Analyzer Interface**

## Test Objectives

The primary objective was to obtain torque-tension data for use of various lubricants such as Braycote 601EF and compounds such as Arathane and Super Korocon. Arathane has been used as a thread locking compound to replace worn out locking features on helical-wire inserts and Super Korocon is used as a corrosion inhibitor/sealer on threaded fasteners and inserts as specified in NASA/JSC PRC-4004, "Sealing of Joints and Faying Surfaces". Some secondary objectives of this testing were to identify the effect of the following variables on torque coefficient (or nut factor) and running torque:

- Multiple cycling of locking inserts.
- Fastener and washer replacement in multiple cycling of inserts.
- The use of multiple lot and or multiple type inserts of a given size.
- The use of ultrasonic cleaning in isopropyl alcohol (IPA) of all hardware as compared to use in as received, un-cleaned condition.

### Small Fastener Testing (#2, #4 & #6) (2.2 mm, 2.8 mm & 3.5 mm)

Torque-tension testing of A286 and 300-series CRES fasteners threaded into free running phosphor bronze and silver-plated CRES helical-wire inserts was performed using the system developed by Posey. Fastener testing was performed both with a low outgassing flight-approved lubricant (Braycote 601EF) and dry insertion.

Torque-tension measurements were taken up to 65% of the fastener yield strength which represents the standard preload currently used at Goddard. Both torque and preload were measured at five equally spaced increments up to the target preload. All hardware was ultrasonically cleaned and handled with gloves using flight hardware processes.

Each fastener tested was torque cycled three times while each insert was cycled six times. After three torque cycles into a given insert, the fasteners and washers were replaced with new hardware and re-lubricated. Separate test plates were used for dry and Braycote lubricated samples. Lubrication was applied to the threads and under the fastener head. The fasteners were torqued at a rate of approximately 6 rpm until the target preload was reached. The data tables and plots below provide a summary of the statistics for the torque coefficient (K) for fasteners installed both lubricated and dry into two different types of helical-wire inserts (Silver-Plated CRES and Phosphor Bronze). The standard deviation of the torque coefficient was calculated for each grouping and also combined for all groups. The B-Basis tolerance limit factors of Kmax and Kmin were also calculated based on the sample size and are given in the tables below. Running torque was included in all measured torque values.

### Small Fastener Test Results and Conclusions

Table 1 and Figures 4 and 5 provide a summary of the statistics for the torque coefficient (K) for each of the types of fasteners into the different types of inserts (Silver-Plated CRES and Phosphor Bronze).



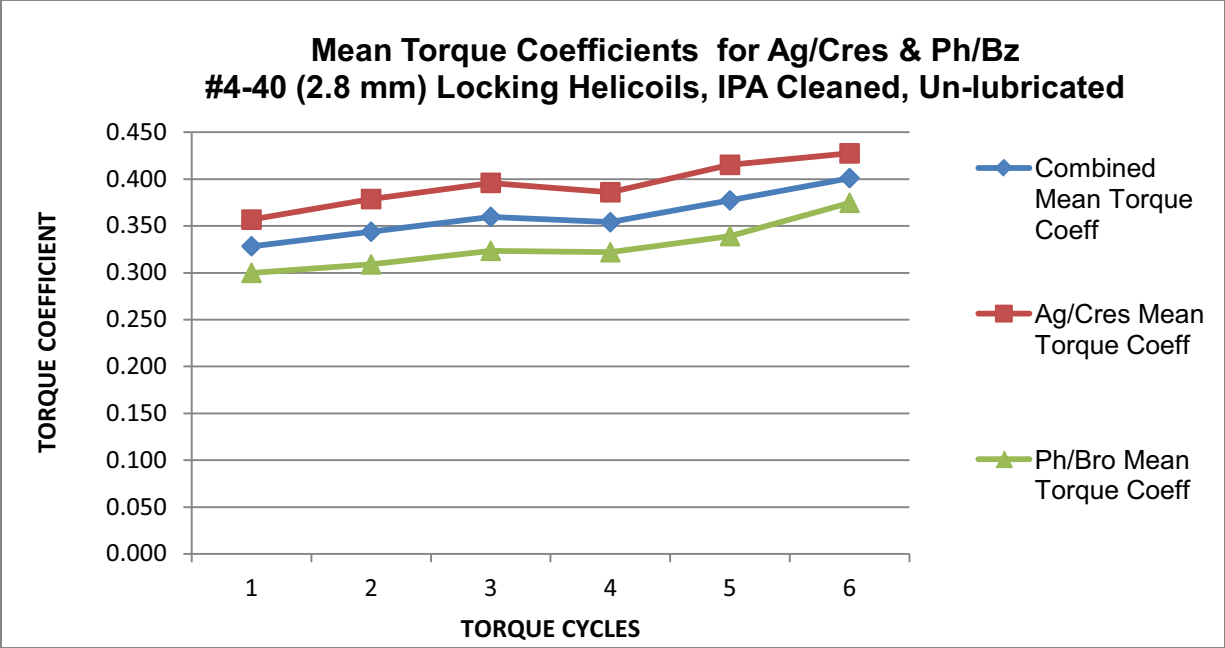


Figure 4. Unlubricated Cyclic Mean Torque Coefficients Example

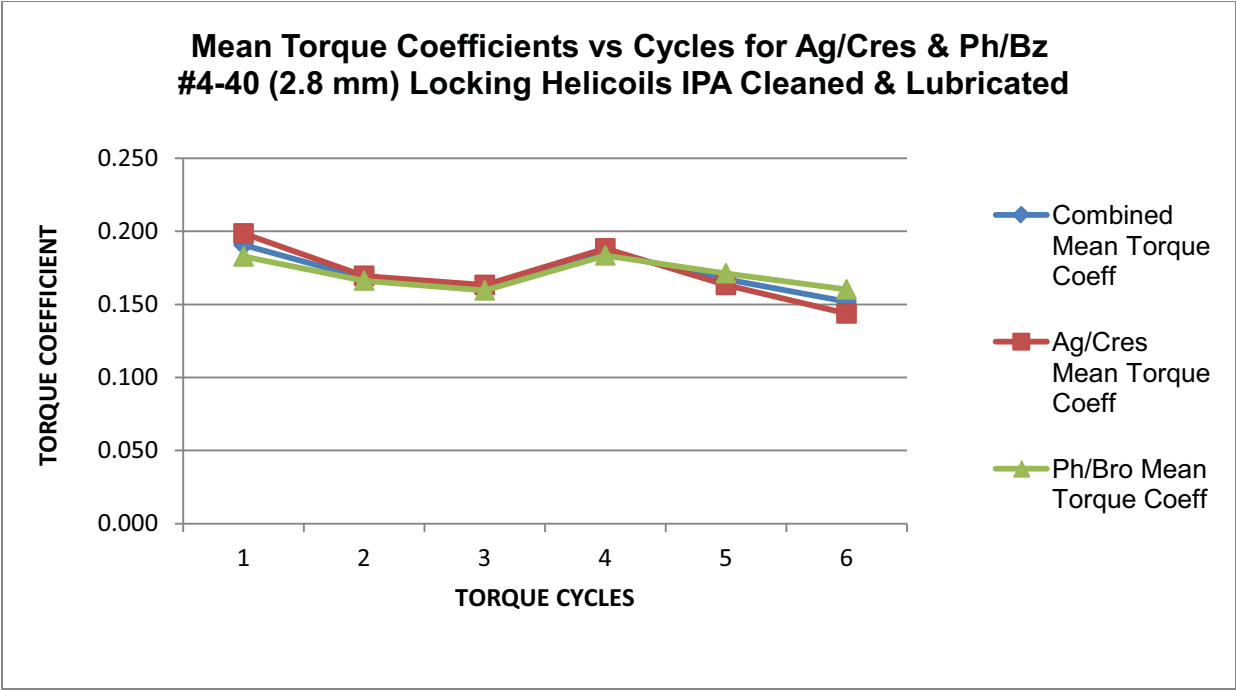


Figure 5. Lubricated Cyclic Mean Torque Coefficients Example

**Table 1. Phosphor Bronze Data Summary**

Phosphor Bronze Inserts												
Fastener	Wet Lubrication						Dry					
	Mean Torque Coefficient K	STD Dev	No. Samples	Tolerance Limit Factor	B-Basis Limits K-Low	B-Basis Limits K-High	Mean Torque Coefficient K	STD Dev	No. Samples	Tolerance Limit Factor	B-Basis Limits K-min	B-Basis Limits K-max
A286	0.169	0.024	48	1.654	0.129	0.210	0.373	0.084	46	1.664	0.233	0.513
300 CRES	0.174	0.022	36	1.725	0.136	0.211	0.339	0.028	36	1.725	0.290	0.387
NAS1352N A286	0.182	0.032	18	1.974	0.119	0.244	0.401	0.102	17	2.002	0.198	0.605
NAS1101 A286	0.167	0.016	18	1.974	0.135	0.198	0.375	0.071	18	1.974	0.236	0.514
NAS8100/1 A286	0.154	0.017	12	2.21	0.117	0.192	0.326	0.056	11	2.275	0.199	0.453
NAS 1352C 300 CRES	0.170	0.018	18	1.974	0.133	0.206	0.333	0.028	18	1.974	0.278	0.389
MS51957 300 CRES	0.181	0.025	18	1.974	0.132	0.231	0.344	0.028	18	1.974	0.289	0.399
Silver Plated Inserts												
Fastener	Wet Lubrication						Dry					
	Mean Torque Coefficient K	STD Dev	No. Samples	B-Basis Tolerance Limit Factor	B-Basis Limits K-Low	B-Basis Limits K-High	Mean Torque Coefficient K	STD Dev	No. Samples	Tolerance Limit Factor	B-Basis Limits K-Low	B-Basis Limits K-High
A286	0.165	0.019	48	1.654	0.134	0.197	0.422	0.098	45	1.664	0.259	0.585
300 CRES	0.180	0.025	36	1.725	0.137	0.224	0.413	0.081	36	1.725	0.273	0.552
NAS1352N A286	0.173	0.022	18	1.974	0.129	0.216	0.432	0.072	17	2.002	0.287	0.577
NAS1101 A286	0.160	0.013	18	1.974	0.134	0.187	0.444	0.106	18	1.974	0.234	0.653
NAS8100/1 A286	0.162	0.017	12	2.210	0.125	0.199	0.225	0.021	10	2.355	0.175	0.275
NAS 1352C 300 CRES	0.174	0.028	18	1.974	0.119	0.230	0.429	0.074	18	1.974	0.283	0.575
MS51957 300 CRES	0.186	0.021	18	1.974	0.145	0.227	0.396	0.086	18	1.974	0.226	0.566

Conclusions and Observations based on the results shown in Table 1:

1. For dry un-lubricated cases, the torque coefficient was found to increase with cycles, whereas for the lubricated cases the reverse was true.
2. The dispersion (standard deviation) of the torque coefficient for all the Dry groups of fasteners was much greater for the dry installation versus the lubricated installation. The smaller dispersion for lubrication make it a better choice (when acceptable to the project) than installing dry since there

is less uncertainty with the torque-tension relationship

3. The torque coefficients for dry silver-plated CRES inserts were higher than for phosphor bronze inserts. In addition, the dispersion was also higher for the dry silver-plated CRES inserts. This was more pronounced for larger size fasteners and goes counter to the assumption that silver plating will act as an effective lubricant. For lubricated samples there was little difference.
4. The torque coefficients for smaller fasteners were found to be higher than those specified by the Goddard Torque Guideline. In this document the lubricated torque coefficient is specified at 0.15 and dry coefficient at 0.2. Based on the small fastener test results, these values were revised to a wet coefficient of 0.18 and dry coefficient of 0.37. Also, based on un-cleaned test results, a coefficient of 0.25 was specified for dry un-cleaned samples.

### Arathane Testing

The purpose of this testing was to determine the differences in torque coefficient when applying Arathane 5753 thread locking compound versus Braycote 601EF lubricant to the fasteners at installation. The use of Arathane as a secondary locking feature was proposed when locking inserts were worn due to repeated torque application cycles. The test sequence was as follows:

- First, the locking phosphor bronze inserts were worn by (10) torque application cycles to 65% yield. This was performed for three different size inserts, #8 (4.2 mm), #10 (4.8 mm) and ¼ inch (6.3 mm) with Braycote lubrication applied to the fastener threads and washer to bolt head bearing surface for first cycles only.
- During each of the (10) torque application cycles, torque-tension measurements were recorded.
- After ten cycles, the worn insert was thoroughly cleaned and a new fastener and washer were installed with Arathane applied to threads and washer to bolt head bearing surface.

Also investigated was the case where a new fastener is installed into a new locking phosphor bronze insert with both Arathane and Braycote. Two different cleaning agents, (IPA and HFE7100) for removal of the Braycote lubricant from worn inserts, were also investigated.

#### Arathane Test Results and Conclusions

The average torque coefficients (Kmean) were determined by two methods as follows:

1. First method was to use the average total torque at the target preload of 65% fastener yield.
2. The second more involved method was to perform a linear regression curve fit of actual test data and determine the torque coefficient from the slope of the linear regression curve. As shown in the Table 2, there was little difference between the two methods for the various data sets.

**Table 2. Torque Coefficient Comparison: Average vs Linear Regression Method**

Configuration	Ave Torque Coeff @ 65%	Ave Torque Coeff Linear Regression (LR)	% Difference of Methods
Worn #8 Braycote	0.145	0.137	5.4
Worn #8 Arathane	0.284	0.277	2.6
Worn #10 Braycote	0.175	0.168	4.2
Worn #10 Arathane	0.314	0.312	0.6
Worn 1/4" Braycote	0.227	0.219	3.5
Worn 1/4" Arathane	0.316	0.321	1.8

A comparison of torque coefficients for use of Arathane and Braycote is shown in Figure 6. The cyclic data was combined into one data set for each fastener/insert size to generate this comparison data plot.

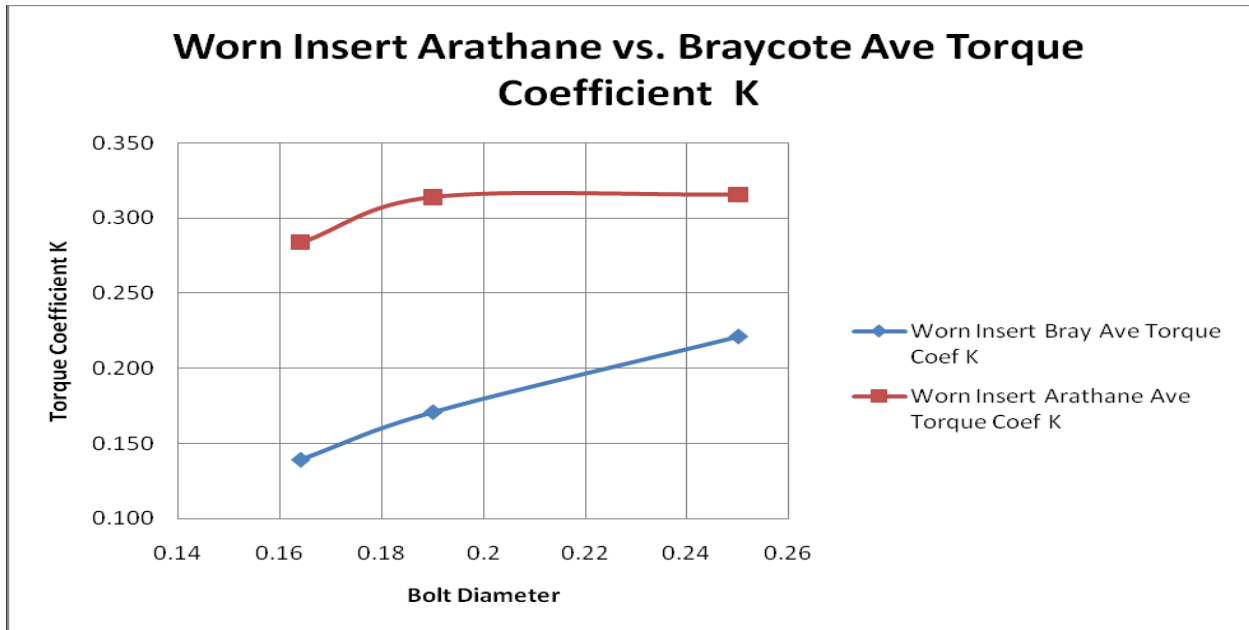


**Figure 6. Arathane and Braycote Torque Coefficient Comparison**

A typical plot of torque coefficients for individual torque application cycles is shown in Figure 7 for #10-32 size fasteners. Cycles 1-10 are Braycote wear cycles, cycle 11 is for a new fastener and washer used in the worn insert with Arathane and cycle 12 for a new fastener and washer used in a new insert with Arathane. The Kmax and Kmin torque coefficients are based on B-basis calculations similar to those used for small fasteners.

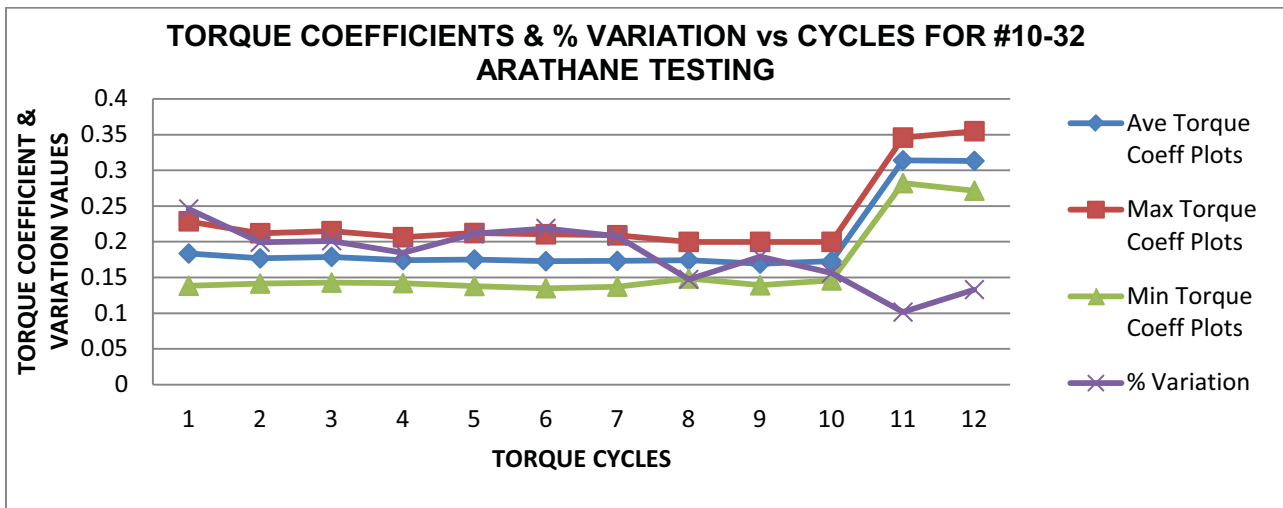


**Figure 7. Cyclic Torque Coefficients, Braycote (1-10), Arathane (11-12)**

The variation curve in Figure 7 is based on data scatter or difference from Kmean and was calculated as follows:

$$\text{Variation} = (K_{\text{max}} - K_{\text{min}}) / (2 * K_{\text{mean}})$$

**Table 3. Data Summary Tables for A286 Fasteners**

Fastener	Braycote Lubrication Phosphor Bronze Insert (Worn)						% Below mean	% Above mean
	Mean Torque Coefficient Kmean	STD Dev	No. Samples	Tolerance Limit Factor	B-Basis Limits Kmin	B-Basis Limits Kmax		
#8 - 0.25 in (4.2 – 6.3 mm)	0.182	0.039	300	1.417	0.127	0.238	30.5	30.5
Fastener	Arathane Installation Phosphor Bronze Insert (Worn)						% Below mean	% Above mean
#8 - 0.25 in (4.2 – 6.3 mm) IPA & HFE Clean	0.304	0.028	30	1.777	0.254	0.355		

Fastener	Arathane and Braycote Comparison New Phosphor Bronze Insert						% Below mean	% Above mean
	Mean Torque Coefficient Kmean	STD Dev	No. Samples	Tolerance Limit Factor	B-Basis Limits Kmin	B-Basis Limits Kmax		
Arathane #8 - 0.25 in (4.2 – 6.3 mm)	0.322	0.024	30	1.777	0.278	0.365	13.5	13.5
Braycote #8 - 0.25 in (4.2 – 6.3 mm)	0.205	0.044	30	1.777	0.128	0.283	37.7	37.7

The following conclusions were noted based on the above test results and Figure 8 for combined Arathane and Small Fastener Testing which were both based on similar A286, 160-ksi (1.1-MPa) strength fasteners installed into Braycote 601EF lubricated phosphor bronze inserts.

1. For both worn and new inserts, the torque coefficient for Arathane installed fasteners was significantly higher than the same size fastener lubricated with Braycote.
2. For worn inserts, the Arathane torque coefficient was ~71% higher than Braycote (K: 0.304 vs. 0.178). It is recommended that for worn inserts the torque should be based on a torque coefficient of 0.30 when Arathane is used.
3. For new inserts, the Arathane torque coefficient was ~57% higher than Braycote (K: 0.322 vs. 0.205). It is recommended that for new wire inserts the torque should be based on a torque coefficient of 0.32 when Arathane is used.
4. There was not an appreciable difference of the Arathane torque coefficient for those inserts cleaned with IPA vs. HFE7100.
5. The torque coefficient was lowest for the #8 (4.2-mm) fasteners and highest for the 0.25-in (6.3-mm) diameter fasteners.
6. If all the data are combined the resulting average torque coefficient is 0.180. As previously noted, the Goddard torque spec tables in 540-PG-8072.1.2 specify a torque coefficient of 0.150 for lubricated fasteners. The data show that for a very commonly used (@ GSFC) combination of



A286/160 ksi (1.1 MPa) fasteners installed with Braycote 601EF into phosphor bronze wire inserts, a change to the Goddard Mechanical Systems Division torque spec should specify a torque coefficient of 0.18

- Also, the B-Basis scatter of the Torque coefficient is  $\pm 30\%$ . Typically a torque coefficient range of  $\pm 25\%$  is commonly used at GSFC.

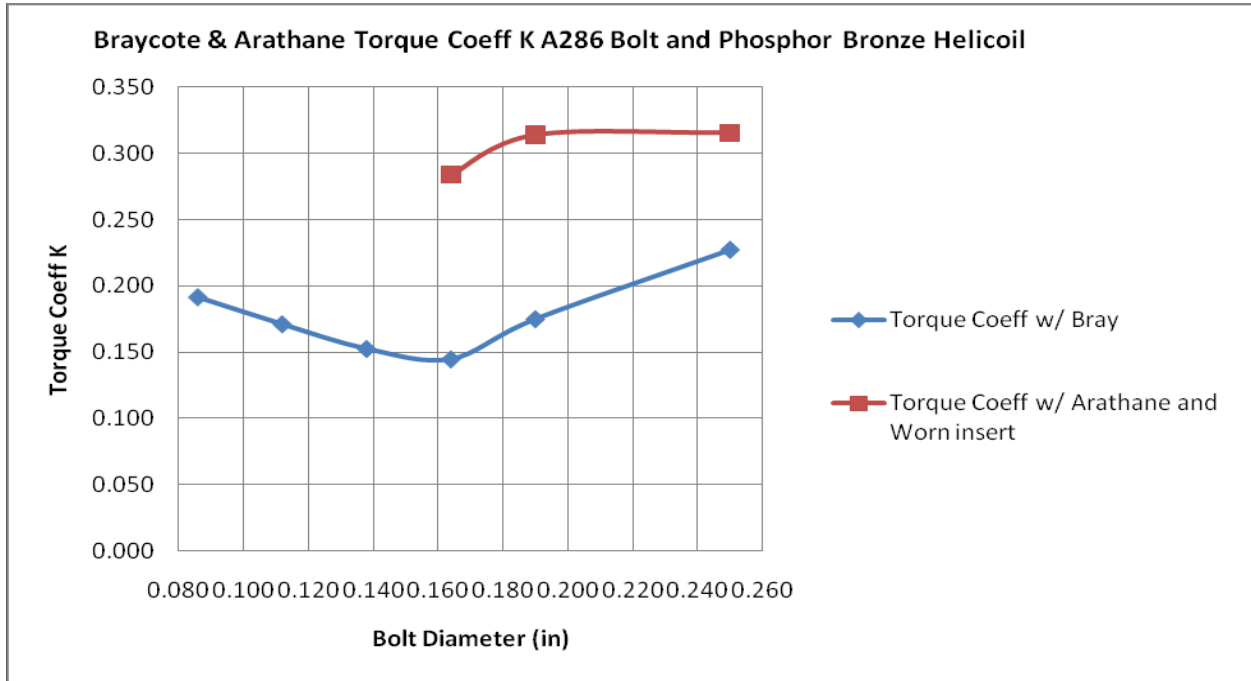


Figure 8. Combined Torque Coefficients Arathane & Small Fastener Testing

### “ORION” Super Koropon Testing

ORION is a manned spacecraft proposed for beyond low Earth orbit that is being designed and built jointly by Lockheed Martin for NASA and the European Space Agency. Two phases of torque-tension testing were performed for ORION. Phase I (6) cycle testing was performed to determine if as-received and un-cleaned fasteners, inserts and washers could be used for assembly of flight hardware. All inserts were received with molybdenum disulfide dry film lubricant applied to the threads by the manufacturer. The fastener and insert combinations tested are shown in Table 4. In addition to the different insert types and cleanliness, various lot numbers for each size and type were also tested to determine the effect on torque coefficient.

Table 4. Test Hardware Phase I & II Fasteners/Inserts & Washers

		Fasteners		Washers	
1	#10-32 Hex Head A286	NAS6703U12		LMC21D5AC3C/A286 CS	
2	1/4-28 Hex Head A286	NAS6704U12		LMC21D5AC3C/A286 CS	
	Keensert	Type	HD	EXHD	LW
1		#10-32	MS51831CA201L	MS51832CA201L	MS51830CA201L
2		1/4-28	MS51831CA202L	MS51832CA202L	

The Phase I (6) cycle test sequence was as follows:

- One half of the fasteners/inserts and washers were cleaned in IPA and the other half were tested as received and un-cleaned.
- Super Koropon, an epoxy-polyimide corrosion inhibitor/sealer for threaded assemblies, was applied to the fastener and washer bearing surfaces of all Koropon installed samples. Fastener threads were not lubricated with Koropon.
- Some cleaned and un-cleaned/as received sample sets were also tested dry without Super Koropon applied to fastener and washer bearing surface.
- All inserts were torqued to 65% fastener yield for total of six cycles with fastener and washer replacement after the third cycle.

Phase II (10) cycle testing was performed to determine the effect of ten cycles on running torque and also if additional benefit could be derived by lubrication of fastener threads with Braycote. All hardware was tested as received and un-cleaned. Super Koropon was applied to fastener and washer bearing surfaces of Koropon samples with some sample sets also being tested dry, without Koropon. Some fastener threads were also lubricated with Braycote to determine the effect on torque coefficient. Two types of Braycote lubricant were tested, Type 601 for anti-rust and Type 602EF with moly disulfide for anti-galling. Phase II test sequence was as follows:

- As received dry film lubricated inserts with no additional Braycote lubrication.
- As received dry film lubricated inserts with fastener threads lubricated with Braycote 601.
- As received dry film lubricated inserts with fastener threads lubricated with Braycote 602EF.
- Fasteners were replaced only if running torque was less than 3 in-lb (0.3 N-m).

#### Phase I and Phase II Test Results

The data plots and tables below provide a summary of the statistics for Phase I and II testing. Figure 9 and Table 5 summarize the Phase I (6) cycle test results. Figure 10 and Table 6 summarize the Phase II (10) cycle results.

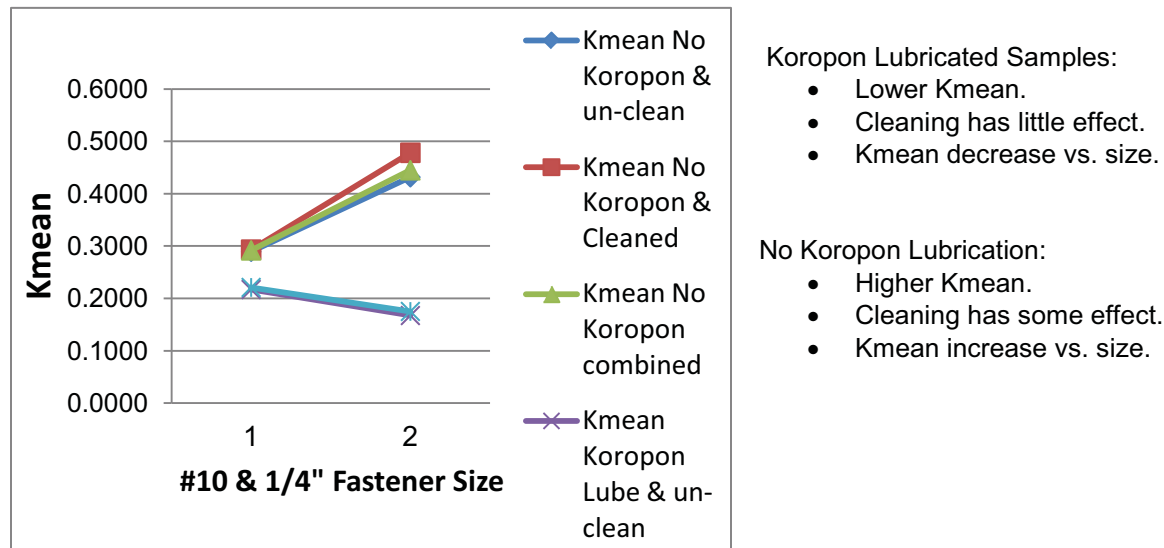
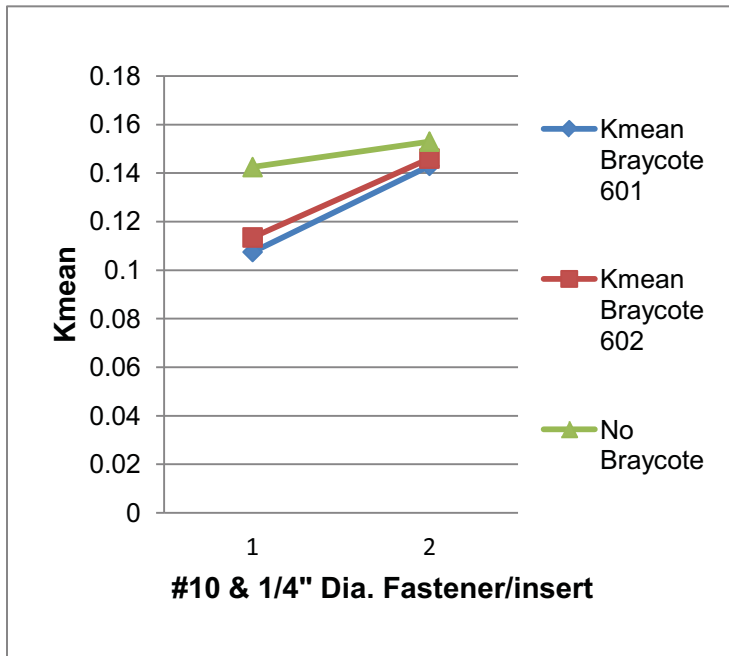


Figure 9. Kmean with and without Koropon Lube

**Table 5. Phase I (6) Cycle Statistics for #10-32 (4.8 mm) & 1/4-28 (6.3 mm) Fasteners**

Koropon Lube cleaned and un-cleaned						
	Koropon/un-clean		Koropon/cleaned		Koropon/Combined	
Size	#10	1/4"	#10	1/4"	#10	1/4"
Kmean	0.217	0.167	0.221	0.175	0.219	0.170
Kmax	0.273	0.203	0.270	0.214	0.268	0.208
Kmin	0.161	0.132	0.172	0.137	0.169	0.132
Variation	0.259	0.212	0.223	0.219	0.226	0.223
N=cycles	60	96	48	90	108	186
No Koropon Lube #10, cleaned and un-cleaned						
	No Koropon/un-clean		No Koropon/cleaned		No Koropon/Combined	
Size	#10	1/4"	#10	1/4"	#10	1/4"
Kmean	0.289	0.432	0.293	0.478	0.292	0.445
Kmax	0.393	0.554	0.390	0.632	0.384	0.568
Kmin	0.186	0.309	0.196	0.325	0.200	0.322
Variation	0.359	0.284	0.331	0.321	0.316	0.277
N=cycles	30	30	54	12	84	42



Additional Braycote Lubrication applied to fastener threads is beneficial for smaller size #10-32 (4.8 mm) fasteners but less so for larger size 1/4-28 (6.3 mm) fasteners.

For larger size fasteners, the head-to-washer bearing surface becomes more dominant and thread friction is less of a factor.

Use of Braycote 601 or 602EF are equally effective with respect to Kmean.

**Figure 10. Kmean for Koropon with and without Braycote Lube**

For Fastener Statistics in Table 5 for (6) cycle test results and Table 6 for (10) cycle test results, the data variation was calculated as follows:

$$\text{Variation} = (K_{\text{max}} - K_{\text{min}}) / (2 * K_{\text{mean}})$$

**Table 6. Phase II Kmean for Koropon with and without use of Braycote**

Size	EXHD & HD Keenserts Koropon Lube Applied							
	Braycote 601		Braycote 602		Combined		No Braycote	
	#10	1/4"	#10	1/4"	#10	1/4"	#10	1/4"
Kmean	0.108	0.143	0.114	0.146	0.111	0.144	0.143	0.153
STDVA	0.013	0.031	0.024	0.022	0.019	0.027	0.025	0.028
Kmax	0.137	0.204	0.168	0.191	0.149	0.195	0.193	0.210
Kmin	0.078	0.082	0.059	0.102	0.072	0.094	0.092	0.097
Variation	0.274	0.427	0.480	0.305	0.351	0.351	0.356	0.369
N	20	50	20	40	40	90	40	50

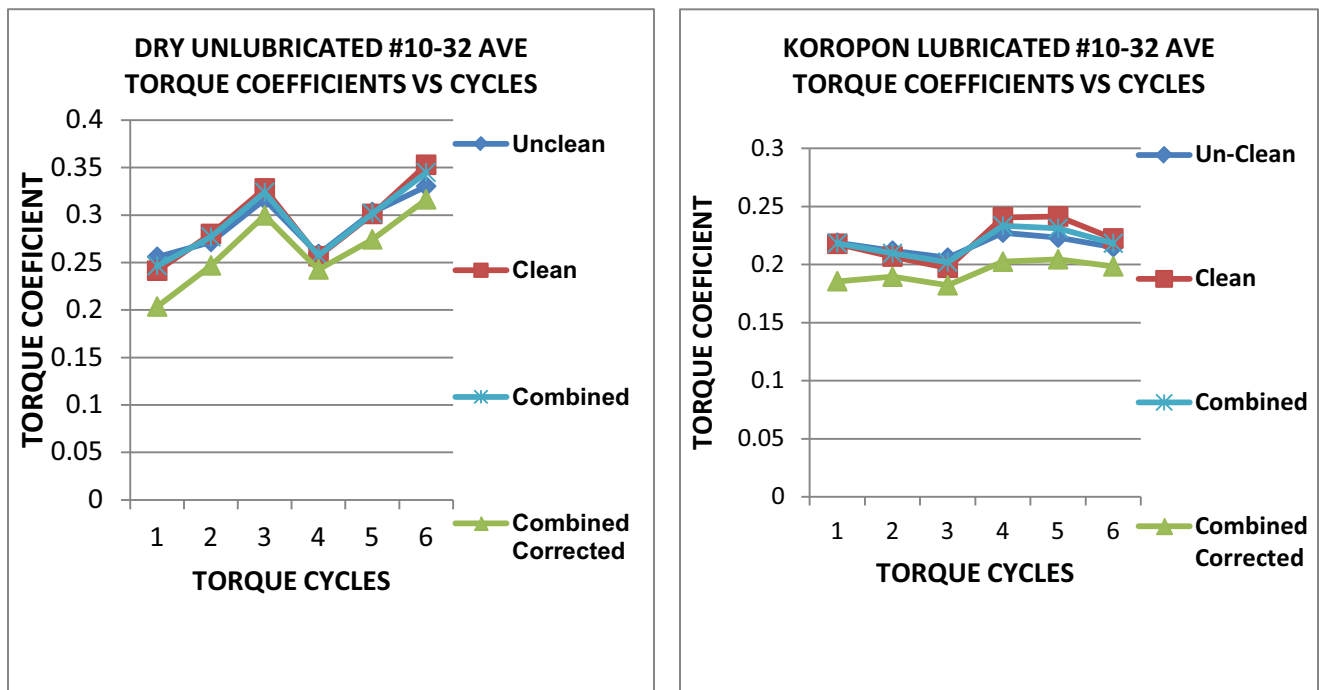
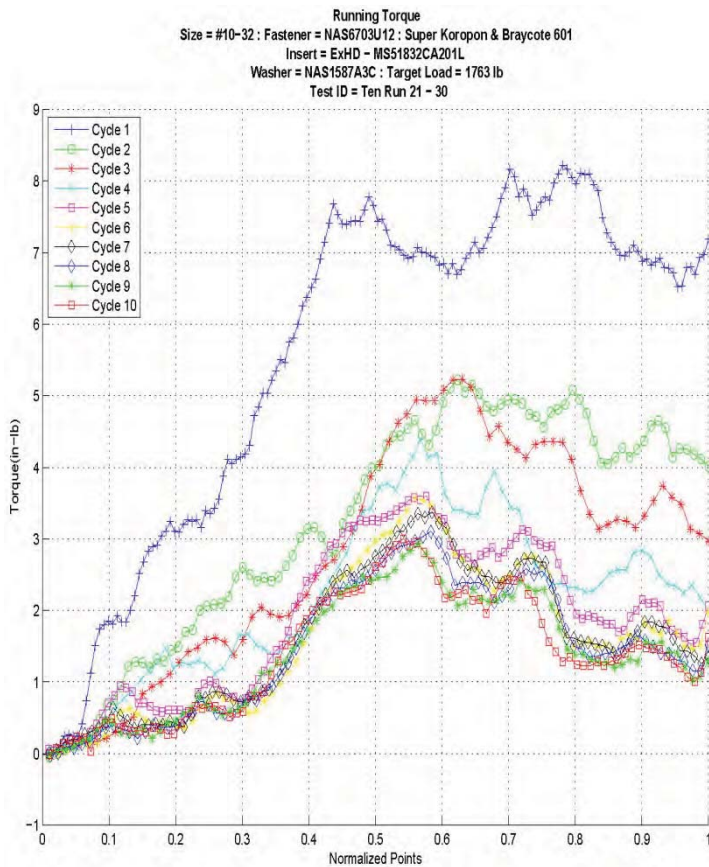


**Figure 11. Cyclic Kmean for Un-lubricated and Lubricated Samples**

The following generalized conclusions can be drawn based on the six and ten cycle testing:

1. For Dry/no-Koropon, Kmean and Variation were found to increase with fastener size. The reverse was true for use of Koropon.
2. There was little difference in Kmean for cleaned and un-cleaned test samples.
3. Removal of running torque was found to reduce Kmean by as much as 20%, refer to corrected plots, Figure 11.
4. The Kmean vs. cycles for un-lubricated samples was found to increase. For lubricated samples, the trend was reversed (refer to Figure 11). Replacement of fastener, washer and re-lubrication after third cycle is beneficial in reducing Kmean.
5. For cycles 1-6 into the same insert without Koropon, there was a large change in torque coefficients. With Koropon use, there was little change.
6. Running Torque was reduced significantly after first torque application but remained above a minimum of 3 in-lb (0.3 N-m) in all but (3) sample sets, Figure 12.



### **With Braycote Lubrication**

Running Torque 8 in-lb (0.9 N-m) max.  
 Is 30% less than 12 in-lb (1.4 N-m) for no Braycote lube.

Follow-on cycles are also lower due to the lubrication effect but remain above minimum required 3 in-lb (0.3 N-m).

**Figure 12. Typical Running Torque Plot for (10) Cycles, Koropon + Braycote Lube**

### **References**

- [1] Bickford, J. H., and Nassar, S. A., 1998, "*Handbook of Bolts and Bolted Joints*", Marcel Dekker, Inc., New York.
- [2] Bickford, J. H., 1997, "*An Introduction to the Design and Analysis of Bolted Joints*", third edition, Marcel Dekker, Inc., New York.
- [3] Alan Posey, August 20, 2008, "Small Bolt Torque/Tension Report", NASA Goddard Space Flight Center, Greenbelt, Maryland.
- [4] Alan Posey, March 24, 2010, "Arathane Bolt Torque/Tension Report", NASA Goddard Space Flight Center, Greenbelt, Maryland.
- [5] Edgar Hemminger, July 2012, Chris McLeod and John Peil, NASA/CR-2012-217587 "*Orion – Super Koropon Torque/Tension Report*", NASA Goddard Space Flight Center, Greenbelt, Maryland.
- [6] Edgar Hemminger and Ray Burkhardt, April 30, 2000, "*Verification of Bolt Pre-Load*", NASA Goddard Space Flight Center, Greenbelt, Maryland.
- [7] NASA/JSC PRC-4004, "*Sealing of Joints and Faying Surfaces*".





# Ultrasonic Method for Deployment Mechanism Bolt Element Preload Verification

Eric C. Johnson\*, Yong M. Kim\*, Fred A. Morris\*\*, Joel Mitchell\*\* and Robert B. Pan\*

## Abstract

Deployment mechanisms play a pivotal role in mission success. These mechanisms often incorporate bolt elements for which a preload within a specified range is essential for proper operation. A common practice is to torque these bolt elements to a specified value during installation. The resulting preload, however, can vary significantly with applied torque for a number of reasons. The goal of this effort was to investigate ultrasonic methods as an alternative for bolt preload verification in such deployment mechanisms. A family of non-explosive release mechanisms widely used by satellite manufacturers was chosen for the work. A willing contractor permitted measurements on a sampling of bolt elements for these release mechanisms that were installed by a technician following a standard practice. A variation of ~ 50% ( $\pm 25\%$ ) in the resultant preloads was observed. An alternative ultrasonic method to set the preloads was then developed and calibration data was accumulated. The method was demonstrated on bolt elements installed in a fixture instrumented with a calibrated load cell and designed to mimic production practice. The ultrasonic method yielded results within  $\pm 3\%$  of the load cell reading. The contractor has since adopted the alternative method for its future production.

## Introduction

What was accomplished here was the adaptation of ultrasonic methodology to assist with the proper installation of satellite deployment mechanisms. The effort was focused on the Frangibolt<sup>®</sup> family of non-explosive actuators marketed by TiNi Aerospace, Inc. [1] These actuators consist of a Shape Memory Alloy (SMA) core that is encased in a heater as depicted in Figure 1. The SMA core is hydraulically compressed prior to installation. A bolt element, tightened to a specified preload, is passed through the SMA core to secure the component that will eventually be deployed. The bolt elements have a notch somewhere along the length. Actuation occurs when the heater is turned on causing the SMA core to

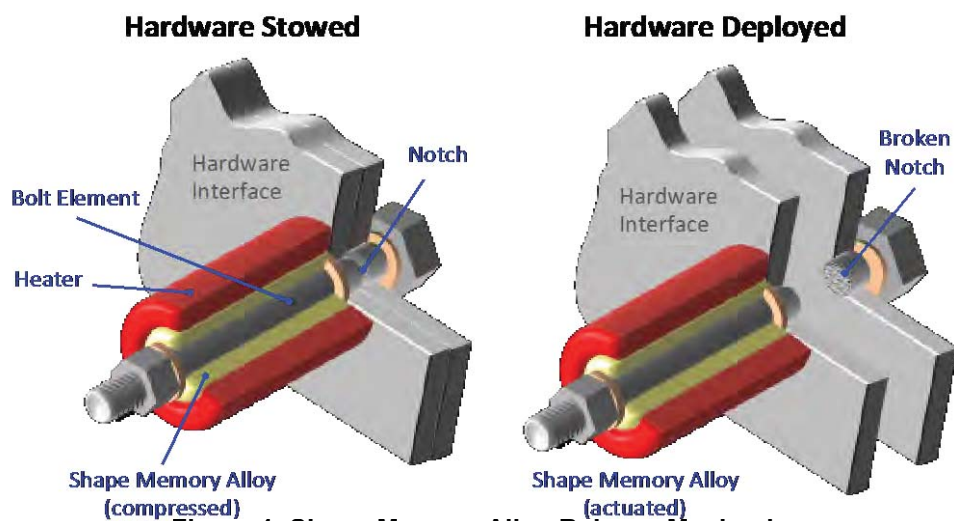


Figure 1. Shape Memory Alloy Release Mechanism

\* The Aerospace Corporation, Los Angeles, CA

\*\* Lockheed Martin Space Systems Company, Littleton, CO

return to (i.e., remember) its uncompressed state, which stretches the bolt element causing it to break at the notch. These ingenious devices are heavily used in a number of satellite programs for deployment of a wide variety of stowed appendages including solar panels, antennae, cover doors, and various payloads. Other uses include latches that lock hinges after deployment and deployment boom restraints.

If the preload is set low for a Frangibolt<sup>®</sup> release mechanism, it can result in a failure to develop fracture load levels in the bolt element, even after the SMA has fully stroked. Given the ramifications associated with a fouled release, bolt element preloads should be carefully set and verified. The most commonly used and easiest approach to setting preloads is to use a torque wrench to tighten the bolt element to a specified value. Unfortunately, the literature [2,3] indicates that preloads set by this method can vary by as much as 50% ( $\pm 25\%$ ). Clearly, a preload verification method more accurate than the standard practice of torque specification is needed. Other options in rough order of increased accuracy, include (1) keeping track of the angular turns of the nut, (2) use of load indicating washers, (3) bolt elongation measurements, and (4) the use of strain gauges or ultrasonic measurements. Ultrasonic Time-of-Flight (TOF) measurements can be used to set preloads with an accuracy of  $\pm 1\%$  for fasteners of simple geometry. The bolt elements in Frangibolt<sup>®</sup> actuators, a sampling of which are depicted in Figure 2, are notched, and can have various head designs, lengths and diameters, depending on the application. In addition, use of ultrasonic instruments generally requires more knowledge than use of a torque wrench. The challenge for this work was to develop a methodology that would overcome these hindrances and prove effective on the shop floor.

### Proof-of-Concept Testing

The key to the ultrasonic approach [4,5] is to accurately measure changes in the Time-of-Flight (TOF) of ultrasonic pulses within the bolt elements as they are loaded. The basic concept is depicted in Figure 3 where the signal traces for two bolt element designs are presented. A small ultrasonic transducer is used to propagate a pulse within the bolt. The pulse traverses the bolt and reflects back to the transducer from features like the notch, thread and end of the bolt. The resulting signal (echo train) can be examined to see how the TOF of an echo changes when the bolt is loaded through tightening.

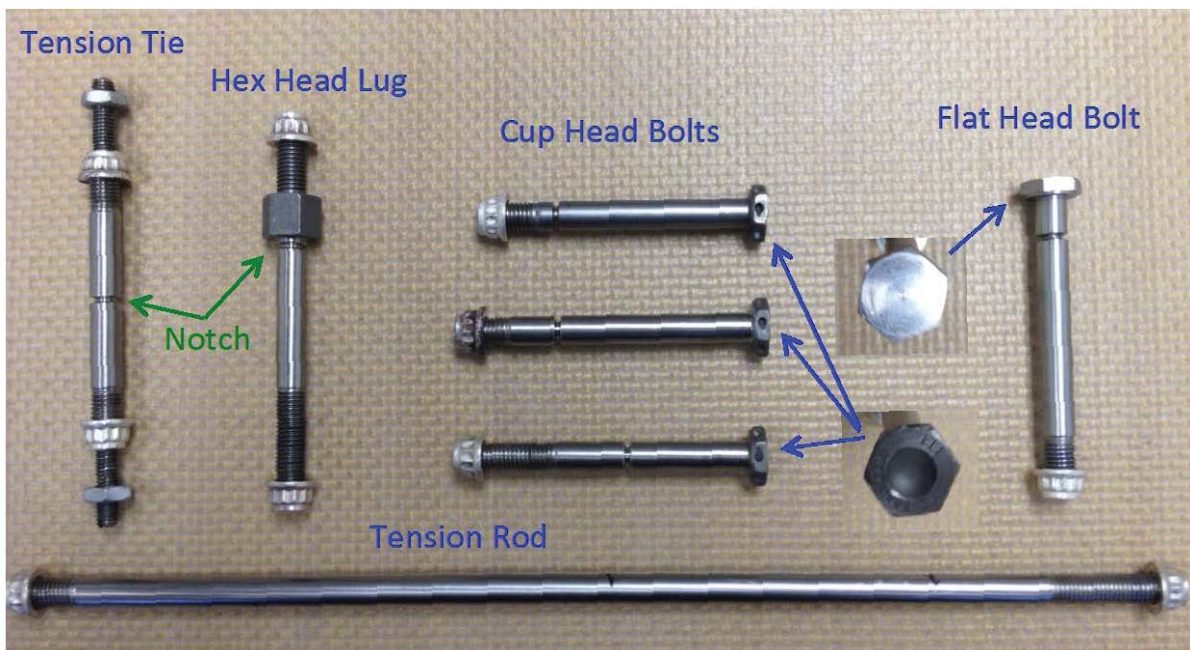
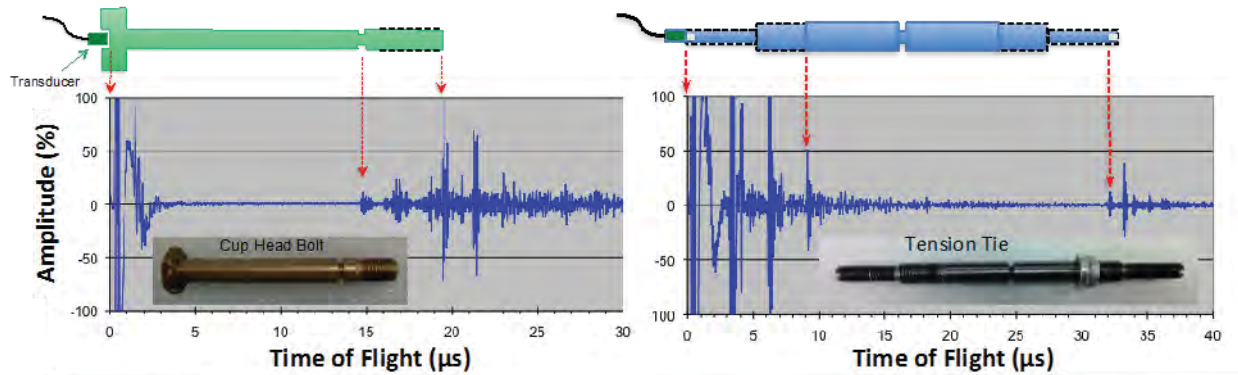


Figure 2. Titanium bolt elements tested in this study.



**Figure 3. Basic Concept for using ultrasonic TOF measurements to determine bolt preloads. Dotted lines indicate threaded shaft. Depicted are typical signal traces from unloaded bolt elements. Amplitude units are % of full screen height.**

### Measurement System

The laboratory system used to perform TOF measurements consisted of a transducer, Panametrics 5052 PRX pulsar-receiver and LeCroy LT354 (1.0 GHz) digitizing scope and, for the purposes of this paper, will be referred to as the “Lab System.” Depending on the application, a selection of flat-faced, contact, ultrasonic transducers from common manufacturers were used with diameters between 3.2 – 6.6 mm ( $1/8$  –  $1/4$  in) and resonant frequencies from 5 – 15 MHz. Generally, broadband (fast rise-time) probes yield a more definitive time measurement. Several methods for coupling of the ultrasonic transducer to the bolt were examined for repeatability. For all, a drop of deionized water or oil provided a sufficient medium for coupling the sound from the transducer into the bolt. The bolt elements used in this study were comprised of titanium and had a 3.3 mm ( $1/4$  inch) diameter main shaft with threaded portions. For some a sensor could simply be coupled to a threaded end through clever use of a magnet and nut as depicted in top photographs of Figure 4. For those where the head was flat, it was enough to just hold the transducer against the head. One heavily used design, however, had a forged head that was cupped. The difficulty encountered in hand-coupling an ultrasonic transducer to these bolt elements in a consistent fashion presented itself as a major problem to be solved. In the end, success was achieved with a custom spring-loaded sensor as depicted in the lower photographs in Figure 4 and Cross-Correlation Processing Scheme (CCPS) to combat operator induced signal variations.



**Figure 4. Methods for attaching an ultrasonic transducer to the bolt elements. In the top photographs the magnets are attracted to the nut that is threaded to pull the sensor against the end of the bolt element. The spring-loaded sensor in the bottom photograph is manually pressed against the bolt head.**

### Cross-Correlation Processing Scheme

The CCPS method is worthy of additional discussion as it was found to be quite effective and could likely prove useful for a number of other field test methods where hand-held sensors are employed. To determine the change in TOF, the signal before the bolt is loaded is subtracted from that after load. The TOF change can be relatively small so that distortions in the shape of the pulse entering the bolt can lead to significant errors. Even when using the custom spring-loaded sensor, small differences in the way the operator holds the sensor can lead to noteworthy changes in the shape of the pulse and subsequent echoes. Consequently, to get the best measurement on a loaded bolt, the operator needs to hold the transducer so as to produce a pulse as similar as possible to that attained for the measurement on the unloaded bolt. Figure 5 illustrates the concept behind the Cross-Correlation Processing Scheme. In essence, while the probe is being held on the loaded bolt, the signal undergoes variations due to inherent instabilities in the way the probe is held. With the CCPS, this changing signal is continuously monitored and compared with the original signal before load until a good match occurs at which point, the signal is saved for further processing. To illustrate the CCPS, three signals from measurement on the same loaded bolt are depicted in Figure 5 and labeled a, b and c. Each of these signals is compared to the reference signal captured on the bolt before the load was applied. The mismatch,  $M$ , defined as the percent Root Mean Square (RMS) difference, between the two signals is then calculated. The lower  $M$ , the better the match. In Figure 5, the signal labeled (a) is the best match. Once the best signal is chosen, a cross-correlation function is used to accurately determine the TOF change,  $\Delta t$ , due to loading of the bolt.

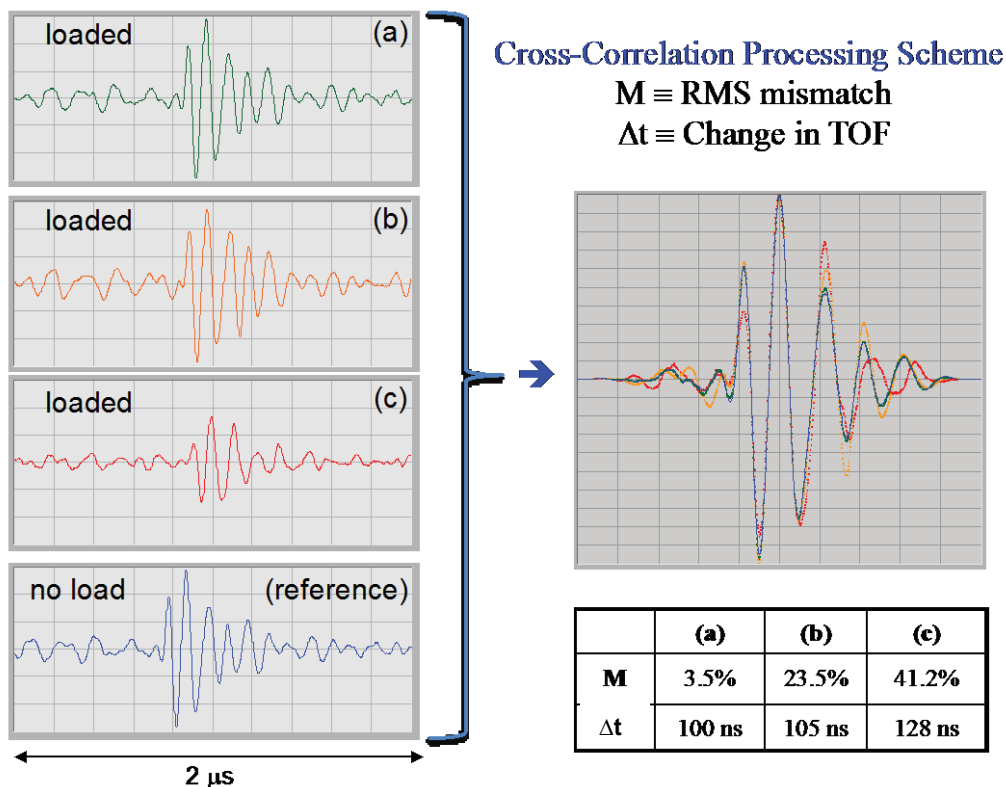


**Figure 5. CCPS Illustration.** Three end echo signals with the transducer held a little differently each time were captured on the same loaded bolt and labeled a, b, and c. Pictured is a  $2 \mu\text{s}$  window zoom from the entire echo train. These signals were compared to the reference to calculate  $M$  and  $\Delta t$ . Signal (a) was the best match.

### Load Frame Tests

With a laboratory TOF measurement system in place and a means for coupling transducers established, several cup head bolts were instrumented with strain gauges and mounted in a load frame for tension



testing. The bolt end was found to be the choice reflector for the measurements. The notch deforms with load, which results in echo distortions that are more pronounced in the later portions of the echo train. As a result, monitoring the TOF of the earliest maximum (or minimum) in the echo from the bolt end was found to produce the most reliable results. Sample results for the bolt end echo are presented in Figure 6. By presenting the TOF data as in terms of fractional change, they can be plotted with the same abscissa and ordinate as the strain data. As indicated in the figure, two major factors contribute linearly, in first order, to the TOF changes with load: (1) acoustic velocity variations with strain [6] and (2) lengthening of the bolt. The TOF data for the echo from the end of the notch was subtracted from that at the beginning of the notch to isolate the fractional TOF change within the notch itself. The results are plotted in Figure 7. The data revealed that the TOF fractional change with load within the notch was ~ 7.8 times that of the body of the bolt. The ratio of the bolt body radius to that of the notch was 1.7. One would expect the ratio of strain in each region to go as the square of the radius ratio, or 2.9. Were the velocity change in the notch equivalent to the average for the whole bolt observed in Figure 6, the TOF change in the notch would have been  $(0.05/0.04 + 1) \times 2.9 = 6.5$  times that of the bolt body, a little short of the observed 7.8 value. The difference likely reflects the fact that the velocity change was larger within the more highly strained notch material. There is also evidence of a subtle slope inflection near 10,675-N (2400-lb) load suggestive of some plastic deformation in the notch. This inflection was confirmed for multiple tensile test runs of the bolt.

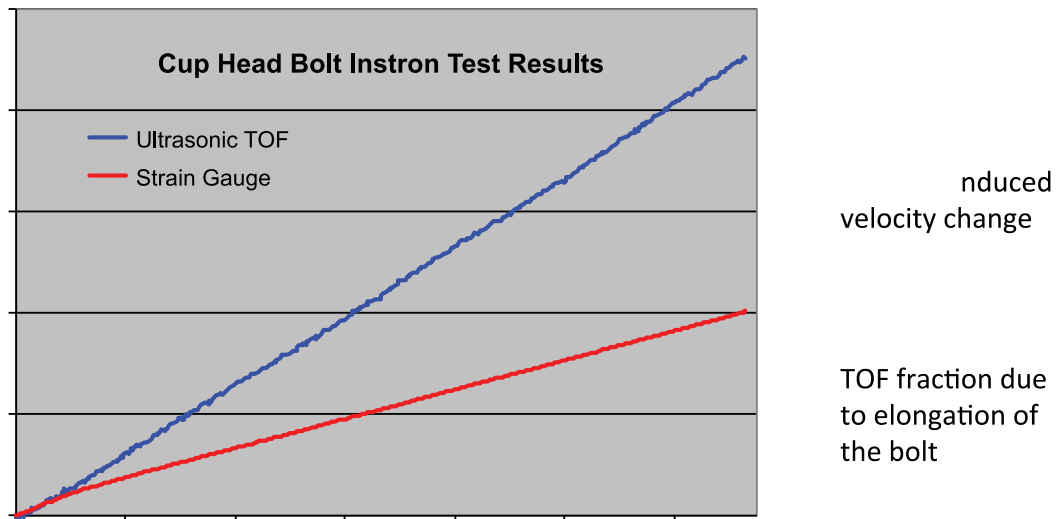


**Figure 6. Load frame test results for a cup head bolt.**

#### Torque Tests

Several unused cup head bolts and bolt elements of a different design dubbed, hex head lugs, were then mounted in a fixture with a load washer and tightened with a torque wrench. At load points, determined from the load washer, ultrasonic TOF measurements were performed. The torque test results are plotted in Figure 8 and can be seen to compare favorably with the load frame results.

#### **Site Visit I**

The above results were presented to a contractor who makes extensive use of Frangibolt® actuators in their product line. This resulted in an opportunity to perform TOF measurements at the contractor facility for a sampling of bolt elements installed by a technician on mock hardware using a standard procedure which included a specific method for pre-lubrication of the bolt threads. A load washer with a digital readout was included in the installation. The test results are presented in Figure 9. As expected, the TOF changes scaled linearly with the preload readings from the load washer. The slope for the two bolt

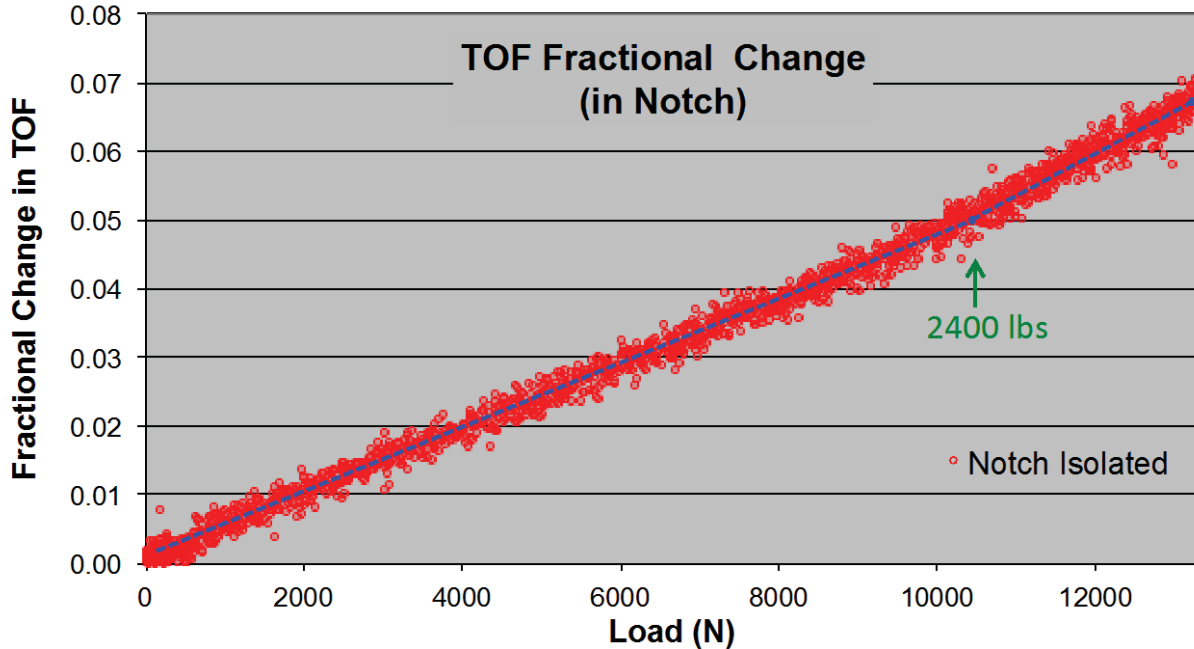


**Figure 7. Fractional change in TOF for the notch.**

element types is slightly different because the loaded lengths were not the same. The bolt-to-bolt preloads varied by  $\pm 25\%$  about the mean for bolts tightened to the same torque, which is consistent with literature reports, but higher than the contractor anticipated, given their carefully controlled installation procedure. The contractor specification called for an accuracy of  $\pm 222$  N (50 lb) for a nominal 13,344-N (3000-lb) preload (e.g.,  $\pm 1.6\%$ ), not the low to high variation of over 4,448 N (1000 lb) observed here. In response, the specification was relaxed to require a method providing  $\pm 10\%$  accuracy, which would still yield a substantial improvement over what was observed in these tests.

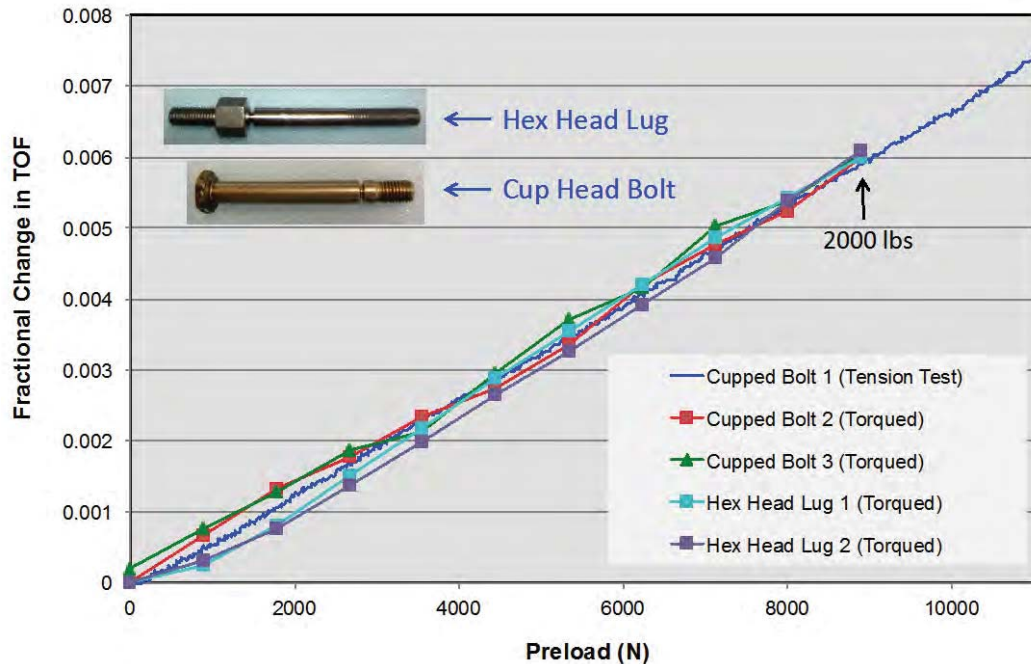
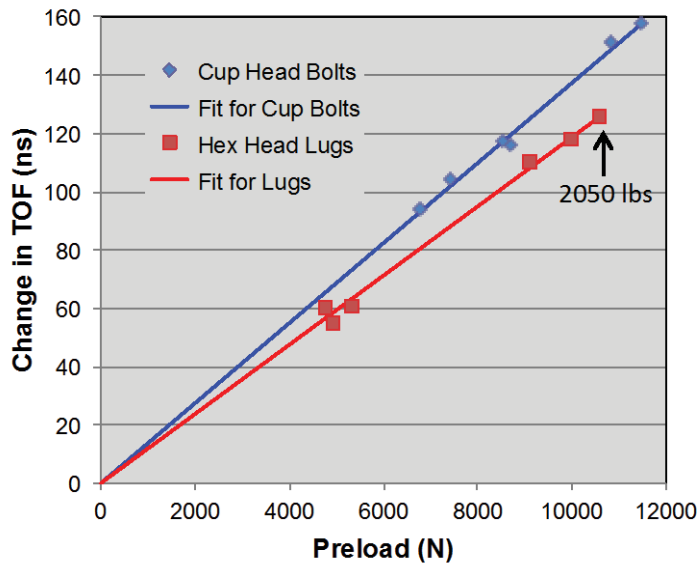


**Figure 8. Comparison of load frame results with those from bolts that were tightened with a torque wrench. A load washer was incorporated into the fixture to measure the preload.**





**Cup Head Bolts**

ID	Torque (N-m)	Torque (in/lbs)	Load (N)	Δt (ns)
Bolt A, Trial 1	5.31	47	7429	104
Bolt A, Trial 2	5.65	50	8687	116
Bolt A, Trial 3	5.65	50	8523	117
Bolt B, Trial 1	5.65	50	10845	151
Bolt B, Trial 2	5.65	50	11485	158
Bolt C, Trial 1	5.65	50	6792	94

**Hex Head Lugs**

ID	Torque (N-m)	Torque (in/lbs)	Load (N)	Δt (ns)
Lug A	2.82	25	4946	55
Lug A	5.65	50	9991	118
Lug B	2.82	25	5347	61
Lug B	5.65	50	10582	126
Lug C	2.82	25	4764	60
Lug C	5.65	50	9119	110

**Figure 9. Change in TOF vs. Preload for bolt elements installed via a standard procedure.**

### Site Visit II

With an eye toward adopting the ultrasonic method for preload verification on the shop floor, the contractor chose to replace the widely used cup head bolts in future builds with some having flat heads that were machined parallel on both ends. This “design for inspection” change simplified adaptation of the ultrasonic method by eliminating the need for the CCPS. A number of devices being marketed to measure residual stresses on the basis of acoustoelasticity were examined with an eye toward finding a portable device that would suffice for the proposed ultrasonic preload measurements. To this end, a unit was procured that Dakota Ultrasonics, [7] and others, market called the Mini-Max Bolt Tension Monitor. This unit is depicted in Figure 10 along with the Lab System.

Additional tests were then performed at the contractor facility. The purposes of these tests were to:

- (1) generate refined TOF calibration curves for 6.3-cm (2.5-in) long, flat head bolts and 24-cm (9.5-in) tension rods,
- (2) measure the error for the ultrasonic method, and
- (3) demonstrate that the, 0.25-GHz sampling rate, Mini-Max Bolt Tension Monitor was sufficient for use in lieu of the more accurate, 1.0-GHz sampling rate, Lab System.

#### Load Frame Tests – Flat Head Bolts

A load frame was used to apply incremental loads up to 15,569 N (3500 lb) to eighteen, 6.3-cm (2.5-in) long, notched, flat head bolts from the same manufacturing lot. At each load increment ultrasonic TOF measurements were made with the Lab System. For the last four bolts, TOF data was also acquired using the Mini-Max unit in its Oscilloscope Mode. In both cases, an Aerotech, Model Alpha, 6.6-mm (1/4-in) diameter, 15-MHz, ultrasonic transducer was used. The data are depicted in Figures 11 and 12. For each bolt, its zero load TOF was subtracted from that of the ensuing higher loads. The Lab System results exhibited an average slope of 0.0126 ns/N (0.056 ns/lb), similar to the 0.0124 ns/N (0.055 ns/lb) value observed for the Mini-Max Bolt Tension Monitor results.

#### Torque Tests– Flat Head Bolts

Bolts 1 – 12 were then each installed in a fixture with a strain-gauge-instrumented load cell of the same length as the associated Frangibolt® actuator and torqued in accordance with the contractor’s installation



**Figure 10. Results obtained with the portable Mini-Max Bolt Tension Monitor (left) were compared with those of the Lab System (right).**

procedure. In preparation for the test, the load frame was used to validate the calibration of the load cell. At three specific levels of loading, as indicated by the load cell, ultrasonic TOF measurements were performed. The calibration slopes derived from the data in Figures 11 and 12, were then used to convert the TOF readings to a load value for comparison with those of the load cell as shown in Figure 13. The discrepancy between the load cell reading and those from both instruments was less than  $\pm 445$  N (100 lb) at 13,344-N (3000-lb) load or  $\pm 3\%$ . For Bolts 11 and 12, where both measurement systems were used, the discrepancy was higher for the lower resolution Mini-Max unit as one would expect, however, it was still well within the  $\pm 10\%$  accuracy desired by the contractor.

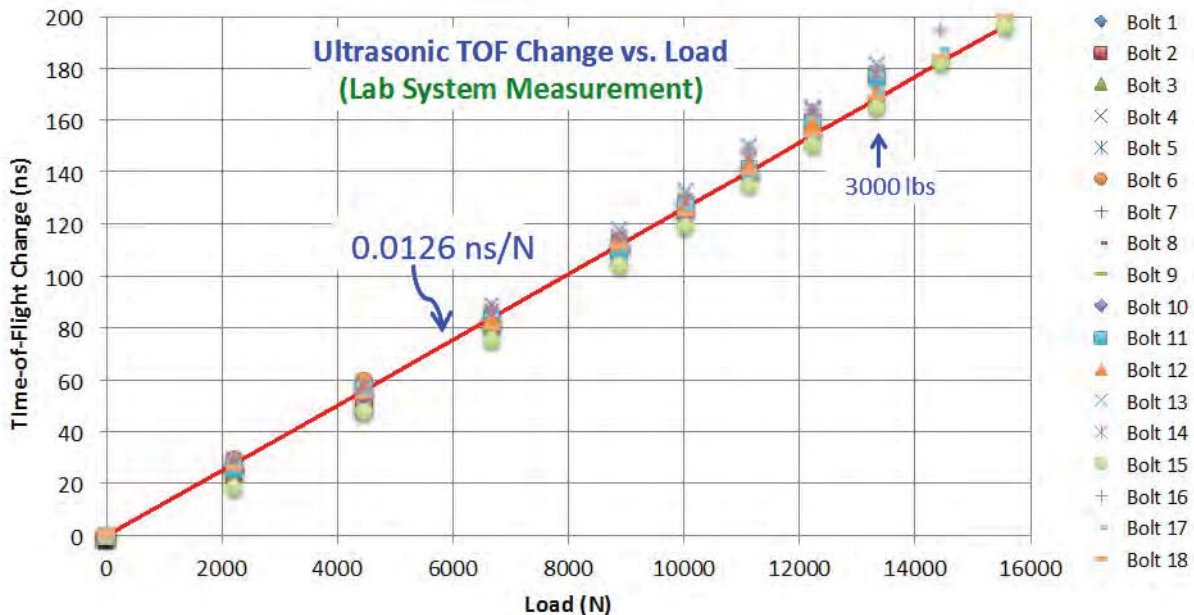


**Figure 11. Ultrasonic TOF change observed for flat head bolt elements as a tensile load was applied. The Lab System depicted in the right photograph of Figure 10 was used to acquire these data points.**

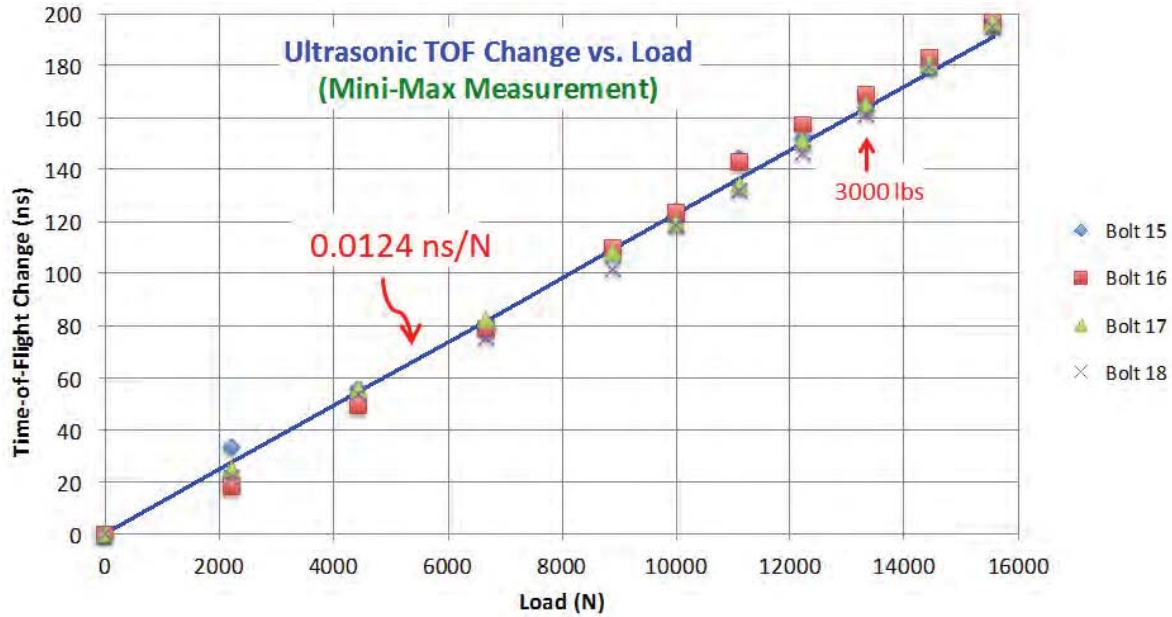


Figure 12. Ultrasonic TOF change observed for flat head bolt elements as a tensile load was applied. The Mini-Max Bolt Tension Meter depicted in the left photograph of Figure 10 was used to acquire these data points.

#### Load Frame - Tension Rods

The contractor also incorporates tension rods of length 24 cm (9.5 in) in some hardware and proper installation requires a specific preload. As with the flat head bolts, the contractor had both ends of the rods machined flat and parallel. These rods, one of which is included in Figure 2, provided a nice avenue for comparison with the bolts, having the same diameter and composition, but no notch. Three tension rods were therefore subjected to the same calibration tests as the bolts. Load frame tests resulted in the data presented in Figure 14. The slope was found to be 0.0468 ns/N (0.208 ns/lb) which when scaled by the length differences yields the same value as was obtained for the bolts:

$$\left(\frac{6.3 \text{ cm}}{24 \text{ cm}}\right) \times 0.0468 \frac{\text{ns}}{\text{N}} = 0.0123 \frac{\text{ns}}{\text{N}}$$

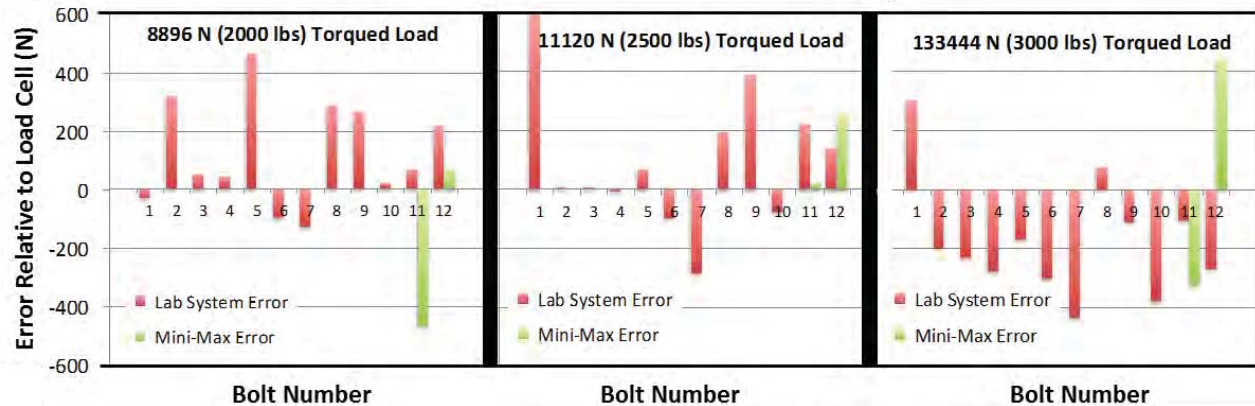
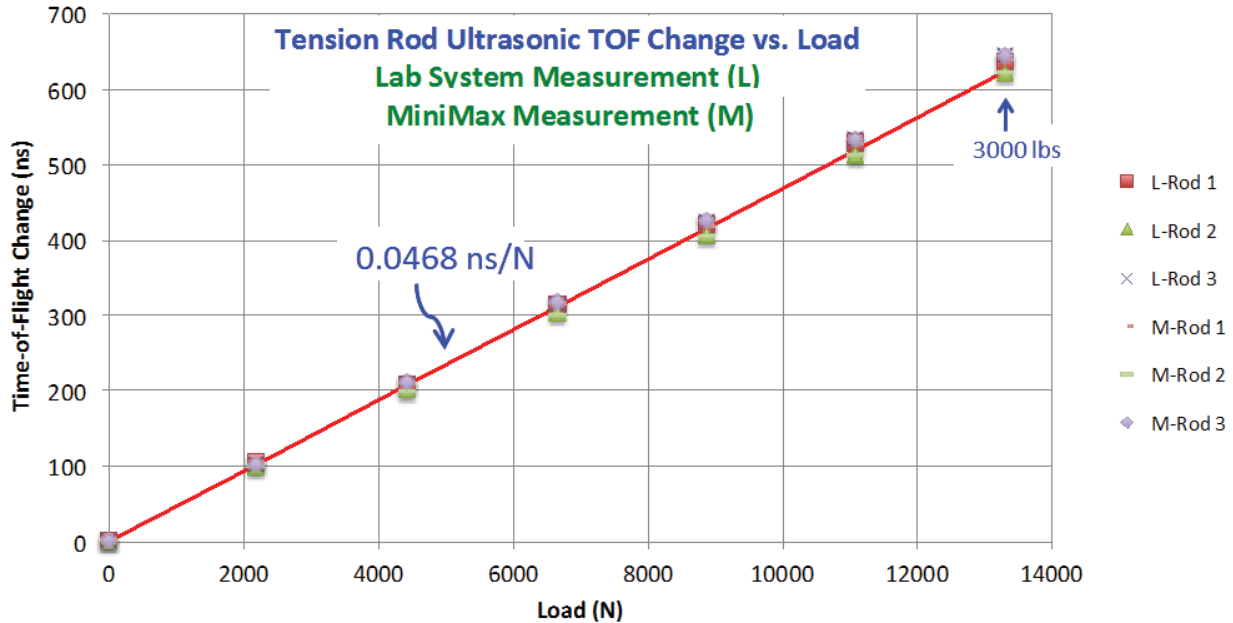


Figure 13. Histograms of the discrepancies noted between the load values registered on a load cell for torqued flat head bolts and that determined ultrasonically.



**Figure 14. Ultrasonic TOF change observed in three 24-cm (9.5-in) tension rods as a tensile load was applied. The measurement was made both with the Lab System and the Mini-Max Bolt Tension Monitor for each tension rod.**

A Panametrics, Model V129, 4.8-mm ( $3/16$ -in) diameter, 10-MHz, transducer was used for the ultrasonic measurements. The 5-MHz version of the same model was found to work equally well. It was also noted that right angle probes (coaxial lead emanates from the side of the sensor) were decidedly easier to hold steadily against the end of the tension rod to produce a consistent signal.

**Torque Tests – Tension Rods**

The tension rods, like the flat head bolts, were then installed in a fixture with the calibrated load cell and torqued in accordance with the contractor’s installation procedure. TOF was measured with both systems and using the previously determined calibration factor of 0.0124 ns/N (0.055 ns/lb), the load was calculated and compared to the associated load cell reading. The results for three load levels are presented in Figure 15. The discrepancy between the load cell reading and those from both instruments was less than  $\pm 400$  N (90 lb) at 13,344-N (3000-lb) load. Again, as expected, the discrepancy was higher for the lower resolution Mini-Max unit, but well within the accuracy required.

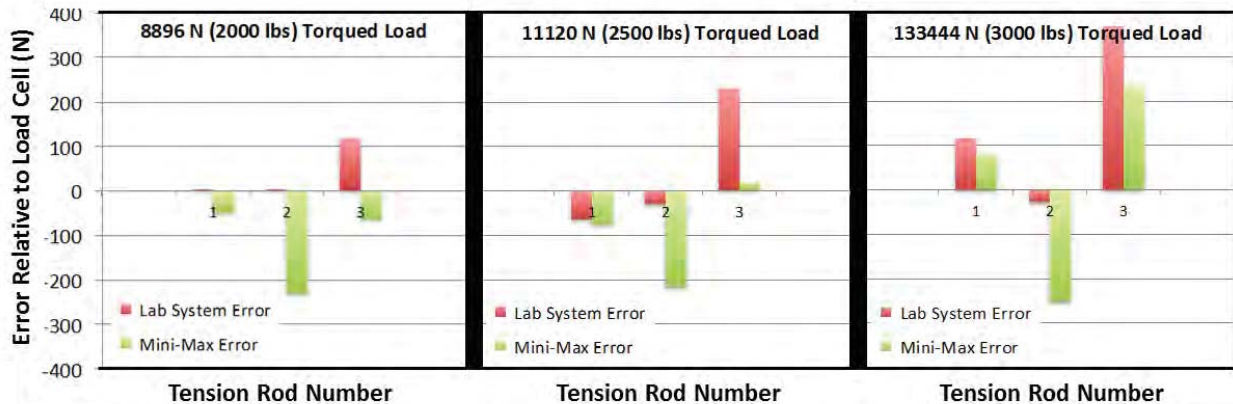


**Figure 15. Histograms of the discrepancies noted between the load values registered on a load cell for torqued tension rods and that determined ultrasonically**



### Possible Contributors to Discrepancy

The magnitude of the discrepancy does not appear to scale monotonically with the applied torque. This suggests that a portion of the observed  $\pm 3\%$  discrepancy between the load cell and TOF measurements may be rooted in factors other than the temporal resolution of the two ultrasonic systems. Such factors include variations in the (1) bolts themselves, (2) actual length of the bolt that is loaded (gage length), and (3) bolt temperature. It should be noted that errors in the gage length (active length of stretch) between calibration and measurement will propagate the same percentage error in the preload determination. For reference, variations in the geometry of the notch for the 18 flat head bolts load tested, plus two that were set aside (all from the same lot), were examined prior to the tests. Image analysis tools were applied to digital radiographs of each bolt to measure its notch diameter, notch radius and notch angle as defined in Figure 16. The notch diameter measured a consistent 3.7 mm (0.146 in) for all bolts. Histograms of the notch radius and notch angle variations are presented on the right of Figure 16. As a final step in the testing of the 18 bolts, an attempt was made to tighten them to 15,568-N (3500-lb) load. These bolts had all previously seen this value during the load frame testing (Figure 11), but one would expect frictional forces to result in a slight twist at the notch during torquing. This load was again achieved with all but one, Bolt Number 2, which broke at the notch. It is noteworthy that this bolt appears as an outlier in the histograms (Figure 16).

For metals, acoustic velocity is a strong function of temperature [8]. To measure the effect of bolt element temperature on the results, one of the tension rods was placed in a heated water bath with a magnetically affixed transducer. The TOF data was then acquired as a function of the water temperature resulting in the plot presented in Figure 17. If one divides the slope of this curve by that of Figure 12, the result indicates that a  $1^\circ\text{C}$  temperature change could lead to a  $>200\text{ N}$  (45 lb) variation in the ultrasonically determined load for the tension rod. This is noteworthy, as it suggests that temperature variations could be a significant contributor to the observed small discrepancies between the load cell readings and the ultrasonic results. Because frictional forces result in heating of the bolt elements during tightening, it would be good practice to wait for at least 15 minutes before making the final ultrasonic determination of preload.

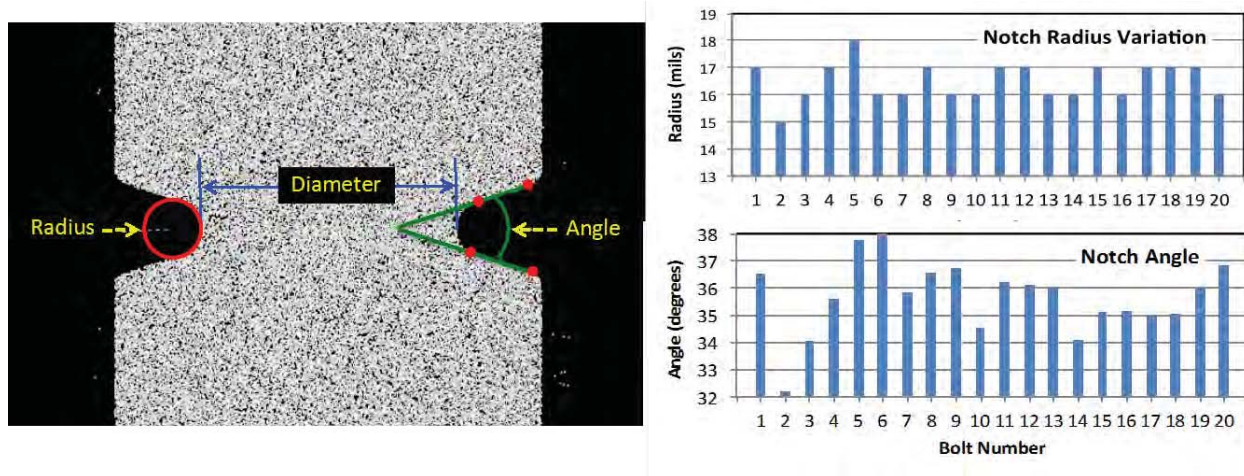
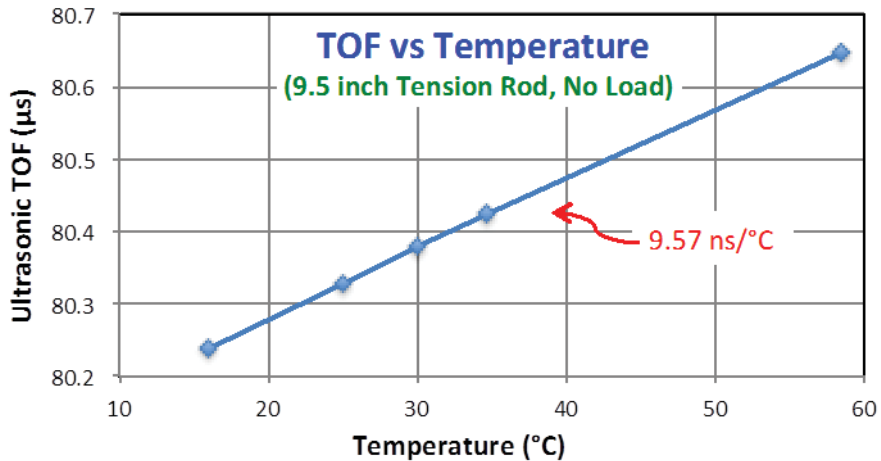


Figure 16. Digital radiographs were analyzed to measure variations in the notch geometry between twenty flat head bolts from the same lot.



**Figure 17. Change in ultrasonic TOF as a function of temperature for a 24-cm (9.5-in) unloaded tension rod.**

### Summary

Ultrasonic TOF measurements were successfully implemented as a means for determining the preload of installed bolt elements for Frangibolt<sup>®</sup> actuators. For each torqued bolt, the load was derived from the measured load-induced ultrasonic TOF change using an average conversion factor determined from load-frame tests. The discrepancy between the ultrasonic and load cell preload readings for 6.3-cm (2.5-in) long, notched bolts nominally torqued to 13,344 N (3000 lb) load was less than  $\pm 445$  N (100 lb) or  $\pm 3\%$ . Similar results were obtained for 24-cm (9.5-in) tension rods. The discrepancies observed likely contained contributions from bolt-to-bolt variations in the actual length loaded, the bolt temperature and bolt geometry. Improvement in the measurement fidelity could be achieved by calibrating the bolt elements individually as opposed to using an average calibration factor. The data suggest that a one-point calibration at 8896-N (2000-lb) load would suffice for the 6.3-cm (2.5-in), notched bolts. Having to load test each bolt, prior to tightening, however is probably not worth the marginal improvement that would be attained.

A commercially available Bolt Tension Monitor with a 0.25-GHz sampling rate was shown to be sufficient for the pre-load measurements. The accuracy gained through use of a system employing a 1.0-GHz digital scope was insignificant. For the notched bolts, it was found that monitoring the earliest maximum (or minimum) in the echo from the bolt end gave the most reliable load measurement result. Broadband transducers in the 5 – 15 MHz range were found to work effectively. The observed  $\pm 3\%$  error obtained with the ultrasonic TOF methodology for setting the bolt element preloads is a significant improvement over the  $\pm 25\%$  error observed with straightforward tightening to a specified torque.

### Acknowledgement

Support of The Aerospace Corporation's Independent Research and Development Program is gratefully acknowledged.



## References

1. TiNi Aerospace, Inc., 2505 Kerner Ave., San Rafael, CA 94901.
2. Bikford, J. H. and Nassar, S. (Eds.) (1998). *Handbook of Bolts and Bolted Joints*, New York, NY: Marcel Dekker, Inc., Chapter 25, Table 2, p. 674.
3. Table showing Accuracy of Bolt Tensioning Methods,  
[http://www.roymech.co.uk/Useful\\_Tables/Screws/Preloading.html](http://www.roymech.co.uk/Useful_Tables/Screws/Preloading.html)
4. Allen, D. R., W. H. B. Cooper, C. M. Sayers, and M. G. Silk (1982). *The Use of Ultrasonics to Measure Residual Stresses*, Research Techniques in NDT, Vol. 6 (R. S. Sharpe, ed.). New York, NY: Academic Press, pp 151-209.
5. Smith, J. F. and J. D. Greiner. "Stress Measurement and Bolt Tensioning by Ultrasonic Methods," *Journal of Metals* (July, 1980), pp 34-36.
6. Pao, Y. H., W. Sachse and H. Fukuoka (1984), *Acoustoelasticity and Ultrasonic Measurements of Residual Stresses*, Vol XVII (W. P. Mason, ed.). New York, NY: Academic Press, pp 61-143.
7. Dakota Ultrasonics, 1500 Green Hills Road, #107, Scotts Valley, CA 95066
8. K. Salama and C. K. Ling, "The Effect of Stress on the Temperature Dependence of Ultrasonic Velocity," *Journal of Applied Physics*, 51, no. 3 (March 1980), pp. 1505-1509

All trademarks, service marks, and trade names are the property of their respective owners



## **LARES Mission: Separation and Retention Subsystem**

Alessandro Bursi<sup>\*</sup>, Pierluigi Camilli<sup>\*</sup>, Claudio Piredda<sup>\*\*</sup>, Gianni Babini<sup>\*</sup> and Elio Mangraviti<sup>\*</sup>

### **Abstract**

As part of the Lares (LAsER RELativity Satellite) mission, an all-Italian scientific mission launched with the Vega maiden flight in February 2012, a mechanical separation and retention subsystem (SSEP) has been developed to retain the LARES satellite during launch and release it in the final orbit. The design flow was based on the identification of the driving requirements and critical areas to guide the trade-off, design, analysis and test activities. In particular, the SSEP had to face very high environmental loads and to minimize the contact areas with the satellite that had a spherical shape. The test activity overview is provided.

### **Introduction**

The scope of this paper is to describe the activities done for the design of the SSEP (Separation Subsystem) developed for the LARES program, give an overview of the test campaign performed, and show the relevant main results underlining the acquired experience.

### **LARES Mission Main Objectives**

LARES (LAsER RELativity Satellite) is an all-Italian scientific mission, developed for the Italian Space Agency and successfully deployed in orbit by the European launch vehicle Vega on its maiden flight on February 13, 2012. The main goal of the LARES mission is to take high accuracy measurements of the Lense-Thirring effect, i.e., the dragging of inertial frame due to additional space-time curvature produced by the Earth's angular momentum. Two secondary objectives were assigned to the mission: to provide a separation platform for additional payloads and to support the launcher qualification. In order to support Vega qualification, the system included a stand-alone avionics system devoted to measure the launcher payload area environmental conditions during flight and to provide video of launcher lift-off, stage separations (by using an external camera), and payload separation in the target orbit.

### **LARES System Architecture and Subsystems**

The LARES system is composed of the following main elements:

- The LARES satellite, a tungsten sphere of ~400 kg with 92 Corner Cube Reflectors embedded;
- The Separation and Retention Subsystem (SSEP) to retain the LARES satellite during the launch flight and release it in the final orbit;
- The Support Subsystem, the main structural interface with the launch vehicle upper stage and to support all the subsystems of LARES system;
- Avionics and Harness Subsystem, the subsystem to provide separation of the payloads, to assist the launch vehicle in acquisition, to monitor key parameters inside the launcher fairing and the separations of the launch stages during ascent by means of video cameras, and to download data to ground stations.
- Eight secondary payloads.

---

<sup>\*</sup> CGS S.p.A., Milan Italy

<sup>\*\*</sup> Consultant

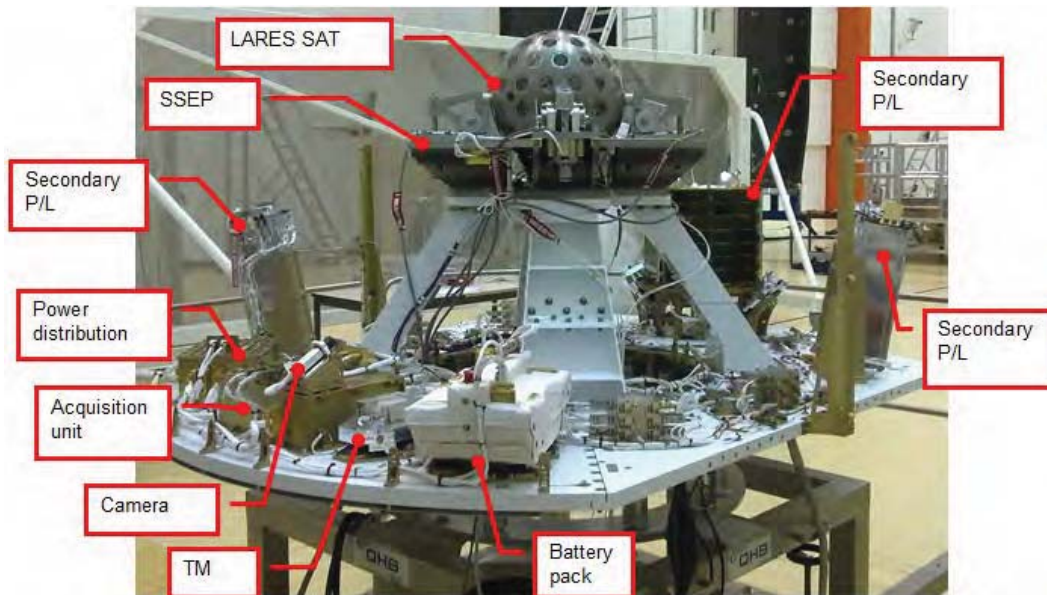


**Figure 1. LARES system before launch**

The industrial contract for LARES development was given to the Compagnia Generale dello Spazio as prime contractor, and a structure of industrial and universities subcontractors for the different subsystems. In particular, Rheinmetall S.p.A. satellite line of business (the line of business later merged with CGS), designed, manufactured and tested the Separation Subsystem.

### **SSEP Design Driving Requirements and Critical Areas Identification**

The main goal of this kind of Subsystem was meeting the following challenging, severe and contradicting requirements:

1. To be stiff with the LARES satellite installed (lateral first frequencies higher than 70 Hz, while vertical frequency higher than 140 Hz);
2. To withstand high environmental loads (i.e., quasi static load of 15 g in each orthogonal directions applied to the 400-kg payload);
3. To lock a spherical body tungsten made by minimizing the contact areas;
4. To be single point failure tolerant in terms of release function (degraded kinematical separation conditions were acceptable);
5. To transmit negligible shock to the LARES during the separation

The structural/stiffness requirements (number 1, 2, 4 and 5) were specified by the launcher in order to be as much conservative as possible as this was the VEGA launcher's maiden flight. The third one was a scientific requirement aimed not to alter the spherical shape of the satellite that for scientific purposes shall be as perfect as possible so as to be modeled as a spherical body. To fulfill the above requirements, the following critical areas have been identified:

1. Reliable, simple and failure tolerant design concept identification;
2. Suitable separation device identification → only non-explosive initiators have been considered;
3. Separable surface design optimization in terms of material selection (with the satellite side fixed), geometry and preload;
4. Robust and repeatable alignment and integration process identification.

### Trade studies

The first trade analysis for the concept selection was performed by taking into account the above listed critical areas. Existing or similar applications have been used as starting point. Several configurations have been analyzed considering applicable requirements in terms mainly of mechanical environment,

available room and taking into account technological, manufacturing and functional aspects. In particular, four basic concepts have been studied:

- Tropical solution: to apply the preload using three pullers hardly engaged in the satellite body.
- Clamp Solution: to apply the preload using four arms on the upper surface of the satellite to push down the satellite against a preloaded pad.
- Equatorial Solution: to apply the preload using four pin-pushers inserted in the equatorial holes and by using a lower supporting circular pad engaging the sphere bottom part providing a vertical support and preload.
- Hinge Solution: the same as solution 3 without using sliding pins but using equatorial hinged pins.

#### Solution n. 1 (Tropical Solution)

The satellite is fastened to the SSEP structure by using three fixation points positioned at  $120^\circ$ . These three points could be threaded bars screwed in the satellite for one side and fixed to the separation device on the other side. After the release, three protruding elements remain attached to the spherical satellite. The benefits of this solution are simplicity and stiffness; simplicity means high reliability and shorter development, manufacturing and testing time. On the other hand several disadvantages exist that lead to discard this solution: the protrusions modify the satellite configuration by adding a small uncertainty source in the Lense-Thirring measure, the preload application to these bars is complicated, and finally the failure tolerance implementation is not easy (if a threaded bar remains engaged no possibility to release the satellite exists).

#### Solution n. 2 (Clamp Solution)

The Clamp Solution was designed to provide the preload using a combination of locked arms in the upper part of the satellite and a pushing cap on the south polar region of the satellite. The clamps are used to obtain a reaction to the preload applied by the pushing cap. The clamps are blocked during the flight until the separation devices receive the separation signal. To provide enough satellite clearance, the clamps have to move when the constraint is unlocked; they are pulled back by a rotational spring inserted inside a hinge.

The contact surface between the clamp and the sphere needs to have an area  $> 23 \text{ cm}^2$ ; which means the clamp has the same curvature of the sphere. In order to avoid damage on the satellite surface due to vibration effects, the same surface finish has to be on the clamp interface area and the satellite. Micro welding is prevented using a suitable material for the clamp. The most important part of this configuration is the clamp that has to hold the satellite. In Figure 2, the main components of this solution are shown; furthermore, the mechanism in open and closed configuration is shown. The conical insert, where the separation device is positioned, is designed in order to withstand shear loads.

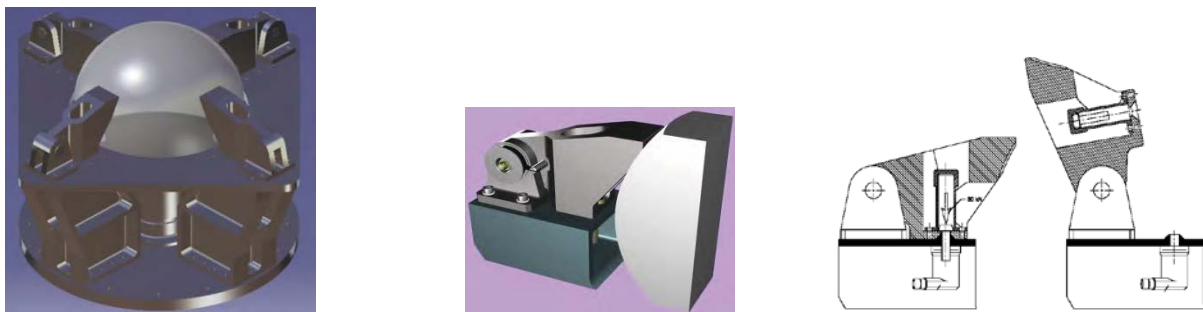


**Figure 2. Clamp Solution assembly on left. Clamp detail in the center. Clamp section in open and closed configuration on right**

The benefits of this solution were simplicity and stiffness; the main drawback is that it is not possible to implement the failure tolerance functionality (if a clamp remains in closed configuration, the vertical force component blocks the satellite on SSEP).

#### Solution n. 3 (Equatorial Solution)

The Equatorial Solution has four equatorial pin-pushers blocking the sphere. Each pin pusher provides a preload by means of non-explosive actuators. During the flight phase, the pins are hardly pressed in the cavities by the devices; once the satellite has reached the separation altitude, the separation devices are activated by removing the preload on the pin-pushers and allowing the pin retraction via springs in order to disengage the satellite. In Figure 3 and Figure 4, the preliminary design of this solution and the two pin working positions are shown.

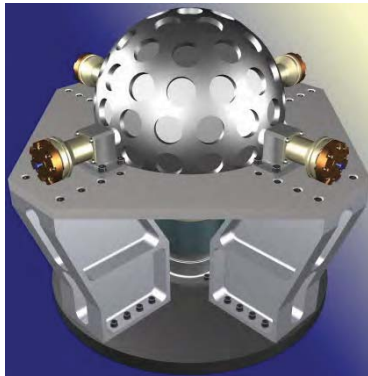


**Figure 3. Equatorial Solution**

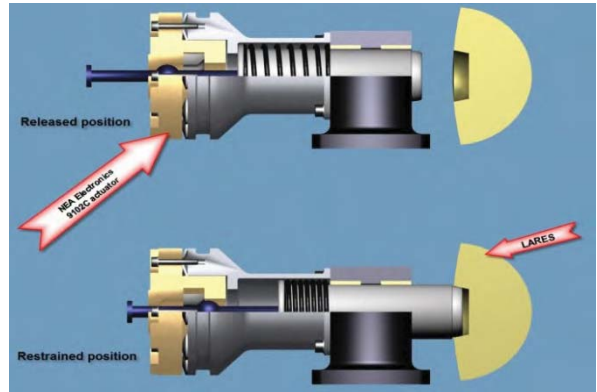


**Figure 4. Pusher working positions**

The benefits of this solution were simplicity, stiffness and the failure tolerance because it is possible to design the interface geometries between pin and satellite to allow the disengagement of the satellite even if a separation device fails; but a problem exists with the loads acting on the pin when the structure is preloaded. The retracting spring on each pin had to be bigger than available space for accommodation.

Solution n. 4 (Hinge Solution)

This solution is an upgrade of the equatorial one, because in it LARES engagement is ensured by four hinges in order to avoid the friction problems in the contact points between LARES and the four pins. The structures must be compacted to improve the stiffness, the vibration behavior, and to reduce the total mass, as shown in Figure 5.

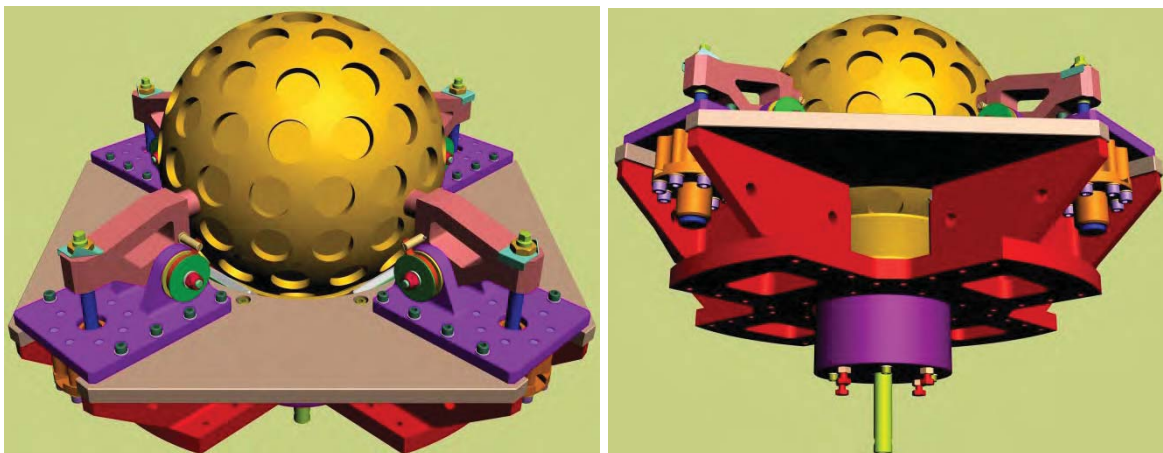


**Figure 5. Hinge Solution**

This solution collects all the advantages of the previous solutions by minimizing the disadvantages; for this reason this has been selected as final configuration for LARES SSEP. The separation device geometrical position and number (4 actuators) required a very good simultaneity in the separation. This simultaneity requirement coupled with high strength and power budget boundaries lead to the usage of a NEA Electronics solution to initiate the LARES separation. In particular, the actuator had to withstand a maximum 195000-N static load applied in compression along the pin axis and had to separate properly



when subjected to a total compressive load of 148000 N along the pin axis. Then the release mechanism, considering an infinitely rigid interface flange, had to guarantee a minimum axial stiffness (against the load direction) of 219 MN/m. Furthermore, the release mechanism allows an angular misalignment of rod corresponding to a 10° cone under the loads above specified.

#### LARES SSEP Selected Configuration Summary

The selected configuration for the SSEP is composed of the following elements:

- A supporting structure that guarantees lower mechanical interface toward the LARES System support structure (white structure in Figure 1).
- An upper main mechanism that is the mechanical interface to the LARES satellite, including:
  - The interface pins to the satellite
  - The hinge system, which allows the retention of the satellite during the launch phase and its separation on orbit.
  - The initiator device that releases the hinge system
  - The switches indicating the opening of the first mechanism and the activation of the second one.
- A support and preloading system
- An ejection LARES mechanism.
- An electrical interface to the avionics, including:
  - The switches lines
  - The initiators lines

The functionality of the release mechanism is explained in the separation sequence shown in Figure 6, from locked configuration (on left) up to the satellite separation (on right):

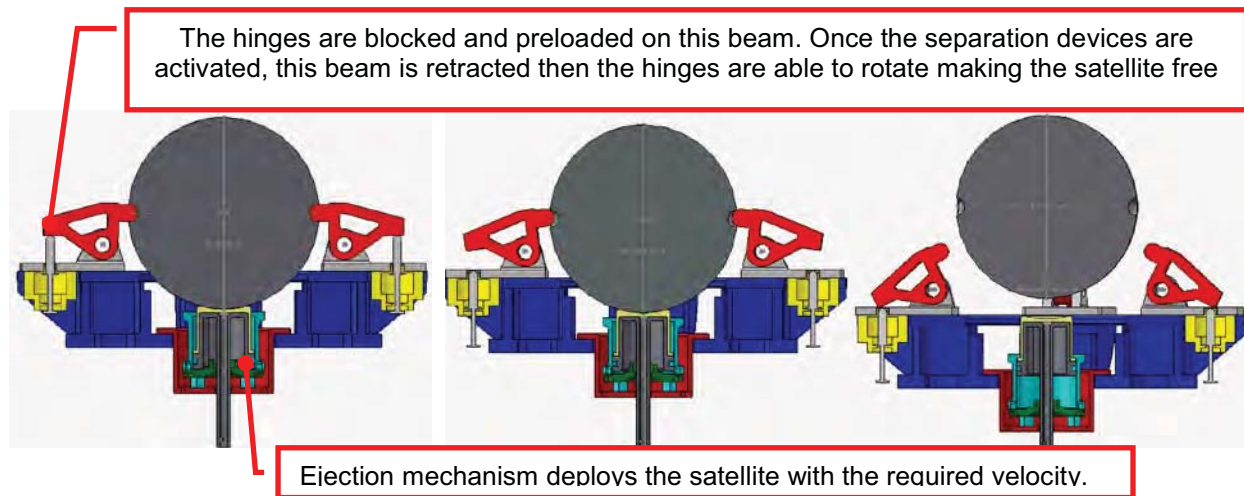


**Figure 6. Separation sequence (from left to right) and functional explanation**

When LARES system reaches its final orbital position and the satellite has to be released, an electrical signal is sent to the actuators that disengage the pin pulled back by means of a retraction spring, thus allowing the hinge to rotate. Hinge rotation is also driven by two spiral springs suitably preloaded.

Once the LARES satellite is set free by the main separation mechanism, the compression spring of the ejection system, in the zero-gravity condition, pushes the LARES satellite along the vertical direction. At the end of compression spring elongation, the LARES satellite will have the nominal vertical speed of 0.75 m/s. The push-out spring has been designed to provide a force of 350 kg for the safety reason to avoid LARES ejection during the operation on ground in case of accidental activation of the SSEP. An electrical device will confirm the release operation.

#### Support and preloading system

A section of the SSEP with the satellite installed and with the description of the preload path is shown in Figure 7.

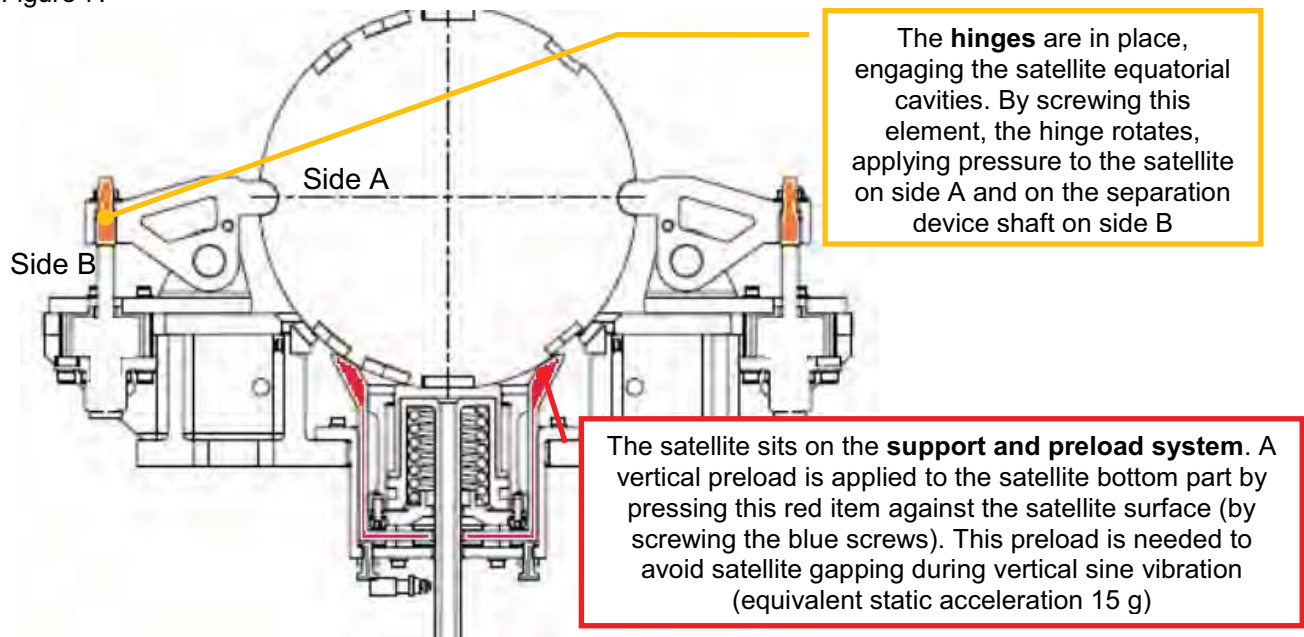


**Figure 7. SSEP Functional Scheme**

The contact surfaces between SSEP and LARES satellite are:

- LARES and support and preload system: Sphere on cone; the SSEP part is covered by Kapton, to avoid LARES surface damage. This contact area is so large that the Hertzian stress is not critical (negligible);
- LARES and hinges: sphere on sphere (cavity on satellite and pin on SSEP). The sphere geometries have been optimized to have an acceptable level of Hertzian stress; in addition, to avoid cold welding issues, Braycote lubricant has been used in between. Both caves on satellite and hinge pins have spherical form.

#### Integration approach

In order to implement the theoretical preload philosophy that has a uniform vertical preload applied by the support system and the hinge preloads acting symmetrically and balanced in the equatorial plane (the preload of two hinges on the same axis null the force contribution in this direction if the forces are the same), an excellent alignment has to be reached during the integration. The SSEP by design was suitable to reach this theoretical condition, but the integration procedure had to be carefully tuned. In particular, the support and preload system has been instrumented with 4 strain gauges placed at 90° in order to evaluate the preload distribution and uniformity on the whole bottom circumference, and each separation device rod has been instrumented too by using strain gauges to measure the force applied to the separation device itself. Additional strain gauges were placed on the structure of the Qualification Model to verify the sensitivity of the preload distribution with respect to the integration approach. Figure 8 shows three integration steps.

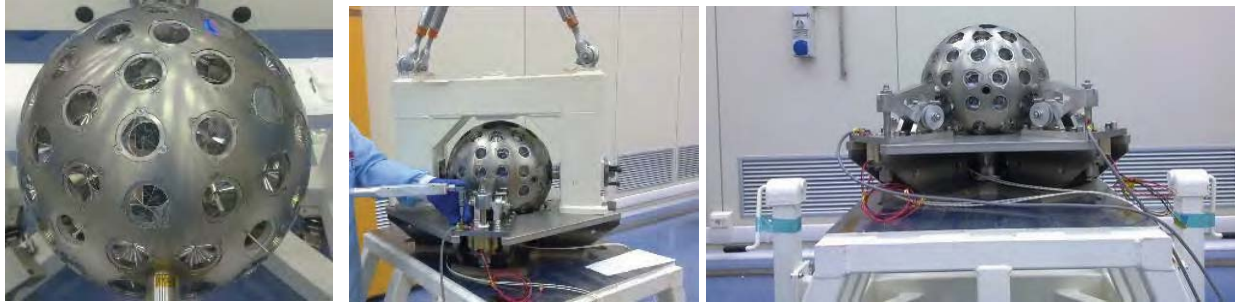


**Figure 8. SSEP Flight Model integration with LARES Flight Model**

The detailed definition of the integration procedure and the decision to perform the shear pin holes execution in an assembled configuration guaranteed the capability to reach a final integration fully compliant to the requirements and with an extremely high repeatability.

### **Model philosophy and tests**

Taking into account the criticality of the subsystem and the requirements to satisfy, the following model philosophy was adopted:

- Two (2) Breadboards models
- One (1) Qualification Model
- One (1) Flight Model

In particular, the Breadboards were to be representative of the two most critical elements - an arm of the bond and the spring of separation / boost system. These models were used for the characterization of the hinges from both the structural point of view (stiffness) and from the functional point of view (torque margin, deployment main parameters). The Qualification Model (QM) was representative of the flight model but the satellite was the LARES Demonstration Model (DM) that was identical to the flight for interfaces but it was the 6% heavier than the flight model to be conservative.

#### Philosophy verification

*Breadboards:* On these models, characterization tests were performed at the extremes of temperature in a climatic chamber (operative range 10°C - 40°C). A cycle in thermal vacuum (non-functional) to verify the compatibility of materials (lubricants) with the space environment was performed too.

*Qualification Model:* On this model the following tests were carried out:

- dimensional test
- mass measurement
- vibration
- separation test at the critical temperature (highlighted by the tests on the breadboard )
- thermal vacuum test exclusively for the electrical part

*Flight model:* On this model the following tests were carried out

- dimensional test
- mass measurement
- functional acceptance tests at room temperature (postponing system-level environmental testing).

#### Breadboard #1 tests

##### *Objectives*

- To demonstrate the functionality of the pin and cave interface (separable surfaces) under operative load (the critical separable surface);
- To demonstrate the functionality of the pin and cave interface under operative load with a load factor of 1.5.

*Pass criteria*

- No plastic deformation on the cave or pin under operative load (measured both via optical method and Coordinate Measurement Machine (CMM));
- No plastic deformation on pin or cave under operative load time 1.5 measured both via optical method and CMM);

*Test article identification*

- 15-5PH H1025 Steel Pin;
- THA-18N Tungsten Cave;



**Figure 9. Steel Pin on left and Tungsten cave on right**

*Tests sequence*

1. Visual inspection with electronic microscope (magnification: 7.5x; 10x; 20x; 40x);
2. Dimensional check with Leitz machine;
3. B/B mounting under compression machine;
4. Visual inspection with photos;
5. Greasing pin and cave with Braycote 600;
6. Slowly applying compression load (26612 N), compression speed equal to 0.0003 mm/s;
7. B/B demounting under compression machine;
8. Visual inspection with electronic microscope (magnification: 7.5x; 10x; 20x; 40x)
9. Dimensional check with Leitz machine;
10. B/B mounting under compression machine;
11. Visual inspection with photos following grease removal;
12. Greasing pin and cave with Braycote 600;
13. Slowly applying compression load times 1.5 (39918 N), compression speed equal to 0.0003 mm/s;
14. Visual inspection with photos following grease removal;
15. B/B demounting from compression machine;
16. Dimensional check with Leitz machine;
17. Visual inspection with electronic microscope (magnification: 7.5x; 10x; 20x; 40x).

To perform a perfect correlation on dimensions in the various performed tests, a measurement points map was used on the cave and pin such that in all the checks the same points were measured.

*Tests results*

A microscope analysis has been performed after the test to look for eventual problems due to plastic deformation on the steel pin and tungsten cave. Figures 10-12 show the test set-up and the microscope steel pin photos. The microscope analysis and the measurements with the Leitz machine showed that no plastic deformation occurred during the test.





Figure 10. BB1 Test set-up



Figure 11. Pin at 10x after first test



Figure 12. Cave at 20x after the test (left) and before (for comparison)

### Breadboard #2 tests

#### *Objectives:*

- To measure the stiffness along the three principal directions of the restraint mechanism;
- To correlate the FEM analysis previously performed on the restraint mechanism with experimental data;
- To evaluate friction coefficient of the restraint mechanism;
- To demonstrate restraint mechanism strength under operative load;
- To demonstrate restraint mechanism strength under operative load with a load factor of 1.5

#### *Pass criteria*

- Check of the complete structural integrity of the BB#2 after the tests
- The value of the friction torque, before and after the tests, must be compatible with the ejection of the LARES satellite

#### *Test article identification*

The test article was composed of the restraint mechanism subdivided in its constituent components:

- Hinge
- Latch
- Pin
- Preload bolt
- Actuator Dummy

All the components were completely representative of flight components, including material, tolerances and dimensions.



**Figure 13. BB2 test set-up**



**Figure 14. Restraint Mechanism**

*Test sequence*

1. Dimensional Check;
2. Visual inspection;
3. Measurement of friction torque;
4. Evaluation of restraint system stiffness;
  - a) Measurement of vertical stiffness;
  - b) Measurement of transverse stiffness
  - c) Measurement of longitudinal stiffness
5. Measurement of strength at nominal max load;
6. Visual Inspection;
7. Measurement of friction torque;
8. Dimensional check;
9. Measurement of friction torque;
10. Measurement of the strength at nominal load times 1.5;
11. Visual Inspection
12. Measurement of friction torque
13. Dimensional check

*Test Results*

- The comparison between the dimensional checks performed with Leitz machine before and after strength tests assures that no plastic deformation occurred on the restraint mechanism during all tests performed up to 1.5 times the qualification load.
- Friction coefficient measured values were acceptable and compatible with the ejection of the LARES satellite, and didn't show variation during the performed tests.
- The obtained results clearly demonstrated the soundness of FE modeling of the entire SSEP subsystem and relevant components (measured stiffness was 20% more than the predicted one in all the 3 directions).

SSEP QM vibration test

*Objectives:*

- To determine the mechanical characteristics of LARES SSEP (in terms of natural frequencies, etc.)
- To demonstrate the validity of the mechanical design with respect to the applicable mechanical environment
- To verify that no degradation or malfunction of LARES SSEP QM components occurs during test.
- To verify that no preload loss occurs before and after testing

*Test article identification*

The LARES SSEP QM Model is shown in Figure 15.



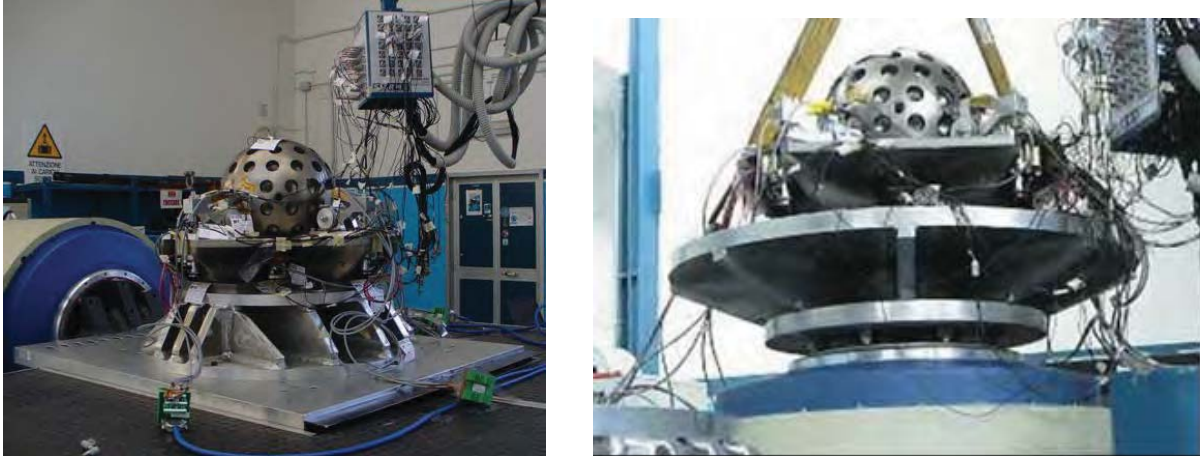


**Figure 15. LARES SSEP Qualification Model on the vibration shaker for lateral test on left and for vertical test on right**

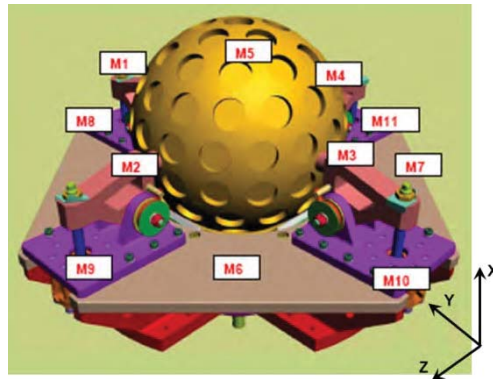


**Figure 16. Accelerometer position and vibration test reference system**

*Test sequence*

On this model, the following tests have been done:

1. Dimensional controls
2. Mass measurement
3. Vibrations
4. Functional tests at the most critical temperature (found during the tests performed on the breadboards) in climatic chamber
5. TVAC test on electrical components only
6. Separation test

*Tests Results*

In the following figures, the results of low sine excitation before and after full-level sine for the accelerometers positioned on the four hinges (M1-M4, see Figure 16) and on LARES satellite (M5, see Figure 16) have been reported for the X direction (that is the vertical one directed as the launcher thrust axis).

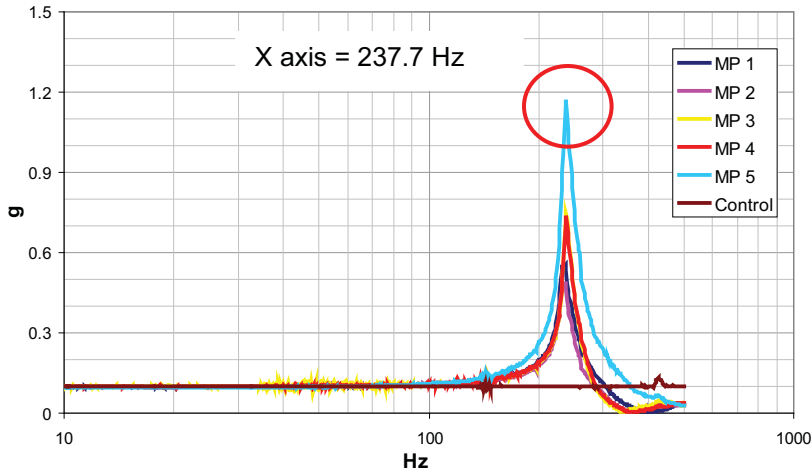


Figure 17. Low sine pre, X direction

In Figure 18, the results of low sine excitation for the same accelerometers after full-level sine are reported.

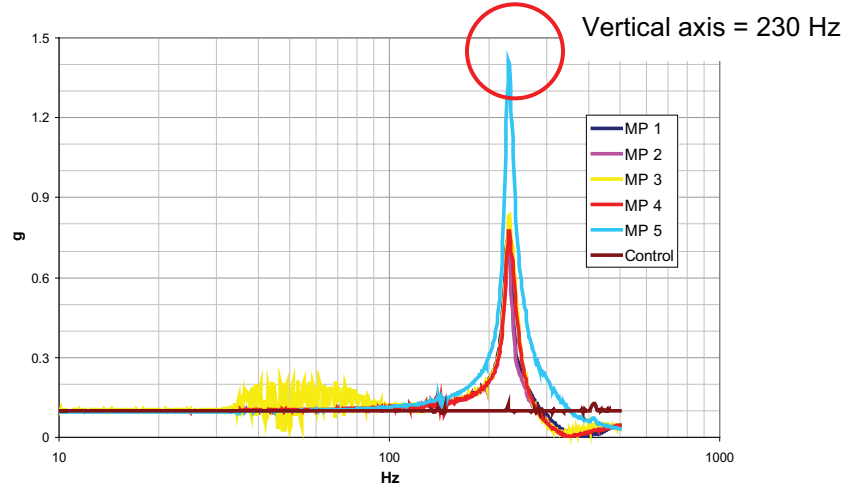


Figure 18. Low sine post, X direction

The previous data show that after a full-level sine a little structure stabilization is present, as revealed by the slight difference between the resonance frequency before and after full level sine test (about 3%). Final value of the first natural frequency on X direction is 230 Hz, greater than the 140 Hz (requirement).

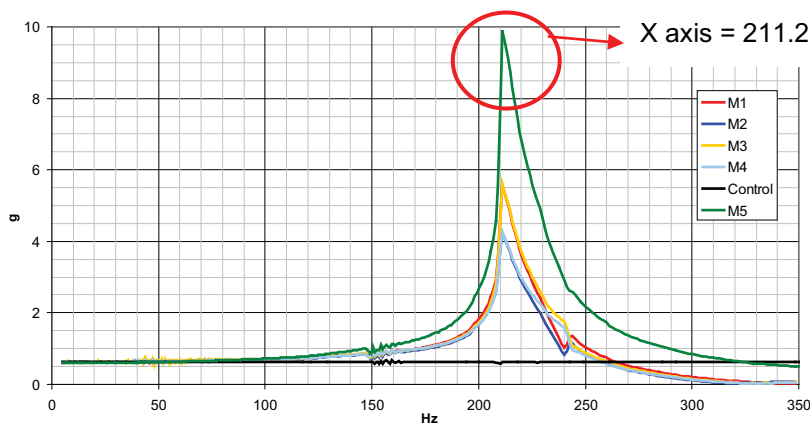


Figure 19. Full sine test, X direction

The full sine test showed a lower value of the first frequency, demonstrating a certain dependence of this parameter with sine amplitude. The low sine test performed after this full sine confirmed that no damage occurred in the mechanism.

*Test Conclusions*

- The Vibration Test has been performed on the SSEP QM and was successfully completed.
- The satellite was in flight configuration and all the success criteria have been satisfied.
- The test confirmed the FEM prediction (the SSEP behaves like a 1 DoF system)
- Loads acting on SSEP during tests are less than expected.
- In the two lateral directions, the same behavior has been measured, in particular 142 Hz first frequency (70 Hz was the requirement) measured during low level sine, while 130 Hz first frequency measured during the full level.

The frequency shift on full level sine is usual when part of a preload structure. Visual inspection did not identify any damage or physical degradation on the item under test.

SSEP QM Separation tests

*Pass Criteria*

- Test conditions according to specification requirements (worst temperature distribution on mechanism was applied);
- “Clean” separation without any problem;
- Separation with an ejection speed  $0.6 < v < 0.9$  m/s;
- Correct activation of the end of stroke switch;
- Acquisition of all the test data (temperatures, video recording, NEA activation parameters, ejection mechanism strains).

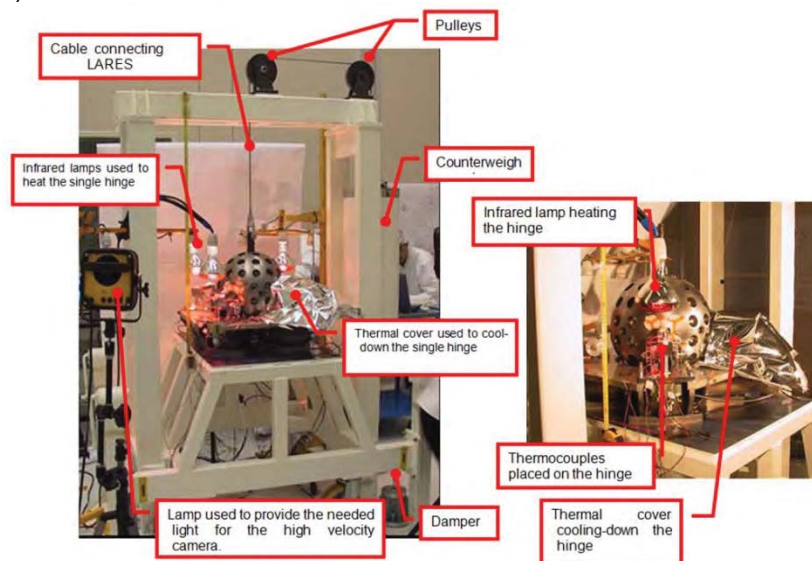


**Figure 20. LARES QM Separation Test configuration**

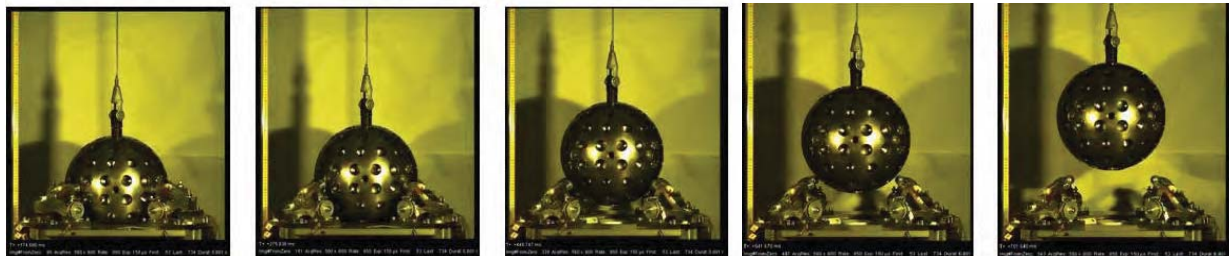


**Figure 21. LARES QM Separation filmed sequence – 527 ms of elapsed time from the first to the last photogram**

#### Tests conclusions

- The Separation Test was performed on the SSEP QM + LARES DM and was successfully completed.
- The SSEP was in flight configuration and all the primary success criteria have been satisfied.
- Visual inspection did not identify any damage or physical degradation on the item under test (no damage occurred after vibration test).
- All the additional controls, measurement and investigations did not show evidence of any degradation or loss of performance of any of the mechanical components.

During the Launch Phase, the on-board camera mounted on the Support Subsystem has shown the nominal performance of the SSEP subsystem.



**Figure 22. Picture of LARES Satellite release on orbit**

#### Lessons Learned

The 'lessons learned' from the positive results obtained in the activities performed on LARES Program SSEP is the confirmation of the importance of:

- developing a design oriented to the integration feasibility;
- using an "over-sensorized" model (in this case SSEP QM) to verify the sensitivity of the integration and alignment mismatches vs performance requirement in order to minimize the influence of operator errors;
- adopting a suitable optimized model philosophy that can allow deep investigations of the critical areas;
- focusing strong effort in the testing activity at breadboard level to correlate in advance the mathematical models in order to minimize the technical risk (the BB model testing phase has been included in the timeframe of CDR).

The importance of the above choices becomes more evident in those programs characterized by very stringent and challenging requirements such as LARES.

## Testing Orion's Fairing Separation System

Henry Martinez\*, Chris Cloutier\*, Heber Lemmon\*, Daniel Rakes\*, Joe Oldham\* and Keith Schlagel\*

### Abstract

Traditional fairing systems are designed to fully encapsulate and protect their payload from the harsh ascent environment including acoustic vibrations, aerodynamic forces and heating. The Orion fairing separation system performs this function and more by also sharing approximately half of the vehicle structural load during ascent. This load-share condition through launch and during jettison allows for a substantial increase in mass to orbit.

A series of component-level development tests were completed to evaluate and characterize each component within Orion's unique fairing separation system. Two full-scale separation tests were performed to verify system-level functionality and provide verification data. This paper summarizes the fairing spring, Pyramidal Separation Mechanism and forward seal system component-level development tests, system-level separation tests, and lessons learned.

### Introduction

The fundamental components of the Orion Multi-Purpose Crew Vehicle fairing are similar to heritage systems as shown in Table 1. However, addition of the load share between the fairings and the Service Module requires a unique architecture and presents challenges requiring substantial testing in order to validate the design can successfully jettison loaded fairings and ensure the safety of Orion astronauts.

**Table 1. Fairing System Comparison**

Vehicle	Segments	Vertical Separation	Horizontal Separation	Separation Energy
Orion MPCV	Trisector	Frangible joint	Frangible joint & PSM	Mechanical springs
Ariane 5 (1)	Bisector	Thrust Rail	Frangible joint	Thrust rail
Atlas V 400 (2)	Bisector	Pyro Sep Bolts	V-Clamp	Spring thrusters
Atlas V 500(2)	Bisector	Thrust rail	Sep bolt	Thrust rail
Delta IV (3)	Bisector	Thrust rail	Sep bolt	Thrust rail
Delta IV Heavy(3)	Trisector	Thrust rail	Sep bolt	Thrust rail
Pegasus (4)	Bisector	Sep bolt / clamp band	Frangible joint	Gas thrusters
Saturn V/Skylab (5)	Quad	Thrust rail	Latchpins	Thrust rail

Extensive development and qualification testing was and is currently being performed on each of the fairing components. This paper focuses on the early development testing for the fairing Pyramidal Separation Mechanism, spring assembly, and forward seal as well as results from the more recent system-level fairing separation testing.

---

\* Lockheed Martin Space Systems Company, Denver, CO



## Orion Fairing Design Overview

The Orion fairing system, referred to as the Spacecraft Adapter Jettisoned Panels shown in Figure 1, provides protection for the Service Module (SM) on the pad and during ascent as well as carries approximately half of the vehicle structural loads up through jettison. During the Orion Exploration Flight Test -1 (EFT-1) mission, the fairings are jettisoned under approximately 0.2g of thrust at an altitude of approximately 1830 m (600,394 ft).

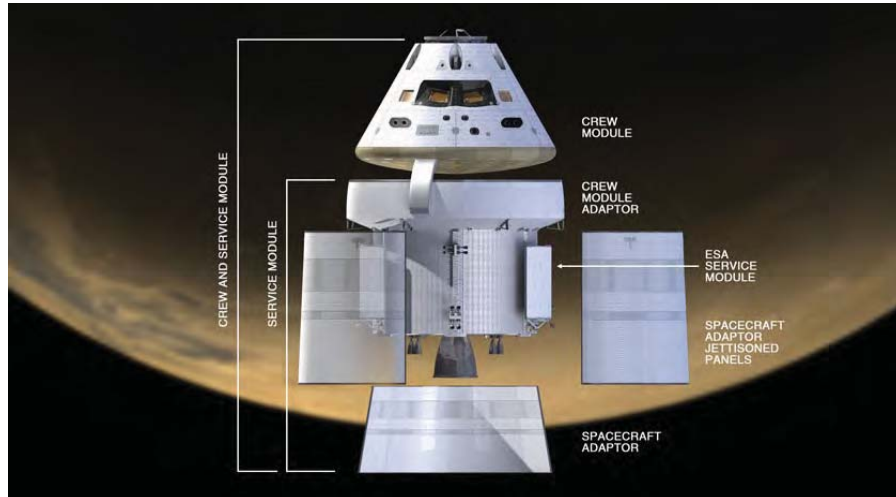


**Figure 1. Orion Configuration (Image Courtesy: NASA)**

The fairing jettison system shown in Figure 2 is comprised of composite tri-sector segments which are severed by frangible joints and pyrotechnic separation bolts, then jettisoned with springs and hinges. The frangible joints are the primary load path between each of the fairing panels along the horizontal and vertical seams. Each frangible joint contains a single core charge initiated by Explosive Transfer Line at opposite ends for redundancy.

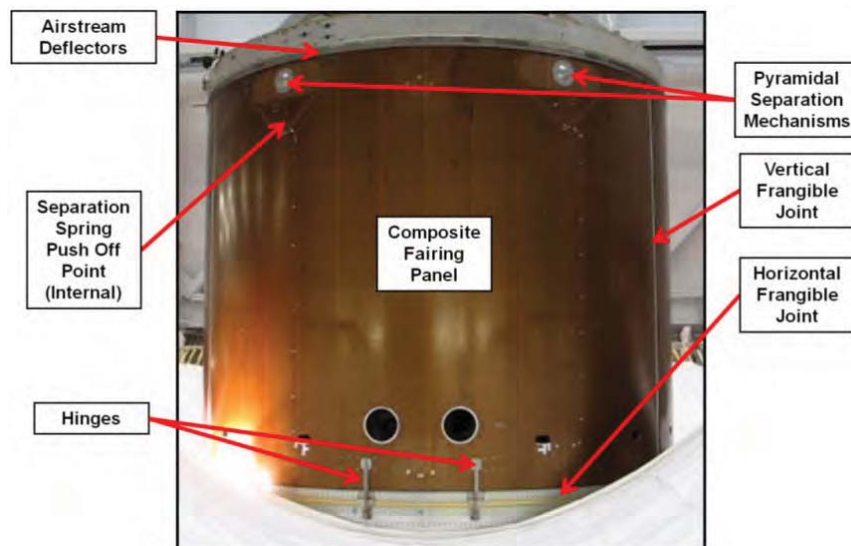


**Figure 2. Fairing Components**

After severance of the frangible joints, each panel is released by two redundantly actuated pyrotechnic separation bolts between cup-cone interfaces called Pyramidal Separation Mechanisms (PSMs). The PSM transfers load from the inner load path (SM) to the outer load path (fairing panels) and allows



clearance of these load bearing surfaces during deployment. Made from titanium with CANADIZE® coating, the PSM incorporates variable angle surfaces with shallow angles taking shear loads and steeper angles providing clearance. Selection of the primary load bearing angle involved a careful balance of minimizing axial force induced into the pyrotechnic separation bolt and frictional resistance during separation.

Once the PSMs are released, the fairings are pushed away with titanium spring actuators which rotate the panels about hinges along the lower separation plane. The Push-Off Springs are located near the top of the panels adjacent to the PSM and provide initial deployment force for the fairing panels. There are two springs per panel sized to provide positive margin in the event of a spring coil fracture per NASA human rating requirements.

The forward seal system is a circumferential seal comprised of an elastomeric p-shaped seal compressed by titanium flexures called airstream deflectors. Together they create an environmental seal between the top of the fairing panels and prevent air ingestion during ascent while allowing for relative deflections between the sealing surfaces. The seal system also acts as a conductive path between the avionics ring and the fairing panels.

### Component Testing

Component-level development testing evaluated the individual components of the system and provided valuable information allowing for mass and performance optimizations. Load testing was performed on the Pyramidal Separation Mechanisms to ensure the material and coatings could endure the high loads and cyclic wear during ascent and still separate. Spring testing was performed to validate design margins and evaluate performance under the stressing ascent vibration environment. The seal system was cycled in order to validate life requirements. Each of these tests provided insight into the performance of each component against its most stressing environment and in most cases required some modification to ensure all performance requirements would be met during qualification.

#### Pyramidal Separation Mechanism Testing

Tests were conducted to evaluate the performance of the cup-cone design to bear load and the effectiveness of the lubricant. Figure 3 shows a cross section of the flight design.

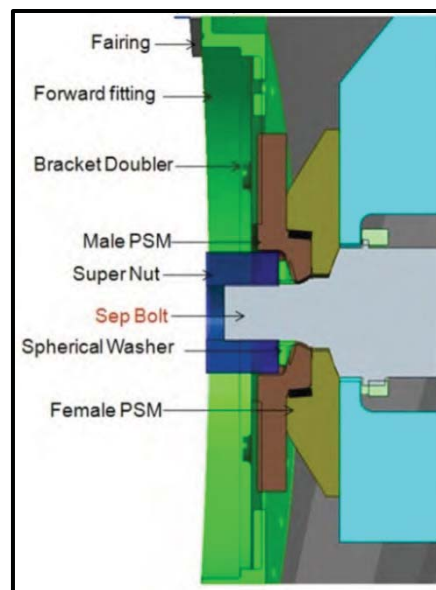


**Figure 3. PSM Cross Section**

There were three rounds of initial PSM development testing that focused on validation of the ramp angles, material and coating performance. The first test identified refinement of the load bearing surfaces and manufacturing tolerances. The second test validated the refinements and changes learned from initial testing and to predict slippage in the joint. The third test was used to verify that the material and coatings would survive the load and life requirements.

Test fixtures were designed to support the PSM halves and mount to a servo-hydraulic load frame. The fixture geometry was designed such that the prescribed ascent loads and moments could be achieved via a single load-axis. Two fixture sets were machined, one for a maximum axial case and the other for a maximum lateral case. Modifications were made to these basic designs to include both forces and moments when the predicted loads changed. In all, the test setup included 10 Linear Displacement Transducers (LDT), an instrumented Strainsert bolt (first and second test), four strain gages mounted on an inert flight-like bolt (third test), a main load cell to control the applied load levels, and an LDT to monitor overall applied displacements.

The first test revealed the critical load bearing surfaces were not engaging properly. In order to correct this, shims were fabricated of variable thicknesses and placed between the two nodes to determine the proper gap. Changes were also made to the interfacing radii for each of the nodes and to the primary critical load bearing surfaces to minimize contact stress between the two halves. The second test conducted validated the changes made to the design. Slippage was more predictable with smoother hysteresis deflection curves. While the test showed heavy burnishing there was no galling and the parts easily separated. Figure 4 shows the wear differences between the first and second test configurations.

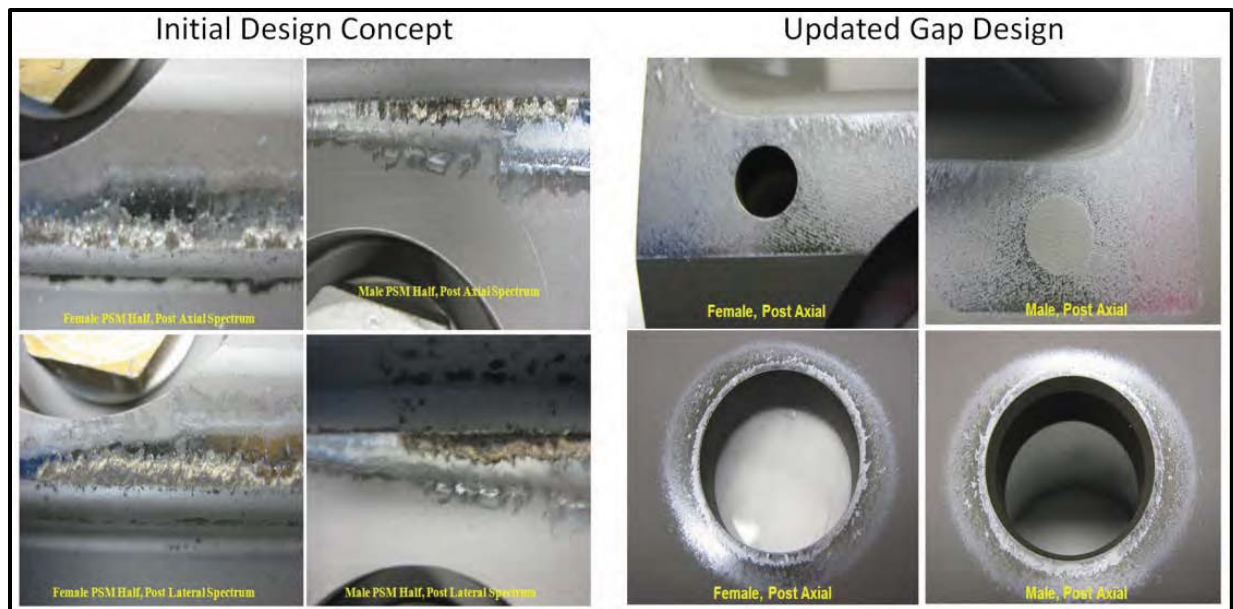


**Figure 4. Wear Characteristics of Initial and Updated Design Concepts**

The third test series used a flight-like inert separation bolt which was instrumented with four uniaxial strain gages as well as a new test fixture. This test evaluated the preload operation and measured the resultant axial and moment loads in the separation bolt over the increased life cycle count based on updated analysis. The cycle count increase was based primarily on updated ground cycle analysis which was typically low load, but had to be accounted for. Data from this round of testing (shown in Figure 5) was also used to determine load when the PSM slipped. This final test confirmed the design was robust enough to survive the loads at twice the number of life cycles and no further modifications were required.

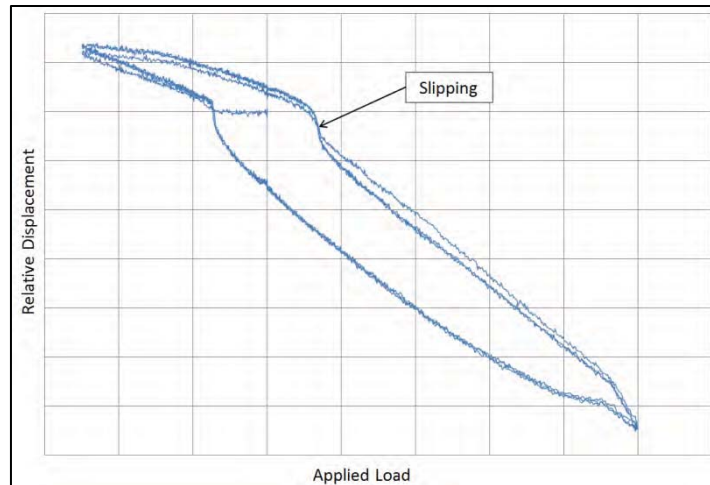


**Figure 5. PSM Load versus Displacement**

Spring Assembly Testing

A “Test Like You Fly” approach was followed for spring testing with initial wear-in/run-in followed by random vibration then multiple functional tests to verify design margin. Figure 6 shows the general cross section of the spring assembly and its various components.

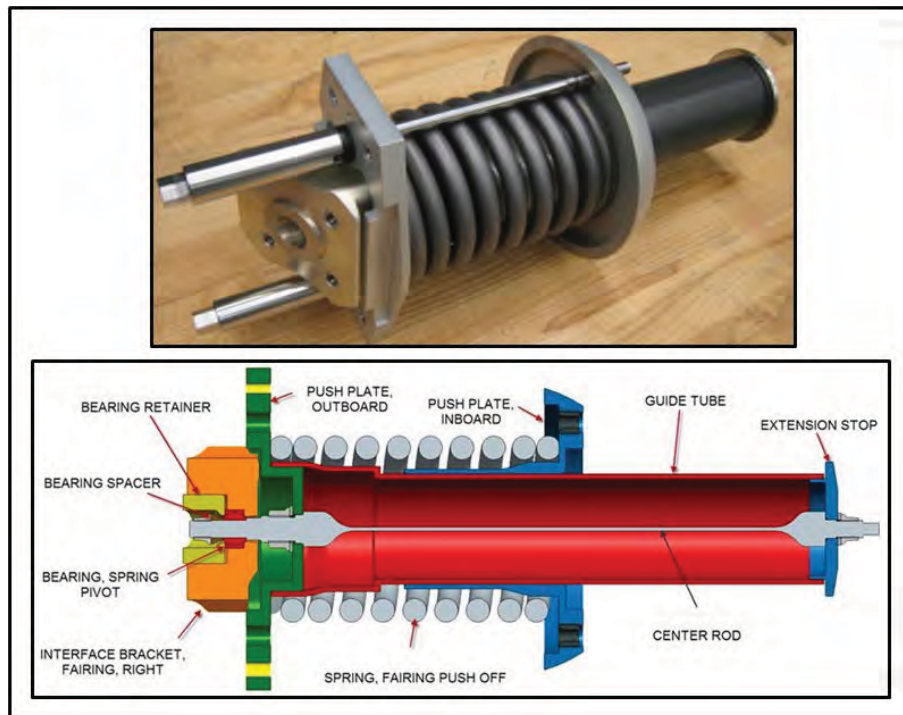


**Figure 6. Fairing Spring Assembly**

Initial wear-in/run-in was performed to burnish close running fit areas and evaluate potential friction losses within the assembly by measuring the force versus displacement over the working height of the spring. Test data showed minimal losses (1% or less) compared to the individual spring coil testing performed by the vendor.

Random vibration test levels initially started out as benign but as dynamic modeling matured the levels more than doubled. This gave cause for concern of excessive loading of the spherical bearing within the assembly which allows for proper spring alignment during deployment. Under random vibration testing, the spring surged in a smooth sinusoidal motion along the coil axis for the most part but at certain levels the peak displacements were significantly amplified and chaotic. This motion induced higher than expected loads into the spherical bearing.

Another noteworthy event was the amount of off-axis displacement resulting in cyclic impacting of the coil with its adjacent assembly hardware. At qualification levels the titanium spring damaged the TUFAM<sup>®</sup>-coated aluminum parts and generated debris which was deemed unacceptable. Three options were selected and tested; bare aluminum, aluminum with hard anodize coating, and 304 CRES stainless steel. Ultimately, the soft 304 CRES stainless steel performed the best by absorbing the impact energy. Post-test results had the appearance of peening but without the effect of creating debris. Figure 7 shows post vibration test results of the original anodized aluminum and the final 304 CRES design.

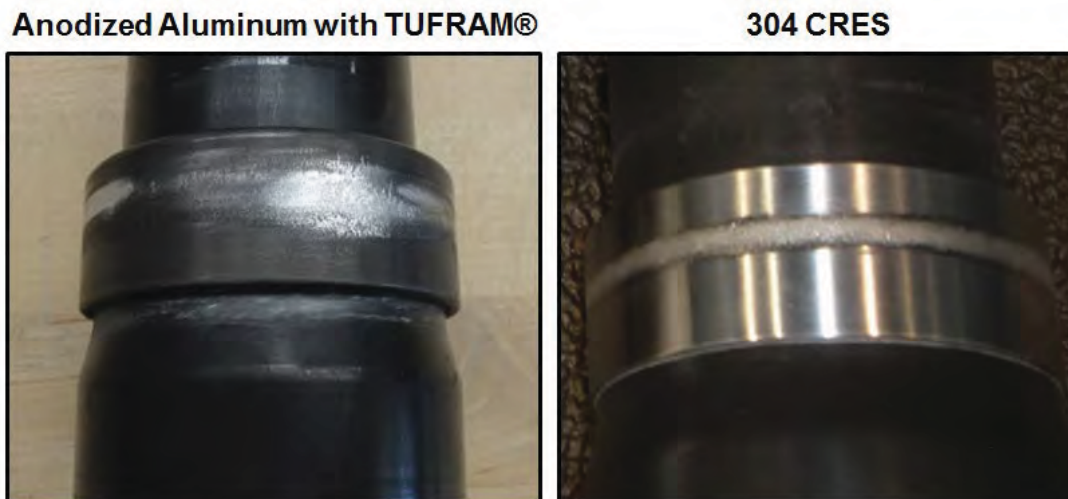


**Figure 7. Anodized Aluminum and 304 CRES Vibration Test Results**

Another issue noted was ground bonding paths. The use of a spherical bearing and a dry film lubricant in the race did not allow for a clean path resulting in intermittent grounding.

Functional testing was conducted after vibration testing to be more flight like with regard to environment exposure. The functional test verified energy margins and hard stop functionality. No issues were found during functional testing. In fact, the functional test fixture was modified to accommodate lanyard connector testing using the same development springs. Overall, the development springs have become a great test asset with some being functioned as many as 15 times with no detrimental damage or wear.



### Forward Seal Testing

The forward seal system shown in Figure 8 is comprised of two components; a specially designed three segmented elastomeric seal and titanium aero deflectors.



Figure 8. Forward Seal System

The aero deflector is essentially a flexure capable of protecting the elastomeric seal from the harsh ascent thermal environment while compressing it against the sealing surface and providing a ground path. The shape of the aero deflector was complex due mainly to the large design deflections (up to 1.3 cm (0.5 in) between sealing surfaces) and required a combination of conventional machining and wire Electrical Discharge Machining (EDM) to maintain the tight manufacturing tolerances. The original avionics ring surface tested was aluminum with electroless nickel which provided a smooth finish with high hardness and excellent wear resistance without any lubricant. However, application of the electroless nickel to the large avionics ring surface was found to be prohibitive due to cost and schedule constraints. Brushed-on nickel coating was eventually chosen. Figure 9 shows the wear on the base material after 2000 cycles of both electroless nickel and brushed-on nickel coatings with no lubricant. From these initial tests it was determined that the addition of lubricant was required if brushed-on nickel plating was to be used.

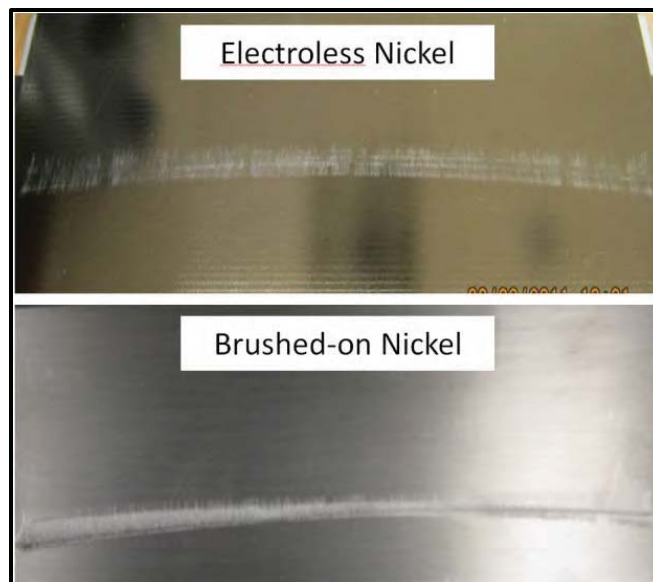
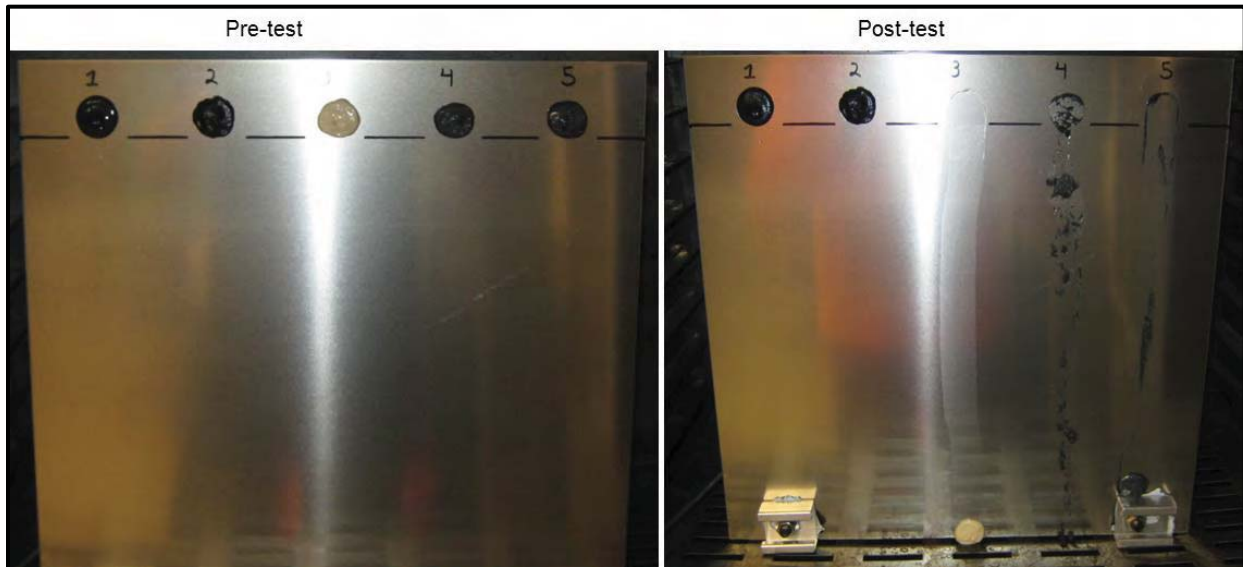


Figure 9. Nickel Coating Wear after 2000 Cycles

Numerous tests followed trying to find a lubricant that would provide the necessary wear resistance with the brushed-on nickel.

Eventually, the trade study was narrowed to five lubricants; Nye Lubricants Inc. special formula paste, Braycote® 602EF, Krytox®, Rheolube™ 2004, and Rheolube™ 2004 with MOS<sub>2</sub>. The first test conducted was an oven test to evaluate the resistance to controlled heat of 66 °C (150 °F) for a short duration (to simulate ascent heating). While several of the lubricants shown in Figure 10 did not remain in place, there is some concern that the test was not representative of flight.



**Figure 10: Controlled Oven Test**

Each of the five lubricants are currently planned to undergo a 30-day environmental exposure test at the Kennedy Space Center. In addition, a final round of wear testing will be performed. After these tests are complete, the final lubricant selection will be made.

## **System Testing**

### Overview

Due to the dynamic nature of fairing jettison induced by the load share event as well as the complex interaction between mechanisms, a system-level test was performed to verify each of the components worked together under flight-like separation conditions. The series of tests designed to verify performance and gather data for the analytical model included test fixture characterization, panel-level testing and full-scale separation tests. Multiple separation tests were required to understand the sensitivity of the system to load and thermal conditions.

### Test Fixture

In order to achieve flight-like boundary conditions, dynamic response and load share, a special test fixture was designed to simulate the Service Module. The fixture incorporated adjustable features allowing the overall structure to be simplified for manufacturability and cost while ensuring proper axial stiffness and dynamic response. The primary stiffness tuning feature was a simple spring plate located at each of the six load path interfaces. The second method for tuning of the structure was adjustability of the load head interface.

Structural stiffness and modal testing of the fixture was performed to help with tuning of the stiffness, adjusting load share, and anchoring the analytical model. Stiffness testing included thirteen load cases to evaluate the axial stiffness of the fixture and PSM interface. Instrumentation of the structure included 156



strain gage channels, 28 displacement measurements and 6 load cells in addition to input load and displacement. Most loads were input using hydraulic actuators tied down to the floor or the reaction frames. Figure 11 shows the test fixture including a frame used to mount instrumentation.

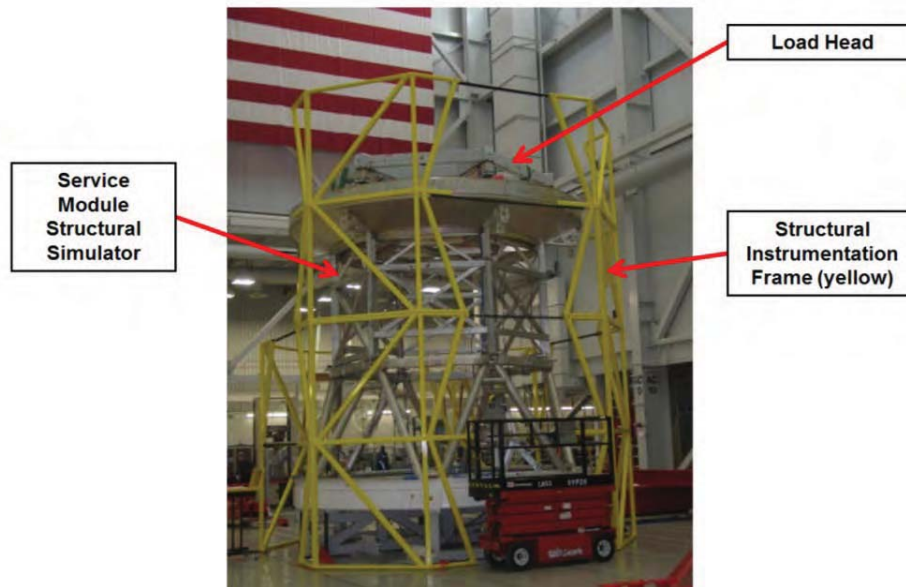


**Figure 11. Test Fixture Stiffness Testing**

Moment loads were applied using pulleys and offloading weights in order to simplify operations. Each load case was applied three times while displacement, load and strain gage data was recorded. The displacement and strain data was used to independently evaluate the stiffness and predict load share. While strain and displacement results were within 3% of each other, the overall initial stiffness prediction was off by ~25%. It was found that interactions between interfaces at the load head and spring plate were more complex than initially modeled. Capturing these differences in the finite element model was crucial in correlating test data to model predictions. Ultimately, results were still within the tuning capability of the fixture and no design changes were required.

After initial axial tuning, local bending and torsion load cases applied to the PSM interface provided additional information which led to further refinement of the stiffness and load input interface. The adjustable features of the fixture were used to obtain loading of both the inner structure and the fairings within acceptable design parameters. In order to reduce schedule, the final load share was adjusted to within 10% of the predicted value with load biased higher to the fairings to ensure a conservative test.

After tuning of the stiffness, modal testing of the fixture was performed to capture flexible body modes in axial, bending and torsion with 129 degrees of freedom over 65 grid points. Ten target modes were initially identified over the frequency range of interest (0-50 Hz) and eleven were excited during testing. Results were then used to refine the finite element model. Similar to a fixture evaluation for vibration or acoustic testing, fixture stiffness characterization is recommended for dynamic separation tests which rely on proper boundary conditions and loads. Even with advances in finite element modeling, complex boundary conditions can be difficult to predict without some level of testing. Adjustability within the Orion fairing test fixture accounted for uncertainties in the predicted stiffness while allowing for simplification of the overall structure to reduce cost and fabrication schedule. In addition, the characterization provided insight into potential model uncertainties with the flight structure and provided valuable information for correlating the test fixture model. Characterization of the flight Service Module is currently scheduled for early 2014.

### Separation Test Results

The first separation test was considered successful even though only two of the three panels fully deployed as seen in Figure 12. The two panels that did fully deploy included the most highly instrumented panel (left side of figure) which provided the necessary data for model correlation and risk reduction.



Figure 12. Separation Test #1 (Image Courtesy: NASA)

The third panel did not fully deploy due to an unexpected asymmetric interference which had not been accounted for in the dynamic separation model.

The nearly 300 channels of instrumentation during the separation test provided sufficient data to gain a better understanding of how the various factors such as gravity, air resistance and friction affect the dynamic behavior of the panels as they deploy. Test results also showed dynamic interaction between the panels was less than predicted and that the single separation event was similar to three independent tests. This was highly beneficial since only two panels deployed. Figure 13 shows the model predictions of the panel deployment before the test and after correlating the model to the data.

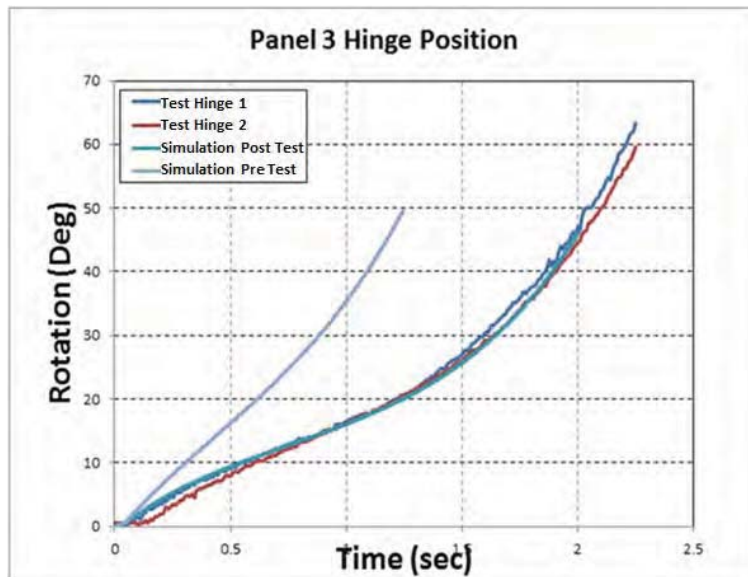
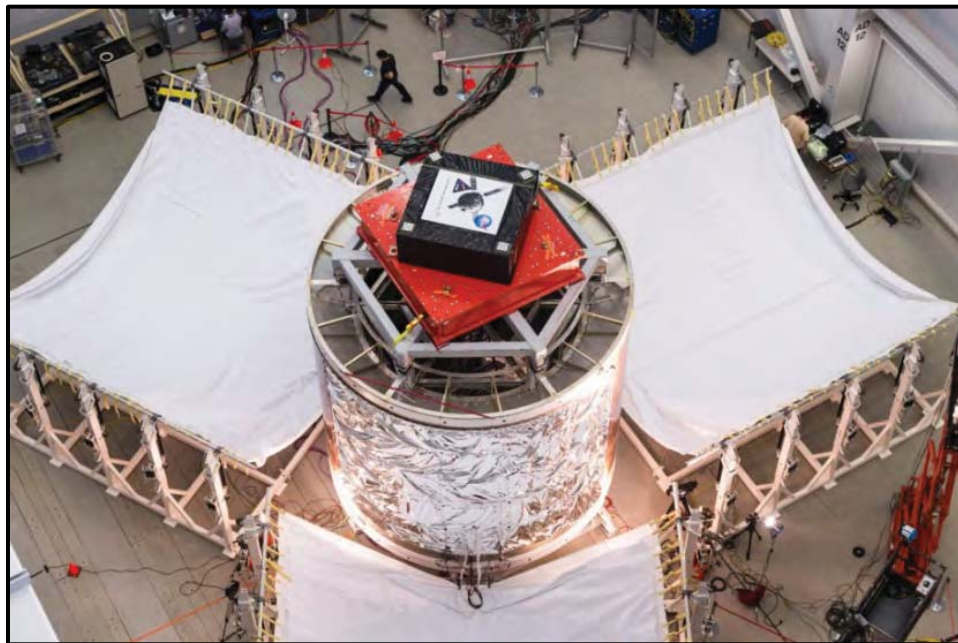


Figure 13. Fairing Position versus Time

After the first separation test, a panel free-fall test was performed on the panel that failed to separate. This test was developed to gather data to reduce uncertainties in the rigid body motion and losses due to air effects and friction. For this test, a single panel was pulled slowly over its center of gravity using an actuator and pulley system. The aero model of a flat plate worked surprisingly well in predicting aero effects during ground testing, however, the aero effects were only a small portion of the total factors that effected the fairing deployment response. It should be noted that while the deployment failure was unexpected, the free-fall test had been previously planned and the un-deployed panel position greatly simplified the logistics and implementation of this test.

The second separation test was performed with one panel heated to 93 °C (200 °F) to simulate flight environments as shown in Figure 14. Panel heating was predicted to increase loads, induce panel warping and amplify the dynamic response of the fairing during separation. Only one panel was heated to save cost and schedule associated with a more complex heating system. Multiple checkout tests of the heater system were performed prior to separation and data was collected for each checkout to gather additional data for model correlation including effects on load share.



**Figure 14. Separation Test #2 Heated Panel**

All three panels successfully jettisoned during the second test (Figure 15). The geometry modification, margins and clearances were validated and it was found that thermal effects were slightly less than predicted.



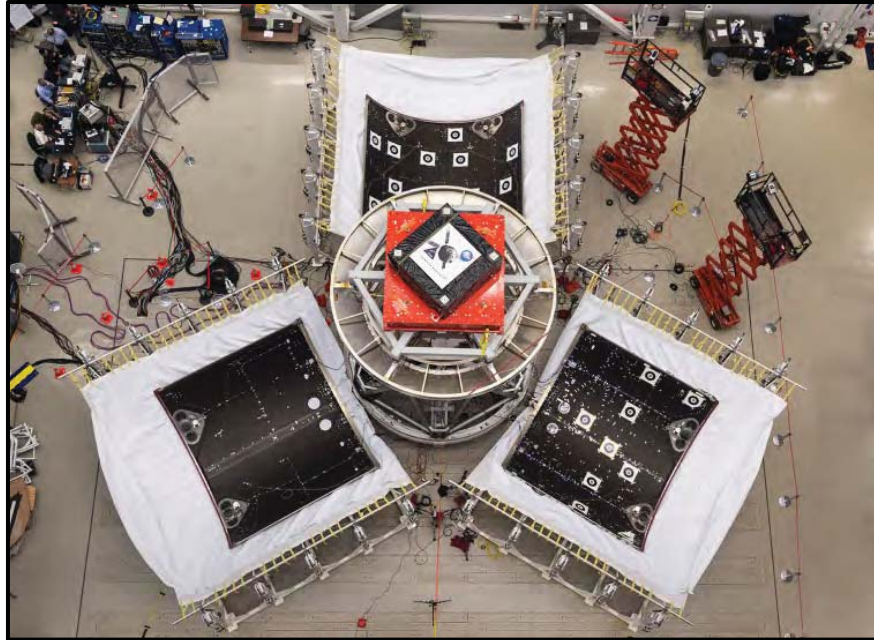


**Figure 15. Separation Test #2 Jettisoned Panels**

### **Lessons Learned**

As with most test programs general lessons learned such as “test early” and “test like you fly” were continually being weighed against design finalization, cost and schedule constraints. However, some specific lessons were learned during the Orion fairing tests. The following is a list of those lessons learned along with some further information and recommendations.

- Titanium with CANADIZE<sup>®</sup> coating with a molydisulfide dry lubricant provided adequate galling resistance for the PSM cup/cone separation interface; however, other materials may have been more efficient as loads and resulting contact stresses increased. Minimizing gaps and overall relative motion reduces wear.
- Coatings and lubricants are very difficult to predict how they will respond to different environments. Testing is critical to understand them and to demonstrate that the selected system will survive both the load levels and the required life span. Part of the selection process and testing should consider what the consequence will be if/when the lubricant fails. Lubricant compatibility with surrounding materials is also a concern. During testing of the aero deflectors, one lubricant tested did not survive; it was discovered later that the lubricant had reactivity issues with both of the interfacing materials. Additionally surface finishes of substrates that receive coatings is critical.
- Titanium is not an ideal material in random vibration environments; it has very little structural damping which often results in very high amplification of vibration inputs. This was evident during the testing of both the spring and the hinge (not discussed in paper). In both cases, the response due to a random vibrate input was significantly higher than expected and in the case of the spring resulted in several issues that had to be resolved.
- Coil springs can exhibit unanticipated response in vibration environments. During random vibration testing of the spring, it was found that the response was highly nonlinear (motion was excited in all directions, not just the input direction). Additionally, the amount of motion seen in the spring was much greater than anticipated, which resulted in the spring contacting the inner guide tube. The spring motion also resulted in a load amplification effect along the spring axis (surging).

- Perform characterization testing for fixtures supporting dynamic events. It is standard practice to perform a bare fixture evaluation for vibration and acoustic testing. This philosophy may also be applied to dynamic separation tests. If the test fixture can have an impact on the dynamic behavior of the test article, it may be necessary to perform some level of characterization testing on the fixture itself. This can include static load, modal or simple functional testing with a known rigid test article. This testing could eliminate analytical uncertainties even with seemingly 'simple' structure. The fixture testing performed for the fairing separation test provided data for adjustments to the analytical model.
- Make sure all design aspects are accounted for in the dynamic simulation of the separation event. When a Finite Element Model is developed for dynamic separation analysis, ensure all proper critical clearance elements are transferred from the CAD. There was a small piece of hardware that snagged on the test fixture in the first separation test and resulted in one of the fairings not separating. Had this part been included in the model, the issue would have been identified and corrected prior to the test.

### Conclusion

Each test has provided critical data necessary for analytical model validation and better understanding of the components and the system. PSM wear testing pushed the limits of the CANADIZE<sup>®</sup> coating which required changes to the geometry. Ultimately, the contact stresses were reduced and the design was able to meet the life requirements under load and provide adequate clearance for separation. Spring testing showed how the vibroacoustic environment was the primary design driver. The softer CRES material was ultimately chosen to mitigate wear and debris generation. Deflector testing validated the flexure design over the relative large deflections required. While the electroless nickel was shown to be far superior for this application, the cost and schedule constraints required an alternative solution. Ultimately, the brushed-on nickel met all design requirements once the proper lubrication was found. System-level fairing separation testing showed how a small geometric interference and reduced ground margins can provide unexpected results. While flight margins are significantly higher, the design changes made increased critical clearances to eliminate any potential recontact during ground or flight jettison. The second separation test was a complete success and all margins and clearances were validated.

Tests discussed here are only a subset of those required to fully verify all requirements necessary for human rating of the Orion fairing system. Additional tests include other component development testing as well as qualification testing being performed in support of the EFT-1 mission. The final test will include a full-scale system-level separation test with flight hardware which is required for human rating the fairing separation system and the Orion vehicle.

### References

1. Couvalt, Craig. "Ariane 5 Fairing Passes Ground Separation Test", *Aviation Week and Space Technology*, 28 November 1994, p. 66.
2. United Launch Alliance. "Atlas V Launch Services User's Guide." March 2010.
3. United Launch Alliance. "Delta IV Payload Planners Guide." September 2007.
4. K. Lucy and J. C. Uht. "Contamination studies of the Pegasus fairing separation", Proc. SPIE 2261, Optical System Contamination: Effects, Measurements, and Control IV, 108 (October 19, 1994); doi:10.1117/12.190132
5. Daye, Charles J. "Skylab Payload Shroud Jettison Tests." National Aeronautics and Space Administration Technical Note D-6913, August 1972.





# Design and Lessons Learned on the Development of a Cryogenic Pupil Select Mechanism used in the Testing and Calibration of the Integrated Science Instrument Module (ISIM) on the James Webb Space Telescope (JWST)

Alissa Mitchell\*, Thomas Capon\*, Jeffrey Guzek\*\*, Claef Hakun\*, Paul Haney\* and Corina Koca\*

## Abstract

Calibration and testing of the instruments on the Integrated Science Instrument Module (ISIM) of the James Webb Space Telescope (JWST) is being performed by the use of a cryogenic, full-field, optical simulator that was constructed for this purpose. The Pupil Select Mechanism (PSM) assembly is one of several mechanisms and optical elements that compose the Optical Telescope Element SIMulator, or OSIM. The PSM allows for several optical elements to be inserted into the optical plane of OSIM, introducing a variety of aberrations, distortions, obscurations, and other calibration states into the pupil plane. The following discussion focuses on the details of the design evolution, analysis, build, and test of this mechanism along with the challenges associated with creating a sub arc-minute positioning mechanism operating in an extreme cryogenic environment. In addition, difficult challenges in the control system design will be discussed including the incorporation of closed-loop feedback control into a system that was designed to operate in an open-loop fashion.

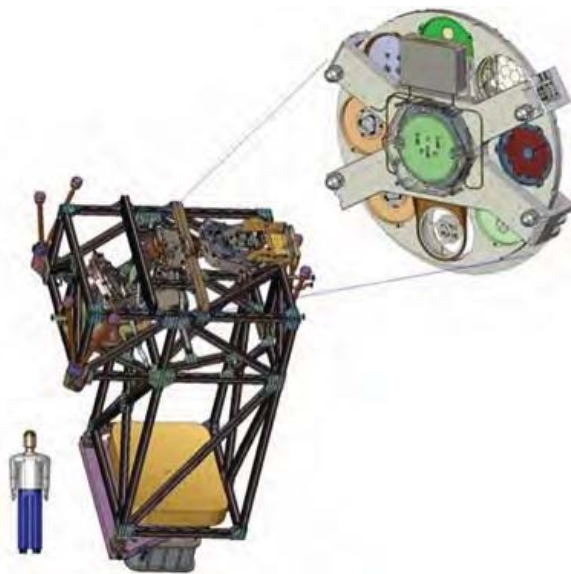


Figure 1. PSM in OSIM Bench

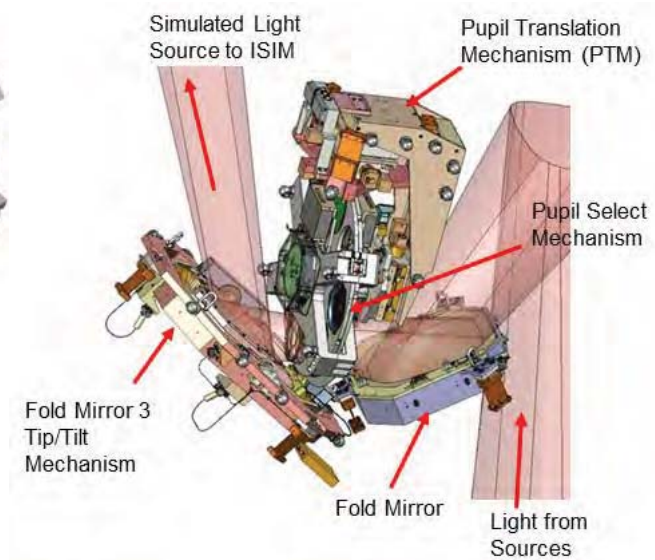


Figure 2. Light Path through PSM

## Introduction

The JWST Optical Simulator (OSIM) is designed to simulate the optical performance of the JWST telescope elements. The simulator consists of the primary imaging optical path, which relays fiber optic point sources to the focal surface of the ISIM over its field of view. OSIM is comprised of several subassemblies, including the Optical Bench Module (OBM), into which the PSM is integrated. The PSM is located at the pupil plane of the OSIM instrument and is mounted on a 2-DOF Pupil Translation

\* NASA Goddard Space Flight Center, Greenbelt, MD

\*\* Design Interface, Inc. Greenbelt, MD

Mechanism. Figures 1 and 2 show the location of the PSM within the OSIM optical bench. For a more detailed description of the OSIM, see reference 2.

Integration of the various modules and subassemblies into OSIM occurred at GSFC in the Spacecraft Systems Development and Integration Facility (SSDIF) and environmental performance of OSIM was verified in the Space Environment Simulator (SES), where OSIM was tested with the Beam Image Analyzer (BIA). The BIA is a cryogenic 5 DOF mechanism system with cold focal planes designed by NASA/GSFC Electromechanical Systems Branch and was used to measure the performance of OSIM as the simulator for the JWST optical telescope. Figure 3 shows the OSIM being lowered in to the SES chamber. Figure 4 shows the OSIM during ambient alignment with the BIA in the SSDIF.



**Figure 3. OSIM Bench being lowered into the SES      Figure 4. OSIM during Ambient Alignment**

The PSM provides OSIM with the capability to configure the OSIM pupil plane with various optical elements, masks, and alignment reference sources. In this mechanism, two 27-inch (68.6-cm) wheel assemblies are assembled adjacent to one another with 0.1 inch (2.5 mm) of clearance between them. Fourteen different optical elements, eight in each wheel, are then rotated into the optical plane of OSIM for testing and calibration purposes. Driving requirements for the PSM are to operate in a cryogenic environment and to provide stable and repeatable positioning of the elements in the optical plane during a powered-off condition. During the testing stages of OSIM, the PSM is required to operate at temperatures as low as 100K and with element position placement of less than 45 arc-seconds. A brief description of the elements located in the two wheels is shown in Figure 5.

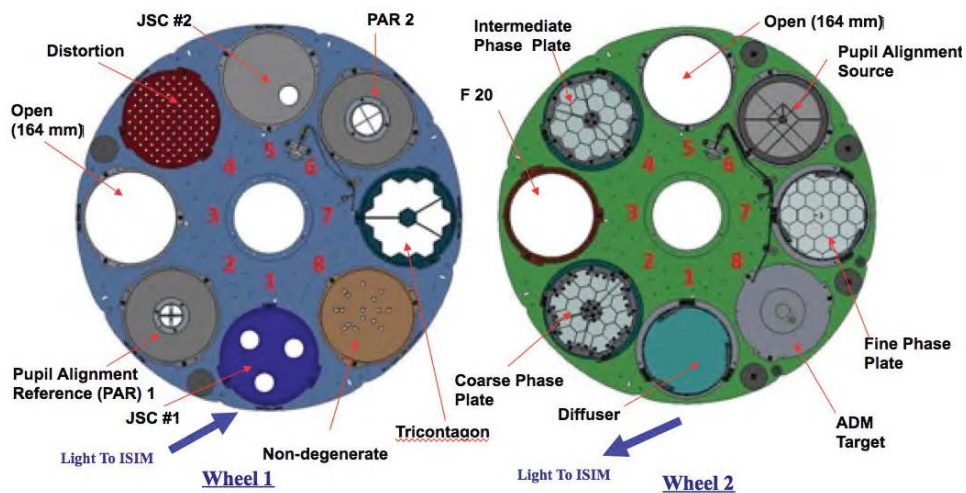


**Figure 5. PSM Wheel Optical Elements**

All of the elements in Wheel 1 were fabricated from 6061 Aluminum and machined to tolerances to meet the requirements of each individual element. It should be noted that, in addition to mounting the optical

elements, heaters and temperature sensors were also mounted on each wheel. In addition, the ADM Target incorporated an LED light source. These necessitated the incorporation of a cable wrap into both wheel assemblies. The optical elements in wheel 2 were more complex, precision opto-mechanical assemblies. An example is the Course Phase Plate Assembly. Figure 6 shows the course phase plate which incorporated sophisticated fabrication and assembly techniques to allow for the individual mounting of 18 segments that would not distort when cooled from ambient temperature to 100 Kelvin.

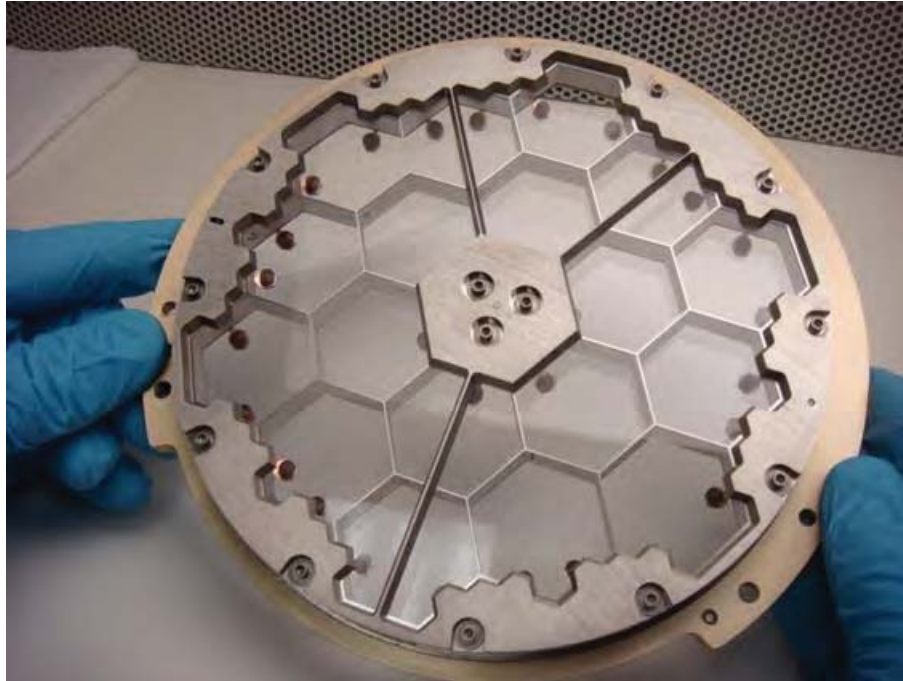


**Figure 6. PSM Optical Element Phase Plate**

### **Design Evolution of the PSM**

During the conceptual design phase of the PSM, the most challenging design task was to develop a system with high pointing stability and repeatability in the powered-off state. Two spare CDA gearhead stepper motors that had been used on a previous JWST mechanism life test were available for the development. This motor was incorporated into the design to turn the primary wheel via friction from a preloaded drive wheel. The step size of the stepper motor allowed for a position resolution of less than 45 arc-seconds, while a high accuracy absolute encoder provided knowledge information to a resolution of approximately 1 arc-second. Figure 7 shows the initial conceptual design of the traction drive system.

A peer review was held on the design and significant resources were dedicated to proof-of-concept. During the initial stages, motor testing was performed as well as testing on high friction representative materials for the optical element wheel and the drive wheel. Several materials were considered for the drive wheel including Vespel, a polymer/carbon fiber blend composite (WearComp<sup>®</sup>), and a polymer/carbon fiber/graphite composite blend (FibreComp<sup>®</sup>). Tests were performed to capture the friction coefficient between these potential materials and the aluminum wheel and to determine a viable pairing that offered a high coefficient of friction with a low risk of debris generation. These tests were performed in ambient pressure and in vacuum at several temperatures, down to 100K, and displayed an unacceptable amount of variation in the coefficient of friction.

Due to concerns with motor life, power dissipation, the variability of the friction data under cold temperature, and a concern that the motor drive wheel would slip during operation, it was decided that pursuing a different design route for the PSM would be less risky. As the development schedule for the



PSM was constrained, the goal was to limit design modifications to the friction-based PSM and to incorporate the high-accuracy, low-bandwidth sensor from the original concept. In addition, restricted wire counts in the flex harness that provided power and signal to the encoders precluded the addition of a high-rate position sensor to the design.

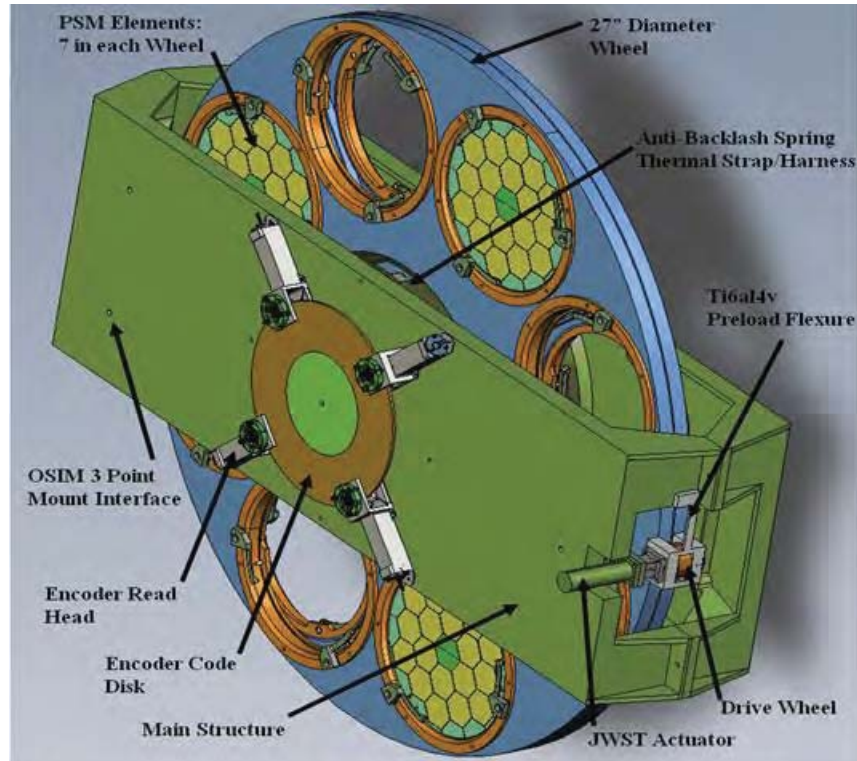


**Figure 7. Preliminary PSM Friction Drive Design**

The team began a conceptual redesign incorporating a brushless DC motor to directly drive each PSM wheel. At a later time, a preloaded follower wheel was added on the outside of the mechanism that would engage mechanical detents machined into the wheel. In addition to preliminary control system design modeling, analyses were initiated to determine the optimal detent and follower wheel geometries as well as the forces on the system. The initial analysis showed that an open-loop control system could be developed to meet the power-off position requirement with minimal changes to the initial friction-based conceptual design.

### **As-Built PSM Design**

In order to rotate the wheels, the stepper motors were replaced by two frameless, 2-phase brushless Aeroflex motors affixed to the center hub assembly, directly driving each wheel. The hub assembly also includes spring-loaded angular contact bearings. In order to meet the 45 arc-second holding and repeatability positioning requirement, a detent is used on the outside of the wheel with a follower assembly to roll in and out of the detents and to hold the wheel in place when power is removed. The encoder system was developed to operate in the 100K environment and provided feedback for the mechanism electronics. Ultimately, it was determined that in order to control the mechanism, a high-fidelity dynamic model was needed. The dynamics of the system were modeled along with a PID gain scheduling controller and trajectory planning which utilized 40-Hz feedback from the absolute encoder system. The final design of the PSM is shown in Figure 8. Details of the maturation will be discussed below.



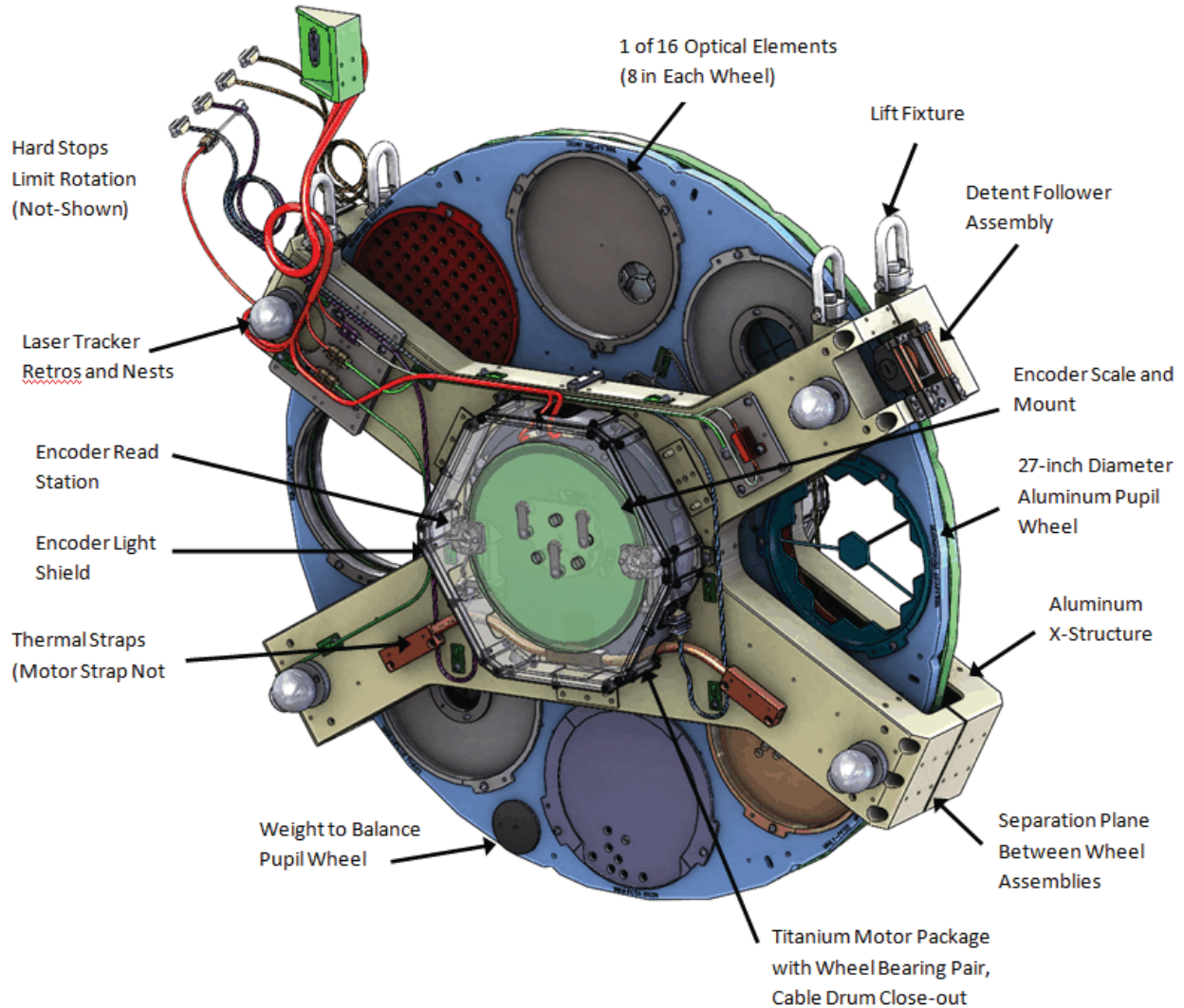


**Figure 8. As-Built PSM Design**

### **Motor/ Bearing Hub Assembly**

To drive the PSM, two frameless, brushless DC motors were selected from Aeroflex and mounted directly to the frame of the structure. In the sizing of these motors, it was assumed that the primary purpose of the motors was to drive the wheels to the capture region of the follower wheel and, therefore, no control authority was required.

Due to the cryogenic operating temperatures, traditional bearing lubricants were not suitable for the application, and the bearings needed to be cold-treated to the 100K operating temperatures of the mechanism. Ultimately, a hybrid, dry-running ceramic bearing from Cerobear was selected for this application. The bearings consisted of a non-magnetic, silicon nitride balls running in Cronidur 30 races with minimum lubrication from PGM-HT (PTFE/MoS<sub>2</sub>/glass fibre composite) retainers. The hardness properties of the ceramic balls coupled with the material differences between the balls and the steel races reduces the risk of fretting, cold welding, and seizing of the bearing at higher Hertzian stresses. The expected number of life cycles for the mechanism was 2000, which is an acceptable lifetime to expect for these bearings. To accommodate the large operating temperature range, the PSM bearings were installed with a soft preload, such that the maximum loaded bearing had a mean Hertzian pressure of

101 ksi (696 MPa), which is less than half the mean recommended Hertzian pressure of 217 ksi (1496 MPa) from the vendor. A cross-section of the wheel assemblies is shown in Figure 9.

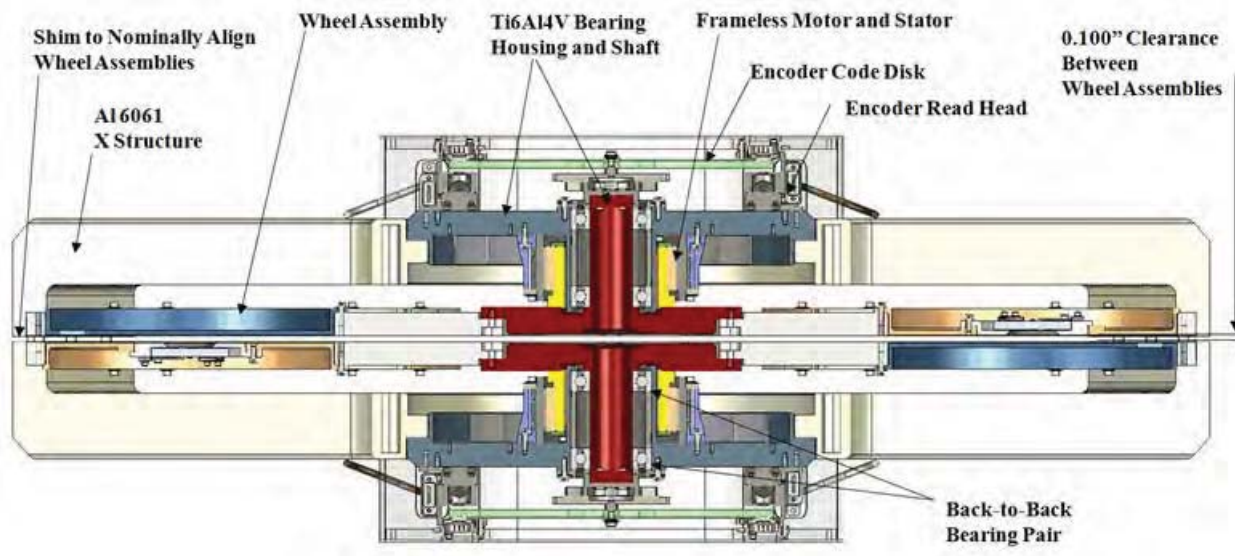


**Figure 9. Cross-section of Wheel Assemblies**

The motors and motor bearings were assembled together in a titanium hub which provided a good coefficient of thermal expansion (CTE) match to the bearing race material. Figure 10 shows the fixture used to assemble the motor rotor and stator. To accommodate CTE mismatch between the titanium hub and the aluminum wheels and X-frame structure, three pin-in-slot interfaces coupled with controlled fastener preload were used to accommodate sliding during cool-down. For signals transverse the rotating axis, a flat ribbon cable from 3M was used in a coiled clock spring design to allow for near 360° rotation. Prior to assembly, this ribbon cable was heated on a mandrel to create a coiled shape, which assisted in assembly. Figure 11 shows the cable wrap assembly.



**Figure 10. Motor Rotor Manually Lowered into Stator Assembly**

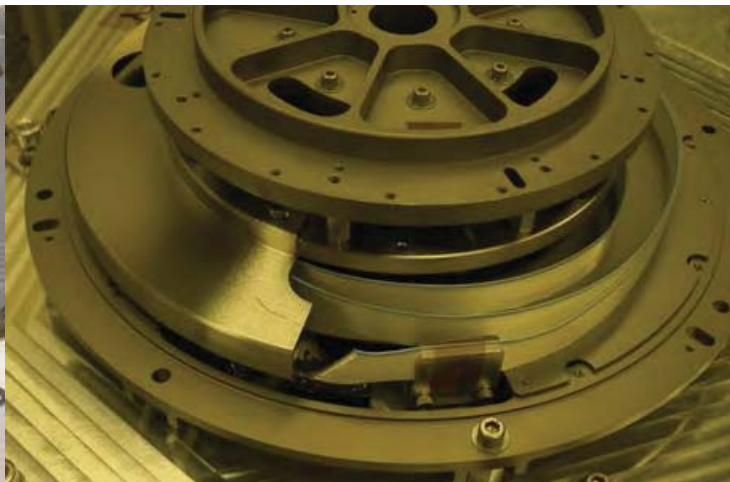


**Figure 11. Cable Wrap Assembly**

## Follower Wheel Assembly

For the follower wheel, Vespel (SP-1) was selected due to the low risk of debris generation with the aluminum wheel. WearComp was also considered for the follower wheel material, but there were concerns that the machined surface finish would generate debris when in contact with the primary wheel. The follower wheel assembly consisted of a face-to-face, spring-loaded duplex bearing pair that supported the follower wheel. The follower wheel was keyed to the rotating shaft while a titanium housing supported the outer races of the bearings. Figure 12 shows the components of the follower wheel assembly.

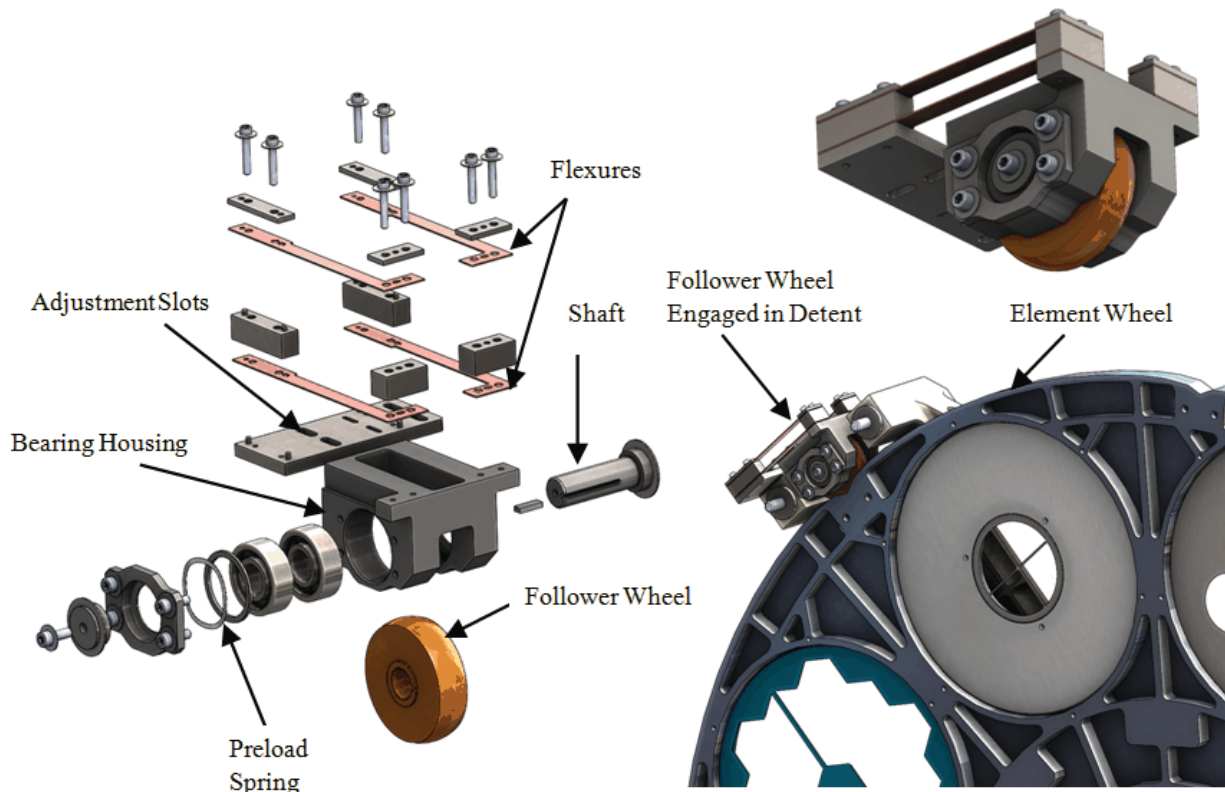


**Figure 12. Follower Wheel Assembly**

The follower wheel was preloaded on the rim of the element wheel via beryllium copper beam flexures. Slots in the flexure bolt holes allowed for circumferential adjustability of the follower assembly on the x-structure while shims allowed for adjustment of the preload.

The initial design of the follower wheel assembly consisted of two cantilever beams which radially preloaded the follower against the outside surface of the wheel and mechanical detents. Once the assembly was integrated, it became apparent that the cantilever beam preload system had a few shortcomings. The cantilever beam spring allowed for the follower to move in and out of the detent, but did not react moments. The arc-shaped tip motion did not adequately provide a purely radial preload to the follower wheel and did not position the elements in the proper location. The system was replaced with a parallel blade arrangement which allows for near perfect radial motion of the follower as it moves in and out of the mechanical detents while resisting internal moments. This allowed for the optical elements to be positioned as originally envisioned. Figure 13 shows the follower wheel assembly integrated onto the X-frame structure of the PSM.



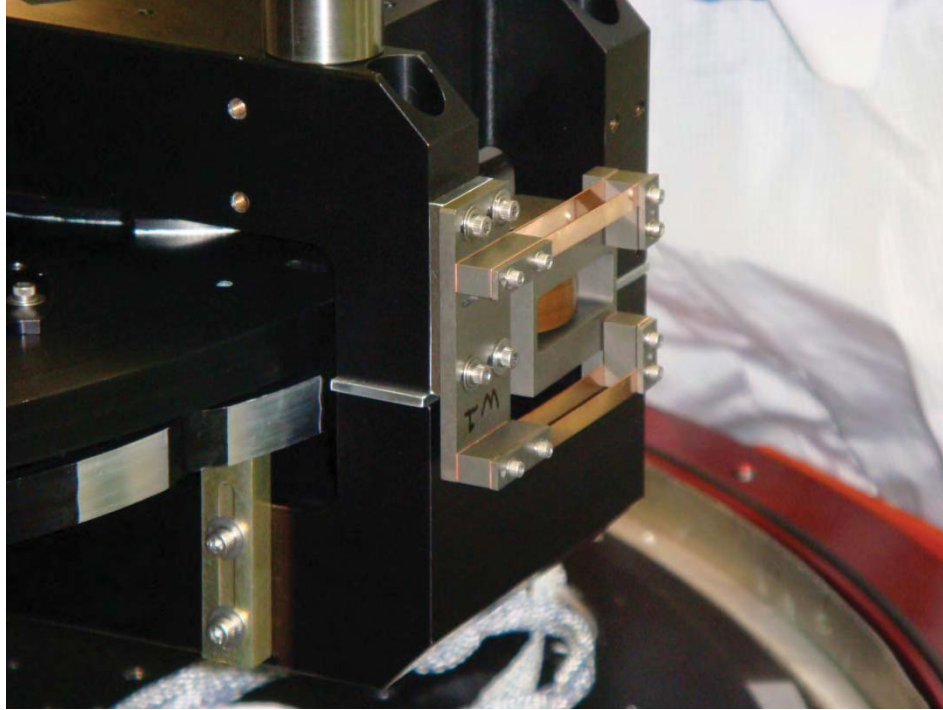


**Figure 11. As-Built Mechanical Follower Wheel Assembly**

### **Optical Encoder Design and Development**

In order to verify the tight positioning and knowledge requirements, cryogenic absolute encoders were developed (see Reference 1 for more details). The PSM absolute encoders were able to achieve less than one arc-second resolution over a nearly 360-degree operational range. The ultra-high resolution was achieved through a unique process of pattern recognition. A PSM Leviton absolute encoder is shown in Figures 14 and 15, and is composed of an LED and LED pinhole mount, a titanium encoder housing with an internal baffle, a mirror and flexure, a detachable titanium CCD mount with accompanying CCD camera and heater and a photolithographic soda lime glass scale. The rotary scale disc was comprised of a pattern containing a periodic series of lines; each line is etched with unique and identifiable features.



**Figure 14. PSM Encoder Readhead**

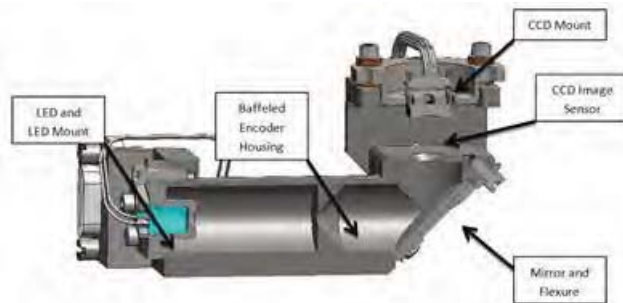


**Figure 15. PSM Encoder Cross Section**

The encoder functions in the following manner. The LED source emits light and the pinhole collimates the light source to a point source. The light then enters the housing, which is baffled to eliminate undesirable stray light. Once the light exits the housing the scale casts a shadow and the image sensor captures the

unique pattern at that location. In addition to capturing the pattern, the image sensor compares its fixed pixel columns with the centroid of each line on the scale. With the combination of unique and identifiable line features and relative line centroid locations, an absolute position measurement with arcsecond resolution is achieved. Figure 16 and 17 show the assembled read head and the code disk kinematically mounted on the wheel hub assembly.

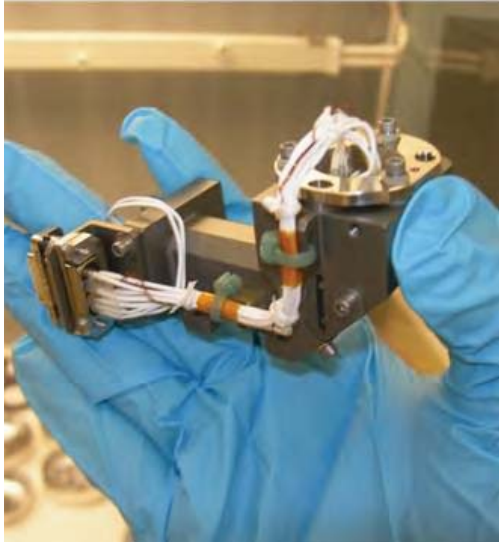


**Figure 16. PSM Encoder Readhead**



**Figure 17. PSM Encoder Disk**

### **Optical Encoder Alignment**

Due to the high accuracy requirement of the PSM encoders, alignment was critical; this includes initial alignment as well as alignment repeatability. Omitting the translation of the object being measured, if the encoder read head and scale move relative to each other, the position measurement is void. Two readheads were included to increase accuracy by removing run-out of the bearing configuration. A challenge when operating in a cryogenic environment is designing and accounting for the differing CTEs of the various materials. To control the position of the CCD relative to its mount, a bonding fixture was used. With the CCD position controlled, bonded and fixed in place on the CCD mount, any additional alignment adjustments were made with the CCD mount, specifically minimal decenter, angular position and image sensor to scale defocus adjustments. To maintain alignment, the CCD mount was pinned to the encoder housing and the encoder housing was pinned to the stationary PSM reference.

To ensure the PSM scale was aligned to the rotor and stator over the temperature range, the scale utilized a titanium 3-point kinematic mount with a flat, a cone, and v-groove features. Titanium flexures and features machined into the glass allowed captured steel balls to remain nestled and preloaded between the glass and the mount. In this configuration, all changes in motion of the scale due to thermal contraction and/or expansion were relative to the kinematic mount cone feature. However, due to CTE differences between the glass scale and the titanium hub of the PSM, scale recalibration at varying operational temperatures was performed as part of the PSM testing. In addition, changes to the bias voltage of the CCD were required to allow for good encoder images to be obtained.

### **PSM Controller Design and Development**

Due to the tight requirements and the torque disturbances from the mechanical detent, controlling the Pupil Select Mechanism proved to be much more challenging than originally anticipated. After the baseline of the friction wheel design with geared stepper motor drives was abandoned, and the direct-drive brushless system was implemented, representative testing was performed with an unpopulated



PSM wheel. This initial testing was promising as the control system was able to command the wheel position using the high-accuracy, low-bandwidth encoders. However, when inertial simulators for the optical elements were installed, an open-loop control was not possible with the torque available from the direct drive motors. Therefore, a closed-loop system was developed within the pre-existing design constraints.

The only sensor on the wheels was the high-precision CCD encoder. The readout software was modified to transmit encoder readings to the motor control rack using UDP packets as TCP packets were not delivered fast enough. There was still some variability, so timestamps were added to each measurement and the controller was designed to account for this in speed calculations. In its normal configuration, this encoder only produced 10 measurements per second, and could not produce readings at all above a certain wheel velocity because of image blurring.

Such low sensor bandwidth meant that the optical positioning requirements could not be met through continuous closed-loop control, so mechanical spring-loaded detents were added to the wheel for this purpose. Thus, in addition to a relatively low amount of motor torque for the given inertia, the control system had to deal with the detent as a torque disturbance. As the roller navigated the sharp V-notch in the wheel, it produced very large torques during entry and exit. It seemed impossible to control wheel-exit trajectories, since the low bandwidth and high disturbance produced high exit velocities, and the resulting blurred images disabled feedback control during recovery. Two critical modifications were made to the system to correct this problem. First, the sharp V-notch was replaced with a rounded notch, making the torque disturbance more gradual (see Figure 18). Second, the encoder readout system was modified to use a shorter exposure time, increasing both the measurement rate and the blurring speed limit. The new detent profile reduced the exit speed to well below the new blurring speed limit. Together, these modifications made the system controllable using a gain-scheduled PID controller.

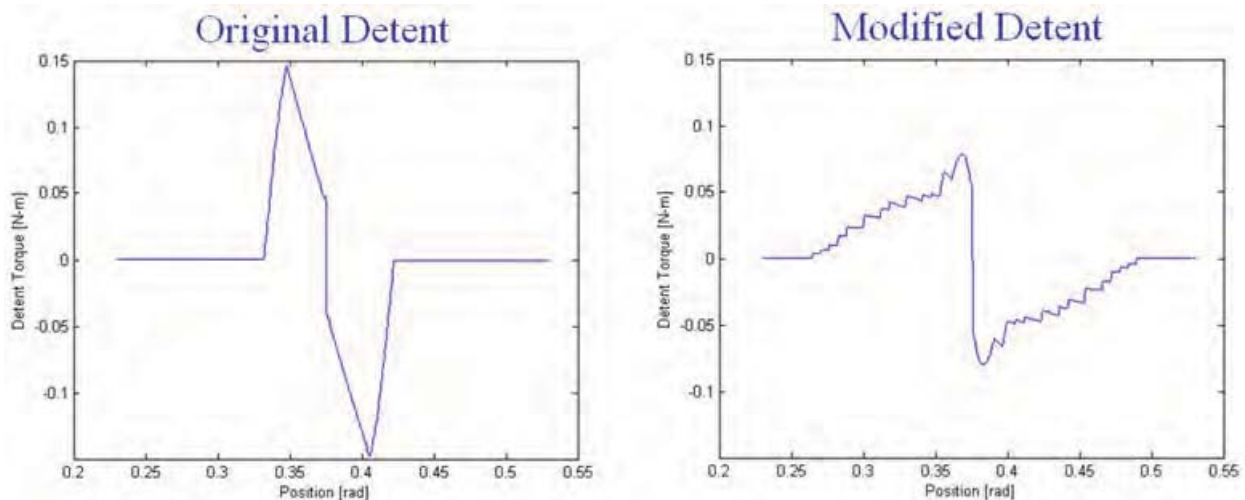


**Figure 18. Simulated Detent Disturbance Torque Profile Before and After Mechanical Modification**

The gain-scheduled PID controller was developed first in a Simulink model of the wheel, motor, detent, and encoder. While it was very helpful in developing the concept of the controller, the simulation proved too unfaithful for the controller to be directly ported to the physical system. Instead, a similar controller was developed in LabVIEW and the gains tuned during testing. The final version of the controller includes four states that are executed to move from one detent to the next (see Figure 19). Longer moves are composed by repeating single moves, since passing through a detent at speed imparts unpredictable and harmful mechanical shocks to the wheels and optical elements. In all the closed-loop states, the motor is commutated in software based on the encoder readings. The states are as follows:

1. **Exit detent.** A simple integrator is used to ramp up the torque until the wheel leaves the detent. This step is effectively open-loop, because the feedback system is too slow to react to the detent torques. Closed-loop control cannot be used while in the “region of influence” of the detent.
2. **Null velocity.** Once the wheel exits the detent, true closed-loop control can begin. A damping controller brings the wheel to a controller stop just outside the detent, so the remaining states are not affected by variations in exit velocity. These variations are clearly visible in circle 2 of Figure 14.
3. **Trajectory travel.** A linear trajectory with acceleration and deceleration curves is generated to guide the wheel from its present location to the edge of the next detent. A carefully tuned PID controller follows this trajectory and ensures the velocity is close to zero when the detent is reached.
4. **Enter detent.** The closed-loop controller is disabled just inside the “region of influence” of the detent. Instead, a high-current open-loop commutation waveform is fed to the motor, lowering the wheel into the detent.

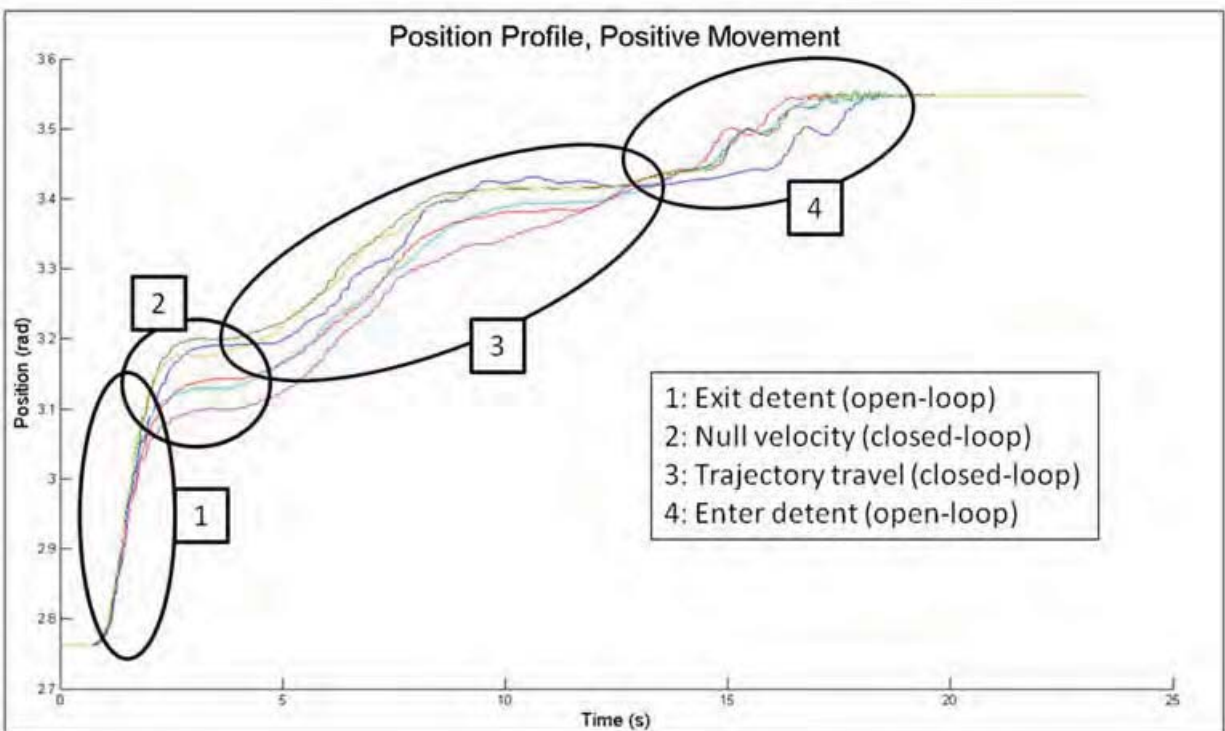


**Figure 19. Pupil Select Mechanism Wheel Position Trajectories During Several Moves. Black Outlines Illustrate the Operation of the Multi-State Controller**

Several types of fault detection and handling are built into the LabVIEW controller. The main purpose is to shut off the wheel if encoder data becomes unusable, but also watch for mechanical blockage of the wheel or unstable behavior. Every error condition sends a telemetry code and records data in the log file for analysis. Triggers include:

- **Encoder data rate.** If not enough packets are received in one time period, the connection is assumed to be set to the wrong frame rate or dropped completely, and the wheel is powered off.
- **Poor image decoding.** When the encoder CCD image cannot be parsed, the encoder system transmits an invalid code. If valid frames are received too infrequently, encoder calibration is the likely cause, and the wheel is powered off.

- **Trajectory tracking error.** If the wheel deviates too far from the command trajectory, it is assumed to be stuck or otherwise out of control, and the wheel is powered off.

The master ground system controls the PSM wheels with a special script that configures the encoder data transmission and performs error detection and automatic retries to move the wheel in a mostly autonomous fashion. This script was developed over the course of several years of use to properly handle edge cases such as powering up the system with the wheel in between two detents.

### **Infinite Microstepping Driver**

The brushless motor was selected with a 60-V, 2.5-A peak winding configuration. This was to keep the current in the previously designed cryogenic harnesses within acceptable limits. However, it made most commercial motor drivers unusable, as they typically provide a maximum output around 28 V. When open-loop control was still intended, an “infinite microstepping” driver was designed for each motor using a pair of 16-bit Texas Instrument digital-to-analog converters and a pair of APEX high-power operational amplifiers configured as voltage-to-current amplifiers. The linear drives provide more stable fine control than pulse-width modulation drivers, and the current-mode output ensures that variations in harness and motor resistance over cryogenic temperatures does not affect the motor current/torque.

Each driver has a dsPIC microcontroller on board that can automatically produce high-fidelity sine/cosine commutation output or produce a desired phase angle and amplitude. The latter feature was used to achieve closed-loop control, where the LabVIEW program reads the encoder position and determines the optimal phase angle and amplitude required to produce the desired control torque. The drivers performed well in this application as well as their originally intended purpose—additional units were built to drive separate stepper motor mechanisms with extreme precision.

### **Assembly of the PSM, Functional and Performance Testing, and Integration into OSIM**

The PSM was assembled at NASA Goddard Space Flight Center in Greenbelt, MD and initial performance testing of the PSM occurred in Spring 2011. The PSM was thermally cycled and taken to survival temperature limits with functional tests occurring at ambient temperature and pressure before testing, during the cold and hot operational limits, and again at ambient after thermal testing. During these functional tests, the PSM was able to show repeatable and stable element placement of less than 20 arc-seconds and was able to show compliance with all other functional and performance requirements. Figure 20 shows the PSM in the “Big Red” test dewar.

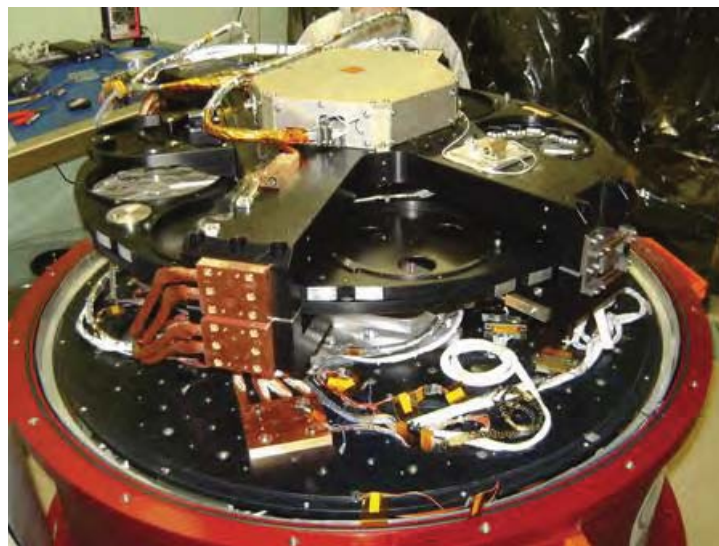


**Figure 20. PSM During Initial Thermal Vacuum Performance Testing**

To perform this testing, retroreflectors were used as alignment targets on the PSM X-Structure as a reference for cathetometer measurements taken of several fiducials and center markings engraved on the optical elements. The known machining error in the fiducial locations was then removed from the final data. For data collection, the wheels were rotated through the range of motion several times, approaching the detent position from different directions, stopping and powering off at each optical element location for measurement. Figure 21 shows the data collected for vacuum optical elements in the wheels.

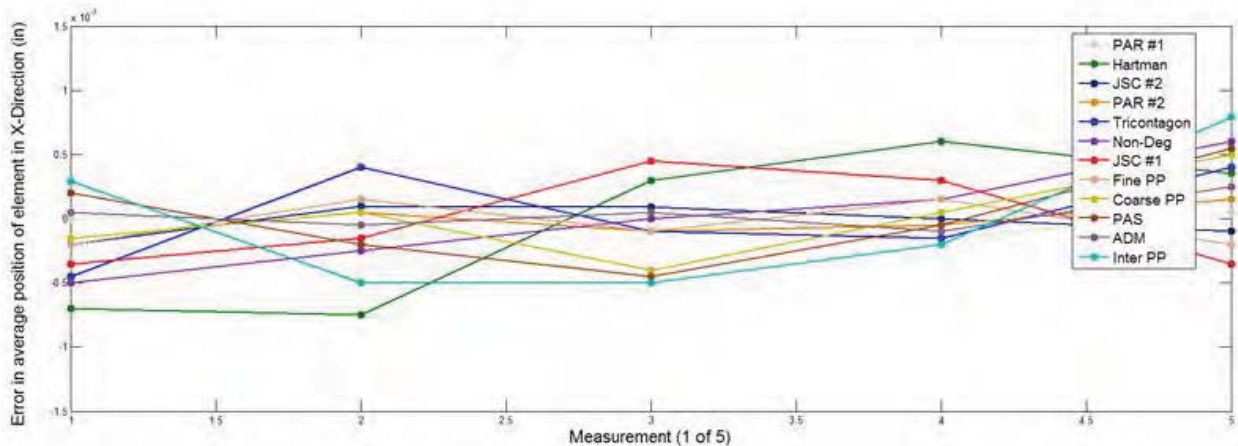


**Figure 21. Error in the Repeatable Average Position (X-Direction) of Central Fiducial on Optical Elements**

The PSM was integrated into OSIM with the other optical elements and mechanisms in the fall of 2011 in the Spacecraft Systems Development and Integration Facility (SSDIF) at GSFC. Figure 22 shows the PSM during integration in the SSDIF. With all of the components installed into OSIM, end-to-end ambient testing was performed and concluded in April 2012. The OSIM structure was then moved to the Space Environment Simulator (SES) chamber for calibration and verification of OSIM performance in a thermal vacuum environment. After 4½ months of testing at 100K, OSIM completed its first cryogenic vacuum test on August 2012. A second OSIM cryogenic test was performed at 100K on March 2013 and lasted 4 months. Figure 23 shows the PSM in the OSIM optical bench at the pupil plane between the two fold mirrors of the optical system.



**Figure 22. PSM in SSDIF during assembly onto the OSIM bench**



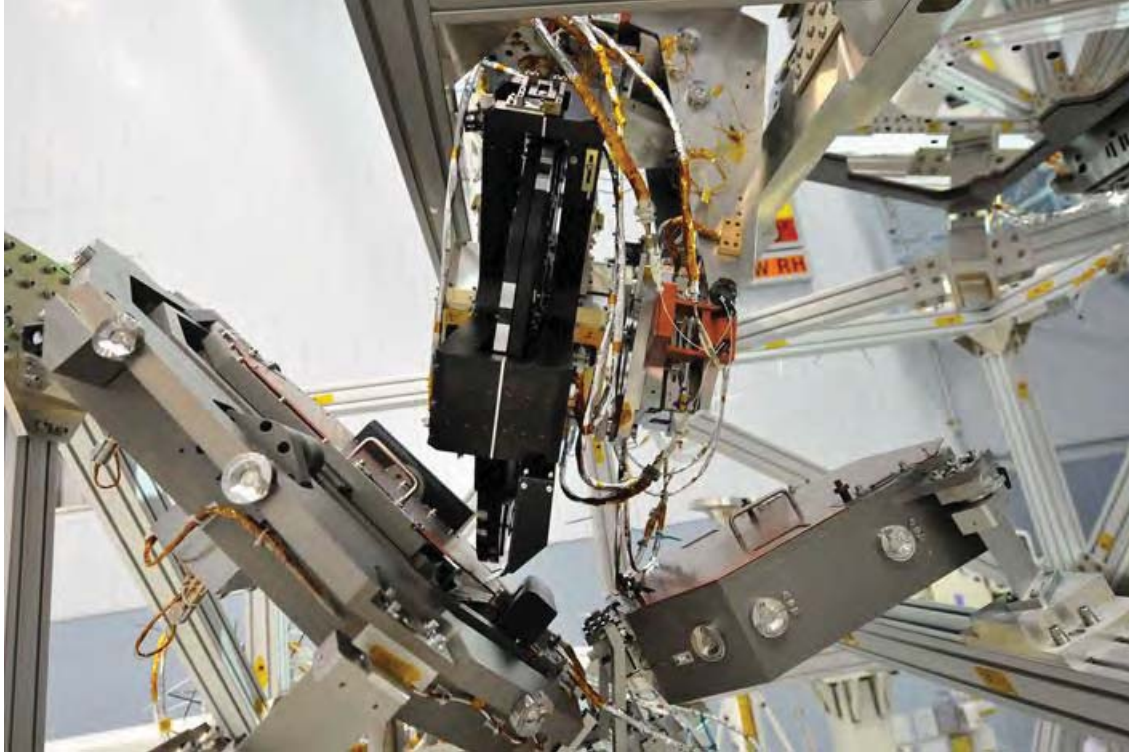


**Figure 23. PSM as oriented in OSIM bench adjacent to fold mirror**

### **Conclusion**

The PSM is currently located in the SES chamber where it being used successfully in concert with other OSIM components for the test and calibration of the Integrated Science Instrument Module for JWST. The first three ISIM tests concluded in November 2013 with the next test projected to begin in May 2014. Due to project schedule constraints, the extreme cryogenic operating temperature of the mechanism, and the tight holding and repeatability requirements, several design features were incorporated into the PSM mechanism during different phases of the development. Included was the incorporation of a bearing and encoder system to survive the extreme operating temperature as well as the implementation of a challenging control system into the design late in the development. A special thank you to the entire OSIM team, especially the integration and test engineers as well as Dr. William Jones at Glenn Research Center for the use of facilities and expertise for friction characterization.

### **Lessons Learned**

- Start early on proof-of-concept testing (especially those related to motor, bearing, and sensor selections) to flush out issues in the design with enough time to affect long lead purchases. Motors and encoder/sensor selection are key decision points in an electromechanical system design development and the suitability of these components should be revisited after any subsequent system level changes.
- Cold treated hybrid bearings consisting of  $\text{Si}_3\text{N}_4$  balls, Cronidur 30 races, and a PGM-HT retainer have been shown to be suitable for cryogenic operations (down to 100K) in mechanisms with a low number of cycles.
- Though WearComp may be suitable for minimal debris in friction-based applications, care must be made that the mating surface is machined appropriately.



- When modeling a plant, ensure the plant is of a high enough fidelity to represent the dynamic response of the system accurately. When testing is used in conjunction with simulation, ensure the test item includes a realistic mass or inertia.
- Closed-loop control always needs a sensor with sufficient bandwidth and speed range. Sensor capabilities limit control possibilities, so selecting a good sensor is critical to anticipating future performance needs.
- In a two-pole system, where position is controlled via torque input, a first-order PID controller cannot track a quadratic position command (i.e. fixed acceleration curve) and it is better to use a higher-order transfer function as a compensator in these cases.
- Automatic event logging is critical in systems with many operators to capture intermittent issues. Producing clear and verbose log files from the very beginning of testing saves a lot of time detecting, diagnosing, and replicating bugs later on without having to re-run tests to duplicate anomalies.

### References

Leviton, D.B. et al. "Cryogenic Optical Position Encoders for Mechanisms in the JWST Optical Telescope Element Simulator (OSIM)" *SPIE 8863* (2013)

Sullivan, J. et al. "Manufacturing and Integration Status of the JWST OSIM Optical Simulator" NTRS (2010)



# GMI Instrument Spin Balance Method, Optimization, Calibration and Test

Laoucet Ayari\*, Michael Kubitschek\*, Gunnar Ashton\*, Steve Johnston\*, Dave Debevec\*,  
David Newell\* and Joseph Pellicciotti\*\*

## Abstract

The Global Microwave Imager (GMI) instrument must spin at a constant rate of 32 rpm continuously for the 3-year mission life. Therefore, GMI must be very precisely balanced about the spin axis and center of gravity (CG) to maintain stable scan pointing and to minimize disturbances imparted to the spacecraft and attitude control on-orbit. The GMI instrument is part of the core Global Precipitation Measurement (GPM) spacecraft and is used to make calibrated radiometric measurements at multiple microwave frequencies and polarizations. The GPM mission is an international effort managed by the National Aeronautics and Space Administration (NASA) to improve climate, weather, and hydro-meteorological predictions through more accurate and frequent precipitation measurements. Ball Aerospace and Technologies Corporation (BATC) was selected by NASA Goddard Space Flight Center to design, build, and test the GMI instrument. The GMI design has to meet a challenging set of spin balance requirements and had to be brought into simultaneous static and dynamic spin balance after the entire instrument was already assembled and before environmental tests began. The focus of this contribution is on the analytical and test activities undertaken to meet the challenging spin balance requirements of the GMI instrument. The novel process of measuring the residual static and dynamic imbalances with a very high level of accuracy and precision is presented together with the prediction of the optimal balance masses and their locations.

## Introduction

The GMI instrument is one of the payload instruments on the GPM core spacecraft and must be spun continuously at 32 revolutions per minute (rpm)  $\pm 0.1\%$  on-orbit for the 3-year operational life of the instrument and to provide the desired geo-location for the science data. Details pertaining to the GMI design and testing were presented in references [1, 2]. The GMI instrument had to be spun balanced to less than 0.032 kg-m (2.77 lbm-in) static imbalance and less than 0.055 kg-m<sup>2</sup> (188 lb-in<sup>2</sup>) dynamic imbalance, total imbalance, for the 123-kg spinning portion of the instrument payload. The design and development of the spin balance method, analytical solution, test setup, design, calibration, and measured test results are described. The verification and validation of the GMI instrument to demonstrate compliance of performance through environmental testing and spin balance has been successfully completed. At the writing of this contribution, GMI has been fully integrated onto the GPM spacecraft, and the GPM spacecraft has been shipped to the launch site in Tanegashima, Japan for launch in February 2014.

The static and dynamic balancing approach consists of spinning GMI on top of an accurately calibrated dynamometer, designed specifically for GMI to measure the imparted forces due to imbalance. This device continues a long tradition of building precision balancing machines, vibration input benches and force measurement instruments for space hardware at Ball Aerospace & Technologies Corporation [5,6].

The dynamometer measures all forces and moments and consists of three force transducers mounted to an aluminum base plate and a corresponding top plate that functions as the mounting interface for the GMI instrument (Figure 1). The calibration of the dynamometer showed that the total measurement error of this technique and dynamometer were much smaller, by an order of magnitude, than the imbalance

---

\* Ball Aerospace & Technologies Corporation, Boulder, CO

\*\* NASA Goddard Space Flight Center, Greenbelt, MD

requirements. Since the balance requirements were tight and the spin balance to be measured was so small, the structural resonances of the GMI instrument, as well as the spin balance test fixture and support structure, also required detailed modeling and design to meet stiffness requirements dictated by the imbalance accuracies to be measured. Figure 2 shows the finite element model of the GMI instrument, the model of the Thermal Vacuum (TVAC) support structure with the dynamometer assembly used for the spin balance, and locations of balance masses available on the GMI instrument.



**Figure 1. Dynamometer Assembly Setup in Calibration and GMI without RDA and MR Assemblies Integrated**

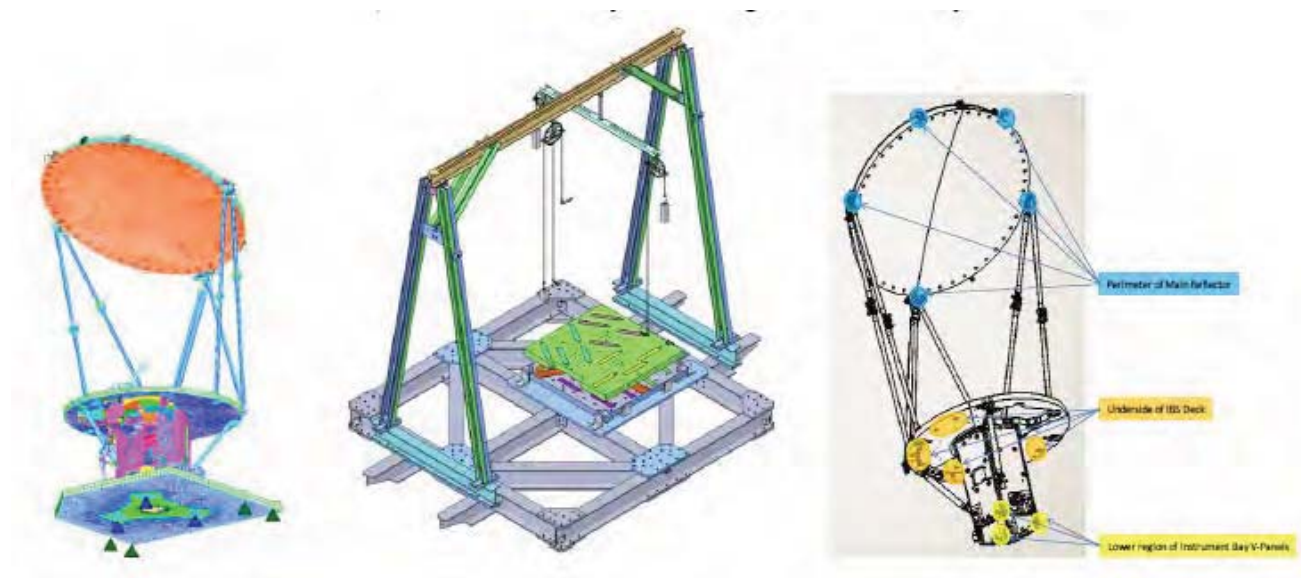


**Figure 2. (a) Structural Model of the GMI Instrument Assembly, (b) Dynamometer**

### **with the Spin Balance Test Fixture, and (c) Balance mass locations on GMI**

Multiple test setups, shown in part in Figures 2 and 3, were developed for balancing GMI at room temperature and in a vacuum chamber to eliminate error terms associated with forces imparted to the dynamometer due to air drag of the GMI instrument spinning in air. A MATLAB computer program was developed to process the resultant forces imparted on the dynamometer, together with position encoder data to derive the magnitude and direction of static and dynamic imbalances, and subsequently perform a linear optimization to predict the optimal balance mass solution. This optimal solution, which meets the static and dynamic imbalance requirements, consists of the values of 21 'balance' masses that can be added and accounts for design constraints specific to each of the balance mass locations, and at the same time minimizing the overall total mass of balance masses to be added simultaneously. The optimization can account for order of preference in the choice of masses by assigning higher weights for particular ones to reflect certain particularities such as ease of access, volume or other situational constraints or preferences. Finally, it has been possible to achieve preliminary balancing of GMI before achieving full integration. The software is capable of balancing a partially integrated GMI while the instrument is being assembled (e.g., before the integration of the RDA – Reflector Deployment Assembly and MR – Main Reflector) by assigning negative inertial properties to the missing subassemblies that were subcontracted elsewhere and would not be integrated for the spin balance testing until late in the environmental test program.

### **Spin Balance Verification**

The GMI instrument underwent an initial spin balance in the clean room in July 2011 and initial balance masses were added prior to GMI instrument environmental testing. Final spin balance and requirement verification and validation was completed in TVAC in February 2012 after the GMI instrument had successfully completed all environmental testing (Figure 3). The methods and steps successfully accomplishing this spin balance of the GMI instrument and showing the requirement was verified via test measurements will be discussed in this paper.



**Figure 3. GMI Instrument in Spin Balance Test Facility on Dynamometer**



### Evaluation of Imbalance Forces

Bringing GMI into balance started from early on in the design phase. As the design progressed, there has been a continuous effort to keep the rotating hardware as close as possible to static and dynamic balance in order to minimize overall total mass of the instrument, with a plan for three separate axial and radial locations to place balancing masses as shown in Figure 2-c. While a minimum of two axial planes for balance masses are required to achieve dynamic balancing, provision to use the RDA/MR for a third location was necessary to maintain lower added masses, because the RDA does not have axial symmetry, is distant from the mounting plane, and due to other production and schedule constraints.

The basic idea is to determine the static and dynamic imbalances from the measurements of the moving imbalance forces imparted at the mounting plane while spinning GMI at some angular velocity. Load cells are ideal for the task as they only pick variations in load magnitudes. In the absence of other disturbances, such as structural resonances, air drag, etc., it can be easily shown that the loads imparted by a non-perfect rotating device on a mounting plane are the result of the centrifugal forces and moments of the imperfection. Assuming an imbalance mass  $m$  centered at a position  $(x,y,z)$  in the GMI reference frame of Figure 4, the reactions are given by the following radial force  $\mathbf{f}_r$  and the radial moment  $\mathbf{M}_r$ ,

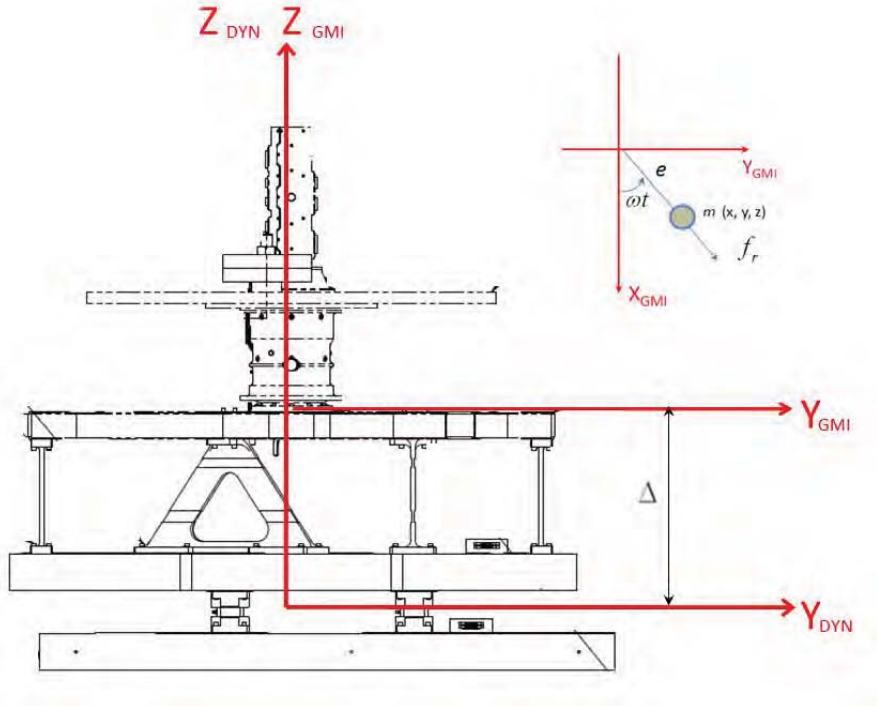


Figure 4. GMI and Dynamometer Coordinate systems

$$\mathbf{f}_r = \begin{Bmatrix} f_x \\ f_y \end{Bmatrix} = me\omega^2 \begin{Bmatrix} \cos \omega t \\ \sin \omega t \end{Bmatrix} = m\omega^2 \begin{Bmatrix} x \\ y \end{Bmatrix}, \quad (1)$$

$$\mathbf{M}_r = \begin{Bmatrix} M_{rx} \\ M_{ry} \end{Bmatrix} = z \begin{Bmatrix} -f_x \\ +f_y \end{Bmatrix} + mg \begin{Bmatrix} -y \\ +x \end{Bmatrix} = \omega^2 \begin{Bmatrix} -m yz \\ +m xz \end{Bmatrix} + mg \begin{Bmatrix} -y \\ +x \end{Bmatrix} = \omega^2 \begin{Bmatrix} -i_{yz} \\ +i_{xz} \end{Bmatrix} + \frac{g}{\omega^2} \begin{Bmatrix} -f_x \\ +f_y \end{Bmatrix}, \quad (2a)$$

where  $e = \sqrt{x^2 + y^2}$  is the radial distance from the spin axis,  $\omega$  is the angular velocity,  $g$  is the magnitude of gravitational acceleration and  $t$  is the time in seconds. Note that we replaced the products  $m yz$  and  $m$

xz by the cross products of inertia  $i_{yz}$  and  $i_{xz}$ , respectively in the last equality of Equation (2a) to account for pure dynamic imbalance situations and therefore address the general case of arbitrary combined static and dynamic imbalances. All forces and moments are functions of time. For example,  $\mathbf{M}_r$  should be written as  $\mathbf{M}_r(t)$ , but the time symbol is omitted for readability. From the dynamometer we can read the exact forces, but the moments will be different due to the height  $\Delta$ , between the mount interface and the elevation of the load cells. On the dynamometer, the readings for the moments are given by:

$$\begin{Bmatrix} M_x \\ M_y \end{Bmatrix} = \begin{Bmatrix} M_{rx} \\ M_{ry} \end{Bmatrix} + \Delta \begin{Bmatrix} -f_y \\ +f_x \end{Bmatrix} = \omega^2 \begin{Bmatrix} -i_{yz} \\ +i_{xz} \end{Bmatrix} + \left(\frac{g}{\omega^2} + \Delta\right) \begin{Bmatrix} -f_y \\ +f_x \end{Bmatrix} \quad (2b)$$

The resultant force in the Z direction is independent of time and therefore would not show on the dynamometer readings since the load cells measure only a change in force. The radial load remains unchanged but the lever arm of the moment is increased by the distance between the mounting surface and the plane of the dynamometer load cells.

Using the expression for the radial load from Equation (1), the magnitude of the radial load is related to the static imbalance  $me$  via

$$me = m\sqrt{x^2 + y^2} = \sqrt{f_x^2 + f_y^2} = \frac{\|\mathbf{f}_r\|}{\omega^2} \quad (3)$$

In order to address the dynamic imbalance requirement, we use Equation (3). The dynamic imbalance is related to the imbalance forces and moments as following:

$$J_{rz} = \left\| \begin{Bmatrix} -i_{yz} \\ +i_{xz} \end{Bmatrix} \right\| = \frac{1}{\omega^2} \left\| M_r - \left(\frac{g}{\omega^2} + \Delta\right) \begin{Bmatrix} -f_y \\ +f_x \end{Bmatrix} \right\| \quad \text{or} \quad (4)$$

$$J_{rz} = \|\mathbf{i}_{rz}^\perp\| = \frac{1}{\omega^2} \left\| M_r - \left(\frac{g}{\omega^2} + \Delta\right) \mathbf{f}_r^\perp \right\| \quad \text{where } \mathbf{f}_r^\perp = \begin{Bmatrix} -f_y \\ +f_x \end{Bmatrix} \quad \text{and} \quad \mathbf{i}_{rz}^\perp = \begin{Bmatrix} -i_{yz} \\ +i_{xz} \end{Bmatrix}.$$

The requirements for static and dynamic balancing have to be compared to the values obtained from the product  $me$  and  $J_{rz}$  computed from Equations (3) and (4) respectively. In addition to the magnitudes of the static and dynamic imbalances, of practical interest are their corresponding directions. To find the precise directions, two coordinate systems can be set on the test setup. One is stationary relative to the dynamometer, while the second rotates with the GMI unit. These two coordinate systems share an origin and the z-axis and initially both x-axes and y-axes are co-linear. Since the angle at which GMI has rotated is known, we can subtract that from the direction of the resultant force to find the physical direction of the imbalance via

$$\theta_f = \tan^{-1} \left( \frac{f_y}{f_x} \right) - \theta_{\text{GMI}} \quad (5)$$

$$\theta_M = \tan^{-1} \left( \frac{M_y - \Delta \cdot f_x}{M_x + \Delta \cdot f_y} \right) - \theta_{\text{GMI}} \quad (6)$$

We have just established that the static and dynamic imbalances form a pair of vectors that may be plotted in a three-dimensional graph to graphically pinpoint the directions of the imbalances together with the physical locations of the balance masses to visually help the technical team understand which masses will be most effective.

#### Optimal Balancing Using Linear Programming

Having determined the levels of static and dynamic imbalances, we now determine the optimal balance masses that would simultaneously make the radial force and moment on the dynamometer nil. In order for GMI to be statically balanced, its center of mass must reside on the axis of rotation. This can be done

by creating equal and opposite forces to the resultant x and y forces imbalance forces, expressed through the following equality constraints

$$\sum_{i=1}^n m_i x_i = -\frac{f_r}{\omega^2} \cos \theta_f, \quad (7)$$

$$\sum_{i=1}^n m_i y_i = -\frac{f_r}{\omega^2} \sin \theta_f. \quad (8)$$

where  $m_i$  is the  $i$ th balancing mass of coordinates  $x_i, y_i$  and  $z_i, i = 1..n.$ , and  $\theta_f$  is the angle of the imbalance radial force. Similarly, the moments created by the dynamic imbalance must be counteracted by the added balancing masses making the combined cross product of inertia nil resulting in the following additional two constraint equations

$$\sum_{i=1}^n m_i x_i \left( z_i + \frac{g}{\omega^2} \right) = -\frac{M_r}{\omega^2} \sin \theta_M \quad (9)$$

$$\sum_{i=1}^n m_i y_i \left( z_i + \frac{g}{\omega^2} \right) = \frac{M_r}{\omega^2} \cos \theta_M \quad (10)$$

Because the locations of the balancing masses are known, we have a system of four linear equilibrium Equations (7-10) to  $n$  unknown mass values  $m_i, i = 1 \dots n.$  For the case of GMI, we have  $n = 21.$  There is no unique solution to this over-determined problem. However, an optimal unique solution may be found by writing a linear programming problem in which we minimize the sum of the balance masses while meeting the static and dynamic balance equality constraints (7-10) and introducing inequality constraints on the balance masses that take into account the feasibility of actual mass placement with respect to size/mass constraints of the balance mass for a given location and the positive nature of the balance masses. The objective function to be minimized is expressed as

$$\varphi(\mathbf{m}) = \sum_{i=1}^n \alpha_i m_i = \boldsymbol{\alpha}^T \mathbf{m} \quad (11)$$

And the optimization problem is written formally as

$$\min_{\mathbf{m}} (\boldsymbol{\alpha}^T \mathbf{m}) \text{ such that } \begin{cases} \mathbf{A}eq \cdot \mathbf{m} = \mathbf{b}eq \\ \mathbf{lb} < \mathbf{m} < \mathbf{ub} \end{cases} \quad (12)$$

The matrix equation  $\mathbf{A}eq \cdot \mathbf{m} = \mathbf{b}eq$  is the set of four equality constraints described above and is set up as shown in Equation (13).

$$\begin{bmatrix} x_1 & x_2 & \dots & x_n \\ y_1 & y_2 & \dots & y_n \\ x_1 \left( z_1 + \frac{g}{\omega^2} \right) & x_2 \left( z_2 + \frac{g}{\omega^2} \right) & \dots & x_n \left( z_n + \frac{g}{\omega^2} \right) \\ y_1 \left( z_1 + \frac{g}{\omega^2} \right) & y_2 \left( z_2 + \frac{g}{\omega^2} \right) & \dots & y_n \left( z_n + \frac{g}{\omega^2} \right) \end{bmatrix} \begin{bmatrix} m_1 \\ m_2 \\ \vdots \\ m_n \end{bmatrix} = \begin{bmatrix} -\frac{f_r}{\omega^2} \cos \theta_f \\ -\frac{f_r}{\omega^2} \sin \theta_f \\ -\frac{M_r}{\omega^2} \sin \theta_M \\ \frac{M_r}{\omega^2} \cos \theta_M \end{bmatrix} \quad (13)$$

The expression  $\mathbf{lb} < \mathbf{m} < \mathbf{ub}$  represents a set of  $2n$  inequality constraints that set the lower and upper bounds on the balance masses. The lower bound must be set to zero, as we are adding mass, and the

upper bound must be a set of mass values that can be handled given the physical reality of space available at each balance mass location. They could also turn off certain masses that are difficult to access due to some practical envelope constraints. The linear problem given by Equation (12) is solvable using MATLAB's linear programming function "linprog" using the same software that collects dynamometer sensor data and encoder position as the test unit spins atop of the dynamometer.

### Calibration of the Dynamometer Setup

The calibration entails three parts. In the first part, the dynamometer is shown to have the necessary sensitivity to accurately make the necessary measurements needed to process the imbalance data. The noise floor of the dynamometer is identified and compared to the requirements on forces and moments that are derived to meet GMI's static and dynamic balancing requirements.

In the second part of the calibration, the forces measured by the dynamometer are checked using two separate data acquisition systems and two loading methods. This was performed to isolate and quantify the sources and magnitudes of systematic and random measurement errors. Finally, the third part in the calibration program evaluates data collected from auxiliary risk mitigation tests which used the GMI SMA (Spin Mechanism Assembly) and simulated payloads with off-axis known masses precisely located on a rotating disk (see Figure 4). These mitigation tests were planned to assess the performance of the tools to be used in the actual balancing of GMI. Three test cases were performed. The first one has a moderate imbalance, while the second test case is intended to achieve extreme static and dynamic imbalances. Finally, the third test case is intended to produce a balanced state from which we demonstrate the capability of the system to meet the required level of balance measurements for GMI.

#### Specified and Derived Requirements

The two GMI balancing requirements are expressed in terms of the product  $me \leq 0.032$  kg-m (2.77 lb-in) for static imbalance and  $J_{rz} \leq 0.055$  kg-m<sup>2</sup> (187 lb-in<sup>2</sup>) for dynamic imbalance. We derive two equivalent requirements that provide the equivalent limits on the static and dynamic imparted forces and moments that GMI needs to meet in order for the balancing effort to be successful. These requirements are shown to be for the radial force  $\leq 0.08$  lb (0.36 N) and the radial moment  $\leq 10$  in-lb (1.1 N-m). In addition, a requirement on the noise floor is set so that accurate and reliable measurements of the balanced state are performed. The noise floor of the dynamometer is checked against 1/10<sup>th</sup> of the requirement levels, padded by a 50% uncertainty levied to account for unknown error contributions to the measurements. The noise floor is found to be  $\leq 0.004$  lb (0.018 N) for reliable measurements to occur.

Using the expression for the radial load from Equation (1) and using an angular frequency of 0.533 Hz (32 rpm), the magnitude of the radial load is related to the imbalance  $me$  via

$$me = \frac{\|f_r\|}{\omega^2} \Rightarrow \|f_r\| = me\omega^2 = 0.032 (2\pi \cdot 0.533)^2 = 0.36N \text{ (0.08 lb)}$$

Furthermore, de-rating this level by 50% to account for unknowns in the setup, we need to bring the radial load to less than 0.04 lb (0.18 N) if we want to show that GMI is statically balanced. Thus, we need to have a noise floor level less than 0.004 lb (0.018 N). In order to address the dynamic balance requirement, we use Equation (3). We have the magnitude of the radial moment given by:

$$\begin{aligned} \|M_r\| &= \left\| \omega^2 \begin{Bmatrix} -i_{yz} \\ +i_{xz} \end{Bmatrix} + \left( \frac{g}{\omega^2} + \Delta \right) \begin{Bmatrix} -f_y \\ +f_x \end{Bmatrix} \right\| \leq \left\| \omega^2 \begin{Bmatrix} -i_{yz} \\ +i_{xz} \end{Bmatrix} \right\| + \left\| \left( \frac{g}{\omega^2} + \Delta \right) \begin{Bmatrix} -f_y \\ +f_x \end{Bmatrix} \right\| = \omega^2 J_{rz} + \left( \frac{g}{\omega^2} + \Delta \right) \|f_r\| \\ \|M_r\| &\leq J_{rz} \omega^2 + me \left( g + \Delta \omega^2 \right) = 0.055 (2\pi \times 0.533)^2 + 0.032 (9.81 + 16.455 \times 0.0254 (2\pi \times 0.533)^2) \\ \|M_r\| &\leq 1.08 Nm \quad (< 10 \text{ in-lb}) \end{aligned}$$

Again, de-rating this level by 50% to account for unknowns in the setup, we need to bring the radial moment to less than 0.6 N-m (5 in-lb) if we want to show that GMI is statically balanced. Thus, we need to have a noise level less than 1/10th of 0.056 N-m (0.496 in-lb). Considering the forces in the sensors from which we compute the moments and the geometry shown in Figure 5, the noise floor needs to be less than 0.5 in-lb (0.06 N-m)  $/(26.035/2.54)$  or 0.05 lb (0.22 N). Accounting for three sensors, we have to have a noise floor better than 0.016 lb (0.071 N). In summary, the requirement imposed on the noise floor of the radial force is 0.004 lb (0.018 N) and the one imposed on the moments is 0.5 in-lb (0.06 N-m) (that is 0.016 lb (0.071 N) in force sensors). The smaller value of the two is 0.004 lb (0.018 N) and is kept for comparison with the performance of the dynamometer.

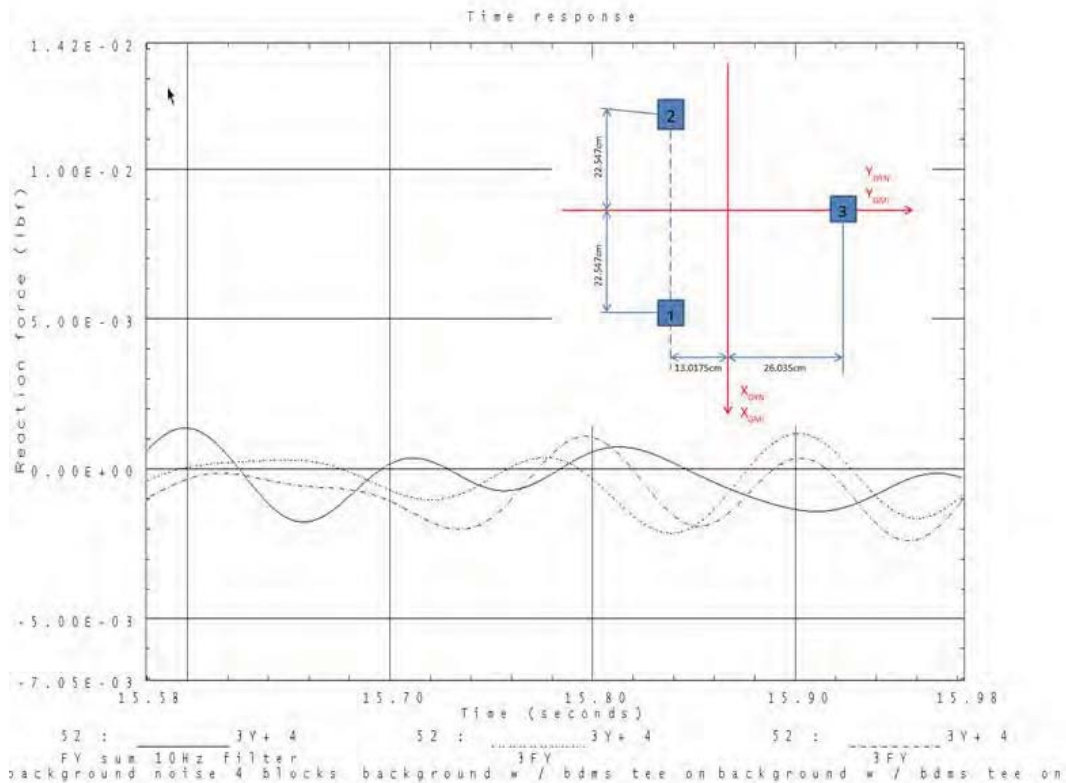


**Figure 5. Noise floor showing measurements filtered using low bandpass of 10 Hz**

To measure the noise floor, the dynamometer was placed on four blocks at the four corners of the lower plate. This configuration was chosen instead of the fully clamped one to simulate the actual balancing configuration in which the dynamometer's own mode is in the vicinity of 30 Hz versus the 120 Hz+ in the fully clamped configuration. Three measurements were taken. In the first measurement, the data from the load cells is channeled only to an independent secondary data acquisition system (VXI system). In the second test, the data from the load cells is channeled to the BDMS data acquisition (processor to be used for balancing) and simultaneously to the VXI through a set of "T" connections. The third test has both data acquisition systems in place except that the data acquisition card of the BDMS was turned off. A digital filter of 10 Hz was applied to the data sets. An example of dynamometer noise floor measurement for the Y-axis is shown in Figure 5. The maximum noise of 0.00175 lb (0.00778 N) is measured and is found to be less than the 0.004 lb (0.018 N) needed to carry out accurate measurements to meet GMI spin balance requirements.

#### Harmonic stinger test

This test is intended to calibrate the measurements performed by the dynamometer as a system. The dynamometer is excited at a frequency of 10 Hz using an MTB 50-lb (220-N) stinger. A calibrated load cell is placed at the interface between the stinger and the dynamometer to measure the input force. The



latter was also measured using the dynamometer as the sum of the contributions of all load cells. The load is applied along the Y direction of the dynamometer. The input loads matched the output load. The Spectral Dynamics Data Acquisition System of BATC's Vibration Lab was also used to further check the response and the results. They were found to be identical to the reference load.

#### Frequency response function (FRF) tests

The FRF shows that the data is unaffected by the fundamental modes of the dynamometer either in a clamped or a simply supported configuration. The difference in loads is negligible in the vicinity of 0.5 Hz. While the results of the excitation illustrated in Figures 6 and 7 are for the Y-axis, similar results are recovered for the X-axis. The FRF was also measured prior to balancing GMI either in the clean room or in the vacuum chamber BRUTUS where additional modes are present due to the mounting equipment. The mount and fixture hosting GMI during spin balance testing in the BRUTUS vacuum chamber is analyzed using the finite element method incorporating a GMI model to ensure that we have no interference from the added structural resonance modes. The mounting beams in BRUTUS (Figure 2b) were stiff enough and produce no modes that interfere with measurements.

#### Speaker tests

The goal of the dynamic calibration using a speaker load input is to verify that we are reading the correct dynamic loads while balancing the GMI instrument, no matter where these loads are applied over the dynamometer. The calibration consists in applying known forces using a speaker precisely oriented and located at different elevations over the dynamometer and measure the reaction forces and moments imparted on the surface of the dynamometer. The speaker is attached to a fixture through an encapsulated load cell to ensure a precise knowledge of the magnitude and location of the excitation. The speaker is actuated using a form generator to deliver an accurate input frequency. The test shows the input load from the speaker force transducer and the measurement from the dynamometer are the same in different orientations. In particular, this test is required to verify the correctness of the measured moments which are crucial for dynamic imbalance predictions.

#### Risk Mitigation Balance Tests

In order for the GMI balancing task to run smoothly, a risk reduction set of tests were carried using the SMA drive and a flywheel on which known masses are placed in well-known locations on the flywheel as shown in Figure 8. The first test consists of the placement of an imbalance mass of about 1.1-lb (4.9-N) at the edge of the flywheel. The second test is an extreme case created by a 16-lb (71-N) imbalance, also placed at the edge of the flywheel. Finally, the last case is of a situation in which an attempt was made to balance the flywheel and the SMA to the best available capabilities. The results of this test points to how a balanced situation results in very small shear and moment loads exported to the mount of the SMA. The data from the dynamometer is compared to the mass tally data. It is found that accurate estimates of the imbalance can be made using the dynamometer. In addition, a balanced state can be easily identified once the shear force and moment become small.

In the first test case, a set of known imbalance masses were placed on the bare flywheel. Knowing the location of the masses, a static imbalance of 13.491 in-lb (1.5243 N-m) and a dynamic imbalance of 139.077 lb-in<sup>2</sup> (0.040699 kg-m<sup>2</sup>) are computed. The total mass of the added hardware consisting of studs, washers and spacers weighs 1.1075 lb (4.9264 N) and its center of mass is located at a radius of 12.18 in (30.93 cm). The radial force and radial moment maintain a nearly constant value as the SMA and its payload rotate. The mean static and dynamic imbalances given by Equations (4) and (5) are computed over a period of 70 seconds at a rate of 1 KHz. These values are within 1% of the expected values as shown in Table 1. The second test is an extreme case in which 18.20 lb (80.95 N) is placed at the edge of the flywheel to produce an imbalance which is about 100 times the imbalance requirement. The static and dynamic imbalances are about 270 lb-in (30.5 N-m) and 2900 lb-in<sup>2</sup> (0.8487 kg-m<sup>2</sup>) respectively. The total mass of the added hardware consisted of two dumbbells, studs, washers and spacers is 18.2025 lb (80.9688 N). Again, the radial force and radial moment maintained constant values as the SMA and its flywheel payload with imbalance mass rotate and the system recovered the static and dynamic imbalances with errors of 0.41% and 1.8% respectively. In the third test case, the measured mean

resultant radial load of 0.015 lb (0.067 N) is below the requirement of 0.08 lb (0.36 N), and the measured mean resultant moment of 0.51 in-lb (0.06 N-m) is below the 10 in-lb (1.1 N-m) equivalent requirement. This last test provided the necessary argument that the system is capable of predicting a balanced state.

**Table 1. Comparison of measured imbalance to correction magnitudes**

Dynamometer		MATLAB		Percent Error	
Static (lb-in)	Dynamic (lb-in <sup>2</sup> )	Static (lb-in)	Dynamic (lb-in <sup>2</sup> )	Static	Dynamic
13.491	139.077	13.371	138.868	0.89%	0.15%
(N-m)	(kg-m <sup>2</sup> )	(N-m)	(kg-m <sup>2</sup> )		
1.5243	0.040699	1.5107	0.040638		

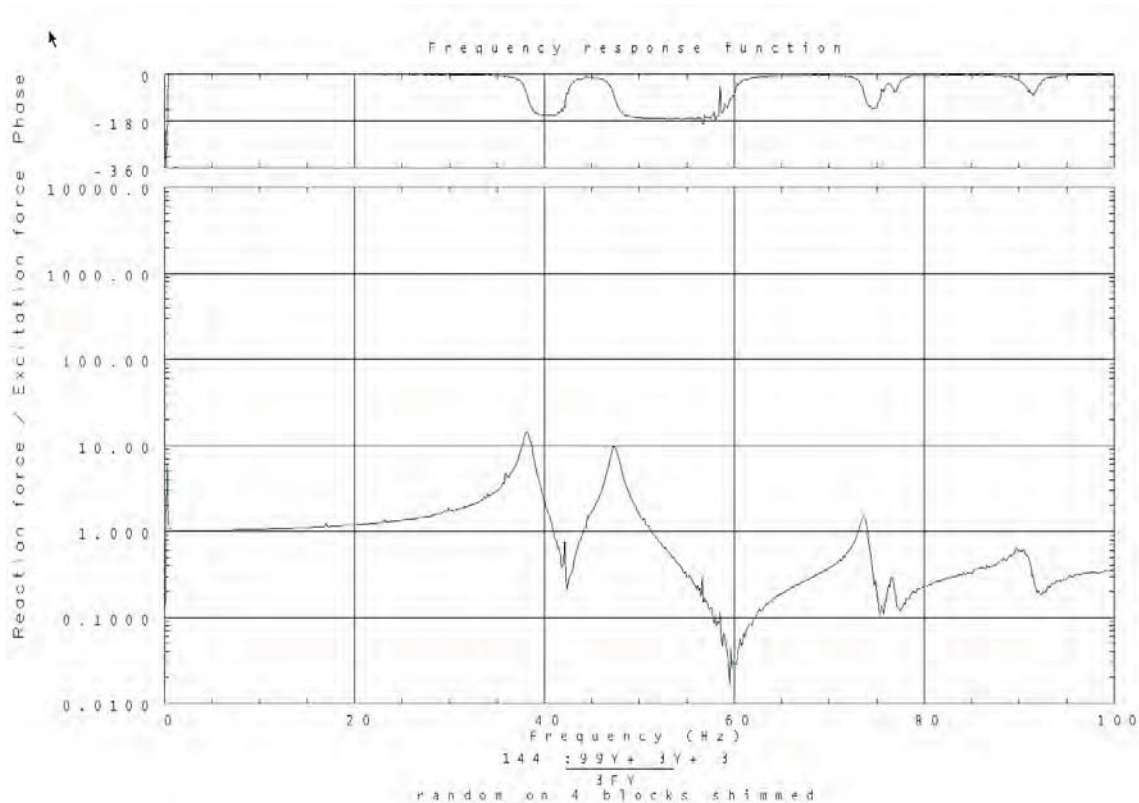


**Figure 6. Frequency Response Function of clamped dynamometer (without GMI)**

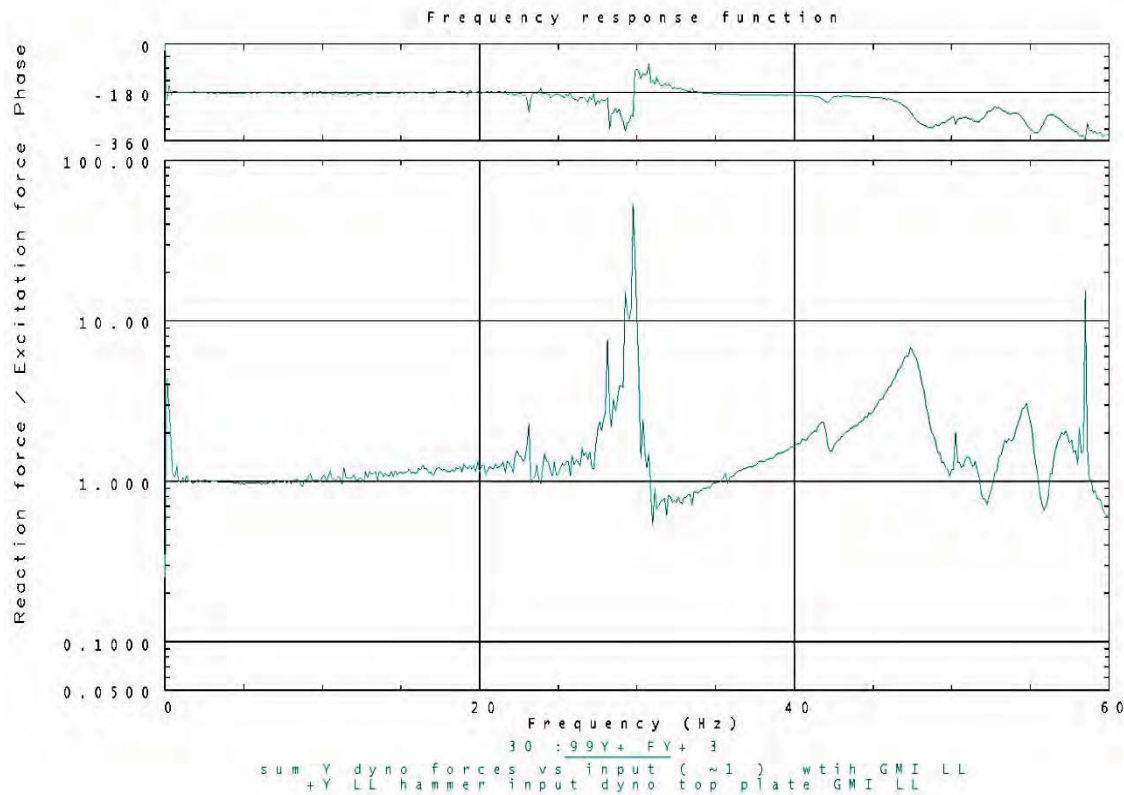


**Figure 7. Frequency Response Function in configuration with GMI installed**

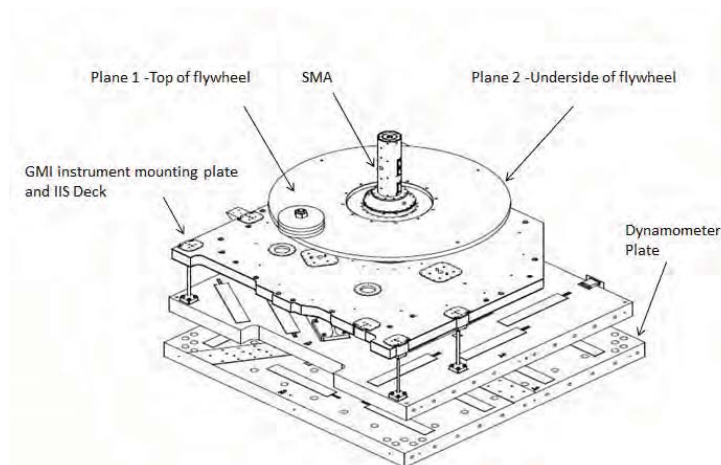


**Figure 8. Spin Balance Risk Mitigation Test Setup**

### Spin Balancing Verification of GMI

It is shown that GMI was adequately balanced to meet both static and dynamic balancing requirements. The measured imbalances in BRUTUS vacuum testing were found to be 0.017 kg-m (1.47 lbm-in) and 0.022 kg-m<sup>2</sup> (75.1 lb-in<sup>2</sup>) meeting the requirements of 0.032 kg-m (2.78 lbm-in) static and 0.055 kg-m<sup>2</sup> (187 lb-in<sup>2</sup>) dynamic imbalances, respectively. The results of Table 2 show the average of three separate measurements of forces, moments and computation of static and dynamic imbalances. Three tests are averaged to give imbalances in vacuum and three other tests carried in open air are averaged to determine final balancing values. All tests are run at 32 rpm and results show all tests met the

requirements. Other test runs, performed to acquire spin balance data at 28 rpm and 33 rpm, were also successful in showing that GMI successfully meets the balancing requirement.

The balancing of GMI takes place in two steps. In the first step, GMI is brought to a pseudo-balanced state, prior to assembling the RDA, MR, and final MLI layers in air in a cleanroom environment. In this configuration, analytical estimates of the RDA, MR, and MLI inertial properties are adopted while computing the balance masses, thus accounting for the future installation of these components. In the second step, the final balancing task is carried out while the fully assembled GMI in its final configuration in a vacuum chamber.

The MATLAB script reads the raw data file and pulls out the relevant ranges for the forces and resolver data. The resolver reading is first converted from the voltage pulse 'zero-crossing' point that, signals a full rotation, into useable angle data with respect to time. A correction value of 94.35 degrees (sensor location) is then added to the angular position to synchronize the zero position on the x-axis of the GICS coordinate system with the SMA resolver readings. This makes it possible to pinpoint the direction of the imbalance, as well as, to properly place balance masses in locations given in a single reference coordinate system. A total of nine forces are read as a function of time once every millisecond, one in each coordinate axis from each one of the three force transducers of the dynamometer. The data collected prior to the first resolver zero-crossing and after the last resolver zero-crossing time is disregarded. The force and moment resultants are then computed, and subjected to a low-pass Butterworth filter at 3 Hz. For each time station, the magnitude of the radial force and radial moment due to imbalance are computed, and plotted together with the static and dynamic imbalance magnitudes and directions as shown in Figure 9.

The mean radial force and mean radial moment are then computed and a linear programming solver is used to find the minimum set of masses that would simultaneously bring the static and dynamic imbalances back to a balanced state. The script has a set of 21 hard-coded mass locations with lower and upper bounds. The optimization is carried to satisfy the four constraint equations with an objective function equal to the sum of all masses as explained in the analytical section. As a default, each mass is equally favored. The user may elect to eliminate contributions from individual masses by bounding their individual lower and upper bounds to zero. Furthermore, the relevance of some weights can be affected through modifying their weights in the objective function. Once the optimization is carried successfully, the command window displays the statement "Optimization terminated." The solution is captured and displayed in three tables. The first table documents the magnitudes of the 21 masses, their locations and their first and second cross moment magnitudes. The resultant forces and moments due to the balancing masses are displayed in the second table. And finally the resultant static and dynamic inertial contributions from the balancing masses are shown in the third table. The initial properties of the imbalance are shown and compared to the solution. The magnitudes of the 21 balancing masses are also displayed in a bar graph for quick visualization. The balancing masses are displayed in their 3D locations as weighted, colored spheres together with the resultant mass. Also displayed are the resultant centrifugal force and moment produced by the balancing masses along with the imbalance radial force and moment. This gives a visual representation that a solution is found in which the balancing radial force and radial moment are equal in magnitude and directly opposite to the force and moment generated by the imbalances (see Figure 9).

The effect of the missing RDA/MR hardware on the static imbalance is based solely on its total mass and CG location. Because of this, it can be treated simply as the 22<sup>nd</sup> balancing mass during the initial optimization process. This 22<sup>nd</sup> presumed unknown mass will have the coordinates of the net CG of the missing RDA/MR assembly and its upper and lower mass bounds are set to the known total mass and inertial properties of the RDA/MR, so that when a solution is found, the 22<sup>nd</sup> mass will be constrained to be equal to its known value.

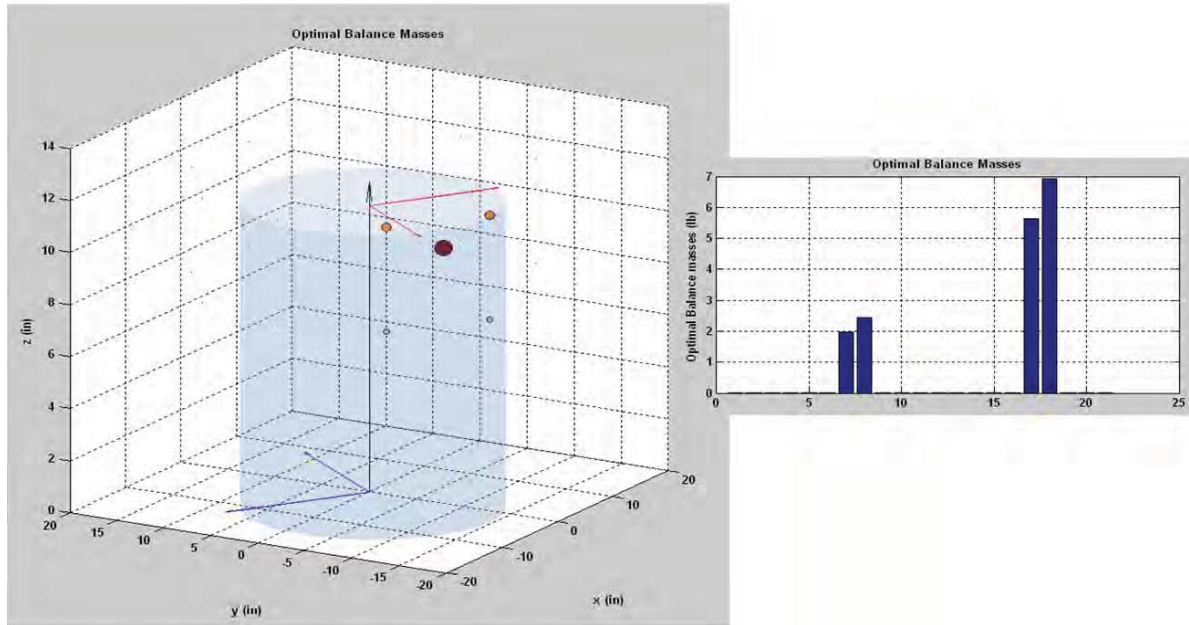


**Figure 9. Plot of Balancing masses, imbalance and balance force and bar graph**

#### Post Vibration Spin Balance Verification (without RDA/MR)

Following the completion of GMI vibration tests, the instrument was spun again on October 5, 2011 to compare with the pre-vibe imbalance measurements carried on August 2, 2011. The test is intended to check for possible shift of cabling and other flexible components. The difference between the two tests amounts to 0.26% in the radial force and 0.48% in the radial moment. It has to be noted that in addition to several changes to the stationary GMI hardware which theoretically would not affect the measurements (as long as we do not excite their modes), there have been slight changes in the configuration of rotating GMI that included the replacement of two 36 GHz flex wave guides, 0.0410 lb (0.183 N) each, with two rigid wave guides, 0.0168 lb (0.0747 N) each, and the re-machining of mounting shims. The wave guides along with the 36-GHz filter were re-staked, and one balance mass was removed, adjusted to account for the change, and then reinstalled in the same spot and re-staked. The overall delta is  $Wt = -0.051$  lb (0.227 N). The new radial load is analytically evaluated and compared well with the measured value, placing all shifts at 0.106%, that is a delta of 0.005 lb (0.022 N), significantly less than the derived requirement of 0.08 lb (0.36 N) (or just 6.7% of the requirement). Therefore, it is safe to state that *vibration loads due to launch will likely shift the rotating mass by 7%, or less, of the requirement of 0.08 lb (0.36 N), on-orbit.*

#### In-Vacuum Final GMI Balancing

Several tests were carried out in vacuum and in air on the dynamometer to show that the requirements were met. It is worth noting that an RDA/MR deployment GSE off-loader structure needed to be removed from Brutus to perform clean test measurements. Table 2 shows the average of three separate measurements of forces, moments and computation of static and dynamic imbalances first in vacuum and then the averages of three other 32-rpm tests also run in the Brutus but in open air rather than in vacuum. Table 3 shows the computed and actual masses that brought GMI to meet requirements.



**Table 2. Average of imbalance measurements (three in vacuum and three in air)**

units (lb,in)	Fx (lb)	Fy (lb)	Fr (lb)	Mx (lb-in)	My (lb-in)	Mr (lb-in)	me (lbm.in)	Jrz (lbm.in <sup>2</sup> )
<b>Vacuum</b>	0.0021	0.0402	0.0436	-0.069	2.805	2.8	1.5	73.5
<b>Air</b>	-0.0098	0.037	0.0398	-0.86	1.104	1.5	1.4	63.9
<b>Requirement</b>			0.08			10	2.77	187
units (Kg,m)	Fx (N)	Fy (N)	Fr (N)	Mx (N.m)	My (N.m)	Mr (N.m)	me (Kg.m)	Jrz (Kg.m <sup>2</sup> )
<b>Vacuum</b>	0.0092	0.1794	0.1946	-0.008	0.318	0.318	0.017	0.022
<b>Air</b>	-0.0438	0.1651	0.1775	-0.097	0.125	0.167	0.016	0.019
<b>Requirement</b>			0.36			1.13	0.032	0.055

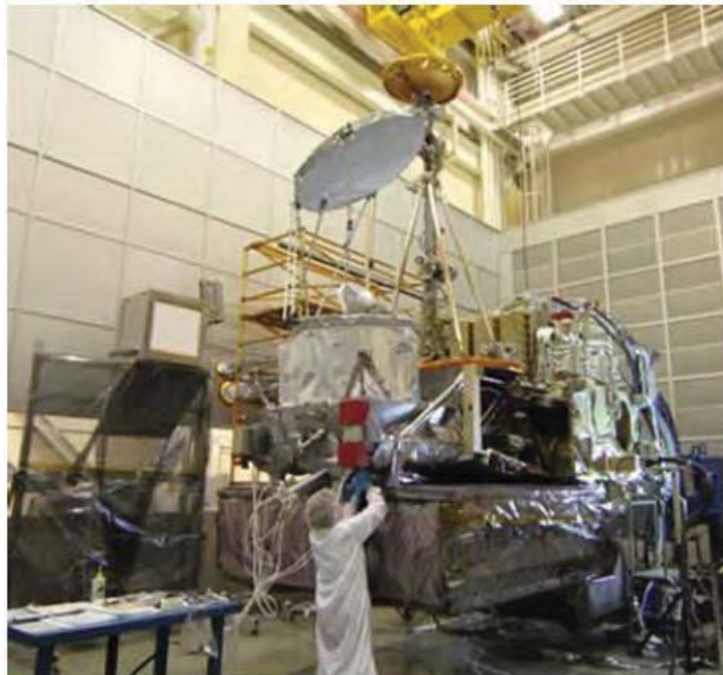


**Figure 10. GMI Integrated on the GPM Spacecraft at NASA Goddard Space Flight Center**

**Table 3. Added masses used to balance GMI**

Balance Mass Location ID	Desired (2) Brutus Spin Balance 2/4/12 (lbm)	Desired (2) Brutus Spin Balance 2/4/12 (kg)	Actual Brutus Spin Balance Final Values 2/9/12 (lbm)	Actual Brutus Spin Balance Final Values 2/9/12 (kg)
1	0.198	0.090	0.196	0.089
2	5.25	2.38	5.25	2.38
3	1.495	0.6781	1.496	0.6786
4	0.19	0.086	0.19	0.086
5				
6				
7				
8				
9	10.17	4.613	10.17	4.613
10				
11	0.063	0.029	0.064	0.029
12	0.393	0.178	0.394	0.179
13				
14	2.77	1.26	2.77	1.26
15				
16				
17				
18	0.006	0.003	0	0
19	0.34	0.15	0.34	0.15
20	0.205	0.0930	0.205	0.0930
21				
Total (lbm)	21.08		21.075	
Total (kg)		9.562		9.559

**Conclusion**

The Global Microwave Imager instrument (GMI) was successfully spin-balanced using a dynamometer as a mounting fixture. GMI was balanced to less than 0.017 kg-m (1.47 lbm-in) static imbalance and 0.022 kg-m<sup>2</sup> (75.2 lb-in<sup>2</sup>) dynamic imbalances, meeting the requirements of 0.032 kg-m (2.77 lbm-in) and 0.055 kg-m<sup>2</sup> (188 lb-in<sup>2</sup>) respectively, total for the 123-kg (271-lb) spinning portion of the instrument payload.

The successful final precision spin balancing of the GMI instrument in vacuum demonstrated the capability of this method to accurately measure the static and dynamic imbalances, and to precisely compute the optimal set of minimal balance masses, accounting for various. The ability to precisely measure the imbalances before and after environmental testing also enabled us to very accurately predict the magnitude of the change in the GMI instrument imbalance on orbit, following launch.

The forces measured by the dynamometer checked well against two other independent measurement systems. In addition, the dynamometer is shown to be capable of reproducing the applied loads and moments with adequate accuracy. The natural structural frequencies of the dynamometer were mapped and their effect on the measurements was identified for the frequency spectrum of interest.

Prior to balancing GMI, both moderate and extreme imbalance risk mitigation tests are shown to be accurately measured using the dynamometer and the necessary balancing forces are accurately computed. The fully balanced state was also recovered from the time traces of the resultant radial loads and radial moments.

Since the successful completion of the final spin balance activity, the GMI instrument was delivered to Goddard Space Flight Center in March 2012, and was successfully integrated onto the GPM spacecraft later in June 2012, see Figure 10. The GPM spacecraft just recently completed spacecraft level Thermal

Vacuum (TVAC) testing in January 2013, vibration testing in July 2013, post-environmental testing in September 2013, and is scheduled to be launched in February 2014 from Tanegashima, Japan on a JAXA MHI-H11A rocket.

A special thanks to Sergey Krimchansky\*\*; GMI instrument COTAR at GSFC for his input over-seeing the technical work on GMI and for his support in writing these GMI-related technical papers.

### References

1. Newell, D., Rait, G., Ta, T., Berdanier, B., Draper, D., Kubitschek, M., Krimchansky, S. "GPM Microwave Imager Design, Predicted Performance and Status", Proceedings of the 2010 IEEE International Geoscience and Remote Sensing Symposium (IGARSS) Publication Date: July 25, 2010.
2. Woolaway, S. Kubitschek, M., Berdanier, B., Newell, D., Dayton, C. and Pellicciotti, J. "GMI Spin Mechanism Assembly Design, Development, and Test Results", *Proceedings of 41<sup>th</sup> NASA Aerospace Mechanisms Symposium*, Langley Research Center, May 2012.
3. Koss, S., Woolaway, S. "Lessons Learned From the WindSat BAPTA Design and On-Orbit Anomalies", Proceedings of 38th NASA Aerospace Mechanisms Symposium, Langley Research Center, May 2006.
4. Pierre, W. "GMI Spin Mechanism Structural Analysis", BATC Internal SER Report No. 2307821B, Ball Aerospace and Technologies Corp., Nov. 2008.
5. Richard P. Wolley, Dynamic Balancing Without Spinning: A New Method for Unwieldy Satellites, SAWE paper No. 1670, Category 6.0, 44th Conference of the Society of Allied Weight Engineers, 1985.
6. Ayari, L. "Hybrid Testing & Simulation - The Next Step in Verification of Mechanical Requirements in the Aerospace Industry," Hybrid Simulation Theory, Implementation and Applications, Victor Saouma, Mettupalayam Sivaselva Editors, 2008.

# The European Robotic Arm: A High-Performance Mechanism Finally on its way to Space

H.J. Cruijssen\*, M. Ellenbroek\*, M. Henderson\*, H. Petersen\*, P. Verzijden\* and M. Visser\*

## Abstract

This paper describes the design and qualification of the European Robotic Arm (ERA), which is planned to be launched by the end of 2015. After years of changes, a shift of launcher and new loads, launch preparation is underway.

The European Robotic Arm ERA has been designed and manufactured by Dutch Space and its subcontractors such as Astrium, SABCA and Stork with key roles for the mechanical aspects. The arm was originally designed to be launched by the STS (mounted on a Russian module for the ISS) in 2001. However, due to delays and the STS disaster, a shift was made to the Russian Proton rocket. ERA will be launched on the Multipurpose Laboratory Module (MLM). This module, which is now planned for launch to the ISS in 2015, will carry the ERA. The symmetrical design of the arm with a complete 3 degree-of-freedom wrist and general-purpose end effector on both sides, allows ERA to relocate on the station by grappling a new base point and releasing the old one, and move to different working locations.

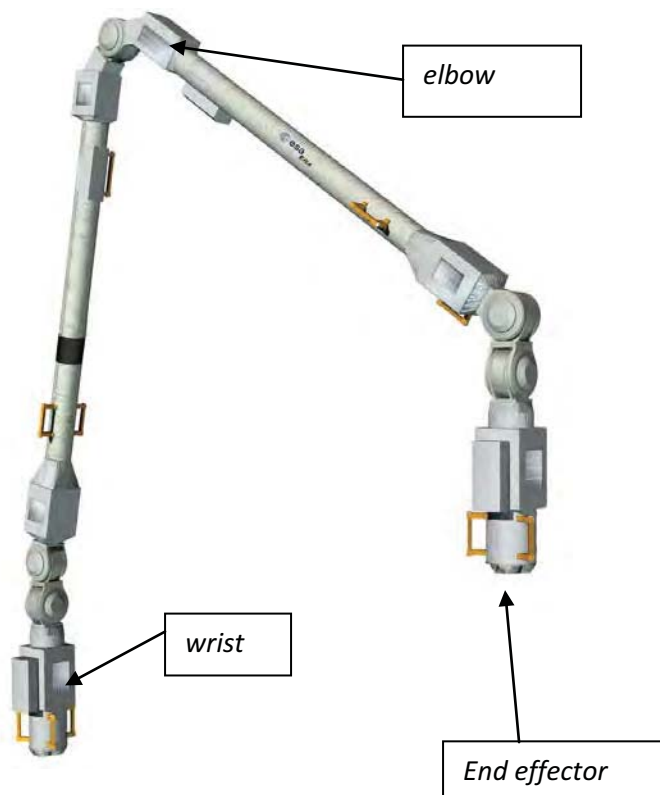


Figure 1. Overall ERA arm architecture

## ERA Overall Design Description

The arm consists of 2 limbs which are connected by motorized hinges. The arm has an end effector which has the possibility of grabbing Space Station components for transport or tools for support of EVA activity.

This end effector includes other features such as electrical connections and a mechanical drive that can operate like a wrench tool. The arm is symmetrically designed, meaning that the arm shoulder joints and wrist joints are identical. This allows the arm to “walk” fully autonomously from base point to base point on part of the ISS. This “walking” arm capability allows it to reach remote grapple points.

The arm structural capability enables it to move 8000-kg payloads. The arm is controlled by an integrated computer and has a camera vision system for close proximity operations and can provide camera images of the working area.

\* Dutch Space BV, Leiden, The Netherlands

ERA has been designed from the beginning to be serviceable and to allow exchange of big parts via EVA in case of failure or an emergency situation. Such parts are called ERU (EVA Replaceable Units). During the launch of STS 132 in 2010, one ERU was launched and put into in space. It has been stored on the outside of the ISS on the MRM-1. A special launch interface had to be designed to allow launch in orbit. This ERU is still fixed in this launch configuration and is protected with a special bag of MLI. In case of failure or specific maintenance, the arm can be activated by EVA. ERA is also designed to perform servicing tasks originally allocated for EVA.

The main technical characteristics are listed in Table 1.

**Table 1. ERA Key Characteristics**

Total Length	11.3 m
Range/span	9.2 m
Degrees of Freedom	7
Mass	630 kg
Peak power dissipation	800 W
Stand-by heat dissipation	420 W
Hibernation heater power	250 W
Accuracy open loop	± 40 mm
Accuracy closed loop	± 5 mm
Maximum moveable mass	8000 kg
Maximum payload dimensions	3x3x8.1 m
Maximum speed of movement	0.10 m/s
Braking distance at max joint speed	0.15 m

The ERA consists of the following major subsystems:

1. The **End Effector Subsystem** (EES) consists of two Basic End Effectors (BEE), Base Points (BP) and Grapple Fixtures (GF).
2. The **Manipulator Joint Subsystem** (MJS) consists of two wrists and one elbow. Each wrist is made of 3 joints (roll, yaw and pitch) and one electronic box for their control. The elbow is made of one joint (pitch) also with its own electronic control box.
3. The **Manipulator Limb Subsystem** (MLS) consists of two limbs of carbon fiber reinforced plastic material.
4. The **ERA Control Computer** subsystem (ECC or On board Computer, OBC), is the brain of the system that communicates with the Space Station through the external data bus and with each subsystem through the internal data bus.
5. The **Camera and Lighting Unit subsystem** (CLU) consists of 4 units. One on each End Effector and one on each side of the elbow mounted on the two limbs.

Other key elements are related to the manual control of ERA. These are:

6. The **EVA Man-Machine Interface** (EMMI) is a control panel that provides the capability to control ERA during EVA.
7. The **IVA Man-Machine Interface** (IMMI) control panel is a laptop computer for control of ERA from the pressurized modules of the station.

The EVA-MMI is a dedicated console with switches and LED displays, designed to be operated by a crew member in EVA suit and able to be exposed to the space environment for extended periods of time. The IVA-MMI is a software application running on an IBM system which is located inside the pressurized module of the Russian Segment of the ISS. The workstation near the IVA-MMI will be able to display ERA camera views.



## ERA Mechanical Subsystems and Mechanisms

The first two above mentioned subsystems represent mechanical subsystems composed of mechanical assemblies. These main subassemblies are:

1. End Effector Subassembly (EES):
  - a) Grapple mechanism (GM) – incl. Base point (BP) and Grapple Fixture (GF)
  - b) Integrated Service Tool (IST) (incl. receptacle in GF)
  - c) Torque Force Sensor (TFS) incl. the Torque Rigidization Mechanism (TRM)
2. Manipulator Joint Subassembly (MJS) consisting of 3 modular hinges of which all are very similar, except the roll. These 3 hinges form together the so called “wrist” joint. See Figure 1 for the overview.
  - a) Pitch Joint / Yaw Joint / Roll Joint; located at both ends of the arm (3 D.O.F)
  - b) Elbow Joint: The elbow joint uses the same basic hardware as the wrist pitch joints but has only one degree of freedom.

A further major mechanical subsystem is:

3. Launch Fixation Mechanism: Its function is to restrain the ERA during launch. The launch fixation mechanism on the Russian Segment-MLM structure consists of:
  - a. Fixation Hooks and support pads, being part of the MLM
  - b. Pins and support pads, being part of the ERA structure

These mechanisms will be activated by EVA, when the unfolding of the arm from the launch support starts. The cosmonauts will release the fixation hooks. Furthermore, special mechanical features are included to allow for EVA. These are implemented to enable repair maintenance, exchange, etc. The design and the size of certain mechanism are driven by the accessibility requirements for EVA tooling.

4. EVA-Compatible Mechanisms:
  - a. Camera & Lighting Unit (CLU): The connector mate/de-mate mechanism.
  - b. EVA Man-Machine Interface (EMMI); only switches.
  - c. EVA overrides for GM, IST, TRM and joints.
  - d. EVA ERU mate/de-mate mechanisms (Elbow/Wrist, CLU, CLU windows).
  - e. EVA placeable handrails.

N.B. For a., c. and d., special EVA tools are used.

The above four mechanical subsystems and mechanisms are described below:

### End Effector Subassembly (EES) Mechanism Design Details

During the operations in orbit, one end effector is connected to a base point in order to provide a sufficiently stiff connection between the Russian Segment of ISS and ERA and to transmit power, data and video signals for the operation of the ERA system. The second end effector then serves as the gripper, able to grapple an object outfitted with a grapple fixture or a basepoint. Furthermore, the second end effector will support ERA by monitoring force/torque values during the insertion/extraction and during the transportation of objects. The second end effector provides mechanical and electrical power to the grappled object and allows for data transfer. In order to provide the above mentioned capabilities, the following functions are assigned to the EES:

- measure torques/forces
- grapple/guide
- power, data and video transfer
- insert the Integrated Servicing Tool (IST) head to provide mechanical power
- provide sufficient stiffness.
- rigidization, if no measurement of torque/force is needed (by design implementation)

The rigidization capability of the torque/force sensor is necessary to provide the required stiffness when the end effector acts as the shoulder and if "hand" stiffness is required during transportation operations.

The End Effector Subsystem (EES) consists of:

1. Structure housing.
2. Actuation and Sensing Unit
  - a) Actuator Unit
  - b) Torque/Force Sensor (TFS)
  - c) TFS Rigidization Mechanism
3. Moving Platform
4. Grapple Mechanisms
5. System Harness Connectors
6. Integrated Servicing Tool (IST)
7. Base points (BP)

The EES is also equipped with specific mechanical elements for EVA manual override.

1. Structure housing The main load-carrying structure of the end effector consists of the lower housing structure and the housing that contains the Electronics Unit. The lower housing structure is built up by the three stiffeners; the cover sheets, which are attached to the stiffeners; interface ring; and the guidance. The Electronics Unit housing provides the interface to the roll joint of the ERA Manipulator Joint System (MJS) and to the Camera and Lighting Unit (CLU). All parts of the housing structures are manufactured from high-strength aluminum alloy, the interfacing ring and the guidance from titanium, the spindles and the hooks from steel.

2. Actuation and Sensing Unit The Actuation and Sensing Unit consists of the Actuator Unit, the Torque Force Sensor, and the TFS Rigidization Mechanism.

- a) Actuator Unit: The actuator unit drives with its electromotor and mechanisms the moving platform. The actuator unit consists of an internally redundant brushless-type electromotor, a redundant set of Hall sensors mounted to the motor shaft, a gear train, and three roller screws with nuts that are mounted to the moving platform. The gear/motor assembly rotates the synchronized roller screws. Three roller screw nuts are mounted with a restricted floating capability to a platform, which will move upwards/downwards by the rotating roller screws.
- b) Torque/Force Sensor (TFS): The TFS is an electro-mechanical unit equipped with strain gauges, which measures torques and forces in 6 degrees of freedom. The analog TFS signals will be acquired and processed by the TFS electronics and will be sent via the Electronic Unit to the ERA OBC. The TFS is temperature compensated and is protected against mechanical overloading by rigid end stops. In case the measured function of the TFS is not needed and an increased stiffness for the TFS is required, the TFS will be blocked by the Torque Force Sensor Rigidization Mechanism.
- c) TFS Rigidization Mechanism: The TFS rigidization mechanism (TRM) will block the TFS when its function is not needed. It will automatically form a stiff structure when not in operation and a flexible structure to protect the arm from overloading when disengaged. The TRM consists of the following items:
  - one electrically redundant brushless motor, which is the same as being used for the Actuator Unit and the Integrated Servicing Tool; the motor control is included within the Electronics Unit;
  - one worm gear, to provide the required gear ratio ( $N= 105$ );
  - three conical shaped blocking elements; each of it consisting of a solid inner cone and a flexible, slotted outer cone;
  - a cam wheel, which is driven via the worm gear by the motor; the cam wheel includes three tracks that transform the rotation of the cam wheel into a translational motion of 3 mm;
  - three rods, which transfer the translational motion of 3 mm from the wheel to the inner cones. The rods are connected to the tracks of the cam wheel via deep groove bearings;

The following procedure will be performed to rigidize the end effector:

- The motor will be switched on and turns the cam wheel by 60° clockwise; two mechanical end switches will monitor the starting and the end position.
- The inner cones, connected to the rods will move 3 mm within the outer cones. The movement will cause the expansion of flexible outer cones. This expansion will now block the TFS.
- The TRM will stay in the blocked condition due to the non-backdriveability of a worm gear and the shape of the cam wheel tracks.

For the de-rigidization of the TFS, the cam wheel will be rotated in the opposite direction. The inner cones will be pushed actively by the rods, to allow for the contraction of the flexible outer cone, which consequently will de-block the TFS.

3. Moving Platform The moving platform actuates the grapple mechanisms, performs the Integrated Servicing Tool (IST) head insertion, and mates the system harness connectors (for power, video and data lines). The male connectors will be mated to the female parts located at the Base Point/Grapple. Redundant switches (3 off) are monitoring the platform position to provide status information for the EES electronic unit. Three platform positions shall be reported by this device:

- the upper end position, which will be used for a zero setting
- the position at which the BEE is aligned with the BP/GF, i.e. the gap between the BEE and BP/FG is closed
- the position where the grapple latches are completely closed and pre-stressed. At this position the connector mating and IST head insertion is also performed.

In addition to monitoring by the switches, the platform position is at any time provided by the Hall-effect sensor output signals of the actuator unit motor.

4. Grapple Mechanism: Grapple fixtures (GF) will be mounted to all objects that have to be handled by the EES. Each GF includes the female part of the connector, through which the power, signal and video data is routed to the grappled object. In addition, a GF contains the IST head receptacle, by which the torque will be provided for the grappled object (e.g. to screw/unscrew). The Grapple Mechanism of ERA consist of a three hook/lever systems, which are coupled to the moving platform The grapple mechanisms start pulling at the grapple fixture (GF) or base point (BP) until the gap between the GF/BP and the end effector is closed and the grapple mechanisms are rigidized and pre-tensioned. The hooks of the grapple mechanism are constantly pressed outwards by coil springs. When one hook touches an obstacle during grappling of a grapple fixture (GF) or a base point (BP), the hook induces a force of about 30 N due to the spring deformation to the obstacle. The reaction force will be measured by the TFS, transmitted via the EU to the ERA OBC. The EES will then be re-positioned with respect to the grapple fixture/base point to ease the induced loading.

5. System Harness Connectors Three connectors, which are mounted to the moving platform, will transfer power, video and data between the end effector on one side and the grapple fixture or base point on the other side. The connectors are mounted via floating devices to the moving platform, to provide a lateral and angular misalignment compensating capability. Each connector provides the capability to monitor the mated/unmated status.

6. Integrated Servicing Tool (IST) The IST will be used to provide torque for a grappled object (e. g. to screw/unscrew bolts or a stowed radiator stack). The IST is mounted within the lower end effector compartment. The IST consists of an electrically redundant brushless motor, similar to the actuator unit motor, a gear box, and a tool head with a “pop-in” device. The gear box output shaft drives the IST head, which will be inserted into the IST head receptacle, located at the grapple fixture to provide the mechanical power to the screw interface. The IST drive shaft will be inserted into the receptacle at the grapple fixture during the platform downwards movement.

The IST head will start rotating slowly upon system command, until it pops into the IST head receptacle. If the tool insertion has not been successfully performed immediately during the platform downwards

movement, the IST receptacle provides a compliance capability. A sensor will detect the proper IST head insertion. A redundant set of Hall sensors will provide the necessary data for the Electronics Unit to control the IST actuation.

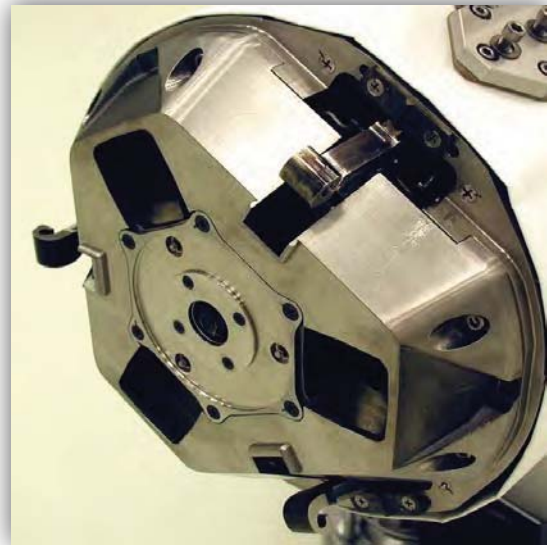
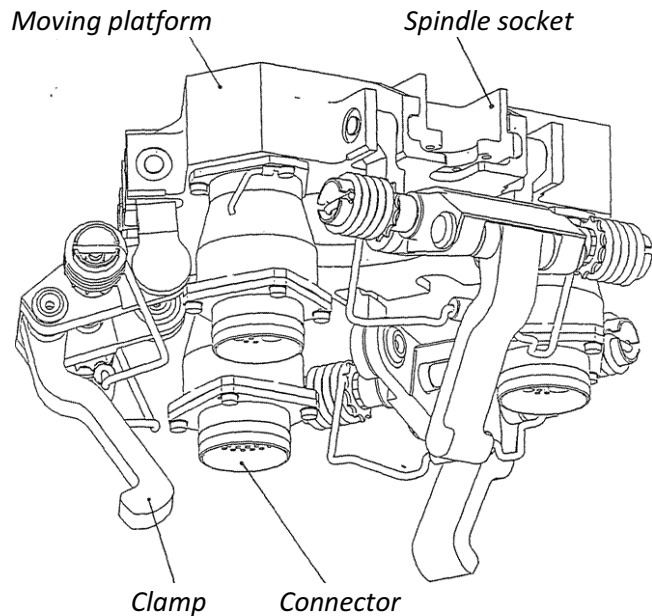


**Figure 2. Grapple mechanism with moving table showing the 3 clamps and 3 connectors (retracted)**

7. Base Points (BP): The base points are mechanically identical to the grapple fixtures. They do not contain the receptacle for the IST but they provide all system harness connections between ERA and the Russian Segment of ISS. They contain the female parts of the three system harness connectors, through which the power, signal and video data for ERA operation are routed. The base points also provide the mechanical interface between the grapple mechanisms on the end effector side and the Russian Segment of ISS on the other side.

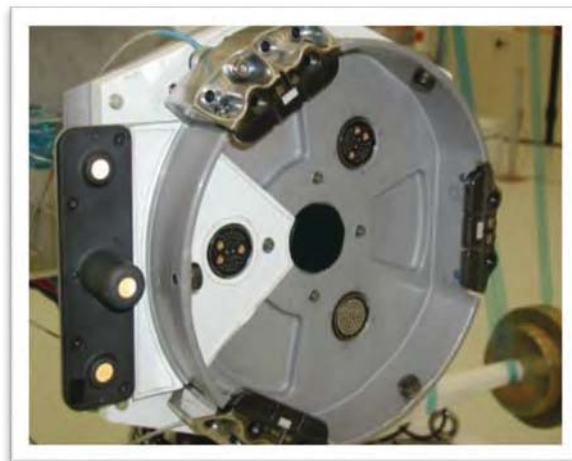


**Figure 3. Base point and engagement hook of end effector**

## Manipulator Joint Subsystem (MJS) Mechanism, Design Details

ERA is approximately 10-m long and has to move large payloads. At the same time, the mass of ERA had to be limited to comply with launch requirements. Its mass is about 620 kg. This makes ERA a much more flexible (elastic) arm than most industrial robots. The first bending mode of the arm is important, as it contains more than 90% of the total inertia. It is the dominant mode to deal with for control. The combination of compactness, limited weight, high stiffness, small backlash, long life time, and thermal vacuum circumstances put high constraints on the development of the joints and the hinge unit.

The wrists and elbow joints are composed of three joints. The pitch and yaw joints are very similar in design. The pitch joint provides a rotation around the Y-axis, the yaw joint around the Z-axis, and the roll X-joint axis. (See Figure 5 below for axis definition).

The wrist contains an electronic box, which drives all the 3 motors independently. Redundancy is included as well in the electronic device via 2 PCBs. Hence, the shoulder joint and the wrist contain a separate electronic box for the drive function, i.e., power and telemetry functions. This is also the case for the elbow. This box is located as a rectangular box in between the limbs and forms part of the structural load path. Hence, the size and the stiffening of the box have been implemented with plates equipped with ribs.

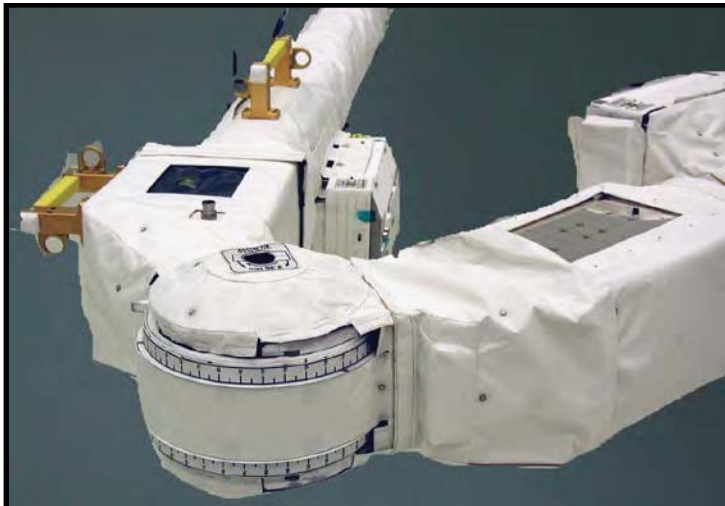


**Figure 4. The elbow joint for pitch motion. Showing the EVA hand rails and the 2 CLU's. In the middle of the hinge is the EVA receptacle hole.**

Each joint consists of the following mechanical elements:

1. Motor unit: Motor, resolver including the Joint Position Sensor for the feedback of the joint position to joint control electronics and brake.
2. Gearbox assembly: Four-stage planetary gear train for torque capability and speed reduction including the bearings including lubrication / grease (N=450)
3. Motor housing and yoke.

In addition, an EVA access provision is included for manual override. Other non-mechanical elements include:

- Cables and connectors; crossing wires passing the joint for external use and entrance wires being connected to electrical components within the joint
- MLI thermal hardware, heaters
- Cable covers / Connector covers.



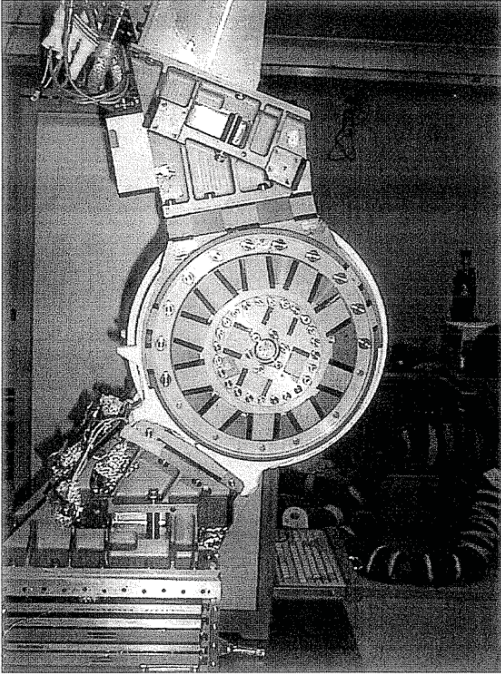


**Figure 5. Elbow joint and brackets launch interfaces; pins and hard plates.**

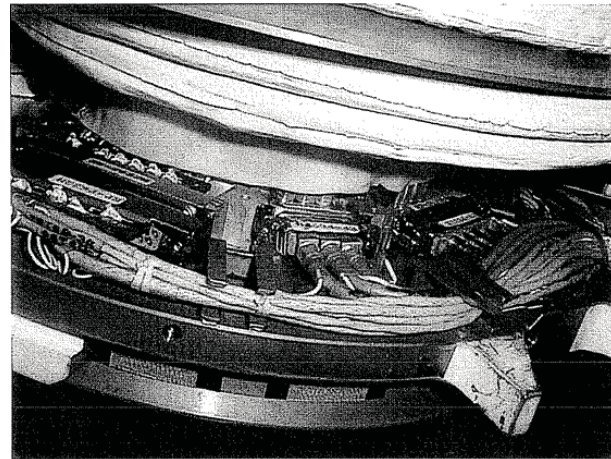


**Figure 6. Elbow joint without cables cover: ribbon cables (data & power) separation wall.**

Details of the mechanical elements are described below.

1) The motor unit: The motor, resolver and brake are integrated as mechanically self-contained device, which interfaces with the Mechanical Unit of the hinge. This unit consists of the following items:

- a) Motor: The motor is based upon a permanent magnet synchronous motor (often called brushless DC motor) and has a two-phase redundant winding. The electronics are adjusted in such a way that the motor provides a ripple-free torque. For this purpose but also for commutation reasons, a resolver is used, providing the instantaneous position information required by the current-torque controller.
- b) Resolver: The resolver is built with a primary winding supplied with a high-frequency voltage, inducing a high-frequency signal in each of the two secondary windings. Both of these signals have an amplitude related directly to the rotor position (e.g., varying respectively with the cosine and sine of the angular position). The analysis of these two signals allows detection of the instantaneous rotor position of the electrical motor drive shaft.
- c) Joint Position Sensor: The sensor measures the angular rotation of the arm joint at the exit axis and provides the angle position input to the joint control electronics. Each Joint Position Sensor contains a redundant set of read stations, light emitting diodes, digital signal processing circuitry, and cable harness.
- d) Brake: A brake is integrated into the joint, providing the braking torque by the contact of two smooth friction surfaces. When the brake coil is not energized, the brakes are engaged, provided by an adequate axial force created by eight dedicated springs (which provide on average a total of approximately 85 N of force). Conversely, the brakes are disengaged by supplying the coil with a constant current, effecting separation of the two braking surfaces by magnetically attracting the moving armature fixed to the axially-translatable brake disc. A microswitch position sensor provides the brake status information (i.e., whether the brake discs are in contact with one

another or separated). This information must be very reliable, as the distance of brake disc separation is on the order of 0.25 mm to 0.30 mm.

## 2) Gear box assembly:

- a) Gear train & bearings: A four-stage planetary gearbox has been chosen with a gear ratio of 1: 450. The gear trains are made from SST. Nitrided steel has been used as gear material. The thermal expansion shall be compatible with the gearwheel material, to keep the influence of thermal deformation on the backlash at the lowest achievable level. Radial deflections at the ends should be small, they are critical for the motor assembly and gearbox. For the gear train, radial deflections affect the backlash; for the motor, they affect the torque ripple due to an adverse effect on the motor resolver.
- b) Number of planet wheels: A strong preference was maintained in the design to apply three planet wheels per stage. This is due to the fact that a three planet wheel system possesses a self-balancing capacity for the loads within the system. This acts as a load distribution system. If more than 3 planet wheels are applied in one carrier, the equal load distribution over the wheels is not ensured automatically. However, to save space, and to make sure that the stress levels do not exceed the maximum allowable Hertzian stress, it was necessary to apply 6 planet wheels in the last stage. To obtain a good load distribution over all 6 planet wheels, the planet wheels are supported by a floating system.
- c) Tandem configuration: Gear stages 1 and 2 share the same ring wheel, as well as stages 3 and 4. Self-adjustment of the stages in one subassembly is improved by this configuration when a torque is applied. In a planetary gear, it is important that the load is distributed equally to the planet wheels to take advantage of the compact arrangement. This can be done by leaving unsupported the sun wheel, the planet wheels carrier assembly, or the ring wheel. The other parts are mutually supported by bearings. In the ERA joint, it was chosen for a floating ring wheel. It can also be considered as a floating planet wheel carrier sun wheel assembly, hence floating with respect to the ring wheel.
- d) The floating component has to be kept aligned with respect to the other gear wheels. In large industrial high-performance gearboxes, this is generally accomplished by the width of the gearwheels. In this case however, the wheel widths are too short for self-aligning per stage. Therefore, two stages are mutually connected by using a common ring wheel. The planet carriers with sun wheels are supporting them mutually by bearings. The self-centering effect of each stage provides the alignment of the assembly, which is called a tandem. The self-aligning effect of a tandem is used to make each set of two gear stages self-supporting. These supports are a flexible plate flexure for the planet carrier sun wheel assembly and a tooth coupling for the ring wheel. Between these interface points there is no connection between the housing and gear train. This ensures isolation from deflections of the housing.
- e) Bearings: The roll joint is equipped with three main bearings: for the radial and axial support one set of two angular contact bearing is used. The single bearing is a deep groove ball bearing which gives only a radial support. The lubrication is with Bray oil. Belleville springs are implemented in the design in order to preload the bearings (to resist launch vibrations). Load on the bearing due to thermal expansion is reduced and is equally distributed on the bearing, due to the lateral elasticity of the yoke fingers that are adapted to the required minimal stiffness.
- f) Flexible elements: The large number of interfacing components inside the joint requires consideration of internal or external disturbances such as :
  - Thermal deformation.
  - Mechanical deformation during launch and during operation.
  - Manufacturing inaccuracies in a statically undetermined support
  - Radial and axial play.

This compensation is realized by the introduction of flexibility to several components. The pitch joint has been equipped with several details by which flexibility is introduced. Because the motor is made of AISI 420 (steel) and the housing material is aluminum, a thermal problem may occur. In order to make it possible that the motor can expand freely, for the coupling between motor and housing the same coupling with square teeth has been used as for the housing and ring wheel connection.

3) Housing and yoke: The yoke structure is replaced by a cylinder rotating around the fixed housing. The hinge construction of the joint consists of two major parts, the housing and the yoke. The housing is the “fixed part”, being the part in which the driving components (gear train and motor) are connected. The yoke is the part that rotates around the housing (the “moving part”). The housing contains the gear train including the EVA-device, the motor, the Joint Position Sensor and cabling. It also supports the main bearings. End stops are incorporated. The housing is designed sufficiently stiff by flanges at the end to reduce radial deflections. Loads shall be transferred with sufficient strength and stiffness of the housing to the main bearings. Care is taken to ensure that loads are equally distributed around the main bearings and excessive loads on the main bearings due to thermal expansion are prevented.

### Launch Fixation mechanism

Launch Configuration: The ERA arm is located in the launch position on this MLM module. Interfaces to the end effector are:

- the Base Points, which are fixed to the Russian Segment of ISS
- the Grapple Fixture, which are fixed to objects to be handled by ERA.

Both base points and grapple fixtures are part of the end effooter subsystem. During launch, both end effectors are grappled to a special base point, each acting as a load suspension system. During the hibernation phases in orbit, both end effectors are also mated to base points. In this configuration all electrical connectors will be mated to the Space Station.

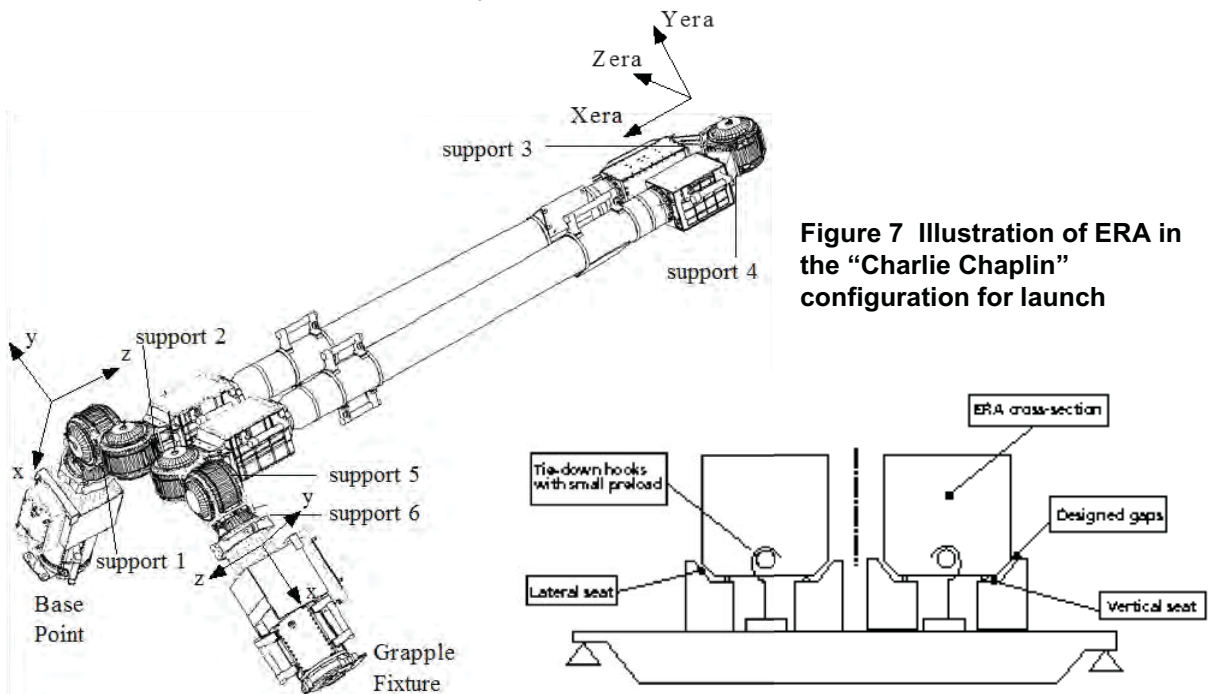


Figure 7 Illustration of ERA in the “Charlie Chaplin” configuration for launch

Figure 8. Schematic illustration of a Launch fixation point for the MLM



***Launch Fixation Mechanism:*** During launch, ERA is configured in its so-called “Charlie Chaplin” configuration (see Fig. 7) and is attached to the MLM by means of six launch fixation mechanisms. Basically, each mechanism consists of one or two EVA-driven hooks to tie down and release ERA from the mounting seats. The hooks are adjustable. The engagement pins on ERA are fixed. The mounting seats are made to fit to minimize the backlash. The preload in the hooks is 500 to 1000 N. Gaps between ERA and its support are introduced in order to allow for easy assembly, to cope with thermal expansion, and to ensure proper release. These attachment points are located at the elbow joint (supports 3 and 4), on the wrist electronic boxes (supports 2 and 5), and on the roll joints (supports 1 and 6). At the Launch BP, the End Effectors are supported in all directions.



**Figure 9. Launch interface points for the MLM**



**Figure 10. ERA integration fit checks on the MLM**

## EVA Compatible Mechanisms, Design Details

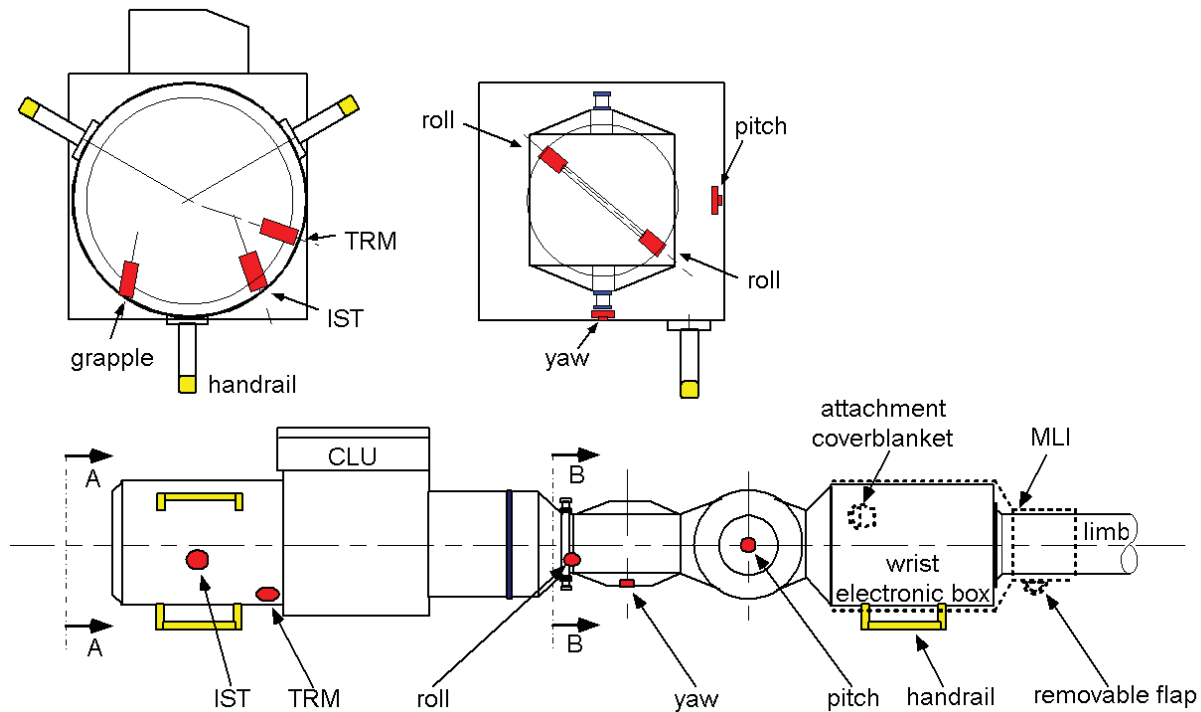


**Figure 11. Location of ERA manual overrides**

*Manual Overrides in the End Effector Subsystem:* An EVA manual override is implemented in the EES Actuator Unit, the Integrated Service Tool (IST) and also for the Torque Force Sensor (TRS) Rigidization Mechanism (TRM). The manual overrides for the Actuator Unit and for the TRM will be blocked during launch to secure the rigidization mechanism is in the closed position. Just after launch during installation of ERA in orbit, the launch lock has to be de-blocked. For de-blocking, the override tool has to be inserted into the 7/16-inch hexagonal receptacle of the Actuator Unit and of the TRM manual override interface. By this first insertion, a pin located within the hexagonal receptacle will be pushed backwards into the de-blocked position. The blocking device ensures that the pin will stay within this de-blocked position during all the following in-orbit operations.

The manual override inlets and position indicators are covered by MLI in order to prevent sun trapping and heat leaks. Before actuating the EVA override, the cosmonauts have to fold back the related parts of the MLI, which then will be secured in the back folded position.

*Manual Overrides in the Manipulator Joint Subsystem:* Each hinge line in the joints contains an override mechanism. The special tooling can be inserted at the locations at the central drive axis. For the pitch and yaw and elbow hinges, the backdriveability is achieved by inserting the pin mechanism in the central hole, directly engaging the electrical motor unit, hence at the input axis. This means that no backdriving of the spur gear is required. For the roll axis, the accessibility of this hinge prevents this approach. A special engage-disengage mechanism ensures that the gear train is by-passed; hence no back driving of this gear train is needed.

As the ERU hinges can also be dismantled from the tube, special bolts are used to allow decoupling. These 6 bolts are accessible via a tool. Handrails are required for momentum equilibrium, when the astronaut is turning these bolts. Again, special tooling is foreseen.



Other EVA interface: Several other interfaces are included to allow opening of MLI blankets, and opening lids of boxes such as the Elbow ERU. Other interfaces which are serviceable are the CLU's. (2 CLUs at the End Effector location as well as the 2 CLUs at the limbs).

### **Qualification Aspects**

Unit Level Qualification Testing: For ERA, a mixture of a normal Qualification Model/Flight Model approach and Proto-flight approach was selected. The Engineering/Qualification models ((EQM) are structurally and thermally representative for the flight standard, but electrically they are built-up from MIL standard B parts. Most of these models do not have complete flight redundancy. Each subsystem has been thoroughly subjected to qualification testing. The testing was first done on subsystem level. Thereafter, the hardware was integrated to form a complete EQM for the system qualification.

System qualification on EQM: Structural and thermal qualification has been done on the EQM. The structural qualification of some external interfaces, which were not possible to test on subsystem level were verified at system level on the flight model. The final end-to-end functional and electrical qualification has been done on the flight model, as only this model contains the Hi-rel Electronic, Electro-Mechanical and Electronic parts, and full redundant electrical circuits.

System-level functional performance testing: For performance testing including alignment, only one plane (the pitch plane) can be tested. The qualification of the three-dimensional robotic operations has been achieved via a combination of two-dimensional tests and three-dimensional simulations with the ERA Simulation Facility.

For functional testing on a flat floor, a special test rig had to be developed. There are 2 versions of this ERA test facility. One rig is for the coarse functional testing and end-to-end performance testing such as grappling. This test set up contains a simple derrick with airpad support near the tip of the arm to allow grappling of a test payload (see Figure 8). For performance measurements, the airpad under the tip was replaced by a more dedicated support vehicle. On this support vehicle, a small flat disc is included which acts as a flat floor on top of the moving flat floor (see Figure 8). The moving carriage is controlled by means of lasers at the corner of the test facility. With this test set-up, calibration of the control model is performed. The following tests have been done:

1. Functional testing:
  - Alignment / Stiffness
  - Free motion control test: for large unconstrained moves, at a safe distance. Feedback will be provided by the encoders.
  - Proximity motion control test: for small unconstrained moves, close to the space station. Feedback will be provided by the encoders in combination with the CLU.
  - Compliant motion test: for constrained moves, very close or in contact with the space station. Feedback will be provided by the encoder, but also the torque force sensor (TFS).
2. Thermal vacuum and thermal balance testing
3. Modal Survey testing and thereafter Boosted Modal Survey testing
4. EMC testing

The functional test with the arm was also done at maximum velocity. These tests were performed with and without payload attached in order to investigate the inertia effects in the control motion software and the response in the hardware. Note that for the functional testing, a protocol has been issued to test the extremities. These tests are executed with and without payload attached to the EES:

- Normal approach mode / fast mode, precision insertion mode
- Contingency mode with EVA
- Safe mode dynamic stopping distance in emergency mode.

The objective of the stopping distance test is to demonstrate that the maximum stopping distance for any part of ERA is maximum 15 cm at a maximum tip velocity of 10 cm/s. The test has been performed with and without a payload grappled to the arm. The measured stopping distances were in the range 4-7.5 cm.



**Figure 8. Moving flat floor disc on large flat floor surface (double decoupled)**

**Boosted Modal Survey:** The aim of the boosted modal survey test was the qualification of the interfaces between ERA and the launcher in terms of proto-flight limit loads. Modes measured during the low-level modal survey test were selected in order to achieve qualification loads at the interfaces by exciting these modes on a high excitation level. Not all predicted qualification levels could be reached since the behavior of the test structure was extremely non-linear. The source of the non-linearity was investigated by additional test runs. The non-linearity was caused by interface conditions, which depend on the loads applied on the ERA. Moreover, the dynamics of ERA were characterized by hammering noises at high excitation levels. The elbow interfaces could be completely qualified during the Boosted Modal Survey testing. Qualification was not feasible for some components of the other interfaces especially for the axial components. Additional static strength tests were performed to complete the qualification. From the boosted modal survey test it could be deduced that the modal parameters like the mode shapes and Eigen frequencies found in the modal survey test do not apply for ERA under high overall launch loads. Thus, they are not directly applicable for the validation of the finite element model. However, qualification was feasible for the lateral components. Qualification for the axial components was expected to be difficult to achieve and turned out to not be feasible. In order to qualify these components, a separate static test was required and performed.

**Finite Element Analysis:** Control performances such as tracking and positioning must rely on good modeling of the arm dynamics. This part is mainly determined by the flexibility in the limbs and the controlled joint behavior. Extensive finite elements analysis with the NASTRAN tool forms the basis for providing model data for the limbs in a multi-body dynamics model within ERA Simulation Facility. For final validation of the modeled flexible behavior of the arm, the real arm will be kicked during test and the position is measured. During this test the joints are not active, and the brakes will be on. The controlled behavior of the joints is mainly driven by the properties of the gearbox. The final achieved backlash including any hysteresis effects was less than 1 mrad.

Flight Acceptance testing: Each subsystem has been thoroughly subjected to flight acceptance testing. The testing was first done on subsystem level. Thereafter, similar functional testing has been executed as done for the EQM.

EVA check by cosmonaut: On the ERA EQM, an astronaut “walk-around” was performed as part of the ERA Critical Design Review. This was the first time that cosmonauts saw the full-sized ERA arm (previously only the MMIs had been seen by cosmonauts). The ERA arm was set in a typical operational pose. In particular, the EVA overrides for all ERA mechanisms, the labels/markings, and the EVA handrails and tether eyes, were presented (MLI was fitted at representative places). No major problems were identified.

### **Lessons Learned**

The Boosted Modal Survey testing can be a good alternative, but keep in mind:

- Non-linear behavior in launch configuration; Hammering (deflections are larger than gaps). Slip and stick motion (frequency change, damping). The qualification may only be partly possible, still requiring static strength testing necessary for other interface points.
- Assessment on non-linearity and damping to find the correct excitation levels / internal loads
- Care should be taken to prevent any over testing.

### **Conclusions**

The ERA arm has been subjected to a rigorous test program on the subsystems and for the EQM. The mechanisms have been designed for EVA and specific tests have been executed to demonstrate this aspect. The flight model has undergone functional testing and integration testing with the MLM. Spare ERA parts have already been launched upfront to the ISS in 2010. The flight model is now ready for final integration on the MLM and launch in 2015.

### **References**

1. *ERA EQM and Flight Model Test Results* by P. Verzijden, W. Admiraal, J. Kouwen, Dutch Space, The Netherlands, ASTRA 2000.
2. *ERA test results Astra 98; Nov 98: Fokker Space BV. C. Hofkamp and P. Verzijden, and J. Schawer DASA; D. Verhoeven; SABCA.*
3. *ERA test philosophy and results: IAF-99-T.2.06; R. Blommenstijn, C. Hofkamp, P. Verzijden.*
4. *Boosted Modal Survey Test on the European Robotic Arm, E. van de Heuvel, G. Glot., M. Degener, 4th International Symposium on Environmental Testing for Space Programmes, Liege 2001.*
5. *Kampen, S., Mandersloot, W., Thirkettle, A., Bentall, R.H., The European Robotic Arm and its role as part of the Russian Segment of the International Space Station Alpha, IAF-95-T.3.03, 46th Int. Astronautical Congress, Oct 2-6, 1995, Oslo, Norway.*
6. *ERA Performance measurements test results, P. Verzijden, H. Petersen, M. Visser, Proceedings of the 7th ESA Workshop on Advanced Space Technologies for Robotics and Automation; ASTRA 2002.*
7. *The ERA System: Control Architecture and Performances Results, F. Didot, M. Oort, J. Kouwen, P. Verzijden, in: Proceedings of the Sixth International Symposium on Artificial intelligence, Research & Development in Space, I-SAIRAS 2001 Conference, Montréal, Canada, June 2001*
8. *Thermal Balance Testing of the European Robotic Arm, E. v.d. Heuvel, J. Doornink, in: 4th International Symposium on Environmental Testing for Space Programmes, ESA SP-467, Liège, Belgium, June 2001*
9. *ERA EQM and Flight Model test results, P. Verzijden, W.J. Admiraal, J. Kouwen, in: Proceedings of the 6th ESA workshop on Advanced Space Technologies for Robotic Applications ‘ASTRA 2000’*
10. *Thermal Balance Testing of the ERA; Jan Doornink, John Kanis and Eduard van den Heuvel, Fokker Space B.V. Leiden, The Netherlands, Giovanni Colangelo ESA/ESTEC Noordwijk, The Netherlands.*
11. *ICES 2000 - Thermal Testing I - Spacecraft & Instrument Testing - ES14A paper no.001CES-83.*

12. *How to build a Space Robot; ERA Lessons Learned, M. Oort, F. Meiboom, C. Heemskerk, in: Proceedings of the 6th ESA workshop on Advanced Space Technologies for Robotic Applications; ASTRA 2000.*

## GPM Solar Array Gravity Negated Deployment Testing

Jonathan Penn\*, Chris Johnson\*, Jesse Lewis\*\*, Trevin Dear\*\* and Alphonso Stewart\*\*

### Abstract

NASA Goddard Space Flight Center (GSFC) successfully developed a g-negation support system for use on the solar arrays of the Global Precipitation Measurement (GPM) Satellite. This system provides full deployment capability at the subsystem and observatory levels. In addition, the system provides capability for deployed configuration first mode frequency verification testing. The system consists of air pads, a support structure, an air supply, and support tables. The g-negation support system was used to support all deployment activities for flight solar array deployment testing.

### Introduction

Global Precipitation Measurement (GPM) is a satellite developed in partnership between NASA and the Japanese Aerospace Exploration Agency (JAXA) to advance scientific understanding of the Earth's water cycles and help forecast extreme climate events.

GPM is the successor to the Tropical Rainfall Measuring Mission (TRMM) that was launched in 1997. Just as for TRMM, GPM depends on solar arrays to deploy once in orbit to provide power. GPM requires a significantly larger amount of power than its predecessor and was designed with a Solar Array Deployment and Drive System (SADDS) that provides approximately 1.75 times more energy. This larger and more efficient array consists of two wings each with four panels per side.



Figure 1. Rendering of GPM in Orbit



Figure 2. Walk Out of Flight GPM Solar Array

One of the challenges at NASA GSFC has been to negate the effects of gravity during deployment testing of the SADDS since it cannot support its own weight in a 1-g environment. The ability to “g-negate” allows the engineers to verify the SADDS deployment capability before and after environmental tests and again prior to launch when fully integrated to the spacecraft. The solar arrays are required to deploy in less than 300 seconds. A consistent time within 10% of baseline performance is required to evaluate performance changes. At full deployment, all hinge hardstops must be contacting and all hinge latches engaged. The

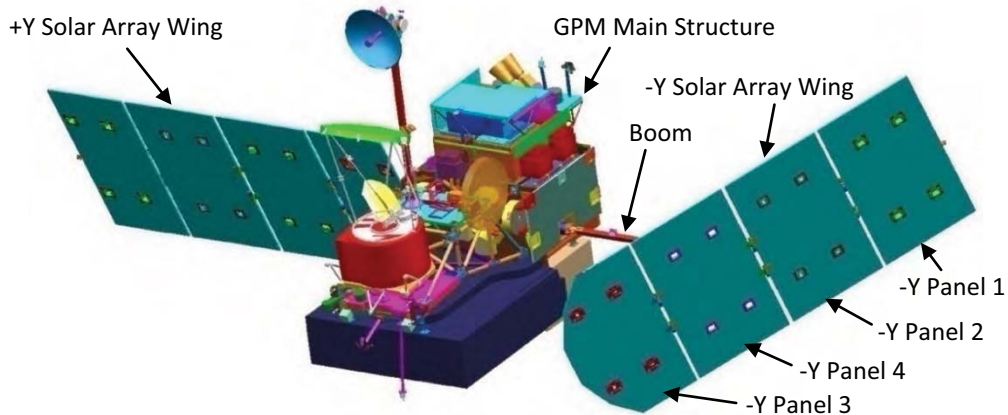
\* Stinger Ghaffarian Technologies, Greenbelt, MD

\*\* NASA Goddard Space Flight Center, Greenbelt, MD



g-negation support system must not compromise the electrostatic sensitivity or contamination requirements of the spacecraft and must be compliant with use on the GPM spacecraft.

The GPM Solar Arrays consist of two Solar Array Wings with one installed to each of the +Y and -Y sides of the GPM Spacecraft. Each Solar Array has a boom that extends approximately 3 m (10 ft) and attaches to the center of four panels. Each panel is approximately 1.5 m (5 ft) by 2.75 m (9 ft) aluminum honeycomb with carbon fiber face sheets. Separately, each Solar Array wing weighs about 177 kg (390 lb). Compared to its predecessor satellite TRMM, GPM's Solar Arrays have about two times the mass.



At the time of publication the SADDs has been shipped to Japan on the GPM Spacecraft for a 2014 launch. Prior to shipment, each wing underwent environmental testing, multiple walk outs, and four official deployment tests. Through the process of developing the g-negation system and working through issues as they arose during deployment testing valuable lessons learned were discovered which are described herein.

## Background

Each of the GPM solar array wing assemblies deploys in the same relative sequence. As such, and because only one wing would be deployed at any given time for testing, only one g-negation system needed to be developed. Initial concepts for the g-negation system included a table system which supported the wing assembly from below and an overhead gantry system which supported the wing assembly from above. Previous GSFC projects TRMM and X-ray Timing Explorer (XTE) had successfully employed table systems that supported the deployable subsystem using air pads. As a result of these prior efforts, air system advantages and disadvantages were fairly well known and additional consideration was given to an overhead gantry system. Gantry research and development was short-lived however, due primarily to the multi-directional deployment sequence and path of the wing assembly panels as shown in Figure 4.

The solar array panel deployment sequence and path would demand a relatively elaborate overhead tracking system. Additionally, that system could neither introduce significant deployment friction nor influence the wing's deployment path in either an inhibitive or assistive manner. Thus, the need for an uninfluenced deployment path eliminated the early gantry concepts and refocused the development on table systems. Furthermore, minimal system friction was more likely to be achieved on the table surface by using an air pad system. Due to the long moment arm created by each Solar Array's wing span, even the small amount of friction created by a castor-supported system could have overwhelmed the solar array wing hinge springs.

Once the decision was made to pursue an air pad table system, the natural progression was to adapt and refine the table system used by the aforementioned spacecraft's TRMM and XTE. Custom tables and air pads were developed for XTE and these would also be employed by GPM. While the table system

concept was very simply a flat level surface big enough for the deployment area, it was required to be modular to facilitate movement within Goddard and to the launch facility at JAXA. The deployment table was an assembly of several tables. Each table was a 1.22 m (4 ft) by 2.44 m (8 ft) aluminum face sheet honeycomb panel on an aluminum frame and legs. Unfortunately, these tables had warped and worn over time and use. Alternative tables were researched but facility compatible materials and weight limits for mobility restricted selection. Cost was an additional constraint restricting table replacement and refurbishment. It was, in result, determined to be most suitable to proceed with the heritage tables and air pads and tailor both for GPM's needs.

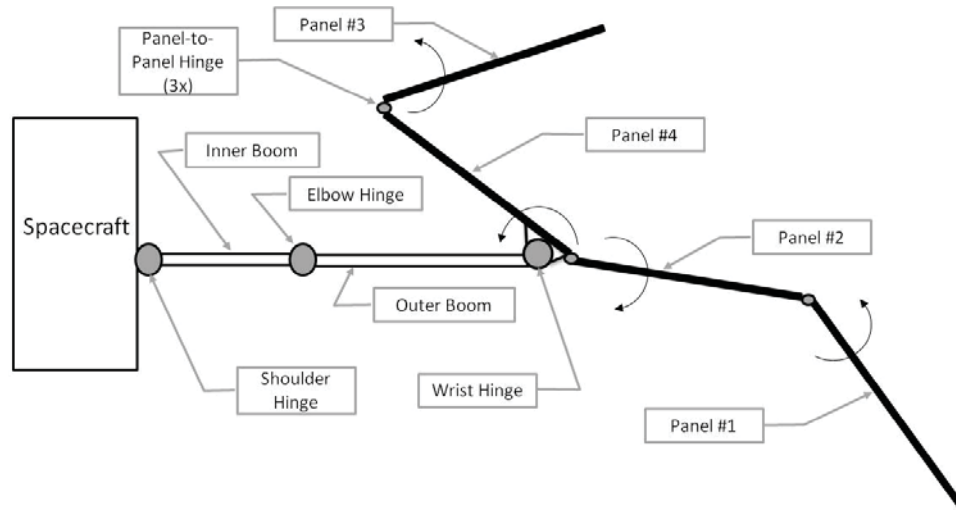


**Figure 4. Solar Array Deployment Path**

### Design and Development

Once the decision was made to use the air pads and deployment tables, the next step was to design additional assemblies that would adapt this hardware to the GPM Solar Array's geometry. This section details how the air pads and deployment tables were optimized and interfaced to the GPM Solar Array to create a working g-negation system.

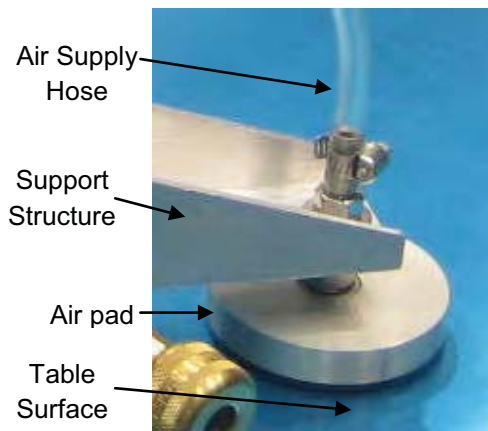


**Figure 5. Air Pad**



**Figure 6. Set of Four Deployment Tables**

#### Air pad Development

To evaluate air pad capabilities, weights were loaded onto structures supported by the same number of total air pads expected to be used on a flight Solar Array Wing and the air flow was opened fully. The

intent of this was to compare the maximum capability of the air supply with the weight of the Solar Array Wing. Unfortunately a problem was encountered as the weight was increased.

Simply increasing the airflow was not sufficient to increase the load capability because the air pads would start to chatter at high frequency once the weight reached a certain threshold. The air pads were acting as air motors, storing and releasing energy from their plenums causing them to rise and fall. The time delay in filling and emptying the plenums caused a time lag between the air flow into the plenums and the resulting pressure buildup below the air outlets. This pressure buildup inside the plenum increased the flow rate through the air outlets, which in turn increased the air pressure below the outlets, increasing the upward force on the load, raising the load, which lowered the pressure below the pad.

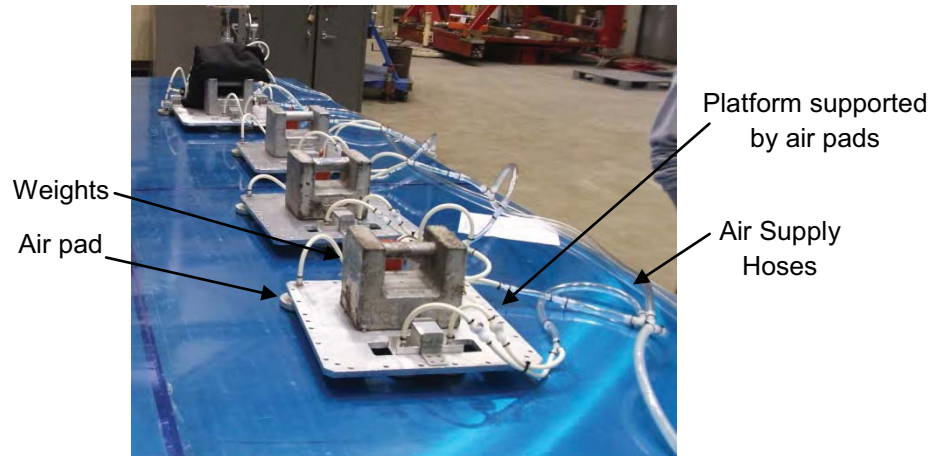


**Figure 7. Air Pad Capability Test**

This chatter was unacceptable as it would introduce friction preventing ground deployment of the Solar Array Wing. The solution was counterintuitive: the team blocked half of the air outlet holes on the bottom of the airpads and eliminated the chatter. This moved the major pressure drop to the air outlets. With the absolute pressure ratio at these outlets now above the critical ratio (0.528 for air), the air velocity through the air outlets rises to Mach 1, and no downstream air pressure changes below the air pads can affect the flow rate. With the pneumatic feedback loop broken, no instability is possible. Once this design fix was implemented it was determined that our facilities could supply enough air to lift the weight of a Solar Array Wing with a 40% margin.

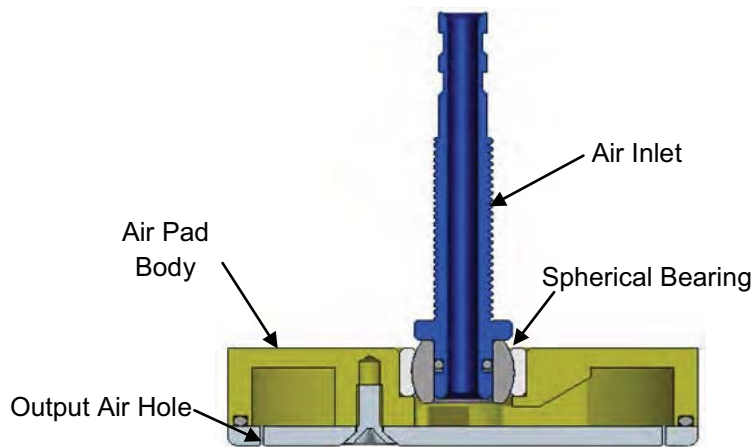


**Figure 8. Air Pad Cross-Section**

### Panel and Boom Supports

A support structure was designed to ensure that the Solar Array Wing had sufficient support to prevent tipping but did not become over-constrained and bind up during deployment. Four panel supports were built that each captured the lower Ground Support Equipment (GSE) attachment inserts of its respective mating panel, shown in Figure 9. Two of the panel supports also had a strut extending to an upper GSE attachment location to stabilize the array against tipping, shown in Figure 10. An additional support was also designed for the boom. The supports were optimized for an even load distribution among 19 air pads, shown in Figure 12. In some cases two or three airpads were placed directly next to one another to support a higher load and were coupled with a universal joint to avoid over constraint. Mockup panels were used to evaluate system performance prior to installing to the ETU assembly.

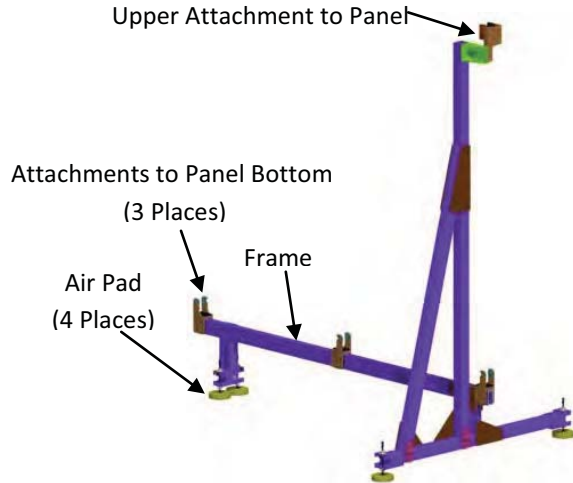


Figure 9. Panel 1 Support

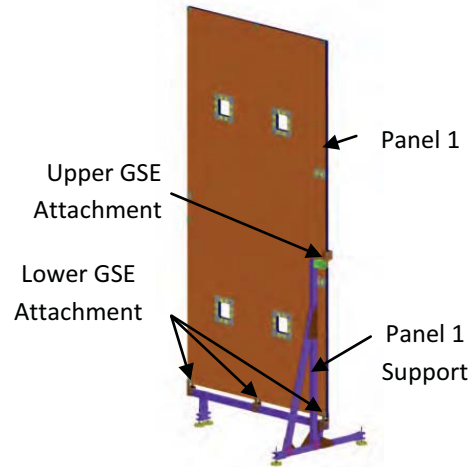


Figure 10. Panel 1 Mounted to Support

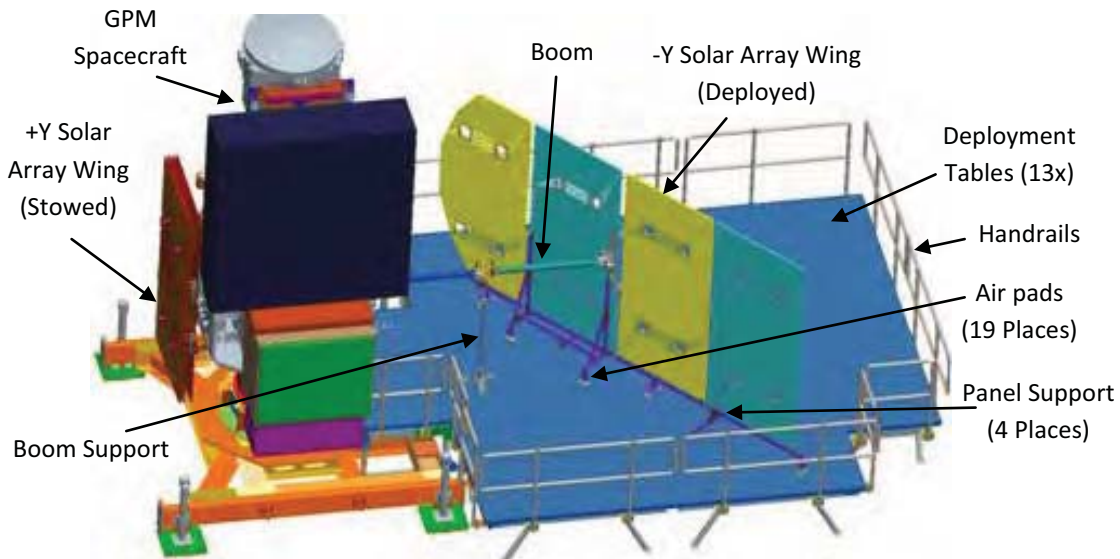
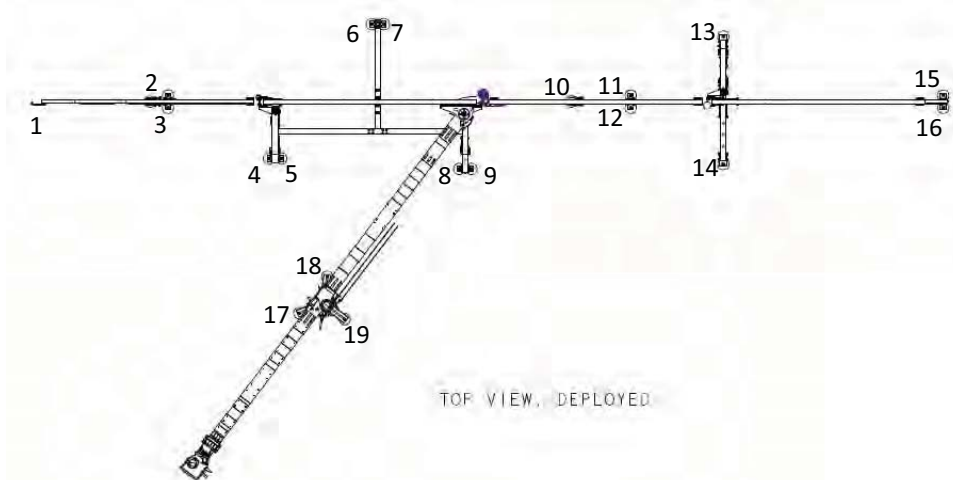


Figure 11. G-Negation System installed to -Y Solar Array Wing



**Figure 12. G-Negation System Air Pad Locations**

Deployment Tables

Problems were experienced immediately on the first tests performed with mockup Solar Array Panels attached to panel supports even though the air pad capability testing proved that the air flow was sufficient to carry a much higher mass. The deployment tables, being over 20 years old, had spent considerable time in storage and warping had occurred on their 1.22 m (4 ft) by 2.44 m (8 ft) honeycomb panel top surfaces. Getting the seams of two tables aligned well was in some cases difficult, and getting all the seams aligned with the full array of 16 tables was not possible. The resulting height differences along the seams of adjacent tables resulted in increased friction or even blocked Air Pad travel. The problem was compounded when multiple air pads attempted to traverse seams at the same time. This table misalignment is illustrated in Figure 13.

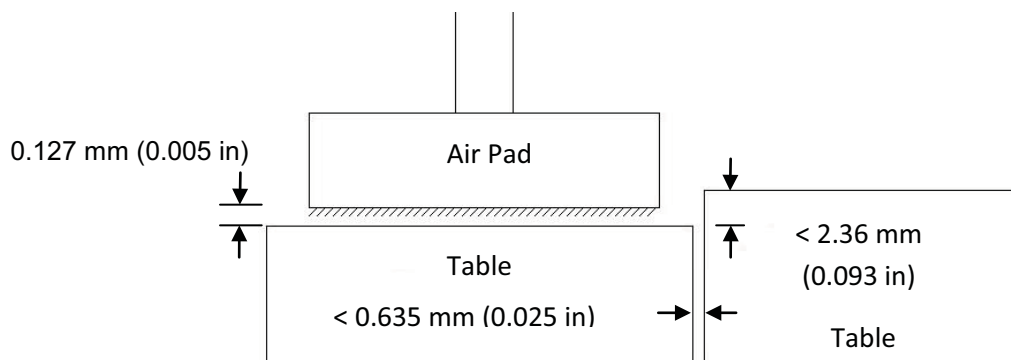


**Figure 13. Table Misalignment (Height Differential)**

Much time and effort was spent optimizing the alignment between tables, however, the team reached a point where any improvement achieved at one location was at the expense of another. It was decided at this point to experiment with laying various materials across the tables to bridge the seams and reduce the effect of the misalignments. It was found that one particular vinyl flooring material vastly improved performance. The reason this particular vinyl material helped so much was not yet fully understood and this topic is discussed in greater depth later in this paper.

With the addition of the table surface cover to the table assembly, table leveling and alignment was revisited. With the table surface cover reducing the misalignment effect at the table-to-table seams, the need for near perfect seam alignment was no longer necessary. Instead, a “best fit” approach to lining up the seams was employed. First, each of the 12 main tables was placed in the appropriate relative



position, shown in Figure 14. Using a laser level and a target block, the first table, table 2 as seen in Figure 14, was leveled by placing the laser on one corner and the target block on the diagonally opposed corner. The target block was then relocated to the opposing corner of table 10 and was leveled relative to table 2. All table leveling was performed at the floor using an adjustable foot at the bottom of each table leg. Following the leveling of table 10 relative to 2, table 11 was leveled relative to 2. Tables 3, 12 and 13 were done similarly. All adjacent tables in between were then leveled and adjusted from level in order to “best fit” their edges and seams to those of the corner tables. Table edge height was assessed by feel across the top surface, from one table to the next. The final step was to bring into position the front table, table 1, and level it to the table assembly. Following leveling and seam adjustment, each table was bolted to the adjacent table(s) to tighten the table seams, stabilize table position, and stabilize the overall table assembly. Once set up was complete, the table assembly was ready for the table surface cover. With the surface cover in place, table set up could be verified with system walk-outs and hand release deployments. Through iterative hand release deployments and adjustments, the table assembly could be optimized for deployment tests. Perhaps the most critical of tables was table 1, seen in Figure 14, which was at the spacecraft interface that supported the entire wing in its stowed state. Deployment time and path were sensitive to the transition of the panels and the elbow support stand across that first seam.

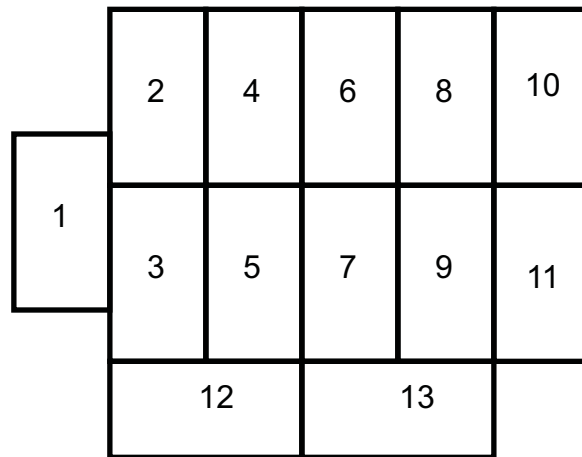


**Figure 14. Table Assembly Layout**

Of equal importance was the adjustment of the g-negation support frames and their respective air pads such that system loads were evenly distributed across all air pads to prevent overloading of any sub-group of air pads. G-negation frames could be adjusted at the interface to the air pads to add or relieve load at pad locations. In this fashion, frame or pad to table interface was optimized at the time of frame installation to the stowed wing assembly. Air pad heights were adjusted so that there was free rotational spin at each pad. Inability to easily rotate any air pad indicated that pad was carrying too much load. Easy rotation and wobble at any air pad indicated that the pad had too much clearance from the table surface and was not loaded enough. Adjustments to the respective frame(s) and pads were made accordingly. Upon release of wing preload and system walk-out, hand release or official deployment, adjustments could be made for further system optimization. This was possible by either adjusting both g-negation frames and air pads, or by adjusting the tables themselves to change table pitch or seam interface issues.

Additionally, the wing itself could be adjusted by modifying the pitch or roll of the spacecraft dolly. This however had to be done with the wing in the stowed position and was only to be done if the dolly was not level in either regard. Spacecraft dolly position and adjustment is covered later in more detail. Of course, proper initial set up would alleviate need for post release adjustments. As such, once the system was refined and understood, initial set up was efficient and all that was required. This was verified through successful post-test deployments which could not be preceded by verification walk outs. Following

successful deployment testing with the mock up panels, the team felt that the development stage was complete. The team was ready to implement the G-Negation System on the Flight Solar Array Wing.

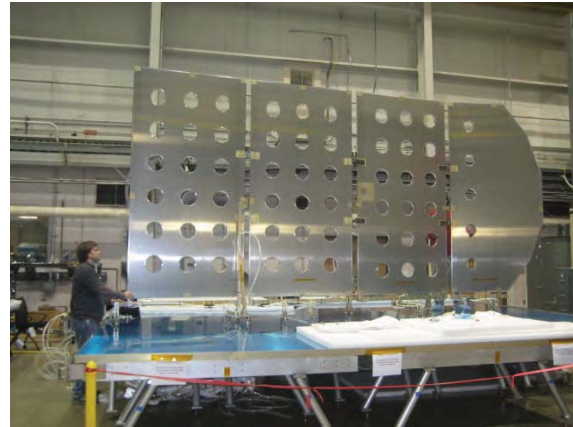


**Figure 15. Testing with Mockup Panels**



**Figure 16. Tables with Vinyl Covering**



**Figure 17. Qual Solar Array Test**

### Adaptation to the Cleanroom

In order to utilize the g-negation system on the flight Solar Array Wings, it was necessary to replace the vinyl surface cover with a low outgassing substitute. Another requirement was the need to dissipate electrostatic charge created by airflow out of the air pads. The particular vinyl used during development testing had specific properties that made it work successfully. This vinyl had a softer lower layer that conformed to the height difference between two tables and a harder layer on top that provided a good ride surface for the air pads, seen in Figure 18.

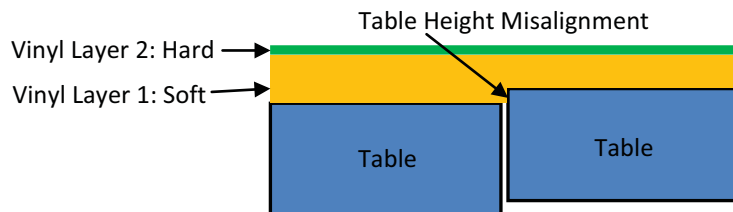


**Figure 18. Vinyl Surface Covering**

After extensive research only two alternatives were found with similar properties to the soft layer of vinyl. The first, Viton Foam, was prohibitively expensive; the amount of material needed to cover the table surface would have cost over \$100k. The second, Poron 4701-30, a material made by Roger's Corporation that is commonly used in aerospace applications was adopted, and large rolls were purchased.

In order to replace the hard layer of vinyl, another material was chosen to place on top of the Poron 4701-30. The material was a 0.254-mm (0.010-in) thick layer of Melinex 515. This material was selected because it could be supplied with a vapor-deposited aluminum (VDA) coating that dissipated the electro-static charge created by the air pads. The combination of these two materials provided a unique solution of soft and hard material properties to properly absorb floor imperfections while simultaneously being able to support the air pads.

Each material was ordered and delivered in factory available sheet sizes. In order to lay out each material on the table, the factory rolls needed to be cut into specific sizes and shapes and placed side by side to fit the table. This was done offline. Once the materials were cleaned and rolled for transport into the cleanroom assembly began.

The cut Poron 4701-30 strips were laid out such that their seams did not overlap the table seams. The Melinex 515 strips were then laid out such that their seams did not overlap the Poron 4701-30 seams. The Melinex 515 seams were then taped using 3M40 tape to prevent air pressure from lifting the strips between the seams. The 3M40 tape was chosen because it has the benefit of dissipating electrostatic build up between any seams of the Melinex 515 or defects in the material. It should be noted that the Poron 4701-30 strips were not taped between the seams to prevent tearing due to the fragility of the material. The layout can be seen in Figure 19.



**Figure 19. Air Pad Gliding on Melinex 515 and Poron 4701-30**

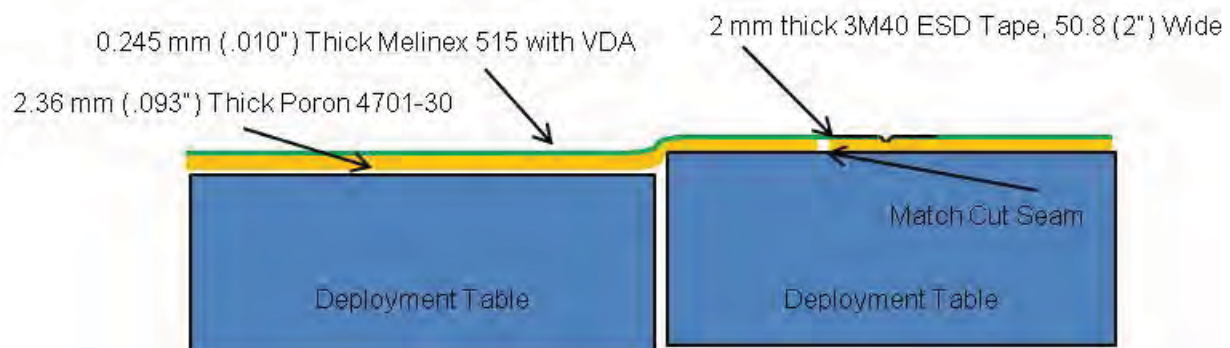


**Figure 20. G-Negation Table Layers**

The finished solar array flooring product is a 20 x 25 foot surface made up of thirteen 8 x 4 foot tables. The tables are first covered by 2.36-mm (0.093-in) thick Poron 4701-30 foam and then topped by 0.254-mm (0.010-in) thick Melinex 515 coated with vapor deposited aluminum and taped together with 2-mm-thick 3M40 ESD tape.



**Figure 21. G-negation Table with Melinex 515 and Poron 4701-30**

Figure 21 shows the completed solar array deployment table surface. The picture portrays the surface such that bubble effects can be seen, however these are an optical illusion due to the reflectivity of the VDA coating on the Melinex 515. Touching the material verifies that there will be no air bubbles in the Poron and Melinex 515 layers once allowed to settle for 24 hours. Minor remaining air bubbles that exist can be pushed out by the test article during testing.

Overall this solution for g-negation worked very well for the largest rigid solar array system built at Goddard Space Flight Center.

### **G-Negation Deployment System Installation Challenges**

While the initial development testing of the air pad system was successful of supporting a higher mass than required, careful implementation of the system with the Solar Arrays was necessary to achieve required performance. The two characteristics used to assess the performance of the solar array deployment system are the total deployment time and deployment path. The deployment time and path varied with characteristics of the g-negation installation specifically in the areas of hose routing and the dolly alignment to the g-negation tables.

During initial testing of the solar array design while working on the protoflight boom assembly, it was found that the deployment time varied greatly with changes in the pitch angle,  $\theta_p$ , between the deployed boom axis and the deployment tables. Initial testing showed any angle outside  $-0.10^\circ$  to  $+0.10^\circ$ , at the shoulder hinge, produced deployments that were longer than expected. Likewise, small changes in the roll angle,  $\theta_R$ , of the shoulder hinge provided variable deployment paths.

The offset in pitch was evident upon visual inspection of the boom hardstops after the deployment finished. A gap at the upper hardstop and contact at the lower hardstop indicates that the pitch angle is greater than zero and the array is attempting to deploy against gravity. A gap at the lower hardstop and contact at the upper hardstop indicates a pitch angle less than zero and that the array is attempting to deploy into the g-negation tables and binding the air pads. Adjusting the pitch angle within  $\pm 0.10^\circ$ , and as close to zero as possible, closed the gap at the hardstops and provided a significantly faster deployment.



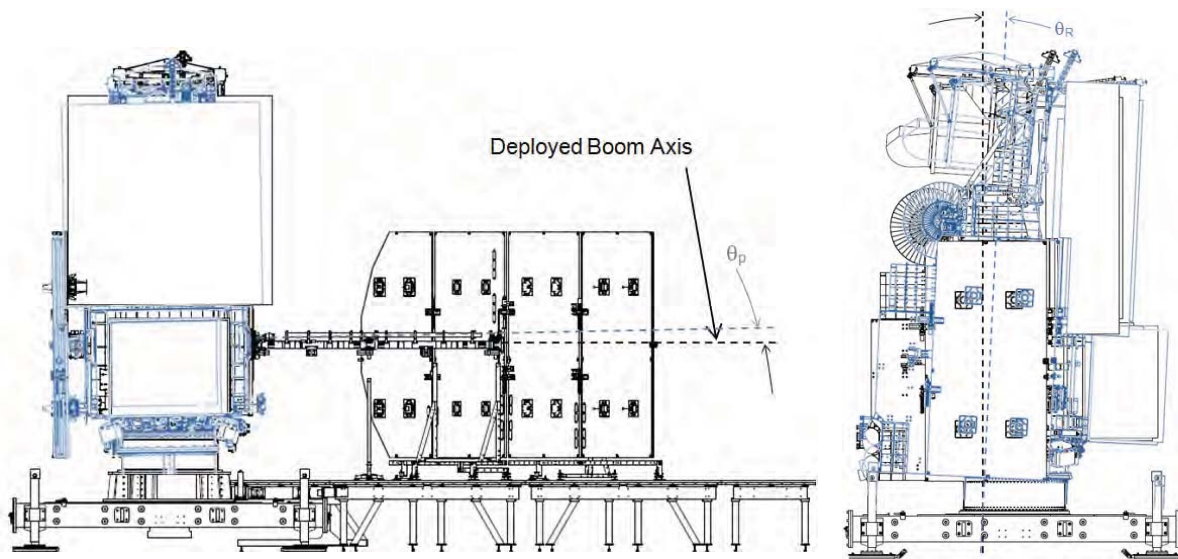


**Figure 22. Definition of Pitch, Left, and Roll, Right.**

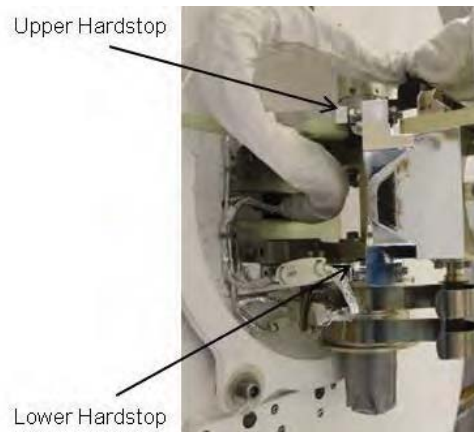


**Figure 23. Dual Hardstop Design of Boom Hinges**

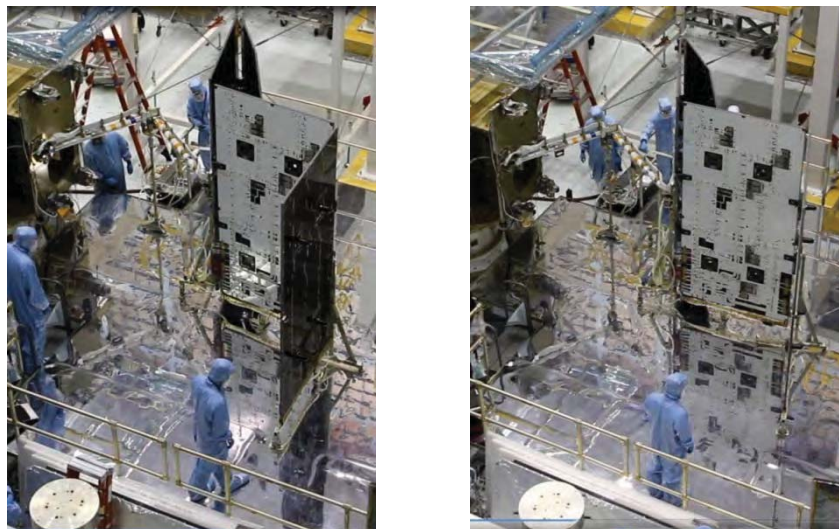


**Figure 24. Excessive roll angle (left), No roll angle (right)**



Likewise, small changes in the roll angle,  $\theta_R$ , of the shoulder hinge provided variable deployment paths. This was evident during the -Y Solar Array's post-vibe deployments. The deployment dolly was inadvertently misaligned and the post-vibe deployment took a much different path than the pre-vibe deployment, resulting in a stalled deployment on a highly warped g-negation table that was specifically placed in a spot where we did not expect the deployment to reach based on pre-vibe results. In Figure 24, at the identical time in deployment, the different deployment trajectories can be seen. With  $\theta_R$  being out of spec by approximately  $\pm 0.10^\circ$ , we can see that the wing is not deployed as much as in the case with less or virtually no roll angle. This deployment with excessive roll angle continues on a path uncharacteristic of the expected deployment. To adjust for pitch and roll, the dolly jacks at each corner of the spacecraft dolly were manipulated.



**Figure 25. Roll Angle Measurement at the Shoulder Hinge**

To achieve an optimal setup for a post-vibe deployment, the pitch and roll angles were measured and adjusted closest to the deployment root hinge, the shoulder hinge, while the arrays were stowed. Figure 25 shows the location that we could measure directly on the shoulder hinge to assess roll. Due to the tight packaging of the stowed array, the closest area we could measure pitch was across the two solar array booms between the Shoulder Hinge and the Elbow Hinge, as seen in Figure 26. A Digi-pas brand 2-axis precision digital level with an accuracy of  $0.01^\circ$  was used for these measurements.



**Figure 26. Pitch Angle Measurement on Deployment Boom**

The air hose configuration of the g-negation system, as seen in Figure 27, is nebulous in design and was photographed repeatedly from different vantage points to achieve a repeatable system. Slight changes in the air routing had the same effects as slight changes in the pitch and roll angle with respect to changing the deployment path and deployment time by generating friction at points in the system different from the desired baseline.

By keeping accurate records of the pitch and roll angles as well as the g-negation hose routing, the solar array deployment times and deployment paths were in family. Telemetry graphs from the +Y Solar Array Wing observatory level pre-vibe and pre-ship deployments, illustrated in Figure 28 and Figure 29, show only a 3 second difference in deployment time, a 2.91% difference, and similar angular velocity characteristics between these two different deployment setups performed 3 months apart

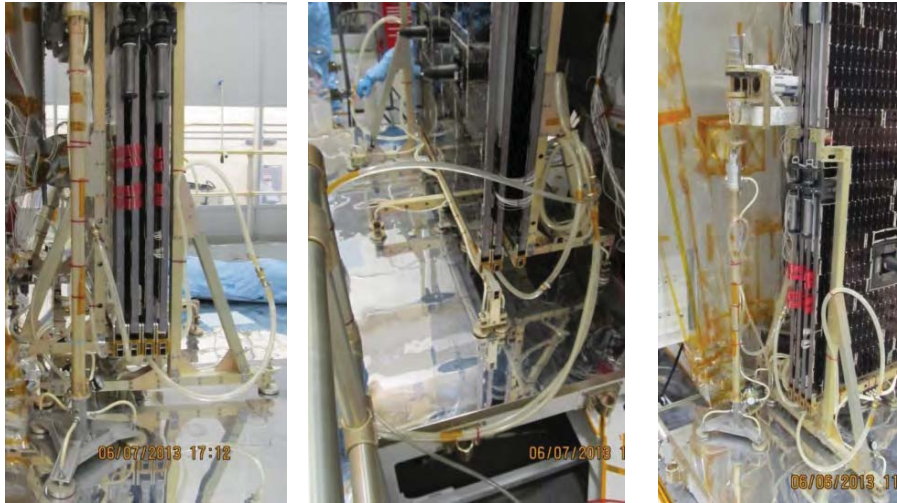


Figure 27. G-negation hose routing documentation

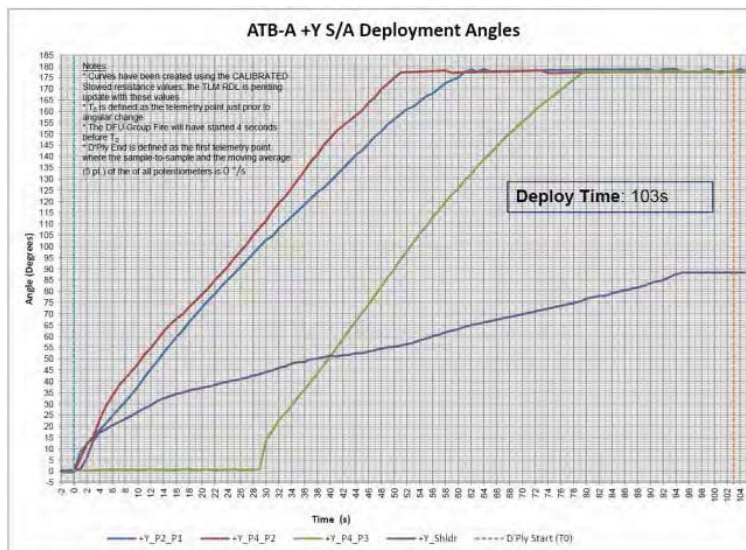


Figure 28. Pre Vibe +Y Wing Deployment Telemetry Comparison, +Y Wing

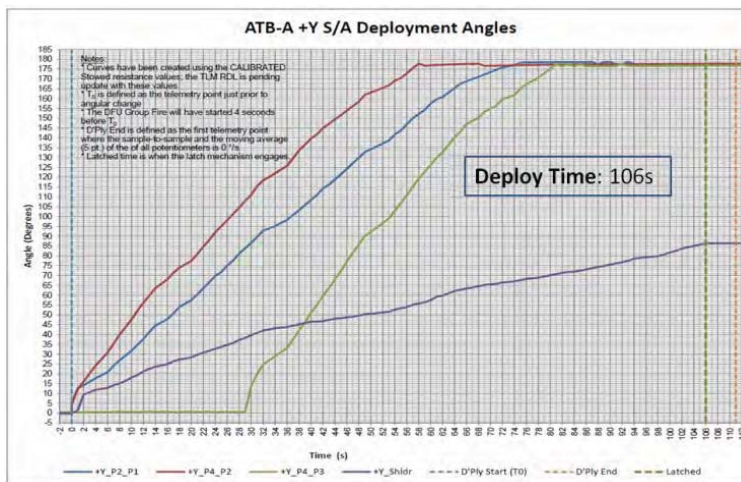


Figure 29. Pre-Ship +Y Wing Deployment Telemetry Comparison

## Ability to Perform First Mode Fundamental Frequency Verification

One of the advantages of the air pad system was that it accommodated first mode frequency verification testing. The Qual -Y Solar Array Wing was configured in the deployed position and a direct measurement of the frequency was able to be performed by placing and releasing side load and examining the oscillating motion of the wing while supported by the airpads. Since the airpads induce almost zero friction and the measured value was found to be close to the predict, the analytical model was verified showing that the Solar Array meets its frequency requirement (Rivera). This test method was found to be more straightforward than others that required suspending the solar array from a cord and performing a twang test as has been used for other projects (Jiang and Gahart).

## Conclusion

In summary, many challenges were overcome developing a system to g-negate the GPM Solar Array Wings so that their ability to deploy once in orbit could be adequately verified. It was decided to implement heritage design air pads even though this type of system had only been used for solar array wings much smaller than those of GPM at NASA GSFC. During this process, it was verified that the facility being used had sufficient air flow and the air pads were optimized to carry the required load. A new support structure was designed in order to capture GSE points on the panels to prevent tipping and allow movement along a flat table surface with the use of air pads. Testing of this design with mass models and full-size mock-ups made it clear that the deployment tables being used, inherited from previous projects, provided an insufficient surface for deployment due to warping of the table top from previous use. Also, difficulties associated with aligning the large array of tables proved inadequate to accommodate the Solar Array's full deployment path. Creative solutions were adopted first to align and provide a surface cover to adequately improve the table surface to allow the Solar Array Wing to deploy. Solutions were also found to modify the table covering to work in the clean room and to dissipating electrostatic charge due to flow from the air pads. Once the table and surface cover solutions were found, additional testing of Solar Array deployments revealed the sensitivity to both the alignment of the wing in pitch and roll and to the air hose routing. Because of these sensitivities, techniques were developed to normalize these parameters. Finally, it was found that this g-negation system was well suited to support first mode fundamental frequency testing. The result of the work involved in developing this system was that the GPM Solar Array Wings were successfully verified through multiple deployment tests while installed to the flight Spacecraft.

## References

1. Rivera, Alejandro, *GPM-SADDS-RPT-0144 - Solar Array Fundamental Frequency Test Results*, <https://gpmmis.nasa.gov/> (accessed 1/8/2014)
2. Jiang and Gahart, *Analysis and Modal Survey Test of Intelsat VIIA Deployed Solar Array*, <http://web.mscsoftware.com/support/library/conf/wuc94/p02794.pdf> (accessed 1/8/2014)

Contributors: Majdi Mukhar, Mike Mutaku, Dick McBirney, Jenny Xu, Robbie Robinson, John Tota, Andrew Scharmann, Chris Matthews, Nick Kwiatkowski, Gary Sheridan, Rodger Farley

# A Recommended New Approach on Motorization Ratio Calculations of Stepper Motors

Ruben Nalbandian\*, Thierry Blais\*\* and Richard Horth†

## Abstract

Stepper motors are widely used on most spacecraft mechanisms requiring repeatable and reliable performance. The unique detent torque characteristics of these type of motors makes them behave differently when subjected to low duty cycle excitations where the applied driving pulses are only energized for a fraction of the pulse duration. This phenomenon is even more pronounced in discrete permanent magnet stepper motors used in the space industry. While the inherent high detent properties of discrete permanent magnets provide desirable unpowered holding performance characteristics, it results in unique behavior especially in low duty cycles. Notably, the running torque reduces quickly to the unpowered holding torque when the duty cycle is reduced. The space industry's accepted methodology of calculating the Motorization Ratio (or Torque Margin) is more applicable to systems where the power is continuously applied to the motor coils like brushless DC motors where the cogging torques are low enough not to affect the linear performance of the motors as a function of applied current.

This paper summarizes the theoretical and experimental studies performed on a number of space-qualified motors under different pulse rates and duty cycles. It is the intention of this paper to introduce a new approach to calculate the Motorization Ratios for discrete permanent magnet steppers under all full and partial duty cycle regimes. The recommended approach defines two distinct relationships to calculate the Motorization Ratio for 100 percent duty cycle and partial duty cycle, when the motor detent (unpowered holding torque) is the main contributor to holding position. These two computations reflect accurately the stepper motor physical behavior as a function of the command phase (ON versus OFF times of the pulses), pointing out how the torque contributors combine.

Important points highlighted under this study are the torque margin computations, in particular for well characterized mechanisms. The rationale at CDR level versus TRR/TRB level will be discussed, aiming at avoiding too much conservatism for units that have extensive test and in flight heritage. A critical topic is related to the magnetic losses and how to sort out such phenomena as a function of the motor type being used. For instance, detent torque is a major contributor that has no reason to evolve during life and is not an uncontrolled torque loss.

## Introduction

A large number of space based mechanisms use stepper motors. They are simple, low cost and reliable. There are several different types of stepper motors, each with different characteristics. The type of stepper motor discussed in this paper is the discrete permanent magnet stepper motor. Its rotor has a discrete magnet for each pole as opposed to a hybrid stepper motor that has only one annulus magnet in its rotor. The specificity of this type of stepper motor is that it exhibits large detent torque, as implemented in the well-known MOOG Type 3 and Type 5 Rotary Actuators and also by MDA for robotics applications.

This detent torque is very useful to hold payloads in position without power when not moving. The effects on the torque produced and the computed Motorization Ratio of different power on duty cycles is

---

\* Moog, Inc., Chatsworth, CA

\*\* Astrium SAS, Toulouse, France

† MDA Corporation, Montreal, Canada



discussed. Different Motorization Ratio computations are compared. Finally, a new motorization ratio computation is proposed.

### Background

The three main institutional bodies that overlook space-based mechanisms are: NASA, ESA and AIAA. They each recommend slightly different methods of computing the margin on electrically driven drives. The three methods are presented below:

#### Presentation of Different Motorization Ratio Requirements

##### (1) NASA-STD-5017

$$\text{Operating Torque Margin} = \frac{\text{Available Driving Torque}}{\text{Total Resisting Torque}} - 1$$

When test verified, an operating torque/force margin of 1.0 or greater is required at all applicable points of travel. Only verification by analysis shall require prior review and approval.

##### (2) ESA - ECSS-E-ST-33-01C

**Table 1. Recommended Theoretical and Measured Uncertainty Factors**

Component of resistance	Symbol	Theoretical Factor	Measured Factor
Inertia	<i>I</i>	1.1	1.1
Spring	<i>S</i>	1.2	1.2
Motor magnetic losses	<i>HM</i>	1.5	1.2
Friction	<i>FR</i>	3	1.5
Hysteresis	<i>Hy</i>	3	1.5
Others (Harness)	<i>HA</i>	3	1.5
Adhesion	<i>HD</i>	3	3

The minimum actuation torque ( $T_{min}$ ) shall be derived by the equation:

$$T_{min} = 2 \times (1.1I + 1.2S + 1.5H_M + 3F_R + 3H_Y + 3H_A + 3H_D) + 1.25T_D + T_L$$

Where:

- $I$  is the inertial torque applied to a mechanism subjected to acceleration in an inertial frame of reference (e.g. spinning spacecraft, payload or other).
- $T_D$  is the inertial resistance torque caused by the worst-case acceleration function specified by the customer at the mechanism level.
- $T_L$  is the deliverable output torque, when specified by the customer.



(3) AIAA-S-114-2005

**Table 2. Minimum Recommended Static Torque or Force Margin for New Designs**

<b>Design Phase</b>	<b>Force or Torque Margin</b>
Conceptual Design Review	175%
Preliminary Design Review	150%
Critical Design Review	125%
Acceptance/Qualification Test	100%

The static torque margin shall be expressed in percentage and is calculated as follows:

$$\% = \left[ \frac{\text{Drive torque}}{\text{Resisting torque}} - 1 \right] \times 100$$

The three methods of calculating Motorization Ratios (MR) as described above are the most widely accepted in the space industry. However, each method results in different ratios. It is quite obvious that defining a standard way of calculating MR to be applicable to every motor technology, design maturity level, and duty cycle is very challenging and not practical, resulting in unnecessary high level of conservatism, especially for well proven heritage designs.

**Effects of Power Off Time on Output Torque and MR**

Extensive testing has shown that output torque drops from the 100% duty cycle value to the unpowered holding torque and below as the time off duration is increased. As expected, when power is removed from the motor, only the magnetic torque prevents the motor rotor from backdriving under the drive train windup torque. It all becomes a question of timing. If the power is removed long enough for the rotor to move back by more than one step, then when the power comes back on to command the rotor to move to the next step, it is too late and the motor loses synchronization.

**Effects of Maturity and Heritage and Available Power on Required MR**

The rotary actuators discussed are of MOOG Type 3 and Type 5 family and have extensive in flight heritage and have gone through several life tests. Each of the life tests have proven that the rotary actuator internal losses do not increase with time in vacuum or mechanical use. The most recent life test on a Moog Type3 actuator accumulated 5.3 million output degrees of motion without any sign of degradation.

The consistency of measured threshold voltage/current throughout the life program at hot, cold and ambient conditions, especially the consistency of the initial functional and final functional is indicative of the fact that the internal losses did not increase after exposure to thermal vacuum and mechanical environments of the life test.

Rotary actuators of this design are also very simple, only one reduction stage (160:1) with the minimum number of bearings and gear meshes.

**Table 3. Summary of Life Test Threshold Voltage Results (Type 3 actuator)**

Test Condition	Primary		Redundant	
	CW	CCW	CW	CCW
Initial Functional @ 22.3°C	11.01	11.00	11.11	11.10
One Times Life @ 107.1°C	13.00	14.00	12.40	13.20
One Times Life @ -54.3°C	10.00	9.50	9.50	9.50
One and a Half Times Life @ 25.1°C	11.61	11.92	11.60	11.62
Final Functional @ 24.2°C	11.30	11.30	11.30	11.20
<b>Partial Disassembly and Examination</b>				
Initial Functional @ 24.6°C	11.40	11.70	11.20	11.60
Initial Functional in Vacuum @ 19.7°C	11.30	11.30	11.50	11.70
One Times Life @ 106.2°C	12.70	13.50	12.60	13.60
One Times Life @ -54.1°C	9.50	9.40	9.50	9.40
One and a Half Times Life @ 105.4°C	12.50	13.20	12.80	13.50
One and a Half Times Life @ -53.7°C	9.80	9.70	9.80	9.80
One and a Half Times Life @ 22.6°C	11.70	11.60	11.50	11.70
Final Functional @ 21.7°C	11.00	11.20	11.00	11.10

**Table 4. Summary of Life Test Threshold voltage Variations**

Condition	Max. Threshold Voltage	Min. Threshold Voltage	Ave. Threshold Voltage	Percent Variation
<b>Ambient</b>	11.7	11.00	11.4	<b>3.0</b>
<b>HOT</b>	14.0	12.50	13.1	<b>5.2</b>
<b>COLD</b>	10.0	9.40	9.6	<b>4.2</b>

**Table 5. Summary of Life Test Threshold Current Results**

Test Step	Motor Housing	Threshold Voltage		Threshold Current		Delta/mean value	
	Temperature	CW	CCW	CW	CCW	CW	CCW
	°C	(V)	(V)	(mA)	(mA)	(mA)	(mA)
Initial functional testing	22.3	11.0	11.0	175	175	-1.1	-2.6
One Times Life testing @ HOT	107.1	13.0	14.0	152	164	4.3	4.7
One Times Life testing @ COLD	-54.3	10.0	9.5	212	203	4.3	-0.3
One and a Half Times Life @ AMB	25.1	11.6	11.9	179	184	2.9	6.4
Final functional testing	24.2	11.3	11.3	178	177	1.9	-0.6
Initial functional testing	24.6	11.4	11.7	173	178	-3.1	0.4
Initial functional testing in vacuum @ AMBIENT	19.7	11.3	11.3	174	174	-2.1	-3.6
One Times Life testing @ HOT	106.2	12.7	13.5	144	158	-3.7	-1.3
One Times Life testing @ COLD	-54.1	9.5	9.4	202	199	-5.7	-4.3
One and a Half Times Life @ HOT	105-4	12.5	13.2	147	156	-0.7	-3.3
One and a Half Times Life @ COLD	-53.7	9.8	9.7	209	206	1.3	4.7
One and a Half Times Life @ AMB	22.6	11.7	11.6	180	178	3.9	0.4
Final functional testing	21.7	11.0	11.2	174	177	-2.1	-0.6

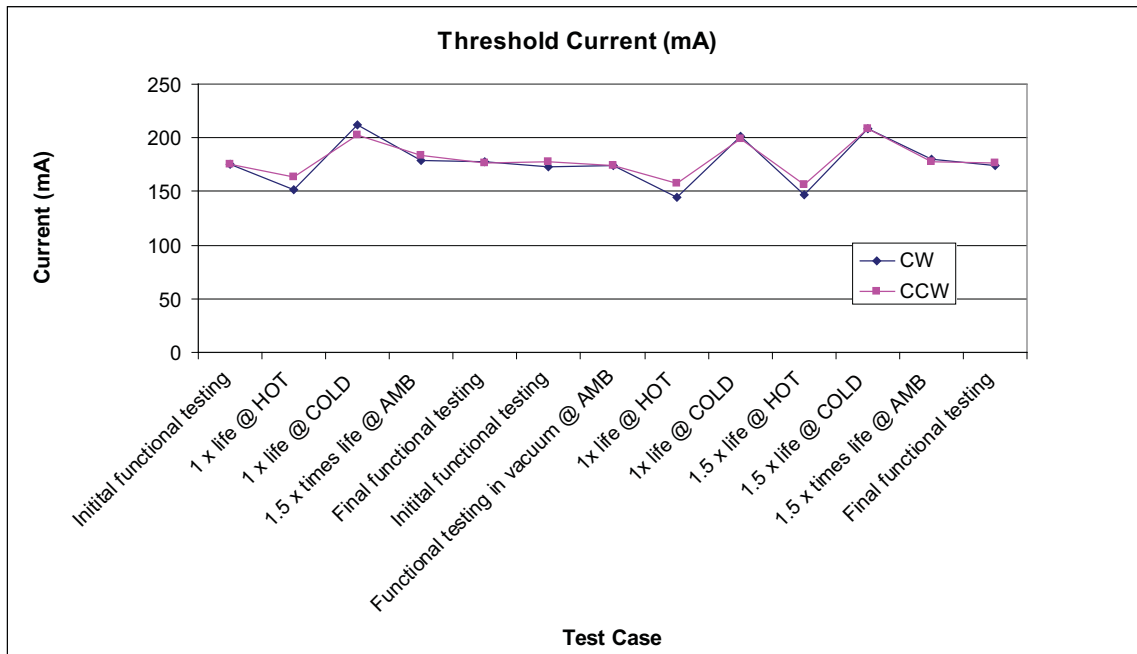


**Figure 1. Life Test Threshold Current Results**

## Space Robotics Example

Other important parameters to take into account when determining what motorization ratio is sufficient is the available power compared to the size of the mechanism and the simplicity of the electric motor used.

When relatively large amounts of power are available and the motor is a brushless DC from which the torque versus speed curve is well known, a reduced motorization ratio might be contemplated.

As an example of this, the drive trains of the Latching End Effector (LEE) of the Space Station Remote Manipulator System (SSRMS) are presented with their characteristics and margins. The SSRMS has been in orbit since April 2001 and has been performing nominally even if its motorization ratios during the design phase were relatively low compared to current requirements.



**Figure 2. SSRMS LEE in orbit** (Courtesy of MDA Corp)

The LEEs have three separate mechanisms each containing complex drive trains. The first mechanism is the snare, it rotates a ring on which cables are attached and permits to snare the grapple probe of the Grapple Fixture (GF) affixed to a payload. The second mechanism is the rigidized mechanism, it pulls back a 45-lbf (200-N) carriage inside the LEE which contains the snare mechanism and applies up to 1,800-lbf (8,000-N) axial preload between the LEE end ring and the GF. This is sufficient to handle small payloads. The third mechanism is the latch; it adds 15,000 lbf (67,000 N) of axial preload between the LEE end ring and the GF to permit handling large payloads and also mates and umbilical. The complete system is designed to fully capture a 100,000-kg space shuttle in 30 seconds. The available electrical power to perform this feat is 300 W. Pictures of each drive train gearbox are presented in Figures 3 and 4.



**Figure 3. SSRMS LEE Snare Gearbox, Scale: OD = 4.86 inches (0.123 m)** (Courtesy of MDA Corp)



**Figure 4. SSRMS LEE Rigidized Gearbox With Ballscrew, Scale: ballscrew = 18-in long (46 cm)**  
(Courtesy of MDA Corp)

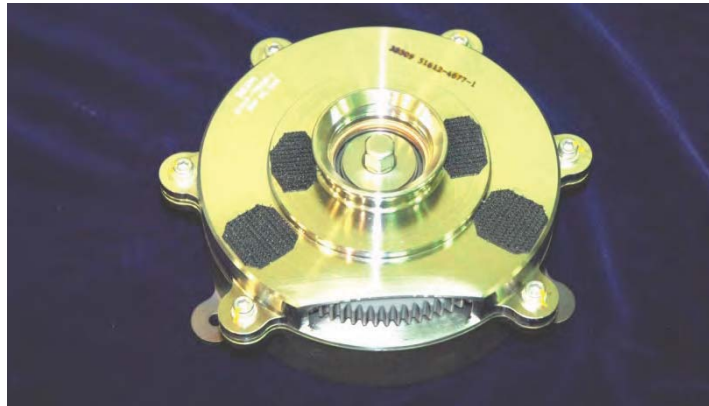


**Figure 5. SSRMS LEE Latch Gearbox, Scale: OD = 5.4 in (14 cm)** (Courtesy of MDA Corp)

The characteristics of each drive train are presented in Table 6. As can be seen in Table 6, during the design phase, the required worst-case torque margins were only 10%. The estimated worst-case torque margins were only 16% for two of the three mechanisms. This compared to the institutional minimum requirement of between 100% and 200%. This is evidence that it is possible to design successful mechanisms with much lower motorization ratios than currently required.

The authors do not believe the same Motorization Ratio should apply to the above designs as that of a newly designed complex multi-stage low-power drive train that has never flown.

#### **Effects of Different External Load Characteristics**

External loads may have different characteristics when applied to the output of the actuators. Pure resistive torques (friction), only resist to the actuator applied output torque. As soon as the actuator stops, the resistive torque drops to zero, as the pure frictional torque only opposes motion.

Spring, dynamical oscillatory response, and gravity torques are very different than the pure friction torques; they remain even when the motion command has stopped. That is why when the applied torque is removed by removing power to the windings, the gravity or the wind-up spring torque may overcome the unpowered holding torque and back-drive the stepper motor. This phenomenon has been investigated by conducting multiple tests at reduced duty cycles when power is removed for a proportion of the pulse period. The effect of the temperature on the performance of actuator for reduced duty cycle has been studied to select an acceptable and appropriate correction factor.



**Table 6. Drive Train Characteristics**

	Gear Ratio	No of Stages	No of gears	No of bearings	Required Torque Margin on nominal case	Estimated Torque Margin on nominal case	Required Torque Margin on Worst Case	Estimated Torque Margin on Worst Case
<b>Snare</b>	230:1	3 planetary, 2 spur	21	19	100%	NA	10%	252%
<b>Rigidize</b>	11.6:1	1 spur, 2 planetary, 1 ballscrew*	15	19	100%	414%	10%	16.7%
<b>Latch</b>	10.2:1	2 planetary, 2 spur, 4 ballscrews*	19	25	100%	134%	10%	16%

\*ballscrew pitch: 0.2 in/rev (5 mm/rev)

**Measuring Torque at Reduced Duty Cycle on Moog Type 3 Actuators**

Background

Moog has measured torque outputs of Type 3 Actuators using two different heritage testing methods.

The first method was to measure the reduced duty cycle torque using a standard torque transducer and magnetic particle brake. In this method, the load applied is increased on the magnetic particle brake until the actuator stalls. This method tends to measure a torque a little less than unpowered holding torque and is a result of the unpowered holding torque and wind-up in the actuator and the test stand.

The second heritage method to measure torque of the actuator at reduced duty cycle was to add weight to a moment arm and gradually add more weight until the actuator backdrives. The results of this test correlated with the unpowered holding torque. When in the power OFF phase, the moment works against the unpowered holding torque. Beyond this level, backdriving occurs. This testing was done at numerous reduced duty cycles at 1 PPS and at 10 PPS. It was shown that the motor and actuator unpowered detents correlate. The values obtained were in the 22.6 N-m (200 lb-in) range (motor level testing showed 14 N-cm, which with a 160:1 gear reduction would result in 22.6 N-m at the output).

Discussion

Both of the methods described in the background section above are thwarted because the dynamic, static and loss loads are combined into a torque that has a 3 times factor on it. This requires the actuator to overcome the torque at both the powered portion of the pulse and the unpowered portion of the pulse. Since movement of the actuator occurs only during the powered portion of the pulse, the demonstrated torque should be 3 X (IL + RT + IT), where IL is internal loss, RT is resistive torque, and IT is a calculated torque from the inertia load. During the unpowered portion of the pulse, the unpowered holding torque needs to hold only the maximum static load, which is the resistive torque and the addition of the inertial torque.

To further pinpoint the problem, internal loss (actuator output turning) is only present during the powered pulse and is not present when the actuator is at the unpowered portion of the pulse (non-dynamic). Inertia is present during actuator powered portion (motion) and the unpowered portion (dynamical response) of the pulse. Accurate measurement of torque during the powered portion of the pulse is needed to be able to show compliance.

## Proposed Motorization Ratio Computation Method for Low Duty Cycle

The Rotary Actuator shall have its powered output torque high enough to successfully operate without adding or losing steps with a minimum motorization margin of 200%, i.e., the ratio of the powered output torque to the total resistive torque at actuator output shaft level shall be greater than 3:1. To that extent, the following two complementary approaches are usually considered:

- Either “mechanism design-oriented” approach: motorization margin shall be sufficient during the design phase considering all contributors – such as IL (internal losses) and customer needs (RT and IT). This is relevant at Critical Design Review
- Or “mechanism user-oriented” approach: motorization margins shall be sufficient to cover possible evolutions of internal properties (IL) and customer needs (RT and IT). This is particularly relevant for mechanisms featuring significant heritage at Acceptance Testing

As the pulse shape has a great influence on the powered output torque, the motorization margin shall be determined in two phases; at Critical Design Review and at Acceptance Testing:

Also, the motorization ratio computation shall properly reflect the two drive possibilities:

- When driven at 100% duty cycle (see DMR formula hereafter);
- When driven at low duty cycle (see DMR & SMR formula hereafter)

### Motorization Ratio Calculations:

- i) When driven at 100 % duty cycle, the so called dynamic motorization ratio (DMR) shall be determined as follows:

$$\text{DMR} = \frac{\text{ART}_{100} - 0.5 \times \text{IL}}{(\text{IT} + \text{RT})} > 3$$

where:

- $\text{ART}_{100}$ : minimum actuator running torque when driven by pulses at 100% duty cycle under any operational conditions. *At CDR,  $\text{ART}_{100}$  is a predicted value by analysis, and during Test  $\text{ART}_{100}$  is a measured value.*
- IL: internal losses due to friction
- IT: inertial torque
- RT: resistive torque

Concerning the DMR, it could be noticed that:

- The formula is relevant during the ON time when the pulse is applied – so not only for the 100% duty cycle case. However, the most reliable way to measure the DMR is to drive the actuator at 100% duty cycle
- The  $\text{ART}_{100}$  is obtained with nominal values as per manufacturing (i.e.,  $1 \times \text{IL}$ ). In order to anticipate any detrimental evolution, an uncertainty factor of 1.5 on IL is considered as per ESA Table 1. The difference corresponds to the term “ $0.5 \times \text{IL}$ ” subtracted in DMR formula numerator.
- The minimum DMR value corresponds to the motor location/step featuring the **highest** detent torque. So it shall be measured at least over a complete motor revolution – and preferably 2 revs.

- ii) When driven at low duty cycle, the rotary actuator is holding during the unpowered time of pulses on its motor detent torque. The unpowered portion of the pulse is the static part of the actuator torque holding capability. The internal loss should not be considered when the actuator is unpowered since it is a result of actuator stepping. Both resistive and inertial torques should use the static motorization ratio (SMR) formula and should be as follows:

$$\text{SMR} = \frac{\text{CF} * (\text{UHT})}{(\text{IT} + \text{RT})} > 3$$

Where:

UHT= Actuator Unpowered Holding Torque Nm (in-lb)

IT = Inertial Torque at output

RT = Resistive Torque

CF = Correction Factor. *CF accounts for loss of holding torque when power is removed while there is some residual kinetic energy*

One can notice that the minimum SMR will correspond to the motor step/location featuring the **minimum** detent torque. To that extent, the SMR shall be determined step by step over at least one motor rev (2 revs preferably), with a sufficient OFF time between each step.

The DMR and SMR are therefore relying on complementary properties of the motor, in particular the mapping of the detent torque over one motor rev. The ideal motor would feature a ratio close to 1 between maximum and minimum values of the detent torque over one rev – as the maximum detent is detrimental to DMR and the minimum detent is detrimental to the SMR. This reflects how accurately the motor is controlled by design and by manufacturing.

### Testing and Results:

#### Unpowered Detent Torque

As stated above, moment arm testing at 1 PPS and 10 PPS at numerous reduced duty cycle values yielded the minimum unpowered holding torque values as the actuator's torque output. These results showed that the actuator could only demonstrate torques less than the unpowered holding torque levels during the un-powered portion of a reduced duty cycle. The test results have fidelity to 0.5 N-m and do not take into account the friction, any wind-up of the torque transducer and couplings between the moment arm and the actuator.

It was demonstrated that the decrease of torque below the unpowered holding torque was caused by a dynamic component with regards to powered cardinal position versus unpowered holding position, test equipment (couplings and torque transducer), harmonic drive wind-up, possible inertia dynamics, and temperature of operation.

**Table 7. Moment Arm (Pendulum) Test Results**

SPEED (PPS)	DUTY CYCLE (%)	DUTY CYCLE (msec)	VOLTAGE (Vdc)	TORQUE PRIMARY (CW) Nm (lb-in)	TORQUE PRIMARY (CCW) Nm (lb-in)	TORQUE RED. (CW) Nm (lb-in)	TORQUE RED. (CCW) Nm (lb-in)
1	4	40	23.13	21.5(190)	21.5(190)	21.5(190)	21.5(190)
1	5.1	51	23.13	21.5(190)	22.6(200)	21.5(190)	22.0(195)
1	8	80	23.13	22.6(200)	22.0(195)	21.5(190)	22.0(195)
1	8	80	27.39	22.6(200)	22.6(200)	22.0(195)	22.0(195)
10	40	40	23.13	21.5(190)	20.9(185)	21.5(190)	20.3(180)
10	51	51	23.13	20.3(180)	19.8(175)	20.9(185)	19.8(175)
10	80	80	23.13	21.5(190)	20.9(185)	21.5(190)	20.9(185)
10	80	80	27.39	21.5(190)	20.9(185)	22.0(195)	21.5(190)

The range of results at 1 PPS through duty cycles of 4%, 5.1% and 8% is between 21.5 to 22.6 N-m of unpowered detent torque. The range of results at 10 PPS, keeping the duration of the powered portion of the pulse equivalent to the 1 PPS data, shows a decrease in the measured torques to 19.8 to 22.0 N-m.

The need for a correction factor for the Static Motorization Ratio calculation can be seen in the difference between the moment arm measured unpowered detent torque and the motor screening values. This particular actuator's motor had a 14 N-cm (22.6 N-m at actuator output) minimum unpowered detent torque during motor screening testing.

***For this reason Moog recommends using a .75 correction factor (CF in SMR formula) for the Static Motorization Ratio calculation.***

Powered Torque

Using a Kistler™ Torque Sensor, a motor was tested to determine the actual torque output of the motor at various speeds and duty cycles. This sensor measures reactive torque of the stator housing when the rotor takes a step. The motor housing was attached to the Kistler™ torque table and the rotor was pulsed. The motor housing resultant (equal but opposite) torque was recorded. This torque was compared to the 100% duty cycle torque measured during motor screening testing. Correlation between the motor screening test at 100% duty cycle and the tests results taken with the Kistler™ Torque Sensor are presented in Table 8.

**Table 8. Kistler™ Torque Sensor vs. Heritage Torque Measurement**

SPEED	DUTY CYCLE (%)	ON time (msec)	KISTLER MEASURED TORQUE N-cm (in-oz)	HERITAGE MEASURED TORQUE N-cm (in-oz)
1	4	40	38.3(54.2)	
1	5.1	51	38.0(53.9)	
1	8	80	38.3(54.2)	
1	50	500	38.4(54.4)	
1	96	960	38.2(54.1)	
1	100	1000	37.5(53.1)	
10	80	80	38.9(55.1)	32.5(46.0)
10	96	96	38.3(55.0)	
10	100	100	37.1(52.5)	35.9(50.8)
16	80	50	38.2(54.1)	
16	96	60	38.3(54.3)	
16	100	62.5	37.2(52.7)	

The consistency of measured torque values show that the torque remains a function of current and windings throughout the testing regimes as measured with the Kistler™ Torque Sensor. See a graph of the results in Figure 6.

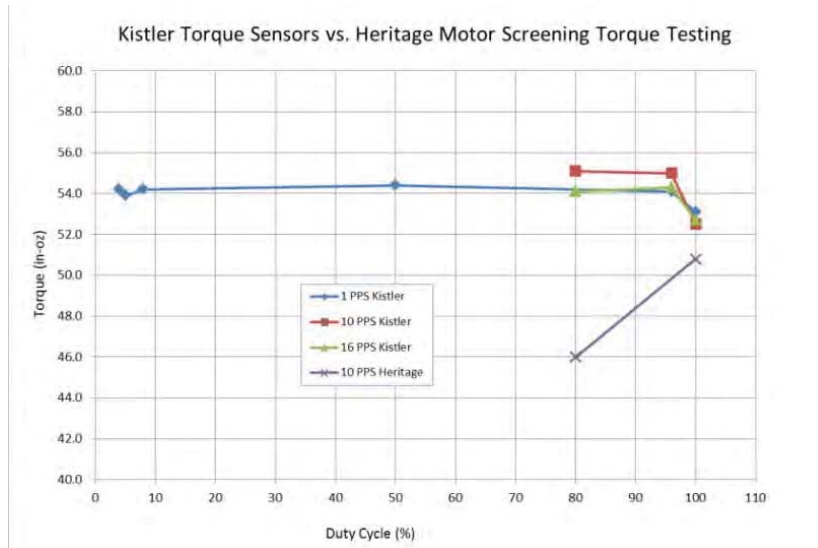


**Figure 6. Kistler™ Torque Sensor vs. Heritage Torque Measurement**

Interestingly, the comparison of wave forms between the slowest speed and shortest powered pulse (1 PPS and 4% duty cycle) and all three of the 100% duty cycle tests (1, 10 and 16 PPS) showed correlation. See the comparison of the wave forms in Figure 7.

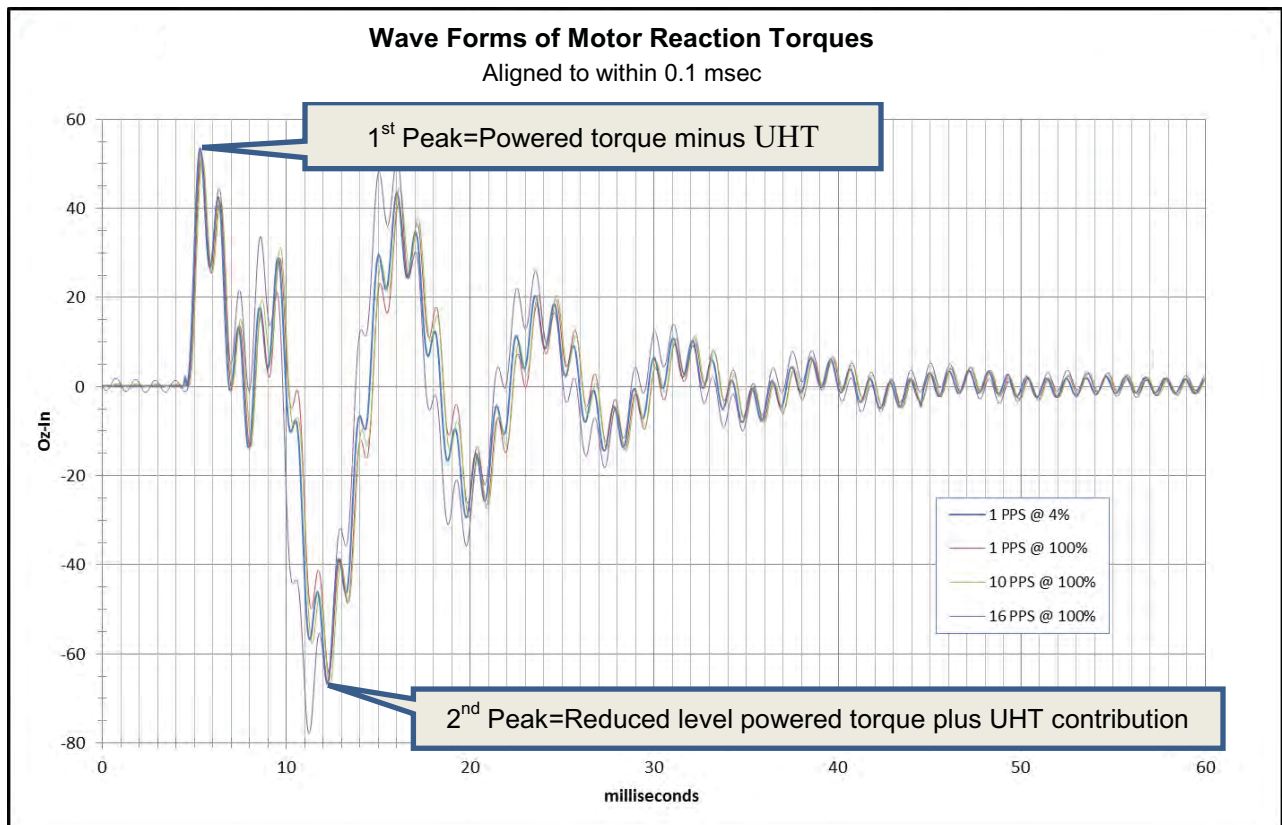


**Figure 7. Wave Forms of Motor Reaction Torques**



Actuator torque capability is reached after unpowered detent torque is overcome. The first peak shows this resulting torque which was used to show the torque capability of the motor. The second peak is the overshoot of the rotor to the cardinal powered position in combination with the unpowered detent torque helping to pull the rotor into the cardinal detent position. It should be noted that the major oscillations dampen out within approximately 45 msec of command at all three speeds and at the one reduced duty cycle compared.

The results above show that there is little change in torque between the powered portions of a pulse when comparing torques at 100% duty cycle and reduced duty cycle pulses. Unpowered Detent Torque is constant throughout the temperature extremes. Heritage testing at 100% duty cycle should be adequate to use in the powered portion

Similar tests were conducted independently on two (2) Moog Rotary Actuators at Astrium. Following is a summary of the tests and the conclusions.

The rotary actuator was gravity loaded using a moment arm. Fine and coarse potentiometers were monitored by the electrical test equipment during the test. To evaluate the dynamic performance, the Back Emf voltages of the redundant phases were plotted using an oscilloscope. Temperature was monitored throughout testing using an ohmmeter measuring the redundant winding resistance. The torque test was performed at 30 to 60 percent duty cycle.

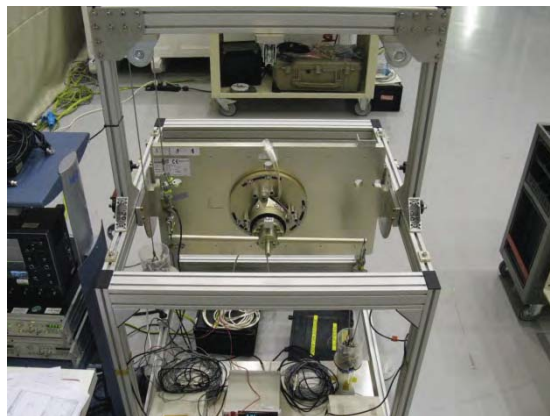


**Figure 8. Mechanical Setup at Astrium** *(Courtesy of Astrium)*

The test method was to increase the gravity loading as long as no miss-stepping is observed (over 240 steps).  $B_{emf}$  voltage was checked on the redundant winding. Figure 9 shows a sample of gathered data.

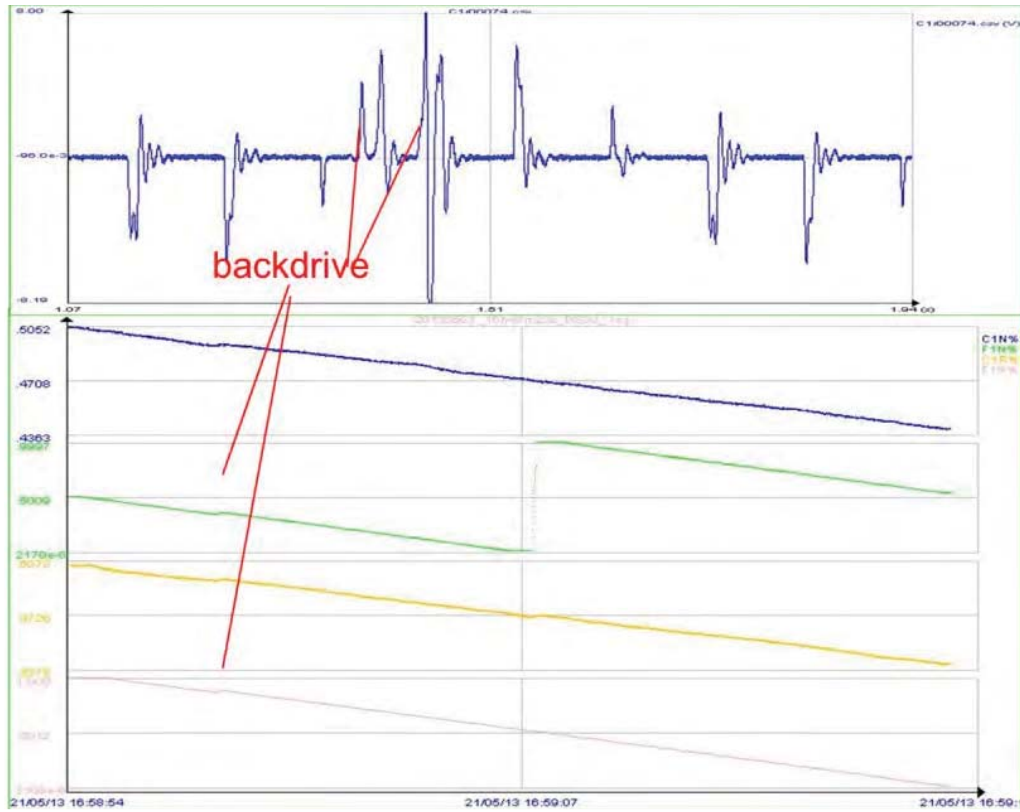


Figure 9. A Sample of Gathered Data (Courtesy of Astrium)

Figure 10 highlights the behavior of the motor during transition from ON to OFF state. The testing concluded that the static torque is at its minimum for OFF time greater than 10 msec and it is independent of the applied voltage  $V_{cc}$  and of duty cycle,

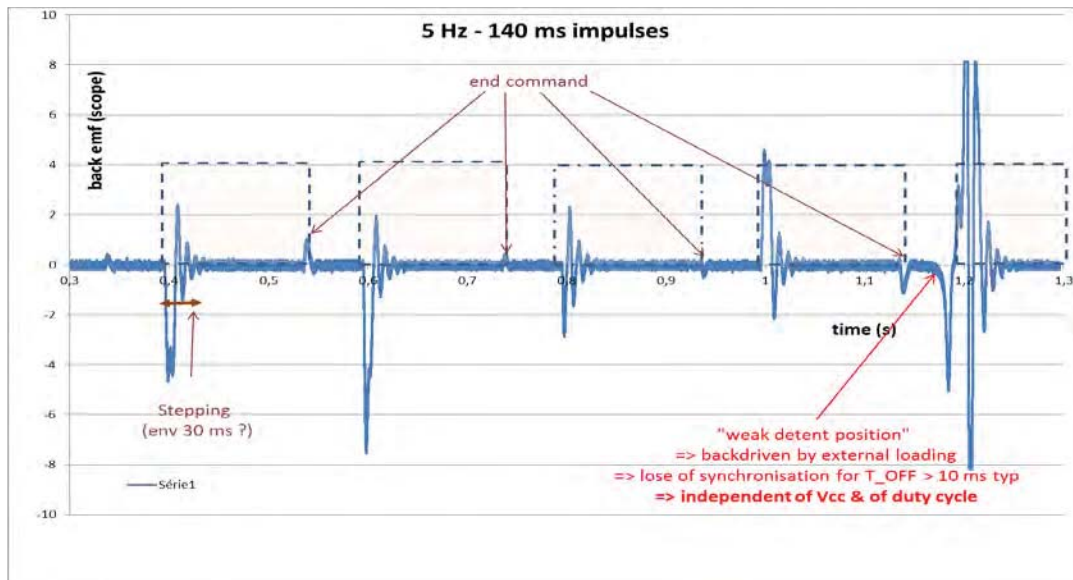


Figure 10.  $B_{emf}$  Scope Plot of  $T_{On}$  &  $T_{Off}$  (Courtesy of Astrium)

A point of interest is also the small spikes recorded at the end of each ON time (end of command pulses). This reflects a transient motion of the rotor, moving between two different quasi-static equilibrium positions:

- During ON time and after completion of the rotor motion, the rotor position is the balance between detent, electromagnetic and external torque
- During OFF time, the rotor position is the balance between only the detent and the external torque.

These locations are not identical and is one origin of the “CF” factor applied in the SMR formula

### Summary of the Predictions versus Measurements

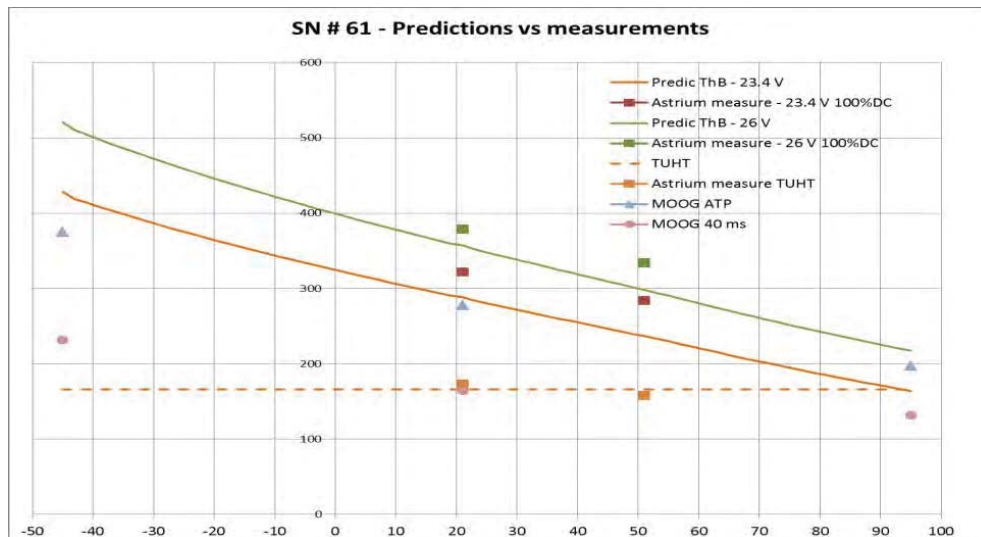


Figure 11. SN#61 Predictions vs Measurements (Courtesy of Astrium)

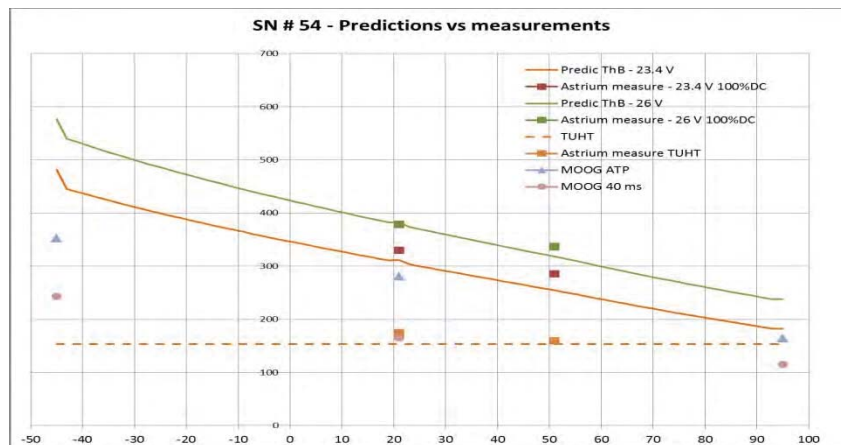


Figure 12. SN#54 Predictions vs Measurements (Courtesy of Astrium)

Similar pendulum (gravity) tests are currently being conducted at MDA, the results of which will be presented during the symposium

## Conclusions

The above examples are presented in an attempt to show that having the same motorization ratio requirement across the board, regardless of several factors like available power vs. size, complexity, design maturity, heritage, knowledge of the system by the designers etc. is neither necessary nor the most effective. In fact, requiring large motorization ratios for well characterized mechanisms might even be detrimental as it could eliminate simpler, higher reliability mechanisms from future designs.

The work presented relies on design heritage gained by MOOG and MDA, together with knowledge acquired during various complementary test campaigns at MOOG, MDA and Astrium premises. It is possible to highlight the following lessons learned:

- 1- Do not blindly apply generic requirements to your designs. Use judgment. The required Motorization Ratio should depend on the design's maturity, complexity and heritage.
- 2- Testing showed that during the powered portion of a pulse, whether the pulse is at 100% or at any reduced duty cycle, the maximum torque will be identical.
- 3- These results indicate that the actuator torque during any powered portion of any reduced duty cycle (as long as it is long enough (> 35 msec) for the rotor to step) pulse will be equal or greater to the heritage actuator torque measured at 100% duty cycle.
- 4- For actuators driven with duty cycles lower than 100%, motorization margin computation methods are proposed, sorting out carefully the two driving phases: during active part of the pulse (DMR formula) and during the off part of the pulse (SMR formula). These formulas aim at reflecting accurately the physical behavior and properties of the actuator.
- 5- Based on test data conducted on several actuators at environmental extreme temperatures, Moog recommends using a 75% correction factor (CF in SMR formula) for worst-case prediction of "static" torque using minimum motor detent torque.
- 6- Test results indicate that the minimum torque at reduced duty cycle, where the 0.75 CF applies, is for operation at hot temperatures.
- 7- Finally, the proposed Motorization Ratio calculation aims at ensuring both a safe utilization of the mechanisms and avoiding too much conservatism. Application of more conservatism could jeopardize the utilization of efficient solution (wrt to mass & heritage) in particular for applications requiring high torque capabilities.

# Magnetic Gearboxes for Aerospace Applications

Jose Luis Perez-Diaz<sup>\*</sup>, Efen Diez-Jimenez<sup>\*</sup>, Marco Antonio Alvarez-Valenzuela<sup>\*</sup>  
Juan Sanchez-García-Casarrubios<sup>\*\*</sup>, Christian Cristache<sup>\*\*\*</sup> and Ignacio Valiente-Blanco<sup>\*\*\*</sup>

## Abstract

Magnetic gearboxes are contactless mechanisms for torque-speed conversion. They present no wear, no friction and no fatigue. They need no lubricant and can be customized for other mechanical properties as stiffness or damping. Additionally, they can protect structures and mechanisms against overloads, limiting the transmitted torque. In this work, spur, planetary and “magdrive” or “harmonic drive” configurations are compared considering their use in aerospace applications. The most recent test data are summarized to provide some useful help for the design engineer.

## Introduction

Magnetic gears were proposed almost a hundred years ago. The absence of contact and wear between teeth seemed a worthy feature to prompt their development, but low efficiency, difficulties with manufacturing techniques, and cost were strong handicaps. It was at the beginning of this century that attention has been paid to their development, using new magnetic materials with higher magnetization or permeability, new precise manufacturing techniques, and advanced magnetomechanical modeling tools. The number of papers devoted to magnetic gears has increased exponentially in the last two years and the technology has overcome many of the first difficulties.

The specific development of magnetic gears for aerospace has been the objective of several projects carried out in Universidad Carlos III and MAG SOAR SL, some of them funded by the European Community's SPACE and CLEAN SKY Programs ([FP7/2007-2013]) under grant agreements n° 263014 and n° 323423. Specific aerospace design techniques have been developed to increase their TRL [1-7].

The main advantages of magnetic gears are a consequence of the absence of contact between teeth. There is no wear. No lubricant is needed. They can be operated at a broad range of temperatures ranging from -270°C up to 350°C. They present intrinsic anti-jamming properties and there is a clutching effect if the applied torque exceeds a limit therefore protecting the output from overloads. This effect is completely reversible. No damage or wear is produced while operating.

The motion direction is also reversible with highly reduced backlash. Input and output axles can also be exchanged so that the same device can be used as a reducer or a multiplier. An additional advantage is that they are suitable for through-wall transmission requiring no joints or sealing. Magnetic gears are also compatible with the presence of dust, sand or non-magnetic particles. As there is a gap between the moving parts, sand can flow not producing significant scratches, wear or stalling.

---

<sup>\*</sup> Dto. Ingeniería Mecánica, Universidad Carlos III de Madrid, Leganés, Spain

<sup>\*\*</sup> MAG SOAR S.L., Valdemoro, Spain

<sup>\*\*\*</sup> Instituto Pedro Juan de Lastanosa, Universidad Carlos III de Madrid, Leganés, Spain



## Classification of Magnetic Gears

Magnetic gears can be designed in configurations similar to conventional gears [8], mainly spur gears, planetary gears and “harmonic drives”.

### Spur gears and planetary gears

Direct spur gears consist of a pinion & wheel set with permanent magnets alternating their poles able to magnetically engage. These poles are equivalent to the teeth in conventional gears. The characteristics of this sort of gears are greatly dependent on size, shape, materials and geometry. As in conventional spur gears only moderate ratios can be achieved. Although useful for some applications, spur gears are more useful when combined in planetary configurations to achieve high ratios with relatively low mass and volume.

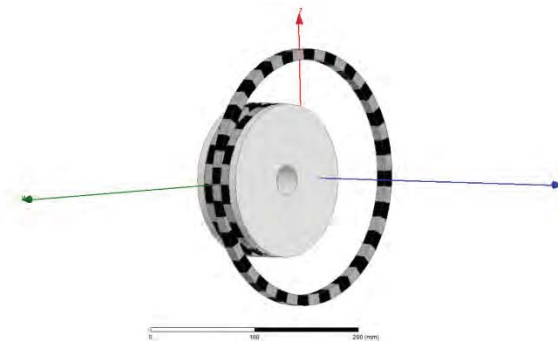


**Figure 1. Model for a 1:2 Magnetic Spur Gear. Calculated Maximum torque: 24.2 N-m.**

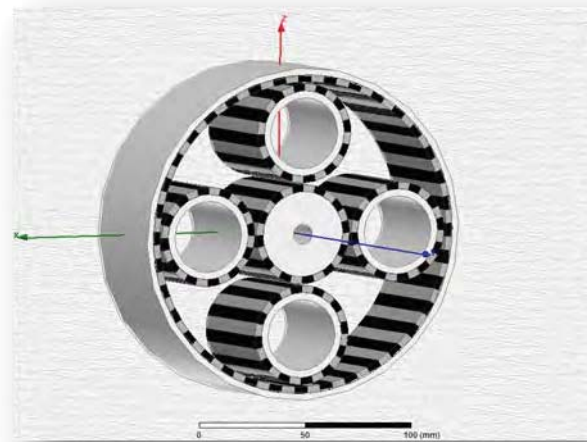


**Figure 2. Model for a 1:5 Magnetic Planetary Gear. Calculated Maximum torque 32.0 N-m.**

Table 1 shows a comparison of a magnetic planetary gear and a mechanical planetary gear. The data shown for the planetary gear correspond to a general configuration not yet optimized. An optimization of parameters with a defined objective can typically improve greatly any of the characteristics.

**Table 1. Comparison of performances of a magnetic planetary gear vs. a mechanical planetary gear.**

Specification	Magnetic Planetary Gear (not optimized)	Mechanical planetary gear from HD company Size 14
Reduction ratio (i)	4	5
Max output torque (N-m)	26	23
Torque Density (kN-m/m <sup>3</sup> )	24	81
Max input speed (rpm)	1500	4000
Max Efficiency (%)	95	-
Mass (kg)	3	1.2
Envelope: Outer Diameter x Length (mm x mm)	166 x 52	60 x 95
Max Operational Temp. (°C)	80	40
Min Operational Temp. (°C)	- 40	0

### Magdrives

Another kind of magnetic gears can be obtained following a “Vernier motor” criteria similar to that of the conventional “Harmonic drives”. We will call them “Magdrive” class. In fact the “harmonic drive” configuration was proposed by Chubb [9] for a magnetic gear some years before the invention of the “Harmonic drive”. Magdrives use a magnetic field wave whilst Harmonic drives use a mechanical deformation wave.

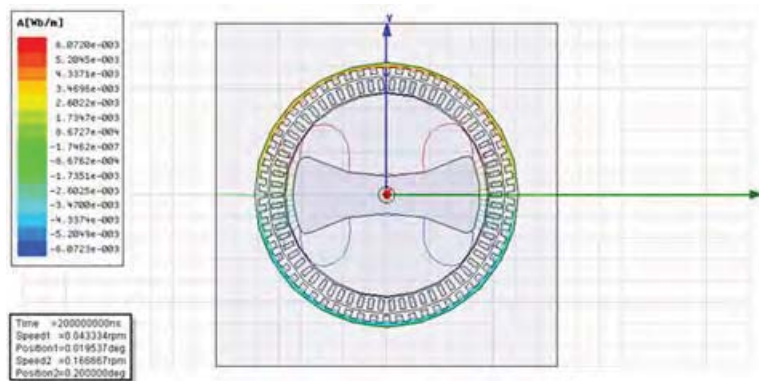


**Figure 3. Model for 1:42 Magdrive.**

Magdrives are provided with a permanent magnet fixed to the input axle that generates a magnetic field wave. This magnetic field induces a magnetization in a set of soft magnetic teeth which tend to align with an outer set of permanent magnets (or outer teeth). If the outer teeth are earthed, then the soft magnetic intermediate teeth are fixed to the output axle although other kinematic inversions are possible as well. This configuration can presumably provide ratios up to 1:200.



**Figure 4. 1:21 Magdrive room temperature prototype and test bench. Max. torque 12 N-m**



**Figure 5. 1:21 Magdrive Cryogenic prototype with superconducting bearing and test bench. A perfectly cryogenic non-contact Magdrive. Max. torque 4 N-m, max speed 1500 rpm at 50-90 K. Weight 7.5 kg. Envelope 130-mm diameter. Length 600 mm.**

Magdrives are suitable for cryogenic conditions. Particularly, a cryogenic Magdrive prototype, supported on non-contact superconducting bearings has been developed. Table 2 summarizes experimental results for this (column 2) and other Magdrive prototypes comparing to some conventional Harmonic drives.

**Table 2. Comparison of experimental tests on Magdrive prototypes vs. Harmonic drives data obtained from manufacturer.**

Specification	MAGDRIVE			Harmonic Drive	
	Room Temp. Prototype	Cryogenic Prototype	MAG SOAR MD-50	HFUC Size 17: Only component without bearings	PMG Size 14: including box
Reduction ratio (i)	21	21	51	80	88
Max output torque (N-m)	15	4	45	43	12.7
Torque Density (kN-m/m <sup>3</sup> )	10.7	2.5	70	470	100
Max input speed (rpm)	500	1500	1500	1500	3000
Max Efficiency (%)	95	-	-	Temperature dependent.	Temperature dependent.
Mass (kg)	5	8	2	0.3	0.5
Envelope: Outer Diameter x Length (mm x mm)	120 x 110	120 x 400	100 x 80	60 x 32	50 x 80
Max. Operational Temp.(°C)	80	-180	+120	40	40
Min Operational Temp. (°C)	-40	-260	-196	0	0

Torque limiters

Other magnetomechanical devices that can be used for power transmission are magnetic torque limiters. They behave as 1:1 transmissions whenever the torque is under a limit. If the applied torque exceeds this limit they present an anti-jamming clutching effect that protects the output structure. Specific and optimized designs make these devices quite compact and competitive.



**Figure 6. MAGSOAR TL-45 Magnetic Torque Limiter. Max. torque 45 N-m**

Additionally, magnetic torque limiters provide a certain degree of torsional elasticity that can be used to reduce the transmission of torsional vibrations. These magnetic torque limiters do not emit any kind of magnetic field around them. They do not dissipate any kind of power while engaging (applied torque below limit). While not engaging (applied torque over limit) a reduced dragging torque and heat release can be customized.

A main and unique feature of magnetic torque limiters is that they do not suffer wear or fatigue independently of the times they act limiting the torque.

Table 3 shows a comparison between experimental data of a magnetic torque limiter and data from the manufacturer of a mechanical torque limiter.

**Table 3. Comparison of a Magnetic torque limiter TL-45 manufactured by MAG SOAR SL and a KTR 01 2TF mechanical torque limiter manufactured by Ruflex.**

Specification	MAGSOAR TL-45	Ruflex KTR 01 2TF
Reduction ratio (i)	1	1
Max output torque (N-m)	45	10-70
Torque Density (kN-m/m <sup>3</sup> )	100	52-300
Max input speed (rpm)	15000	6000
Max Efficiency (%)	95	-
Mass (kg)	2	-
Envelope: Outer Diameter x Length (mm x mm)	135 x 40	68 x 52
Max Operational Temp. (°C)	80	80
Min Operational Temp. (°C)	-40	-20

### Torque and Torsional Stiffness in Magnetic Gears

The most outstanding properties of magnetic gears are derived from the torque/torsion behavior. It is radically different from that of the conventional gears. If we block the output axle of a gear and increase the torque in the input axle to try to move it we will make evident the difference between magnetic and mechanical gears.

Magnetic gears will admit a shift angle in the input axle that increases linearly with the applied torque. Figure 7 shows experimental data of torque vs. shift angle for a 1:21 Magdrive (black dots). If we decrease the torque and change the sign of it, the angle will follow the torque without any significant hysteresis. In this sense magnetic gears do have zero backlash. If we increase the torque up to its maximum value, a non-linear dependence appears. If we try to increase the torque and pass the limit, then the axle simply turns. For the magnetic gears nothing breaks down.

The case is quite different in conventional gears (blue line in Fig. 7). A backlash is present due to the clearances needed for the movement. Therefore, if the movement is reversed there is a small but not negligible backlash around the origin. Once the gears are engaging, then the input axle presents a rigid behavior with stiffness on the order of magnitude of the flexural stiffness of the teeth. Once the maximum applied torque is reached, a plastic deformation and fracture appears with permanent damage of the conventional gear.

The radically different behavior of magnetic and mechanical gears makes the meaning of “maximum applied torque” to be quite distinct. For mechanical gears it means “if you exceed that value you break the device”. For magnetic gears it means “it will transmit the movement up to that value of the torque, but if you try to exceed it, it will slide and nothing breaks down”.

Non-contact and elasticity of magnetic gears make magnetic gears natural isolators for vibrations. Figure 8 shows axial vibrations measured on a bearing supporting the input axle of a 1:21 Magdrive and the corresponding vibrations measured on the bearing supporting the output axle. Damping is evident.



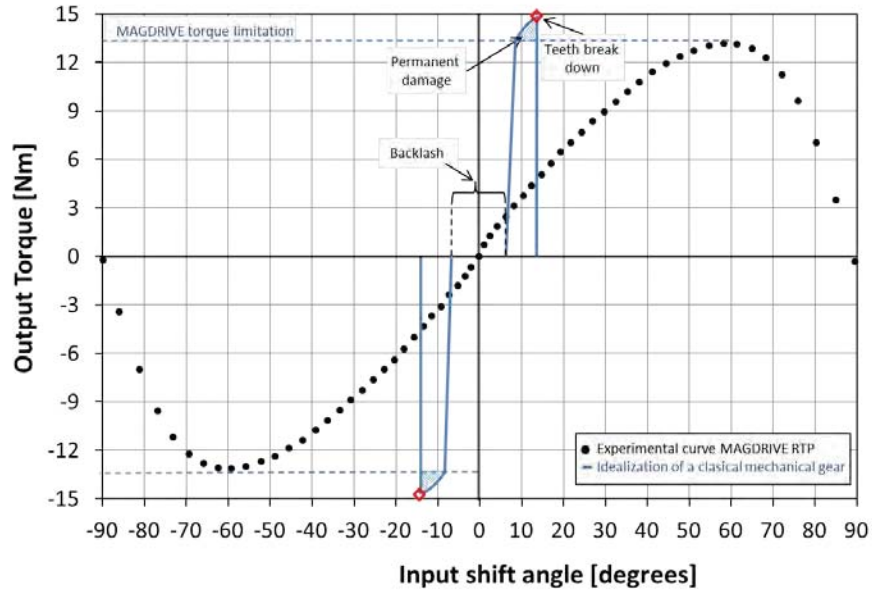


Figure 7. Experimental Torque vs. angle shift in MAGDRIVE Room Temperature Prototype (black dots) compared to a perfect mechanical gear (blue line). Magnetic gears do not present backlash but a linear dependence around the zero point. Magnetic gears, unlike mechanical ones, do not present damage if the torque overpasses the maximum.

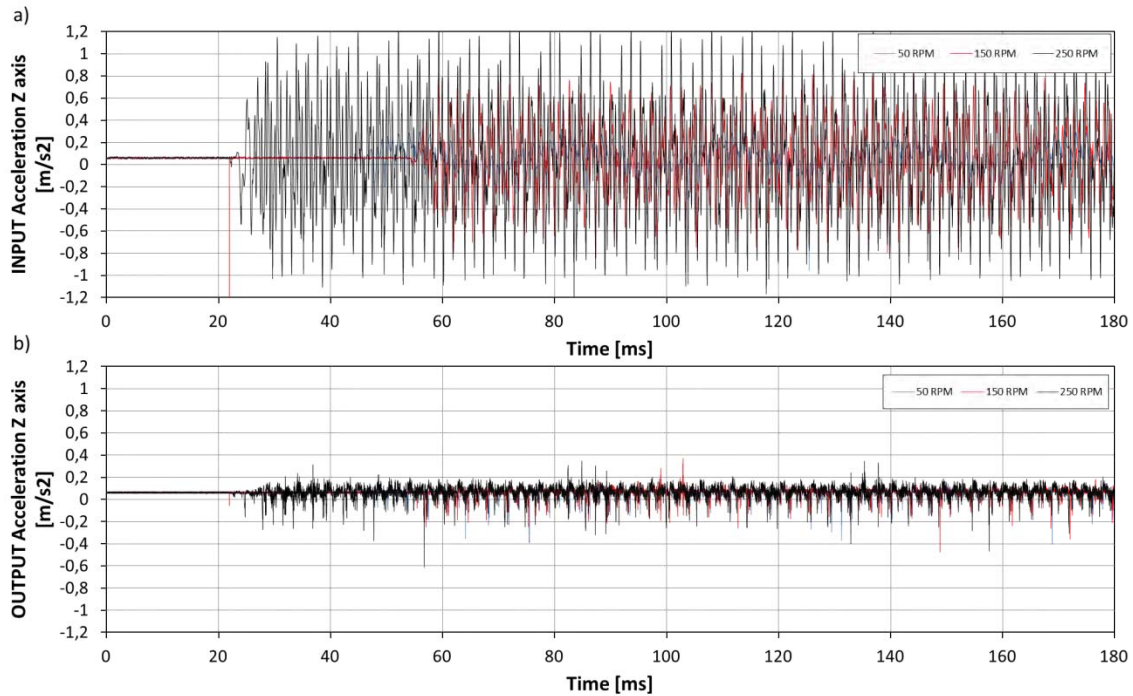


Figure 8. a) Transversal Acceleration on a bearing supporting the input axle of a 1:21 Magdrive when vibrations are induced on it. b) Transversal Acceleration on the bearing supporting the output axle of the same system.

## Conclusions

Magnetic gears are becoming competitive alternatives to conventional gears. They present no contact and no wear. They do not produce debris and they do not require lubricant, being able to be operated at a broad range of temperature ranging from  $-270^{\circ}\text{C}$  up to  $350^{\circ}\text{C}$ . They present intrinsic anti-jamming properties and there is a clutching effect if the applied torque exceeds a limit therefore protecting the output from overloads. This effect is completely reversible without any damage or wear. The TRL of this technology is currently increasing making it available for consideration for aerospace uses.

The radically different behavior against torque overloads, the isolation of vibrations, the absence of maintenance, the compatibility with sand or dust, broad temperature range and the through wall capability are some properties that make these devices attractive for aerospace.

Table 4 summarizes the state of the art of magnetic gears and torque limiters with a qualitative comparison of magnetic torque limiters, magnetic planetary gears and magdrives with respect to their best available mechanical equivalents. For the elaboration of Table 4, the authors have developed original software able to interpolate current-state data of magnetic gears. The user can select the ratio, speed and some other parameters. The software provides maximum torque, size, weight and even an estimation of the cost of the magnets for a magnetic spur gear, a magnetic planetary gear and a Magdrive.

**Table 4. Qualitative comparison of magnetic torque limiters, magnetic planetary gears and magdrives with respect to their best available mechanical equivalents.**

Specification/characteristic	Magnetic Torque Limiters	Magnetic Planetary Gears	Magdrives	Mechanical equivalent
Reduction ratio	1:1	1:50	1:100	1:160
Torque density	+++	++	++	★
Torque specific density	++++	++	++	★
Max output torque	★	+++	+++	★
Max input speed	★	++++	★	+++
Accuracy (Low Backlash)	★	★	★	+
Torsional stiffness	+++	++	++	★
Damping/Isolation of Vibrations	++++	++++	★	+
Efficiency at room temperature	++++	+++	+++	++++
Efficiency at low temperature (-40°C)	++++	+++	+++	+++
Efficiency at cryogenic temperature	++++	+++	++++	++
Compactness	++++	++	++	★
Wide Operational Temperature Range	★	★	★	+++
Lifetime at room temperature	++++	++++	++++	++
Lifetime at cryogenic temperature	++++	++++	++++	+
Outgassing	++++	++++	++++	++++
Time between maintenance ops.	★	★	★	+++
Low generation of debris	★	★	★	++
Lubrication	Not required	Not required	Not required	Yes
TRL of technology	TRL 7	TRL 5-6	TRL 5-6	★

### Acknowledgements

This work has been partially funded by the European Community's Seventh Framework Program ([FP7/2007-2013]) under grant agreements n° 263014 and n° 323423.

## References

1. C. Cristache, I. Valiente-Blanco, E. Diez-Jimenez, M.A. Alvarez Valenzuela, N. Pato and J.L. Perez-Diaz; "Mechanical characterization of journal superconducting magnetic bearings: stiffness, hysteresis and force relaxation", Journal of Physics: Conference Series EUCAS, (2013). IEEE Council on Superconductivity Best contributed EUCAS 2013 Award: Mechanical characterization of journal superconducting magnetic bearings: stiffness, hysteresis and force relaxation.
2. I.Valiente-Blanco, E. Díez-Jiménez, Cristian Cristache, Marco A. Álvarez-Valenzuela and J.L. Pérez-Díaz, "Characterization and Improvement of Axial and Radial Stiffness of Contactless Thrust Superconducting Magnetic Bearings", Tribology Letters, (2013).
3. J.L. Pérez-Díaz, I. Valiente-Blanco, E. Díez-Jiménez, and J. Sanchez García-Casarrubios, "Superconducting Noncontact Device for Precision Positioning in Cryogenic Environments," IEEE/ASME Transaction on Mechatronics, (2013).
4. Pérez-Díaz, J.L.; Valiente-Blanco,I., et al., "Contactless Superconducting Magnetic Instrument for Precise Positioning in Cryogenic Environments", Proceedings of ASME International Mechanical Engineering Congress & Exposition, San Diego, E.E.U.U, (2013).
5. Perez-Diaz, J.L.; Diez-Jimenez, E., Valiente-Blanco, I. et al., "Magnetic Non-Contact Harmonic Drive", Proceedings of ASME International Mechanical Engineering Congress & Exposition, San Diego, USA, (2013).
6. Valiente-Blanco I., Cristache C., Diez-Jimenez, E., Alvarez-Valenzuela M.A., Sanchez-Garcia-Casarrubios J. and Perez-Diaz, J. L (2013) Characterization and improvement of axial and radial stiffness of contactless thrust superconducting magnetic bearings, 5th World Tribology Congress, Torino, Italia, (2013).
7. Cristache C., Diez-Jimenez, E., Valiente-Blanco I., Alvarez-Valenzuela M.A, Sanchez-Garcia-Casarrubios J. and Perez-Diaz, J. L.; Levitation force relaxation and hysteresis in a frictionless superconducting magnetic bearing, VII Iberian Conference on Tribology, Porto, Portugal, (2013).
8. X. Li, K.-T Chau, M. Cheng and W. Hua ; « Comparison of Magnetic-Geared permanent-magnet machines », Prog. In Elec. Res., 133, 177-198 (2013)
9. L.W. Chubb, "Vernier Motor", US Patent 1894979, (1933).

# Primer – Stepper Motor Nomenclature, Definition, Performance and Recommended Test Methods

Scott Starin\* and Cutter Shea\*

## Abstract

There has been an unfortunate lack of standardization of the terms and components of stepper motor performance, requirements definition, application of torque margin and implementation of test methods. This paper will address these inconsistencies and discuss in detail the implications of performance parameters, affects of load inertia, control electronics, operational resonances and recommended test methods. Additionally, this paper will recommend parameters for defining and specifying stepper motor actuators. A useful description of terms as well as consolidated equations and recommended requirements is included.

## Introduction

Stepper Motor Actuators are desired in space mechanisms because of their precise incremental control, yet they are inherently under-damped and susceptible to inertial mismatch. These issues will be addressed in detail. While linear straight-line approximation of Stepper Motor performance may be simulated with simple relationships and equations, actual performance in a system with inertia, friction, and compliance may result in dramatically different performance compared to simulations. Often, performance requirements in specifications do not fully reflect the actual requirements, including torque margin. More importantly, an inadequately designed test set-up or incomplete testing could erroneously hide a latent performance issue that may not be identified until the actuator is integrated at a higher assembly.

## Linear Performance Approximation

There are many factors that contribute to the actual dynamic performance of a stepper motor actuator. Simple linear extrapolation, however, yields conservative results that works for the vast majority of applications. The linear approximation may be obtained by determining key motor parameters, which are included in most motor manufacturers' catalogs. For our example, Table 1 delineates the key parameters and values used in our example.

<b>Parameter</b>	<b>Units</b>	<b>Symbol</b>	<b>Value</b>
Motor Constant (Non-Redundant)	mN-m/ $\sqrt{\text{Watt}}$	$K_M$	34
Motor Inertia	kg-m <sup>2</sup>	$J_M$	7.06E-07
Step Angle at Motor	Degrees/step	$\Delta\theta_M$	30
Simplex No Load Response Rate Constant	RPM/ $\sqrt{\text{Watt}}$	$K_{RR}$	325
Motor Bearing Friction (-20° C)	mN-m	$f_{BM}$	1.0
Magnetic Coulomb Torque	mN-m	$f_{CM}$	5.0

---

\* Avior Control Technologies, Inc., Longmont, CO



Figure 1, graphs a linear simulation of a geared Stepper Motor Actuator at room temperature and at +50° C. The figure points out key performance parameters and introduces some nomenclature that will be used throughout the paper.

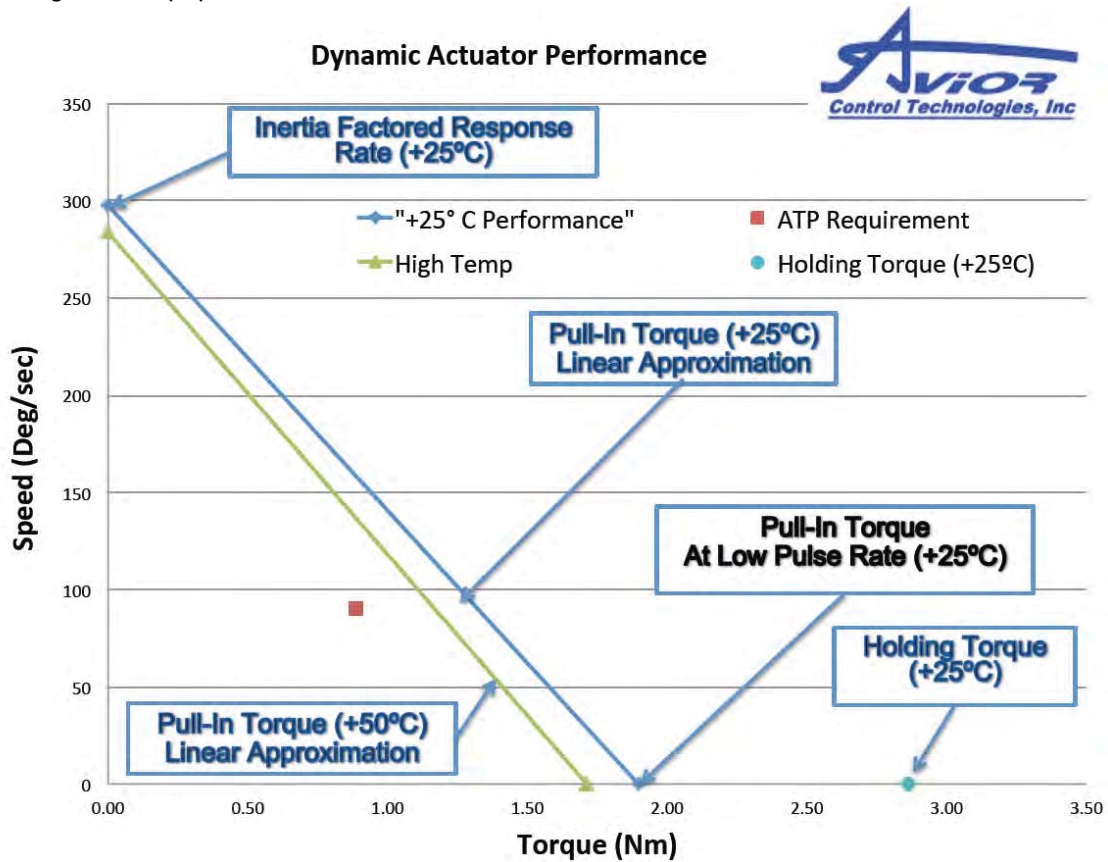


Figure 1. Linear Simulation of Geared Stepper Motor

The designated operating point “ATP Requirement” refers to the required Torque margin requirements, as defined in GSFC-STD-7000 (GEVS) [2]. This will be discussed in detail later in the paper.

Inertia Factor Calculations

Perhaps one of the most important parameters in the utilization of Stepper Motor Actuators is determining the *Inertia Factor* ( $J_F$ ). This parameter is the sum of the load inertia reflected to the motor ( $J_{LM}$ ), and the motor inertia ( $J_M$ ), all divided by the motor inertia:

$$J_F = \frac{J_{LM} + J_M}{J_M} \dots\dots\dots(1)$$

Where  $J_{LM}$  is the load inertia ( $J_L$ ), divided by the entire gear ratio ( $N$ ), squared.

$$J_{LM} = \frac{J_L}{N^2} \dots\dots\dots(2)$$

Many times, the gear ratio is determined by the step resolution required at the system level, but the driving factor may also be reducing the Inertia Factor. There are several schools of thought on what is an acceptable Inertia Factor. Some engineers insist on an Inertia Factor less than or equal to 2.0 (That is  $J_{LM} \leq J_M$ ). While a  $J_F$  less than 2.0 is conservative, there are times this may be impractical. A maximum

Inertia Factor less than 5.0 is recommended, but higher reflected inertias may be used with proper testing and analysis.

Response Rate and Torque at Low Pulse Rate Calculations

The Inertia Factored Response Rate ( $RR_{JF}$ ), or No Load Speed, of a Stepper Motor Actuator is directly effected by the Power Input at Holding ( $P_H$ ), the Inertia Factor, and Response Rate Constant ( $K_{RR}$ ). Equation 3 reflects the Inertia Factored Response Rate at the output of the Actuator, in RPM. As a note; the Response Rate Constant for redundantly wound Stepper Motors ( $K_{RR'}$ ) will be higher than a non-redundant winding, because of lower inductive losses ( $Ldi/dt$ ). The Inertia Factored Response Rate calculation is presented in Equation 3. The factor of 6 converts the units to degrees per second from RPM.

$$RR_{JF} = \frac{K_{RR} \cdot 6.0 \cdot \sqrt{P_{H25}}}{N \cdot \sqrt{J_F}} \dots\dots\dots(3)$$

The Torque at Low Pulse Rate ( $T_{PPS_0}$ ), presented in Equation 4, is a function of the Holding Torque at 25°C ( $T_{H25}$ ) and the sum of the Motor Magnetic Coulomb ( $f_{CM}$ ) Motor Bearing Friction ( $f_{BM}$ ) Gearbox Bearing Friction ( $f_{BG}$ ) Torques, and Gearbox Efficiency ( $\eta_G$ ).

$$T_{PPS_0} = (T_{H25} \cdot 0.707) - N(f_{BM} + f_{CM} + f_{BG}) \dots\dots\dots(4)$$

$$T_{H25} = (N \cdot \eta_G) \cdot K_{M25} \cdot \sqrt{P_{H25}} \dots\dots\dots(5)$$

Equation 4 is a point of discrepancy to be resolved. Professionals in the aerospace industry argue that the Magnetic Coulomb Torque ( $f_c$  or Detent Torque) is a function of position and typically integrates out over a course of a step. In other words, part of the cycle, the Detent Torque is working against the electro-magnetically generated torque, and part of the cycle, the Detent Torque *works with* the generated torque. Strict interpretation of Torque Margin requirements, these components of torque should be factored as we show in Equation 4, above [2]. *While analyzing Pull-In Torque, the detent torque must be subtracted from the available torque to accelerate.* Note, torque margin factors are not applied to torque components such as  $f_{BM}$  in this equation because it will be addressed later in the dynamic analysis. The rationale and application of torque margin are discussed in detail in the Comprehensive Torque Margin Analysis section of this paper.

Table 2 delineates the variable values used in our simulation, shown in Figure 1. Data represented in blue herein is a reminder the values are an example.

Table 2. Actuator and System Variables for Sample Simulation			
Parameter	Units	Symbol	Value
Load Inertia	kgm <sup>2</sup>	J <sub>L</sub>	5.7E-04
Holding Power (at +25°C)	Watts	P <sub>H</sub>	28
Gear Ratio	-	N	20:1
Gearbox Efficiency	%	η <sub>G</sub>	90
Elevated Temperature	°C	t <sub>2</sub>	50

Performance at Elevated Temperatures

To determine performance of voltage control systems at temperatures other than room temperature (+25°C) the change in DC Resistance must be determined. The example will analyze a two-phase motor. Refer to supplier catalogs for three phase calculations. For a two-phase bipolar drive, the room temperature DC Resistance ( $\Omega_{25}$ ) per phase may be easily calculated by using Equation 6.

$$\Omega_{25} = \frac{2 \cdot V^2}{P_{H25}} \dots\dots\dots(6)$$

Where “V” is the supply voltage. In our example, this yields a nominal motor resistance of 48.3 ohms per phase. Use Equation 7 to calculate the DC resistance at temperatures other than 25° C (t<sub>2</sub>).

$$\Omega_{t_2} = \Omega_{25} [1 + .004(t_2 - 25)] \dots\dots\dots(7)$$

Knowing the change in resistance at any temperature allows the change in current and power to be calculated. Thus allowing the Torque at Low Pulse Rate and Inertia factored Response Rate to be determined at temperature. Calculations are detailed in Appendix A.

Equation 7 works while analyzing the system is increasing or decreasing temperatures, within limited temperature ranges. Exercise caution when going down in temperature. Colder temperatures could yield higher viscosity in a wet lubrication system and will affect available torque calculations. Avior has modeled multiple wet lubrication options and introduced a functional component of bearing friction (f<sub>BM</sub>) that accounts for the increased viscosity at colder temperatures. This method is recommended for accurate performance models. Additionally, the relationship of Equation 7 does not work down to cryogenic temperatures where the purity of the copper must be factored.

### **Actual Dynamic Performance (What Really Happens)**

As mentioned, the linear approximation provides a conservative estimate for most applications. Figure 2 shows an empirical test of the Pull-In Torque of the geared stepper motor for the example. It is extremely important to realize that the characteristic oscillations of the dynamic performance will be unique to the test set-up and drive electronics. If high stiffness couplings were replaced with more compliant couplings, the characteristics could dramatically change. The portions of dynamic torque that increase and decrease will be exaggerated with lower compliance, reduced damping, or increased load inertia.

## Dynamic Actuator Performance

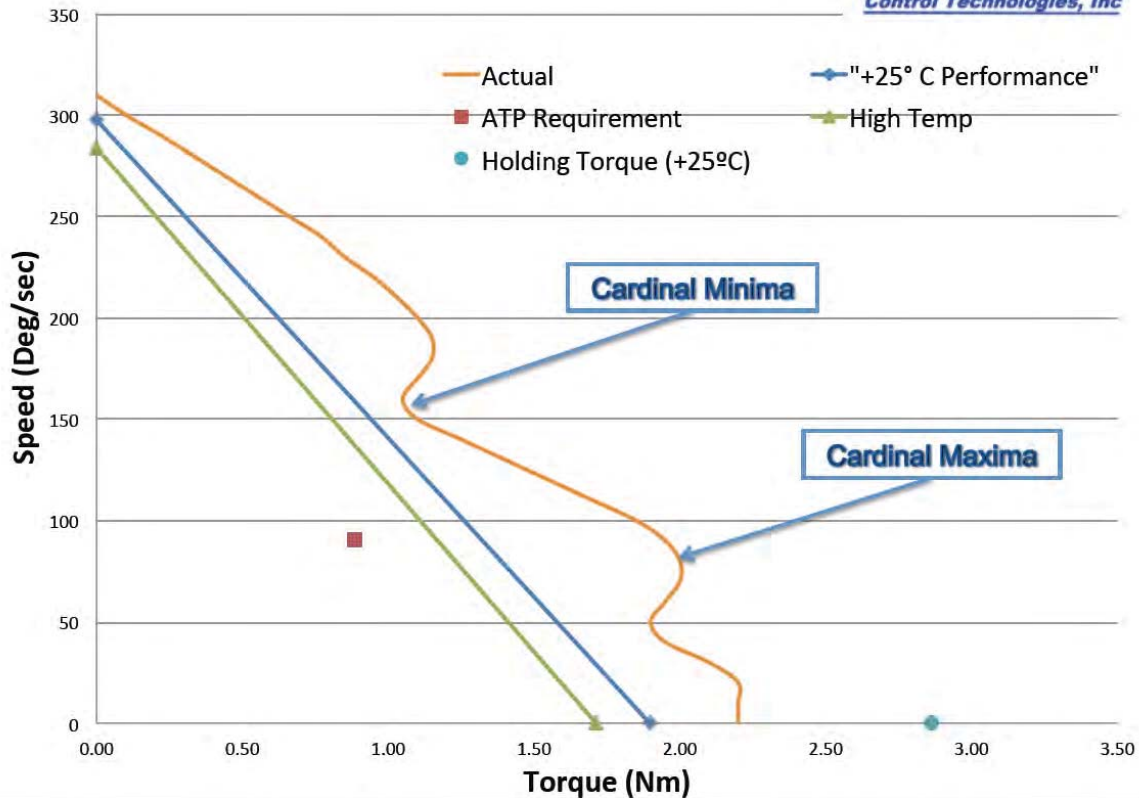


Figure 2. Empirical Dynamic Performance versus Linear Simulation

### Why This Happens

The inherent kinematics of a stepper motor mirrors an under-damped step function of a servo system. As the stepper motor moves to each stable step point, there is overshoot of position. Also note that as the motor crosses each step point, the angular velocity, and therefore the kinetic energy, is at a maximum. Even when stepper motors are driven at low pulse rates, the instantaneous angular velocity can be extremely high at these crossover points. The cardinal oscillatory frequencies of these overshoots will result in an increase in torque at some step rates (Cardinal-Maxima), and a reduction of torque at other step rates (Cardinal-Minima). As the Inertia Factor increases, the variation of the torque peaks and valleys will be exaggerated. When the Inertia Factor is greater than 5.0, it is recommended that additional margin be applied from the linear performance assumption before a system prototype has been tested.

There are several important aspects to take into account, considering these phenomena. The characteristic cardinal torque step rates will vary with test set inertia, drive electronics and coupling compliance. This is why it is recommended the drive electronics and test set configuration simulate the actual system parameters as closely as practical. Additionally, performance at multiple step rates should be conducted to verify that dynamic torque performance is not conditionally marginal. In other words, during a test, the system may be at a cardinal torque increase point. If you test multiple step rates around the system operating step rate, you may better characterize the performance. It is important to realize that more torque is not necessarily better. Torque margin is desirable, but increasing torque may actually increase kinematic overshoot and further exaggerate the dynamic cardinal torque variations.

Determining the damping ratio of a Stepper Motor system can be an excellent indicator for susceptibility of a system to extreme cardinal exaggerations. From actual test data, Figures 3 and 4 show the same system with two actuators with different drive methods and damping ratios ( $\zeta$ ). The total inertia, inertia

factor, power input and drive systems were identical but the system in Figure 3 was driven bipolar and Figure 4 was controlled with wave drive electronics. This clearly demonstrates the bipolar system provides more damping.

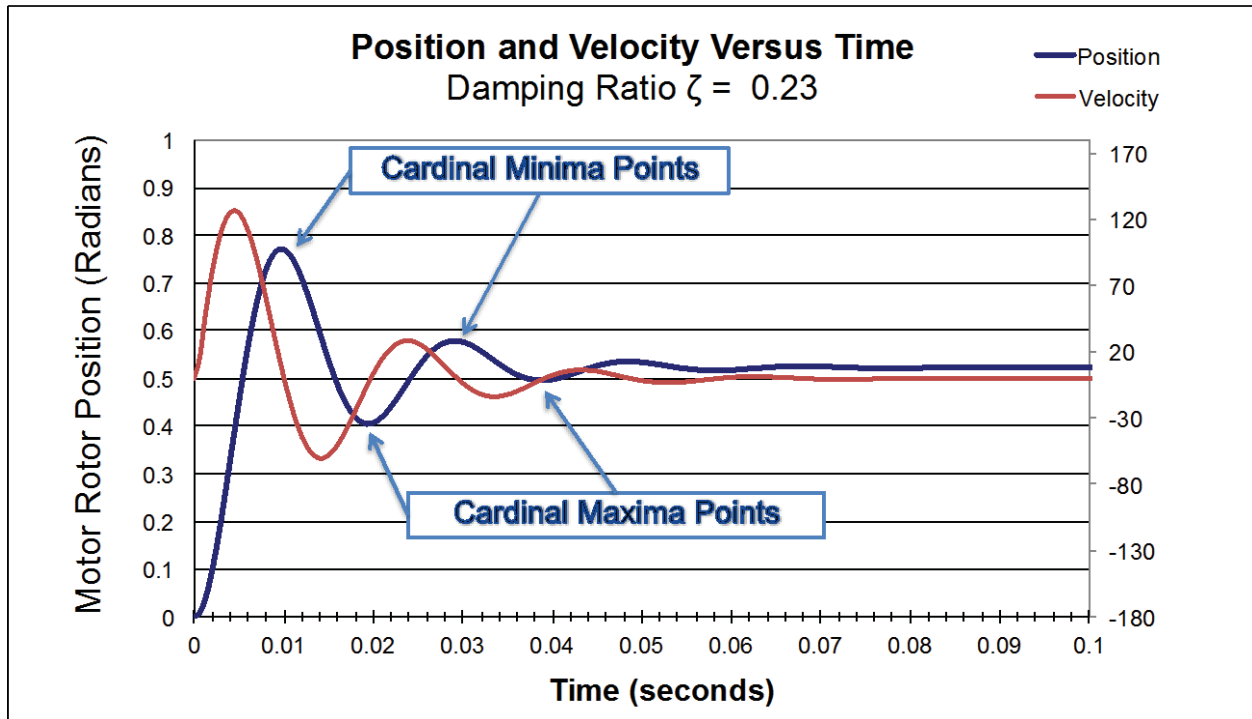


Figure 3. Bipolar Driven Actuator System  
Position and Velocity versus Time

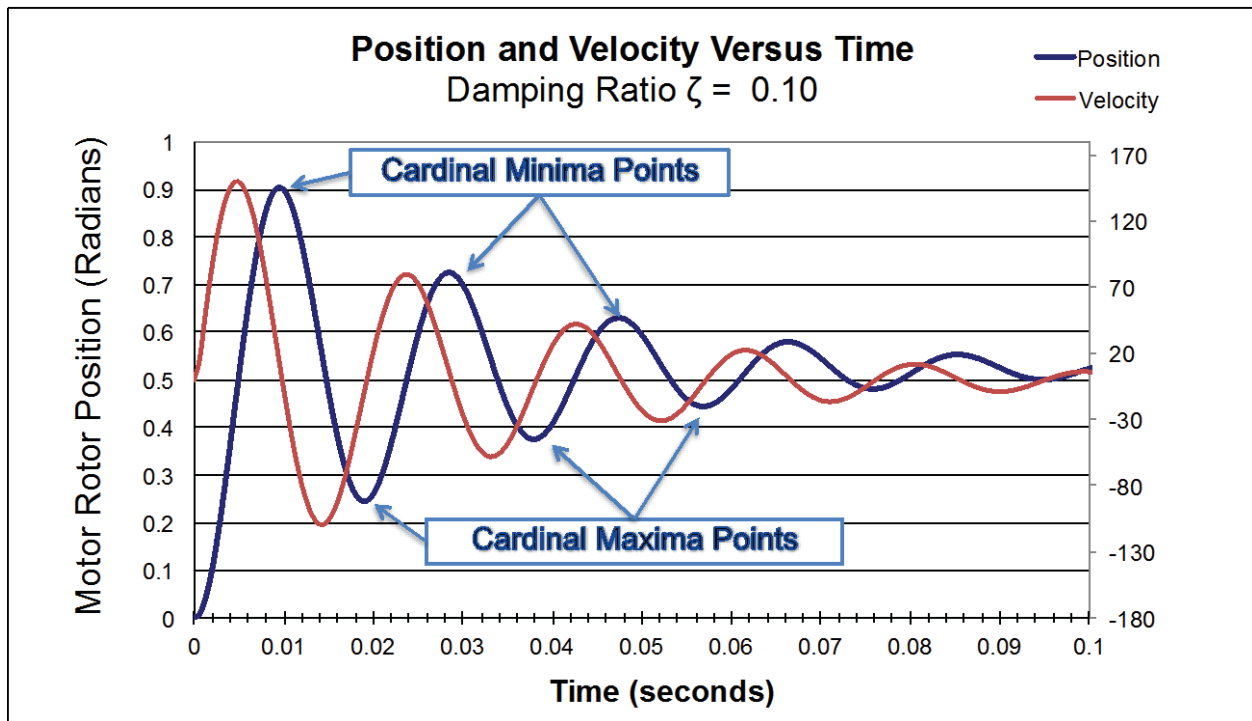


Figure 4. Wave Driven Actuator System



## Position and Velocity versus Time

The Cardinal Minima points occur at the peak overshoot points of step because the electromechanically generated torque drops off with the cosine of the position of the overshoot. Obviously, to minimize the impact and number of Minima occurrences, it is desirable to minimize the magnitude and number of overshoots, and the best method to do so is to increase damping.

### How to Compensate (How to Increase Damping)

If you find yourself at a conditionally marginal operating rate (or Cardinal-Minima) there are several approaches that may be taken to address the issue. Fundamentally, the main issue with these conditionally marginal operating points is damping. While technically, damping is the loss of torque at speed, an under-damped stepper motor that loses dynamic torque at resonant frequencies can regain torque margin by increasing damping through drive methods or adding electromechanical damping in the actuator. Reference [3] details consequences, options and results of an under-damped system.

Perhaps the two most common causes of under-damped resonant torque losses are drive method or too excess inertia (Inertia Factor). Bipolar drives, whether two phase or three phase, are far superior to unipolar or wave drive methods, in terms of adequately damped systems. As discussed, Inertia Factors greater than 5.0 can tend to have significant resonant torque losses at cardinal-operating frequencies. If bipolar drive is already implemented, then internal electro-mechanical damping methods may be the best solution to remedy under-damped systems. These methods, however, take away from copper volume for motor torque generation, so the effective motor constant, or torque per square root watt, is reduced. Other methods, such as response shaping networks through sensor feedback and processing are effective, but increase the complexity and development of the drive electronics.

### Slew Operation (Operating in the Pull-Out Region)

Thus far pull-in torque performance or the torque capacity to pull-in from rest has been discussed. Increased dynamic performance is achievable while operating in the pull-out or slew region. Increased torque capacity or velocity may be achieved by ramping (or slewing) up the step rate of the motor. This will allow the actuator to operate in a performance region that may not be achievable from a dead stop. It is important to not only ramp-up, but also ramp down step rate. It is not advisable to depend on counting steps for positional information if operating in the slew region.

Calculating the linear performance in the slew region is similar to the pull-in analysis described above, but Inertia Factor does not affect the Slew Rate Constant ( $K_{SR}$ ), as it affects Response Rate Constant ( $K_{RR}$ ). The pull-out Torque is calculated by a linear approximation from the Slew Rate to the Torque at Low Pulse Rate. Cardinal Oscillatory effects as described above may impact slew operation, just as they effect pull-in operation.

## Comprehensive Torque Margin Analysis

Torque Margin has been calculated, defined and interpreted by almost every imaginable method. Many companies have their own methods to define and apply Torque Margin, but as described above and addressed in [3], too much torque can result in under-damped performance. In addition to exaggerating the cardinal minima, too much torque and severely under-damped systems may introduce fatigue and stressing of mechanical components. Additionally, too much torque equates to excess power, unnecessary heat loss and energy consumption. It is certainly prudent to assure torque requirements are satisfied, but this does not mean the design engineer should simply increase torque at a mechanism to ensure a robust system.

### Components of Torque

Know your torque contributors and their characteristics. In addition to bearing friction, gear frictions and magnetic coulomb torques, acceleration torques must be accounted for at the step rate of the actuator.

Reference [2] requires different application of torque margin at different stages of the program. Table 3 details the requirements for Factors of Safety for Known ( $K_C$ ) and Variable ( $K_V$ ) components of Torque.

<b>Table 3. Applied Factors of Safety to Torque Components per GEVS</b>		
<b>Program Phase</b>	<b>Known Factor of Safety (<math>K_C</math>)</b>	<b>Variable Factor of Safety (<math>K_V</math>)</b>
Preliminary Design Review	2.00	4.0
Critical Design Review	1.50	3.0
Acceptance / Qualification Test	1.50	2.0

Variable torque components ( $K_V$ ) are values that may vary from unit to unit or may increase over time, such as friction. Known torque components ( $K_C$ ) are much more stable and cannot increase over time. Examples of these torque components are Motor Coulomb Torque and torque to accelerate inertias. The strict interpretation of the GEVS requires high safety factors at early stages of the program. These factors are intended to apply to new development efforts. Most times for actuator applications, characteristic frictions and performance are characterized on standard motor and gearbox frame sizes. For applications that have functionally tested or qualified components, it is entirely appropriate to use CDR level factors for early program margins, and use Acceptance / Qualification levels for the specification and final deliverable product.

One of the torque contributing components is accelerating the motor and load inertia at each step of the actuator. This component, reflected to the load is as follows:

$$T_{\alpha L} = \frac{J_M \cdot K_C \cdot N^2 \cdot \Delta\theta_A}{\Delta t^2} + \frac{J_L \cdot K_C \cdot \Delta\theta_A}{\Delta t^2 \cdot \eta_G} \dots\dots\dots(8)$$

Where  $\Delta t$  is the pulse time or 1/PPS.

Note:  $\Delta\theta_L$  must be in radians for this equation. Additionally, gearbox efficiency is not applied to the motor inertia component because that torque is applied directly to the motor rotor. Motor acceleration torque is simply reflected to the output to provide consistent analysis.

Using the margins described above to determine the minimum required torque at Rated Velocity (PPS) of a geared stepper motor actuator, apply Equation 9, where  $F_L$  is the nominal friction at the load:

$$T_{PPS\_Min} = (F_L \cdot K_V) + (F_L(1 - \eta_G)(K_V - 1)) + T_{\alpha L} + (N(K_V - 1)(F_{BM} + F_{BG})) + (N(K_C - 1)F_{CM}) \dots\dots(9)$$

While there are many terms in this equation, it is simply summing the separate components that contribute to torque loads with their margin. For this equation, *only the margin terms that apply are added to the motor and gearbox bearing friction and gearbox efficiency*. Those losses have already been factored in the  $T_{PPS\_0}$  term. Only the margins have been added here because taking the margin out at the  $T_{PPS\_0}$  would lead to a mathematical linear assumption error that would apply insufficient margin in proportion to velocity. The calculation for the conservative linear approximation torque of our actuator may be completed with known information. Actuator output velocity ( $\omega_A$ ) and the Inertia Factored Response Rare ( $RR_{JF}$ ) are in degrees per second.

$$T_{PPSA} = \frac{(RR_{JF} - \omega_A) \cdot (T_{PPS\_0})}{RR_{JF}} \dots\dots\dots(10)$$

The Dynamic Margin of Safety (MoS) is calculated in Equation 11. Note: MoS must be greater than zero, for adequate torque margin.

$$MoS = \frac{T_{PPS\_A}}{T_{PPS\_Min}} - 1 \dots \dots \dots (11)$$

### Properly Specifying a Stepper Motor Actuator

Perhaps the most important aspect of selecting and integrating a geared stepper motor actuator into a system is properly defining and testing the product. This may sound obvious, but many specifications for these products fall short of the goal. A properly specified actuator should specify the components of loading and electro-magnetically generated torque components for the load (system) side as well as the actuator side. Using the example, Tables 4 and 5 delineate the components, values and tolerances.

Table 4. System Level Parameters (+25° C Unless Specified)					
Parameter	Units	Symbol	Value	Tolerance	Margin Type
Load Inertia	kg-m <sup>2</sup>	J <sub>L</sub>	5.7E-04	Nominal	Kc
Load Friction	N-m	F <sub>L</sub>	0.294	Nominal	Kv
Dynamic Velocity at Load	Degrees/sec	ω <sub>L</sub>	90	Nominal	-
Maximum System Temperature	°C	t <sub>max</sub>	+50°	Max	-
Minimum System Temperature	°C	t <sub>min</sub>	-20°	Min	-
Maximum Supply Voltage	VDC	V <sub>max</sub>	34	Max	-
Minimum Supply Voltage	VDC	V <sub>min</sub>	24	Min	-
System Step Resolution	Degrees/Step	Δθ <sub>A</sub>	1.5	Min	-
	Radians/Step	Δθ <sub>A</sub>	0.02618	Min	-
Unpowered Holding Torque	N-m	T <sub>BD</sub>	0.08	Min	-

Of course there are many other requirements that contribute to an aerospace quality component, but presenting the nominal system characteristics are the first step in deriving the requirements for the actuator that will drive that system. From the System Level Parameters, defined in Table 4, simulation is used to determine the requirements for the actuator, using the Torque Margin Requirements and methods discussed above. It is important to communicate the NOMINAL values for the torque contributing parameters because otherwise, margin will be applied on top of margin. When calculating worst-case conditions, an application may be over-powering the actuator unnecessarily, or forcing a larger actuator frame size than need be.

Table 5 delineates the derived Actuator parameters, broken down to the components and composite assembly level. As with the System Level Parameters, the contributing components of torque and applicable type of margin is utilized for those factors. Additionally, verification method using conventional (A) Analysis, (D) Demonstration, (I) Inspection, (S) Similarity and (T) Test is provided.

Table 5. Actuator Level Parameters (+25° C Unless Specified)						
Parameter	Units	Symbol	Value	Tolerance	Margin Type	Verification Method
<b>Motor Performance</b>						
Motor Inertia	kg-m <sup>2</sup>	J <sub>M</sub>	7.06E-07	Nominal	-	A
Bearing Friction Torque (at -20°C)	mN-m	f <sub>BM</sub>	1.0	Max	Kv	D, S
Magnetic Coulomb Torque	mN-m	f <sub>CM</sub>	5.0	Max	Kc	D, S
Composite Motor Friction Torques (See Note 1)	mN-m	f <sub>TM</sub>	6.0	Max	-	T
<b>Rated Pulse Rate</b>	Pulses per sec	PPS	60	Nominal	-	A

Table 5. Actuator Level Parameters (+25° C Unless Specified)						
Parameter	Units	Symbol	Value	Tolerance	Margin Type	Verification Method
DC Resistance Per Phase	Ohms	$\Omega_{25}$	50	±10%	-	T
Motor Inductance Per Phase	Henries	L	0.025	±10%	-	T
Torque Constant Per Phase	mN-m/Amp	$K_T$	240	Min	-	T
Back emf Constant Per Phase	V/Rad/sec	$K_B$	0.24	Nominal	-	T
<b>Rated</b> Minimum Current Per Phase ( <b>See Note 3</b> )	ADC	I <sub>min</sub>	0.436	Ref	-	A
Holding torque at <b>Rated</b> ADC Per Phase	mN-m	T <sub>H25</sub>	0.135	Min	-	T
No Load Response Rate	PPS	RR <sub>M</sub>	275	Min	-	T
	Deg/Sec	RR <sub>M</sub>	8250	Min	-	T
Motor Winding (Simplex or Redundant)	-	-	Simplex	-	-	A, I
<b>Gearbox Performance</b>						
Gearbox Ratio	-	N	20	Nominal	-	A, D
Fore-driving Friction	mN-m	F <sub>BG</sub>	2.0	Max	Kv	T
Gearbox Dynamic Efficiency	%	$\eta_G$	90	Min	Kc	D, S
Gearbox Torsional Stiffness	N-m/Rad	K <sub>G</sub>	1000	Reference	-	D, S
Gearbox Backlash	Degrees	$\theta_{BL}$	0.10	Max	-	I
Output Shaft Axial Play	mm/kg	$\theta_{BA}$	0.05	Max	-	I
Output Shaft Radial Play (measured at shaft end)	mm/kg	$\theta_{BR}$	0.05	Max	-	I
<b>Composite Actuator Performance (Performance at Minimum Supply Voltage)</b>						
No Load Response Rate	PPS	RR <sub>A</sub>	275	Min	-	T
	Deg/sec	RR <sub>A</sub>	412	Min	-	T
Rated Load Inertia for Dynamic Testing	kg-m <sup>2</sup>	J <sub>L</sub>	5.7E-04	Nominal	-	A
Response Rate with Rated Load Inertia	PPS	RR <sub>JFA</sub>	185	Min	-	T
	Deg/sec	RR <sub>JFA</sub>	277	Min	-	T
Resonant Frequency For Dynamic Testing ( <b>See Note 4</b> )	Hz	F <sub>n</sub>	90	Min	-	A
Torque to Accelerate at Rated PPS ( <b>See Note 2 / Equation 8</b> )	N-m	T <sub>αL</sub>	0.139	Reference	Kc	A
Velocity at <b>Rated</b> Pulse Rate	Deg/sec	$\omega_A$	90	Nominal	-	D
Pull-In Torque at <b>Rated</b> Pulse Rate ( <b>See Equation 10</b> )	N-m	T <sub>PPS_A</sub>	1.30	Min	-	T
Unpowered Back-driving Torque ( <b>See Note 5</b> )	N-m	T <sub>BD</sub>	0.09 / 0.18	Min / Max	-	T
Step Angle at Actuator Output	Degrees	$\Delta\theta_A$	1.5	Nominal	-	I

**Notes on Table 5:**

1. The Composite Motor Friction Torque is the only parameter that is testable in the final motor configuration. Bearing Friction Torque may be characterized with a preloaded set of bearings on a shaft with no magnets. Magnetic Coulomb Torque may be determined from subtracting the measured  $f_{BM}$  from the measured  $f_{TM}$ .
2. The Torque to accelerate the motor and load inertia at the required pulse rates was presented in Equation 8, above. This is provided as a reference value.
3. To calculate the **Rated** minimum current per phase divide the maximum Resistance at 25° C ( $\Omega_{25\_Max}$ ) by the minimum Supply Voltage ( $V_{Min}$ ). It is recommended to test the Holding Torque ( $T_{H25}$ ) at this value.
4. It is highly recommended that the Test Set Resonant Frequency be calculated to be greater than the operational Pulse Rate (**Rated PPS**). See Equation 12.
5. Unpowered Back-driving Torque should be specified as a minimum when the actuator detent torque is used to maintain position during launch. A maximum value should be specified in all cases, to identify a potential high-spot that may impede performance or create a latent issue.
6. Any test verification with (S) Similarity, should be characterized on a representative unit. Customer determination if Similarity verification must be conducted on Flight Production unit.

### Properly Testing a Stepper Motor Actuator

Since the performance of the actuator starts with the performance of the motor, testing the components of the actuator at each modular level, as indicated in Table 5, is highly recommended. These tests are intuitive and self-explanatory and not discussed in detail here. However, dynamic testing of the actuator assembly is vital. It is imperative to simulate the system load conditions as much as *practically* possible. It is also desirable to measure performance at the integrated system but measuring performance at the actuator level can avoid issues that may arise at a higher-level assembly. Some actuator suppliers believe that as long as back emf is tested, the actuator has been characterized. This is an over-simplified and potentially dangerous approach. Too many factors contribute to the dynamic performance of geared stepper motor actuation and the “test-as-you-fly” mantra flows down to the actuator level.

Figure 5 shows a typical geared actuator test set with simulated load inertia and performance torque transducer. A variant of this test configuration is advantageous. Rather than utilizing a loading magnetic particle brake, replace that component with a geared velocity control motor to back-drive the actuator. Employing torque transducers with integral position information is useful for position versus torque (or Torque-Theta) testing.



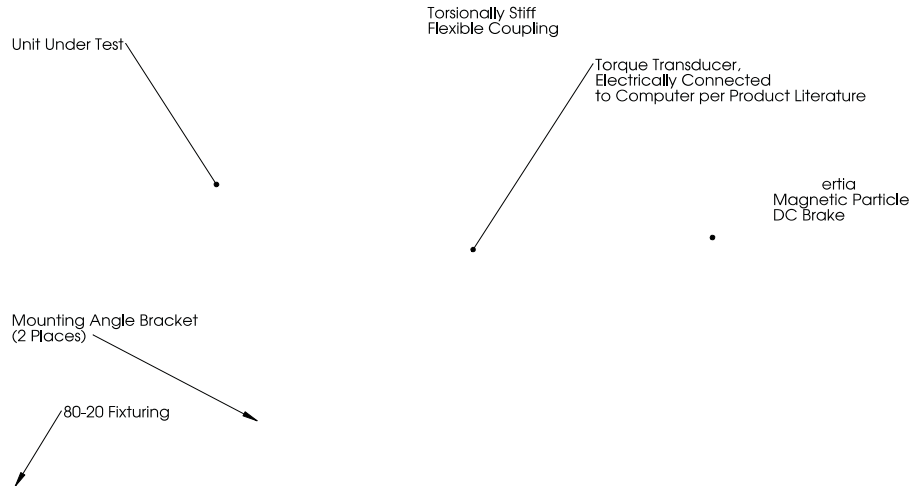


**Figure 5. Example Stepper Motor Actuator Test Set-up**

As stated in Table 5 and following notes, determining the resonant frequency of the test set-up is recommended. The Resonant Frequency ( $F_n$ ), in Hz, of the test set-up is presented in Equation 12.

$$F_n = \frac{1}{2\pi} \sqrt{\frac{K_o(J_L + J_M \cdot N^2)}{J_L \cdot J_M \cdot N^2}} \dots \dots \dots (12)$$

Where  $K_o$  is the overall system stiffness, which may be calculated by the taking the inverse of the sum of all the compliances in series:

$$\frac{1}{K_o} = \frac{1}{K_G} + \frac{1}{K_{FC1}} + \frac{1}{K_X} + \frac{1}{K_{FC2}} + \frac{1}{K_{MPB}} \dots \dots \dots (13)$$

Where  $K_G$  is the gearbox torsional stiffness, and  $K_{FC1}$  is the stiffness of Flexible Coupling 1,  $K_X$  is the stiffness of the Torque Transducer,  $K_{FC2}$  is the stiffness of Flexible Coupling 2, and  $K_{MPB}$  is the stiffness of the Magnetic Particle Brake, all in N-m/rad. To achieve our desired load inertia of 5.4E-04 kg-m<sup>2</sup> it is necessary to hard couple a flywheel on the rear end of the magnetic particle brake. By connecting the simulated load inertia here, the compliance of the magnetic particle brake must be added into the equation. When stiffness components and inertia are factored into Equations 12 and 13, we obtain a resonant frequency ( $F_n$ ) of over 220 Hz, well above the desired goal of 90 Hz. Minimum. Therefore it is known that resonances in the test set will not affect the dynamic test results at rated operational velocity.

Once the Unit Under Test (UUT) is fixtured to the test set, static and dynamic runout measurements should be made to assure alignments are proper. Also, there must not be any improper loading on the UUT or the test fixturing. It is recommended that No Load and Inertia Factored Response Rates be measured first. If there are any anomalous features of the UUT or the test set, these tests will highlight an issue quickly.

To check the Pull-In Torque, it is advised to set the magnetic particle brake to the minimum required dynamic torque value, or  $T_{PPS\_Min}$ , and start the actuator from random rest position to verify the unit pulls-in at the specified pulse rate at minimum voltage. This is a Pass / Fail method that does not verify the actual magnitude of the pull-in torque, but rather that the minimum required value is achieved. To test the

actual magnitude of the pull-in torque at a desired pulse rate is more of an iterative process. A relatively simple method that is not as laborious of continually increasing the torque test by test is to run the actuator at the desired pulse rate and increase the torque until the unit pulls-out of synchronous operation. While the unit is “buzzing” in this pulled out condition, decrease the brake torque until the actuator regains synchronous operation. Stop the unit and allow the actuator to return to room temperature, then test the pull-in torque at the torque value that returned the actuator to synchronous operation. A final minor adjustment may be necessary, but this value should be a negligible difference to the actual pull-in torque value.

Now that the performance at room temperature has been characterized, it may be desired to simulate or test the performance at maximum temperature. It is actually simple to simulate high temperature performance at ambient room temperature by calculating the motor resistance and power input as described in Equation 7 and Appendix A. With the reduced power calculated, simply adjust the power input to the supply to apply the high temperature input power, and duplicate the dynamic tests described above.

Adjusting the supply voltage cannot simulate testing an actuator at colder temperatures. While the electromagnetically generated torques are proportional in decreasing temperature, increased lube viscosity could dominate at colder temperatures and increase torque losses greater than the increased generated torque through reduced resistance. Testing inside a temperature chamber may be the only alternative, but if the cold temperature values are well within a lubricant’s rating, room temperature performance may be acceptable.

### **Conclusion**

Linear interpretation to simulate stepper motor performance when introduced to load inertia, given motor performance parameters, such as Motor Constant, Response Rate Constant and Motor frictional components has been presented. The analysis shows how to predict performance at room temperature as well as elevated temperatures. The linear approximation, however, does not predict actual variances (Cardinal Maxima and Minima) that naturally occur in stepper motor actuators. The magnitude and frequency of these variances that occur can be minimized through damping techniques.

The industry has applied the requirements of Torque Margin in many ways. To consolidate efforts and avoid over-margining, a breakdown of torque components and applied reasonable margins, in accordance with GSFC-STD-7000 has been presented.

Finally, recommendations for proper actuator specification and verification requirements were detailed. It is extremely important to conduct acceptance testing with a controller and test set-up that reflects the actual drive method and operational conditions that the actuator will see in the instrument.

### **References**

1. Scott Starin “Stepper Motor Product Catalog and Design Guidelines V2.3” November, 2013
2. GSFC-STD-7000, “General Environmental Verification Standard” (GEVS), NASA Goddard Space Flight Center, Greenbelt, MD USA, 2005
3. Shane Brown, Scott Starin “Implications of Underdamped Stepper Mechanism Performance and Damping Solution Methodology”, Proceedings of the 39<sup>th</sup> Aerospace Mechanism Symposium, NASA Marshall Space Flight Center, May 7 – 9, 2008

<b>Appendix A</b>			
<b>Stepper Motor Performance Equations (Two Phase Motor)</b>			
<b>Parameter</b>	<b>Symbol</b>	<b>Units</b>	<b>Equation</b>
Step Angle at Actuator Output	$\Delta\theta_A$	Degrees	$\Delta\theta_A = \frac{\Delta\theta_M}{N}$
Velocity at Actuator Output	$\omega_A$	$\frac{Deg}{Sec}$	$\omega_A = \frac{\Delta\theta_M * PPS}{N}$
Load Inertia Reflected to Motor	$J_{LM}$	kg-m <sup>2</sup>	$J_{LM} = \frac{J_L}{N^2}$
Inertia Factor	$J_F$	-	$J_F = \frac{J_{LM} + J_M}{J_M}$
Total Power Input at Holding (at +25° C)	$P_{H25}$	Watts	$P_{H25} = \left[ \frac{T_{H25}}{K_M} \right]^2$
Motor Constant (at +25° C)	$K_M$	$\frac{Nm}{\sqrt{Watt}}$	$K_M = \frac{T_{H25}}{\sqrt{P_{H25}}}$
Motor Constant (alternate equation)	$K_M$	$\frac{Nm}{\sqrt{Watt}}$	$K_M = \frac{K_T}{\sqrt{\Omega_{25}}}$
DC Resistance (at +25° C)	$\Omega_{25}$	Ohms	$\Omega_{25} = \frac{2 * V^2}{P_{H25}}$
DC Resistance at other Temperature (t <sub>2</sub> )	$\Omega_{t2}$	Ohms	$\Omega_{t2} = \Omega_{25} [1 + .004(t_2 - 25)]$
DC Current at Holding	$I_{25}$	Amps Per Phase	$I_{25} = \frac{V}{\Omega_{25}}$
DC Current at Holding at other Temperature (t <sub>2</sub> )	$I_{t2}$	Amps Per Phase	$I_{t2} = \frac{V}{\Omega_{t2}}$
Total Power Input at Holding, at other Temperature (t <sub>2</sub> )	$P_{Ht2}$	Watts	$P_{Ht2} = \frac{2V^2}{\Omega_{t2}}$
Torque Constant	$K_T$	$\frac{Nm}{Amp}$	$K_T = \frac{T_{H25}}{1.414 * I_{25}}$
Torque Constant (alternate equation)	$K_T$	$\frac{Nm}{Amp}$	$K_T = K_M * \sqrt{\Omega_{25}}$
Holding Torque at +25° C	$T_{H25}$	N-m	$T_{H25} = (N * \eta_G) * K_{M25} * \sqrt{P_{H25}}$
Holding Torque at +25° C (alternate equation)	$T_{H25}$	N-m	$T_{H25} = (N * \eta_G) * K_T * I_{25} * 1.414$
Holding Torque at other Temperature (t <sub>2</sub> )	$T_{Ht2}$	N-m	$T_{Ht2} = (N * \eta_G) * K_T * I_{t2} * 1.414$
Torque at Low Pulse Rate at +25°C	$T_{PPS_0}$	N-m	$T_{PPS_0} = (T_{H25} * 0.707) - N(f_{BM} + f_{CM} + f_{BG})$
No Load Response Rate at Actuator Output (at +25° C)	RR	$\frac{Deg}{Sec}$	$RR = \frac{K_{RR} * 6 * \sqrt{P_{H25}}}{N}$

Appendix A			
Stepper Motor Performance Equations (Two Phase Motor)			
Parameter	Symbol	Units	Equation
Inertia Factored Response Rate at Motor (at +25° C)	$RR_{JF}$	$\frac{Deg}{Sec}$	$RR_{JF} = \frac{K_{RR} \cdot 6 \cdot \sqrt{P_{H25}}}{N * \sqrt{J_F}}$
Acceleration Torques, Reflected to Load <b>Note- <math>\Delta\theta_A</math> must be in radians for this equation</b>	$T_{\alpha L}$	N-m	$T_{\alpha L} = \frac{J_M \cdot K_C \cdot N^2 \cdot \Delta\theta_A}{\Delta t^2} + \frac{J_L \cdot K_C \cdot \Delta\theta_A}{\Delta t^2 \cdot \eta_G}$
Available Pull In Torque at Required Pulse Rate at Actuator Output	$T_{PPSA}$	N-m	$T_{PPSA} = \frac{(RR_{JF} - \omega_A) (T_{PPS_0})}{RR_{JF}}$
Required Pull In Torque at Required Pulse Rate at Actuator Output (Interpreted from GSFC-STD-2000)	$T_{PPS_{Min}}$	N-m	$T_{PPS_{Min}} = (F_L \cdot K_V) + (F_L(1 - \eta_G)(K_V - 1)) + T_{\alpha L} + (N(K_V - 1)(F_{BM} + F_{BG})) + (N(K_C - 1)F_{CM})$
Margin of Safety (must be >0 for adequate torque margin)	MoS	-	$MoS = \frac{T_{PPS_A}}{T_{PPS_{Min}}} - 1$
Natural Circular Resonant Frequency	$F_n$	Hertz	$F_n = \frac{1}{2\pi} \sqrt{\frac{K_o(J_L + J_M \cdot N^2)}{J_L \cdot J_M \cdot N^2}}$

## Appendix A Variable Definition

Symbol	Units	Definition / Comment
$\Delta\theta_M$	Degrees/step	Step Angle at Motor. Supplier provided value.
PPS	Steps Per Second	Application Dynamic Pulse Rate (Pulses Per Second)
N	-	Gearbox Ratio. Supplier provided value.
$J_L$	kg-m <sup>2</sup>	Load Inertia
$J_M$	kg-m <sup>2</sup>	Motor Inertia. Supplier provided value.
$K_{RR}$	$\frac{RPM}{\sqrt{Watt}}$	Motor Response Rate Constant – Supplier provided value. Value will change for drive method and whether unit is simplex or redundant.
$\eta_G$	%	Gearbox Efficiency. Supplier provided value.
$f_{BM}$	N-m	Motor Bearing Rolling Friction. Supplier provided value.
$f_{CM}$	N-m	Motor Coulomb or Detent Torque. Supplier provided value.
$f_{BG}$	N-m	Gearbox fore-driving bearing friction. Supplier provided value.
$K_C$	-	Torque Margin Factor for Known (Stable) Source. Value changes at maturity stage of the program. See Table 3.
$K_V$	-	Torque Margin Factor for Variable (Potentially Changing) Source. Value changes at maturity stage of the program. See Table 3.
$F_L$	N-m	Friction at the Load
$K_O$	N-m/Radian	System Overall Torsional Stiffness.
V	Volts, DC	Supply Voltage (should be de-rated for electronics headroom)
$\Delta t$	Seconds	Seconds per step or 1/PPS



# Development Testing and Subsequent Failure Investigation of a Spring Strut Mechanism

Jared Dervan<sup>\*</sup>, Brandan Robertson<sup>\*\*</sup>, Lucas Staab<sup>+</sup>, Michael Culberson<sup>\*\*</sup> and Joseph Pellicciotti<sup>+++</sup>

## Abstract

The NASA Engineering and Safety Center (NESC) and Lockheed Martin (LM) performed random vibration testing on a single spring strut development unit to assess its ability to withstand qualification-level random vibration environments. Failure of the strut while exposed to random vibration resulted in a follow-on failure investigation, design changes, and additional development tests. This paper focuses on the results of the failure investigations referenced in detail in the NESC final report [1] including identified lessons learned to aid in future design iterations of the spring strut and to help other mechanism developers avoid similar pitfalls.

## Introduction

Commodities are transferred between the Multi-Purpose Crew Vehicle (MPCV) crew module (CM) and service module (SM) via an external umbilical that is driven apart with spring-loaded struts after the structural connection is severed, as shown in Figure 1. The spring struts must operate correctly for the modules to separate safely. The MPCV program plan did not include development vibration testing of this strut for the Exploration Flight Test 1 (EFT-1) mission, thus any design problems discovered as a result of vibration testing would not have been found until the component verification testing, potentially causing large program schedule delays. The MPCV Program Chief Engineer submitted a request to the NESC to perform random vibration testing on a single spring strut development unit to mitigate this risk.

The objective of the NESC assessment was to perform development vibration testing on a flight-like umbilical spring strut and evaluate the strut's behavior during and after the test. Roles and responsibilities were distributed between NESC personnel and the MPCV Program prime contractor, LM.

As part of the test program, low-level vibration and performance tests (consisting of force-displacement curve generation) were to be performed prior to and following a qualification-level random vibration testing to characterize the baseline system response and performance and help detect changes as a result of the random vibration testing. The random vibration portion of the test was to begin at low levels, ramping in increments through maximum predicted environment (MPE) levels to qualification levels (MPE +6 dB for the MPCV Program) and held at qualification levels for 3 minutes in each axis while in a stowed configuration. Pre- and post-test inspections and collection of digital imagery were planned. Following the testing and performance evaluations, the strut was to be disassembled and inspected for damage/wear with a report detailing the findings.

During random vibration testing of the last test configuration, the spring strut encountered a failure of the forward locking elements resulting in a rotation of the strut and subsequent fatigue failure. A follow-on root cause investigation was performed that identified supporting rationale for a failure scenario that included aspects of design, analysis, test, and workmanship. Lessons learned pertaining to areas of joint

---

<sup>\*</sup> NASA Marshall Space Flight Center, Huntsville, AL

<sup>\*\*</sup> NASA Johnson Space Center, Houston, TX

<sup>+</sup> NASA Glenn Research Center, Cleveland, OH

<sup>\*\*</sup> Lockheed Martin Space Systems Company, Littleton, CO

<sup>+++</sup> NASA Goddard Space Flight Center, Greenbelt, MD

design, significance of secondary effects, material selection, and processing, to name a few, were identified to aid in future design iterations.



**Figure 1. MPCV EFT-1 CM-SM Umbilical in its Stowed Configuration**

### **Hardware Description and Development**

The CM-SM umbilical spring strut consists of multiple piece parts assembled with sliding contact interfaces. A detailed image of the assembly with piece parts identified can be found in Figure 2. The titanium actuator spring is compressed when configured to the strut flight length (780 mm (30.7 in) between end fitting spherical bearings). The compression force is applied to the aft cap, located on the SM side, and piston located internal to the actuator housing. The piston transfers the load to the secondary piston through a contact constraint normal to the strut axis. The contact surface between the piston and secondary piston is permitted to rotate relative to one another and is only opposed by friction. When the strut is permitted to actuate, after release of the umbilical interface at the CM, the compressed spring forces the piston forward sliding through the actuator housing and driving the secondary piston forward. Dual spring-loaded latches slide over the piston as it moves through the actuator housing. Once the piston traveled past the latches, the latches are forced into the actuator housing cavity prohibiting the piston from returning to its pre-actuation position. During the actuation, the driven secondary piston will move until it contacts the aluminum honeycomb damper dissipating the energy of the forward stroke.

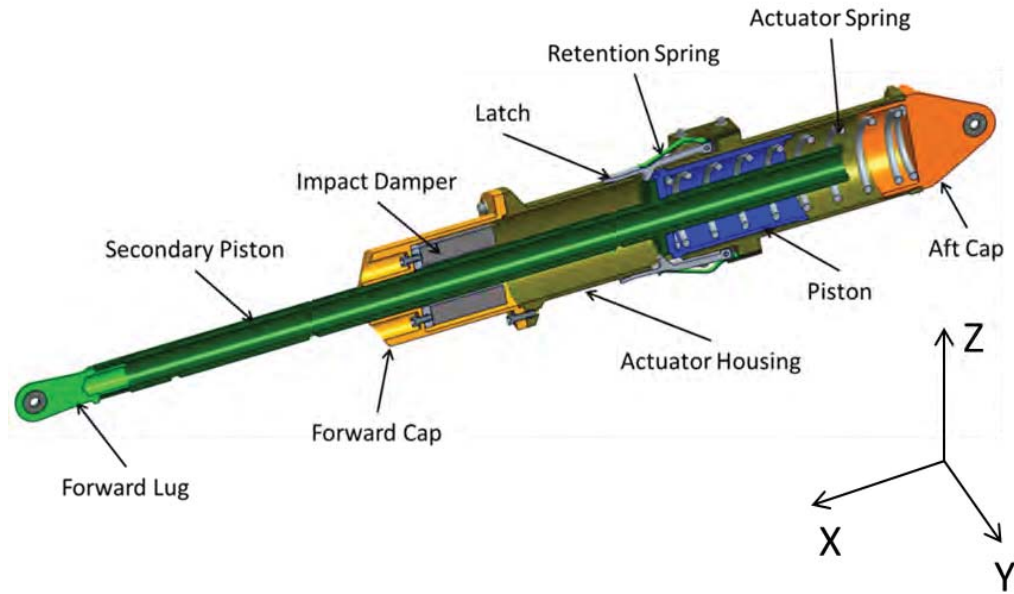


**Figure 2. MPCV CM-SM Umbilical Spring Strut Detail Cross Section**

The forward lug interfaces with the umbilical side of the CM-SM umbilical mechanism while the aft cap interfaces with the SM side. A spherical bearing in both end fittings is pinned in a clevis and permits some misalignment when installed in the flight vehicle or test fixtures. The umbilical side test interface consisted of a test fixture and the SM side interface a flight-like actuator bracket. The forward lug and aft cap have threaded aluminum 7050 interfaces to their adjoining parts, the secondary piston and actuator housing, respectively. The threads for these parts were cut and have an applied polyester locking patch and single braided lockwire between the elements to serve as secondary locking features.

As-designed, aluminum 7050 parts with sliding contact interfaces, the secondary piston, forward cap, actuator housing, and piston, have a General Magnaplate proprietary Tufram L-4 surface treatment. This treatment is a polymer (i.e., polytetrafluoroethylene (PTFE)) impregnated Type III hard anodize to minimize stick/slip. During NESC fabrication, a Type III hard anodize was mistakenly applied instead of the as-designed surface treatment. The test hardware surface treatment was considered to provide a conservative wear condition at the sliding surfaces and deemed acceptable by the joint NESC and LM team for the development test program.

After compressing the strut to the stowed flight length, a retention tool (shown in Figure 3) was applied to sustain the compressed state of the strut. The retention tool interfaces with two through tooling holes located in the secondary piston and the body of the actuator housing. The tool was applied after initial assembly, after pre- and post-random vibration performance testing, and during reconfiguration between random vibration test axes.



**Figure 3. CM-SM Umbilical Spring Strut with Retention Tool**

## Development Testing

Random vibration testing was performed after initial performance testing (described below) to assess the umbilical spring struts capability to meet applicable functional requirements following exposure to qualification levels of random vibration environments. This process included acceptance testing intended to screen production units for latent manufacturing, material, and workmanship defects.

Two random vibration environments in each axis were provided by LM for the umbilical and SM side inputs. Several options were initially evaluated for the random vibration test configuration before reaching an agreement to utilize two T-2000 Unholtz-Dickie 80068 N (18000 lb<sub>f</sub>) shakers with two shaker control systems and two random vibration environments applied simultaneously and uncorrelated. By using two shakers, the umbilical strut was exposed to the required environments and was the closest to qualification of a “flight-like” configuration. The dual shaker configuration can be found in Figure 4.

Strain gages (four total) were initially installed only on the aft housing due to channel number limits. After Z-axis testing, three strain gages were added to the secondary piston and used in place of three of the aft housing gages. The control 3-axis accelerometers for test control, channels 1-12, were placed on the test fixtures (two on each end).

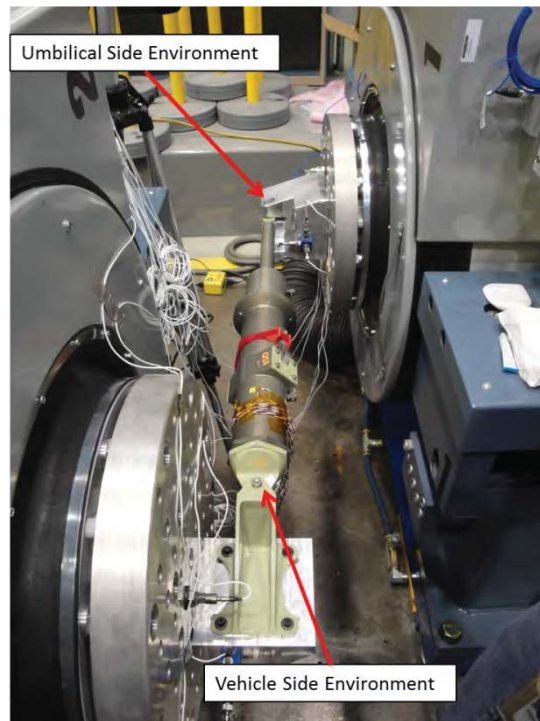


**Figure 4. Dual Shaker Configuration (Z-axis)**

The test proceeded with the Z-axis first followed by the X-axis and finally the Y-axis. Each testing axis followed a similar pattern: minimum workmanship screening (MWS) and acceptance level loads were applied for 60 seconds, followed by the qualification levels for 3 minutes, and finally another MWS for comparison to the first MWS to assess changes in stiffness. Figure 5 illustrates discrepancies in responses that were seen upon comparison of the pre- and post-qualification level MWS runs in the Z-axis. The difference was found to be loosening of the aft cap during the qualification level testing. The aft cap was re-torqued and additional lockwire at a larger gauge was applied for follow-on testing. Figure 5 shows the minimal difference in the X-axis pre- and post-qualification level MWS runs. Additionally, the assessment team noted debris was observed exiting the spring strut when qualification levels were



applied in both Z- and X-axes. A borescope was used after testing in each axis to qualitatively assess the magnitude of internal wear and provide a comparison from axis to axis. For the Z- and X-axis testing, the hardware was exposed to the target levels with no significant (i.e., operation-inhibiting) damage observed and thus deemed successful.

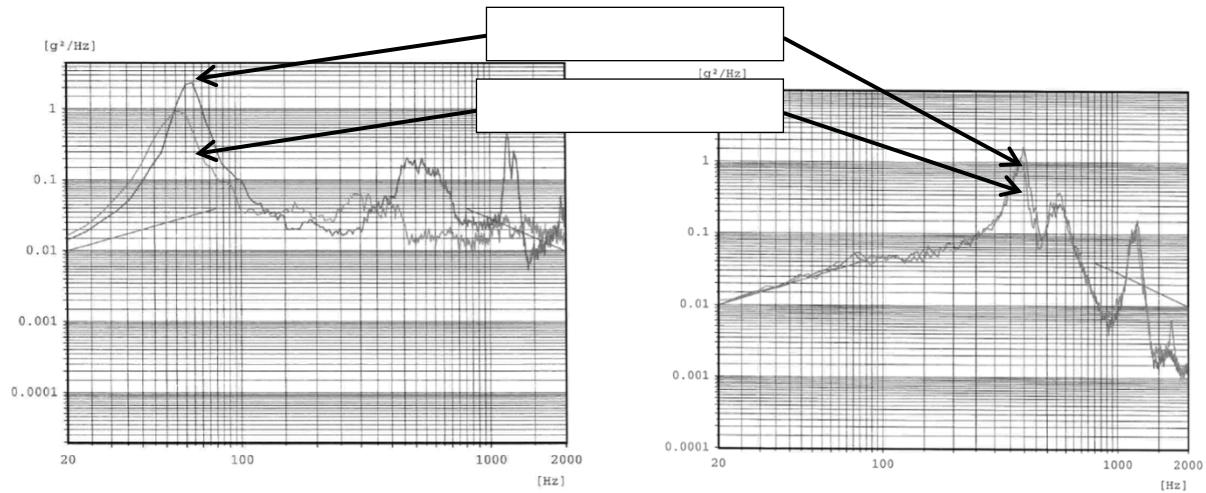


**Figure 5. Typical Pre- and Post-Qualification MWS Differences (Z-axis [left]; X-axis [right])**

The Y-axis was anticipated to be the worst environment for the hardware. MWS and acceptance levels were completed in the Y-axis. However, during the qualification level test, a distinct change in the sound and response produced by the hardware was observed 27 seconds into the full level qualification run. A lack of clear visual failure indicators coupled with ill-defined criteria for test stoppage resulted in continuation of the testing to the full duration (3 minutes). Upon completion of the test, the NESC team found the secondary piston had failed at the aft tooling hole and the lockwire restraining the forward lug from rotating had failed (Figure 6). Due to the failure of the spring strut hardware, no further random vibration testing could be completed and the hardware was taken back for investigation and performance testing. Note that even though the test hardware incurred a failure, the testing was ultimately considered successful because it flagged design deficiencies before they were encountered late in the test and verification cycle.

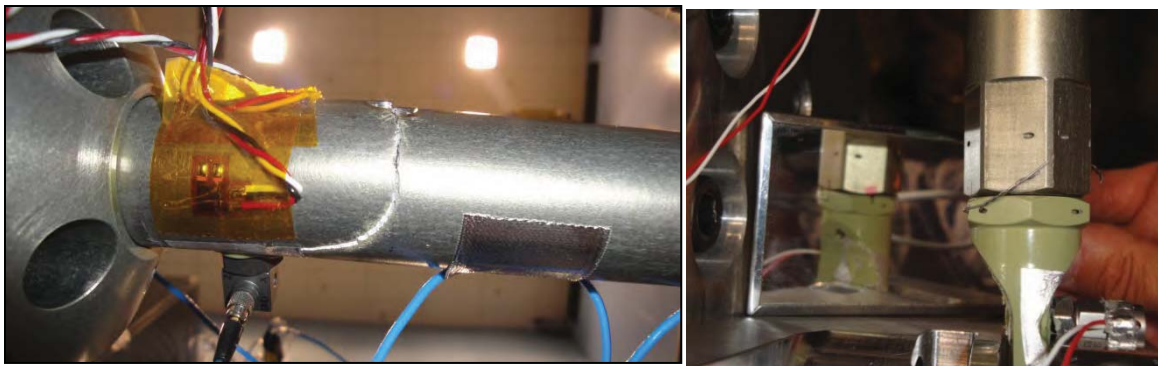


**Figure 6. Structural Failure of Secondary Piston at Aft Tooling Hole [left]; Lockwire Failure at Forward Lug [right]**

In the performance test, the development spring strut was exercised at a slow rate from the flight configuration (stowed) to the extended position (Figure 7) to measure the load versus displacement characteristics and observe the function of the anti-back-travel latches. In the wear-in test, the strut was



exercised 15 times at nominal deployment speeds (394 mm/s (15.5 in/s)). During the test, the strut was stroked from the flight length to the extended position to reach steady state performance and to observe potential wear or performance degradation. After wear-in, the strut was stored at the flight configuration with the retention tool applied and shipped to the random vibration testing facility.

After failure during the random vibration testing, the strut was returned to the performance testing facility with a truncated secondary piston to remove the failed portion of the strut. Using a cupping interface, post-vibe performance deployment tests were performed with the strut assembled in the load frame. The post-vibration performance test served primarily to assess whether there were any large excursions from the nominal force-deflection curve. These excursions could be indicative of significant damage to the spring strut sliding surface. The post-vibration performance test satisfied the nominal expected end of travel force of  $165 \text{ N} \pm 27 \text{ N}$  ( $37 \pm 6 \text{ lbf}$ ) and resulted in nominal engagement of the anti-back travel latches. Force versus displacement within the expected tolerance yielded acceptable force margin based on the next high assembly assumptions and calculations. A comparison of the pre- and post-random vibration performance test is shown in Figures 8.

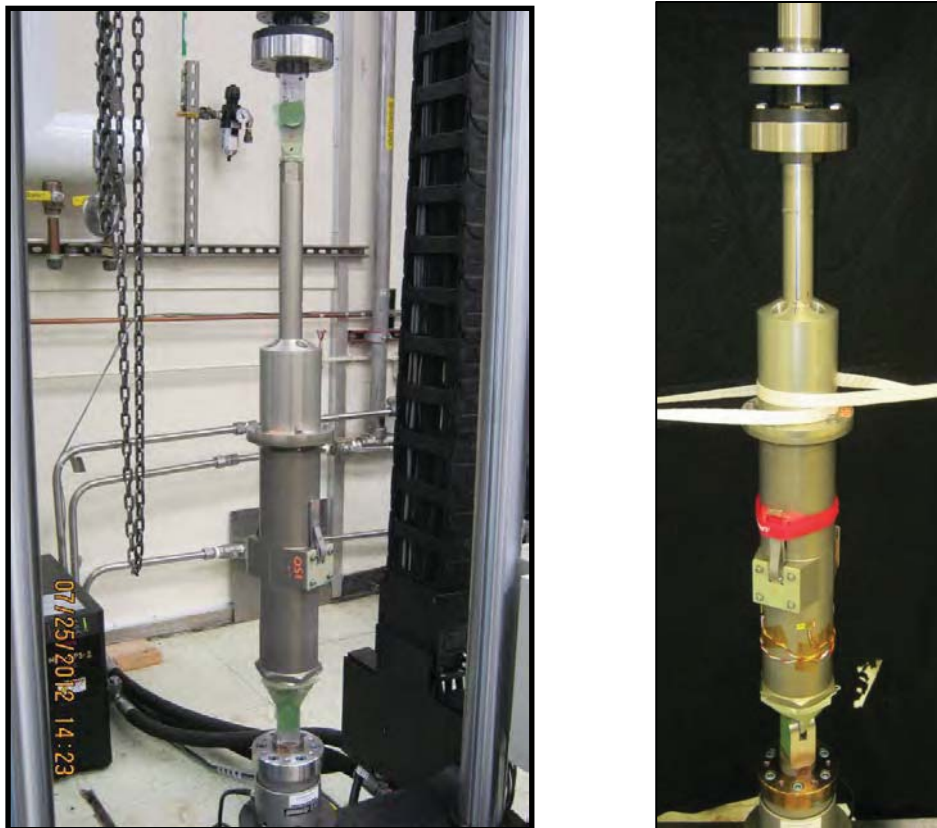
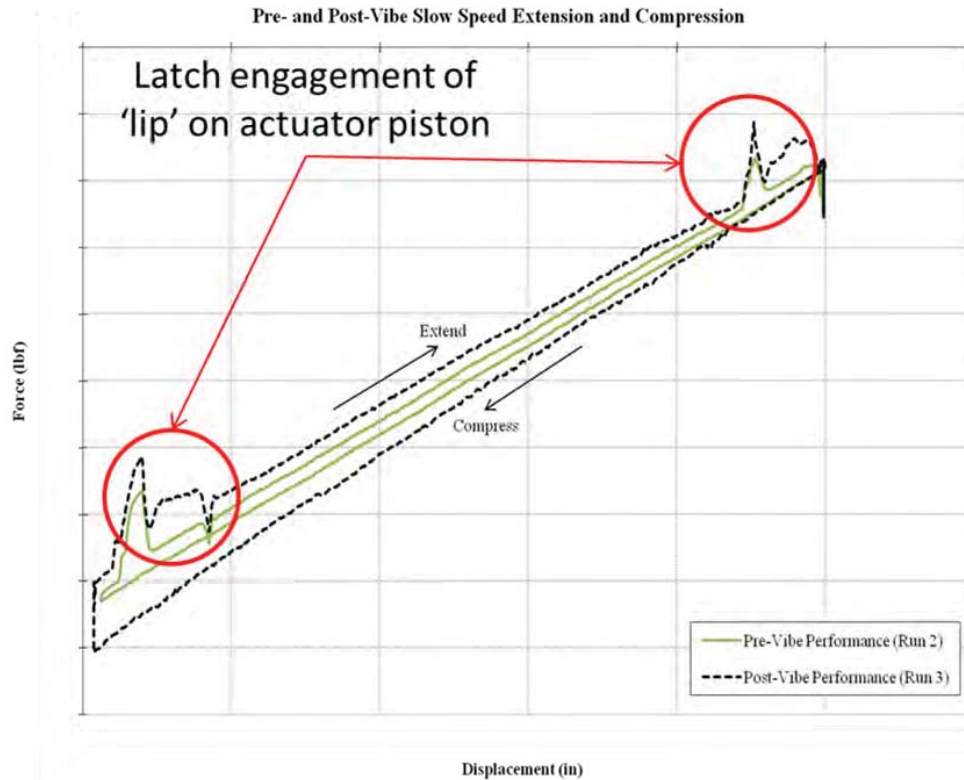


Figure 7. Test Setup for Performance Testing (Pre-Vibe [left] and Post-Vibe [right])



**Figure 8. Force versus Displacement Plot for Slow Speed Extension**

### Root Cause Investigation and Findings

Immediately following the strut failure, the joint NESC and LM team generated a fishbone diagram. Individual elements were classified as aspects of design, analysis, test, and/or workmanship. Related and supporting evidence was gathered to disposition those elements as either most probable cause, contributor, credible, credible but unlikely, or non-credible. The NESC/LM joint investigation occurred over a month whereupon, due to MPCV Program schedule pressure, LM chose to implement corrective actions addressing identified proximate causes and assumed ownership of the CM-SM umbilical spring strut development test program. The NESC team continued the investigation in an effort to identify root cause and the most probable failure scenario. Supporting analyses were completed, photographic evidence was reviewed, and inspections were conducted to provide rationale for fishbone element classifications shown in Figure 9. Detailed information regarding the root cause investigation, including classification definition, can be found in the full NESC assessment report [1].

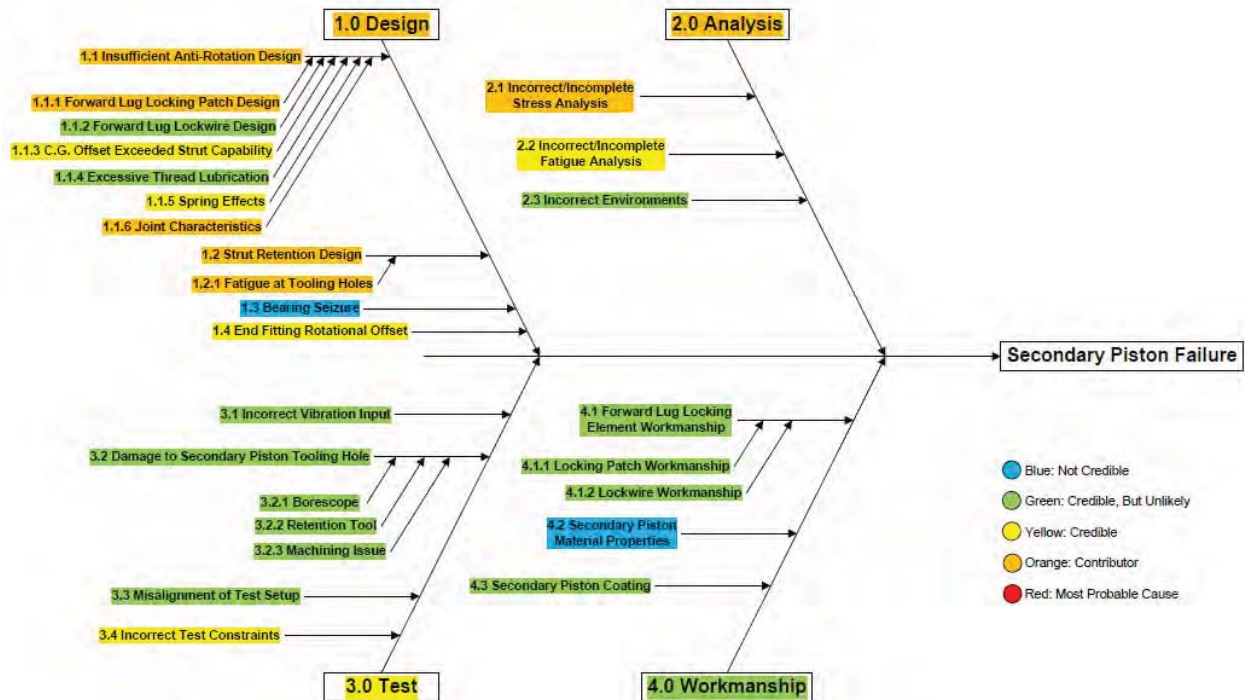


Figure 9. Fishbone Diagram

### Failure Scenario Supporting Elements

The following key findings related to the root cause investigation elements were utilized to devise a most probable failure scenario.

- Test Video and Strain Gauge Data:** Immediately after application of the qualification levels, the SM side assembly (aft cap, actuator housing, and forward cap) rotated clockwise (looking SM to umbilical side). Lagging this rotation, the secondary piston was observed to rotate counterclockwise. Inspection of data from strain gauges mounted on the secondary piston and visual indicators of mounted accelerometers indicated a rotation of approximately 90 degrees. Strain gauge data with indicators of tooling hole orientation relative to the Y-axis applied load can be found in Figure 10. Approximately 27 seconds after application of qualification levels (242 seconds) there was a noticeable decrease in noise and strut dynamic response. No noticeable damage was observed, so the test was continued to the full duration at 395 seconds.
- Forward Lug Locking Patch Design:** Load requirements for the locking patch were not defined prior to developmental testing. Designers did not anticipate any applied loosening torque to aid in the patch sizing in part due to the fact that the strut would be in compression during vibration testing. Additionally, it is not standard practice to perform supporting analyses of locking patch capability. Locking patches are not intended to serve as torque reaction features; rather, they should be used to reduce the rate of preload loss in a joint. The prevailing torque requirement was less than the minimum recommended running torques specified for fine thread series threads 38.1 mm (1.500 in) in diameter or less. The locking patch vendor indicated the patch size was small relative to the thread size and pitch to which they were applied.
- Joint Characteristics:** The threads utilized for testing had an as-designed preload limited to 25 percent of the tensile yield strength ( $F_{ty}$ ), which was constrained by Material Usage Agreement (MUA) dictating sustained stresses to be less than 50 percent  $F_{ty}$  due to stress corrosion cracking (SCC) susceptibility of the joint material, aluminum 7050-T7451. Preload is the primary means of joint loosening when subjected to cyclic, transverse loads. Typical torques sufficient to prevent loosening

during vibration are in the 70 percent  $F_{ty}$  range [2]. Preload was applied to the joint by tightening to a predetermined torque range. Galling, typical for threaded aluminum joints, would have added to the resistive torque measured during application of a final assembly torque and resulted in a reduced as-assembled preload. Additionally, the profile of the forward lug and aft cap could have contributed to lower preload values given the end fittings were hollow and more susceptible to flexure and joint relaxation. The requirements and analysis methods utilized in the assessment of joint preload [3, 4] did not consider bending as a potential source of joint separation and are primarily focused on typical bolted joints and fasteners, the definitions of which are not completely applicable to the spring strut joints.

4. **Strut Retention Design and Fatigue Analysis:** The retention tool utilized to hold the spring strut in a compressed state interfaces with secondary piston tooling holes and clamps onto the actuator housing body just aft of the actuator housing-to-forward cap interface. The two tooling holes were machined as a part of the spring strut assembly process whereupon the forward lug is fastened to the secondary piston, the location of the tooling holes relative to this subassembly are identified, and the forward lug is removed and holes machined. Since this machining operation occurs during the assembly phase, the tooling holes did not have the surface treatment that was applied to the rest of the secondary piston.

Prior stress and fracture analyses did not include the tooling holes, and the secondary piston was not considered fracture critical. Large structural margins in this analysis deemed the secondary piston satisfied the definition of a 'low risk' component and were subsequently classified as non-fracture critical. These prior analyses were based on flight load factors found to be inadequate and inconsistent with the EFT-1 flight configuration. After the secondary piston failure, an updated fatigue analysis was performed accounting for the off-nominal secondary piston rotation to quantify the Cumulative Damage Index (CDI) using Rayleigh's distribution and Miner's Rule for response to the base input Power Spectral Density (PSD). In summary, the analysis results showed exceedance of the secondary piston fatigue life capability at the tooling hole ( $CDI = 1.519 > 1.0$ ) when subjected to Y-axis qualification levels in a maximum bending condition. After the failure, the spring strut was evaluated by LM and Marshall Space Flight Center (MSFC) failure analysis groups with both groups concluding the structural failure occurred at the aft-most secondary piston tooling hole initiated in fatigue followed by ductile overload. The opposite side of the failed tooling hole also showed the beginnings of fatigue cracking.

5. **CG Offset:** Through hardware inspection and as-designed tolerance limitations on select dimensions, the spring strut center of gravity (CG) could be approximated as 1.09 mm (0.043 in) offset for the forward assembly (i.e., secondary piston, forward lug, actuator spring, and piston) and 0.76 mm (0.030 in) offset for the aft assembly (i.e., aft cap, actuator housing, forward cap, damper module assembly, latch, retention spring, and fasteners) in the Z-axis. With random vibration loads applied to the strut, the CG offset in the forward assembly could contribute to a moment being applied in the direction of rotation of the secondary piston during the Y-axis random vibration testing. Other factors that may have contributed to the applied torque on secondary piston are the static, induced torque from compression of the actuator spring and the instrumentation mass offset from the strut centerline, neither of which was incorporated into the pre-test analysis.

Application of recorded time history data permitted an across-the-board comparison of applied torque versus estimated torque capability as a function of CG offset. It was shown that the required torque to overcome the forward lug-to-secondary piston secondary locking feature's capability would have been exceeded given a 3- and 4- $\sigma$  load and 1.09-mm (0.043-in) CG offset. Similarly, reasonably attainable CG offsets would have resulted in significant induced torques relative to the predicted capability of the joint for a 3- $\sigma$  load. Therefore, the CG offset in the forward assembly could have led to induced torques capable of overcoming the torque-resistive capability of the forward strut interface with reasonable assumptions, known input environments, and predicted dynamic responses. Note that no such reasonably attainable CG offset would have induced significant enough torque to



overcome the aft cap-to-actuator housing secondary locking feature with increased capability (augmented after Z-axis testing).

6. **Spring Effects:** In addition to bias torques induced by compression of the in-line spring, hand calculations confirmed the potential for an offset spring mass. Given the free length, compressed length, spring diameter, and pitch, the titanium spring would have experienced buckling in its compressed state. As a significant mass contributor, this buckling would have further offset the CG from the strut centerline. Evidence of this offset can be found in wear observed internal to the actuator housing from an apparent contact with the spring.
7. **End Fitting Rotational Offset:** Indications of wear are evident on the end fittings and adjoining clevises (Figure 11). Contact due to misalignment/rotational offset would have imparted a force off-axis from the strut and induced a torque applied to the end fittings. If the force was sufficient to overcome resistive elements of the joint, then the end fittings could have tightened or loosened. Loosening at the forward strut interface would have permitted an applied torque to more easily rotate the secondary piston relative to the forward lug.

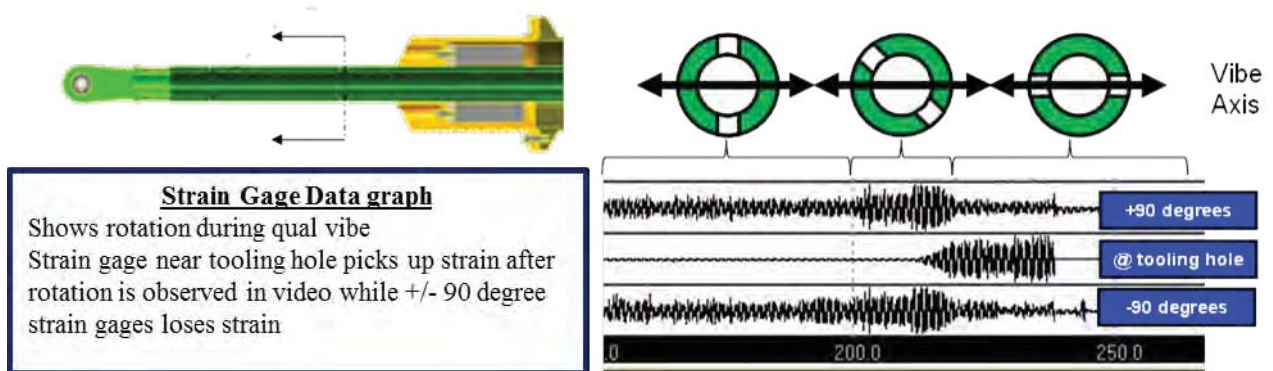


**Figure 10. Strain Gauge Data and Strut Rotation**



**Figure 11. Wear Post-Vibration Testing (Forward Lug [left]; Test Fixture [right])**

**Failure Scenario**

The following failure scenario was identified to best correlate with the evidence collected during the root cause investigation. Due to the varied classifications of elements identified, this failure scenario should not be considered definitive. Technical limitations for failure scenario supporting elements are provided and discussed in reference 1.



During vibration testing there was contact between the aft cap and SM side actuator bracket and the forward lug and test fixture, with significant wear observed during post-test inspection. This produced a constraint and source of induced reaction force off-axis from the strut. The strut design also permitted a CG offset due to a combination of sliding contact interfaces, machining tolerances, non-axisymmetric nature of select piece parts, elastically buckled spring, and gravity loads as installed in the random vibration test fixture. The design also did not include an alignment feature integral to the strut, therefore forward lug and aft cap strut end fitting alignment was not guaranteed and permitted rotational misalignment between the two rod ends.

In the first test configuration (Z-axis), this contact constraint, combined with inertial forces from an offset of the strut CG and maximum SM side environments, resulted in an induced loosening torque on the aft cap. The lack of prevailing torque from an undersized aft cap locking patch increased the joint's susceptibility to loosening. The aft cap was observed to have loosened after Z-axis testing whereupon it was retightened to the required torque. Lockwire was then re-applied in larger quantities and gauge thickness to further increase the torque reaction capability of the joint.

In the last test configuration (Y-axis), a similar contact condition induced a torque at the forward strut interface. The maximum umbilical side environments were applied during Y-axis testing, which, when combined with the CG offset, induced a significant torque about the forward lug. Given a contact condition, again observed through post-test inspection, the forward lug relative to the secondary piston could have been free to rotate in the direction of tightening while contacting the test fixture off-axis from the strut centerline in the direction of loosening. The contact condition would have induced a torsional load to loosen the forward cap-to-secondary piston interface. Once the inertia-induced torque exceeded the capability of the joint which includes a combination of breakaway torque, prevailing torque from the locking patch, and lockwire capability, the secondary piston rotated relative to the forward lug breaking the lockwire. At this point the resistive torque was limited to that provided by the undersized locking patch. The rotation continued until the CG offset was small enough relative to the applied force vector that the prevailing torque of the locking patch exceeded the applied torque (i.e., approximately 90 degrees).

Due to the rotation, strut tooling holes, nominally in the neutral bending axis during the Y-axis vibration test, were placed in maximum bending. Once the fatigue life capability at the tooling hole was exceeded, the secondary piston failed by crack growth and overload.

### **Additional Development Testing**

After assessing the results of the NESC-led test and identifying proximate causes of the failure, LM reclaimed responsibility for further strut development testing. Programmatic pressure drove LM to make immediate, low-impact design changes based on proximate cause. The NESC continued the investigation into root cause in parallel with the spring strut redesign effort.

The NESC team was kept apprised of the redesign activities by the MPCV CM subsystem management team. LM made design changes intended to prevent loosening of the threaded parts and eliminate fatigue initiation sites, then retested the strut. These changes included an increase in the size of the secondary locking patches, quantity and diameter of lockwire, and preload at the end fitting joints (50 percent of  $F_{ty}$ ). Additionally, the tooling holes were removed and a new retention tool design was devised. Once the initial redesign effort was complete, LM began with the Y-axis test, which was the worst case and the axis in which the secondary piston failed. Shortly after reaching qualification levels, the strut suffered another failure. This time, the forward lug fractured at the secondary piston interface. A subsequent investigation by LM determined fatigue failure was the cause and that the corrections made appeared to be working up to the point at which the testing was stopped. The LM retest had reused a majority of the hardware from the original test unit (including the forward lug) without a residual life assessment. Analysis revealed the fractured rod end had exceeded its fatigue life capability. Gapping in the joint between the rod end and the secondary piston exacerbated the problem.

LM performed a residual life assessment on all parts to identify any other components at risk. Those items with insufficient life were replaced. Numerous design changes as shown in Figure 12 were also incorporated: the secondary piston was redesigned to eliminate the joint between the rod end and the secondary piston by replacing the assembly with a rod end integral to the secondary piston, the tooling hole interface to the retention tool was replaced with a clamp-style tool, and the aft cap-to-actuator housing interface was adhesively bonded after application of the required preload. The new design was placed through a new random vibration test, this time using an approach that included qualification for AVT per reference 5, and the unit passed the vibration test and post-vibration performance testing.

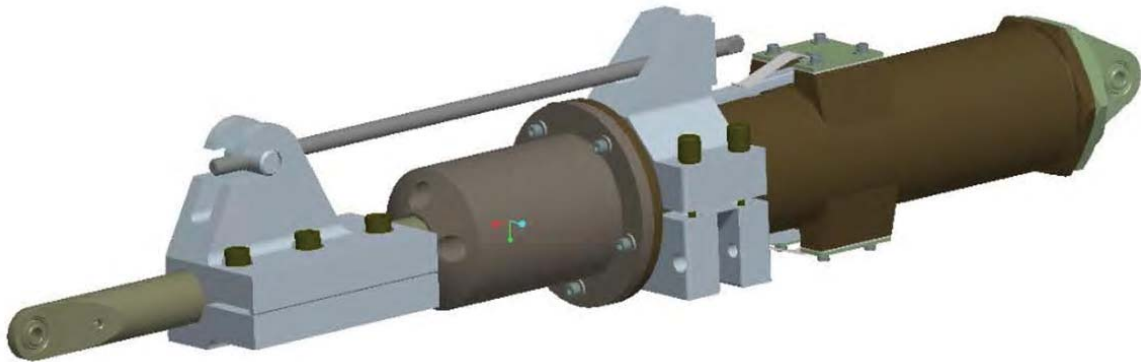


**Figure 12. Updated Spring Strut Design**

#### **Lessons Learned**

The assessment and the subsequent failure investigation resulted in a number of lessons learned. Those described above are reflected below in addition to others more fully described in the NESC final report [1].

1. **Care must be taken in adapting heritage designs to new applications.** An actuator design from a mars lander support leg design was adapted for the spring strut application. As the design evolved and was scaled to the new application, some of the features became obsolete, but were retained; this was the case with the forward lug/secondary piston interface. A focused evaluation of the interface would have led to its elimination earlier in the design cycle.
2. **Threaded aluminum parts should only be used in lightly loaded applications (e.g., an application that does not see severe, cyclic bending loads).** The threaded interface in the bending load path of the piston was able to be eliminated in the subsequent design. With regard to the aft cap, an alternative to the aluminum threaded interface could be designed to include a flange mounted interface with a pattern of standard fasteners providing the structural connection.
3. **Avoid designs that have the potential to utilize fastener thread locking features to react applied or induced torque in the higher level assembly.** Thread locking features are intended only to resist self-loosening. However, in this strut design they were used in a way that depended on them to react any torque that was applied to the entire strut by the environments. Thread locking features are not intended or designed to react applied torques that are part of the structural load path and should not be used to do so.
4. **Ensure sufficient preloads are obtained (e.g., through joint material selection) to reduce the potential for joint loosening.** Due to the choice of aluminum 7050-T7451, the permissible preload of the joints was reduced to avoid the potential for stress corrosion cracking. Given preload is the primary means to combat joint loosening, the design was highly susceptible to the failure observed when subjected to a significant random vibration environment.

5. **Conduct machining operations prior to surface treatments to reduce the potential for crack initiation.** Machining of the holes after applying the anodic coating likely influenced crack initiation of ~12  $\mu\text{m}$  (4.7E-4 in) depth through the anodic coating and into the base material. The tooling hole machining process may have contributed to the fatigue crack initiation. MSFC failure analysis noted that '[h]ard anodized coatings reduce the fatigue life and increase the number of crack initiation site [sic] when applied to aluminum 7050-T7451.' There is evidence that '[a]nodic oxidation of light alloys reduces bending endurance limits by as much as 39 percent'.
6. **Utilize dedicated tooling for locking patch process development.** This prevents unneeded cycling of the test article or flight unit's threads during the locking patch development.
7. **Utilize visual movement indicators (e.g., torque striping) for threaded joints.** The umbilical strut had torque stripes applied to certain indicators that were of high value during the investigation. However, not all threaded interfaces had torque stripes so the state of some could not be ascertained. Torque striping is typically very easy and inexpensive to apply.
8. **Conduct testing to determine the required limits on running torque for joint designs not conforming to available standards and specifications.** The running torques and preload torques found in most tables have been determined through testing of specific joint combinations. Applying those torques to configurations other than those from which the values were derived may result in large differences from what is needed. In the case of this strut, the material modulus was three times lower than a steel fastener and the threaded body was hollow, generating a much different stiffness in the joint than assumed in the torque tables.
9. **Perform a bounding fatigue analysis in all possible orientations on mechanism components that are subject to rotation.** The fatigue analysis assumed that the strut remained in its ideal rotational alignment, resulting in the tooling holes being at the neutral axis of the strut. However, normal limits of rotation allowed by the strut design could move these holes somewhat out of the neutral axis and begin to have an impact on fatigue life. Fatigue analysis (as well as all other analyses) should examine the worst-case orientations allowed by the design, not just the ideal orientation.
10. **Review requirements, references, and methodologies used in analyses for design applicability.** The requirements and analysis methods utilized in the assessment of joint preload did not consider bending as a potential source of joint separation. Additionally, the references are primarily focused on typical bolted joints and fasteners, the definitions of which are not completely applicable to the spring strut joints. This resulted in a false confidence in the understanding of the behavior of these joints.
11. **Assess the contribution of assumed secondary effects (e.g., CG offsets, induced compression spring static torques, nonlinear behavior, etc.) to the analysis results, and perform an analysis and correlation study that reflects the major contributors.** Assumptions about what will be a small contributor to strut response to environments are appropriate for initial design phases, but those assumptions should be checked via sensitivity studies or other means once the design and analysis are more fully developed. In this case, some of the factors assumed to be unimportant turned out to have non-negligible effects on the hardware.

## Conclusions

The strut, with corrective actions employed, has since successfully completed qualification and acceptance vibration testing with no failures or anomalies and is slated to fly on the Exploration Flight Test-1 (EFT-1) in September, 2014.

While no single root cause was identified, numerous contributors and credible elements were found that may have attributed to the failure. Based on these elements, a most probable failure scenario was identified that points to a number of design and process deficiencies that led to a contact condition with the interfacing test hardware, that, when combined with a center of gravity offset of the mechanism assembly and significant applied environments, produced a loosening torque at the forward lug-to-secondary piston interface overcoming the resistive torque of the remaining locking elements and a subsequent rotation of the secondary piston. The tooling holes in the secondary piston, nominally located in the neutral bending axis, were then subjected to maximum bending stresses. When the fatigue life at the hole stress concentration was exceeded, the secondary piston failed.

Results from this assessment identified key lessons learned for the spring strut design and mechanisms in general. These key takeaways focus on design as well as process concerns in areas of design, analysis, test, and workmanship. The value added by the development test program will help satisfy the future needs of the MPCV through increased confidence in the mechanism's reliability and ability to meet future programmatic constraints.

## References

1. Dervan, Jared; Staab, Lucas; Robertson, Brandan; Song, Kyong; Irvine, Tom; Knight, Joseph. *Multi-Purpose Crew Vehicle (MPCV) Crew Module (CM) – Service Module (SM) Umbilical Spring Strut Testing*. Doc. no. 11-00747. November 14, 2013
2. *Design and Development Requirements for Mechanisms*. NASA-STD-5017. June 13, 2006
3. *NASA Space Transportation System: Space Shuttle Criteria for Preloaded Bolts*. NSTS 08307A. July 6, 1998
4. *NASA Technical Memorandum: Preloaded Joint Analysis Methodology for Space Flight Systems*. NASA-TM-106943. December 1995
5. *Mechanical Engineering Design*, 5th Edition. Joseph Shigley. November 1, 1988

# Development of a Tendon-Actuated Lightweight In-Space MANipulator (TALISMAN)

William R. Doggett<sup>\*</sup>, John T. Dorsey<sup>\*</sup>, Thomas C. Jones<sup>\*</sup> and Bruce King<sup>\*\*</sup>

## Abstract

An invention of a new and novel space robotic manipulator is described. By using a combination of lightweight truss links, a novel hinge joint, tendon-articulation and passive tension stiffening, this new robotic manipulator architecture achieves compact packaging, high strength, stiffness and dexterity while being very lightweight compared to conventional manipulators. The manipulator is also very modular; easy to scale for different reach, load and stiffness requirements; enabling customization for a diverse set of applications. Novel features of the new manipulator concept are described as well as some of the approaches to implement these design features. Two diverse applications are presented to show the versatility of the concept. First generation prototype hardware was designed, manufactured and has been assembled into a working manipulator that is being used to refine and extend development efforts.

## Introduction

Devices for maneuvering and precisely placing payloads are critical for efficient space operations involving reusable assets or in-space assembly and construction. Key to the success of many of NASA's space activities has been the availability of long-reach manipulators, such as the Shuttle Remote Manipulation System (SRMS) and the Space Station Remote Manipulation System (SSRMS) (Refs. 1 and 2). These devices have been used for many operations including berthing spacecraft, space station assembly, astronaut positioning, payload transfer, satellite deployment, and spacecraft inspection prior to reentry. New missions and applications currently being considered, such as asteroid retrieval and redirection, asteroid mining, satellite servicing, and small payload delivery to space stations, can all benefit from long-reach manipulators.

Current manipulators embody an architecture whereby carbon composite tubes are joined by revolute joints, with the joints accounting for the majority of the device mass. Generally, the joints are driven by a gear train that applies the joint torque relatively close to the joint axis (Ref. 3). This results in the need to generate large torques, which in turn, requires large and massive gear-train-motor combinations. The area around the joint becomes a crowded location from a design stand point due to joint articulation, gearing, motors, and associated electronics all vying for space. Design is further complicated by the need to route a large electrical harness through the joint area to transmit power, sensor data, control and video signals between the joints and end-effector.

The current state-of-the-art in long-reach space robotics is represented by the SRMS and the SSRMS mentioned previously. Both of these incorporate traditional manipulator architectures, consisting of lightweight booms connected by massive rotary joints that are systems of motors, gearboxes and brakes. The rotary joints account for 85 to 90 percent of the manipulator mass and manipulator compliance in response to an applied load (Ref. 1). The long booms result in restrictive packaging options, and adding joints to improve packaging would incur an extremely high mass penalty. The high mass associated with the joints also results in practical limits to: reach, packaging, stiffness and tip force that can be achieved with the conventional architecture.

---

<sup>\*</sup> NASA Langley Research Center, Hampton, VA

<sup>\*\*</sup> Northrop Grumman, Hampton, VA



In order to enable future missions and applications, it is desirable to improve space manipulator state-of-the-art by significantly increasing manipulator reach, dexterity and packaging efficiency while reducing manipulator mass and complexity. The Tendon Actuated Lightweight In-Space MANipulator (TALISMAN) is an invention (patent application has been filed) of a new robotic manipulator architecture that incorporates a tendon-actuated joint with a novel hinge that allows a full 360-degree rotation between connecting links and the capability to incorporate auxiliary and passive tension stiffening. Tendon actuation incorporates spreaders to achieve longer moment arms between the force applied by tension cables and the joint rotation axis, thus gaining mechanical advantage for generating moments and actuating the joints.

Key features of the new TALISMAN architecture and approach are:

- Uses tendon actuation, which can be semi or fully antagonistic, with major components being the link, spreader, and lightweight cables, motors, gearboxes,
- Increased joint stiffness due to tendon architecture,
- Lightweight joints enable the number of joints to be optimized to achieve desired packaging efficiency, range-of-motion, dexterity, etc.,
- Potential to increase manipulator stiffness using passive tension elements (very lightweight),
- Versatility; many different cable/motor/control options can be implemented,
- Modularity; links and joints are easy to scale for different applications, can combine link and joints as needed for packaging, dexterity, etc. to achieve operational needs,
- Novel hinge joint allows full 360-degree rotation between adjacent links, improving dexterity and range of motion,
- Uses lightweight truss structures for links.

The TALISMAN architecture embodies and adds to many of the features that were developed for a new planetary surface hybrid crane/manipulator, the Lightweight Surface Manipulation System (LSMS) (Ref. 4). The LSMS is a cable-actuated manipulator that achieves high structural efficiency by using a pure tension / compression architecture (as opposed to bending in conventional robotic manipulators). Further mass efficiency is achieved by using the tension structure (cables) to also articulate the LSMS arm hinges. The tension cables provide mechanical advantage about the joint enabling small lightweight hoists or capstans to reel cable in and out (thus articulating the hinge), replacing the massive high-torque motor gear-boxes used in a conventional boom manipulator.

### **TALISMAN: New Approach for Space Manipulators**

In conventional space manipulator architectures, a majority of the manipulator mass resides in the joints. TALISMAN's new and unique approach significantly reduces motor mass while simultaneously stiffening the links and allowing more compact packaging. In addition, a new joint architecture is described that allows a full 360-degree rotation of the joint. The invention described here creates a new class of manipulators through innovative use of tension networks to actuate the joints and stiffen the manipulator structure in a modular fashion. Both tension actuation of the manipulator joints and tension stiffening of the links are novel approaches to manipulator design. Each of these approaches enhances the performance of the manipulators and can be used independently or together depending on mission requirements for reach, packaging efficiency, weight and dexterity. Tensioning can be accomplished in a variety of ways including through cables, metallic tapes, rigid bars, etc., or some combination of these approaches. Actuating the manipulator joints using tension elements that are offset from the joint rotation axis (by the spreaders) provides large mechanical advantage for the joint motor enabling use of smaller lighter weight motors requiring less power. Low-precision motors can be used because the tension elements can be designed to damp out irregularities in the motor torque, further reducing motor complexity and costs. In addition, the tension actuation provides a large effective gear reduction, so that a motor revolution produces only a small change in joint angle.

Figure 1 illustrates an example of a manipulator that uses tension elements for actuation and stiffening. The manipulator in the figure shows 2 joints and 3 links; however any number and size of joints and links

can be combined into a manipulator, depending on the requirements for a particular application. The primary parts of a manipulator are labeled on the left of the figure and the components of a joint are labeled on the right. When developing a manipulator with the architecture depicted in Figure 1, tension elements can be used to actuate and stiffen a joint as well as stiffen a link. The motors used to actuate the joint can either drive hoists, where excess tension material (for example cable) is spooled, or drive capstans where the tension elements circulate from one side to the other. These tension networks increase the stiffness of the manipulator dramatically, allowing compression members with smaller cross sections to be used and lighter overall systems to be realized compared to the current state-of-the-art manipulators such as the SSRMS and SRMS. The spreaders (identified in the figure) are used to provide joint stiffening and mechanical advantage about the joint. Single spreaders above and below the joint, or multiple spreaders (depending on design requirements) can be incorporated as shown. Similar to joint spreaders that aid articulation, link towers (which are fixed elements along the link) can be used to provide a tension path to increase link stiffness.

The components of a single joint are identified on the right side of Figure 1. The joint rotates about the joint axis, identified in red in the middle of the figure. In this example, the capstan (B) and pulleys (A,C,D) are located equidistant from the joint axis and a single capstan (with dual warping profiles) located along one of the links is used to actuate the joint. The number and location of the drive motor(s) that actuate the joint can be varied, allowing significant design freedom to meet mission requirements. The link-mounted capstan in the figure has two warping end profiles of different diameters that operate two circulating cable loops simultaneously to achieve joint articulation. Extension/contraction of the springs shown in the figure are used to accommodate changes in the total cable path as the joint articulates.

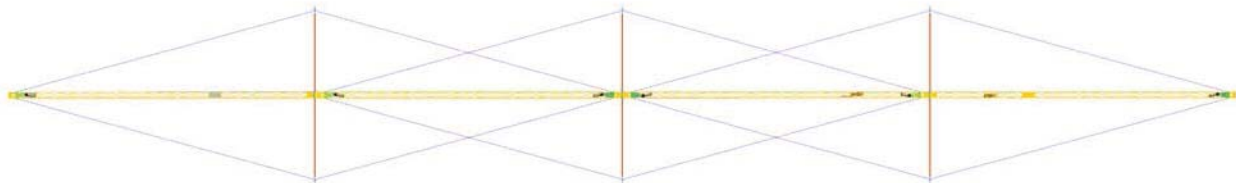
Many variations of the joint architecture shown in Figure 1 are possible, with four possibilities shown in Figure 2. Starting in the upper left with image "I" and using the nomenclature defined on Figure 1, first the distance from "A" and "B" to the joint axis does not need to be equal as shown in Figure 2. In image "I" of Figure 2, "B" has moved to the end of the link. This arrangement uses a single cable, one each above and below the link, to not only stiffen the link, but also to stiffen and actuate the joint. The location of "B" in Figure 2 can be selected to be at any point along the link. The image also shows a manipulator configuration where the tension element is no longer in contact with the spreader, referred to as "spreader liftoff". Allowing liftoff is optional because it results in the tension element sweeping through a large portion of the workspace which might cause interference. However, a benefit of liftoff is that it enables significantly increased force to be applied between the link ends, achieving a large amount of joint torque. In Figure 2, image "II" in the upper right, the dual capstan warping end profiles may be the same diameter and combined with a single motor located along one of the spreaders. This results in one of the simplest configurations from a control standpoint. In the lower right of Figure 2, image "III" shows multiple spreaders used above the links. Additional spreaders can be located above or below the links and any number of spreaders can be used. In the final image in the lower left of Figure 2, four motors are used to actuate the joint, each one driving separate tension elements that run between the link end point and the top of the spreader. For optimal performance, each motor must be synchronized to keep the spreader tips equidistance from the links. Using multiple motors allows for many advanced control schemes including dynamic damping of structural modes. Image "IV" also depicts constrained lift-off, where the tension element along the lower portion of the joint is encapsulated and forced to remain affixed to the spreader, in this case, by a telescoping member that allows for some increase in spreader height. In Figures 1 and 2 the joint rotation axes between successive joints have been shown as parallel and tension stiffening is only shown in the plane of articulation. Successive joint rotation axes can also be rotated relative to one another and tension stiffening can be applied in multiple directions.

Tension stiffening enables much smaller truss cross sections to be used while achieving equivalent in tip deflection performance. For example, the 4-link manipulator shown in Figure 3, where the actuation tendons are connected to the link ends, places the links in pure compression, avoiding bending loads. Stiffness provided by the tension network enables a reduced link cross section and a smaller overall packaged device. When packaged for launch (middle of Figure 3) the spreaders slide in between the links allowing their maximum length to approach the length of the links without requiring any additional

complexity to collapse the spreaders. For the links, a large portion of the cross section is open, allowing integration of cable bundles as required.

In Table 1, the TALISMAN prototype shown in Figure 3 is compared to the SRMS. In this example, the TALISMAN has been sized for the SRMS tip force and stiffness requirements; 53.4 N (12 lbf) at the tip and 17.5 N/cm (10 lbf/in) deflection constraint (Ref. 2). Although the SRMS is a flight system and the TALISMAN is a laboratory prototype that have different levels of design fidelity, major advantages of the TALISMAN architecture are apparent. The TALISMAN prototype has not been optimized and is constructed from readily available rectangular tubes to allow inexpensive development, with the focus being on implementing and obtaining experience with the unique cable actuated joint. Currently, a single joint/two-link test bed has been fabricated using 7.62 x 15.2 cm (3 x 6 inch) rectangular aluminum tubes with a 6-mm (0.25-inch) wall thickness for the links. For the version summarized in Table 1, the links and spreaders are assumed to have the same geometry as the test bed, but are constructed from a polymeric composite material that has a Young's modulus of 138 GPa ( $20 \times 10^6$  psi); the joint mass is based on the as-built hardware that was designed and fabricated from aluminum and installed into the laboratory prototype and has a mass of 0.54 kg (1.2 lb); and the spreader is assumed to be a polymeric composite tube with its height fixed at 1 m (39.4 in). As shown in the table, the TALISMAN system mass is an order of magnitude less than that of the SRMS, with the link system mass (including the links, spreaders and cables) being significantly less than that of the SRMS tubes. When packaged for launch, the TALISMAN occupies only 1/7<sup>th</sup> of the SRMS volume. For comparison, at the bottom of Figure 3, the packaged TALISMAN is shown in two views packaged inside one of the two SRMS links (depicted as folded side by side for this image), where the SRMS links are each 0.381 m (15 in) in diameter and 7.65-m (25-feet) long. In the end view on the lower right, a dashed line is included showing the 0.33-m (13-in) diameter of the SRMS composite tubes. The SRMS composite tubes are thin walled and are encased in a protective bumper resulting in the 0.381-m (15-in) diameter shown. In contrast, the TALISMAN truss uses solid members, and does not require a protective covering. Finally, based on parametric motor sizing equations, the TALISMAN is expected to use significantly less power because less torque is required at the motors resulting in smaller lighter motors (Ref 5).

A limitation of the TALISMAN design used for the prototype configuration is that it is a planar system, having significantly more stiffness in the plane of articulation than out of that plane. If required, out-of-plane stiffness can be increased by adding passive tension elements or by increasing the depth of the truss cross-section perpendicular to the plane of actuation. Another limitation of the prototype is that the TALISMAN motors included in the comparison are not redundant as are the SRMS motors. Also, the TALISMAN does not include a wrist with roll, pitch and yaw capability or a snare end-effector as the SRMS does. However, the TALISMAN design does assume all joints have full articulation capability, but if this is not required, a much simpler and lighter deployment hinge and lock can be used.



**A Novel Joint Enabling Full 360-Degree Rotation**

Joint range of motion directly affects the ability of a manipulator to reach locations, i.e. the useable manipulator workspace. Here a novel joint will be described that provides a full 360-degree rotation, while simultaneously supporting free rotation of a third member, the spreader, about the active joint rotation axis. The mechanism of interest is the center of a tension articulated joint that is shown in the top left of Figure 4. In the close up view of the joint shown on the top right of the figure, the yellow and purple components (on the left and right of the hinge) are the link plugs used to attach the joint to the links

(which are depicted as grey rectangles in the figure). Three components make up the center of the hinge, two identical linkage arms and a central spreader support component. Three hinge lines, labeled A, B and C, enable the range of motion as depicted in the bottom of the figure: where starting on the left, the hinge is at 0 degrees and progresses through to 360 degrees on the right. From 0 to 180 degrees, the top hinge line (B) is active, while from 180 to 360 the bottom hinge lines (A and C) are active. During joint rotation, the spreader support bisects the angle formed by the links, which keeps the transverse force resultants at the tip of the spreader balanced and the spreader in pure compression.

### **Tendon Routing Options: Evaluation and Selection**

A large number of options are available for implementing the TALISMAN architecture including: the number of motor/drive systems used per joint, the location of the motor/drive systems along the links or on the spreaders, cable routes, and full versus partial antagonistic control. A simple test bed was designed and constructed to allow a variety of tendon-drive options to be easily implemented, operated and evaluated so that a configuration could be chosen to implement into a full-scale two-link articulating joint prototype. The test bed consists of two arm links connected at a central hub, with the left arm fixed, as shown in Figure 5. The spreader is attached to the hub and under ideal operations, would remain centered between the two arms. A counter-balance is attached to the rotating arm to off-load the arm weight so that the actuation system essentially experiences zero load as it rotates the joint.

Four major architecture options were evaluated by varying the number and location of motor/gear-box systems on the arms or spreader, as summarized in Figure 6. In the figure, the locations of motors, springs, pulleys, capstans and stops (tendon tie-down points) are indicated with icons. The figure also uses sequences of numbers and/or letters to indicate tendon routing and circulation. None of the options tested in the lab were the full antagonistic actuation version (the required control system is still being developed); all included springs so that the stiffness in one rotation direction reached that of the cables while the stiffness in the other direction was limited to that of the passive springs. The major attributes of each of the tendon routing and motor/spring position options, all of which are shown in Figure 6, are:

- Option 1: one motor/gearbox system, two capstans with one having half the diameter of the other, the motor/gear-box is mounted at a distance along the arm equal to  $\frac{1}{2}$  the length of the spreader.
- Option 2: two motor/gearbox systems, each motor/gearbox system has a single capstan, both capstans are the same diameter, the motor/gear-boxes are each mounted at a distance along the arm equal to  $\frac{1}{2}$  the length of the spreader, one on either side of the center of rotation, two independent cable loops used.
- Option 3a: two motor/gear-box systems; each motor/gearbox system has a single capstan, both capstans are the same diameter; the motor/gear-boxes are each mounted at a distance along the arm that is approximately equal to the length of the spreader, one on either side of the center of rotation; cable routing is top of spreader, around drive capstan system, around pulley on bottom of spreader, up spreader arm to hub (with the spring between the pulley and hub).
- Option 3b: this option is the same as Option 3a except; the cable routing was modified to; top of spreader, around drive capstan system, around pulley on bottom of spreader, through pulley (only) on opposite drive system along arm to hub (with the spring between the pulley and hub); modified 3a such that two springs are attached to each other with their connection point to the right of the hub.
- Option 4: one motor/gear-box system; motor/gearbox system has two capstans, one capstan is half the diameter of the other; the motor/gear-box is mounted at the top of the spreader; two independent cable loops, identical to Option 2; used the new constant-spring-force mechanisms for each loop.
- Option N: not evaluated in test-bed, but his option would be a fully antagonistic arrangement with no passive spring elements.

All of the options were rated against the set of criteria listed in Table 2. The fully antagonistic option (N) would be preferred in an implemented system, due to its high stiffness over the full 360-degree rotation range and its high degree of controllability and performance. However, the control system for this option is the most complex, and although it is currently being developed, was not available immediately. In order

to proceed with the TALISMAN joint prototype, Option 3b was chosen because of its good stiffness and spreader synchronization characteristics as well as its very good packaging capability. The packaging capability is important because the next phase of TALISMAN development will be focusing on demonstrating: efficient packaging; deployment, including the spreader, from a fully packaged state; and, full 360-degree articulation of the joint. A prototype section of the Option 3b has been fabricated and undergone limited operational testing in the laboratory, as shown in Figure 7. The prototype section has two aluminum truss links connected by a single-degree-of-freedom hinge joint. Each link is 3.66-m (144-inches) long and has a 7.62 x 15.24 cm (3 x 6 inch) cross-section and the total height of the spreader is 1 m (39.4 inches) above the joint rotation axis. Articulation of the prototype has been demonstrated from 0 degrees (straight out position) through 180 degrees (where the outer link is folded adjacent to the inner link).

### **Example TALISMAN Applications and Sizing Results**

Two distinct embodiments of the TALISMAN are emerging: A Long Reach (LR) variant and a Compactly Stowable (CS) variant. LR applications would be focused on achieving long reach and maintaining high stiffness with less emphasis on high dexterity and the ability to stow and deploy multiple times. CS applications would be focused on achieving high dexterity, a large reach envelope, applying and reacting large tip forces, being able to deploy and restow multiple times, and packaging into a limited volume (for launch or within a spacecraft storage location).

#### 300-meter LR Application

A Space Act Agreement was signed between Langley Research Center and Altius Space Machines to investigate and develop applications for a LR TALISMAN (LRT) design. As a result of this collaboration, Altius Space Machines investigated a mission concept for enabling inexpensive and rapid commercial payload delivery/recovery from the International Space Station (ISS). The mission concept requires that ISS payloads be captured and released beyond a strictly controlled 200-m radius keep-out sphere. Altius baselined a LRT having a reach of 300 meters, assuming a capture distance at 250 meters from the ISS. Due to the lack of additional mission definition at this time, the LRT was designed to achieve a reasonable and robust operational capability (dexterity for example) coupled with efficient structural performance. Due to the extreme length of the manipulator, passive tension stiffening is used to augment the stiffening provided by the tendon-actuation architecture. In this case, the tension-stiffened manipulator was designed to have 10 times the stiffness of the bare central truss. Features of the LRT are illustrated in Figure 8 and design/performance specifications are given in Table 3.

#### Asteroid Capture System CS Application

A current mission option being investigated within NASA is to capture an asteroid and return it to cislunar space where it would be examined by an astronaut crew. The original mission concept was limited to capturing a free-floating asteroid, assumed to be either an approximately 7-meter diameter sphere, or a 5 meter x 10 meter ellipsoid. The associated capture/enclosure concept used a series of deployable links, tensioning cables and inflatable envelopes to accomplish the mission. In order to improve mission versatility and increase the probability of mission success, a CS TALISMAN (CST) based concept for an asteroid retrieval mechanism was developed with the goal of accommodating many possible different mission scenarios (including retrieving a boulder from a large asteroid body) while also enabling and supporting astronaut Extra-Vehicular Activity asteroid evaluation operations in cislunar space. By leveraging TALISMAN technology currently being developed by NASA it might also be possible to reduce system cost and development schedule.

The complete asteroid material capture and enclosure system would consist of two major subsystems; a set of three 4-link TALISMANs attached to the retrieval spacecraft bus and a simple lightweight bag to enclose the asteroid and prevent loose particles from escaping as shown in Figure 9. The capture system is assumed to integrate with a solar electric retrieval stage at a 3-meter-diameter circular interface. The four links are folded for launch so that the packaged TALISMAN easily fits into the baseline launch vehicle (Atlas V) medium or long payload shroud. The three CSTs are attached along the outside edge of



the spacecraft interface at 120-degree intervals. Each CST has four truss links and four tendon-actuated hinge joints with the base of each CST mounted to a simple turntable (to provide a [fifth] rotary degree of freedom). The enclosure bag (EB) is attached to the circular interface structure at its base and folded in the center portion of the space between the stowed CSTs. The EB has a simple inflatable ring integrated at its open end that is inflated to provide a large circular opening for acquiring an asteroid. The system is redundant since the mission can be successfully completed even if one of the CSTs completely fails to operate. Design and performance specifications for the CST are given in Table 3.

#### TALISMAN Structural Sizing Analysis

One of the key advantages of the TALISMAN architecture is its structural simplicity and efficiency. These attributes are achieved by using a modular, periodic tension-compression design that lends itself well to analytical modeling. Closed-form, parametric equations were derived to calculate the member loads and tip deflection and allow systematic optimization of the key structural components of TALISMAN, including the core truss links, the spreaders and the tension elements. The analytical equations were derived using the following assumptions; spreaders and truss links have small axial deformations, all tension elements are always under load (achieved in practice using either active actuator control or passive springs) and material behavior is linear elastic. Typical requirements that must be specified are for in-plane (refers to those aligned with the plane of the spreaders; the stiffest plane), out-of-plane and torsional tip loads, and the required tip stiffness. The derived equations can be used to determine the optimum sizing, pretension level and mass of the system while taking into account constraints on the minimum gauge of thin-walled members, and local strength and buckling. A spreadsheet-based TALISMAN design tool was generated using these equations to enable rapid design studies and to investigate the sensitivities of various parameters including: number, length and cross-section of primary arm links; spreader height and geometry; cross-section of tension elements; material properties; safety factors on strength and buckling; lacing pattern of truss diagonals and; in-plane, out-of-plane and torsional tip loads and tip deflection. Figure 10 illustrates the geometry used in the model as well as load and displacement variables.

The TALISMAN design tool requires the user to input the basic geometry, tip loading and material properties and it outputs the internal loads, sizing and masses of all members. The geometric parameters include the length, number and cross-section of the arm links and the height of the spreaders. These parameters are not included in the optimization since they are typically dictated by the requirements for a specific application, such as component packaging volume, or spreader impingement into the operational work space. The links and spreaders are optimized by iterating on and requiring the value of a sizing parameter (either area or thickness) be equivalent when both strength and buckling constraints are satisfied. The tendons are sized for axial stiffness and strength, as they provide the primary in-plane stiffness. Separate safety factors are specified for the compressive and tension members, due to the typically higher factor on strength for tendons. The TALISMAN is designed for high structural efficiency in the plane of articulation. However, off-nominal loads, such as out-of-plane or torsion, are accounted for in the design process. Some examples of these off-nominal loads include push-off lateral loads induced by an attached Extra Vehicular Astronaut (EVA) astronaut, or torsional loads induced by lateral loads when the arm links are at different angles. For the CST, the worst-case torsional load was used for sizing. This torsional load occurs when all of the arm links ahead of the root link are perpendicular to the root and a lateral tip load is applied, thus creating a large moment that is reacted by the truss diagonals in the first bay of the link closest to the root or base.

The current design tool is intended to produce optimized TALISMAN architectures that are conservative by using reasonable and current material properties and worst-case loading scenarios. The structural members are sized for a tip load applied to a fully extended (straight-out) manipulator pose (i.e. the longest moment arm), with any lateral loads inducing compression in the truss longerons (through bending and torsion). The sizing is based on the maximum loads induced in the structural members, usually those that are at or near the root; this allows equivalent cross-sections to be used for each set of members, resulting in easy and inexpensive manufacture or purchase of off-the-shelf components. For example, extruded beam sections with standard rectangular cross-sections were inexpensively purchased and cut on a water-jet machine to obtain the optimal truss lacing pattern determined by this

design tool. Additional optimization could be included at a later date to allow: tapered members, different spreader sizes from root to tip, sizing based on specific member loads rather than maximum loads, and sizing based on nominal, as opposed to worst case loads (with safety factors). For instance, a fully extended manipulator pose is unlikely to be used for most applications; typical operations would have the links at some angle. In addition, the worst-case torsional load results from a highly unlikely manipulator pose. With a well-defined and actively controlled work envelope, the severity of the load cases could be reduced. The current sizing for tip stiffness assumes purely passive operation, i.e. the members are sized so that when a tip load is applied the structure deforms to a set tip displacement. However, with full antagonistic control, the tip displacement can be driven back to zero by actuating the tendons. This operation would result in a mid-manipulator displacement rather than a tip displacement, but could significantly reduce the mass of the system if tip stiffness is a primary objective, but at the cost of greater structural flexibility. Depending on the application and control system this might be an attractive option for future analysis. Since the tip stiffness requirement also determines the tendon sizing; a reduction in required passive tip stiffness would reduce the tendon diameters allowing smaller/faster gear trains and motors. This could allow greater actuation speeds that might be necessary to actively control the dynamic response of a flexible system. Any of these optimization features could be added in the future if desired.

The TALISMAN sizing tool is primarily used to explore the parameter design space and currently only calculates the structural mass. Future work will include adding mass estimating tools for joints, motors, gear trains, electronics and any additional hardware needed. A simple, pinned truss analysis tool, based on matrix structural analysis, was written in MATLAB and used successfully to verify and validate the results of the spreadsheet output and the analytical equations. To enable more refined analysis of a specific TALISMAN design, an ABAQUS Finite Element Model script was also written to recreate the geometry from the spreadsheet design tool. The Finite Element Model can then be used for dynamic, frequency and global buckling analyses. The script can create different operational poses, and can be integrated with structural models of candidate spacecraft. Loads can be applied at other points along the structure if needed and all internal loads and displacements can be interrogated. With these tools the TALISMAN architecture can be adapted and optimized for a wide range of applications and designs created that have accurate estimates of their structural performance and system mass.

## Conclusions

Devices for maneuvering and precisely placing payloads are critical for efficient space operations involving reusable assets or in-space assembly and construction. New missions and applications currently being considered, such as asteroid retrieval and redirection, asteroid mining, satellite servicing, and small payload delivery to space stations can all benefit from having long reach manipulators that are also light weight and have high dexterity. The limits resulting from the current state-of-the-art in long reach space manipulators are discussed and a novel new manipulator architecture, the TALISMAN that directly addresses and mitigates these limits is introduced. By using a combination of lightweight truss links, a novel hinge joint, tendon-articulation and passive tension stiffening, this new robotic manipulator architecture achieves compact packaging, high strength, stiffness and dexterity while being very lightweight compared to conventional manipulators. There is a great deal of freedom and versatility in designing manipulators based on this new architecture and accompanying details and options are discussed. A hardware test-bed was created and several different manipulator options were implemented and tested. The results from the hardware assessment were used to rate and prioritize design options and a specific configuration was chosen for further development. The design and operation of this manipulator prototype is presented along with the development focus of current research. The extreme versatility of the TALISMAN architecture is demonstrated by presenting two different (a long-reach and a compactly stowable) applications and summarizing the design and performance attributes of the resulting manipulators. Finally, tools are described that have been developed to perform structural analysis, size structural members and estimate the mass of different TALISMAN implementations designed for different mission requirements.

## References

1. Hunter, J. A.; Ussher, T. H.; and Gossain, D. M.: Structural Dynamic Design Considerations of The Shuttle Remote Manipulator System. AIAA 82-0762, pp. 500 - 505.
2. Kumar, P.; Truss, P.; and Wagner-Bartak, C. G.: System Design Features of the Space Shuttle Remote Manipulator. Proceedings of the Fifth World Congress on Theory of Machines and Mechanisms 1979. Published by the ASME, pp. 839 - 842.
3. Craig, John J.: Introduction to Robotics, Mechanics and Control, Third Edition. New Jersey: Pearson Prentice Hall, 2005.
4. Doggett, William R.; Dorsey, John T.; Collins, Timothy J.; King, Bruce; and Mikulas, Martin M.: A Versatile Lifting Device for Lunar Surface Payload Handling, Inspection and Regolith Transport Operations. Presented at the Space Technology and applications International Forum – STAIF 2008, Albuquerque NM, 10 – 14 February 2008. AIP Conference Proceedings Volume 969, Editor Mohamed S. El-Genk, 2008 American Institute of Physics.
5. Dorsey, John T.; Mikulas, Martin M.; and Doggett, William R.: Preliminary Structural Design Considerations and Mass Efficiencies for Lunar Surface Manipulator Concepts. Presented at the AIAA Space 2008 Conference and Exposition, 9 – 11 September 2008, San Diego, California. Available as AIAA-2008-7916.

**Table 1. Comparison of TALISMAN to Shuttle Remote Manipulator System. (Refs. 1, 2)**

Design Parameter	SRMS	TALISMAN
Total manipulator length	15.3 m (50 ft)	15.3 m (50 ft)
Number of joints in manipulator	6 (2 shoulder, 1 elbow, 3 wrist)	5 (2 base, 4 links)
Number of links in manipulator	2	4
Tube/Link System Mass [kg]	46 kg (101.4 lbf)	7.03 kg (15.5 lbf)
Manipulator Mass	410 kg (904 lbf)	36.1 kg (79.6 lbf)
Packaged Volume	1.74 m <sup>3</sup> (61.4 ft <sup>3</sup> )	0.23 m <sup>3</sup> (8 ft <sup>3</sup> )

**Table 2. Results from tendon-routing option evaluation**

Criteria	Option.1	Option.2	Option.3a	Option.3b	Option.4	Option.N
# of Motors	1	2	2	2	1	4
Control System Simplicity	5/5	4/5	4/5	4/5	5/5	1.67/5
Power Consumption	3/5	3/5	3.67/5	3.67/5	3.67/5	4.67/5
Stiffness Properties	2.5/5	1/5	2.5/5	2.5/5	2.5/5	5/5
Strength / Stiffness Symmetry	180° Full+ Bending / 180° Spring	180° Full Bending / 180° Spring	180° Full / 180° Spring	180° Full / 180° Spring	180° Full / 180° Spring	360° Full
Cable Mass	4/5	4.5/5	2.5/5	2/5	2.5/5	4/5
Packaging	2.5/5	2.5/5	3/5	4.5/5	3/5	4.5/5
Cable Routing Simplicity	1/5	2.5/5	3/5	1.5/5	3/5	5/5
Ease of Spreader Liftoff	2/5	3.5/5	3/5	3/5	2/5	5/5
Spring Travel	1/5	1.5/5	3.5/5	3/5	3.5/5	5/5
Ease of Motor Repair	1.5/5	2/5	2/5	1/5	4/5	4.5/5
Spreader Synchronization Robustness	1/5	3.5/5	3.5/5	3.5/5	1/5	5/5
<b>TOTAL</b>	<b>23.5/50</b>	<b>28/50</b>	<b>30.67/50</b>	<b>28.67/50</b>	<b>30.17/50</b>	<b>44.34/50</b>

**Table 3. Specifications for two TALISMAN applications**

<b>Design Parameter, Specification</b>	<b>LR: ISS Payload Application</b>	<b>CS: Asteroid Capture Application</b>
Total manipulator length, m (ft)	300.0 (984.3)	20.0 (65.6)
Number of links in manipulator	6	4
Link length, m (ft)	50.0 (164)	5.0 (16.4)
Number/types of degrees-of-freedom (dof)	7 total: 1 base rotation; 6 single dof hinges	5 total: 1 base rotation; 4 single dof hinges
Number of motor/gear-boxes per hinge joint	2	2
Control method	Fully antagonistic	Fully antagonistic
Hinge joint articulation range, degrees	From 0: +125; -180	From 0: +180; -180
Location of motor/gear-boxes	Link mid-point	Link end-point
Link structure	1m by 1m polymeric composite truss with titanium joints	7.62cm by 15.24cm (3in by 6in) polymeric composite integral truss
Structural assembly concept	Assembled robotically on orbit using Electron-Beam welding	Fully assembled & packaged on ground, deployed in space
Spreader height (tip to joint axis), m(ft)	4.5 (14.8)	1.0 (3.3)
Passive tension stiffening?	Yes: tower height 4.5 m (same as spreaders)	No
Tower base location	Link mid-point	NA
Design load: manipulator fully extended, transverse load at tip, N (lb)	100.0 (22.5)	66.7 (15.0)
Tip deflection, m (ft)	5.38 (17.7) [1.8% of length]	0.20 (0.66) [1.0% of length]
Mass estimate, kg (lb)	2200 (4840)	48.8 (107)
Mass per unit length, kg/m (lb/in)	7.33 (0.41)	2.44 (0.14)



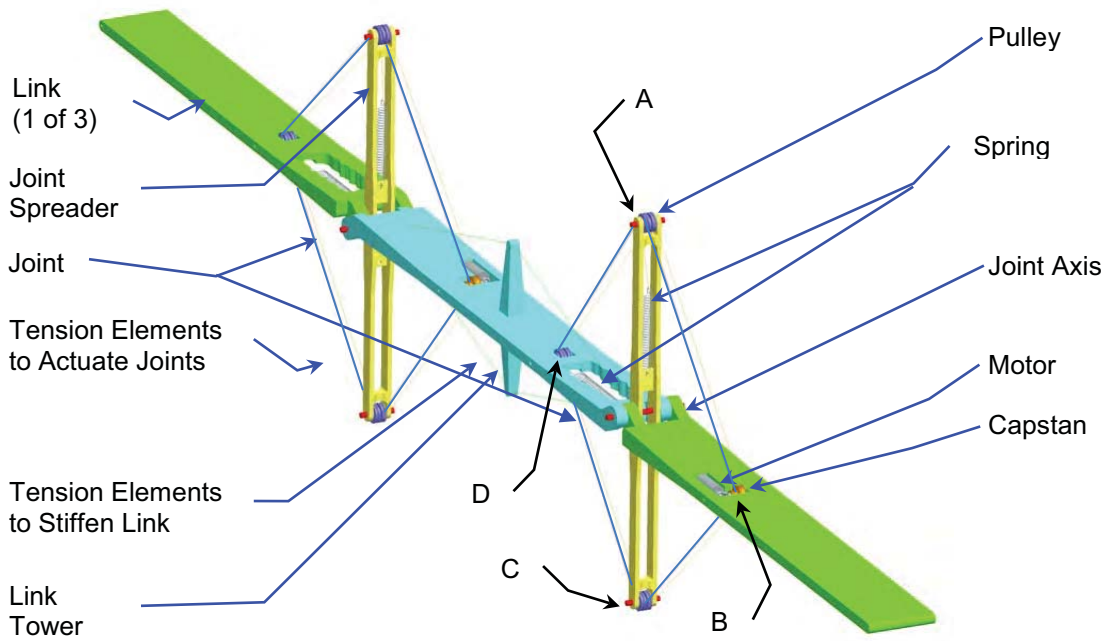


**Figure 1. Planar embodiment of the Invention with Multiple Joints**

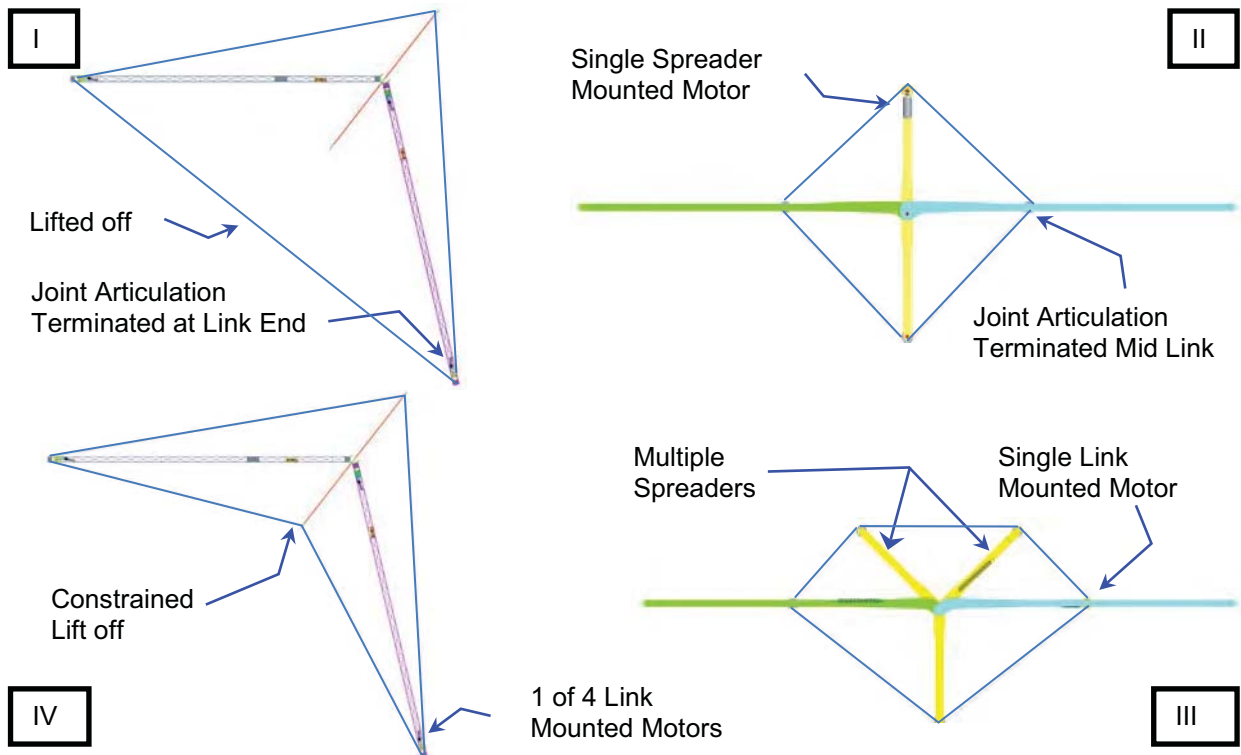


**Figure 2. Variations of Tension Actuated Joint**

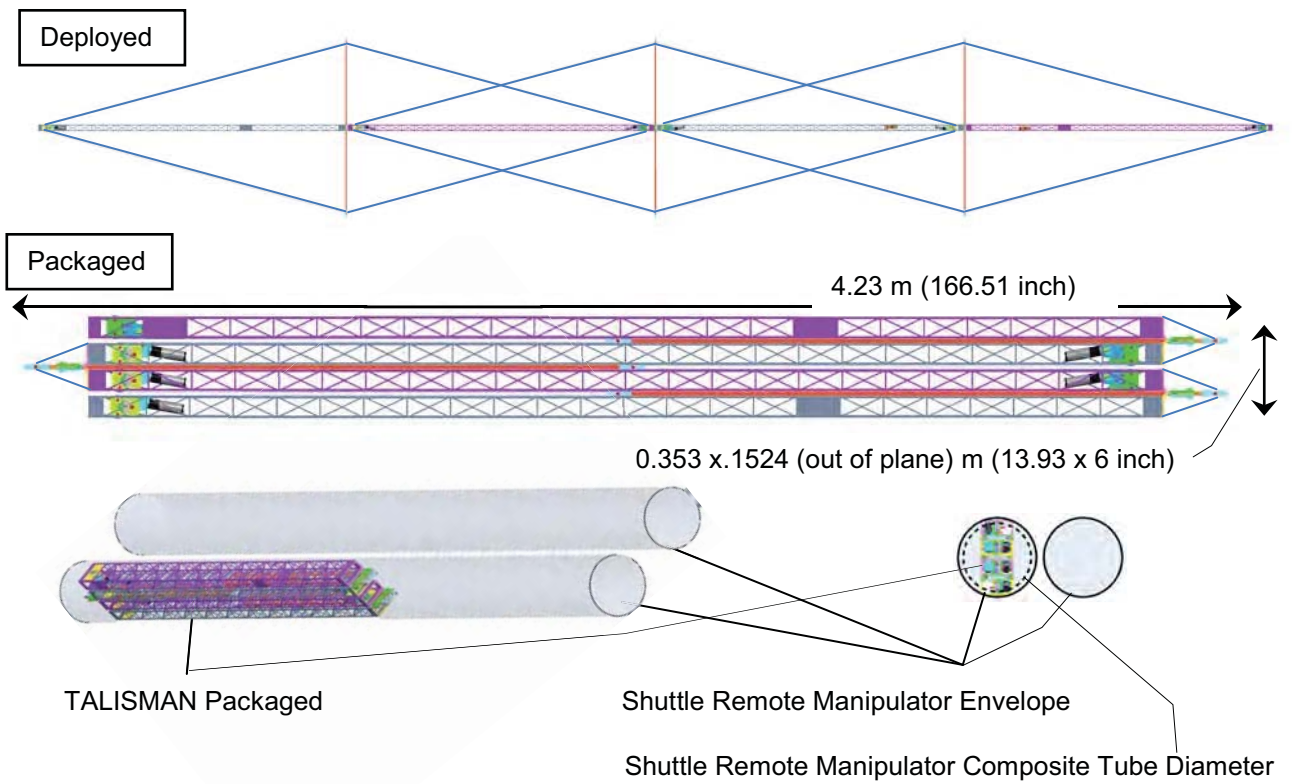


**Figure 3. Packaging of TALISMAN**

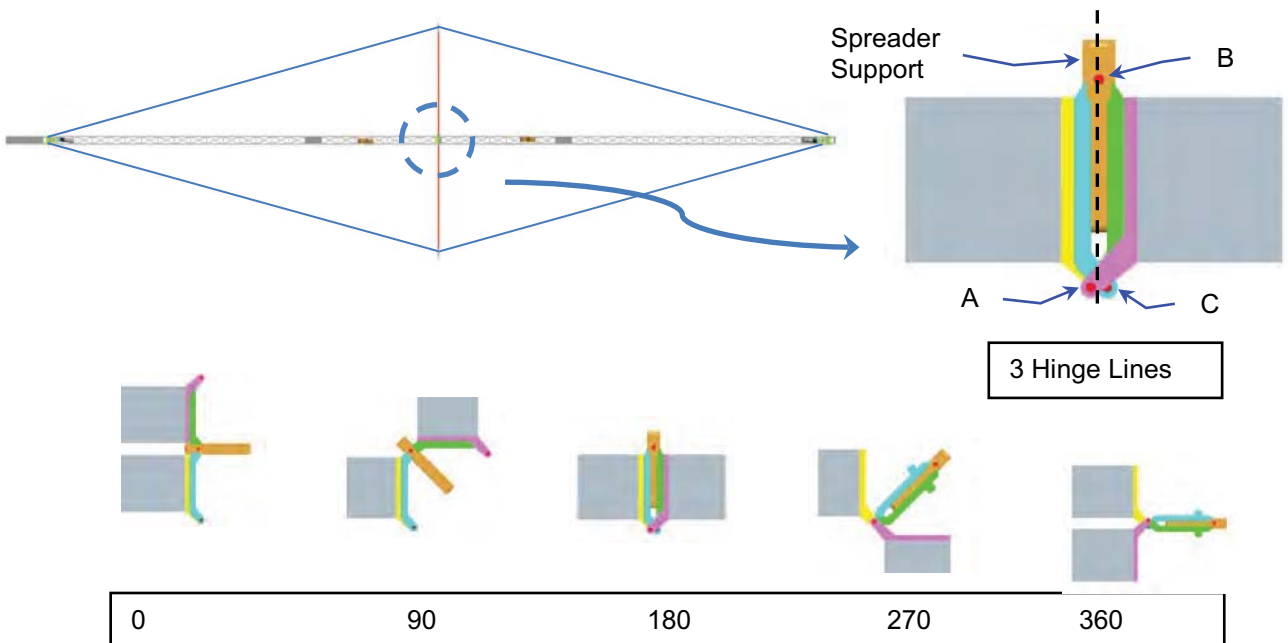


**Figure 4. Novel Joint Provides 360 Degree Rotation**



Figure 5. Tendon evaluation test bed set up showing option 1.

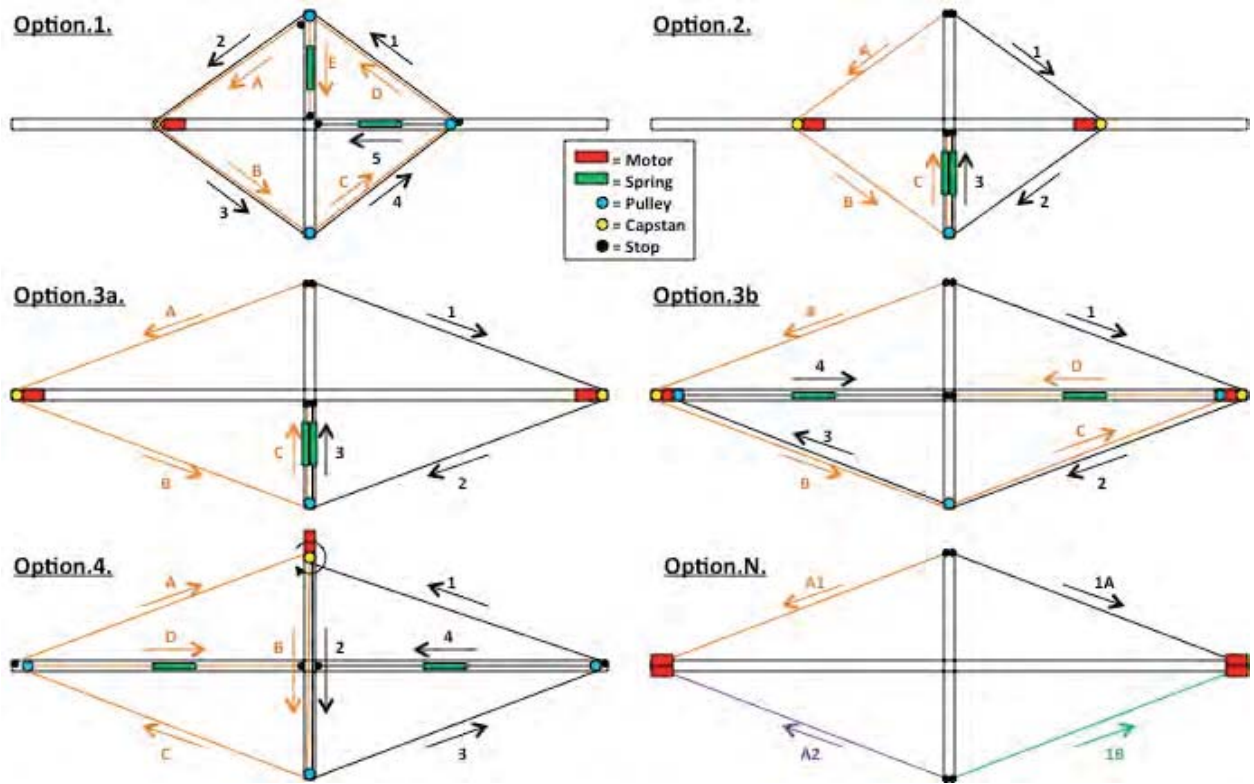


Figure 6. Tendon evaluation test bed set up.



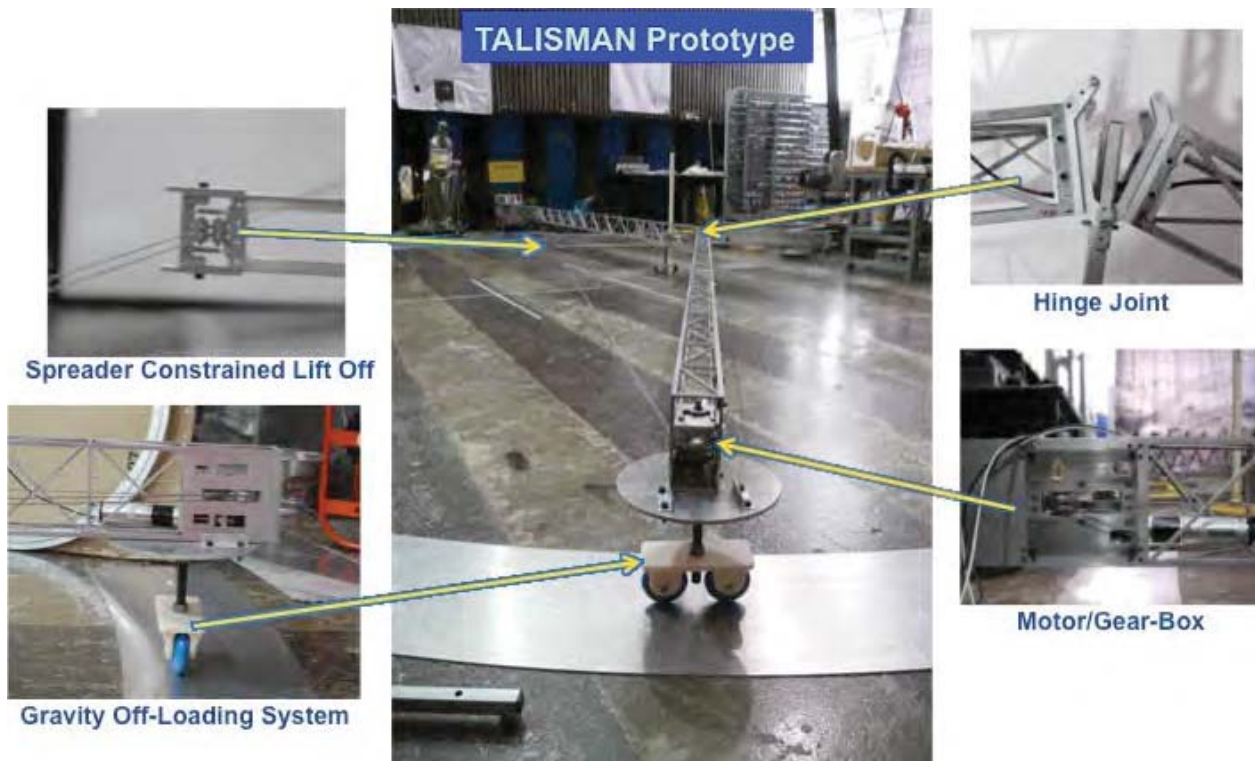


Figure 7. Prototype of TALISMAN tendon actuated joint section.

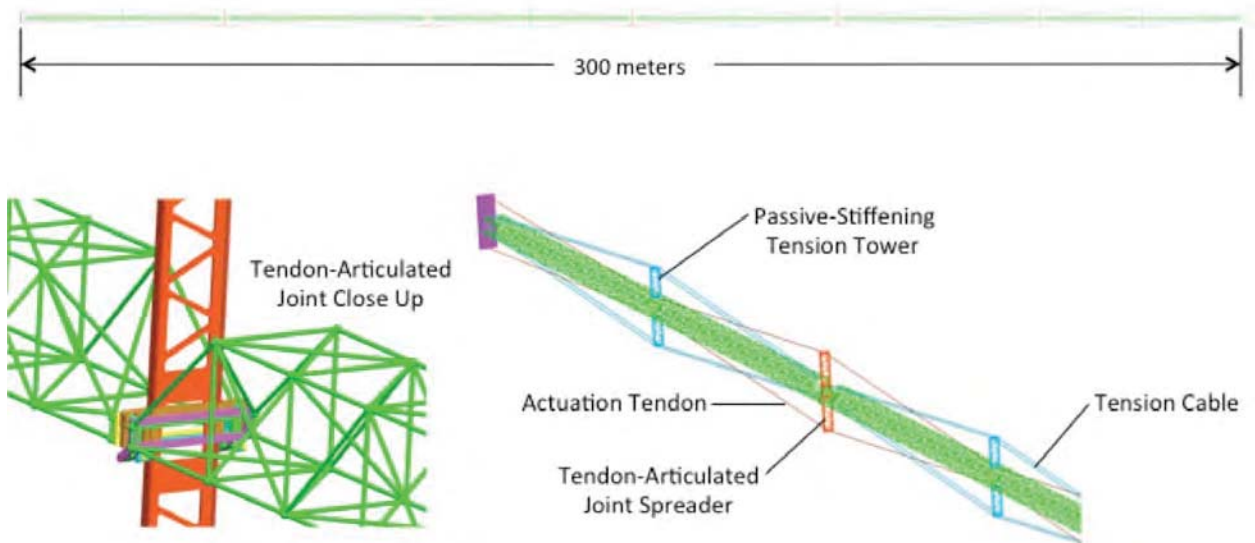


Figure 8. 300-meter-long TALISMAN configuration.

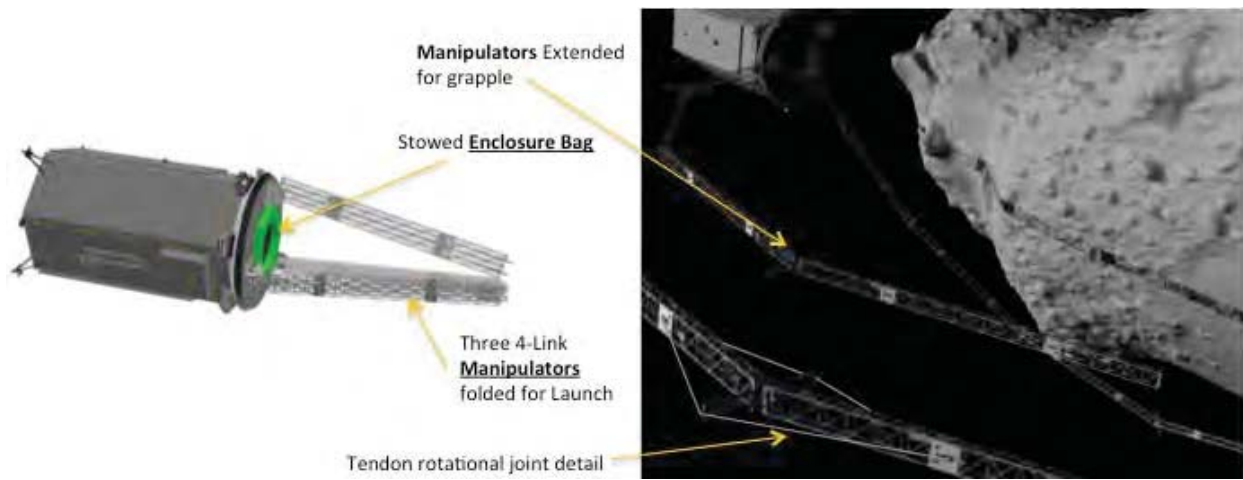


Figure 9. Asteroid capture mechanism TALISMAN configuration.

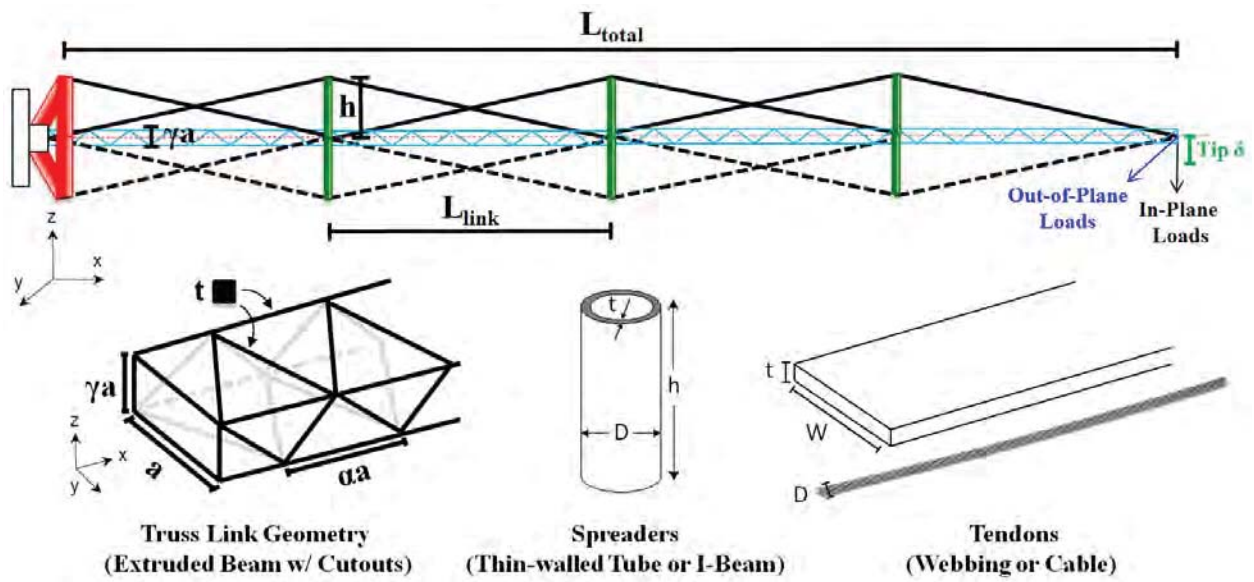


Figure 10. TALISMAN design tool member geometry, loads and tip displacement



# The Use, Evolution and Lessons Learnt of Deployable Static Solar Array Mechanisms

Mark Ferris\* and Andrew Haslehurst\*

## Abstract

This paper focuses on the mechanisms incorporated into SSTL's static deployable arrays; namely the sprung-hinges and hold down and release mechanism (HDRM). Combined, the HDRM and hinges form the hold down release system (HDRS). The deployable static solar array HDRS has been successfully used on several missions, first launched upon the DMC-CFESAT spacecraft in 2007 for a U.S. customer (Figure 1), and later used on DMC-UK2 and EXACTVIEW-1 launched in 2009 and 2012, respectively. The simple, robust and low-cost solution HDRS has been evident in allowing missions to satisfy an ever-increasing power demand, allowing the solar arrays to increase in size and have a preferable sun angle for increased cell efficiency. The system is now being employed on the first mission out of SSTL's U.S. office (SST-US) on the Orbital Test Bed platform. This paper shall cover details of the original design and development program, problems incurred on latter missions, and evolution of the HDRS for the present Orbital Test Bed mission. Both the original development and recent evolutions have taken place in rapid timescales, to satisfy the high-turnaround of SSTL missions.



**Figure 1. DMC-CFESAT platform with deployable solar panels partially deployed**  
(Ph. Credit LeRoy N. Sanchez94)

## Introduction

### The SSTL approach to Spacecraft Engineering

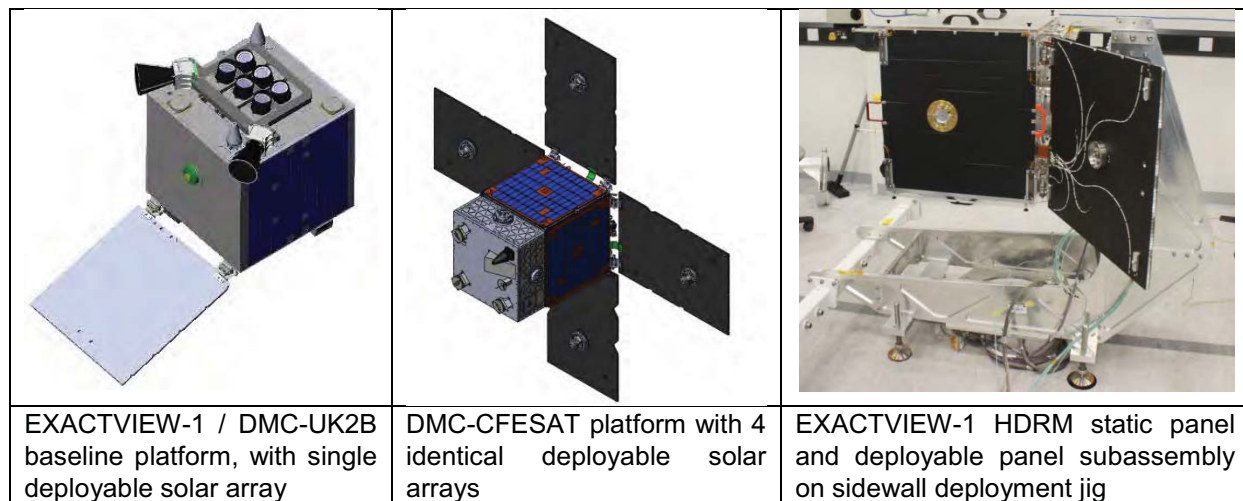
Surrey Satellite Technology Ltd (SSTL) is a unique supplier of low-cost satellites to international customers from its headquarters based near London, UK. SSTL's success within the industry and to meeting the increasing market need for more cost-effective satellite solutions has meant SSTL expanding into the U.S. with a dedicated office (SST-US) with design and assembly integration and test (AIT) facilities. SST-US' first mission, Orbital Test Bed, is now live, with AIT of the spacecraft commencing in summer 2014. SSTL-UK shall be supplying the modules and platform bus, while SST-US provides the payloads and conducts the remaining AIT campaign on the entire spacecraft. SSTL's traditional simple, low-cost platforms used fixed body-mounted solar arrays on all 4 side-panels (non-Earth and Space facing facets) as the satellite's power source. As SSTL's mission capabilities grew and payloads became more power hungry, SSTL had to achieve higher-power capacity platforms. Options to do this included higher-performance solar cells; static deployable solar arrays; and tracking deployable arrays. Static deployable arrays were selected over the other two options for the most popular SSTL-100 class of

---

\* Surrey Satellite Technology Ltd, Surrey, United Kingdom

platforms (100 kg) to give a noble compromise between increased power delivery and attributed cost (development and recurring). Static deployable arrays vary from the more complex tracking arrays in as much as the array is deployed from the body of the craft once and to a fixed position which does not change throughout life. This means that the sun angle is improved over the traditional fixed body-mounted panels, but not as optimized as a tracking array which actively follows the sun. The cost and complexity of a tracking array was not deemed necessary for SSTL-100 platforms since the needed power could be achieved via the simpler static-deployable arrays (Figure 2).

SSTL operates uniquely compared to traditional space companies as it makes extensive use of commercial off the shelf (COTS), which gives the benefit that technology is typically advanced ahead of space-rated hardware. SSTL's matrix structure and use of COTS components both allow for rapid development schedules with the manufacture and test of Qualification Models (QM) taking place early in the project cycle. SSTL invests a focused effort and duration on design and analysis, and spends significant time on thorough test campaigns in order to gain confidence in module developments and fix problems quickly along the way. In this way, SSTL can build and test Flight Models ready for satellite integration quickly from 'blank-sheet' design specifications. The deployable static solar arrays and attributed mechanisms demonstrate this approach to spacecraft engineering.

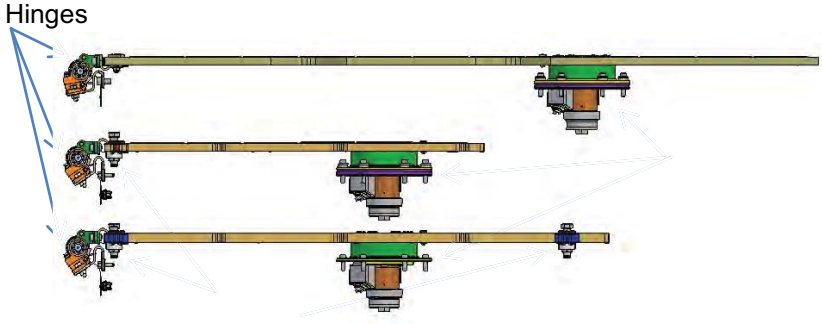



**Figure 2. SSTL-100 platforms with deployable solar panels**

#### Deployable Static Solar Arrays Overview

Existing SSTL platforms utilize static deployable arrays, with each deployable array having 2 spring-driven hinges, damping interface brackets, and a HDRM. The complete system (hinges, brackets and HDRM) is termed the Hold Down Release System (HDRS). The original HDRS philosophy was to form a generic set of units that could cope with a variety of panel sizes and launch loads to keep future platform non-recurring engineering costs low. The HDRM unit constrains the array against the panel craft during launch, and once actuated, releases the panel. During launch, the HDRM therefore limits the movement of the panel both laterally and axially and thus share the loads with the hinges to prevent their bearings being overloaded. The HDRM incorporates push-off springs to physically release the array from the craft, however, full array deployment is only possible because of the hinges. Once released, the sprung-hinges drive the panel through deployment and a sprung latch locks into position to prevent over travel and recoil upon reaching full deployment.

SSTL has utilized the HDRS successfully on several SSTL-100 platform missions, as captured in Figure 3. Other requirements of the platform types mean that the panel size and position of the HDRM has varied across the missions. Depending upon the position of the HDRM, size of panel, and launcher choice, some platforms also incorporate array snubbers to further control panel displacements during launch.

	DMC-CFESAT (launched 2007) No snubbers. 908-mm panel length. Original HDRM and Hinges
	DMC-UK2 (launched 2009) Lower snubbers only. 482-mm panel length. Original HDRM and Hinges.
	EXACTVIEW-1 (launched 2012) Lower and upper snubbers. 641-mm panel length. Original HDRM and Hinges.
	Orbital Test Bed (launch expected 2015) No snubbers. 908-mm panel length. New HDRM evolution and original Hinges.

**Figure 3. Evolution of the SSTL deployable Solar Array**

### History of HDRS Original Development for DMC-CFESAT

#### Original Hinge Development for DMC-CFESAT

Initial concepts were based on the Surrey Rigid Array program, which took place at a similar time and used tape springs for a 2-panel 1-yoke system with  $\sim 1.2 \times 1.5$  m panels for  $\sim 1$ -kW power generation (see Figure 4). The tape springs provide simple low part count mechanisms but due to their nature during  $180^\circ$  rotation, there are points of negative torque margin, and when coupled with the high retarding torques of the flexprint power harness, a positive torque margin cannot be guaranteed. Initial testing proved that this could be overcome by giving the array an initial push-off, however, there was permanent deformation (creases) exhibited in the tape springs and although they still worked, it was deemed not suitable for flight systems which require multiple deployments, so a new hinge concept was undertaken.

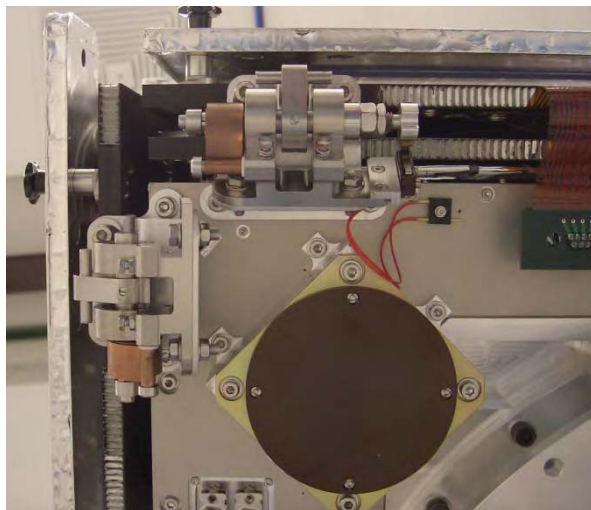


**Figure 4. Surrey Rigid Array in deployed position**

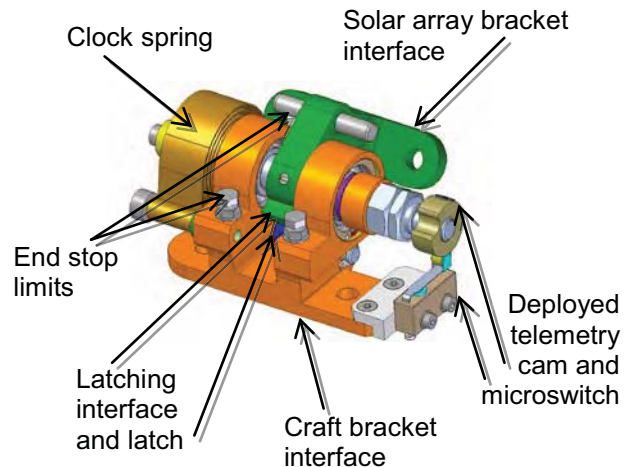
The subsequently developed hinge system design is relatively simple, utilizing two hinges very similar in design; one fixed and one free to slide on its shafts to manage the material thermal expansion mismatch from the CFRP solar panel and the aluminum body of the spacecraft. The constraints of limited volume and mass for the hinges meant that a damped system could not be implemented. Instead, the system

energy needed to be carefully balanced so as not to over-design the parts or cause the brackets to break at the end of deployment latch up. The hinge design is kept generic and latches in the same position, and hence different deployment angles between missions are achieved by simply changing the bracket geometry and not touching the hinge mechanism itself. Each hinge has a simple latch which has a PTFE-coated running surface with a carefully profiled end to give positive locking at the end of deployment. Early versions of these did disengage if enough moment was applied on the hinge so a change was made to bead blast the end surface and after this they never disengaged.

The first design used plain bushings; however, the torque of these was too high and varied considerably over temperature, so this simple and small volume solution was replaced with deep groove radial ball bearings with dry-lubricated PGM-HT cages similar to the ones used in SSTL 10SP reaction wheels. These had a large radial load capacity and very low and consistent running torque (see Figure 5). The initial hinge design used a regular coil torsional spring, but this proved to give unreliable torque performance, and to keep the stresses low in the spring it ended up being quite long and thus not fitting in the design volume on the spacecraft. Instead, a custom beryllium copper clock spring was designed, which had good torque performance through the rotation angle.



DMC-CFESAT hinges insitu with platform



Details of fixed hingewith microswitch

**Figure 5. An overview of heritage deployable array hinges and interface brackets**

The deployable panel went through an extensive unit-level qualification; the same unit also went through spacecraft-level testing doubling some of the typical tests performed. Over 20 deployments were performed at ambient pressure cold / hot and well as a Thermal Vacuum Test (TVT) campaign to remove the air drag on the system. During TVT, one test was performed hot with the maximum system energy and the other cold with one spring removed, the other at low torque and no push-off springs to represent different possible failure modes and a worst case deployment case; all tests were successful.

#### Original HDRM Development for DMC-CFESAT

SSTL started investigating the use of Frangibolts (see [www.tiniaerospace.com](http://www.tiniaerospace.com)) in early 2000's for use on its static and multiple panel deployed tracking solar arrays due to the simple design, ease of use, volume, mass and cost of these devices. The development for DMC-CFESAT was particularly mass and volume critical which suited the Frangibolt design. This section discusses the initial Frangi-HDRM (i.e., Frangibolt-based HDRM) development through engineering trials, qualification campaigns, and into flight manufacture and in-orbit deployment of multiple modules. The development was challenging at times; an early release trial on some ground support equipment resulted in a non-fracture of the bolt, however, these problems were overcome to fulfill the successful design qualification and release of multiple devices in-orbit.



The HDRM unit is predominantly bespoke SSTL design in terms of the separation interfaces and housings; however, the central release actuator is a purchased unit (Frangibolt and Shape Memory Alloy (SMA)). The basic principle of the Frangibolt relies on a pre-compressed SMA tube and a titanium bolt with a special notched section which is positioned through the cylinder and restrained at either end. When heated up to a temperature of  $\sim 90^{\circ}\text{C}$ , the SMA undergoes a phase change returning to its original size thus developing enough tensile force to fracture the notched section of the titanium Frangibolt. Redundant heaters wrapped around the SMA are used to apply the heat which only requires unregulated DC power from 10 – 100 V to activate, and with temperature sensors built-in this makes a very simple mechanism with no real moving parts. The Frangi-SMA actuator was selected because it was cost effective, could be reset in-house, and energized via low-power switches.

The Frangibolt is thus designed to fracture in a controlled fashion at a specific tensile load, which occurs because of a stress concentration region via a notch – the frangible portion of the bolt. The notch however limits the load capacity of the Frangibolt and in turn, of the HDRM. In order to ensure that the Frangibolt performs as intended, tight control over the applied preload must be established in order to absorb all clearances so that the subsequent SMA expansion  $\sim 0.1\text{ mm}$  is successful in fracturing the bolt, while not overloading the Frangibolt.

There were a few design requirements on the HDRM over the aforementioned. One requirement was that the parts of the cup-cone should require no match-machining of parts or special alignment impact to the spacecraft structure or arrays. Instead, the cup-cones simply had to ‘bolt-on’ over multiple interfaces which could create up to 0.5 mm of axial and lateral alignment error. To do this, the HDRM was designed to include multiple parallel and tapered shims in the form of a fixed swash plate to allow for parallel and angular misalignments. However, the shimming capacity (parallel and angular) were never used and always set at nominal as the spacecraft assembly errors were minor during the flight builds. The actuator also had to be easily re-set without dismantling the spacecraft or misaligning previously set HDRM and panel hinges. Figure 6 shows a cross section of the Frangi-HDRM assembly.

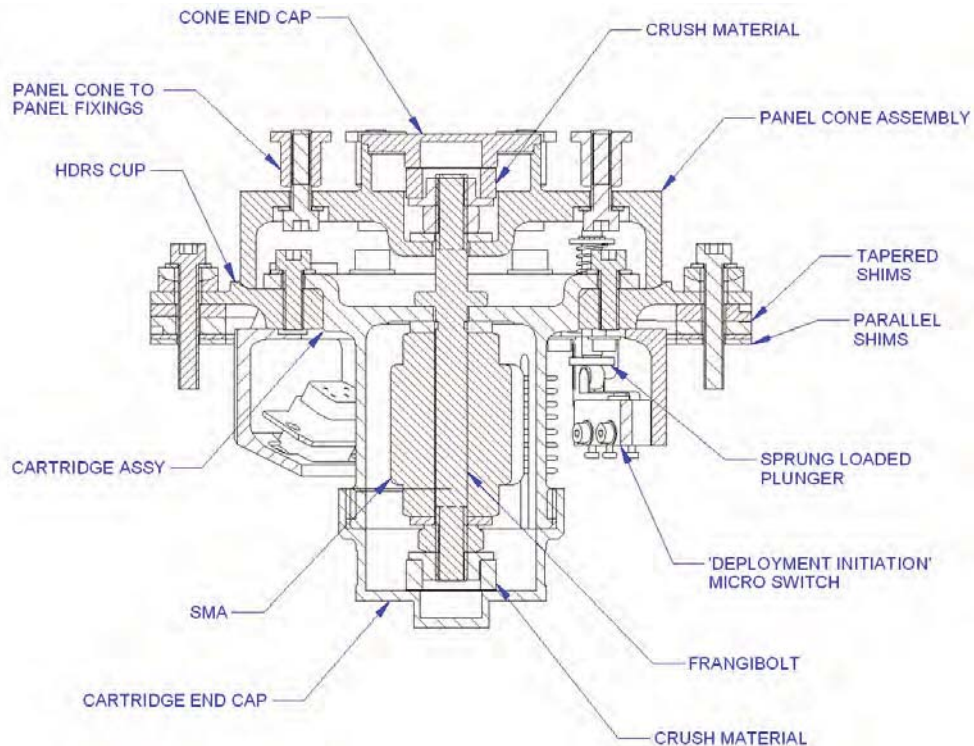


**Figure 6. Cross section of the Hold Down and Release mechanism (HDRM)**



Redundant push-off springs mounted on COTS bushings are configured inside the cone to give the panel an initial separation. A COTS microswitch (~\$2) is housed behind one of these push-off plungers and used to confirm separation of the hold down. A similar microswitch used on the hinges then confirms full deployment and latching. The solar arrays use triple-junction gallium arsenide solar cells which are in close proximity of the HDRM in order to achieve maximum panel coverage. The induced shock from the HDRM bolt fracture was a concern on the micrometer-thick fragile cover glass on the cells, in addition to the hinge's deep groove radial ball bearings and other electronic components within the spacecraft. To reduce the shock, thin film aluminum honeycomb core material was located at each end of the Frangibolt which serves to absorb the shock forces when the bolt fractures.

A ¼-inch Frangibolt was selected for the HDRM and is assembled into a removable cartridge which attaches to the cup. The Frangibolt passes through the cup (craft side) and protrudes through the mating cone (array side) to allow the array to be attached. The cup-cone is thus fastened together via the Frangibolt, and a preload is applied to the front side via torquing a high-tensile nut up to ~5 N-m. The preload of this bolt is critical to prevent the cup-cone slipping and gapping.

In order to prevent cold welding during launch, the Titanium 6Al-4V cup is coated with Titanium Nitride, while the Titanium 6Al-4V cone is left un-plated. To help accommodate the alignment and assembly constraints at spacecraft level, a design trade was made and it was decided that the cup-cone interface did not bear on the cone angle itself as in a typical cup-cone interfaces. Instead, the cup-cone elements bear on flat portions of the corresponding elements with a very small gap (<0.2 mm) to the cone interface so if slipping did occur, it would then engage.

The practical limit of tensile load capability of the Frangibolt is ~6.5 kN. If a larger preload is applied on the cone-side over the maximum in the actuator section, there is risk of creating a gap which could risk non-fracture of the bolt. There was no space in the design to implement a load cell to give accurate preloads so the torque scatter was accommodated in the design. Early testing did lead to further calibration of the test up and an increase in this value to 6.5 N-m as slipping did occur on the engineering qualification model (EQM) vibration test which was evident by visible fretting (Figure 7), but it should be noted that this did not prevent any deployments.

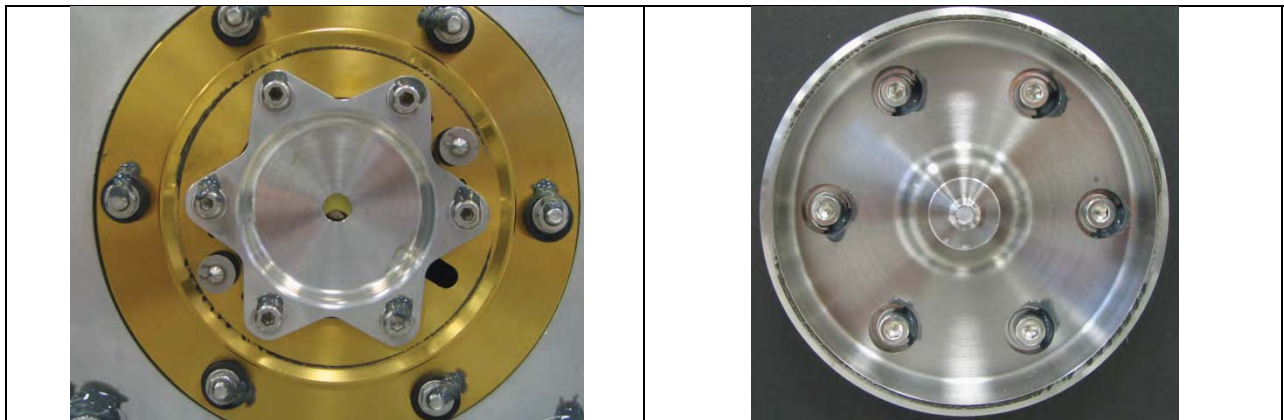


**Figure 7. Engineering Qualification Model cup / cone interfaces showing fretting**

Early on in the design process of the hold downs it was acknowledged that the temperature of the device is critical to its operation. Some work was undertaken to better understand the upper temperature limits of the SMA in the Frangibolt as thermal mission predictions show high temperatures in excess of 80-90°C during early phases of the missions prior to array deployment. This environmental temperature could result in premature array deployment. It was during this testing that one bolt failed to fracture, upon disassembly there was nothing obvious to show why and the actuator in question subsequently successfully fractured a bolt under normal actuation. The full root cause was never clearly identified but

during the detailed investigations several lessons learned were made which were to be later implemented in the flight designs:

- Radii under some of the mating interfaces could have caused a gap if they interfered so tolerances were tightened and 100% optical inspection was made on all Frangibolts and mating parts.
- There was a hexagon broached section in the end of the Frangibolt used to stop rotation with an Allen key while the nut torque was applied during assembly. It was realized that this section could be too long and extend into the working section of the bolt under the main nut and thus changing the local stiffness of the bolt possibly causing elongation of the bolt during extension of the Frangibolt. This was tested and found to be inconclusive although during one tensile test the broached section did fail at a low load and thus it was removed from the design – subsequently changed to a male hex feature.
- Upon disassembly of the setup, a slither of metal was found in the nut and the thread of the bolt was damaged. It was thought that debris could have prevented the nut from being correctly torqued up thus insignificant preload being applied which when the SMA went through its elongation it was not restrained and could extend / gap.

The latter concern coupled with the fretting required indicated that accurate knowledge of the preload in the frangible section of the Frangibolt was needed and so a new setup (Figure 8) was defined in a tensile test machine. Here a known load  $\sim 7$  kN is applied and then a locking nut installed to 1 N-m thus guaranteeing the preload in the assembly is greater than the newly defined 6.5 kN required on the front.

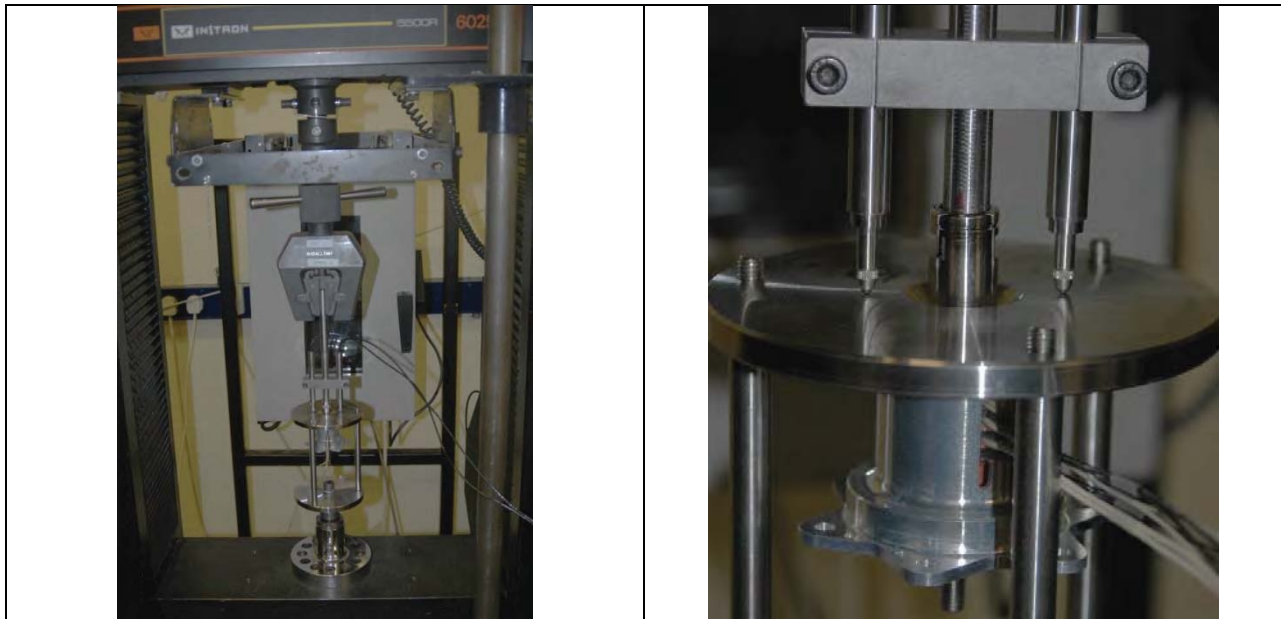


Figure 8. Frangibolt preloading set up

### Challenges Experienced with HDRM Actuator Selection on Later SSTL-100 Missions

#### DMC-UK2

The HDRS successfully deployed all four DMC-CFESAT solar arrays in orbit following launch in 2007. Following this success, the HDRS was employed on another SSTL-100 platform type, DMC-UK2. For this mission, the deployable panel was significantly smaller than the original DMC-CFESAT (Figure 3), therefore direct use of the HDRS was deemed feasible. While the HDRS had sufficient load capacity to cope with the panel's induced forces during launch, the launch environment was harsher and solar array panel deflections were a concern. In order to avoid possible damage to the solar cells, then snubbers

were incorporated into the design to limit the array deflection. DMC-UK2's single solar array deployed in-orbit in 2009 - a successful application of the heritage HDRS design.

#### Problems Experienced During EXACTVIEW-1 Environmental Test Campaign

The load capacity was suitable for the baseline two platforms – DMC-CFESAT & DMC-UK2 – however problems arose during the third platform (EXACTVIEW-1). For this mission, the panel size grew. While still smaller than the original DMC-CFESAT panels, the relative distance from the hold down to the top of the panel increased and a different launcher was selected late in the program, which imparted higher loads into the structure. Subsequent analysis showed a coupling of a spacecraft mode at ~280 Hz (Figure 9) with the deployable panel so two additional upper corner snubbers were incorporated into the design, which helped, but the design margins at the hold down against gapping were low to negative. As this was late into the spacecraft EVT program with all hardware manufactured and built onto the spacecraft, the spacecraft was taken for a low-level vibration transmissibility test which confirmed the analysis / negative margins and lead to a speedy re-design.

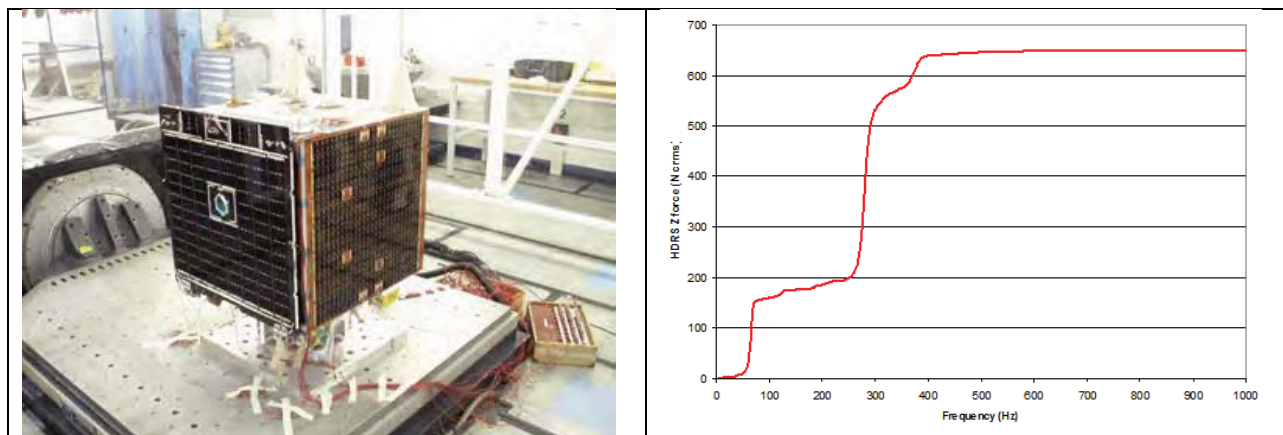


**Figure 9. EXACTVIEW-1 at vibration test with HDRM sine loading shown**

All the interfaces were fixed and there was no time to procure / implement another hold down device with a higher load capacity, so the preloading of the nut was investigated as preloading either side of the actuator using a torque wrench is known to have a large scatter. The torque scatter means that the resulting preload in the bolted joint could vary by as much as  $\pm 30\%$  due to friction on the thread and washer. In order not to exceed the Frangibolt's 6.5-kN load capacity, a nominal preload of 4.55 kN would be necessary and at the lower end of the scatter would result in a preload of 3.19 kN. At this lowest tolerance preload, the resulting margin of safety against HDRM gapping was negative (gapping is the ability of the mating release interfaces to separate temporarily), this could lead to:

- HDRM pushing additional loads onto the hinges, and the hinge bearings being overloaded - thus increasing friction and risk of deployment failure
- During dynamic vibrations, fretting on the release interface could occur, which could lead to cold welding preventing the panel from deploying
- Gapping hold down portions could in turn induce additional lateral loads and bending moments on the Frangibolt which could cause it to fracture prematurely and deploy during launch.

It was not possible to implement a load cell or load washer into the design so the HDRM housing was re-designed and instrumented with strain gauges to monitor deflection to better determine the preload reducing the scatter to  $\pm 10\%$  (see Figure 10). As a result of this method, the nominal preload could be increased to 6 kN, however, this alone was only just sufficient to avoid the potential for gapping so a further change was made to achieve more favorable margins of safety by employing the true cup-cone interface instead of the previous flat-on-flat friction contact used on CFE-SAT and DMC-UK2. Shear Tests

were conducted, that showed the true cup-cone interface could support approximately 25% increased lateral forces for the same preload than a flat-on-flat friction contact (see Figure 11).

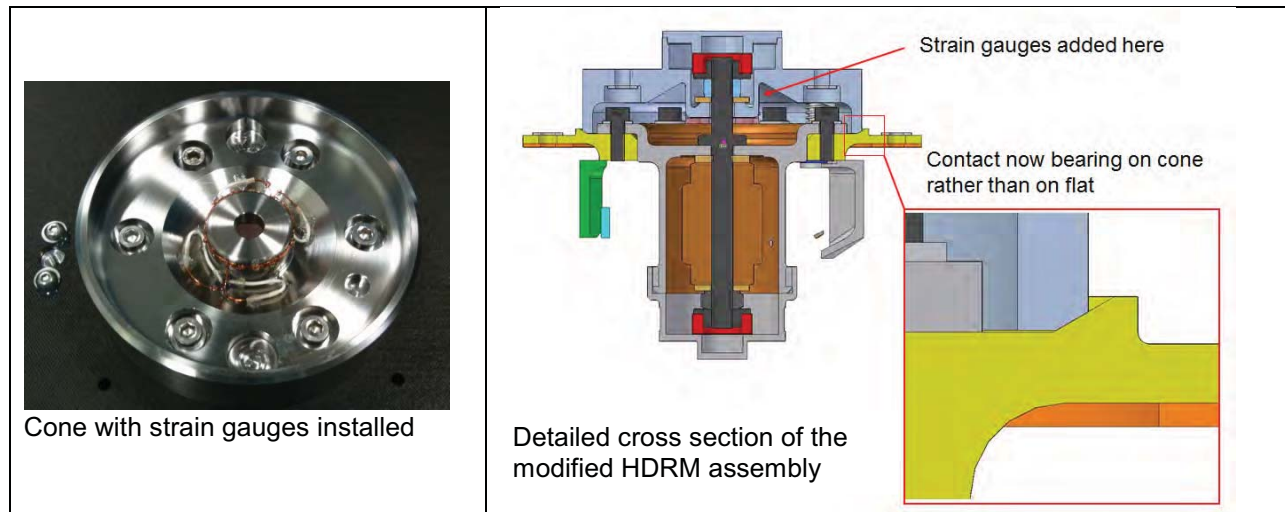


**Figure 10. EXACTVIEW-1 HDRM Modifications**

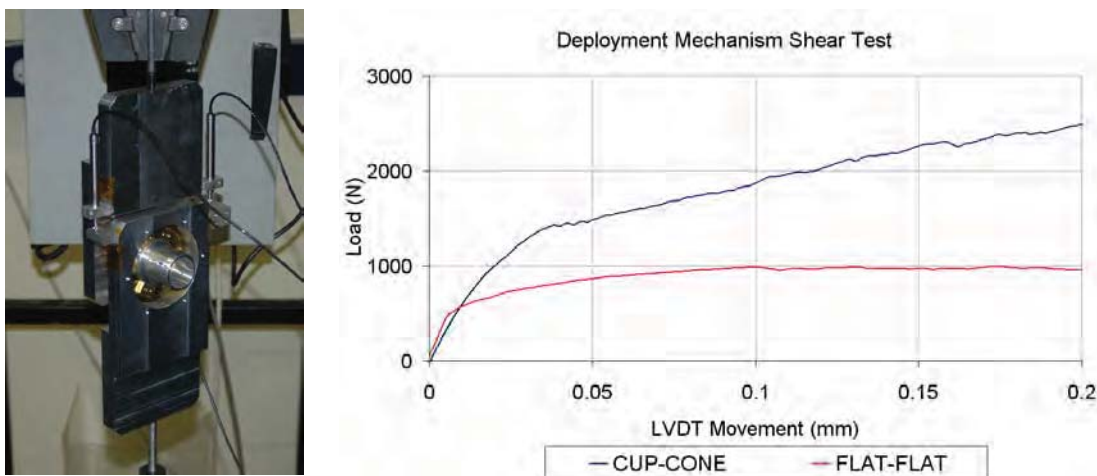


**Figure 11. Deployment interface shear test setup comparing flat-flat interface with cup-cone interface, for a nominal preload of 6075 N**

The cup-cone interface and reduced preload scatter was sufficient to change the baseline negative design margins to positive for the EXACTVIEW-1 mission, whose panel successfully deployed in-orbit in 2012. While the campaign was successful, it highlighted the design's load capacity limitations and the criticality of the preload method. The man effort now associated with using this design due to the different assembly and calibration steps had increased the overall unit price of the system. When also considering the increased analysis non-recurring effort which would be required on each future program due to the Frangi-HDRM's sensitivities, a recommendation was made by the material review board to implement a different higher load capacity solution on the next mission. The material review board's analysis suggested a preload greater than 12 kN was required to give confident margins.

It is also worth noting that DMC-UK2 and EXACTVIEW-1 platforms provided the benefit over the DMC-CFESAT craft such that the HDRM and hinges are mounted directly to a single fixed body-mounted panel interface, allowing the HDRS, static and deployable panels to be assembled and tested separate to the rest of the satellite structure (see Figure 2). Whereas, on DMC-CFESAT, the hinges mount to one spacecraft interface, and the HDRM to another driven by the craft's need for an alternative payload bay



arrangement. The stacked tolerances on the multi-interface of DMC-CFESAT means that after craft de-stack and re-stack operation, the hinges and HDRM need realigning carefully, whereas DMC-UK2 and EXACTVIEW-1 can remain as a separate single subassembly, saving time and reducing variability.

### **HDRM Evolution and Actuator Change**

#### Hold Down Actuator Change

Following on from the successful in-orbit deployment of EXACTVIEW-1 solar panel, there were substantial lessons learned regarding the heritage hold down actuator choice. Firstly, the load capacity proved more restricting than previously thought to the extent where a launcher change caused the hold down to have negative margins on gapping and slippage. Secondly, the attraction of being able to perform in-house refurbishment via frangible bolt change after hard deployments was offset by problems experienced during the setup whereby the exact preload achieved was questionable. This latter issue could be resolved for future use by better methodology and with additional instrumentation – for example by monitoring the deflection of the hold down cup body.

However, the decision was taken that a much higher load capacity was needed in order to avoid future problems similar to EXACTVIEW-1, such that in terms of HDRM loading, the launcher selection could largely be ignored and the need for detailed analysis would almost disappear. Therefore, upon signing the contract for the SST-US mission Orbital Test Bed, the decision was taken to change the hold down actuator. SSTL could have alternatively changed other design features of the HDRM, such as the cup-cone angle, however, the actuator change and experience with a viable alternative proved favorable.

Another actuator market study was conducted, but revealed that the availability was very constrained based on the recurring cost budget permitted. Due to the criticality of the application, only established actuators were considered and the possibility of new developments in-house or external was ignored. This market study identified two possible solutions: either select a larger size in the frangible bolt and SMA family from the existing selection (1/4") or change to a non-explosive separation nut. The larger frangible-bolt was rejected since the corresponding SMA body would impart a significant increase in volume of the HDRM unit. Thus the non-explosive separation nut (see [www.neaelectronics.com](http://www.neaelectronics.com)) was chosen. This was also based on good experience gained with the separation nut on the SSTL NigeriaSat-2 mission which used these to support a deployable optical payload bench.

The separation nut actuator works on the basis that a spigot shaft is constrained by a multi-piece nut, which is held radially by a wrapped spring and fuse wire. When the fuse wire burns, the released spring allows the nut to separate and release the spigot. The separation nut housing is fastened to the cup portion of the HDRM in place of the previous SMA and the mating cone is fastened by screwing a stud into the separation nut's spigot. Therefore, the spigot shaft is merely released in contrast to the fracturing nature of the frangible bolt in the previous system.

For a similar size separation nut to the previous SMA, the load capacity increased threefold, with a rated release load of >33 kN. This allows a Sep-Nut-HDRM to be assembled efficiently without any instrumentation by torqueing alone. A nominal preload of 22 kN is sufficient to ensure that the achieved preload always exceeds the 12-kN minimum requirement and is well within the actuator's load capacity, even factoring in  $\pm 30\%$  torque scatter. The significant load capacity allows the Sep-Nut-HDRM to remain a generic solution for many more applications supporting larger panels/payloads over higher launch loads. The requirements for the HDRM development are summarized in Table 1.

Due to the hinged deployment nature of the solar arrays, once released, the spigot tip's movement describes an arc and thus the spigot tip would catch and snag on the bore of the cup. This was not a problem on the existing SSTL separation nut application on the deployable optical payload bench, since the bench was released parallel to the static panel, as opposed to being hinged from one edge. Any snagging of the spigot tip on the cup could result in partial deployment and corresponding mission degradation via loss of power.



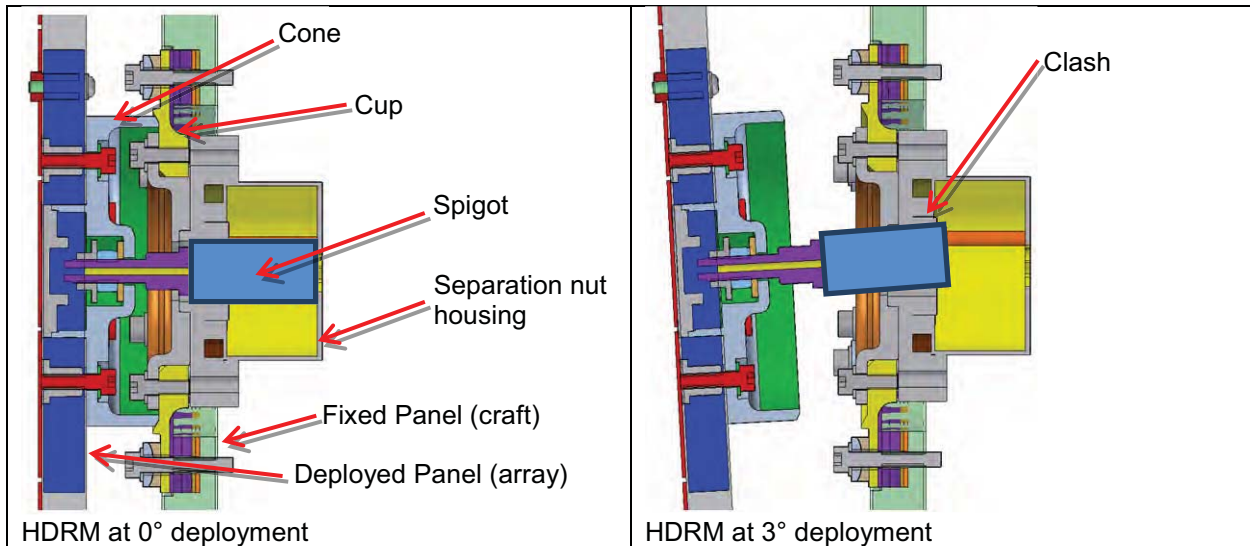


**Figure 12. Separation Nut and HDRM arrangement and arcing effect of panel deployment profile**

**Table 1. HDRM and Actuator Requirements**

Parameter	Magnitude	Notes
Hold down actuator load capacity	Minimum load capacity 15 kN	The selected Separation Nut is rated to loads <33 kN, hence providing margin even given $\pm 30\%$ torque scatter
HDRM mass	< 1.0 kg	
Operating voltage	20 – 33 VDC	
Operating current	< 3 A	Traditionally actuated by a low-power switch.
Survival temperature	-70°C to +80°C	Based on preliminary mission analysis.
Low Shock	<< 3000 g	
Physical Envelope	Compatible with heritage interfaces	The redesigned HDRM shall have the same spacecraft interfaces to both the static and deployable panels. The overall volume of the HDRM shall be largely unchanged, and compatible with existing craft layouts.

Due to the complex way in which the separation nut releases the spigot, the separation nut actuator provides the limitation that it cannot be refurbished in-house and needs to be sent back to the supplier, in contrast to the original actuator where the frangible bolt could merely be replaced. This external refurbishment limitation was outweighed by the confidence obtained through SSTL's existing use of the separation nut and large margin on load capacity. The other limitation was that the separation nut actuator choice was also ITAR-restricted which limits the applications and slows the procurement process. However, there is a significant lack of European cost-effective, high-load capacity, low-shock and proven hold down actuators, so there was no alternative at this time.

#### Retraction and Non-Retracting Mechanisms

Due to the spigot arcing hang-up effect described in Figure 12, it was foreseen necessary that the released spigot shall be withdrawn through the cup bore, prior to significant panel movement in order to prevent the possibility of hang-up. The most elegant way to do this is to incorporate a retraction spring which pulls the released spigot through the deployable panel immediately upon deployment to ensure that the spigot is out of the way and will not clash. This is done using a compression spring mounted between the cone and stud to act as a spigot retraction spring. The nature of the NEA's function means that the deployment is low-shock; however, the retracting spring on the spigot will impart some low-magnitude shock which shall be absorbed by a simple O-ring, instead of the previous honeycomb core material.

Initially, it was conceived that a retraction cap would be integrated onto the cone assembly to 'catch' the released spigot and stud shaft during deployment. Figure 13 shows that the retraction cap for a full-retraction system would protrude significantly above the panel surface with two notable drawbacks: the likelihood of cell-shadowing in-orbit and the restriction of launch vehicle accommodation due to growth of craft footprint. The cell shadowing effect was deemed low risk since the small diameter (30 mm) protrusion above the array surface would only cause significant shadowing at large angles of incidence (60°), at which point the cell's efficiency is significantly reduced and little power produced anyway.

As an alternative to the retraction spring, it was also conceived feasible that the spigot could merely be provided with a degree of freedom (rather than rigidly constrained to the cone), and thus without retraction, the spigot would clash with the cup during deployment but rotate and drag along the surface, rather than snagging and preventing deployment. Therefore, 3 configurations were envisaged: full retraction, partial retraction, and non-retracting (see Figure 13). The non-retracting variant has the advantage that the cone can be kept low profile without a retraction cap, but the mechanism details are less elegant. The degree of freedom is provided by a spherical washer interface, and the amount of spigot deflection needed to drag across the cup is <math><3^\circ</math>.

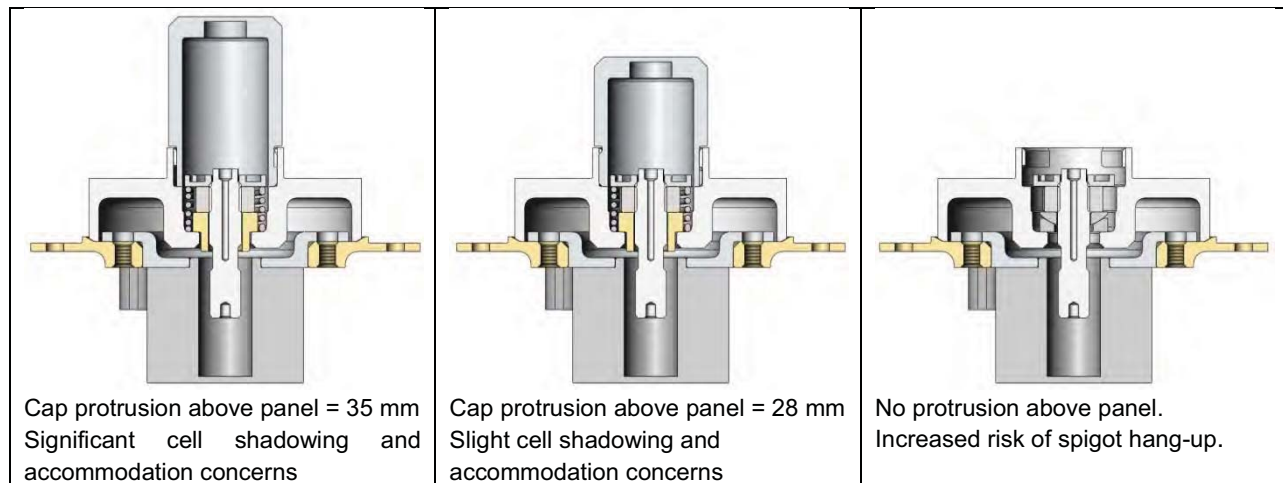


**Figure 13. Partial-retraction, Full-retraction and Non-retraction variants of HDRM**

#### HDRM Variant Breadboard Engineering Testing

The 3 HDRM design variants were taken forward to breadboard engineering testing in order to assess which one to select and evolve to the final mechanism. For this testing, a simple separation nut spigot was used instead of a complete separation nut actuator, and rapid-prototype additive-layer manufactured plastic parts represent the cup, cone and retraction cap. This low-cost and quickly compiled test setup was invaluable for providing some initial indications of design success.

All testing was done on the already existing sidewall deployment jig, with qualification model (QM) hinges and panels. Two sized panels were used: the smaller DMC-UK2 QM with short offset between the hinge rotation axis and HDRM position, worsening the arcing effect; and the larger DMC-CFESAT QM panel. The deployment tests were conducted in two stages: initially a 'light' retraction spring was used ( $k = 0.189 \text{ N/mm}$ ) to reduce risk of damage to the plastic; then the testing was repeated with a 'hard' spring (the intended design,  $k = 0.98 \text{ N/mm}$ ). To give confidence, three deployment tests were done for each variant across several deployment scenarios, varying the hinge spring torque and the push-off spring presence to mimic different failure scenarios.

The breadboard engineering tests provided the following conclusions:

1. Deployment was successful in all attempts for all variants for all feasible scenarios and the choice between full, partial and no retraction does not influence the reliability of deployments.
2. Retraction spring energy imparts notable energy into the panel deployment – the effect on hinge bracket energy dissipation shall need further work.
3. The time for full retraction with the hard retraction spring is 6 ms corresponding to 0.3° panel deployment. This provides margin on the spigot-cone collision which occurs at 1° deployment.
4. The light retraction spring still provides fast enough retraction time (12 ms to full); however under 1g conditions, the spring was so light that the spigot would droop under its own weight once released, and this meant that it could be heard to make contact with the cone during deployment.
5. Spigot-cone collision does not prevent deployment provided the spigot has >2° free rotation.

This test campaign has demonstrated that all variants (partial-, full- and non-retraction HDRMs) are suitable to ensure reliable deployment of both the DMC-UK2 and DMC-CFESAT solar arrays.

#### Design Finalization and Qualification Plan

In true SSTL-style, the early breadboard engineering test campaigns gave opportunity to make observations and tailor the design to final design quickly, with final flight design drawings being released 5 months after HDRM evolution kick-off. It was agreed that the full-retraction variant was most attractive from a mechanism-reliability perspective; this could also be done without the need for the undesirable rigid retraction cap. Instead, the natural shoulder available on the separation nut spigot could be used to constrain the spigot in the cone to prevent full withdrawal. In this way, the HDRM retained the low-profile stowed volume of the non-retracting variant.

An O-ring on the underside of the cone is used to dampen the impact of the spigot shoulder, to permit the spigot to be reused to refurbishment after hard-deployments. In addition, the arrangement of the spigot, stud and retraction spring mean that if the retraction spring were to fail, the assembly allows the spigot to retain degrees of freedom, which have been shown to provide successful deployment – giving additional confidence to the design. The final design is shown in Figure 14 and Figure 15.

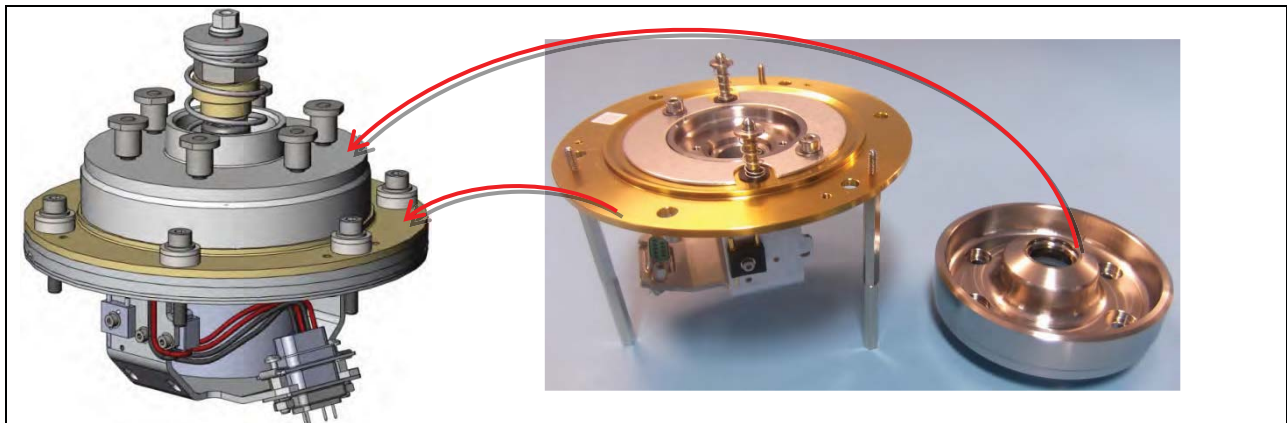


**Figure 14. Sep-Nut-HDRM: Left – CAD, Right – partially-built hardware (cup assembly and cone)**

In order to remove and replace the separation nut on the spacecraft for hard deployments during AIT, the actuator must be inserted from the ‘front’ of the cup only. In this configuration, the stress analysis of the design showed that the fasteners initially used to hold the actuator body to the cup was overstressed in tension, and enough larger fasteners to cope with the stressing could not be accommodated. Therefore a novel solution was incorporated to offload the fasteners by using a bayonet interface between the actuator carrier and the cup as shown in Figure 16. In this way, 2 small fasteners are merely used to stop the actuator falling out upon assembly – they do not experience any load, which instead is transferred directly through the cup body.

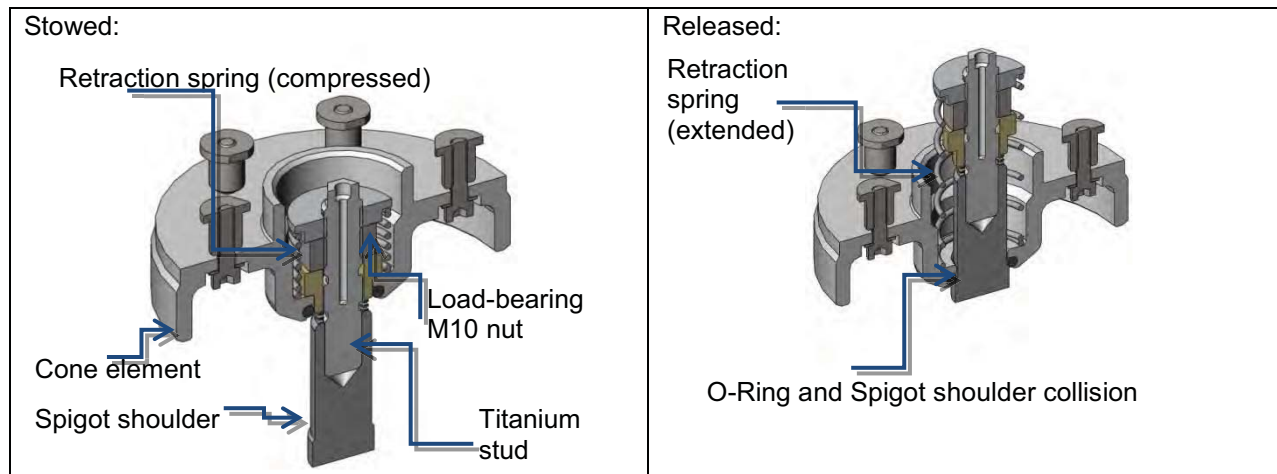


**Figure 15. Sep-Nut-HDRM Retraction Mechanism Overview**

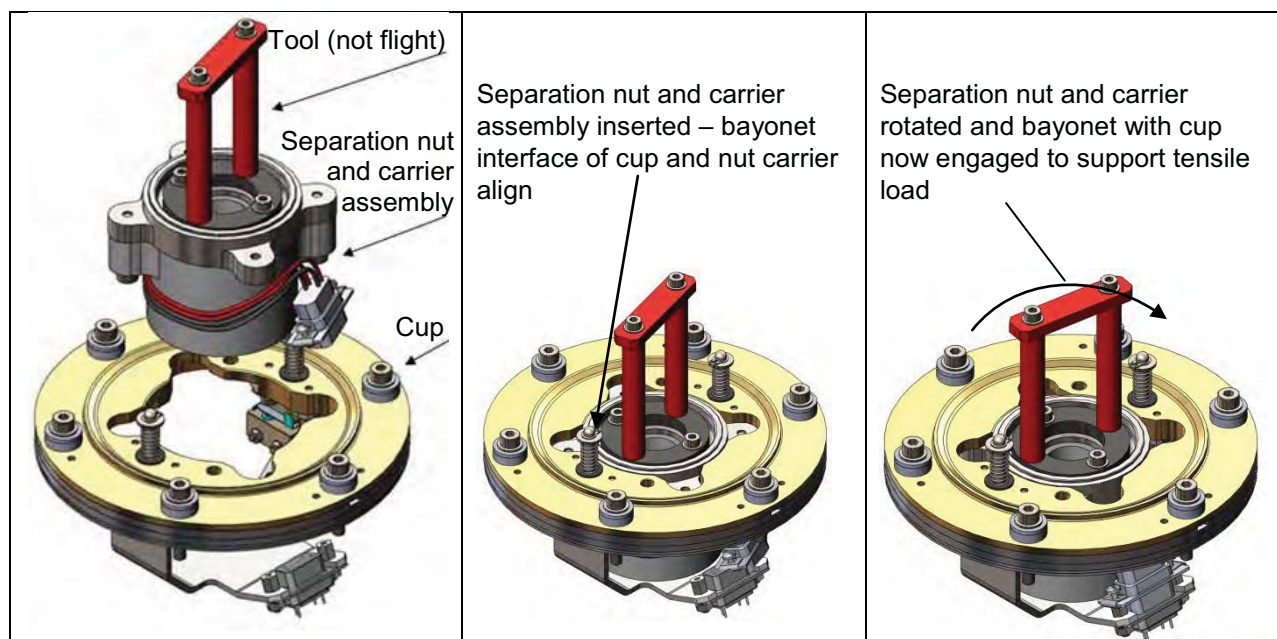


**Figure 16. Separation nut carrier and cup bayonet load transfer**

### Conclusions

The revised Sep-Nut-HDRM assembly weighs <1 kg and supports up to 33-kN preload. The original Frangi-HDRM design weighed 750 g and could only support 7-kN preload. The significant increase in load capacity far outweighs the small increase in mass; and allows for a very generic HDRM design for future applications such as larger/multi-panel arrays or deployable boom/antenna. The QM Sep-Nut-HDRM has been built and is about to undergo hard-deployment testing. The decision has been taken that vibration testing is not necessary since the QM HDRM design load capacity is far larger than the intended use, and thus the assembly does not experience any live load above its own preload. Instead, only thermal hard deployment testing shall be undertaken on the QM HDRM to prove the design is fit for flight while also covering the torque scatter possibility to avoid instrumentation and reduce recurring flight build costs. Subsequently, 4 FM HDRMs shall be built and integrated onto the craft during summer 2014.



# Deployment Mechanism for Thermal Pointing System

Kraig Koski\*

## Abstract

The Deployment Mechanism for the Total and Spectral Solar Irradiance Sensor (TSIS) is responsible for bringing the Thermal Pointing System (TPS) from its stowed, launch locked position to the on-orbit deployed, operational position. The Deployment Mechanism also provides structural support for the TSIS optical bench and two-axis gimbal. An engineering model of the Deployment Mechanism has been environmentally qualified and life tested. This paper will give an overview of the TSIS mission and then describe the development, design, and testing of the Deployment Mechanism.

## Introduction

The goal of the TSIS instrument suite is to accurately measure Total Solar Irradiance (TSI) and Solar Spectral Irradiance (SSI) and make the data available to the research community and public. TSI is defined as the Sun's radiant power per unit area ( $\text{watts/m}^2$ ) incident on a plane surface at the top of the atmosphere that is normal to the direction from the Sun and normalized to 1 astronomical unit. SSI is the power per unit area per unit wavelength interval. These two measurements are important for measuring the magnitude and variability of natural radiative forcing on the Earth's climate system. Radiative forcings are variations in the radiant energy received by the Earth or the energy radiated back to space. Long term measurements of solar and spectral irradiance provided by TSIS are required to continue the Climate Data Record and to fully understand the causes of climate change.

The University of Colorado/Laboratory for Atmospheric and Space Physics (LASP) is responsible for the delivery of the TSIS instrument. The TSIS dual instrument package was originally selected to fly on National Polar-orbiting Operational Environment Satellite System (NPOESS). It was de-manifested in 2006 during the restructuring of NPOESS, and then restored in 2007 following a decision by the NPOESS Executive Committee because of its critical role in determining the natural forcings of the climate system and the high priority given by the Earth Science Decadal Survey. Further restructuring of NPOESS transitioned all climate sensors, including TSIS, to the Joint Polar Satellite System (JPSS). The JPSS is the next generation of low Earth, polar orbiting, environmental satellites that are procured by the National Oceanic and Atmospheric Administration (NOAA) through NASA [1].

### TSIS Mission Design

TSIS is comprised of two instruments: the Total Irradiance Monitor (TIM) and the Spectral Irradiance Monitor (SIM). The TIM instrument measures TSI, integrating all wavelengths of solar energy ( $\text{W/m}^2$ ) at the outer boundaries of the atmosphere. The SIM instrument measures SSI from 200 nm to 2400 nm (96% of TSI)[2]. Both instruments along with associated electronics boxes are mounted to an optical bench which is mounted on a two-axis gimbal that provides the required solar pointing accuracy. The two-axis gimbal is mounted inside a mast that can be deployed and stowed (see Figure 1).

The TSIS is slated to launch in 2017 on JPSS Free Flyer 1 (JPSS-FF1), which is a smaller spacecraft relative to NPOESS with solar pointing capability. Since the JPSS-FF1 spacecraft will provide solar pointing, the need for the TPS and Deployment Mechanism is eliminated. Much of the fabrication and assembly of the TPS and Deployment Mechanism was already completed at the time of this decision, so approval was provided to continue the design and testing. This decision was based on the possibility that

---

\* Laboratory for Atmospheric and Space Physics, University of Colorado, Boulder, CO



the TPS and Deployment Mechanism may be used on a future mission with similar requirements to the original NPOESS mission. The Deployment Mechanism was successfully built and tested in 2012. Currently an engineering model with increased functionality is being fabricated, and the assembly will be tested in the spring of 2014.

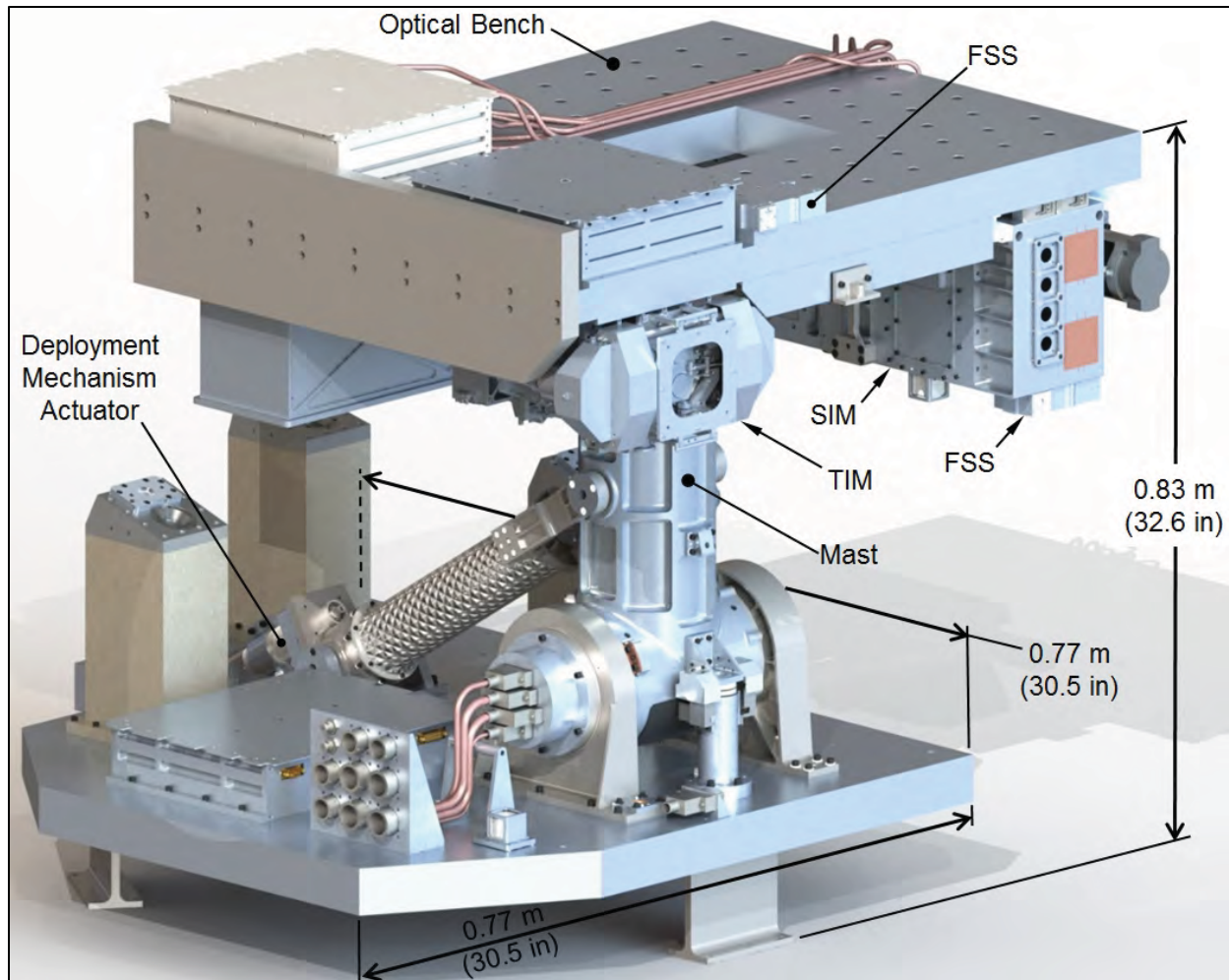


Figure 1. TSIS Rendering

Table 1. TPS Key Driving Requirements

Requirement	Method
Precise tracking of the sun	Gimbaled optical bench
Stable thermal environment for optical bench	Material selection, subsystem layout
Steady-state pointing error of TPS with respect to sun center <64 arcsec 1 $\sigma$	FSS (Fine Sun Sensor), precision actuators, control system
Dynamic pointing error of TPS with respect to sun center <61 arcsec 1 $\sigma$	Precision actuators, control system
Operational Temperature Range -20C to +40C	Material selection & platings, design
Survival Temperature Range -30C to +50C	Material selection & platings, design
Natural frequency of TSIS during launch >50 Hz	Launch latch design, structural design
Natural frequency of TSIS on orbit >6 Hz	Gimbal design, deployment mechanism
TPS shall be operable in any orientation in 1G environment	Gimbal design, deployment mechanism
Uncompensated momentum contribution from TPS < $\pm$ 0.5 N-m per axis	Precision actuators, control system, structural design

### Thermal Pointing System Design

The TPS was designed to meet the original NPOESS requirements summarized in Table 1. The natural frequency at launch must be  $>50$  Hz and this requires the TPS to have both stowed and deployed configurations. In the stowed configuration, the TPS is locked down to three launch towers with a 2-2-2 kinematic mount. The three attachment points are fastened with ground resettable non-pyro separation nuts. The kinematic restraint uses a vee-spherolinder-cone design (Figure 8) to accommodate launch loads. The TPS is moved from the stowed to the deployed configuration by the Deployment Mechanism (the subject of this paper). Figure 2 illustrates the phases that the TPS goes through after the separation nuts are fired and it is deployed by the Deployment Mechanism.

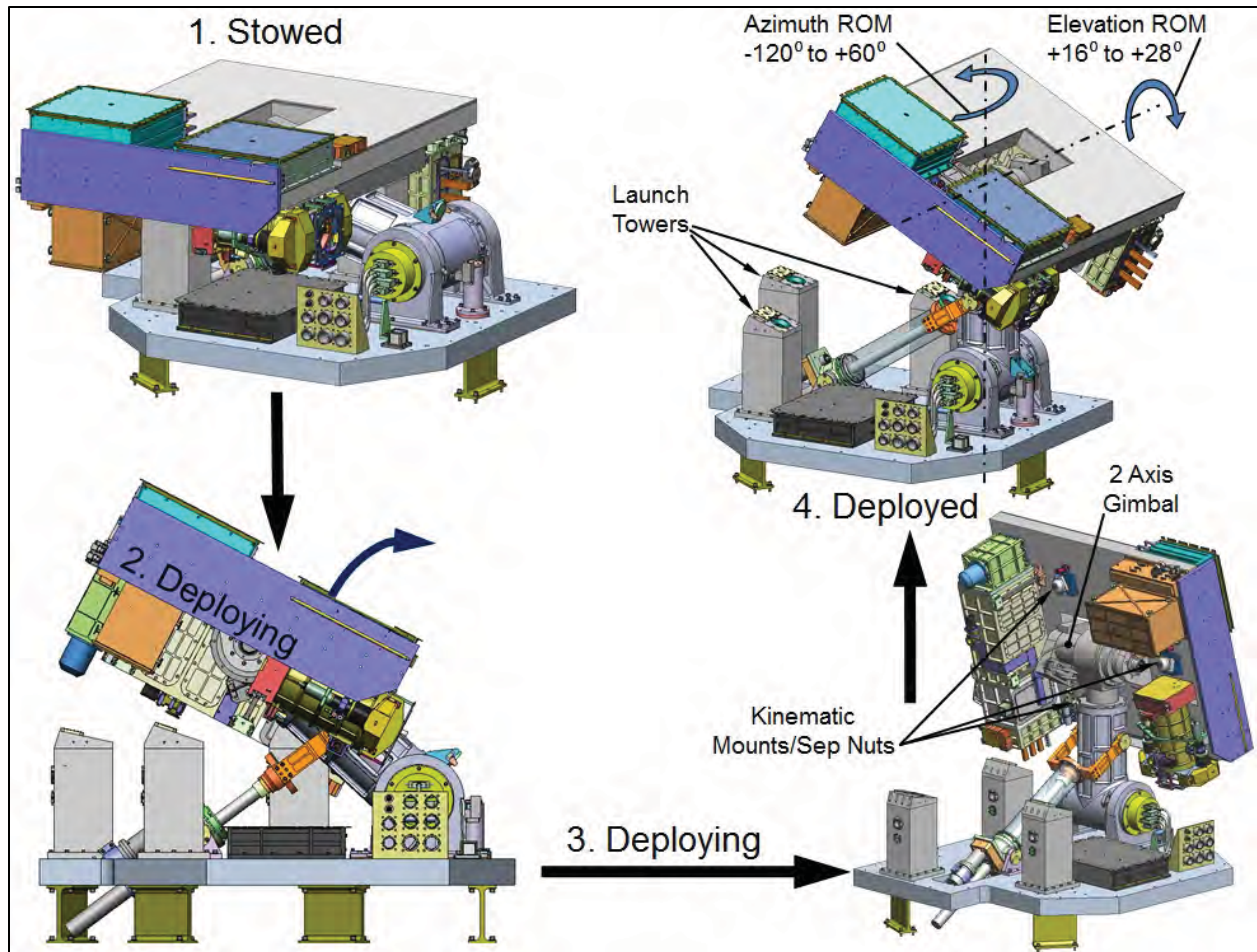
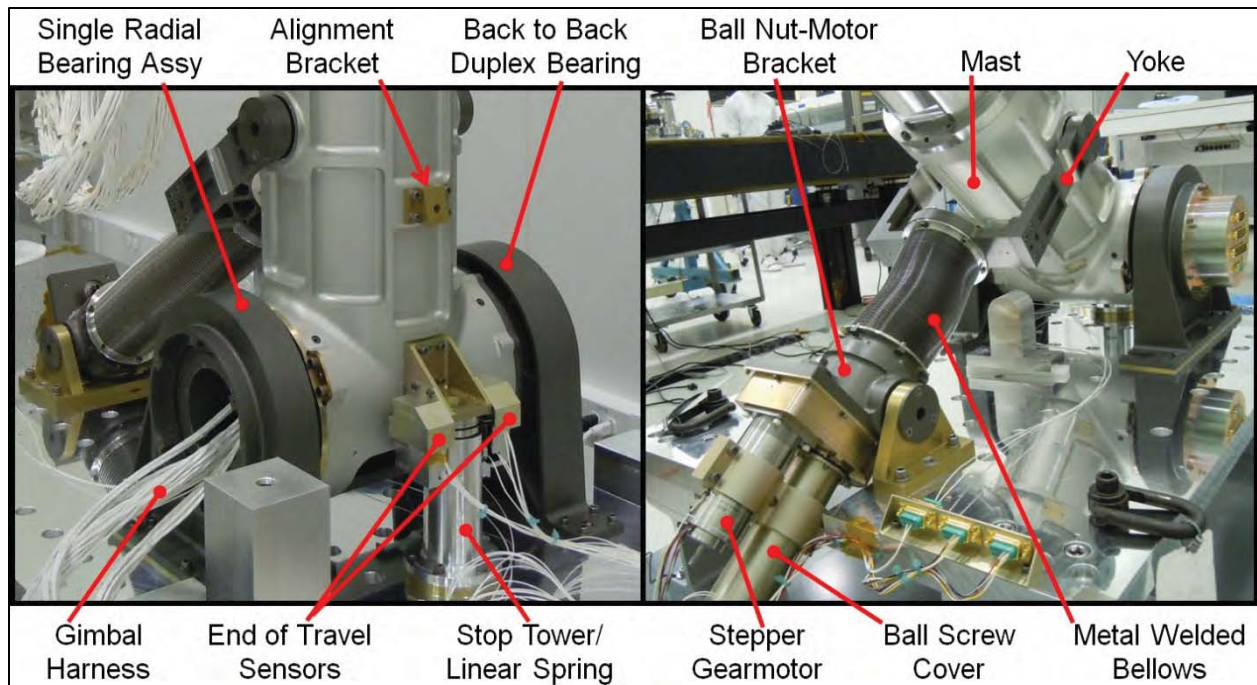


Figure 2. TPS Deployment Phases

### Deployment Mechanism Design Overview

The Deployment Mechanism incorporates a unique design that utilizes a variety of moving mechanical components to drive the TPS from stowed to deployed and back again. A stepper gear motor drives the system that includes a ball screw, gears, bearings, flexures, welded bellows and position sensors. The mechanism has a  $75^\circ$  range of motion between the stowed and deployed positions. Redundancy has been included where it is feasible with redundant motor windings and positions sensors. Front and aft views of the Deployment Mechanism engineering model are shown in Figure 3.





**Figure 3. Front and Aft Views of the Deployment Mechanism Engineering Model**

#### Deployment Mechanism Function

The Deployment Mechanism is driven by a 45°, 2-phase stepper motor with an integral 3-stage, 384:1 planetary gear head and a detent brake. The output shaft of the gearmotor attaches to a 2:1 pinion-spur gear reduction as shown in Figures 4 & 7. The spur gear is attached to a ball nut which is housed inside a titanium bracket and is supported by thin section duplex bearings at the top and a radial thin section bearing at the base. The ball nut rotates to advance a 6.35-mm (.25-in) pitch ball screw shaft with 25.4 cm (10 in) of total travel. The top end of the ball screw shaft is attached to a titanium yoke with flexures. A stiff linear spring along the axis of the ball screw shaft at the interface joint with the yoke provides an over travel gage during the stowing operation. The yoke is attached to the TPS mast and pivots on radial bearings at each fork end. The TPS mast is supported by 3<sup>rd</sup> axis bearings at its base. The 3<sup>rd</sup> axis bearings include 80-mm (3.15-in) bore duplex back-to-back pair angular contact bearings on one side and an 80-mm bore single radial bearing on the other side. The single radial bearing is preloaded with a beryllium copper flexure.

When the stepper motor drives the ball nut, the mast is driven between the stowed position at 15° and the deployed position at 90°. Optical end of travel sensors indicate when the mechanism is in either the stowed or deployed positions. A stop tower with a stiff linear spring that is compressed when the unit is in the deployed position is used to preload the system. Detent magnets integral to the stepper motor are used to prevent backdriving the system when it is deployed. To prevent the ball screw from over traveling, a non-jamming hard stop engages slightly beyond the nominal deployed position. Figure 4 shows a section view of the Deployment Mechanism CAD model.

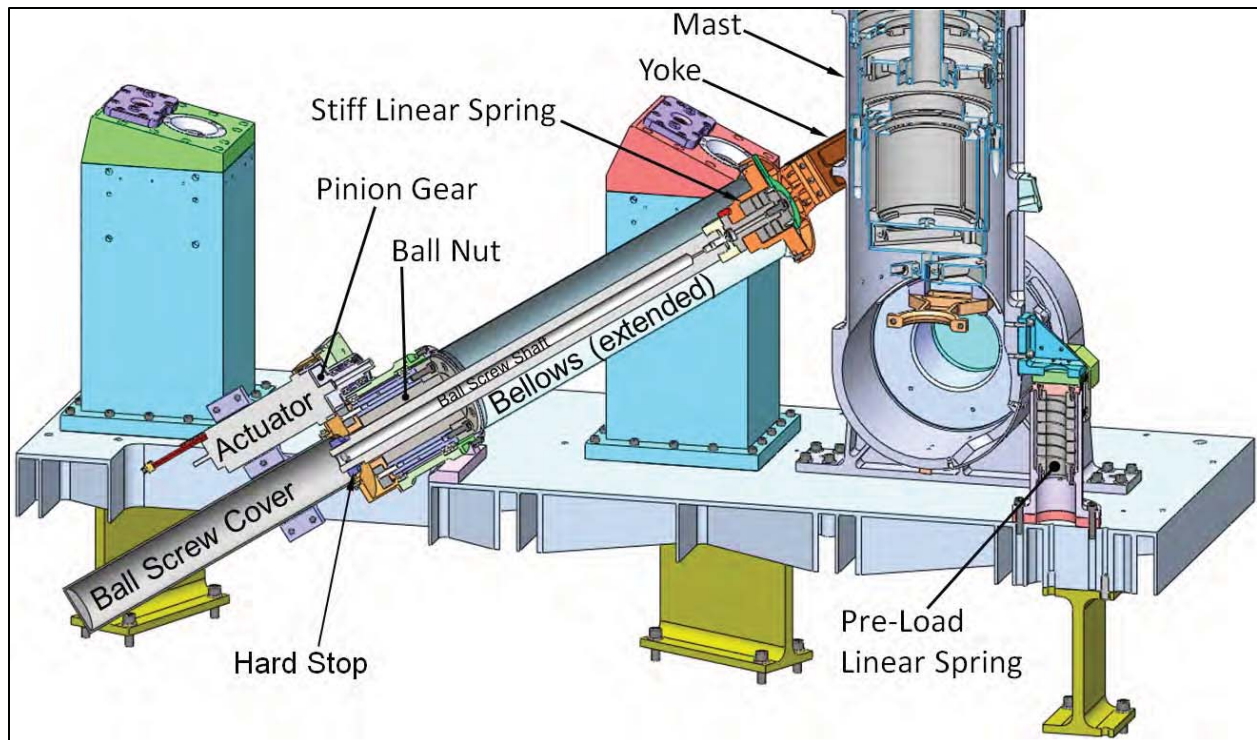


**Figure 4. Deployment Mechanism Section View, Deployed Configuration**

#### TPS Deployment Mechanism Design Background

The initial conceptual development for the TPS Deployment Mechanism began in 2007 by LASP engineer Ryan Lewis. The design concept shown in Figure 5 utilized a 7-stage stepper gearmotor to deploy and stow the unit. A latch tower was used to lock the system in the deployed position. Prior to the Critical Design Review (CDR) in 2009, the design evolved and the 7-stage stepper gearmotor was eliminated due to cost, schedule and vendor response concerns. Other design changes that occurred around the CDR time frame are listed below.

1. Ball Screw with yoke attachment to the Mast used to give better mechanical advantage.
2. Smaller and more readily available actuator chosen to drive the ball screw.
3. Latch tower eliminated.
4. Bellows used to contain ball screw shaft lubricant.
5. Stiff compression spring/stop tower compressed in the deployed position to preload the system.
6. Duplex and single radial ball bearings used to support the mast.
7. End of travel sensors and hard stops incorporated into the design.
8. Ability to manually actuate the system when the actuator is removed.
9. Stiff compression spring with over-travel gage added for stowing the system.

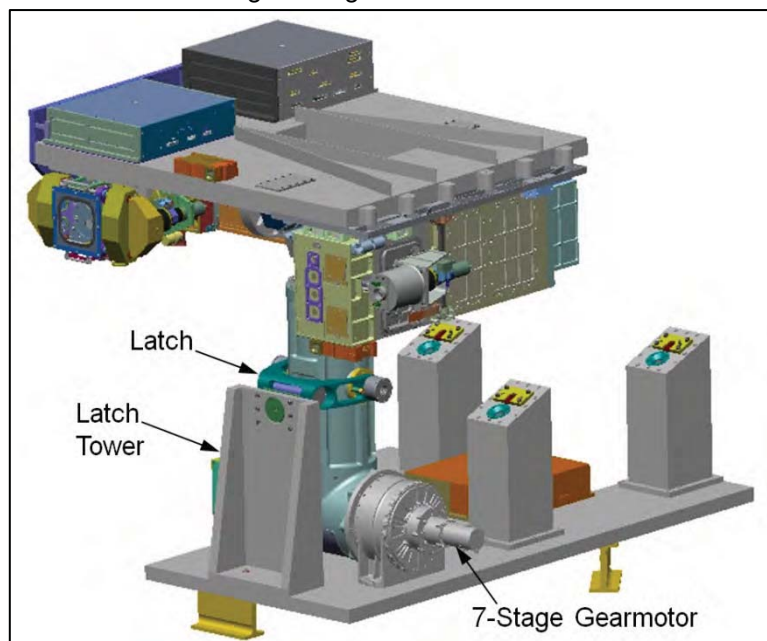


**Figure 5. Deployment Mechanism Initial Concept, 2007.**



## Design Discussion

### Motor

The Deployment Mechanism is driven by a 45°, 2-phase and 4-pole stepper motor with redundant windings. This actuator includes a detent brake and a 3-stage, 384:1 planetary gear head integral to the unit. The large gear reduction combined with the 2:1 transfer gears and ball screw results in a large mechanical advantage for the mechanism. The actuator detent torque, 3.4 N·m (30 in·lbf) at the output shaft, combined with the reduced torque reflected back through the ball screw and transfer gears eliminates the need for a latching device in the deployed state.

The 45° step angle equates to 0.12° of rotation at the actuator output shaft per step. The nominal operational rate of the actuator is 128 PPS (Pulses Per Second) which results in an operational speed of 2.5 RPM (Revolutions Per Minute) at the output shaft. At this nominal operational rate, the Deployment Mechanism requires 31.2 minutes to travel from the stowed configuration to the deployed configuration and vice-versa.

The maximum backlash in the gear-motor was measured at <0.0029 radian (<10 arcminutes). This backlash is not an issue for the TPS because when the Deployment Mechanism is in the deployed state, the preload from the stiff compression spring in the stop tower removes all of the play in the system.

The bearings in the motor were lubricated with low vapor pressure Braycote 601EFVB grease and the gears were lubricated with Braycote 601EFVB with 3% MoS<sub>2</sub>. All materials in the actuator assembly were chosen to meet the outgassing specification of <1.0% Total Mass Loss (TML) and <0.1% Collected Volatile Condensable Material (CVCM).

A thermal clamp bracket is used to conduct heat away from the actuator and into the ball screw cover as shown in Figure 6. Polypad 1000, a 0.23-mm (.009-in) thick thermal conducting material, is compressed between the actuator and clamp to enhance the thermal conductivity between the actuator and ball screw cover.

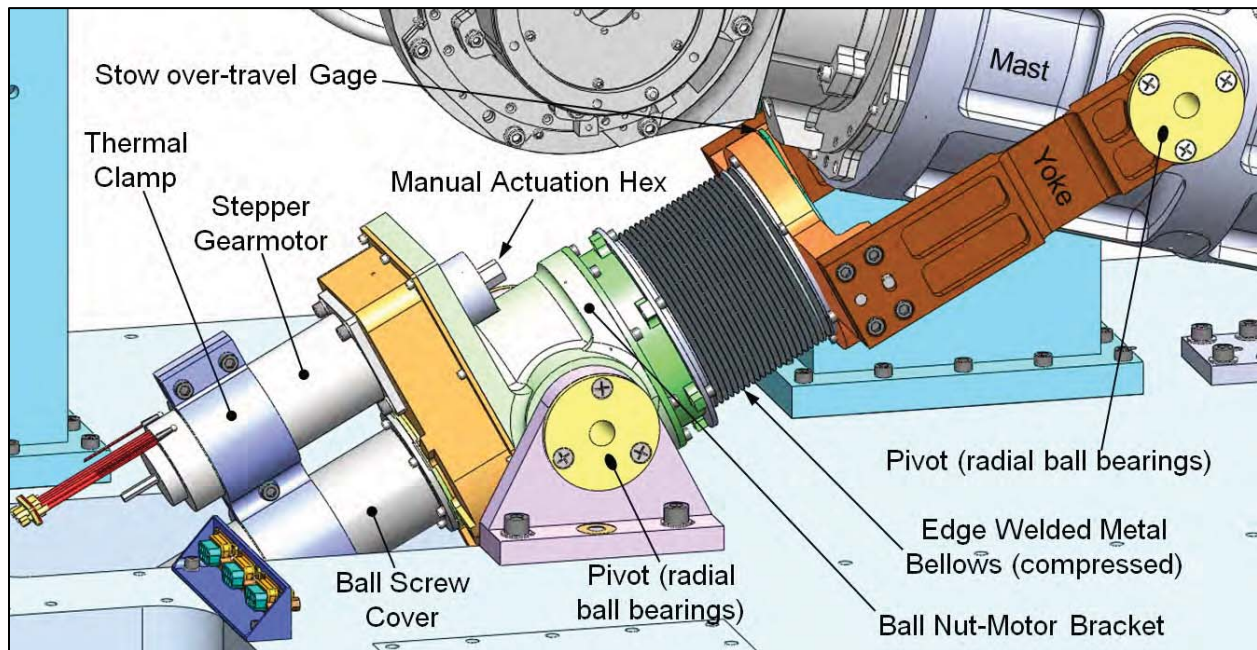


Figure 6. Deployment Mechanism Drive Components



On orbit, the Deployment Mechanism will only be operated one time, moving the TPS from the stowed to deployed configurations. During this one-time deploy sequence the Deployment Mechanism is open-loop controlled. The actuator is commanded to move in the deploy direction and then it will automatically be commanded to stop when either one of the redundant deploy position sensors is triggered.

On the ground during Integration and Testing (I&T), the deploy command sequence is closed-loop controlled, identical to what it is in space. Stowing on the ground is open-loop. The actuator is commanded to move in the stow direction until it is manually commanded to stop slightly prior to reaching the stow position. The actuator is then incrementally commanded to approach the stowed position so that the kinematic interfaces of the 3X vee-spherolinder-cones can be closely monitored and dialed-in for optimal positioning and a flush, slightly preloaded interface.

### Transfer Gears

Both the pinion and spur gear have a 20 diametral pitch and 20° pressure angle. The 28-tooth pinion gear is a custom part fabricated from 15-5 PH stainless steel and heat treated to condition H1000. This pinion gear part includes an integral precision shaft for two radial bearings to slip fit over. There is also a 8-mm (5/16-in) hex head at the end of the integral shaft that allows for the Deployment Mechanism to be manually stowed or deployed without an actuator. The 56-tooth spur gear is a standard off-the-shelf part made from 303 stainless steel. The spur gear is modified to add mounting holes, a precision central through hole and a dowel pin slot. Both gears were lubricated with Braycote 601EFVB. There is a small amount of backlash [ $<0.0026$  radian ( $<9$  arcminutes)] in the transfer gears, but as was stated in the motor section above, this is not a concern due to the preload in the deployed state that removes all play in the system.

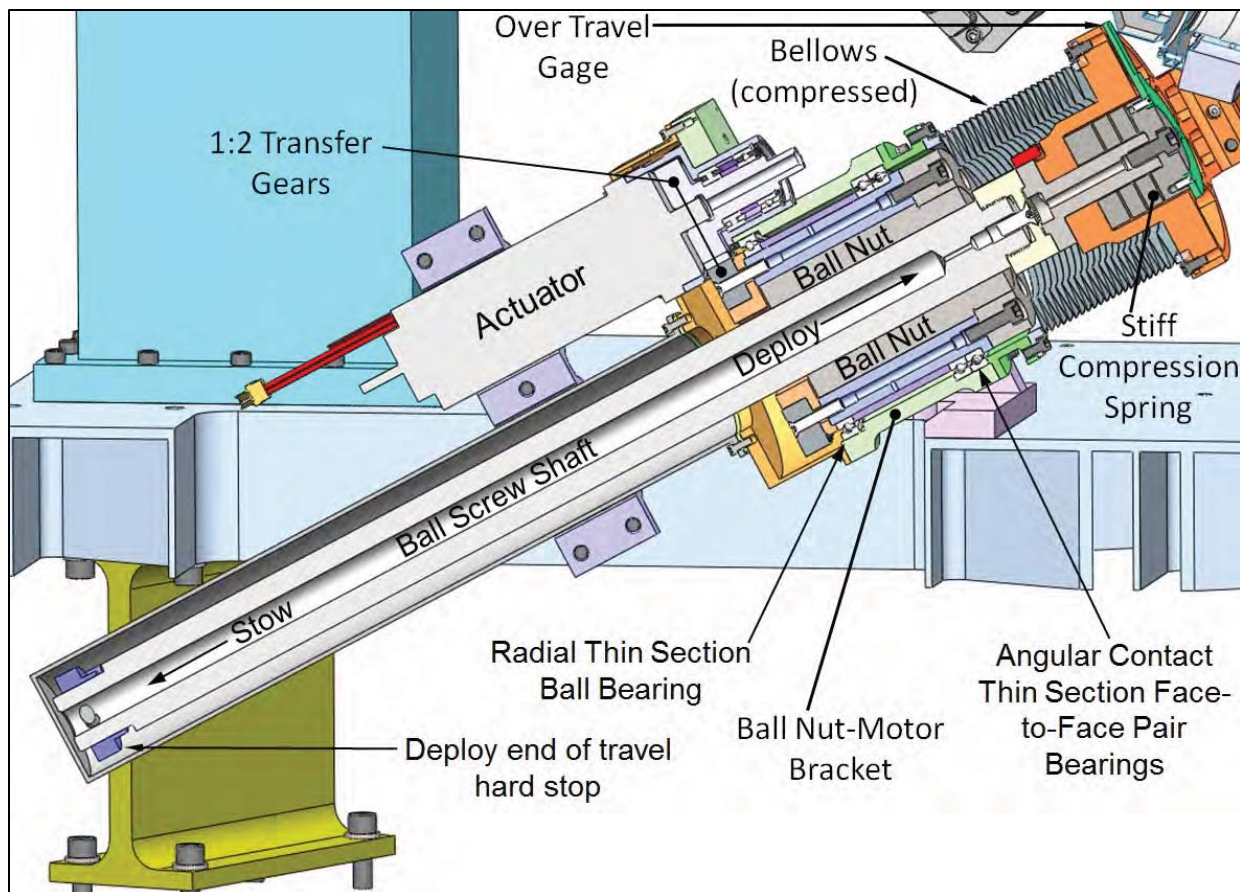


**Figure 7. Focus Mechanism Drive Components, Section View**

### Ball Screw/Nut

The right handed ball screw has a 25.4-mm (1-in) diameter shaft and 6.35-mm (0.25-in) pitch. The ball nut has two tracks/return tubes with 2.5 circuits per track. The ball screw was sized to handle worst case mechanism loads with positive margin. The ball nut is not preloaded and the nut-to-screw backlash is .13-.38 mm (.005-.015 in). As stated earlier, the backlash is removed from the system when the mechanism is in the deployed state due to the preload imparted by the stiff compression spring in the stop tower. The ball screw shaft is fabricated from 4150 alloy steel Rc 56-60 and is chrome plated to .005-.010 mm (.0002-.0004 in) thick. The ball nut is made from AISI 1117, nitrided to Rc 56-60 and electroless nickel coated to .005-.010 mm (.0002-.0004 in) thick. The balls have a nominal diameter of 3.96 mm (.156 in) and are made from AISI 52100 steel. The ball screw shaft grooves, nut and balls are lubricated with Braycote 601EFVB. Barrier film is applied to each end of the ball screw shaft to prevent lubricant migration.

All of the critical drive components of the Deployment Mechanism are brought together by the ball nut-motor bracket. The section view in Figure 7 illustrates how the actuator, transfer gear and ball nut interface with the ball nut-motor bracket. This bracket is fabricated from Titanium 6AL-4V to reduce the CTE mismatch between the ball nut, thin section bearings and bracket. The ball nut rotates on thin section bearings within the bracket when it is driven by the actuator through the transfer gears. The ball screw shaft does not rotate as it advances either in the deployed or stow direction. Throughout the deployment the ball nut-motor bracket pivots on two radial ball bearings that are located in pockets machined into each side of the bracket. The ball nut-motor bracket is attached to a base bracket that is mounted to the baseplate as shown in Figure 6.

### Thin Section Bearings

The thin section bearings that support the ball nut are an angular contact face-to-face pair and a single floating radial bearing. The face-to-face style angular contact bearing pair was chosen for their ability to withstand high axial loads. The main load path of the mechanism travels along the axis of the ball screw and through this face-to-face bearing pair. The bearing pair was sized to handle the maximum thrust load with positive margin. The single radial bearing is floating axially and only provides radial support to the ball nut. The load and lifetime cycle requirements make preloading this bearing unnecessary. Both the angular contact bearing pair and single radial bearing are lubricated with Braycote 601EF. The material of the thin section bearing races and balls is 440C stainless steel.

### Bellows

The expandable and collapsible bellows is used to contain the lubricant on the ball screw shaft. The completed assembly has a compressed length of 4.8 cm (1.9 in) and it can be expanded to 31.5 cm (12.4 in) resulting in a 26.7-cm (10.5-in) stroke capacity which meets the requirements of the Deployment Mechanism. The bellows is fabricated using pieces of .10-mm (.004-in) thick AM350 stainless steel that are hydraulically stamped into diaphragms. Once stamped, several of the diaphragms

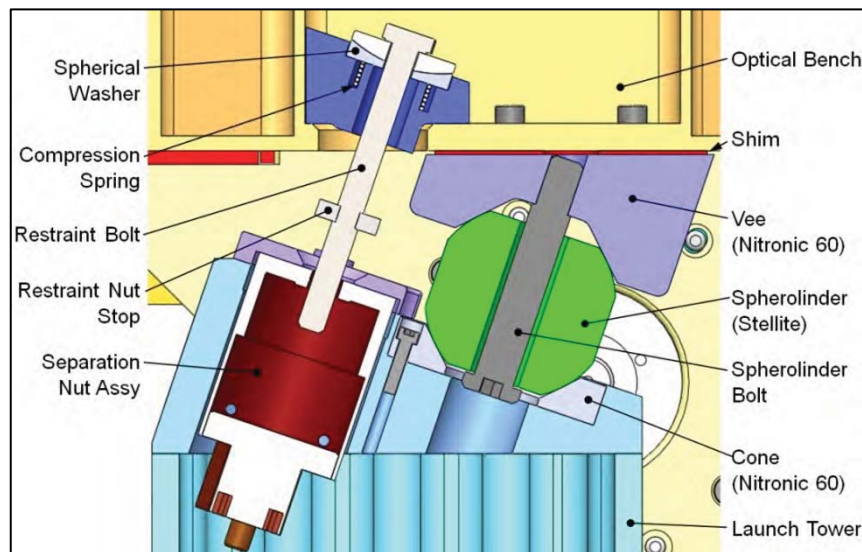


**Figure 8. Kinematic Mounts/Restraint Bolt Section View in the Launch Configuration**

are placed back-to-back and welded together at both the inside and outside edges. Custom 316L stainless steel mounting flanges are then welded to each end of the bellows. The spring rate of the completed bellows is 670 N/m (3.8 lbf/in) and it has a rated cycle life of 100,000 cycles. Initially, there was a concern that the bellows might sag, buckle or squirm during the deploy/stow cycles and thereby interfere with the ball screw. The buckling and squirming issues were eliminated by venting the bellows (the bellows does not need to hold a vacuum or pressure). The bellows has only minimal sag in the deployed state such that the inside of the bellows does not touch the shaft of the ball screw at any time during the deployment.

#### Stow Over-Travel Gage

During the stow operation, the actuator must drive the mast down so that the 3X kinematic vee-spherolinder-cones are in flush contact with each other (see Figure 8). Only at that point can the restraint bolts be torqued for launch configuration. An over-travel gage has been designed into the system to avoid over driving the ball nut once nominal kinematic engagement has been reached. This gage includes a stiff linear spring [2,600 N/mm (15,000 lbf/in)] attached to the end of the ball screw shaft along with a simple aluminum gage mounted to the top of the spring as shown in Figure 7. The nominal gap between the aluminum gage and the yoke base is 1 mm (.04 in). If the ball nut is driven past nominal engagement, this gap will decrease. Monitoring this gap during the stowing operation is essential to avoid over-driving the ball nut.

#### Hard Stop

The deployed hard stop is used to avoid damaging the ball nut/screw in the unlikely event that both end-of-travel position sensors fail during deployment. The hard stop uses a radial face-to-face design that is non-jamming and minimizes stress on the ball screw. During the initial build of the Deployment Mechanism, the hard stop was positioned onto the ball screw such that it engaged with a stop tab on the ball nut at a position slightly beyond the nominal deployed position. In this nominal position the stop tower compression spring is displaced by 2.54 mm (.100 in). The hard stop engages when the stop tower compression spring is displaced by 3.18 mm (.125 in). During normal operation, the end-of-travel will be reached before the hard stop will engage. Figure 9 shows the hard stop when it is engaged. After the hard stop was correctly positioned, the ball screw was removed from the assembly and the hard stop was match drilled to it. During this operation the threads of the ball screw were completely covered to prevent contamination. A screw and a dowel pin were used to fasten the two pieces together. The ball screw and hard stop were then reassembled into the mechanism after the match drilling operation.

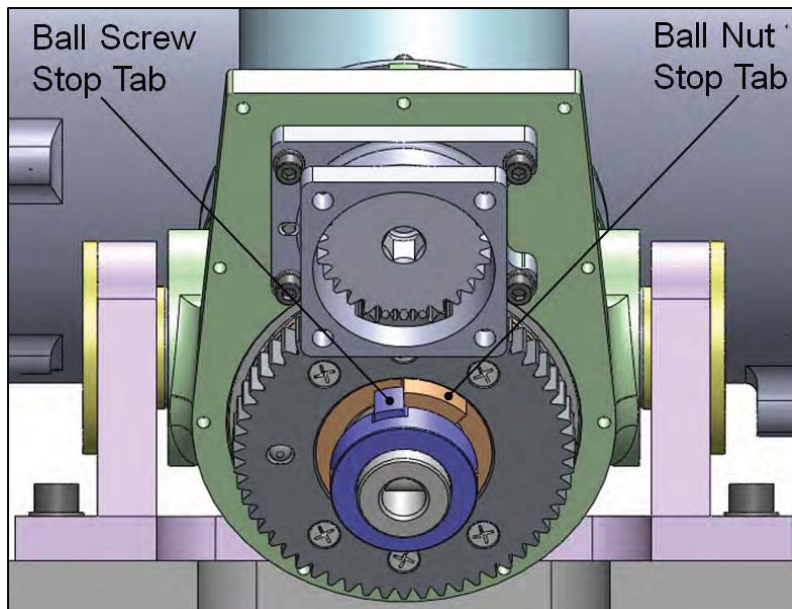


**Figure 9. Deployed Hard Stop**

#### Yoke to Mast Interface

The titanium yoke is attached to the aluminum mast via two radial ball bearings that fit into pockets machined into the side of the mast as shown in Figure 11. A titanium ring is placed around each 440C ball bearing to prevent damaging the ball bearings during cold survival due to the CTE mismatch between the aluminum mast and 440C bearing rings. Each yoke arm has a single blade flexure machined into it to allow for some compliance in the system.



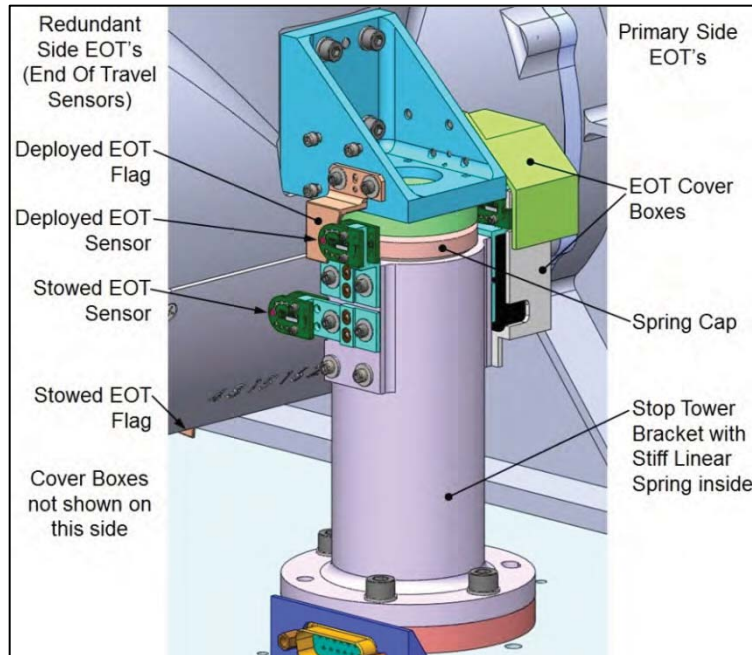


**Figure 10. Stop Tower and End of Travel Sensors**

Stop Tower and End of Travel Sensors

The stop tower assembly is used to preload the system in the deployed state. This is accomplished with a stiff compression spring that is mounted inside the stop tower bracket. As was mentioned earlier, the spring is compressed by 2.54 mm (.100 in) in the nominal deployed position, which results in a force of 1,628 N (366 lbf). When this force is opposed by the ball screw, all backlash in the system is removed. This results in a stiff design that meets the solar tracking requirements of >6 Hz in the deployed configuration. Redundant end-of-travel sensors are also mounted to the stop tower bracket. These sensors are phototransistor/infrared emitting diode pairs and their positions are dialed into the ideal spot during the initial assembly of the Deployment Mechanism. Interrupt flags are mounted

to the mast as shown in Figure 10. Cover boxes are mounted around the sensors to prevent external light from potentially causing sensor reading errors.

3<sup>rd</sup> Axis Bearings

The 3<sup>rd</sup> axis bearings that support the mast assembly (see Figures 3 and 11) are comprised of an angular contact duplex pair on one side and a single radial ball bearing on the opposite side. The duplex back-to-back pair was chosen for excellent radial, axial and moment stability. The bearing pair size is: 80-mm bore x 125-mm outside diameter x 22-mm wide and there is a 311-N (70-lbf) preload. The single radial bearing size is: 80-mm bore x 140-mm outside diameter x 26-mm wide. This bearing has an axial preload of 44.5 N (10 lbf) that is applied with

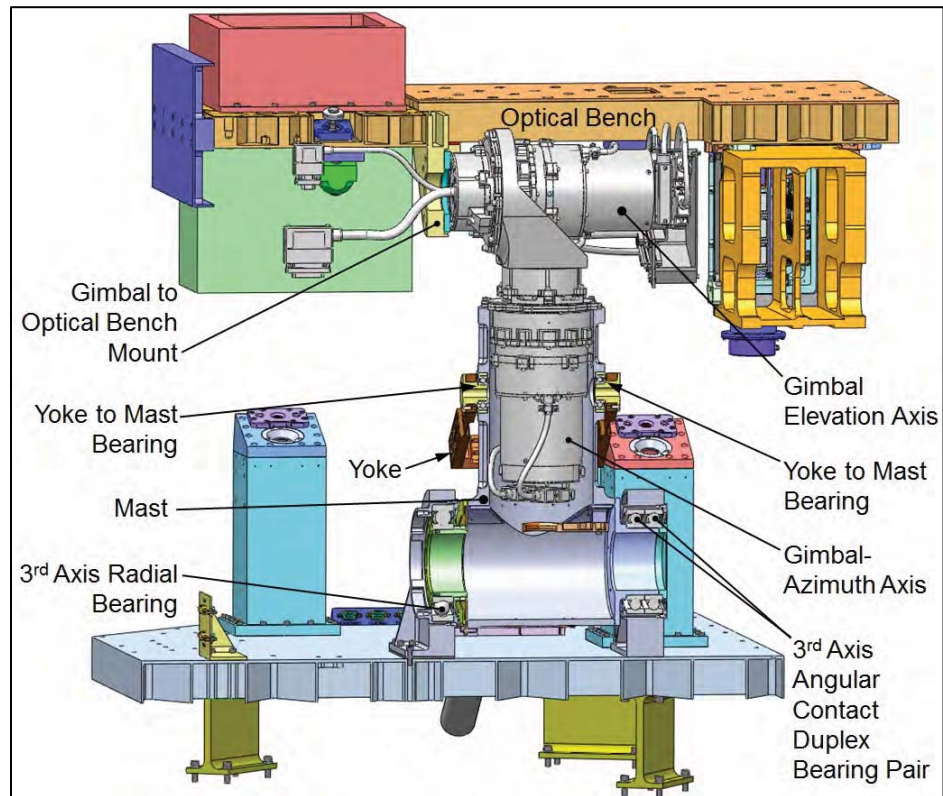


**Figure 11. Deployment Mechanism Vertical Section View**

a beryllium copper diaphragm flexure to maintain ball-race contact and prevent skidding. The 3<sup>rd</sup> axis bearings were sized to handle worst case loads with positive margins. The support brackets were fabricated from Titanium 6AL-4V for excellent strength and stiffness characteristics plus low CTE to prevent damaging the bearings during cold survival temperatures. The bearings were lubricated with Braycote 601EFVB. Labyrinth seals and barrier film are used to prevent lubrication migration.

#### Gimbal

The 2-axis gimbal is mounted to the top of the mast with the azimuth axis actuator located mostly inside the vertical shaft of the mast as shown in Figure 11. The optical bench is mounted to the elevation axis actuator via a gimbal to bench mounting bracket. The gimbal harness is routed through the bottom of the mast and out of the 3<sup>rd</sup> axis single radial bearing bore.

#### Analysis

The major components of the TPS were designed and analyzed to meet the requirements of the NPOESS mission. ANSYS Workbench was used to predict structural and thermal stresses along with modes during the launch and deployed configurations. The predicted 1<sup>st</sup> mode is 67 Hz in the stowed configuration and 8.1 Hz in the deployed configuration. Individual piece parts and small sub-assemblies that are in the load path were analyzed in ANSYS and the geometry was modified as required to result in positive margins of safety for worst case load configurations. All moving parts including the actuator, bearings, gears and ball screw were analyzed and sized to withstand lifetime cycles. The mean Hertz contact stress was calculated for all bearings in the system to verify that they met the requirement of <400 ksi (<2760 MPa). All had healthy margins of safety.

### **Testing**

#### Life Test

In early 2012, the TPS successfully completed a life test of 100 stow-deploy cycles. A mass model that matched the mass and Center of Gravity (CG) of the populated optical bench was attached to the top of the mast for this test. Fifteen of the cycles occurred in the thermal vacuum chamber with 5 cycles at ambient temperature, 5 cycles at -20C, and 5 cycles at +40C. The remaining 85 cycles took place at ambient temperature and pressure in a cleanroom. Each cycle required just over 60 minutes to complete. Figure 12 shows the TPS about to enter the thermal vacuum chamber. Figure 13 shows life test data for cycles 34-40.

During the 100 cycle life test, the actuator operated nearly continuously for a total of 100 hours. A thermocouple was bonded to the body of the motor and the temperature was continuously monitored throughout the entire test. An automatic shut off set at +150C was built into the control software to avoid damaging the actuator. The actuator temperature limits specified by the manufacturer are -80C to +225C. The specified temperature limits for Braycote 601EFVB are -80C to +204C. The temperature gradient between the external surface of the actuator and the thermocouple along with a healthy safety factor were the rationale behind the +150C shut off. The automatic shut off was never triggered during the life test. The maximum temperature that the thermocouple measured was +134C during the hot (+40C) test in the thermal vacuum chamber.



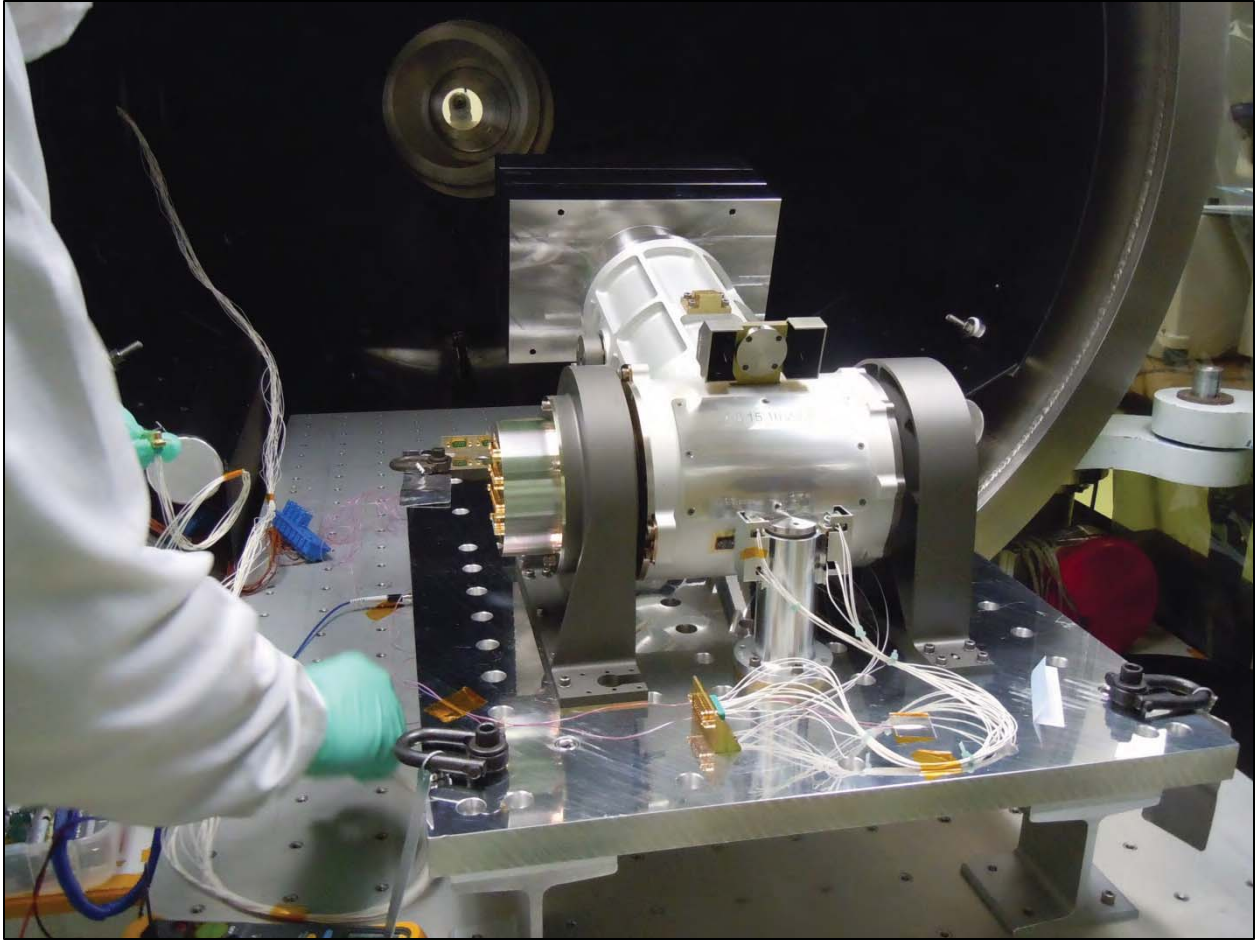


**Figure 12. Deployment Mechanism entering the Thermal Vacuum Chamber during the Life Test**

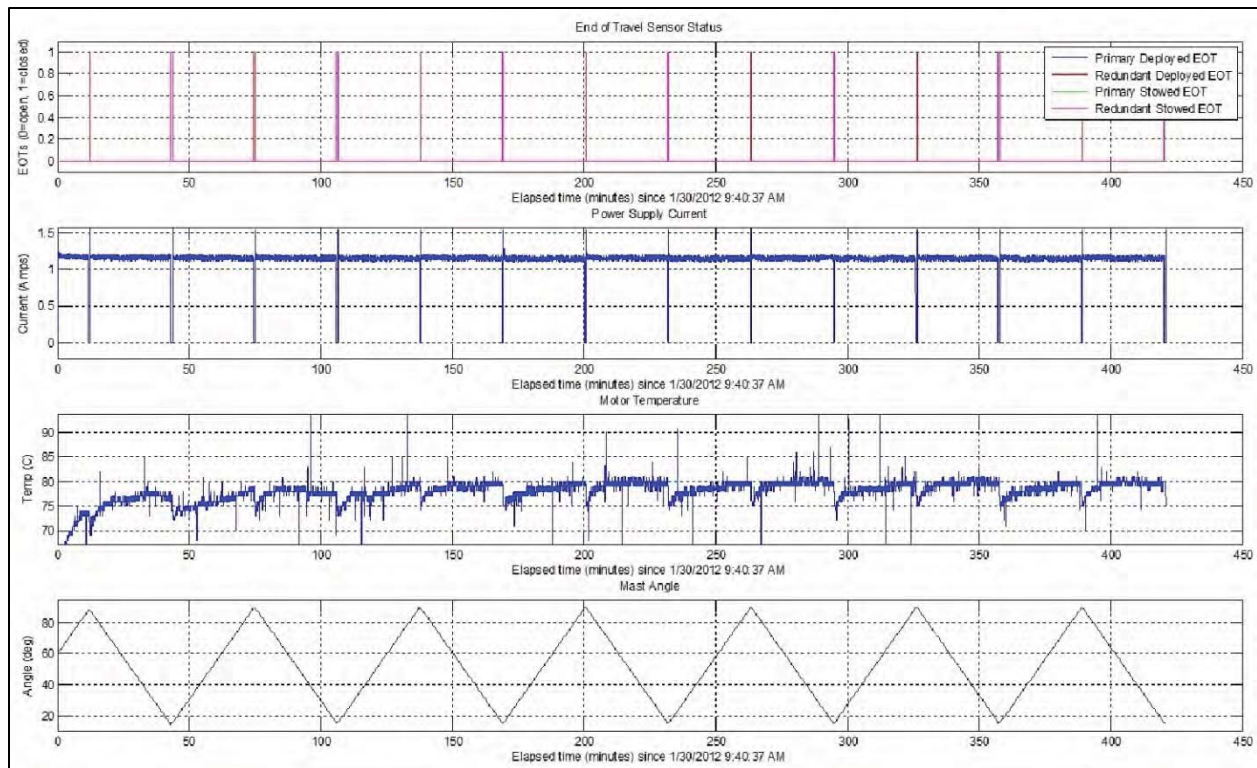


**Figure 13. Deployment Mechanism Life Test Data for Cycles 34-40**

The maximum current observed during the life test was 1.2 amps at the nominal operation voltage of 28 volts. This correlates to 0.89 N·m (7.9 in-lbf) of torque required by the actuator to stow or deploy the mechanism. This number was calculated using the actuator's torque constant of 26.8 mN·m (3.8 in-oz/watt). During qualification testing at the vendor prior to shipment,

the actuator pull-in torque at the nominal rate of 128 PPS

was measured to be 14.1 N·m (125 in-lbf), see Figure 14. From these measurements, and using a safety factor of 1.5, the actuator torque margin was calculated to be +9.4.

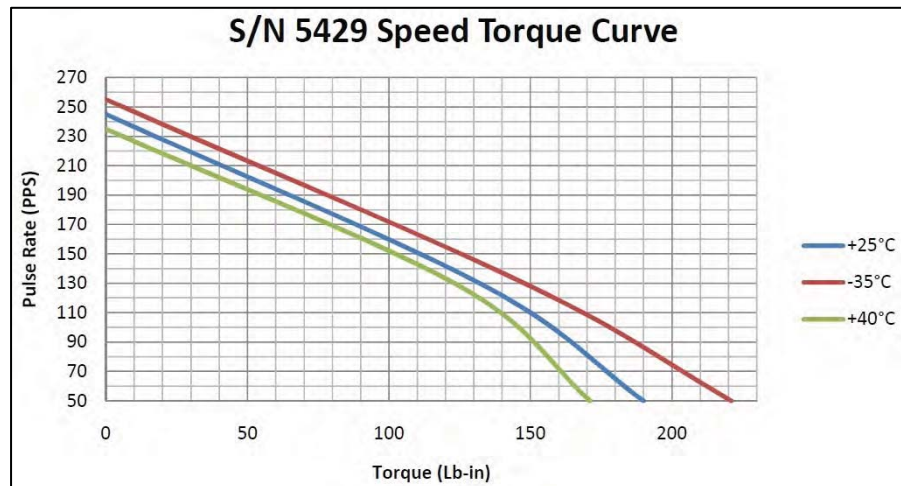


**Figure 14. Actuator Speed-Torque Curve at Various Temperatures**

#### Backdriving Test

In early 2012, shortly after the life test, the Deployment Mechanism successfully passed the backdriving test. This test verified that the Deployment Mechanism is able to deploy and stow in any orientation in a 1G environment. A Flotron was used to perform this test as shown in Figure 15. The Deployment Mechanism had healthy torque margin while deploying and stowing in all orientations.

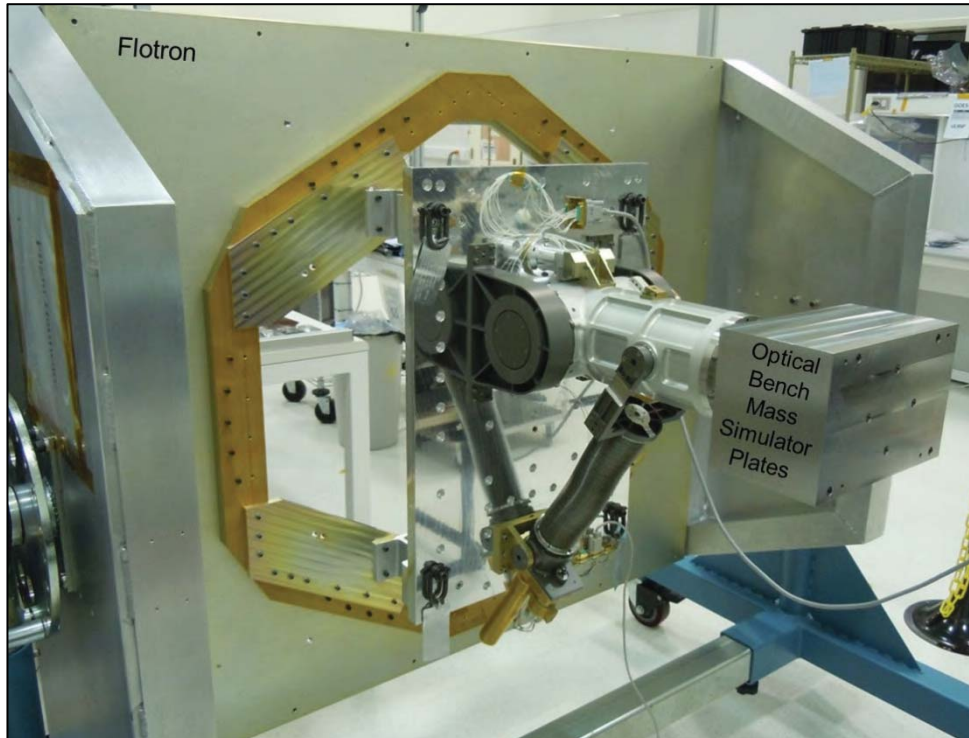


**Figure 15. Deployment Mechanism Back Driving Test on the Flotron**

The backdriving test also verified that the TPS remains in a stable position in the worst case vertical orientation due to gravity. This was done by measuring the gap between the spring cap and the stop tower bracket (see Figure 10) while the TPS was in the deployed configuration. The gap remained unchanged after 24 hours, thus verifying that the system did not back drive and that the detent torque in the motor was appropriately sized.

The torsional spring rate of the Deployment Mechanism system in the stowed configuration was calculated during this test. During the test, gap measurements between the mast and the baseplate were taken at various times and it was noticed that the gap would change slightly after the Flotron was rotated to a new position. This gap change was the result of the gravitational force acting on the optical bench mass simulator mounted to the top of the mast as shown in Figure 15. Certain orientations resulted in more torque imparted to the mast rotation axis compared to other orientations, thus resulting in a smaller or larger gap. The angle between the mast vertical axis and the baseplate is easily calculated from this gap measurement.

The torsional spring rate in the stowed configuration was calculated with the Flotron in the horizontal position. A gap measurement verified that the mast angle was at the nominal  $15^\circ$ . At this point the optical bench mass simulator plates were removed and the gap was measured again. This time the gap increased by 1.14 mm (.045 in) which correlates to the mast angle increasing to  $15.386^\circ$ . Using this change in angle measurement along the moment torque caused by the mass simulator plates, the torsional spring constant of the Deployment Mechanism system in the stowed configuration was calculated to be 674 N·m (5,967 in-lbf/degree).

#### Future Testing

A gimbal characterization test will be performed early in 2014 with an optical bench mounted to the gimbal and representative mass models mounted to the optical bench. This test will characterize the gimbal pointing performance when it is mounted to the TPS. Following that test, the engineering model assembly will be expanded to include the launch towers and resettable separation nuts. This unit will then undergo tests to verify deployment and stow/alignment capability. A modal test is also planned in both stow and deployed configurations and the results will be correlated to the structural model.

## **Conclusions**

The Deployment Mechanism design has been proven to be a viable method for deploying and stowing the TPS. The mechanism successfully passed the lifetime and back driving tests. Future testing will undoubtedly reveal more nuances about the design and its features.

### Lessons Learned

During the life test, the actuator thermocouple produced transient spikes that exceeded the +150C temperature limit, setting off alarms in the software that resulted in the test automatically stopping and causing delays. This was fixed by increasing the thermocouple sample rate to 200 msec and averaging 5 samples.

The peer review process is extremely helpful in producing a successful design. Prior to CDR, two peer reviews were held at LASP with many LASP mechanical, electrical and systems engineers in the audience. The insightful questions from the audience and the action items that came out of the reviews resulted in improvements to the design. Because of these design improvements the fabrication, assembly and testing of the assembly went smoothly without any major problems.

## **Acknowledgements**

The author would like to thank all of the LASP machinists, technicians, engineers, scientists and managers who played a role in developing and building the Deployment Mechanism. The success of this effort was a direct result of their skill, commitment, hard work and enthusiasm.

## **References**

1. JPSS website. <http://www.jpss.noaa.gov/>
2. TSIS mission Quick Facts. LASP website. <http://lasp.colorado.edu/home/missions-projects/quick-facts-tsis/>





# ISS Ammonia Pump Failure, Recovery, and Lesson Learned – A Hydrodynamic Bearing Perspective

Robert J. Bruckner\* and Richard A. Manco II\*\*

## Abstract

The design, development, and operation of long duration spaceflight hardware has become an evolutionary process in which meticulous attention to details and lessons learned from previous experiences play a critical role. Invaluable to this process is the ability to retrieve and examine spaceflight hardware that has experienced a premature failure. While these situations are rare and unfortunate, the failure investigation and recovery from the event serve a valuable purpose in advancing future space mechanism development. Such a scenario began on July 31, 2010 with the premature failure of an ammonia pump on the external active thermal control system of the International Space Station. The ground-based inspections of the returned pump and ensuing failure investigation revealed five potential bearing forces that were un-accounted for in the design phase and qualification testing of the pump. These forces could combine in a number of random orientations to overload the pump bearings leading to solid-surface contact, wear, and premature failure. The recovery plan identified one of these five forces as being related to the square of the operating speed of the pump and this fact was used to recover design life through a change in flight rules for the operation of the pump module. Through the course of the failure investigation, recovery, and follow-on assessment of pump wear life, design guidance has been developed to improve the life of future mechanically pumped thermal control systems for both human and robotic exploration missions.

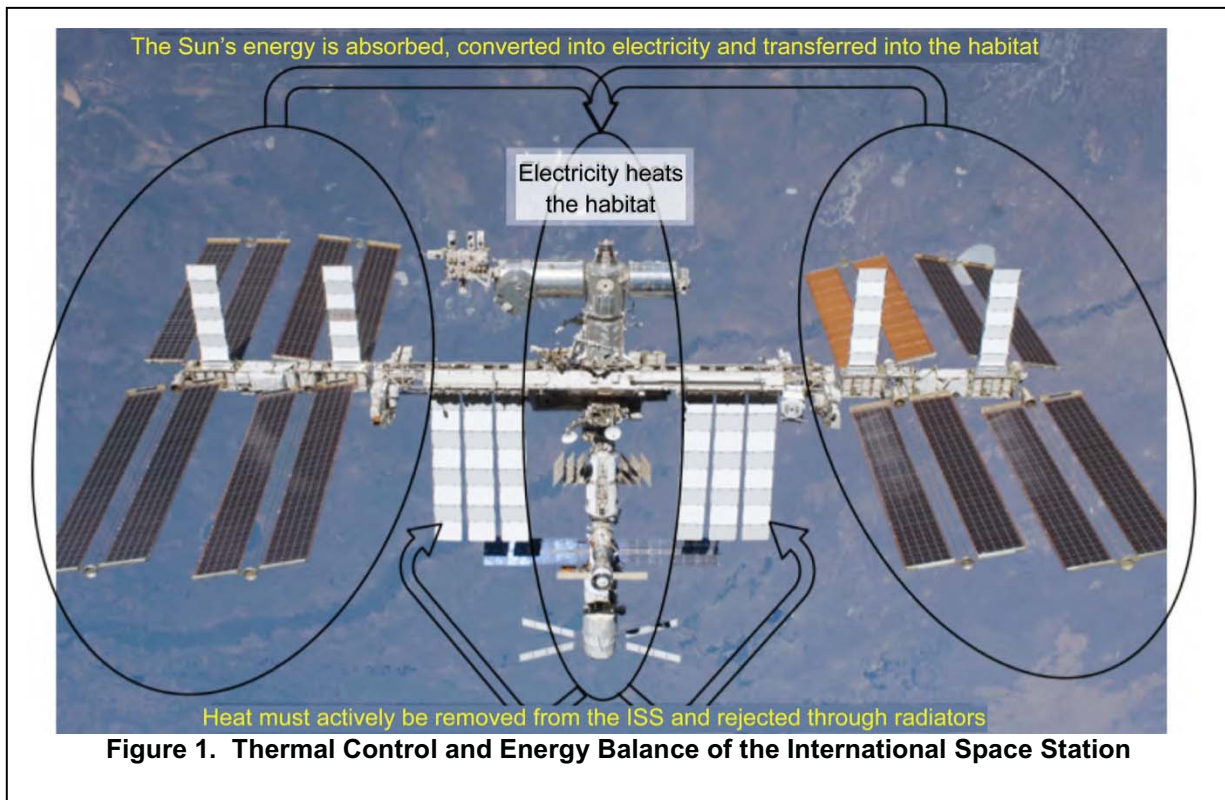
## Introduction

The International Space Station (ISS) is an engineering marvel. This micro-gravity laboratory was the result of decades of engineering, design, international cooperation, construction, and operation. One of the most significant engineering accomplishments of this laboratory has been the power generation and active thermal control system. These two systems must be considered in the same context because of their integral relationship in the operation of the ISS. Both of these systems contain large-scale mechanisms and control schemes to continuously optimize the performance of the system. The Photovoltaic Arrays (PVA) pivot and rotate in order to maximize the capture of energy from the sun, while the heat rejection radiators rotate to seek shade in order to maximize heat rejection to space through radiation. In addition the active thermal control system utilizes a high-speed centrifugal pump to maintain adequate flowrate of the heat transfer fluid throughout the system. In highly simplified terms, the thermal control of the inhabited volume of the ISS is a precise balancing act between electrical power input from the PVA and waste heat rejection through the radiator panels. An additional requirement of the active thermal control system is to maintain a uniform temperature on critical parts of the ISS structure such as habitat interfaces and airlocks. The energy balance of the system is illustrated in Figure 1. The thermal control system is symmetric having independent port and starboard loops. Although flight rules dictate that both systems shall run at all times, there is limited redundancy on the ISS such that limited operation is possible with only one functional loop. The working fluid in the heat rejection system is high-pressure liquid, anhydrous ammonia at a nominal system pressure and temperature of 2.62 MPa and 275 K (380 psia, 36°F). Additional components of the system are shown in Figure 2. The specific arrangements of the components of the active thermal control system are also shown in the figure. The pump module is an Orbital Replacement Unit (ORU) designed so that it could be exchanged with spare units during an

---

\* NASA Glenn Research Center, Cleveland, OH, USA

\*\* Sierra Lobo Inc. at the NASA Glenn Research Center, Cleveland, OH, USA



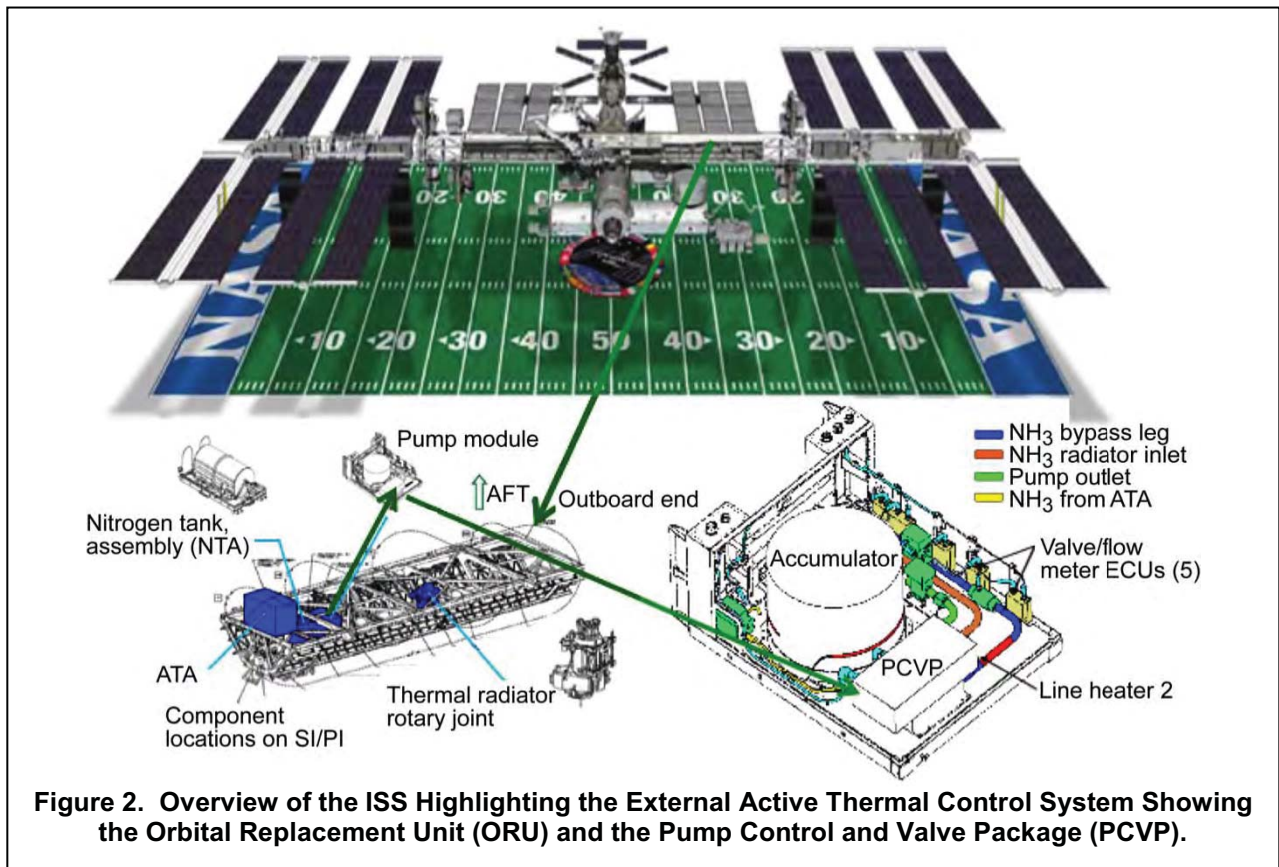
ExtraVehicular Activity (EVA). The pump module ORU houses the pump, controls, and valves required to maintain proper temperature in the heat rejection loop. A canned motor cartridge pump circulates this heat transfer fluid through the thermal control system. A typical canned motor cartridge pump lies at the heart of the system. The pump must run continuously for the 15-year predicted life of the module in order to maintain safe operation of the ISS.

#### The 2010 Cooling Pump Shutdown

Shortly before midnight on July 31, 2010 the ISS cooling Loop A on the Starboard side of the vehicle went offline when a Remote Power Control Module opened during a high current draw event. As a result the crew was instructed to reconfigure the ISS thermal management system to rely solely on Loop B. Subsequent remote procedures were unable to restart the pump and very likely caused additional mechanical damage to the hardware. Over the course of the next 17 days the ISS operated in a zero-fault tolerant mode, relying only on Loop B for all active thermal control. During this time period electrical power input to the habitat was limited and many of the scientific experiments were placed in standby mode. Astronauts Doug Wheelock and Tracy Caldwell-Dyson performed three EVAs totaling over 25 hours to replace the failed pump module with a spare ORU. The EVAs proved to be much more difficult and dangerous than anticipated due to frozen ammonia that jammed the quick disconnect fluid couplings used to connect the pump module to the rest of the thermal control loop. During the de-mating procedure on the failed unit, frozen ammonia particles were liberated from the connectors and caused both a micrometeorite type of hazard for the two astronauts and a health concern upon re-entry to the ISS as the frozen ammonia particles were stuck to the outside of the spacesuits. On August 17, 2010 function of cooling Loop A was restored and ISS operations returned to nominal.

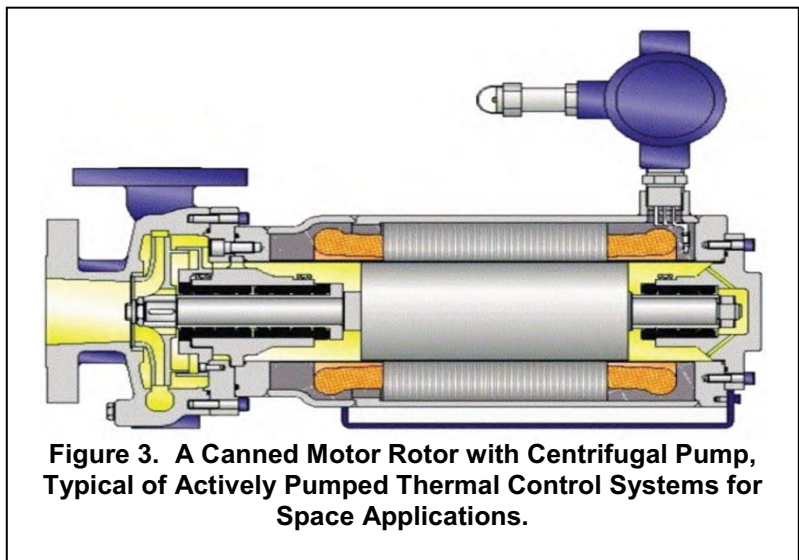
The failed pump module was stored on the ISS external structure for 11 months. The module was returned to earth on the final Space Shuttle mission, STA-135. During these initial 11 months, a team was assembled and failure investigation was initiated. Early root cause failure paths focused on the electrical power and control system. Initially this approach was logical since the primary data that was available to the team was the initial over-current RPCM shutdown and the inability to restart the motor due to persistent high current draw. Once the pump module was returned to earth, inspections revealed severe

mechanical damage to the motor and in particular the graphitic carbon bearings. A new fault tree branch was then investigated with emphasis on the hydrodynamic bearings, rotordynamic vibrations, and wear life of the bearing materials.



### Pump Mechanical Design

The pump used in the ISS external active thermal control system is a custom-built and space-qualified canned motor cartridge pump. A typical canned motor cartridge pump is shown in Figure 3. This type of pump design was selected for several reasons. The main driver for the selection of this type of pump is the elimination of fluid seals on the shaft. High-speed shaft seals are typically the life-limiting component on pumps and a seal failure on the ISS ammonia system poses a great risk to the vehicle and crew. An additional reason for the selection of this type of pump is its compact and lightweight architecture. Finally, this type of pump has a robust heritage in spaceflight hardware from the early manned vehicles to the Mars Pathfinder rover; canned motor cartridge pumps have proven to be robust and reliable. The challenge





faced by the pump designer is to increase the life of these pumps as space missions become more challenging. The operating life requirements for micro-gravity operation of high-speed centrifugal pumps has increased from days, to weeks, to years with the expectation of extending pump life to decades. The pump module failure of 2010 has provided invaluable experience in damage initiation and the progression of very light wear accumulation over a long period of time.

The main complication of this type of pump is the dual use of the working fluid as the hydrodynamic bearing lubricant. Characteristics of good heat transfer fluids and good lubricants are not complimentary. For high heat capacity at modest temperatures and low pressure drops through pumped loops, heat transfer fluids required high fluid density and low absolute viscosity. However, hydrodynamic bearings perform best with fluids having a low density and high absolute viscosity. For reference, typical fluid properties for anhydrous ammonia, SAE10 lubricating oil, and Carbon Dioxide gas are shown in Table 1. The technical challenge of using the process fluid as the hydrodynamic bearing lubricant often leads to a low bearing load capacity, low vibrational damping characteristics, and wear in the bearings. This bearing wear then becomes the primary life limiting factor for the pump. The canned motor type of pump is ubiquitous in terrestrial operations especially in applications where explosive, corrosive, and caustic liquids are processed such as petroleum refineries and chemical plants. In such ground-based applications, additional instrumentation is utilized to monitor machine health, rotor vibrations, and bearing wear, which permits maintenance intervals to be scheduled accordingly. However, for operation on spacecraft additional instrumentation and frequent maintenance intervals are not a reasonable solution. Therefore, design details that impact the wear life must be considered as important design parameters and qualification tests must be conducted to flesh out these details prior to mission launch.

The bearings used to support the rotor in this pump were rigid, hydrodynamic bearings. Two journal bearings supported the rotor in the radial direction, while a single sided thrust bearing positioned the rotor axially. A thrust washer was used to limit the axial rotor motion in the negative thrust direction, but in normal use the single sided thrust bearing was biased against the impeller inlet suction. During low speed operation and on startup and shutdown the thrust bearing was loaded by a skewed magnetic force generated by the electric rotor. The rotor-bearing system was a rigid shaft design with the permanent magnet motor straddle mounted between the journal bearings and the pump impeller was cantilevered. The journal bearings were 9 mm and 18 mm in diameter on the rear and front bearing respectively and separated axially by 144 mm. The clearance ratio of the journal bearings was 0.26% for both bearings. This created a static angular misalignment at zero speed of 79 microradians. The stationary sleeves of the bearing were fabricated from a special ammonia tolerant grade of graphitic carbon for low startup friction and low wear during solid surface contact events. Each bearing sleeve had four axial grooves machined at roughly equal spacing around the circumference to reduce the probability of half frequency whirl, impede the onset of turbulent flow, and to provide additional area for the secondary flow. A secondary flowpath from the pump discharge provides lubricant flow to both journal bearings and the thrust bearing. The secondary flow also passed between the rotor-stator gap to provide cooling for the eddy current losses. The typical operating speed range of the pump is 11,000 to 14,700 revolutions per minute.

### **Hydrodynamic Bearing Performance**

The hydrodynamic performance of the journal bearings is challenged in terms of fluidic instabilities and turbulence due to the relatively large clearances, high rotor speed, and low absolute viscosity of the lubricant. Figure 4 demonstrated this feature by overlaying the Taylor number region for the two journal bearings of the pump on top of experimental data taken for journal bearings operating with lubricants having very low kinematic viscosity. The data shown in Figure 4 used various high pressure gases as the lubricant in a concentric cylinder type of journal bearing. Despite the challenging conditions for the journal bearings, they are still able to generate meaningful film pressures and load support. The main reason that these bearings do not lose all film pressure to turbulence is the four axial grooves machined into the carbon sleeves. These grooves serve to reduce the turbulent length scale and maintain load support across each sector of the bearing. In order to calculate hydrodynamic load capacity for any journal

bearing, the first challenge is to determine a reasonable minimum film thickness for the bearings in a particular application. Typically, there exists a range in which the minimum film thickness may fall and the true value depends on a variety of factors. Numerically, the range for minimum film thickness lies between 7.5 and 2.5 micrometers (0.0003 and 0.0001 in). The large variation in this range is attributed to specific machine characteristics such as surface finish of the bearing and shaft, wear couple, expected rotor motion due to various excitation forces, and lubricant rheology. In the present case, the first three characteristics are very good, the surface finish of the bearings, wear couple, and rotor motion tend toward an acceptance of low film thicknesses. However, the low lubricant viscosity and high density do not permit the most aggressive minimum film thickness to be chosen. For this application two assumptions for minimum film thickness are used, 3.8 and 7.5 micrometers. These two levels of film thickness bound the hydrodynamic problem by providing an aggressive and a conservative estimate to bearing performance. A Stribeck curve containing calculated performance for both front and rear journal bearings is shown in Figure 5.

Figure 6 contains results of the bearing load capacity calculation for the rear bearing as a function of pump speed for both levels of minimum film thickness. This figure clearly demonstrates the desire to operate at the smallest possible film thickness because the hydrodynamic load capacity of the bearing roughly follows an inverse square trend with film thickness. Therefore, a well-designed, well-built, well-lubricated, smooth running machine would have over four times the load capacity of an inferior machine running in a challenging environment.

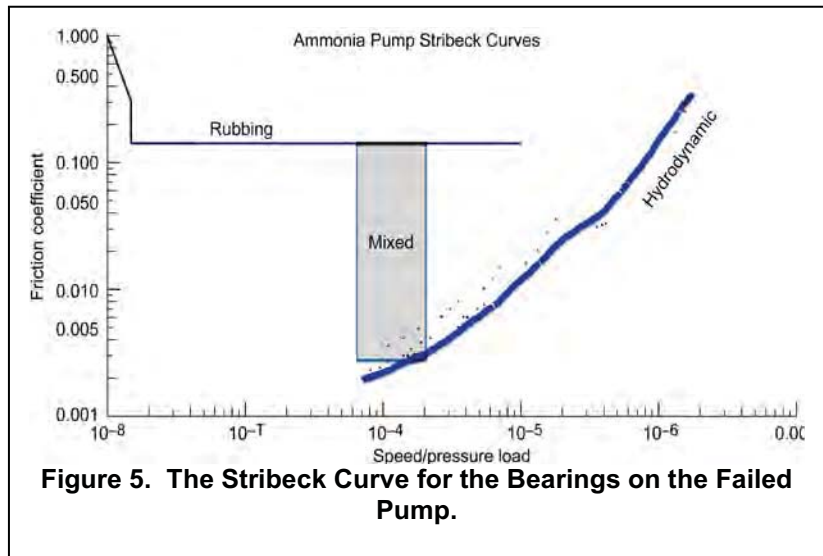


Figure 5. The Stribeck Curve for the Bearings on the Failed Pump.

Although the analytic models for bearing performance correlate well with industry standards on low viscosity bearings, the models have not been validated with test data. As the design life of these pumps is driven to fifteen years and beyond, it is recommended to quantitatively validate bearing performance and dynamic coefficients with component testing.

### Pump Rotordynamic Characteristics

A rotordynamic analysis was conducted on the ISS cooling pump and the graphical results are shown in Figure 7. Computed bearing coefficients for stiffness and damping were utilized since no individual bearing test data was available for these bearings. The composite, permanent magnet shaft was modeled with discrete elements and the bend frequency was compared to static vibration tests to verify that total shaft stiffness was consistent from model to test. Good agreement was achieved between test and modeling. The first two rigid body modes are shown in figure 7. A notable feature of these two modes is that they are both angular modes. In other words there is no cylindrical mode present in this machine and, most importantly, the machine is predisposed to angular misalignment and vibrations. Most likely this is caused by the asymmetric journal bearing configuration where both the size and absolute clearance is different between the two bearings. This feature is not desirable for long wear life since angular misalignment leads to edge loading on the bearings and high wear rates. For future pump designs it is recommended to maintain cylindrical rigid body modes to reduce the high wear caused by angular contact. Additionally, qualification testing is recommended to quantitatively validate the rotordynamic models.



## Post-Failure Inspection Findings

The pump module was returned from orbit in 2011 on the final Space Shuttle mission, STS-135. After post-flight processing and ammonia decontamination were completed, a comprehensive inspection procedure was conducted on the returned hardware. This inspection covered electric power and controls, material microscopy and crack progression analysis, debris analysis, x-ray, ultrasound and visual examinations of the physical hardware. The electrical and control systems were deemed to be in acceptable condition given the long-term exposure to ammonia. No evidence was found to further pursue these components as the root cause. The most significant finding was severe wear of the carbon bearings at all three bearing locations, two journals and one thrust bearing. The most severe wear occurred at the rear journal bearing. An additional significant finding was that the wear was organized in a manner that indicates an angular misalignment. In other

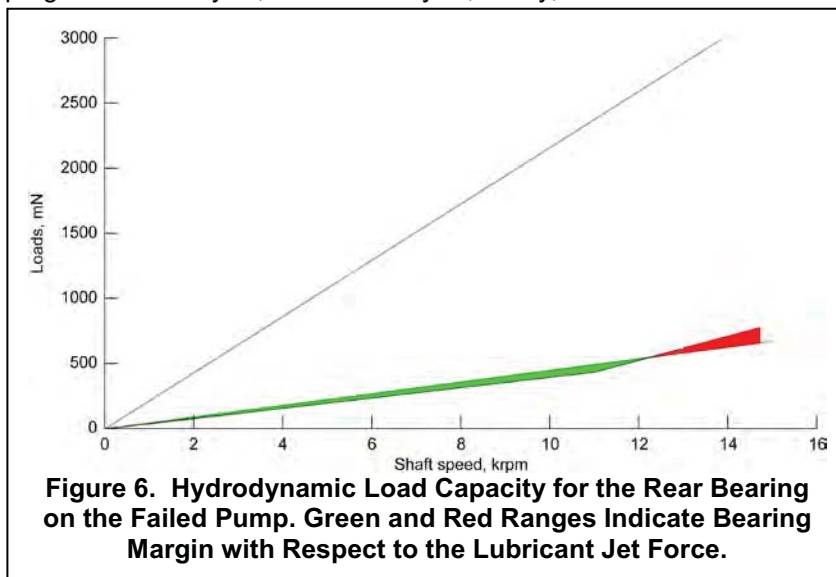


**Figure 6. Hydrodynamic Load Capacity for the Rear Bearing on the Failed Pump. Green and Red Ranges Indicate Bearing Margin with Respect to the Lubricant Jet Force.**

words, a specific load acting in a specific direction on the rear bearing was the most likely root cause. Typically, in high speed rotating machinery the expectation is that wear would occur throughout the circumference of the bearing either in a cylindrical or conical shape. However, in this case the wear was concentrated in one quadrant and mainly on one bearing. Again, this is a strong indication a specific static force was acting directly on the rear bearing.

## Uncharacterized Bearing Loads

The severe damage found on the bearings in the post-failure investigation initiated a quest to identify and quantify all potential loads that may act on the bearings. For most pumps that are operated on the ground in standard gravity conditions and for these pumps during ground-based qualification testing, the most significant force that must be reacted by the bearings is the deadweight load of the rotating mass. This load typically dominates the bearing performance calculation and all other forces are considered insignificant. In fact, the gravity load often tends to stabilize a rotating system because it provides a preferred location for minimum film thickness and hence health monitoring instrumentation can be located accordingly. However, once this load is removed by operating the machine in orbit, the remaining small forces can contribute to instabilities, vibrations, and even a static overloading of the bearing. During the course of the failure investigation, five loads were discovered that were uncharacterized during the design phase and qualification testing of these pumps. It is recommended that vertical qualification testing be implemented for future pumps designed to operate in microgravity environments. Vertical testing relieves the radial system of deadweight forces and uncovers potential deleterious effects of an unloaded system.

### Residual Unbalance of Rotating Assembly

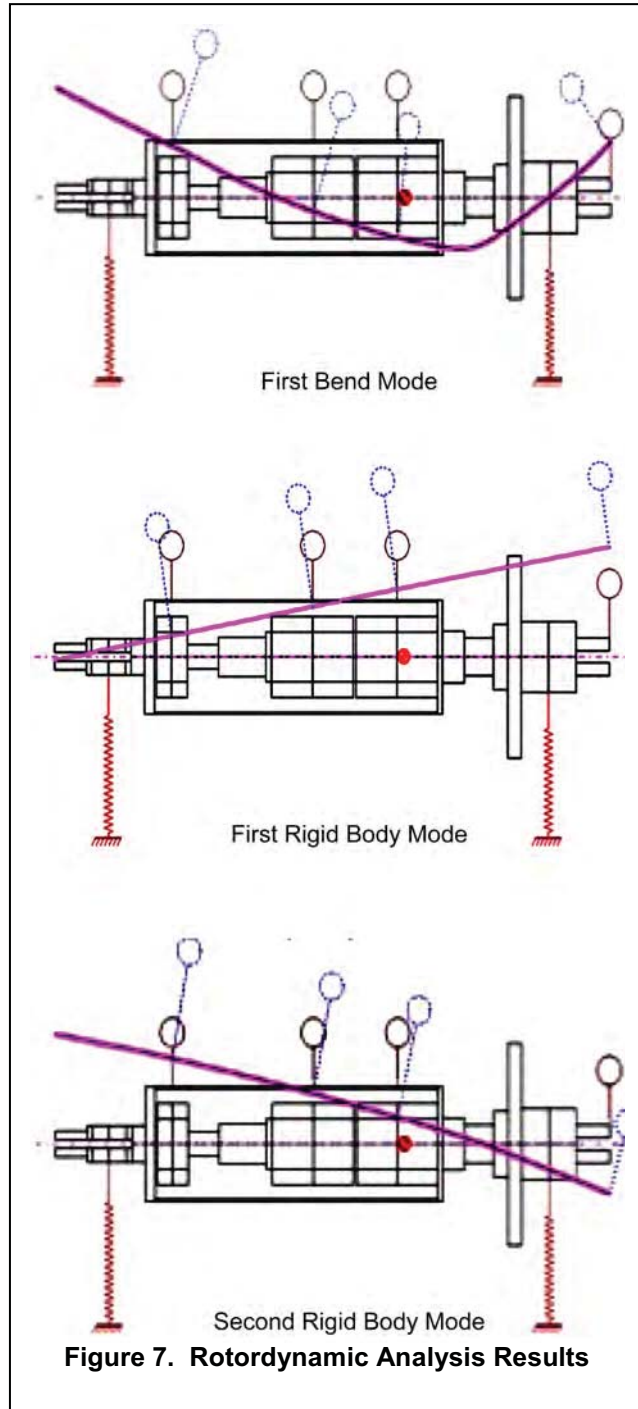
Residual unbalance exists in all rotating systems and exists when the line of mass centers does not coincide with the rotational axis. This offset when combined with the rotational speed of the machine manifests itself as a synchronous, rotating force on the bearings. Typically, high-speed rotating equipment is dynamically balanced after final machining and prior to assembly. The dynamic balance process aims to return the mass center to the rotation axis by adding mass or removing material from the

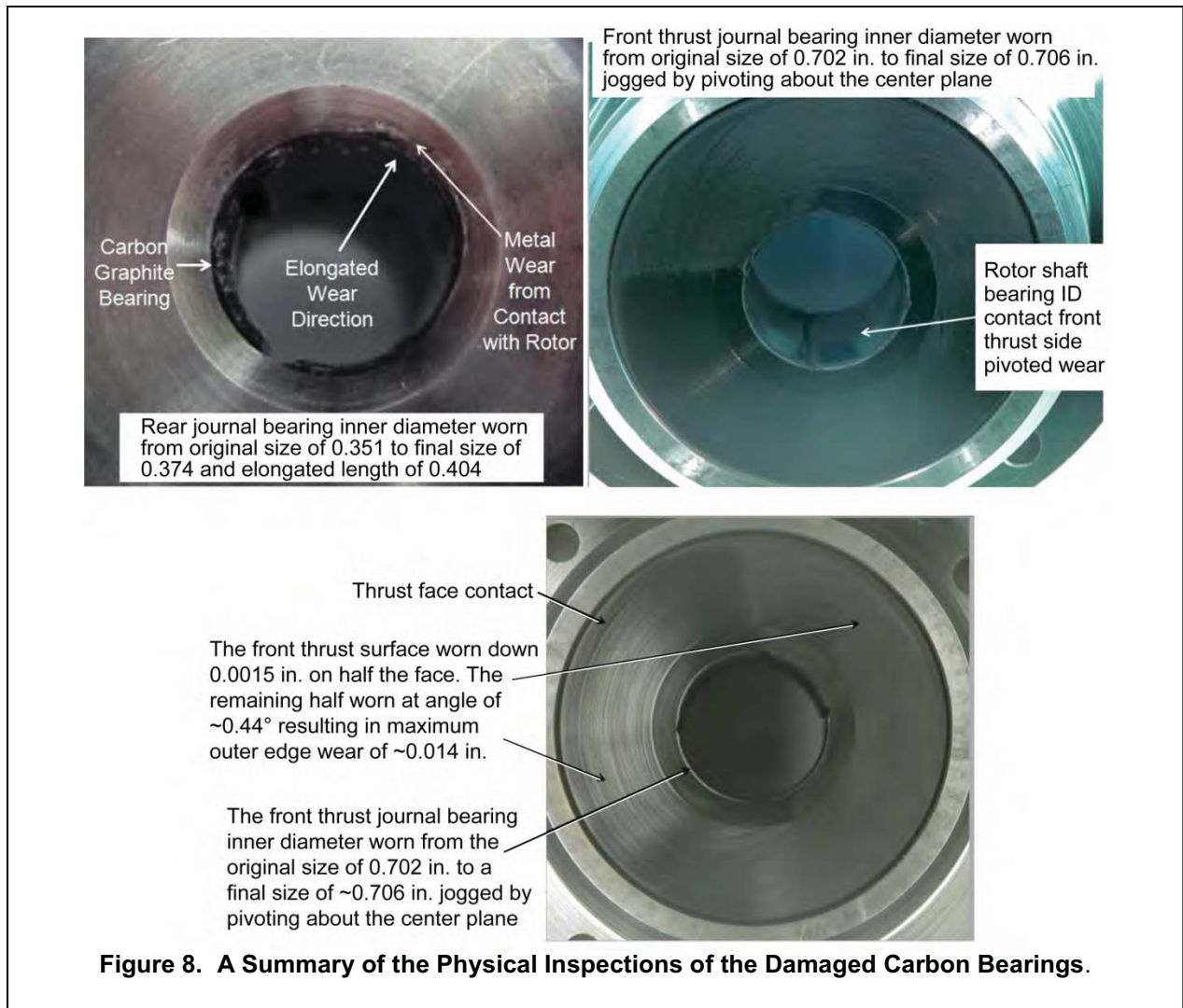
rotor. It is good design practice to specify the correction planes as near the bearings as is practical. By locating the balance planes near the bearings, the final unbalance recorded by the dynamic balance process can be used to calculate bearing loads directly. For the specific pumps in question here, the balance planes are located near the rear bearing and on the thrust disc near the front bearing. Build records were examined for all motors and pumps, not just for the failed unit, and bearing loads were calculated. The results indicate that the imbalance load on the rear bearing goes from 0.11 N at 12000 rpm to 0.17 N at 14700 rpm. These loads are well within the capacity of the rear bearing but do approach 20% of the load capacity. The residual imbalance alone would not overload the bearing and cause damage; however, it may either excite a rotordynamic vibration or combine with other forces to overload the bearing. Damage associated with a bearing overload from residual unbalance would manifest itself around the entire periphery of the bearing. This type of damage was not found during the physical inspection of the failed pump. Therefore, this force could not be the root cause, as it needs a force that organizes the overload in one specific direction.

Radial Magnetic Asymmetry

The drive for the pump is a four-pole permanent magnet motor. As such, there exists the possibility that radial asymmetries of the stator or rotating group position could cause a radial load on the bearings due to the negative stiffness of the magnets. During the design, build, and qualification of the motors no testing was conducted to quantify the radial force due to asymmetry. However, this quantity is bounded by the contract specifications to the motor supplier to be no greater than 10.7 Newton. Assuming this load would be equally split between the two bearings since the motor is straddle mounted, this would impose a 5.35

Newton load on each bearing. This magnitude of load is sufficient to overload the rear journal bearing and cause wear. However, the asymmetry would have to manifest itself through at least two poles of the motor stator in order to cause the angular misalignment damage found during the physical inspections of the failed hardware. A two pole stator asymmetry would manifest itself in reduced motor efficiency. Qualification testing of the motor did not reveal this characteristic. A magnetic asymmetry in the rotating group would manifest itself around the entire periphery of the bearing while a single stator pole asymmetry would cause the damage on both bearings to be in the same angular orientation. Therefore, this force could not be the root cause, as it needs a force that organizes the overload in one specific direction.





### Annulus Fluid Inertia Forces

Annulus fluid inertia forces were first discovered and analyzed by R. J. Fritz in the early 1970's. These forces arise in canned motors where high density fluids fill the rotor-stator gap of the machine. When accompanied by high speed, non-concentric operation, the fluid in this gap can impose a negative stiffness between rotor and stator, similar to the asymmetric magnetic forces. This causes a bearing load that increases with increasing eccentricity and speed. At 14700 rpm and an assumed eccentricity of 25 micrometers, the load on each bearing would be 2.58 Newton from the annular fluid force. This force is sufficient to overload the rear bearing under most hydrodynamic conditions. However, these annular fluid inertia forces for canned motors are well understood for eccentric rotor motion in a cylindrical mode. For the failed ISS ammonia pump an angular misalignment was found from physical hardware inspections. It is unclear whether these inertial forces behave in a similar fashion for this type of misalignment. Additionally, this force would rotate with the eccentricity causing wear around the entire periphery of the bearing, which is inconsistent with the findings of the physical inspections. It is unlikely that this force was the root cause of the wear because, like the previous forces, it requires an additional force that organizes the overload to occur in one specific angular location.

### Load Alignment with Respect to Bearing Pad

Both the front and the rear journal bearings used in this pump utilize axial grooves machined into the carbon sleeves. These grooves serve to disrupt the half frequency whirl flow pattern and delay the transition to turbulence in the fluid film. A detriment to bearing performance caused by this feature is to weaken the load capacity of the bearing when the load is oriented on or near one of these grooves. This orientation can reduce bearing load capacity by 55% compared with an orientation where the load is well-centered on the pad. During the assembly procedures of the pumps, no control measures were put in place to dictate the orientation of these grooves. Therefore this is a truly random variable, which may or may not become significant depending also on the orientation of the additional imposed loads. Physical inspections of the failed hardware revealed that the rear bearing wear was concentrated at one of these axial grooves. In fact, the wear was so severe that the 1.5-mm-deep groove was no longer a visible feature and the wear had gone deeper than the bottom of the groove. The evidence strongly implies that the orientation of the load on a groove is a major contributing factor to the failure of the ammonia pump. However, the load orientation only serves to diminish the load capacity, a force acting in this specific direction must be present to overload the bearing and cause the damage.

### Lubricant Jet Force on Rear Bearing

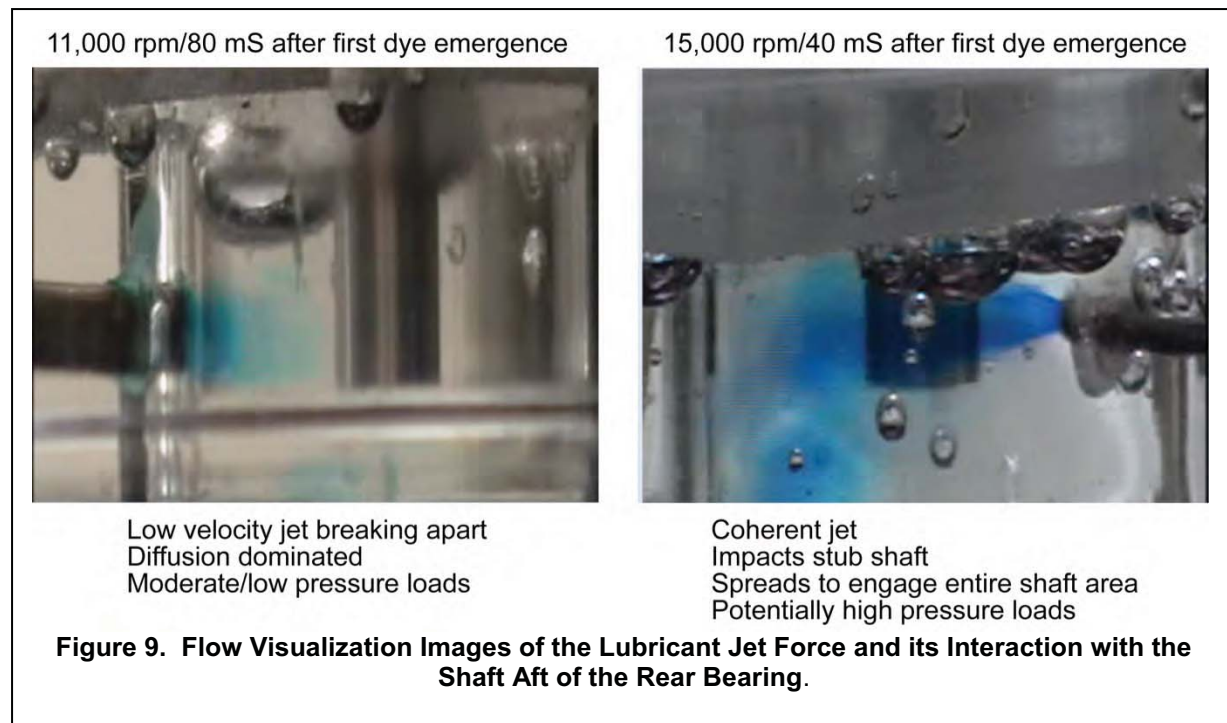
A unique feature of the secondary flowpath on the failed ISS ammonia pump was the single lubricant feed supply hole to the rear bearing. In addition to having just one supply hole to the rear bearing the lubricant was directed radially toward the shaft extension aft of the bearing. This is in contrast to the notional pump shown in Figure 3. Examination of the right side of this figure shows that the lubricant to the rear bearing is canted toward the rear endplate of the motor, not toward the shaft, and that there are symmetric supply holes to the rear bearing. This design practice ensures that no net force is imposed on the rear bearing due to the lubricant supply and secondary flowpath of the motor. However, the design that was implemented on the failed ammonia pump permitted a radial load to be imposed on the rear bearing due to the jet force of the lubricant feed. An analysis was conducted on the magnitude of this force as a function of pump rotational speed. The results of this analysis are cross-plotted on Figure 6 and show that this force can overload the 7.5 micrometer load capacity limit of the bearing at 12500 rpm. Furthermore, the finding of the physical inspections revealed that the wear on the rear bearing was in the direct opposite direction from the lubricant feed hole. There are two strong indications that the lubricant jet force on the rear bearing was the root cause of the bearing failure and initiated the damage to the rear bearing carbon. First, the load margin analysis showed that the jet force alone could overload the rear bearing at 12500 rpm without considering the additional effects of the previous four factors providing additional bearing loads or reduced capacity. Second, the wear pattern was consistent with a uni-directional load causing a static angular misalignment, which is the expected manifestation of the single jet force aft of the rear bearing.

## **Recovery and Modified Operations**

The tactical recovery for the ISS from the 2010 ammonia pump failure was the replacement of the pump ORU with a functional on-orbit spare. Three EVAs were used to accomplish this task. Full function and operation of the ISS was restored by this activity. The strategic recovery focused on restoring the full 15-year operational life of the pump module and ensuring that the ISS had a full complement of spares available to complete its projected life. In order to accomplish the strategic objective, additional questions needed to be answered and the root cause of the failure needed to be verified. Of primary importance was the determination that the failed pump was an 'in family' pump and no extenuating factors impacted the reduced life of the pump. A comprehensive review was conducted on all of the build records and qualification tests. No information was uncovered that would suggest that the failed pump had a unique history that would predispose it to premature failure. This finding placed an emphasis on the verification of the root cause and potential modifications to the operating procedures to restore pump life for future modules. The lack of a ground asset that could be instrumented to validate a root cause scenario limited the ability of the team to conduct comprehensive validation testing. A recommendation for future system development is to maintain ground assets such that in-space anomalies can readily be investigated.



Verification was needed to confirm the hypothesis that the lubricant jet force on the rear bearing served as the root cause for the ammonia pump failure. While analysis of the bearing capacity, analysis of the magnitude of the lubricant jet force, and the findings of the physical inspections were consistent with this fact, experimental validation of the analyses was needed to run the issue to ground. To this end, a flow visualization experiment of the rear bearing lubricant feed geometry was conducted. Still pictures of the lubricant jet characteristics at 11000 rpm and 15000 rpm are shown in Figure 9. In these experiments water was used to simulate the anhydrous ammonia in order to match the kinematic viscosity between the two fluids. In the flow visualization blue dye was added to the lubricant jet in order to distinguish between the fluid in the jet and the fluid resident in the aft bearing pocket. The pictures clearly show a change in the character of the jet force between the low speed operating point of 11000 rpm and the high speed operating point of 15000 rpm. At the low speed point, the jet is slow to emerge from the feedhole and diffuses into the surrounding fluid. These characteristics are consistent with a low imposed jet force. By contrast, at the high-speed condition the jet remains organized and coherent up to the point of impact with the shaft extension. This characteristic is consistent with a significant jet force imposed on the shaft and rear bearing. Because the bearing load capacity increases linearly with rotational speed but the jet force increases with the square or cube of shaft speed, a crossover point can be identified at which the rear bearing margin goes negative. Once the bearing margin goes negative, solid surface contact occurs and wear damage of the carbon bearing begins to accumulate. This initial damage changes the geometry of the bearing, which in turn predisposes the rotor-bearing system to angular misalignment in this direction. These flow visualization experiments provided verification that the lubricant jet force initiated damage to the rear bearing and contributed to the premature failure of the pump. In order to restore operational life of the remaining pump modules, procedures were modified to limit maximum speed to 12500 rpm, minimize changes to pump speed, and minimize start-stop cycles on the pump.





## Conclusions

The premature failure of the ISS external thermal control system provided an unprecedented opportunity to retrieve and examine spaceflight hardware that has operated for years in a microgravity environment. The ground-based inspections of the returned pump and ensuing failure investigation revealed five potential bearing forces that were un-accounted for in the design phase of the pump. While these forces are relatively small compared to the deadweight load of the rotating group in standard gravity operation, when on orbit, these forces could combine in a number of random orientations to overload the pump bearings leading to solid-surface contact, wear, and premature failure. The recovery plan identified the lubricant jet force on the rear bearing as being the damage-initiating event for the failure. Since this force is directly related to the square or cube of the operating speed of the pump, there exists a crossover speed at which bearing margin becomes negative and carbon wear begins to occur. Design life for the remaining pumps was recovered through a change in flight rules for the operation of the pump module that limits rotational speed and minimizes speed changes and start stop cycles. Through the course of the failure investigation, recovery, and follow-on assessment of pump wear life, design guidance has been developed to improve the life of future mechanically pumped thermal control systems for both human and robotic exploration missions. The following six recommendations are proposed for future development of high speed pumps designed for long-term microgravity operation:

- Maintain an axially symmetric journal bearing design
- Ensure that cylindrical rigid body modes dominate over conical modes
- Perform vertical testing to unmask dead weight loading effects
- Perform qualification tests that quantitatively validate bearing performance
- Perform qualification tests that quantitatively validate rotordynamic performance
- Maintain ground assets to experimentally probe and verify in-space anomalies

**Table 1. Typical Fluid Properties at 2.62 MPa and 275 K**

	Ammonia	SAE 10	Carbon Dioxide	Water @ 325K
<b>Density (kg / m<sup>3</sup>)</b>	<b>637</b>	<b>865</b>	<b>67</b>	<b>1001</b>
<b>Absolute Viscosity (mPoise)</b>	<b>1.68</b>	<b>2600</b>	<b>0.14</b>	<b>5.47</b>
<b>Kinematic Viscosity (mm<sup>2</sup> / s)</b>	<b>0.264</b>	<b>301</b>	<b>0.209</b>	<b>0.546</b>

## References

1. Active Thermal Control System (ATCS) Overview, The Boeing Company, <http://www.boeing.com/assets/pdf/defense-space/space/spacestation/systems/docs/ISS%20Active%20Thermal%20Control%20System.pdf>
2. Birur, G.C., Bhandari, P., Gram, M.B., Durkee, J., "Integrated Pump Assembly – An Active Cooling System for Mars Pathfinder Thermal Control", Society of Automotive Engineers, 26th International Conference on Environmental Sciences, Monterey, CA, 1996
3. Bloch, P.E., "Understanding Canned Motor Pumps", Maintenance Technology, 01 September 2008.
4. Duchesne, S.M., Sweterlitsch, J. J., Son, C. H., Perry, J. L., "Impacts of an Ammonia Leak on the Cabin Atmosphere of the International Space Station", American Institute of Aeronautics and Astronautics, International Conference on Environmental Systems (ICES); San Diego, CA; 15-19 Jul. 2012; United States, 2012.
5. Lockwood, M.K., Ercol, C.J., Cho, W.L., Hartman, D., Adamson, G., "An Active Cooling System for the Solar Probe Power System", American Institute of Aeronautics and Astronautics, International Conference on Environmental Systems, AIAA-2010-6294, 2010.
6. Ticker, R., "Engineering Test Beds on the International Space Station", IEEE A&E Systems Magazine, August 2009.
7. Swanson, T.D., Birur, G. C., "NASA Thermal Control Technologies for Robotic Spacecraft", National Aeronautics and Space Administration, N20030031332, 2003.
8. Westheimer, D. T., Tuan, G. C., "Active Thermal Control System Considerations for the Next Generation of Human Rated Space Vehicles", American Institute of Aeronautics and Astronautics AeroSpace Sciences Meeting, AIAA-2005-342, 2005.
9. Paris, A.D., Bhandari, P., Birur, G.C., "High Temperature Mechanically Pumped Fluid Loop for Space Applications – Working Fluid Selection", SAE International, 04ICES-282, 2004.
10. Jimenez, A.P., Hoberecht, M.A., "Space Station Freedom Photovoltaic Power Module Design Status", National Aeronautics and Space Administration, 899271, IEEE , 1989.
11. Shen, F., Drolen, B., Prabhu, J., Harper, L., Eichinger, E., Hgyuen, C., "Long Life Mechanical Fluid Pump for Space Applications", American Institute of Aeronautics and Astronautics AeroSpace Sciences Meeting, AIAA-2005-273, 2005.
12. Son, C.H., "Numerical Study of Ammonia Leak and Dispersion in the International Space Station", American Institute of Aeronautics and Astronautics, International Conference on Environmental Systems (ICES); San Diego, CA; 15-19 Jul. 2012; United States, 2012
13. Baldauf R. W., Kawecki, T., Purdy, W., Hoang, T.T., "Development of a Bearingsless Ammonia Pump for Spacecraft Thermal Control", NRL Review, 2008
14. Midgley, J.W., Teer, D. G., "An Investigation of the Mechanism of the Friction and Wear of Carbon", Transactions of the ASME, American Society of Mechanical Engineers, December, 1963.
15. Fritz, R.J., "The Effects of an Annular Fluid on the Vibrations of a Long Rotor, Part 1 – Theory", Journal of basic Engineering, December 1970.
16. Fritz, R.J., "The Effects of an Annular Fluid on the Vibrations of a Long Rotor, Part 2 – Test", Journal of basic Engineering, December 1970.

# Wide Range Vacuum Pumps for the SAM Instrument on the MSL Curiosity Rover

Paul Sorensen\*, Robert Kline-Schoder\* and Rodger Farley\*\*

## Abstract

Creare Incorporated and NASA Goddard Space Flight Center developed and space qualified two wide range pumps (WRPs) that were included in the Sample Analysis at Mars (SAM) instrument [1]. This instrument was subsequently integrated into the Mars Science Laboratory (MSL) “Curiosity Rover,” launched aboard an Atlas V rocket in 2011, and landed on August 6, 2012, in the Gale Crater on Mars. The pumps have now operated for more than 18 months in the Gale Crater and have been evacuating the key components of the SAM instrument: a quadrupole mass spectrometer, a tunable laser spectrometer, and six gas chromatograph columns. In this paper, we describe the main design challenges and the ways in which they were solved. This includes the custom design of a miniaturized, high-speed motor to drive the turbo drag pump rotor, analysis of rotor dynamics for super critical operation, and bearing/lubricant design/selection.

## Introduction

Approximately 15 years ago, the Jet Propulsion Laboratory started an initiative to fund the development of a miniaturized vacuum system. JPL saw a need for small vacuum systems to support astrobiological science missions, including mass spectrometers and gas chromatographs. At the time, mass spectrometers and other instruments for astrobiology were being reduced in size, mass, and power. However, the bulk of the accompanying vacuum system had come to dominate the overall system design, especially since commercial vacuum systems were not designed with the constraints of space missions in mind. For astrobiological science missions such as MSL, the main requirements are the highest vacuum level and longest life in the smallest possible package with the least amount of power consumption. These are requirements not unlike what is required for terrestrial applications of portable mass spectrometers. This paper will present miniaturized pumping system design and test data and will discuss continuing efforts, supported by Goddard Space Flight Center (GSFC), to demonstrate long life time with repeated start-stop cycles.

## Miniature Vacuum Pump Background

In order to achieve high vacuum levels, only a few pumping technologies are available (turbomolecular-, cryogenic-, or diffusion-pumps). Considering size and power limitations, the choices are further restricted so that the only viable technology for long term operation is a turbomolecular pump. In a turbomolecular pump, the rotor and stator blades push gas molecules from low to high pressure. In order to achieve high compression ratios on each turbo stage, the pump rotor tip speed needs to be comparable to the most probable molecular speed of the gas being pumped. This means that when the size of the rotor decreases to reduce pump size and mass, the rotor speed needs to increase in proportion. Also, as pump size decreases, the pumping speed is reduced, which necessitates tighter clearances between the moving parts of the pumps in order to control leakage back flow. Both the higher speed and the tighter clearance affect higher demand on pump parts fabrication and assembly. For astrobiological science, and Mars missions in particular, a turbomolecular pump (TMP) is coupled with a molecular drag pump (MDP) on the same shaft driven by the same electric motor drive. The molecular drag pump exhausts directly to

---

\* Creare Incorporated, Hanover, NH

\*\* NASA Goddard Space Flight Center, Greenbelt, MD

the Martian atmosphere at pressure 10 Torr or greater. Similar demands for high precision manufacture and assembly of the molecular drag pump exist as for the turbo-molecular pump.

In collaboration with GSFC, Creare has been developing and demonstrating the technologies required to design and build miniature high vacuum pumps. In particular, we have designed and built two of the smallest available high vacuum pumps that have the following pumping characteristics: a compression ratio for air that is greater than  $10^8$ ; a pumping speed of about 5 L/sec; 10-W power consumption for an exhaust pressure of 10 Torr; and operation over a very wide range of temperatures (from  $-40^{\circ}\text{C}$  to  $65^{\circ}\text{C}$ ). The smallest of these pumps (Figure 1a) has a mass of 130 g, a diameter of 3.3 cm (1.3 in), and an overall length of 5.8 cm (2.3 in) (i.e., the size of a C-cell battery). The slightly larger pump (Figure 1b) has a mass of 500 g, a diameter of 5.1 cm (2.0 in), and an overall length of 11.7 cm (4.6 in) (i.e., the size of a soda can). The larger version was space qualified for use on the Mars Science Laboratory (MSL) Sample Analysis at Mars (SAM) instrument that was launched in 2011 and is currently being used operationally on Mars. The smaller version was tested to TRL 6 in the laboratory for potential use on ExoMars, a reformulated Mars mission, or other astrobiological missions.

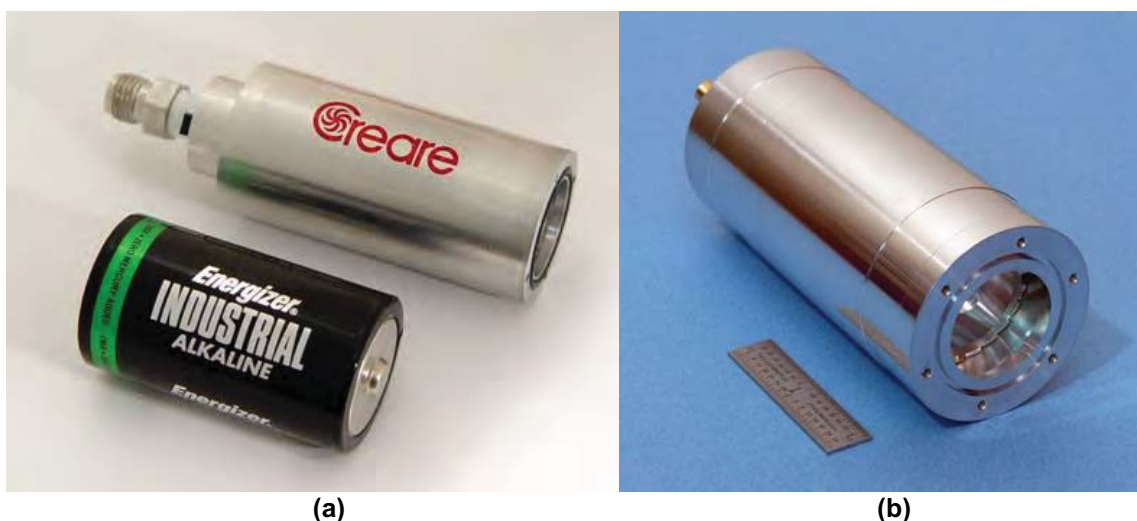


**Figure 1. (a) Smallest Turbomolecular/Molecular Drag Pump. (b) Space-Qualified Turbomolecular/Molecular Drag Pump That is Part of the SAM Instrument on MSL.**

### **Vacuum Pump Fabrication Challenges**

As described above, in order to greatly reduce the size and mass of a TMP/MDP, very high rotor speeds are required since the pump tip speed must remain constant as the pump diameter is decreased. In order to achieve the desired size and mass for space missions, the miniaturized pumps that we have developed require motor operation at 100,000 rpm (for the 5.1-cm-diameter pump) and 200,000 rpm (for the 3.3-cm-diameter pump). Table 1 summarizes the features enabled by miniaturization and those required for space qualification and the corresponding consequence and fabrication challenge. While the need for tight dimensional control, the selection of proper materials, and accommodating the consequences of thermal and structural interactions require careful engineering design, the most difficult challenge that we faced was the impact of very high speed operation of the motors on lifetime of the pumps. In particular, since the miniaturized pumps need to operate at such high speeds, the combined motor and rotor structural resonances are below the operating speed of the pump, which results in super-critical operation. This, combined with the need for relatively long-life under harsh operating conditions (i.e., many starts/stops) resulted in the key limitation that needed to be overcome during space qualification. In fact, TMP/MDPs designed for use on Earth are turned on once and rarely, if ever, turned off and on again, in order to avoid the wear-and-tear associated with starting and stopping the pumps. In addition, terrestrial TMP/MDPs are operated at sub-critical speeds.

### Miniaturized TMP/MDP Design

The design of the miniaturized, space-qualified TMP/MDP is shown in Figure 2. Figure 2a provides an exploded view and Figure 2b provides a cross sectional view of the pump. This figure shows that the pump rotor is cantilevered over the pump motor and that the turbomolecular blades are on the outside of the pump rotor near the gas inlet and that the smooth molecular drag pump rotor begins on the outside of the pump rotor and continues on the inside of the pump rotor, making use of the bottom end of the pump stator and the outside of the pump motor for the molecular drag pump “grooves”.

**Table 1. Summary of Miniaturized Turbomolecular/Molecular Drag Pump Fabrication Challenges.**

Feature	Consequence	Fabrication challenge
Lower pumping speed	Good internal leakage control	Tight dimensional control
Smaller dimensions	Small clearances in flow channels	Tight dimensional control
High speed	Super critical operation	Advanced balancing procedures
High speed, lightweight	Material structural limits	Use high strength alloys
Wide temperature range	Compatible material selection	Incorporate heater and heat rejection
Wide temperature swing	CTE mismatch	Careful thermal/structural design

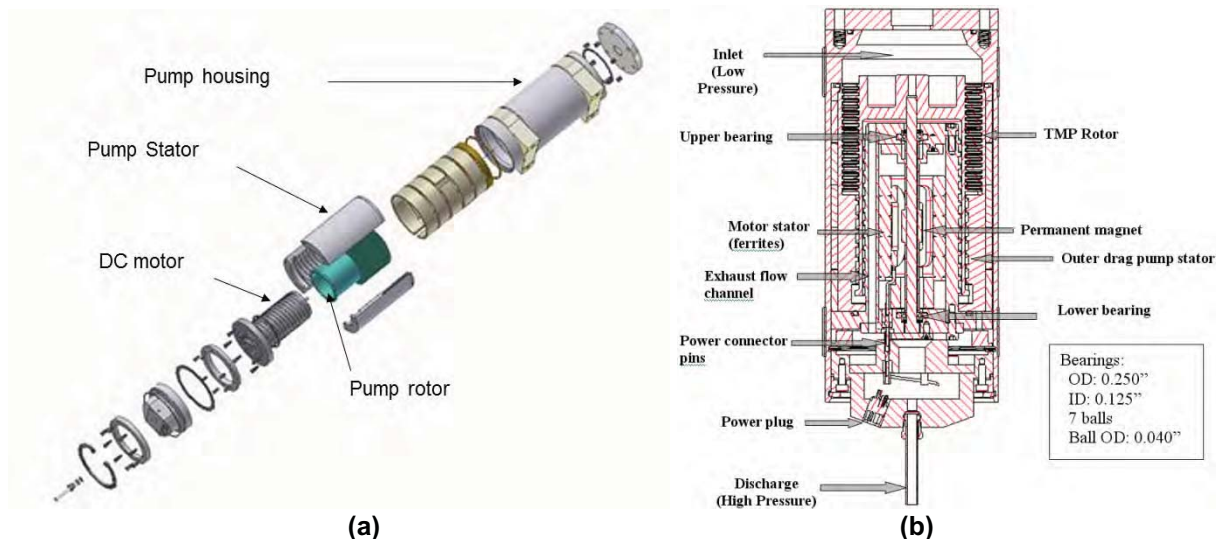


**Figure 2. (a) Exploded, Three-Dimensional View of Space-Qualified 100,000 rpm TMP/MDP  
(b) Cross Section of Space-Qualified 100,000 rpm TMP/MDP**

### Resonant Frequency Analysis Optimization

Analysis of the motor rotor/pump rotor combination (see Figure 3) show that the lowest natural frequency of the combined system is approximately 985 Hz (e.g. approximately 59,000 rpm) and that the mode shape is such that the pump rotor acts like a bell on the “stiff”, tungsten-carbide shaft with the bearings providing the support points. In order to make the natural frequency of this mode as high as possible, we have designed the pump so that the bearings are as close as possible to each other given the other constraints of the motor design (namely the electro-magnetic requirements of the low-power, high-speed motor). In order to enable the pump motor to pass through this resonance, we have mounted the bearings in an elastomer, which provides both greater damping and lower stiffness as compared to hard-mounted bearings. While these properties enable super-critical operation, they also presented operational



temperature range challenges and necessitated the introduction of a heater on the pump to ensure that the elastomer was soft enough during startup to provide these important properties.

### Lifetime Optimization

As described above, high-speed operation, super-critical operation, and the need for many start and stop cycles contributed to the need to optimize the lifetime of the pump to meet the mission requirements. In addition, since science considerations limited the choice of lubricant to non-hydrocarbon greases, the bearing-lubricant combination selection became the focus of an effort to optimize the pump lifetime. We used a combination of screening tests at room temperature with hardware that consisted of the pump motor and a pump rotor simulator (i.e., “Life Test Simulators”) as well as complete pumps that were tested over the complete operational temperature range of the mission.

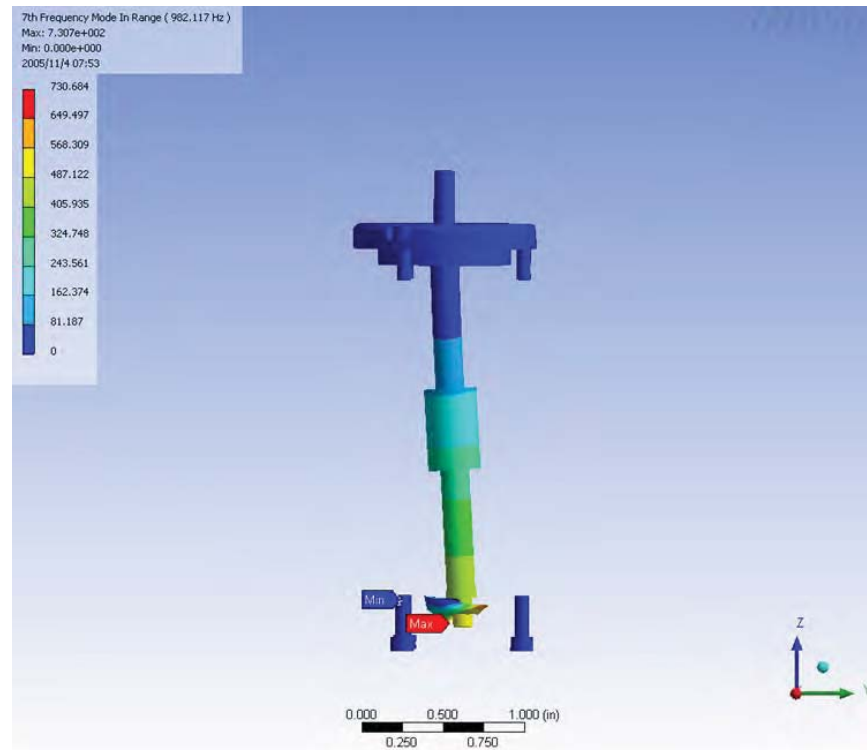


**Figure 3. Fundamental Structural Resonance Mode Shape From Finite Element Analysis**

A summary of the test configurations and the results of the life testing using the Life Test Simulators are shown in Table 2. Based on the results of similar previous tests and input from bearing and lubricant experts, we focused our testing on two retainer materials and various pre-load values. We focused our testing on these variations because results of our previous testing indicated that cracking or wear of the retainers was the primary, life-limiting, failure mechanism. In addition, based on results of our testing, the bearing manufacturer revised the design of their standard Meldin retainer to provide additional a larger cross section of material. Finally, we considered the effect of pre-load since the overall design required that the bearings be pre-loaded and past experience showing a significant effect of pre-load on bearing and lubricant life. The results show that the Vespel retainers, which are strong, but which do not absorb much lubricant, can be made to last twice the desired lifetime specification. However, the performance of this material and the lubricant is strongly related to the pre-load. The Meldin retainer material, being porous, stores lubricant and can therefore achieve a longer life time – up to and beyond three times the desired lifetime specification.

**Table 2. Summary of Life Test Simulator Configurations and Results**

Test Unit #	Retainer Material	Pre-Load (N)/(lb)	Lifetime (hr)	Fraction of Spec
3	Vespel	2.7 / 0.6	801	1.59
4	Vespel	1.8 / 0.4	1027	2.04
5	Vespel	4.0 / 0.9	575	1.09
6	Meldin (original)	2.7 / 0.6	1160	2.21
7	Meldin (revised)	1.8 / 0.4	1736	3.31
8	Meldin (revised)	2.7 / 0.6	1690	3.22
9	Meldin (revised)	2.7 / 0.6	1343	2.56

Vacuum Pump Measured Performance

The Martian atmosphere, though much lower pressure than Earth (e.g., approximately 10 torr of mostly CO<sub>2</sub>), is still much too dense for mass spectrometers to work. The SAM instrument requires two vacuum pumps that are able to exhaust directly to the Martian atmosphere and much achieve high vacuum levels. In order to meet the high compression ratio, we developed a miniaturized hybrid turbomolecular and molecular drag pump with unique features. The pump is shown in Figure 4 after installation in the SAM instrument. The pump is less than half the size of the smallest turbo drag vacuum pump available commercially and consumes only one-tenth of the power. As a consequence of the smaller size, this turbo drag spins at 100,000 rpm.



**Figure 4. Wide Range Pump Installed in SAM Instrument**

During the course of the pump development, we measured the ultimate pressure and flow rate of the pump design. The ultimate pressure test measures high vacuum pressure on the upstream side of the WRP while maintaining a given exhaust pressure on the downstream side of the WRP and the flow is only that due to outgassing in the test chamber (assumed to be very small). The tests are conducted first with the pump purged with CO<sub>2</sub> and CO<sub>2</sub> on the exhaust side and subsequently with a thorough Helium purge and Helium on the exhaust side. The pressure measurements are conducted in an environmental chamber with the chamber temperature set at 22 °C, +50 °C and -40 °C respectively.

The pump was started at room temperature, brought up to full speed, 100,000 rpm, and maintained at this speed during temperature cycling. The pump was initially brought up to +50 °C to allow as much of the entrained gas in the high vacuum chamber to outgas as possible. We did observe a steady decline of the high vacuum pressure throughout the test as the chamber was cleaned of outgassing material. The chamber had been rough pumped for several days prior to testing, but even so improved high vacuum performance will probably be possible with a more thorough bake out and cleaning with a turbo pump. So, the results reported here can be seen as conservative and provide a lower limit on vacuum pump

compression ratio. At each of the three temperatures, we recorded the steady-state high vacuum pressure, the pump foreline pressure, the DC voltage and current into the motor controller, and the pump housing temperature. The high vacuum pressure was collected with a Bayard-Albert (BA) tube. A correction factor was applied to the indicated pressure to account for the difference in gas performance of the BA tube. The foreline pressure is measured with a Convector gauge and properly corrected for the difference in gas convection properties.

The measured ultimate pressure and resulting compression ratio for CO<sub>2</sub> as a function of foreline pressure are given in Figure 5. We see that the pump maintains a virtually constant high vacuum pressure, but that this pressure is highly dependent on the temperature. The pumping ability of the turbo molecular pump is expected to be reduced with increased mean molecular speed. However, this only accounts for a very minor amount (<10%) of change in no-flow pressure. Barring any increase in leakage across the pump, we expect the main reason for increased ultimate pressure at high temperature to be due to increased outgassing in the vacuum chamber, which is also supported by the fact that the pressure at similar operating conditions kept dropping during the test as the chamber was baked out. We see that the compression ratio at Mars operating conditions exceeds 5e6 at high temperature and is close to 10e8 at low temperature.

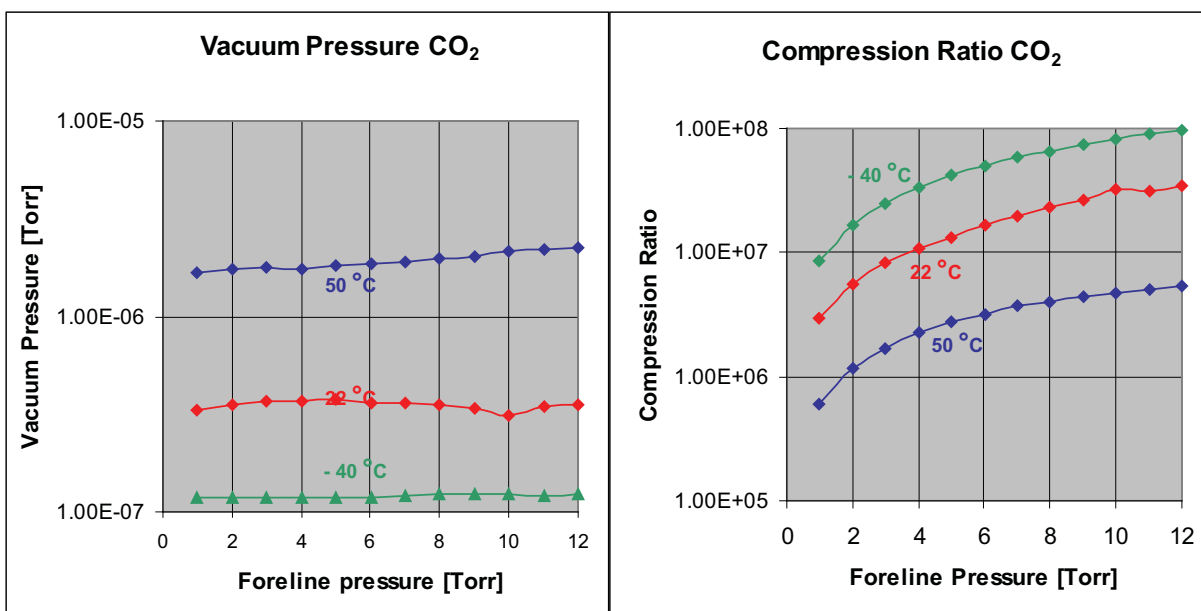


Figure 5. Ultimate Pressure and Compression Ratio Pumping CO<sub>2</sub>

The flow test measures the pumping speed of the WRP while maintaining an exhaust pressure on the downstream side of the WRP similar to Martian conditions of 12 Torr. The tests were conducted in three configurations: (1) the pump purged with CO<sub>2</sub> and CO<sub>2</sub> on the exhaust side; (2) a thorough Helium purge and CO<sub>2</sub> on the exhaust side; and (3) N<sub>2</sub> on both high vacuum and exhaust side of the pump. During the tests CO<sub>2</sub>, Helium, or N<sub>2</sub> is bled into the high vacuum chamber through an orifice and the pressure drop across the orifice is used to determine the flow rate and thereby the pumping speed. The measurements are conducted in an environmental chamber with the chamber temperature set at +20°C, +50°C and -40°C respectively.

The pump was started at room temperature, brought up to full speed, 100,000 rpm, and maintained at this speed during temperature cycling. The chamber was initially brought up to +50 °C to allow as much of the entrained gas in the high vacuum chamber to outgas as possible. We did observe a steady decline of the high vacuum pressure throughout the test as the chamber was cleaned of outgassing material. The chamber had been rough pumped for several days prior to testing, but even so improved high vacuum performance will probably be possible with a more thorough bake out and cleaning with a turbo pump.

The pumping speed measurements will be affected by the outgassing rates, in particular at low temperatures where it will underestimate the flow rate. The pumping speed is derived by bleeding the gas through a short circular duct of known dimensions into the high vacuum chamber. Assuming that the gas flow through the duct is much larger than outgassing rates, the duct flow rates will equal pumping speed. The duct flow rate can be determined from measurements of gas pressure on either side of the duct.

At each of the three temperatures, we recorded the steady-state high vacuum pressure, the gas leak pressure upstream from the metering duct, the pump foreline pressure, the DC voltage and current into the motor controller, and the pump housing temperature. We also measured the temperature of the chamber wall upstream of the orifice and used this temperature as a measure of the temperature of the gas flowing through the orifice. Since this chamber is large both in length and diameter relative to the gas mean free path, and since the gas flow through this chamber is very slow, the gas has ample time to reach thermal equilibrium with the chamber walls. If the real gas temperature is actually different, the duct conductance will be wrong but we estimate that this error will be less than a few percent. The high vacuum pressure was measured with a BA tube. A correction factor was applied to the indicated pressure to account for the difference in gas performance of the BA tube. The foreline pressure is measured with a Convectron gauge and properly corrected for the difference in gas convection properties. The bleed pressure was measured with a calibrated Pirani gauge, and corrected for the difference in gas conductivity of Helium, CO<sub>2</sub>, and N<sub>2</sub>. The main uncertainty in the flow measurement is due to the error in the BA tube measurement. This will directly affect the pumping speed measurement. We estimate the total relative error on the pumping speed to be 20-25%.

We measured the pumping speed by adjusting the setting of a leak valve on the upstream side of the metering duct. We covered flow rates through the duct from zero to a value where the pressure upstream of the metering duct (the leak pressure) gave a mean free path of the gas molecules ten times longer than the duct diameter. This ensures that the duct conductance can be treated as purely molecular flow far from transitioning to continuum flow. The measured pumping speed is shown in Figure 6 for the three gasses and three gas temperatures spanning the temperature extremes for the WRP operation. We see that the pumping speed at high vacuum pressure (i.e., small differential pressure across the orifice) reaches a constant level of approximately 6 L/sec. This level is consistent with model values for the turbo-molecular stage at zero differential pressure across the turbo molecular stages. When the high vacuum pressure (i.e. inlet to the pump) is lowered the pumping speed decreases, since the probability of a molecule hitting the pump inlet goes down to the point where as many molecules enter the pump inlet as exit it.

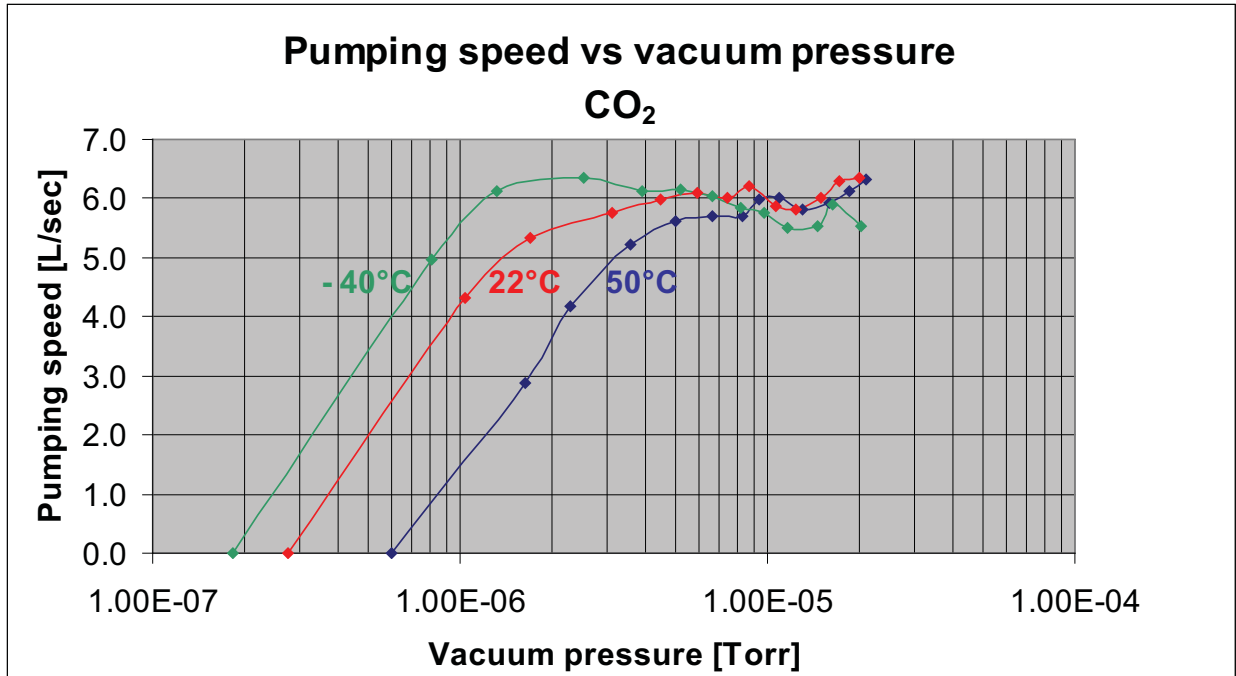


Figure 6. WRP Pumping Speed When Pumping CO<sub>2</sub> With Exhaust of CO<sub>2</sub> at 12 torr

The pumping speed is clearly affected by temperature, the pump being less efficient at higher temperature. The main difference between high and low temperatures is believed to be the level of outgassing from the vacuum chamber wall. At higher temperatures, the outgassing will increase substantially, thereby adding leak flow to the orifice flow that the WRP must pump. The pumping speed at high temperatures will therefore be artificially low. By proper bake out procedures we believe that the outgassing leak rate may be lowered substantially, which will result in increased measured pumping speed of the WRP.

### Conclusions

In this paper, we described the main design challenges of designing and developing a space-qualified, miniature turbomolecular/molecular drag pump and the ways in which they were solved. This included a discussion of the custom design of a miniaturized high speed motor to drive the turbo drag pump rotor, analysis of rotor dynamics for super critical operation, and bearing/lubricant design and selection. Measured performance and lifetime data proved that the pump design achieved the mission specifications and current operation on Mars proves that the pump is meeting mission requirements.

### References

1. Mahaffy, P.R., et al. "The Sample Analysis at Mars Investigation and Instrument Suite." Space Science Reviews, September 2012, Volume 170, Issue 1-4, pp 401-478.



# SLM Produced Hermetically Sealed Isolation Valve

James Richard\*

## Abstract

Marshall Space Flight Center (MSFC) has developed a valve concept to replace traditional pyrotechnic-driven isolation valves. This paper will describe the valve design and development process. The valve design uses a stem/wedge to support a disk inside the valve. That disk hermetically seals the pressurized fluids. A release mechanism holds the stem/wedge and a large spring in place. When required to open, a solenoid is energized and pulls the release mechanism allowing the spring to pull the stem/wedge away from the disk. Now the disk is unsupported and the pressure ruptures the disk allowing flow to the outlet of the valve. This paper will provide details of this design, describe the development testing, and show the results from the valve level tests performed. Also, a trade study is presented to show the advantages of this design to a conventional pyrotechnic-based valve.

## Introduction

National Aeronautics and Space Administration (NASA) spacecraft and commercial payloads are faced with similar issues of isolation of toxic propellants, limited propellant or pressurant resources, precision of timed events, reliability of operations, and/or limited budgets. Hermetically sealed valves that use pyrotechnics to rupture internal passages are the state of the art in achieving the isolation, resource, and timing objectives. However, handling issues associated with pyrotechnics, quality control issues requiring lot sampling of valves, and costs associated with the handling, access, and design of these devices has made the state-of-the-art valves a costly and involved solution. This effort was to utilize the Selective Laser Melting (SLM) technology to offer valve solutions that would reduce or eliminate the cost and handling disadvantages of the state-of-the-art valves, while maintaining the necessary sealing requirements of the valves. Valve vendors have in the past endeavored to manufacture these valves, but the costs associated with the actuators, sealing elements, and other production costs kept this from becoming a reality.

NASA missions have had disconcerting experiences using the state-of-the-art pyrovalves. MSFC generally used these valves for launch vehicles and larger payloads. Goddard Space Flight Center (GSFC) uses these valves in their fleet of earth observation satellites. Others NASA centers have had issues using these devices for everything from deep space missions to manned vehicles. Each had different needs and concerns and each had concepts to resolve the issues. MSFC and GSFC teamed to provide a proposal to pool ideas and resources, and design a valve that could replace pyrovalves at similar costs and equal or greater reliability.

## Discussion

Generally, the approach was to combine the MSFC and GSFC application requirements into a single set of performance requirements that enveloped the needs of both centers' missions, develop concepts for the valves, perform a trade study of various concepts based on the performance requirements, select a single design, complete a detailed Design, Develop, Test, and Evaluation effort for that single concept, and perform limited testing to demonstrate viability.

---

\* Marshall Space Flight Center, Huntsville, AL

### Risk & Cost Study

Before this work began, a study was conducted revealing the risks and costs associated with the current pyrotechnic valves. Elimination of these risks and costs was the primary goal of this effort and the reason for the effort.

MSFC and GSFC each provided input to this study. The team's data and experience showed that there were three areas of concern: 1) Spacecraft System Development Costs driven by component reliability, 2) Component Development and Qualification Cost associated to the single use nature of the components, and 3) Spacecraft Operational Costs driven by the operational proximity of the personnel and payload to pyrotechnic devices.

**Spacecraft Development Costs:** Given that the pyrotechnic valves offer no redundancy of operation, should the main charge fail, the designers of the systems require multiple pressurant and propellant fluid system legs with multiple valves in series and/or parallel to ensure reliability of the spacecraft. This is based on operational history where failures of these valves result in the loss of the spacecraft or loss of the mission. Many examples were found where incorrect wiring, loose wiring, or failed igniters resulted in a spacecraft valve not opening/closing and the mission was lost. So, designers now routinely install parallel (and often series in addition) fluid legs assuring opening (or closing) actions. Design of these systems with multiple parallel (and/or series) legs drives the vehicle costs. If the valves can be assured to have true redundancy and high reliability, multiple paths could be eliminated and the development cost of the spacecraft reduced. A goal for these new valves was to allow end-to-end verification of the electrical system, and to have capability for true redundancy in the actuation system.

**Component Development Costs:** This area has at least two costs associated with the total. The first is an igniter system. The second is the method required to qualify the valves/systems for spaceflight. The first requires development and qualification of the igniter subsystems and controls to ensure the system meets all performance requirements. Generally, pyrotechnic valves use a chain of explosive events consisting of multiple pyrotechnics, each more stable and more energetic than the one before. As an example, an electrical impulse is used to set off a small squib in the igniter, which sets off a high explosive, which ignites a low explosive. These low explosives are used to generate the high pressure gases needed to open the valve. Figure 1 shows a typical pyrovalve cross-section and the location of each of these explosive elements. Each of the elements, the interconnections, and the controllers, which provide the initiation, all have to be designed, tested, qualified, and installed on the spacecraft. These costs must be considered when looking at the total cost of a spacecraft. A new pyrotechnic system development cost can be \$2 to \$5 million dollars, depending on the operational requirements, number of interlocks required for range safety, and the type system chosen. For this reason, many spacecraft use previously designed systems and stay within the previously qualified requirement ranges. This introduces additional analysis and spacecraft design costs. Elimination of these systems and changing to standard solenoid driver systems offers large program-level component development cost savings beyond the cost of the valve itself. However, the valves also must be developed and qualified. Each valve must be shown to be reliable through batch and or lot testing. As many as 5 to 10 valves can be lost from a build due to lot testing required to assure the valves function as specified. These tests destroy the valves, so the cost to the must include these lot/batch testing units. If there are only 4 valves on a spacecraft, lot testing could more than double the unit cost of the valve.

**Operational Costs:** Operations costs associated with working around pyrotechnic devices can be significant. The vehicles must be designed for late in-process access to install the devices' igniters. These generally have been removed to prevent inadvertent initiation caused by stray electrical signals and system check-outs. When the spacecraft systems are loaded onto the launch vehicle and the vehicle is rolled to the launch pad, technicians must install the initiators/igniters within a few hours of the launch. This late access costs time and money, not only in the manpower to actually do the work, but in the design of the spacecraft, launch systems, and ground towers to allow access late in the launch flow.

From these considerations, it is easy to see that if the costs of the valves themselves are similar, the total savings to a spacecraft (and the development program) could be very significant.

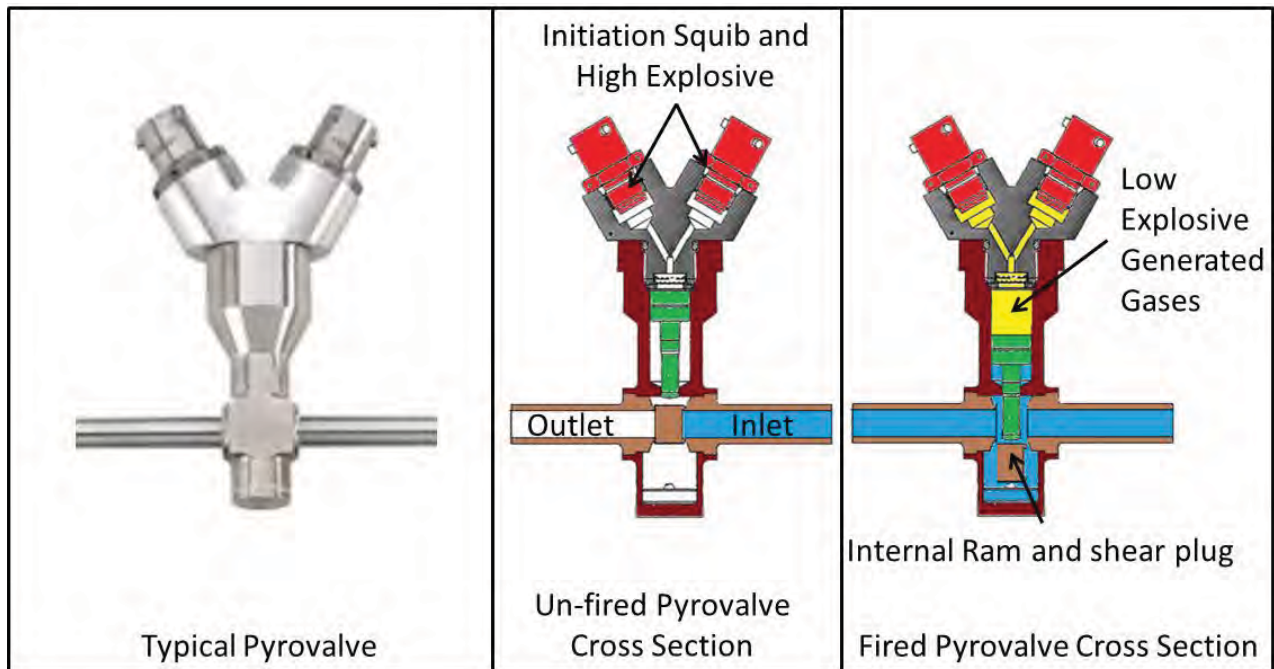


**Figure 1. Typical Pyrotechnic Valve and Explosive Chain**

#### Accomplishments

This project produced many accomplishments over the year. Although generally in chronological order, some of the accomplishments were a result of the entire effort. This report will detail these accomplishments by category.

Teaming: MSFC led the effort. GSFC provided Dan Ramspacher, a committed designer, and systems engineering overview. Mr. Ramspacher and his supervisor, Caitlin Bacha, were instrumental in making this team work. Ms. Bacha provided Mr. Ramspacher with the resources needed for the detailed design, offered peer review of the project, and provided leadership in the development of the task and team.

The team had weekly teleconference calls, worked issues as they arose, interacting and communicating well as they performed the assigned tasks. Generally, MSFC provided overall project control: managed schedule and funding, made top-level technical decisions, and performed most of the reporting activities. MSFC and GSFC each performed technical tasks. MSFC provided valve engineering, launch vehicle, engine, and cryogenic payload expertise. GSFC provided additional valve engineering, small near-earth satellite, and operations/handling expertise.

This effort has resulted in a relationship that will extend well beyond this project and has established a collaborative environment for the two centers in the areas of valve and actuation systems, and component design and development.

Requirements Definition: The first task the team performed was to define a set of performance requirements that satisfied the needs of all systems. MSFC provided launch vehicle and stage requirements, as well as long duration experiments. GSFC provided requirements for handling, reliability, and near-earth satellites.

Table 1 provides the results of that collaboration. This single sheet of requirements formed the basic specification for the valve design effort. This also became the list used in the selection of trade study Figures of Merit (FOM) and weighting factors.

**Table 1. Valve Performance Requirements**

<b>Hermetically Sealed Isolation Valve Performance Requirements</b>		
<b>Requirement</b>	<b>General</b>	<b>Detail Requirement Goals</b>
Media	Inert Gas, Solvent, Propellant Compatibility	Wetted surface non-reactive with helium, nitrogen, argon, IPA, hydrazine. MMH, NTO, kerosene, dimethylhydrazine, etc.
Internal Leakage	Shall provide a leak-tight seal until actuated	Internal and external leak rate < $10^{-6}$ sccs - Parent metal seal is fractured during actuation.
Pressure Rating	Maximum Design Pressure and ability to be actuated over a range of pressures	Minimum operating pressure shall be 350 psig (2,400 kPa); design shall be shown as extensible to up to 4500 psig (31,000 kPa).
Actuation Time	Low Response Time	Response in less than 50 msec.
Repeatability	Actuations repeatable within a narrow range	Repeatable to within 10 msec.
Actuator Force Margin	Force available from the actuator should be significantly greater than required to operate the valve	All external inputs (e.g., heat, electrical interference, vibrations, or other external stimuli) must not cause the valve to actuate prematurely and actuator shall provide a required 100% margin to these loads.
APT and In Situ Testing	Ability to actuate individual valve during testing without loss of seal	The valves shall withstand testing pressurized or depressurized without loss of the hermetic seal. This will ensure individual valve functionality, which will significantly mitigate mission risks and decrease overall unit cost.
Particulate generation	Particulate generation shall be minimized	Particulate can clog filters and plug components downstream; must be minimized both in number and size. Largest passable particulate is 0.5 micron.
Construction and End fittings	All-welded fluid flow path	This is a basic requirement of in-space propulsion system components to limit the possible propellant leak paths. Mechanical fitting-type or O-ring seals cannot be used as primary seals. Proposed valve uses a parent metal seal, which is fractured during actuation, maintaining all welded fluid path. Development valves can be bolted, but must show path to all welded design.
Flow Rate and DP Performance	Low pressure drop/ High Flow Coefficient	$\Delta P < 3$ psia (20kPa) @ 0.15 kg/s – from pyrovalve spec from SDO. – typical of in-space propulsion systems
Interfaces	General interface requirements, valve designs shall be show extensibility to larger and smaller requirements.	¼" to ½" inlet/outlet tube fittings. Electrical connector or leads. Mechanical mounting feet to allow for integration to spacecraft structure.
Electrical Requirements	Typical of in-space propulsion system electric limits.	Power < 60 W, Voltage < 28 V, E < 1 Wh, Current > 2 amps.
Mass	Mass should be comparable to existing pyrovalves.	Mass should be less than 2.5 lbm (1.1kg).
Construction	To the extent possible, SLM shall be used for this valve	Using SLM offers the opportunity to design new and complex geometries to meet the performance requirements. Designs that utilize SLM are required.

**Concepts Development:** MSFC and GSFC each were then asked to develop a set of concepts that met the above requirements. They were given a few weeks to perform a preliminary analysis of each concept and present the ideas back to the team. Figure 2 shows these concepts.

MSFC developed 4 concepts:

- 1) A modified version of the Vacco design developed in 2002,
- 2) A shear disk or “Dual Disk” Valve,
- 3) A wedge-supported rupture disk or “Wedge Seat” Valve, and
- 4) A piloted balance disk or “Pilot Pressure” Valve.

GSFC developed a concept for a fracture plate or “Linear Disk” Valve based on previous work.

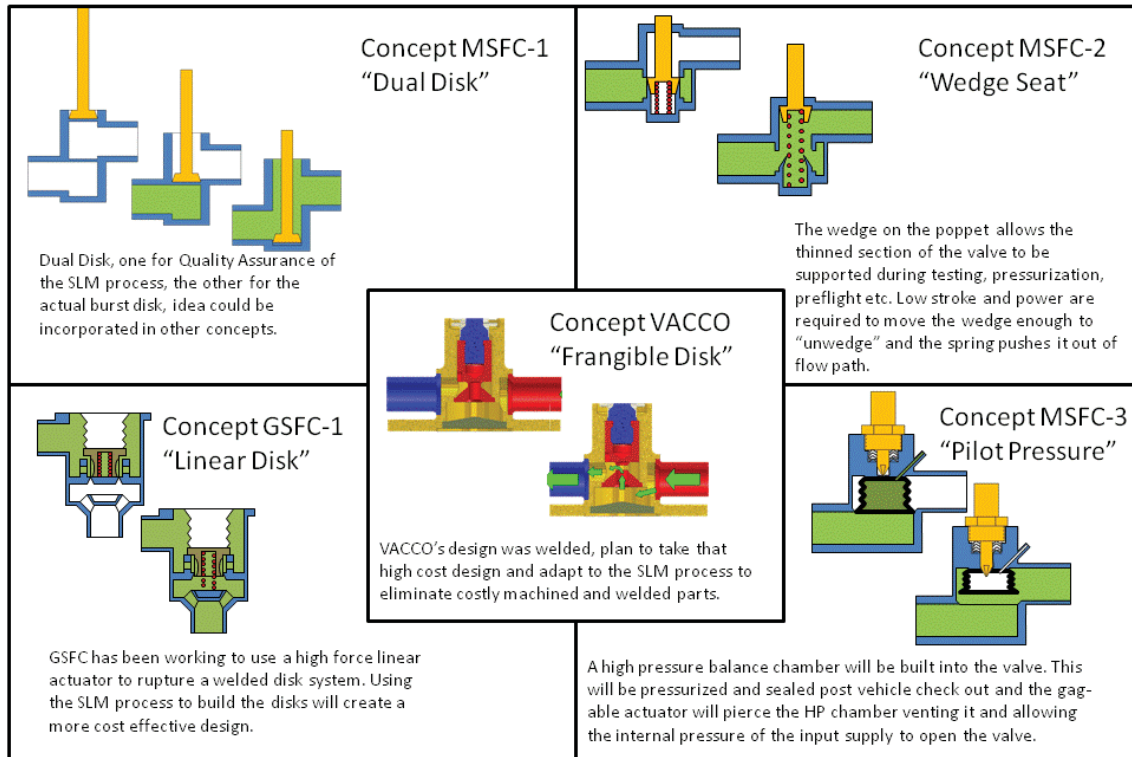


**Figure 2. Concepts Used in the Trades.**

The Vacco design was attractive given that they had fully developed the valve concept. However, they encountered large manufacturing costs, which could not be reduced with their current suppliers and assembly methods. The valve was designed to have a small poppet embedded in the body that was supported by the actuator. The pressure times area (PA) and spring (Sp) loads are carried through to the actuator at all times. This loads the actuator with high forces from time the valve is assembled until it is used. Thus the actuator requires some method to limit travel during testing. MSFC’s concept for this valve was to use an actuator that had been developed under a task for the NASA Engineering and Safety Center (NESC). This design could hold these loads continuously and release them through the use of a traditional solenoid system. This actuator uses a unique ball latch system. The MSFC concept for modifications to the Vacco design was to reduce the high touch labor valve parts using SLM manufacturing methods. This concept was analyzed and found to be possible, but the valve body would still require some machine time and some welding. The forces required for this valve were directly tied to the supply pressure and would escalate with pressure, going up with the square of the area. Scaling up would further increase the actuator load requirements.

The MSFC Dual Disk design was conceived to have an internal fracture disk that was sheared by the release of a large spring load. That spring would push a shear plunger through the internal hermetic seal.



This design required a large-force high-stroke actuator. This could be made possible with the use of a very long stroke spring and the same actuator. This would be simple conceptually, but resulted in high loads causing an increase in weight. It also would have limited extensibility to larger or smaller designs and higher pressure systems.

The MSFC Wedge Disk design incorporated a wedge to support a thin disk internally. The wedge would support the PA loads on the disk. The disk was to be thin enough to rupture reliably at roughly  $\frac{1}{2}$  the minimum MDP (hence 100% margin). The biggest unknown was how the loads would scale with the pressure and disk size. Quick calculations showed it should scale linearly and assuming a very high coefficient of friction (0.9), the spring loads required for a wide pressure range were manageable. The NESC actuator could easily handle these variable loads. The valve could be made to have a relatively short stroke and a high equivalent square edged orifice diameter.

The pilot design was conceived to use one of the other concepts as a pilot system to balance scaling for pressure or size. The idea was to develop a small pilot system that was reliable and light, and then build a valve that had internal force balancing of the PA and Sp loads. As this concept was developed, it became clear that it was going to be costly and complex. But the valve looked feasible and was the most scalable of all the designs considered.

The GSFC valve used a fracture plate that supported the inlet pressure, but could be overloaded with the addition of a high force, low stroke actuator. This concept had much heritage to previous work and was simple, scalable within a range of sizes and pressures, and was a fairly mature concept. The main issue was the original concept used a Nitinol bar stroke actuator. This actuator, although reliable and capable of very high loads, was very slow and depending on the initial temperature, varied in response time. So, MSFC and GSFC conceived a magnetostrictive actuator. This actuator was based on MSFC-patented valve concepts, but is high force, low stroke as required, and is very fast. These two concepts (the GSFC valve and the modified MSFC actuator) were combined into the GSFC valve that was included in the trade space.

#### Trade Study

With the five concepts fleshed out, each was evaluated by a team of MSFC and GSFC personnel. The first step was to develop a methodology for evaluation. This consisted of a matrix of figures of merit and weighting factors in a pair-wise analysis to provide a ranking of each concept.

The figures of merit were derived from the performance requirements shown in Table 1, but down-selected to those felt most critical. Team members each voted on a weighting factor for each requirement. Table 2 and Table 3 show the teams suggested figures of merit and weighting factors, respectively.

#### Down Selection

The results of this trade showed that two concepts, the MSFC Wedge Seat Design and the GSFC Fracture Disk Design, were nearly equal in performance.

With GSFC needing to develop a detailed analysis of the actuator, but having a nearly completed the valve design, and MSFC only needing to complete the NESC actuator design started to do a new valve design. It appeared there was manpower available to do both designs. A review of the budget showed that with the rapidly de-escalating costs of SLM due to increased competition in the market, there was budget to build and test an example of each. With the total cost to design, build, and test both valves within the available resources allocated for this program, the decision was to produce both designs and have a real hardware trade study down-select at the end of the program.

**Table 2. Figures of Merit and Pair-wise Study Analysis Matrix**

Pairwise Comparison								
	9	5	3	1	3	5	9	
Unit Cost				X				Force Margin
Unit Cost				X				Repeatability
Unit Cost				X				Serviceability
Unit Cost				X				Scalability
Unit Cost				X				Integration
Force Margin				X				Repeatability
Force Margin				X				Serviceability
Force Margin				X				Scalability
Force Margin				X				Integration
Repeatability				X				Serviceability
Repeatability				X				Scalability
Repeatability				X				Integration
Serviceability				X				Scalability
Serviceability				X				Integration
Scalability				X				Integration

**Table 3. Weighting Factors Applied to the Designs**

FOM Ranking	Vector	Weight
Unit Cost	1.348	0.177
Force Margin	1.348	0.173
Repeatability	1.348	0.176
Serviceability	1.348	0.163
Scalability	1.348	0.161
Integration	1.348	0.152
	8.088	1.0018

### Detailed Design

The following will provide details of the analysis and design efforts performed to develop the MSFC valve design. GSFC will write a separate paper on the development of their valve, so it is not covered in this paper. A future development activity will down-select to the final single valve using the performance, cost, and reliability data obtained from this testing and activity.

#### MSFC's Design

The original concept of the wedge design was to have a conical internal disk in the SLM body that was supported radially by a removable conical wedge. The concept was to have the SLM disk as a feature built directly to the needed thickness and sizes in the body. This was thought to only require a minor reaming machine operation for clean-up of the wedge interface surfaces before assembly. Working with

the builders of SLM hardware, it became clear that the tolerances required by the design to achieve reliable rupture performance were beyond the capability of the SLM equipment. Thus access to both sides of the disk would be required to clean up the build material. The radial design would have not allowed 360 degrees of access to the underside of the disk for the machine operations.

The design was changed to a linear wedge configuration. Figure 3 shows the basic concept for each. The overall design of the radial concept would have been smaller given the flow area was larger for a specific design. The linear wedge design allows access to both sides and is simpler to manufacture. This concept was the one taken to final design and used for development testing.

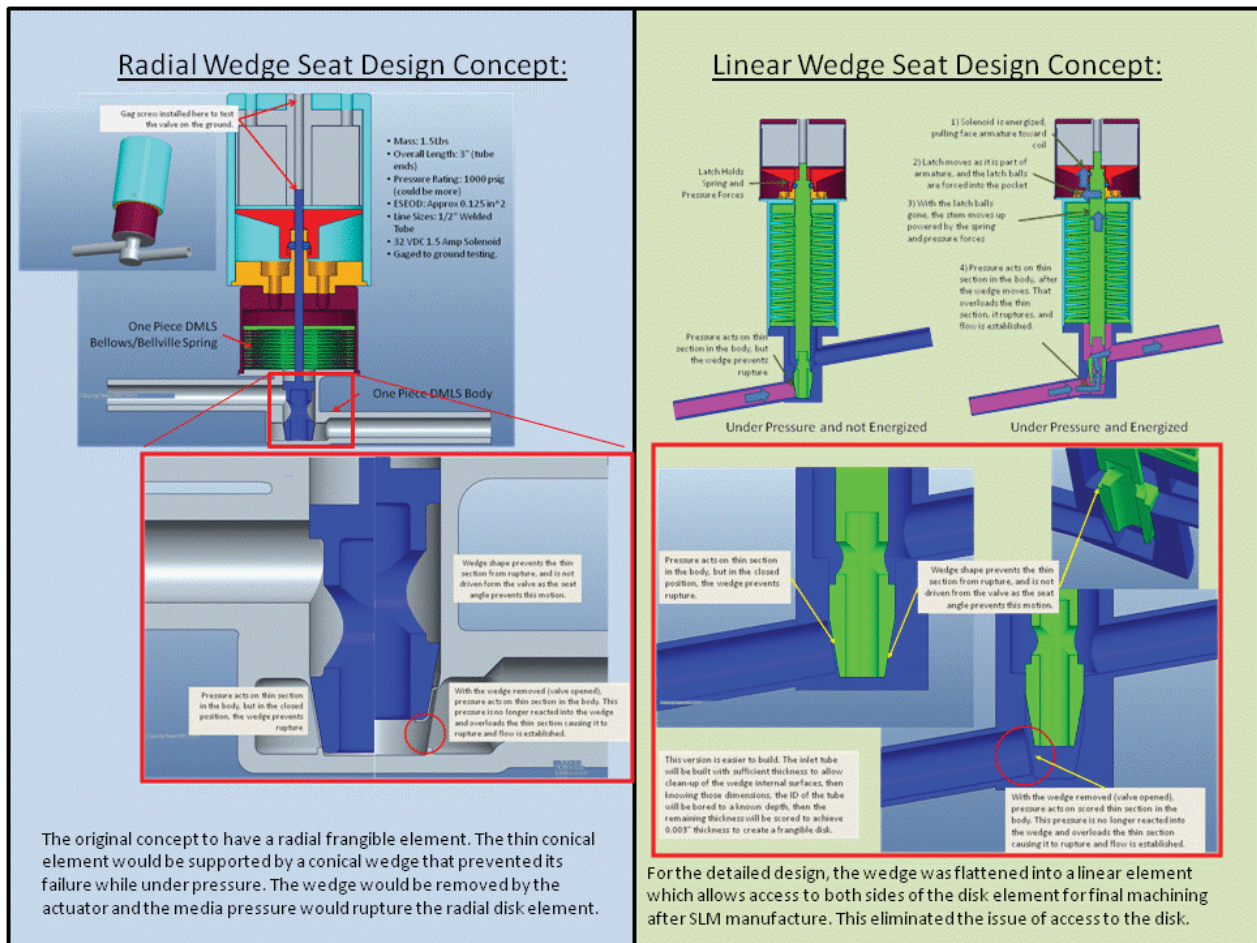


**Figure 3. Comparison of the MSFC Radial Wedge vs. Linear Wedge Designs**

From this point, the analysis for the actuator load spring sizes and other calculations was performed. Four big issues were uncertain:

1. First was the variability of the coefficient of friction between the wedge and the disk. This drove the loads as a function of supply pressure from as few as 30 (130 N) to nearly 350 lbf (1560 N), depending on the values of pressure and coefficient.
2. The second was whether the valve would generate particulate greater than allowed.
3. The third uncertainty was the actual spring rate and capability of the unique spring/bellows concept.
4. And the final uncertainty was the consistency of the as-ruptured flow discharge coefficient.

To address the first concern, a 10-degree angle was selected to minimize the effect of load on the force needed to pull the wedge from the pressurized disk, however, the actual effect was uncertain, because

this type of analysis was highly dependent on actual coefficients and the nominal load transmitted through the diaphragm. To address that part of the issue, development tests were performed to determine the actual loads needed to remove the wedge as pressure was varied. The development tests were performed with materials that had higher than as-designed couples to drive the coefficient of friction to the highest possible. The valve was to be all Inconel 718. The development test was performed with an Inconel 718 wedge and an aluminum body. These tests showed that the 350-lbf (1560 N) maximum design point was twice the highest value recorded. Twenty tests were run and none had loads greater than 185 lbf (823 N), with pressure ranging from as little as 100 psig (600 kPa) to over 3500 psig (24,000 kPa). With a requirement for 100% force margin, the spring load required was set at 700 lbf (3000 N).

An unforeseen issue was found during testing. We showed that the analysis of the disk, assuming a thin membrane, was predicting failure at much lower pressures than those found. Using a disc diameter of 0.25 in (6.4 mm) and thickness of 0.002 to 0.003 inch (0.051 to 0.076 mm), a Roark's pure membrane analysis indicated that rupture would occur at around 50 psig (344 kPa) to 150 psig (1,000 kPa). Testing showed this to be a variable from 300 (2,000 kPa) to 900 psig (6,200 kPa). Review of the actual failure and analysis from the MSFC analysis branch showed that the actual failure mechanism is a combination of shear, bending, and membrane type failures. An empirical method was developed to match the test data to the analysis, and it was determined that disk area needed to increase as thickness could not be consistently controlled to less than 0.002 inch (0.051 mm). This drove the disk size to a 0.75-inch (0.02-m) diameter.

Figure 4 shows some of the development test articles and a graph of the load results. Visually, the test revealed that the rupture disk stayed intact, fractured cleanly along the "petals", and opened fully to achieve the required flow area. Flow testing of this design will be performed to prove the flow is acceptable. This was to be accomplished following final assembly or the completed design later in the development effort. Flow testing was never an objective of this development. Additional development testing showed this to be satisfactory given that no test article failed to rupture at 250 psig (1,700 kPa) or less. So, this larger disk concept was incorporated into the valve.

To address the second concern, the fluid used to burst the development valves was collected and sampled for particulate generation. This testing showed that there were no particles over the limit of 0.5 micron found. In fact, none were ever detected. This validated the burst disk design features of a circular cut 340 degrees around the edge of the opening and an "X" shape in the center to force the ruptured disk to open like pedals when the disk failed. For each test, the development hardware disk failure matched this configuration.

The third issue was the spring-rate. MSFC built two trial springs (see Figure 5) and each was tested. Even though neither was heat treated, a minimum spring rate of 4000 lbf/in (700,000 N/m) was achieved. The actual loads are assumed to be 10% to 20% greater when heat treated. Even this lower number provided the ideal 800 lbf (3600 N) required at 0.200-in (5-mm) stroke for this design, and still yielded the required 100% margin.

The results of these test showed that the spring/bellows system and the disk concept were valid, and the design was completed. The only remaining concern was the flow consistency. This could only be addressed with the final design and in a lot test program. Additional funding was requested and obtained later in the year. The results from that effort will be reported when available. The development testing resulted in similar failures for each test over the wide range of test pressures. The concern was mitigated with this qualitative data. Hard quantitative data is to be obtained later in Fiscal Year (FY) 14.



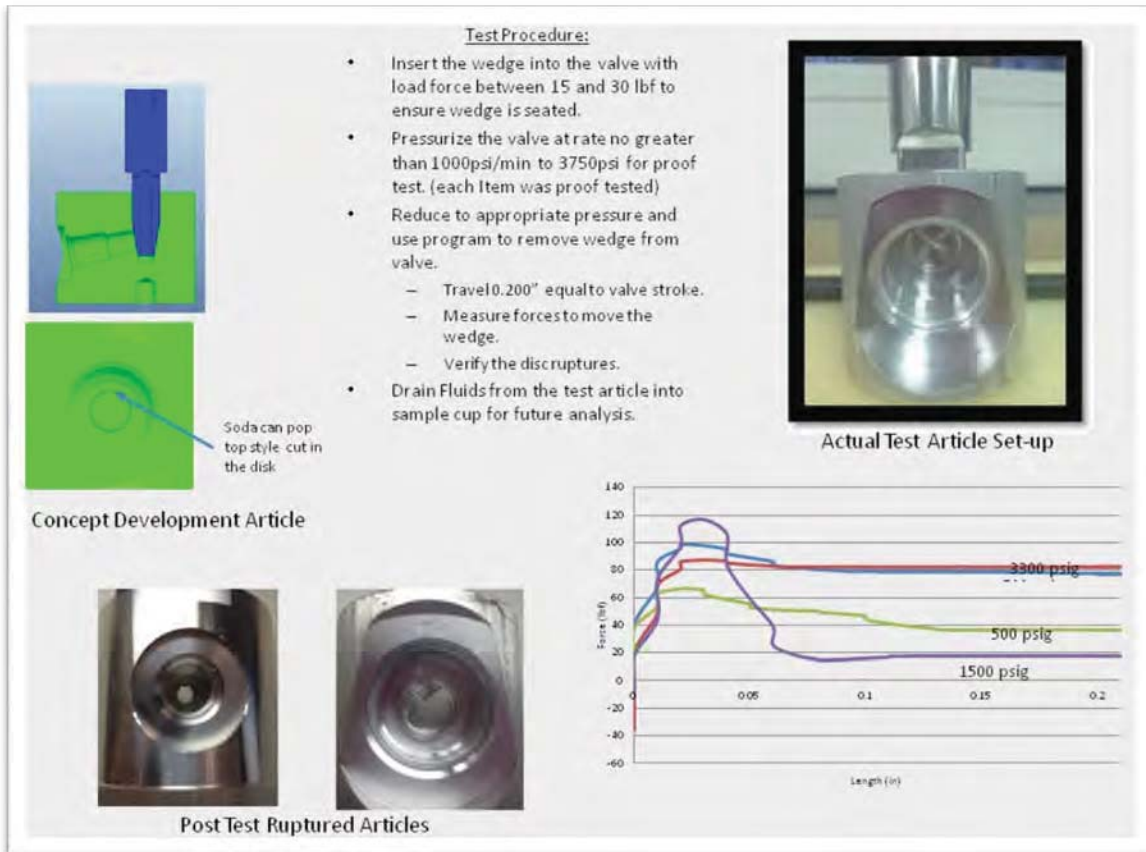


**Figure 4. Development Test Results**



**Figure 5. Trial Spring Builds Showed Acceptable Build and Performance Goals were achieved**



Once the spring design was completed and assured that the loads were well known, the actuator design was adjusted to provide the needed load holding and release capability. The biggest obstacle was to size the solenoid to provide the needed loads. A free-body loads analysis was used to define the actuator load.

$$\text{Spring Force} = F_s = 700 \text{ lbf (3100 N)}$$

$$\text{Reaction Load Per Ball on the Slip Ring} = F_r = F_s/4 \text{ balls} * \sin 10 = 30 \text{ lbf (130 N)}$$

$$\text{Actuator Pull Requirement } I = F_a$$

$$F_a = 24 \text{ lbf (110 N)} = \{(30 \text{ lb (130 N) reaction load)} * (0.2 \text{ coefficient of friction}) * (4 \text{ balls})\}$$

This is the force needed for the actuator. With a 100% force margin, the required solenoid force is 48 lbf (213 N). Figure 6 shows this in detail. Several available solenoids were tested, and a Marotta MV583 coil was selected. Tests showed the coil needed 0.04-in (1-mm) stroke to generate the 48 lbf (213 N) required. However, with the need for 0.0625-in (1.6-mm) actuator stroke (1/2 of the ball 0.125-in (3-mm) dia), the design required a slip feature, such that the ball would push the slip ring axially past the stroke of the armature to allow the ball to completely unlatch. This feature and a spring incorporated to reset the balls following actuation.

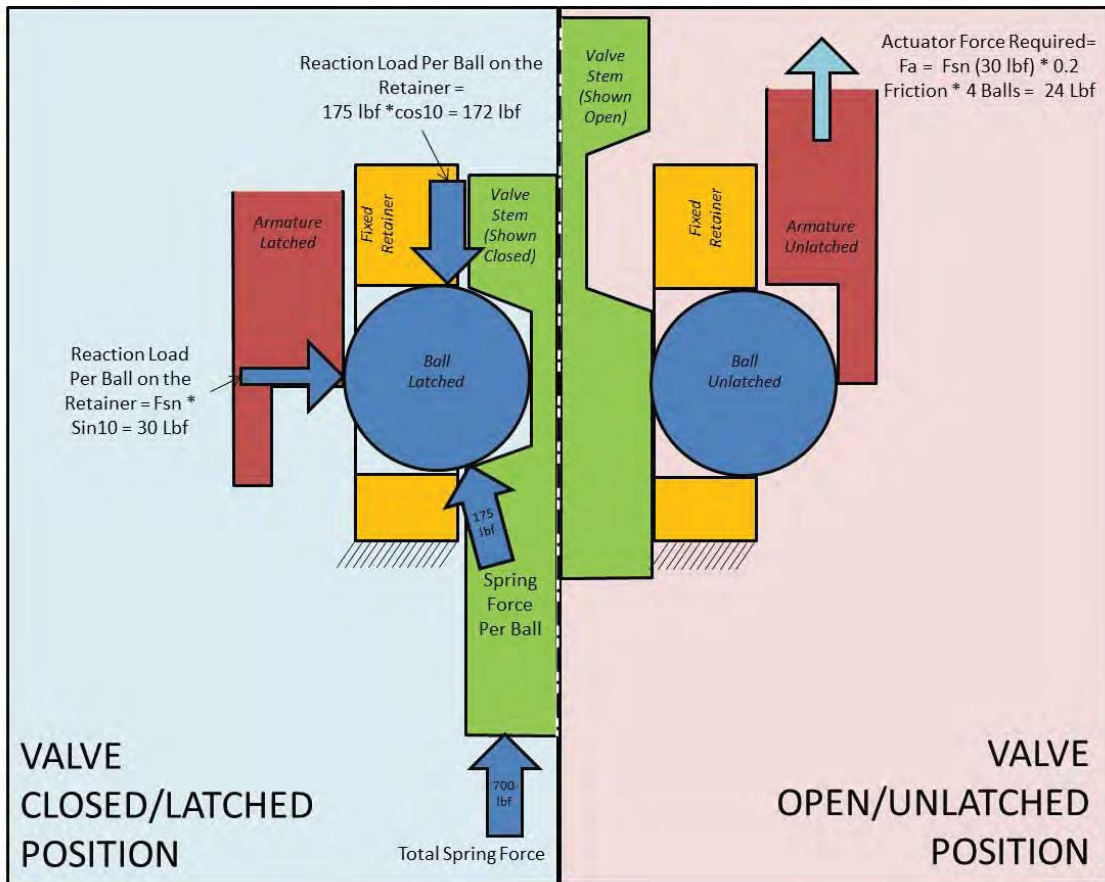


**Figure 6. Actuator Detail Layout**

The final MSFC valve drawings were completed and the hardware has been manufactured. Some of the hardware is shown in Figure 7. The final assembly drawing is shown in Figure 8. Final assembly and testing is underway as of the date of this paper's writing.



**Figure 7. Fabricated Hardware**

### **Summary**

The MSFC hermetically sealed valve isolation valve has been designed as a replacement for the traditional pyrotechnic valve. This valve was designed from the ground up to address the system designs, which result in operational complexity. This effort has shown that this design, although maybe not optimal for all applications, does meet the requirements of many pyrotechnic valve applications for spacecraft, launch vehicle, and lander applications.

The valves MSFC built were “one off” and the cost was high. An estimate of the unit production cost is provided in Table 4. At roughly \$10K per valve, this cost is very similar to the costs of an existing pyrovalve. So, the direct cost of the valve is a “wash”. The savings from the system design simplifications and operations enhancements are the primary benefits to be expected. Additionally there is no requirement for lot testing and depending on the size of the program, the cost of lot test units can be anywhere from \$30K to \$100K.

Table 4. Projected Unit Costs

MSFC Hermetically Sealed Isolation Valve Costs Data					
Part Name	Hours To Build	Hourly Rate	Part Labor Costs	Material Cost	Total Part Cost
Machined and DMLS Body					\$ 2,500.00
Machined and DMLS Bellows/Spring					\$ 1,150.00
Direct Purchased Coil					\$ 550.00
Machined Coil Housing					\$ 150.00
Machined Spring Housing					\$ 250.00
Machined Tube Adapter					\$ 275.00
Machined Adapter Rings					\$ 50.00
Machined Armature					\$ 250.00
Machined Wedge					\$ 150.00
Ball Support					\$ 75.00
Gland Adjuster					\$ 150.00
Washer					\$ 20.00
Balls					\$ 20.00
Wavy Spring					\$ 25.00
O-ring					\$ 10.00
Bellows Clamp					\$ 15.00
Misc Shims					\$ 15.00
Misc Screws					\$ 100.00
Welding Labor					\$ 2,100.00
Assembly Labor					\$ 600.00
ATP Labor and Consumables					\$ 2,250.00
				Projected Unit Cost	\$ 10,705.00

Details Not Provided

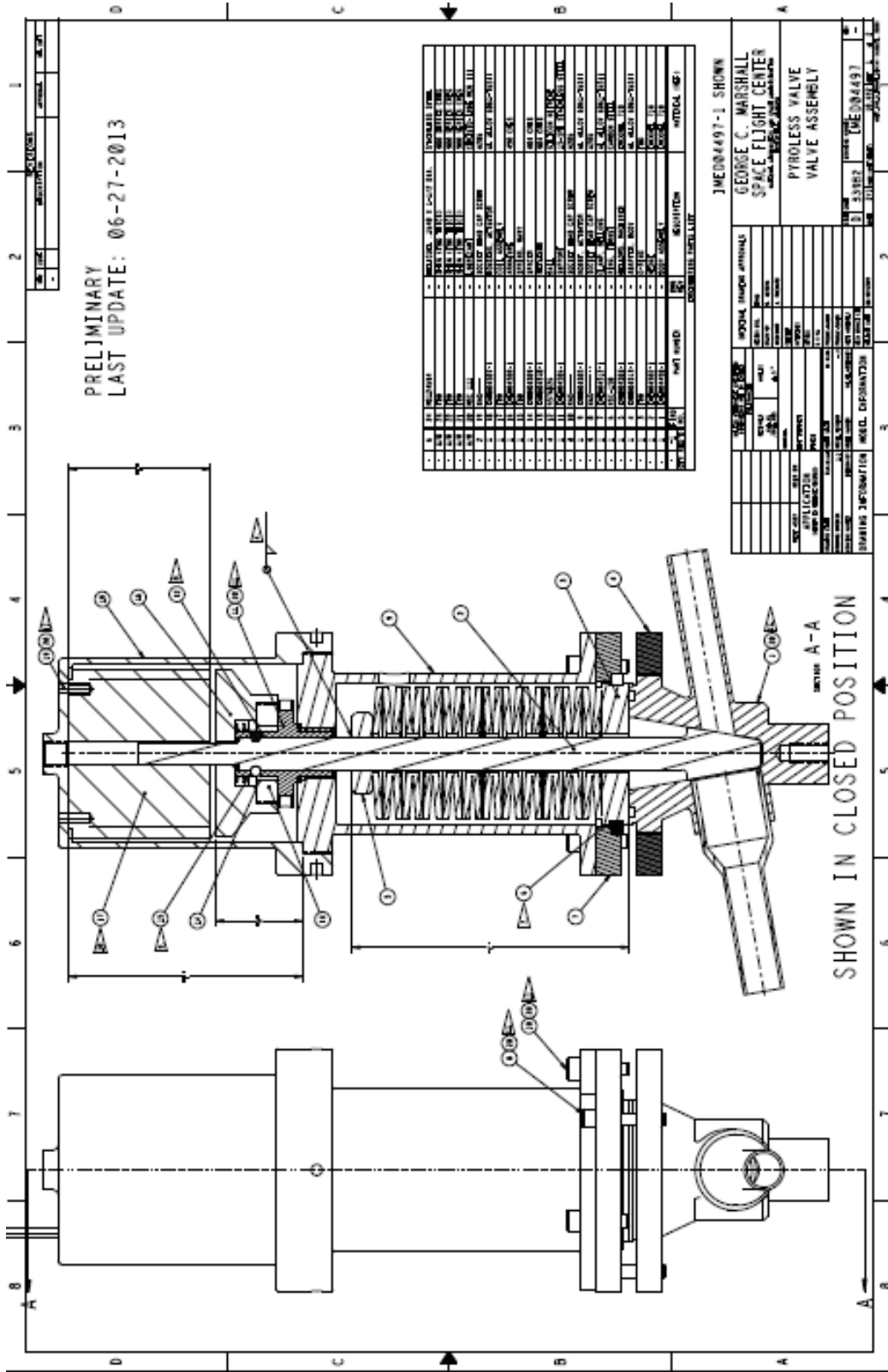


Figure 8. Final Drawing

Conclusions

The MSFC hermetically-sealed valve has been shown to meet the general requirements as a replacement for traditional pyrotechnic valves. The valve design offers the potential of being cost

competitive with pyrovalves at the component level. If this is true, the systems utilizing these designs could potentially save millions of dollars relating to simplification of system architecture design, qualification, and operations.

Cost and reliability data is to be determined from a follow-on task that is currently being worked at NASA/MSFC.

Discussions with several projects have indicated interest in this concept and an e-mail from the Project Manager of the Lunar Prospector Project has suggested that with more cost and reliability data, it could be considered as a flight alternative for their low-cost project.

A valve vendor has been shown the concepts and they have expressed interest in using some of these concepts in their product line. They would also like to see additional cost and reliability data. They have provided a letter stating this interest.

#### Publications and Patent Application

Three NASA Technology Report (NTR) disclosures have been submitted.

1. The unique latch system was submitted as an NTR. The application of a standard ball release appeared to be a unique design.
2. The retractable wedge support system for the disk was considered unique. No other systems like this were found, so an NTR was submitted.
3. The use of the two previous innovations makes the valve itself a unique design, so an NTR was issued for the valve concept.

These NTR's will be evaluated to determine the uniqueness and patentability of the design(s). MSFC submitted a final report on the two designs (MSFC and GSFC valve) in late November 2013 to the funding organization.

#### Status of Investigation

The final steps required to complete this effort include final machining of the undelivered parts, assembly, and the noted basic testing. This should be performed before February 2014.

#### Planned Future Work

Production of a complete lot of valves for testing and evaluation focused on the manufacturing costs, reliability, and performance necessary to meet projected goals. This effort was submitted as a follow-up TIPs proposal. If not funded in FY14, it will be submitted again in FY15. Additionally, the proposal was submitted to the ED Technology Excellence committee for potential funding. If the TIPs follow-on is not awarded, then the TE board has said that it will fund this effort.





## DRAGON - 8U Nanosatellite Orbital Deployer

Marcin Dobrowolski\*, Jerzy Grygorczuk\*, Bartosz Kędziora\*, Marta Tokarz\* and Maciej Borys\*

### Abstract

The Space Research Centre of the Polish Academy of Sciences (SRC PAS) together with Astronika company have developed an Orbital Deployer called DRAGON for ejection of the Polish scientific nanosatellite BRITE-PL Heweliusz (Fig. 1). The device has three unique mechanisms including an adopted and scaled lock and release mechanism from the ESA Rosetta mission MUPUS instrument. This paper discusses major design restrictions of the deployer, unique design features, and lessons learned from development through testing.

### Introduction

BRITE Constellation is a group of scientific nanosatellites whose purpose is to study oscillations in the light intensity of the most luminous stars (brighter than magnitude +3.5) in our galaxy. The observations will have a precision at least 10 times better than achievable using ground-based observations. The BRITE (BRight Target Explorer) mission formed by Austria, Canada and Poland will send to space a constellation of six nanosatellites, two from each country. BRITE-PL satellite is based on the Generic Nanosatellite Bus (GNB) from the Canadian SFL/UTIAS (Space Flight Laboratory / University of Toronto, Institute for Aerospace Studies). The spacecraft are to use the SFL XPOD (Experimental Push Out Deployer) as a separation system.

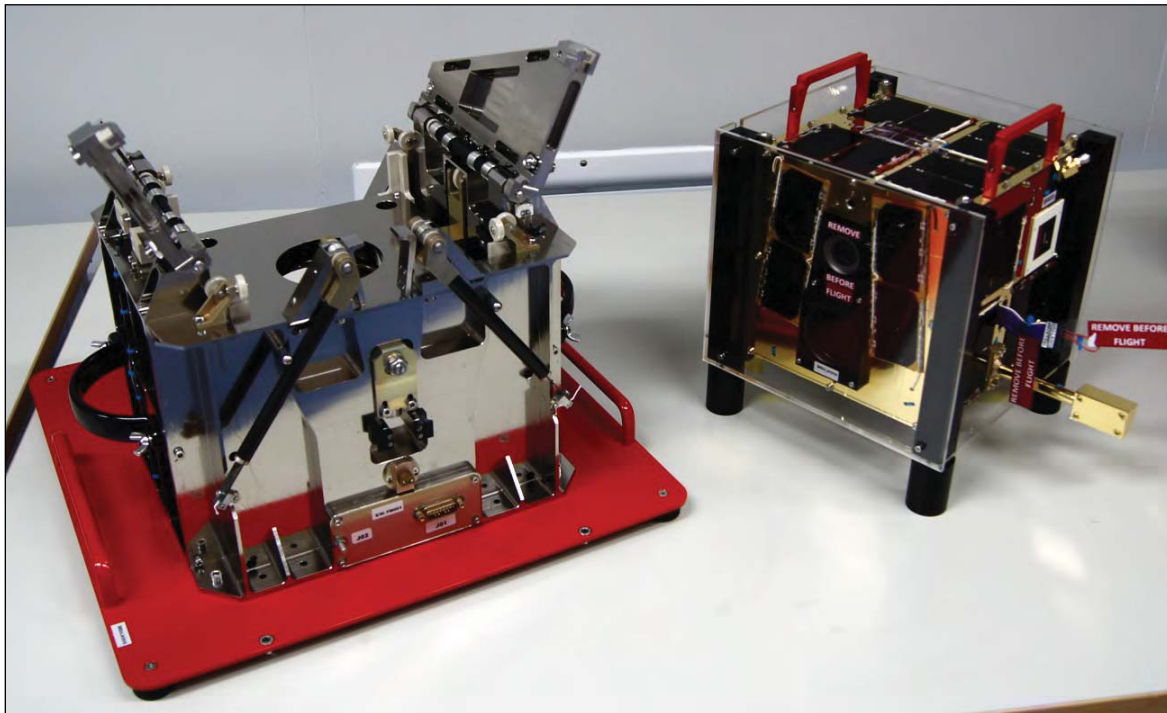


Figure 1. DRAGON Orbital Deployer and BRITE-PL Heweliusz Spacecraft (in a safety box)

\* Space Research Centre of the Polish Academy of Sciences, Warsaw, Poland

The first scientific satellite, BRITE-PL Lem, is a modified version of the original SFL design. The second one, BRITE-PL Heweliusz, has the significant changes – it carries additional technological experiments implemented by SRC PAS. Lem satellite was launched into orbit on November, 2013 as a secondary payload, using the XPOD, on a Dnepr vehicle from the Yasny Cosmodrome. Heweliusz will be launched from China by a Long March 4B rocket. In regards to its launch, a decision was made not to use XPOD and to develop a Polish-made separation device. The lack of a compatible device on the market prompted SRC to propose its own design.

### Overview of Nanosatellite Deployers

To speed up and simplify placing nanosatellites in orbit in a cost effective way, a few standards and rules of building nanosatellites was established. The smallest standard unit of nanosatellite, so called 1U CubeSat, is a spacecraft that is a 10-centimeter cube with a mass of 1 kilogram. Each larger standard nanosatellite is a multiple of one unit. The first CubeSats were launched in 2000, with many more having been launched since then on a myriad of different launch vehicles. To facilitate the launch of nanosatellites as a secondary payload, several orbital deployers have been developed.

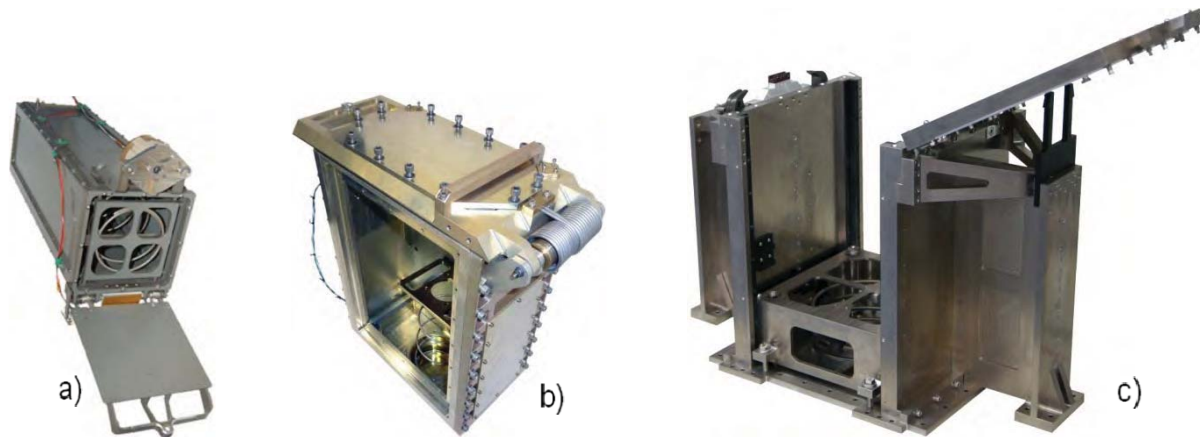


**Figure 2. Popular nanosatellite deployers: a) CalPoly 3U P-POD; b) NASA WWF 6U Deployer (with one wall removed); c) SFL 8U GNB X-POD**

Being first, California Polytechnic State University developed the Poly Picosatellite Orbital Deployer (P-POD), which became a virtual industry standard. Shown in Fig. 2a, the P-POD accommodates three CubeSats in a linear configuration of individual satellites but also combinations of satellites occupying the same volume, including a single 3U (triple-unit) CubeSat. By using the entire dispenser, a 3U CubeSat can have a maximum length of approximately 34 cm and mass of 4.5 kg. A similar but larger deployer is the NASA Wallops Flight Facility (WWF) 6U Deployer, which is able of carrying a 10x23x35-cm cuboid payload with a maximum mass of 12 kg (Fig. 2b). Both are characterized by a closed structure that does not allow for the projection of any part of the satellite outside the container and block electrical noise. A little different ejector is designed by SFL. Shown in Figure 2c, XPOD has a partially open structure, which allows the ejection of satellites with sticking out elements beyond the outline of the deployer. XPOD is designed to carry a GNB-type satellite platform that has the shape of a cube with dimensions of 20x20x20 cm, an equivalent of 8U and mass of around 7 kg. Common features of these three deployers include satellite sliding along guide rails during ejection pushed by a pusher plate that is driven by a linear spring. Other features are a single satellite clamp plate with a hinge on one side and a lock and release system on the other side. During launch, the spacecraft structure is maintained in tension by locking pins located in corresponding sockets on the top and bottom of the spacecraft.

## Design Requirements

The DRAGON project was subject to a very tight schedule. Satellite requirements included size, ejected mass, ball-pin interfaces, and protruding elements like UHF antennas and a magnetometer. The Launcher requirements included spacecraft deployment speed less than 1.5 m/s; electrical signal for releasing to be 0.6 A for 10 sec at  $28 \pm 4$  V; telemetry signals indicate door opening and spacecraft escape; up to 12 g of overload level; and a shock of 1000 g. Since original plans assumed the usage of XPOD, the launch provider supplied an interface bracket mounted to the main spacecraft adapter, which followed XPOD-like footprint guidelines. This resulted in constraints such as the mounting hole arrangement, limited overall deployer dimensions, and lower dry mass, which was almost 10 kg in the case of the XPOD.

## Mechanical Design

DRAGON deployer design includes three main mechanisms: a pushing platform, doors with latches, and the hold down & release mechanism (HDRM). The deployer structure is made of a nickel-plated 7075 aluminum. It consists of four walls connected at the bottom by a thinner panel. Two opposing side walls provide hinge support and the front wall provides mounting for the HDRM. The general view of the deployer is shown in Figure 3.

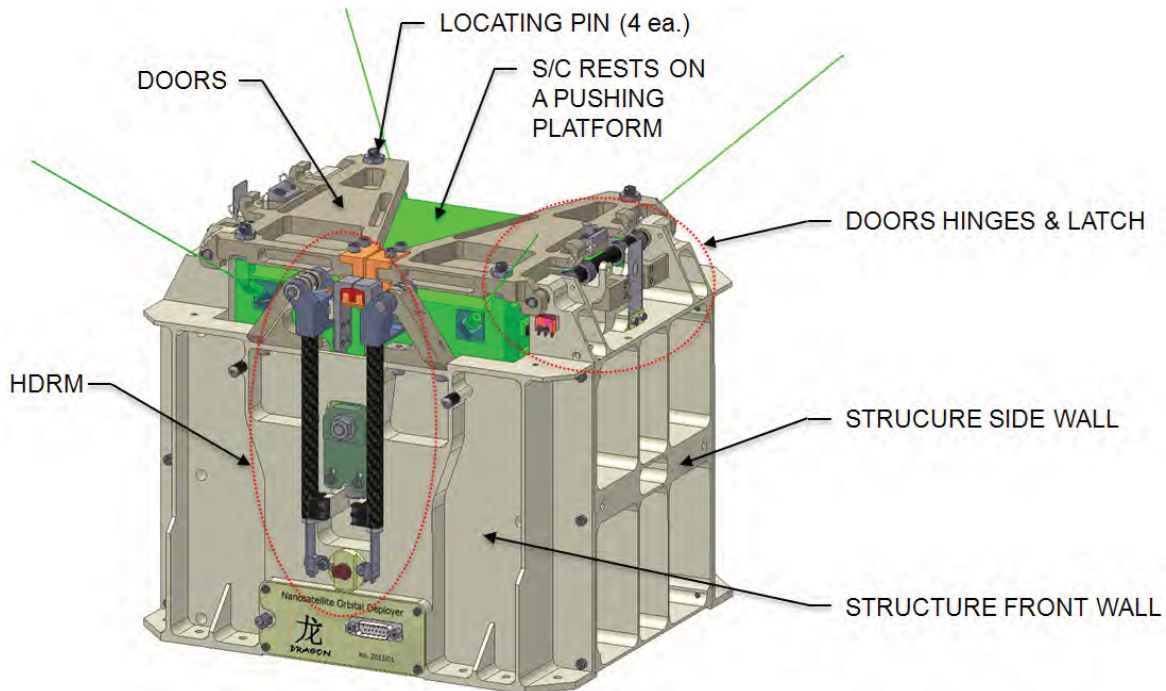


Figure 3. DRAGON CAD model (in stowed position)

### Pushing Platform

Although BRITE-PL Heweliusz has a structure suitable for sliding along guide rails, it was decided not to apply this solution. In order to protect the spacecraft better during deployment, a sliding motion along rails was replaced by a rolling motion. This is accomplished using a pushing platform shown in Figure 4a. The platform consists of an aluminum base to which are mounted two sets of wheels located opposite to each other. Wheels roll in a groove in the structure's side panels (Fig. 4b). In the stowed position, four conical elements are touching the sockets in the base panel of the structure, thus transferring all loads. The spacecraft is located on the platform base in the appropriate slots, and safety brackets prevent it from sliding off. The energy needed to eject the satellite is stored in a conical spring located between the



platform base and the bottom plate of the structure. A conical spring was used instead of a simpler linear spring to decrease its length in the stowed position, which resulted in a reduction of height of the ejector as well as its mass. Initial force of the spring is 83 N. The pushing platform end positions are shown in Figure 4c.

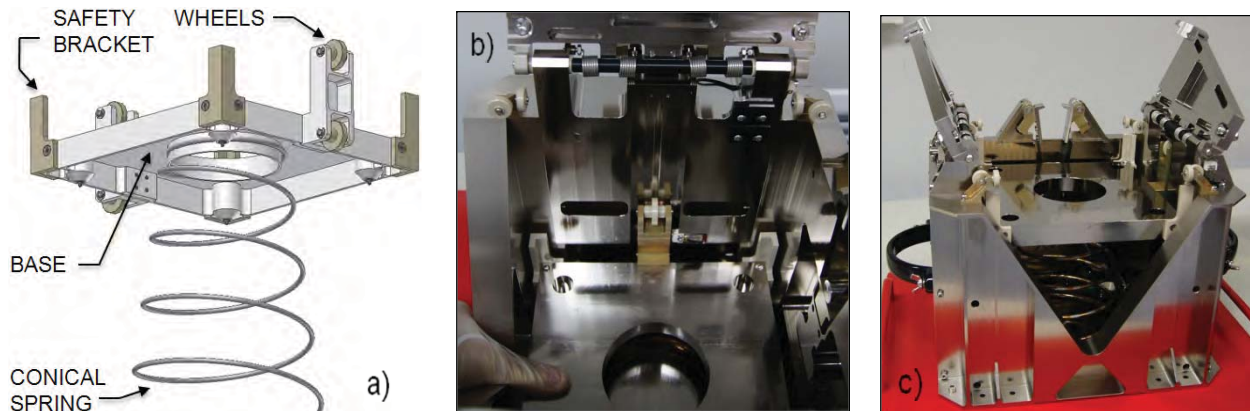


**Figure 4. Pushing platform: a) main components; b) view of the initial position; c) view in the deployed position**

#### Doors with Latches

From the top, the spacecraft is secured by locating pins fastened in a pair of symmetrical doors containing their own latches. The doors are equipped with locking brackets on one side and are driven by hinges, attached on the opposite side.

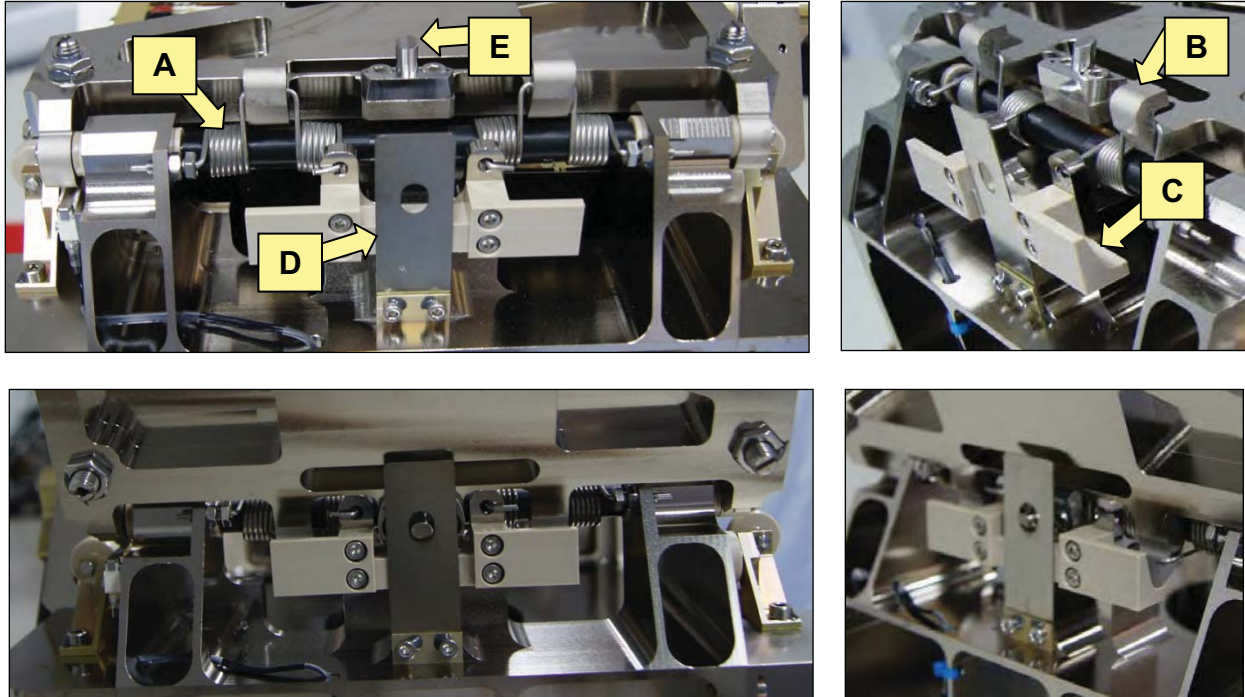


**Figure 5. DRAGON door hinge and latch in the initial (top) and locked position (bottom)**

Figure 5 shows one of two pivotally mounted doors which opens rapidly due to the torque from two double torsion springs (A). To slow down the opening of the door, friction was used to act between a



specially profiled bracket (B) to which a hinge spring hook was attached and a plastic wedge (C) attached to the structure side wall. The wedge element is also used as a soft stop component. To prevent violent door bouncing and subsequent satellite damage, the latching system is used. The latch works with the leaf spring (D) which, when pressed by the moving door deflects until the latch pin (E) slips into the hole in the leaf spring. Thus the door is caught, preventing the rebound and stays wide open at an angle of 110 deg. A microswitch is used to verify and confirm door opening.

#### Hold Down & Release Mechanism (HDRM)

To hold the door during take-off, a very reliable HDRM was used, which is released by the Dyneema cord melting system. This type of lock and release mechanism has been tested during the ESA Rosetta mission preparation of the MUPUS instrument. In DRAGON, the mechanism, shown in Figure 6, has been scaled to meet higher loads.

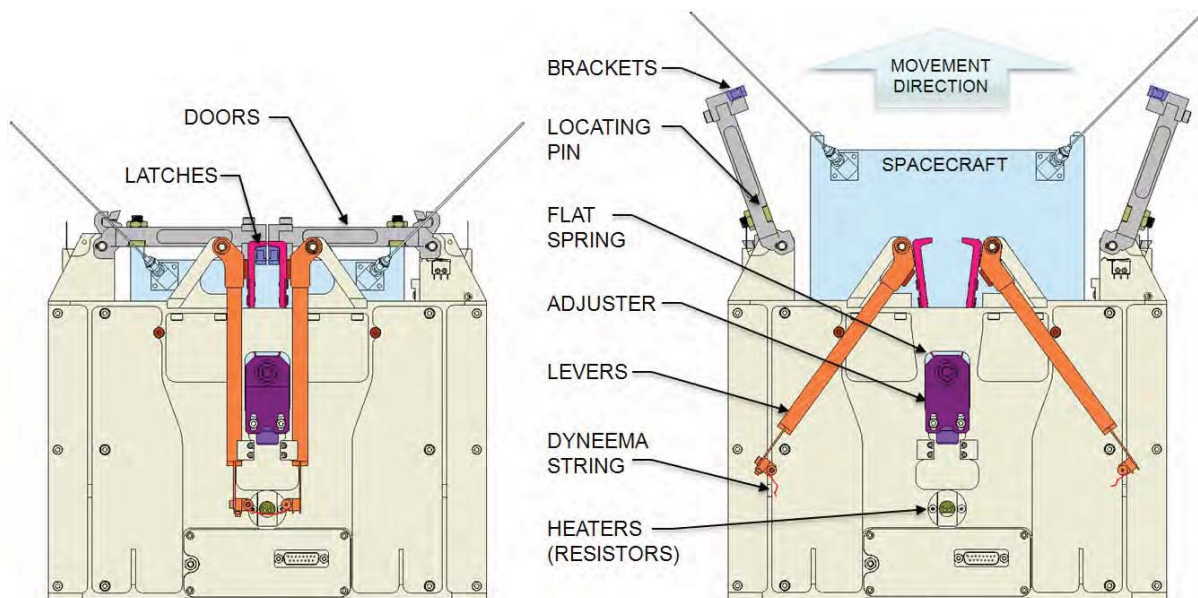


**Figure 6. DRAGON Hold Down & Release Mechanism principle of operation shown in stowed (left) and released (right) position**

When stowed, the doors are held by latches mounted to the tensioned elastic flat spring and adjusted by tightening an M10 screw that changes the position of an adjusting element with respect to a structural wall. Latches are held in place by the levers constructed of carbon fiber tubes (to decrease its mass and inertia). At the ends of the levers, flat springs are provided with attachments for the Dyneema string. The use of these flat springs guarantees the mechanism not to loosen during Dyneema creep. Therefore, it is possible to use a string with a small diameter (0.5 mm) that is easy to melt with little power. Melting of the Dyneema string releases the levers rotated by torsion springs, which allow the latches to slip from the door brackets and thus letting the doors open. The clamp ratio between shear pins and Dyneema string for this mechanism is 200:1.

#### **Test and Qualification**

The Dragon deployer passed a full series of tests, beginning with functional and ending with environmental. Functional tests have been carried out on the existing test bench located at SRC, to actively simulate the lack of gravity and were recorded by high-speed camera. A system, shown in Figure 7, uses a spring that generates constant torque and is able to compensate the impact of gravity acting on the suspended object. The system relies on feedback from a force sensor that is turned on by the PID controller that sends a signal to a DC motor, which adjusts the tension of the spring tape by

appropriate rotation. During the test, a spacecraft mass model mock-up was used. The mock-up suspended on a rope was ejected from the deployer located below the test stand. Motion of the satellite during ejection is quite a fast phenomenon. Therefore, setting parameters of the PID controller play an important role in simulating zero gravity.

Three tests were conducted with different settings of control parameters. In an ideal case, the satellite ejection speed is increased in accordance with the characteristics of the force generated by the conical spring. The satellite separates from a pushing platform after the pushing action stops. From that moment, the spacecraft should move at the same final speed. Tests results shown in Figure 8 are presented in the form of plots of time vs. speed and speed vs. displacement. They were obtained from the analysis of high-speed camera images.

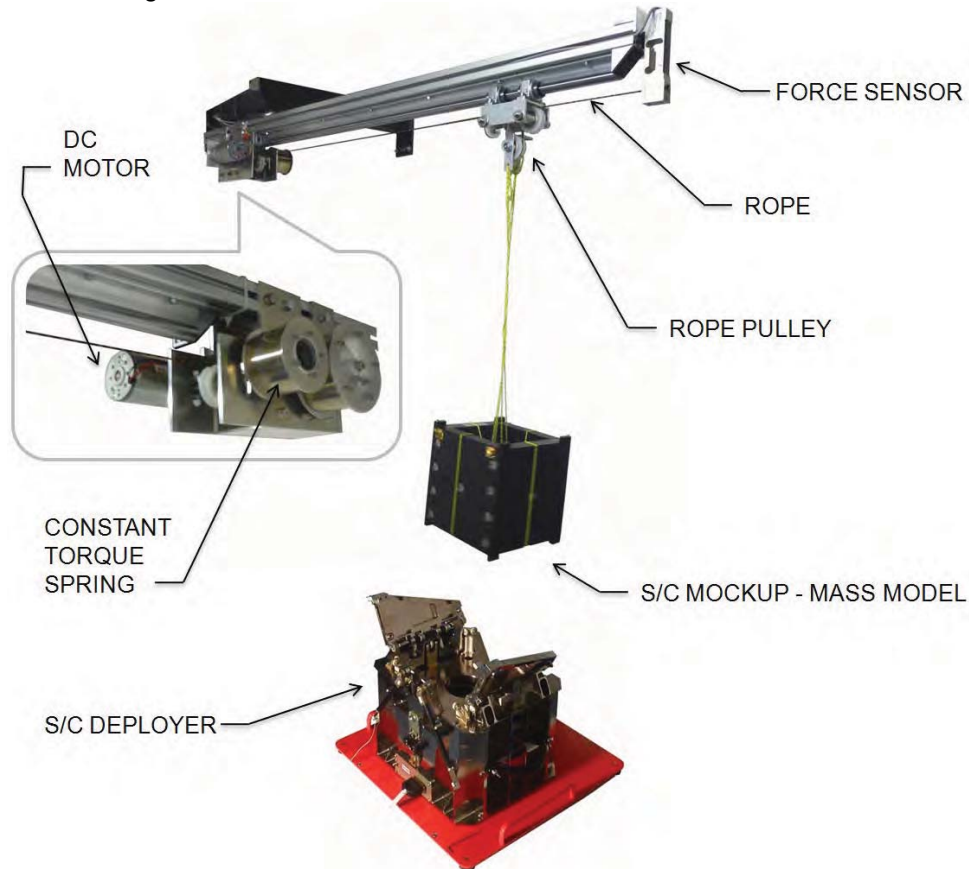


**Figure 7. Functional test stand to actively simulate the lack of gravity**

Triangular marks on the plots indicate the time when a pushing platform reached its end position and thus the point at which the satellite begins free flight. Square marks indicate both time and location when the satellite passes remaining protruding elements of the deployer and is considered to be outside of it.

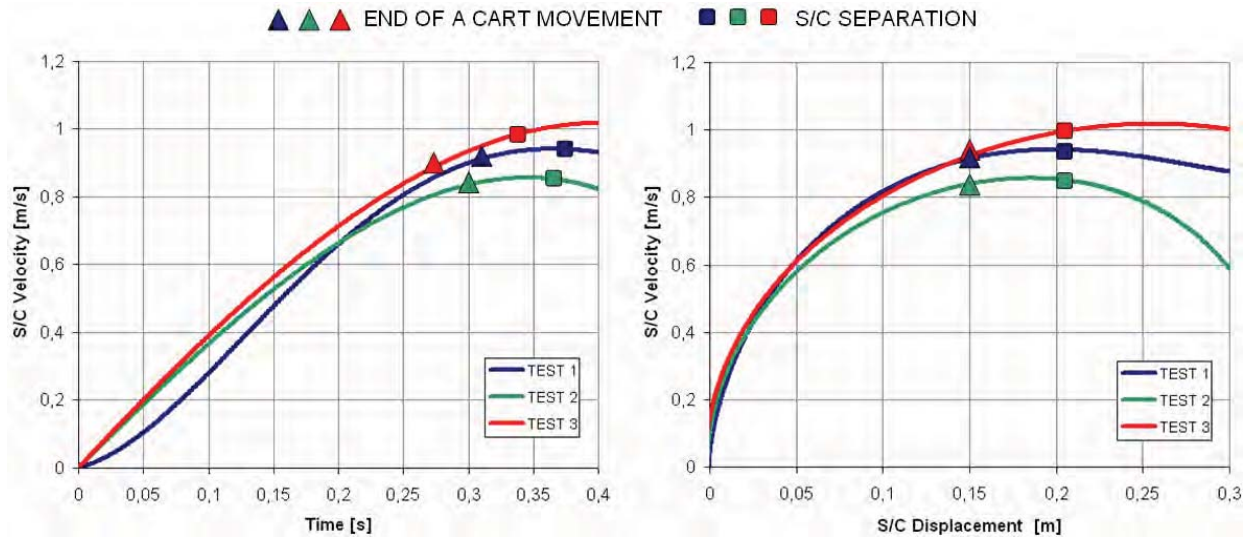


**Figure 8. Satellite ejection speed graphs**

Results from test 1 and 3 best fit the theoretical movement conditions of the spacecraft in zero gravity. Test 2 is characterized by a sudden drop in speed of the satellite after separation which indicates that the mass was not supported adequately. From the time of the doors' release, the pushing platform supporting the satellite moves 150 mm in about 0.3 sec to reach an end speed slightly less than 1 m/s. The speed limit was set at 1.5 m/s and the expected value, which did not take into account motion resistance, was 1.2 m/s. The test demonstrated that assumptions have been met, and a video recorded with a high-speed camera showed that the ejection takes place very smoothly and doors open much faster than the spacecraft is ejected.

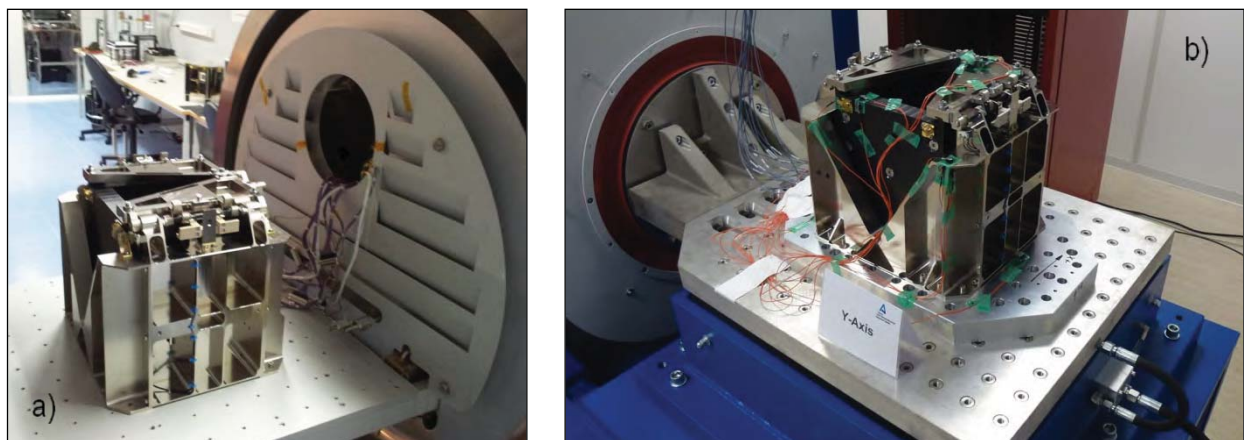


**Figure 9. Deployer qualification tests: a) thermal-vacuum; b) vibration**

The next functional test was performed in the thermal-vacuum chamber shown in Figure 9a. The time of Dyneema string melting and mass model ejection was less than 1 sec at  $-20^{\circ}\text{C}$  and a  $0.0004\text{-Pa}$  vacuum level. There was no destruction or change of resistance of the heating element. DRAGON passed all required vibration and shock tests. No change was observed in resonant frequencies after sine and random vibration. The resonant frequencies in the X and Y axes (the base plane axes) were 205 Hz and 278 Hz in Z axis (along which spacecraft ejection occurs). Light ringing could be seen coming from the deployer main spring.

Finally, a fit check was performed on a launch vehicle. DRAGON was attached to the bracket on the adapter ring between the rocket and the main satellite. A deployment signal was sent from the launch vehicle and the deployer opened safely. Telemetry with sensor confirmation of deployment was sent to the rocket computer.

### **Lessons Learned**

There was not enough time to design a new suitable and reliable separation device or order it from an outside source. In the deployer, a scaled hold down & release mechanism from MUPUS instrument was used. This approach has been proven as reliable. A general lesson connected with this issue is to carefully analyze a scaled device that will be used in a new application. We dedicated a lot of attention to redesign with this new mechanism so it could withstand higher loads. What we did not notice originally was that the MUPUS mechanism levers were arranged in a position towards the operator, while in DRAGON that position was just opposite. The use of components to mount the Dyneema string in a way similar to that used in MUPUS made arming of the mechanism very difficult. So two new redesigned components had to be manufactured.

To cut costs and to speed up the deployer production, all rotating joints used commercially available PEEK flanged sleeve bearings and polished stainless steel (SS) shafts. This combination was also used for latches made from stainless steel pressed against PEEK lever blocks and sliding across PEEK door brackets. Tests showed that such a combination is sufficient for applications working in not too low nor too high temperatures.

Two utility issues have sprung up during the deployer testing with the Heweliusz spacecraft. Both concern satellite safety. DRAGON is not a tightly closed container but has a structure with many open spaces that could expose a spacecraft to danger. Also, deployer doors have open cutouts to save mass. This causes the possibility of damage in case of an unintended fall of some piece on spacecraft solar cells during locating pins set up. To avoid it, suitable ground-use covers were designed to protect the satellite. In Figure 10, the satellite integration procedure is shown on the left and the deployer with a safety cover on the right.

DRAGON, different from other separation ejectors, is equipped with a pushing platform. Satellite structure rails are not supported. This results in a possibility of hitting satellite parts, for example solar cells, during satellite insertion into the deployer. To prevent this, four wheel assemblies were added in every corner with a 1-mm gap between the spacecraft and every wheel. Figure 11 shows wheel assemblies that also help to provide a very stable low friction guiding during satellite deployment.



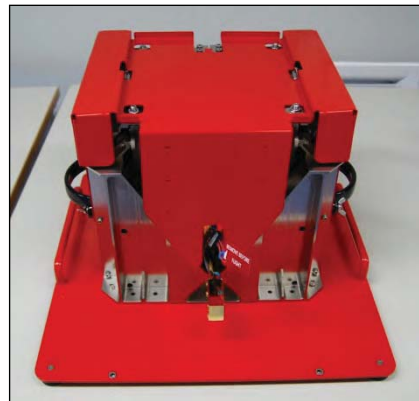
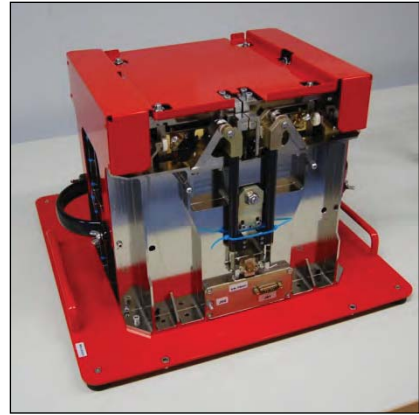
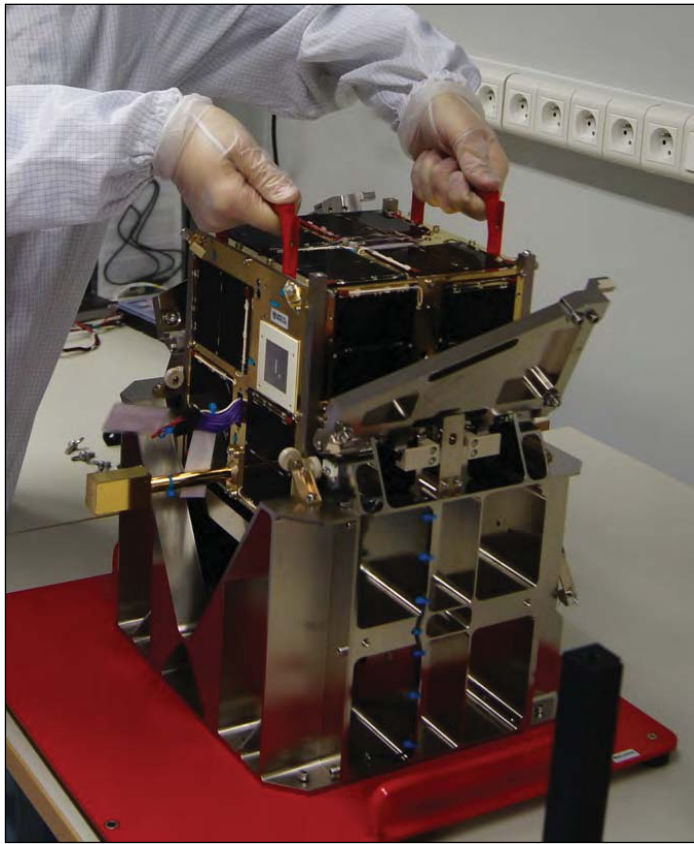


**Figure 10. Spacecraft insertion procedure (left) and ground-use cover (right)**

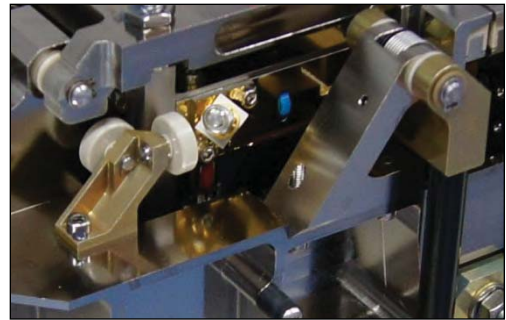
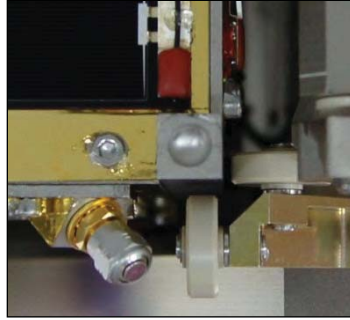
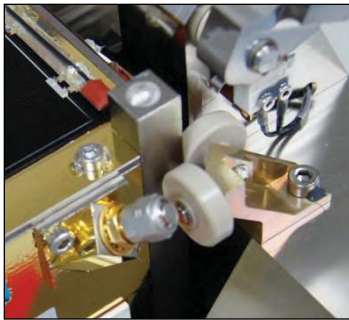


**Figure 11. Wheels assemblies added for spacecraft safety during insertion**



## Conclusions

A nanosatellite orbital separation device was designed, manufactured, assembled and successfully tested. The overall dimensions of the deployer are 282x320x287 mm and its mass is 7.2 kg. It is able to deploy a small cuboid BRITE-PL Heweliusz spacecraft of dimensions 200x200x200 mm and mass of 7 kg.

Commercially available standard orbital deployers are usually developed with particular spacecraft in mind. DRAGON separation device was developed with a target to satisfy preexisting specific constraints. The mass ratio of DRAGON deployer to satellite is about 1. In the author's opinion, such a system should have a mass ratio less than 0.8, preferably 0.5, and that is possible to achieve with a closed-type deployer and structure optimization. Figure 12 show graphs where masses of aforementioned popular deployers and Dragon are plotted. In the deployer mass vs. payload mass graph (left ) markers that represent standard American-made container-type ejectors are joined by a line (CalPoly P-POD 3U and NASA WWF 6U). If we take this line as a determinant of representative orbital deployers, it turns out that the ejector designed for 7 kg payload should have a mass of about 5 kg.

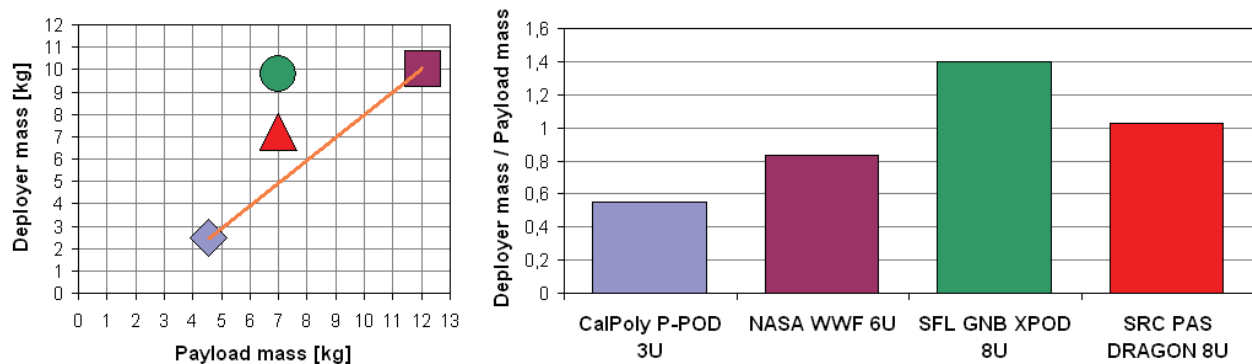


**Figure 12. Deployers mass vs. payload mass that they are able to eject**

General conclusion: it is very hard to design, manufacture, integrate and test a space device in two months. It is even more challenging during the holiday period which was the case of DRAGON development. But all this was possible with a well-motivated team that was using solutions already proven and previously tested during development of the space instruments in SRC PAS.

## References

1. Dobrowolski M., Grygorczuk J. "Lock and release mechanism for the CHOMIK penetrator device and its tribological properties" *Proceedings of the 41st AMS*; NASA/CP-2012-217653 pp. 29-37
2. Grygorczuk, J., Banaszkiewicz, M., Seweryn, K., Spohn, T. "MUPUS Insertion device for the Rosetta mission" *Journal of Telecommunications and Information Technology* (1/2007), pp50-53.
3. Toorian A., Blundell E., Puig Suari J., Twiggs R. "Cubesats as responsive satellites" *Proceedings of the 3rd Responsive Space Conference 2005 AIAA-RS3 2005-3001*
4. Thompson L. D. "Development of a NASA 6-U Satellite" *Proceedings of the 25th Annual AIAA/USU Conference on Small Satellites SSC11-X-8*

# Mechanism Design and Testing of a Self-Deploying Structure Using Flexible Composite Tape Springs

Joseph N. Footdale\* and Thomas W. Murphey\*\*

## Abstract

The detailed mechanical design of a novel deployable support structure that positions and tensions a membrane optic for space imaging applications is presented. This is a complex three-dimensional deployment using freely deploying rollable composite tape spring booms that become load bearing structural members at full deployment. The deployment tests successfully demonstrate a new architecture based on rolled and freely deployed composite tape spring members that achieve simultaneous deployment without mechanical synchronization. Proper design of the flexible component mounting interface and constraint systems, which were critical in achieving a functioning unit, are described. These flexible composite components have much potential for advancing the state of the art in deployable structures, but have yet to be widely adopted. This paper demonstrates the feasibility and advantages of implementing flexible composite components, including the design details on how to integrate with required traditional mechanisms.

## Introduction

Current efforts in advancing the art of deployable structures include developing deployment architectures that maximize the packaging efficiency while minimizing mass and satisfying dimensional stability constraints. A number of developed and conceptual architectures are making such advancements with the implementation of flexible Fiber Reinforced Polymer (FRP) composite laminate components in place of traditional hinge and latching mechanisms. The Air Force Research Laboratory (AFRL) Space Vehicles Directorate has developed multiple deployable architectures [1-3], including a boom [4] that employed rollable composite tape spring members. These example structures also utilized the stored strain energy of the structure in the packaged configuration to provide the motive force to drive the deployment, eliminating the need for external energy sources (motors or springs for example). The tape spring members are similar in shape and functionality as the Storable Tubular Extendable Member (STEM) boom [5]. The difference lies in the engineered laminate design that allows the tape spring to tightly wrap around a cylindrical drum without requiring containment mechanisms or shroud to prevent radial billowing during deployment. FRP composite laminates are the preferred material because of the increased strain capability, higher modulus, lower mass, and increased dimensional stability over conventionally used metallic materials for flexure applications.

This paper presents the design and testing of a novel, self-deployable support structure that implements rollable composite tape spring members. The structure is a departure from existing architectures due to the synchronous deployment of the structure in three dimensions simultaneously. The synchronous deployment is achieved without any mechanical components to enforce the desired kinematics. This was accomplished through a combination of a tape spring laminate and geometry and constraint mechanism designs. When compared to the relatively large number of mechanisms and support components required in traditional systems to enable the deployment of a three-dimensional structure, the freely-deploying architecture presented offers significant advantages with respect to complexity (and associated cost) and performance.

---

\* LoadPath, Albuquerque, NM

\*\* High Strain Dynamics, Phoenix, NY

A CubeSat-scale telescope with a membrane primary optic was selected as an example three-dimensional deployment application to demonstrate the flexible composite technology. The primary objective of this effort was to design the tape springs and determine the required mechanisms to develop a kinematic functional unit. There are many features required for an operational CubeSat payload not designed in detail, such as a primary deployment stage that would be required to translate the telescope from the bus interior such that the extendable booms do not impinge the CubeSat walls. These features were a factor in the design of the deployment mechanism and fixtures of the prototype unit, such that there is a feasible transition from the prototype to a flight system. This is the first known documentation of the fabrication and demonstration of this specific class of a three-dimensional deployable structure featuring flexible composite mechanisms. Two papers [6,7] regarding this structure were previously published and presented that primarily focused on the overall structure and membrane design for the deployable membrane telescope. This paper describes in detail the designs of the mechanisms required to enable successful operation of the structure and aims to serve as a design guide for integrating flexible composite components in existing or conceptual deployable structure architectures. The detail mechanical design of the mechanism is first described. An overview of flexible composite research is then presented along with the tape spring laminate and geometry design. Results of the functional deployment tests are discussed next, followed by the lessons learned from this effort.

## **Mechanism Design**

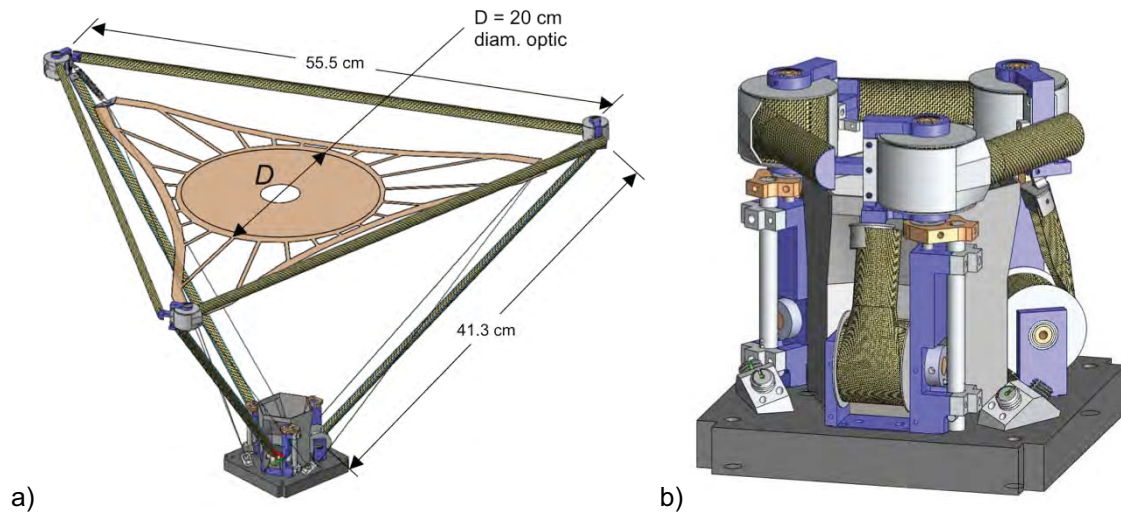
### Design Summary

The telescope design in the deployed and stowed configurations is illustrated in Figure 1. The deployable structure subsystem consists of a planar tri-member frame (“top frame”) that is extended from the base mechanism by three deployable booms. Three pull points to tension the membrane was selected because this represents the minimum number to uniquely define a plane. Introducing additional pull points creates an over-determined set that will introduce out-of-plane deformations in the membrane if all points are not precisely located on the nominal plane. The positions of the membrane pull points are controlled by high-stiffness bipedal lanyards at each corner location. The membrane corner pull points are attached to the deployable support structure by high-compliance decoupling spring. Membrane tension is then set by the deployed structure dimensions. A decoupling spring with relatively high compliance reduces the tension sensitivity to the structure dimensional stability. The support structure in this effort was designed to deploy and position a 20-cm-diameter optic with an f-number of 2, and stow within 1U (10 cm x 10 cm x 10 cm) CubeSat volume. The associated compaction ratio to achieve this objective is traceable to the requirements of desired larger diameter applications. The assembled system stows into a volume of 9.4 cm x 9.4 cm x 8.3 cm tall with an assembled mass of 133 g. All tape spring members had a semi-circular cross section and radius of 5.56 mm.

### Tape Spring Hub Mechanism

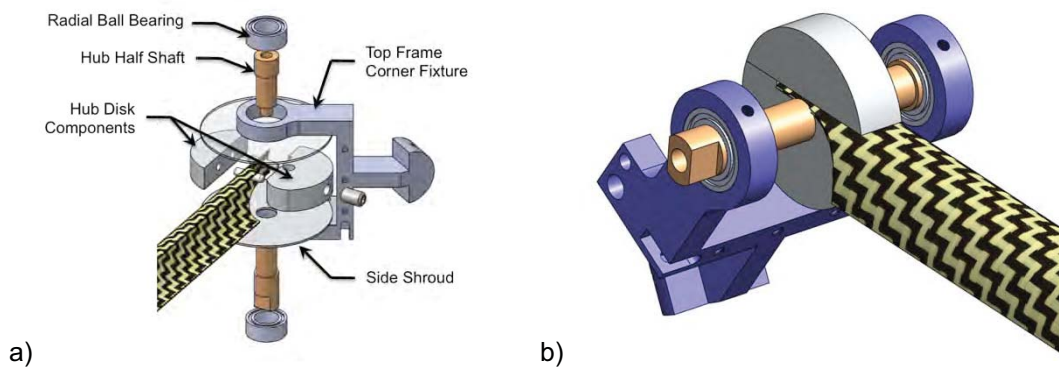
The deployed structure shown in Figure 1 is fully determinant when using only pin-type joints at the tape spring ends. This allows elimination of any latching mechanism for each tape spring at full deployment. The hub mechanism is a simple bearing-supported shaft free to rotate. Exploded and assembled renderings of the top frame hub corner assembly are shown in Figure 2. The tape spring hub assembly is identical for the top frame members and the booms mounted to the base plate. The only difference is in the design of the hub assembly mounting fixture. The central hub disk is fabricated from two pieces that clamp the tape spring end. Hub disk and tape spring components are aligned using two dowel pins and the assembly is bonded with adhesive. The hub disk controls the tape spring roll diameter in the stowed state and mates with the hub shafts, which are concentric with the hub disc. Thickness of the hub disk was kept to a minimum to keep the rotary inertia low during deployment. The geometry and laminate of the FRP composite tape spring are designed such that no containment devices are required to maintain a tight roll of the tape spring around the central hub disk while stowed or during the deployment process. Circumferential and side containment shrouds (circumferential shrouds not shown in Figure 2 for clarity) are included to prevent anomalous deployment events. The side shrouds are circular disks that mounted to the hub shafts and rotate with the tape spring roll. This basic shroud design was first implemented in

the SIMPLE boom [4], which demonstrated effective functionality. The design was adapted for this application. Further details on the tape spring design are described in a later section below.



**Figure 1. Membrane optic prototype support structure in a) deployed and b) stowed configurations.**

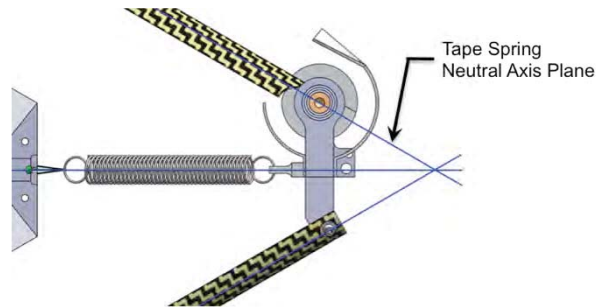
Each tape spring is subjected to a compression load at full deployment to react the design tension in the membrane optic. To eliminate the need of a rotation lockout mechanism for the hub assembly at full deployment, the tape spring neutral axis must be coincident with the shaft axis (see Figure 3). This prevents an induced moment at the hub axis from the eccentric loading, which may result in hub rotation if the moment is greater than the tape spring bending stiffness. The same principle determines the required location for the mounting of the adjacent tape spring end, also shown in Figure 3. The intersection of the tape spring neutral axes is coincident with the membrane loading vector, which bisects the angle formed by tape spring neutral axes and is normal to the edge of the membrane end tab.



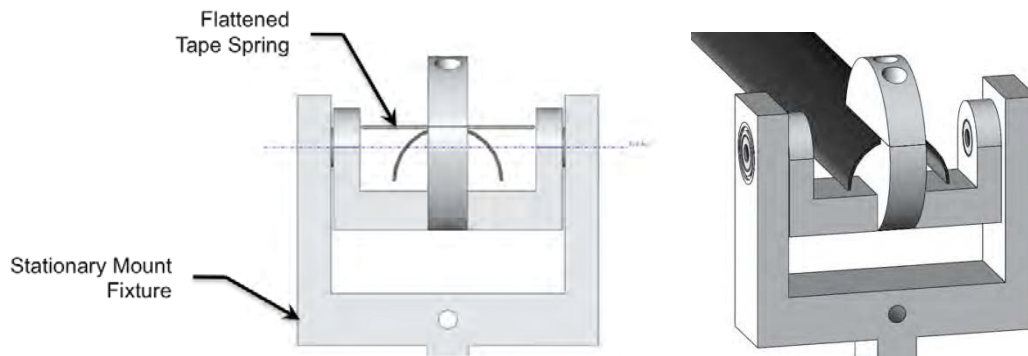
**Figure 2. a) Exploded and b) Assembled renderings of top frame corner hub.**

The tape spring is located within the central hub to minimize the overall strain in the transition region from the clamped end to the final roll diameter. This mounting position, in addition to constraining the tape spring roll axis to be concentric with the hub shaft axis, results in interference between the tape spring and the hub rotation axis in the fully deployed state. The first option considered, illustrated in Figure 4, eliminates this interference with a U-shaped fixture fastened to the hub disk. This allows the tape spring

to flatten during rolling. The assembly center of gravity was designed to be coincident with the rotation axis as to not induce dynamic imbalance loads during deployments. This design was not selected since the overall width of the hub fixture resulted in the system dimensions to exceed the 1U CubeSat volume requirement.



**Figure 3. Top frame tape spring neutral axes locations.**



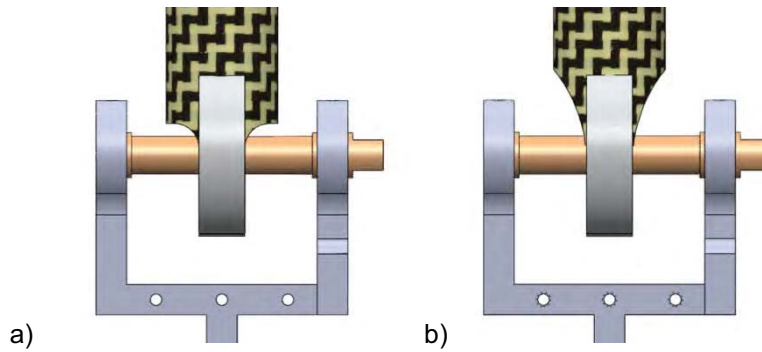
**Figure 4. Tape spring hub mechanism design concept requires no clearance trimming**

Figure 2b) shows the selected design of trimming the tape spring end to clear the hub shaft. The tape spring clearance cut geometry has a significant effect on the deployment torque and despite only a small reduction in deployed buckling strength [7]. A tight clearance cut, shown in Figure 5a), will maximize these parameters. Fabricated prototypes with this trim profile were observed to have a high failure rate in the radius cut region during rolling of the tape spring. This configuration could be successfully rolled if the tape spring is initially flattened. Sufficient available torque and buckling margins allowed for a more gradual taper cut, shown in Figure 5b), which provided a robust solution capable of repeated stow-deploy cycles without special handling requirements. If the fixture dimensions can be accommodated, it is preferred to have a tape spring with constant cross section, i.e. no clearance trimming.

#### Constraint/Release Mechanism

In the stowed configuration, the rotation degree of freedom (dof) of each tape spring hub must be constrained until deployment is initiated. The tape spring laminate was designed such that containment fixtures are not required to prevent the tape spring roll from radially billowing out in the stowed state. However, if the free end of the tape spring is held fixed, but the roll rotation dof is unconstrained or opened, the tape spring is in an unstable state and the tape spring roll will begin to rotate. The constraint and release mechanism components to control the deployment for all six tape spring rolls are shown in Figure 6. To prevent binding and have a synchronous deployment, this constraint must be released from all six hubs simultaneously.





**Figure 5. Two example tape spring end clearance cuts.**

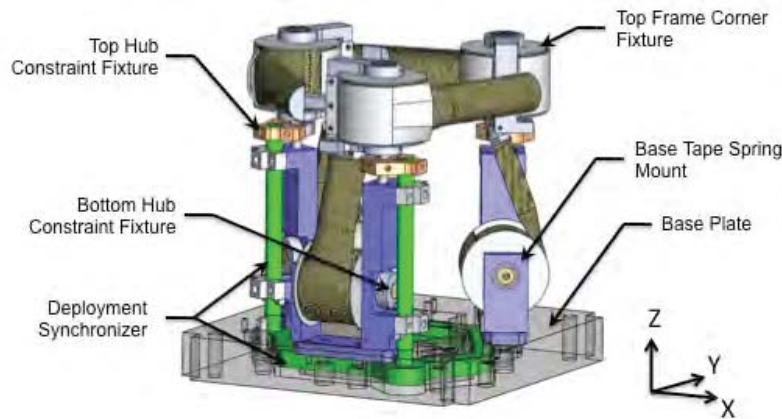


**Figure 6. Constraint mechanism components.**

The boom tape spring hub fixtures are fastened to the base plate equally spaced  $120^\circ$  apart. Each boom fixture is paired with a top frame tape spring hub assembly, which is positioned above the vertical extension. A cylindrical rod controls the deployment of the pair by vertical (Z-axis) motion. The deployment control rods are mechanically coupled via a rigid ring. For this prototype unit, deployment is initiated by manual actuation of the deployment synchronizer ring. Details for the interface of the deployment control rod and the boom tape spring roll is shown in Figure 7. The tape spring hub half shaft protrudes through the fixture wall. A notched, thin cylindrical disk with a slip fit-sized hole is placed on the shaft. The slip disk also contains a radial tapped hole for a setscrew that mechanically couples/decouples the slip disk from the hub shaft. During tape spring rolling, the setscrew is loosened such that the slip disk can remain stationary. The deployment control rod contains a protruding pin. The rod is actuated vertically such that pin fits within the tape spring notch. Once the tape spring is rolled to the desired length, the setscrew is fastened down. The boom tape spring roll is now locked or constrained. Actuating the control rod vertically down clears the pin from the disk notch, which releases the constraint allowing the tape spring to deploy.

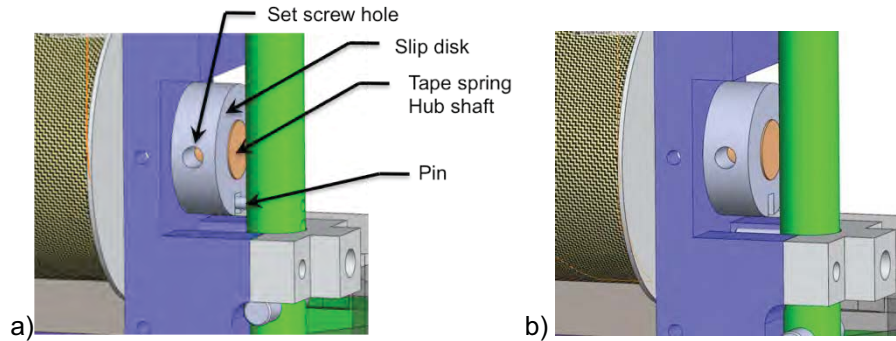


**Figure 7. Boom tape spring constraint design in the a) locked and b) released states.**

A similar methodology is implemented to control the deployment of the top frame tape spring. The operation and design features of the top frame constraint mechanism are best explained by describing the structure stow procedure. The structure starts in the fully deployed state shown in Figure 1a). The top frame tape springs are simultaneously rolled until the relative distances between the hubs approximate the stowed state shown in Figure 1b). The top frame is temporarily constrained using tape or Velcro applied circumferentially around the assembly. The tape spring booms are then simultaneously rolled until the extending hub shaft (Figure 8b) can be placed into the respective slip disks. The temporary top frame constraint is removed to allow manipulation into the slip disks. The boom tape springs are further rolled such that the top frame hubs are preloaded against the vertical hard stop (Figure 8a). The fixture prevents the top frame from deploying at this stage. Each top frame tape spring is then tightened around the hub disk and held, while setscrews in the constraint fixture (Figure 8a) are fastened to lock the rotation. All tape springs are now fully constrained. Actuating the deployment control rod clears the constraint fixture from the tape spring hub shaft (Figure 8b). The height of the vertical hard stop is set such that the top frame and boom constraints are released simultaneously.

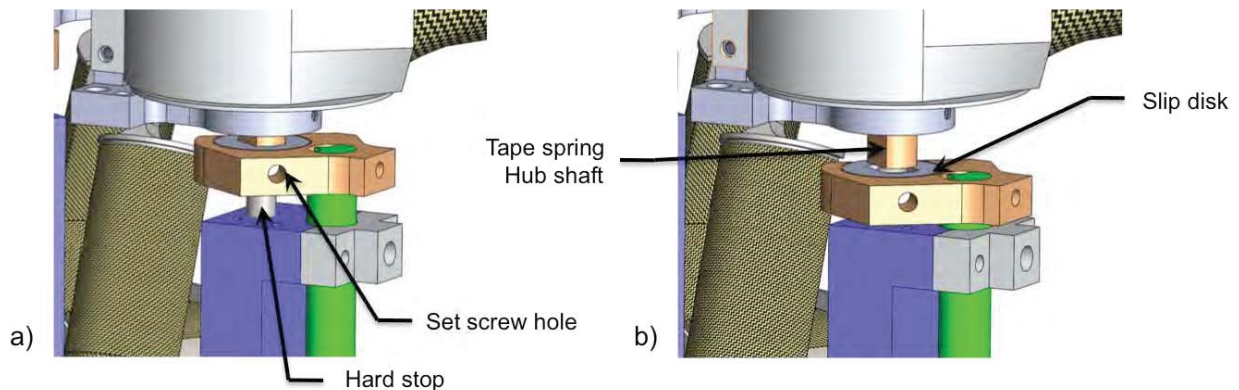


**Figure 8. Top frame hub constraint mechanism design in the a) locked and b) released states.**

### Flexible Composite Components

The flexible composites described for deployable structure applications are traditional stiff matrix composites with traditional aerospace-grade resin systems (977-2 and 8552 epoxies, cyanate esters, etc.). The laminate total thickness is kept relatively small such that it can be subjected to large bending strains without failure. The mechanics of flexible FRP composite have been analyzed and tested

extensively. References [8-14] are a small subset of published work on the subject. This section first presents a summary of the fundamental equations used to estimate the rollable tape spring primary characteristics, such as roll radius and deployment torque, that are fabricated from FRP materials. Current and future research in flexible composites that is needed to have a comprehensive understanding of the underlying physics is then discussed. Finally, details of the tape spring design for this effort are reported.

### Tape Spring Design Basics

Classical Laminate Theory (CLT) describes the linear-elastic relationship between applied loads and the laminate strains by the **ABD** matrix [15]. The terms of the **ABD** matrix are a function of the lamina material properties and the fiber orientations in the construction. For rollable tape spring applications, the terms in the **D** matrix are of particular interest. AFRL Space Vehicles directorate has developed a general composite laminate construction [10] that exhibits high stiffness, is dimensionally stable, and can be subjected to high strains, which are essential characteristics for this class of tape spring applications. Reference 11 provides further details and high strain flexure test data demonstrating laminate performance. The laminate consists of unidirectional plies sandwiched between bias plain weave plies, as illustrated in Figure 9. The unidirectional lamina stores the primary strain energy upon stowage, which drives the deployment upon release. It is also characterized by high axial stiffness, low susceptibility to creep/relaxation along the fiber direction, and relatively low transverse and shear stiffness. The plain weave lamina provides the required transverse/shear stiffness and contributes to laminate transverse bending stiffness. This significantly increases structural stability of the laminate. Due to the bias orientation, the plain weave lamina is subjected to relatively high shear loads under bending conditions. The viscoelasticity of the matrix significantly factors into the response, resulting in very high susceptibility to creep/relaxation. If solely used in the laminate design, it will fail to deploy due to excessive relaxation.

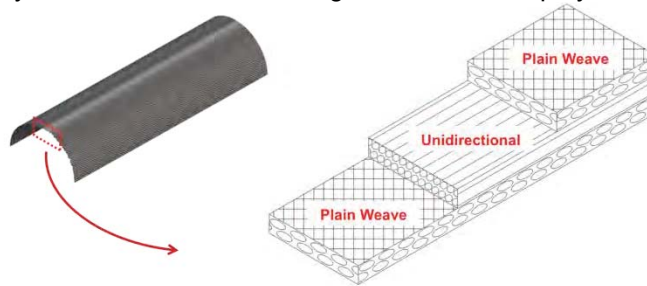


**Figure 9. Typical laminate construction for rollable tape springs.**

Rollable tape springs are fabricated and strain free in the deployed configuration. The defining geometric characteristics (illustrated in Figure 10) are the cross-section radius,  $R$ , subtended angle,  $\beta$ , and overall length,  $L$ . Suitable tape spring laminates for this application will have local minimum strain energy state in the rolled configuration in addition to the other local minimum for the deployed state. This property keeps the tape spring from automatically billowing when in the rolled state without constraint. The corresponding inner stowed roll radius,  $R_s$ , tends to be approximately equal to the cross-section radius, but can be further estimated by:

$$R_s = R \frac{D_{11}}{D_{12}} \quad (1)$$

The central hub disk radius,  $R_H$ , should be set equal to, or slightly larger than  $R_s$ . The tape spring is capable of being wound at a tighter radius without failure, but will billow to the stable radius if not constrained. A strain energy gradient exists between the rolled and the deployed states. To make the tape spring self-deployable, it is constrained in an unstable configuration where free end and rolled sections are in their respective low-energy states. Releasing this constraint allows the tape spring to proceed to the lowest energy state, which is the initial strain-free deployed configuration. The transition is

stable and follows a single kinematic path that manifests as unrolling of the tape-spring. Figure 10 illustrates the transition from the free end that is mechanically held in the deployed state and the tape spring roll section. The unstable transition zone is where the deployment force is generated. Tape spring deployment torque is a weak function of the wrap thickness, which decreases as deployment progresses and is at the minimum right before full deployment where the roll radius is equal to the  $R_H$ . The torque value at this state can be roughly approximated by:

$$\tau = \frac{R_H \beta}{2R} \left[ D_{22} - \frac{D_{12}^2}{D_{11}} \right] \quad (2)$$

The above equations are used to observe the sensitivity of the stowed radius and deployment torque to the laminate construction and initial geometry to aid in the design process. The predicted performance, determined from either the rigorous calculations, such as described in Ref. 8, or through finite element analyses are naturally only as accurate as the input parameters. For example, the results for thin flexible composites have been shown [11] to be highly sensitive to the lamina thickness terms. Simply using the measured cured thickness can result in a significant over estimation of the available torque. The laminates are designed to be relatively insensitive to creep/relaxation effects; however, torque degradation should be taken into account. One method to approximate the long-term available torque is to assume that the in-plane shear modulus terms ( $G_{12}$ ) of the plain weave layers is several orders of magnitude less than the initial value found from CLT. Accurate prediction of this degradation is one area of active study in thin flexible composites.

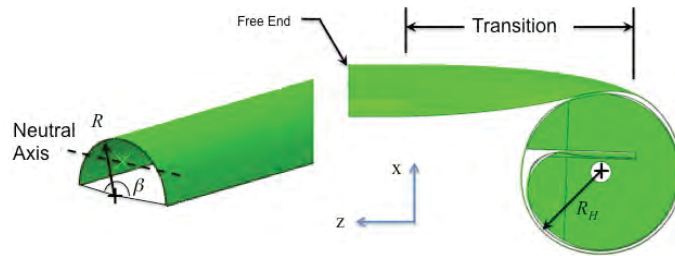


**Figure 10. Geometrics definitions of a cylindrical shell.**

#### Current and Future Research in Flexible Composites

The sizeable body of research and development in flexible composite tape springs enables implementation into space deployable architectures with an acceptable level of risk. The components are constructed with space-qualified traditional fibers and material systems to achieve high strains. Also, space-qualified methods are followed to produce consistent, high-quality parts. Engineering methods to predict bending stiffness/deployment torque have been verified [11] to acceptable accuracy. One remaining critical area of current research is to develop the engineering methods to accurately predict flexible composite strength based on stress/strain state for a given laminate. Large deformation bending of composite materials in flexure routinely yield strain levels not attainable by standard ASTM axial tensile test methods. Traditional thick composites ASTM tests fail in compression at lower strains, where the fibers subjection to tensile loads are the failure mode in bending tests. AFRL Space Vehicles directorate has developed a test and analysis methodology to determine stress/strain state at flexural failure [12]. The method constructs a nonlinear constitutive model of the lamina material based on empirical data from a combination of axial and bending tests. With an adequate understanding of lamina nonlinear constitutive behavior, laminate bending response can be predicted and through thickness stresses and strains can be calculated as a function of curvature and at failure. Material failure criteria can then rationally be developed that are pertinent to the large strains achieved in thin flexures.

Experience has shown that traditional CFRP laminates gradually lose strain energy (deployment force) or change dimensions over time while packaged due to stress relaxation. The laminate can be designed to

reduce the degradation, but this results in a high-energy system that results in an unacceptable shock event upon full deployment. Excessive degradation can lead to deployment failure. A simple means to control deployment rate and avoid shock loads has not been developed. Strain energy deployable structures often employ complex mechanisms that control deployment paths and rates using housings, motors and fluid based dampers. These devices can double the system mass, negating any improvements in structural performance and increasing the system and launch costs. A simple material-based solution is currently being investigated, where a CFRP laminate with discrete *elastic* laminas provides deployment force and *viscoelastic* laminas to passively control the deployment rate of the structure. The challenge here is to tailor the net viscoelastic response for deployment rate control. The proposed idea can be thought of as a spring (provided by the low creep elastic lamina) in parallel with a damper (provided by the viscoelastic lamina).

#### Telescope Structure Tape Spring Design

From previous experience, a composite laminate consisting of an S-2 glass unidirectional fiber sandwich by an Astroquartz plain weave layers at 45° bias has shown good roll stability property with high resistance to creep. The unidirectional lamina was AGY 933-AA-750 S-2 Glass fiber pre-impregnated with Patz Materials & Technologies PMT-F7 with 10% by weight 3M nanosilicate. The JPS Style 525 Astroquartz II plain weave was also pre-impregnated with the PMT-F7 epoxy. Material properties are listed in Table 1. The effective orthotropic properties for the laminate are presented in Table 2.

**Table 1. Tape spring material properties**

Property (units)	Astroquartz II/PMT-F7 Plain Weave	S2 Glass/PMT-F7 Unidirectional
$E_1$ (GPa)	21.7	56.9
$E_2$ (GPa)	21.7	16.8
$G_{12}$ (GPa)	3.4	6.1
$\nu_{12}$	0.11	0.27
t (mm)	0.1016	0.0762

**Table 2. Tape spring laminate properties**

Property (units)	Astroquartz II/PMT-F7 Plain Weave
$E_1$ (GPa)	21.7
$E_2$ (GPa)	21.7
$G_{12}$ (GPa)	3.4
$\nu_{12}$	0.11
t (mm)	0.254

The stress in the membrane was a critical design parameter. The membrane design stress level of 68.9 kPa (10 psi) was chosen, which translates to the corner pull-point load of approximately 0.5 N. The load-carrying members in the structure are illustrated in the side view of one corner location in Figure 11. The position of point A in Figure 11 was considered fixed for the initial calculations, which sets the vectors of the membrane force,  $F_m$ , and the positioning lanyard force,  $F_l$ . The vector of the spring force,  $F_s$ , and decoupling spring stiffness,  $k_s$ , were varied in a Matlab script to calculate the forces in the top frame and boom tape spring members and their respective lengths. This study gave the position tolerance of point A to maintain  $F_m$  within  $\pm 0.05$  N and the required tape spring cross-section radius to resist buckling with margin. A commercial off-the-shelf extension spring with stiffness of approximately



45.5 N/m with an initial length of 3.2 cm was selected for the prototype unit. A spring force vector that bisects the membrane and lanyard vectors minimized the required minimum tape spring radii. The resulting boom tape spring length was 41.3 cm and is subjected to a compressive load of 0.52 N. The frame tape spring is 55.5 cm in length with a compressive load of 0.27 N.

When sizing the tape spring to resist the compressive loading, the tape spring cross-section was assumed to have a constant radius with a subtended angle of  $\beta = \pi$  radians. A half-sine wave shape imperfection with peak amplitude assumed to be 5% of the member length was used to calculate the total load in the member. The minimum tape spring radius was then determined such that the total load in the tape spring was one third of the Euler buckling load. Solving for the top frame and boom cases resulted in the same required minimum tape spring radius of 0.38 cm. However, strain limitations for the layup limit the radius to be greater than 0.48 cm.

The tape spring should have sufficient torque to fully deploy quasi-statically, i.e., not relying on the kinetic energy of the system to assist in the process. A torque margin of 3 was used to calculate the minimum required tape spring cross-section radius to overcome the resistive moment resulting from the axial compressive load in the member. To account for long-term creep effects, the shear modulus in the outer plain weave layers was assumed to be effectively zero. For a constant cross section with  $\beta = \pi$  radians, the minimum radius is 0.41 cm. The trimmed tape spring shown in Figure 5b) has an effective subtended angle of  $\beta = 0.86$  radian at the root. The resulting minimum radius was 0.54 cm. This was rounded up to a standard mandrel size 0.56 cm (7/16 in) for manufacturing purposes.

A finite element model of the tape spring was created to compare the deployment torque and buckling. Abaqus/Standard was used to perform buckling analyses to compare the buckling loads of the trimmed tape spring geometry to the pristine member. Various trials were performed with initial shape imperfections applied. The trimmed geometry was observed to have a consistent 4% reduction in buckling load capability. A buckling analysis using was then performed by continuously increasing the tension in the compliant member that connects the membrane corner point to the corner of the top triangular frame. The system buckles at an applied load of approximately 48 N, which is two orders of magnitude above the design load of 0.9 N.

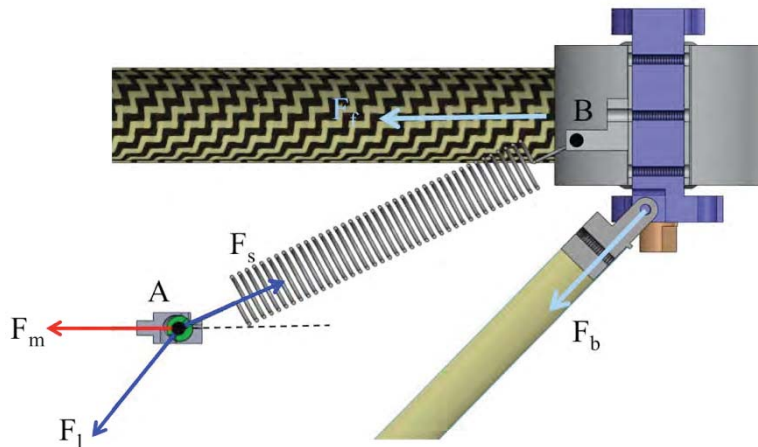


**Figure 11. Top frame corner free body diagram.**

The central disk radius of 8.5 mm was selected for the hub assembly. The moment generated from the 0.52-N compressive load in the boom tape spring required a deployment torque of at least 4.4 mN-m. The estimated deployment torque from Equation 2 at this radius and taking into account the cross section at

the root due to the clearance trimming was calculated to be 13.3 mN-m. Deployment torque for the untrimmed tape spring is approximately 48.5 mN-m.

### Deployment Testing

The assembled prototype unit is shown in the deployed and stowed configurations in Figure 12. The membrane was cut from 50.8- $\mu\text{m}$  (0.002-inch) thick Kapton using a Gerber ply cutting table. This thickness is approximately 3x that of the anticipated operational material. The positioning lanyards were constructed from braided Spectra cord. The ends were bonded to steel spheres with a hole drilled through the centroid. The membrane was folded in a conical coffee-filter-type fold pattern and guided into the containment shroud located with the tape spring members. Minus the base plate, which was intentionally oversized for testing purposes, the assembled system mass was 113 g.

The initial functional deployment test of the fully assembled structure shown in Figure 12 did not finish in the fully deployed configuration. High-speed video shows the booms would fully deploy, but the shock loading at full deployment caused buckling in the members, at which there was insufficient torque from the boom tape spring members to overcome the compressive load and fully lock out. Manual assistance was given to fully deploy the boom tape springs, which confirmed the system's integrity in the deployed configuration. The boom tape springs were then perturbed to induce buckling and observe the response quasi-statically. The booms did not have sufficient torque to return to the locked state. Original deployment torque calculations did not include parasitic torques from bearing and side shroud friction, or gravitational loading. Preliminary deployment testing without the position control lanyards was successful with no failures observed. Gravity offload support to negate the top frame mechanism mass was included for subsequent testing. The relatively small mass of the corner fixture, coupled with the large vertical deployment distance of 0.26 m, presents a challenge to not overly influence the true dynamics of the deployable structure with a passive offload system. Each top frame fixture was connected to a series of extensional springs with an effective stiffness of 0.28 N/m. The spring ends were connected to a common point approximately 12 m above the test article. Braided Spectra cord was used to connect the springs to the frame fixtures. This height resulted in a negligible parasitic lateral load of approximately 3% of the vertical offload force of 0.19 N. The deviation of vertical offload force from the stowed to the deployed state was roughly 0.07 N (37%). The top frame assembly was disconnected and supported by the offload lines. The height of the upper offload point was adjusted until the top frame was offset at the nominal distance from the base plate. Therefore, the offload system provides additional deployment assistance at the beginning of deployment. The high deployment rate observed in preliminary testing showed sufficient deployment torque was present and the additional force from the offload system was not enabling a deployment that would otherwise fail. After assembly in the deployed state, the booms were manually buckled and returned to the locked state as desired.

Eight deployment tests were performed on the updated test article to demonstrate the feasibility of the novel structure design. Deployments were considered successful if all tape springs fully transitioned to the deployed state and lanyards tensioned as shown in Figure 12. Three attempts resulted in deployment failure, which was due to lanyard snagging on the deployment mechanism. Lanyard control features were not implemented during the first round of testing in order to minimize the effort required to demonstrate deployment feasibility. The membrane containment shroud was redesigned with features to stow the lanyards and provide a more deterministic method to deploy without catching on the mechanism. Four additional deployments were performed with no failures observed. Selected captured images from a successful deployment are presented in Figure 13. The deployment duration was approximately 0.65 second. Deployments were initiated immediately after stowage, such that any torque degradation due to stress relaxation was insignificant. Visual inspection of the tape springs did not reveal any noticeable damage.

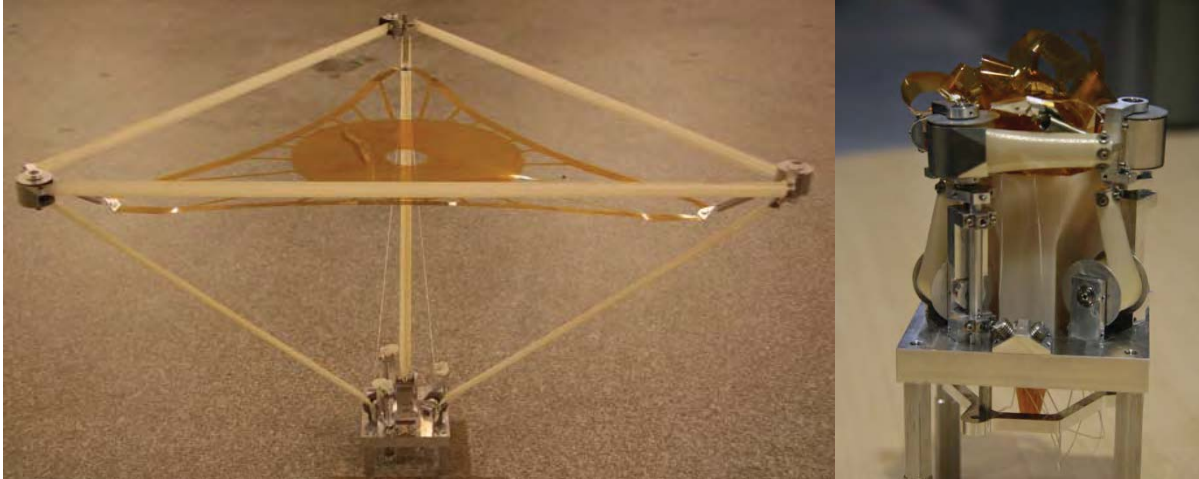


**Figure 12. Fabricated structure in the deployed and stowed configurations.**

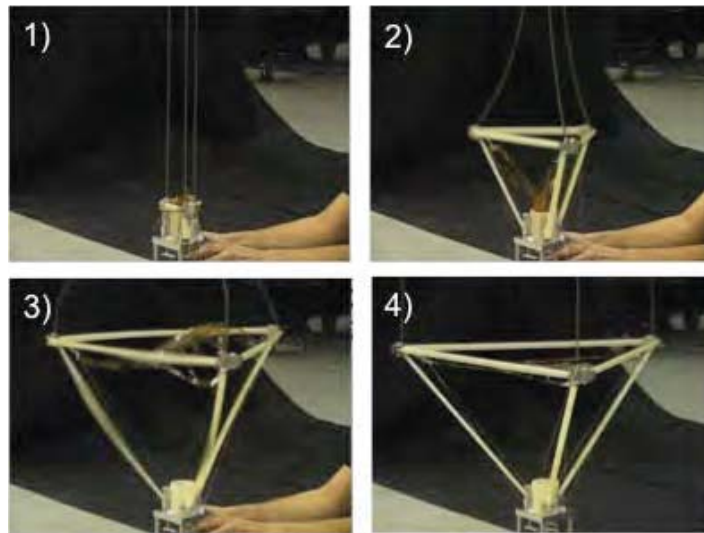


**Figure 13. Captured sequence from deployment test**

In order to verify the deployable telescope satisfies the structural requirements for an operational system, tests such as deployment repeatability, deployed dimensional stability, and dynamic vibration are needed. Observations from handling and testing of the prototype structure presented a number of departures from a conceived operational unit. The combination of these factors justified reserving the characterization testing for the next structure revision that incorporates the identified design features.

### **Conclusions**

The structure presented in this work incorporated flexible composite tape springs in a novel manner to produce a relatively simple and mass efficient solution for a three-dimensional, self-deployable structure. Through the development process a number of mechanism design requirements were discovered to enable the desired functionality. The tape spring-hub interface design was a driving factor in the overall system design and available torque factor of safety. A hub design that accommodated an untrimmed tape spring did not satisfy the structure volume constraints. Calculations supported the trimmed tape spring end would provide sufficient deployment torque with margin. Gravitational and other parasitic loads

originally unaccounted for, required gravity offload support for ground deployment testing. The off-nominal and inertial loading imparted by the passive offload system yields added uncertainty to the observed structure kinematics. Microgravity testing, or at a minimum active gravity offload support, is suggested for this class of freely deployable structure. The tape springs can be designed to deploy with no gravity offloading, but at the expense of an overly designed system that increases the deployment rate and imparted shock.

Rate control has been a critical design factor in deployable structures. As mentioned previously, a viable rate control solution for this scale of deployable structure is not available. Known methods either add excessive mass and complexity or excessively increase deployment failure risk. The relatively low mass of the deploying structure is a small fraction of a notional 3U CubeSat spacecraft. Free deployment testing of the SIMPLE boom (work not yet published) qualitatively had little impact on bus dynamics. The shock loading on the membrane optic in this application is of larger concern.

The test data required per Reference 11 to more accurately predict the deployment torque was not available for the selected laminate. AFRL Space Vehicles directorate is currently constructing a database of commonly used lamina and laminates to provide this data for future efforts. A test to directly measure the operational tape spring torque over the full deployment would also be beneficial to verify the calculations.

Successful deployment tests were observed to be highly sensitive to simultaneous release of the tape spring rotation constraints. Preliminary functional testing during the design development phase revealed deployment failures often resulted when one top frame hub was released before the other two. Because the top frame deployment does not work against gravity, the rapid motion of the top frame corner fixture would cause the boom tape spring to deploy in a lateral, rather than vertical, fashion that resulted in gross lateral shifting of the top frame assembly. The final hub constraint mechanism using the locking/unlocking slip disk allowed all tape spring rolls to be consistently stowed in a more deterministic fashion against the hard stops and tightly wound about the central hub disk. Proper packaging in this manner was found to be critical for synchronous deployment. The resulting hub and constraint mechanism design enabled repeatable functional three-dimensional deployments. The deployment tests successfully demonstrate that flexible composite tape spring members can be utilized to enable simple and efficient deployable structures.

### **Acknowledgments**

This work was financially supported by Integrated Design, Analysis, and Testing Of Space Structures (IDATS) [Contract #FA9453-11-C-0265] Program Manager: Andrew Williams, and executed at the Air Force Research Laboratory Space Vehicles Directorate, Kirtland AFB 87117. The authors would also like to thank Michael Peterson for his contribution in solid modeling tasks and Daniel Roldan for assisting in hardware assembly and deployment testing.

## References

1. Mejia-Ariza, J. M., Murphey, T. W., and Dumm, H. P., "Deployable Trusses Based on Large Rotation Flexure Hinges," *Journal of Spacecraft and Rockets*, Vol. 47, 2010, pp. 1053–1062.
2. Murphey, T. W., Jeon, S. K., Biskner, A., and Sanford, G., "Deployable Booms and Antennas Using Bi-stable Tape-springs," 24th Annual AIAA/USU Conference on Small Satellites, 2010.
3. Pollard, E., Murphey, T. W., and Sanford, G. E., "Experimental and Numerical Analysis of a DECSMAR Structure's Deployment and Deployed Performance," 48th AIAA/ASME/ASCE/AHS/ASC Structures, Structural Dynamics, and Materials Conference, 2007.
4. Jeon, S. K. and Murphey, T. W., "Design and analysis of a meter-class CubeSat boom with a motor-less deployment by bi-stable tape springs," 52nd AIAA/ASME/ASCE/AHS/ASC Structures, Structural Dynamics, and Materials Conference, April 2011.
5. Rimrott, F. P. J. and Fritzsche, G., "Fundamentals of STEM Mechanics," IUTAM-IASS Symposium on Deployable Structures, Theory and Applications, Sep 06-09, 1998.
6. Footdale, J. N. and Murphey, T. W., "Structural Design of a CubeSat-Based Diffractive Optic Telescope," 52nd AIAA/ASME/ASCE/AHS/ASC Structures, Structural Dynamics, and Materials Conference, 2011.
7. Footdale, J. N. and Murphey, T. W., "Design and Testing of Self-Deploying Membrane Optic Support Structure Using Rollable Composite Tape Springs," Proceedings of the 54<sup>th</sup> AIAA Structures, Structural Dynamics, and Materials Conference, Boston, MA, 2013.
8. Seffen, K. A. and Pellegrino S. "Deployment Dynamics of Tape Springs," Proceedings of the Royal Society London Series A, Vol. 455, pp 1003-1048, 1999.
9. Pellegrino, S., "Bi-Stable Structures," *Deployable Structures*, SpringerWien, New York, 2001, pp. 99-111.
10. Pollard, E. L., and Murphey, T. W., "Development of Deployable Elastic Composite Shape Memory Alloy Reinforced (DECSMAR) Structures," 47th AIAA/ASME/ASCE/AHS/ASC Structures, Structural Dynamics, and Materials Conference, Newport, RI: AIAA, 2006.
11. Peterson, M. E. and Murphey, T. W. "Large Deformation Bending of Thin Composite Tape Spring Laminates," 54th AIAA/ASME/ASCE/AHS/ASC Structures, Structural Dynamics, and Materials Conference, Boston, MA, 2013.
12. Murphey, T. W. and Peterson, M. E., "Four Point Bending of Thin Unidirectional Composite Laminas," 54th AIAA/ASME/ASCE/AHS/ASC Structures, Structural Dynamics, and Materials Conference, Boston, MA, 2013.
13. Domber, J. L., Hinkle, J. D., Peterson, L. D., and Warren, P. A., "Dimensional Repeatability of an Elastically Folded Composite Hinge for Deployed Spacecraft Optics," *Journal of Spacecraft and Rockets*, Vol. 39, No. 5, pp. 646-652, 2002.
14. Kwok, K. and Pellegrino, S., "Folding, Stowage, and Deployment of Viscoelastic Tape Springs," *AIAA Journal*, Vol. 51, No. 8, 2013, pp. 1908-1918.
15. Hyer, M. W., *Stress Analysis of Fiber-Reinforced Composite Materials*, WCB/McGraw-Hill, 1998.



# Innovative Escapement-Based Mechanism for Micro-Antenna Boom Deployment

Marta Tokarz\*, Jerzy Grygorczuk\*, Stanisław Jarzynka\* and Henryk Gut\*\*

## Abstract

This paper presents the prototype of a tubular boom antenna developed for the Polish BRITE-PL satellite by the Space Research Center of the Polish Academy of Sciences (CBK PAN). What is unique about our work is that we developed an original type of the tubular boom antenna deployment mechanism that can be used widely as a basic solution for compact electrical antennas, booms deploying sensitive instruments, ultra-light planetary manipulators etc. The invented electromagnetic driving unit provides a dual complementary action – it adds extra energy to the driving spring, making the system more reliable, and at the same time it moderates the deployment speed acting as a kind of damper. That distinguishing feature predetermines the mechanism to be applied wherever the dynamic nature of a spring drive introducing dangerous vibrations and inducing severe local stress in the structure needs to be mitigated. Moreover, the paper reveals a product unique in Europe – a miniature beryllium bronze tubular boom free of geometry and strain defects, which is essential for stiffness and fatigue resistance. Both the deployment mechanism and the technology of tubular boom manufacturing are protected by patent rights.

## Introduction

In December 2009, The Minister of Science and Higher Education signed a decision to grant funding for the project: 'BRITE: First Polish Scientific Satellite'. Two satellites: BRITE-PL Lem and BRITE-PL Heweliusz are the Polish contribution to the BRITE mission, developed by a consortium of Canadian, Austrian and Polish institutes. In total, six satellites will perform astronomical observations of the brightest stars, two from each partnering country [1].

The BRITE-PL satellites are almost identical (both measure 20 x 20 x 20 cm and weigh about 7 kg), although BRITE-PL Heweliusz contains some additional experiments designed by CBK PAN. Among them there is an experiment called Micro-Antenna Boom (MAB) – a miniature tubular antenna driven by a modified escapement mechanism. This paper describes the MAB background, technical features of the new deployment mechanism used in MAB, conducted test campaign and lessons learned from the project. It also concisely presents the technology developed for manufacturing a miniature Ø6 mm beryllium bronze tubular boom, not available in Europe before.

## CBK PAN Heritage

CBK PAN has successfully developed devices based on a tubular boom technology since 1993, gaining therefore an outstanding experience in development of space mechanisms with the use of tubular booms as a lightweight construction material, ideal for antennas and special manipulators where the relation between mass and operational range is crucial. Some of its achievements are shown in Figure 1 and thoroughly described in [2, 3].

---

\* The Space Research Center of the Polish Academy of Sciences, Warsaw, Poland

\*\* GUTRONIC Henryk Gut, Warsaw, Poland

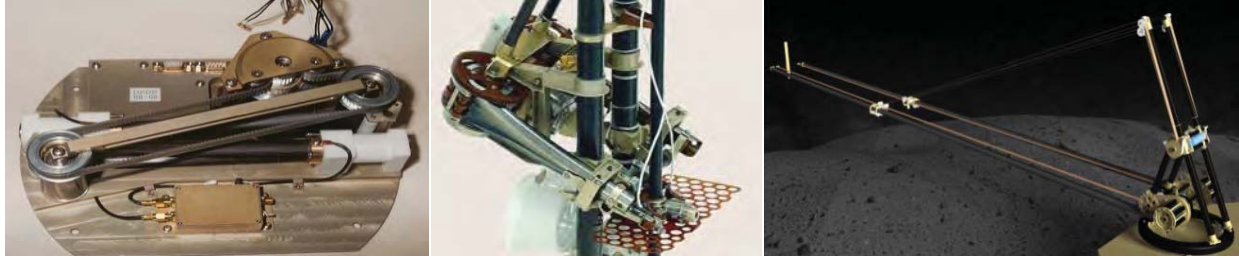


**Figure 1. (Left) 2 x 2 m, 40-MHz Rubber antenna, three times successfully launched by Indian rocket, (Middle) MUPUS Deployment Device for Rosetta mission, (Right) laboratory model of Ultra-Light Planetary Manipulator (ULPM) – 3-dof, 3-m operational range, mass of 2.5 kg.**

All the above-presented devices used  $\varnothing 15$ -mm or  $\varnothing 25$ -mm tubular booms of stainless steel strips produced in Ukraine. Recently, the CBK PAN activities were concentrated on application of a miniature  $\varnothing 6$ -mm tubular boom made of beryllium bronze, more compact and lighter than the stainless steel ones (it weighs 8 g per 1 m, while the previous booms weigh 50 g and 100 g per 1 m respectively). The original manufacturing method developed by the Polish enterprise GUTRONIC, a longtime CBK PAN partner, will be described later in the paper.

The demand for such an ultra-light and scaled-down solution arose from the Russian RELEC mission. Within the framework of that mission, CBK PAN developed the Radio Frequency Analyser (RFA) – an instrument devoted to measure three electrical components of radio frequency emissions in the frequency range from 50.0 kHz up to 18.0 MHz. One of the main units of RFA was a three dimensional electric antenna set shown in Figure 2.



**Figure 2. RFA – set of three orthogonal 1 m long antennas for RELEC mission.**

As mentioned above, the RFA antenna set is based on miniature  $\varnothing 6$ -mm tubular booms stored on a reel. In principle, the tubular boom is to extend itself by spring energy, which is released during transformation of the input flat profile to the original round one. The storage reel is on the front and performs rotational and translational motion. The reel is attached to the tubular boom to never become space debris after deployment. This solution, despite intrinsic advantages like design simplicity and lack of a motor drive, cannot be recommended as the perfect one, for three reasons:

- The deployment process is characterized by high and uncontrolled speed. This can be against certain mission constraints, especially in small satellites threatened with stability loss in case of rapid and dynamic actions.
- As a baseline, a reel is separated from the boom at the end of deployment and becomes space debris. A design allowing keeping the reel at the antenna end, like in RFA, is applied, however, from the electrical point of view, it is an unfavourable solution.
- The tubular boom acts as a driving spring. In case of spring relaxation (e.g. as a result of a long flight to a destination) or an unexpected boom jam, there is no deployment salvage.

### MAB Background

Bearing in mind the aforesaid disadvantages of free deployment with the leading reel, CBK PAN undertook a task to create an alternative solution with significant improvements. Roughly at the same time CBK PAN was allowed to place additional payload instruments on board BRITE-PL Heweliusz satellite. In this way, MAB was proposed as a prototype of the tubular boom antenna driven by the modified escapement mechanism. MAB is a technology demonstrator aimed only at showing correctness of the novel deployment mechanism idea without testing the antenna performance itself (i.e., reception characteristics, antenna response and sensitivity). The fully functional prototype developed for the BRITE-type spacecraft is presented in Figure 3.

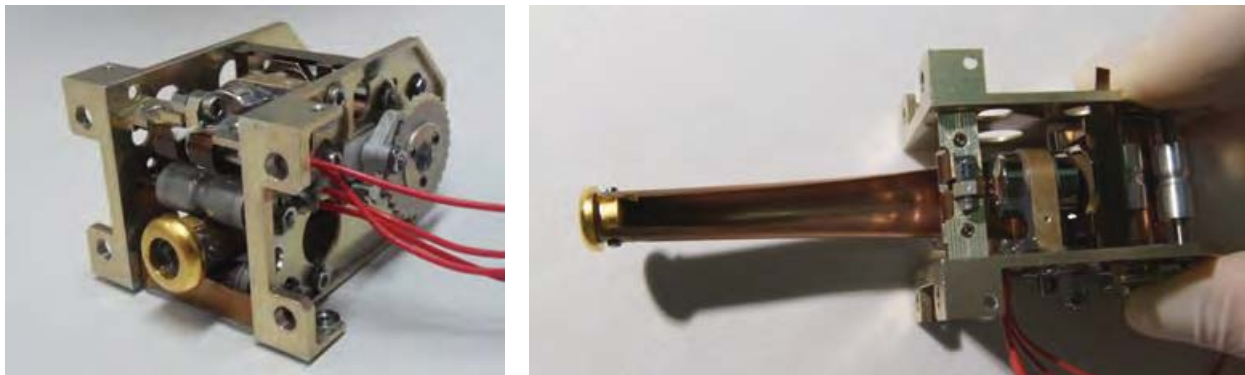


**Figure 3. MAB – technology demonstrator for BRITE-PL Heweliusz satellite: (left) stowed, (right) partially deployed configuration.**

In general, the tubular boom strip made of beryllium bronze (like the one used in MAB) can be stored on a reel and when deployed, it can form a 1.5-m long cylindrical tube. However, for safety reasons, in case of antenna deployment failure, the tube on BRITE mission is only 120-mm long and deployed inside a cylindrical casing (Figure 4). A closing contact placed at the free end of the safety casing verifies and confirms the antenna deployment.

The device passed qualification tests, described in detail hereinafter, achieving therefore TRL 6, and is ready for launch. BRITE-PL Heweliusz was to be launched in December 2013 on board the Chinese CZ-4B rocket. Unfortunately, due to the failure of the preceding flight of the same rocket type, the launch was postponed. The Chinese investigation is still ongoing and, according to recent update, the satellite will be probably launched in February 2014. Following the performance in a space environment, MAB is expected to gain TRL 7.

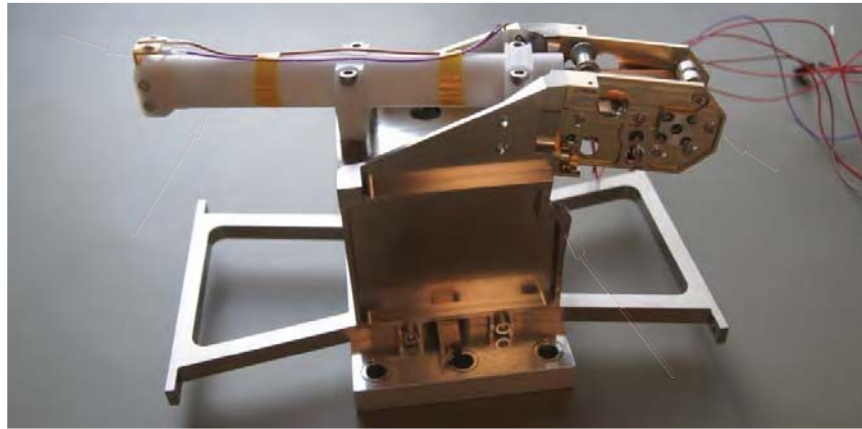


Figure 4. Flight model: 1 – MAB, 2 – safety casing, 3 – closing contact, 4 – bracket.

### Technical Features of the New Deployment Mechanism

The idea of the new deployment mechanism applied in MAB originates from an escapement – a device commonly used in mechanical watches and clocks.

#### Traditional clock escapement

A perfect example to show the principle of operation of a traditional escapement mechanism is a gravity clock (Figure 5). The escapement is driven by force from a suspended weight (1) while a pendulum (2) acts as a timekeeping element. An escape wheel (3) works with a detent (4). The detent releases a tooth of the wheel, which therefore changes from a locked state to a drive one until the opposite detent arm strikes another tooth on the gear, which locks the gear again. Such a mechanism, with meticulously selected pendulum properties, allows clocks to precisely indicate the passage of time. A characteristic clock ticking is nothing but the sound of the gear stopping when the escapement locks.

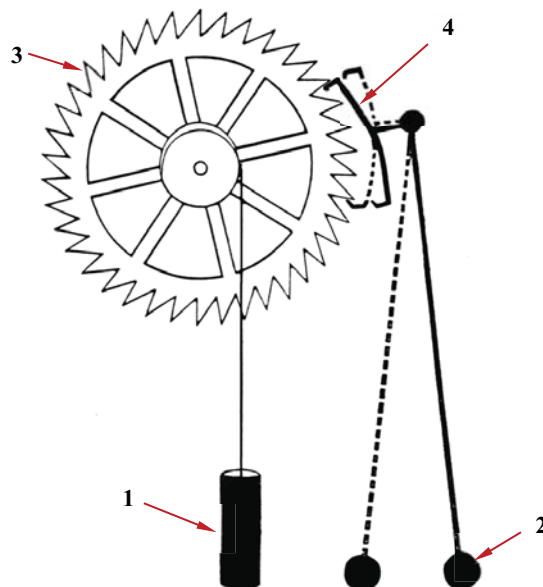


Figure 5. Gravity clock escapement mechanism: 1 – weight, 2 – pendulum, 3 – escape wheel, 4 – detent.

Initially, the traditional Graham escapement (an escapement type used in almost all modern pendulum clocks) was developed in MAB that constituted the antenna solution with the reel joined to the spacecraft and the escape wheel fixed to the reel shaft. The tubular boom, stored on the reel, performed a function of a weight and thus a driving force. A pendulum was replaced with an electromagnet. In that way MAB was provided with a very precise speed regulation dependent only on the electromagnet timing rate. One of the main RFA disadvantages – high and uncontrolled deployment speed – was eliminated. However, the solution was still not free of consequences of the driving spring relaxation or accidental boom jam.

Innovative escapement-based mechanism

The modified escapement mechanism proposed by CBK PAN turned out to be an innovative solution free and clear of any RFA defects. The geometry of the detent and escape wheel underwent a significant change aimed at the breaking properties decrease corresponding with efficiency improvement and higher deployment reliability. The main modification was that the escapement lost its self-locking attribute.

The schematic of MAB deployment mechanism is shown in Figure 6. The tubular boom (1) is rolled up on the reel coupled with the escape wheel (2). The wheel works with the detent (3) fixed to the armature (4) which is driven by the electromagnet (5) and return spring (6). Once released, tubular boom starts free unwinding. The detent, sliding on the escape wheel teeth, is forced to perform swinging motion. The deployment speed is regulated via eigenfrequency of the detent mechanism. No electromagnet action is required.

In case of a much lower than desired deployment speed or unexpected boom jam, the escapement-based mechanism serves as a motion-inducing unit. With the use of electromagnet and return spring the detent swinging movement is forced, the escape wheel begins to rotate and thereby aiding the unreeling action. Moreover, the electromagnet working at high frequencies can act as a generator of vibration, also valuable in providing better unwinding (confirmed by tests).

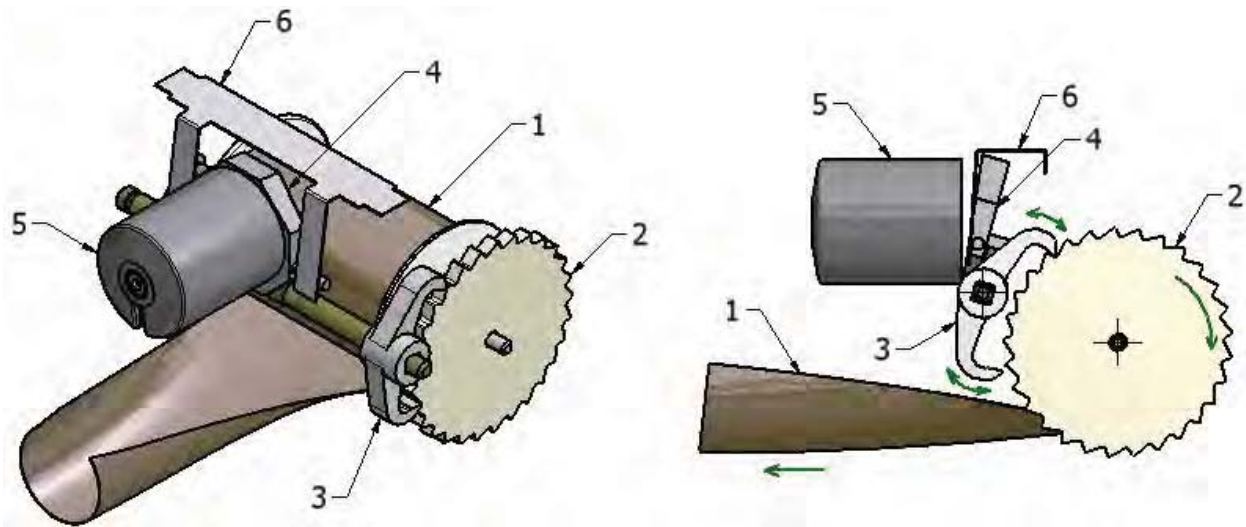


**Figure 6. Modified escapement mechanism for MAB deployment: (left) isometric view, (right) side view; 1 – tubular boom stored on the reel, 2 – escape wheel, 3 – detent, 4 – armature, 5 – electromagnet, 6 – return spring**

The only inconvenience of the proposed mechanism is the limited speed control. The deployment rate, although satisfactorily mitigated and slowed down, depends closely on the detent mechanism inertia. The inertia properties of the detent subassembly strictly determine the deployment speed. The pictures in Figure 7 present two versions of MAB: initial (with the traditional Graham escapement) and the final one



(with the modified escapement). CBK PAN has made an effort to obtain a patent for the invention described in this paper since the special escapement mechanism has a potential to be reused in other devices in the future. The property rights registration process commenced in October 2013 (Polish Patent Office no. P.405646).

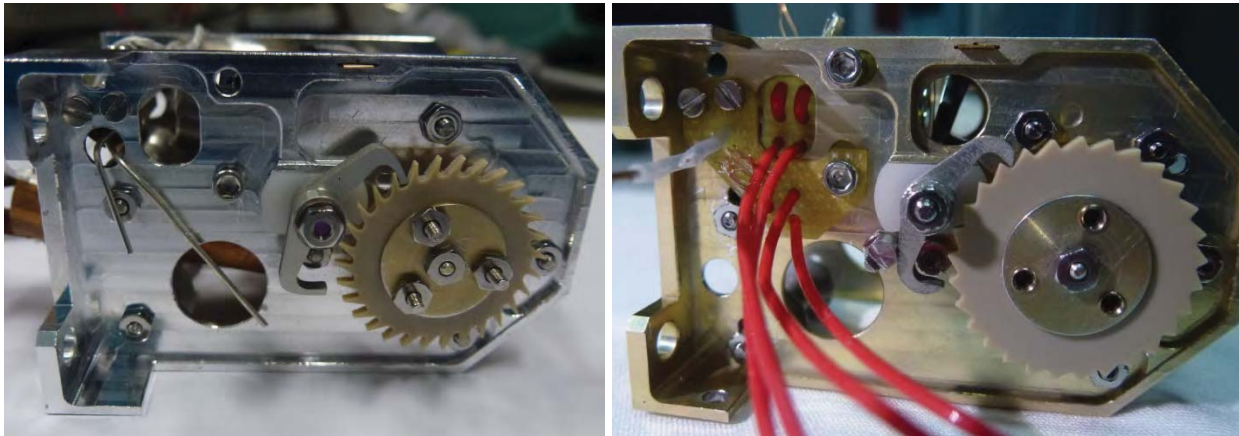


**Figure 7. Comparison of MAB versions: (left) with Graham escapement, (right) with modified one.**

#### MAB basic characteristics

MAB is a prototype of the antenna equipped with: the innovative escapement drive acting simultaneously as a speed damper and a new type of a miniature tubular boom – these are paramount distinguishing MAB features. A non-explosive lock & release mechanism is also noteworthy (Figure 8). It is based on the Dyneema string melting system (with the use of a resistor as a heater), which was space proven in several CBK PAN previous instruments [4]. This kind of actuator is very reliable, especially at low temperature applications. The Dyneema string continuous tension is realized by an extra kick-off spring that also supports the release action.

The MAB operation is fully controlled by an external control board. Once initiated, the deployment system receives a deployment command – the resistor is heated up for 10 s, which makes the Dyneema filaments melt. The released tubular boom starts free unwinding at moderated speed until leaning against the closing contact. Then a signal is sent that stops the operation.

In case of the boom jam (and hence the lack of the stop signal after 10 s), the electromagnet serving as an extra motion-inducing unit is powered and thereby the unreeling action takes place. The procedure is stopped either via the stop signal sent from the closing contact or after 120 s. In the latter case (or in any when the unplugging signal is not sent), the deployment would be considered as unsuccessful.

The main MAB characteristic features:

- miniature size and low weight: 30 x 40 x 50 mm, 35 g,
- smooth and regular deployment without rapid and dynamic actions (no risk of satellite stability loss), deployment speed – 10 cm/s,
- usage of no electrical motors resulting in a simpler construction and higher reliability – the electromagnet individually optimized to the specific requirements must be a more reliable and higher-class solution than a common motor, especially the one with a reduction gearbox, where the number of moving parts and frictional joints is significant,
- advantageous length to weight ratio (120-mm-long boom weighs less than 1 g),
- relatively low power consumption: 4 W for 10 s (for lock & release mechanism), 1.25 W for 30 s (for electromagnet, if needed to be used),
- once deployed, the antenna cannot be retracted.

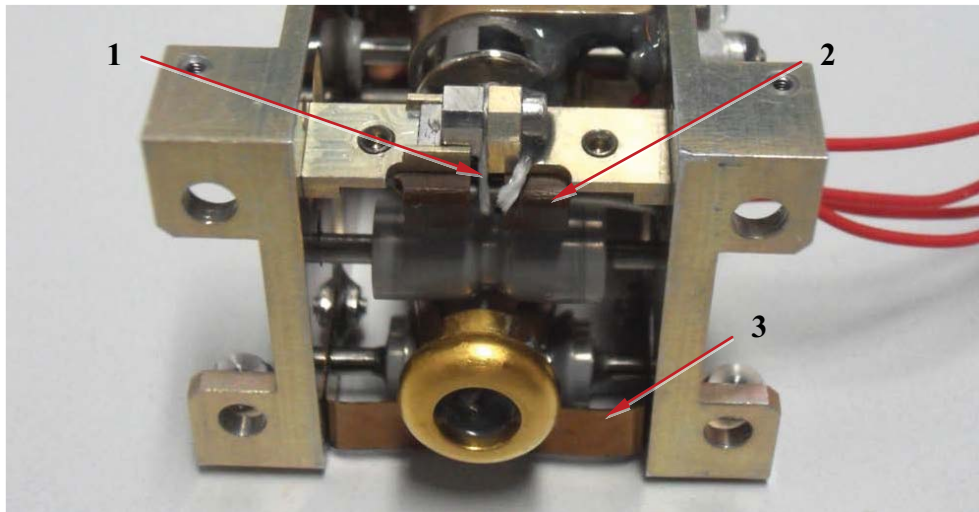


**Figure 8. Lock & release mechanism used in MAB: 1 – Dyneema string, 2 – heater, 3 – kick-off spring**

### **Technical Features of the New Manufacturing Technology**

Another challenging and innovative issue is the manufacture of the new kind of miniature tubular booms (6 mm in diameter). The manufacturing process requires several factors to be taken into account: low thickness of the boom, its fragility, tendency to torsional/bending deformations, and geometry degradation arising from multitude of manufacturing effects such as heterogeneous material properties, uneven heat treatment, and aging of material. A careful control of dimensional tolerances during production of the boom may be crucial for a successful mission [5]. Therefore, the chosen production method must ensure as precise manufacturing of tubes – free of any material defects – as possible.

Analyses showed that none of the reviewed existing methods of open profile metal tubes manufacturing fits completely to such a specific task as production of thin-walled tubular booms. The innovative method for producing beryllium bronze tubular boom – 0.05-mm thick, 1.5-m long and 6 mm in diameter – has been developed by the Polish enterprise GUTRONIC during the ESA PECS 4000105010/11/NL/KML project. That innovative method, undeniably unique in Europe, has been a subject of a patent since April 2013 (Polish Patent Office no. P.403660). The employed method of tubular booms manufacturing is presented in Figures 9 and 10 in a simplified form. The scheme is shown in Figure 9.

The tape (1) is placed on a susceptible tie (2) travelling in a prismatic base (3). The tie is clamped to the prism by a forming rod (4) being a part of the pressure providing unit. A beryllium tape being formed travels on a tie and is inserted under a forming rod and thereby into the working area (5). The rod rolls on the tape making it bend. The working area is determined by radiuses of the rod cross-section, perpendicular to the prism surface.

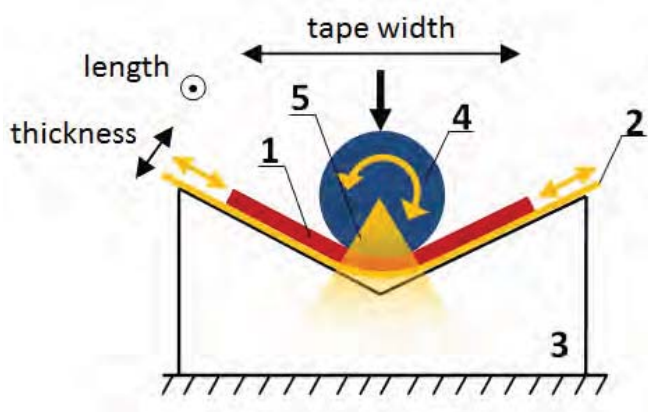


**Figure 9. Local bending – process scheme:**  
 1 – tape, 2 – susceptible tie,  
 3 – prismatic base, 4 – forming rod,  
 5 – working area

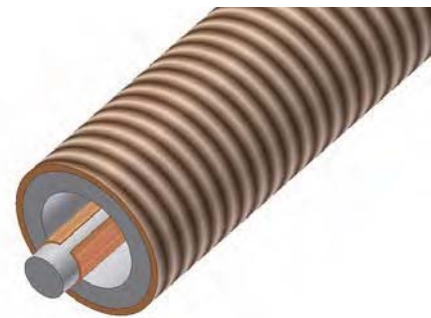


**Figure 10. Hardening heater – pictorial view:**  
 1 – aluminium tube, 2 – tubular boom,  
 3 – heating element,  
 4 – mandrel rod

An advantage of the proposed solution is a fully controlled, precise shape of the manufactured tubular boom, homogeneity of the material deformation, no folding either bending of beryllium tape during production process, economical construction and easy control. A disadvantage is dependence of the manufactured tubular boom length on the device size (the longer the tape, the longer the device) and low production rate. At the moment the maximum length of the manufactured tape is 1.5 m.

A separate issue worth paying attention to is the hardening of the final product – a process necessary for obtaining the required stiffness and elastic properties of the final tubular boom. The proposed method (Figure 10) is the one of hardening with a thick-wall aluminium tube (1), inside of which there is a segment of the tubular boom (2). The aluminium tube is reeled with a heating element (3) that heats it evenly. The tubular boom is loaded over a mandrel rod (4) and heated to the hardening temperature of 315°C (according to the heat treatment procedure provided by the BERYLCO 25 distributor).

Numerous optimization tests were conducted using 25-cm prototypes of the bender and hardening heater that allowed some parameters to be determined, i.e. the tape pulling strength, the tape travel time, the tape leading system, the pressure force, the forming rod diameter, the mandrel rod diameter, etc. Based on the results of a foregoing analysis, the target device, including two modules – the bender and hardening heater – was developed and the first series of 1.5-m long tubular booms was successfully manufactured (Figure 11).

In space applications the tubular boom is to be stored on a reel. When deployed it is to form a cylindrical tube. In order to confirm such a possible use of the manufactured tubular booms and to characterize them as well, the final product underwent a series of relevant validation tests carried out by GUTRONIC in close cooperation with CBK PAN. The tests-proved the mechanical and resilient properties of the product met all requirements.



**Figure 11. First series of five hardened 1.5 m long tubular booms**

#### **MAB functional tests**

MAB underwent a series of acceptance and qualification tests, all conducted at CBK PAN. Table 1 shows the sequence of tests performed on the MAB flight model and their results.

**Table 1. MAB Test Campaign**

No.	Test	Result	Remarks
1.	Functional test at room temperature (~20°C)	passed	
2.	T-shock test (25 cycles of rapidly changing temperature in the range of +60°C ÷ -25°C )	passed	
3.	Functional test at room temperature (~20°C)	passed	
4.	Vibration test	passed	
5.	Functional test in Thermal-Vacuum Chamber (-6°C)	failed	
6.	Functional test in Climate Chamber (-20°C)	–	Investigation of failure cause
7.	Functional test at room temperature (~20°C)	passed	
8.	Vibration test	passed	
9.	Functional test in Climate Chamber (-10°C)	Passed	
10.	Functional test in Thermal-Vacuum Chamber (-6°C)	Passed	Approved for flight

As indicated in Table 1, the first functional test in the Thermal-Vacuum Chamber at -6°C ended up in a failure. A number of failure scenarios were considered in order to explain this result, however two causes were most likely:

- thermal shrinkage causing mechanical jam of the rotating components,
- failure of the Dyneema string melting – the force with which the string leaned against the resistor could be too low, causing poor adhesion and resulting in ineffective temperature dissipation.



As a part of a thorough investigation test 6 was carried out. It showed that thermal shrinkage was the cause of the detent deadlock and consequently the mechanism malfunction. At a low temperature (below 0°C) the detent axle could not rotate despite the proper electromagnet drive action. Remedial measures were taken: MAB was disassembled and the hole in the bearing bush was enlarged. The normal running fit became the easy running one. During MAB disassembly, an extra tension spring was added to increase the lock & release mechanism reliability (showed in Figure 8). The main spring task was to generate an additional tension force for the Dyneema fiber to better wrap it over the heater.

Since the problem was successfully detected and eliminated, the set of tests was repeated. The device passed all subsequent tests, achieving TRL 6. Figure 12 shows MAB during functional and vibration tests.

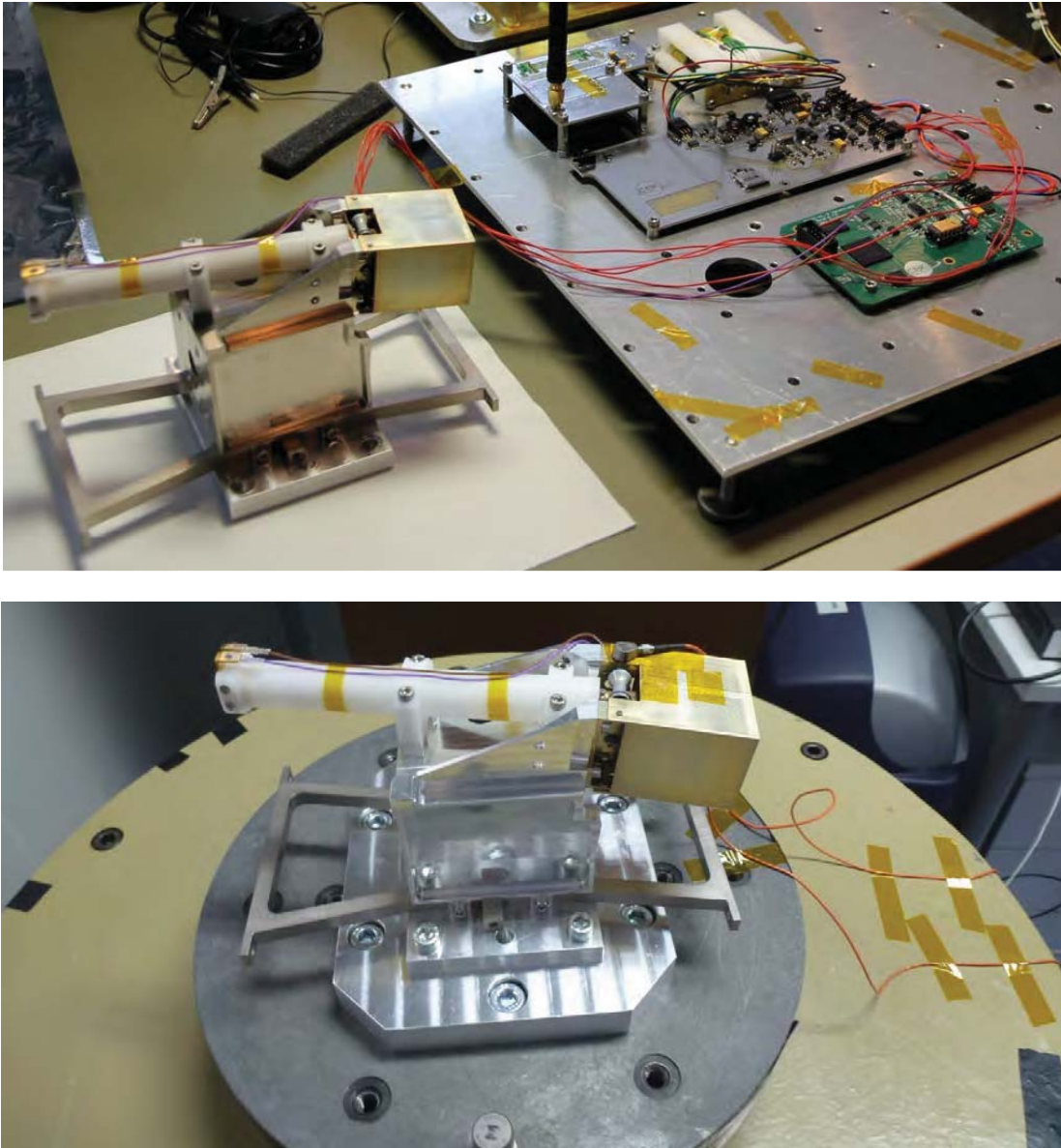


**Figure 12. MAB during: (top) functional test at room temperature, (bottom) vibration test.**



## Conclusions & Lessons Learned

The prototype of the miniature antenna called MAB, driven by the modified escapement mechanism, has been successfully developed together with the innovative technology of tubular boom manufacturing. The mechanism has been qualified through the dedicated test campaign, thereby proving correctness of the novel deployment mechanism idea – the idea assuming a dual complementary action of the driving system which simultaneously performs a role of a drive unit and a kind of moderator.

As with any mechanisms development, some important lessons were learned:

- Dealing with the new type of tubular boom showed how delicate and troublesome the tape is. It was very easy to damage it at every stage of assembly and testing. Once the project team had to cope with a tape crack (Figure 13) as a result of numerous winding and unwinding actions. It was initialized by rugged edges caused by careless hole drilling. Working on MAB, the team got to know the mechanical properties of the tubular boom.



**Figure 13. Tubular boom fatigue (marked in red)**

- Thermal difficulties – in the case of such a miniature mechanism thermal phenomena is of a key importance. During the first series of tests MAB failed the functional test at low temperature due to the detent deadlock. It turned out that the normal running fit was too restrictive.
- Assembly and manufacturing difficulties – the mechanism assembly and miniature components manufacturing turned out to be very challenging. A pinpoint accuracy was required.

Furthermore, GUTRONIC company, for many years closely cooperating with CBK PAN, gained a complete and unique knowledge of manufacturing tubular booms of BERYLCO 25. It got to know advantages and disadvantages of the developed method as well as the comprehensive characteristics of the final product. Now GUTRONIC specializes in manufacturing tubular booms for space applications and is able to improve its method, at the same time enriching the range of products with various tubular booms lengths, diameters and materials.

### Possible application

The foreseen applications of the MAB-type deployment mechanism equipped with the miniature tubular boom or another spring drive are as follows:

- compact electrical antennas,
- ultra-light planetary manipulators (the torsional stiffness of structure can be strengthened by combining booms into a pair),
- dual action units used wherever the dynamic nature of spring drive introduces dangerous vibrations and induces severe local stress in the structure that need to be mitigated and

smoothed (i.e. in hinges with a latching system commonly used to deploy booms with small sensors or measuring instruments, in solar panels systems, etc.),

- active dampers/actuators.

As it was shown in this paper, MAB is a properly functioning and reliable instrument. Its miniature character predetermines the device to be applied particularly on board nano- and micro-satellites.

#### Future development

The already studied solution seems to be a perfect starting point for future space projects. The subject aroused ESA's interest. Under Polish Industry Incentive Scheme, the agreement between ESA and ASTRONIKA (spin-off company founded by a CBK PAN group of engineers), GUTRONIC and CBK PAN was signed. Within the framework of the contract, a new generation of the electrical antenna will arise. The device will be significantly improved in comparison to MAB – it will be a fully functional, 2.5-m long antenna designed on the basis of the new type Ø10-mm tubular booms. The existing one (Ø6 mm) does not cover applications on small and medium satellites, representing a large number of present-day projects. Therefore, taking into account a more common use of tubular booms, production of Ø10-mm profiles of thicker beryllium bronze strips seems to be favorable.

#### **References**

1. Matthews S. E.: "The Seven Most Incredible Telescopes In Existence. The Biggest, Smallest and Most Robotic Stargazing Tools." *Popular Science*, 12 (2013).
2. Grygorczuk, J., Banaszkiwicz, M., Seweryn, K., Spohn, T.: "MUPUS Insertion Device for the Rosetta Mission". *Journal of Telecommunications and Information Technology*, 1 (2007), 50-53.
3. Grygorczuk, J. et al.: "Prototype of Ultra-Light Planetary Manipulator – Design, Test and Simulations". *Proceedings of the 12<sup>th</sup> Symposium on Advanced Space Technologies in Robotics and Automation (ASTRA 2013)*, Noordwijk, the Netherlands.
4. Grygorczuk, J. et al.: "Advanced Mechanisms and Tribological Tests of the Hammering Sampling Device CHOMIK". *Proceedings of the 14<sup>th</sup> European Space Mechanisms and Tribology Symposium (ESMATS 2011)*, Constance, Germany.
5. Collective work: "Tubular spacecraft booms (extendible, reel stored)". *NASA space vehicle design criteria (guidance and control)*, February 1971

# Design and Functional Validation of a Mechanism for Dual-Spinning CubeSats

Eric Peters<sup>\*</sup>, Pratik Dave, Ryan Kingsbury, Anne Marinan, Evan Wise, Chris Pong, Meghan Prinkey, Kerri Cahoy, David W. Miller, Devon Sklair, Joshua Emig

William J. Blackwell<sup>\*\*</sup>, G. Allen, C. Galbraith, R. Leslie, I. Osaretin, M. Shields, E. Thompson, D. Toher, D. Townzen and A. Vogel

## Abstract

The mission of the Micro-sized Microwave Atmospheric Satellite (MicroMAS) is to collect useful atmospheric images using a miniature passive microwave radiometer payload hosted on a low-cost CubeSat platform. In order to collect this data, the microwave radiometer payload must rotate to scan the ground-track perpendicular to the satellite's direction of travel. A custom motor assembly was developed to facilitate the rotation of the payload while allowing the spacecraft bus to remain fixed in the local-vertical, local-horizontal (LVLH) frame for increased pointing accuracy. This paper describes the mechanism used to enable this dual-spinning operation for CubeSats, and the lessons learned during the design, fabrication, integration, and testing phases of the mechanism's development lifecycle.

## Introduction

The Micro-sized Microwave Atmospheric Satellite (MicroMAS) project is a three-unit (3U) CubeSat under joint development by the MIT Space Systems Laboratory and MIT Lincoln Laboratory, currently scheduled to launch in May 2014. Its mission to deliver useful images of hurricanes, cyclones, and tropical storms using a low-cost satellite stretches the limit of what has been previously accomplished using the CubeSat platform. The payload is a multispectral passive microwave radiometer that has been developed by MIT Lincoln Laboratory in collaboration with the University of Massachusetts-Amherst. The payload is contained within a standard 1U CubeSat structure, occupying one-third of the total vehicle volume. All spacecraft support functions are integrated within the remaining 2U volume as part of a separate bus structure that has been developed by the MIT Space Systems Laboratory (SSL).

In order to effectively collect data with the radiometer sensor, the spacecraft must simultaneously sweep the radiometer field of view perpendicular to the ground-track while maintaining sub-degree pointing accuracy fixed in the local-vertical, local-horizontal (LVLH) frame. A satellite stabilized in this way is considered a "dual-spinning" spacecraft. Figure 1 illustrates how MicroMAS will be oriented during on-orbit operations. The following sections discuss the development of the mechanism, dubbed the Scanner Assembly (SA), used to enable this motion – including design requirements; early prototypes and design trades; and functional validation.

## Motivation for Dual-Spinning Design

Preliminary design analyses<sup>1,2</sup> determined that precessing the angular momentum of an entire spinning CubeSat as it progresses through its orbit would require torque in excess of the capabilities of available commercial, off-the-shelf (COTS) CubeSat mechanisms for attitude control. This includes the MAI-400 unit, developed by Maryland Aerospace, Inc. (Crofton, MD), which was selected for MicroMAS attitude determination and control. The MAI-400 incorporates an attitude computer, a 3-axis reaction wheel set, a 3-axis magnetorquer set, and earth-horizon sensors in a single package.<sup>3</sup> To maintain the spacecraft's alignment with the LVLH frame, MicroMAS would need to slew at a rate equal to the angular velocity of

---

<sup>\*</sup> Space Systems Laboratory, Massachusetts Institute of Technology, Cambridge, MA

<sup>\*\*</sup> Lincoln Laboratory, Massachusetts Institute of Technology, Lexington, MA

the spacecraft's orbit. For a simple spinner, the system's angular momentum is simply its moment of inertia about the axis of rotation times its spin rate. Assuming a spin rate of 0.8 Hz and a 500-km orbit, the torque required to slew in this manner exceeds the capabilities of our magnetic torque rods by roughly two orders of magnitude.<sup>1</sup>

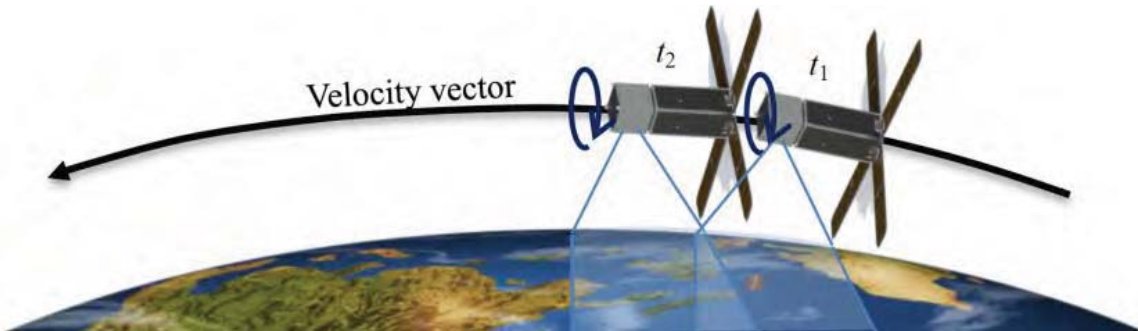


**Figure 1. MicroMAS Orbit and Swath Overlap<sup>2</sup>**

Since MicroMAS does not possess enough torque to precess the entire angular momentum bias of a simple spinner, it must leave its angular momentum oriented in a constant direction, which is illustrated in Figure 2. Because of this arrangement, a simple spinner version of MicroMAS must exchange the momentum of the spacecraft between internal storage devices (such as reaction wheels) to maintain proper orientation of the radiometer payload as the spacecraft traverses its orbit. At point (c), the momentum storage device would have to account for twice the angular momentum produced by the rotating system. For a simple spinner rotating at 0.8 Hz, this angular momentum would be an order of magnitude greater than the momentum storage capability provided to MicroMAS by the reaction wheels in the MAI-400.<sup>3</sup> Additionally, at points (b) and (d) in the orbit, the momentum storage devices must trade between themselves the entirety of the spacecraft's momentum four times during the course of a single rotation of the spacecraft, which would require a torque nearly five orders of magnitude greater than the maximum torque available to the MAI-400's reaction wheels.<sup>3</sup> No miniature reaction wheel set could realistically transfer momentum fast enough between its wheels to keep a simple spinner aligned with the LVLH frame.<sup>1</sup>

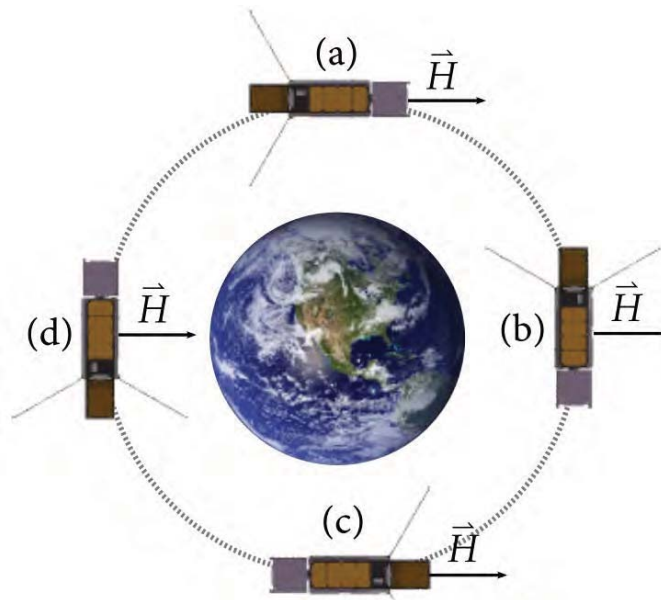


**Figure 2. MicroMAS Maintaining LVLH Alignment with Constant Momentum<sup>1</sup>**

For these reasons, MicroMAS was designed as a zero-momentum, dual-spinning spacecraft, in which a purpose-designed “scanner assembly” mechanism would provide the actuating mechanical and electrical interface between the spinning payload module and the spacecraft bus fixed in the LVLH frame. Figure 3 provides a system overview of MicroMAS in its dual-spinning configuration.

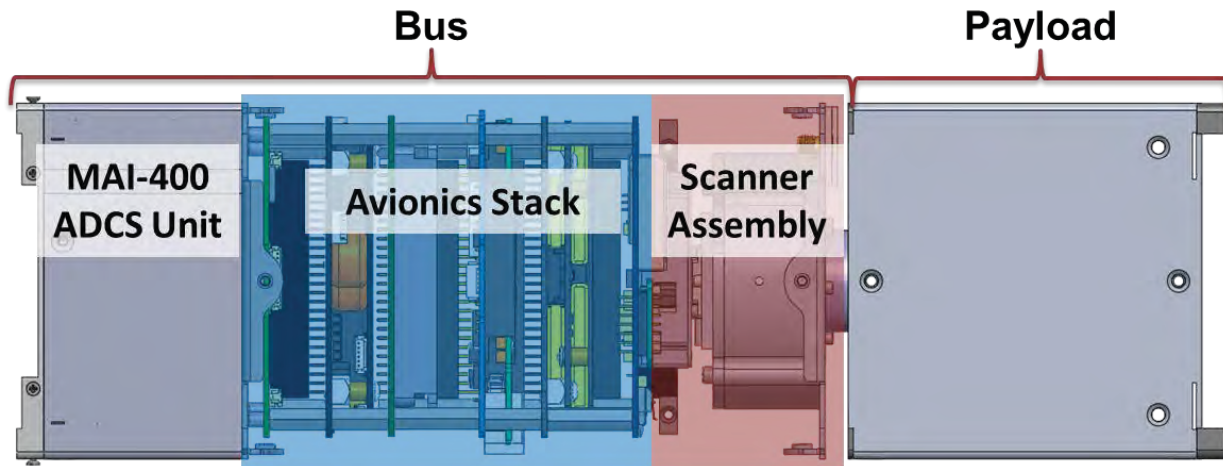


**Figure 3. MicroMAS System Overview**

It was determined early in the design phase that to ensure mission success, the scanning mechanism would need to possess a specific set of capabilities (presented in Table 1). This list of capabilities was then formalized into specific design requirements, against which the performance of the finalized mechanism could be validated.

**Table 1. Scanner Assembly Design Requirements**

Requirement	Justification/Rationale
Must fit within a 10 cm by 10 cm by 3.5 cm volume	This ensures that the mechanism fits within the CubeSat cross-section and that all components will fit within the length available in a 2U bus structure
Must be able to continuously operate in a space environment for a nominal mission lifetime of one year.	This is the only system onboard that requires continuous mechanical (rather than electrical) operation
The scanning assembly shall exert a maximum torque less than or equal to 7 mN-m	Maximum torque available at the reaction wheels at 0 rpm is 7.4 mN-m
Must be capable of rotating a 1U, 1-kg payload at a nominal rate of 1 Hz (60 rpm)	Requirement for data collection at target altitude
Must have angular position knowledge to a precision higher than 0.1 deg (6 arcmin)	Minimize error for geolocation accuracy
Must have at least 8 electrical feed-lines	Minimum number of lines required for power/data transfer between bus and payload



## Scanner Assembly Design

The design of the MicroMAS scanner assembly (shown in Figure 4) incorporates both COTS and custom-designed hardware in order to satisfy the aforementioned design requirements. Commercial parts include a brushless DC motor (rotor/stator only); an incremental rotary encoder; a thin-section radial ball bearing; and a miniature slip ring capsule. Custom parts were then designed to incorporate the COTS components into a single assembly and provide the necessary mechanical interfaces between the bus and payload structures. The entire assembly fits within the 10 cm x 10 cm x 3.5 cm (3.937 in x 3.937 in x 1.378 in) volume constraints imposed by the design requirements.

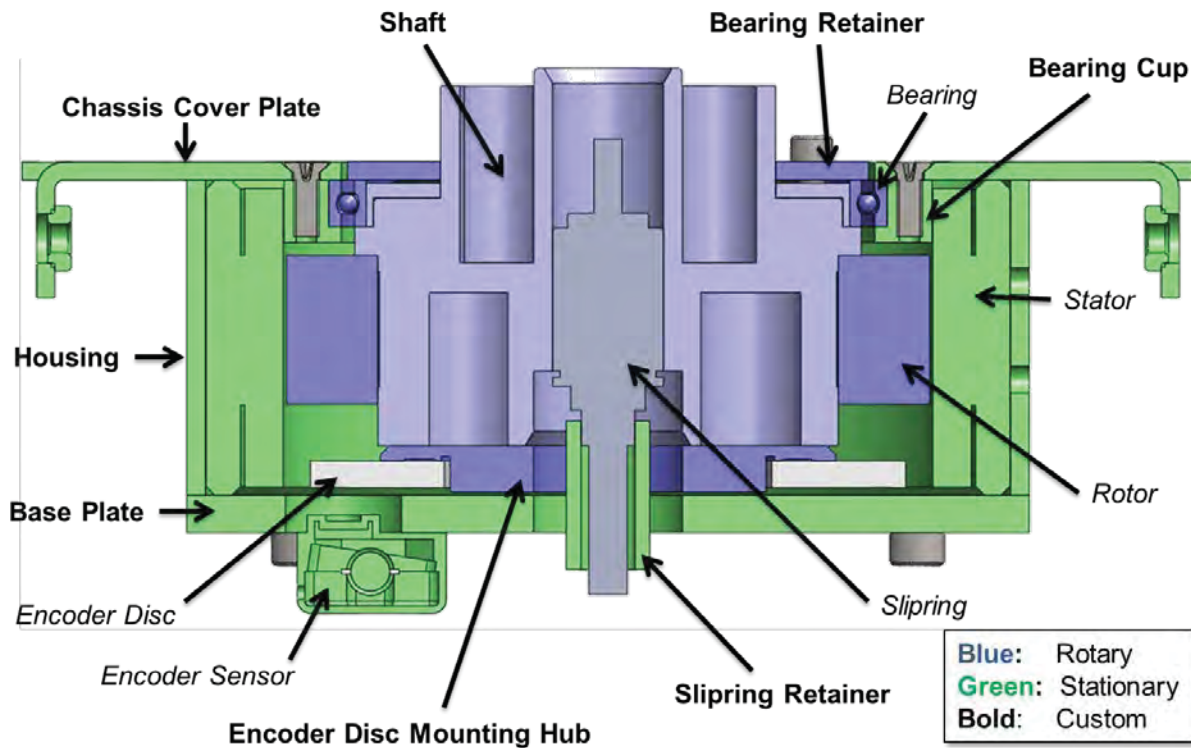


Figure 4. Cross-section view of Scanner Assembly

### COTS Component Selection

The need for low-speed vacuum operation led to the selection of a zero-cogging brushless DC motor as the basis of operation for the scanner assembly. A brushless motor was selected over conventional brushed motors because of the electrical arcing that can occur between the brushes during vacuum operation. Furthermore, the low iron content of the zero-cogging rotor allows for smooth rotation at the relatively low speed of 60 rpm. The selected component was an Aeroflex<sup>\*</sup> Z-0250-050-3-104 rotor and stator combination, due to its continuous torque capabilities, and large internal bore. Its continuous torque capability of 254 mN-m (36 in-oz) was well above the 7 mN-m operating requirement, leaving the system with a large performance margin for future applications. The dimensions, while not the most compact of all the options surveyed, fit within the design space, though the 2.7-cm (1.060-in) height of the stator necessitated that several components be mounted internal to the assembly.

To provide angular position knowledge, the MicroE<sup>\*\*</sup> M1500V optical rotary encoder system was chosen, for its vacuum operation capability and its available array of optical gratings of various diameters and resolutions.<sup>5</sup> The selected grating has an outer diameter of 5.04 cm (2.0 in), which allows it to be placed

<sup>\*</sup> Aeroflex Incorporated, Plainview, NY

<sup>\*\*</sup> MicroE Systems, GSI Group, Bedford, MA

inside of the stator, minimizing the impact on the overall assembly height. Additionally, the chosen grating has a resolution of 7,200 counts per revolution, which on its own leads to an angular position knowledge of 0.05 deg (3 arcmin). Coupled with the 4x interpolation of the encoder head, the system has a total of 28,800 counts per revolution, providing angular position knowledge down to 0.0125 deg (0.75 arcmin).

The Aeroflex<sup>\*</sup> CAY-1398 miniature slip ring capsule was selected to provide the electrical interfaces between the bus and payload.<sup>6</sup> With a diameter of 0.95 cm (0.375 in) and an overall length of around 2.5 cm (1 in), the compact size of this unit allowed it to be mounted within the shaft of this motor assembly. Additionally, its twelve electrical lines exceeded the minimum of eight set by the design requirements.

The final COTS component is the bearing. Given the assembly volume constraint and the height already occupied by the stator, cover plate and encoder head, it was determined that only a single bearing could be accommodated in the assembly. This led to the selection of an NHBB<sup>\*</sup> deep groove, thin-section radial ball bearing,<sup>7</sup> as it did not need to be mounted in a duplex configuration like angular contact bearings.

Simulations of the spacecraft attitude control system were used to determine the maximum static imbalance of the rotating payload that the system could tolerate before control authority no longer met mission-required levels. From this, the team was able to determine that the CG of the payload had to be within 1.3 mm (0.051 in) of the axis of rotation.<sup>1</sup> The selected bearing is manufactured to Class 5 tolerances as specified by the Annular Bearing Engineering Committee (ABEC 5), which allows for a maximum radial runout of 0.005 mm (0.0002 in), well below the static imbalance requirement.<sup>8</sup> To prevent a loss of contact between the inner race of the bearing and the shaft that would be caused by differential thermal expansion between the steel and aluminum, a stainless steel ring was added to the shaft to serve as the bearing mounting surface. Its diameter was sized to provide a light interference fit of 0.0025 mm (0.0001 in), as recommended by the manufacturer. Furthermore, the height of the mounting ring was sized 0.13 mm (0.005 in) shorter than the bearing height, allowing the inner race of the bearing to be compressed by tightening the ring used to axially retain the bearing on the shaft. The deformations to the inner race caused by the interference fit and the compression serve to preload the bearing and mitigate some of the inherent radial play.

## Design Units

The development cycle of the scanner assembly leveraged the use of an iterative design process, using stages of prototypes and engineering models such that any lessons learned and design changes in the current iteration could be integrated into the following iteration. Each prototype served as a risk reduction measure, proving different aspects of the design (and therefore increasing TRL) with each iteration.

### 3-D Print Unit

Once the basic design of the scanner assembly was established, a 3D printer was used to fabricate mockups of each component (shown in Figure 5). This was done early in the design process in order to identify any issues that may have been overlooked during the initial design. The component mockups were used to visualize the physical envelope of each part in the assembly, check the fit between components (especially those that were custom designed to interface with and between COTS components), visualize the volume of the overall assembly, and most importantly, verify that the unit could be assembled.

---

<sup>\*</sup> New Hampshire Ball Bearings, Inc., Chatsworth, CA

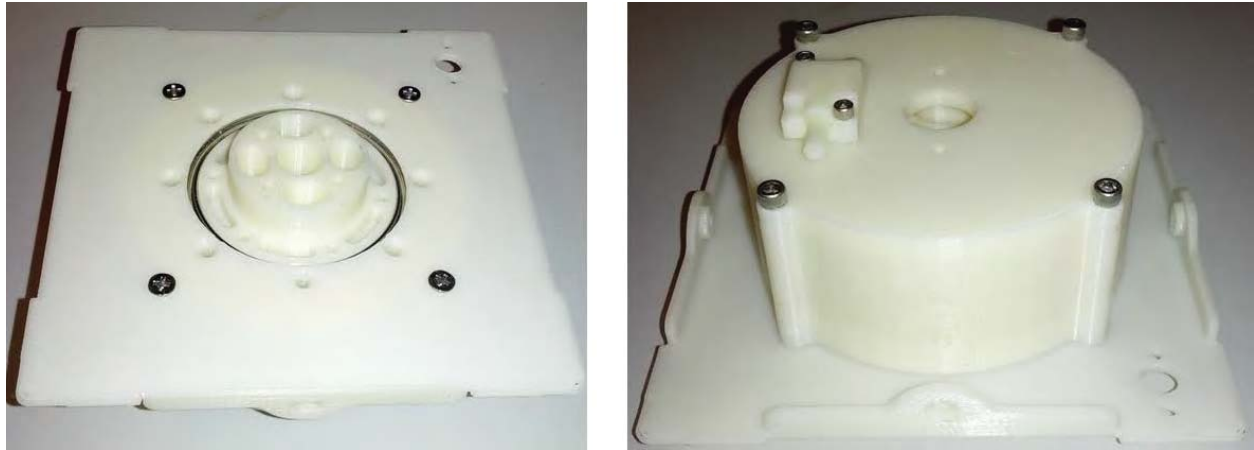


**Figure 5. 3-D Printed Scanner Assembly Mockup**

Engineering Design Unit

The next unit fabricated was an Engineering Design Unit (EDU). The purpose of this assembly was to verify mass properties of the custom components, assess whether any part posed manufacturing issues, and provide an initial functional unit for early testing and driver development. Due to component lead time, mass mockups for the rotor and stator were used, and functionality was provided through the use of a surrogate motor mounted externally to the assembly, as shown in Figure 6. At this point in the design process, a mass mockup of the satellite – with the Engineering Design Unit scanner assembly joining bus and payload mockups – was subjected to random vibration testing at “qualification” level, as prescribed by GSFC-STD-7000.<sup>9</sup> Post-test inspection of the hardware showed that the glass grating disk did not shatter or separate in any way from the hub to which it was mounted, quelling two concerns that the team had about using a glass grating. Additionally, the shaft still spun freely after the test, showing that the bearing could survive the combined loading imposed by random vibrations and from stowage in a CubeSat deployment device.\*

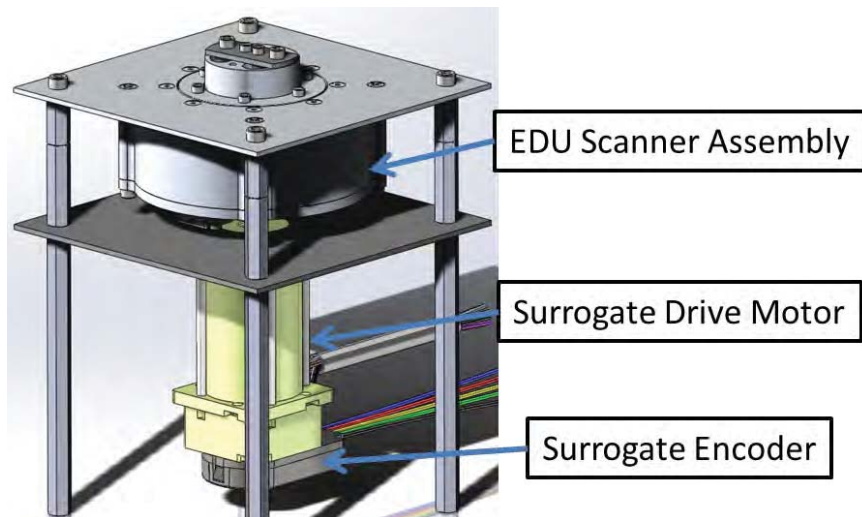


**Figure 6. Engineering Design Unit with surrogate drive motor**

\* MicroMAS will be deployed by a NanoRacks CubeSat Deployer (NRCSD), which can be seen at <http://nanoracks.com/nanoracks-completes-flight-integration-cubesats-bound-orb1-iss/>.

### Engineering Test Unit

After incorporating these design changes, an Engineering Test Unit (ETU) was built utilizing flight-spare COTS components (shown in Figure 7). This unit was used for full functional testing and validation, and also served as a baseline estimate for cost and schedule of the flight-model scanner assembly.



**Figure 7. Engineering Test Unit scanner assembly**

### **Structural Validation**

Considering the lack of flight heritage of a dual-spinning CubeSat, and the criticality of the scanner assembly to the MicroMAS mission, a broad series of tests were conducted to qualify the mechanism for successful performance in relevant environments. Structural tests and analyses were conducted to identify the most effective method for securing the rotor to the motor shaft, due to concern for loss of contact during thermal expansion/contraction. Three mating methods were evaluated – epoxy, tolerance rings, and mechanical press-fit. Though tolerance rings seemed most directly applicable for the task, a lack of knowledge regarding their space heritage (and a lack of experience using them) resulted in the choice for epoxy securing the rotor and shaft in the flight-model assembly.

### Rotor/Shaft Interface Test Units

Occurring in parallel with fabrication of the engineering test unit scanner assembly, a series of tests were conducted to determine which method would be used to secure the rotor to the shaft in the flight unit. This trade was motivated by the concern that differential thermal expansion between the stainless steel rotor and the aluminum shaft would cause a loss of contact between the two parts at the low temperatures.

Calculations were performed to determine the change in rotor and shaft diameters at the expected (cold) operational temperature, along with three temperatures below that operational point. The three classifications of interference fits are presented in Table 2.

**Table 2. Diameter ranges for interference fits<sup>10</sup>**

<b>Fit Classification</b>	<b>Symbol</b>	<b>Minimum Size Above Basic Shaft Diameter (mm) [in]</b>	<b>Maximum Size Above Basic Shaft Diameter (mm) [in]</b>
Locational Interference Fit	H7/p6	0.026 [0.0010]	0.042 [0.0016]
Medium Drive Fit	H7/s6	0.043 [0.0017]	0.059 [0.0023]
Force Fit	H7/u6	0.060 [0.0024]	0.076 [0.0030]

For the calculations that follow, a worst-case scenario was assumed where the rotor inner diameter was the largest value allowed by the H7 fit class. Table 3 summarizes the material interference between the shaft and the rotor diameters for various temperatures.

**Table 3. Change in interference fit between shaft/rotor under various temperature differentials**

Temperature (°C)	$\Delta T$ (°C)	Interference (mm) [in]	Fit Classification
25	0	0.051 [0.0020]	Medium Drive
0	-25	0.038 [0.0015]	Locational Interference
-10	-35	0.033 [0.0013]	Locational Interference
-15	-40	0.030 [0.0012]	Locational Interference
-25	-50	0.025 [0.00099]	Locational Transition

The results of the above calculations showed that although the press fit mating method would be acceptable for the expected operating temperature range, it did not leave much margin for survival if the system got colder than expected. This led to a study of different mating methods and a series of tests to characterize the performance of the options under consideration.

The two additional mating methods considered were epoxy and tolerance rings. The selected epoxy was Lord 3135, due to extensive institutional knowledge of the product and known flight heritage on the Chandra X-ray Observatory and the Suzaku satellite.<sup>11</sup> A tolerance ring, shown in Figure 8, is a corrugated metal strip specifically designed for mating concentric, cylindrical parts. Sample units were provided by USA Tolerance Rings.\*



**Figure 8. Tolerance ring<sup>12</sup>**

The tolerance ring is installed between the shaft and the bore, providing a radial spring force that maintains alignment of the two parts. The rings are available in a wide variety of stock styles and sizes, making them ideal for nearly any combination of loading and geometry. However, the lack of internal experience with this product, coupled with no known flight heritage added two critical risks to this option. Table 4 summarizes the advantages and disadvantages of three methods that were considered.

The press fit method was used in the engineering test unit, and was thus tested through the functional tests the ETU scanner assembly was subjected to. The other two options, epoxy and the tolerance ring, were tested separately. The purpose of this series of tests was to assess the strength of the rotor-shaft interface provided by both methods. This was accomplished by creating two sets of surrogate shafts and rings, with dimensions identical to the flight components. The shaft was made from 6061-T6 aluminum alloy – the same material that the flight shaft would be made from – with a 9.9-mm wide by 0.127-mm deep (0.390 in by 0.005 in) circumferential groove cut into it, as depicted in Figure 9. The initial dimensions for the groove were established by combining required dimensions of both the tolerance ring and the epoxy – the tolerance ring size set the groove width while the recommended epoxy bond line

\* USA Tolerance Rings, Inc., Pennington, NJ



thickness set the groove depth. When testing began, it was found that a deeper groove was needed to fit the tolerance ring. The surrogate ring was made from A513 mild steel with a height of 12.7 mm (0.500 in) and a wall thickness of 1.59 mm (0.0625 in). This material differs from the material of the flight rotor, Custom 455 stainless steel, but its low cost, accessibility, and ease of machining made it the best option.

**Table 4. Rotor-mounting Options**

	Press-Fit	Epoxy	Tolerance Ring
Advantages	<ul style="list-style-type: none"> <li>No additional parts required</li> <li>Simple to design</li> </ul>	<ul style="list-style-type: none"> <li>Flight heritage (ACIS instrument, bond held with <math>\Delta T</math> of <math>-145\text{ }^{\circ}\text{C}</math>)</li> </ul>	<ul style="list-style-type: none"> <li>Robust to thermal expansion/contraction</li> <li>Known torque and radial load capacities</li> </ul>
Disadvantages	<ul style="list-style-type: none"> <li>Loss of fit with thermal variation</li> <li>Requires additional equipment for installation</li> </ul>	<ul style="list-style-type: none"> <li>High CTE</li> <li>Estimated elastic modulus</li> <li>Requires careful application, curing</li> </ul>	<ul style="list-style-type: none"> <li>No prior experience</li> <li>No (known) flight heritage</li> <li>Tests needed to get groove fit right</li> </ul>
Testing Performed	Thermal testing	Torque testing	Torque testing

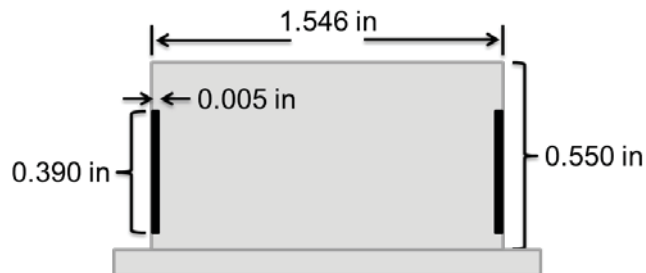


**Figure 9. Dimensions of shaft/rotor test rig**  
*(0.390 in = 10 mm), (0.005 in = 1 mm), (1.546 in = 39.2 mm), (0.550 in = 14 mm)*

During assembly of the test shafts, it quickly became apparent that the chosen groove depth was too shallow to securely hold the tolerance ring. On the first assembly attempt, the tolerance ring was forced out of the groove when even minimal force was applied to the surrogate rotor ring. Attempts to mate the two pieces with excessive force only served to buckle the tolerance ring. A new surrogate shaft was machined for the tolerance ring unit, this time with a groove depth of 0.056 cm (0.022 in); this depth was selected to fully retain the 0.051-cm (0.020-in) base thickness of the tolerance ring along with 25% of the corrugated portion. The circumference of the ring was trimmed to maintain a gap of 0.15 cm (0.060 in) between edges, which fell within range of 0.10 to 0.20 cm (0.040 to 0.080 in) recommended by the product engineers.

A 1/2-13 bolt was secured through a bore through the center of the test shaft. Flat washers were placed on either side of the bolt and the installation was torqued to 13.6 N-m (120 in-lb). The assembly was then placed in a vise and the jaws were tightened around the ring. A torque wrench was then placed on the bolt head and torque was applied to the assembly. The test procedure continued as follows: (1) Test both units to the peak torque provided by the motor during nominal operations (4 in-lb or 0.5 N-m); (2) If successful, continue application of torque until failure occurs; (3) Note the torque at which the assembly failed.

Both test units survived an applied torque of 7.34 N-m (64.9 in-lb). At this point, the aluminum test shafts suffered material failures where the lock washers dug into the aluminum. After this occurred, the tests were halted and the application of higher torques was not attempted. It is important to note that the neither the epoxy nor the tolerance ring were tested to the point of failure. Post-test analysis showed that the applied torque was an order of magnitude less than the rated torque capacity of 76.3 N-m (675 in-lb) for a ring of that size. For the epoxy shaft, a simple analysis (shown in Equations 1 and 2) converted the applied torque to shear stress at the interface between the shaft and the epoxy layer. Results showed that the applied torque caused a shear stress of 303 kPa (44 psi) in the epoxy layer, which is nearly two orders of magnitude lower than the epoxy's rated shear strength of 26 MPa (3800 psi).

$$F = \frac{\tau}{r} = 374 \text{ N (84 lbf)} \quad (1)$$

$$\sigma_{shear} = \frac{F}{A} = \frac{F}{\pi dh} = 303 \text{ kPa (44 psi)} \quad (2)$$

The aforementioned testing indicated that both the epoxy and the tolerance ring were well-suited to handle the torques exerted by the scanner assembly. Due to schedule constraints, it was not possible to conduct additional tests in order to fully characterize both the epoxy and the tolerance ring. Despite the disadvantages mentioned in Table 4, epoxy was selected as the mating mechanism because of institutional knowledge of working with epoxies and its known flight heritage.

For future applications, we would like to reopen the trade and continue characterization of the two methods, particularly the behavior of a tolerance ring assembly subjected to random vibration. The benefits that the tolerance ring provides over epoxy, such as a simplified installation process and ease of disassembly, make the tolerance ring a desirable option. During assembly, the process had to be halted for 24 hours in order to let the epoxy cure. Had a tolerance ring been used to mate the rotor and the shaft, this portion of the assembly process would have only taken minutes. However, installation of the tolerance ring requires the use of an arbor press, which is typically not found in a clean assembly room. Another possible issue is the interaction between a steel arbor press and the high-strength permanent magnets in the rotor; a special assembly jig would likely be needed to protect the rotor from damage during installation.

#### Bearing Lifetime Analysis

The critical component inside the scanner assembly is the bearing, which mechanically supports the motor shaft and facilitates rotation with a low-friction lubricant. Failure of the bearing would cause the motor to seize, and lead to a science mission failure. Design requirements state that the scanner assembly motor must survive for a minimum of 6 months of continuous operation, with 12 months being the objective. Assuming continuous rotation at 60 rpm, the bearing must survive for 15.8 million revolutions to meet the 6-month nominal mission lifetime, and 31.5 million revolutions to meet the 12-months objective mission lifetime. A lifetime analysis of the bearing was performed, using equations provided by the vendor.<sup>13</sup> The equation used to estimate bearing lifetime is presented in Equation 3.

$$L = a_1 a_2 \left( \frac{C}{P_r} \right)^3 \quad (3)$$

$L$  is the number of revolutions (in millions),  $C$  is the dynamic load rating of the bearing,  $P_r$  is the equivalent radial load acting on the bearing,  $a_1$  is an adjustment factor for reliability percentage, and  $a_2$  is an adjustment factor for ball material. The equivalent radial load is defined as the purely radial load that, if applied to the bearing, would result in the same lifetime as a bearing under radial and/or axial loading. Mathematically, it is defined by Equation 4.

$$P_r = XVF_r + YF_a \quad (4)$$

$V$  is a rotation adjustment factor,  $X$  is a radial load factor,  $Y$  is an axial load factor,  $F_r$  is the applied radial load, and  $F_a$  is the applied axial load. The factors  $V$ ,  $X$  and  $Y$  are tabulated for different values of the quantity presented in Equation 5.

$$\frac{F_a}{ZD^2} \quad (5)$$

$F_a$  is again the axial load,  $Z$  is the number of balls in the bearing, and  $D$  is the ball diameter. For the bearing used in the scanner assembly,  $Z = 42$ ,  $D = 1.59$  mm (0.0626 in), and the dynamic load rating,  $C$  is 961 N (216 lbf).

The axial and radial loads were determined by assuming payload rotation in a 1-G environment, as the force of gravity acting on the payload mass is higher than any loads that will be experienced on orbit. Assuming a payload mass of 1 kg (2.2 lbf), the axial load on the bearing is 10 N (2.2 lbf). After performing the calculation for  $F_a/ZD^2$ , it was found that  $V = 1.2$ ,  $X = 0.0056$ , and  $Y = 2.3$ . The equivalent radial load was then calculated to be 23 N (5.17 lbf):

The default lifetime equation gives the expected lifetime that 90% of the bearings in a given application will meet. To determine the expected lifetime that 99% of the bearings in a given application will meet, the  $a_1$  factor must be changed to  $a_1 = 0.21$ . This provides a conservative estimate of the expected bearing lifetime. Finally, a factor of  $a_2 = 0.8$  is used to account for the softer 440C stainless steel material that the balls are made of.

With all of the constants determined, the expected lifetime of the bearing could then be calculated, as presented in Equation 6.

$$L = a_1 a_2 \left( \frac{C}{P_r} \right)^3 = 13068 \text{ [x 1 million]} \quad (6)$$

The expected lifetime of the bearing under operation in a 1-G environment is 13 billion revolutions, which is three orders of magnitude larger than the 12-month operational objective of 31.5 million revolutions.

### Thermal Validation

Thermal-vacuum testing was also used to validate the hardware. A two-day test was conducted on the flight-like Engineering Test Unit in order to characterize the performance of the full scanner assembly over predicted operating temperature ranges, and also verify the workmanship of the individual parts used in the assembly.

Thermal modeling analyses, performed in Thermal Desktop, showed a predicted operating temperature range of -5 to +25 °C for a circular 450-km orbit at 52° inclination. This conflicted with the 0 to +70 °C operational temperature range of the MicroE 1500V encoder sensor as specified by the manufacturer. Therefore, a major goal of this thermal-vacuum test was to qualify the encoder for colder temperatures in order to gain margin from the manufacturer's specifications. A procedure for the cold operating temperature qualification is shown in Figure 10.

Scenario	Chamber State		Test Procedure
TS Test Setup	Room Pressure & Temperature		<ul style="list-style-type: none"> <li>• Prep chamber, test rigs, articles, + sensors</li> <li>• Check function + calibrate test articles + sensors</li> <li>• Collect benchmark data</li> </ul>
T-0 Functional Checks	Ambient Vacuum (25 °C)		<ul style="list-style-type: none"> <li>• Pump-down chamber to ~1e-05 torr</li> <li>• Functional checks on test articles + sensors</li> <li>• Command motor to 60 rpm</li> <li>• Collect data until thermally stable</li> </ul>
T-1 Cold Test	Cold Vacuum (< 0 °C)		<ul style="list-style-type: none"> <li>• Continue running motor at 60 rpm</li> <li>• Continue collecting data</li> <li>• Supply LN2 to bring encoder temperature to 0°C</li> <li>• Monitor encoder, slowly lower T to -10 °C</li> </ul>
T-2 Thermal Cycling	Cold Vacuum (0 °C)	Hot Vacuum (70 °C)	<ul style="list-style-type: none"> <li>• Command motor to 60 rpm, collect data</li> <li>• Complete 1+ full thermal cycles by switching between LN2 cooling and resistor heating</li> </ul>

Figure 10. Thermal-vacuum testing procedure

The encoder performance was evaluated as a function of temperature by routing the encoder sensor's analog output to an oscilloscope outside of the thermal-vacuum chamber, and monitoring changes in signal strength (measured as voltage amplitude). As specified by the manufacturer, the signal strength is deemed nominal around 800 mV, and considered acceptable above 400 mV.

During the test, the encoder was operational through a temperature range of -8.5 to +61.5 °C, adding margin beyond the predicted operating temperature range. Though the encoder was subjected to temperatures colder than its specified operating range, the signal strength stayed within the acceptable range (shown in Figure 11). This provided the team with confidence in the encoder's performance at colder-than-specified temperatures for short periods of time (< 3 hours, or 2 orbits).

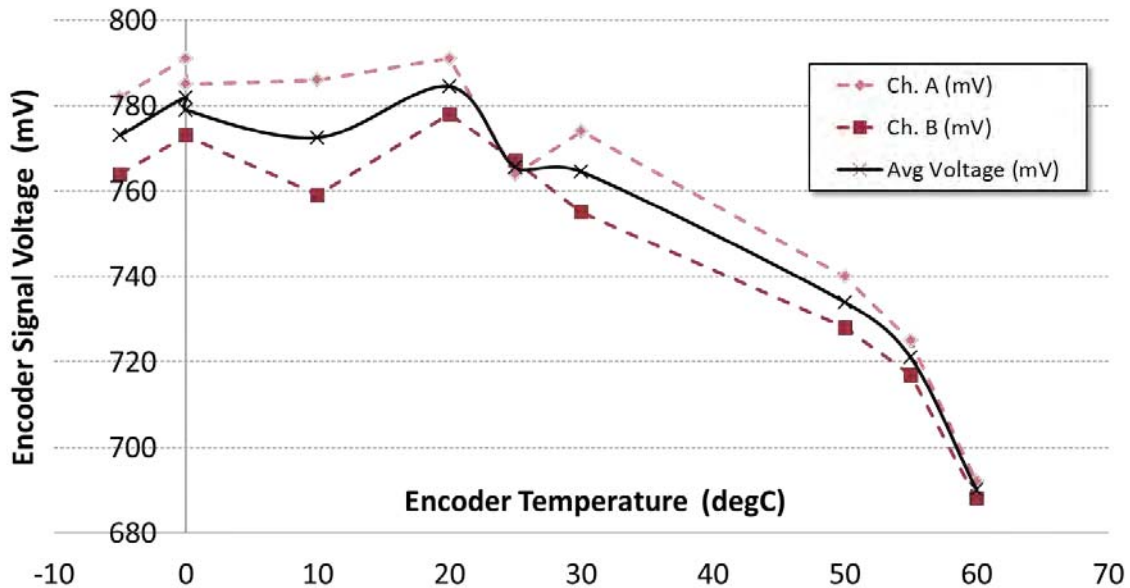
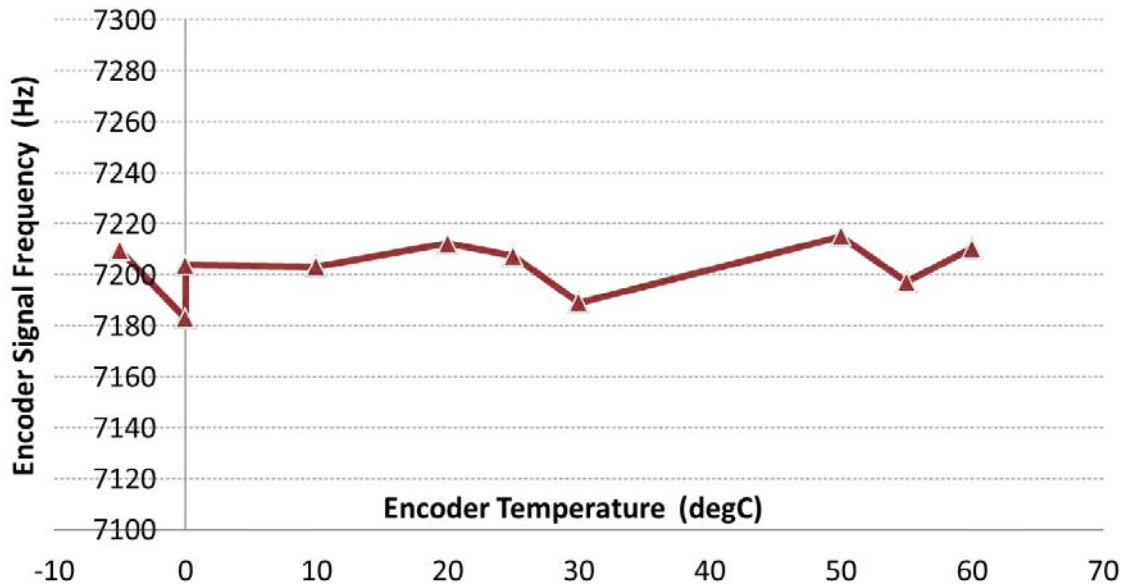


Figure 11. Encoder signal strength over expected operating temperature range

The overall scanner assembly performance was evaluated as a function of temperature by monitoring the frequency of the encoder sensor's analog output. The scanner assembly was set to spin at 60 rpm, or 7200 counts/sec (based on the 7200 gratings on the encoder disk). As set in our design requirements, this frequency should be maintained within 5% of nominal, or 360 counts/sec at 60 rpm. If one of the parts were to fail, expand, contract, or degrade as a function of temperature, this could be seen in the frequency of the encoder signal.

Over the tested temperature range of -8.5 to +61.5 °C, the encoder frequency stayed well within the 5% requirement even when tested beyond the predicted operating temperature range (shown in Figure 12), and did not show any trend as a function of temperature. This provided the team with confidence in the scanner assembly's design and performance for operation in the predicted space environment.



**Figure 12. Scanner assembly performance over expected operating temperature range**

Workmanship, however, was deemed to be an issue after the epoxy bond between the glass encoder disk and titanium mounting hub failed during bench testing several weeks after the thermal-vacuum test. Post-failure inspection determined that the epoxy did not successfully bond to the smooth glass surface of the encoder disk. As a result, greater care was taken in the surface preparation and epoxy application processes of mounting the encoder disk to the titanium hub, with the help of product engineers at MicroE Systems. The new unit was thermal-cycled and successfully tested for bond strength up to 111 N (25 lbf) prior to re-integration into the flight-model scanner assembly.

### **Conclusions**

The MicroMAS scanner assembly is a novel new mechanism designed to provide satellites utilizing the CubeSat form factor with dual-spin functionality. The utilization of multiple COTS components allowed for successful development of a flight assembly that satisfies all of its subsystem requirements under a condensed timeline. The scanner assembly is capable of producing a continuous torque of 250 mN-m while providing sub-arcminute angular position knowledge, and allows for the transmission of 12 electrical signals between the stationary and rotating hardware. Testing has shown that the scanner assembly can functionally operate in a vacuum environment and withstand temperatures in the range of -10 to +70 °C.

The scanner assembly mechanism expands the possible science missions that can be accomplished with the low-cost CubeSat platform. After successfully passing verification of the design and performance requirements and undergoing final integration and testing within the full space vehicle, the scanner



assembly has reached TRL 8. As of this writing, MicroMAS awaits launch, scheduled for May 2014. The MicroMAS team looks forward to a successful launch, deployment, and on-orbit operation.

### Acknowledgments

The authors would like to thank the following individuals for all of their help throughout the design process: Neal Erickson from UMass-Amherst Department of Astronomy; Steve Fujikawa, Tzer Leei Ng, and Kirk Volland from Maryland Aerospace, Inc.; Karl Anderson from Aeroflex Incorporated; Pat Liessner, Paul Costello, and Dave Smith from MicroE Systems; and George Spais from USA Tolerance Rings.

This work is sponsored by the Assistant Secretary of Defense for Research & Engineering under Air Force Contact FA8721-05-C-0002. Opinions, interpretations, conclusions, and recommendations are those of the authors and are not necessarily endorsed by the United States Government.

### References

1. Wise, Evan D. "Design, Analysis, and Testing of a Precision Guidance, Navigation, and Control System for a Dual-Spinning CubeSat." Thesis, Massachusetts Institute of Technology, 2013. Found online at <<http://dspace.mit.edu/handle/1721.1/82509>>.
2. Wise, Evan D., et al. "A Dual-Spinning, Three-Axis-Stabilized CubeSat for Earth Observations." AIAA GNC Conference. American Institute of Aeronautics and Astronautics, 2013.
3. "The 1/2U MAI-400: A La Carte." Maryland Aerospace Inc. April 2012. Found online at <[http://www.miniadacs.com/miniadacs\\_012.htm](http://www.miniadacs.com/miniadacs_012.htm)>.
4. "Zero Cogging Motors." *Aeroflex Motion Control Products: DC Motors*. Aeroflex Incorporated. Found online at <<http://www.aeroflex.com/ams/motion/motion-motors.cfm>>.
5. "Mercury 1500V Vacuum Rated Digital Output Encoders." MicroE Systems. Found online at <<http://www.microesys.com/specifications/vacuum-encoders/mercury-1500V>>.
6. "Airflyte: CAY-1398, CAY-1544." *Slip Ring Assemblies*. Aeroflex Incorporated. Found online at <<http://www.aeroflex.com/ams/motion/motion-sliprings.cfm>>.
7. "Thin Section - Radial and Gothic Arch." *Ball Bearings*. New Hampshire Ball Bearings, Inc. Found online at <[http://nhbb.com/files/catalog\\_pages/HiTech-29-30.pdf](http://nhbb.com/files/catalog_pages/HiTech-29-30.pdf)>.
8. "Tolerances." *Reference Center*. New Hampshire Ball Bearings, Inc. Web. Accessed 12 Dec. 2012. <<http://nhbb.com/reference/ball-roller-bearings/tolerances.aspx>>
9. "General Environmental Verification Standard (GEVS) For GSFC Flight Programs and Projects." NASA. GSFC-STD-7000. April 2005.
10. Budynas, R. G., Nisbett, J. K., & Shigley, J. E. "Shigley's mechanical engineering design." 2011. New York: McGraw-Hill.
11. Bralower, Harrison. "Mechanical Design, Calibration, and Environmental Protection of the REXIS DAM." Thesis, Massachusetts Institute of Technology, 2013.
12. "How Tolerance Rings Work." USA Tolerance Rings, Inc. Web. Accessed 12 Dec. 2012. <<http://www.usatolerancerings.com/index.php?page=how-tolerance-rings-work>>.
13. "Load Ratings and Bearing Life." *Reference Center*. New Hampshire Ball Bearings, Inc. Web. Accessed 12 Dec. 2012. <<http://www.nhbb.com/reference/ball-roller-bearings/load-ratings-bearing-life.aspx>>.



